Volume 237, Nos. 14–17, 15 August 2008

ISSN 0167-2789

ELSEVIER

PHYSICA D
NONLINEAR PHENOMENA

Euler Equations: 250 Years On

Proceedings of an international conference

18–23 June 2007
Aussois, France

Guest Editors:

Gregory Eyink
Uriel Frisch
René Moreau
Andreĭ Sobolevskiĭ

Available online at
ScienceDirect
www.sciencedirect.com

http://www.elsevier.com/locate/physd

Available online at www.sciencedirect.com
ScienceDirect
ELSEVIER
Physica D 237 (2008) v–viii
PHYSICA D
www.elsevier.com/locate/physd

Contents

Available online at www.sciencedirect.com

ScienceDirect

Physica D 237 (2008) ix

PHYSICA D

www.elsevier.com/locate/physd

International Conference

EULER EQUATIONS: 250 YEARS ON

Aussois, France, June 18–23, 2007

An initiative
of CNRS (France)

Under the patronage
of the French Academy of Sciences,

the Berlin-Brandenburg
Academy of Sciences,

and the Swiss Academy of Sciences'
Committee of the Euler Tercentenary

Co-sponsored by the International Union
of Theoretical and Applied Mechanics

Organized by the Observatory of Côte d'Azur, the Cassiopée Laboratory,
and the Wolfgang Döblin Institute (Nice, France)
with participation of the J.-V. Poncelet Laboratory (Moscow, Russia)

Supported by the National Science Foundation (US),
the Grenoble Institute of Technology, the Joseph Fourier University,
and the Rhône-Alpes region (France)

0167-2789/$ - see front matter
doi:10.1016/j.physd.2008.05.007

Available online at www.sciencedirect.com
ScienceDirect
Physica D 237 (2008) xi–xv
PHYSICA D
www.elsevier.com/locate/physd

General introduction

To the dear memory of Akiva Yaglom (06 March 1921–13 December 2007) and Robert Kraichnan (15 January 1928–26 February 2008)

The international conference *Euler Equations: 250 Years On* (EE250) was held in Aussois, France, June 18–23, 2007, on an initiative of the Centre National de la Recherche Scientifique, under the patronage of the French Academy of Sciences, the Berlin–Brandenburg Academy of Sciences, and the Swiss Academy of Science's Committee of the Leonhard Euler Tercentenary, and the co-sponsorship of the International Union of Theoretical and Applied Mechanics.

The Conference was organized by the Laboratoire Cassiopée of the Observatoire de la Côte d'Azur and the Wolfgang Döblin Institute, Nice, with participation of the Jean-Victor Poncelet Laboratory, Moscow.

Support of the Institut National Polytechnique and the Université Joseph Fourier, Grenoble, of the Région Rhône–Alpes, and of the US National Science Foundation is gratefully acknowledged.

We are very grateful to our colleagues of the EE250 Scientific Committee, listed at the Conference web site http://www.oca.eu/etc7/EE250/, who helped with the organization of the Conference and sometimes also with these Proceedings.

We are also very grateful to the archivists of the French Academy of Sciences and of the Berlin-Brandenburg Academy, Florence Greffe and Wolfgang Knobloch, who have provided us with important documents and manuscripts from Euler's time.

Many persons have helped us in organizing this conference; we are most grateful to Sébastien Bott, Hélène Frisch, Rafaela Hillerbrand, Takeshi Matsumoto, Walter Pauls and Rose Pinto. Fathi Namouni is thanked for having named the Conference. The improvement of the scientific content of the Proceedings owes much to Olivier Darrigol and Gleb K. Mikhailov and to numerous anonymous referees. Many thanks are due also to the scientific and production staff of the journal *Physica D* and especially to Joceline Lega, Eline van Mourik and Gary Anderton.

The EE250 conference, held on the occasion of the 250th anniversary of the publication of Euler's founding paper of hydrodynamics 'Principes généraux du mouvement des fluides', brought together about 95 invited senior researchers and 45 selected young scientists from all over the world, representing various scientific communities. In loyalty to Euler's legacy, which embraces theory as well as applications, the Conference covered a broad range of disciplines and approaches. It provided a snapshot of the state-of-the-art in a research field started in the eighteenth century and still thriving.

One of the outcomes of the EE250 conference is this collection of papers, part of which are surveys written by established experts whereas the rest cover active research conducted by other participants of the Conference and in particular by the younger generation. The Conference itself had a number of presentations that have not led to papers in the Proceedings and for which we refer the reader to the EE250 web pages http://www.oca.eu/etc7/EE250/ that contain the detailed program and slides of most presentations. We have not tried to summarize the numerous discussion panels which were a highlight of the Conference.

The articles are organized in seven sections corresponding to different kinds of scientific outlooks on the Euler equations and hydrodynamics.[1] To remain faithful to Euler's vision of science, we have avoided separating the more fundamental papers from those devoted to applied science and engineering.

What follows is an overview of the organization and contents of the Proceedings.

The volume starts with two of **Euler's founding papers on hydrodynamics**, 'Principes généraux du mouvement des fluides' (written in 1755 and published in 1757) and 'Principia motus fluidorum' (written in 1752 and published in 1761). Both are here rendered in modern English. The former was written in amazingly modern French, so that we decided on a faithful translation (p. 1825); the latter uses not only Latin but a rather heavy style which may have been easily understood 250 years ago but whose literal translation would put some hardship on the modern fluid dynamicist; hence we opted for a somewhat modernized adaptation (p. 1840).

As is well known, Euler was an extremely prolific author. All his publications are reproduced in the *Opera omnia*, undertaken

[1] At the beginning of each section the reader will find the papers having a review character, followed by the other papers in alphabetic order.

0167-2789/$ - see front matter
doi:10.1016/j.physd.2008.05.006

one century ago, in 1907, and published first by Teubner (Leipzig/Berlin), then by Orell Füssli (Zürich) and now by Birkhäuser (Basel). Scanned copies of most original papers are available from the EULER ARCHIVE, at Dartmouth College (http://www.math.dartmouth.edu/~euler). A guide to the Euler bibliography, *Euleriana*, written by Gleb K. Mikhailov, is found just after this General Introduction.

Next we have the modern scientific papers, beginning with the **historical perspective** section. The paper of Darrigol & Frisch (p. 1855)[2] shows how modern fluid dynamics was born in the eighteenth century through the work of many important figures, not only Euler, but also the Bernoullis and d'Alembert. A case study by Grimberg, Pauls & Frisch (p. 1878), based on the d'Alembert paradox, gives evidence that quite a lot was already understood before the availability of the modern formulation in terms of partial differential equations. Euler spent a quarter of a century living through peace and war in the Berlin of Frederick the Great (Friedrich II), King of Prussia, with whom he had increasingly strained relations. These years come to life in the contributions of Eckert (p. 1870), and Knobloch (p. 1887) who also demonstrate that Euler was frequently involved in very practical matters, including engineering problems. For lack of material we are unable to pay similar attention to the societal context of Euler's two Russian periods, but this is somewhat alleviated by the *Euleriana* of Mikhailov. Another historical contribution, regarding advanced rocketry in the eighteenth century in India, was presented by Narasimha.

Next come the many papers of the section devoted to **singularities** and related questions, one of the most central issues discussed at EE250 and among the most conspicuous themes of this volume. The survey paper of Gibbon (p. 1894) sets up the scene for the issue of occurrence or non-occurrence, for incompressible three-dimensional Euler flow, of *spontaneous singularities* appearing after a finite time (blow up). More than 250 years after the Euler equations had been written, it is still unknown if they always possess solutions that stay smooth indefinitely when the initial data are smooth; the available proofs of existence either are local in time or establish global existence of weak solutions whose smoothness is not guaranteed. In this section we also have the paper of Constantin (p. 1926), who investigates the local geometry of the Euler flow with an eye on the singularity problem, the paper of Childress (p. 1921), who investigates conditions for explosive vorticity growth, and various papers devoted to the numerical investigation of singularities: Bustamante & Kerr (p. 1912), Grafke et al. (p. 1932), Hou & Li (p. 1937), and Matsumoto, Bec & Frisch (p. 1951). We note that for analytic initial data there is now strong numerical evidence – and even a proof in special cases as shown by Li & Sinai (p. 1945) – of the existence of singularities in the complex space domain in both Eulerian and Lagrangian coordinates. However for real singularities and finite-time blow up, the current numerical results are still pointing in different directions. There is also a well-known class of non-smooth Euler flows, the vortex sheets, for which the equivalent of the blow up issue is whether or not the shape of the sheet, governed by the Birkhoff–Rott equation, remains regular when sufficient regularity is assumed initially. The analyticity of solutions of the Birkhoff–Rott equation was discussed by Wu.[3] The structure of such solutions implies very pathological behavior of the interface, but Bardos, Linshitz & Titi (p. 1905) show there exists a non-dissipative α-regularization which ensures indefinite smoothness.

Actually, the topic of Euler blow up is intimately connected with the problem of singularities in the Navier–Stokes equations, which is one of the famous Millennium Prize problems of the Clay Mathematics Institute. During the EE250 conference an informal poll among the participants on the problem of finite-time singularities was conducted by C. Bardos and E.S. Titi. The question was: how confident are you, on a 0–10 scale, that solutions to the Euler (Navier–Stokes) equations can develop finite-time singularities? The results are given in the following table.

Response	0	1	2	3	4	5	6	7	8	9	10	*Tot.*
# of votes (Euler)	**8**	2	2	4	2	**9**	0	3	3	3	**7**	43
# of votes (N.-S.)	**20**	8	4	0	1	**5**	0	1	0	0	2	41

Highest peaks are marked in bold.

Next comes the section on **weak solutions, high Reynolds numbers and statistical mechanics**, in which turbulent or random solutions of the hydrodynamical equations are considered. A particularly important topic concerns weak dissipative solutions of the Euler equation; in spite of its "singular" nature it is not necessarily related to blow up and fits more naturally here because of strong connections with the fact that turbulence remains dissipative even at infinite Reynolds numbers. Actually the weak solution approach takes globally non-smooth, everywhere densely singular, Hölder continuous solutions to the Euler equation for models of the infinitely fine structure of turbulent flow at *infinite Reynolds numbers*. In the present volume the state-of-the-art of this approach, which has its origins in the 1940s work of Andrei Kolmogorov and Lars Onsager pertaining to the classics of turbulence research, is summarized in the survey of Eyink (p. 1956). Such work, which reveals the hidden dissipative nature of the Euler equation, is central to the current rebirth of interest in the Euler equation. From a different point of view the relation between the inviscid limit and totally inviscid behavior is studied numerically by Ohkitani (p. 2020).

The weaker and broader the notion of solution is, the easier it lends itself to mathematically rigorous investigation, but lack of immediate relation to physics leaves this investigation vulnerable to paradoxes. Eyink points out that one of the open problems is how to constrain weak solutions to the

2 Presentations at EE250 or papers in these Proceedings are referenced by the last name(s) of their author(s), followed by the relevant page number where the paper is to be found in these Proceedings.

3 This work and many mathematical aspects of the Euler equations are discussed in a review paper by C. Bardos and E.S. Titi [1].

Euler equations, with appropriate admissibility conditions, so that uniqueness does not fail. Such is the case with the weak solutions obtained by adding to the 2D Euler equation very rapidly fluctuating forces that, smeared by smooth test functions, vanish in a suitable limit while still creating energy [2,3]. If this kind of weak solution is permitted, a fluid at rest may suddenly develop motion and then come to rest again without any apparent forcing or dissipation. The contribution of Bronzi, Lopes Filho & Nussenzveig Lopes (p. 1989) provides a numerical model of this phenomenon which turns out to be connected with forcing acting in a counter-entropic way at infinitesimal scales. Another important notion of weak solution, the Shnirelman–Brenier *generalized flow* [4,5], is still weaker than solutions considered by Eyink. Brenier (p. 1982) reviews paradoxes of the generalized flow but at the same time he shows that it still may have physical significance of a different kind, being similar to stratified geophysical flows in the hydrostatic approximation. Here it is of interest to point out that C. De Lellis and L. Székelyhidi proved, using differential inclusions, the non-uniqueness of the solution in any space dimension for a class of dissipative weak solutions with bounded velocity and pressure [6].

A different kind of connection between ideal Euler dynamics and dissipative dynamics has been discovered recently by Cichowlas et al. [7] who showed that the 3D Euler equations with a Galerkin truncation, chosen such that a finite but very large number of Fourier modes survive, behaves at large and intermediate scales just as the Navier–Stokes equations. Indeed small-scale (high-wavenumber) modes thermalize and provide a suitable eddy viscosity for the larger scales. Krstulovic & Brachet (p. 2015) carry this interesting theme further (see also Ref. [8]).

Another topic is that of the statistical mechanics of 2D ideal turbulence, a subject pioneered by Onsager [9]. Bouchet (p. 1976) investigates several variational formulations of this theory, while Capel & Pasmanter (p. 1993) and Chavanis (p. 1998) use vorticity instead of the Casimir functions to constrain and leverage flows. Another connection between statistical mechanics and 2D turbulence is provided by the recent work on conformal turbulence, which was presented by Falkovich [10]. Gallavotti reviewed dynamical-systems perspectives in fluid turbulence and non-equilibrium statistical mechanics and, in particular, the "chaotic hypothesis" and its predictions for fluid experiments [11].

The most natural way to connect statistical mechanics and hydrodynamics is of course to start from kinetic (molecular) theory. The mathematical foundations of the passage from the Boltzmann equation to the Euler equation are examined by Saint-Raymond (p. 2028). Boltzmann models with discrete velocities, such as discussed by Chen & Shan (p. 2003), can now give very good practical approximations to hydrodynamical equations. A discussion session was devoted to the use of kinetic approaches in computing high Reynolds-number flow.

High-Reynolds number 3D fully developed turbulence is discussed in a number of papers, mostly presented in separate sections on Lagrangian aspects or on the influence of boundaries (see below). Here we find papers discussing the issues of universality and intermittency: Biferale, Lanotte & Toschi (p. 1969) and Ching, Guo & Cheng (p. 2009). A major breakthrough on intermittency was initiated by the so-called Kraichnan model of passive scalar intermittency [12,13]. The subject was reviewed at the Conference in the lecture of Lebedev.

The section on **Lagrangian description and mixing** gathers papers in which one either follows idealized fluid particles – the Lagrangian approach pioneered by Euler near the end of his 'Principes généraux du mouvement des fluides' – or tracks real particles, which tend to lag behind fluid particles because of inertia. There is a strong renewal of interest in Lagrangian approaches: the Lagrangian description connects with the important problems of mixing and dispersion and new experimental developments, involving for example ultra-fast cameras, are about to provide us with a wealth of Lagrangian information (this was reviewed by Mordant). Inertial particles arise in a host of practical problems from PIV flow imaging to spreading of pollutants in water and air. A discussion session was devoted to the various Lagrangian problems.

Theoretical aspects of inertial particles are discussed in the review paper of Bec et al. (p. 2037); experimental aspects are presented by Volk et al. (p. 2084) and Xu & Bodenschatz (p. 2095). Lagrangian aspects of vortex flow are discussed by Branicki (p. 2056) and by Wilczek, Kamps & Friedrich (p. 2090). Boatto & Simó (p. 2051) and Sakajo & Yagasaki (p. 2078) discuss problems with point vortices. We also have mathematical papers in which a Lagrangian approach plays a role by Kambe (p. 2067) and Khesin & Lee (p. 2072). Last, but not least, there has been much discussion at the Conference of the magnetohydrodynamic dynamo problem,[4] for example in the presentation of Cardin, that of Pinton and also in a special discussion session with strong emphasis on the recent breakthrough made on experimental turbulent dynamos and magnetic field reversals (see, e.g. Refs. [14, 15]). Finally there is a paper by Burattini et al. (p. 2062), dealing with magnetohydrodynamics in the infinite-magnetic-diffusivity limit in the presence of a background magnetic field, which results in an increasing anisotropy of the decaying turbulence.

We move now to the section on **geophysical and astrophysical fluid dynamics**. Arguably, studies of the Euler equations are also motivated by the fact that they proved to be of crucial relevance to nature and technology. This was of course something Euler was aware of, as revealed by his studies of naval and fluvial hydrodynamics. Busse's review (p. 2101) considers rotating fluid flow characteristic of stellar and planetary interiors; Fedele (p. 2127) and the first part of Ghil, Chekroun & Simonnet (p. 2111) deal with oceanic flow; the second part of Ghil, Chekroun & Simonnet introduces one of the hottest topics of current science, climate dynamics, in the setting of the Euler equations and the wider context of

[4] The dynamo problem has a loose connection to the Lagrangian structure insofar as, at zero magnetic diffusivity, a transported magnetic field behaves as a pair of infinitesimally close fluid particles.

nonlinear dynamics. A separate note of Hillerbrand & Ghil (p. 2132) raises ethical issues of climate research; if ethics do not belong to the physicist's perspective proper, they ought to be part of the world outlook of any conscious scientist. Gravity currents, within the shallow water approximations, are discussed by Zemach & Ungarish (p. 2162).

A few decades after Euler's work, Gaspard Monge [16] posed the following problem: how should one optimally move material from one place to another, knowing only its initial and final spatial distributions, the cost being a prescribed function of the distance travelled by 'molecules' of material. This optimal transportation problem started being deeply understood only 160 years later when Leonid Kantorovich [17] showed that Monge's query was an instance of the linear-programming problem and developed for it a theory that found numerous practical applications. Some of the current developments of this very active area of research were triggered by Brenier's observation that optimal transportation can be applied to the variational formulation of the incompressible Euler equation [18]. More recently, cosmological applications have been discovered, which, from the infinite-dimensional geometric viewpoint, may be seen as the opposite of the Euler dynamics of incompressible fluid; indeed dark matter on scales of millions of parsecs is infinitely compressible.[5] Nusser (p. 2158) discusses the current state of the variational formulation of cosmological reconstruction introduced by Jim Peebles [19] in which the goal is to reconstruct the past dynamical history of the Universe from the present observable large-scale structures of galaxies and clusters. Mohayaee & Sobolevskiĭ (p. 2145) and Lavaux (p. 2139) show how optimal transportation, coupled with modern optimization algorithms can be used very efficiently for cosmological reconstruction on the largest scales where the dynamics are governed by the Zel'dovich approximation [20], closely related to the 3D Burgers equation. Here we mention that Nguyen van yen et al. (p. 2151) develop a new wavelet filtering method which they test on the 1D Burgers equation and which they plan to extend to higher dimensions.

The Conference also had a general discussion on climate issues (in the context of the recent report of the Intergovernmental Panel on Climate Change [21]) and presentations by Shaw on cloud physics and inertial particles, and by Nordlund on solar hydrodynamics.

The final section on **boundaries and vortical structures** gathers all the papers in which boundaries or vortices (other than point vortices) play a decisive role. Euler himself definitely did not ignore boundaries. For example, he was the first to formulate the correct boundary condition at a wall for ideal flow. However, one of his major achievements was also to free fluid dynamics from the earlier paradigm, totally dominated by confining vessels and mostly unable to think of pressure as generating internal forces also. For reasons of technical convenience the paradigm of homogeneous turbulence free of boundaries (or having just "periodic boundary conditions") has perhaps been excessively popular with theoreticians, but a more balanced view has emerged in recent years. Of course engineers never stopped studying boundary effects. As for vortical structures, they are discussed for the first time in Euler's French memoir (p. 1825), after having been missed in the Latin memoir (p. 1840). We also mention that, in the course of the discussion of singularities, Constantin invited us to look at local geometric structure of the flow.

This section opens with a joint review of Procaccia & Sreenivasan (p. 2167), dealing with such topics as anisotropic and wall-bounded turbulence, drag reduction by additives, and superfluid turbulence. This is followed by a number of papers discussing boundary effects: Ali et al. (p. 2184) on aeroacoustics, Araya, Leonardi & Castillo (p. 2190) on passive scalars in a turbulent channel, Eliasson, Henshaw & Appelö (p. 2203) on the influence of obstacles on converging shock waves, Schneider & Farge (p. 2228) on the influence of boundaries on the long-time decay of 2D turbulence, Singh & Pedley (p. 2234) on the hydrodynamics of fish motion, and Sznitman & Rösgen (p. 2240), on creeping flow in a cavity which, nevertheless, has inviscid steady states. We also have papers on vortex rings by Fukumoto & Moffatt (p. 2210) and by Krueger (p. 2218) and papers on vortex tangles (superfluid or classical) by Barenghi (p. 2195) and by Ricca (p. 2223).

The Conference also had a survey lecture by Perrier on multiphysics numerical simulations for complex engineering flow, illustrated by problems in aerospace and ground transportation, a presentation by Monkewitz on cavitation, a subject pioneered by Euler, and one by van Heijst on the production of vorticity near the boundaries in 2D turbulent flow.

Research on the Euler equations has been going on for a quarter of a millennium. It is far from being over. We are particularly glad that so many young researchers have participated in the EE250 Conference who will carry the torch further.

[5] Only a few presentations and papers at EE250 dealt with *compressible* flow, a very active area of research, also pioneered by Euler, and which would have deserved its own conference.

References

[1] C. Bardos, E.S. Titi, Euler equations for incompressible ideal fluids, Uspekhi Mat. Nauk. 62 (2007) 5–46; English version Russian Math. Surv. 62 (2007) 409–451.

[2] V. Scheffer, An inviscid flow with compact support in space-time, J. Geom. Anal. 3 (1993) 343–401.

[3] A.I. Shnirelman, On the nonuniqueness of weak solutions of the Euler equation, Comm. Pure Appl. Math. 50 (1997) 1261–1286.

[4] A.I. Shnirelman, Generalized fluid flows, their approximation and applications, Geom. Funct. Anal. 4 (1994) 586–620.

[5] Y. Brenier, The least action principle and the related concept of generalized flows for incompressible perfect fluids, J. Amer. Math. Soc. 2 (1989) 225–255.

[6] C. De Lellis, L. Székelyhidi Jr., On admissibility criteria for weak solutions of the Euler equations, preprint, 2007. arXiv:0712.3288 [math.AP].

[7] C. Cichowlas, P. Bonaïti, F. Debbasch, M.E. Brachet, Effective dissipation and turbulence in spectrally truncated flows, Phys. Rev. Lett. 95 (2005) 264502.

[8] U. Frisch, S. Kurien, R. Pandit, W. Pauls, A. Wirth, J.-Z. Zhou, Hyperviscosity, Galerkin truncation and bottlenecks in turbulence, preprint, 2008. arXiv:0803.4269 [nlin.CD].

[9] L. Onsager, Statistical hydrodynamics, Nuovo Cimento (Suppl. 6) (1949) 279–287.
[10] G. Falkovich, Conformal invariance in hydrodynamic turbulence, Russian Math. Surv. 62 (2007) 497–510.
[11] G. Gallavotti, Dynamical ensemble equivalence in fluid mechanics, Physica D 105 (1997) 163–184.
[12] R.H. Kraichnan, Anomalous scaling of a randomly advected passive scalar, Phys. Rev. Lett. 72 (1994) 1016–1019.
[13] G. Falkovich, K. Gawędzki, M. Vergassola, Particles and fields in fluid turbulence, Rev. Modern. Phys. 73 (2001) 913–975.
[14] R. Monchaux, M. Berhanu, M. Bourgoin, M. Moulin, P. Odier, J.F. Pinton, R. Volk, S. Fauve, N. Mordant, F. Pétrélis, A. Chiffaudel, F. Daviaud, B. Dubrulle, C. Gasquet, L. Marié, F. Ravelet, Generation of magnetic field by dynamo action in a turbulent flow of liquid sodium, Phys. Rev. Lett. 98 (2007) 044502.
[15] M. Berhanu, R. Monchaux, S. Fauve, N. Mordant, F. Pétrélis, A. Chiffaudel, F. Daviaud, B. Dubrulle, L. Marié, F. Ravelet, M. Bourgoin, P. Odier, J.-F. Pinton, R. Volk, Magnetic field reversals in an experimental turbulent dynamo, Europhys. Lett. 77 (2007) 59001.
[16] G. Monge, Mémoire sur la théorie des déblais et des remblais, Hist. de l'Académie Royale des Sci. (1781) 666–704.
[17] L.V. Kantorovich, On the translocation of masses, C. R. Dokl. Acad. Sci. USSR 321 (1942) 199–201; English translation J. Math. Sci. (2006) 1381–1382.
[18] Y. Brenier, A combinatorial algorithm for the Euler equations of incompressible flows, Comput. Methods Appl. Mech. Eng. 75 (1989) 325–332.
[19] P.J.E. Peebles, Tracing galaxy orbits back in time, Astrophys. J. 344 (1989) L53–L56.
[20] Y.B. Zel'dovich, Gravitational instability: An approximate theory for large density perturbations, Astron. Astrophys. 5 (1970) 84–89.
[21] IPCC, 2007: Climate Change 2007: The Physical Science Basis. Contribution of Working Group I to the Fourth Assessment Report of the Intergovernmental Panel on Climate Change [S. Solomon, D. Qin, M. Manning, Z. Chen, M. Marquis, K.B. Averyt, M. Tignor and H.L. Miller (Eds.)]. Cambridge University Press, Cambridge, United Kingdom, New York, NY, USA, 996 pp.

Gregory Eyink
Baltimore,
United States

Uriel Frisch*
Nice,
France

René Moreau
Grenoble,
France

Andreĭ Sobolevskiĭ
Moscow,
Russia

Available online 27 May 2008

* Corresponding address: Observatoire de la Côte d' Azur, BP 4229, 06304 Nice Cedex 4, France. *E-mail address:* uriel@obs.nice.fr.

Available online at www.sciencedirect.com
ScienceDirect
Physica D 237 (2008) xvii–xviii
PHYSICA D
www.elsevier.com/locate/physd

Euleriana
A short bibliographical note

1. Leonhard Euler's scientific heritage is immense. His published scientific studies, numbering close to 800, comprise about 30 000 printed pages and consist of roughly 600 papers in periodicals and various collections of the Petersburg Academy of Sciences, 130 papers published in Berlin and in Western European journals, 15 memoirs, which were awarded prizes and promoted by the Paris Academy of Sciences, and 40 books of individual essays. A century ago a publication of Euler's "Complete Works" *(Opera omnia)* was undertaken. It was planned to divide them into three series: I. Mathematics (29 vols); II. Mechanics and Astronomy (31 vols); III. Physics and Varia (12 vols). The first volume was published in 1911, and the publication of the final two volumes, out of the planned 72, is expected in the next two or three years. In the 1970s it was decided to publish an additional series (IVA) of the *Opera omnia* that would contain Euler's scientific correspondence.[1] The first volume of ser. IVA (1975) consists of an annotated list of the whole scientific correspondence. Of the planned approximately ten volumes of this series only four have been published so far. They contain Euler's correspondence with Johann I and Niklaus I Bernoulli (vol. IVA-2, 1998), A.C. Clairaut, J. d'Alembert, J.L. Lagrange (vol. IVA-5, 1980), P.-L.M. Maupertuis and Friedrich II (vol. IVA-6, 1986). Three volumes of Euler's correspondence with Petersburg (from 1726–1774) were published independently earlier (*Die Berliner und die Petersburger Akademie der Wissenschaften im Briefwechsel Leonhard Eulers*, 3 T. Berlin: Akademie-Verlag, 1959–1976).

A comparatively full list of Euler's published works was prepared by G. Eneström: *Verzeichnis der Schriften Leonhard Eulers*, in: *Jahresber. Deutsch. Math.-Verein.*, Ergänzungsb. 4, 1–2, 1–388, 1910–1913.[2] Since then all Euler works are usually mentioned with the corresponding number of the Eneström list supplemented with the symbol E.

Euler's works are commented in introductory notes of the corresponding volumes of *Opera omnia*. Particularly comprehensive surveys of Euler's work in continuum mechanics have been written by Clifford A. Truesdell: *Rational fluid mechanics, 1687–1765* (Editor's introduction to Euleri Opera omnia, II-12, 1954, pp. vii–cxxv); Editor's introduction to Opera omnia, II-13, 1955, pp. vii–cv; *The rational mechanics of flexible or elastic bodies, 1638–1788* (Opera omnia, II-11(2), 1960, 435 p.). In the 1950s Truesdell essentially rediscovered Leonhard Euler as the creator of rational mechanics (cf.: C. Truesdell, *Essays in the history of mechanics*. Springer-Verlag, 1968).

Now Leonhard Euler's *Opera omnia*, together with the full Eneström list, are available on the Internet: http://www.math.dartmouth.edu/˜euler.

Original minutes of the Petersburg Academy of Sciences, written mainly in Latin and French and containing a huge amount of information on Euler's work, were published at the beginning of the 20th century: *Procès-verbaux des séances de l'Académie Impériale des sciences depuis sa fondation jusqu'à 1803*. 4 t. SPb., 1897–1911. Cf. annotated *Chronicles of the Russian Academy of Sciences*, 4 vols (*Letopis' Rossiĭskoĭ Akademii nauk, 1724–1934*). SPb., 2000–2004.[3] Many documents concerning Euler's work in Petersburg (till 1750) have been published (in original languages) in the *Materials for the history of the Imperial Academy of Sciences*, 10 vols (*Materialy dlya istorii Imperatorskoĭ Akademii nauk*). SPb., 1885–1900.

A *Scientific description* (*Nauchnoe opisanie*) of all the Euler documents from the Archives of the Russian Academy of Sciences is published in the *Works* (*Trudy*) of the Archives of the USSR Academy of Sciences, 1962, vol. 17: *Manuscripta Euleriana Archivi Academiae scientiarum URSS*, t. I (*Rukopisnye materialy L. Èĭlera v Arkhive Akademii nauk SSSR*, I = *Trudy Arkhiva AN SSSR*, 17).

The Berlin Academy has not kept full texts of its minutes for the middle of the 18th century. Only their extracts

[1] At the same time it was proposed to prepare Series IVB dedicated to unpublished manuscripts of Euler. For a number of reasons, including lack of funds, this idea had to be abandoned. However it is not ruled out that the manuscripts will be made available in an electronic form, provided that a suitable source of financing is found in the future.

[2] The Eneström list is reproduced, without detailed descriptions, in the *Works* (*Trudy*) of the Archives of the USSR Academy of Sciences, vol. 17 (1962) mentioned below.

The Archives of the USSR Academy of Sciences published later a volume (vol. 20, 1965) containing some manuscripts of Euler's early papers on mechanics (*Opera mechanica*, vol. 1, ed. G.K. Mikhailov).

[3] Transliteration of Russian titles is according to the new (since 1983) system of Mathematical Reviews; the Russian titles themselves are given according to the modern (post-1918) orthography.

0167-2789/$ - see front matter
doi:10.1016/j.physd.2008.05.005

exist: *Die Registres der Berliner Akademie der Wissenschaften 1746–1766*. Berlin: Akademie-Verlag, 1957.

There is a published description of Euler documents kept in the Archives of the Berlin Academy: *Leonhard Eulers Wirken an der Berliner Akademie der Wissenschaften, 1741–1766*. Berlin: Akademie-Verlag, 1984.

2. The number of studies dedicated to Leonhard Euler and his work is truly enormous.

Among special monographs on Leonhard Euler it is necessary to mention:

L.-Gustave du Pasquier, 1927 *Léonard Euler et ses amis*, Paris: Hermann.

Otto Spieß, 1929 *Leonhard Euler: Ein Beitrag zur Geistesgeschichte des XVIII. Jahrhunderts*, Frauenfeld, Leipzig: Huber.

Rüdiger Thiele, 1982 *Leonhard Euler*, Leipzig: Teubner (in German).

Emil A. Fellmann, 1995 *Leonhard Euler*, Reinbek bei Hamburg: Rowohlt (in German).

Emil A. Fellmann, 2007 *Leonhard Euler*, Basel: Birkhäuser (English translation by Erika Gautschi and Walter Gautschi).

Let us also mention many interesting collections of papers associated to various Euler jubilee years:

Berliner mathematische Gesellschaft, 1907 *Festschrift zur Feier des 200. Geburtstages Leonhard Eulers*, Leipzig, Berlin: Teubner (collection of four papers in German).

Académie des sciences de l'URSS, l'Institut de l'histoire de la science et de la technique, 1935 *Léonard Euler 1707–1783: Recueil des articles et matériaux en commémoration du* 150^{e} anniversaire du jour de sa mort (*Leonard Èĭler 1707–1783: Sbornik stateĭ i materialov k 150-letiyu so dnya smerti*), Moscow, Leningrad (collection of 10 papers in Russian).

M.A. Lavrent'ev, A.P. Yushkevich, A.T. Grigor'yan (eds), 1958 *Sammelband der zu Ehren des 250. Geburtstages Leonhard Eulers der Akademie der Wissenschaften der UdSSR vorgelegten Abhandlungen* (*Leonard Èĭler: Sbornik stateĭ v chest' 250-letiya so dnya rozhdeniya, predstavlennykh Akademii nauk SSSR*), Moscow (collection of 20 papers in Russian, with German abstracts).

Kurt Schröder (ed.), 1959 *Sammelband der zu Ehren des 250. Geburtstages Leonhard Eulers der Deutschen Akademie der Wissenschaften zu Berlin vorgelegten Abhandlungen*, Berlin: Akademie-Verlag (collection of 26 papers, mostly in German, except one in French and one in Italian, with Russian abstracts).

J.J. Burckhardt, E.A. Fellmann, W. Habicht (eds), 1983 *Leonhard Euler 1707–1783: Beiträge zu Leben und Werk*, Basel: Birkhäuser (collection of 30 papers, mostly in German, except 6 in French and 3 in English).

E. Knobloch, I.S. Louhivaara, J. Winkler (eds), 1984 *Zum Werk Leonhard Eulers: Vorträge des Euler-Kolloquiums im Mai 1983 in Berlin*, Basel: Birkhäuser (collection of 7 papers in German, 5 in English and one in French).

Wolfgang Engel (ed.), 1985 *Festakt und wissenschaftliche Konferenz aus Anlaß des 200. Todestages von Leonhard Euler*, Berlin: Akademie-Verlag (collection of 13 papers, mostly in German, except one in English).

N.N. Bogolyubov, G.K. Mikhaĭlov, and A.P. Yushkevich (eds), 1988 *Development of Leonhard Euler's ideas and modern science* (*Razvitie ideĭ Leonarda Èĭlera i sovremennaya nauka*), Moscow: Nauka (collection of 28 papers in Russian).

One can find a detailed (but, of course, not exhaustive) bibliography of Euleriana in the Basel volume mentioned above (1983, pp. 511–552).

The last Euler year (2007) prompted an extremely wide jubilee activity throughout the world, both in the form of international and national conferences and publications.

A grandiose international Euler conference was organized in St. Petersburg (its Book of abstracts contains 470 pages!). A separate volume with selected papers presented at the Conference is now in print: V.N. Vasil'ev (ed.), 2008 *Leonhard Euler: On the tercentenary of his birth* (*Leonard Èĭler: K 300-letiyu so dnya rozhdeniya*), St. Petersburg: Nestor-Istoriya (collection of about 30 papers, in Russian and in English).

The Mathematical Association of America published five special Euler volumes:

C. Edward Sandifer, 2007 *The Early Mathematics of L. Euler*, Washington, DC: Math. Assoc. Amer.

William Dunham (ed.), 2007 *The Genius of Euler: Reflections on his life and work*, Washington DC: Math. Assoc. Amer. (collection of 30 selected papers in English on the life and work of Euler, dating from 1872 to 2006).

C. Edward Sandifer, 2007 *How Euler did it*, Washington, DC: Math. Assoc. Amer.

N.N. Bogolyubov, G.K. Mikhaĭlov and A.P. Yushkevich (eds), 2007 *Euler and Modern Science*, Washington, DC: Math. Assoc. Amer. (English translation by Robert Burns of the aforementioned Russian collection of 1988).

Robert E. Bradley, Lawrence A. D'Antonio, and C. Edward Sandifer (eds), 2007 *Euler at 300: An Appreciation*, Washington, DC: Math. Assoc. Amer. (collection of 21 papers on various aspects of Euler's work, in English).

The Tercentenary was also marked by the publication of the volume:

Robert E. Bradley and C. Edward Sandifer (eds), 2007 *Leonhard Euler: Life, Work and Legacy*, Amsterdam: Elsevier (collection of 24 papers on Euler's life and work, in English).

Gleb K. Mikhailov
Moscow

Available online 24 May 2008

Available online at www.sciencedirect.com

ScienceDirect

Physica D 237 (2008) xix–xxii

PHYSICA D

www.elsevier.com/locate/physd

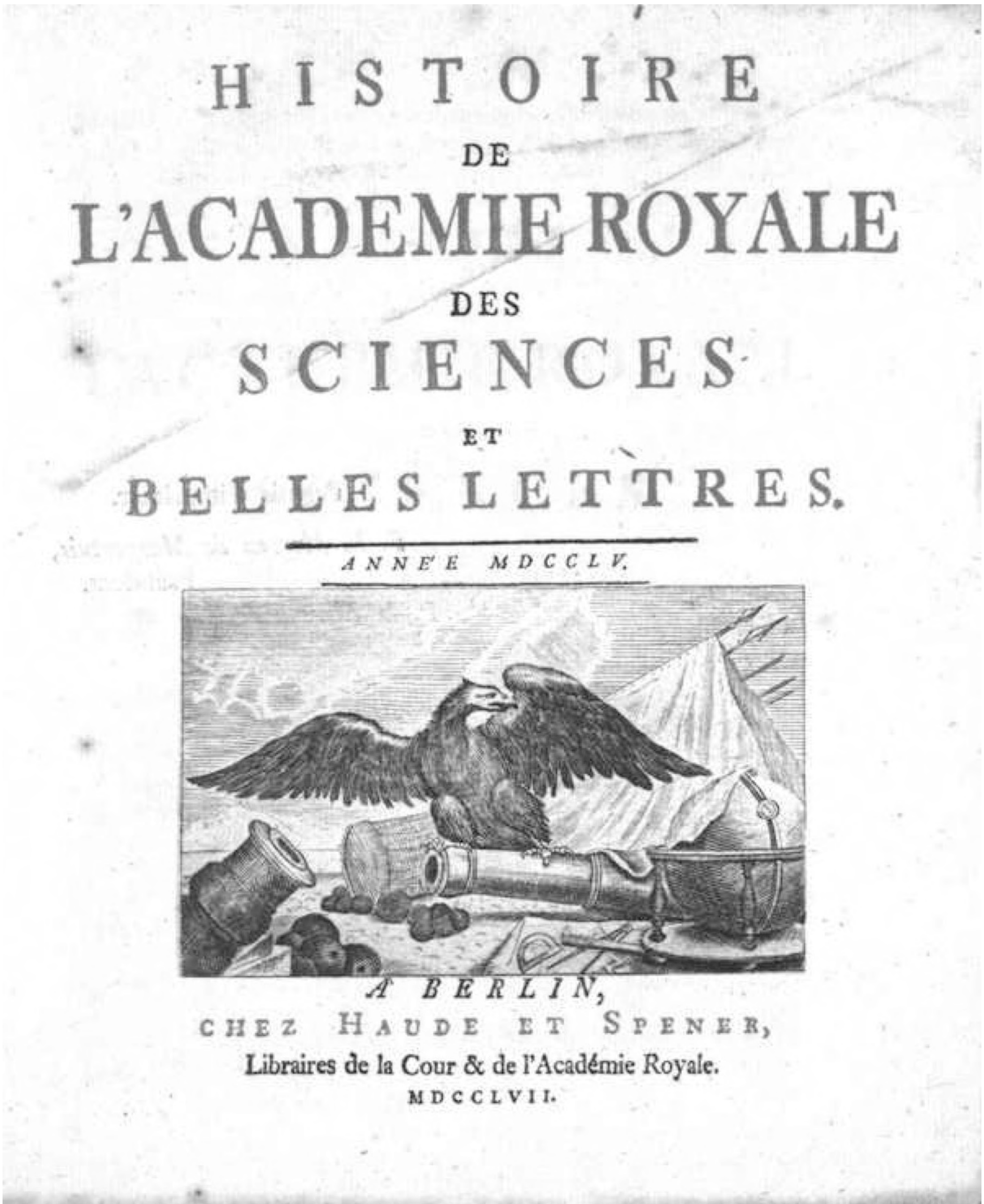

HISTOIRE
DE
L'ACADEMIE ROYALE
DES
SCIENCES
ET
BELLES LETTRES.

ANNÉE MDCCLV.

À BERLIN,
CHEZ HAUDE ET SPENER,
Libraires de la Cour & de l'Académie Royale.
MDCCLVII.

0167-2789/$ - see front matter
doi:10.1016/j.physd.2008.05.004

Permis d'imprimer.

P. L. Moreau de Maupertuis,
Préſident.

538

CLASSE
de Mathématique.

CLASSE
de Philosophie Spéculative.

CLASSE

PRINCIPES GÉNÉRAUX DU MOUVEMENT DES FLUIDES.

PAR M. EULER.

I.

Ayant établi dans mon Mémoire précedent les principes de l'équilibre des fluides le plus généralement, tant à l'égard de la diverſe qualité des fluides, que des forces qui y puiſſent agir ; je me propoſe de traiter ſur le même pied lè mouvement des fluides, & de rechercher les principes géneraux, ſur lesquels toute la ſcience du mouvement des fluides eſt fondée. On comprend aiſément que cette matiere eſt beaucoup plus difficile, & qu'elle renferme des recherches incomparablement plus profondes : cependant j'eſpère d'en venir auſſi heureuſement à bout, de ſorte que s'il y reſte des difficultés, ce ne ſera pas du côté du méchanique, mais uniquement du côté de l'analytique: cette ſcience n'étant pas encore portée à ce degré de perfection, qui ſeroit néceſſaire pour déveloper les formules analytiques, qui renferment les principes du mouvement des fluides.

II. Il s'agit donc de découvrir les principes, par lesquels on puiſſe déterminer le mouvement d'un fluide, en quelque état qu'il ſe trouve, & par quelques forces qu'il ſoit ſollicité. Pour cet effet examinons en détail tous les articles, qui conſtituent le ſujet de nos recherches, & qui renferment les quantités tant connues qu'inconnues. Et d'abord la nature du fluide eſt ſuppoſée connue, dont il faut conſidérer les diverſes eſpeces : le fluide eſt donc, ou incompreſſible, ou compreſſible. S'il n'eſt pas ſusceptible de compreſſion, il faut diſtinguer deux cas, l'un où toute la maſſe eſt compoſée de parties homogenes, dont la denſité eſt partout & demeure toujours la même, l'au-

tre

Euler’s founding papers on hydrodynamics

Available online at www.sciencedirect.com
ScienceDirect
Physica D 237 (2008) 1825–1839
PHYSICA D
www.elsevier.com/locate/physd

General principles of the motion of fluids[☆]

Leonhard Euler

Available online 4 March 2008

1. Having established in my previous Memoir[1] the principles of fluid equilibrium in their most general form, regarding both the diverse nature of fluids and the forces that act upon them, I now propose to deal with the motion of fluids in the same way and to seek out the general principles on which the entire science of fluid motion is based. It will readily be understood that this is a much more difficult undertaking and involves studies of incomparably greater depth. Nevertheless, I hope to arrive at an equally successful conclusion, so that, if difficulties remain, they will pertain not to Mechanics but purely to Analysis, this science not yet having been brought to the degree of perfection necessary to develop analytical equations [*formules*][2] that embody the principles of fluid motion.

2. The task, then, is to discover the principles by means of which the motion of a fluid can be determined, whatever its state and whatever the forces to which it is subjected. To this end, we shall examine in detail all the elements which form the subject of our research and contain quantities both known and unknown. First of all, the nature of the fluid is assumed to be known, in which case it is necessary to consider its various forms since it may be compressible or incompressible. If it is not compressible, then there are two possibilities: either the entire mass is composed of homogeneous parts, whose density is everywhere and always the same, or it is composed of heterogeneous parts and in this case it is necessary to know the density of each component and the proportions of the mixture. If the fluid is compressible and its density is variable, we must know the law according to which its elasticity[3] depends on the density and whether the elasticity depends only on the density or also on some other property, such as heat,[4] which is proper to each particle of fluid, at least for each instant of time.

3. It must also be assumed that the state of the fluid at a certain moment of time is known and I shall call this the initial state [*état primitif*] of the fluid. As this state is quasi-arbitrary, it is necessary, first of all, to know the distribution of the particles of which the fluid is composed and, unless in the initial state the fluid is at rest, the motion impressed upon them. However, the initial motion is not entirely arbitrary since both the continuity and the impenetrability of the fluid impose a certain limitation which I shall investigate below. Often, however, nothing is known of the initial state, for example when it is a question of determining the motion of a river, and then it is usually only possible to seek the steady state at which the fluid finally arrives, thereafter undergoing no further changes. Now, neither this circumstance nor the initial state in any way will affect the investigation to be made and the calculations will always be the same. It is only in the integrations that they need to be taken into account for the purpose of determining the constants which every integration involves.

4. Thirdly, the data must include the external forces to which the fluid is subjected. I shall call these forces external to distinguish them from the internal forces which the fluid particles exert on each other and which will constitute the main topic for subsequent investigation. Thus, it could be assumed that the fluid is not exposed to any external force, unless it be natural gravity which is everywhere considered to be constant in magnitude and to act in the same direction. However, to generalize the investigation, I shall consider the fluid to be acted upon by forces which may be directed towards one or more centers or obey some other law with respect to both magnitude

[☆] This is an adaptation by U. Frisch of an English translation by Thomas E. Burton of Euler's memoir 'Principes généraux du mouvement des fluides' (Euler, 1775b). Burton's translation appeared in *Fluid Dynamics* **34** (1999) pp. 801–822, Springer and is here adapted by permission. A detailed presentation of Euler's published work can be found in Truesdell, 1954. Euler's work is discussed also in the perspective of eighteenth century fluid dynamics research by Darrigol and Frisch, 2008.
Explanatory footnotes have been supplied where necessary by G.K. Mikhailov and a few more by U. Frisch and O. Darrigol. Euler's memoir had neither footnotes nor a list of references.

[1] Euler, 1755a.

[2] Bracketed words are from the original eighteenth century French text.

[3] By elasticity [*élasticité*] Euler means that property of a fluid which is expressed in the creation of internal pressure and therefore uses the term on an equal footing with the term "pressure" (see § 5 below).

[4] Essentially, heat [*chaleur*] should be taken to mean temperature.

doi:10.1016/j.physd.2008.02.023

and direction. As far as these forces are concerned, only their accelerating action is directly known, irrespective of the masses upon which they act. Accordingly, I shall introduce into the calculations only the accelerative forces, from which it will be easy to obtain the true motive forces by multiplying in each case the accelerative forces by the masses to which they are applied.[5]

5. Let us now turn to those elements which contain that which is unknown. In order to properly understand the motion that will be imparted to the fluid it is necessary to determine, for each instant and for each point, both the motion and the pressure [*pression*] of the fluid situated there. And if the fluid is compressible, it is also necessary to determine the density, knowing the above-mentioned other property which, together with the density, makes it possible to determine the elasticity. The latter, being counterbalanced by the fluid pressure, must be considered equal to that pressure, exactly as in the case of equilibrium, where I have developed these ideas more thoroughly.[6] Clearly, then, the number of quantities which enter into the study of fluid motion is much greater than in the case of equilibrium, since it is necessary to introduce letters which denote the motion of each particle and all these quantities may vary with time. Thus, in addition to the letters which determine the location of each conceivable point in the fluid, another is required which denotes the time already elapsed and which, by virtue of its variability, can be applied to any given time.

6. Suppose (Fig. 1) that from the initial state a time t has elapsed and that the fluid is now in a state of motion which is to be determined.[7] Whatever the volume that the fluid now occupies, I begin by considering any point Z in the fluid mass and in order to introduce the location of this point Z into the calculations I relate it to three fixed axes, OA, OB and OC, mutually perpendicular at the point O and having a given position. Let the two axes OA and OB lie in the plane represented by the page and let the third OC be perpendicular to it. Then from the point Z we draw a perpendicular ZY to the plane AOB and from the point Y a normal YX to the axis OA to obtain three coordinates: $\mathrm{OX} = x$, $\mathrm{XY} = y$ and $\mathrm{YZ} = z$ parallel to our three axes. For each point in the fluid mass, these three coordinates x, y and z will have specific values and by successively giving these three coordinates all possible values, both positive and negative, we can run through all the points of infinite space, including those lying in the volume occupied by the fluid at each instant of time.

7. Secondly, I shall consider the accelerative forces which act at a given moment on the fluid particle located at Z. Now,

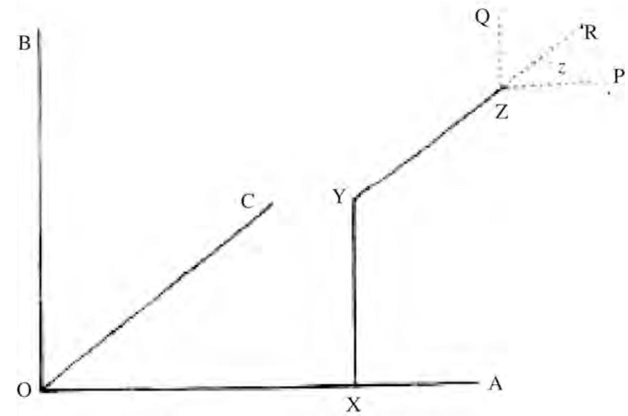

Fig. 1.

whatever these forces may be, they can always be reduced to three acting in the three directions ZP, ZQ and ZR parallel to our three axes 0A, OB and OC. Taking the accelerative force of natural gravity[8] as the unit, we let P, Q and R be the accelerative forces acting on the point Z in the directions ZP, ZQ and ZR, the letters P, Q and R denoting abstract numbers [*nombres absolus*].[9] If unchanging forces always act at the same point in space Z, the quantities P, Q and R will be expressed by certain functions of the three coordinates x, y and z. However, if the forces also vary with time t, these functions will likewise contain time t. I shall assume that these functions are known, since the acting forces must be included among the known quantities, whether they depend only on the variables x, y, z or also on time t.

8. Let r now express the heat at the point Z or that other property which, in addition to the density, influences the elasticity in the case of a compressible fluid. The quantity r must also be considered to be a function of the three variables x, y, z and time t, since it might vary with time t at the same point Z in space. Thus, this function may be regarded as being known.[10] Moreover, let the present density of the fluid particle located at Z be equal to q. As the unit of density I shall take the density of a certain homogeneous substance which I shall use to measure pressures in terms of heights, as explained at greater length in my memoir on the equilibrium of fluids.[11] Let, moreover, the present value of the fluid pressure at the point Z, expressed in terms of height, be equal to p, which will thus also denote the elasticity. Since the nature of the fluid is assumed to be known, we will know the relation between the height p and the quantities q and r.[12] Thus, p and q will likewise be

[5] Newton distinguishes between the "accelerative" and "motive" aspects of a force, the former being "a measure proportional to the velocity which it generates" and the latter "a measure proportional to the quantity of motion which it generates in a given time". Thus, the "accelerative force" is the ratio of the acting force to the mass of the particle on which it acts, i.e. the acceleration which it imparts, and the "motive force" is that which, strictly speaking, we now understand by force. The neutral term "acting forces" [*forces sollicitantes*], not used by Newton, was widely employed by Euler, starting with his well-known "Mechanics" (Euler, 1736).

[6] Cf. Euler, 1755a.

[7] In the original publication all figures are on the fourth table following the end (on p. 402) of the part of the volume dedicated to the Mathematics Class. As was the rule at the time figures are devoid of captions.

[8] The acceleration of gravity is intended.

[9] The non-dimensionality of the values of P, Q and R is emphasized.

[10] Euler is confining himself to the consideration of fluid motion in a given temperature field.

[11] Clearly, for Euler the density q is non-dimensional, being divided by the constant density ρ_0 of a certain auxiliary fluid: $q = \rho/\rho_0$. Euler defines the pressure in the fluid as the height p of a column of this same homogeneous auxiliary fluid. Thus, for Euler pressure is measured by a quantity with the dimension of length — the ratio of the acting pressure to the constant quantity $\rho_0 g$ (where g is the acceleration of gravity). For further details see Euler, 1755a.

[12] That is, the "equation of state" of the moving medium is assumed to be known.

functions, albeit unknown, of the four variables x, y, z and t; however if the fluid is not compressible,[13] the pressure p will be independent of the density q and the other property [*qualité*] r will not enter into consideration at all.

9. Finally, whatever the motion corresponding at a given time to the fluid element located at the point Z, it too can be decomposed in the directions ZP, ZQ and ZR parallel to our three axes. Thus, let u, v and w be the velocities of this motion decomposed in the three directions ZP, ZQ and ZR. It is then obvious that these three quantities must also be considered to be functions of the four variables x, y, z and t. Indeed, having found the nature of these functions, if the time t is assumed to be constant, then by varying the coordinates x, y and z the three velocities u, v and w and hence the true motion imparted to each element of the fluid at a given time will be known. If, the coordinates x, y and z are assumed to be constant and only the time t is considered to be variable, we shall find the motion not of some particular element of the fluid but of all the elements that pass successively through the same point Z; in other words, at each moment of time the motion of that fluid element which is then located at the point Z will be known.

10. Let us consider what path will be described by a fluid element now at Z during the infinitely small[14] time dt; or the point at which it will be an instant later.[15] If we express the distance as the product of velocity and time, a fluid element currently at Z will travel a distance udt in the direction ZP, a distance vdt in the direction ZQ and a distance wdt in the direction ZR. Therefore, if we set

$$\mathrm{ZP} = udt, \quad \mathrm{ZQ} = vdt, \quad \text{and} \quad \mathrm{ZR} = wdt$$

and from these three sides complete the construction of the parallelepiped, then the corner opposite to the point Z will represent the point at which the fluid element in question will be after the time dt and the diagonal of the parallelepiped, which is equal to $dt\sqrt{(uu+vv+ww)}$ will give the true path described.[16] Consequently, the velocity of this true motion will be equal to $\sqrt{(uu+vv+ww)}$ and the direction can easily be determined from the sides of the parallelepiped since it will be inclined to the plane AOB at an angle whose sine is equal to

$$\frac{w}{\sqrt{(uu+vv+ww)}},$$

to the plane AOC at an angle whose sine is equal to

$$\frac{v}{\sqrt{(uu+vv+ww)}},$$

and, finally, to the plane BOC at an angle whose sine is equal to

$$\frac{u}{\sqrt{(uu+vv+ww)}}.$$

11. Having determined the motion of a fluid element which at a given instant is located at the point Z, let us now also examine that of some other infinitely close element located at the point z with the coordinates $x + dx$, $y + dy$ and $z + dz$. The three velocities of this element in the direction of the three axes can thus be expressed by u, v, w after substituting in those quantities $x+dx$, $y+dy$ and $z+dz$ or after adding to them their differentials while assuming the time t to be constant. Thus, when $x + dx$ is substituted for x, the increments of u, v and w will be:[17]

$$dx\left(\frac{du}{dx}\right), \quad dx\left(\frac{dv}{dx}\right), \quad dx\left(\frac{dw}{dx}\right),$$

and when $y + dy$ is substituted for y, the increments will be:

$$dy\left(\frac{du}{dy}\right), \quad dy\left(\frac{dv}{dy}\right), \quad dy\left(\frac{dw}{dy}\right),$$

and the same will apply to the variation of z. Then, the three velocities of the fluid element currently located at z will be: in the direction OA

$$u + dx\left(\frac{du}{dx}\right) + dy\left(\frac{du}{dy}\right) + dz\left(\frac{du}{dz}\right),$$

in the direction OB

$$v + dx\left(\frac{dv}{dx}\right) + dy\left(\frac{dv}{dy}\right) + dz\left(\frac{dv}{dz}\right),$$

in the direction OC

$$w + dx\left(\frac{dw}{dx}\right) + dy\left(\frac{dw}{dy}\right) + dz\left(\frac{dw}{dz}\right).$$

12. These are the velocities corresponding to a fluid element at the point z, which is infinitely close to the point Z and whose position is determined by the three coordinates $x + dx$, $y + dy$ and $z+dz$. Thus, if we choose a point Z (Fig. 2) such that only x changes by dx, the other two coordinates y and z remaining the same as for the point Z, the three velocities of the fluid element located at this point z will be:

$$u + dx\left(\frac{du}{dx}\right), \quad v + dx\left(\frac{dv}{dx}\right), \quad w + dx\left(\frac{dw}{dx}\right).$$

These velocities will transport the element in the time dt to another point z' whose position must be determined relative to the point Z′, namely the point to which the fluid element which was at Z is transported in the same time dt and whose position

[13] The 1757 printed version of the memoir has "not incompressible" [*pas incompressible*], but a handwritten copy of the manuscript dated 1755, henceforth cited as Euler, 1755c has "not compressible" [*pas compressible*] which is obviously the correct form.

[14] The differential operator d, now denoted using roman fonts, was at the time of Euler italicized; we shall follow his usage.

[15] The intuitive derivation of the equations of motion and continuity of an ideal (inviscid and non-heat-conducting) compressible fluid proposed by Euler is valid provided that the functions in question have bounded derivatives, up to and including the second. The modern derivation of these equations, based on the integral laws of conservation of mass and momentum of the fluid particles and the use of the Gauss theorem, is free of this limitation.

[16] In the 1757 printed version, which we here follow, we usually find the old notation xx rather than x^2 for the square of the quantity x and $\sqrt{(\ldots)}$ rather than $\sqrt{\ldots}$ for the square root of an expression. The manuscript Euler, 1755c, which is not in Euler's hand, uses modern notation.

[17] Rather than the now customary notation for partial derivatives using the symbol ∂, Euler employs only the symbol d but encloses the expressions for partial derivatives in round brackets.

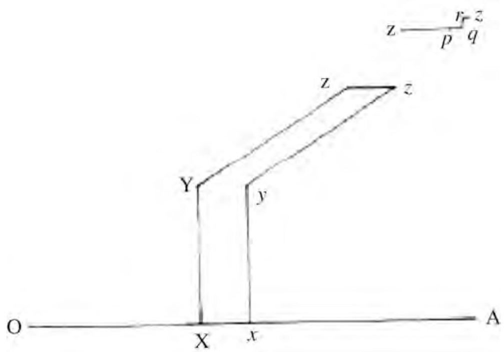

Fig. 2.

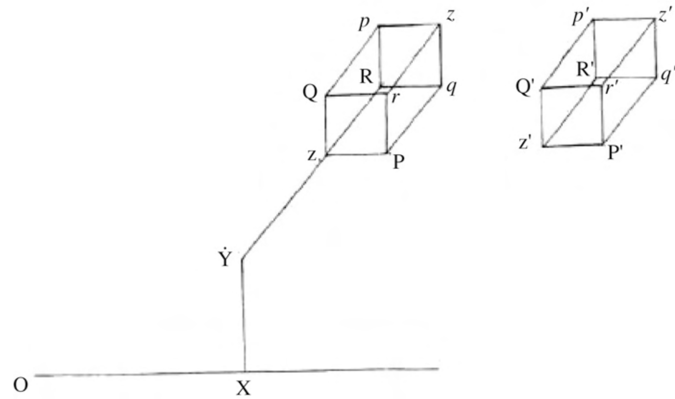

Fig. 3.

was determined above (see § 10). For determining this point z', I note that if the velocities of the point z were exactly the same as those of Z, then the point z' would fall at the point p,[18] such that the distance $\mathrm{Z}'p$ would be equal and parallel to the distance $\mathrm{Z}z$. Since, by hypothesis, $\mathrm{Z}z$ is parallel to the OA axis and equal to dx, the segment $\mathrm{Z}'p$ will also be equal to dx and parallel to the OA axis.

13. Now, since the velocity along OA is not u but $u + dx\left(\frac{du}{dx}\right)$, this velocity increment will transport the element in question from p to q in the direction $\mathrm{Z}'p$, such that $pq = dtdx\left(\frac{du}{dx}\right)$: this element would thus be at q, if the other two velocities were equal to v and w. However, since the velocity along the OB axis is $v + dx\left(\frac{dv}{dx}\right)$, this increment will transport our element from q to r, through the distance $qr = dtdx\left(\frac{dv}{dx}\right)$, and parallel to the axis OB. Finally, the increment $dx\left(\frac{dw}{dx}\right)$ of the velocity w will transport the element from r to z' through the infinitesimal distance [*particule d'espace*][19] $rz' = dtdx\left(\frac{dw}{dx}\right)$, and parallel to the third axis OC. From this I conclude that the fluid element which occupied the small linear segment $\mathrm{Z}z$ would be transported in the time dt to the segment $\mathrm{Z}'z'$, inclined at an infinitely small angle to the OA axis, whose length by virtue of the fact that $\mathrm{Z}'q = dx\left(1 + dt\left(\frac{du}{dx}\right)\right)$ will be

$$dx\sqrt{\left(\left(1 + dt\left(\frac{du}{dx}\right)\right)^2 + dt^2\left(\frac{dv}{dx}\right)^2 + dt^2\left(\frac{dw}{dx}\right)^2\right)}.$$

Thus, neglecting the terms that contain the square of dt, the length $\mathrm{Z}'z'$ will not differ from $\mathrm{Z}'q$ and we shall have: $\mathrm{Z}'z' = dx\left(1 + dt\left(\frac{du}{dx}\right)\right)$. For the inclination of this line to the OA axis, it will suffice to note that it is an infinitely small quantity of the first order and can be expressed as αdt.

14. If the small segment $\mathrm{Z}z$ had been taken equal to dy and parallel to the OB axis, by the same reasoning it could have been shown that the fluid which occupied that segment would have been transported to another segment $\mathrm{Z}'z' = dy\left(1 + dt\left(\frac{dv}{dy}\right)\right)$, and which would have been inclined to the OB axis at an infinitely small angle. And if we had taken the segment $\mathrm{Z}z = dz$, and parallel to the third axis OC, the fluid which occupied it would have have been transported to another segment $\mathrm{Z}'z' = dz\left(1 + dt\left(\frac{dw}{dz}\right)\right)$, and which would have been inclined to the OC axis at an infinitely small angle. Thus, if we consider a rectangular parallelepiped ZPQR$zpqr$ (Fig. 3) formed by the three sides $\mathrm{ZP} = dx$, $\mathrm{ZQ} = dy$, $\mathrm{ZR} = dz$, the fluid occupying that volume would be transported in the time dt to fill a volume $\mathrm{Z'P'Q'R'}z'p'q'r'$ differing infinitely slightly from a rectangular parallelepiped whose three sides would be

$$\mathrm{Z'P'} = dx\left(1 + dt\left(\frac{du}{dx}\right)\right);$$

$$\mathrm{Z'Q'} = dy\left(1 + dt\left(\frac{dv}{dy}\right)\right);$$

$$\mathrm{Z'R'} = dz\left(1 + dt\left(\frac{dw}{dz}\right)\right).$$

Since the sides ZP, ZQ, ZR go over into Z′P′, Z′Q′, Z′R′, there is no doubt that the fluid contained in the first volume will be transported into the other in the time dt.

15. We can now judge whether the volume of fluid occupying the parallelepiped $\mathrm{Z}z$ has increased or decreased in the time dt. For this we need only to find the volume or the capacity of each of these two solids. Since the first is a parallelepiped formed by the sides dx, dy, dz, its volume is equal to $dxdydz$. As for the other, whose plane angles differ infinitely slightly from a right angle, I note that its volume can also be found by multiplying its three sides, since the error due to the infinitesimal distortion of the angles will enter into terms which contain the square of the time element dt and can therefore be neglected. Thus, the volume $\mathrm{Z}'z'$ can be represented by the expression:

$$dxdydz\left(1 + dt\left(\frac{du}{dx}\right) + dt\left(\frac{dv}{dy}\right) + dt\left(\frac{dw}{dz}\right)\right).$$

Anyone still harboring doubts about the reasonableness of this conclusion need only consult my Latin paper *Principia motus fluidorum* in which I calculate this volume without neglecting anything.[20]

[18] Euler frequently uses the same notation for different quantities. Thus, both here and later on, the letters p and q, which in this article are mainly employed to denote pressure and density, are used to denote certain auxiliary points.

[19] The 1757 printed version of the memoir has "through the particle" [*par la particule*], but Euler, 1755c has "through the particle of distance" [*par la particule d'espace*].

[20] See Euler, 1756–1757. This memoir was originally entitled *De motu fluidorum in genere*, but the final title has been used here.

16. Thus, if the fluid is not compressible, these two volumes should be equal, since the mass occupying the volume Zz would not fit into either a larger or a smaller volume. However, since I propose to examine the problem in the most general possible form and have denoted the density at Z by q, considering q to be a function of the three coordinates and time, I note that to find the density at Z' it will first be necessary to increase the time t by its differential dt; then, as the point Z' is different from Z, the quantities x, y, z will have to be increased by the small increments udt, vdt, wdt; whence the density at Z' will be:

$$q + dt\left(\frac{dq}{dt}\right) + udt\left(\frac{dq}{dx}\right) + vdt\left(\frac{dq}{dy}\right) + wdt\left(\frac{dq}{dz}\right)$$

and since the density is inversely proportional to the volume, this quantity will be to q as $dxdydz$ to

$$dxdydz\left(1 + dt\left(\frac{du}{dx}\right) + dt\left(\frac{dv}{dy}\right) + dt\left(\frac{dw}{dz}\right)\right).$$

Thus, dividing by dt, we find that consideration of the density leads to the following equation:

$$\left(\frac{dq}{dt}\right) + u\left(\frac{dq}{dx}\right) + v\left(\frac{dq}{dy}\right) + w\left(\frac{dq}{dz}\right) + q\left(\frac{du}{dx}\right) + q\left(\frac{dv}{dy}\right) + q\left(\frac{dw}{dz}\right) = 0.$$

17. Here, then, is a very remarkable condition which already establishes a certain relation between the three velocities u, v and w and the fluid density q. Now this equation can be reduced to a simpler form.[21] Thus, $u\left(\frac{dq}{dx}\right)$ is no different from $\left(u\frac{dq}{dx}\right)$ since this form of expression must be taken to mean that in differentiating q only the quantity x is taken to be a variable, and similarly $q\left(\frac{du}{dx}\right) = \left(q\frac{du}{dx}\right)$; from which it follows that

$$q\left(\frac{du}{dx}\right) + u\left(\frac{dq}{dx}\right) = \left(\frac{udq + qdu}{dx}\right) = \left(\frac{d.qu}{dx}\right),$$

the differential of the product qu being so understood that only the quantity x is regarded as a variable. Accordingly, the equation obtained can be reduced to the following:

$$\left(\frac{dq}{dt}\right) + \left(\frac{d.qu}{dx}\right) + \left(\frac{d.qv}{dy}\right) + \left(\frac{d.qw}{dz}\right) = 0.$$

If the fluid was not compressible, the density q would be the same at both Z and Z' and for this case we would have the equation:

$$\left(\frac{du}{dx}\right) + \left(\frac{dv}{dy}\right) + \left(\frac{dw}{dz}\right) = 0,$$

which is also that on which I based my Latin memoir mentioned above.[22]

[21] In Euler's subsequent exposition the use of round brackets goes beyond the scope of simple partial derivative notation, but the meaning of the operations is still clear, in Euler's notation $d.qu = d(qu)$, etc.

[22] See Euler, 1756–1757.

18. This equation, obtained by considering the continuity of the fluid, already contains a certain relation which must exist between the quantities u, v, w and q. The other relations must be obtained by considering the forces to which each fluid particle is subjected. Thus, in addition to the accelerative forces[23] P, Q, R, which act on the fluid at Z, the fluid is also subjected to the pressure [*pression*] exerted from all sides on the fluid element contained at Z. Combining these two forces, we obtain three accelerative forces in the direction of the three axes. Since the accelerations themselves can be determined by considering the velocities u, v and w, we can derive three equations which, together with that which we have just found, will contain everything that relates to the motion of fluids, so that we shall then have the general and complete laws of the entire science of fluid motion.

19. In order to find the accelerations undergone by a fluid element at Z, we need only compare the velocities u, v, w which currently correspond to the point Z with the velocities corresponding to the point Z' after the lapse of the time dt. Thus, a double change takes place: with respect to the coordinates x, y, z, which receive the increments udt, vdt, wdt, as well as with respect to time, which increases by dt. Hence it follows that the three velocities at the point Z' are: in the direction OA

$$u + dt\left(\frac{du}{dt}\right) + udt\left(\frac{du}{dx}\right) + vdt\left(\frac{du}{dy}\right) + wdt\left(\frac{du}{dz}\right),$$

in the direction OB

$$v + dt\left(\frac{dv}{dt}\right) + udt\left(\frac{dv}{dx}\right) + vdt\left(\frac{dv}{dy}\right) + wdt\left(\frac{dv}{dz}\right),$$

in the direction OC

$$w + dt\left(\frac{dw}{dt}\right) + udt\left(\frac{dw}{dx}\right) + vdt\left(\frac{dw}{dy}\right) + wdt\left(\frac{dw}{dz}\right),$$

and hence the accelerations, expressed in terms of the velocity increments divided by the time element dt, will be: in the direction OA

$$\left(\frac{du}{dt}\right) + u\left(\frac{du}{dx}\right) + v\left(\frac{du}{dy}\right) + w\left(\frac{du}{dz}\right),$$

in the direction OB

$$\left(\frac{dv}{dt}\right) + u\left(\frac{dv}{dx}\right) + v\left(\frac{dv}{dy}\right) + w\left(\frac{dv}{dz}\right),$$

in the direction OC

$$\left(\frac{dw}{dt}\right) + u\left(\frac{dw}{dx}\right) + v\left(\frac{dw}{dy}\right) + w\left(\frac{dw}{dz}\right).$$

20. We will now seek the accelerative forces acting in these same directions due to the pressure exerted by the fluid on the parallelepiped Zz, whose volume is equal to $dxdydz$, the mass of the fluid occupying that volume thus being equal to $qdxdydz$. Since the pressure at the point Z is expressed in terms of the height p, the motive force acting on the face

[23] Concerning the concept of "accelerative" (body) forces, see footnote 5.

ZQRp is equal to $pdxdydz$. For the opposite face zqrP with the area $dydz$, the height p is increased by its differential $dx\left(\frac{dp}{dx}\right)$, obtained on the assumption that only x is variable. Accordingly, this fluid mass Zz is driven in the direction AO by the motive force $dxdydz\left(\frac{dp}{dx}\right)$ or by the accelerative force $\frac{1}{q}\left(\frac{dp}{dx}\right)$. Similarly, we find that the fluid mass Zz is subjected to the action of the accelerative force $\frac{1}{q}\left(\frac{dp}{dy}\right)$ in the direction BO and to that of the accelerative force $\frac{1}{q}\left(\frac{dp}{dz}\right)$ in the direction CO. To these forces we add the given forces P, Q, R, and the total accelerative forces will be:

in the direction OA: $\mathrm{P}-\dfrac{1}{q}\left(\dfrac{dp}{dx}\right)$

in the direction OB: $\mathrm{Q}-\dfrac{1}{q}\left(\dfrac{dp}{dy}\right)$

in the direction OC: $\mathrm{R}-\dfrac{1}{q}\left(\dfrac{dp}{dz}\right).$

21. Thus, it only remains to equate these accelerative forces with the actual accelerations which we have just found. We then obtain the following three equations:[24]

$$\mathrm{P}-\frac{1}{q}\left(\frac{dp}{dx}\right)=\left(\frac{du}{dt}\right)+u\left(\frac{du}{dx}\right)+v\left(\frac{du}{dy}\right)+w\left(\frac{du}{dz}\right)$$
$$\mathrm{Q}-\frac{1}{q}\left(\frac{dp}{dy}\right)=\left(\frac{dv}{dt}\right)+u\left(\frac{dv}{dx}\right)+v\left(\frac{dv}{dy}\right)+w\left(\frac{dv}{dz}\right)$$
$$\mathrm{R}-\frac{1}{q}\left(\frac{dp}{dz}\right)=\left(\frac{dw}{dt}\right)+u\left(\frac{dw}{dx}\right)+v\left(\frac{dw}{dy}\right)+w\left(\frac{dw}{dz}\right).$$

If we add to these three equations, first, that obtained from considering the continuity of the fluid, namely

$$\left(\frac{dq}{dt}\right)+\left(\frac{d.qu}{dx}\right)+\left(\frac{d.qv}{dy}\right)+\left(\frac{d.qw}{dz}\right)=0,$$

and then the equation[25] which gives the relation between the elasticity p, the density q and the other property r which, in addition to the density q influences the elasticity p, we shall have five equations encompassing the entire Theory of the motion of fluids.

22. Whatever be the nature of the forces P, Q, R, provided that they are real, it should be noted that $\mathrm{P}dx+\mathrm{Q}dy+\mathrm{R}dz$ is always a total [*réel*] differential of a certain finite and determinate quantity,[26] assuming the three coordinates x, y and z to be variables. Thus, we will always have:

$$\left(\frac{d\mathrm{P}}{dy}\right)=\left(\frac{d\mathrm{Q}}{dx}\right);\quad\left(\frac{d\mathrm{P}}{dz}\right)=\left(\frac{d\mathrm{R}}{dx}\right);\quad\left(\frac{d\mathrm{Q}}{dz}\right)=\left(\frac{d\mathrm{R}}{dy}\right),$$

and if we set this finite quantity equal to S, then, we have

$$d\mathrm{S}=\mathrm{P}dr+\mathrm{Q}dy+\mathrm{R}dz,$$

assuming the time t to be constant for the case in which the forces P, Q, R also vary with time at the same points. The quantity S expresses what I shall call the effort [*l'effort*] of the acting forces[27] and is equal to the sum of the integrals of each force multiplied by the elementary interval in the direction of that force or by the small distance through which it would drag a body subjected to its action. This notion of effort is of the utmost importance for the entire theory of both equilibrium and motion, since it makes it possible to see that the sum of all the efforts is always a maximum or a minimum. This excellent property fits in admirably with the splendid principle of least action whose discovery we owe to our illustrious President, Mr. de Maupertuis.[28]

23. The equations just obtained contain four variables x, y, z and t which are absolutely independent of each other since the variability of the first three extends to all elements of the fluid and that of the fourth to all times. Therefore, for the equations to continue to hold, the other variables u, v, w, p and q must be certain functions of the former. For although a differential equation with two variables[29] is always possible,[30] we know that a differential equation containing three or more variables is possible only under certain conditions, by virtue of which a certain relationship must exist between the terms of the equation. Therefore, before we can begin solving the equations, we need to know what sort of functions of x, y, z and t must be used to express the values of u, v, w, p and q in order for these same equations to be possible.

24. We now multiply the first of the three equations obtained by dx, the second by dy and the third by dz, and since $dx\left(\frac{dp}{dx}\right)+dy\left(\frac{dp}{dy}\right)+dz\left(\frac{dp}{dz}\right)$ represents the differential of p, assuming only time t to be constant, we obtain[31]

$$\begin{aligned}d\mathrm{S}-\frac{dp}{q}=&\\ &+dx\left(\frac{du}{dt}\right)+udx\left(\frac{du}{dx}\right)+vdx\left(\frac{du}{dy}\right)+wdx\left(\frac{du}{dz}\right)\\ &+dy\left(\frac{dv}{dt}\right)+udy\left(\frac{dv}{dx}\right)+vdy\left(\frac{dv}{dy}\right)+wdy\left(\frac{dv}{dz}\right)\\ &+dz\left(\frac{dw}{dt}\right)+udz\left(\frac{dw}{dx}\right)+vdz\left(\frac{dw}{dy}\right)+wdz\left(\frac{dw}{dz}\right).\end{aligned}$$

24 Despite the outward resemblance between Euler's equations and modern notation, they have been written here in dimensionless form. As mentioned above, the pressure p is measured as the ratio of the acting pressure to the specific weight $\rho_0 g$ of a certain homogeneous auxiliary fluid, the density q is dimensionless ($q=\rho/\rho_0$), the components of the body forces have been divided by the acceleration of gravity g, the transition from the Eulerian velocities u, v, w to the real velocities U, V, W is effected by means of a transformation of the form $u\mapsto U/\sqrt{g}$ and the transition from Eulerian time to real time by means of the transformation $t\mapsto T\sqrt{g}$. (For further details concerning Euler's system of physical units, see Mikhailov, 1999.)

25 What we now call the equation of state.

26 Euler is thinking here of real body forces possessing a potential (more correctly, a force function). By "finite" quantities (functions) Euler means quantities that do not contain differentials.

27 Euler's "effort" is equivalent to the modern notion of potential.

28 Maupertuis was president of the Berlin Academy at the time.

29 Here, by variable Euler means both independent variables and their functions.

30 We would now say "soluble".

31 The first term on the r.h.s. is correct in the manuscript Euler, 1755c but misprinted as $dz\left(\frac{du}{dt}\right)$ in the printed version.

It is now a question of finding the integral of this equation in which time is assumed to be constant. It should be noted that this single equation contains the three equations of which it is composed and that as soon as it is satisfied the conditions of all three will be fulfilled. Thus, if the expression $d\mathrm{S} - \frac{dp}{q}$ is equal to the three lines, where x, y and z are variables, the portion of $d\mathrm{S} - \frac{dp}{q}$ due to the variability of x alone, namely $\mathrm{P}dx - \frac{dx}{q}\left(\frac{dp}{dx}\right)$ must necessarily be equal to the first line, and similarly for the other two. The terms $\left(\frac{du}{dt}\right)$, $\left(\frac{dv}{dt}\right)$, and $\left(\frac{dw}{dt}\right)$, found by assuming the variability of time t, since they denote certain finite functions, do not prevent time t from now being taken to be constant.

25. Suppose that this equation has already been solved and the quantities u, v, w, q and p have been found as certain finite functions of x, y, z and t. The substitution of these functions in the differential equation, with time t assumed constant, yields an identity. Since after this substitution we will have three types of terms, the first associated with dx, the second with dy and the third with dz, the identity leads us to three equations whence it is clear that although only one differential equation is being considered, it actually has the force of three and determines three of our unknowns. What is also clear is that a differential equation with three variables, such as $\mathrm{L}dx + \mathrm{M}dy + \mathrm{N}dz = 0$, cannot be solved unless a certain relationship exists between the quantities L, M and N. However, since very little work has yet been done on solving these three-variable equations, we cannot hope to obtain a complete solution of our equation until the limits of Analysis have been extended much further.

26. The best approach would therefore be to ponder well on the particular solutions of our differential equation that we are in a position to obtain, as this would enable us to judge which path to follow in order to arrive at a complete solution. I have already pointed out[32] that where the density q is assumed to be constant a very elegant solution can be obtained when the velocities u, v and w are such that the differential expression [*formule*] $udx + vdy + wdz$ can be integrated. Suppose, then, that W is that integral, being any function of x, y, z and time t, and that its differentiation, also including t as a variable, gives

$$d\mathrm{W} = udx + vdy + wdz + \Pi dt.$$

Then the quantities u, v, w and Π will be related as follows:[33]

$$\left(\frac{du}{dy}\right) = \left(\frac{dv}{dx}\right); \quad \left(\frac{du}{dz}\right) = \left(\frac{dw}{dx}\right); \quad \left(\frac{du}{dt}\right) = \left(\frac{d\Pi}{dx}\right);$$
$$\left(\frac{dv}{dz}\right) = \left(\frac{dw}{dy}\right); \quad \left(\frac{dv}{dt}\right) = \left(\frac{d\Pi}{dy}\right); \quad \left(\frac{dw}{dt}\right) = \left(\frac{d\Pi}{dz}\right).$$

27. Using these equalities, we can reduce our differential equation to the following form:

$$\begin{aligned} d\mathrm{S} - \frac{dp}{q} = {} & \\ & + dx\left(\frac{d\Pi}{dx}\right) + udx\left(\frac{du}{dx}\right) + vdx\left(\frac{du}{dy}\right) + wdx\left(\frac{du}{dz}\right) \\ & + dy\left(\frac{d\Pi}{dy}\right) + udy\left(\frac{dv}{dx}\right) + vdy\left(\frac{dv}{dy}\right) + wdy\left(\frac{dv}{dz}\right) \\ & + dz\left(\frac{d\Pi}{dz}\right) + udz\left(\frac{dw}{dx}\right) + vdz\left(\frac{dw}{dy}\right) + wdz\left(\frac{dw}{dz}\right). \end{aligned}$$

Since here time t is assumed to be constant, using the same hypothesis we will have

$$dx\left(\frac{d\Pi}{dx}\right) + dy\left(\frac{d\Pi}{dy}\right) + dz\left(\frac{d\Pi}{dz}\right) = d\Pi$$
$$dx\left(\frac{du}{dx}\right) + dy\left(\frac{du}{dy}\right) + dz\left(\frac{du}{dz}\right) = du$$
....

Thus, our equation will become

$$d\mathrm{S} - \frac{dp}{q} = d\Pi = udu + vdv + wdw,$$

or

$$dp = q\,(d\mathrm{S} - d\Pi - udu - vdv - wdw)\,.$$

Hence, if the density of the fluid is everywhere the same, or $q = g$, as a result of integration we obtain:[34]

$$p = g\left(\mathrm{C} + \mathrm{S} - \Pi - \frac{1}{2}uu - \frac{1}{2}vv - \frac{1}{2}ww\right).$$

28. For brevity, let us set

$$\mathrm{C} + \mathrm{S} - \Pi - \frac{1}{2}uu - \frac{1}{2}vv - \frac{1}{2}ww = \mathrm{V},$$

where it should be noted that the constant C may well contain the time t, since it is considered to be constant in this integration and, as $dp = qd\mathrm{V}$, it is clear that the hypothesis

$$d\mathrm{W} = udx + vdy + wdz + \Pi dt,$$

also makes our differential equation possible, when the elasticity p depends in any way on the density q only or q is any function of p. It will also become possible if the fluid is not compressible but the density q varies in such a way that it is an arbitrary function of the quantity V. And in general, if the elasticity p depends both on the density q and on some other quantity represented by the letter r, the hypothesis may also be satisfied provided that r is a function of V. In all these cases, for the motion to exist under this hypothesis it is also necessary for the following condition to be satisfied:

$$\left(\frac{dq}{dt}\right) + \left(\frac{d.qu}{dx}\right) + \left(\frac{d.qv}{dy}\right) + \left(\frac{d.qw}{dz}\right) = 0.$$

29. This hypothesis is so general that it seems that there is not a single case that is not included and hence that, generally

[32] Euler, 1756–1757: §§ 60–67.

[33] In modem terminology, the function introduced by Euler $W = W(x, y, z, t)$ is the velocity potential; here, the equality of the cross derivatives of W with respect to the coordinates (condition of integrability of dW) is the condition of absence of vorticity.

[34] The subsequent equation, which generalizes the Bernoulli integral, is usually associated with the names of Cauchy and Lagrange.

speaking, the equation $dp = qd\mathrm{V}$, together with the other equations which present hardly any difficulty, incorporates all the foundations of the Theory of the motion of fluids. Thus, I concerned myself exclusively with this case in my Latin memoir on the laws of fluid motion[35] in which I considered incompressible fluids only and showed that all the cases previously considered, in which the fluid moves through pipes of arbitrary shapes, are contained in this supposition and that the velocities u, v and w are always such that the differential expression $udx + vdy + wdz$ is integrable. However, I have since noted that there are also cases, even when the fluid is incompressible and everywhere homogeneous, in which this condition does not hold, which is enough to convince me that the solution I have just given is only a particular one.[36]

30. To give an example of a real motion which would be perfectly consistent with all the equations that follow from the laws of Mechanics, but without the expression $udx+vdy+wdz$ being integrable, let us assume that the fluid is incompressible and everywhere homogeneous, i.e. that q is constant and equal to g, and that there are no forces acting on the fluid, so that $\mathrm{P} = 0$, $\mathrm{Q} = 0$ and $\mathrm{R} = 0$. Then, let $w = 0$, $v = \mathrm{Z}x$ and $u = -\mathrm{Z}y$, where Z denotes any function of $\sqrt{(xx + yy)}$. It is now obvious that the expression $udx + vdy + wdz$, which takes the form $-\mathrm{Z}ydx + \mathrm{Z}xdy$, is integrable only in the case $\mathrm{Z} = \frac{1}{xx+yy}$. However, these values[37] satisfy all our formulas so that the possibility of this motion cannot be questioned. Since Z is a function of $\sqrt{(xx + yy)}$, its differential will have the form $d\mathrm{Z} = \mathrm{L}xdx + \mathrm{L}ydy$, where L will again be any function of $\sqrt{(xx + yy)}$.

31. Using these values of u, v and w, we obtain:

$$\left(\frac{du}{dt}\right) = 0; \qquad \left(\frac{dv}{dt}\right) = 0; \qquad \left(\frac{dw}{dt}\right) = 0;$$
$$\left(\frac{du}{dx}\right) = -\mathrm{L}xy; \qquad \left(\frac{dv}{dx}\right) = \mathrm{Z} + \mathrm{L}xx; \qquad \left(\frac{dw}{dx}\right) = 0;$$
$$\left(\frac{du}{dy}\right) = -\mathrm{Z} - \mathrm{L}yy; \qquad \left(\frac{dv}{dy}\right) = \mathrm{L}xy; \qquad \left(\frac{dw}{dy}\right) = 0;$$
$$\left(\frac{du}{dz}\right) = 0; \qquad \left(\frac{dv}{dz}\right) = 0; \qquad \left(\frac{dw}{dz}\right) = 0;$$

and since $d\mathrm{S} = 0$, assuming time t to be constant, we have the following differential equation:

$$\begin{aligned}\frac{dp}{g} &= \mathrm{LZ}xyydx - \mathrm{ZZ}xdx \\ &\quad - \mathrm{LZ}xyydx - \mathrm{ZZ}ydy - \mathrm{LZ}xxydy + \mathrm{LZ}xxydy \\ &= -\mathrm{ZZ}(xdx + ydy).\end{aligned}$$

Consequently $dp = g\mathrm{ZZ}(xdx + ydy)$, since Z is assumed to be a function of $\sqrt{(xx + yy)}$, this equation will definitely be possible and will yield the integral $p = g\int \mathrm{ZZ}(xdx + ydy)$. We see that the differential equation would also be possible if the fluid were subjected to the action of certain arbitrary forces P, Q, R, provided that the expression $\mathrm{P}dx + \mathrm{Q}dy + \mathrm{R}dz$ was a total [*possible*] differential equal to $d\mathrm{S}$, since then $p = g\mathrm{S} + g\int \mathrm{ZZ}(xdx + ydy)$.

32. As these values $u = -\mathrm{Z}y$, $v = \mathrm{Z}x$ and $w = 0$ satisfy our differential equation, they can also be seen to satisfy the condition contained in the equation:[38]

$$\left(\frac{dq}{dt}\right) + \left(\frac{d.qu}{dx}\right) + \left(\frac{d.qv}{dy}\right) + \left(\frac{d.qw}{dz}\right) = 0.$$

By virtue of the fact that $q = g$, this equation goes over into

$$-g\mathrm{L}xy + g\mathrm{L}xy = 0$$

which, being an identity, satisfies the required conditions. Thus, it is quite possible for a fluid to have a motion such that the velocities of each of its elements are $u = -\mathrm{Z}y$, $v = \mathrm{Z}x$ and $w = 0$, although the differential expression $udx + vdy + wdz$ is not possible;[39] this confirms that there are cases in which fluid motion is possible without this condition, which seemed general, being fulfilled. Thus, the assumption that the differential expression $udx+vdy+wdz$ is possible yields only a particular solution of the equations we have found.

33. Clearly, the motion corresponding to this case reduces to a rotational motion about the axis OC and since what has been said about the axis OC can be applied to any other fixed axis, we may conclude that it is possible for a fluid acted upon by any forces whose effort[40] is equal to S to have a motion about a fixed axis such that the rotational velocities are proportional to any function of the distance to that axis. Thus, if the distance to that axis is denoted by s and the rotation velocity at that distance by ℧,[41] then since $xx + yy = ss$ and $\mathrm{ZZ}ss = ℧℧$, the pressure there will be expressed by the height $p = g\mathrm{S} + g\int \frac{℧℧ ds}{s}$. Thus, such a motion, which corresponds to that of a vortex [*tourbillon*], is just as possible as those contained in the expression $udx + vdy + wdz$ when the latter is integrable. No doubt there is an infinity of other motions, which satisfying our equations, are also equally possible.

34. Let us now return to our general formulas and, since they are somewhat too complicated, introduce, for greater conciseness, the notation:

$$\left(\frac{du}{dt}\right) + u\left(\frac{du}{dx}\right) + v\left(\frac{du}{dy}\right) + w\left(\frac{du}{dz}\right) = \mathrm{X}$$
$$\left(\frac{dv}{dt}\right) + u\left(\frac{dv}{dx}\right) + v\left(\frac{dv}{dy}\right) + w\left(\frac{dv}{dz}\right) = \mathrm{Y}$$
$$\left(\frac{dw}{dt}\right) + u\left(\frac{dw}{dx}\right) + v\left(\frac{dw}{dy}\right) + w\left(\frac{dw}{dz}\right) = \mathrm{Z}.$$

[35] See Euler, 1756–1757.

[36] Here, Euler recognizes that his previous memoir on fluid motion was too restricted, in so far as it ignored what we now call vorticity.

[37] The corresponding values of u, v and w.

[38] Strictly speaking, it cannot be said that the values of u, v and w assumed in § 30 also satisfy the equation of motion from § 31; in reality, this equation determines the corresponding pressure $p = p(s)$ $(s = \sqrt{(xx + yy)}$, the continuity equation being satisfied irrespective of the equations of motion.

[39] That is a total differential.

[40] See footnote 27.

[41] In modern terms Z is the angular velocity at the radial distance s and ℧ $= \mathrm{Z}s$ is the tangential velocity.

Whatever the nature of the three accelerative forces P, Q and R, granted that[42] $dS = Pdx + Qdy + Rdz$, the differential equation

$$\frac{dp}{q} = (P - X)\,dx + (Q - Y)\,dy + (R - Z)\,dz,$$

in which t is assumed to be constant must be satisfied. Moreover, the continuity of the fluid requires that:

$$\left(\frac{dq}{dt}\right) + \left(\frac{d.qu}{dx}\right) + \left(\frac{d.qv}{dy}\right) + \left(\frac{d.qw}{dz}\right) = 0.$$

In whatever manner these two equations are satisfied, there will always be a motion which can actually take place in the fluid.

35. If the fluid is everywhere incompressible and homogeneous, i.e. the density q is constant and equal to g, then, clearly, the differential equation cannot be satisfied unless the differential

$$(P - X)dx + (Q - Y)dy + (R - Z)dz,$$

is possible or total, i.e. unless it can be obtained as a result of the actual differentiation of some finite function of the variables x, y and z, which may also contain the time t, although in the differentiation the latter is assumed to be constant. It is also obvious that this differential expression must be soluble or total when the fluid is compressible and the density q is expressed in terms of any function of the elasticity p. In both cases, if we denote by V the finite quantity whose differential has the form:

$$dV = (P - X)dx + (Q - Y)dy + (R - Z)dz,$$

our differential equation will yield either $\frac{p}{g} = V$ or $\int \frac{dp}{q} = V$. In addition, however, for the motion to be possible the other condition derived from the continuity must also be fulfilled.

36. If the fluid is not incompressible, but its density q is variable and can be expressed in terms of any function of position, i.e. of the three coordinates x, y, z and time t, it is not sufficient for the expression

$$(P - X)dx + (Q - Y)dy + (R - Z)dz = dV,$$

to be integrable; in addition, the integral V must be a function of q. Since $\frac{dp}{q} = dV$ or $dp = qdV$, it is clear that the pressure p cannot have a definite value unless the expression qdV can be integrated. However, it should also be noted that in this case it is not necessary that the expression

$$(P - X)dx + (Q - Y)dy + (R - Z)dz$$

be integrable, only that on being multiplied by a certain function U it becomes integrable. Thus, let

$$U(P - X)dx + U(Q - Y)dy + U(R - Z)dz = dW,$$

since $\frac{dp}{q} = \frac{dW}{U}$, or $dp = \frac{qdW}{U}$ for this equation to be possible it is sufficient that W be a function of $\frac{q}{U}$, or that W be a function of zero dimension of the quantities q and U.[43]

[42] Here, Euler assumes that all real body forces have a potential $S = S(x, y, z)$.

[43] This latter expression is equivalent, in 18th century terminology, to the condition that W should depend only on the ratio q/U.

37. In general, however the elasticity p depends on the density q or on some other property denoted by r which is any function of the coordinates x, y, z that could also contain time t, it is clear from our equation $q = \frac{dp}{dV}$ that the differential dp must always be divisible by dV, where dV denotes not so much a total differential than the expression

$$(P - X)dx + (Q - V)dy + (R - Z)dz,$$

and this so much that, as a result of division the differentials dx, dy and dz are entirely eliminated from the calculations, because both p and q must always be expressed in terms of finite functions of the variables x, y and z, without their differentials entering into these functions. Now this could not be so unless there were a function U, multiplication by which rendered the expression dV integrable: indeed, setting $\int UdV = W$, clearly, p must be a function of W in order for the expression $\frac{dp}{dV}$ to take a definite value corresponding to the density q.

38. Since $U\,dV = dW$, we have $q = \frac{Udp}{dW}$. Consequently, if we choose W to be any function of the coordinates x, y and z, which contains time t among the constants, and if we set p equal to any function of W, namely[44] $p = \varphi, W$, and $dp = dW.\varphi', W$, we will have $q = U.\varphi', W$, whence $U = \frac{q}{\varphi', W}$. Thus, in whatever way the density q is expressed in terms of the elasticity p and some other function r of the coordinates x, y and z, we obtain the value $U = \frac{q}{\varphi', W}$ and, consequently, the value $dV = \frac{dW.\varphi', W}{q}$, which then gives us the following equation:

$$(P - X)dx + (Q - V)dy + (R - Z)dz = \frac{dW.\varphi', W}{q} = \frac{dp}{q}.$$

This will yield the values of X, Y, Z, from which we must then look for the values of the velocities u, v and w: and when the latter also satisfy the continuity condition, we shall have a case of possible motion of the fluid.

39. The question of the nature of the expression $(P-X)dx + (Q-Y)dy + (R-Z)dz$ then reduces to the following. When the density q is constant or depends only on the elasticity p, this expression must be absolutely integrable and to this end one must determine suitable values of the three velocities u, v and w.When the density q depends on a given function of place and time,[45] the expression must be such that it becomes integrable on multiplication by some given function U. In both cases, then, the velocities u, v and w must be such that the equation

$$(P - X)dx + (Q - Y)dy + (R - Z)dz = 0$$

be soluble;[46] and we know the conditions under which a differential equation with three variables is soluble; having

[44] For representing the functional dependence, now denoted $f(x)$, Euler used the notation f, x or $f : x$. For example Euler's φ, W and φ', W would now be denoted $\varphi(W)$ and $\varphi'(W)$. In Euler, 1755c, the comma is omitted.

[45] The function r.

[46] Indeed, if $\Phi(x, y, z) = \text{Cnst.}$ is the general integral of this equation, then the form $(P - X)dx + (Q - Y)dy + (R - Z)dz$ must vanish whenever the differential $d\Phi$ vanishes; hence the two forms are proportional, which means that there exists an integrating factor for the first form.

satisfied these conditions, it remains to satisfy that imposed by continuity.

40. These are the conditions which restrict the functions expressing the three velocities u, v and w, and the study of the motion of fluids reduces to determining, in general form, the nature of those functions such that the conditions of our differential equation and of continuity be fulfilled. Since the quantities X, Y and Z depend not only on the velocities u, v and w themselves but also on their variability with respect to each of the coordinates x, y and z and, moreover, on time t, this study would appear to be the most far-reaching of those to be encountered in the field of Analysis, and if we are unable to achieve a complete understanding of the motion of fluids, it is not Mechanics or the inadequacy of the known laws of motion but Analysis itself that is to blame, given that the entire Theory of the motion of fluids has just been reduced to the solution of analytical equations.

41. Since a general solution must be deemed impossible due to the shortcomings of Analysis, we must content ourselves with the consideration of certain particular cases, especially as the study of several cases seems to be the only means of perfecting our knowledge. Now the simplest case imaginable is, no doubt, that in which the three velocities u, v and w are set equal to zero, namely the case in which the fluid remains at perfect rest and which I dealt with in my previous Memoir.[47] The formulas we have obtained for motion in general also include the case of equilibrium, since when $\mathrm{X} = 0$, $\mathrm{Y} = 0$ and $\mathrm{Z} = 0$ we have: $\frac{dp}{q} = \mathrm{P}dx + \mathrm{Q}dy + \mathrm{R}dz$, and $\left(\frac{dq}{dt}\right) = 0$, from which it follows, first of all, that the density q cannot depend on time t, i.e. should remain always the same at the same place. Furthermore, the forces P, Q and R must be such that the differential expression $\mathrm{P}dx + \mathrm{Q}dy + \mathrm{R}dz$ either is integrable, when q is constant or depends only on the elasticity p, or becomes integrable upon being multiplied by a suitable function.

42. In my Memoir on fluid equilibrium[48] I only considered cases of the acting forces P, Q, R for which the differential expression $\mathrm{P}dx + \mathrm{Q}dy + \mathrm{R}dz$ is integrable, since this seemed to be the only case that could occur in Nature. In fact, if the density q is either constant or depends only on the pressure p, the fluid could never be in equilibrium unless this condition relating to the acting forces is satisfied. However, if it were possible for the acting forces to obey some other law, there could be equilibrium provided that the forces were such that there existed some function U which when multiplied by the expression $\mathrm{P}dx + \mathrm{Q}dy + \mathrm{R}dz$ made that expression integrable, or, equivalently, provided that the differential equation $\mathrm{P}dx + \mathrm{Q}dy + \mathrm{R}dz = 0$ were integrable; for then if the density q is equated to this function U or to the product of this function U and some arbitrary function of the elasticity p, equilibrium may also exist. However, since these cases may not be possible, I shall not consider them in greater detail.

[47] Euler, 1755a.
[48] Euler, 1755a.

43. After the case of equilibrium, the simplest state that could exist in a fluid is that in which the entire fluid is in uniform motion in the same direction. Let us see, then, how this state is described by our two formulas. In this case, the three velocities being constant, we set $u = a$, $v = b$ and $w = c$; we have $\mathrm{X} = 0$, $\mathrm{Y} = 0$ and $\mathrm{Z} = 0$. Then our two equations assume the form:

$$\frac{dp}{q} = \mathrm{P}dx + \mathrm{Q}dy + \mathrm{R}dz,$$
$$\left(\frac{dq}{dt}\right) + a\left(\frac{dq}{dx}\right) + b\left(\frac{dq}{dy}\right) + c\left(\frac{dq}{dz}\right) = 0,$$

and hence it is clear that if the density q is constant, the condition of the second equation is satisfied; however, the first equation cannot be satisfied unless the expression $\mathrm{P}dx + \mathrm{Q}dy + \mathrm{R}dz$ admits integration, just as if the fluid were at rest. Of course, such motion can have no effect on the pressure.

44. If, however, the density q is not constant, let us first see what function of x, y, z and t it must be for the second equation to be satisfied. This leads us to the curious analytical question of what function of the variables x, y, z and t must be taken for q in order that:

$$\left(\frac{dq}{dt}\right) + a\left(\frac{dq}{dx}\right) + b\left(\frac{dq}{dy}\right) + c\left(\frac{dq}{dz}\right) = 0.$$

This would appear to be very difficult to answer if formulated in its broadest possible form. However, since when $a = 0$, $b = 0$, $c = 0$ the quantity q is any function of x, y, z that does not contain time t, if we reduce this case[49] to that of rest by imposing on the volume an equal and opposite motion, then, clearly, after time t the coordinates x, y and z will be transformed by the change into $x - at$, $y - bt$, $z - ct$. From this we conclude that our equation will be satisfied if as q we take any function of the three quantities $x - at$, $y - bt$, $z - ct$.[50] And in fact it is easy to see that such a function satisfies the equation, since

$$dq = \mathrm{L}(dx - a\,dt) + \mathrm{M}(dy - b\,dt) + \mathrm{N}(dz - c\,dt),$$

and, consequently,

$$\left(\frac{dq}{dt}\right) = -a\mathrm{L} - b\mathrm{M} - c\mathrm{N}; \quad \left(\frac{dq}{dx}\right) = \mathrm{L};$$
$$\left(\frac{dq}{dy}\right) = \mathrm{M}; \quad \text{and} \quad \left(\frac{dq}{dz}\right) = \mathrm{N}.$$

45. Now, as I have already noted, in order to satisfy the first equation it is necessary that after multiplication by some function U the differential expression $\mathrm{P}dx + \mathrm{Q}dy + \mathrm{R}dz$ be integrable. Therefore let $\int \mathrm{U}(\mathrm{P}dx + \mathrm{Q}dy + \mathrm{R}dz) = \mathrm{W}$, where the constant of integration also in some way contains time t. Clearly, the expression $\mathrm{P}dx + \mathrm{Q}dy + \mathrm{R}dz$ will also be integrable if it is multiplied by $\mathrm{U}f, \mathrm{W}$,[51] where U and W are known functions, since the acting forces are assumed to be known.

[49] The case of motion.
[50] Here Euler performs a Galilean transformation.
[51] The equivalent modern notation would be $\mathrm{U}f(\mathrm{W})$, cf. footnote 44.

Thus, if q does not depend on p, then necessarily $q = \mathrm{U}f, \mathrm{W}$, whence the function of the three quantities $x - at$, $y - bt$ and $z - ct$ must be so determined that it can be reduced to the form $\mathrm{U}f, \mathrm{W}$. If, however, q depends only on p, the expression $\mathrm{P}dx + \mathrm{Q}dy + \mathrm{R}dz$ must be absolutely integrable or $\mathrm{U} = 1$; then, since p will be found in the form of a function of W, the density q will likewise be a function of W, which must also be a function of the quantities $x - at$, $y - bt$ and $z - ct$, and from this we can deduce the nature of this function.

46. However, it can be seen that, in general, the pressure p must always be a function of W, since otherwise the density could not be a finite function. Therefore let $p = f, \mathrm{W}$ and $dp = d\mathrm{W}.f', \mathrm{W}$; then, by virtue of the fact that $\mathrm{P}dx + \mathrm{Q}dy + \mathrm{R}dz = \frac{d\mathrm{W}}{\mathrm{U}}$, we obtain $q = \mathrm{U}f', \mathrm{W}$. Consequently, this case could not arise unless the density q was proportional to the product of the quantity U and a function of the pressure p or to the product of the quantity $\mathrm{U}\varphi, \mathrm{W}$ and any function of p, where φ, W is used to denote a given function of W. For example, let $q = pp\mathrm{U}\varphi, \mathrm{W}$; we then have $f', \mathrm{W} = \frac{d(f,\mathrm{W})}{d\mathrm{W}} = (f, \mathrm{W})^2\varphi, \mathrm{W}$,[52] whence we find that the unknown function f, W is composed of W, for in this example we have $\frac{1}{f,\mathrm{W}} = -\int d\mathrm{W}, \varphi\mathrm{W} = \frac{1}{p}$ and hence p can be expressed in terms of W and thus, the quantity q will also be known. When the latter can be reduced to the form of a function of $x - at$, $y - bt$ and $z - ct$, the assumed state of the fluid will be possible and we shall know the pressure and the density at any time and at any point.

47. An example[53] will throw more light on these operations which, as they are not yet sufficiently familiar, might appear overly obscure. Thus, let $\mathrm{P} = y$, $\mathrm{Q} = -x$ and $\mathrm{R} = 0$; since $\frac{dp}{q} = ydx - xdy$, we obtain $\mathrm{U} = \frac{1}{yy}$ and $\mathrm{W} = \frac{x}{y} + \mathrm{T}$, where T is any function of time t. Moreover, let $q = \frac{pp}{yy}$; since $\frac{dp}{pp} = \frac{ydx - xdy}{yy}$, we shall obtain $\frac{1}{p} = \Theta - \frac{x}{y}$, and $p = \frac{y}{\Theta y - x}$, where the constant Θ also contains time t. As a result, we have $q = \frac{1}{(\Theta y - x)^2}$, and this expression must be a function of $x - at$ and $y - bt$, since z does not enter into it and this is only possible when $\Theta = \frac{a}{b}$; we then have $q = \frac{bb}{(ay - bx)^2}$, and $p = \frac{by}{ay - bx}$. Thus, neither the pressure nor the density depends on time and at a given point will be always the same. This example shows how the calculations should be performed in other cases that might be imagined.

48. Having dealt with this case in which the three velocities are constant, let us now assume that two velocities u and v vanish, which corresponds to the case in which all the fluid particles move in the direction of the OA axis, so that the trajectory described by each is a straight line[54] parallel to the OA axis; this case differs from the previous one, since the velocity u is assumed to vary with respect to both place and time. Since

$$\mathrm{X} = \left(\frac{du}{dt}\right) + u\left(\frac{du}{dx}\right); \quad \mathrm{Y} = 0; \quad \mathrm{Z} = 0,$$

our two equations will take the form:

$$\frac{dp}{q} = \mathrm{P}dx + \mathrm{Q}dy + \mathrm{R}dz - dx\left(\frac{du}{dt}\right) - udx\left(\frac{du}{dx}\right),$$

$$\& \left(\frac{dq}{dt}\right) + \left(\frac{d.qu}{dx}\right) = 0.$$

This latter equation tells us, first of all, that the expression $qdx - qudt$ must be integrable, the quantities y and z being considered constant with respect to this integration. Thus, the product of q and $dx - udt$ must be a total differential, i.e. must be integrable.

49. If the density of the fluid is everywhere and always the same, i.e. if q is a constant equal to g, then, since $\left(\frac{du}{dx}\right) = 0$, it is clear that the velocity u must be independent of the variable x. Let u be any function of the two coordinates y, z and time t. Then our differential equation will take the form:

$$\frac{dp}{q} = \mathrm{P}dx + \mathrm{Q}dy + \mathrm{R}dz - dx\left(\frac{du}{dt}\right),$$

where time t is assumed to be constant; thus, this expression must be integrable. Accordingly, if the expression $\mathrm{P}dx + \mathrm{Q}dy + \mathrm{R}dz$ obtained from considering the acting forces is integrable in itself, then $dx\left(\frac{du}{dt}\right)$ must also be integrable. The expression $\left(\frac{du}{dt}\right)$ does not contain x, but if it were to contain y and z, the expression $dx\left(\frac{du}{dt}\right)$ could not be integrable. Thus, $\left(\frac{du}{dt}\right)$ must not contain y and z. Let Z be any function of y and z, and T any function of time t only; then the quantity $u = \mathrm{Z} + \mathrm{T}$ will satisfy this condition, whence by virtue of the fact that $\mathrm{P}dx + \mathrm{Q}dy + \mathrm{R}dz = d\mathrm{V}$ and $\left(\frac{du}{dt}\right) = \left(\frac{d\mathrm{T}}{dt}\right)$, we obtain the following integral: $\frac{p}{q} = \mathrm{V} - x\left(\frac{d\mathrm{T}}{dt}\right) + \mathrm{Cnst}$.

50. As a further clarification of this case, it should be noted that each fluid particle Z moves exclusively in the direction ZP parallel to the ZA axis and hence the motion of each fluid element will describe a straight line parallel to that axis, so that for the same element there is no change in the values of the two coordinates y and z. Thus, the motion of each particle will either be uniform or will vary with time in such a way that at each instant all the particles undergo the same changes in their motions, which is obvious from the equation $u = \mathrm{Z} + \mathrm{T}$. As to the state of pressure, given that we have $p = g\mathrm{V} - gx\left(\frac{d\mathrm{T}}{dt}\right) + \mathrm{Cnst}$. where the constant has any dependence on time t, it depends not only on the effort[55] V but also on the change of velocity undergone by each element of the fluid; and, moreover, it may vary in any way with time.

51. This case provides me with an opportunity to deal with certain questions which naturally arise and whose clarification is of the utmost importance for the theory of both fluid equilibrium and fluid motion. First of all, surprisingly, a change in the velocity of the fluid can occur without the acting forces P, Q, R helping to produce it. Since such a change could take place even when the acting forces vanish, it is reasonable to inquire how it is produced. Next, it also seems paradoxical that the pressure can vary arbitrarily at any instant, and that irrespective

52 The equivalent modern form would be $f'(\mathrm{W}) = df(\mathrm{W})/d\mathrm{W} = f^2(\mathrm{W})\varphi(\mathrm{W})$.

53 In this example forces are considered which do not derive from a potential and the integrating factor U is found for these forces.

54 This is the case of the so-called shear flow.

55 See footnote 27.

of the aforesaid change to which the motion is subjected. The latter difficulty remains even in the state of equilibrium. Thus, letting the three velocities u, v, w vanish, for incompressible fluids we have the integral $\frac{p}{g} = \mathrm{V} + \mathrm{Cnst.}$, where the constant may contain the time t in any way.

52. To understand this more clearly, one need only imagine a certain mass enclosed in a vessel. Clearly, the state of pressure depends not only on the acting forces but also on any extraneous forces which might be exerted on the vessel. For, even if there were no acting forces, by means of a piston applied to the fluid one could successively produce every possible state of pressure without the equilibrium being disturbed. This is precisely what we can conclude from our formula, which in this case shows that $\frac{p}{g}$ is a function of time t. From this we see that the state of pressure may vary at any instant, irrespective of the equilibrium. However, if for each instant of time the pressure at any point is known, then the pressures at all the other points can be determined, and since the force applied to the piston might now increase and now decrease, the calculations must reflect all these possible changes. The same variability should also be observed when the fluid is subjected to the action of arbitrary accelerative forces, so that at each instant the state of pressure is indeterminate and depends on the force then acting on the piston.

53. Here, then, is a vital difference between the accelerative forces, which act on all the elements of the fluid, and the force of a piston that presses on the fluid. Only the accelerative forces enter into our differential equation, while the piston force enters into the calculations only after integration and only affects the constant of integration. Consequently, in each case the constant must be so determined that at the point at which the piston acts the pressure is exactly equal to the force driving the piston at each instant, and it is for this reason that the constant contains time, so that it can be varied with time at will, as the circumstances require. This variability can always be represented by the action of a piston since, whatever the nature of the case considered, for it to be determined it must always be assumed that at one point at least in the fluid the pressure is known at every instant, and it is precisely this which makes it possible to determine the constant introduced into the calculations through the integration of our differential equation.

54. However, in our case of the motion considered in § 49, let us also assume that the accelerative forces vanish, i.e. that $\mathrm{V} = 0$, and to make this case perfectly determinate, let us assume that $u = a + \alpha y + \beta t$.[56] Then the equation for the pressure will take the form $\frac{p}{g} = \mathrm{Cnst.} - \beta x$. Let us assume, moreover, that this constant is equal to $\gamma + \delta t$, so that $\frac{p}{g} = \gamma + \delta t - \beta x$, and let us see under what conditions this motion can take place. Since each fluid element moves in the direction of the OA axis, the motion could only take place in a cylindrical pipe laid in the same direction. Let ABIO (Fig. 4) be that pipe and initially, at $t = 0$, let the fluid occupy the portion ABCD bounded by cross sections AB and CD perpendicular to the pipe. We will reckon

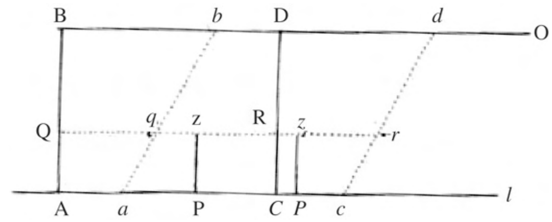

Fig. 4.

the abscissas from the point A along the straight line AI and let the pressure p be equal to γg everywhere along the base AB and to $\gamma g - \beta g.\mathrm{AC}$ along the other base CD. In the interior of the fluid, however, at any point Z with the coordinates $\mathrm{AP} = x$, $\mathrm{PZ} = y$, the pressure will be equal to $\gamma g - \beta g x$. Consequently, it is impossible to consider the fluid in the pipe beyond CD, taking $\mathrm{AC} = \frac{\gamma}{\beta}$, so that the pressure at CD does not become negative.

55. Let us set for this determinate fluid mass the length $\mathrm{AC} = b$ and the width $\mathrm{AB} = \mathrm{CD} = c$, the height not entering into consideration since neither the velocities nor the pressures depend on the third coordinate z; when $\gamma = \beta b$, in the initial state ABCD the pressure is equal to $\beta b g$ on the base AB and zero on the base CD, while at any point Z it is equal to $\beta g(b - x) = \beta g.\mathrm{CP}$. We will assume that in this state the fluid has a motion in the direction of the pipe such that the velocity on the line AC is equal to a and that on the line BD equal to $a + \alpha c$, while on any line QR parallel to the direction of the pipe it is equal to $a + \alpha y$, where $\mathrm{AQ} = \mathrm{CR} = y$. Thus, we believe that something has caused this motion to be impressed on the fluid and that, at the initial instant, the surface AB is subjected to the said force $\beta b g$, exerted by means of a piston, while the other base CD is not subjected to any pressure. However, at subsequent moments of time the forces acting on the end faces could vary arbitrarily. Now this variability is determined by the hypotheses we have just established. Therefore let us see how by virtue of these hypotheses the motion of the fluid will be continued.

56. After the lapse of a time t, all the fluid elements on the line QR will have a velocity in that same direction equal to $a + \alpha y + \beta t$, as a result of which in the time dt they will travel a distance $(a + \alpha y + \beta t)dt$; thus, from the beginning of the motion they will have traveled a distance $at + \alpha yt + \frac{1}{2}\beta tt$; and the alignment of fluid particles[57] initially at QR will now have advanced to qr, having traversed the distance $\mathrm{Q}q = at + \alpha yt + \frac{1}{2}\beta tt$. Thus, the thread AC will have arrived at ac, having traveled a distance $\mathrm{A}a = at + \frac{1}{2}\beta tt$, while the thread BD will have arrived at bd, having traveled a distance $\mathrm{B}b = at + \alpha ct + \frac{1}{2}\beta tt$, so that the fluid mass will now be bounded by the faces ab and cd, which are straight but inclined to the direction of the pipe. The pressure on the face ab at q must now be $g(\beta b + \delta t - \beta.\mathrm{Q}q) = g(\beta b + \delta t - \beta at - \alpha\beta yt - \frac{1}{2}\beta\beta tt)$,

[56] In Euler, 1755b the symbol β is used in the r.h.s. of this equation; in the printed version it is replaced by a symbol resembling a capital C with curled ends.

[57] Euler uses "filée du fluide" where "filée" is a somewhat poetic variant of "file" (alignment, file) or "fil" (thread); this is just a line of fluid elements and not what is now called a fillet of fluid, the latter having also an infinitesimal width, a concept introduced by Euler, 1745 (see Grimberg et al., 2008).

and on the face cd at r it must now be $g(\beta b + \delta t - \beta.\mathrm{Q}r) = g(\delta t - \beta at - \alpha\beta yt - \frac{1}{2}\beta\beta tt)$. Thus, we need to visualize pistons which act with these forces on the two end faces ab and cd, and since the pressures are not the same over the entire length of these faces, the pistons must be imagined as being flexible and pliable enough to exert such pressures.

57. This motion would remain the same if in integrating the pressure p we were to take any function of t instead of δt, but then the state of pressure in the fluid mass would be different at each instant of time, even though the assumed motion of the fluid itself would not be affected in any way. Thus, let us set $\delta t = \beta at + \alpha\beta ct + \frac{1}{2}\beta\beta tt$; after a time t the pressure at any point q on the face ab will be $g[\beta b + \alpha\beta(c-y)t]$, and at any point z on the line qr it will be equal to $g[\beta b + \alpha\beta(c-y)t - \beta.qz]$; therefore the pressure at the other end r will be $\alpha\beta g(c-y)t$. Hence, on the face ab the pressure will be equal to $\beta g(b + \alpha ct)$ at a and to βgb at b, while on the other face cd the pressure will be equal to $\alpha\beta gct$ at c and to zero at d. Moreover, each thread QR will move in its own direction with uniform acceleration, i.e. will receive equal increments of velocity in equal times. The study of this particular case could serve to elucidate the calculations to be made in all other cases.

58. Let us now return to the case proposed (§ 48) and assume the density q to be constant and equal to g, while making the forces P, Q, R such that the fluid could never be in equilibrium. To this end, let $\mathrm{P} = 0$, $\mathrm{Q} = -\frac{x}{a}$ and $\mathrm{R} = -\frac{x}{a}$ and let $u = b + \frac{(y+z)t}{a}$, so that we have $\left(\frac{du}{dx}\right) = 0$ and $\frac{dp}{g} = -\frac{xdy+xdz}{a} - \frac{ydx+zdx}{a}$,[58] whence by integration we obtain $\frac{p}{g} = \mathrm{Cnst.} - \frac{xy+xz}{a}$, where the constant may contain time in any way. Thus, it is not possible for the entire fluid mass ever to remain at rest, since even if we set $b = 0$ in order to have the fluid at rest at the outset when $t = 0$, immediately after that first instant it would be agitated and only the elements for which $y = 0$ or $z = 0$ or $y + z = 0$ would remain at rest; all the others would be set in motion either forward or backward, depending on whether $y + z$ was positive or negative. It is also easy to determine the pressures required to maintain the assumed motion.

59. Let, however, the density be no longer constant but variable, i.e. let the fluid be compressible. Then in order for the expression $qdx - qudt$ to be a total differential we can take for u any function of the variables x, y, z and t. Here, since only x and t are regarded as variable, while y and z are taken constant, it will always be possible to assign a quantity s such that $s(dx - udt)$ is integrable. Let S be that integral; then this condition will be satisfied if we take $q = sf : \mathrm{S}$.[59] Furthermore, it is now necessary that the following differential be integrable:

$$\frac{dp}{q} = \mathrm{P}dx + \mathrm{Q}dy + \mathrm{R}dz - dx\left(\frac{du}{dt}\right) - udx\left(\frac{du}{dx}\right).$$

Note that if the forces P, Q, R were to vanish, the pressure p would become a function of x and t and hence the quantity $q\left(\left(\frac{du}{dt}\right) + u\left(\frac{du}{dx}\right)\right)$ would only involve the two variables x and t, from which the nature of the function u must be determined, insofar as it involves y and z.

60. Although I have assumed that $v = 0$ and $w = 0$, these formulas cover all the cases in which all the fluid particles always move in the same direction, the only requirement being that the OA axis be taken in that direction. Therefore we will also be able to solve our equations when the direction of motion is inclined to the three axes, which cannot fail to throw further light on the analysis. To this end, let us consider the true velocity of any fluid particle Z and let that velocity be equal to $\Taurus$, and since its direction is given with respect to the three axes, the velocity components will hold certain ratios to it. Let $u = \alpha\Taurus$, $v = \beta\Taurus$ and $w = \gamma\Taurus$; setting $d\Taurus = \mathrm{K}dt + \mathrm{L}dx + \mathrm{M}dy + \mathrm{N}dz$, we shall have

$$\begin{aligned}
\mathrm{X} &= \alpha\mathrm{K} + \alpha\alpha\mathrm{L} + \alpha\beta\mathrm{M} + \alpha\gamma\mathrm{N}\\
\mathrm{Y} &= \beta\mathrm{K} + \alpha\beta\mathrm{L} + \beta\beta\mathrm{M} + \beta\gamma\mathrm{N}\\
\mathrm{Z} &= \gamma\mathrm{K} + \alpha\gamma\mathrm{L} + \beta\gamma\mathrm{M} + \gamma\gamma\mathrm{N}.
\end{aligned}$$

Consequently, if, for conciseness, we write $\mathrm{K} + \alpha\mathrm{L} + \beta\mathrm{M} + \gamma\mathrm{N} = \mathrm{O}$, having $\mathrm{X} = a\mathrm{O}$, $\mathrm{Y} = \beta\mathrm{O}$, $\mathrm{Z} = \gamma\mathrm{O}$, our equations will take the form:

$$\frac{dp}{q} = \mathrm{P}dx + \mathrm{Q}dy + \mathrm{R}dz - \mathrm{O}(\alpha dx + \beta dy + \gamma dz)$$

$$\left(\frac{dq}{dt}\right) + \alpha\left(\frac{d.q\Taurus}{dx}\right) + \beta\left(\frac{d.q\Taurus}{dy}\right) + \gamma\left(\frac{d.q\Taurus}{dz}\right) = 0.$$

61. First, let the density $q = g$. As we have seen in § 44, in order to satisfy the equation $\alpha\left(\frac{d\Taurus}{dx}\right) + \beta\left(\frac{d\Taurus}{dy}\right) + \gamma\left(\frac{d\Taurus}{dz}\right) = 0$ the quantity $\Taurus$ must be any function of the quantities $\alpha y - \beta x$ and $\alpha z - \gamma x$ or $\beta z - \gamma y$ and, in addition, may in an arbitrary way contain time t. Thus, let $\Taurus$ be any function of the quantities $\alpha y - \beta x$, $\alpha z - \gamma x$, and t, since the expression $\beta z - \gamma y$ has already been formed from the other two. From this it is easy to see that at each instant the velocity of particles on the same straight line parallel to the direction of motion will be everywhere the same, just as the nature of the hypothesis requires. Hence the differential of $\Taurus$ will have the following form:

$$d\Taurus = \mathrm{F}dt + \mathrm{G}(\alpha dy - \beta dx) + \mathrm{H}(\alpha dz - \gamma dx),$$

so that $\mathrm{K} = \mathrm{F}$; $\mathrm{L} = -\beta\mathrm{G} - \gamma\mathrm{H}$; $\mathrm{M} = \alpha\mathrm{G}$; and $\mathrm{N} = \alpha\mathrm{H}$. Consequently, $\mathrm{O} = \mathrm{F}$ is a function of $\alpha y - \beta x$, $\alpha z - \gamma x$ and of t. Hence the differential equation, which remains to be solved, will be :

$$\frac{dp}{q} = \mathrm{P}dx + \mathrm{Q}dy + \mathrm{R}dz - \mathrm{F}(\alpha dx + \beta dy + \gamma dz).$$

62. The time t being here assumed constant, if the expression $\mathrm{P}dx + \mathrm{Q}dy + \mathrm{R}dz = d\mathrm{V}$ is integrable in itself, the other part of the equation $\mathrm{F}(\alpha dx + \beta dy + \gamma dz)$ must be likewise, and this could not be so unless F were a function of $\alpha x + \beta y + \gamma z$ and of time t. In addition, however, F must must also be a function of the quantities $\alpha y - \beta x$, $\alpha z - \gamma x$ and time t; consequently, since the expression $\alpha x + \beta y + \gamma z$ cannot be formed from the expressions $\alpha y - \beta x$ and $\alpha z - \gamma x$, it is clear that the quantity

[58] In the printed version the two fractions in the r.h.s. have a minus instead of a correct plus in the numerator; in the manuscript Euler, 1755c, the handwritten notation is ambiguous.

[59] This equation would now be written $q = sf(\mathrm{S})$.

F must be a function of time t only. Consequently, the velocity $\mho$ will have the form $\mho = \mathrm{Z} + \mathrm{T}$, where Z denotes an arbitrary function of the two quantities $\alpha y - \beta x$ and $\alpha z - \gamma x$ that does not contain time t, while T is an arbitrary function of time t only, so that $d\mathrm{T} = \mathrm{F}dt$. Hence the integral of our differential equation will be $\frac{p}{g} = \mathrm{V} - \mathrm{F}(\alpha x + \beta y + \gamma z) + \mathrm{Cnst.}$, where the constant may contain time t in an arbitrary way. Together with the relation $\mho = \mathrm{Z}+\mathrm{T}$, this integral contains everything relating to the motion in the case in question.

63. But if the density q is not constant, it will be important to obtain the solution of the following equation:

$$\left(\frac{dq}{dt}\right) + \alpha\left(\frac{d.q\mho}{dx}\right) + \beta\left(\frac{d.q\mho}{dy}\right) + \gamma\left(\frac{d.q\mho}{dz}\right) = 0.$$

However difficult this may appear, reduction to the previous case shows that the velocity $\mho$ can be an arbitrary function of the four variables x, y, z and t, while the value of q must be determined as follows. Let us consider, generally, an expression

$$s(ldx + mdy + ndz - \mho dt) = d\mathrm{S},$$

which has become integrable after multiplication by s, and let $q = sf : \mathrm{S}$; then, if we set $d.f : \mathrm{S} = d\mathrm{S}.f' : \mathrm{S}$,[60] our expression will take the form

$$\begin{aligned} & f : \mathrm{S}\left(\frac{ds}{dt}\right) - sf' : \mathrm{S}.s\mho \\ & \quad + \alpha sf : \mathrm{S}\left(\frac{d\mho}{dx}\right) + \alpha\mho f : \mathrm{S}\left(\frac{ds}{dx}\right) + \alpha\mho sf' : \mathrm{S}.ls \\ & \quad + \beta sf : \mathrm{S}\left(\frac{d\mho}{dy}\right) + \beta\mho f : \mathrm{S}\left(\frac{ds}{dy}\right) + \beta\mho sf' : \mathrm{S}.ms \\ & \quad + \gamma sf : \mathrm{S}\left(\frac{d\mho}{dz}\right) + \gamma\mho f : \mathrm{S}\left(\frac{ds}{dz}\right) + \gamma\mho sf' : \mathrm{S}.ns \end{aligned}$$

which must be equal to zero.

64. First of all, we equate to zero the terms containing $f' : \mathrm{S}$, as a result of which we obtain $1 = \alpha l + \beta m + \gamma n$; after division by $f' : \mathrm{S}$ the remaining terms give

$$\left(\frac{ds}{dt}\right) + \alpha\left(\frac{d.s\mho}{dx}\right) + \beta\left(\frac{d.s\mho}{dy}\right) + \gamma\left(\frac{d.s\mho}{dz}\right) = 0,$$

which is indeed similar to the expression proposed; however, it should be noted that the integrability of the quantity $d\mathrm{S}$ is conditioned by:

$$\left(\frac{d.s\mho}{dx}\right) = -\left(\frac{d.ls}{dt}\right); \quad \left(\frac{d.s\mho}{dy}\right) = -\left(\frac{d.ms}{dt}\right); \quad \left(\frac{d.s\mho}{dz}\right) = -\left(\frac{d.ns}{dt}\right);$$

whence we obtain: $\left(\frac{ds}{dt}\right)(1 - \alpha l - \beta m - \gamma n) = 0$,[61] which is consistent with the previous condition. Thus, provided that $\alpha l + \beta m + \gamma n = 1$, and s is a function such that $s(ldx + mdy + ndz - \mho dt) = d\mathrm{S}$, or integrable, our equation will be satisfied if we take $q = sf : \mathrm{S}$, or $\frac{q}{s}$ equal to any function of S. The quantities l, m and n do not have to be constant, but then the following must hold

$$\alpha\left(\frac{dl}{dt}\right) + \beta\left(\frac{dm}{dt}\right) + \gamma\left(\frac{dn}{dt}\right) = 0,$$

a condition already contained in the equation $1 = \alpha l + \beta m + \gamma n$.

65. In addition, l, m and n must be functions such that the differential equation $ldx + mdy + ndz - \mho dt = 0$ becomes possible, since without this condition it would be impossible to find a multiplier s which made the equation integrable. Thus, if we arbitrarily choose some value for l, the values of m and n will be already determined and we can avoid having to find them. We will set $\alpha l = 1$ or $l = \frac{1}{\alpha}$; then, necessarily, $\beta m + \gamma n = 0$ and it remains only to find the factor s for which the expression $s\left(\frac{dx}{\alpha} - \mho dt\right)$ is integrable, the two quantities y and z being regarded as constants. Thus, let $\mathrm{S} = \int s\left(\frac{dx}{\alpha} - \mho dt\right)$, so that y and z are contained in S as constants; we can now take $q = sf : \mathrm{S}$, which gives us the same solution as if we had changed the position of the three axes so much that one of them coincided with the direction of motion of all the fluid elements. Hence we see that this apparent restriction in no way diminishes the generality of the solution.

66. In the same way it would be possible to study several other particular cases of sometimes greater and sometimes lesser scope, but we would not find a case more general than that in which the three velocities u, v and w are such that the expression $udx + vdy + wdz$ becomes integrable.[62] Let S be an integral which also contains time t and let its total differential be $d\mathrm{S} = udx + vdy + wdz + \Pi dt$. Since we have

$$\left(\frac{du}{dt}\right) = \left(\frac{d\Pi}{dx}\right); \quad \left(\frac{dv}{dt}\right) = \left(\frac{d\Pi}{dy}\right); \quad \left(\frac{dw}{dt}\right) = \left(\frac{d\Pi}{dz}\right);$$
$$\left(\frac{du}{dy}\right) = \left(\frac{dv}{dx}\right); \quad \left(\frac{du}{dz}\right) = \left(\frac{dw}{dx}\right); \quad \left(\frac{dv}{dz}\right) = \left(\frac{dw}{dy}\right),$$

we shall have

$$\begin{aligned} \mathrm{X} &= \left(\frac{d\Pi}{dx}\right) + u\left(\frac{du}{dx}\right) + v\left(\frac{dv}{dx}\right) + w\left(\frac{dw}{dx}\right) \\ \mathrm{Y} &= \left(\frac{d\Pi}{dy}\right) + u\left(\frac{du}{dy}\right) + v\left(\frac{dv}{dy}\right) + w\left(\frac{dw}{dy}\right) \\ \mathrm{Z} &= \left(\frac{d\Pi}{dz}\right) + u\left(\frac{du}{dz}\right) + v\left(\frac{dv}{dz}\right) + w\left(\frac{dw}{dz}\right) \end{aligned}$$

and our differential equation now becomes:

$$\frac{dp}{q} = \mathrm{P}dx + \mathrm{Q}dy + \mathrm{R}dz - d\Pi - udu - vdv - wdw$$

[60] Here, $q = sf : \mathrm{S}$ and $d.f : \mathrm{S} = d\mathrm{S}.f' : \mathrm{S}$ would now be denoted $q = sf(\mathrm{S})$ and $df(\mathrm{S}) = d\mathrm{S}f'(\mathrm{S})$, respectively.

[61] The r.h.s. = 0 is missing both in the printed version and in Euler, 1755c.

[62] In §§ 30–33 above, Euler has already pointed out the possibility and given examples of non-potential fluid flows. Truesdell, 1954 considers that Euler based § 66 of his memoir on his previous work (Euler, 1756–1757) which was completed before he had discovered the existence of non-potential flows. This seems all the more likely in that, as Truesdell points out, Euler here denotes the velocity potential not by W, as in § 26, but by S, as in his earlier study.

(the last member of which is absolutely integrable), while the other equation remains as before:

$$\left(\frac{dq}{dt}\right)+\left(\frac{d.qu}{dx}\right)+\left(\frac{d.qv}{dy}\right)+\left(\frac{d.qw}{dz}\right)=0.$$

67. Thus, everything reduces to finding suitable values for the three velocities u, v and w that satisfy our two equations, which contain everything we know about the motion of fluids. For if these three velocities are known, we can determine the trajectory described by each element of the fluid in its motion. Let us consider a particle which at a given instant is located at the point Z; for finding the trajectory which it has already described and which it has yet to describe, since its three velocities u, v and w are assumed to be known, for its position at the next instant we have $dx = udt$, $dy = vdt$ and $dz = wdt$. Eliminating time t from these three equations, we obtain two more equations in the three coordinates x, y and z which will determine the unknown trajectory of the fluid element now at Z and, in general, we shall know the path which each particle has traveled and has yet to travel.

68. The determination of these trajectories is of the utmost importance and should be used to apply the Theory to each case considered. If the shape of the vessel in which the fluid moves is given, the fluid particles which touch the surface of the vessel must necessarily follow its direction; therefore the velocities u, v and w must be such that the trajectories derived therefrom lie on that same surface.[63] This makes it quite clear how far removed we are from a complete understanding of the motion of fluids and that my exposition is no more than a mere beginning. Nevertheless, everything that the Theory of Fluids contains is embodied in the two equations formulated above (§ 34), so that it is not the laws of Mechanics that we lack in order to pursue this research but only the Analysis, which has not yet been sufficiently developed for this purpose. It is therefore clearly apparent what discoveries we still need to make in this branch of Science before we can arrive at a more perfect Theory of the motion of fluids.

References

Darrigol Olivier, Frisch Uriel, 2008 ‘From Newton’s mechanics to Euler’s equations,’ these Proceedings. Also at www.oca.eu/etc7/EE250/texts/darrigol-frisch.pdf.

Euler Leonhard, 1736 *Mechanica sive motus scientia analytice exposita* 2 volumes, (St. Petersburg 1736). Also in *Opera ommia*, ser. 2, **1** and **2**, [Eneström index] **E015** and **E016**.

Euler Leonhard, 1745 *Neue Grundsätze der Artillerie, aus dem englischen des Herrn Benjamin Robins übersetzt und mit vielen Anmerkungen versehen* [from B. Robins, *New principles of gunnery* (London,1742)], Berlin. Also in *Opera ommia*, ser. 2, **14**, 1–409, **E77**.

Euler Leonhard, 1755a ‘Principes généraux de l’état d’équilibre d’un fluide.’ Académie Royale des Sciences et des Belles-Lettres de Berlin, *Mémoires*, **11** [printed in 1757], 217–273. Also in *Opera omnia*, ser. 2, **12**, 2–53, **E225**.

Euler Leonhard, 1755b ‘Principes généraux du mouvement des fluides.’ Académie Royale des Sciences et des Belles-Lettres de Berlin, *Mémoires*, **11** [printed in 1757], 274–315. Also in *Opera omnia*, ser. 2, **12**, 54–91, **E226**.

Euler Leonhard, 1755c. Handwritten copy of Euler, 1775b, not in Euler’s hand. Académie des sciences de l’Institut de France (Paris) in ‘Dossier biographique de Leonhard Euler’.

Euler Leonhard, 1756–1757 ‘Principia motus fluidorum’ [written in 1752]. *Novi commentarii academiae scientiarum Petropolitanae*, **6** [printed in 1761], 271–311. Also in *Opera omnia*, ser. 2, **12**, 133–168, **E258**.

Grimberg Gérard, Pauls Walter, Frisch Uriel, 2008 ‘Genesis of d’Alembert’s paradox and analytical elaboration of the drag problem,’ these Proceedings.

Mikhailov Gleb K., 1999 ‘The origins of hydraulics and hydrodynamics in the work of the Petersburg Academicians of the 18th century.’ *Fluid dynamics*, **34**, 787–800.

Truesdell Clifford, 1954 ‘Rational fluid mechanics, 1657–1765.’ In Euler, *Opera omnia*, ser. 2, **12** (Lausanne), IX–CXXV.

[63] Here, Euler is drawing attention to the fact that in order to calculate the motion of a fluid, in addition to the equations of motion, continuity and state and the initial conditions, we also need the boundary conditions, namely the vanishing of the normal component of the velocity.

Available online at www.sciencedirect.com
ScienceDirect
Physica D 237 (2008) 1840–1854
PHYSICA D
www.elsevier.com/locate/physd

Principles of the motion of fluids☆

Leonhard Euler

Available online 5 May 2008

Abstract

The elements of the theory of the motion of fluids in general are treated here, the whole matter being reduced to this: given a mass of fluid, either free or confined in vessels, upon which an arbitrary motion is impressed, and which in turn is acted upon by arbitrary forces, to determine the motion carrying forward each particle, and at the same time to ascertain the pressure exerted by each part, acting on it as well as on the sides of the vessel. At first in this memoir, before undertaking the investigation of these effects of the forces, the Most Famous Author[1] carefully evaluates all the possible motions which can actually take place in the fluid. Indeed, even if the individual particles of the fluid are free from each other, motions in which the particles interpenetrate are nevertheless excluded, since we are dealing with fluids that do not permit any compression into a narrower volume. Thus it is clear that an arbitrary small portion of fluid cannot receive a motion other than the one which constantly conserves the same volume; even though meanwhile the shape is changed in any way. It would hold indeed, as long as no elementary portion would be compressed at any time into a smaller volume; furthermore[2] if the portion expanded into a larger volume, the continuity of the particles was violated, these were dispersed and no longer clung together, such a motion would no longer pertain to the science of the motion of fluids; but individual droplets would separately perform their motion. Therefore, this case being excluded, motion of the fluids must be restricted by this rule that each small portion must retain for ever the same volume; and this principle restricts the general expressions of motion for elements of the fluid. Plainly, considering an arbitrary small portion of the fluid, its individual points have to be carried by such a motion that, when at a moment of time they arrive at the next location, until then they occupy a volume equal to the previous one; thus if, as usual, the motion of a point is decomposed parallel to fixed orthogonal directions, it is necessary that a certain established relation hold between these three velocities, which the author has determined in the first part.

In the second part the author proceeds to the determination of the motion of a fluid produced by arbitrary forces, in which matter the whole investigation reduces to this that the pressure with which the parts of the fluid at each point act upon one another shall be ascertained; which pressure is denoted most conveniently, as customary for water, by a certain height; this is to be understood thus, that each element of the fluid sustains a pressure the same as if were pressed by a heavy column of the same fluid, whose height is equal to that amount. Thus, in such way in each point of the fluid the height referring to the state of the pressure will be given; since it is not equal to the one in the neighbourhood, it will perturb the motion of the elements. But this pressure depends as well on the forces acting on each element of the fluid, as on those, acting in the whole mass; thus, by the given forces, the pressure in each point and thereupon the acceleration of each element – or its retardation – can be assigned for the motion, all which determinations are expressed by the author through differential formulas. But, in fact, the full development of these formulas mostly involves the greatest difficulties. But nevertheless this whole theory has been reduced to pure analysis, and what remains to be completed in it depends solely upon subsequent progress in Analysis. Thus it is far from true that purely analytic researches are of no use in applied mathematics; rather, important additions in pure analysis are now required.

I. First part

1. Since liquid substances differ from solid ones by the fact that their particles are mutually independent of each other, they can also receive most diverse motions; the motion performed by an arbitrary particle of the fluid is not determined by the motion

☆ This is an English adaptation by Walter Pauls of Euler's memoir 'Principia motus fluidorum' (Euler, 1756–1757). Updated versions of the translation may become available at http://www.oca.eu/etc7/EE250/texts/euler1761eng.pdf. For a detailed presentation of Euler's fluid dynamics papers, cf. Truesdell, 1954, which has also been helpful for this translation. Euler's work is discussed in the perspective of eighteenth century fluid dynamics research by Darrigol and Frisch (2008). The help of O. Darrigol, U. Frisch, G. Grimberg and G. Mikhailov is also acknowledged. Explanatory footnotes and references have been supplied where necessary; Euler's memoir had neither footnotes nor a list of references.

1 Summaries, which at that time were not placed at the beginning of the corresponding paper, were published under the responsibility of the Academy; the presence of the words "Most Famous Author", rather common at the time, cannot be taken as evidence that Euler usually referred to himself in this way.

2 In the original, we find "verum quoniam"; the literal translation "since indeed" does not seem logically consistent.

0167-2789/$ - see front matter © 2008 Published by Elsevier B.V.
doi:10.1016/j.physd.2008.04.019

of the remaining particles to the point that it cannot move in any other way. The matter is very different in solid bodies, which, if they were inflexible, would not undergo any change in their shape; in whatsoever way they be moved, each of their particles would constantly keep the same location and distance with respect to other particles; it thus follows that, the motion of two or, if necessary, three of all the particles being known, the motion of any other particle can be defined; furthermore the motion of two or three particles of such a body cannot be chosen at will, but must be constrained in such a way that these particles preserve constantly their positions with respect to each other.[3]

2. But if, moreover, solid bodies are flexible, the motion of each particle is less constrained: because of bending, the distance as well as the relative position of each particle can be subject to change. However, the manner itself of bending constitutes a certain law which various particles of such a body have to obey in their motion: certainly what has to be taken care of is that the parts that experience in their neighbourhood such a strong bending with respect to each other are neither torn apart from the inside nor penetrate into each other. Indeed, as we shall see, impenetrability is demanded for all bodies.

3. In fluid bodies, whose particles are united among themselves by no bond, the motion of each particle is much less restricted: the motion of the remaining particles is not determined from the motion of any number of particles. Even knowing the motion of one hundred particles, the future motion permitted to the remaining particles still can vary in infinitely many ways. From which it is seen that the motion of these fluid particles plainly does not depend on the motion of the remaining ones, unless it be enclosed by these so that it is constrained to follow them.

4. However, it cannot happen that the motion of all particles of the fluid suffers no restrictions at all. Furthermore, one cannot at will invent a motion that is conceived to occur for each particle. Since, indeed, the particles are impenetrable, it is immediately clear that a motion cannot be maintained in which some particles go through other particles and, accordingly, penetrate each other: also, because of this reason such motion certainly cannot be conceived to occur in the fluid. Therefore, infinitely many motions must be excluded; after their determination the remaining ones are grouped together. It is seen worthwhile to define them more accurately regarding the property which distinguishes them from the previous ones.

5. But before the motion by which the fluid is agitated at any place can be defined, it is necessary to see how every motion, which can definitely be maintained in this fluid, be recognized: these motions, here, I will call possible, which I will distinguish from impossible motions which certainly cannot take place. We must then find what characteristic is appropriate to possible motions, separating them from impossible ones. When this is done, we shall have to determine which one of all possible motions in a certain case ought actually to occur. Plainly we must then turn to the forces which act upon the water, so that the motion appropriate to them may be determined from the principles of mechanics.

6. Thus, I decided to inquire into the character of the possible motions, such that no violation of impenetrability can occur in the fluid. I shall assume the fluid to be such as never to permit itself to be forced into a lesser space, nor should its continuity be interrupted. Once the theory of fluids has been adjusted to fluids of this nature, it will not be difficult to extend it also to those fluids whose density is variable and which do not necessarily require continuity.[4]

7. If, thus, we consider an arbitrary portion in such a fluid, the motion, by which each of its particles is carried has to be set up so that at each time they occupy an equal volume. When this occurs in separate portions, any expansion into a larger volume, or compression into a smaller volume is prohibited. And, if we turn attention to this only property, we can have only such motion that the fluid is not permitted to expand or compress. Furthermore, what is said here about arbitrary portions of the fluid, has to be understood for each of its elements; so that the volume of its elements must constantly preserve its value.

8. Thus, assuming that this condition holds, let an arbitrary motion be considered to occur at each point of the fluid; moreover, given any element of the fluid, consider the brief translations of each of its boundaries. In this manner the volume, in which the element is contained after a very short time, becomes known. From there on, this volume is posed to be equal to the one occupied previously, and this equation will prescribe the calculation of the motion, in so far as it will be possible. Since all elements occupy the same volumes during all periods of time, no compression of the fluid, nor expansion can occur; and the motion is arranged in such a way that this becomes possible.

9. Since we consider not only the velocity[5] of the motion occurring at every point of the fluid but also its direction, both aspects are most conveniently handled, if the motion of each point is decomposed along fixed directions. Moreover, this decomposition is usually carried out with respect to two or three directions[6]: the former is appropriate for decomposition, if the motion of all points is completed in the same plane; but if their motion is not contained in the same plane, it is appropriate to decompose the motion following three fixed axes. Because the latter case is more difficult to treat, it is more convenient to begin the investigation of possible motions with the former case; once this has been done, the latter case will be easily completed.

10. First I will assign to the fluid two dimensions in such a way that all of its particles are now not only found with certainty in the same plane, but also their motion is performed in it. Let this plane be represented in the plane of the table (Fig. 1), let an arbitrary point l of the fluid be considered, its position being denoted by orthogonal coordinates $\mathrm{AL} = x$ and $\mathrm{L}l = y$. The motion is decomposed following these directions, giving a

[3] Here Euler refers to the motion of rigid solid bodies treated previously in Euler, 1750.

[4] See the English translation of “General laws of the motion of fluids” in these Proceedings.

[5] Meaning here the absolute value of the velocity.

[6] Depending on the dimension: Euler treats both the two- and the three-dimensional cases.

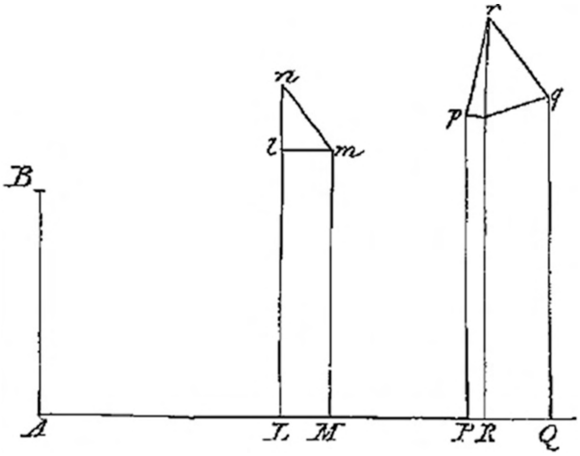

Fig. 1.

velocity $lm = u$ parallel to the axis AL and $ln = v$ parallel to the other axis AB: so that the true future velocity of this point is $\sqrt{(uu + vv)}$, and its direction with respect to the axis AL is inclined by an angle with the tangent $\frac{v}{u}$.

11. Since the state of motion, presented in a way which suits each point of the fluid, is supposed to evolve, the velocities u and v will depend on the position l of the point and will therefore be functions of the coordinates x and y. Thus, we put upon a differentiation

$$du = \mathrm{L}dx + ldy \quad \text{and} \quad dv = \mathrm{M}dx + mdy,$$

which differential formulas, since they are complete,[7] satisfy furthermore $\frac{d\mathrm{L}}{dy} = \frac{dl}{dx}$ and $\frac{d\mathrm{M}}{dy} = \frac{dm}{dx}$. Here it is noted that in such expression $\frac{d\mathrm{L}}{dy}$, the differential of L itself or $d\mathrm{L}$, is understood to be obtained from the variability with respect to y; in similar manner in the expression dl/dx, for dl the differential of l itself has to be taken, which arises if we take x to vary.

12. Thus, it is in order to be cautious and not to take in such fractional expressions $\frac{d\mathrm{L}}{dy}$, $\frac{dl}{dx}$, $\frac{d\mathrm{M}}{dy}$, and $\frac{dm}{dx}$ the numerators $d\mathrm{L}$, dl, $d\mathrm{M}$, and dm as denoting the complete differentials of the functions L, l, M and m; but they designate such differentials constantly that are obtained from variation of only one coordinate, obviously the one, whose differential is represented in the denominator; thus, such expressions will always represent finite and well defined quantities. Furthermore, in the same way are understood $\mathrm{L} = \frac{du}{dx}$, $l = \frac{du}{dy}$, $\mathrm{M} = \frac{dv}{dx}$ and $m = \frac{dv}{dy}$; which notation of ratios has been used for the first time by the most enlightened *Fontaine*,[8] and I will also apply it here, since it gives a non negligible advantage of calculation.

13. Since $du = \mathrm{L}dx + ldy$ and $dv = \mathrm{M}dx + mdy$, here it is appropriate to assign a pair of velocities to the point which is at an infinitely small distance from the point l; if the distance of such a point from the point l parallel to the axis AL is dx, and parallel to the axis AB is dy, then the velocity of this point parallel to the axis AL will be $u + \mathrm{L}dx + ldy$; furthermore, the velocity parallel to the other axis AB is $v + \mathrm{M}dx + mdy$. Thus, during the infinitely short time dt this point will be carried parallel to the direction of the axis AL the distance $dt(u + \mathrm{L}dx + ldy)$ and parallel to the direction of the other axis AB the distance $dt(v + \mathrm{M}dx + mdy)$.

14. Having noted these things, let us consider a triangular element lmn of water, and let us seek the location into which it is carried by the motion during the time dt. Let lm be the side parallel to the axis AL and let ln be the side parallel to the axis AB: let us also put $lm = dx$ and $ln = dy$; or let the coordinates of the point m be $x + dx$ and y; the coordinates of the point n be x and $y + dy$. It is plain, since we do not define the relation between the differentials dx and dy, which can be taken negative as well as positive, that in thought the whole mass of fluid may be divided into elements of this sort, so that what we determine for one in general will extend equally to all.

15. To find out how far the element lmn is carried during the time dt due to the local motion, we search for the points p, q and r, to which its vertices, or the points l, m and n are transferred during the time dt. Since

	of point l	of point m	of point n
Velocity w.r.t. AL=	u	$u + \mathrm{L}dx$	$u + ldy$
Velocity w.r.t. AB=	v	$v + \mathrm{M}dx$	$v + mdy$

in the time dt the point l reaches the point p, chosen such that:

$$\mathrm{AP} - \mathrm{AL} = udt \quad \text{and} \quad \mathrm{P}p - \mathrm{L}l = vdt.$$

Furthermore, the point m reaches the point q, such that

$$\mathrm{AQ} - \mathrm{AM} = (u + \mathrm{L}dx)dt \quad \text{and}$$
$$\mathrm{Q}q - \mathrm{M}m = (v + \mathrm{M}dx)dt.$$

Also, the point n is carried to r, chosen such that

$$\mathrm{AR} - \mathrm{AL} = (u + ldy)dt \quad \text{and} \quad \mathrm{R}r - \mathrm{L}n = (v + mdy)dt.$$

16. Since the points l, m and n are carried to the points p, q and r, the triangle lmn made of the joined straight lines pq, pr and qr, is thought to be arriving at the location defined by the triangle pqr. Because the triangle lmn is infinitely small, its sides cannot receive any curvature from the motion, and therefore, after having performed the translation of the element of water lmn in the time dt, it will conserve the straight and triangular form. Since this element lmn must not be either extended to a larger volume, nor compressed into a smaller one, the motion should be arranged so that the volume of the triangle pqr is rendered to be equal to the area of the triangle lmn.

17. The area of the triangle lmn, being rectangular at l, is $\frac{1}{2}dxdy$, value to which the area of the triangle pqr should be put equal. To find this area, the pair of coordinates of the points p, q and r must be examined, which are:

$$\begin{aligned} \mathrm{AP} &= x + udt; & \mathrm{AQ} &= x + dx + (u + \mathrm{L}dx)dt; \\ \mathrm{AR} &= x + (u + ldy)dt; & \mathrm{P}p &= y + vdt \\ \mathrm{Q}q &= y + (v + \mathrm{M}dx)dt, & \mathrm{R}r &= y + dy + (v + mdy)dt. \end{aligned}$$

[7] Exact differentials.

[8] A paper "Sur le calcul intégral" containing the notation $\frac{df}{dx}$ for the partial derivative of f with respect to x was presented by Alexis Fontaine des Bertins to the Paris Academy of Sciences in 1738, but it was published only a quarter of a century later (Fontaine, 1764). Nevertheless, Fontaine's paper was widely known among mathematicians from the beginning of the 1740s, and, particularly, was discussed in the correspondence between Euler, Daniel Bernoulli and Clairaut; cf. Euler, 1980: 65–246.

Then, indeed, the area of the triangle pqr is found from the area of the succeeding trapezoids, so that

$$pqr = \mathrm{P}pr\mathrm{R} + \mathrm{R}rq\mathrm{Q} - \mathrm{P}pq\mathrm{Q}.$$

Since these trapezoids have a pair of sides parallel to and perpendicular to the base AQ, their areas are easily found.

18. Plainly, these areas are given by the expressions

$$\mathrm{P}pr\mathrm{R} = \frac{1}{2}\mathrm{PR}(\mathrm{P}p + \mathrm{R}r)$$
$$\mathrm{R}rq\mathrm{Q} = \frac{1}{2}\mathrm{RQ}(\mathrm{R}r + \mathrm{Q}q)$$
$$\mathrm{P}pq\mathrm{Q} = \frac{1}{2}\mathrm{PQ}(\mathrm{P}p + \mathrm{Q}q).$$

By putting these together we find:

$$\Delta pqr = \frac{1}{2}\mathrm{PQ}.\mathrm{R}r - \frac{1}{2}\mathrm{RQ}.\mathrm{P}p - \frac{1}{2}\mathrm{PR}.\mathrm{Q}q.$$

Let us set for brevity

$$\mathrm{AQ} = \mathrm{AP} + \mathrm{Q}; \quad \mathrm{AR} = \mathrm{AP} + \mathrm{R}; \quad \mathrm{Q}q = \mathrm{P}p + q; \quad \text{and} \quad \mathrm{R}r = \mathrm{P}p + r,$$

so that PQ $=$ Q, PR $=$ R, and RQ $=$ Q $-$ R, and we have $\Delta pqr = \frac{1}{2}\mathrm{Q}(\mathrm{P}p + r) - \frac{1}{2}(\mathrm{Q} - \mathrm{R})\mathrm{P}p - \frac{1}{2}\mathrm{R}(\mathrm{P}p + q)$ or $\Delta pqr = \frac{1}{2}\mathrm{Q}.r - \frac{1}{2}\mathrm{R}.q$.

19. Truly, from the values of the coordinates represented before it follows that

$$\mathrm{Q} = dx + \mathrm{L}dxdt; \quad q = \mathrm{M}dxdt$$
$$\mathrm{R} = ldydt; \quad r = dy + mdydt,$$

upon the substitution of these values, the area of the triangle is obtained

$$pqr = \frac{1}{2}dxdy(1 + \mathrm{L}dt)(1 + mdt) - \frac{1}{2}\mathrm{M}l\,dxdydt^2, \quad \text{or}$$
$$pqr = \frac{1}{2}dxdy(1 + \mathrm{L}dt + mdt + \mathrm{L}mdt^2 - \mathrm{M}ldt^2).$$

This should be equal to the area of the triangle lmn, that is $= \frac{1}{2}dxdy$; hence we obtain the following equation

$$\mathrm{L}dt + mdt + \mathrm{L}mdt^2 - \mathrm{M}ldt^2 = 0 \quad \text{or}$$
$$\mathrm{L} + m + \mathrm{L}mdt - \mathrm{M}ldt = 0.$$

20. Since the terms $\mathrm{L}mdt$ and $\mathrm{M}ldt$ are negligible for finite L and m, we will have the equation $\mathrm{L} + m = 0$. Hence, for the motion to be possible, the velocities u and v of any point l have to be arranged such that after calculating their differentials

$$du = \mathrm{L}dx + ldy, \quad \text{and} \quad dv = \mathrm{M}dx + mdy,$$

one has $\mathrm{L}+m = 0$. Or, since $\mathrm{L} = \frac{du}{dx}$ and $m = \frac{dv}{dy}$, the velocities u and v, which are considered to occur at the point l parallel to the axes AL and AB, must be functions of the coordinates x and y such that $\frac{du}{dx} + \frac{dv}{dy} = 0$, and thus, the criterion of possible

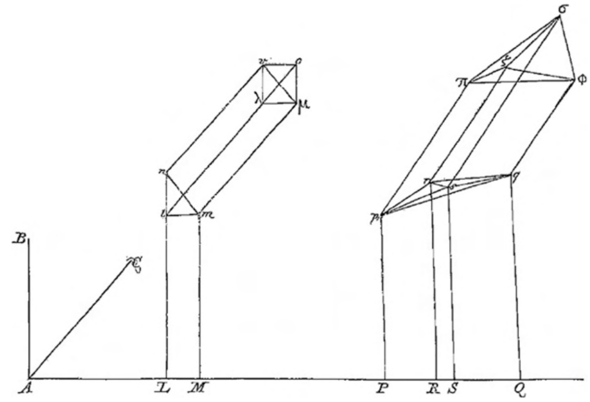

Fig. 2.

motions consists in this that $\frac{du}{dx} + \frac{dv}{dy} = 0$;[9] and unless this condition holds, the motion of the fluid cannot take place.

21. We shall proceed identically when the motion of the fluid is not confined to the same plane. Let us assume, to investigate this question in the broadest sense, that all particles of the fluid are agitated among themselves by an arbitrary motion, with the only law to be respected that neither condensation nor expansion of the parts occurs anywhere: in the same way, we seek which condition should apply to the velocities that are considered to occur at every point, so that motion be possible: or, which amounts to the same, all motions that are opposed to these conditions should be eliminated from the possible ones, this being the criterion of possible motions.

22. Let us consider an arbitrary point of the fluid λ. To represent its location we use three fixed axes AL, AB and AC orthogonal to each other (Fig. 2). Let the triple coordinates parallel to these axes be AL $= x$, L$l = y$ and $l\lambda = z$; which are obtained if firstly a perpendicular λl is dropped from the point λ to the plane determined by the two axes AL and AB; and then a perpendicular lL is drawn from the point l to the axis AL. In this manner the location of the point λ is expressed through three such coordinates in the most general way and can be adapted to all points of the fluid.

23. Whatever the later motion of the point λ, it can be resolved following the three directions $\lambda\mu$, $\lambda\nu$, λo, parallel to the axes AL, AB and AC. For the motion of the point λ we set

the velocity parallel to the direction $\lambda\mu = u$,
the velocity parallel to the direction $\lambda\nu = v$,
the velocity parallel to the direction $\lambda o = w$.

Since these velocities can vary in an arbitrary manner for different locations of the point λ, they will have to be considered as functions of the three coordinates x, y and z. After differentiating them, let us put to proceed

$$du = \mathrm{L}dx + ldy + \lambda dz$$
$$dv = \mathrm{M}dx + mdy + \mu dz$$
$$dw = \mathrm{N}dx + ndy + \nu dz.$$

[9] This is the two-dimensional incompressibility condition, which in a slightly different form has already been established by D'Alembert, 1752; cf. also Darrigol and Frisch, 2008:§III.

Henceforth the quantities L, l, λ, M, m, μ, N, n, ν will be functions of the coordinates x, y and z.

24. Because these formulas are complete differentials, we obtain as above

$$\frac{d\mathrm{L}}{dy}=\frac{dl}{dx};\ \frac{d\mathrm{L}}{dz}=\frac{d\lambda}{dx};\ \frac{dl}{dz}=\frac{d\lambda}{dy}$$
$$\frac{d\mathrm{M}}{dy}=\frac{dm}{dx};\ \frac{d\mathrm{M}}{dz}=\frac{d\mu}{dx};\ \frac{dm}{dz}=\frac{d\mu}{dy}$$
$$\frac{d\mathrm{N}}{dy}=\frac{dn}{dx};\ \frac{d\mathrm{N}}{dz}=\frac{d\nu}{dx};\ \frac{dn}{dz}=\frac{d\nu}{dy},$$

where it is assumed that the only varying coordinate is that whose differential appears in the denominator.[10]

25. Thus, this point λ will be moved in the time dt by this threefold motion, which is considered to take place at the point X; hence it moves

parallel to the axis AL the distance $= udt$

parallel to the axis AB the distance $= vdt$

parallel to the axis AC the distance $= wdt$.

The true velocity of the point λ, denoted by V, which clearly arises from the composition of this triple motion, is given in view of orthogonality of the three directions by $V=\sqrt{(uu+vv+ww)}$ and the elementary distance, which is travelled in time dt through its motion, will be Vdt.

26. Let us consider an arbitrary solid element of the fluid to see whereto it is carried during the time dt; since it amounts to the same, let us assign a quite arbitrary shape to that element, but of a kind such that the entire mass of the fluid can be divided into such elements; to investigate by calculation, let the shape be a right triangular pyramid, bounded by four vertices λ, μ, ν and o, so that for each one there are three coordinates

	of point λ	of point μ	of point ν	of point o
w.r.t. AL	x	$x+dx$	x	x
w.r.t. AB	y	y	$y+dy$	y
w.r.t. AC	z	z	z	$z+dz$.

Since the base of this pyramid is $\lambda\mu\nu = lmn = \frac{1}{2}dxdy$ and the hight $\lambda o = dz$, its volume will be $= \frac{1}{6}dxdydz$.

27. Let us investigate, whereto these vertices λ, μ, ν and o are carried during the time dt: for which purpose their three velocities parallel to the directions of the three axes must be considered. The differential values of the velocities u, v and w are given by

Velocity	of point λ	of point μ	of point ν	of point o
w.r.t. AL	u	$u+\mathrm{L}dx$	$u+ldy$	$u+\lambda dz$
w.r.t. AB	v	$v+\mathrm{M}dx$	$v+mdy$	$v+\mu dz$
w.r.t. AC	w	$w+\mathrm{N}dx$	$w+ndy$	$w+odz$

28. If we let the points λ, μ, ν and o be transferred to the points π, Φ, ρ and σ in the time dt, and establish the three coordinates of these points parallel to the axes, the small displacement parallel to these axes will be

$$\begin{array}{lcl}
\mathrm{AP}-\mathrm{AL} &=& u\,dt\\
\mathrm{AQ}-\mathrm{AM} &=& (u+\mathrm{L}\,dx)\,dt\\
\mathrm{AR}-\mathrm{AL} &=& (u+l\,dy)\,dt\\
\mathrm{AS}-\mathrm{AL} &=& (u+\lambda\,dz)\,dt\\
\hline
\mathrm{P}p-\mathrm{L}l &=& v\,dt\\
\mathrm{Q}q-\mathrm{M}m &=& (v+\mathrm{M}\,dx)\,dt\\
\mathrm{R}r-\mathrm{L}n &=& (v+m\,dy)\,dt\\
\mathrm{S}s-\mathrm{L}l &=& (v+\mu\,dz)\,dt\\
\hline
p\pi-l\lambda &=& w\,dt\\
q\Phi-m\mu &=& (w+\mathrm{N}\,dx)\,dt\\
r\rho-n\nu &=& (w+n\,dy)\,dt\\
s\sigma-lo &=& (w+\nu\,dz)\,dt.
\end{array}$$

Thus the three coordinates for these four points π, Φ, ρ and σ will be

$\mathrm{AP}=x+udt$; $\mathrm{P}p=y+vdt$;

$p\pi=z+wdt$

$\mathrm{RQ}=x+dx+(u+\mathrm{L}dx)dt$; $\mathrm{Q}q=y+(v+\mathrm{M}dx)dt$;

$q\Phi=z+(w+\mathrm{N}dx)dt$

$\mathrm{AR}=x+(u+ldy)dt$; $\mathrm{R}r=y+dy+(v+mdy)dt$;

$r\rho=z+(w+ndy)dt$

$\mathrm{AS}=x+(u+\lambda dz)dt$; $\mathrm{S}s=y+(v+\mu dz)dt$;

$s\sigma=z+dz+(w+\nu dz)dt$.

29. Since after time dt has elapsed the vertices λ, μ, ν and o of the pyramid are transferred to the points π, Φ, ρ and σ, $\pi\Phi\rho\sigma$ defines a similar triangular pyramid. Due to the nature of the fluid the volume of the pyramid $\pi\Phi\rho\sigma$ should be equal to the volume of the pyramid $\lambda\mu\nu o$ put forward, that is $\frac{1}{6}dxdydz$. Thus, the whole matter is reduced to determining the volume of the pyramid $\pi\Phi\rho\sigma$. Clearly, it remains a pyramid, if the solid $pqr\pi\Phi\rho\sigma$ is removed from the solid $pqr\pi\Phi\rho\sigma$; the latter solid is a prism orthogonally incident to the triangular basis pqr, and cut by the upper oblique section $\pi\rho\Phi$.

30. The other solid $pqr\pi\Phi\rho\sigma$ can be divided by similarly into three prisms truncated in this manner, namely

I.$pqrs\pi\Phi\sigma$; II.$prs\pi\rho\sigma$; III.$qrs\Phi\rho\sigma$.

This has to be accomplished in such a way that

$$\frac{1}{6}dxdydz = pqs\pi\Phi\sigma + prs\pi\rho\sigma + qrs\Phi\rho\sigma - pqr\pi\Phi\rho.$$

Since such a prism is orthogonally incident to its lower base, and furthermore has three unequal heights, its volume is found by multiplying the base by one third of the sum of these heights.

31. Thus, the volumes of these truncated prisms will be

$$\begin{array}{lcl}
pqs\pi\Phi\sigma &=& \frac{1}{3}pqs(p\pi+q\Phi+s\sigma)\\
prs\pi\rho\sigma &=& \frac{1}{3}prs(p\pi+r\rho+s\sigma)\\
qrs\Phi\rho\sigma &=& \frac{1}{3}qrs(q\Phi+r\rho+s\sigma)\\
pqr\pi\Phi\rho &=& \frac{1}{3}pqr(p\pi+q\Phi+r\rho).
\end{array}$$

[10] The partial differential notation was so new that Euler had to remind the reader of its definition.

Since $pqr = pqs + prs + qrs$, the sum of the first three prisms will definitely be small, or

$$\frac{1}{6}dxdydz = -\frac{1}{3}p\pi.qrs - \frac{1}{3}q\Phi.prs - \frac{1}{3}r\rho.pqs + \frac{1}{3}s\sigma.pqr,$$

or

$$dxdydz = 2pqr.s\sigma - 2pqs.r\rho - 2prs.q\Phi - 2qrs.p\pi.$$

32. Thus, it remains to define the bases of these prisms: but before we do this, let us put

$$\begin{aligned} \mathrm{AQ} &= \mathrm{AP} + \mathrm{Q}; & \mathrm{Q}q &= \mathrm{P}p + q; & q\Phi &= p\pi + \Phi; \\ \mathrm{AR} &= \mathrm{AP} + \mathrm{R}; & \mathrm{R}r &= \mathrm{P}p + r; & r\rho &= p\pi + \rho; \\ \mathrm{AS} &= \mathrm{AP} + \mathrm{S}; & \mathrm{S}s &= \mathrm{P}p + s; & s\sigma &= p\pi + \sigma, \end{aligned}$$

in order to shorten the following calculations. After the substitution of these values, the terms containing $p\pi$ will annihilate each other, and we shall have

$$dxdydz = 2pqr.\sigma - 2pqs.\rho - 2prs.\Phi$$

so that the value of the bases to be investigated is smaller.

33. Furthermore the triangle pqr is obtained by removing the trapezoid PpqQ from the figure PprqQ, the latter being the sum of the trapezoids PprR and RrqQ; from which it follows that

$$\Delta pqr = \frac{1}{2}\mathrm{PR}(\mathrm{P}p + \mathrm{R}r) + \frac{1}{2}\mathrm{RQ}(\mathrm{R}r + \mathrm{Q}q) - \frac{1}{2}\mathrm{PQ}(\mathrm{P}p + \mathrm{Q}q);$$

or, because of PR = R; RQ = Q − R; and PQ = Q we shall have

$$\Delta pqr = \frac{1}{2}\mathrm{R}(\mathrm{P}p - \mathrm{Q}q) + \frac{1}{2}\mathrm{Q}(\mathrm{R}r - \mathrm{P}p) = \frac{1}{2}\mathrm{Q}r - \frac{1}{2}\mathrm{R}q.$$

In the same manner we have

$$\Delta pqs = \frac{1}{2}\mathrm{PS}(\mathrm{P}p + \mathrm{S}s) + \frac{1}{2}\mathrm{SQ}(\mathrm{S}s + \mathrm{Q}q) - \frac{1}{2}\mathrm{PQ}(\mathrm{P}p + \mathrm{Q}q),$$

or

$$\Delta pqs = \frac{1}{2}\mathrm{S}(\mathrm{P}p + \mathrm{S}s) + \frac{1}{2}(\mathrm{Q} - \mathrm{S})(\mathrm{S}s + \mathrm{Q}q) - \frac{1}{2}\mathrm{Q}(\mathrm{P}p + \mathrm{Q}q),$$

from where it follows that:

$$\Delta pqs = \frac{1}{2}\mathrm{S}(\mathrm{P}p - \mathrm{Q}q) + \frac{1}{2}\mathrm{Q}(\mathrm{S}s - \mathrm{P}p) = \frac{1}{2}\mathrm{Q}s - \frac{1}{2}\mathrm{S}q.$$

And finally

$$\Delta prs = \frac{1}{2}\mathrm{PR}(\mathrm{P}p + \mathrm{R}r) + \frac{1}{2}\mathrm{RS}(\mathrm{R}r + \mathrm{S}s) - \frac{1}{2}\mathrm{PS}(\mathrm{P}p + \mathrm{S}s),$$

or

$$\Delta prs = \frac{1}{2}\mathrm{R}(\mathrm{P}p + \mathrm{R}r) + \frac{1}{2}(\mathrm{S} - \mathrm{R})(\mathrm{R}r + \mathrm{S}s) - \frac{1}{2}\mathrm{S}(\mathrm{P}p + \mathrm{S}s)$$

from where it follows that

$$\Delta prs = \frac{1}{2}\mathrm{R}(\mathrm{P}p - \mathrm{S}s) + \frac{1}{2}\mathrm{S}(\mathrm{R}r - \mathrm{P}p) = \frac{1}{2}\mathrm{S}r - \frac{1}{2}\mathrm{R}s.$$

34. After the substitution of these values we will obtain

$$dxdydz = (\mathrm{Q}r - \mathrm{R}q)\sigma + (\mathrm{S}q - \mathrm{Q}s)\rho + (\mathrm{R}s - \mathrm{S}r)\Phi;$$

thus the volume of the pyramid $\pi\Phi\rho\sigma$ will be

$$\frac{1}{6}(\mathrm{Q}r - \mathrm{R}q)\sigma + \frac{1}{6}(\mathrm{S}q - \mathrm{Q}s)\rho + \frac{1}{6}(\mathrm{R}s - \mathrm{S}r)\Phi.$$

From the values of the coordinates presented above in §. 28 follows

$$\begin{aligned} &\mathrm{Q} = dx + \mathrm{L}dxdt \quad q = \mathrm{M}dxdt \quad \Phi = \mathrm{N}dxdt \\ &\mathrm{R} = ldydt \quad r = dy + mdydt \quad \rho = ndydt \\ &\mathrm{S} = \lambda dzdt \quad s = \mu dzdt \quad \sigma = dz + \nu dzdt. \end{aligned}$$

35. Since here we have

$$\begin{aligned} \mathrm{Q}r - \mathrm{R}q &= dxdy(1 + \mathrm{L}dt + mdt + \mathrm{L}mdt^2 - \mathrm{M}ldt^2) \\ \mathrm{S}q - \mathrm{Q}s &= dxdz(-\mu dt - \mathrm{L}\mu dt^2 + \mathrm{M}\lambda dt^2) \\ \mathrm{R}s - \mathrm{S}r &= dydz(-\lambda dt - m\lambda dt^2 + l\mu dt^2) \end{aligned}$$

the volume of the pyramid $\pi\Phi\rho\sigma$ is found to be expressed as

$$\frac{1}{6}dxdydz \left\{ \begin{array}{llll} 1 & +\mathrm{L}\,dt & +\mathrm{L}m\,dt^2 & +\mathrm{L}m\nu\,dt^3 \\ & +m\,dt & -\mathrm{M}l\,dt^2 & -\mathrm{M}l\nu\,dt^3 \\ & +\nu\,dt & +\mathrm{L}\nu\,dt^2 & -\mathrm{L}n\mu\,dt^3 \\ & & +m\nu\,dt^2 & +\mathrm{M}n\lambda\,dt^3 \\ & & -n\mu\,dt^2 & -\mathrm{N}m\lambda\,dt^3 \\ & & -\mathrm{N}\lambda\,dt^2 & +\mathrm{N}l\mu\,dt^3 \end{array} \right\},$$

which (volume), since it must be equal to that of the pyramid $\lambda\mu\nu o = \frac{1}{6}dxdydz$, will satisfy, after performing a division by dt the following equation[11].

$$\begin{aligned} 0 = \mathrm{L} + m + \nu &+ dt(\mathrm{L}m + \mathrm{L}\nu + m\nu - \mathrm{M}l - \mathrm{N}\lambda - n\mu) \\ &+ dt^2(\mathrm{L}m\nu + \mathrm{M}n\lambda + \mathrm{N}l\mu - \mathrm{L}n\mu - \mathrm{M}l\nu - \mathrm{N}l\mu). \end{aligned}$$

36. Discarding infinitely small terms, we get this equation:[12] $\mathrm{L} + m + \nu = 0$, through which is determined the relation between u, v and w, so that the motion of the fluid be possible. Since $\mathrm{L} = \frac{du}{dx}$, $m = \frac{dv}{dy}$ and $\nu = \frac{dw}{dz}$, at an arbitrary point of the fluid λ, whose position is defined by the three coordinates x, y and z, and the velocities u, v and w are assigned in the same manner to be directed along these same coordinates, the criterion of possible motions is such that

$$\frac{du}{dx} + \frac{dv}{dy} + \frac{dw}{dz} = 0.$$

This condition expresses that through the motion no part of the fluid is carried into a greater or or lesser space, but perpetually the continuity of the fluid as well as the identical density is conserved.

37. This property is to be interpreted further so that at the same instant it is extended to all points of the fluid: of course, the three velocities of all the points must be such functions of the three coordinates x, y and z that we have $\frac{du}{dx} + \frac{dv}{dy} + \frac{dw}{dz} = 0$:

[11] This is the calculation to which Euler refers in his later French memoir Euler, 1755.

[12] This is the three-dimensional incompressibility condition.

in this way the nature of those functions defines the motion of every point of the fluid at a given instant. At another time the motion of the same points may be howsoever different, provided that at an arbitrary point of time the property holds for the whole fluid. Up to now I have considered the time simply as a constant quantity.

38. If however, we also wish to consider time as variable so that the motion of the point λ whose position is given by the three coordinates $\mathrm{AL} = x$, $\mathrm{L}l = y$ and $l\lambda = z$ has to be defined after the elapsed time t, it is certain that the three velocities u, v and w depend not only on the coordinates x, y and z but additionally on the time t, that is they will be functions of these four quantities x, y, z and t; furthermore, their differentials are going to have the following form

$$\begin{aligned} du &= \mathrm{L}dx + ldy + \lambda dz + \mathfrak{L}dt;\\ dv &= \mathrm{M}dx + mdy + \mu dz + \mathfrak{M}dt;\\ dw &= \mathrm{N}dx + ndy + \nu dz + \mathfrak{N}dt; \end{aligned}$$

Meanwhile we shall always have $\mathrm{L} + m + \nu = 0$, having in view that at every arbitrary instant the time t is considered to be constant, or $dt = 0$. Howsoever the functions u, v and w vary with time t, it is necessary that at every moment of time the following holds:

$$\frac{du}{dx} + \frac{dv}{dy} + \frac{dw}{dz} = 0.$$

Since the condition expresses that any arbitrary portion of the fluid is carried in a time dt into a volume equal to itself, the same will have to happen, due to the same condition, in the next time interval, and therefore in all the following time intervals.

II. Second part

39. Having presented what pertains to all possible motions, let us now investigate the nature of the motion which can really occur in the fluid. Here, besides the continuity of the fluid and the constancy of its density, we will also have to consider the forces which act on every element of the fluid. When the motion of any element is either non-uniform or varying in its direction, the change of motion must be in accordance with the forces acting on this element. The change of motion becomes known from known forces, and the preceding formulas contain this change; we will now deduce new conditions[13] which single out the actual motion among all those possible up to this point.

40. Let us arrange this investigation in two parts as well; at first let us consider all motions being performed in the same plane. Let $\mathrm{AL} = x$, $\mathrm{L}l = y$ be, as before, the defining coordinates of the position of an arbitrary point l; now, after the elapsed time t, the two velocities of the point l parallel to the axes AL and AB are u and v: since the variability of time has to be taken into account, u and v will be functions of x, y and t themselves. In respect of which we put

$$du = \mathrm{L}dx + ldy + \mathfrak{L}dt \quad \text{and} \quad dv = \mathrm{M}dx + mdy + \mathfrak{M}dt$$

and we have established above that because of the former condition encountered above, we have $\mathrm{L} + m = 0$.

41. After an elapsed small time interval dt the point l is carried to p, and it has travelled a distance udt parallel to the axis AL, a distance vdt parallel to the other axis AB. Hence, to obtain the increments in velocities u and v of the point l which are induced during time dt, for dx and dy we must write the distance udt and vdt, from which will arise these true increments of the velocities

$$du = \mathrm{L}udt + lvdt + \mathfrak{L}dt \quad \text{and} \quad dv = \mathrm{M}udt + mvdt + \mathfrak{M}dt.$$

Therefore the accelerating forces, which produce these accelerations are

$$\text{Accel. force w.r.t. AL} = 2(\mathrm{L}u + lv + \mathfrak{L})$$
$$\text{Accel. force w.r.t. AB} = 2(\mathrm{M}u + mv + \mathfrak{M})$$

to which therefore the forces acting upon the particle of water ought to be equal.[14]

42. Among the forces which in fact act upon the particles of water, the first to be considered is gravity; its effect, however, if the plane of motion is horizontal, amounts to nothing. Yet if the plane is inclined, the axis AL following the inclination, the other being horizontal, gravity generates a constant accelerating force parallel to the axis AL, let it be α. Next we must not neglect friction, which often hinders the motion of water, and not a little. Although its laws have not yet been explored sufficiently, nevertheless, following the law of friction for solid bodies, probably we shall not wander too far astray if we set the friction everywhere proportional to the pressure with which the particles of water press upon one another.[15]

43. First, must be brought into the calculation the pressure with which the particles of water everywhere mutually act upon each other, by means of which every particle is pressed together on all sides by its neighbours; and in so far as this pressure is not everywhere equal, to that extent motion is communicated to that particle.[16] The water simply will be put everywhere into a state of compression similar to that which still water experiences when stagnating at a certain depth. This depth is most conveniently employed for representing the pressure at an arbitrary point l of the fluid. Therefore let that height, or depth, expressing the state of compression at l, be p, a certain function of the coordinates x and y, and should the pressure at l vary also with the time, the time will also enter into the function p.

44. Thus let us set $dp = \mathrm{R}dx + rdy + \mathfrak{R}dt$, and let us consider a rectangular element of water, $lmno$, whose sides are $lm = no = dx$ and $ln = mo = dy$, whose area is $dxdy$ (Fig. 3). The pressure at l is p, the pressure at m is $p + \mathrm{R}dx$, at n it is $p + rdy$ and at o it is $p + \mathrm{R}dx + rdy$. Thus the side lm is pressed by a force $= dx(p + \frac{1}{2}\mathrm{R}dx)$, while the opposite side no will be pressed by a force $= dx(p + \frac{1}{2}\mathrm{R}dx + rdy)$;

[13] Here Euler probably has in mind the condition of potentiality, which he will obtain in §§. 47 and 54 for the two-dimensional case and in §. 60 for the three-dimensional case.

[14] The unusual factors of 2 in the previous equations have to do with a choice of units which soon became obsolete; cf. Truesdell, 1954; Mikhailov, 1999.

[15] It is actually not clear why Euler takes the friction force proportional to the pressure.

[16] Here Euler makes full use of the concept of internal pressure, cf. Darrigol and Frisch, 2008.

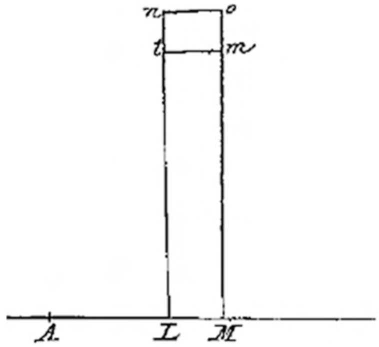

Fig. 3.

therefore by these two forces the element $lmno$ will be impelled in the direction ln by a force $= -rdxdy$. Moreover, in a similar manner from the forces $dy(p+\frac{1}{2}rdy)$ and $dy(p+\mathrm{R}dx+\frac{1}{2}rdy)$, which act on the sides ln and mo will result a force $= -\mathrm{R}dxdy$ impelling the element in the direction lm.

45. Thus will originate an accelerating force parallel to $lm = -\mathrm{R}$ and an accelerating force parallel to $ln = -r$, of which the one directed along the force of gravity α gives $\alpha - \mathrm{R}$. Having ignored friction so far, we obtain the following equations[17]:

$$\begin{array}{lll} \alpha - \mathrm{R} = 2\mathrm{L}u + 2lv + 2\mathfrak{L} & \text{or} & \mathrm{R} = \alpha - 2\mathrm{L}u - 2lv - 2\mathfrak{L} \\ -r \quad = 2\mathrm{M}u + 2mv + 2\mathfrak{M} & \text{and} & r \ = -2\mathrm{M}u - 2mv - 2\mathfrak{M} \end{array}$$

from which we gather that

$$dp = \alpha dx - 2(\mathrm{L}u + lv + \mathfrak{L})dx - 2(\mathrm{M}u + mv + \mathfrak{M})dy + \mathfrak{N}dt,$$

a differential which must be complete or integrable.

46. Because the term $\alpha\, dx$ is integrable by itself and nothing is determined for $\mathfrak{N}$, from the nature of complete differentials it is necessary that the following holds in the notation already employed:

$$\frac{d.\mathrm{L}u + lv + \mathfrak{L}}{dy} = \frac{d.\mathrm{M}u + mv + \mathfrak{M}}{dx}.$$

Since $\frac{du}{dx} = \mathrm{L}$, $\frac{du}{dy} = l$; $\frac{dv}{dx} = \mathrm{M}$, and $\frac{dv}{dy} = m$ it follows that

$$\mathrm{L}l + \frac{ud\mathrm{L}}{dy} + lm + \frac{vdl}{dy} + \frac{d\mathfrak{L}}{dy} = \mathrm{ML} + \frac{ud\mathrm{M}}{dx} + m\mathrm{M} + \frac{vdm}{dx} = \frac{d\mathfrak{M}}{dx}$$

which is reduced to this form:

$$(\mathrm{L} + m)(l - \mathrm{M}) + u\left(\frac{d\mathrm{L}}{dy} - \frac{d\mathrm{M}}{dx}\right) + v\left(\frac{dl}{dy} - \frac{dm}{dx}\right) + \frac{d\mathfrak{L}}{dy} - \frac{d\mathfrak{M}}{dx} = 0.$$

47. In fact, since we knew $\mathrm{L}dx + ldy + \mathfrak{L}dt$ and $\mathrm{M}dx + mdy + \mathfrak{M}dt$ to be complete differentials,

$$\frac{d\mathrm{L}}{dy} = \frac{dl}{dx}; \quad \frac{dm}{dx} = \frac{d\mathrm{M}}{dy}; \quad \frac{d\mathfrak{L}}{dy} = \frac{dl}{dt} \quad \text{and} \quad \frac{d\mathfrak{M}}{dx} = \frac{d\mathrm{M}}{dt}$$

after the substitution of which values we have the following equation

$$(\mathrm{L} + m)(l - \mathrm{M}) + u\left(\frac{dl - d\mathrm{M}}{dx}\right) + v\left(\frac{dl - d\mathrm{M}}{dy}\right) + \frac{dl - d\mathrm{M}}{dt} = 0.$$

Plainly, this is satisfied if $l = \mathrm{M}$: so that $\frac{du}{dy} = \frac{dv}{dx}$. Since this condition requires that $\frac{du}{dy} = \frac{dv}{dx}$,[18] it appears finally that the differential formula $udx + vdy$ must be complete; in this lies the criterion of actual motion.

48. This criterion is independent from the preceding one, which was provided by the continuity of the fluid and its uniform constant density. Therefore even if the fluid in motion changes its density, as happens in the motion of elastic fluids such as air, this property will hold nonetheless, namely $udx + vdy$ has to be a complete differential. In other words, the velocities u and v must always be functions of the coordinates x and y, together with time t, in such a way that when the time is taken constant the formula $udx + vdy$ admits an integration.

49. We shall now determine the pressure p itself, which is absolutely necessary for perfectly determining the motion of the fluid. Since we have found that $\mathrm{M} = l$ we have

$$dp = \alpha dx - 2u(\mathrm{L}dx + ldy) - 2v(ldx + mdy) - 2\mathfrak{L}dx - 2\mathfrak{M}dy + \mathfrak{N}dt.$$

Moreover $\mathrm{L}dx + ldy = du - \mathfrak{L}dt$; $ldx + mdy = dv - \mathfrak{M}dt$; hence we have

$$dp = \alpha dx - 2udu - 2vdv + 2\mathfrak{L}udt + 2\mathfrak{M}vdt - 2\mathfrak{L}dx - 2\mathfrak{M}dy + \mathfrak{N}dt.$$

Therefore, if we wish to ascertain for the present time the pressure at each point of the fluid, with no account of its variation in time, we shall have to consider this equation

$$dp = \alpha dx - 2udu - 2vdv - 2\mathfrak{L}dx - 2\mathfrak{M}dy,$$

and in our notation $\mathfrak{L} = \frac{du}{dt}$ and $\mathfrak{M} = \frac{dv}{dt}$.[19] Hence

$$dp = \alpha dx - 2udu - 2vdv - 2\frac{du}{dt}dx - 2\frac{dv}{dt}dy,$$

in the integration of which the time is to be taken constant.

50. This equation is integrable by hypothesis, and is indeed understood as such, if we consider the criterion of the motion which, as we have seen, consists in that $udx + vdy$ be a complete differential when the time t is taken constant. Let therefore S be its integral, which consequently will be a function of x, y and t themselves. For $dt = 0$ we obtain $d\mathrm{S} = udx + vdy$, while assuming the time t variable as well,

[17] Here the so-called Euler equations of incompressible fluid dynamics appear for the first time, but the notation and the units are not very modern, in contrast to the memoir he will write three years later (Euler, 1755).

[18] Here there are two problems. The minor problem is a typographical error in the published version ($\frac{du}{dx}$ instead of $\frac{dv}{dx}$), which is not present in a 1752 copy of the manuscript (not in Euler's hand), henceforth referred to as Euler, 1752. A more serious problem is that Euler here repeats the mistake of D'Alembert, 1752 who confused a sufficient condition – the vanishing of the vorticity – with a necessary one.

[19] The printed version has $L = \frac{dv}{dt}$ instead of $\mathfrak{L} = \frac{du}{dt}$. Euler, 1752 is correct.

let us write

$$dS = udx + vdy + Udt,$$

on which account we obtain $\frac{du}{dt} = \frac{dU}{dx}$ and $\frac{dv}{dt} = \frac{dU}{dy}$. Then, in fact $U = \frac{dS}{dt}$.

51. After inserting these values we will obtain

$$\frac{du}{dt}.dx + \frac{dv}{dt}.dy = \frac{dU}{dx}.dx + \frac{dU}{dy}.dy$$

and this differential formula is manifestly integrated at constant time t to give U. For this to become clearer, let us set $dU = Kdx + kdy$; thus $\frac{dU}{dx} = K$ and $\frac{dU}{dy} = k$, so that $\frac{dU}{dx}.dx + \frac{dU}{dy} = Kdx + kdy = dU$. Since its integral is $U = \frac{dS}{dt}$, we shall have

$$dp = \alpha dx - 2udu - 2vdv - 2dU$$

from where it appears by integration:

$$p = \text{Const.} + \alpha x - uu - vv - \frac{2dS}{dt}$$

with a given function S of the coordinates x, y and t themselves, whose differential, for $dt = 0$ is $udx + vdy$.

52. In order to understand better the nature of these formulas, let us consider the true velocity of the point l, which is $V = \sqrt{(uu + vv)}$. And the pressure will be: $p = \text{Const.} + \alpha x - VV - \frac{2dS}{dt}$: in which the last term dS denotes the differential of $S = \int(udx + vdy)$ itself, where the time t is allowed to vary.

53. If we now wish to also take friction into account, let us set it proportional to the pressure p. While the point l travels the element ds, the retarding force arising from the friction is $= \frac{p}{f}$; so that, setting $\frac{dS}{dt} = U$, our differential equation will be for constant t

$$dp = \alpha dx - \frac{p}{f}ds - VdV - 2dU,$$

from where we obtain by integration, taking e for the number whose hyperbolic[20] logarithm is $= 1$,

$$p = e^{\frac{-s}{f}} \int e^{\frac{s}{f}} (\alpha dx - 2VdV - 2dV) \quad \text{or}$$

$$p = \alpha x - VV - 2U - \frac{1}{f} e^{\frac{-s}{f}} \int e^{\frac{s}{f}} (\alpha x - VV - 2U) ds.$$

54. The criterion of the motion which drives the fluid in reality consists in this that, fixing the time t, the differential $udx + vdy$ has to be complete: also continuity and constant uniform density demand that $\frac{du}{dx} + \frac{dv}{dy} = 0$, hence it follows too that this differential $udy - vdx$ will have to be complete.[21] From where both velocities u and v jointly must be functions of the coordinates x and y with the time t in such a way that both differential formulas $udx + vdy$ and $udy - vdx$[22] be complete differentials.

55. Let us set up the same investigation in general, giving the point λ three velocities directed parallel to the axes AL, AB, AC. Let u, v, w denote these functions, which depend on coordinates x, y, z, besides t. After a differentiation we obtain

$$du = Ldx + ldy + \lambda dz + \mathfrak{L}dt$$
$$dv = Mdx + mdy + \mu dz + \mathfrak{M}dt$$
$$dw = Ndx + ndy + \nu dz + \mathfrak{N}dt.$$

Although here the time t is also taken as variable, nonetheless for the motion to be possible, by the preceding condition[23] we have $L + m + \nu = 0$, or, which reexpresses the same

$$\frac{du}{dx} + \frac{dv}{dy} + \frac{dw}{dz} = 0,$$

a condition on which the present examination does not depend.

56. After the passage of time interval dt the point λ is carried to π, and it travels a distance udt parallel to the axis AL, a distance vdt parallel to the axis AB and a distance wdt parallel to the axis AC. Thus the three velocities of the point which has moved from λ to π will be:

parallel to AL $= u + Lu\,dt + lv\,dt + \lambda w\,dt + \mathfrak{L}\,dt$;
parallel to AB $= v + Mu\,dt + mv\,dt + \mu w\,dt + \mathfrak{M}\,dt$;
parallel to AC $= w + Nu\,dt + nv\,dt + \nu w\,dt + \mathfrak{N}\,dt$,

and the accelerations parallel to the same directions will be

par. AL $= 2(Lu + lv + \lambda w + \mathfrak{L})$;
par. AB $= 2(Mu + mv + \mu w + \mathfrak{M})$;
par. AC $= 2(Nu + nv + \nu w + \mathfrak{N})$.

57. If we take the axis AC to be vertical, in such a way that the remaining two AL and AB are horizontal, the accelerating force due to gravity arises parallel to the axis AC with the value -1. Then indeed, denoting the pressure at λ by p, its differential, at constant time is

$$dp = R\,dx + rdy + \rho dz,$$

from which we obtain the three accelerating forces

par. AL = R; par. AB $= -r$; par. AC $= -\rho$

which are in fact easily collected in the same manner as was done in §§. 44 and 45, so that it is not necessary to repeat the same computation. Hence we obtain the following equations[24]

$$R = -2(Lu + lv + \lambda w + \mathfrak{L})$$
$$r = -2(Mu + mv + \mu w + \mathfrak{M})$$
$$\rho = -1 - 2(Nu + nv + \nu w + \mathfrak{N}).$$

58. Since the differential formula $dp = Rdx + rdy + \rho dz$ has to be a complete differential, we have

$$\frac{dR}{dy} = \frac{dr}{dx}; \quad \frac{dR}{dz} = \frac{d\rho}{dx}; \quad \frac{dr}{dz} = \frac{d\rho}{dy}.$$

20 Natural.
21 The published version has $udx + vdy$, a mistake not present in Euler, 1752.
22 Previous mistake repeated in the published version.
23 From Part I.
24 These are the three dimensional Euler equations.

After a differentiation and a division by -2 the following three equations are obtained[25]

$$\mathrm{I}\begin{cases}\dfrac{u d\mathrm{L}}{dy}+\dfrac{v dl}{dy}+\dfrac{w d\lambda}{dy}+\dfrac{d\mathfrak{L}}{dy}+\mathrm{L}l+lm+\lambda n=\\ \dfrac{u d\mathrm{M}}{dx}+\dfrac{v dm}{dx}+\dfrac{w d\mu}{dx}+\dfrac{d\mathfrak{M}}{dx}+\mathrm{ML}+m\mathrm{M}+\mu\mathrm{N}\end{cases}$$

$$\mathrm{II}\begin{cases}\dfrac{u d\mathrm{L}}{dz}+\dfrac{v dl}{dz}+\dfrac{w d\lambda}{dz}+\dfrac{d\mathfrak{L}}{dz}+\mathrm{L}\lambda+l\mu+\lambda\nu=\\ \dfrac{u d\mathrm{N}}{dx}+\dfrac{v dn}{dx}+\dfrac{w d\nu}{dx}+\dfrac{d\mathfrak{N}}{dx}+\mathrm{NL}+n\mathrm{M}+\nu\mathrm{N}\end{cases}$$

$$\mathrm{III}\begin{cases}\dfrac{u d\mathrm{M}}{dz}+\dfrac{v dm}{dz}+\dfrac{w d\mu}{dz}+\dfrac{d\mathfrak{M}}{dz}+\mathrm{M}\lambda+m\mu+\mu\nu=\\ \dfrac{u d\mathrm{N}}{dy}+\dfrac{v dn}{dy}+\dfrac{w d\nu}{dy}+\dfrac{d\mathfrak{N}}{dy}+\mathrm{N}l+nm+\nu n.\end{cases}$$

59. Moreover, because of the nature of the complete differentials, we have

$$\begin{aligned}
&\frac{dL}{dy}=\frac{dl}{dx};\quad \frac{dm}{dx}=\frac{dM}{dy};\quad \frac{d\lambda}{dy}=\frac{dl}{dz};\\
&\frac{d\mu}{dx}=\frac{dM}{dz};\quad \frac{d\mathfrak{L}}{dy}=\frac{dl}{dt};\quad \frac{d\mathfrak{M}}{dx}=\frac{dM}{dt}\\
&\frac{dL}{dz}=\frac{d\lambda}{dx};\quad \frac{dl}{dz}=\frac{d\lambda}{dy};\quad \frac{dn}{dx}=\frac{dN}{dy};\\
&\frac{d\nu}{dx}=\frac{dN}{dz};\quad \frac{d\mathfrak{L}}{dz}=\frac{d\lambda}{dt};\quad \frac{d\mathfrak{N}}{dx}=\frac{dN}{dt};\\
&\frac{dM}{dz}=\frac{d\mu}{dx};\quad \frac{dN}{dy}=\frac{dn}{dx};\quad \frac{dm}{dz}=\frac{d\mu}{dy};\\
&\frac{d\nu}{dy}=\frac{dn}{dz};\quad \frac{d\mathfrak{M}}{dz}=\frac{d\mu}{dt};\quad \frac{d\mathfrak{N}}{dy}=\frac{dn}{dt},
\end{aligned}$$

after substituting of which values those three equations will be transformed into these[26]

$$\left(\frac{dl-d\mathrm{M}}{dt}\right)+u\left(\frac{dl-d\mathrm{M}}{dx}\right)+v\left(\frac{dl-d\mathrm{M}}{dy}\right)+ w\left(\frac{dl-d\mathrm{M}}{dz}\right)+(l-\mathrm{M})(\mathrm{L}+m)+\lambda n-\mu\mathrm{N}=0,$$

$$\left(\frac{d\lambda-d\mathrm{N}}{dt}\right)+u\left(\frac{d\lambda-d\mathrm{N}}{dx}\right)+v\left(\frac{d\lambda-d\mathrm{N}}{dy}\right)+ w\left(\frac{d\lambda-d\mathrm{N}}{dz}\right)+(\lambda-\mathrm{N})(\mathrm{L}+\nu)+l\mu-n\mathrm{M}=0,$$

$$\left(\frac{d\mu-dn}{dt}\right)+u\left(\frac{d\mu-dn}{dx}\right)+v\left(\frac{d\mu-dn}{dy}\right)+ w\left(\frac{d\mu-dn}{dz}\right)+(\mu-n)(m+\nu)+\mathrm{M}\lambda-\mathrm{N}l=0.$$

60. Now it is manifest that these three equations are satisfied by the following three values

$$l=\mathrm{M};\quad \lambda=\mathrm{N};\quad \mu=n$$

in which is contained the criterion furnished by the consideration of the forces. Here therefore follows that in the notation chosen we have[27]

$$\frac{du}{dy}=\frac{dv}{dx};\quad \frac{du}{dz}=\frac{dw}{dx};\quad \frac{dv}{dz}=\frac{dw}{dy}$$

these conditions moreover are the same as those which are required in order that the formula $udx+vdy+wdz$ be a complete differential. From which this criterion consists in that the three velocities u, v and w have to be functions of x, y and z together with t in such a manner that for fixed constant time the formula $udx+vdy+wdz$ admits an integration.

61. Taking the time t constant or $dt=0$, we have

$$\begin{aligned}
du&=\mathrm{L}dx+\mathrm{M}dy+\mathrm{N}dz\\
dv&=\mathrm{M}dx+mdy+ndz\\
dw&=\mathrm{N}dx+ndy+\nu dz
\end{aligned}$$

moreover, for R, r and ρ the values are

$$\begin{aligned}
\mathrm{R}&=-2(\mathrm{L}u+\mathrm{M}v+\mathrm{N}w+\mathfrak{L})\\
r&=-2(\mathrm{M}u+mv+nw+\mathfrak{M})\\
\rho&=-1-2(\mathrm{N}u+nv+\nu w+\mathfrak{N}).
\end{aligned}$$

Regarding the pressure p, we obtain the following equation

$$\begin{aligned}
&dp=-dz\\
&-2u(\mathrm{L}dx+\mathrm{M}dy+\mathrm{N}dz)=-dz-2udu-2vdv-2wdw\\
&-2v(\mathrm{M}dx+mdy+ndz)\qquad -2\mathfrak{L}dx-2\mathfrak{M}-2\mathfrak{N}dz\\
&-2w(\mathrm{N}dx+ndy+\nu dz)\\
&-2\mathfrak{L}dx-2\mathfrak{M}dy-2\mathfrak{N}dz.
\end{aligned}$$

62. Since in truth $\mathfrak{L}=\frac{du}{dt}$; $\mathfrak{M}=\frac{dv}{dt}$; $\mathfrak{N}=\frac{dw}{dt}$, we obtain by integration

$$p=\mathrm{C}-z-uu-vv-ww-2\int\left(\frac{du}{dt}dx+\frac{dv}{dt}dy+\frac{dw}{dt}dz\right).$$

By the previously ascertained condition $udx+vdy+wdz$ is integrable. Let us denote its integral by S, which can also involve the time t; taking also the time t variable, we have

$$d\mathrm{S}=udx+vdy+wdz+\mathrm{U}dt,$$

and we have $\frac{du}{dt}=\frac{d\mathrm{U}}{dx}$; $\frac{dv}{dt}=\frac{d\mathrm{U}}{dy}$; $\frac{dw}{dt}=\frac{d\mathrm{U}}{dz}$. From where, with time generally taken constant, it can be assumed in the above integral that

$$\frac{d\mathrm{U}}{dx}dx+\frac{d\mathrm{U}}{dy}dy+\frac{d\mathrm{U}}{dz}dz=d\mathrm{U},$$

and we obtain[28]

$$p=\mathrm{C}-z-uu-vv-ww-2\mathrm{U},\quad\text{or}$$
$$p=\mathrm{C}-z-uu-vv-ww-2\frac{d\mathrm{S}}{dt}.$$

63. Thus, $uu+vv+ww$ is manifestly expressing the square of the true velocity of the point λ, so that, if the true velocity of

[25] The printed version contains mistakes not present in Euler, 1752: in the formula labelled II, instead of L there is $\mathfrak{L}$; in the formula labelled III there is a v instead of u.

[26] These are the equations for the vorticity.

[27] Here Euler repeats the mistake of assuming that the only solution is zero-vorticity flow; in Euler, 1755 this will be corrected.

[28] The published version has a ds in the denominator, instead of the correct dt, found in Euler, 1752.

this point is denoted V, the following equation is obtained for the pressure[29]

$$p = \mathrm{C} - z - \mathrm{VV} - \frac{2d\mathrm{S}}{dt}.$$

To use this, firstly one must seek the integral S of the formula $udx + vdy + wdz$ which should be complete. This is differentiated again, taking only the time t as variable. After division by dt, one obtains the value of the formula $\frac{d\mathrm{S}}{dt}$, which enters into the expression for the state of the pressure p.

64. But before we may add here the previous criterion, regarding possible motion, the three velocities u, v and w must be such functions of the three coordinates x, y and z, and of time t that, firstly, $udx + vdy + wdz$ be a complete differential and, secondly, that the condition $\frac{du}{dx} + \frac{dv}{dy} + \frac{dw}{dz} = 0$ holds. The whole motion of fluids endowed with invariable density is subjected to these two conditions.

Furthermore, if we take also the time t to be variable, and the differential formula $udx + vdy + wdz + \mathrm{U}dt$ is a complete differential, the state of the pressure at any point λ, expressed as an altitude p, will be given by

$$p = \mathrm{C} - z - uu - vv - ww - 2\mathrm{U},$$

if only the fluid enjoys the natural gravity and the plane BAL is horizontal.

65. Suppose we had attributed another direction to the gravity or even adopted arbitrary variable forces acting on the particles of the fluid. Differences would arise in the values of the pressure, but the law which the three velocities of the fluid have to obey would not suffer any changes. Thus, whatever the acting forces, the three velocities u, v and w have to satisfy the conditions that the differential formula $udx + vdy + wdz$ be complete and that $\frac{du}{dx} + \frac{dv}{dy} + \frac{dw}{dz} = 0$ should hold. Therefore, the three velocities u, v and w can be fixed in infinitely many ways while satisfying the two conditions; and then it is possible to prescribe the pressure at every point of the fluid.[30]

66. However, much more difficult would be the following question: given the acting forces and the pressure at all places, to determine the motion of the fluid at all points. Indeed, we would then have some equations[31] of the form $p = \mathrm{C} - z - uu - vv - ww - 2\mathrm{U}$, from which the relation of the functions u, v and w would have to be defined in such a way that not only the equations themselves would be satisfied, but also the previously contributed rules[32] would have to be obeyed; this work would certainly require the greatest force of calculation. It is fitting therefore to inquire in general into the nature of functions proper to satisfy both criteria.

67. Most conveniently therefore let us begin with the characterization of the integral quantity S, whose differential is $udx + vdy + wdz$, when time is held constant. Let thus S be a function of x, y and z, the time t being contained in constant quantities. When S is differentiated, the coefficients of the differentials dx, dy and dz are the velocities u, v and w which at the present time suit the point of fluid λ, whose coordinates are x, y and z. The question thus arises here to find the functions S of x, y and z such that $\frac{du}{dx} + \frac{dv}{dy} + \frac{dw}{dz} = 0$; now, since we have $u = \frac{dS}{dx}$, $v = \frac{dS}{dy}$ and $w = \frac{dS}{dz}$ it follows that $\frac{dd\mathrm{S}}{dx^2} + \frac{dd\mathrm{S}}{dy^2} + \frac{dd\mathrm{S}}{dz^2} = 0$.[33]

68. Since it is not plain how this can be handled in general, I shall consider certain rather general cases. Let

$$\mathrm{S} = (\mathrm{A}x + \mathrm{B}y + \mathrm{C}z)^n.$$

We have

$$\frac{d\mathrm{S}}{dx} = n\mathrm{A}(\mathrm{A}x + \mathrm{B}y + \mathrm{C}z)^{n-1} \text{ and}$$
$$\frac{dd\mathrm{S}}{dx^2} = n(n-1)\mathrm{AA}(\mathrm{A}x + \mathrm{B}y + \mathrm{C}z)^{n-2}$$

and the expressions for $\frac{dd\mathrm{S}}{dy^2}$ and $\frac{dd\mathrm{S}}{dz^2}$ will be similar. Thus we have to satisfy

$$n(n-1)(\mathrm{A}x + \mathrm{B}y + \mathrm{C}z)^{n-2}(\mathrm{AA} + \mathrm{BB} + \mathrm{CC}) = 0$$

which is plainly satisfied when either $n = 0$ or $n = 1$. Thus we have the solutions S = Const. and $\mathrm{S} = \mathrm{A}x + \mathrm{B}y + \mathrm{C}z$, where the constants A, B and C are arbitrary.

69. But if n is neither 0, nor 1, we necessarily have: $\mathrm{AA} + \mathrm{BB} + \mathrm{CC} = 0$: and then S is given by

$$\mathrm{S} = (\mathrm{A}x + \mathrm{B}y + \mathrm{C}z)^n$$

for any value of the exponent n; even the time t itself will possibly enter in n. Furthermore we can add up arbitrarily many such S and obtain yet another solution.[34] The function

$$\mathrm{S} = \alpha + \beta x + \gamma y + \delta z + \epsilon(\mathrm{A}x + \mathrm{B}y + \mathrm{C}z)^n + \zeta(\mathrm{A}'x + \mathrm{B}'y + \mathrm{C}'z)^{n'} + \eta(\mathrm{A}''x + \mathrm{B}''y + \mathrm{C}''z)^{n''} + \theta(\mathrm{A}'''x + \mathrm{B}'''y + \mathrm{C}'''z)^{n'''} \text{ etc.}$$

will satisfy the condition only if we have:

$$\mathrm{AA} + \mathrm{BB} + \mathrm{CC} = 0; \quad \mathrm{A}'\mathrm{A}' + \mathrm{B}'\mathrm{B}' + \mathrm{C}'\mathrm{C}' = 0;$$
$$\mathrm{A}''\mathrm{A}'' + \mathrm{B}''\mathrm{B}'' + \mathrm{C}''\mathrm{C}'' = 0 \text{ etc.}$$

70. Here suitable values are given for S in which the coordinates x, y, z have either one, or two, or three, or four dimensions[35]

I. $\mathrm{S} = \mathrm{A}$
II. $\mathrm{S} = \mathrm{A}x + \mathrm{B}y + \mathrm{C}z$
III. $\mathrm{S} = \mathrm{A}xx + \mathrm{B}yy + \mathrm{C}zz + 2\mathrm{D}xy + 2\mathrm{E}xz + 2\mathrm{F}yz$ with $\mathrm{A} + \mathrm{B} + \mathrm{C} = 0$

29 This is basically the Bernoulli pressure law for potential flow.

30 Many statements in this paragraph are rendered invalid by the generally incorrect assumption of potential flow.

31 The plural is here used probably because this relation has to be satisfied at all points.

32 Incompressibility and potentiality.

33 This is what will later be called Laplace's equation.

34 In modern terms, Euler is here using the linear character of the Laplace equation.

35 In modern terms we would say "which are polynomials in x, y, z of degrees up to four".

IV. $S = Ax^3 + By^3 + Cz^3 + 3Dxxy + 3Fxxz + Hyyz + 6Kxyz + 3Exyy + 3Gxzz + 3Iyzz$ with $A + E + G = 0$; $B + D + I = 0$; $C + F + H = 0$

V.

$$S = \begin{array}{l} + Ax^4 + 6Dxxyy + 4Gx^3y + 4Hxy^3 + 12Nxxyz \\ + By^4 + 6Exxzz + 4Ix^3z + 4Kxz^3 + 12Oxyyz \\ + Cz^4 + 6Fyyzz + 4Ly^3z + 4Myz^3 + 12Pxyzz \end{array}$$

with

$$\begin{array}{ll} A + D + E = 0 & G + H + P = 0 \\ B + D + F = 0 & I + K + O = 0 \\ C + E + F = 0 & L + M + N = 0. \end{array}$$

71. Hence it is clear how these formulas are to be obtained for any order. First, simply give to the various terms the numerical coefficients which belong to them from the law of permutation, or, equivalently, which arise when the trinomial $x + y + z$ is raised to that same power. Let indefinite letters A, B, C, etc., be adjoined to the numerical coefficients. Then, ignoring the coefficients, observe whenever there occur three terms of the type $LZx^2 + MZy^2 + NZz^2$ having a common factor Z formed from the variables. Whenever this occurs, set the sum of the literal coefficients $L + M + N$ equal to zero. For example, for the fifth power we have

$$\begin{aligned} S = {} & Ax^5 + 5Dx^4y + 5\mathfrak{D}x^4z + 10Gx^3yy + \mathfrak{G}x^3zz + \\ & 20Kx^3yz + 30Nxyyzz + \\ & Bx^5 + 5Ex^4y + 5\mathfrak{E}x^4z + 10Hx^3yy + \mathfrak{H}x^3zz + \\ & 20Lx^3yz + 30Oxyyzz \\ & + Cx^5 + 5Fx^4y + 5\mathfrak{F}x^4z + 10Ix^3yy + \mathfrak{I}x^3zz + \\ & 20Mx^3yz + 30Pxyyzz \end{aligned}$$

and the following determinations of the coefficient letters are obtained

$$\begin{array}{lll} A + G + \mathfrak{G} = 0; & D + H + O = 0; & \mathfrak{D} + I + P = 0; \\ B + H + \mathfrak{H} = 0; & E + G + N = 0; & \mathfrak{G} + F + P = 0; \\ K + L + M = 0; & & \\ C + I + \mathfrak{F} = 0; & F + \mathfrak{G} + N = 0; & \mathfrak{F} + \mathfrak{H} + O = 0. \end{array}$$

In the same way for the sixth order such determinations will give 15, for the seventh 21, for the eighth 28 and so on.

72. In the very first formula $S = A$ the coordinates x, y and z are clearly not intertwined. Thus the three velocities u, v and w are equal to zero, and hence this describes a quiet state of fluid. Also the pressure at an arbitrary point for different times will be able to vary in an arbitrary manner. Indeed A is an arbitrary function of time and, for a given time t, the pressure at the point λ is $p = C - \frac{2dA}{dt} - z$. Through this formula is revealed the state of the fluid, when it is subjected at an arbitrary instant to arbitrary forces, which nevertheless balance each other, so that no motion in the fluid can arise from them: where it happens, if the fluid is enclosed in a vase from which it can nowhere escape, it is also compressed by suitable forces inside.

73. Moreover, the second formula $S = Ax + By + Cz$, after differentiation, gives these three velocities to the point λ:

$$u = A; \quad v = B \quad \text{and} \quad w = C.$$

Thus simultaneously, all points of the fluid are carried by an identical motion in the same direction. From which the whole fluid moves in the same manner as a solid body, carried only by a forward motion. But at different times the velocities as well as the direction of this motion are able to be varied in an arbitrary way, depending on what the extrinsic driving forces require. Therefore, the pressure at the point λ at the time t on which A, B, C depend, is[36] $p = C - z - AA - BB - CC - 2x\frac{dA}{dt} - 2y\frac{dB}{dt} - 2z\frac{dC}{dt}$.

74. The third formula $S = Axx + Byy + Czz + 2Dxy + 2Exz + 2Fyz$, where $A + B + C = 0$, gives the following three velocities[37] of the point λ: $u = 2Ax + 2Dy + 2Ez$; $v = 2By + 2Dx + 2Fz$; $w = 2Cz + 2Ex + 2Fy$, or $w = 2Ex + 2Fy - 2(A + B)z$. Here, at a given instant, different points of the fluid are carried by different motions; moreover, in the time development an arbitrary motion of a given point is permitted, because A, B, D, E, F can be arbitrary functions of the time t. Finally, a much greater variety can take place, if more elaborate values are given to the function S.

75. In the second case the motion of the fluid was corresponding to the forward motion of a solid body in which, plainly, at any instant the different parts are carried by a motion equal and parallel to itself. In other cases the motion of the fluid could be suspected to correspond to solid-body motion, either rotational or anomalous. It suffices to put forward such a hypothesis – beyond the second case – to find that it cannot take place. Indeed, in order to happen, not only would it be necessary that the pyramid $\pi\Phi\rho\sigma$ would be equal,[38] but also similar to the pyramid $\lambda\mu\nu o$, or that the following holds

$$\begin{aligned} &\pi\Phi = \lambda\mu = dx = \surd(QQ + qq + \Phi\Phi) \\ &\pi\rho = \lambda\nu = dy = \surd(RR + rr + \rho\rho) \\ &\pi\sigma = \lambda o = dz = \surd(SS + ss + \sigma\sigma) \\ &\Phi\rho = \mu\nu = \surd(dx^2 + dy^2) = \\ &\surd((Q - R)^2 + (q - r)^2 + (\Phi - \rho)^2) \\ &\Phi\sigma = \mu o = \surd(dx^2 + dz^2) = \\ &\surd((Q - S)^2 + (q - s)^2 + (\Phi - \sigma)^2) \\ &\rho\sigma = \nu o = \surd(dy^2 + dz^2) = \\ &\surd((R - S)^2 + (r - s)^2 + (\rho - \sigma)^2), \end{aligned}$$

where we applied the values taken from §. 32.

76. Then the three latter equations, combined with the former, are reduced to these:

$$QR + qr + \Phi\rho = 0; \; QS + qs + \Phi\sigma = 0 \text{ and } RS + rs + \rho\sigma = 0.$$

36 The printed version, but not Euler, 1752, has a missing BB in the formula.

37 In both the printed version and in Euler, 1752, the first velocity component is mistakenly denoted by α.

38 In volume.

Moreover, if the values assigned in §. 34 are substituted for the letters Q, R, S, q, r, s, Φ, ρ, σ and the higher-order terms for the rests are neglected, the three former will give

$$1 = 1 + 2\mathrm{L}dt; \quad l + \mathrm{M} = 0;$$
$$1 = 1 + 2m dt; \quad \lambda + \mathrm{N} = 0;$$
$$1 = 1 + 2\nu dt; \quad \mu + n = 0,$$

so that we have $\mathrm{L} = 0\, m = 0$ and $\nu = 0$, $\mathrm{M} = -l$, $\mathrm{N} = -\lambda$ and $n = -\mu$.

77. Thus, the three velocities of this point λ would have to be compared to the condition that the following hold[39]

$$du = l dy + \lambda dz;$$
$$dv = -l dx + \mu dz;$$
$$dw = -\lambda dx - \mu dy.$$

But the second condition demands a motion of the fluid such that $l = \mathrm{M}$, $\lambda = \mathrm{N}$ and $n = \mu$; hence all the coefficients l, λ and μ vanish; also the velocities u, v and w will take the same value everywhere in the fluid. Therefore it is plain that the motion of the fluid cannot correspond to solid-body motion other than pure translational.

78. To ascertain the effect of the forces which act from the outside upon the fluid, it is first necessary to determine those forces[40] which are required for effecting the motion which we have assumed to exist in the fluid. These are equivalent to the forces which in fact work upon the fluid; furthermore we have seen above in §. 56 that three accelerating forces are required, which are here repeated. If an element of fluid is conceived here, whose volume, or mass is $dxdydz$, the moving forces required for the motion are

$$\text{par. AL} = 2dxdydz(\mathrm{L}u + lv + \lambda w + \mathfrak{L}) = 2dxdydz\left(u\frac{du}{dx} + v\frac{du}{dy} + w\frac{du}{dz} + \frac{du}{dt}\right);$$
$$\text{par. AB} = 2dxdydz(\mathrm{M}u + mv + \mu w + \mathfrak{M}) = 2dxdydz\left(u\frac{dv}{dx} + v\frac{dv}{dy} + w\frac{dv}{dz} + \frac{dv}{dt}\right);$$
$$\text{par. AC} = 2dxdydz(\mathrm{N}u + nv + \nu w + \mathfrak{N}) = 2dxdydz\left(u\frac{dw}{dx} + v\frac{dw}{dy} + w\frac{dw}{dz} + \frac{dw}{dt}\right),$$

so that by triple integration the components of the total forces which must act on the whole mass of fluid may be obtained.

79. But since the second condition requires that $udx+vdy+wdz$ be a complete differential, whose integral is S, let us put as before, with time allowed to vary, $d\mathrm{S} = udx+vdy+wdz+\mathrm{U}dt$. Since $\frac{du}{dy} = \frac{dv}{dx}$; $\frac{du}{dz} = \frac{dw}{dx}$; $\frac{du}{dt} = \frac{d\mathrm{U}}{dx}$ those three moving forces emerge[41]:

$$\text{par. AL} = 2dxdydz\left(\frac{udu + vdv + wdw + d\mathrm{U}}{dx}\right)$$
$$\text{par. AB} = 2dxdydz\left(\frac{udu + vdv + wdw + d\mathrm{U}}{dy}\right)$$
$$\text{par. AL} = 2dxdydz\left(\frac{udu + vdv + wdw + d\mathrm{U}}{dz}\right).$$

80. Let us set now $uu + vv + ww + 2\mathrm{U} = \mathrm{T}$. The function T depends on the coordinates x. y, z; take it at a given instant of time t:[42]

$$d\mathrm{T} = \mathrm{K}dx + kdy + \kappa dz.$$

The three moving forces of the element $dxdydz$ are[43]

$$\text{par. AL} = \mathrm{K}dxdydz$$
$$\text{par. AB} = kdxdydz$$
$$\text{par. AC} = \kappa dxdydz$$

and by triple integration these formulas ought to be extended throughout the mass of the fluid; thus forces equivalent to all[44] and their directions may be obtained. Truly this discussion is for a later investigation, which I shall not deepen here.

81. Furthermore, the quantity $\mathrm{T} = uu+vv+ww+2\mathrm{U}$, which is analyzed in this calculation, furnishes a simpler formula for expressing the pressure through the height p; we have indeed $p = \mathrm{C} - z - \mathrm{T}$ when the particles of the fluid are pressed upon solely by the gravity. But if an arbitrary particle λ is acted upon by three accelerating forces which are Q, q and Φ, acting parallel to the directions of the axes AF, AB and AC, respectively, after a calculation similar to the previous one has been carried out, the pressure will be given by

$$p = \mathrm{C} + \int (\mathrm{Q}dx + qdy + \Phi dz) - \mathrm{T}.$$

Thus it is plain that the differential $\mathrm{Q} + qdy + \Phi dz$ must be complete, as otherwise a state of equilibrium, or at least a possible one, could not exist. That this condition must be imposed on the acting forces Q, q and Φ was shown very clearly by the most famous Mr. Clairaut.[45]

82. Here are, therefore, the principles of the entire doctrine of the motion of fluids, which, even if they at first sight may seem insufficiently fruitful, nevertheless embrace almost everything treated both in hydrostatics and in hydraulics, so that these principles must be regarded as having very broad extent. For this to appear more clearly, it is worthwhile to show how the precepts learned in hydrostatics and hydraulics follow.

83. Let us therefore consider first a fluid in a state of rest, so that we have $u = 0$, $v = 0$ and $w = 0$; in view of $\mathrm{T} = 2\mathrm{U}$, the pressure in an arbitrary point λ of the fluid is

$$p = \mathrm{C} + \int (\mathrm{Q}dx + qdy + \Phi dz) - 2\mathrm{U}.$$

Here, U is a function of the time t itself which we take as constant. Indeed, we investigate the pressure at a given time;

39 In the printed version, but not in Euler, 1752, there are several sign mistakes.

40 Here, internal forces are meant.

41 There is a misprint in the printed version, w instead of $+$.

42 There is a misprint: u instead of κ.

43 Here is again a misprint: k instead of κ.

44 The pressure forces.

45 Clairaut, 1743.

the quantity U can be included in the constant C, so that we obtain

$$p = \mathrm{C} + \int (\mathrm{Q}dx + qdy + \Phi dz)$$

where Q, q an Φ are the forces acting on the particle of water λ, parallel to the axes AL, AB and AC.

84. The pressure p can only depend on the position of the point λ that is on the coordinates x, y and z; it is thus necessary that $\int(\mathrm{Q}dx + qdy + \Phi dz)$ be a prescribed function of them, which therefore admits integration. Thus it is firstly clear that in the manner indicated the fluid cannot be sustained in equilibrium, unless the forces acting on each element of the fluid are such that the differential formula $\mathrm{Q}dx + qdy + \Phi dz$ is complete. Thus, if its integral is denoted P, the pressure at λ will be $p = \mathrm{C} + \mathrm{P}$. Therefore, if the only force present is gravity, impelling parallel to the direction CA, we shall have $p = \mathrm{C} - z$; hence, if the pressure is fixed at one point λ, the constant C can be obtained. From which the pressure at a given time will be defined completely at all points of the fluid.

85. However, with time passing, the pressure at a given place can change; and this plainly occurs, if variability is assumed for the forces impelling on the water, whose calculation cannot be made from those forces which are assumed to act on each element of the fluid,[46] but in such a way that they keep each other in equilibrium and produce no motion. But if, moreover, these forces are not subject to any change, the letter C will indeed denote a constant quantity, not depending on time t; and at a given location λ we will always find the same pressure $p = \mathrm{C} + \mathrm{P}$.

86. It is possible to determine the extremal shape of a fluid in a permanent state, when it is not subjected to any force.[47] Certainly, at the extreme surface of the fluid at which the fluid is left to itself and not contained within the walls of the vase in which it is enclosed, the pressure must be zero. Thus we shall obtain the following equation: $\mathrm{P} = \text{const}$; the shape of the external surface of the fluid is then expressed through a relation between the three coordinates x, y and z. And if for the external circumference held $\mathrm{P} = \mathrm{E}$, since $\mathrm{C} = -\mathrm{E}$, in another arbitrary internal location λ the pressure would be $p = \mathrm{P} - \mathrm{E}$. In this manner, if the particles of the fluid are driven by gravity only, and because $p = \mathrm{C} - z$, the following will hold at for the external surface $z = \mathrm{C}$; from which the external free surface is perceived to be horizontal.

87. Next, everything which has so far been brought out concerning the motion of a fluid through tubes is easily derived from these principles. The tubes are usually regarded as very narrow, or else are assumed to be such that through any section normal to the tube the fluid flows across with equal motion: from there originates the rule, that the speed of the fluid at any place in the tube is reciprocally proportional to its amplitude. Let therefore λ be an arbitrary point of such a tube, of which the shape is expressed by two equations relating the three coordinates x, y and z, so that thereupon for any abscissa x the two remaining coordinates y and z can be defined.

88. Let henceforth the cross section of this tube at λ be rr; in another fixed location of the tube, where the cross-section is ff, let the velocity at the present time be $\Taurus$; now after time dt has elapsed, let the velocity become $\Taurus + d\Taurus$, so that $\Taurus$ is a function of time t, and similarly with $\frac{d\Taurus}{dt}$. Hence the true velocity of the fluid at λ will be at the present time $V = \frac{ff\Taurus}{rr}$. Since now y and z are obtained from the shape of the tube, we have $dy = \eta dx$ and $dz = \theta dx$; thus the three velocities of the point λ in the fluid, parallel to directions AL, AB and AC, are

$$u = \frac{ff\Taurus}{rr}\,\frac{1}{\surd(1+\eta\eta+\theta\theta)}; \quad v = \frac{ff\Taurus}{rr}\,\frac{\eta}{\surd(1+\eta\eta+\theta\theta)};$$
$$w = \frac{ff\Taurus}{rr}\,\frac{\theta}{\surd(1+\eta\eta+\theta\theta)},$$

and hence, $uu + vv + ww = \mathrm{VV} = \frac{f^4\Taurus\Taurus}{r^4}$: and rr is function of x itself, thus of the dependent variables y and z.

89. Since $udx + vdy + wdz$ must be a complete differential, the integral of which is denoted $= S$, we have:

$$d\mathrm{S} = \frac{ff\Taurus}{rr}\,\frac{dx(1+\eta\eta+\theta\theta)}{\surd(1+\eta\eta+\theta\theta)} = \frac{ff\Taurus}{rr}\,dx\surd(1+\eta\eta+\theta\theta).$$

Moreover, $dx\surd(1+\eta\eta+\theta\theta)$ expresses the element of the tube itself; if we denote it by ds, we shall obtain $d\mathrm{S} = \frac{ff\Taurus ds}{rr}$: although $\Taurus$ is a function of the time,[48] here we fix the time and, furthermore, the quantities s and rr do not depend on time but only on the shape of the tube; thus we have $\mathrm{S} = \Taurus\int\frac{ffds}{rr}$.

90. Turning now to the pressure p which is found at the point of the tube λ, the quantity U has to be considered; it arises from the differentiation of the quantity S, if the time only is considered as variable, so that we have $\mathrm{U} = \frac{d\mathrm{S}}{dt}$. Thus, since the integral formula $\int\frac{ffds}{rr}$ does not involve time t, on the one hand we shall have $\frac{d\mathrm{S}}{dt} = \mathrm{U} = \frac{d\mathrm{U}}{dt}\int\frac{ffds}{rr}$, and on the other hand it will follow from §. 80 that:

$$\mathrm{T} = \frac{f^4\Taurus\Taurus}{r^4} + \frac{2d\Taurus}{dt}\int\frac{ffds}{rr}.$$

Therefore, after introducing arbitrary actions of forces Q, q and Φ, the pressure at λ will be

$$p = \mathrm{C} + \int(Q\,dx + q\,dy + \Phi\,dz) - \frac{f^4\Taurus\Taurus}{r^4} - \frac{2d\Taurus}{dt}\int\frac{ffds}{rr}.$$

This is that same formula which is commonly written for the motion of a fluid through tubes; but now much more widely valid, since arbitrary forces acting on the fluid are assumed here, while this formula is commonly restricted to gravity alone. Meanwhile it is in order to remember that the three forces Q, q and Φ must be such that the differential formula $Q\,dx + q\,dy + \Phi\,dz$ be complete, that is, admit integration.

[46] That is the internal pressure forces.

[47] Here, Euler will comment on the shape of the free (extreme) surface of a fluid contained in an open vessel.

[48] As was stated in §. 88.

References

D'Alembert Jean le Rond, 1752 *Essai d'une Nouvelle Théorie de la Résistance des Fluides*, Paris.

Clairaut Alexis, 1743 *Théorie de la Figure de la Terre, Tirée des Principes de l'Hydrostatique*, Paris.

Darrigol Olivier, Frisch Uriel, 2008 'From Newton's mechanics to Euler's equations', these Proceedings. Also at www.oca.eu/etc7/EE250/texts/darrigol-frisch.pdf.

Euler Leonhard, 1750 'Découverte d'un nouveau principe de mécanique'. Académie Royale des Sciences et des Belles-Lettres de Berlin, *Mémoires*, **6** [printed in 1752], 185–217. Also in *Opera omnia*, ser. 2, **5**, 81–108, **E177**.

Euler Leonhard, 1752 'De motu fluidorum in genere', early version of Euler, 1756–1757 [handwritten copy], deposited at the Berlin-Brandenburg Akademie der Wissenschaften, Akademie-Archiv call number: I-M 120.

Euler Leonhard, 1755 'Principes généraux du mouvement des fluides', Académie Royale des Sciences et des Belles-Lettres de Berlin, *Mémoires* **11** [printed in 1757], 274–315. Also in *Opera omnia*, ser. 2, **12**, 54–91, [Eneström index] **E226**. English translation in these Proceedings.

Euler Leonhard, 1756–1757 'Principia motus fluidorum' [written in 1752]. *Novi commentarii academiae scientiarum Petropolitanae*, **6** [printed in 1761], 271–311. Also in *Opera omnia*, ser. 2, **12**, 133–168, **E258**.

Euler Leonhard, 1980 *Commercium epistolicum*, ser. 4A, **5**, eds. A. Juskevic and R. Taton. Basel.

Fontaine Alexis, 1764 *Le calcul intégral.—Mémoires donnés à l'Académie royale des sciences, non imprimés dans leur temps*, Paris.

Mikhailov Gleb K., 1999 'The origins of hydraulics and hydrodynamics in the work of the Petersburg Academicians of the 18th century'. *Fluid dynamics*, **34**, 787–800.

Truesdell Clifford, 1954 'Rational fluid mechanics, 1657–1765'. In Euler, *Opera omnia*, ser. 2, **12** (Lausanne), IX–CXXV.

Historical perspective

Available online at www.sciencedirect.com
ScienceDirect
Physica D 237 (2008) 1855–1869
PHYSICA D
www.elsevier.com/locate/physd

From Newton's mechanics to Euler's equations[☆]

O. Darrigol[a], U. Frisch[b,*]

[a] CNRS:Rehseis, 83, rue Broca, 75013 Paris, France
[b] Labor. Cassiopée, UNSA, CNRS, OCA, BP 4229, 06304 Nice Cedex 4, France

Available online 17 August 2007

Abstract

The Euler equations of hydrodynamics, which appeared in their present form in the 1750s, did not emerge in the middle of a desert. We shall see in particular how the Bernoullis contributed much to the transmutation of hydrostatics into hydrodynamics, how d'Alembert was the first to describe fluid motion using partial differential equations and a general principle linking statics and dynamics, and how Euler developed the modern concept of internal pressure field which allowed him to apply Newton's second law to infinitesimal elements of the fluid.

Keywords: History of science; Fluid dynamics; Euler equations

Quelques sublimes que soient les recherches sur les fluides, dont nous sommes redevables à Mrs. *Bernoullis, Clairaut*, & *d'Alembert*, elles découlent si naturellement de mes deux formules générales : qu'on ne scauroit assés admirer cet accord de leurs profondes méditations avec la simplicité des principes, d'où j'ai tiré mes deux équations, & auxquels j'ai été conduit immédiatement par les premiers axiomes de la Mécanique.[1]

(Leonhard Euler, 1755)

1. Introduction

Leonhard Euler had a strong interest in fluid dynamics and related subjects during all his adult life. In 1827, at age twenty, he published an important paper on the theory of sound. In that paper, he gave a quantitative theory of the oscillations of the column of air in a flute or similar instruments. On a slate found after his death on 7 September 1783 he had developed a theory of aerostatic balloons, having just learned about the first manned ascent of a balloon designed by the Montgolfier brothers. Altogether, he published more than forty papers or books devoted to fluid dynamics and applications. After his arrival in Saint-Petersburg in 1727, and perhaps before, Euler was planning a treatise on fluid mechanics based on the principle of live forces. He recognized the similarity of his project with Daniel Bernoulli's and left the field open to this elder friend. During the fourteen years of his first Petersburg stay, Euler was actively involved in establishing the theoretical foundations of naval science, thereby contributing to the ongoing effort of the Russian state in developing a modern and powerful fleet. His *Sciencia Navalis*, completed by 1738 and published in 1749, contained a clear formulation of hydrostatic laws and their application to the problem of ship stability. It also involved a few Newtonian considerations on ship resistance. Soon after his move to Berlin in 1741, he edited the German translation of Benjamin Robins's *New Principles of Gunnery*, as a consequence of Frederick II's strong interest in the science of artillery. Published in 1745, this edition included much innovative commentary on the problem of the resistance of the air to the motion of projectiles, especially regarding the effects of high speed and cavitation.[2]

☆ The present article includes large sections of Chapter 1 of Darrigol, 2005, thanks to the kind permission of Oxford University Press. We mention that one of the authors (OD) is a theoretical physicist by early training who became a historian of science some twenty years ago, while the other one (UF) is a fluid dynamicist interested in Euler's equations since the seventies.

* Corresponding author. Tel.: +33 4 92003035; fax: +33 4 92003058.
E-mail address: uriel@obs-nice.fr (U. Frisch).

1 Euler, 1755c: 316[original publication page]/92[*omnia* page]: However sublime the researches on fluids that we owe to Messrs *Bernoullis*, *Clairaut*, and *d'Alembert* may be, they derive so naturally from my two general formulas that one could not cease to admire this agreement of their profound meditations with the simplicity of the principles from which I have drawn my two equations and to which I have been immediately driven by the first axioms of Mechanics.

2 Euler, 1727, [1784] (balloons), 1745, 1749. For general biography, cf. Youschkevitch, 1971; Knobloch, 2008 and references therein. On Euler and

0167-2789/$ - see front matter
doi:10.1016/j.physd.2007.08.003

Today's fluid dynamics cannot be conceived without the fundamental basis of Euler's equations, as they appear in "Principes généraux du mouvement des fluides", presented to the Académie Royale des Sciences et Belles-Lettres (Berlin) on 4 September 1755 and published in 1757. In Euler's own notation, they read:

$$\left.\begin{aligned}
&\left(\frac{\mathrm{d}q}{\mathrm{d}t}\right)+\left(\frac{\mathrm{d}.qu}{\mathrm{d}x}\right)+\left(\frac{\mathrm{d}.qv}{\mathrm{d}y}\right)+\left(\frac{\mathrm{d}.qw}{\mathrm{d}z}\right)=0\\
&P-\frac{1}{q}\left(\frac{\mathrm{d}p}{\mathrm{d}x}\right)\\
&\quad=\left(\frac{\mathrm{d}u}{\mathrm{d}t}\right)+u\left(\frac{\mathrm{d}u}{\mathrm{d}x}\right)+v\left(\frac{\mathrm{d}u}{\mathrm{d}y}\right)+w\left(\frac{\mathrm{d}u}{\mathrm{d}z}\right)\\
&Q-\frac{1}{q}\left(\frac{\mathrm{d}p}{\mathrm{d}y}\right)\\
&\quad=\left(\frac{\mathrm{d}v}{\mathrm{d}t}\right)+u\left(\frac{\mathrm{d}v}{\mathrm{d}x}\right)+v\left(\frac{\mathrm{d}v}{\mathrm{d}y}\right)+w\left(\frac{\mathrm{d}v}{\mathrm{d}z}\right)\\
&R-\frac{1}{q}\left(\frac{\mathrm{d}p}{\mathrm{d}z}\right)\\
&\quad=\left(\frac{\mathrm{d}w}{\mathrm{d}t}\right)+u\left(\frac{\mathrm{d}w}{\mathrm{d}x}\right)+v\left(\frac{\mathrm{d}w}{\mathrm{d}y}\right)+w\left(\frac{\mathrm{d}w}{\mathrm{d}z}\right).
\end{aligned}\right\}\qquad(1)$$

Here, P, Q, and R are the components of an external force, such as gravity. The modern reader with no special training in the history of science will nevertheless recognize these equations and be barely distracted by the use of q instead of ρ for density, of $\left(\frac{\mathrm{d}u}{\mathrm{d}x}\right)$ instead of $\frac{\partial u}{\partial x}$ and of $\mathrm{d}.qu$ instead of $\partial(qu)$.[3]

Euler's three memoirs on fluid dynamics written in 1755 contain, of course, much more than these equations. They are immediately intelligible to the modern reader, the arguments being strikingly close to those given in modern treatises. They mark the emergence of a new style of mathematical physics in which fundamental equations take the place of fundamental principles formulated in ordinary or geometrical language. Euler's equations are also the first instance of a *nonlinear* field theory and remain to this day shrouded in mystery, contrary for example to the heat equation introduced by Fourier in 1807 and the Maxwell equations discovered in 1862.

Our main goal is to trace the development and maturation of the physical and mathematical concepts, such as internal pressure, which eventually enabled Euler to produce his memoirs of the 1750s.[4] The emergence of Euler's equations was the result of several decades of intense work involving such great figures as Isaac Newton, Alexis Clairaut, Johann and Daniel Bernoulli, Jean le Rond d'Alembert ... and Euler himself. It is thus also our goal to help the reader to see how such early work, which is frequently difficult because it is not couched in modern scientific language, connects with Euler's maturing views on continuum mechanics and his papers of the 1750s.

Section 2 is devoted to the first applications of Newtonian mechanics to fluid flow, from Newton to the Bernoullis. Whereas Isaac Newton treated a few particular problems with heteroclite and ad hoc methods, Daniel and Johann Bernoulli managed to solve a large class of problems through a uniform dynamical method. Section 3 shows how Jean le Rond d'Alembert's own dynamical method and mathematical creativity permitted a great extension of the investigated class of flows. Despite its now antiquated formulation, his theory had many of the key concepts of the modern theory of incompressible flows. In Section 4 we discuss Euler's memoirs of the 1750s. Finally, a few conclusions are presented in Section 5. Another paper in these Proceedings focuses on Euler's 1745 third remark (Theorem 1) à propos Robins's Gunnery. This remark, which actually constitutes a standalone paper of eleven pages on the problem of steady flow around a solid body, is at the crossroads of eighteenth-century fluid dynamics: it uses many ideas of the Bernoullis to write the equations in local coordinates and has been viewed, correctly or not, as a precursor of d'Alembert's derivation of the paradox of vanishing resistance (drag) for ideal flow.[5]

2. From Newton to the Bernoullis

2.1. Newton's principia

Through the eighteenth century, the main contexts for studies of fluid motion were water supply, water-wheels, navigation, wind-mills, artillery, sound propagation, and Descartes's vortex theory. The most discussed questions were the efflux of water through the short outlet of a vessel, the impact of a water vein over a solid plane, and fluid resistance for ships and bullets. Because of its practical importance and of its analogy with Galilean free-fall, the problem of efflux got special attention from a few pioneers of Galilean mechanics. In 1644, Evangelista Torricelli gave the law for the velocity of the escaping fluid as a function of the height of the water level; in the last quarter of the same century, Edme Mariotte, Christiaan Huygens, and Isaac Newton tried to improve its experimental and theoretical foundations of this law.[6]

More originally, Newton devoted a large section of his *Principia* to the problem of fluid resistance, mainly to disprove the Cartesian theory of planetary motion. One of his results, the proportionality of inertial resistance to the square of the velocity of the moving body, only depended on a similarity argument. His more refined results required some drastically simplified models of the fluid and its motion. In one model, he treated the fluid as a set of isolated particles individually impacting the head of the moving body; in another, he preserved the continuity of the fluid but assumed a discontinuous, cataract-like motion around the immersed body. In addition, Newton

hydraulics, cf. Mikhailov, 1983. On sound, cf. Truesdell, 1955: XXIV–XXIX. On the early treatise on fluids, cf. Mikhailov, 1999, and pp. 61–62, 80 in Euler, 1998. On naval science, cf. Nowacki, 2006; Truesdell, 1954: XVII–XVIII, 1983. On gunnery, cf. Truesdell, 1954: XXVIII–XLI.

3 Euler, 1755b.

4 Detailed presentations of these may be found in Truesdell's 1954 landmark work on Euler and fluid dynamics.

5 Grimberg, Pauls and Frisch, 2008. Truesdell, 1954: XXXVIII–XLI.

6 Cf. Truesdell, 1954: IX–XIV; Rouse and Ince, 1957: Chaps. 2–9; Garbrecht, 1987; Blay, 1992, Eckert, 2005: Chap. 1.

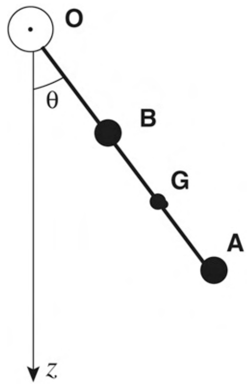

Fig. 1. Compound pendulum.

investigated the production of a (Cartesian) vortex through the rotation of a cylinder and thereby assumed shear stresses that transferred the motion from one coaxial layer of the fluid to the next. He also explained the propagation of sound through the elasticity of the air and thereby introduced the (normal) pressure between successive layers of the air.[7]

To sum up, Newton introduced two basic, long-lasting concepts of fluid mechanics: internal pressure (both longitudinal and transverse), and similarity. However, he had no general strategy for subjecting continuous media to the laws of his new mechanics. While his simplified models became popular, his concepts of internal pressure and similarity were long ignored. As we will see in a moment, much of the prehistory of Euler's equation has to do with the difficult reintroduction of internal pressure as a means to derive the motion of fluid elements. Although we are now accustomed to the idea that a continuum can be mentally decomposed into mutually pressing portions, this sort of abstraction long remained suspicious to the pioneers of Newtonian mechanics.

2.2. *Daniel Bernoulli's hydrodynamica*

The Swiss physician and geometer Daniel Bernoulli was the first of these pioneers to develop a uniform dynamical method to solve a large class of problems of fluid motion. His reasoning was based on Leibniz's principle of live forces, and modeled after Huygens's influential treatment of the compound pendulum in his *Horologium oscillatorium* (1673).[8]

Consider a pendulum made of two point masses A and B rigidly connected to a massless rod that can oscillate around the suspension point O (Fig. 1). Huygens required the equality of the "potential ascent" and the "actual descent," whose translation in modern terms reads:

$$\frac{m_A(v_A^2/2g) + m_B(v_B^2/2g)}{m_A + m_B} = z_G, \tag{2}$$

where m denotes a mass, v a velocity, g the acceleration of gravity, and z_G the descent of the gravity center of the two

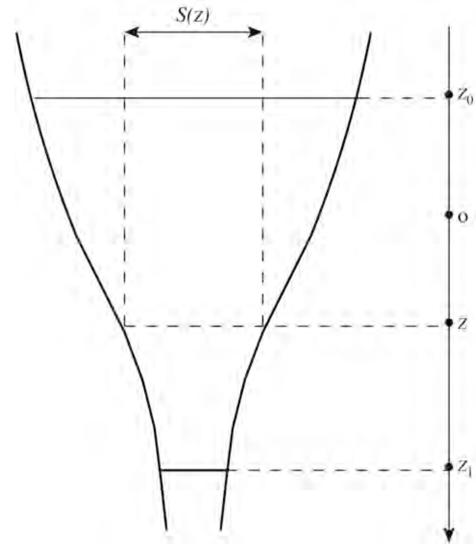

Fig. 2. Parallel-slice flow in a vertical vessel.

masses measured from the highest elevation of the pendulum during its oscillation. This equation, in which the modern reader recognizes the conservation of the sum of the kinetic and potential energies, leads to a first-order differential equation for the angle θ that the suspending rod makes with the vertical. The comparison of this equation with that of a simple pendulum then yields the expression $(a^2 m_A + b^2 m_B)/(a m_A + b m_B)$ for the length of the equivalent simple pendulum (with a = OA and b = OB).[9]

As D. Bernoulli could not fail to observe, there is a close analogy between this problem and the hydraulic problem of efflux, as long as the fluid motion occurs by parallel slices. Under the latter hypothesis, the velocity of the fluid particles that belong to the same section of the fluid is normal to and uniform through the section. If, moreover, the fluid is incompressible and continuous (no cavitation), the velocity in one section of the vessel completely determines the velocity in all other sections. The problem is thus reduced to the fall of a connected system of weights with one degree of freedom only, just as is the case of a compound pendulum.

This analogy inspired D. Bernoulli's treatment of efflux. Consider, for instance, a vertical vessel with a section S depending on the downward vertical coordinate z (Fig. 2). A mass of water falls through this vessel by parallel, horizontal slices. The continuity of the incompressible water implies that the product Sv is a constant through the fluid mass. The equality of the potential ascent and the actual descent implies that at every instant[10]

$$\int_{z_0}^{z_1} \frac{v^2(z)}{2g} S(z)\mathrm{d}z = \int_{z_0}^{z_1} z S(z)\mathrm{d}z, \tag{3}$$

where z_0 and z_1 denote the (changing) coordinates of the two extreme sections of the fluid mass, the origin of the z-axis

[7] Cf. Smith, 1998. Newton also discussed waves on water and the shape of a rotating fluid mass (figure of the Earth).

[8] Bernoulli, 1738; Huygens, 1673.

[9] Cf. Vilain, 2000: 32–36.

[10] Bernoulli, 1738: 31–35 gave a differential, geometric version of this relation.

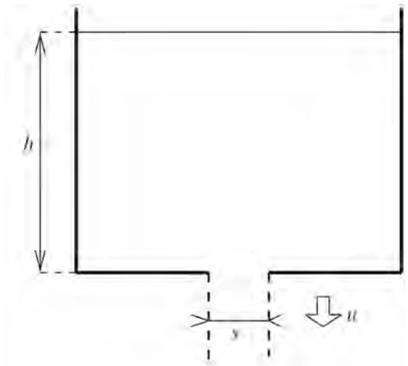

Fig. 3. Idealized efflux through small opening (without *vena contracta*).

coincides with the position of the center of gravity of this mass at the beginning of the fall, and the units are chosen so that the density of the fluid is *one*. As $v(z)$ is inversely proportional to the known function S of z, this equation yields a relation between z_0 and $v(z_0) = \dot{z}_0$, which can be integrated to give the motion of the highest fluid slice, and so forth. D. Bernoulli's investigation of efflux amounted to a repeated application of this procedure to vessels of various shapes.

The simplest sub-case of this problem is that of a broad container with a small opening of section s on its bottom (Fig. 3). As the height h of the water varies very slowly, the escaping velocity quickly reaches a steady value u. As the fluid velocity within the vessel is negligible, the increase of the potential ascent in the time $\mathrm{d}t$ is simply given by the potential ascent $(u^2/2g)su\mathrm{d}t$ of the fluid slice that escapes through the opening at the velocity u. This quantity must be equal to the actual descent $hsu\mathrm{d}t$. Therefore, the velocity u of efflux is the velocity $\sqrt{2gh}$ of free fall from the height h, in conformity with Torricelli's law.[11]

D. Bernoulli's most innovative application of this method concerned the pressure exerted by a moving fluid on the walls of its container, a topic of importance for the physician and physiologist he also was. Previous writers on hydraulics and hydrostatics had only considered the hydrostatic pressure due to gravity. In the case of a uniform gravity g, the pressure per unit area on a wall portion was known to depend only on the depth h of this portion below the free water surface. According to the law enunciated by Simon Stevin in 1605, it is given by the weight gh of a water column (of unit density) that has a unit normal section and the height h. In the case of a moving fluid, D. Bernoulli defined and derived the "hydraulico-static" wall pressure as follows.[12]

The section S of the vertical vessel ABCG of Fig. 4 is supposed to be much larger than the section s of the appended tube EFDG, which is itself much larger than the section ε of the hole o. Consequently, the velocity u of the water escaping through o is $\sqrt{2gh}$. Owing to the conservation of the flux, the velocity v within the tube is $(\varepsilon/s)u$. D. Bernoulli goes on to say:[13]

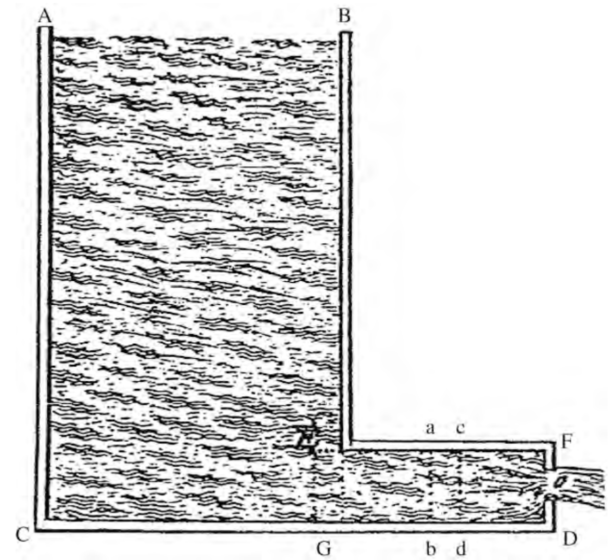

Fig. 4. Daniel Bernoulli's figure accompanying his derivation of the velocity-dependence of pressure (1738: plate).

If in truth there were no barrier FD, the final velocity of the water in the same tube would be [s/ε times greater]. Therefore, the water in the tube tends to a greater motion, but its pressing [*nisus*] is hindered by the applied barrier FD. By this pressing and resistance [*nisus et renisus*] the water is compressed [*comprimitur*], which compression [*compressio*] is itself kept in by the walls of the tube, and thence these too sustain a similar pressure [*pressio*]. Thus it is plain that the pressure [*pressio*] on the walls is proportional to the acceleration... that would be taken on by the water if every obstacle to its motion should instantaneously vanish, so that it were ejected directly into the air.

Based on this intuition, D. Bernoulli imagined that the tube was suddenly broken at ab, and made the wall pressure P proportional to the acceleration $\mathrm{d}v/\mathrm{d}t$ of the water at this instant. According to the principle of live forces, the actual descent of the water during the time $\mathrm{d}t$ must be equal to the potential ascent it acquires while passing from the large section S to the smaller section s, plus the increase of the potential ascent of the portion EabG of the fluid. This gives (the fluid density is *one*)

$$hsv\mathrm{d}t = \frac{v^2}{2g}sv\mathrm{d}t + bs\mathrm{d}\left(\frac{v^2}{2g}\right), \tag{4}$$

where $b = \mathrm{Ea}$. The resulting value of the acceleration $\mathrm{d}v/\mathrm{d}t$ is $(gh - v^2/2)/b$. The wall pressure P must be proportional to this quantity, and it must be identical to the static pressure gh in the limiting case $v = 0$. It is therefore given by the equation

$$P = gh - \frac{1}{2}v^2, \tag{5}$$

[11] Bernoulli, 1738: 35. This reasoning assumes a parallel motion of the escaping fluid particle. Therefore, it only gives the velocity u beyond the contraction of the escaping fluid vein that occurs near the opening (Newton's *vena contracta*): cf. Lagrange, 1788: 430–431; Smith, 1998.

[12] Bernoulli, 1738: 258–260. Mention of physiological applications is found in D. Bernoulli to Shoepflin, 25 Aug 1734, in Bernoulli, 2002: 89: "Hydraulico-statics will also be useful to understand animal economy with respect to the motion of fluids, their pressure on vessels, etc."

[13] Bernoulli, 1738: 258–259, translated in Truesdell, 1954: XXVII. The *compressio* in this citation perhaps prefigures the internal pressure later introduced by Johann Bernoulli.

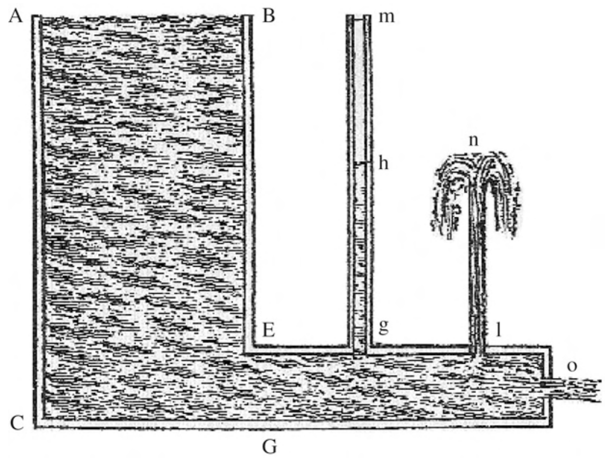

Fig. 5. Effects of the velocity-dependence of pressure according to Bernoulli (1738: plate).

which means that the pressure exerted by a moving fluid on the walls is lower than the static pressure, the difference being half the squared velocity (times the density). D. Bernoulli illustrated this effect in two ways (Fig. 5): by connecting a narrow vertical tube to the horizontal tube EFDG, and by letting a vertical jet surge from a hole on this tube. Both reach a water level well below AB.

The modern reader may here recognize Bernoulli's law. In fact, D. Bernoulli did not quite write Eq. (5), because he chose the ratio s/ε rather than the velocity v as the relevant variable. Also, he only reasoned in terms of *wall* pressure, whereas modern physicists apply Bernoulli's law to the *internal* pressure of a fluid.

There were other limitations to D. Bernoulli's considerations, of which he was largely aware. He knew that in some cases, part of the live force of the water went to eddying motion, and he even tried to estimate this loss in the case of a suddenly enlarged conduit. He was also aware of the imperfect fluidity of water, although he decided to ignore it in his reasoning. Most importantly, he knew that the hypothesis of parallel slices only held for narrow vessels and for gradual variations of their sections. But his method confined him to this case, since it is only for systems with one degree of freedom that the conservation of live forces suffices to determine the motion.[14]

To summarize, by means of the principle of live forces, Daniel Bernoulli was able to solve many problems of quasi-onedimensional flow and thereby related wall pressure to fluid velocity. This unification of hydrostatic and hydraulic considerations justified the title *Hydrodynamica* which he gave to the treatise he published in 1738 in Strasbourg. Besides the treatment of efflux, this work included all the typical questions of contemporary hydraulics except fluid resistance (which D. Bernoulli probably judged as being beyond the scope of his methods), a kinetic theory of gases, and considerations on Cartesian vortices. It is rightly regarded as a major turning point in the history of hydrodynamics, because of the uniformity and rigor of its dynamical method, the depth of physical insight, and the abundance of long-lasting results.[15]

2.3. *Johann Bernoulli's hydraulica*

In 1742, Daniel's father Johann Bernoulli published his *Hydraulica*, with an antedate that made it seem anterior to his son's treatise. Although he had been the most ardent supporter of Leibniz's principle of live forces, he now regarded this principle as an indirect consequence of more fundamental laws of mechanics. His asserted aim was to base hydraulics on an incontrovertible, Newtonian expression of these laws. To this end he adapted a method he had invented in 1714 to solve the paradigmatic problem of the compound pendulum.

Consider again the pendulum of Fig. 1. According to J. Bernoulli, the gravitational force $m_{\mathrm{B}}g$ acting on B is equivalent to a force $(b/a)m_{\mathrm{B}}g$ acting on A, because according to the law of levers two forces that have the same moment have the same effect. Similarly, the "accelerating force" $m_{\mathrm{B}}b\ddot{\theta}$ of the mass B is equivalent to an accelerating force $(b/a)m_{\mathrm{B}}b\ddot{\theta} = m_{\mathrm{B}}(b/a)^2a\ddot{\theta}$ at A. Consequently, the compound pendulum is equivalent to a simple pendulum with a mass $m_{\mathrm{A}} + (b/a)^2m_{\mathrm{B}}$ located on A and subjected to the effective vertical force $m_{\mathrm{A}}g + (b/a)m_{\mathrm{B}}g$. It is also equivalent to a simple pendulum of length $(a^2m_{\mathrm{A}} + b^2m_{\mathrm{B}})/(am_{\mathrm{A}} + bm_{\mathrm{B}})$ oscillating in the gravity g, in conformity with Huygens' result. In sum, Johann Bernoulli reached his equation of motion by applying Newton's second law to a fictitious system obtained by replacing the forces and the momentum variations at any point of the system with equivalent forces and momentum variations at one point of the system. This replacement, based on the laws of equilibrium of the system, is what J. Bernoulli called "translation" in the introduction to his *Hydraulica*.[16]

Now consider the canonical problem of water flowing by parallel slices through a vertical vessel of varying section (Fig. 2). J. Bernoulli "translates" the weight $gS\mathrm{d}z$ of the slice $\mathrm{d}z$ of the water to the location z_1 of the frontal section of the fluid. This gives the effective weight $S_1g\mathrm{d}z$, because according to a well-known law of hydrostatics, a pressure applied at any point of the surface of a confined fluid is uniformly transmitted to any other part of the surface of the fluid. Similarly, J. Bernoulli translates the "accelerating force" (momentum variation) $(\mathrm{d}v/\mathrm{d}t)S\mathrm{d}z$ of the slice $\mathrm{d}z$ to the frontal section of the fluid, with the result $(\mathrm{d}v/\mathrm{d}t)S_1\mathrm{d}z$. He then obtains the equation of motion by equating the total translated weight to the total translated accelerating force as:

$$S_1\int_{z_0}^{z_1} g\mathrm{d}z = S_1\int_{z_0}^{z_1}\frac{\mathrm{d}v}{\mathrm{d}t}\mathrm{d}z. \tag{6}$$

For J. Bernoulli the crucial point was the determination of the acceleration $\mathrm{d}v/\mathrm{d}t$. Previous authors, he contended, had failed

[14] Bernoulli, 1738: 12 (eddies), 124 (enlarged conduit); 13 (imperfect fluid).

[15] On the *Hydrodynamica*, cf. Truesdell, 1954: XXIII–XXXI; Calero, 1996: 422–459; Mikhailov, 2002.

[16] Bernoulli, 1714; 1742: 395. In modern terms, J. Bernoulli's procedure amounts to equating the sum of moments of the applied forces to the sum of moments of the accelerating forces (which is the time derivative of the total angular momentum). Cf. Vilain, 2000: 448–450.

to derive correct equations of motion from the general laws of mechanics because they were only aware of one contribution to the acceleration of the fluid slices: that which corresponds to the instantaneous change of velocity at a given height z, or $\partial v/\partial t$ in modern terms. They ignored the acceleration due to the broadening or to the narrowing of the section of the vessel, which J. Bernoulli called a *gurges* (gorge). In modern terms, he identified the convective component $v(\partial v/\partial z)$ of the acceleration. Note that his use of partial derivatives was only implicit: thanks to the relation $v = (S_0/S)v_0$, he could split v into a time dependent factor v_0 and a z-dependent factor S_0/S and thus express the total acceleration as $(S_0/S)(\mathrm{d}v_0/\mathrm{d}t) - (v_0^2 S_0^2/S^3)(\mathrm{d}S/\mathrm{d}z)$.[17]

Thanks to the *gurges*, J. Bernoulli successfully applied Eq. (6) to various cases of efflux and retrieved his son's results.[18] He also offered a novel approach to the pressure of a moving fluid on the side of its container. This pressure, he asserted, was nothing but the pressure or *vis immaterialis* that contiguous fluid parts exerted on one another, just as two solids in contact act on each other:[19]

The force that acts on the side of the channel through which the liquid flows... is nothing but the force that originates in the force of compression through which contiguous parts of the fluid act on one another.

Accordingly, J. Bernoulli divided the flowing mass of water into two parts separated by the section $z = \zeta$. Following the general idea of "translation", the pressure that the upper part exerts on the lower part is:

$$P(\zeta) = \int_{z_0}^{\zeta} (g - \mathrm{d}v/\mathrm{d}t)\mathrm{d}z. \tag{7}$$

More explicitly, this is:

$$\begin{aligned} P(\zeta) &= \int_{z_0}^{\zeta} g\mathrm{d}z - \int_{z_0}^{\zeta} v\frac{\partial v}{\partial z}\mathrm{d}z - \int_{z_0}^{\zeta} \frac{\partial v}{\partial t}\mathrm{d}z \\ &= g(\zeta - z_0) - \frac{1}{2}v^2(\zeta) + \frac{1}{2}v^2(z_0) - \frac{\partial}{\partial t}\int_{z_0}^{\zeta} v\mathrm{d}z. \end{aligned} \tag{8}$$

In a widely different notation, J. Bernoulli thus obtained a generalization of his son's law to non-stationary parallel-slice flows.[20]

J. Bernoulli interpreted the relevant pressure as an *internal* pressure analogous to the tension of a thread or the mutual action of contiguous solids in connected systems. Yet, he did not rely on this new concept of pressure to establish the equation of motion (6). He only introduced this concept as a short-cut to the velocity-dependence of wall-pressure.[21]

To summarize, Johann Bernoulli's *Hydraulica* departed from his son's *Hydrodynamica* through a more direct reliance on Newton's laws. This approach required the new concept of a convective derivative. It permitted a generalization of Bernoulli's law to the pressure in a non-steady flow. J. Bernoulli had a concept of internal pressure, although he did not use it in his derivation of his equation of fluid motion. Like his son's, his dynamical method was essentially confined to systems with one degree of freedom only, so that he could only treat flow by parallel slices.

3. D'Alembert's fluid dynamics

3.1. The principle of dynamics

In 1743, the French geometer and philosopher Jean le Rond d'Alembert published his influential *Traité de dynamique*, which subsumed the dynamics of connected systems under a few general principles. The first illustration he gave of his approach was Huygens's compound pendulum. As we saw, Johann Bernoulli's solution to this problem leads to the equation of motion:

$$m_{\mathrm{A}} g \sin\theta + (b/a) m_{\mathrm{B}} g \sin\theta = m_{\mathrm{A}} a\ddot{\theta} + (b/a) m_{\mathrm{B}} b\ddot{\theta}, \tag{9}$$

which may be rewritten as

$$a(m_{\mathrm{A}} g \sin\theta - m_{\mathrm{A}} a\ddot{\theta}) + b(m_{\mathrm{B}} g \sin\theta - m_{\mathrm{B}} b\ddot{\theta}) = 0. \tag{10}$$

The latter is the condition of equilibrium of the pendulum under the action of the forces $m_{\mathrm{A}}\mathbf{g} - m_{\mathrm{A}}\boldsymbol{\gamma}_{\mathrm{A}}$ and $m_{\mathrm{B}}\mathbf{g} - m_{\mathrm{B}}\boldsymbol{\gamma}_B$ acting respectively on A and B. In d'Alembert's terminology, the products $m_{\mathrm{A}}\mathbf{g}$ and $m_{\mathrm{B}}\mathbf{g}$ are the motions impressed (per unit time) on the bodies A and B under the sole effect of gravitation (without any constraint). The products $m_{\mathrm{A}}\boldsymbol{\gamma}_{\mathrm{A}}$ and $m_{\mathrm{B}}\boldsymbol{\gamma}_{\mathrm{B}}$ are the actual changes of their (quantity of) motion (per unit time). The differences $m_{\mathrm{A}}\mathbf{g} - m_{\mathrm{A}}\boldsymbol{\gamma}_A$ and $m_{\mathrm{B}}\mathbf{g} - m_{\mathrm{B}}\boldsymbol{\gamma}_B$ are the parts of the impressed motions that are destroyed by the rigid connection of the two masses through the freely rotating rod. Accordingly, d'Alembert saw in Eq. (10) a consequence of a general dynamic principle following which the motions destroyed by the connections should be in equilibrium.[22]

D'Alembert based his dynamics on three laws, which he regarded as necessary consequences of the principle of sufficient reason. The first law is that of inertia, according to which a freely moving body moves with a constant velocity in a constant direction. The second law stipulates the vector

[17] Bernoulli, 1742: 432–437. He misleadingly called the two parts of the acceleration the "hydraulic"and the "hydrostatic" components. Truesdell (1954: XXXIII) translates *gurges* as "eddy" (it does have this meaning in classical latin), because in the case of sudden (but small) decrease of section J. Bernoulli imagined a tiny eddy at the corners of the gorge. In his treatise on the equilibrium and motion of fluids (1744: 157), d'Alembert interpreted J. Bernoulli's expression of the acceleration in terms of two partial differentials.

[18] D'Alembert later explained this agreement: see below, pp. 7–8.

[19] Bernoulli, 1742: 442.

[20] Bernoulli, 1742: 444. His notation for the internal pressure was π. In the first section of his *Hydraulica*, which he communicated to Euler in 1739, he only treated the steady flow in a suddenly enlarged tube. In his enthusiastic reply (5 May 1739, in Euler, 1998: 287–295), Euler treated the accelerated efflux from a vase of arbitrary shape with the same method of "translation," not with the later method of balancing gravity with internal pressure gradient, contrary to Truesdell's claim (1954: XXXIII). J. Bernoulli subsequently wrote his second part, where he added the determination of the internal pressure to Euler's treatment.

[21] For a different view, cf. Truesdell, 1954: XXXIII; Calero, 1996: 460–474.

[22] D'Alembert, 1743: 69–70. Cf. Vilain, 2000: 456–459. D'Alembert reproduced and criticized Johann Bernoulli's derivation on p. 71. On Jacob Bernoulli's anticipation of d'Alembert's principle, cf. Lagrange, 1788: 176–177, 179–180; Dugas, 1950: 233–234; Vilain, 2000: 444–448.

superposition of motions impressed on a given body. According to the third law, two (ideally rigid) bodies come to rest after a head-on collision if and only if their velocities are inversely proportional to their masses. From these three laws and further recourse to the principle of sufficient reason, d'Alembert believed he could derive a complete system of dynamics without recourse to the older, obscure concept of force as cause of motion. He defined force as the motion impressed on a body, that is, the motion that a body would take if this force were acting alone without any impediment. Then the third law implies that two contiguous bodies subjected to opposite forces are in equilibrium. More generally, d'Alembert regarded statics as a particular case of dynamics in which the various motions impressed on the parts of the system mutually cancel each other.[23]

Based on this conception, d'Alembert derived the principle of virtual velocities, according to which a connected system subjected to various forces remains in equilibrium if the work of these forces vanishes for any infinitesimal motion of the system that is compatible with the connections.[24] As for the principle of dynamics, he regarded it as a self-evident consequence of his dynamic concept of equilibrium. In general, the effect of the connections in a connected system is to destroy part of the motion that is impressed on its components by means of external agencies. The rules of this destruction should be the same whether the destruction is total or partial. Hence, equilibrium should hold for that part of the impressed motions that is destroyed through the constraints. This is d'Alembert's principle of dynamics. Stripped of d'Alembert's philosophy of motion, this principle stipulates that a connected system in motion should be at any time in equilibrium with respect to the fictitious forces $\mathbf{f} - m\boldsymbol{\gamma}$, where $\mathbf{f}$ denotes the force applied on the mass point m of the system, and $\boldsymbol{\gamma}$ is the acceleration of this mass point.

3.2. *Efflux revisited*

At the end of his treatise on dynamics, d'Alembert considered the hydraulic problem of efflux through the vessel of Fig. 2. His first task was to determine the condition of equilibrium of a fluid when subjected to an altitude-dependent gravity $g(z)$. For this purpose, he considered an intermediate slice of the fluid, and required the pressure from the fluid above this slice to be equal and opposite to the pressure from the fluid below this slice. According to a slight generalization of Stevin's hydrostatic law, these two pressures are given by the integral of the variable gravity $g(z)$ over the relevant range of elevation. Hence the equilibrium condition reads:[25]

$$S(\zeta)\int_{z_0}^{\zeta} g(z)\mathrm{d}z = -S(\zeta)\int_{\zeta}^{z_1} g(z)\mathrm{d}z, \tag{11}$$

or

$$\int_{z_0}^{z_1} g(z)\mathrm{d}z = 0. \tag{12}$$

According to d'Alembert's principle, the motion of the fluid under a constant gravity g must be such that the fluid is in equilibrium under the fictitious gravity $g(z) = g - \mathrm{d}v/\mathrm{d}t$, where $\mathrm{d}v/\mathrm{d}t$ is the acceleration of the fluid slice at the elevation z. Hence comes the equation of motion

$$\int_{z_0}^{z_1}\left(g - \frac{\mathrm{d}v}{\mathrm{d}t}\right)\mathrm{d}z = 0, \tag{13}$$

which is the same as Johann Bernoulli's equation (6). In addition, d'Alembert proved that this equation, together with the constancy of the product Sv, implied the conservation of live forces in Daniel Bernoulli's form (Eq. (3)). In his subsequent treatise of 1744 on the equilibrium and motion of fluids, d'Alembert provided a similar treatment of efflux, including his earlier derivations of the equation of motion and the conservation of live forces, with a slight variant: he now derived the equilibrium condition (13) by setting the pressure acting on the bottom slice of the fluid to zero.[26] Presumably, he did not want to base his equations of equilibrium and motion on the concept of internal pressure, in conformity with his general avoidance of internal contact forces in his dynamics. His statement of the general conditions of equilibrium of a fluid, as found at the beginning of his treatise, only required the concept of wall-pressure. Yet, in a later section of his treatise d'Alembert introduced "the pressure at a given height":

$$P(\zeta) = \int_{z_0}^{\zeta}(g - \mathrm{d}v/\mathrm{d}t)\mathrm{d}z, \tag{14}$$

just as Johann Bernoulli had done, and for the same purpose of deriving the velocity dependence of wall-pressure.[27]

In the rest of his treatise, d'Alembert solved problems similar to those of Daniel Bernoulli's *Hydrodynamica*, with nearly identical results. The only important difference concerned cases involving the sudden impact of two layers of fluids. Whereas Daniel Bernoulli still applied the conservation of live forces in such cases (save for possible dissipation into turbulent motion), d'Alembert's principle of dynamics there implied a destruction of live force. Daniel Bernoulli disagreed with these and a few other changes. In a contemporary letter to Euler, he expressed his exasperation over d'Alembert's treatise:[28]

> I have seen with astonishment that apart from a few little things there is nothing to be seen in his hydrodynamics but an impertinent conceit. His criticisms are puerile indeed, and show not only that he is no remarkable man, but also that he never will be.[29]

[23] D'Alembert, 1743: xiv–xv, 3. Cf. Hankins, 1968; Fraser, 1985.

[24] The principle of virtual velocities was first stated generally by Johann Bernoulli and thus named by Lagrange (1788: 8–11). Cf. Dugas, 1950: 221–223, 320. The term 'work' is, of course, anachronistic.

[25] D'Alembert, 1743: 183–186.

[26] D'Alembert, 1743: 19–20.

[27] D'Alembert, 1743: 139.

[28] D. Bernoulli to Euler, 7 Jul 1745, quoted in Truesdell, 1954: XXXVIIn.

[29] This is but an instance of the many cutting remarks exchanged between eighteenth-century geometers; further examples are not needed here.

3.3. The cause of winds

In this judgment, Daniel Bernoulli overlooked that d'Alembert's hydrodynamics, being based on a general dynamics of connected systems, lent itself to generalizations beyond parallel-slice flow. D'Alembert offered striking illustrations of the power of his approach in a prize-winning memoir published in 1747 on the cause of winds.[30] As thermal effects were beyond the grasp of contemporary mathematical physics, he focused on a cause that is now known to be negligible: the tidal force exerted by the luminaries (the Moon and the Sun). For simplicity, he confined his analysis to the case of a constant-density layer of air covering a spherical globe with uniform thickness. He further assumed that fluid particles originally on the same vertical line remained so in the course of time and that the vertical acceleration of these particles was negligible (owing to the thinness of the air layer), and he neglected second-order quantities with respect to the fluid velocity and to the elevation of the free surface. His strategy was to apply his principle of dynamics to the motion induced by the tidal force $\mathbf{f}$ and the terrestrial gravity $\mathbf{g}$, both of which depend on the location on the surface of the Earth.[31]

Calling $\boldsymbol{\gamma}$ the absolute acceleration of the fluid particles, the principle requires that the fluid layer should be in equilibrium under the force $\mathbf{f} + \mathbf{g} + \boldsymbol{\gamma}$ (the density of the air is *one* in the chosen units). From earlier theories of the shape of the Earth (regarded as a rotating liquid spheroid), d'Alembert borrowed the equilibrium condition that the net force should be perpendicular to the free surface of the fluid. He also required that the volume of vertical cylinders of fluid should not be altered by their motion, in conformity with his constant-density model. As the modern reader would expect, from these two conditions d'Alembert derived some sort of momentum equation, and some sort of incompressibility equation. He did so in a rather opaque manner. Some features, such as the lack of specific notation for partial differentials or the abundant recourse to geometrical reasoning, disconcert modern readers only.[32] Others were problematic to his contemporaries: he often omitted steps and introduced special assumptions without warning. Also, he directly treated the utterly difficult problem of fluid motion on a spherical surface without preparing the reader with simpler problems.

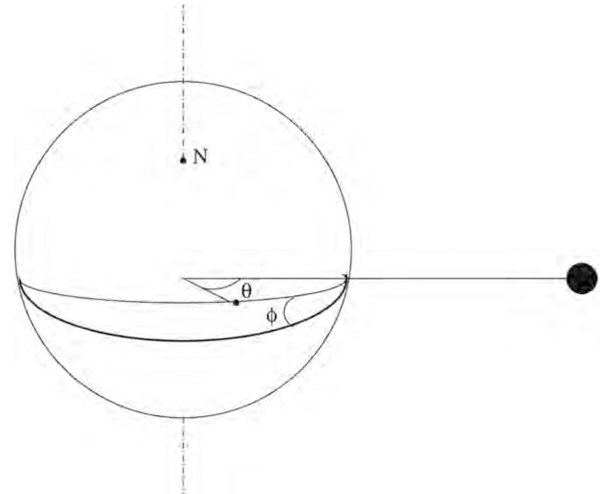

Fig. 6. Spherical coordinates for d'Alembert's atmospheric tides. The fat line represents the visible part of the equator, over which the luminary is orbiting. N is the North pole.

Suppose, with d'Alembert, that the tide-inducing luminary orbits above the equator (with respect to the Earth).[33] Using the modern terminology for spherical coordinates, call θ the colatitude of a given point of the terrestrial sphere with respect to an axis pointing toward the orbiting luminary, ϕ the longitude measured from the meridian above which the luminary is orbiting (this is *not* the geographical longitude), η the elevation of the free surface of the fluid layer over its equilibrium position, v_θ and v_ϕ the θ- and ϕ-components of the fluid velocity with respect to the Earth, h the depth of the fluid in its undisturbed state, and R the radius of the Earth (see Fig. 6).

D'Alembert first considered the simpler case when ϕ is negligibly small, for which he expected the component v_ϕ also to be negligible. To first order in η and v, the conservation of the volume of a vertical column of fluid yields:

$$\frac{1}{h}\dot{\eta} + \frac{1}{R}\frac{\partial v_\theta}{\partial \theta} + \frac{v_\theta}{R\tan\theta} = 0, \tag{15}$$

which means that an increase of the height of the column is compensated for by a narrowing of its basis (the dot denotes the time derivative at a fixed point of the Earth surface). Since the tidal force $\mathbf{f}$ is much smaller than the gravity $\mathbf{g}$, the vector sum $\mathbf{f} + \mathbf{g} - \boldsymbol{\gamma}$ makes an angle $(f_\theta - \gamma_\theta)/g$ with the vertical. To first order in η, the inclination of the fluid surface over the horizontal is $(\partial\eta/\partial\theta)/R$. Therefore, the condition that $\mathbf{f} + \mathbf{g} - \boldsymbol{\gamma}$ should be perpendicular to the surface of the fluid is approximately identical to[34]

$$\gamma_\theta = f_\theta - \frac{g}{R}\frac{\partial\eta}{\partial\theta}. \tag{16}$$

As d'Alembert noted, this equation of motion can also be obtained by equating the horizontal acceleration of a fluid slice

[30] As a member of the committees judging the Berlin Academy's prizes on winds and on fluid resistance (he could not compete as a resident member), Euler studied d'Alembert's submitted memoirs of 1747 and 1749. The subject set for the first prize, probably written by Euler, was "to determine the order & the law wind should follow, if the Earth were surrounded on all sides by the Ocean; so that one could at all times predict the speed & direction of the wind in all places." The question is here formulated in terms of what we now call Eulerian coordinates ("all places"), cf. Grimberg, 1998: 195.

[31] D'Alembert, 1747. D'Alembert treated the rotation of the Earth and the attraction by the Sun and the Moon as small perturbing causes whose effects on the shape of the fluid surface simply added (D'Alembert, 1747: xvii, 47). Consequently, he overlooked the Coriolis force in his analysis of the tidal effects (in D'Alembert, 1747: 65, he writes he will be doing as if it were the luminary that rotates around the Earth).

[32] D'Alembert used a purely geometrical method to study the free oscillations of an ellipsoidal disturbance of the air layer.

[33] The sun and the moon actually do not, but the *variable* part of their action is proportional to that of such a luminary.

[34] D'Alembert, 1747: 88–89 (formulas A and B). The correspondence with d'Alembert's notation is given by: $\theta \mapsto u$, $v_\theta \mapsto q$, $\partial\eta/\partial\theta \mapsto -v$, $R/h\omega \mapsto \varepsilon$, $R/gK \mapsto 3S/4pd^3$ (with $f = -K\sin 2\theta$).

to the sum of the tidal component f_θ and of the difference between the pressures on both sides of this slice. Indeed, the neglect of the vertical acceleration implies that at a given height, the internal pressure of the fluid varies as the product $g\eta$. Hence, d'Alembert was aware of two routes to the equation of motion, through his dynamic principle, or through an application of the momentum law to a fluid element subjected to the pressure of contiguous elements. In some sections he favored the first route, in others the second.[35]

In his expression of the time variations $\dot\eta$ and $\dot v_\theta$, d'Alembert considered only the forced motion of the fluid for which the velocity field and the free surface of the fluid rotate together with the tide-inducing luminary at the angular velocity $-\omega$. Then the values of η and v_θ at the colatitude θ and at the time $t + \mathrm{d}t$ are equal to their values at the colatitude $\theta + \omega\mathrm{d}t$ and at the time t. This gives

$$\dot v_\theta = \omega\frac{\partial v_\theta}{\partial\theta}, \qquad \dot\eta = \omega\frac{\partial\eta}{\partial\theta}. \tag{17}$$

D'Alembert equated the relative acceleration $\dot v_\theta$ with the acceleration γ_θ, for he neglected the second-order convective terms, and judged the absolute rotation of the Earth as irrelevant (he was aware of the centripetal acceleration, but treated the resulting permanent deformation of the fluid surface separately; and he overlooked the Coriolis acceleration). With these substitutions, his Eqs. (15) and (16) become ordinary differential equations with respect to the variable θ.

D'Alembert eliminated η from these two equations, and integrated the resulting differential equation for Newton's value $-K\sin 2\theta$ of the tide-inducing force f_θ. In particular, he showed that the phase of the tides (concordance or opposition) depended on whether the rotation period $2\pi/\omega$ of the luminary was smaller or larger than the quantity $2\pi R/\sqrt{gh}$, which he had earlier shown to be identical with the period of the free oscillations of the fluid layer.[36]

In another section of his memoir, d'Alembert extended his equations to the case when the angle ϕ is no longer negligible. Again, he had the velocity field and the free surface of the fluid rotate together with the luminary at the angular velocity $-\omega$. Calling $\mathbf{R}_{\omega\mathrm{d}t}$ the operator for the rotation of the angle $\omega\mathrm{d}t$ around the axis joining the center of the Earth and the luminary and $\mathbf{v}(\mathrm{P}, t)$ the velocity vector at point P and at time t, we have:

$$\mathbf{v}(\mathrm{P}, t + \mathrm{d}t) = \mathbf{R}_{\omega\mathrm{d}t}\mathbf{v}(\mathbf{R}_{\omega\mathrm{d}t}\mathrm{P}, t). \tag{18}$$

Expressing this relation in spherical coordinates, d'Alembert obtained:

$$\dot v_\theta = \omega\left(\frac{\partial v_\theta}{\partial\theta}\cos\phi - \frac{\partial v_\theta}{\partial\phi}\frac{\sin\phi}{\tan\theta} - v_\phi\sin\phi\sin\theta\right), \tag{19}$$

$$\dot v_\phi = \omega\left(\frac{\partial v_\phi}{\partial\theta}\cos\phi - \frac{\partial v_\phi}{\partial\phi}\frac{\sin\phi}{\tan\theta} + v_\theta\sin\phi\sin\theta\right). \tag{20}$$

For the same reasons as before, d'Alembert identified these derivatives with the accelerations γ_θ and γ_ϕ. He then applied his dynamic principle to get:

$$\gamma_\theta = f_\theta - \frac{g}{R}\frac{\partial\eta}{\partial\theta}, \tag{21}$$

$$\gamma_\phi = -\frac{g}{R\sin\theta}\frac{\partial\eta}{\partial\phi}. \tag{22}$$

Lastly, he obtained the continuity condition:

$$\dot\eta = \omega\left(\frac{\partial\eta}{\partial\theta}\cos\phi - \frac{\partial\eta}{\partial\phi}\frac{\sin\phi}{\tan\theta}\right) = -\left(\frac{\partial v_\theta}{\partial\theta} + \frac{v_\theta}{\tan\theta} + \frac{1}{\sin\theta}\frac{\partial v_\phi}{\partial\phi}\right), \tag{23}$$

in which the modern reader recognizes the expression of a divergence in spherical coordinates.[37]

D'Alembert judged the resolution of this system to be beyond his capability. The purpose of this section of his memoir was to illustrate the power and generality of his method for deriving hydrodynamic equations. For the first time, he gave the complete equations of motion of an incompressible fluid in a genuinely two-dimensional case. Thus emerged the velocity field and partial derivatives with respect to two independent spatial coordinates. Although Alexis Fontaine and Euler had earlier developed the needed calculus of differential forms, d'Alembert was first to apply it to the dynamics of continuous media. His notation of course differed from the modern one: where we now write $\partial f/\partial x$, Fontaine wrote $\mathrm{d}f/\mathrm{d}x$, and d'Alembert often wrote A, with $\mathrm{d}f = A\mathrm{d}x + B\mathrm{d}y + \cdots$.

3.4. The resistance of fluids

In 1749 d'Alembert submitted a Latin manuscript on the resistance of fluids for another Berlin prize, and failed to win. The Academy judged that none of the competitors had reached the point of comparing his theoretical results with experiments. D'Alembert did not deny the importance of this comparison for the improvement of ship design. But he judged that the relevant equations could not be solved in the near future, and that his memoir deserved consideration for its methodological innovations. In 1752, he published an augmented translation of this memoir as a book.[38]

35 D'Alembert, 1747: 88–89. He represented the internal pressure by the weight of a vertical column of fluid. In his discussion of the condition of equilibrium (1747: 15–16), he introduced the balance of the horizontal component of the external force acting on a fluid element and the difference of weight of the two adjacent columns as "another very easy method" for determining the equilibrium. In the case of tidal motion with $\phi \approx 0$, he directly applied this condition of equilibrium to the "destroyed motion" $\mathbf{f} + \mathbf{g} - \boldsymbol{\gamma}$. In the general case (D'Alembert, 1747: 112–113), he used the perpendicularity of $\mathbf{f} + \mathbf{g} - \boldsymbol{\gamma}$ to the free surface of the fluid.

36 The elimination of η leads to the easily integrable equation $(gh - R^2\omega^2)\mathrm{d}v_\theta + gh\mathrm{d}(\sin\theta)/\sin\theta - R^2\omega K\sin\theta\mathrm{d}(\sin\theta) = 0$.

37 D'Alembert, 1747: 111–114 (Eqs. E, F, G, H, I). To complete the correspondence given in note (36), take $\phi \mapsto A$, $v_\phi \mapsto \eta$, $\gamma_\theta \mapsto \pi$, $\gamma_\phi \mapsto \varphi$, $g/R \mapsto p$, $\partial\eta/\partial\theta \mapsto -\rho$, $\partial\eta/\partial\phi \mapsto -\sigma$, $\partial v_\theta/\partial\theta \mapsto r$, $\partial v_\theta/\partial\phi \mapsto \lambda$, $\partial v_\phi/\partial\theta \mapsto \gamma$, $\partial v_\phi/\partial\phi \mapsto \beta$. D'Alembert has the ratio of two sines instead of the product in the last term of Eqs. (19) and (20). An easy, modern way to obtain these equations is to rewrite (18) as $\dot{\mathbf{v}} = [(\boldsymbol{\omega}\times\mathbf{r})\cdot\nabla]\mathbf{v} + \boldsymbol{\omega}\times\mathbf{v}$, with $\mathbf{v} = (\mathbf{0}, \mathbf{v}_\theta, \mathbf{v}_\phi)$, $\mathbf{r} = (\mathbf{R}, \mathbf{0}, \mathbf{0})$, $\boldsymbol{\omega} = \omega(\sin\theta\sin\phi, \cos\theta\sin\phi, \cos\phi)$, and $\nabla = (\partial_r, \partial_\theta/R, \partial_\phi/(R\sin\theta))$ in the local basis.

38 D'Alembert, 1752: xxxviii. For an insightful study of d'Alembert's work on fluid resistance, cf. Grimberg, 1998 (which also contains a transcript of the Latin manuscript submitted for the Berlin prize). See also Calero, 1996: Chapter 8.

Compared with the earlier treatise on the equilibrium and motion of fluids, the first important difference was a new formulation of the laws of hydrostatics. In 1744, d'Alembert started with the uniform and isotropic transmissibility of pressure by any fluid (from one part of its surface to another). He then derived the standard laws of this science, such as the horizontality of the free surface and the depth-dependence of wall-pressure, by qualitative or geometrical reasoning. In contrast, in his new memoir he relied on a mathematical principle borrowed from Alexis-Claude Clairaut's memoir of 1743 on the shape of the Earth. According to this principle, a fluid mass subjected to a force density $\mathbf{f}$ is in equilibrium if and only if the integral $\int \mathbf{f} \cdot d\mathbf{l}$ vanishes over any closed loop within the fluid and over any path whose ends belong to the free surface of the fluid.[39]

D'Alembert regarded this principle as a mathematical expression of his earlier principle of the uniform transmissibility of pressure. If the fluid is globally in equilibrium, he reasoned, it must also be in equilibrium within any narrow canal of section ε belonging to the fluid mass. For a canal beginning and ending on the free surface of the fluid, the pressure exerted by the fluid on each of the extremities of the canal must vanish. According to the principle of uniform transmissibility of pressure, the force $\mathbf{f}$ acting on the fluid within the length $d\mathbf{l}$ of the canal exerts a pressure $\varepsilon f \cdot d\mathbf{l}$ that is transmitted to both ends of the canal (with opposite signs). As the sum of these pressures must vanish, so does the integral $\int \mathbf{f} \cdot d\mathbf{l}$. This reasoning, and a similar one for closed canals, establish d'Alembert's new principle of equilibrium.[40]

Applying this principle to an infinitesimal loop, d'Alembert obtained (the Cartesian-coordinate form of) the differential condition

$$\nabla \times \mathbf{f} = \mathbf{0}, \tag{24}$$

as Clairaut had already done. Combining it with his principle of dynamics, and confining himself to the steady motion ($\partial \mathbf{v}/\partial t = \mathbf{0}$, so that $\boldsymbol{\gamma} = (\mathbf{v} \cdot \nabla)\mathbf{v}$) of an incompressible fluid, he obtained the two-dimensional, Cartesian-coordinate version of

$$\nabla \times [(\mathbf{v} \cdot \nabla)\mathbf{v}] = \mathbf{0}, \tag{25}$$

which means that the fluid must formally be in equilibrium with respect to the convective acceleration. D'Alembert then showed that this condition was met whenever $\nabla \times \mathbf{v} = \mathbf{0}$. Confusing a sufficient condition with a necessary one, he concluded that the latter property of the flow held generally.[41]

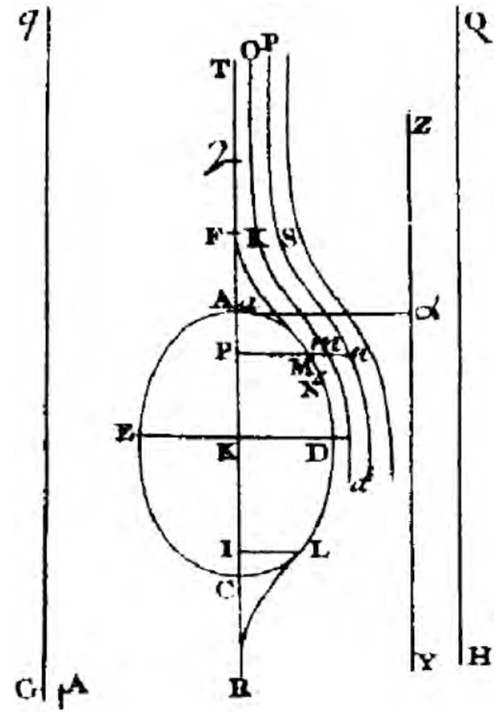

Fig. 7. Flow around a solid body according to D'Alembert (1752: plate 13).

This property nonetheless holds in the special case of motion investigated by d'Alembert, that is, the stationary flow of an incompressible fluid around a solid body when the flow is uniform far away from the body (Fig. 7). In this limited case, d'Alembert gave a correct proof of which a modernized version follows.[42]

Consider two neighboring lines of flow beginning in the uniform region of the flow and ending in any other part of the flow, and connect the extremities through a small segment. According to d'Alembert's principle together with the principle of equilibrium, the integral $\oint (\mathbf{v} \cdot \nabla)\mathbf{v} \cdot d\mathbf{r}$ vanishes over this loop. Using the identity

$$(\mathbf{v} \cdot \nabla)\mathbf{v} = \nabla \left(\frac{1}{2} \mathbf{v}^2 \right) - \mathbf{v} \times (\nabla \times \mathbf{v}), \tag{26}$$

this implies that the integral $\oint (\nabla \times \mathbf{v}) \cdot (\mathbf{v} \times d\mathbf{r})$ also vanishes. The only part of the loop that contributes to this integral is that corresponding to the little segment joining the end points of the two lines of flow. Since the orientation of this segment is arbitrary, $\nabla \times \mathbf{v}$ must vanish.

D'Alembert thus derived the condition

$$\nabla \times \mathbf{v} = \mathbf{0} \tag{27}$$

from his dynamical principle. In addition, he obtained the (incompressibility) condition

$$\nabla \cdot \mathbf{v} = \mathbf{0} \tag{28}$$

by considering the deformation of a small parallelepiped of fluid during an infinitesimal time interval. More exactly, he

[39] D'Alembert, 1752: 14–17. On the early history of theories of the figure of the Earth, cf. Todhunter, 1873. On Clairaut, cf. Passeron, 1995. On Clairaut's principle and Newton's and MacLaurin's partial anticipations, cf. Truesdell, 1954: XIV–XXII.

[40] As is obvious to the modern reader, this principle is equivalent to the existence of a single-valued function (P) of which $\mathbf{f}$ is the gradient and which has a constant value on the free surface of the fluid. The canal equilibrium results from the principle of solidification, the history of which is discussed in Casey, 1992.

[41] D'Alembert, 1752: art. 78. The modern hydrodynamicist recognizes in Eq. (25) a particular case of the vorticity equation. The condition $\nabla \times \mathbf{v} = \mathbf{0}$ is that of irrotational flow.

[42] For a more literal rendering of d'Alembert's proof, cf. Grimberg, 1998: 43–48.

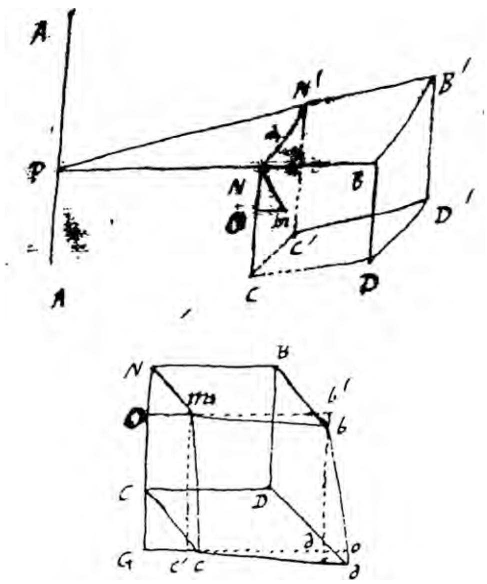

Fig. 8. D'Alembert's drawing for a first proof of the incompressibility condition. He takes an infinitesimal prismatic volume NBDCC'N'B'D' (upper figure). The faces NBDC and N'B'D'C' are rectangles in planes passing through the axis of symmetry AP; after an infinitesimal time dt the points NBDC have moved to nbdc (lower figure). Expressing the conservation of volume and neglecting higher-order infinitesimals, he obtains Eq. (29). From the 1749 manuscript in the Berlin-Brandeburgische Akademie der Wissenschaften; courtesy Wolfgang Knobloch and Gérard Grimberg.

obtained the special expressions of these two conditions in the two-dimensional case and in the axially-symmetric case. In the latter case, he wrote the incompressibility condition as:

$$\frac{\mathrm{d}q}{\mathrm{d}x} + \frac{\mathrm{d}p}{\mathrm{d}z} = \frac{p}{z}, \tag{29}$$

where z and x are the radial and axial coordinates and p and q the corresponding components of the velocity. D'Alembert's 1749 derivation (repeated in his 1752 book) is illustrated by a geometrical construction (Fig. 8).[43]

In order to solve the system Eqs. (27) and (28) in the two-dimensional case, d'Alembert noted that the two conditions meant that the forms $u\mathrm{d}x + v\mathrm{d}y$ and $v\mathrm{d}x - u\mathrm{d}y$ were exact differentials (u and v denote the velocity components along the orthogonal axes Ox and Oy). This property holds, he ingeniously noted, if and only if $(u - \mathrm{i}v)(\mathrm{d}x + \mathrm{i}\mathrm{d}y)$ is an exact differential. This means that u and $-v$ are the real and imaginary parts of a (holomorphic) function of the complex variable $x + \mathrm{i}y$. They must also be such that the velocity is uniform at infinity and at a tangent to the body along its surface. D'Alembert struggled to meet these boundary conditions through power-series developments, to little avail.[44]

The ultimate goal of this calculation was to determine the force exerted by the fluid on the solid, which is the same as the resistance offered by the fluid to the motion of a body with a velocity opposite to that of the asymptotic flow.[45] D'Alembert expressed this force as the integral of the fluid's pressure over the whole surface of the body. The pressure is itself given by the line integral of $-\mathrm{d}\mathbf{v}/\mathrm{d}t$ from infinity to the wall, in conformity with d'Alembert's earlier derivation of Bernoulli's law. This law still holds in the present case, because $-\mathrm{d}\mathbf{v}/\mathrm{d}t = -(\mathbf{v}\cdot\nabla)\mathbf{v} = -\nabla(\mathbf{v}^2/2)$. Hence the resistance could be determined, if only the flow around the body was known.[46]

D'Alembert was not able to solve his equations and to truly answer the resistance question. Yet, he had achieved much on the way: through his dynamical principle and his equilibrium principle, he had obtained hydrodynamic equations for the steady flow of an incompressible axisymmetrical flow that we may retrospectively identify as the incompressibility condition, the condition of irrotational flow, and Bernoulli's law. The modern reader may wonder why he did not try to write general equations of fluid motion in Cartesian-coordinate form. The answer is plain: he was following an older tradition of mathematical physics according to which general principles, rather than general equations, were applied to specific problems.

D'Alembert obtained his basic equations without recourse to the concept of pressure. Yet, he had a concept of internal pressure, which he used to derive Bernoulli's law. Curiously, he did not pursue the other approach sketched in his theory of winds, that is, the application of Newton's second law to a fluid element subjected to a pressure gradient. Plausibly, he favored a derivation that was based on his own principle of dynamics and thus avoided the kind of internal forces he judged obscure.

It was certainly well known to d'Alembert that his equilibrium principle was nothing but the condition of uniform integrability (potentiality) for the force density $\mathbf{f}$. If one then introduces the integral, say P, one obtains the equilibrium equation $\mathbf{f} = \nabla P$ that makes P the internal pressure! With d'Alembert's own dynamical principle, one then reaches the equation of motion

$$\mathbf{f} - \rho\frac{\mathrm{d}\mathbf{v}}{\mathrm{d}t} = \nabla P, \tag{30}$$

[43] It thus would seem appropriate to use "d'Alembert's condition" when referring to the condition of incompressibility, written as a partial differential equation.

[44] D'Alembert, 1752: 60–62. D'Alembert here discovered the Cauchy–Riemann condition for u and $-v$ to be the real and imaginary components of an analytic function in the complex plane, as well as a powerful method to solve Laplace's equation $\Delta u = 0$ in two dimensions. In 1761: 139, d'Alembert introduced the complex potential $\varphi + \mathrm{i}\psi$ such that $(u - \mathrm{i}v)(\mathrm{d}x + \mathrm{i}\mathrm{d}y) = \mathrm{d}(\varphi + \mathrm{i}\psi)$. The real part φ of this potential is the velocity potential introduced by Euler in 1752; its imaginary part ψ is the so-called stream function, which is a constant on any line of current, as d'Alembert noted.

[45] D'Alembert gave a proof of this equivalence, which he did not regard as obvious.

[46] D'Alembert had already discussed fluid resistance in part III of his treatise of 1744. There, he used a molecular model in which momentum was transferred by impact from the moving body to a layer of hard molecules. He believed, however, that this molecular process would be negligible if the fluid molecules were too close to each other – for instance when fluid was forced through the narrow space between the body and a containing cylinder. In this case (1744: 205–206), he assumed a parallel-slice flow and computed the fluid pressure on the body through Bernoulli's law. For a head-tail symmetric body, this pressure does not contribute to the resistance if the flow has the same symmetry. After noting this difficulty, d'Alembert invoked the observed stagnancy of the fluid behind the body to retain only the Bernoulli pressure on the prow.

which is nothing but Euler's second equation. But d'Alembert did not proceed along these lines, and rather wrote equations of motion not involving internal pressure.[47]

4. Euler's equations

We finally turn to Euler himself, for whom we shall be somewhat briefer than we have been with the Bernoullis and d'Alembert (whose papers are not easily accessible to the untrained modern reader; not so with Euler). "Lisez Euler, lisez Euler, c'est notre maître à tous" (Read Euler, read Euler, he is the master of us all) as Pierre-Simon Laplace used to say.[48]

4.1. Pressure

After Euler's arrival in Berlin, he wrote a few articles on hydraulic problems, one of which was motivated by his participation in the design of the fountains of Frederick's summer residence Sanssouci. In these works of 1750–51, Euler obtained the equation of motion for parallel-slice pipe flow by directly relating the acceleration of the fluid elements to the combined effect of the pressure gradient and gravity. He thus obtained the differential version

$$\frac{\mathrm{d}v}{\mathrm{d}t} = g - \frac{\mathrm{d}P}{\mathrm{d}z} \tag{31}$$

of Johann Bernoulli's equation (7) for parallel-slice efflux. From this, he derived the generalization (8) of Bernoulli's law to non-permanent flow, which he applied to evaluate the pressure surge in the pipes that would feed the fountains of Sanssouci.[49]

Although d'Alembert had occasionally used this kind of reasoning in his theory of winds, it was new in a hydraulic context. As we saw, the Bernoullis did not rely on internal pressure in their own derivations of the equations of fluid motion. In contrast, Euler came to regard internal pressure as a key concept for a Newtonian approach to the dynamics of continuous media.

In a memoir of 1750 entitled "Découverte d'un nouveau principe de mécanique," he claimed that the true basis of continuum mechanics was Newton's second law applied to the infinitesimal elements of bodies. Among the forces acting on the elements he included "connection forces" acting on the boundary of the elements. In the case of fluids, these internal forces were to be identified to the pressure.[50]

Euler's first attempt to apply this approach beyond the approximation of parallel-slices was a memoir on the motions of rivers written around 1750–1751. There he analyzed steady two-dimensional flow into fillets and described the fluid motion through the Cartesian coordinates of a fluid particle expressed as functions of time and of a fillet-labeling parameter (a partial anticipation of the so-called Lagrangian picture). He wrote partial differential equations expressing the incompressibility condition and his new principle of continuum dynamics. Through a clever combination of these equations, he obtained for the first time the Bernoulli law along the stream lines of an arbitrary steady incompressible flow. Yet he himself judged that he had reached a dead end, for he could not solve any realistic problem of river flow in this manner.[51]

4.2. The Latin memoir

An English translation of the Latin memoir will be included in these Proceedings.

This relative failure did not discourage Euler. Equipped with his new principle of mechanics and probably stimulated by the two memoirs of d'Alembert, which he had reviewed, he set out to formulate the equations of fluid mechanics in their full generality. A memoir entitled "De motu fluidorum in genere" was read in Berlin on 31 August 1752 and published under the title "Principia motus fluidorum" in St. Petersburg in 1761 as part of the 1756–1757 proceedings. Here, Euler obtained the general equations of fluid motion for an incompressible fluid in terms of the internal pressure P and the Cartesian coordinates of the velocity $\mathbf{v}$.[52]

In the first part of the paper, he derived the incompressibility condition. For this, he studied the deformation during a time $\mathrm{d}t$ of a small triangular element of water (in two dimensions) and of a small triangular pyramid (in three dimensions). The method here is a slight generalization of what d'Alembert did in his memoir of 1749 on the resistance of fluids. Euler obtained, in his own notation:

$$\frac{\mathrm{d}u}{\mathrm{d}x} + \frac{\mathrm{d}v}{\mathrm{d}y} + \frac{\mathrm{d}w}{\mathrm{d}z} = 0. \tag{32}$$

In the second part of the memoir, he applied Newton's second law to a cubic element of fluid subjected to the gravity $\mathbf{g}$ and to the pressure P acting on the cube's faces. By a now familiar bit of reasoning, this procedure yields (for unit density) in modern notation:

$$\frac{\partial \mathbf{v}}{\partial t} + (\mathbf{v}\cdot\nabla)\mathbf{v} = \mathbf{g} - \nabla P. \tag{33}$$

Euler then eliminated the pressure gradient (basically by taking the curl) to obtain what we now call the vorticity equation:

$$\left[\frac{\partial}{\partial t} + (\mathbf{v}\cdot\nabla)\right](\nabla\times\mathbf{v}) - [(\nabla\times\mathbf{v})\cdot\nabla]\mathbf{v} = 0, \tag{34}$$

[47] In this light, d'Alembert's later neglect of Euler's approach should not be regarded as a mere expression of rancor.

[48] Reported by Libri, 1846: 51.

[49] Euler, 1752. On the hydraulic writings, cf. Truesdell, 1954: XLI–XLV; Ackeret, 1957. On Euler's work for the fountains of Sanssouci, cf. Eckert, 2002, 2008. As Eckert explains, the failure of the fountains project and an ambiguous letter of the King of Prussia to Voltaire have led to the myth of Euler's incapacity in concrete matters.

[50] Euler, 1750: 90 (the main purpose of this paper was the derivation of the equations of motion of a solid).

[51] Euler, 1760, Truesdell, 1954: LVIII–LXII.

[52] Euler, 1756–1757. Cf. Truesdell, 1954: LXII–LXXV. D'Alembert's role (also the Bernoullis's and Clairaut's) is acknowledged by Euler somewhat reluctantly in a sentence at the beginning of the third memoir cited in epigraph to the present paper.

in modern notation. He then stated that "It is manifest that these equations are satisfied by the following three values [$\nabla \times \mathbf{v} = \mathbf{0}$], in which is contained the condition provided by the consideration of the forces [i.e. the potential character of the r.h.s. of (33)]". He thus concluded that the velocity was potential, repeating here d'Alembert's mistake of confusing a necessary condition with a sufficient condition. This error allowed him to introduce what later fluid theorists called the velocity potential, that is, the function $\varphi(\mathbf{r})$ such that $\mathbf{v} = \nabla\varphi$. Eq. (33) may then be rewritten as:

$$\frac{\partial}{\partial t}(\nabla\varphi) + \frac{1}{2}\nabla\left(v^2\right) = \mathbf{g} - \nabla P. \tag{35}$$

Spatial integration of this equation yields a generalization of Bernoulli's law:

$$P = \mathbf{g}\cdot\mathbf{r} - \frac{1}{2}v^2 - \frac{\partial\varphi}{\partial t} + C, \tag{36}$$

wherein C is a constant (time-dependence can be absorbed in the velocity potential). Lastly, Euler applied this equation to the flow through a narrow tube of variable section to retrieve the results of the Bernoullis.

Although Euler's Latin memoir contained the basic hydrodynamic equations for an incompressible fluid, the form of exposition was still in flux. Euler frequently used specific letters (coefficients of differential forms) for partial differentials rather than Fontaine's notation, and he measured velocities and accelerations in gravity-dependent units. He proceeded gradually, from the simpler two-dimensional case to the fuller three-dimensional case. His derivation of the incompressibility equation was more intricate than we would now expect. And he erred in believing in the general existence of a velocity potential. These characteristics make Euler's Latin memoir a transition between d'Alembert's fluid dynamics and the fully modern foundation of this science found in the French memoirs.[53]

4.3. The French memoirs

An English translation of the second French memoir will be included in these Proceedings.

The first of these memoirs "Principes généraux de l'état d'équilibre des fluides" is devoted to the equilibrium of fluids, both incompressible and compressible. Euler realized that his new hydrodynamics contained a new hydrostatics based on the following principle: the action of the contiguous fluid on a given, internal element of fluid results from an isotropic, normal pressure P exerted on its surface. The equilibrium of an infinitesimal element subjected to this pressure and to the force density $\mathbf{f}$ of external origin then requires:

$$\mathbf{f} - \nabla P = 0. \tag{37}$$

As Euler showed, all known results of hydrostatics follow from this simple mathematical law.[54]

The second French memoir, "Principes généraux du mouvement des fluides," is the most important one. Here, Euler did not limit himself to the incompressible case and obtained the "Euler's equations" for compressible flow:

$$\partial_t\rho + \nabla\cdot(\rho\mathbf{v}) = 0, \tag{38}$$

$$\partial_t\mathbf{v} + (\mathbf{v}\cdot\nabla)\mathbf{v} = \frac{1}{\rho}(\mathbf{f} - \nabla P), \tag{39}$$

to which a relation between pressure, density, and heat must be added for completeness.[55]

The second French memoir is not only the coronation of many decades of struggle with the laws of fluid motion by the Bernoullis, d'Alembert and Euler himself, it also contains much new material. Among other things, Euler now realized that $\nabla \times \mathbf{v}$ needed not vanish, as he had assumed in his Latin memoir, and gave an explicit example of incompressible vortex flow in which it did not.[56] In a third follow-up memoir entitled "Continuation des recherches sur la théorie du mouvement des fluides," he showed that even if it did not vanish, Bernoulli's law remained valid along any stream line of a steady incompressible flow (as he had anticipated on his memoir of 1750–1751 on river flow). In modern terms: owing to the identity

$$(\mathbf{v}\cdot\nabla)\mathbf{v} = \nabla\left(\frac{\mathbf{1}}{\mathbf{2}}\mathbf{v}^2\right) - \mathbf{v}\times(\nabla\times\mathbf{v}), \tag{40}$$

the integration of the convective acceleration term along a line of flow eliminates $\nabla \times \mathbf{v}$ and contributes the $v^2/2$ term of Bernoulli's law.[57]

In his second memoir, Euler formulated the general problem of fluid motion as the determination of the velocity at any time for given values of the impressed forces, for a given relation between pressure and density, and for given initial values of fluid density and the fluid velocity. He outlined a general strategy for solving this problem, based on the requirement that the form $(\mathbf{f} - \rho\dot{\mathbf{v}})\cdot d\mathbf{r}$ should be an exact differential (in order to be equal to the pressure differential). Then he confined himself to a few simple, soluble cases – for instance uniform flow (in the second memoir), or flow through a narrow tube (in the third memoir). In more general cases, he recognized the extreme difficulty of integrating his equations under the given boundary conditions:[58]

> We see well enough ... how far we still are from a complete knowledge of the motion of fluids, and that what I have explained here contains but a feeble beginning. However, all that the Theory of fluids holds, is contained in the two equations above [Eq. (1)], so that it is not the principles of Mechanics which we lack in the pursuit of these researches, but solely Analysis, which is not yet sufficiently cultivated for this purpose. Thus we see clearly what discoveries remain for us to make in this Science before we can arrive at a more perfect Theory of the motion of fluids.

53 Cf. Truesdell, 1954: LXII–LXXV.

54 Euler, 1755a.

55 Euler, 1755b: 284/63, 286/65. Cf. Truesdell, 1954: LXXXV–C.

56 As observed by Truesdell, 1954: XC–XCI), in Section 66 Euler reverts to the assumption of non-vortical flow, a possible leftover of an earlier version of the paper.

57 Euler, 1755c: 345/117.

58 Euler, 1755b: 315/91.

5. Conclusions

In retrospect, Euler was right in judging that his "two equations" were the definitive basis of the hydrodynamics of perfect fluids. He reached them at the end of a long historical process of applying dynamical principles to fluid motion. An essential element of this evolution was the recurrent analogy between the efflux from a narrow vase and the fall of a compound pendulum. Any dynamical principle that solved the latter problem also solved the former. Daniel Bernoulli appealed to the conservation of live forces; Johann Bernoulli to Newton's second law together with the idiosyncratic concept of *translatio*; d'Alembert to his own dynamical principle of the equilibrium of destroyed motions. With this more general principle and his feeling for partial differentials, d'Alembert leapt from parallel-slice flows to higher problems that involved two-dimensional anticipations of Euler's equations. Although his method implicitly contained a general derivation of these equations in the incompressible case, his geometrical style and his abhorrence of internal forces prevented him from taking this step.

Despite d'Alembert's reluctance, another important element of this history turns out to be the rise of the concept of internal pressure. The door on the way to general fluid mechanics opened with two different keys, so to speak: d'Alembert's principle, or the concept of internal pressure. D'Alembert (and Lagrange) used the first key, and introduced internal pressure only as a derivative concept. Euler used the second key, and ignored d'Alembert's principle. As Euler guessed (and as d'Alembert suggested *en passant*), Newton's old second law applies to the volume elements of the fluid, if only the pressure of fluid on fluid is taken into account. Euler's equations derive from this deceptively simple consideration, granted that the relevant calculus of partial differentials is known. Altogether, we see that hydrodynamics rose through the symbiotic evolution of analysis, dynamical principles, and physical concepts. Euler pruned the unnecessary and unclear elements from the abundant writings of his predecessors, and combined the elements he judged most fundamental in the clearest and most general manner. He thus obtained an amazingly stable foundation for the science of fluid motion.

The discovery of sound foundations only marks the beginning of the life of a theory. Euler himself suspected that the integration of his equations would in general be a formidable task. It soon became clear that their application to problems of resistance or retardation led to paradoxes. In the following century, physicists struggled to solve these paradoxes by various means: viscous terms, discontinuity surfaces, instabilities. A quarter of a millennium later, some very basic issues remain open, as many contributions to this conference amply demonstrate.

Acknowledgments

We are grateful to G. Grimberg, W. Pauls and two anonymous reviewers for many useful remarks. We also received considerable help from J. Bec and H. Frisch.

References

Ackeret, Jakob 1957 'Vorrede', in L. Euler, *Opera omnia*, ser. 2, **15**, VII–LX, Lausanne.

Bernoulli, Daniel 1738 *Hydrodynamica, sive de viribus et motibus fluidorum commentarii*, Strasbourg.

Bernoulli, Daniel 2002 *Die Werke von Daniel Bernoulli*, vol. 5, ed. Gleb K. Mikhailov, Basel.

Bernoulli, Johann 1714 'Meditatio de natura centri oscillationis.' *Acta Eruditorum* Junii 1714, 257–272. Also in *Opera omnia* **2**, 168–186, Lausanne.

Bernoulli, Johann 1742 'Hydraulica nunc primum detecta ac demonstrata directe ex fundamentis pure mechanicis. Anno 1732.' Also in *Opera omnia* **4**, 387–493, Lausanne.

Blay, Michel 1992 *La naissance de la mécanique analytique: La science du mouvement au tournant des XVII^e et XVIII^e siècles*, Paris.

Calero, Julián Simón 1996 *La génesis de la mecánica de los fluidos (1640–1780)*, Madrid.

Casey, James 1992 'The principle of rigidification.' *Archive for the history of exact sciences* **43**, 329–383.

D'Alembert, Jean le Rond 1743 *Traité de dynamique*, Paris.

D'Alembert, Jean le Rond 1744 *Traité de l'équilibre et du mouvement des fluides*. Paris.

D'Alembert, Jean le Rond 1747 *Réflexions sur la cause générale des vents*, Paris.

D'Alembert, Jean le Rond [1749] *Theoria resistenciae quam patitur corpus in fluido motum, ex principiis omnino novis et simplissimis deducta, habita ratione tum velocitatis, figurae, et massae corporis moti, tum densitatis & compressionis partium fluidi*; manuscript at Berlin-Brandenburgische Akademie der Wissenschaften, Akademie-Archiv call number: I–M478.

D'Alembert, Jean le Rond 1752 *Essai d'une nouvelle théorie de la résistance des fluides*, Paris.

D'Alembert, Jean le Rond 1761 'Remarques sur les lois du mouvement des fluides.' In *Opuscules mathématiques* vol. 1 (Paris, 1761), 137–168.

Darrigol, Olivier 2005 *Worlds of flow: A history of hydrodynamics from the Bernoullis to Prandtl*, Oxford.

Dugas, René 1950 *Histoire de la mécanique*. Paris.

Eckert, Michael 2002 'Euler and the fountains of Sanssouci. *Archive for the history of exact sciences* **56**, 451–468.

Eckert, Michael 2005 *The dawn of fluid mechanics: A discipline between science and technology*, Berlin.

Eckert, Michael 2008 'Water-art problems at Sans-souci — Euler's involvement in practical hydrodynamics on the eve of ideal flow theory,' in these Proceedings.

Euler, Leonhard 1727 'Dissertatio physica de sono', Basel. Also in *Opera omnia*, ser. 3, **1**, 183–196, [Eneström index] **E002**.

Euler, Leonhard 1745 *Neue Grundsätze der Artillerie, aus dem englischen des Herrn Benjamin Robins übersetzt und mit vielen Anmerkungen versehen* [from B. Robins, *New principles of gunnery* (London,1742)], Berlin. Also in *Opera ommia*, ser. 2, **14**, 1–409, **E77**.

Euler, Leonhard 1749 *Scientia navalis seu tractatus de construendis ac dirigendis navibus*, 2 volumes (St. Petersburg 1749) [completed by 1738]. Also in *Opera ommia*, ser. 2, **18** and **19**, **E110** and **E111**.

Euler, Leonhard 1750 'Découverte d'un nouveau principe de mécanique.' Académie Royale des Sciences et des Belles-Lettres de Berlin, *Mémoires* [abbreviated below as *MASB*], **6** [printed in 1752], 185–217. Also in *Opera omnia*, ser. 2, **5**, 81–108, **E177**.

Euler, Leonhard 1752 'Sur le mouvement de l'eau par des tuyaux de conduite.' *MASB*, **8** [printed in 1754], 111–148. Also in *Opera omnia*, ser. 2, **15**, 219–250, **E206**.

Euler, Leonhard 1755a 'Principes généraux de l'état d'équilibre d'un fluide.' *MASB*, **11** [printed in 1757], 217–273. Also in *Opera omnia*, ser. 2, **12**, 2–53, **E225**.

Euler, Leonhard 1755b 'Principes généraux du mouvement des fluides' *MASB*, **11** [printed in 1757], 274–315. Also in *Opera omnia*, ser. 2, **12**, 54–91, **E226**.

Euler, Leonhard 1755c 'Continuation des recherches sur la théorie du mouvement des fluides.' *MASB*, **11** [printed in 1757], 316–361. Also in *Opera omnia*, ser. 2, **12**, 92–132, **E227**.

Euler, Leonhard 1760 'Recherches sur le mouvement des rivières'[written around 1750–1751]. *MASB*, **16** [printed in 1767], 101–118. Also in *Opera omnia*, ser. 2, **12**, 272–288, **E332**.

Euler, Leonhard 1756–1757 'Principia motus fluidorum' [written in 1752]. *Novi commentarii academiae scientiarum Petropolitanae*, **6** [printed in 1761], 271–311. Also in *Opera omnia*, ser. 2, **12**, 133–168, **E258**.

Euler, Leonhard [1784] 'Calculs sur les ballons aérostatiques, faits par le feu M. Euler, tels qu'on les a trouvés sur son ardoise, après sa mort arrivée le 7 septembre 1783', Académie Royale des Sciences (Paris), *Mémoires*, 1781 [printed in 1784], 264–268. Also in *Opera omnia*, ser. 2, **16**, 165–169, **E579**.

Euler, Leonhard 1998 *Commercium epistolicum*, ser. 4A, **2**, eds. Emil Fellmann and Gleb Mikhajlov (Mikhailov). Basel.

Fraser, Craig 1985 'D'Alembert's principle: The original formulation and application in Jean d'Alembert's *Traité de dynamique* (1743).' *Centaurus* **28**, 31–61, 145–159.

Günther Garbrecht (ed.), 1987 *Hydraulics and hydraulic research: A historical review*, Rotterdam.

Grimberg, Gérard 1998 *D'Alembert et les équations aux dérivées partielles en hydrodynamique*, Thèse. Université. Paris 7.

Grimberg, Gérard; Pauls, Walter and Frisch, Uriel 2008 In these Proceedings.

Hankins, Thomas 1968 Introduction to English transl. of d'Alembert 1743 (New York, 1968), pp. ix–xxxvi.

Huygens, Christiaan 1673 *Horologium oscillatorium, sive, de motu pendulorum ad horologia aptato demonstrationes geometricae*. Paris.

Knobloch, Eberhard 2008 In these Proceedings.

Lagrange, Joseph Louis 1788 *Traité de méchanique analitique*. Paris.

Libri, Gugliemo (della Somaia) 1846 'Correspondance mathématique et physique de quelques célèbres géomètres du XVIII^{e} siècle, ...' *Journal des Savants* (1846), 50–62.

Mikhailov, Gleb K. 1983 *Leonhard Euler und die Entwicklung der theoretischen Hydraulik im zweiten Viertel des 18. Jahrhunderts.* In Johann Jakob Burckhardt and Marcel Jenni (eds.), Leonhard Euler, 1707–1783: Beiträge zu Leben und Werk. Gedenkband des Kantons Basel-Stadt (Basel: Birkhäuser, 1983), 229–241.

Mikhailov, Gleb K. 1999 'The origins of hydraulics and hydrodynamics in the work of the Petersburg Academicians of the 18th century.' *Fluid dynamics*, **34**, 787–800.

Mikhailov, Gleb K. 2002 Introduction to *Die Werke von Daniel Bernoulli* 5, ed. Gleb K. Mikhailov (Basel), 17–86.

Nowacki, Horst 2006 'Developments in fluid mechanics theory and ship design before Trafalgar.' Max-Planck-Institut für Wissenschaftsgeschichte, Preprint 308 (2006). *Proceedings, International Congress on the Technology of the Ships of Trafalgar*, Madrid, Universidad Politécnica de Madrid, Escuela Técnica Supérior de Ingenieros Navales. Available at http://www.mpiwg-berlin.mpg.de/en/forschung/Preprints/P308.PDF (in press).

Passeron, Irène 1995 *Clairaut et la figure de la Terre au XVIII^{e}, Thèse. Université Paris 7*.

Rouse, Hunter and Ince, Simon 1957 *History of hydraulics*, Ann Arbor.

Smith, George E. 1998 'Newton's study of fluid mechanics.' *International journal of engineering science*. **36**, 1377–1390.

Todhunter, Isaac 1873 *A history of the mathematical theories of attraction and the figure of the Earth*, London.

Truesdell, Clifford 1954 'Rational fluid mechanics, 1657–1765.' In Euler, *Opera omnia*, ser. 2, **12** (Lausanne), IX–CXXV.

Truesdell, Clifford 1955 'The theory of aerial sound, 1687–1788.' In Euler, *Opera omnia*, ser. 2, **13** (Lausanne), XIX–LXXII.

Truesdell, Clifford 1983 'Euler's contribution to the theory of ships and mechanics.' *Centaurus* **26**, 323–335.

Vilain, Christiane 2000 'La question du centre d'oscillation' de 1660 à 1690; de 1703 à 1743.' *Physis* **37**, 21–51, 439–466.

Youschkevitch, Adolf Pavlovitch 1971 'Euler, Leonhard.' In *Dictionary of scientific biography* **4**, 467–484.

Available online at www.sciencedirect.com

ScienceDirect

Physica D 237 (2008) 1870–1877

PHYSICA D

www.elsevier.com/locate/physd

Water-art problems at Sanssouci—Euler's involvement in practical hydrodynamics on the eve of ideal flow theory

M. Eckert*

Deutsches Museum, Forschungsinstitut, D 80306 Munich, Germany

Available online 14 September 2007

Abstract

Frederick the Great blamed Euler for the failure of fountains at his summer palace Sanssouci. However, what is regarded as an example for the proverbial gap between theory and practice, is based on dubious evidence. In this paper I review Euler's involvement with pipeflow problems for the Sanssouci water-art project. Contrary to the widespread slander, Euler's ability to cope with practical challenges was remarkable. The Sanssouci fountains did not fail because Euler was unable to apply hydrodynamical theory to practice, but because the King ignored his advice and employed incompetent practitioners. The hydrodynamics of the Sanssouci problem also deserves some interest because it happened on the eve of the formulation of the general equations of motion for ideal fluids. Although it seems paradoxical, the birth of ideal flow theory was deeply rooted in Euler's involvement with real flow problems.

Keywords: Hydrodynamics; Euler; Euler equation

1. Introduction

Since the beginning of his career as an academician in St. Petersburg, Euler dealt with practical problems of fluid dynamics, from ballistics to naval architecture. When the Prussian King, Frederick II, called him to Berlin as director of the mathematical class of the Prussian Academy of Science, founded under the motto *theoria cum praxi*, Euler was eager to display his disposedness for practical affairs. In 1744, for example, Euler recommended the translation of an English treatise on ballistics into German because of its practical value for the artillery. He intended to add "suitable remarks to perfect the usefulness of the matter", and therefore offered himself as a translator. He accomplished this task in 1745 and dedicated the translation to the King. According to Clifford A. Truesdell, the editor of Euler's treatises on hydrodynamics, it changed the character of the English original from a "little budget of rules, experiments, and guesses" into "the first scientific work on gunnery". A historian of ballistics remarked that Euler revealed with this work "a highly perceptive engineering mentality that illustrates the depths of his technical knowledge". With regard to the history of fluid dynamics, Euler's treatise on ballistics deserves particular interest because it contains a consideration of fluid resistance which led Euler to closely anticipate "d'Alembert's paradox".[1]

During the years prior to his formulation of the general theory in 1755, Euler reported to the academy every year at least once on practical matters involving one or another aspect of fluid motion. In May 1749, for example, Euler investigated the navigability of a canal which connected two rivers north of Berlin. The inspection of the canal may well have contributed to shape his thoughts on the forces which act on a fluid element under free-surface flow conditions; two years later, on 6 May 1751, he communicated to the academy a memoir on 'Research concerning the flow of rivers', in which he studied the balance of forces along streamlines. Euler did not arrive at a general solution (for this reason he probably regarded it to be of

* Tel.: +49 89 2179538; fax: +49 89 2179273.
E-mail address: m.eckert@deutsches-museum.de.

[1] Robins, 1742; Euler to Frederick II, undated, in *Opera omnia*, ser. 4a, **6**: p. 309; Euler, 1745; Truesdell, 1954: p. XXXVIII; Steele, 2006: p. 290; Szabó, 1987: pp. 243–245; Darrigol, 2005: p. 103; Eckert, 2006: pp. 13–15; Darrigol, Frisch, 2008. However, the early derivation of the "Euler–d'Alembert-paradox"—as it was labeled by Szabó —should not be interpreted uncritically as an anticipation of d'Alembert's paradox because Euler combined his derivation with dubious considerations about momentum transfer in fluids; I thank Olivier Darrigol for this clarification.

0167-2789/$ - see front matter © 2007 Elsevier B.V. All rights reserved.
doi:10.1016/j.physd.2007.09.006

minor value and published it only much later). "In any case it is likely", Truesdell argued, "that Euler then threw aside the manuscript on rivers and started afresh on a new plan". At about the same time, in 1750, Euler formed his thoughts about how to apply Newton's Second Law more generally to contiguous infinitesimal volume elements. This combined effort to solve practical problems on the basis of general principles led him to the famous 1755 memoirs, the 'Principes généraux'.[2]

Shortly after the canal investigation in summer 1749, did Euler become also involved in the Sanssouci water-art project. If the canal project brought him into contact with open channel flow, the Sanssouci project confronted him with pipeflow problems. In contrast to his manuscript concerning river flow, Euler regarded his pipeflow study not as provisional. He solved the equations of motion for water which is pumped through a pipeline to an elevated reservoir. In this study, as well as in others concerning pumps and mills, Euler combined a deep theoretical insight with a "good feel" for practice, as the editor of Euler's hydraulic work attested.[3]

Why, then, became Euler a role model of the pure scientist divorced from the practice to which his scholarship was supposed to refer? In popular books on the history of physics and mathematics Euler is portrayed as a "second rate physicist" and blamed for "letting his mathematics run away with his sense of reality". One physicist mused: "When Euler applied his equations to design a fountain for Frederick the Great of Prussia, it failed to work," and he offered as a cause for Euler's mishap: "Unfortunately, he omitted the effects of friction, with embarrassing practical consequences".[4]

At first sight such a verdict does not seem implausible. The water-art in the Park at Sanssouci, as conceived in the 18th century, indeed was malfunctioning. As early as in 1783, Euler's contemporary, the Marquis de Condorcet, wrote in an obituary, addressed to the Paris Academy, that Euler at times "appeared only to enjoy the pleasures of calculation" and "only wished to exhibit the power of his art"; he was full of praise for Euler as a mathematical genius, but "Mr. Euler the Metaphysician or even the Physicist was not as great as the Geometer".[5] Was Euler, as Condorcet suggested, using practical applications only as a pretext to "enjoy the pleasures of calculation"—without real concern about the physical problems? Even more support for this view comes from the King himself. In 1778 Frederick II wrote in a letter to Voltaire[6]:

"I wanted to make a fountain in my Garden; the Cyclop Euler calculated the effort of the wheels for raising the water to a basin, from where it should fall down through canals, in order to form a fountain jet at Sanssouci. My mill was constructed mathematically, and it could not raise one drop of water to a distance of fifty feet from the basin. Vanity of Vanities! Vanity of geometry."

The derogative tenor in this letter ("le Ciclope Euler")[7] already hints at tensions in the relationship between Euler and Frederick II. Euler had left Berlin in 1766 after he was repeatedly neglected by the King as a candidate for the presidency of the academy. Euler's biographers report a growing alienation between Euler and Frederick II. Therefore, the King's utterance, made almost thirty years after Euler's involvement in the Sanssouci project, is of dubious value as a historical evidence. Yet it became the widely accepted source for the slander against Euler—a slander which accompanied Euler like a symbol for the gulf which separates ideal from real flows. Even Truesdell, who was otherwise very critical with regard to the slander against Euler, did not cast doubt on Euler's alleged mishap: The King "expected Euler to supervise the laying of aqueducts. Unfortunately Euler was willing and able to undertake such tasks, thus giving Frederick occasion for the complaint that the work was not well done".[8]

2. Euler's involvement at Sanssouci

In order to sort out historical fact from anecdotes and myths, it is necessary to reconstruct the circumstances of Euler's involvement in the Sanssouci project from other sources than eulogies and biased recollections. When was Euler's advice for the water-art project solicited? What was the particular problem? Did Euler's advice misdirect the project so that the King lost confidence in Euler's ability to combine theory with practice?

The water-art project at Sanssouci had started in 1748, shortly after the inauguration of the King's new summer palace. The design foresaw a system with several fountains; the major fountain close to the palace was supposed to have a jet with a height of at least 30 m, higher than the jets of the fountains at Versailles. Water from the Havel river should be raised to an elevated reservoir at a distance of about one kilometer on top of a hill 50 m above the river level in order to provide for the required pressure for the fountain jets in the Park underneath. The water had to be guided first by a canal from the river to the site of a windmill connected to pumps which would press the water through a pipeline into the reservoir. Other pipes would connect the reservoir with the fountains. By the end of 1748, the canal from the Havel to the pump station, the windmill and the pumps were accomplished; so far the project progressed according to the expectations. But problems arose as soon as water was pumped into the elevated reservoir. The tubes for the pipeline had been constructed from wooden boards, each 24 feet long, which were put together like barrels and strengthened

2 Eichler, 1974: Appendix, pp. 243–251; Frederick to Euler, 30 April 1749, Euler et al. 1749 to Frederick, 14 May 1749, in *Opera omnia*, ser. 4a, **6**, 311–316; Euler, 1760; Truesdell, 1954: p. LXII; Euler, 1750; Euler, 1755a,b

3 Ackeret, 1957: p. LVI.

4 Hermann, 1991: p. 81, Bell, 1937: p. 168; Perkovitz, 1999: p. 38.

5 Condorcet, 1783.

6 Frederick to Voltaire, 25 January 1778, in Besterman, 1976: pp. 184–186. ("Je voulus faire un jet-d'eau en mon Jardin; le Ciclope Euler calcula l'effort des roües, pour faire monter l'eau dans un bassin d'oú elle devoit retomber par des Canaux, afin de jaillir à Sanssouci. Mon Moulin a été éxécuté géométriquement, et il n'a pu élever une goutte d'eau à Cinquante pas du Bassin. Vanité des Vanités; Vanité de la géométrie".)

7 In 1738, Euler lost the sight in his right eye as a consequence of a severe illness; in the 1760s a cataract in his left eye further deteriorated his remaining visual faculty; in his later years Euler was almost completely blind. For biographical details see Fellmann, 2007.

8 Truesdell, 1954: p. XC.

by iron bands. The pipeline was assembled from eight hundred such tubes. But when water was pumped into this pipeline, it reached only about halfway up to the reservoir before the pipes at the lower end began to burst. After this failure the barrel-like tubes were replaced by entire spruce tree trunks whose cores had been drilled out. Between March and December of 1749, the new pipeline was assembled—but it experienced the same mishap: the pipes burst.[9]

At this stage, Euler became involved. Frederick trusted Euler as an expert whom he could ask for advice whenever problems of a mathematical, physical or technical nature arose. In the summer of 1749, for example, shortly after the canal investigation, the King requested Euler's advice also on a number lottery which had been recently introduced in Italian cities and which Frederick considered as an additional source of income for the state's treasury. Like with the lottery and the canal issues, Euler responded swiftly. On 18 September 1749 he informed the academy's president, Pierre Louis Maupertuis, "that I sent my researches about the projected lottery yesterday to the King, and that I hope to accomplish within a couple of days those about the hydraulic machine". Three days later he sent Maupertuis the first results concerning "la Machine Hydraulique de Sans Soucy". With regard to the mighty fountain jet he cautioned already in this first response "that it would require a huge effort to make it as high as the King wishes". A week later, Euler expressed severe doubts about the present design, in particular concerning the dimensions of the pipes. He complained that the architect "does not give any rule for estimating the pressure which the conduit pipes have to sustain: apparently he believes that these pipes would have to sustain the weight of the water column which corresponds the state of rest". Euler surveyed the literature on water-art hydraulics and suspected that the dynamically increased pressure due to the action of the pumps had never been taken into account before. Nevertheless, practitioners elsewhere had usually chosen thick metal tubes rather than wooden tubes for pipelines where high pressures were to be expected. In view of a lack of theoretical methods for calculating the strength of materials Euler referred to the experiences made by Edme Mariotte in Versailles where it was shown "that a lead pipe with a diameter of 12 in., and a wall thickness of 2 lignes (1 ligne = 2.2558 mm), is able to sustain a 100 feet high water column," but cautioned to simply extrapolate: "But if Mariotte's experience was wrong, or corrupted by a misprint, I would not know how to determine the thickness of the pipes for the case in question other than making new experiments about the force which the lead pipes are able to sustain. For one would risk too much if the determination of the thickness of the pipes would be made only haphazardly".[10]

From this letter it is obvious that Euler was not resorting to mere theoretical considerations. He referred explicitly to Bernard Forest de Bélidor and Edme Mariotte, whose treatises *Architecture hydraulique* and *Traité du mouvement des eaux et des autres corps fluides* contained the contemporary empirical knowledge of hydraulic constructions. A good deal of this knowledge was derived from experiments undertaken upon request of the Paris Academy and motivated, among other practical interests, by the constructions of the water-art system for Versailles.[11] The major theoretical part to which Euler could contribute useful considerations concerned the magnitude of the pressure which the pipeline had to sustain under the action of the driving pumps. The motion of the pump's pistons resulted in a nonstationary pipeflow. Euler's theory (see next section) provided a formula from which the maximal pressure in the pipeline could be estimated if the dimensions of the tubes and the driving force of the pumps (delivered by a wind mill or horse power) were given. On 21 October 1749, he explained to Maupertuis why the wooden pipeline was doomed to burst[12]:

> "The true cause of this awkward accident was only due to the fact that the capacity of the pumps was too big, and if one does not reduce it very considerably, either by diminishing their diameter or their height, or the number of cycles per one turn of the mill, the machine will not be in the state to raise one drop of water into the reservoir."

Two days later, Euler presented his theory 'On the motion of water in conduits' to the academy. At subsequent meetings of the academy, on 20 November 1749 and 5 February 1750, he drew a number of practical consequences 'concerning different methods with which to raise water through pumps with the greatest effectiveness' and 'the most advantageous arrangement of the machines used to raise water via pumps'.[13]

Euler did not content himself with academic presentations. On 17 October 1749 he communicated a summary of his results together with related problems concerning windmills to the King. Like in his letter to the president of the academy, Euler left no doubt that he regarded the present design as doomed to failure unless major changes were made[14]:

> "For in the state in which they are at present it is quite certain that one will never raise one drop of water to the reservoir, and the entire force would be employed only for the destruction of the machine and the pipes."

Frederick II thanked Euler for the "remarks you have made concerning your calculations about the pumps and pipes of the

[9] Manger, 1789: vol. 1, pp. 91–106.

[10] Euler to Maupertuis, 18 September, 21 September and 30 September 1749, in *Opera omnia*, ser. 4a, **6**: pp. 135–138. ("Mais en cas que l'expérience de Mariotte ne fût pas juste, ou gâtée par une faute d'impression, je ne saurois rien déterminer sur l'épaisseur des tuyaux dans le cas dont il s'agit, à moins qu'on ne fît de nouveau des expériences sur la force que des tuyaux de plomb sont capables de soutenir. Car on risqueroit trop si l'on vouloit confier au seul hazard la détermination de l'épaisseur des tuyaux".)

[11] Bélidor, 1737-1739; Mariotte, 1718; for the role of the Paris Academy see Blay, 1986.

[12] Euler to Maupertuis, 21 October 1749, in *Opera omnia*, ser. 4a, **6**: pp. 139–140. ("La veritable cause de ce facheux accident consistoit uniquement en ce que la capacité des pompes étoit trop grande, et à moins qu'on ne la diminue très considerablement, ou en diminuant leur diametre ou leur hauteur, ou le nombre des jeux qui repond à un tour de moulin, la machine ne sera pas en etat de fournir une seule goutte d'eau dans le reservoir".)

[13] Euler, 1752a,b,c.

[14] Euler to Frederick, 17 October 1749, in *Opera omnia*, ser. 4a, **6**: p. 322 ("Car sur le pied qu'elles se trouvent actuellement, il est bien certain, qu'on n'éleveroit jamais une goutte d'eau jusqu' au reservoir, et toute la force ne seroit employée qu'à la destruction de la machine et des tuyaux".). He also elaborated his related treatises on windmills as academy memoirs: Euler, 1758a,b.

machine of Sanssouci. They have been very agreeable to me, and I am very obliged to you for the effort which you have made for it".[15] Beyond this exchange of letters in autumn 1749, and the subsequent presentation of the related memoirs to the academy, there is no evidence for any further involvement of Euler with the water-art project at Sanssouci.

What happened thereafter at Sanssouci? According to the available historical evidence, no consequences were drawn from Euler's advice. The bungling in the Park at Sanssouci proceeded unabatedly. No experiments were undertaken to determine the wall thickness of lead pipes, as Euler had recommended in his letters in September 1749. Although Euler regarded the choice of lead pipes as obvious for pipelines that had to sustain high pressure, the practitioners in the Park continued to use wooden pipes for a second trial—with the same mishap: the pipes burst again. Only in summer 1752, more than two years after Euler had presented his advice, the wooden pipes were replaced by metal pipes. But the pipes were not properly dimensioned. As one could have anticipated from Euler's analysis, the new pipeline was rather inefficient. By Spring 1754, a little amount of water was raised to the reservoir, so that the King was given a demonstration. But the fountain jet rose to only about half the expected height, and after an hour the reservoir was empty. Two years later, the Seven Years' War broke out and caused an interruption of the bungling at Sanssouci. In 1763, new efforts were started, but the King was unwilling to afford the high costs involved with the replacement of the inappropriate installations. A few years later, the project was stopped, and those materials of the dysfunctional water-art which had not been rotten in the meantime were used for other purposes. In 1841, under the reign of another King, the water-art project at Sanssouci was started anew. With pumps driven by a steam engine and properly dimensioned pipes the project was successfully completed within only two years.[16]

3. Nonstationary pipeflow theory

Although Euler's advice was ignored, and thus had no impact on the further developments of the water-art project at Sanssouci, it is interesting to study his pipeflow theory which he presented to the Berlin academy as a result of his short-termed involvement. Euler introduced his academy memoir with references to Johann and Daniel Bernoulli, as well as to Jean le Rond d'Alembert, but regarded the "hydraulic theory"

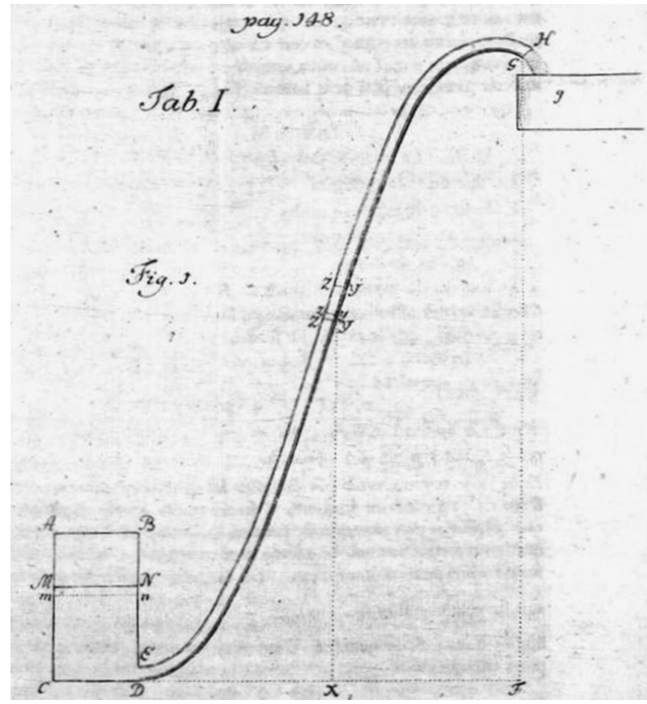

Fig. 1. Euler's pump–pipeline arrangement: $DX = x$ and $XY = y$ are the Cartesian coordinates of the centerline of the pipeline, specified by a curve $s = s(x, y)$; $z = z(s)$ is the inner diameter of the pipe; $AB = a$ and $AC = b$ is the inner diameter of the pump cylinder and its height; MN indicates an intermediate position of the piston at time t when it is at $b - r$ above the ground, with $r = r(t)$ and $r(0) = 0$; within $\mathrm{d}t$ the piston moves down by $\mathrm{d}r$ to the new position mn; the driving pump force is represented by the weight of an equivalent water column of height k exerted on the piston.

still too general for practical application. Without explicitly mentioning the Sanssouci project, he chose the case of water rising to an elevated reservoir by means of a piston pump in order to demonstrate what theory could do for practical applications. But he mentioned at the outset that he employed a different method compared to those which had been used before, with the explicit goal "to facilitate the researches which one has still to undertake in this Science".[17]

In a nutshell, Euler's approach was based on the internal pressure gradient which is involved in the balance of forces on a slice of water in the tube; Euler succeeded to derive from there an expression for the pressure at an arbitrary location of the pipeline (Fig. 1).

Unfortunately, the originality of his approach is obscured by the use of a notation that makes it difficult to follow from a modern perspective. But in order to understand both the conceptual problems with which 18th century pipeflow theories were confronted, and the merits of Euler's memoir for practical applications, it is useful to transmit a flavor for Euler's memoir in the original notation before it is adapted to our modern vantage point.

Euler expressed the force on the piston of the pump in terms of an equivalent water column of height k; for the velocity of the piston he wrote $\mathrm{d}r/\mathrm{d}t = \sqrt{v}$, where v indicates the height from which a falling weight would acquire the corresponding velocity. The equation of continuity allowed him to express the velocities at the corresponding locations YZ and $Y'Z'$ of the tube in terms of the piston velocity v. Euler assumed the diameter z of the tube as variable,

[15] Frederick to Euler, 21 October 1749, in *Opera omnia*, ser. 4a, **6**: p. 330 ("... remarques, que vous avez fait sur vos calculs sur les pompes et les tuyaux de la Machine de Sanssouci. Elles M'ont été fort agréables, et Je vous suis bien obligé de la peine que vous en avez pris".)

[16] Although the archival material about the constructions at Sanssouci was largely destroyed in World War II, the bungling by the practitioners is well-documented in several accounts, most comprehensively in Manger, 1789 and Artelt, 1893. Heinrich Ludewig Manger served as architect under Frederick II; Paul Artelt's account was written at the occasion of the fiftieth birthday of the steam engine at Sanssouci. In both accounts, written from the perspective of practitioners, Euler's name is not even mentioned—which is plausible because of the short period of his involvement in autumn 1749 and the long duration of mishaps. If there had been the slightest reason to blame Euler for the failures, the authors of these accounts would surely not have missed the opportunity to elaborate on Euler's role as a consultant.

[17] Euler, 1752a: pp. 222–223 ("ce qui ne manquera pas de faciliter les recherches qu'on a encore à entreprendre dans cette Science".)

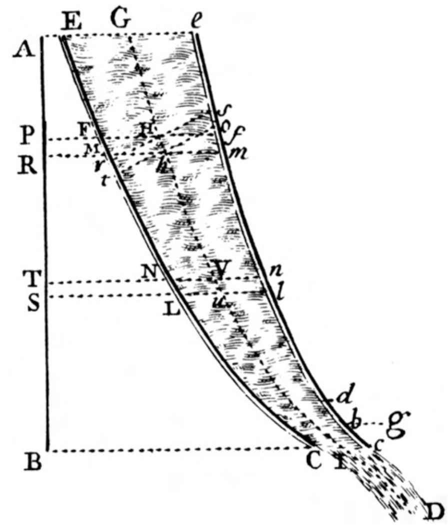

Fig. 2. Nonstationary pipeflow in Johann Bernoulli's *Hydraulica*. For the derivation of Bernoulli's formula and its relation to (2) see Szabó, 1987: pp. 181–185.

which further complicated his analysis. For the velocity of the water in the tube at $Y'Z'$, which corresponds to the piston velocity $\sqrt{(v+\mathrm{d}v)}$ at mn, he obtained

$$\frac{a^2}{z+\frac{a^2}{z^2}S\mathrm{d}r}\sqrt{(v+\mathrm{d}v)}$$

with $S=\mathrm{d}z/\mathrm{d}s$ accounting for the variation of the diameter of the tube. Euler derived from this expression an incremental velocity increase along the passage YY', expressed in equivalent height of fall, as

$$\frac{a^4}{z^4}\mathrm{d}v-\frac{4a^6}{z^7}Sv\mathrm{d}r$$

corresponding to an accelerating force (exerted by the pump's piston) which Euler balanced with the force due to the pressure gradient and the weight upon the infinitesimal slice of water $YZzy$: "Now one has to find the accelerating force which acts on the section YZ," he introduced this stage of his analysis. The crucial passage of Euler's analysis reads in the original[18]:

"Adjacent to this slice from the side YZ acts the pressure of the water which follows, and from the side yz the pressure from the preceding water; and if these two pressures would be equal, one would destroy the effect of the other, and no acceleration or retardation would result therefrom. Be the height p the expression for the pressure of the water on the surface YZ, and p a function of x or s; then the pressure on the surface yz is expressed by the height $p+\mathrm{d}p$".

The balance of forces finally yielded the result:

$$\mathrm{d}p+\mathrm{d}y=-\frac{a^2\mathrm{d}s}{z^2}\frac{\mathrm{d}v}{\mathrm{d}r}+\frac{4a^4S\mathrm{d}s}{z^5}v$$

where the left-hand side contained the action of the pressure gradient and gravity, and the right-hand side the accelerating force due to the pump. After integration Euler obtained for the pressure at YZ[19]:

$$p=C-y-\frac{a^2\mathrm{d}v}{\mathrm{d}r}\int\frac{\mathrm{d}s}{z^2}-a^4v\frac{1}{z^4}.$$

Determining the integration constant by considering the pressure at $y=0$, Euler obtained the final result for the pressure at an arbitrary location YZ:

$$p=k-y+(b-r)\left(1-\frac{\mathrm{d}v}{\mathrm{d}r}\right)-\frac{a^2\mathrm{d}v}{\mathrm{d}r}\int\frac{\mathrm{d}s}{z^2}+v\left(1-\frac{a^4}{z^4}\right).$$

So much for the flavor of the contemporary work. In modern notation the result may be rewritten as[20]

$$p(y)=\rho g(k+b-r-y)+\frac{1}{2}\rho w^2\left(1-\frac{a^4}{z^4}\right)$$
$$-\rho\left(b-r+\frac{\mathrm{d}w}{\mathrm{d}t}\int\frac{a^2}{z^2}\mathrm{d}s\right) \quad (1)$$

ρ is the density of the fluid, g the acceleration of gravity; w instead of v is used here for the velocity of the piston in modern notation in order to avoid confusion with Euler's velocity $\sqrt{v}$; the integral is taken along s from the pump to the location at y. (1) is equivalent to the "Bernoulli equation" for nonstationary pipeflow:

$$p_1+\frac{1}{2}\rho w_1^2+\rho g y_1+\rho\int_0^1\frac{\partial w}{\partial t}\mathrm{d}s=p_0+\frac{1}{2}\rho w_0^2+\rho g y_0 \quad (2)$$

where the subscripts 0 and 1 refer to different locations along a streamline (or, to put it less anachronistically, along the centerline of an arbitrarily shaped cylindrical pipe). Formulae for nonstationary pipeflow, which imply (2), had been obtained earlier; when Johann Bernoulli sent Euler the first part of his *Hydraulica* in 1739, Euler responded by calculating a formula for the vertical efflux of water from an arbitrarily shaped vase through a hole in the bottom.[21]

Johann Bernoulli elaborated the theory of nonstationary pipeflow in the second part of his treatise for the more general case of a flow through an arbitrarily oriented pipe (Fig. 2): by a rather complicated procedure he obtained a formula which may be transformed with hindsight directly into (2).[22]

Johann Bernoulli's *Hydraulica* had appeared in 1742. Why did not Euler start from (2) and merely specify the variables at location 0 and 1 for the particular pump–pipeline configuration (as modern hydraulic engineers would do)? Such reasoning ignores that Johann Bernoulli did not write (1) in its modern form, and that the earlier methods used for nonstationary pipeflow became the subject of heated debates among the Bernoullis and d'Alembert. Euler, presumably, regarded the older methods with some suspicion and therefore chose a novel approach—an approach in which "for the first time in the history of fluid mechanics, the pressure p in its modern sense has made its appearance", as Truesdell remarked about Euler's

[18] Euler, 1752a: p. 227 ("Outre cela cette couche se trouve du coté YZ sollicitée par la pression de l'eau suivante, et du coté yz de la pression de l'eau précédente; et si ces deux pressions étoient égales, l'une détruiroit l'effet de l'autre, et il n'en résulteroit aucune accélération ou retardation. Que la hauteur p exprime la pression de l'eau sur la surface YZ, et p étant une fonction de x ou s, la pression sur la surface yz sera exprimée par la hauteur $p+\mathrm{d}p$".)

[19] Euler, 1752a: p. 230.

[20] For the conversion of Euler's units see Truesdell, 1954: pp. XLIII–XLIV and Ackeret, 1957: pp. XIX-XXI.

[21] Darrigol, Frisch, 2008: Footnote 21; Euler, 1998: pp. 287–304; for earlier unpublished work by Euler and Daniel Bernoulli on nonstationary pipeflow see Gleb Mikhailov's introduction in Euler, 1998: pp.60–62; for the priority dispute between Johann and Daniel Bernoulli see Mikhailov, 1999, 2002.

[22] Szabó, 1987: pp. 175–185. With hindsight, Szabó also interpreted Johann Bernoulli's somewhat mysterious notion of "gurges" merely as a sort of construct which enabled Bernoulli the application of the momentum principle for the motion of a parallel slice of fluid from a wider to a narrower passage.

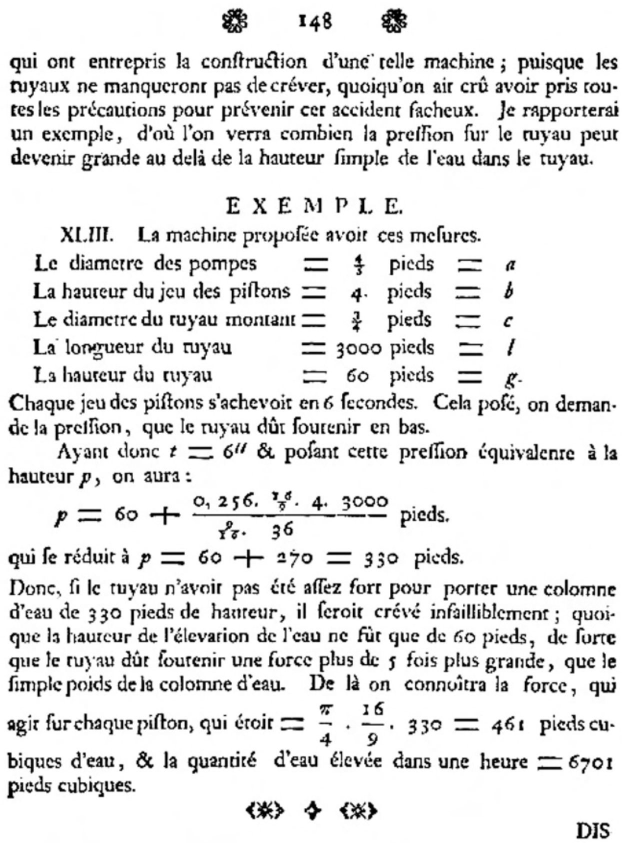
148

qui ont entrepris la conſtruction d'une telle machine ; puisque les tuyaux ne manqueront pas de créver, quoiqu'on ait crû avoir pris toutes les précautions pour prévenir cet accident facheux. Je rapporterai un exemple, d'où l'on verra combien la preſſion ſur le tuyau peut devenir grande au delà de la hauteur ſimple de l'eau dans le tuyau.

EXEMPLE.

XLIII. La machine propoſée avoit ces meſures.

Le diametre des pompes	$=$	$\frac{4}{3}$ pieds	$=$	a
La hauteur du jeu des piſtons	$=$	4. pieds	$=$	b
Le diametre du tuyau montant	$=$	$\frac{3}{4}$ pieds	$=$	c
La longueur du tuyau	$=$	3000 pieds	$=$	l
La hauteur du tuyau	$=$	60 pieds	$=$	g.

Chaque jeu des piſtons s'achevoit en 6 ſecondes. Cela poſé, on demande la preſſion, que le tuyau dût ſoutenir en bas.

Ayant donc $t = 6''$ & poſant cette preſſion équivalente à la hauteur p, on aura :

$$p = 60 + \frac{0,256 \cdot \frac{16}{9} \cdot 4 \cdot 3000}{\frac{9}{16} \cdot 36} \text{ pieds.}$$

qui ſe réduit à $p = 60 + 270 = 330$ pieds.

Donc, ſi le tuyau n'avoit pas été aſſez fort pour porter une colomne d'eau de 330 pieds de hauteur, il ſeroit crévé infailliblement ; quoique la hauteur de l'élevation de l'eau ne fût que de 60 pieds, de ſorte que le tuyau dût ſoutenir une force plus de 5 fois plus grande, que le ſimple poids de la colomne d'eau. De là on connoîtra la force, qui agit ſur chaque piſton, qui étoit $= \frac{\pi}{4} \cdot \frac{16}{9} \cdot 330 = 461$ pieds cubiques d'eau, & la quantité d'eau élevée dans une heure $= 6701$ pieds cubiques.

DIS

Fig. 3. Euler's example for the pressure increase caused by the action of the pump, compared with the pressure in the hydrostatic case.

pipeflow memoir.[23] From this perspective, Euler's pipeflow memoir may be regarded as a turning point in the history of hydrodynamics because the new method of balancing forces on a fluid volume element by using internal pressure gradients also yielded the general "Euler equations" a few years later.

However, this is another retrospective evaluation. Euler's memoir was not motivated by a concern about the foundations of fluid mechanics but by the desire to solve practical problems. Once he had derived (1) it was straightforward (but tedious) to calculate the technically important quantities of the pump–pipeline assembly.[24] Euler could have left this effort to lesser geometers if he had been interested only in foundational matters or mathematical challenges. But he proceeded to derive formulae for the quantities of practical interest, particularly the pressure at the lower end of the pipeline and the discharge flow, and he explained in great detail their practical relevance. His formula for the pressure at the lower end of the pipeline made particularly clear how much the dynamical action of the pump added to the hydrostatic pressure (corresponding to the height difference between the level of the pump and the elevated reservoir):

$$p = g + \frac{0.256a^2bl}{c^2t^2}.$$

Note again, that in Euler's notation the pressure is expressed in length units; g is the vertical height difference (not to be confused with the acceleration of gravity in our modern notation), l the length of the pipeline, and c its inner diameter (assumed to be constant, i. e. $z = c$); t is the time within which the piston moves from the upper to the lower position in the pump.[25]

Euler formulated the practical lessons from this result not only in the language of mathematics but also as "rules"[26]:

"For the same force acting on the pistons of the pumps being able to deliver a maximal amount of water into the reservoir, one must make the rising pipe as wide as possible (...). In order to deliver a maximal quantity of water into the reservoir by the same force acting on the pistons, one must make the rising pipe as short as possible."

He concluded his memoir with a numerical example (Fig. 3): For a discharge of 6701 cubic feet per hour, pumped to a height of 60 feet through a 3000 feet long pipeline, the pressure at the lower end of the pipeline amounted to an equivalent height of a 330 feet high water column. If the pipeline would have been designed to withstand only the hydrostatic pressure, Euler warned, "it would inevitably have burst".[27] In his letter to the King on 17 October 1749, Euler had presented the same lesson—here with direct reference to the mishap at Sanssouci (which he did not mention in his memoir) when the pipes burst at the first trials[28]:

"Having made the calculation about the first trials of this machine, where the wooden pipes have burst as soon as the water was raised to a height of 70 feet, I find that the pipes actually experienced the pressure of a more than 300 feet high water column: this is a certain indication that the disposition of the machine is still very far from its perfect state."

4. Conclusion

Despite its practical goals, Euler's pipeflow theory was not meant as an engineering blueprint for the pumps, pipelines and fountains at Sanssouci. The neglect of friction, of course, would not be permissible if the theory would have had to predict detailed power and discharge values. But to demand such a theory in 1750 would not only be anachronistic; it also ignores that even without taking friction into account Euler's theory correctly explained why the Sanssouci water-art system was doomed to fail. As an exposition of a tangible nonstationary-flow problem, it could well have helped to correct the deficiencies of the initial design. Metal pipes and a shorter distance from the pumps to the elevated reservoir would have sufficed to turn the failure into success.

[23] Truesdell, 1954: p. XLV. This statement, however, seems exaggerated, see Darrigol, Frisch, 2008 for earlier appearances of internal pressure.

[24] Ackeret, 1957; Eckert, 2002.

[25] Euler, 1752a: pp. 247–248.

[26] Euler, 1752a: pp. 240–242. ("Pour que la meme force qui agit sur les pistons des pompes soit en état de fournir dans le réservoir la plus grande quantité d'eau, il faut avoir soin de faire le tuyau montant aussi large qu'il sera possible (...) Pour fournir une plus grande quantité d'eau dans le réservoir par la meme force qui agit sur les pistons, il faut rendre le tuyau montant aussi court qu'il sera possible".)

[27] Euler, 1752a: pp. 249–250 ("il seroit crevé infalliblement".)

[28] Euler to Frederick, 17 October 1749, in *Opera omnia*, ser. 4a, **6**: p. 322 ("Ayant fait le calcul sur les premiers essais de cette machine, oú les tuyaux de bois sont crevés, dès que l'eau fut élevée à la hauteur de 70 pieds, je trouve que les tuyaux ont alors effectivement souffert la pression d'une colonne d'eau de plus de 300 pieds de hauteur: ce qui est une marque certaine, que la disposition de la machine étoit encore fort éloignée de son état de perfection".)

Water-raising installations elsewhere, for example in mines or for the water supply of cities, tacitly followed Euler's rules: In the pits of mines or in water towers the pipelines rose vertically upwards—thus resulting in the shortest possible distance between pumps and water reservoirs. The fact that such widespread contemporary practice was ignored at Sanssouci, and that even after Euler's explicit warning the bungling proceeded unabatedly, renders further speculations, such as about the neglect of friction, superfluous.

Why was Euler's advice ignored? One reason may be that Frederick II had little understanding of mathematics. In contrast to poetry, music and philosophy, for which he had high esteem, mathematics and natural sciences were alien to him. In his later years his ignorance turned into outspoken contempt, as the diary entries of a frequent guest at the King's dinner table, Girolamo Marchese Lucchesini, illustrate: "Because he understands nothing of mathematics," Lucchesini entered after a conversation on 19 June 1782 in his diary, "he has difficulties to acknowledge that representatives of this science merit great renown. It caused him little worry to see Euler depart, and he does not regard Lagrange's merits very high".[29] Furthermore, the King seems to have been unwilling to afford the high costs for changing the original design. He employed inexperienced personnel who must have felt constantly under pressure to use cheap materials. "Economizing is a virtue for everyone; but if it is exaggerated, it loses its meaning; and nowhere is exaggerated economizing so damaging as with constructions," the last architect of Frederick II complained about the stinginess of his King.[30] Perhaps both traits of Frederick's character, contempt for mathematics and stinginess, combined when he chose in his letter to Voltaire, quoted in the introduction, Euler as a scapegoat for the failure at Sanssouci. With biting sarcasm, he perverted into derision what Euler had meant as warning ("Mon Moulin a été éxécuté géométriquement, et il n'a pu élever une goutte d'eau à Cinquante pas du Bassin. Vanité des Vanités; Vanité de la géométrie".)—using almost Euler's own words ("qu'on n'éleveroit jamais une goutte d'eau jusqu'au réservoir...").

Apart from the injustice against Euler, the uncritical acceptance of the King's slander has misguided some scientists, historians of science and technology and popular writers to misrepresent 18th century science as utterly remote from practical applications. Although there are certainly cases which confirm a deep gulf between theory and practice, the Sanssouci case definitely does not fall into this category. The fountains did not fail because the theory was remote from practice, but because the practical men at Sanssouci ignored the standards of contemporary practice. Water-art installations elsewhere could have served as role models. Euler's pipeflow theory was as practical as a theory could be at the time; further mishaps could have been avoided if the lessons from Euler's theory had been taken into account. With regard to the history of fluid dynamics, Euler's pipeflow memoir also deserves more than a cursory mentioning: It illustrates that Euler approached the general theory from practical corners. He had solved a number of special flow problems in naval architecture, ballistics, hydraulic machinery and pipeflow, before he arrived at the general equations of fluid motion. His famous 'Principes généraux du mouvement des fluides' did not emerge in a single stroke of genius but in several stages, mediated through his involvement in practical affairs, among which the Sanssouci project was not the least important one. Although it seems paradoxical, Euler's ideal flow theory was deeply rooted in real flow problems.

[29] Bischoff, 1885. Other examples of Frederick's "intellectual insufficiency" are given in Fellmann, 2007: pp. 92–93.

[30] Manger, 1789: vol. 3, p. 547.

References

Ackeret, Jakob, 1957 'Vorrede' in L. Euler's *Opera omnia*, ser. 2, **15**, VII-LX. Lausanne.

Artelt, Paul, 1893 *Die Wasserkünste von Sanssouci. Eine geschichtliche Entwickelung von der Zeit Friedrichs des Großen bis zur Gegenwart*. Berlin.

Bélidor, Bernard Forest de, 1737-1739 *Architecture hydraulique ou l'art de conduire, d'elever et de ménager les eaux pour les differentes besoins de la vie.* 2 vols. Paris.

Bell, E.T., 1937 *Men of Mathematics*, London.

Besterman, Theodore ed. 1976 *The Complete Works of Voltaire, Vol. 129: Correspondence and related documents, XLV September 1777-May 1778, letters D20780-D21221*. Banbury.

Bischoff, Fritz (ed.) 1885 *Gespräche Friedrichs des Großen mit H. de Catt und dem Marchese Lucchesini*. Leipzig.

Blay, Michel, 1986 'Recherches sur les forces exercées par les fluides en mouvement á l'Académie Royale des Sciences: 1668-1669', in Pierre Costabel (ed.), *Mariotte, Savant et Philosophe (+ 1684)*. Paris, 91-124.

Condorcet, Marquis de, 1783 'Eulogy to Mr. Euler,' in *History of the Royal Academy of Sciences 1783, Paris 1786*, 37-68 (translated by John S. D. Glaus from The Euler Society, available online via http://www.math.dartmouth.edu/ euler/).

Darrigol, Olivier, 2005 *Worlds of flow: A history of hydrodynamics from the Bernoullis to Prandtl*. Oxford.

Darrigol, Olivier, Frisch, Uriel, 2008 'From Newton's mechanics to Euler's equations'. *these Proceedings*.

Eckert, Michael, 2002 'Euler and the fountains of Sanssouci'. *Archive for the history of exact sciences* **56**, 451-468.

Eckert, Michael, 2006 *The dawn of fluid mechanics: A discipline between science and technology*. Berlin.

Eichler, Helga, 1974 *Die Preußische Akademie der Wissenschaften zwischen 1740 und 1812–unter besonderer Berücksichtigung ihrer Bedeutung für die Entwicklung der gewerblichen Produktivkräfte*. Dissertation at the Academy of Sciences of the GDR, Berlin (East).

Euler, Leonhard, 1745 *Neue Grundsätze der Artillerie, aus dem Englischen des Herrn Benjamin Robins übersetzt und mit vielen Anmerkungen versehen* [from B. Robins, *New principles of gunnery* (London,1742)]. Berlin. Also in *Opera omnia*, ser. 2, **14**, 1-409, [Eneström index] **E77**.

Euler, Leonhard, 1750 'Découverte d'un nouveau principe de mécaniqué'. Académie Royale des Sciences et des Belles-Lettres de Berlin, *Mémoires* [abbreviated below as *MASB*], **6** [printed in 1752], 185-217. Also in *Opera omnia*, ser. 2, **5**, 81-108, **E177**.

Euler, Leonhard, 1752a 'Sur le mouvement de l'eau par des tuyaux de conduite'. *MASB*, **8** [printed in 1754], 111-148. Also in *Opera omnia*, ser. 2, **15**, 219-250. **E206**.

Euler, Leonhard, 1752b 'Discussion plus particuliére de diverses maniéres d'élever l'eau par le moyen des pompes avec le plus grand avantage'. *MASB*, **8** [printed in 1754], 149-184. Also in *Opera omnia*, ser. 2, **15**, 251-280. **E207**.

Euler, Leonhard, 1752c 'Maximes pour arranger le plus avantageusement les machines destinées á élever de l'eau par le moyen des pompes'. *MASB*, **8** [printed in 1754], 185-232. Also in *Opera omnia*, ser. 2, **15**, 281-318. **E208**.

Euler, Leonhard, 1755a 'Principes généraux de l'état d'équilibre d'un fluide'. *MASB*, **11** [printed in 1757], 217-273. Also in *Opera omnia*, ser. 2, **12**, 2-53, **E225**.

Euler, Leonhard, 1755b 'Principes généraux du mouvement des fluides' *MASB*, **11** [printed in 1757], 274-315. Also in *Opera omnia*, ser. 2, **12**, 54-91, **E226**.

Euler, Leonhard, 1758a 'De constructione aptissima molarum alatarum' *Novi Commentarii academiae scientiarum Petropolitanae*, **4**, [printed in 1758] 41-108. Also in *Opera omnia*, ser. 2, **16**, 1-64, **E229**.

Euler, Leonhard, 1758b 'Recherches plus exactes sur l'effet des moulins á vent' *MASB*, **12** [printed in 1758], 165-234. Also in *Opera omnia*, ser. 2, **16**, 65-125, **E233**.

Euler, Leonhard, 1760 'Recherches sur le mouvement des rivières'[written around 1750–1751. *MASB*, **16** [printed in 1767], 101-118. Also in *Opera omnia*, ser. 2, **12**, 272-288, **E332**.

Euler, Leonhard, 1998 *Commercium epistolicum*, ser. 4A, **2**, eds. Emil Fellmann and Gleb Mikhailov. Basel.

Fellmann, Emil A., 2007 *Leonhard Euler*, Basel, Boston, Berlin.

Hermann, Armin, 1991 *Weltreich der Physik*. Von Galilei bis Heisenberg, Stuttgart.

Manger, Heinrich Ludewig, 1789 *Baugeschichte von Potsdam*, 3 Vols. Berlin.

Mariotte, Edme, 1718 *Traité du mouvement des eaux et des autres corps fluides*. Paris.

Mikhailov, Gleb K. (ed.) 1999 'The origins of hydraulics and hydrodynamics in the work of the Petersburg Academicians of the 18^{th} century. *Fluid dynamics*, **34**, 787-800.

Mikhailov, Gleb K. (ed.) 2002 *Die Werke von Daniel Bernoulli*, vol. 5, ed. Gleb K. Mikhailov. Basel.

Perkovitz, Sidney, 1999 'The Rarest Element,' *The Sciences* **39** (January/February 1999), 34-38.

Robins, Benjamin, 1742 *New Principles of Gunnery*, London.

Steele, Brett D., 2006 'Rational Mechanics as Enlightenment Engineering: Leonhard Euler and Interior Ballistics,' in B. Buchanan, ed., *Gunpowder, Explosives, and the State: A Technological History*, Ashgate, 281-302.

Szabó, István, 1987 *Geschichte der mechanischen Prinzipien und ihrer wichtigsten Anwendungen*, third edition, Basel, Boston, Stuttgart.

Truesdell, Clifford, 1954 Rational fluid mechanics, 1657-1765. In Euler, *Opera Omnia*, ser. 2, **12** (Lausanne), IX-CXXV.

Available online at www.sciencedirect.com
ScienceDirect
Physica D 237 (2008) 1878–1886
PHYSICA D
www.elsevier.com/locate/physd

Genesis of d'Alembert's paradox and analytical elaboration of the drag problem

G. Grimberg[a], W. Pauls[b,c], U. Frisch[b,*]

[a] Instituto de Matemática, Universidade Federal do Rio de Janeiro (IM-UFRJ), Brazil
[b] Labor. Cassiopée, UNSA, CNRS, OCA, BP 4229, 06304 Nice Cedex 4, France
[c] Fakultät für Physik, Universität Bielefeld, Universitätsstraße 25, 33615 Bielefeld, Germany

Available online 20 January 2008

Abstract

We show that the issue of the drag exerted by an incompressible fluid on a body in uniform motion has played a major role in the early development of fluid dynamics. In 1745 Euler came close, technically, to proving the vanishing of the drag for a body of arbitrary shape; for this he exploited and significantly extended the existing ideas on decomposing the flow into thin fillets; he did not however have a correct picture of the global structure of the flow around a body. Borda in 1766 showed that the principle of live forces implied the vanishing of the drag and should thus be inapplicable to the problem. After having at first refused the possibility of a vanishing drag, d'Alembert in 1768 established the paradox, but only for bodies with a head–tail symmetry. A full understanding of the paradox, as due to the neglect of viscous forces, had to wait until the work of Saint-Venant in 1846.

PACS: 47.10.A-; 47.15.ki

Keywords: History of science; Fluid dynamics; D'Alembert's paradox

1. Introduction

The first hint of d'Alembert's paradox – the vanishing of the drag for a solid body surrounded by a steadily moving ideal incompressible fluid – had appeared even before the analytical description of the flow of a "perfect liquid"[1] was solidly established. Leonhard Euler in 1745, Jean le Rond d'Alembert in 1749 and Jean-Charles Borda in 1766 came actually very close to formulating the paradox, using momentum balance (in an implicit way) or energy conservation arguments, which actually predate its modern proofs.[2] D'Alembert in 1768 was the first to recognize the paradox as such, although in a somewhat special case. Similarly to Euler and Borda, his reasoning did not employ the equations of motion directly, but nevertheless used a fully constituted formulation of the laws of hydrodynamics, and exploited the symmetries he had assumed for the problem. A general formulation of d'Alembert's paradox for bodies of an arbitrary shape was given in 1846 by Adhémar Barré de Saint-Venant, who pointed out that the vanishing of the drag can be due to not taking into account viscosity. Other explanations of the paradox involve unsteady solutions, presenting for example a wake, as discussed by Birkhoff.[3]

Since the early derivations of the paradox did not rely on Euler's equation of ideal fluid flow, it was not immediately recognized that the idealized notion of an inviscid fluid motion was here conflicting with the physical reality. The difficulties encountered in the theoretical treatment of the drag problem were attributed to the lack of appropriate analytical tools rather than to any hypothetical flaws in the theory. In spite of the great achievements of Daniel and Johann Bernoulli, of d'Alembert

* Corresponding author. Tel.: +33 4 92003035; fax: +33 4 92003058.
E-mail addresses: gerard.emile@terra.com.br (G. Grimberg), uriel@obs-nice.fr (U. Frisch).

[1] Kelvin's name of an incompressible inviscid fluid.

[2] See, e.g. Serrin, 1959 and Landau and Lifshitz, 1987.

[3] Euler, 1745; D' Alembert, [1749]; Borda, 1766; Saint-Venant, 1846, 1847; Birkhoff, 1950: Chap. 1, §9.

0167-2789/$ - see front matter © 2008 Elsevier B.V. All rights reserved.
doi:10.1016/j.physd.2008.01.015

and of Euler[4] the theory of hydrodynamics seemed beset with insurmountable technical difficulties; to the contemporaries it thus appeared of little help, as far as practical applications were concerned. There was a dichotomy between, on the one hand, experiments and the everyday experience and, on the other hand the eighteenth century's limited understanding of the nature of fluids and of the theory of fluid motion. This dichotomy is one of the reasons why neither Euler nor Borda nor the early d'Alembert were able to recognize and to accept the possibility of a paradox.

We shall also see, how the problem setting became more and more elaborated in the course of time. Euler, in his early work on the drag problem appeals to several physical examples of quite different nature, such as that of ships navigating at sea and of bullets flying through the air. D'Alembert's 1768 formulation of the drag paradox is concrete, precise and much more mathematical (in the modern sense of the word) than Euler's early work. This is how d'Alembert was able to show – with much disregard for what experiments or (sometimes irrelevant) physical intuition might suggest – that the framework of inviscid fluid motion necessarily leads to a paradox.

For the convenience of the reader we begin, in Section 2, by recalling the modern proofs of d'Alembert's paradox: one proof – somewhat reminiscent of the arguments in Euler's 1745 work – relies on the calculation of the momentum balance, the other one – connected with Borda's 1766 paper – uses conservation of energy. In Section 3 we describe Euler's first attempt, in 1745, to calculate the drag acting on a body in a steady flow using a modification of a method previously introduced by D. Bernoulli.[5] In Section 4 we discuss d'Alembert's 1749 analysis of the resistance of fluids. In Section 5 we review Euler's contributions to the drag problem made after he had established the equations of motions for ideal fluid flow. Section 6 is devoted to Borda's arguments against the use of a live-force (energy conservation) argument for this problem. In Sections 7 and 8 we discuss d'Alembert's and Saint-Venant's formulation of the paradox. In Section 9 we give the conclusions.

Finally, we mention here something which would hardly be necessary if we were publishing in a journal specialized in the history of science: the material we are covering has already been discussed several times, in particular by such towering figures as Saint-Venant and Truesdell.[6] Our contributions can only be considered incremental, even if, occasionally, we disagree with our predecessors.

2. Modern approaches to d'Alembert's paradox

Let us consider a solid body K in a steady potential flow with uniform velocity U at infinity. In the standard derivation of the vanishing of the drag[7] one proceeds as follows: Let Ω be the domain bounded in the interior by the body K and in the exterior by a sphere S with radius R (eventually, $R \to \infty$). The force acting upon K is calculated by writing a momentum balance, starting from the steady incompressible 3D Euler equation

$$\boldsymbol{v} \cdot \nabla \boldsymbol{v} = -\nabla p, \qquad \nabla \cdot \boldsymbol{v} = 0. \tag{1}$$

The contribution of the pressure term gives the sum of the force acting on the body K and of the force exerted by the pressure on the sphere S. It may be shown, using the potential character of the velocity field, that the latter force vanishes in the limit $R \to \infty$. The contribution of the advection term can be written as the flux of momentum through the surface of the domain Ω: the flux through the boundary of K vanishes because of the boundary condition $\boldsymbol{v} \cdot \boldsymbol{n} = 0$; the flux through the surface of S vanishes because the velocity field is asymptotically uniform ($v \simeq U$ for $R \to \infty$). From all this it follows that the force on the body vanishes. This approach proves the vanishing of both the drag and the lift.[8]

Alternatively, one can use energy conservation to show the vanishing of the drag.[9] Roughly, the argument is that the work of the drag force, due to the motion with velocity U, should be balanced by either a dissipation of kinetic energy (impossible in ideal flow when it is sufficiently smooth) or by a flow to infinity of kinetic energy, which is also ruled out for potential flow. This argument shows only the vanishing of the drag.

A more detailed presentation of such arguments may be found in the book by Darrigol.[10]

In the following we shall see that many technical aspects of these two modern approaches were actually discovered around the middle of the eighteenth century.

3. Euler and the new principles of Gunnery (1745)

In 1745 Euler published a German translation of Robins' book "New Principles of Gunnery" supplemented by a series of remarks whose total amount actually makes up the double of the original volume. In the third remark of the first proposition (Dritte Anmerkung zum ersten Satz) of the 2nd Chapter Euler attempts to calculate the drag on a body at rest surrounded by a steadily moving incompressible fluid.[11]

In 1745 the general equations governing ideal incompressible fluid flow were still unknown. Nevertheless, Euler managed the remarkable feat of correctly calculating the force acting on an element of a 2D steady flow around a solid body. For this, as we shall see, he borrowed and extended the results obtained by D. Bernoulli a few years earlier.[12]

4 See, e.g., Darrigol, 2005; Darrigol and Frisch, 2008.
5 Bernoulli, 1736.
6 Truesdell, 1954; Saint- Venant [1888].
7 See, e.g., Serrin, 1959.
8 The lift need not vanish if there is circulation.
9 See, e.g., Landau and Lifshitz, 1987: §11.
10 Darrigol, 2005: Appendix A.
11 For the German original of the third remark, cf. Euler, 1745: 259–270 (of *Opera omnia* which we shall use for giving page references); an English version, taken from Hugh Brown's 1777 translation is available at www.oca.eu/etc7/EE250/texts/euler1745.pdf. We shall sometimes use our own translations.
12 Bernoulli, 1736, 1738.

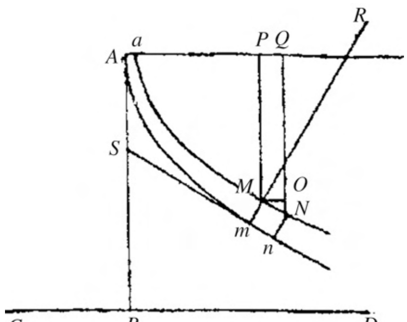

Fig. 14

Fig. 1. Figure 14 of Euler, 1745: 263: this figure represents a fillet of fluid aAMm, deflected by the solid body, but the shape of the body is not fully specified.

Euler begins by noting that instead of calculating the drag acting on a body moving in a fluid one can calculate the drag acting on a resting body immersed in a moving fluid. Thus, he considers a fluid moving into the direction AB[13] (cf. Figs. 1 and 3), past a solid body CD.[14] Then Euler continues by describing the motion of fluid particles and establishes a relation between the trajectory and velocity of each fluid particle and the force which is acting on this particle. He observes that, instead of determining the force on the body, one can evaluate the reaction on the fluid:

But since all parts of the fluid, as they approach the body, are deflected and change both their speed and direction [of motion], the body has to experience a force of strength equal to that needed for this change in speed as well as direction of the particles.[15]

Thus, one has to determine the force which is applied at each point of the fluid. Euler chooses a fillet[16] AaMm of fluid with an infinitesimal width and observes that the velocity[17] v of the particles passing through the section Mm is inversely proportional to its (infinitesimal) width $Mm = \delta z$; so that $v\,\delta z = v_0\,\delta z_0$, where $\delta z_0 =$ Aa and v_0 are the width of the fillet and the velocity at the reference point A.[18] For later reference let us call this relation mass conservation. Euler assumes that the particles passing through the section Aa follow the fillet AaMm. This is equivalent to assuming that the velocity in each section Mm along the trajectory depends only on the location of the point M and not on time, in modern terms a stationary flow. Here the concepts of streamline and of stationarity in two dimensions appear for the first time explicitly.

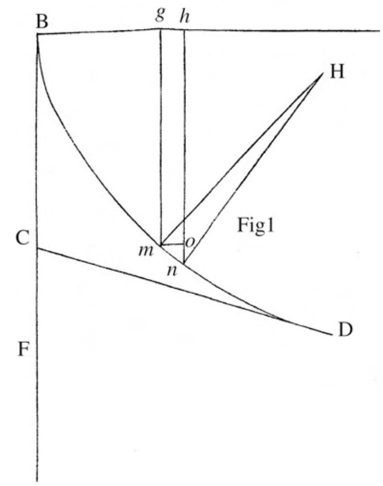

Fig. 2. Figure 1 of Bernoulli, 1736. A centripetal argument is used to calculate the normal force acting along a fillet of fluid represented here just by the curve BD (changes in width are ignored).

With the above assumption, Euler defines

$$\begin{aligned} &AP = x, \qquad PQ = \mathrm{d}x, \qquad PM = y, \qquad ON = \mathrm{d}y, \\ &p = \mathrm{d}y/\mathrm{d}x, \qquad MN = \sqrt{\mathrm{d}x^2 + \mathrm{d}y^2} = \mathrm{d}x\sqrt{1+p^2}. \end{aligned} \tag{2}$$

Since the force exerted by the body on the fluid is oriented upward, we prefer orienting the vertical axis upward. Hence y and p will be negative in what follows. Otherwise we shall mostly follow Euler's notation. Euler calculates the normal and tangential components, $\mathrm{d}F_\mathrm{N}$ and $\mathrm{d}F_\mathrm{T}$, of the infinitesimal force acting on the element of fluid fillet MNnm (see Fig. 1).[19]

With the assumed unit density, the mass of fluid in MNnm is

$$\delta z \times MN = \delta z \mathrm{d}x\sqrt{1+p^2}. \tag{3}$$

The normal acceleration $\mathrm{d}F_\mathrm{N}$ in the direction MR is calculated by Euler as a centripetal acceleration, i.e., given by the product of the square of the velocity v^2 and the curvature $(1+p^2)^{\frac{3}{2}}\mathrm{d}p/\mathrm{d}x$. Euler may here be following D. Bernoulli.[20] The latter, in a paper concerned among other things with jets impacting on a plane, had developed an analogy between an element of fluid following a curved streamline and a point mass on a curved trajectory (cf. Fig. 2). Multiplying the acceleration by the elementary mass and using mass conservation,[21] Euler then obtains

$$\mathrm{d}F_\mathrm{N} = v_0\delta z_0 v\mathrm{d}p/(1+p^2), \tag{4}$$

in which the velocity v along the fillet is considered to be a function of the slope p.

13 Here, contrary to the usage in Eulers' memoir, all geometrical points will be denoted by roman letters, leaving italics for algebraic quantities.

14 These are Euler's own words; examination of various of his figures and of the scientific context shows that the body extends below CD and, perhaps also above.

15 Euler, 1745: 263. Weil aber alle Theile der flüßigen Materie, so bald sich dieselben dem Körper nahen, genöthiget werden auszuweichen, und so wohl ihre Geschwindigkeit, als ihre Richtung zu verändern, so muß der Körper eine eben so große Kraft empfinden, als zu dieser Veränderung so wohl in der Geschwindigkeit, als der Richtung der Theilchen, erfordert wird.

16 Euler uses the word "Canal" (channel).

17 Following early eighteenth century notation, Euler represents a velocity by the corresponding height of free fall to achieve the given velocity, starting a rest; in modern notation this would be $\sqrt{2gh}$. In the 1745 paper Euler takes mostly $g = 1$ – but occasionally $g = 1/2$ – and denotes the height by v. In order not to confuse the reader, we shall here partially modernize the notation and in particular denote the velocity by v.

18 Euler denotes our δz, δz_0 and v_0 by z, a and $\sqrt{2b}$, respectively.

19 The notation $\mathrm{d}F_\mathrm{N}$ and $\mathrm{d}F_T$ is ours.

20 Bernoulli, 1736 and 1738: Section XIII, §13.

21 Bernoulli, 1738: 287 assumed a fillet of uniform width (*fistulam implantatam esse uniformis quidem amplitudinis*) and thus did not use mass conservation to relate the varying width and velocity.

To obtain the tangential force $\mathrm{d}F_{\mathrm{T}}$ in the direction mS on the element of fillet, Euler writes

$$\delta z \mathrm{d}x\sqrt{1+p^2}\mathrm{d}(v^2/2) = -\mathrm{d}F_{\mathrm{T}}\,\mathrm{d}x\sqrt{1+p^2}, \tag{5}$$

and thus

$$\mathrm{d}F_{\mathrm{T}} = -\delta z \mathrm{d}(v^2/2) = -\delta z_0(v_0/v)\mathrm{d}(v^2/2). \tag{6}$$

For the case of Fig. 1 the force is oriented in the direction mS, because the fluid is moving more slowly at N than at M. Euler does not elaborate on how he derives (5) but this seems typically a "live-force" argument of a kind frequently used at that time, for example by the Bernoullis.[22] Indeed the l.h.s. is the variation of the live force (kinetic energy) and the r.h.s. is what we would now call the work of the tangential force per unit mass.

So as to later determine the drag, that is the force on the body in the vertical direction, Euler adds these normal and tangential elementary forces, projected onto the vertical axis oriented in the direction BA. He thus obtains the following elementary vertical force on the fluid:

$$\mathrm{d}F_{\mathrm{BA}} = v_0\delta z_0\left(\frac{v\mathrm{d}p}{(1+p^2)^{\frac{3}{2}}} + \frac{p\mathrm{d}v}{\sqrt{1+p^2}}\right). \tag{7}$$

Here a "miracle" happens: the r.h.s. of (7) is the exact differential of

$$v_0\delta z_0\left(\frac{vp}{\sqrt{1+p^2}}\right). \tag{8}$$

Finding the exact form of the function $v(p)$, as we now know, requires the solution of a non-trivial boundary value problem. The exact form does however not matter for the integrability property and – from a modern perspective – can be related to the global momentum conservation property of the Euler equation. In 1745 Euler did not comment on the miracle. It is worth stressing that it does not survive if any error is made regarding the numerical factors appearing in the normal and tangential forces.

Euler is now able to exactly integrate the elementary force along a fillet from its starting point A, assumed to be far upstream ($p = -\infty$), to a point m with a finite slope p. Noting that $-p/\sqrt{1+p^2}$ is the cosine of the angle MSB, he obtains the following force on the body, due to the fillet:

$$F_{\mathrm{AB}} = -v_0^2\delta z_0\left(1 - \frac{v}{v_0}\cos \mathrm{MSB}\right). \tag{9}$$

Note that this is a force from a given fillet of infinitesimal width which must still be integrated over a set of fillets encompassing the whole fluid. More important here is where to terminate the fillet. It is clear that the relevant fillets start far upstream in the vertical direction; but where do they lead after having come close to the solid body? Euler considers various possibilities, such as a 90° deflection. He then envisages a very interesting case:

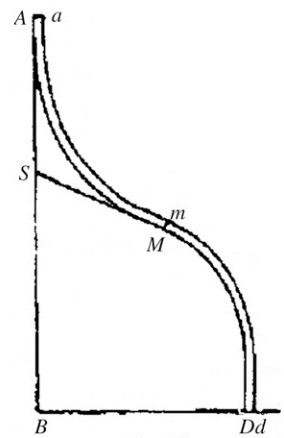

Fig. 3. Figure 15 of Euler, 1745: 268 from which he tries to explain that the drag should be calculated using only the portion AM of the fillet.

It remains therefore only to fix upon the point which is to be esteemed the last of the canal. If we go so far that the fluid may pass by the body, and attain its first direction and velocity then shall $\delta z = \delta z_0$, and the angle mSB vanish, and therefore its cosine = 1, then shall the force acting on the body in the direction AB $= -v_0^2\delta z_0(1-1) = 0$, and the body suffers no resistance. [23]

From a technical point of view Euler's 1745 derivation of the vanishing of the drag force has many features of the modern proof. However Euler refuses here to see a paradoxical property of the model of ideal fluid flow (for which the equations are not even completely formulated). He accepts the possibility that the vanishing of the drag applies to certain exotic fluids which are "infinitely fluid ... and also compressed by an infinite force"[24] such as the hypothetical ether surrounding celestial bodies (called by him "subtle heavenly material"), but he firmly rejects it for water and air. Indeed, immediately after the previous citation he writes:

Hence it appears, that for air or water, we are not to take the point of the canal for last, where the motion behind the body corresponds exactly with that at the beginning of the canal. [25]

Euler then explains why in his opinion the "last point" should not at all be taken far downstream, but rather near the inflection point M where the angle MSB achieves its maximum value, as shown in Fig. 3.[26] As pointed out to us by Olivier Darrigol, in Euler's opinion the portion AM of the canal AD is the only one that exerts a force on the body, the alleged reason

[22] Cf., e.g., Darrigol, 2005: Chap. 1.

[23] Euler, 1745: 267. Hier kömmt es also nur darauf an, wo das Ende des Canals angenommen werden soll. Geht man so weit, biß die flüßige Materie um den Körper völlig vorbey geflossen, und ihren vorigen Lauf wiederum erlanget hat, so wird ..., und der Winkel mSB verschwindet, dahero der Cosinus desselben = 1 wird. In diesem Fall würde also die auf den Körper nach der Direction AB würkende Kraft ... und der Körper litte gar keinen Wiederstand.

[24] Euler, 1745: 268–269. ... unendlich flüßig ... und von einer unendlichen Kraft zusammen gedruckt ...

[25] Euler, 1745: 267. Woraus erhellet, daß man für Wasser und Luft nicht denjenigen Punkt des Canals, wo die Bewegung hinter dem Körper mit der ersten wiederum völlig übereinkommt, für den letzten annehmen könne.

[26] Truesdell, 1954: XL writes that "Euler supposes that the oncoming fluid turns away from the axis, leaving a dead-water region ahead of the body"; actually, Euler does not assume any dead-water region in his Third Remark.

being that the force caused by the deflection in the portion MD is not directed toward the body:

The other part DM produces a force which is opposite to the first, and would cause the body to move back in the direction BA. Now, as only a true pressure [a positive one] can set a body into motion, the latter force can only act on the body insofar as the pressure of the fluid matter from behind is strong enough to move the body forwards .[27]

Hence he departed from strict dynamical reasoning to follow a dubious intuition of the transfer of force through the fluid.[28]

To sum up, Euler performed a real *tour de force* by deriving the correct expression for the force on a fillet of fluid without having the equations of motion but practically he was not able to reach much beyond Newton's impact theory when considering the global interaction between the fluid and the body.

4. d'Alembert and the treatise on the resistance of fluids (1749)

In a treatise[29] written for the prize of the Berlin Academy of 1749 whose subject was the determination of the drag a flow exerts upon a body, d'Alembert gives a description of the motion of the fluid analogous to that of Euler. It is not clear if d'Alembert knew about Euler's "Commentary on Gunnery". As noted by Truesdell,[30] some figures in d'Alembert's treatise are rather similar to those found in the Gunnery but there are also arguments in the Gunnery which would have allowed d'Alembert, had he been aware of them, to extend his 1768 paradox to cases not possessing the head–tail symmetry he had to assume. Anyway, d'Alembert was fully aware of D. Bernoulli's work on jet impact in which, as we already pointed out, a similar figure is found.

In the treatise d'Alembert described the motion of an incompressible fluid in uniform motion at large distance, interacting with a localized axisymmetric body. He observed that the streamlines and the velocity of the fluid at each point in space are time-independent. The velocity a of the fluid far upstream of the body is directed along the axis of symmetry (which he takes for the abscissa); the other axis is chosen to be perpendicular to this direction. In this frame a point M of the fluid is characterized by the cylindrical coordinates (x, z) and the corresponding velocity has the components av_x and av_z.[31]

D'Alembert's first aim is to derive the partial differential equations which determine the motion of the fluid, and the appropriate boundary conditions with which they must be supplemented. He observed that, in order to determine the drag on the body, one must first determine

...the pressure of the fillet of Fluid which glides immediately on the surface of the body. For this it is necessary to know the velocity of the particles of the fillet. [32]

By considering the motion of fluid particles during an infinitesimal time interval, d'Alembert is able to find the expressions of the two components of the force acting on an element of fluid:

$$\gamma_z = a^2\left(-v_x\frac{\partial v_z}{\partial x} - v_z\frac{\partial v_z}{\partial z}\right), \tag{10}$$

and

$$\gamma_x = a^2\left(-v_x\frac{\partial v_x}{\partial x} - v_z\frac{\partial v_x}{\partial z}\right). \tag{11}$$

From this d'Alembert derived for the first time the partial differential equations for axisymmetric, steady, incompressible and irrotational flow, but he does not use such equations in considering the problem of "fluid resistance".[33]

How does d'Alembert calculate the drag? From an assumption about the continuity of the velocity he infers, contrary to Euler, that there must be a zone of stagnating fluid in front of the body and behind it, bordered by the streamline TFMDLa which attaches to the body at M and detaches at L (see Fig. 4).[34]

In his calculation of the drag d'Alembert used an approach which differed from that of Euler in the Gunnery: instead of calculating the balance of forces acting on the fluid he considered the pressure force exerted on the body by the fluid fillet in immediate contact with it. D'Alembert noted first that, for each surface element of the body, the force exerted by the fluid particles is perpendicular to this surface, because of the vanishing of the tangential forces, characterizing the flow of an ideal fluid.[35]

In conformity with Bernoulli's law, d'Alembert expressed the pressure along the body as $a^2(1-v_x^2-v_z^2)$. With ds denoting the element of curvilinear length along the sections of the body by an axial plane such as that of Fig. 4, the infinitesimal element of surface of revolution of the body upon which this pressure is acting is $2\pi z\mathrm{d}s$. The component along the axis of the pressure force exerted is

$$2\pi a^2(1 - v_x^2 - v_z^2)z\mathrm{d}z. \tag{12}$$

Further integration along the profile AMDLC yields the vertical component of the drag.

Then came a very important remark. D'Alembert noted that in the case of a body which is not only axisymmetric but has

[27] Euler, 1745: 268. Aus dem andern Theil DM aber ensteht eine Kraft, welche jener entgegen ist, und von welcher des Körper nach der Direction BA zurück gezogen werden sollte. Da nun kein Körper anders, als durch einen würklichen Druck in Bewegung gesetzt werden kann, so kann auch die letztere Kraft nur in so ferne auf den Körper würken, als der Druck der flüßigen Materie von hinten stark genug ist, den Körper vorwärts zu stossen.

[28] Darrigol, private communication, 2007.

[29] D'Alembert, [1749], 1752.

[30] Truesdell, 1954: LII.

[31] D'Alembert uses a similarity argument to prove that the velocity field around a body of a given shape is proportional to the incoming velocity a (D'Alembert, [1749]: §42–43, 1752: §39).

[32] D'Alembert, 1752: xxxi. ...la pression du filet de Fluide qui glisse immédiatement sur la surface du corps. Pour cela il est nécessaire de connoître la vitesse des particules de ce filet.

[33] Cf. Truesdell, 1954: LIII, Grimberg, 1998: 44–46, Darrigol, 2005: 20–21.

[34] D'Alembert, [1749]: §39, 1752: §36.

[35] D'Alembert, [1749]: §40, 1752: §37. This vanishing, as we know, characterizes an ideal fluid; d'Alembert did not relate it to the nature of the fluid.

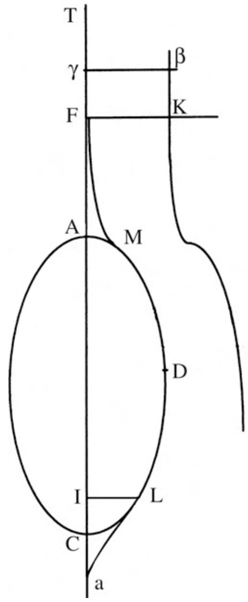

Fig. 4. Figure 14 of D'Alembert, [1749] redrawn. Not all elements shown here are used in our arguments.

a head–tail symmetry,[36] the contributions to the drag from two symmetrically located points would be equal and of opposite sign and thus cancel.[37] In order to avoid the vanishing of the drag, he assumed that the attachment point M and the separation point L are not symmetrically located:

From there it follows that the arcs LD and DM cannot be equal; because, if they were, the quantity—$\int 2\pi y \mathrm{d}y(p^2+q^2)$ would be equal to zero so that the body would not experience any force from the fluid: which is contrary to experiments.[38]

This stress on "experiments", already present in the 1749 manuscript and which will not reappear in d'Alembert's 1768 paradox paper, seems to reflect just common sense. It cannot be explained by d'Alembert's hypothetical desire to adhere to late recommendations by the Berlin Academy which emphasized comparisons with experiments for the 1750 prize on resistance of fluids. D'Alembert did not seem pleased with such late changes and these recommendations were probably formulated only in May 1750.[39]

D'Alembert's new idea, compared to Euler, is to consider the drag as the resultant of the pressure forces directed along the normal to the surface of the body over its entirety. But for d'Alembert it is still unimaginable to obtain a vanishing drag.

5. Euler and the 'Dilucidationes' (1756)

The *Dilucidationes de resistentia fluidorum* (Enlightenment regarding the resistance of fluids) have been written in 1756, one year after Euler established his famous equations in their final form.[40] In his review of previous efforts to understand the drag problem for incompressible fluids, Saint-Venant[41] writes the following about the *Dilucidationes*:

And it is obvious that, when the flow is assumed indefinite or very broad, the theory of the *Dilucidationes* can only be and actually is just a return to the vulgar theory, ... [42]

Here, Saint-Venant understands by "vulgar theory" the impact theory which goes back to the seventeenth century. Actually, in 1756 Euler was rather pessimistic regarding the applicability of his equations to the drag problem:

But the results which I have presented in several previous memoirs on the motion of fluids do not help much here. Because, even though I have succeeded in reducing everything that concerns the motion of fluids to analytical equations, the analysis has not reached the sufficient degree of completion which is necessary for the solving of such equations.[43]

Truesdell discusses the *Dilucidationes* in detail.[44] Actually this paper is quite famous because of a remark Euler made on the cavitation that arises from negative pressure in incompressible fluids. Truesdell is also rightly impressed by Euler's success in doing something non-trivial with his equation for flows around a parabolic cylinder; for this Euler uses a system of curvilinear coordinates based on the streamlines and their orthogonal trajectories.

The *Dilucidationes* are however not contributing much to our understanding of drag. In Section 15, Euler expresses his doubts regarding the applicability of his 1745 calculation to both the front and the back of a body (which would result in vanishing drag):

...the boat would be slowed down at the prow as much as it would be pushed at the poop ....[45]

We must mention here that, because of a possible non-vanishing transfer of kinetic energy to infinity, the modern theory of the d'Alembert paradox does not apply to flow with a free surface, such as a boat on the sea.

Thus, in the *Dilucidationes* we find a first attempt to introduce a new analytical treatment of streamlines unrelated to the previous theories and coming closer to the modern description of a fluid flow. Nevertheless, Euler does not succeed in using his 1755 equations to improve our understanding of the drag problem.

36 In d'Alembert [1752] this additional symmetry is explicitly assumed; in d'Alembert, [1749] the language used only suggests such a symmetry.

37 D'Alembert, [1749]: §62, 1752: §70.

38 D'Alembert, 1752: §70. Delà il s'ensuit que les arcs LD, DM ne sauroient être égaux ; car s'ils l'étoient, alors la quantité $-\int 2\pi y \mathrm{d}y(p^2+q^2)$ seroit égale à zéro de manière que le corps ne souffriroit aucune pression de la part du fluide : ce qui est contre l'expérience.

39 D'Alembert, 1752: xxxviii; Yushkevich and Taton, 1980: 312–314; Grimberg, 1998: 9.

40 Euler, 1755, 1756.

41 Saint-Venant, [1888], probably mostly written around 1846.

42 Saint-Venant, [1888]: 35. Et il est évident que, lorsque le courant est supposé indéfini ou très large, la théorie des *Dilucidationes* d'Euler ne peut être et n'est réellement qu'un retour pur et simple à la théorie vulgaire,

43 Euler, 1760: 200. Quae ego etiam nuper in aliquot dissertationibus de motu fluidorum exposui, nullum subsidium huc afferunt. Etiamsi enim omniam quae ad motum fluidorum pertinent, ad aequationes analyticas reduxi, tamen ipsa Analysis minime adhuc ita est exculta, ut illis aequationibus resoluendis sufficiat.

44 Truesdell, 1954: C–CVII.

45 Euler, 1760: 206 ...puppis nauis paecise tanta vi propelleretur, quanta prora repellitur....

6. Borda's memoir (1766)

In his memoir Borda, a prominent French "Geometer" and experimentalist, studies the loss of "live force" (energy) in incompressible flows, in particular in pipes whose section is abruptly enlarged.[46] At the end of his memoir Borda gives an example of what would be, in his opinion, "a bad use" of the principle of conservation of live forces. This is precisely the problem of determining the drag force that a moving fluid exerts upon a body at rest. The particles of the fluid in the neighborhood of the body "delineate curved lines or rather move in small curved channels"; the pressure force acting upon the body has to be determined. But the channels become narrower at certain locations similarly to a siphon, so that the principle of live forces cannot be used. To prove this point he then presents the following argument for the vanishing of the drag:

> ... suppose that the body D moves uniformly through a quiescent fluid, driven by the action of the weight P. According to this principle [of live forces], the difference of the live force of the fluid must be equal to the difference of the actual descent of the weight; however, since the motion is supposed to have reached uniformity, the difference of the live forces equals zero. Therefore, the difference of the actual descent is also zero, which cannot happen unless the weight P is itself zero. As the weight P measures the resistance of the fluid, the supposition of the principle [of live forces] necessarily leads to a vanishing resistance.[47]

This constitutes the first derivation of the d'Alembert paradox using an energy dissipation argument. Borda's explanation of why the live-force conservation argument is inapplicable rests on the aforementioned analogy with the siphon problem. This is illustrated by a figure[48] not reproduced here because of its poor quality. There one sees a fillet of fluid narrowing somewhat as it approaches the body. The modern concept of dissipation in high-Reynolds-number flow being confined to regions with very strong velocity gradients is definitely not what Borda had in mind.

Borda's reasoning is correct, but like Euler in 1745 and d'Alembert in 1749, he does not formulate the vanishing of the drag as a paradox. In his remarks Borda addresses neither the question of the nature of the fluid, nor the consequences of having stationary streamlines, nor the problem of the contact between the fluid and the body (absence of viscosity in the case of ideal flow) which, as we know, are quite central to the understanding of the paradox.

7. D'Alembert's memoirs on the paradox (1768 and 1780)

In Volume V of his "Opuscules" published in 1768, a part of a memoir is entitled "Paradox on the resistance of fluids proposed to geometers."[49] D'Alembert considers again an axisymmetric body, but now with a head–tail symmetry. More precisely, he assumes a plane of symmetry perpendicular to the direction of the incompressible flow at large distance and dividing the body into two mirror-symmetric pieces. To avoid the problem of possible separation of streamlines upstream and downstream of the body, he assumes that the front part and the rear part of the body have needle-like endings. First of all he asserts that the velocities at every location in the fluid are perfectly symmetric in front/rear of the body, and that

> ... under this assumption the law of the equilibrium and the incompressibility of the fluid will be perfectly obeyed, because, the rear part of the body being similar and equal to its front part, it is easy to see that the same values of p and q [i.e. the velocity components] which will give at the first instant the equilibrium and incompressibility of the fluid at the front part will give the same results for the rear part.[50]

This statement is directly related to the remark in Section 70 of d'Alembert's 1752 treatise. In fact, the assumption used by d'Alembert in 1749 and 1752 to avoid a paradox is here lifted, since no separation of streamlines occurs except at the needle-like end points. D'Alembert here assumes that the solution with mirror symmetry is the only one: "The fluid has only one way to be moved by the encounter of the body." The pressure forces at the front and rear part of the body are then also axisymmetric and mirror symmetric. Hence they combine into a force of resistance (drag) which vanishes. D'Alembert concluded:

> Thus I do not see, I admit, how one can satisfactorily explain by theory the resistance of fluids. On the contrary, it seems to me that the theory, developed in all possible rigor, gives, at least in several cases, a strictly vanishing resistance; a singular paradox which I leave to future Geometers to elucidate.[51]

It is clear that d'Alembert's argument is less general than that of Borda, since he is restricting the formulation of the paradox to bodies with a head–tail symmetry. Nevertheless, d'Alembert is the first one to seriously propose the vanishing of the drag as a paradox. Twelve years later in Volume VIII of his "Opuscules" d'Alembert revisits the paradox in the light of a letter received from "a very great Geometer" who is not named and who points out that, when considering the flow inside or around a

---

46 Borda, 1766.

47 Borda, 1766: 604–605. ...supposons que le corps D se meuve uniformément dans un fluide tranquille, entraîné par l'action du poids P: on sait que suivant le principe, la différence de la force vive du fluide devra être égale à la descente actuelle du poids P; mais puisque le mouvement est censé parvenu à l'uniformité, la différence des forces vives $= 0$; donc la différence de la descente actuelle sera aussi $= 0$, ce qui ne se peut pas à moins que le poids P ne soit lui-même $= 0$: or le poids P marque la résistance du fluide : donc la supposition du principe dont il s'agit, donne toujours une résistance nulle.

48 Borda, 1766: Figure 14, found at the end of the 1766 volume on p. 847.

49 D'Alembert, 1768. In the eighteenth century "Geometer" was frequently used to mean "mathematician" (pure or applied).

50 D'Alembert, 1768: 133. ...dans cette supposition les loix de l'équilibre & de l'incompressibilité du fluide seront parfaitement observées; car la partie postérieure étant (*hyp.*) semblable et égale à la partie antérieure, il est aisé de voir que les mêmes valeurs de p & de q; qui donneront au premier instant l'équilibre & l'incompressibilité du fluide à la partie antérieure, donneront les mêmes résultats à la partie postérieure.

51 D'Alembert, 1768: 138. Je ne vois donc pas, je l'avoue, comment on peut expliquer par la théorie, d'une maniere satisfaisante, la résistance des fluides. Il me paroît au contraire que cette théorie, traitée & approfondie avec toute la rigueur possible, donne, au moins en plusieurs cas, la résistance absolument nulle ; paradoxe singulier que je laisse à éclaircir aux Géometres [*sic*].

symmetric body, there may be, in addition to the symmetric solution, another one which does not possess such symmetry and to which d'Alembert's argument for the vanishing of the resistance does not apply.[52] D'Alembert concurs and discussed the issue at length. It should however be noted that a breaking of the symmetry was already assumed by him in his early work on the resistance when he assumed that the (hypothetical) points of attachment and detachment of the streamline following the body are not symmetrically located (see Section 4).

Thus d'Alembert was definitely the first to formulate the vanishing of the drag as a paradox within the accepted model of that time, namely incompressible fluid flow, implicitly taken as ideal.[53] He was however formulating it only for bodies with head–tail symmetry, not realizing that techniques introduced by Euler and Borda could have allowed him to obtain the paradox for bodies of arbitrary shapes.

8. Saint-Venant and the first precise formulation of the paradox (1846)

In three notes published in 1846 and then in a memoir published in 1847, Saint-Venant gives for the first time a general formulation of the paradox. A detailed write-up, mostly dating from the same period, was published only posthumously in 1888 and contains also a very interesting discussion of previous work.[54] Saint-Venant's memoir marks the beginning of the modern theory of the d'Alembert paradox which was to flourish, in particular with major contributions by Ludwig Prandtl.[55]

We here give only a very brief description of the key results of Saint-Venant. He first specified the properties of the incompressible fluid: the pressure force is normal to the surface element on which it is acting and therefore equal in all directions. The fluid moves steadily around a body at rest. He gives a derivation of the paradox, closely related to Borda's. Indeed, it suffices to establish the equation for the live forces acquired by the fluid to see that the live-force (energy) loss of the system is zero:

> If the motion has reached, as one always assumes, a steady state, the live force acquired by the system at every instant is zero; the work performed by the exterior pressures is also zero and the same applies to the work of the interior actions of the fluid whose density is assumed to be unchanging. Thus, the work of the impulse of the fluid on the body, and, consequently, the impulse itself, is necessarily equal to zero. [56]

He adds that the situation is different for a real fluid made of molecules in which there is friction at the contact between two neighboring fluid elements:

> But one finds another result if, instead of an ideal fluid – object of the calculations of the geometers of the last century – one uses a real fluid, composed of a finite number of molecules and exerting in its state of motion unequal pressure forces or forces having components tangential to the surface elements through which they act; components to which we refer as the friction of the fluid, a name which has been given to them since Descartes and Newton until Venturi.[57]

Thus, d'Alembert's paradox is explained by Saint-Venant for the first time as a consequence of ignoring viscous forces. Of course, a precise formulation of the paradox would not have been possible without a clear distinction between ideal and viscous fluids.

9. Conclusion

The problem of the resistance of bodies moving in fluids was – and still is – of great practical importance. It was thus naturally one of the first non-trivial problems tackled within the nascent eighteenth century hydrodynamics. Euler, who was not only a great "Geometer" but a person acutely aware of the needs of gunnery and ship building, tried – as we have seen – reaching beyond the old impact theory of Newton—and failed. He was lacking both the concept of viscous forces and a deep understanding of the global aspects of the topology of the flow around a body. His "failure" – as is frequently the case with major scientists – was however very creative: born was the idea of analyzing a steady flow into a set of fluid fillets of infinitesimal and non-uniform section; he also managed to calculate the forces acting on such fillet several years before there was any representation of the dynamics in terms of partial differential equations. Borda, being both a Geometer and an experimentalist, felt compelled to qualify as non-sensical a very simple live-force argument discovered by himself and which predicted a vanishing drag for bodies of arbitrary shape. D'Alembert, another brilliant Geometer, was probably less constrained by experimental considerations, and dared eventually to present the paradox known by his name. His proof reveals a very good understanding of the global topology of the flow but otherwise is very simple and limited intrinsically to bodies with a head–tail symmetry.

We must stress that the statement as a paradox is very much tied to the type of analytical representation of an ideal flow. From this point of view, experiments on flow past bodies, be they real or thought experiments, have rather been an obstacle to grasping the distinction between an ideal fluid and a real one. The same kind of epistemological obstacle has

[52] D'Alembert, 1780: 212; Birkhoff, 1950: 21–22.

[53] The idea of viscosity ripened only in the XIXth century, see e.g. Darrigol, 2005; in the eighteenth century there was only a concept of tenaciousness, e.g. resistance to the introduction of a body into fluid, which was still a long way from actual viscosity.

[54] Saint-Venant, 1846, 1847, [1888].

[55] Cf., e.g. Darrigol, 2005: Chap. 7.

[56] Saint-Venant, 1847: 243–244. Si le mouvement est arrivé, comme on le suppose toujours, à l'état de permanence, la force vive, acquise à chaque instant par le système, est nulle ; le travail des pressions extérieures est nul aussi, et il en est de même du travail des actions intérieures du fluide dont nous supposons que la densité ne change pas. Donc le travail de l'impulsion du fluide sur le corps, et, par conséquent, cette impulsion elle-même, est nécessairement zéro.

[57] Saint-Venant, 1847: 244. Mais on trouve un autre résultat si, au lieu du fluide idéal, objet des calculs des géomètres du siècle dernier, on remet un fluide réel, composé de molécules en nombre fini, et exercant dans l'état du mouvement, des pressions inégales ou qui ont des composantes tangentielles aux faces à travers desquelles elles agissent; composantes que nous désignons par le nom de frottement du fluide, qui leur a été donné depuis Descartes et Newton jusqu'à Venturi.

accompanied the earlier birth of the principle of inertia, which no experiment could at that time truly reveal; it was necessary to distance oneself from real conditions and to find an appropriate mathematical representation. Finding such representations for fluid dynamics was a painfully slow process: a full century elapsed between Euler's fragmentary results on drag and Saint-Venant's full understanding of the d'Alembert paradox.

Acknowledgments

Olivier Darrigol has been a constant source of inspiration to us while we investigated the issues discussed here. We also thank Gleb K. Mikhailov for numerous remarks and Rafaela Hillerbrand and Andrei Sobolevskii for their help.

References

Bernoulli Daniel, 1736 'De legibus quibusdam mechanicis, quas natura constanter affectat, nondum descriptis, earumque usu hydrodynamico, pro determinanda vi venae aqueae contra planum incurrentis', *Commentarii academiae scientarum imperialis Petropolitanae,* 8, 99-127. Also in Bernoulli, 2002, 425–444.

Bernoulli Daniel, 1738 *Hydrodynamica, sive de viribus et motibus fluidorum commentarii*, Strasbourg, 425–444.

Bernoulli Daniel, 2002 *Die Werke von Daniel Bernoulli*, vol. 5, ed. Gleb K. Mikhailov, Basel.

Birkhoff Garrett, 1950 *Hydrodynamics*, Princeton.

Borda Jean-Charles de, 1766 'Sur l'écoulement des fluides par les orifices des vases.' Académie Royale des Sciences (Paris), *Mémoires* [printed in 1769], 579–607.

D'Alembert Jean le Rond, [1749] *Theoria resistentiae quam patitur corpus in fluido motum, ex principiis omnino novis et simplissimis deducta, habita ratione tum velocitatis, figurae, et massae corporis moti, tum densitatis & compressionis partium fluidi*; manuscript at Berlin-Brandenburgische Akademie der Wissenschaften, Akademie-Archiv call number: I-M478.

D'Alembert Jean le Rond, 1752 *Essai d'une nouvelle théorie de la résistance des fluides*, Paris.

D'Alembert Jean le Rond, 1768 'Paradoxe proposé aux géomètres sur la résistance des fluides,' in *Opuscules mathématiques*, vol. 5 (Paris), Memoir XXXIV, Section I, 132–138.

D'Alembert Jean le Rond, 1780 'Sur la Résistance des fluides,' in *Opuscules mathématiques*, vol. 8 (Paris) Memoir LVII, Section 13, 210–230.

Darrigol Olivier, 2005 *Worlds of flow: A history of hydrodynamics from the Bernoullis to Prandtl*, Oxford.

Darrigol Olivier, Frisch Uriel, 2008 'From Newton's mechanics to Euler's equations,' these Proceedings. Also at www.oca.eu/etc7/EE250/texts/darrigol-frisch.pdf.

Euler Leonhard, 1745 *Neue Grundsätze der Artillerie, aus dem englischen des Herrn Benjamin Robins übersetzt und mit vielen Anmerkungen versehen* [from B. Robins, *New principles of gunnery* (London,1742)], Berlin. Also in *Opera ommia*, ser. 2, 14, 1-409, [Eneström index] E77. This was retranslated into English as *The true principles of gunnery investigated and explained. Comprehending translations of Professor Eulers observations upon the new principles of gunnery, published by the late Mr. Benjamin Robins, and that celebrated authors Discourse upon the track described by a body in a resisting medium, inserted in the memoirs of the Royal academy of Berlin for the year 1753. To which are added, many necessary explanations and remarks, together with Tables calculated for practice, the use of which is illustrated by proper examples; with the method of solving that capital problem, which requires the elevation for the greatest range with any given initial velocity*, by Hugh Brown, London, printed for I. Nourse, Bookseller to His Majesty 1777, E77A.

Euler Leonhard, 1755 'Principes généraux du mouvement des fluides,' Académie Royale des Sciences et des Belles-Lettres de Berlin, *Mémoires* 11 [printed in 1757], 274–315. Also in *Opera omnia*, ser. 2, 12, 54–91, E226.

Euler Leonhard, 1756 'Dilucidationes de resistentia fluidorum' [written in 1756]. *Novi Commentarii academiae scientiarum imperialis Petropolitanae*, 8 [contains the Proceedings for 1755 and 1756, printed in 1763], 197–229. Also in *Opera omnia*, ser. 2, 12, 215–243, E276.

Euler Leonhard, 1760 'Recherches sur le mouvement des rivières,' [written around 1750–1751] Académie Royale des Sciences et des Belles-Lettres de Berlin, *Mémoires* 16 [printed in 1767], 101–118. Also in *Opera omnia*, ser. 2, 12, 272–288, E332.

Grimberg Gérard, 1998 *D'Alembert et les équations aux dérivées partielles en hydrodynamique*, Thèse. Université Paris 7.

Landau Lev Davydovich, Lifshitz Evgeniĭ Mikhailovich, 1987 *Fluid Mechanics*, 2nd Edition, Oxford.

Saint-Venant Adhémar Barré de, 1846 *Société Philomathique de Paris*, Extraits des procès verbaux (1846), 25–29, 72–78, 120–121.

Saint-Venant Adhémar Barré de, 1847 'Mémoire sur la théorie de la résistance des fluides. Solution du paradoxe proposé à ce sujet par d'Alembert aux géomètres. Comparaison de la théorie aux expériences,' Académie des Sciences (Paris), *Comptes rendus*, 24, 243–246.

Saint-Venant Adhémar Barré de, [1888] 'Résistance des fluides: considérations historiques, physiques et pratiques relatives au problème de l'action dynamique mutuelle d'un fluide et d'un solide, dans l'état de permanence supposé acquis par leurs mouvements,' [posthumous work, edited by Joseph Valentin Boussinesq] Académie des Science (Paris), *Mémoires* 44, 1–280.

Serrin James, 1959 'Mathematical principles of classical fluid mechanics' in *Handbuch der Physik. Stroemungsmechanik I* (ed. C. Truesdell) Springer.

Truesdell Clifford, 1954 Rational fluid mechanics, 1657–1765. In Euler, *Opera omnia*, ser. 2, 12 (Lausanne), IX–CXXV.

Yushkevich Adol'f-Andrei Pavlovich, Taton René, 1980 Introduction to 'Leonhard Euler in Correspondence with Clairaut, d'Alembert and Lagrange,' *Opera omnia*, ser. 4, 5.

Available online at www.sciencedirect.com
ScienceDirect
ELSEVIER
Physica D 237 (2008) 1887–1893
PHYSICA D
www.elsevier.com/locate/physd

Euler, the historical perspective

E. Knobloch*

Technische Universität Berlin, Germany
Berlin-Brandenburgische Akademie der Wissenschaften, Germany

Available online 18 March 2008

Abstract

This paper is meant to give some interesting details of Euler's unusual life and extraordinary creativity. A fast-rising scientist, he became Europe's teacher of mathematics by his numerous textbooks. Yet, he, too, had to manage the problems of daily academic and private life. He was a pioneer in solving special cases of the famous three-body problem: the problem of two gravitational centers and the collinear configuration.

Keywords: Euler

1. Introduction

The Irish satirist Jonathan Swift once said[1]:

Elephants are drawn always smaller than life, but a flea always larger.

Whoever would like to speak about Euler has to solve exactly this problem: How to do justice to this mathematician, "universal, richly detailed and inexhaustible"[2]? The following essay is meant to emphasize some less well-known details of Euler's unusual life and work, especially his pioneering work in celestial mechanics regarding the three-body problem.

2. The fast-rising scientist

1720 13 years old, Leonhard Euler enrolls at the University of Basel;
1721 14 years old, he obtains the Bachelor's degree;
1722 still 14 years old, he is for the first time opponent in an appointment procedure for a professorship (of logic);
1722 15 years old, he is for the second time opponent in an appointment procedure for a professorship (of history of law);
1723 16 years old, he obtains his Master's degree (A.L.M. = Artium Liberalium Magister);
1726 18 years old, he publishes his first (faulty) paper on isochronic curves[3];
1726 19 years old, he submits his paper on ship's masts, thus gaining an honourable mention by the French Academy of sciences[4];
1727 19 years old, he submits his habilitation thesis without having obtained the Ph.D. degree[5];
1727 20 years old, he begins his work in St. Petersburg.

Euler submitted the thesis in order to receive the vacant professorship of physics at the University of Basel. Its complete title reads[6]:

Q.F.F.Q.S.[7] Physical dissertation on sound which Leonhard Euler, Master of the liberal arts submits to the public examination of the learned in the juridical lecture-room on February 18, 1727 at 9 o'clock looking at the free professorship of physics by order of the magnificent and wisest class of philosophers whereby

* Corresponding address: Technische Universität Berlin, Germany.
E-mail address: Eberhard.Knobloch@TU-Berlin.DE.

[1] Cf. Fellmann, 2007: p. XIII.
[2] Simmons, 2007: p. 168.
[3] Sandifer, 2007: p. 5.
[4] Euler, 1728.
[5] Euler, 1727.
[6] Euler, 1727: p. 181 ("Q.F.F.Q.S. [=Quod felix faustumque sit] Dissertatio physica De sono, quam annuente numine divino jussu magnifici et sapientissimi philosophorum ordinis pro vacante professione physica ad d. 18. Febr. A. MDCCXXVII. In Auditorio Juridico hora 9. Publico Eruditorum Examini subjicit Leonhardus Eulerus A.L.M. Respondente Praestantissimo Adolescente Ernesto Ludovico Burcardo Phil. Cand.").
[7] Quod felix faustumque sit (May it bring you happiness and good fortune).

0167-2789/$ - see front matter
doi:10.1016/j.physd.2008.03.005

the divine will is nodding assent. The most eminent young man Ernst Ludwig Burchard, candidate of philosophy, is responding.

But all imploring was in vain: Euler did not get the position. In the appendix he raised the following problem: What would happen if a stone dropped into a straight tunnel drilled to the center of the earth and onward to the other side of the planet? According to Euler it reaches infinite velocity at the center and immediately returns to the same point from which it had fallen down. Only in his *Mechanica* did Euler justify this false solution saying[8]:

This seems to differ from truth ... . However that may be, here we have to confide more in the calculation than in our judgement and have to confess that we do not understand at all the jump if it is done from the infinite into the finite.

Euler's result was the consequence of his mathematical modelling of the situation (a non-permitted commutation of limits). Benjamin Robins put it as follows[9]:

When y, the distance of the body from the center, is made negative, the terms of the distance expressed by y^n, when n may be any number affirmative, or negative, whole number or problem are sometimes changed with it. The centripetal force being as some power of the fraction; if, when y is supposed negative, y^n be still affirmative, the solution gives the velocity of the body in its subsequent ascent from the center; but if y^n by this supposition becomes also negative, the solution exhibits the velocity, after the body has passed the center, upon condition, that the centripetal force becomes centrifugal; and when on this supposition y^n becomes impossible, the determination of the velocity beyond the center is impossible, the condition being so.

Such mistakes are not uncommon in the writings of great men. Curiously, Euler never recanted.

3. Euler's publications and posthumous works

Euler published more than 800 books or papers, mainly in Latin or French, some in German or Russian. His posthumous works are kept in the archives of the Russian Academy of Sciences in St. Petersburg. The Euler Archives in Basel dispose of microfilms of all preserved Eulerian manuscripts. They are described in a volume published in Moscow and Leningrad.[10] The twelve mathematical notebooks covering the period 1725 to 1783 are of special interest. They consist of 2300 sheets of paper written nearly exclusively in Latin. Russian, German, and English surveys appeared in 1988, 1989, and 2007, respectively.[11] The notebooks will not be published in the *Opera omnia*. Their digitization is planned.

Euler dealt with all aspects of pure and applied mathematics and likewise with philosophy and theology.[12] Differential and integral calculus; logarithmic, exponential, and trigonometric functions; ordinary and partial differential equations; elliptic functions and integrals; hypergeometric integrals; classical geometry (theorem on polyhedra); number theory; algebra; continued fractions; Zeta and other (Euler) products; infinite series and products (Basel problem); divergent series; mechanics of particles and solid bodies; calculus of variations; theory and practice of optics; hydrostatics; hydrodynamics; astronomy; lunar and planetary motions; topology; graph theory (Königsberg bridge problem); philosophy; theology; shipbuilding; engineering; music theory.

The following enumeration gives a survey of Euler's most important monographs or textbooks. They are chronologically ordered according to the date of publication and assigned to Euler's three stays in St. Petersburg (1727–1741), Berlin (1741–1766), and again in St. Petersburg (1766–1783).

3.1. St. Petersburg (1727–1741)[13]

- Mechanics or the science of motion set forth analytically, 1736 (so-called First Mechanics)
- Introduction to the art of arithmetic for the use of the high school at the Imperial Academy of Sciences in St. Petersburg, 1738
- Essay of a new theory of music set forth clearly according to the most certain principles of harmony, 1739
- Naval science or treatise on the construction and navigation of ships, 1749 (so-called First naval theory, already written in 1738 while still in St. Petersburg).

3.2. Berlin (1741–1766)[14]

- Method of finding curvilinear lines having a property to a highest or smallest degree or solution of the isoperimetric problem understood in the largest sense, 1744
- Theory of the motion of planets and comets, 1744
- New principles of gunnery, 1745
- Introduction into the analysis of the infinite, 1748
- Theory of the motion of the moon, setting forth all of its inequalities, 1753 (so-called First lunar theory; its publication was paid for by the Russian Academy of Sciences)
- Elements of instruction of the differential calculus together with its application in the analysis of the finite and theory of series, 1755 (its publication was paid for by the Russian Academy of Sciences)
- Theory of the motion of solid or rigid bodies stabilized according to the first principles of our cognition and accommodated to all motions that can fall in such bodies, 1765 (so-called Second Mechanics)
- Letters to a German princess on diverse subjects of physics and philosophy, 1768–1772 (already written in the years 1760–1762 while still in Berlin)
- Elements of instruction of the integral calculus, 1768–1770, 1794 (already written in 1763 while still in Berlin)

[8] Euler, 1736: p. 88. ("Hoc quidem veritati minus videtur consentaneum; ... Quicquid autem sit, hic calculo potius quam nostro iudicio est fidendum atque statuendum, nos saltum, si fit ex infinito in finitum, penitus non comprehendere.")

[9] Robins, 1739: p. 12.

[10] Kopelevic, Krutikova, Mikhailov, Raskin, 1962.

[11] Knobloch, 1988, 1989, 2007.

[12] Cf. Varadarajan, 2006: p. 2.

[13] Euler, 1736, 1738, 1739, 1749.

[14] Euler, 1744a,b, 1745, 1748, 1753, 1755a, 1765c, 1768–1772, 1794.

3.3. St. Petersburg (1766–1783)[15]

- Dioptrics, 1769–1771
- Complete introduction to algebra, 1770
- Theory of the motions of the moon dealt with by a new method together with astronomical tables, 1772 (so-called Second lunar theory)
- Complete theory of the construction and navigation of ships, 1773 (so-called Second naval theory).

Through these textbooks Euler became Europe's teacher not only in his own time, but also for mathematicians of the 19th century.[16]

4. The troubles of daily life

In spite of all intellectual flights of fancy Euler had to manage the problems of daily academic and private life. Three examples may illustrate this aspect of his activities.

4.1. The quadrature of the circle

In his capacity as director of the mathematical class of the Berlin Academy he had to evaluate mathematical writings and projects, for example the writing of a certain Thibault from Avignon about the quadrature of the circle.[17] The report dates from the 15th of March, 1750 (cf. Fig. 1). It begins by saying[18]:

> After reading the writing of Mr. Thibault where he pretends to have found the quadrature of the circle, I doubt very much that one has ever seen a paper on this subject being just as absurd as this one.

The report ends by saying[19]:

> This suffices to demonstrate that the author not only does not have the slightest notion of the question he is dealing with but that he does not know either anything about the first elements of geometry.

4.2. The supply of dead bodies

Since the departure of Maupertuis from Berlin Euler was his proxy. He had to inform the administrator David Köhler of the Academy's financial affairs to pay the due honorarium to the widow of the grave-digger Schünemann for supplying the Anatomy with dead bodies.[20] The Anatomical Theatre had been constructed in 1713.

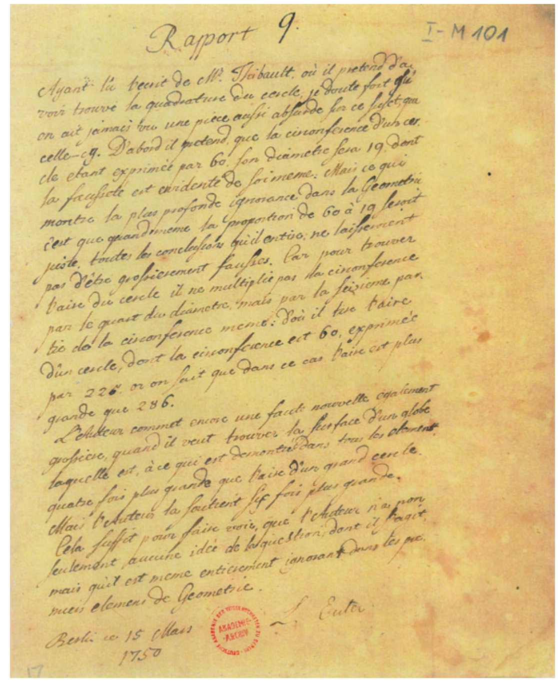

Fig. 1. Euler's report on Thibault's quadrature of the circle dating from March 15, 1750; Archives of the Berlin-Brandenburg Academy of Sciences and Humanities I–M 101, sheet 1.

4.3. The plundering of Euler's estate

During the Seven Years War between England and Prussia on the one side, Russia, Austria, and France on the other side, Euler's estate in the village Lietzow (outside of but near to Berlin in those days) was plundered by Saxon troops, allies of the Russians. The still existing list of damages elaborated by the mayor of Lietzow enumerates 1 Wispel, 5 Scheffel rye (1 Wispel = 24 Scheffel, 1 Scheffel = 54,73 l), 1 Wispel, 6 Scheffel barley/oat, 30 metric hundred-weights, two horses, thirteen cows, seven pigs, twelve sheep (cf. Fig. 2).[21]

In his letter to the Russian secretary Gerhard Friedrich Müller in St. Petersburg Euler spoke of four horses thus doubling the damage.[22]

5. Euler's work in celestial mechanics

When Euler published his *Mechanica* in 1736, it was preceded by the copperplate engraving presented in Fig. 3.

The head of the celestial deity carries the sun revolved by the six planets that can be seen with the naked eye. The planet Uranus discovered only in 1781 is still absent. In the right hand the deity holds an opened book. The figures represent the whole or partial elliptic orbit of a planet. The message is clear: Celestial mechanics is a part of mechanics wherein the Newtonian law of gravitation plays the crucial role.

---

15 Euler, 1769–1771, 1770, 1772, 1773.

16 Spieß, 1929: p. 206.

17 W. Knobloch, 1984: p. 27, no. 64. Publication of the following citations by courtesy of the Archives of the Berlin-Brandenburg Academy of Sciences and Humanities.

18 "Ayant lu l'écrit de Mr. Thibault, où il prétend d'avoir trouvé la quadrature du cercle, je doute fort qu'on ait jamais vu une pièce aussi absurde sur ce sujet que celle-cy."

19 "Cela suffit pour faire voir, que l'Auteur n'a non seulement aucune idée de la question, dont il s'agit, mais qu'il est même entièrement ignorant dans les premiers élémens de Géométrie."

20 W. Knobloch, 1984: p. 252, no. 1430; p. 270, no. 1553; p. 315, no. 1857–1860.

21 Brandenburgisches Landeshauptarchiv, Kurmärkische Kriegs- und Domänenkammer, Städte-Registratur: De anno 1760, Nr. S 3498; reproduction by courtesy of these archives.

22 Fellmann, 2007: p. 101f.

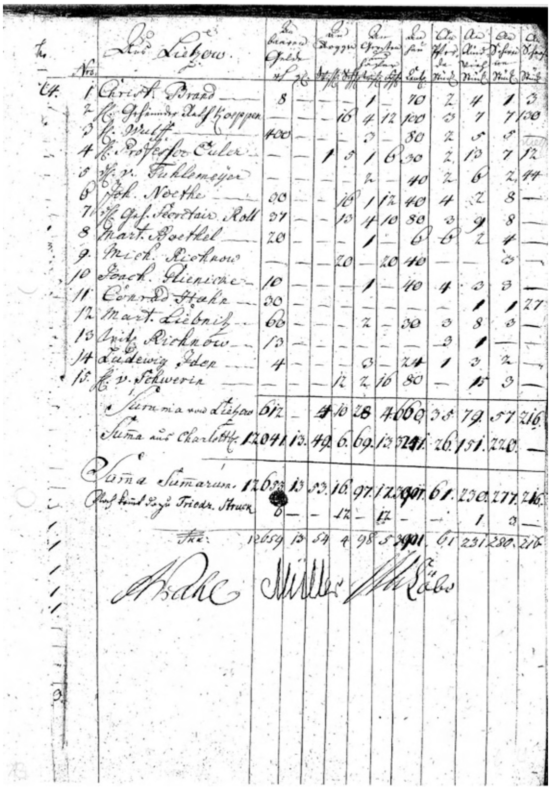

Fig. 2. List of damages regarding the village Lietzow. It was elaborated by the mayor of Lietzow dating from October 24, 1760. Lietzow was plundered by Saxon troops commanded by a Russian general. The fourth line of the list enumerates "Prof. Euler's" damages. Brandenburgisches Landeshauptarchiv Potsdam, Rep. 2 Kurmärkische Kriegs- und Domänenkammer Nr. S 3498.

Fig. 3. Copperplate in Euler's *Mechanics* (published in 1736) at the beginning of the dedication to Johann Albert Korff (Euler 1736: p. 5).

The message on the right part of the copperplate is not so evident. Euler himself does not give any explanation. Yet, a boy obviously throws rings into a water basin by means of a sling that he holds in his left hand. He observes the curved line the rings are describing sinking to the ground of the water basin. This might be an illustration of a motion in a resisting medium as dealt with in the second volume of Euler's *Mechanica*.

When Euler came to Berlin in 1741, he at once elaborated a corresponding research program for astronomy at the Berlin Academy of Sciences. He defined the true theory of astronomy as follows[23]:

> The true theory of astronomy mainly consists of a thorough understanding of the so-called Newtonian philosophy which does not only explain all already known celestial motions but it also shows the reason why one makes more and more new discoveries in the long run and recognizes more precisely the true motions of all celestial bodies. By this science an astronomer can relate all of his observations to a final aim and derive all kinds of profit from them.

Euler's own contributions to celestial mechanics can be divided into three groups: 1. Planetary perturbations, 2. Lunar theories, 3. Three-body problem. The first two subjects have been dealt with by Curtis Wilson very recently.[24] Hence this section will confine itself to the third subject.

First trials to solve the three-body problem where the bodies are moving in the same plane are to be found in Euler's mathematical notebooks dating from 1750 to 1755.[25] In his publications he emphasized the importance of the problem saying that we have to solve the famous three-body problem in order to arrive at the culmination of astronomy.[26] The solution turned out to be extremely difficult. Yet, Euler did not question the solvability. He only stated that first we have to study special cases, to introduce certain restrictions before we can hope to solve the general problem.[27] Euler was indeed "the first to investigate restricted forms of the three-body problem with a view to obtaining exact integrals".[28] He considered two special cases: the problem of two gravitational centers and the collinear configuration.

5.1. The problem of two gravitational centers

It can be explained in the following way: Two fixed bodies A, B of masses a, b act on a third body Z according to the Newtonian law of gravitation. What will be the curve described by Z?

Euler dealt with it in three papers.[29] In the first two of them he presupposed that the curve described by Z lies in the same plane as the two centers of gravitation. In the third paper he dropped this restriction (cf. Fig. 4).

His method of solving the problem consisted of four steps[30]:

---

23 Kirsten, 1977: p. 9 ("Die wahre Theorie der Astronomie bestehet aber hauptsächlich in einer gründlichen Erkenntnüß der sogenannten Newtonianischen Philosophie, als welche nicht nur alle schon erkannten Motus Coelestes sehr herrlich erkläret, sondern auch Anlaß gibt in der Astronomie je länger je mehr Entdeckungen zu machen, und die wahren Bewegungen aller Himmlischen Cörper genauer zu erkennen. Durch diese Wissenschaft wird ein Astronom in Stand gesetzt, nicht nur alle seine Observationen auf einen gewissen Endzweck zu dirigiren, sondern daraus auch allen möglichen Nutzen zu ziehen.")

24 Wilson, 2007.

25 Kopelevic/Krutikova/Mikhailov/Raskin 1962–1965, vol. 1: no. 401, fol. 76v; no. 402, fol. 49r–50r, 78v, 93v.

26 Euler, 1765b: p. 281.

27 Euler, 1764b, 1765b.

28 Wilson, 1994: p. 1054; cf. Subbotin, 1958; Volk, 1983.

29 Euler, 1760, 1764a, 1765a.

30 This is explained in Euler, 1760.

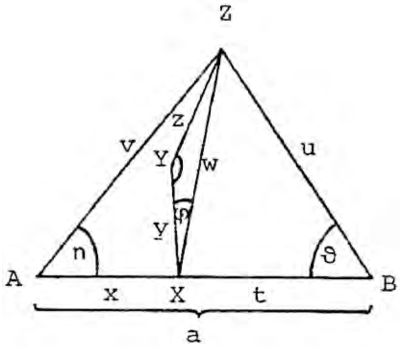

Fig. 4. The configuration of the problem of two gravitational centers as dealt with by Euler in Euler, 1765a: p. 248. A, B are the gravitational centers, the moving body Z describes a curve that does not lie in the same plane as the two centers.

1. Find the general differential equations of the second order which determine the motion of the body.
2. Integrate these equations in order to obtain differential equations of the first order.
3. Apply separation of variables to these equations in order to construct the solution.
4. Determine the cases where the described curve becomes algebraic.

Eventually, he was able to deduce an equation with two elliptic integrals with separated variables, and recognized the advantage of introducing the sum and difference of the distances v, u of the centers A, B from Z as new variables. If Z moves in a plane where A, B are to be found, the curve is an ellipse or a hyperbola. Dropping this condition Euler discussed the case where the curve lies on a hyperbolic conoid or on an elliptic spheroid.

He elaborated the first paper[31] in 1759, in my opinion presumably because he was stimulated by Clairaut's paper published exactly in this year.[32] Therein Clairaut abandoned the plan of finding the complete solution of the three-body problem in favour of approximative solutions:

Now integrate who will be able to do it! I have found the six equations which I have just found since the first times that I have considered the three-body problem. But I made only few efforts to solve them because they always seemed to me to be hardly manageable.

In 1762, Euler, too, was inclined to set aside exact integrals and worked out an iteration method based on series expansions praising its simplicity, practicality, and generality.[33]

On the 9th of November of the same year, Euler wrote to Lagrange about his relative researches on the subject:

I am utmost delighted, Sir, that my investigations on the motion of a body attracted by two fixed centers of force have deserved your attention. But you have only seen what has been inserted into the Memoirs of Berlin and what mainly regards the algebraic curves included in my solution. Yet, I have written still two other memoirs on that subject. One of them is to be found in the 10th volume of our Commentaries and the other in the 11th volume.

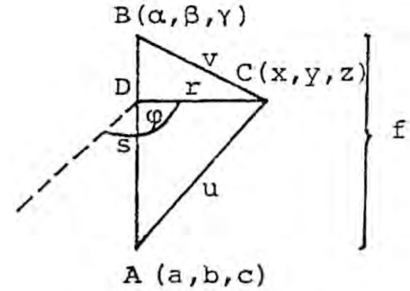

Fig. 5. The configuration of the problem of two gravitational centers as dealt with by Lagrange in Lagrange, 1766–1769a: p. 73.

Only in 1767 did Lagrange come back to this problem, when all three Eulerian papers had already been printed.[34] In his own paper[35] Lagrange at once considered the generalized case dealt with in Euler's third paper and used $v + u$, $v - u$ as variables (cf. Fig. 5). Apparently in order to avoid unpleasant suspicions, he claimed that he had written his paper before he knew Euler's third paper. The reader will be able to judge whose method was more direct or simpler.[36]

5.2. The collinear configuration

The three bodies A, B, C with masses a, b, c remain on a straight line that turns uniformly around itself.

Euler investigated this collinear case in four papers.[37] It presents the first particular solution of the three-body problem. Either the two distances between A, B and B, C remain constant. Then they can be determined thanks to the quintic equation

$$1 - 2x + x^2 - mx^2 - x^3 + 2x^4 - x^5 = 0 \qquad (1)$$

with $m = \frac{n^2c^3}{d^3}$ = constant, c mean distance of the 'moon' from the 'earth', n:1 ratio of the mean motion of the 'moon' to the mean motion of the 'sun', d mean distance between 'sun' and 'earth'.

Or the ratio n of the distances p, q between the three bodies remains constant. On the understanding that an arbitrary angular velocity is given, the mutual distances are periodical functions of time and can be determined thanks to the quintic

31 Euler, 1764a.

32 Clairaut, 1759: p. 566. ("Intègre maintenant qui pourra ! J'ai trouvé les six équations que je viens de trouver dès les premiers temps que j'ai envisagé le problème des trois corps, mais je n'ai jamais fait que peu d'efforts pour les résoudre, parce qu'elles m'ont toujours paru peu traitables.")

33 Euler, 1763a.

34 Euler to Lagrange, November 9, 1762, in Euler, *Opera omnia*, ser. 4A, 5, p. 450 ("Je suis extrêmement ravi, Monsieur, que mes recherches sur le mouvement d'un corps attiré à deux centres de forces fixes aient mérité votre attention; mais vous n'en avez vu que ce qui a été inséré dans les Mémoires de Berlin et qui regarde principalement les courbes algébriques que ma solution renferme. Or j'en ai composé encore deux autres mémoires, dont l'un se trouve dans le Xe Volume de nos Commentaires et l'autre dans le XIe."); Lagrange to Euler, October 29, 1767, in Euler, *Opera omnia*, ser. 4A, 5, p. 460.

35 Lagrange, 1766–1769a, 1766–1769b.

36 Lagrange, 1766–1769a: p. 94.

37 Euler, 1764b, 1765b, 1763b, 1785.

equation

$$(a+b)n^5 + (3a+2b)n^4 + (3a+b)n^3 - (b+3c)n^2 - (2b+3c)n - b - c = 0. \quad (2)$$

Euler derived Eq. (1) in his first paper, Eq. (2) in all three subsequent papers.

When in 1771 Lagrange submitted his famous prize 'Essay on the three-body problem',[38] he did not employ a new method (as he claimed), using only the distances between the three bodies in order to determine the orbits. He applied Euler's method to a more general case than Euler had considered.

He investigated the two cases that the distances remain constant or that they maintain a constant ratio. Both conditions can only be fulfilled again in two cases: the bodies move along the same straight line (collinear case) or they form an equilateral triangle (triangular solution). No wonder that he derived again Euler's quintic equation for a constant ratio in the collinear case.

Nowadays we know that the triangular configuration is approximately realized in the solar system by the sun, Jupiter, and the Trojan group of the asteroids Achilles, Patrocles, Hector, and Nestor.

One might say that Euler paved the way, Lagrange gathered the fruits. The three-body problem demonstrates how he initiated new inquiries. Other fields of knowledge could demonstrate how he invented new methods (Zeta-function), defended new ideas (divergent series), developed new theories (theory of music). In his eyes mathematical problems were solvable. If necessary they have to be formulated in such a way that they become solvable. Or to put it as Eduard Fueter in 1941: "For where mathematical reason did not suffice, for Euler began the kingdom of God."[39]

6. Conclusion

Fueter's affirmation is especially true, too, of Euler's epochal contributions to hydromechanics that were comprehensively described by Truesdell in 1954.[40] In 1983, Gleb Mikhailov[41] analysed the complicated relationship between Daniel Bernoulli's, John Bernoulli's, and Euler's achievements in this respect. Euler praised John Bernoulli's *Hydraulica* printed in 1742 (it appeared only in 1743) because therein Bernoulli had calculated the force acting on an infinitesimal element. This essential idea helped Euler to create his general theory of fluids. Euler completed and perfected classical hydromechanics. His *Scientia navalis* begins with the fundamental lemma that the pressure which the water exerts upon a submerged body in its several points is normal to the surface of the body. A long series of papers followed wherein Euler reintroduced internal pressure as a means to derive the motion of fluid elements. This series culminated in the three French written treatises forming the core of Euler's general theory of fluids. They appeared in 1757. The second treatise *Principes généraux du mouvement des fluides* (General principles of the motion of fluids)[42] first introduced the famous Euler equations of fluid motion. The 250th anniversary of its publication gave rise to the conference that took place in Aussois. The history of this development is thoroughly analysed and reconstructed by Darrigol and Frisch.[43]

[38] Lagrange, 1772.
[39] Fellmann, 2007: p. 172.
[40] Truesdell, 1954.
[41] Mikhailov, 1983.
[42] Euler, 1755b.
[43] Darrigol and Frisch, 2008.

References

Alexis Claude Clairaut, 1759 'Mémoire contenant des réflexions sur le problème des trois corps, avec les équations différentielles qui expriment les conditions de ce problème.' *Journal des Sçavants*, 563–566.

Olivier Darrigol, Uriel Frisch, 2008 'From Newton's mechanics to Euler's equations, How the equations of fluid dynamics were born 250 years ago' (these *Proceedings*).

Leonhard Euler, 1727 *Dissertatio physica de sono*. Basel, also in *Opera omnia*, ser. 3, 1, 181–196, **E2**.

Leonhard Euler, 1728 *Meditationes super problemate nautico, quod illustrissima regia Parisiensis academia scientiarum proposuit*. Paris, also in *Opera omnia*, ser. 2, **20**, 1–35, **E4**.

Leonhard Euler, 1736 *Mechanica sive motus scientia analytice exposita*. 2 vols. St. Petersburg, also in *Opera omnia*, ser. 2, **1** and **2**, **E15** and **E16**.

Leonhard Euler, 1738 *Einleitung zur Rechen-Kunst zum Gebrauch des Gymnasii bey der Kayserlichen Academie der Wissenschaften in St. Petersburg*. St. Petersburg, also in *Opera omnia*, ser. 3, **2**, 1–303, **E17**.

Leonhard Euler, 1739 *Tentamen novae theoriae musicae ex certissimis harmoniae principiis dilucide expositae*. St. Petersburg, also in *Opera omnia*, ser. 3, **1**, 197–427, **E33**.

Leonhard Euler, 1744a *Methodus inveniendi lineas curvas maximi minimive proprietate gaudentes, sive solutio problematis isoperimetrici latissimo sensu accepti*. Lausanne, Genf, also in *Opera omnia*, ser 1, **24**, E65.

Leonhard Euler, 1744b. *Theoria motuum planetarum et cometarum*. Berlin, also in *Opera omnia*, ser. 2, **28**, 105–268, **E66**.

Leonhard Euler, 1745 *Neue Grundsätze der Artillerie enthaltend die Bestimmung der Gewalt des Pulvers nebst einer Untersuchung über den Unterschied des Wiederstands der Luft in schnellen und langsamen Bewegungen aus dem Englischen des Hrn. Benjamin Robins übersetzt und mit den nöthigen Erläuterungen und vielen Anmerkungen versehen*. Berlin, also in *Opera omnia*, ser. 2, **14**, 1–409, **E77**.

Leonhard Euler, 1748 *Introductio in analysin infinitorum*. 2 vols. Lausanne, also in *Opera omnia*, ser. 1, **8** and **9**, **E101** and **E102**.

Leonhard Euler, 1749 *Scientia navalis seu tractatus de construendis ac dirigendis navibus*. 2 parts. St. Petersburg, also in *Opera omnia*, ser. 2, **18** and **19**, **E110** and **E111**.

Leonhard Euler, 1753 *Theoria motus lunae exhibens omnes ejus inaequalitates*. Berlin, also in *Opera omnia*, ser. 2, **23**, 64–336, **E187**.

Leonhard Euler, 1755a *Institutiones calculi differentialis cum ejus usu in analysi finitorum ac doctrina serierum*, ser. 1, **10**, **E212**.

Leonhard Euler, 1755b 'Principes généraux du mouvement des fluides' MASB, **11** [printed in 1757], 274–315. Also in *Opera omnia*, ser. 2, **12**, 54–91, **E226**.

Leonhard Euler, 1760 'Problème: Un corps étant attiré en raison réciproque quarrée des distances vers deux points fixes donnés trouver les cas où la courbe décrite par ce corps sera algébrique.' Académie Royale des Sciences et des Belles Lettres de Berlin, *Mémoires* [abbreviated below as MASB], 16 [printed in 1767], 228–249, also in *Opera omnia*, ser. 2, **6**, 273–293, **E337**.

Leonhard Euler, 1763a 'Nouvelle méthode de déterminer les dérangemens dans le mouvement des corps célestes, causés par leur action mutuelle.' *MASB*, 19 [printed in 1770], 141–179, not yet published in *Opera omnia*, ser. 2, **26** (in preparation), **E398**.

Leonhard Euler, 1763b ‘Considérations sur le problème des trois corps.’ *MASB*, 19 [printed in 1770], 194–220, not yet published in *Opera omnia*, ser. 2, **26** (in preparation), **E400**.

Leonhard Euler, 1764a De motu corporis ad duo centra virium fixa attracti.’ *Novi commentarii academiae scientiarum Petropolitanae*, 10 [printed in 1767], 207–246, also in *Opera omnia*, ser. 2, **6**, 209–246, **E301**.

Leonhard Euler, 1764b ‘Considerationes de motu corporum colestium.’ *Novi commentarii academiae scientiarum Petropolitanae*, 10 [printed in 1766], 544–558, also in *Opera omnia*, ser. 2, **25**, 246–257, **E304**.

Leonhard Euler, 1765a ‘De motu corporis ad duo centra virium fixa attracti.’ *Novi commentarii academiae scientiarum Petropolitanae*, 11 [printed in 1767], 152–184, also in *Opera omnia*, ser. 2, **6**, 247–272, **E328**.

Leonhard Euler, 1765b ‘De motu rectilineo trium corporum se mutuo attrahentium.’ *Novi commentarii academiae scientiarum Petropolitanae*, 11 [printed in 1767], 144–151, also in *Opera omnia*, ser. 2, **25**, 281–289, **E327**.

Leonhard Euler, 1765c *Theoria motus corporum solidorum seu rigidorum ex primis nostrae cognitionis stabilita et ad omnes motus, qui in hujusmodi corpora cadere possunt, accommodata*. Rostock, Greifswald, also in *Opera omnia*, ser. 2, **3** and **4**, **E289**.

Leonhard Euler, 1768–1770, 1794 *Institutiones calculi integralis*. 3 vols., 1 post. vol. St. Petersburg, also in *Opera omnia*, ser. 1, **11**, **12**, and **13**, **E342**, **E366**, **E385** and **E660**.

Leonhard Euler, 1768–1772 *Lettres à une princesse d’Allemagne sur divers sujets de physique et de philosophie*. 3 vols. St. Petersburg, also in *Opera omnia*, ser. 3, **11** and **12**, **E343**, **E344**, and **417**.

Leonhard Euler, 1769–1771 *Dioptrica*. 3 vols. St. Petersburg, also in *Opera omnia*, ser. 3, **3** and **4**, **E367**, **E386**, and **E404**.

Leonhard Euler, 1770 *Vollständige Anleitung zur Algebra*. 2 vols. St. Petersburg, also in *Opera omnia*, ser. 1, **1**, **E387** and **388**.

Leonhard Euler, 1772 *Theoria motuum lunae, nova methodo pertractata una cum tabulis astronomicis*. St. Petersburg, also in *Opera omnia*, ser. 2, **22**, **E418**.

Leonhard Euler, 1773 *Théorie complette de la construction et de la manœuvre des vaisseaux mise à la portée de ceux, qui s’appliquent à la navigation*. St. Petersburg, also in *Opera omnia*, ser. 2, **21**, **E426**.

Leonhard Euler, 1785 ‘De motu trium corporum se mutuo attrahentium super eadem linea recta.’ *Nova acta academiae scientiarum Petropolitanae*, 3 [printed in 1788], 126–141, not yet published in *Opera omnia*, ser. 2, **27** (in preparation), **E626**.

Emil Alfred Fellmann, 2007 *Leonhard Euler*, translated by Erika Gautschi and Walter Gautschi. Basel, Boston, Berlin.

Christa Kirsten, 1977 ‘Leonhard Eulers Programm für die Berliner Sternwarte’, in G. Jackisch (ed.), *Sternzeiten (Zur 275jährigen Geschichte der Berliner Sternwarte, der heutigen Sternwarte Babelsberg)*, vol. 1. Berlin, 7–12.

Eberhard Knobloch, 1988 ‘Matematicheskie zapisnye knizhki Leonarda Eilera’, in N. N. Bogolyubov, G. K. Mikhailov, A. P. Yushkevich (eds.), *Razvitie idei Leonarda Eilera i sovremennaya nauka*. Moscow, 102–129.

Eberhard Knobloch, 1989 ‘Leonard Eulers mathematische Notizbücher.’ *Annals of Science***46**, 277–302.

Eberhard Knobloch, 2007 *‘Euler’s mathematical notebooks’*, in N. N. Bogolyubov, G. K. Mikhailov, A. P. Yushkevich (eds.), Euler and modern science, translated by Robert Burns. Washington, DC, 97–118.

Wolfgang Knobloch, (ed.) 1984 *Leonhard Eulers Wirken an der Berliner Akademie der Wissenschaften 1741–1766*, Spezialinventar Regesten der Euler-Dokumente aus dem Zentralen Archiv der Akademie der Wissenschaften der DDR. Berlin.

Kopelevic, J. Ch., Krutikova, M. V., Mikhailov, G. K., Raskin, N. M. (eds.) 1962 *Manuscripta Euleriana Archivi Academiae Scientiarum URSS*. Moscow, Leningrad.

Joseph Louis Lagrange, 1766–1769a ‘Recherches sur le mouvement d’un corps qui est attiré vers deux centres fixes. Premier mémoire.’ *Miscellanea Taurinensia*, **4** [printed in 1773], also in *Œuvres*, vol. 2, 65–94.

Joseph Louis Lagrange, 1766–1769b ‘Recherches sur le mouvement d’un corps qui est attiré vers deux centres fixes. Second mémoire. *Miscellanea Taurinensia*, **4** [printed in 1773], also in *Œuvres*, vol. 2, 94–121.

Joseph Louis Lagrange, 1772 *‘Essai sur le problème des trois corps.’ Recueil des pièces qui ont remporté le prix de l’académie royale des sciences*, **9** [printed in 1777], also in *Œuvres*, vol 6, 229–331.

Gleb K. Mikhailov, 1983 ‘Leonhard Euler und die Entwicklung der theoretischen Hydraulik im zweiten Viertel des 18. Jahrhunderts’, in *Leonhard Euler 1707–1783, Beiträge zu Leben und Werk, Gedenkband des Kantons Basel-Stadt*. Basel, 229–241.

Benjamin Robins, 1739 *Remarks on Mr. Leonhard Euler’s treatise entitled Mechanica, Dr. Smith’s Compleat system of opticks, and Dr. Jurin’s essay upon distinct and indistinct vision*, London.

C.Edward Sandifer, 2007 *The Early Mathematics of Leonhard Euler*. Washington, DC.

George F. Simmons, 2007 *Calculus gems, Brief Lives and Memorable Mathematics*. Washington, DC..

Otto Spieß, 1929 *Leonhard Euler, Ein Beitrag zur Geistesgeschichte des XVIII. Jahrhunderts*. Frauenfeld, Leipzig.

M.F. Subbotin, 1958 ‘Astronomicheskie raboty Leonarda Eilera’ (Leonhard Euler’s astronomical works), in M. A. Lavrentev, A. P. Yushkevich, A. T. Gregoryan (eds.), *Leonard Eiler, Sbornik statei v chest 250-letiya so dnya rozhdeniya, predstavlennykh Akademii Nauk SSSR*. Moscow, 268–276.

Clifford Truesdell, 1954 ‘Rational fluid mechanics, 1657–1765’, in Euler, *Opera omnia*, ser. 2, **12**, IX-CXXV.

V.S. Varadarajan, 2006 *Euler Through Time: A New Look at Old Themes*. Providence.

Otto Volk, 1983 ‘Eulers Beiträge zur Theorie der Bewegungen der Himmelskörper,’ in: *Leonhard Euler, Beiträge zu Leben und Werk, Gedenkband des Kantons Basel-Stadt*. Basel, 345–361.

Curtis Wilson, 1994 ‘The three-body problem’, in: I. Grattan-Guinness (ed.), *Companian Encyclopedia of the History and Philosophy of the Mathematical Sciences*, vol. 2. London, New York, 1054–1062.

Curtis Wilson, 2007 ‘Euler and Applications of Analytical Mathematics to Astronomy,’ in: Robert E. Bradley, C. Edward Sandifer (eds.), *Leonhard Euler: Life, Work and Legacy*. Amsterdam etc., 121–145.

Singularities

Available online at www.sciencedirect.com

ScienceDirect

Physica D 237 (2008) 1894–1904

PHYSICA D

www.elsevier.com/locate/physd

The three-dimensional Euler equations: Where do we stand?

J.D. Gibbon*

Department of Mathematics, Imperial College London, London SW7 2AZ, United Kingdom

Available online 1 November 2007

Abstract

The three-dimensional Euler equations have stood for a quarter of a millenium as a challenge to mathematicians and physicists. While much has been discovered, the nature of solutions is still largely a mystery. This paper surveys some of the issues, such as singularity formation, that have cost so much effort in the last 25 years. In this light we review the Beale–Kato–Majda theorem and its consequences and then list some of the results of numerical experiments that have been attempted. A different line of endeavour focuses on work concerning the pressure Hessian and how it may be used and modelled. The Euler equations are finally discussed in terms of their membership of a class of general Lagrangian evolution equations. Using Hamilton's quaternions, these are reformulated in an elegant manner to describe the motion and rotation of fluid particles.

PACS: 47.10.A-; 47.15.ki

Keywords: Vorticity; Singularities; Hessian; Quaternions

1. Introduction

The Apocryphal book Ecclesiasticus says [1]

Let us now praise famous men, and our fathers that begat us. ...All these were honoured in their generations, and were the glory of their times ...

and goes on to conclude in the same passage

There be of them that have left a name behind them, that their praises might be reported.

Leonhard Euler was certainly honoured in his own generation and has left a name behind him in manifold and diverse ways. Not only has his star shone ever more brightly, but the equations of inviscid fluid dynamics that bear his name have also stood the test of a quarter of a millennium of investigation and still stand proudly today as a challenge to the mathematical, physical and engineering sciences [2]. The incompressible Euler equations have a deceptively innocent simplicity about them; indeed their siren song has tempted many young scientists, somewhat like Ulysses, towards the twin rocks called Frustration and Despair. After a career spent in puzzlement, the sadder but wiser researcher is forced to admit how subtle and difficult they are.

They can be expressed as a set of partial differential equations relating the velocity vector field $\boldsymbol{u}(\boldsymbol{x}, t)$ to the pressure $p(\boldsymbol{x}, t)$

$$\frac{\mathrm{D}\boldsymbol{u}}{\mathrm{D}t} = -\nabla p, \tag{1}$$

$$\frac{\mathrm{D}}{\mathrm{D}t} = \frac{\partial}{\partial t} + \boldsymbol{u}\cdot\nabla, \tag{2}$$

where $\operatorname{div}\boldsymbol{u} = 0$ is an incompressibility condition. Applying this condition to (1) and (2) forces the pressure to satisfy an elliptic equation $-\Delta p = u_{i,j}u_{j,i}$ that involves products of velocity gradients. This can also be re-expressed in terms of the strain matrix $S_{ij} = \frac{1}{2}(u_{i,j} + u_{j,i})$

$$-\Delta p = u_{i,j}u_{j,i} = \mathrm{Tr}\left(S^2\right) - \frac{1}{2}\omega^2. \tag{3}$$

The vorticity $\boldsymbol{\omega} = \operatorname{curl}\boldsymbol{u}$ obeys the Euler equations in their vorticity form

$$\frac{\mathrm{D}\boldsymbol{\omega}}{\mathrm{D}t} = \boldsymbol{\omega}\cdot\nabla\boldsymbol{u}. \tag{4}$$

* Tel.: +44 207 594 8504.
E-mail address: j.d.gibbon@ic.ac.uk.

0167-2789/$ - see front matter
doi:10.1016/j.physd.2007.10.014

On a domain Ω, the energy $\int_\Omega |\boldsymbol{u}|^2 \mathrm{d}V$, the circulation $\int_C \boldsymbol{u}\cdot \mathrm{d}\boldsymbol{r}$ and the helicity $\int_\Omega \boldsymbol{u}\cdot\boldsymbol{\omega}\mathrm{d}V$ are all conserved; for historical observations on these quantities see [3].

Given the large volume of work on the two- and three-dimensional Euler equations, it would be vacuous to attempt to cover every aspect, but there are certain significant areas I wish to mention before moving on to other material in more detail. It is appropriate at this point to pay tribute to Viktor Yudovich who died in the Spring of 2006 and whose work on establishing weak solutions in the two-dimensional case made him one of the fathers of modern Euler analysis [4]. Unfortunately these solutions have no such counterpart in the three-dimensional case for arbitrary initial data in L^2, which would be the analogue of Leray solutions [5]. Their absence creates difficulties for the mathematician who wishes to make each step rigorous. In these terms, standard manipulations of the three-dimensional Euler equations have to be undertaken in a formal way. Along-side this, but closer in spirit to two-dimensional Euler analysis, is a sizable literature on weak and distributional formulations of vortex sheets and the numerical methods needed to describe their roll-up. These areas have their own specialist literature which can be found in the book by Majda and Bertozzi [6].

A particular area deserving of special mention is what is now referred to as "topological fluid dynamics". Inspired by ideas based on the conservation of helicity [7–9], Moffatt [10] studied the Euler equations and those of ideal magneto-hydrodynamics through the respective tangling and knotting of vortex lines and of magnetic field lines. Together with the book by Arnold and Khesin [11], which takes a more general mathematical approach, the distillation of almost 40 years of literature in references [10,12–15] should be read by every graduate student wishing to study this area.

2. The difference between the three- and two-dimensional cases

2.1. Vortex stretching

Let us formally consider the vortex stretching term $\boldsymbol{\omega}\cdot\nabla\boldsymbol{u}$ in (4) in more detail for the three-dimensional case. Splitting the velocity gradient matrix $\nabla\boldsymbol{u} = \{u_{i,j}\}$ into its symmetric and anti-symmetric parts gives

$$(\nabla\boldsymbol{u})\boldsymbol{h} = S\boldsymbol{h} + \frac{1}{2}\boldsymbol{\omega}\times\boldsymbol{h}, \tag{5}$$

where $\boldsymbol{h}$ is an arbitrary 3-vector. It is then easy to see that if $\boldsymbol{h}\equiv\boldsymbol{\omega}$ then the anti-symmetric part plays no role and (4) becomes

$$\frac{\mathrm{D}\boldsymbol{\omega}}{\mathrm{D}t} = S\boldsymbol{\omega}. \tag{6}$$

At first glance this appears to be a deceptively simple eigenvalue problem, except the three eigenvalues $\{\lambda_1,\lambda_2,\lambda_3\}$ of S are functions of space-time and are subject to the divergence-free constraint $\lambda_1+\lambda_2+\lambda_3 = 0$. Rapid changes of size and sign in λ_i, subject to this constraint, could violently stretch or compress the vorticity field in various directions, thereby producing the fine-scale vortical structures that are so familiar in the graphical output of three-dimensional numerical computations.

In two dimensions, however, $\boldsymbol{\omega}$ is perpendicular to the plane in which the gradient lies, and so the vortex stretching term $\boldsymbol{\omega}\cdot\nabla\boldsymbol{u} = 0$. This observation illustrates the fact that the absence or presence of the vortex stretching term makes a huge difference to the vortical behaviour and suggests that the two and three-dimensional cases are fundamentally different equations with significantly different properties.

As its title suggests, this paper concentrates mainly on the three-dimensional case, but some short remarks on the two-dimensional and two-and-a-half-dimensional cases are nevertheless in order.

2.2. The two-dimensional Euler equations

Because $\boldsymbol{\omega}\cdot\nabla\boldsymbol{u} = 0$ in two-dimensions, (4) becomes

$$\frac{\mathrm{D}\boldsymbol{\omega}}{\mathrm{D}t} = 0, \tag{7}$$

and thus $\boldsymbol{\omega}$ is a constant of the motion. One difficult and subtle problem is the evolution of a two-dimensional patch of vorticity with an initially smooth closed boundary, inside which $\boldsymbol{\omega}$ = const. Whether the boundary of the patch remains smooth if it starts smooth, or whether it develops a cusp in a finite time, was once a long-standing open question until Chemin [16] proved that if an initial boundary Γ_0 is smooth (C^r for $r > 1$) then Γ_t must remain smooth. The bounds are parameterized by a double exponential in time so it is possible that numerical computations might suggest the development of a cusp even though the proof rules one out. An alternative proof using methods of harmonic analysis by Bertozzi and Constantin [17] can also be seen in [6].

2.3. The two-and-a-half-dimensional Euler equations

The class of solutions of the three-dimensional Euler equations that take the form

$$\boldsymbol{U}_{3D}(x,y,z,t) = \{\boldsymbol{u}(x,y,t), z\gamma(x,y,t)\} \tag{8}$$

are usually referred to as being of "two-and-a-half-dimensional type" because the predominant two-dimensional part in the cross-section is stretched linearly into a third dimension. This class of solutions generalizes those investigated some years ago by Stuart [18] who found a class of solutions in which two independent spatial variables were taken to be linear. The resulting partial differential equation has solutions that develop a singularity in a finite time. Eq. (8) suggests that an appropriate domain should be infinite in z with a circular periodic cross-section $\mathcal{A}$ of radius L. The two-dimensional velocity field $\boldsymbol{u}(x,y,t)$ in Eq. (8) satisfies

$$\frac{\mathrm{D}\boldsymbol{u}}{\mathrm{D}t} = -\nabla p \tag{9}$$

while $\operatorname{div}\boldsymbol{u} = -\gamma$. The fact that $\operatorname{div}\boldsymbol{u}\neq 0$ means that $\boldsymbol{u}(x,y,t)$ does not fully satisfy the two-dimensional Euler equations and that fluid particles in any one cross-section are allowed to move through any other. $\gamma(x, y, t)$ itself satisfies

$$\frac{D\gamma}{Dt} + \gamma^2 = \frac{2}{\pi L^2}\int_{\mathcal{A}} \gamma^2 dA. \tag{10}$$

While the above formulation can be found in Ohkitani and Gibbon [19], it turns out a time-independent form of these equations was written down long ago by Oseen in an appendix to a double paper [20]. He took the idea no further, however. Ohkitani and Gibbon [19] showed numerically $\gamma \to -\infty$ in a finite time. Later, using Lagrangian arguments, Constantin [21] proved analytically that $\gamma \to \pm\infty$. In other words, the blow-up is two-sided and occurs in different parts of the cross-section $\mathcal{A}$. An important point to note is that this blow-up does not represent a true singularity in the fluid, for this would need infinite energy to draw particles from infinity. More realistically, it suggests the full system will not sustain a solution of the form of (8) beyond the singular time. Before this singular time, the solution physically represents a class of stretched Burgers vortices: when $\gamma \to +\infty$ the vortex is tube-like but when $\gamma \to -\infty$ the vortex is ring-like [19]. This orthogonal pair of vortices, locked non-linearly together, has only a finite lifetime and is destroyed by the two-sided blow-up. Moreover, the finite lifetime of these vortices is consistent with experimental observations in turbulent flows where, among the collective set, individual tubes squirm around and then vanish after a short period [22–24]. A class of analytical singular solutions of a special case of (8)–(10) has been found using the method of characteristics [25].

3. The three-dimensional Euler singularity problem

One of the great open questions in mathematical fluid dynamics today is whether the incompressible three-dimensional Euler equations develop a singularity in the vorticity field in a finite time. Opinion is largely divided on the matter with strong positions taken on each side. That the vorticity accumulates rapidly from a variety of initial conditions is not under dispute, but whether the accumulation is sufficiently rapid to manifest singular behaviour or whether the growth is merely exponential, or double-exponential, has not been answered definitively. The interest in singularities comes from many directions. Physically their formation may signify the onset of turbulence and may be a mechanism for energy transfer to small scales: see the companion article in this issue by Eyink [26]. Numerically they require very special methods and are thus a challenge to computational fluid dynamics. Finally, the question is of interest to mathematicians because of the question of global existence of solutions. This section reviews some of the theoretical and computational work of the last 25 years.

3.1. The Beale–Kato–Majda Theorem

Work on the existence of solutions culminated in what is known as the Beale–Kato–Majda Theorem [27]. It was originally proved on an infinite domain with solutions decaying sufficiently rapidly at infinity but the domain Ω could easily be taken to be periodic instead. We refer the reader to the recent review by Bardos and Titi [28]. There are various ways of stating the result but the following form will be used:

Theorem 1. *There exists a global solution of the 3D Euler equations* $\boldsymbol{u} \in C([0,\infty]; H^s) \cap C^1([0,\infty]; H^{s-1})$ *for* $s \geq 3$ *if, for every* $T > 0$

$$\int_0^T \|\boldsymbol{\omega}(\cdot,\tau)\|_{L^\infty(\Omega)} d\tau < \infty. \tag{11}$$

Ferrari [29] has also proved a version of this result on boundary conditions where $\boldsymbol{u}\cdot\hat{\boldsymbol{n}} = 0$. Kozono and Taniuchi [30] have more recently proved a version of this theorem in the BMO-norm (bounded mean oscillations) which is weaker than the L^∞-norm. For literature on variations of the BKM theorem see Ponce [31] and Chae [32–35].

There are several other points to note about this important result which settled several outstanding questions. First it says that only one object, the maximum norm, needs to be monitored in a numerical calculation. Second, this object is different from the point-wise enstrophy $\|\boldsymbol{\omega}\|_{L^2(\Omega)}$. Having the latter bounded guarantees the regularity of the three-dimensional Navier–Stokes equations but this is not enough for Euler; it is theoretically possible that $\|\boldsymbol{\omega}\|_{L^2(\Omega)}$ could remain finite but $\|\boldsymbol{\omega}\|_{L^\infty(\Omega)}$ blow up.

Third, the result also says something subtle about the nature of singular behaviour in numerical experiments. For instance, say that a numerical integration of the three-dimensional Euler equations produces data that suggests that the maximum norm grows like ($\beta > 0$)

$$\|\boldsymbol{\omega}(\cdot,t)\|_{L^\infty(\Omega)} \sim (T-t)^{-\beta}. \tag{12}$$

The theorem says that the solution remains regular, including $\|\boldsymbol{\omega}\|_{L^\infty(\Omega)}$ itself, if the time integral in (11) is finite. If the observed value of β lies in the range $0 < \beta < 1$, however, the time integral of (12) is finite and thus the theorem contradicts the numerical result. The observed singularity is likely to be an artefact of the numerics. The theorem contains no information on whether a singularity occurs but it does say that β must satisfy $\beta \geq 1$ for the singularity to be genuine.

3.2. Numerical search for singularities

There have been many numerical experiments over the last quarter of a century that have attempted to determine, from specific initial data, whether the vorticity field in the three-dimensional Euler equations develops a singularity in a finite time. At this stage I would like to pay tribute to Richard Pelz (1957–2002), who was a much-valued and gentlemanly member of our community. His interests lay in the potential development of Euler singularities under Kida's high-symmetry conditions [36]. His work and that with his collaborators is referenced in the list below. Shigeo Kida has also edited a volume in his memory [37]. The list is a revised and updated version of one originally compiled by Rainer Grauer of Bochum. The "yes/no" in each item refers to whether the authors detected the development of a singularity from their initial data. Except for item 2 all calculations refer to the 3D Euler equations.

1. Morf, Orszag and Frisch [38–40]: complex time singularities of the 3D Euler equations were studied using Padé-approximants. Singularity; yes.
2. Pauls, Matsumoto, Frisch and Bec [41]: this paper is a recent study of complex singularities of the 2D Euler equations and contains a good list of references for the student.
3. Chorin [42]: Vortex–method. Singularity; yes.
4. Brachet, Meiron, Nickel, Orszag and Frisch [43]: Taylor–Green calculation. Singularity; no.
5. Siggia [44]: Vortex–filament method; became anti–parallel. Singularity; yes.
6. Pumir and Siggia [45]: results from their adaptive grid method showed a tendency to develop quasi-two-dimensional structures with exponential growth of vorticity. Singularity; no.
7. Bell and Marcus [46]: the evolution of a perturbed vortex tube was studied using a projection method with 128^3 mesh points; amplification of vorticity by 6. Singularity; yes.
8. Brachet, Meneguzzi, Vincent, Politano and Sulem [47]: pseudospectral code, Taylor–Green vortex, with a resolution of 864^3. They achieved an amplification of vorticity by 5. Singularity; no.
9. Kerr [48,49]: Chebyshev polynomials with anti–parallel initial conditions; resolution $512^2 \times 256$. Amplification of vorticity by 18. Observed vorticity growth $\|\boldsymbol{\omega}\|_{L^\infty(\Omega)} \sim (T-t)^{-1}$. Singularity; yes.
10. Between 1994–2001 Boratav and Pelz [50,51], Pelz and Gulak [53] and Pelz [52,54] performed a series of 1024^3 grid-point simulations under Kida's high-symmetry condition. Singularity; yes.
    The recent memorial issue for Pelz [37] contains:
    (a) Cichowlas and Brachet [55]: Singularity; no.
    (b) Gulak and Pelz [56]: Singularity; yes.
    (c) Pelz and Ohkitani [57]: Singularity; no.
11. Grauer, Marliani and Germaschewski [58]: using an adaptive mesh refinement of the Bell and Marcus initial condition [46] with 2048^3 mesh points, they achieved an amplification factor of vorticity of 21. Singularity; yes.
12. Hou and Li [59]: A $1536 \times 1024 \times 3072$ pseudo-spectral calculation agreed with Kerr [48] until the final stage and then the growth slowed; the vorticity grew no faster than double-exponential in time. Singularity; no.
13. Germaschewski and Grauer (2001, unpublished): revisited the Boratav-Pelz simulations but observed strong vortex flattening that halted singular growth. This is consistent with the results of Hou and Li [59]. Singularity; no.
14. Orlandi and Carnevale [60]: using Lamb dipoles as initial conditions, they performed a 1024^3 finite difference calculation with two symmetry planes. They found a period of rapid growth of vorticity consistent with $\|\boldsymbol{\omega}\|_{L^\infty(\Omega)} \sim (T-t)^{-1}$: Singularity; yes.

The interested reader may wish to consult the other articles in this volume written by Hou [61], Bustamente and Kerr [62] and Grauer [63] which contain more references on this topic.

3.3. Results on the direction of vorticity

The yes/no aspect of the results in Section 3.2 is deceptive because the list may have hidden the fact that while a result may have been "no" the vorticity growth may nevertheless have been very strong. It is easy to overlook the directional mechanisms that induce strong early growth even if that growth slows during the final stage. Thus it is important to consider the direction of vorticity growth in its own right [64]. The reader is referred to the companion article in this volume by Constantin [65].

The pioneering paper by Constantin, Fefferman and Majda [66] contains a discussion on the idea of how vortex lines may be considered to be "smoothly directed" in a region of their greatest curvature. A digest of their results is the following: consider the three-dimensional Euler equations with smooth localized initial data and assume the solution is smooth on $0 \le t < T$. The velocity field defines particle trajectories $\boldsymbol{X}(\boldsymbol{x}_0, t)$ that satisfy

$$\frac{\mathrm{D}\boldsymbol{X}}{\mathrm{D}t} = \boldsymbol{u}(\boldsymbol{X}, t), \tag{13}$$

where $\boldsymbol{X}(\boldsymbol{x}_0, 0) = \boldsymbol{x}_0$. The image $\boldsymbol{W}_t$ of a set $\boldsymbol{W}_0$ is given by $\boldsymbol{W}_t = \boldsymbol{X}(\boldsymbol{W}_0, t)$. Then the set $\boldsymbol{W}_0$ is said to be *smoothly directed* if there exists a length $\rho > 0$ and a ball $0 < r < \frac{1}{2}\rho$ such that the following conditions are satisfied: (i) $\hat{\boldsymbol{\omega}}(\cdot, t)$ has a Lipschitz extension to the ball $B_{4\rho}$ of radius 4ρ centred at $\boldsymbol{X}(\boldsymbol{x}_0, t)$; (ii) if the velocity is finite in a ball $B_{4\rho}$; (iii) if

$$\lim_{t\to T} \sup_{W_0} \int_0^t \|\nabla\hat{\boldsymbol{\omega}}(\cdot,\tau)\|^2_{L^\infty(B_{4\rho})}\mathrm{d}\tau < \infty. \tag{14}$$

One needs a chosen neighbourhood that captures large and growing vorticity which does not overlap with another similar region. Under these circumstances, there can be no singularity at time T. Cordoba and Fefferman [67] have weakened condition (ii) in the case of vortex tubes to

$$\int_0^T \|\boldsymbol{u}(\cdot, s)\|_{L^\infty(\Omega)}\mathrm{d}s < \infty. \tag{15}$$

A result a decade later by Deng, Hou and Yu [68,69] follows in the same spirit; they take the arc length $L(t)$ of a vortex line L_t with $\hat{\boldsymbol{n}}$ the unit normal and κ the curvature. Let $0 < B \le 1 - A$, and C_0 be a positive constant with $M(t)$ defined as

$$M(t) \equiv \max\left(\|\nabla\cdot\hat{\boldsymbol{\omega}}\|_{L^\infty(L_t)}, \|\kappa\|_{L^\infty(L_t)}\right). \tag{16}$$

They prove that there will be no blow-up at time T if

$$U_{\hat{\omega}}(t) + U_{\hat{n}}(t) \lesssim (T-t)^{-A}, \tag{17}$$

$$M(t)L(t) \le C_0, \tag{18}$$

$$L(t) \gtrsim (T-t)^{B}. \tag{19}$$

$U_{\hat{\omega}}(t)$ is the maximum value of the tangential velocity of the difference between any two points x and y on the vortex line length L_t; likewise for $U_{\hat{n}}(t)$ with respect to the normal velocity.

4. The pressure Hessian

4.1. Ertel's Theorem and its consequences

The traditional view in fluid mechanics has taken the velocity vector field $\boldsymbol{u}$ as the dominant variable with the pressure p considered as an auxiliary. Given that there exists no evolution equation for p, which must be determined from the elliptic equation (3), there is much to be said for this philosophy. Following Leray, this is normally put into practice in Navier–Stokes and Euler analysis by projection onto divergence-free vector fields, thus covertly hiding the pressure. An alternative route is to avoid this projection process and make a virtue of openly keeping the pressure in the calculation. The key to this route is to use what is generally called Ertel's theorem, which is stated as the following formal result [71]:

Theorem 2. *If $\boldsymbol{\omega}$ satisfies the three-dimensional incompressible Euler equations then any arbitrary differentiable μ satisfies*

$$\frac{\mathrm{D}}{\mathrm{D}t}(\boldsymbol{\omega}\cdot\nabla\mu) = \boldsymbol{\omega}\cdot\nabla\left(\frac{\mathrm{D}\mu}{\mathrm{D}t}\right). \tag{20}$$

The proof is a simple exercise: consider $\boldsymbol{\omega}\cdot\nabla\mu \equiv \omega_i\mu_{,i}$

$$\begin{aligned}\frac{\mathrm{D}}{\mathrm{D}t}(\omega_i\mu_{,i}) &= \frac{\mathrm{D}\omega_i}{\mathrm{D}t}\mu_{,i} + \omega_i\left\{\left(\frac{\mathrm{D}\mu}{\mathrm{D}t}\right)_{,i} - u_{k,i}\mu_{,k}\right\}\\ &= \omega_i\left(\frac{\mathrm{D}\mu}{\mathrm{D}t}\right)_{,i} + \{\omega_j u_{i,j}\mu_{,i} - \omega_i u_{k,i}\mu_{,k}\}.\end{aligned}$$

The last term is zero under summation. Another way of expressing this result is that $\mathrm{D}/\mathrm{D}t$ and $\boldsymbol{\omega}\cdot\nabla$ commute

$$\left[\frac{\mathrm{D}}{\mathrm{D}t}, \boldsymbol{\omega}\cdot\nabla\right] = 0. \tag{21}$$

In Lie-derivative form this means that $\boldsymbol{\omega}\cdot\nabla(t) = \boldsymbol{\omega}\cdot\nabla(0)$ is a Lagrangian invariant and is "frozen in".

In geophysical fluid dynamics, if μ is chosen as the density ρ in a Boussinesq fluid then

$$\frac{\mathrm{D}\rho}{\mathrm{D}t} = 0 \tag{22}$$

implies that $\boldsymbol{\omega}\cdot\nabla\rho$ (potential vorticity) is a constant of the motion [70]. Credit is normally given to Ertel [71] although the general result has been known for much longer [72–74]. Both Klainerman [75] and Ohkitani [76,77] used Theorem 2 in the following way. The choice of $\mu = u_i$ gives a relation for the vortex stretching vector

$$\frac{\mathrm{D}(\boldsymbol{\omega}\cdot\nabla\boldsymbol{u})}{\mathrm{D}t} = \boldsymbol{\omega}\cdot\nabla\left(\frac{\mathrm{D}\boldsymbol{u}}{\mathrm{D}t}\right) = -P\boldsymbol{\omega}, \tag{23}$$

where P is the Hessian matrix of the pressure

$$P = \{p_{,ij}\} = \left\{\frac{\partial^2 p}{\partial x_i\partial x_j}\right\}. \tag{24}$$

This result illustrates the relative merits or demerits of cancelling non-linearity of $O(|\boldsymbol{\omega}||\nabla\boldsymbol{u}|^2)$ while being forced to include the Hessian of the pressure.

4.2. Restricted Euler equations: Modelling the pressure Hessian

The results of the previous subsection have shown that if the pressure field is to remain in the calculation then it is important to understand its Hessian matrix. Because there are numerical difficulties in accurately computing this matrix there have been a variety of attempts at modelling it. In effect, this produces restricted versions of the Euler equations. Consider the gradient matrix $M_{ij} = u_{i,j}$ which satisfies the matrix Riccati equation

$$\frac{\mathrm{D}M}{\mathrm{D}t} + M^2 + P = 0, \tag{25}$$

$$\mathrm{Tr}\,P = -\mathrm{Tr}\,(M^2), \tag{26}$$

where Eq. (26) has its origins in the divergence-free condition $\mathrm{Tr}\,M = 0$ and is an economical way of writing $\Delta p = -u_{i,j}u_{j,i}$. Several attempts have been made to model the Lagrangian-averaged pressure Hessian by introducing a constitutive closure — see [78] for a summary. The idea goes back to Léorat [79], Vieillefosse [80], Novikov [81] and Cantwell [82]. The Eulerian pressure Hessian P is generally assumed to be isotropic

$$P = -\frac{1}{3}I\,\mathrm{Tr}\,(M^2), \quad \mathrm{Tr}\,I = 3, \tag{27}$$

which results in the "restricted Euler equations". There is a also a variety of literature on modelling the velocity gradient matrix [83–86]. The elliptic pressure constraint given in (3), re-expressed as $-\mathrm{Tr}\,P = \mathrm{Tr}\,(S^2) - \frac{1}{2}\omega^2$, is concerned solely with the diagonal elements of P, whereas in computations its off-diagonal elements turn out to be important.

An different attempt at modelling the effect of the Hessian has been made by Constantin who derived the "distorted Euler equations" [87]. The Euler equations for the gradient composed with the Lagrangian path map $\boldsymbol{a} \mapsto \boldsymbol{X}(\boldsymbol{a},t)$, $N = M\circ\boldsymbol{X}$ are rewritten in Lagrangian form as

$$\frac{\partial N}{\partial t} + N^2 + Q(\boldsymbol{x},t)\mathrm{Tr}(N^2) = 0, \tag{28}$$

$$Q_{ij} = R_iR_j\circ\boldsymbol{X}, \qquad R_i = (-\Delta)^{-1/2}\frac{\partial}{\partial x_i}, \tag{29}$$

where R_i is the Riesz transform and $\boldsymbol{X}$ represents the Lagrangian path-map $\boldsymbol{a} \mapsto \boldsymbol{X}(\boldsymbol{a},t)$. The distorted equations arise through replacing $Q_{ij}(t)$ with $Q_{ij}(0)$, solutions of which have been proved to blow up [87]. Other models of interest include the tetrad model of Chertkov, Pumir and Shraiman [88] which has recently been developed by Chevillard and Meneveau [89]. More ideas regarding the modelling of the pressure Hessian through a transformation from Eulerian to Lagrangian coordinates using a Lagrangian flow map have recently been discussed in [78].

5. A formulation in quaternions

The material of Section 3.3 has been devoted to the issue of the directional growth of vorticity. Ultimately, the mechanisms that guide this growth will determine whether the Euler equations develop a finite-time singularity and so alternative ways of formulating this problem may be of value. It turns out that Hamilton's quaternions are useful not only for this purpose but are also ideal for understanding how fluid particles rotate within their trajectories. Before moving on to more technical aspects of quaternions some motivation is in order to explain why their introduction into Euler analysis is natural.

Firstly, based on the unit vector of vorticity $\hat{\boldsymbol{\omega}}$, let us define the respective scalar and 3-vector variables designated as α and $\boldsymbol{\chi}$

$$\alpha = \hat{\boldsymbol{\omega}} \cdot S\hat{\boldsymbol{\omega}}, \qquad \boldsymbol{\chi} = \hat{\boldsymbol{\omega}} \times S\hat{\boldsymbol{\omega}}. \tag{30}$$

These respectively represent the rates of growth and swing of the vorticity. Then the vortex stretching vector $S\boldsymbol{\omega}$ can be decomposed into components parallel and perpendicular to $\boldsymbol{\omega}$

$$S\boldsymbol{\omega} = \alpha\boldsymbol{\omega} + \boldsymbol{\chi} \times \boldsymbol{\omega}, \tag{31}$$

from which it is trivial to show that $\omega = |\boldsymbol{\omega}|$ and $\hat{\boldsymbol{\omega}}$ satisfy

$$\frac{\mathrm{D}\omega}{\mathrm{D}t} = \alpha\omega, \qquad \frac{\mathrm{D}\hat{\boldsymbol{\omega}}}{\mathrm{D}t} = \boldsymbol{\chi} \times \hat{\boldsymbol{\omega}}. \tag{32}$$

It is clear that in the evolution of $\alpha(\boldsymbol{x}, t)$ and $\boldsymbol{\chi}(\boldsymbol{x}, t)$ lies the key to the growth and direction of vorticity. Given that α and $\boldsymbol{\chi}$, by definition, contain $S\boldsymbol{\omega}$, it is also clear from (23) that material differentiation of them will introduce the pressure Hessian P into the problem and thus the advantages and disadvantages discussed in Section 4 regarding its use come into play. Combining α and $\boldsymbol{\chi}$ into a 4-vector quaternion is an obvious first step; thereafter we wish to exploit the elegant algebraic properties that quaternions possess.

The second area where quaternions have an application lies in the recent experimental advances that have made in the detection of the trajectories of tracer and other particles in fluid flows [90–99]. The curvature of their paths can be used to extract statistical information about velocity gradients from a single trajectory. Fluid particles not only take complicated trajectories but they also rotate in motion. Recent work has shown that Hamilton's quaternions are applicable to this type of problem [78,100–103]. In his lifetime Hamilton's ideas did not meet with the approval of his contemporaries [104–106] but in the context of modern-day problems the crucial property that quaternions possess – that they represent a composition of rotations – has made them the technical foundation of modern inertial guidance systems in the aerospace industry where tracking the paths and the orientation of satellites and aircraft is critical [107]. The graphics community also uses them to control the orientation of tumbling objects in computer animations [108] because they avoid the difficulties incurred at the poles when Euler angles are used [108–110]. When quaternions are applicable to a problem it is usually evidence that geometrical structures are dominant. This aspect of the Euler equations has been long been debated [64,103,111–114]. Given the available equations for the evolution of the vorticity $\boldsymbol{\omega}$, the strain matrix S, and the Hessian matrix P, a pertinent question to ask is whether this is enough information to make a satisfactory formulation of this problem.

In the first of future subsections a general class of Lagrangian evolution equations will be considered of which Euler is the most important member. Then the properties of quaternions and their association with rigid body dynamics is summarized in Section 5.2 and applied in Section 5.3 to the description the flight and rotation of fluid particles. In this it will be seen how the pressure Hessian is the key factor in driving the system. Sections 5.4 and 5.5 are devoted to some of the properties of the Euler equations themselves.

5.1. A class of Lagrangian evolution equations

Suppose $\boldsymbol{w}$ is a contravariant vector quantity attached to a particle following a flow along the characteristic paths $d\boldsymbol{x}/dt = \boldsymbol{u}$ of a velocity field $\boldsymbol{u}(\boldsymbol{x}, t)$. Now consider the formal Lagrangian flow equation [78]

$$\frac{\mathrm{D}\boldsymbol{w}}{\mathrm{D}t} = \boldsymbol{a}(\boldsymbol{x}, t), \tag{33}$$

where the material derivative is given by (2). Let us also suppose that $\boldsymbol{a}$ itself is formally differentiable

$$\frac{\mathrm{D}\boldsymbol{a}}{\mathrm{D}t} = \boldsymbol{b}(\boldsymbol{x}, t), \tag{34}$$

where $\boldsymbol{b}(\boldsymbol{x}, t)$ is known. Together (2), (33) and (34) define a quartet of 3-vectors

$$\{\boldsymbol{u}, \boldsymbol{w}, \boldsymbol{a}, \boldsymbol{b}\}. \tag{35}$$

For a passive particle, $\boldsymbol{u}$ and $\boldsymbol{w}$ are independent vectors but for the three-dimensional Euler equations $\boldsymbol{u}$ and $\boldsymbol{w} \equiv \boldsymbol{\omega}$ are tied by the fact that $\boldsymbol{\omega} = \operatorname{curl} \boldsymbol{u}$. The quartet in (35) is now

$$\{\boldsymbol{u}, \boldsymbol{w}, \boldsymbol{a}, \boldsymbol{b}\} = \{\boldsymbol{u}, \boldsymbol{\omega}, S\boldsymbol{\omega}, -P\boldsymbol{\omega}\}, \tag{36}$$

where P is the pressure Hessian discussed in Section 4. This is not the whole story because the divergence-free condition means that P, S and $\boldsymbol{\omega}$ are not independent of each other because of the elliptic pressure constraint

$$-\mathrm{Tr}\, P = \mathrm{Tr}\left(S^2\right) - \frac{1}{2}\omega^2. \tag{37}$$

Another example that could be cast into this format are the equations of ideal MHD in Elsasser form (see [78,100,101] although the existence of two material derivatives requires some generalization.

In Section 5.3 it will be shown how the quartet in (35), based upon the pair of Lagrangian evolution equations (33) and (34), can determine the evolution of an ortho-normal frame for a fluid particle in a trajectory. In graphics problems the usual practice is to consider the Frenet-frame of a trajectory. This consists of the unit tangent vector, a normal and a bi-normal [108]. In navigational language, this represents the corkscrew-like pitch, yaw and roll of the motion. In turn, the tangent vector and normals are related to the curvature and torsion. While the Frenet-frame describes the path, it ignores the dynamics that generates the motion. Here we will discuss another ortho-normal frame associated with the motion of each Lagrangian fluid particle, designated the *quaternion-frame*. This may be envisaged as moving with the Lagrangian particles, but their evolution derives from the Eulerian equations of motion.

5.2. Quaternions and rigid body dynamics

Rotations in rigid body mechanics have given rise to a rich and longstanding literature in which Whittaker's book is a classic example [110]. This gives explicit formulae relating the Euler angles to the Euler parameters and Cayley–Klein parameters of a rotation. Quaternions are not only much more efficient but they also circumvent the messy inter-relations that are unavoidable when Euler angle formulae are involved [105, 110].

In terms of any scalar p and any 3-vector $\boldsymbol{q}$, the quaternion $\mathfrak{q} = [p, \boldsymbol{q}]$ is defined as

$$\mathfrak{q} = [p, \boldsymbol{q}] = pI - \sum_{i=1}^{3} q_i \sigma_i, \tag{38}$$

in which Gothic fonts denote quaternions (see [78,100]). The three Pauli spin matrices σ_i are defined by

$$\sigma_1 = \begin{pmatrix} 0 & i \\ i & 0 \end{pmatrix} \quad \sigma_2 = \begin{pmatrix} 0 & 1 \\ -1 & 0 \end{pmatrix} \quad \sigma_3 = \begin{pmatrix} i & 0 \\ 0 & -i \end{pmatrix} \tag{39}$$

and I is the 2×2 unit matrix. The relations between the Pauli matrices $\sigma_i \sigma_j = -\delta_{ij} I - \epsilon_{ijk} \sigma_k$ then give a non-commutative multiplication rule

$$\mathfrak{q}_1 \circledast \mathfrak{q}_2 = [p_1 p_2 - \boldsymbol{q}_1 \cdot \boldsymbol{q}_2,\, p_1 \boldsymbol{q}_2 + p_2 \boldsymbol{q}_1 + \boldsymbol{q}_1 \times \boldsymbol{q}_2]. \tag{40}$$

It is not difficult to demonstrate that they are associative.

Let $\hat{\mathfrak{p}} = [p, \boldsymbol{q}]$ be a unit quaternion with inverse $\hat{\mathfrak{p}}^* = [p, -\boldsymbol{q}]$: this requires $\hat{\mathfrak{p}} \circledast \hat{\mathfrak{p}}^* = [p^2 + q^2, 0] = [1, 0]$. For a pure quaternion $\mathfrak{r} = [0, \boldsymbol{r}]$ there exists a transformation

$$\mathfrak{r} = [0, \boldsymbol{r}] \mapsto \mathfrak{R} = [0, \boldsymbol{R}] \tag{41}$$

that can explicitly be written as

$$\mathfrak{R} = \hat{\mathfrak{p}} \circledast \mathfrak{r} \circledast \hat{\mathfrak{p}}^* = [0, (p^2 - q^2)\boldsymbol{r} + 2p(\boldsymbol{q} \times \boldsymbol{r}) + 2\boldsymbol{q}(\boldsymbol{r} \cdot \boldsymbol{q})]. \tag{42}$$

Choosing p and $\boldsymbol{q}$ such that $\hat{\mathfrak{p}} = \pm[\cos \frac{1}{2}\theta, \hat{\boldsymbol{n}} \sin \frac{1}{2}\theta]$, where $\hat{\boldsymbol{n}}$ is the unit normal to $\boldsymbol{r}$, we find that

$$\begin{aligned} \mathfrak{R} = \hat{\mathfrak{p}} \circledast \mathfrak{r} \circledast \hat{\mathfrak{p}}^* &= [0, \boldsymbol{r} \cos\theta + (\hat{\boldsymbol{n}} \times \boldsymbol{r}) \sin\theta] \\ &\equiv O(\theta, \hat{\boldsymbol{n}})\boldsymbol{r}. \end{aligned} \tag{43}$$

Eq. (43) is the *Euler–Rodrigues formula* for the rotation $O(\theta, \hat{\boldsymbol{n}})$ by an angle θ of the 3-vector $\boldsymbol{r}$ about its normal $\hat{\boldsymbol{n}}$ and $(\theta, \hat{\boldsymbol{n}})$ are called the Euler parameters. The elements of the unit quaternion $\hat{\mathfrak{p}}$ are the Cayley–Klein parameters which are related to the Euler angles [110], and form a representation of the Lie group $SU(2)$. When $\hat{\mathfrak{p}}$ is time-dependent, the Euler–Rodrigues formula in (43) can be rewritten as

$$\mathfrak{r} = \hat{\mathfrak{p}}^* \circledast \mathfrak{R}(t) \circledast \hat{\mathfrak{p}} \tag{44}$$

and thus the time derivative $\dot{\mathfrak{R}}$ is given by

$$\dot{\mathfrak{R}}(t) = (\dot{\hat{\mathfrak{p}}} \circledast \hat{\mathfrak{p}}^*) \circledast \mathfrak{R} - ((\dot{\hat{\mathfrak{p}}} \circledast \hat{\mathfrak{p}}^*) \circledast \mathfrak{R})^*, \tag{45}$$

where we have used the fact that $\mathfrak{R}^* = -\mathfrak{R}$. Because $\hat{\mathfrak{p}} = [p, \boldsymbol{q}]$ is of unit length, and thus $p\dot{p} + q\dot{q} = 0$, this means that $\dot{\hat{\mathfrak{p}}} \circledast \hat{\mathfrak{p}}^* = [0, \frac{1}{2}\boldsymbol{\Omega}_0(t)]$ which is also a pure quaternion. The 3-vector entry in this defines the angular frequency $\boldsymbol{\Omega}_0(t)$ as $\boldsymbol{\Omega}_0 = 2(-\dot{p}\boldsymbol{q} + \dot{\boldsymbol{q}}p - \dot{\boldsymbol{q}} \times \boldsymbol{q})$ thereby giving the well-known formula for the rotation of a rigid body

$$\dot{\boldsymbol{R}} = \boldsymbol{\Omega}_0 \times \boldsymbol{R}. \tag{46}$$

For a Lagrangian particle, the equivalent of $\boldsymbol{\Omega}_0$ is the Darboux vector $\boldsymbol{\mathcal{D}}_a$ in Theorem 3 of Section 5.3.

5.3. An ortho-normal frame and particle trajectories

Having set the scene in Section 5.2 by describing some of the essential properties of quaternions, it is now time to apply them to the Lagrangian relation (33) between the two vectors $\boldsymbol{w}$ and $\boldsymbol{a}$. Through the multiplication rule in (40) quaternions appear in the decomposition of the 3-vector $\boldsymbol{a}$ into parts parallel and perpendicular to $\boldsymbol{w}$, which is expressed as

$$\boldsymbol{a} = \alpha_a \boldsymbol{w} + \boldsymbol{\chi}_a \times \boldsymbol{w} = [\alpha_a, \boldsymbol{\chi}_a] \circledast [0, \boldsymbol{w}]. \tag{47}$$

The scalar α_a and 3-vector $\boldsymbol{\chi}_a$ in (47) are defined as

$$\alpha_a = w^{-1}(\hat{\boldsymbol{w}} \cdot \boldsymbol{a}), \quad \boldsymbol{\chi}_a = w^{-1}(\hat{\boldsymbol{w}} \times \boldsymbol{a}). \tag{48}$$

It is now easily seen that α_a is the growth rate of the scalar magnitude ($w = |\boldsymbol{w}|$) which obeys

$$\frac{\mathrm{D}w}{\mathrm{D}t} = \alpha_a w, \tag{49}$$

while $\boldsymbol{\chi}_a$, the swing rate of the unit tangent vector $\hat{\boldsymbol{w}} = \boldsymbol{w}w^{-1}$, satisfies

$$\frac{\mathrm{D}\hat{\boldsymbol{w}}}{\mathrm{D}t} = \boldsymbol{\chi}_a \times \hat{\boldsymbol{w}}. \tag{50}$$

Now define the two quaternions

$$\mathfrak{q}_a = [\alpha_a, \boldsymbol{\chi}_a], \qquad \mathfrak{w} = [0, \boldsymbol{w}], \tag{51}$$

where $\mathfrak{w}$ is a pure quaternion. Then (33) can automatically be rewritten equivalently in the quaternion form

$$\frac{\mathrm{D}\mathfrak{w}}{\mathrm{D}t} = \mathfrak{q}_a \circledast \mathfrak{w}. \tag{52}$$

Moreover, if $\boldsymbol{a}$ is differentiable in the Lagrangian sense so that its material derivative is $\boldsymbol{b}$, as in (34) then another quaternion $\mathfrak{q}_b$ can be defined, based on the variables

$$\alpha_b = w^{-1}(\hat{\boldsymbol{w}} \cdot \boldsymbol{b}), \qquad \boldsymbol{\chi}_b = w^{-1}(\hat{\boldsymbol{w}} \times \boldsymbol{b}), \tag{53}$$

where

$$\mathfrak{q}_b = [\alpha_b, \boldsymbol{\chi}_b]. \tag{54}$$

Clearly there exists a similar decomposition for $\boldsymbol{b}$ as that for $\boldsymbol{a}$ as in (47)

$$\frac{\mathrm{D}^2\mathfrak{w}}{\mathrm{D}t^2} = [0, \boldsymbol{b}] = [0, \alpha_b \boldsymbol{w} + \boldsymbol{\chi}_b \times \boldsymbol{w}] = \mathfrak{q}_b \circledast \mathfrak{w}. \tag{55}$$

Using the associativity property, compatibility of (55) and (52) implies that ($w = |\boldsymbol{w}| \neq 0$)

$$\left(\frac{\mathrm{D}\mathfrak{q}_a}{\mathrm{D}t} + \mathfrak{q}_a \circledast \mathfrak{q}_a - \mathfrak{q}_b\right) \circledast \mathfrak{w} = 0, \tag{56}$$

which establishes a *Riccati relation* between $\mathfrak{q}_a$ and $\mathfrak{q}_b$

$$\frac{\mathrm{D}\mathfrak{q}_a}{\mathrm{D}t} + \mathfrak{q}_a \circledast \mathfrak{q}_a = \mathfrak{q}_b, \tag{57}$$

whose components yield

$$\frac{\mathrm{D}}{\mathrm{D}t}[\alpha_a, \boldsymbol{\chi}_a] + [\alpha_a^2 - \chi_a^2, 2\alpha_a \boldsymbol{\chi}_a] = [\alpha_b, \chi_b]. \tag{58}$$

These lead to a general theorem on the nature of the dynamics of the ortho-normal frame (see Fig. 1):

Theorem 3 (*[78,100]*). *The ortho-normal quaternion-frame* ($\hat{\boldsymbol{w}}, \hat{\boldsymbol{\chi}}_a, \hat{\boldsymbol{w}} \times \hat{\boldsymbol{\chi}}_a) \in SO(3)$ *has Lagrangian time derivatives expressed as* ($w \neq 0$)

$$\frac{\mathrm{D}\hat{\boldsymbol{w}}}{\mathrm{D}t} = \boldsymbol{\mathcal{D}}_a \times \hat{\boldsymbol{w}}, \tag{59}$$

$$\frac{\mathrm{D}(\hat{\boldsymbol{w}} \times \hat{\boldsymbol{\chi}}_a)}{\mathrm{D}t} = \boldsymbol{\mathcal{D}}_a \times (\hat{\boldsymbol{w}} \times \hat{\boldsymbol{\chi}}_a), \tag{60}$$

$$\frac{\mathrm{D}\hat{\boldsymbol{\chi}}_a}{\mathrm{D}t} = \boldsymbol{\mathcal{D}}_a \times \hat{\boldsymbol{\chi}}_a. \tag{61}$$

The Darboux angular velocity vector $\boldsymbol{\mathcal{D}}_a$ *is defined as*

$$\boldsymbol{\mathcal{D}}_a = \boldsymbol{\chi}_a + \frac{c_b}{\chi_a}\hat{\boldsymbol{w}}, \quad c_b = \hat{\boldsymbol{w}} \cdot (\hat{\boldsymbol{\chi}}_a \times \boldsymbol{\chi}_b). \tag{62}$$

Remark 1. The proof of Theorem 3 is simple and can be found in [78,100]. The Darboux vector $\boldsymbol{\mathcal{D}}_a$ sits in a two-dimensional plane and is driven by the vector $\boldsymbol{b}$ which itself sits in c_b in (62). The analogy with rigid body rotation expressed in (46) is clear.

Remark 2. This theorem is much more general than might be initially apparent. It provides an elegant and simple means of constructing the dynamic equations for an ortho-normal frame for any system driven by a field $\boldsymbol{b}$. An example of this is the construction of a frame for the Kepler system which is illustrated in [114].

5.4. Relation to the Euler equations

For the three-dimensional Euler equations themselves the scalar and vector variables $\alpha, \boldsymbol{\chi}$ have already been defined in (30) as the scalar and vector products between $\boldsymbol{\omega}$ and $S\boldsymbol{\omega}$. The variables $\alpha_p, \boldsymbol{\chi}_p$ corresponding (53) (with a change of sign) are defined in the same manner [101,102]

$$\alpha_p = \hat{\boldsymbol{\omega}} \cdot P\hat{\boldsymbol{\omega}}, \qquad \boldsymbol{\chi}_p = \hat{\boldsymbol{\omega}} \times P\hat{\boldsymbol{\omega}}, \tag{63}$$

which avoids the null points that arise in the definition in (48) and (53). The definitions of $\alpha, \alpha_p, \boldsymbol{\chi}, \boldsymbol{\chi}_p$ were first written down in [103]. In fact, α and α_p are Rayleigh quotient estimates for eigenvalues of S and P respectively although they are only exact eigenvalues when $\boldsymbol{\omega}$ aligns with one of their eigenvectors. Constantin [64] has a Biot–Savart formula for α. These variables form natural tetrads associated with $[0, \boldsymbol{\omega}]$

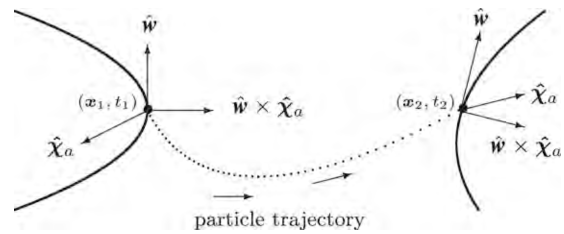

Fig. 1. Three unit vectors $[\hat{\boldsymbol{w}}, \hat{\boldsymbol{\chi}}, \hat{\boldsymbol{w}} \times \hat{\boldsymbol{\chi}}]$ form an ortho-normal coordinate system on a characteristic curve $\mathrm{d}\boldsymbol{x}/\mathrm{d}s = \boldsymbol{u}$. The two curves are drawn at times t_1 and t_2: the dotted curve represents the particle trajectory.

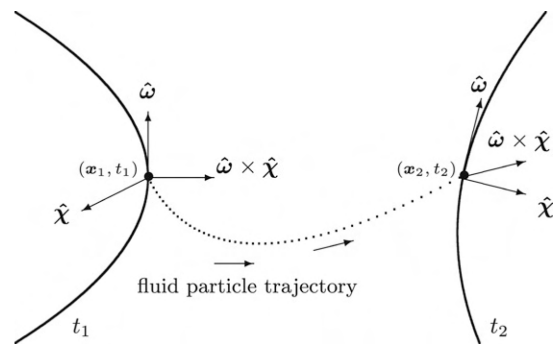

Fig. 2. Vortex lines (solid) on which sit an ortho-normal frame $\hat{\boldsymbol{\omega}}, \hat{\boldsymbol{\chi}}, \hat{\boldsymbol{\omega}} \times \hat{\boldsymbol{\chi}}$ for the Euler equations. The two curves are drawn at times t_1 and t_2: the dotted curve represents a fluid particle trajectory.

$$\mathfrak{q} = [\alpha, \boldsymbol{\chi}], \qquad -\mathfrak{q}_b = \mathfrak{q}_p = \left[\alpha_p, \boldsymbol{\chi}_p\right]. \tag{64}$$

Thus it is the pressure Hessian P that lies in $\mathfrak{q}_p$ and controls the particle trajectories through

$$\frac{\mathrm{D}\mathfrak{q}}{\mathrm{D}t} + \mathfrak{q} \circledast \mathfrak{q} + \mathfrak{q}_p = 0. \tag{65}$$

Theorem 3 furnishes us with an equivalent set of equations for the ortho-normal frame ($\hat{\boldsymbol{\omega}}, \hat{\boldsymbol{\chi}}, \hat{\boldsymbol{\omega}} \times \hat{\boldsymbol{\chi}}$) of a fluid particle through (62) where

$$c_p = -\hat{\boldsymbol{\omega}} \cdot (\hat{\boldsymbol{\chi}} \times \boldsymbol{\chi}_p). \tag{66}$$

The dynamics of the ortho-normal frame could be seen as a competition between S and P with the divergence-free constraint (37) applied.

5.5. The Frenet frame

Modulo a rotation around the unit tangent vector $\hat{\boldsymbol{\omega}}$ of Fig. 2, with $\hat{\boldsymbol{\chi}}$ as the unit bi-normal $\hat{\boldsymbol{b}}$ and $\hat{\boldsymbol{\omega}} \times \hat{\boldsymbol{\chi}}$ as the unit principal normal $\hat{\boldsymbol{n}}$ to the vortex line, the matrix F can be formed

$$F = \left(\hat{\boldsymbol{\omega}}^T, (\hat{\boldsymbol{\omega}} \times \hat{\boldsymbol{\chi}})^T, \hat{\boldsymbol{\chi}}^T\right), \tag{67}$$

and (59)–(61) can be re-written as

$$\frac{DF}{\mathrm{D}t} = AF, \quad A = \begin{pmatrix} 0 & -\chi & 0 \\ \chi & 0 & c_p\chi^{-1} \\ 0 & -c_p\chi^{-1} & 0 \end{pmatrix}. \tag{68}$$

For a space curve parameterized by arc-length s, then the Frenet equations relating $\mathrm{d}F/\mathrm{d}s$ to the curvature κ and the torsion τ of the vortex line curve are

$$\frac{\mathrm{d}F}{\mathrm{d}s} = NF, \quad \text{where } N = \begin{pmatrix} 0 & \kappa & 0 \\ -\kappa & 0 & \tau \\ 0 & -\tau & 0 \end{pmatrix}. \tag{69}$$

It is now possible to relate the t and s derivatives of F given in (68) and (69). At any time t the integral curves of the vorticity vector field define a space-curve through each point $\boldsymbol{x}$. The arc-length derivative is defined by

$$\frac{\mathrm{d}}{\mathrm{d}s} = \hat{\boldsymbol{\omega}} \cdot \nabla. \tag{70}$$

The evolution of the curvature κ and torsion τ of a vortex line may be obtained from Ertel's theorem in (21), expressed as the commutation of operators

$$\left[\frac{\mathrm{d}}{\mathrm{d}s}, \frac{\mathrm{D}}{\mathrm{D}t}\right] = \alpha \frac{\mathrm{d}}{\mathrm{d}s}. \tag{71}$$

Applying this to F and using the relations (68) and (69) establishes the following consistency relation on the matrices N and A

$$\frac{\mathrm{D}N}{\mathrm{D}t} - \alpha N = \frac{\mathrm{d}A}{\mathrm{d}s} + [A, N] \tag{72}$$

which relates the evolution of the curvature κ and the torsion τ to α, χ and c_p defined in (30) and (62).

6. Final remarks

It is clear that despite past endeavours there is still a very long way to go before we can say that there exists a clear mathematical understanding of the behaviour of solutions of the incompressible three-dimensional Euler equations. While weak solutions in the conventional sense of Leray are not known to exist, certain very special weak solutions have been found, such as those constructed by Brenier [115] and Shnirelman [116]. These are obtained by relaxing the variational problem and are not the same as weak solutions of the initial value problem for the Euler equations themselves.

The existence or non-existence of singularities is still an open problem. The numerical results of Hou and Li [59], which have focused anew on Kerr's numerical calculations performed fourteen years ago [48], suggest that a new generation of numerical experiments may be needed to look more carefully at not only the amplitude but also the direction of vorticity at high amplitudes. Even with a combination of analysis, as in [59,66–69], and with potentially much greater computing power, we may still have to wait some time until this matter is settled decisively. Much of the literature in modern mechanics has stressed that the three-dimensional Euler equations have inherent geometrical properties [11,64,66,111–113]. It is thus possible that the open problem of the regularity of solutions may become clearer after using a combination of geometrical and topological fluid mechanics [10–15] in combination with analysis and large-scale numerical computations. However, it is not clear what theorem might emerge from these considerations. Until then, the singularity problem will remain as one of the great challenges in modern applied mathematics.

A further area of endeavour has lain in the modelling of the pressure Hessian and the velocity gradient matrix. The traditional view in fluid mechanics holds that the pressure should be treated as an auxiliary variable. The alternative is to treat the Hessian P on an equal footing with the strain matrix S. Out of necessity this is certainly the case when quaternions are used to describe the problem. The elliptic equation for the pressure

$$-\Delta p = -\mathrm{Tr}\, P = \mathrm{Tr}\left(S^2\right) - \frac{1}{2}\omega^2, \tag{73}$$

is by no means fully understood and *locally* holds the key to the formation of vortical structures through the sign of $\mathrm{Tr}\, P$. In this relation, which is often thought of as a constraint, may lie a deeper knowledge of the geometry of both the Euler and Navier–Stokes equations. In turn, this may lead to a better understanding of the role of the pressure. Eq. (73) certainly plays a role in three-dimensional Navier–Stokes turbulence calculations in which the vortical topology has the classic signature of what are called "thin sets", where the vorticity concentrates into quasi-two-dimensional vortex sheets which later have a tendency to roll up into quasi-one-dimensional tubes. These tubes have a complicated topology and a finite lifetime, vanishing in one location and reappearing in another [22]. The fact that these thin sets are dynamically favoured may be explained by inherent geometrical properties of the Euler equations but little is known about these features.

Let us end with an analogy: if work on the Euler equations, beginning as a spring of water in the hills 250 years ago, has now become a mature river in full flow, it is probable that it still has far to go before it reaches its distant estuary and ocean. Will the participants at the meeting *Euler 500 years on* in the year 2257 be able to testify that sufficient progress has been made that many of the outstanding problems in this area have been solved?

Acknowledgments

Thanks are due to Uriel Frisch and his collaborators for the excellence of their organization of the meeting *Euler 250 years on*. I would like to thank Claude Bardos, Peter Constantin, Uriel Frisch, Rainer Grauer, Raymond Hide, Darryl Holm, Tom Hou, Bob Kerr, Keith Moffatt, Koji Ohkitani, Ian Roulstone, Trevor Stuart and Edriss Titi for helpful comments and corrections on the material both in this paper and the content of my lecture.

References

[1] Ecclesiasticus 44:1-15, King James Bible (1611), The Oxford Text Archive, http://ota.ahds.ac.uk/.

[2] L. Euler, Principia motus fluidorum, Novi Commentarii Acad. Sci. Petropolitanae 6 (1761) 271–311.

[3] O. Darrigol, Worlds of Flow, Oxford University Press, Oxford, 2007.
[4] V.I. Yudovich, Non-stationary flow of an incompressible liquid, Zh. Vychisl. Mat. Mat. Fiz. 3 (1963) 1032–1066.
[5] P. Constantin, C. Foias, Navier–Stokes Equations, The University of Chicago Press, Chicago, 1988.
[6] A.J. Majda, A.L. Bertozzi, Vorticity and Incompressible Flow, Cambridge University Press, Cambridge, 2001.
[7] L. Woltjer, A theorem on force-free magnetic fields, Proc. Natl. Acad. Sci. 44 (1958) 489–491.
[8] H.K. Moffatt, Magnetic Field Generation in Electrically Conducting Fluids, Cambridge University Press, Cambridge, 1978.
[9] R. Moreau, Magnetohydrodynamics, Kluwer, Dordrecht, 1990.
[10] H.K. Moffatt, The degree of knottedness of tangled vortex lines, J. Fluid Mech. 35 (1969) 117–129.
[11] V.I. Arnold, B.A. Khesin, Topological Methods in Hydrodynamics; Springer Series: Applied Mathematical Sciences, Berlin, 1998.
[12] H.K. Moffatt, Magnetostatic equilibria and analogous Euler flows of arbitrarily complex topology, J. Fluid Mech. 159 (1985) 359–378.
[13] H.K. Moffatt, A. Tsinober (Eds.), Topological Fluid Mechanics: Proceedings of the IUTAM Symposium, Cambridge University Press, 1990.
[14] H.K. Moffatt, A. Tsinober, Helicity in laminar and turbulent flow, Ann. Rev. Fluid Mech. 24 (1992) 281–312.
[15] R.L. Ricca, H.K. Moffatt, The helicity of a knotted vortex filament, in: H.K. Moffatt, G.M. Zaslavsky, P. Compte, M. Tabor (Eds.), Topological Aspects of Fluid Dynamics and Plasmas, Kluwer, Dordrecht, 1992, pp. 235–236.
[16] J.Y. Chemin, Persistance de structures geometriques dans les fluides incompressibles bidimensionnels, Ann. Ec. Norm. Supér. 26 (4) (1993) 1–16.
[17] A. Bertozzi, P. Constantin, Global regularity for vortex patches, Comm. Math. Phys. 152 (1993) 19–28.
[18] J.T. Stuart, Singularities in three-dimensional compressible Euler flows with vorticity, Theoret. Comput. Fluid Dyn. 10 (1998) 385–391.
[19] K. Ohkitani, J.D. Gibbon, Numerical study of singularity formation in a class of Euler and Navier–Stokes flows, Phys. Fluids 12 (2000) 3181–3194.
[20] C.W. Oseen, Exakte Lösungen der hydrodynamischen Differentialgleichungen II, Arkiv für Mat., Astronomi och Fysik 20A (1927) 1.
[21] P. Constantin, The Euler equations and nonlocal conservative Riccati equations, Int. Math. Res. Not. 9 (2000) 455–465.
[22] S. Douady, Y. Couder, M. Brachet, Direct observation of the intermittency of intense vorticity filaments in turbulence, Phys. Rev. Lett. 67 (1991) 983–986.
[23] R.M. Kerr, Higher-order derivative correlations and the alignment of small-scale structures in isotropic numerical turbulence, J. Fluid Mech. 153 (1985) 31–58.
[24] S. Kishiba, K. Ohkitani, S. Kida, Interaction of helical modes in formation of vortical structures in decaying isotropic turbulence, J. Phys. Soc. Japan 64 (1994) 2133–2148.
[25] J.D. Gibbon, D.R. Moore, J.T. Stuart, Exact, infinite energy, blow-up solutions of the three-dimensional Euler equations, Nonlinearity 16 (2003) 1823–1831.
[26] G. Eyink, Dissipative anomalies in singular Euler flows, Physica D 237 (14–17) (2008) 1956–1968.
[27] J.T. Beale, T. Kato, A.J. Majda, Remarks on the breakdown of smooth solutions for the 3D Euler equations, Comm. Math. Phys. 94 (1984) 61–66.
[28] C. Bardos, E. Titi, Euler equations of incompressible ideal fluids, Russian Math. Surveys 62 (3) (2007) 409–451.
[29] A. Ferrari, On the blow-up of solutions of the 3D Euler equations in a bounded domain, Comm. Math. Phys. 155 (1993) 277–294.
[30] H. Kozono, Y. Taniuchi, Limiting case of the Sobolev inequality in BMO, with applications to the Euler equations, Comm. Math. Phys. 214 (2000) 191–200.
[31] G. Ponce, Remarks on a paper by J.T. Beale, T. Kato and A. Majda, Comm. Math. Phys. 98 (1985) 349–353.
[32] D. Chae, Remarks on the blow-up of the Euler equations and the related equations, Comm. Math. Phys. 245 (2003) 539–550.
[33] D. Chae, Local existence and blow-up criterion for the Euler equations in the Besov spaces, Asymptot. Anal. 38 (2004) 339–358.
[34] D. Chae, Remarks on the blow-up criterion of the 3D Euler equations, Nonlinearity 18 (2005) 1021–1029.
[35] D. Chae, On the finite time singularities of the 3D incompressible Euler equations, Comm. Pure Appl. Math. 60 (2007) 597–617.
[36] S. Kida, Three-dimensional periodic flows with high-symmetry, J. Phys. Soc. Japan 54 (1985) 2132–2136.
[37] S. Kida (Ed.), Special issues in memory of Richard Pelz Fluid Dynam. Res. 36 (4–6) (2005).
[38] R.H. Morf, S. Orszag, U. Frisch, Spontaneous singularity in three-dimensional, inviscid incompressible flow, Phys. Rev. Lett. 44 (1980) 572–575.
[39] C. Bardos, S. Benachour, M. Zerner, Analyticité des solutions périodiques de léquation d'Euler en deux dimensions, C. R. Acad. Sci. Paris 282A (1976) 995–998.
[40] C. Bardos, S. Benachour, Domaine d'analyticité des solutions de l'équation d'Euler dans un ouvert de R^n, Ann. Sc. Norm. Super. Pisa, Cl. Sci. IV Ser. 4 (1977) 647–687.
[41] W. Pauls, T. Matsumoto, U. Frisch, J. Bec, Nature of complex singularities for the 2D Euler equation, Physica D 219 (2006) 40–59.
[42] A.J. Chorin, The evolution of a turbulent vortex, Comm. Math. Phys. 83 (1982) 517–535.
[43] M.E. Brachet, D.I. Meiron, S.A. Orszag, B.G. Nickel, R.H. Morf, U. Frisch, Small-scale structure of the Taylor–Green vortex, J. Fluid Mech. 130 (1983) 411–452.
[44] E.D. Siggia, Collapse and amplification of a vortex filament, Phys. Fluids 28 (1984) 794–805.
[45] A. Pumir, E. Siggia, Collapsing solutions to the 3D Euler equations, Phys. Fluids A 2 (1990) 220–241.
[46] J.B. Bell, D.L. Marcus, Vorticity intensification and transition to turbulence in the three-dimensional Euler equations, Comm. Math. Phys. 147 (1992) 371–394.
[47] M.E. Brachet, V. Meneguzzi, A. Vincent, H. Politano, P.-L. Sulem, Numerical evidence of smooth self-similar dynamics and the possibility of subsequent collapse for ideal flows, Phys. Fluids 4A (1992) 2845–2854.
[48] R.M. Kerr, Evidence for a singularity of the three-dimensional incompressible Euler equations, Phys. Fluids A 5 (1993) 1725–1746.
[49] R.M. Kerr, Vorticity and scaling of collapsing Euler vortices, Phys. Fluids A 17 (2005) 075103–075114.
[50] O.N. Boratav, R.B. Pelz, Direct numerical simulation of transition to turbulence from a high-symmetry initial condition, Phys. Fluids 6 (1994) 2757–2784.
[51] O.N. Boratav, R.B. Pelz, On the local topology evolution of a high-symmetry flow, Phys. Fluids 7 (1995) 1712–1731.
[52] R.B. Pelz, Locally self-similar, finite-time collapse in a high-symmetry vortex filament model, Phys. Rev. E 55 (1997) 1617–1626.
[53] R.B. Pelz, Y. Gulak, Evidence for a real-time singularity in hydrodynamics from time series analysis, Phys. Rev. Lett. 79 (1997) 4998–5001.
[54] R.B. Pelz, Symmetry and the hydrodynamic blow-up problem, J. Fluid Mech. 444 (2001) 299–320.
[55] C. Cichowlas, M.-E. Brachet, Evolution of complex singularities in Kida–Pelz and Taylor–Green inviscid flows, Fluid Dynam. Res. 36 (2005) 239–248.
[56] Y. Gulak, Richard B. Pelz, High-symmetry Kida flow: Time series analysis and resummation, Fluid Dynam. Res. 36 (2005) 211–220.
[57] R.B. Pelz, K. Ohkitani, Linearly strained flows with and without boundaries — the regularizing effect of the pressure term, Fluid Dynam. Res. 36 (2005) 193–210.
[58] R. Grauer, C. Marliani, K. Germaschewski, Adaptive mesh refinement for singular solutions of the incompressible Euler equations, Phys. Rev. Lett. 80 (1998) 4177–4180.
[59] T.Y. Hou, R. Li, Dynamic depletion of vortex stretching and non-blowup of the 3-D incompressible Euler equations, J. Nonlinear Sci. 16 (2006) 639–664.

[60] P. Orlandi, G. Carnevale, Nonlinear amplification of vorticity in inviscid interaction of orthogonal Lamb dipoles, Phys. Fluids 19 (2007) 057106.
[61] T.Y. Hou, Blowup or no blowup? The interplay between theory and numerics, Physica D 237 (14–17) (2008) 1937–1944.
[62] M.D. Bustamente, R.M. Kerr, 3D Euler in a 2D symmetry plane, Physica D 237 (14–17) (2008) 1912–1920.
[63] T. Grafke, H. Homann, J. Dreher, R. Grauer, Numerical simulations of possible finite time singularities in the incompressible Euler equations: Comparison of numerical methods, Physica D 237 (14–17) (2008) 1932–1936.
[64] P. Constantin, Geometric statistics in turbulence, SIAM Rev. 36 (1994) 73–98.
[65] P. Constantin, Singular, weak and absent: Solutions of the Euler equations, Physica D 237 (14–17) (2008) 1926–1931.
[66] P. Constantin, Ch. Fefferman, A. Majda, A. Geometric constraints on potentially singular solutions for the 3D Euler equation, Comm. Partial Differential Equations 21 (1996) 559–571.
[67] D. Cordoba, Ch. Fefferman, On the collapse of tubes carried by 3D incompressible flows, Comm. Math. Phys. 222 (2001) 293–298.
[68] J. Deng, T.Y. Hou, X. Yu, Geometric properties and non-blowup of 3D incompressible Euler flow, Comm. Partial Differential Equations 30 (2005) 225–243.
[69] J. Deng, T.Y. Hou, X. Yu, Improved geometric condition for non-blowup of the $3D$ incompressible Euler equation, Comm. Partial Differential Equations 31 (2006) 293–306.
[70] B. Hoskins, M. McIntyre, A.W. Robertson, On the use and significance of isentropic potential vorticity maps, Quart. J. Roy. Met. Soc. 111 (1985) 877–946.
[71] H. Ertel, Ein Neuer Hydrodynamischer Wirbelsatz, Met. Z. 59 (1942) 271–281.
[72] C. Truesdell, R.A. Toupin, Classical field theories, in: S. Flugge (Ed.), Encyclopaedia of Physics III/1, Springer, 1960.
[73] E. Kuznetsov, V.E. Zakharov, Hamiltonian formalism for nonlinear waves, Phys. Uspekhi 40 (1997) 1087–1116.
[74] A. Viudez, On Ertel's potential vorticity theorem. On the impermeability theorem for potential vorticity, J. Atmos. Sci. 56 (1999) 507–516.
[75] S. Klainerman, 1984, unpublished.
[76] K. Ohkitani, Eigenvalue problems in three-dimensional Euler flows, Phys. Fluids A 5 (1993) 2570–2572.
[77] K. Ohkitani, S. Kishiba, Nonlocal nature of vortex stretching in an inviscid fluid, Phys. Fluids A 7 (1995) 411–421.
[78] J.D. Gibbon, D.D. Holm, Lagrangian particle paths and ortho-normal quaternion frames, Nonlinearity 20 (2007) 1745–1759.
[79] J. Léorat, Thèse de Doctorat, Université Paris-VII, 1975.
[80] P. Vieillefosse, Internal motion of a small element of fluid in an inviscid flow, Physica A 125 (1984) 150–162.
[81] E.A. Novikov, Internal dynamics of flows and formation of singularities, Fluid Dynam. Res. 6 (1990) 79–89.
[82] B.J. Cantwell, Exact solution of a restricted Euler equation for the velocity gradient tensor, Phys. Fluids 4 (1992) 782–793.
[83] S. Girimaji, C. Speziale, A modified restricted Euler equation for turbulent flows with mean velocity gradients, Phys. Fluids 7 (1995) 1438–1446.
[84] A. Ooi, J. Martin, J. Soria, M.S. Chong, A study of the evolution and characteristics of the invariants of the velocity-gradient tensor in isotropic turbulence, J. Fluid Mech. 381 (1999) 141–174.
[85] J. Martin, A. Ooi, A., M. Chong, J. Soria, Dynamics of the velocity gradient tensor invariants in isotropic turbulence, Phys. Fluids 10 (1998) 2336–2346.
[86] A. Naso, A. Pumir, Scale dependence of the coarse-grained velocity derivative tensor structure in turbulence, Phys. Rev. E 72 (2005) 056318–056326.
[87] P. Constantin, Note on loss of regularity for solutions of the 3D incompressible Euler and related equations, Comm. Math. Phys. 104 (1986) 311–326.
[88] M. Chertkov, A. Pumir, B.I. Shraiman, Lagrangian tetrad dynamics and phenomenology of turbulence, Phys. Fluids 11 (1999) 2394–2410.
[89] L. Chevillard, C. Meneveau, Lagrangian dynamics and statistical geometric structure of turbulence, Phys. Rev. Lett. 97 (2006) 174501–174504.
[90] G. Falkovich, K. Gawedzki, M. Vergassola, Particles and fields in fluid turbulence, Rev. Modern Phys. 73 (2001) 913–975.
[91] A. La Porta, G.A. Voth, A. Crawford, J. Alexander, E. Bodenschatz, Fluid particle accelerations in fully developed turbulence, Nature 409 (2001) 1017–1019.
[92] N. Mordant, J.F. Pinton, Measurement of Lagrangian velocity in fully developed turbulence, Phys. Rev. Lett. 87 (2001) 214501–214504.
[93] G.A. Voth, A. La Porta, A. Crawford, E. Bodenschatz, J. Alexander, Measurement of particle accelerations in fully developed turbulence, J. Fluid Mech. 469 (2002) 121–160.
[94] N. Mordant, A.M. Crawford, E. Bodenschatz, Three-dimensional structure of the Lagrangian acceleration in turbulent flows, Phys. Rev. Lett. 93 (2004) 214501–214504.
[95] N. Mordant, E. Leveque, J.F. Pinton, Experimental and numerical study of the Lagrangian dynamics of high Reynolds turbulence, New J. Phys. 6 (2004) 116–160.
[96] B.A. Lüthi, A. Tsinober, W. Kinzelbach, Lagrangian measurement of vorticity dynamics in turbulent flow, J. Fluid Mech. 528 (2005) 87–118.
[97] L. Biferale, G. Boffetta, A. Celani, A. Lanotte, F. Toschi, Particle trapping in three-dimensional fully developed turbulence, Phys. Fluids 17 (2005) 021701–021704.
[98] A.M. Reynolds, N. Mordant, A.M. Crawford, E. Bodenschatz, On the distribution of Lagrangian accelerations in turbulent flows, New J. Phys. 7 (2005) 58–67.
[99] W. Braun, F. De Lillo, B. Eckhardt, Geometry of particle paths in turbulent flows, J. Turbulence 7 (2006) 1–10.
[100] J.D. Gibbon, Ortho-normal quaternion frames, Lagrangian evolution equations and the three-dimensional Euler equations, Uspekhi Mat. Nauk 62 (3) (2007) 47–72. In English Russian Math. Surveys 62 (3) (2007) 1–26.
[101] J.D. Gibbon, D.D. Holm, R.M. Kerr, I. Roulstone, Quaternions and particle dynamics in Euler fluid flow, Nonlinearity 19 (2006) 1969–1983.
[102] J.D. Gibbon, A quaternionic structure in the three-dimensional Euler and ideal magneto-hydrodynamics equation, Physica D 166 (2002) 17–28.
[103] B. Galanti, J.D. Gibbon, M. Heritage, Vorticity alignment results for the 3D Euler and Navier–Stokes equations, Nonlinearity 10 (1997) 1675–1695.
[104] J. O'Connor, E. Robertson, Sir William Rowan Hamilton. http://www-groups.dcs.st-and.ac.uk/history/.
[105] P.G. Tait, An Elementary Treatise on Quaternions, 3rd ed., Cambridge University Press, Cambridge, 1890.
[106] W.R. Hamilton, Elements of Quaternions, Cambridge University Press, Cambridge, Repub. Chelsea, 1969.
[107] J.B. Kuipers, Quaternions and Rotation Sequences: A Primer with Applications to Orbits, Aerospace, and Virtual Reality, Princeton University Press, Princeton, 1999.
[108] A.J. Hanson, Visualizing Quaternions, Morgan Kaufmann Elsevier, London, 2006.
[109] K. Shoemake, Animating rotation with quaternion curves, in: Computer Graphics, SIGGRAPH Proceedings 19 (1985) 245–254.
[110] E.T. Whittaker, A Treatise on the Analytical Dynamics of Particles and Rigid Bodies, Dover, New York, 1944.
[111] V.I. Arnold, Mathematical methods of Classical Mechanics, Springer Verlag, Berlin, 1978.
[112] J.E. Marsden, Lectures on geometric methods in mathematical physics, in: CBMS-NSF Regional Conference Series in Applied Mathematics, vol. 37, SIAM, Providence, 1981.
[113] J.E. Marsden, Lectures on Mechanics, Cambridge University Press, Cambridge, 1992.
[114] D.D. Holm, Geometric Mechanics, Part II: Rotating, Translating and Rolling, Imperial College Press, London, 2007 (in press).
[115] Y. Brenier, Minimal geodesics on groups of volume-preserving maps and generalized solutions of the Euler equations, Comm. Pure Appl. Math. 52 (1999) 411–452.
[116] A. Shnirelman, On the non-uniqueness of weak solution of the Euler equation, Comm. Pure Appl. Math. 50 (12) (1997) 1261–1286.

Available online at www.sciencedirect.com

ScienceDirect

Physica D 237 (2008) 1905–1911

PHYSICA D

www.elsevier.com/locate/physd

Global regularity for a Birkhoff–Rott-α approximation of the dynamics of vortex sheets of the 2D Euler equations

Claude Bardos[a], Jasmine S. Linshiz[b,*], Edriss S. Titi[b,c,d]

[a] Université Denis Diderot and Laboratory J.-L. Lions, Université Pierre et Marie Curie, Paris, France
[b] Department of Computer Science and Applied Mathematics, Weizmann Institute of Science, Rehovot 76100, Israel
[c] Department of Mathematics, University of California, Irvine, CA 92697-3875, USA
[d] Department of Mechanical and Aerospace Engineering, University of California, Irvine, CA 92697-3875, USA

Available online 6 January 2008

Abstract

We present an α-regularization of the Birkhoff–Rott equation, induced by the two-dimensional Euler-α equations, for the vortex sheet dynamics. We show that an initially smooth self-avoiding vortex sheet remains smooth for all times under the α-regularized dynamics, provided the initial density of vorticity is an integrable function over the curve with respect to the arc-length measure.

PACS: 47.32.C; 47.20.Ma; 47.20.Ft; 47.15.ki

Keywords: Inviscid regularization of Euler equations; Birkhoff–Rott regularization; Birkhoff–Rott-α; Vortex sheet regularization

1. Introduction

One of the novel approaches for subgrid scale modeling is the α-regularization of the Navier–Stokes equations (NSE). The inviscid Euler-α model was originally introduced in the Euler–Poincaré variational framework in [1,2]. In [3–7] the corresponding Navier–Stokes-α (NS-α) [also known as the viscous Camassa–Holm equations or the Lagrangian-averaged Navier–Stokes-α (LANS-α)] model was obtained by introducing the appropriate viscous term into the Euler-α equations. The extensive research into the α-models (see, e.g., [3–24]) stems from the successful comparison of their steady state solutions to empirical data, for a large range of huge Reynolds numbers, for turbulent flows in infinite channels and pipes. On the other hand, the α-models can also be viewed as numerical regularizations of the original, Euler or Navier–Stokes, systems. The main practical question arising is that of the applicability of these regularizations to the correct predictions of the underlying flow phenomena.

In this paper we present some results concerning the α-regularization of the two-dimensional (2D) Euler equations in the context of vortex sheet dynamics. A vortex sheet is a surface of codimension 1 (a curve in the plane) in inviscid incompressible flow, across which the tangential component of the velocity has a jump discontinuity, while the normal component is continuous. The evolution of the vortex sheet can be described by the Birkhoff–Rott (BR) equation [25–27]. This is a nonlinear singular integro-differential equation, which can be obtained formally from the Euler equations assuming that the evolution of a vortex sheet retains a curve-like structure. However, the initial data problem for the BR equation is ill-posed due to the Kelvin–Helmholtz instability [25,28]. Numerous results show that an initially real analytic vortex sheet can develop a finite time singularity in its curvature. This singularity formation was studied with asymptotic techniques in [29,30] and numerically in [30–32]. Specific examples of solutions were constructed in [33,34], where the development, in a finite time, of curvature singularity from initially analytic data was rigorously proved.

The problem of the evolution of a vortex sheet can also be approached, in the general framework of weak solutions (in the distributional sense) of the Euler equations, as a problem of

* Corresponding author. Tel.: +972 8 9342761; fax: +972 8 9342945.
E-mail addresses: bardos@ann.jussieu.fr (C. Bardos), jasmine.tal@weizmann.ac.il (J.S. Linshiz), etiti@math.uci.edu, edriss.titi@weizmann.ac.il (E.S. Titi).

0167-2789/$ - see front matter
doi:10.1016/j.physd.2008.01.003

evolution of the vorticity, which is concentrated as a measure along a surface of codimension 1. The general problem of existence for mixed-sign vortex sheet initial data remains an open question. However, in 1991, Delort [35] proved a global in time existence of weak solutions of the 2D incompressible Euler equation for the vortex sheet initial data with initial vorticity being a Radon measure of a distinguished sign; see also [36–41]. This result was later obtained as an inviscid limit of the Navier–Stokes regularizations of the Euler equations [37, 39], and as a limit of vortex methods [38,40]. The Delort result was also extended to the case of mirror-symmetric flows with distinguished sign vorticity on each side of the mirror [42]. However, the problem of uniqueness of a weak solution with fixed sign vortex sheet initial data is still unanswered; numerical evidence of non-uniqueness can be found, e.g., in [43,44]. Furthermore, the structure of weak solutions given by Delort's theorem is not known, while the Birkhoff–Rott equations assume *a priori* that a vortex sheet remains a curve at a later time. A proposed criterion for the equivalence of a weak solution of the 2D Euler equations with vorticity being a Radon measure supported on a curve, and a weak solution of the Birkhoff–Rott equations can be found in [45]. Also, another definition of weak solutions of Birkhoff–Rott equation has been proposed in [46,47]. For a recent survey of the subject, see [48].

The question of global existence of weak solutions for the three-dimensional Euler-α equations is still an open problem. On the other hand, the 2D Euler-α equations were studied in [49], where it has been shown that there exists a unique global weak solution to the Euler-α equations with initial vorticity in the space of Radon measures on $\mathbb{R}^2$, with a unique Lagrangian flow map describing the evolution of particles. In particular, it follows that the vorticity, initially supported on a curve, remains supported on a curve for all times.

We present in this paper an analytical study of the α-analogue of the Birkhoff–Rott equation, the Birkhoff–Rott-α (BR-α) model, which is induced by the 2D Euler-α equations. The BR-α model was implemented computationally in [50], where a numerical comparison between the BR-α regularization and the existing regularizing methods, such as a vortex blob model method [38,51–54], has been performed. We remark that, unlike the vortex blob methods that regularize the singular kernel in the Birkhoff–Rott equation, the α-model method regularizes instead the Euler equations themselves to obtain a smoother kernel.

We report in Section 4 our main result, which states that the initially smooth self-avoiding 2D vortex sheet, evolving under the BR-α equation, remains smooth for all times. In this short communication we only report the results and sketch some of their proofs; the full details will be reported in a forthcoming paper. In Section 2 we describe the BR-α equation. Section 3 studies the linear stability of a flat vortex sheet with uniform vorticity density for the 2D BR-α model. The linear stability analysis shows that the BR-α regularization controls the growth of high wavenumber perturbations, which is the reason for the well-posedness. This is unlike the case for the original BR problem which exhibits the Kelvin–Helmholtz instability, the main mechanism for its ill-posedness.

2. Birkhoff–Rott-α equation

The incompressible Euler equations in $\mathbb{R}^2$ in the vorticity form are given by

$$\begin{aligned} &\frac{\partial q}{\partial t} + (v \cdot \nabla)\, q = 0, \\ &v = K * q, \\ &q(x,0) = q^{in}(x), \end{aligned} \tag{1}$$

where $K(x) = \frac{1}{2\pi} \nabla^{\perp} \log|x|$, v is the fluid velocity field, $q = \operatorname{curl} v$ is the vorticity, and q^{in} is the given initial vorticity.

The 2D Euler-α model [1,2,5,55–57] is an inviscid regularization of the Euler equations, such that the vorticity is governed by the system

$$\begin{aligned} &\frac{\partial q}{\partial t} + (u \cdot \nabla)\, q = 0, \\ &u = K^{\alpha} * q, \\ &q(x,0) = q^{in}(x). \end{aligned} \tag{2}$$

Here u represents the "filtered" fluid velocity, and $\alpha > 0$ is a length scale parameter, which represents the width of the filter. At the limit $\alpha = 0$, we formally obtain the Euler equations (1). The smoothed kernel is $K^{\alpha} = G^{\alpha} * K$, where G^{α} is the Green function associated with the Helmholtz operator $\left(I - \alpha^2 \Delta\right)$, given by

$$G^{\alpha}(x) = \frac{1}{\alpha^2} G\left(\frac{x}{\alpha}\right) = -\frac{1}{\alpha^2}\frac{1}{2\pi} K_0\left(\frac{|x|}{\alpha}\right), \tag{3}$$

where $x = (x_1, x_2) \in \mathbb{R}^2$ and K_0 is a modified Bessel function of the second kind [58].

Let $\mathcal{M}(\mathbb{R}^2)$ denote the space of Radon measures on $\mathbb{R}^2$; $\mathcal{G}$ denote the group of all homeomorphisms of $\mathbb{R}^2$ which preserve the Lebesgue measure; and $\eta = \eta(\cdot, t)$ denote the Lagrangian flow map induced by (2) and obeying the equation $\partial_t \eta(x,t) = u(\eta(x,t),t)$, $\eta(x,0) = x$.

Oliver and Shkoller [49] showed global well-posedness of the Euler-α equations Eq. (2) with initial vorticity in $\mathcal{M}(\mathbb{R}^2)$ (which includes point-vortex data).

Theorem 1 (*Oliver and Shkoller [49]*). *For initial data $q^{in} \in \mathcal{M}(\mathbb{R}^2)$, there exists a unique global weak solution (in the sense of distribution) to (2) with*

$$\eta \in C^1(\mathbb{R}; \mathcal{G}), \qquad u \in C\left(\mathbb{R}; C\left(\mathbb{R}^2\right)\right),$$
$$q \in C\left(\mathbb{R}; \mathcal{M}(\mathbb{R}^2)\right).$$

The Birkhoff–Rott-α equation, based on the Euler-α equations, is derived similarly to the original Birkhoff–Rott equation. Detailed descriptions of the Birkhoff–Rott equation as a model for the evolution of the vortex sheet can be found, e.g., in [27,41,59]. We remark that while the BR equations assume *a priori* that a vortex sheet remains a curve at a later time, in the 2D Euler-α case, if the vorticity is initially supported on a curve, then due to the existence of the unique

Lagrangian flow map given by Theorem 1, it remains supported on a curve for all times. Hence the BR-α equation gives a description of the vortex sheet evolution equivalent to the description given by the 2D Euler-α equations. It is described in the following proposition.

Proposition 2. *Let q be the solution of (2) in the sense of Theorem 1. Assume, furthermore, that q has the density $\gamma(\sigma,t)$ supported on the sheet (curve) $\Sigma(t) = \left\{x = x(\sigma,t) \in \mathbb{R}^2 | \sigma_0(t) \leq \sigma \leq \sigma_1(t)\right\}$, that is, the vorticity $q(x,t)$ satisfies*

$$\int_{\mathbb{R}^2} \varphi(x) \mathrm{d}q(x,t) = \int_{\sigma_0(t)}^{\sigma_1(t)} \varphi(x(\sigma,t))\, \gamma(\sigma,t) |x_\sigma(\sigma,t)| \mathrm{d}\sigma,$$

for every $\varphi \in C_0^\infty(\mathbb{R}^2)$. Then this sheet evolves according to the equation

$$\frac{\partial}{\partial t} x(\sigma,t) = \int_{\sigma_0(t)}^{\sigma_1(t)} K^\alpha\left(x(\sigma,t) - x(\sigma',t)\right) \gamma(\sigma',t) \left|x_\sigma(\sigma',t)\right| \mathrm{d}\sigma'.$$

Additionally, if $\Gamma(\sigma,t) = \int_{\sigma^*}^{\sigma} \gamma(\sigma',t)\left|x_\sigma(\sigma',t)\right| \mathrm{d}\sigma'$, where $x(\sigma^*,t)$ is some fixed reference point on $\Sigma(t)$, defines a strictly increasing function of σ (e.g., as in the case of positive vorticity), then the evolution equation is given by the Birkhoff–Rott-α (BR-α) equation

$$\frac{\partial}{\partial t} x(\Gamma,t) = \int_{\Gamma_0}^{\Gamma_1} K^\alpha\left(x(\Gamma,t) - x(\Gamma',t)\right) \mathrm{d}\Gamma' \tag{4}$$

with $\gamma = 1/|x_\Gamma|$ being the vorticity density along the sheet.

Here σ_0, σ_1 (and, consequently, Γ_0, Γ_1) can represent either a finite length curve, or an infinite one. In our existence Theorem 3, stated in Section 4, we will make the assumption that $\gamma(\cdot,t) \in L^1(|x_\sigma| \mathrm{d}\sigma)$, i.e., $|\Gamma_0|, |\Gamma_1| < \infty$.

Notice that

$$K^\alpha(x) = \nabla^\perp \Psi^\alpha(|x|) = \frac{x^\perp}{|x|} D\Psi^\alpha(|x|),$$

where

$$\Psi^\alpha(r) = \frac{1}{2\pi}\left[K_0\left(\frac{r}{\alpha}\right) + \log r\right]$$

and

$$D\Psi^\alpha(r) = \frac{\mathrm{d}\Psi^\alpha}{\mathrm{d}r}(r) = \frac{1}{2\pi}\left[-\frac{1}{\alpha}K_1\left(\frac{r}{\alpha}\right) + \frac{1}{r}\right].$$

K_0 and K_1 denote modified Bessel functions of the second kind of orders zero and one, respectively. For details on Bessel functions, see, e.g., [58]. We remark that the smoothed kernel $K^\alpha(x)$ is a bounded continuous function, that for $\frac{|x|}{\alpha} \to 0$ behaves as $K^\alpha(x) = -\frac{1}{4\pi}\frac{1}{\alpha^2} x^\perp \log\frac{|x|}{\alpha} + O\left(\frac{|x|}{\alpha^2}\right)$. That is, it is non-singular kernel. The assumption $\gamma(\cdot,t) \in L^1(|x_\sigma| \mathrm{d}\sigma)$ allows us to show the integrability of the relevant terms, even though $|K^\alpha(x)|$ is decaying like $|x|^{-1}$ at infinity.

3. Linear stability of a flat vortex sheet with uniform vorticity density for 2D BR-α model

The initial data problem for the BR equation is highly unstable due to an ill-posed response to small perturbations called Kelvin–Helmholtz instability [25,28]. The linear stability analysis of the BR-α equation shows that the ill-posedness of the original problem is mollified, and the Kelvin–Helmholtz instability of the original system now disappears.

When the vortex sheet can be parameterized as a graph of a function in the form $x_2 = x_2(x_1,t)$ the BR-α system (4) takes the form

$$\frac{\partial x_2}{\partial t} = -\frac{\partial x_2}{\partial x_1} u_1 + u_2, \qquad \frac{\partial \gamma}{\partial t} = -\frac{\partial}{\partial x_1}(\gamma u_1), \tag{5}$$

with velocity $u = (u_1, u_2)^t$ given by

$$u(x_1,t) = \text{p.v.} \int_{\mathbb{R}} K^\alpha\left(x(x_1,t) - x(x_1',t)\right) \gamma(x_1',t) \mathrm{d}x_1',$$

where $x(x_1,t) = (x_1, x_2(x_1,t))^t$. The flat sheet $x_2^0 \equiv 0$ with uniformly concentrated intensity γ_0 is a stationary solution of (5). By linearization about the flat sheet we obtain the following linear system:

$$\frac{\partial \tilde{x}_2}{\partial t} = \tilde{u}_2, \qquad \frac{\partial \tilde{\gamma}}{\partial t} = -\gamma_0 \frac{\partial \tilde{u}_1}{\partial x_1},$$

where

$$\tilde{u}_1(x_1,t) = -\gamma_0(\operatorname{sgn}(x_1) D\Psi^\alpha(|x_1|)) * \frac{\partial \tilde{x}_2}{\partial x_1},$$
$$\tilde{u}_2(x_1,t) = \left(\operatorname{sgn}(x_1) D\Psi^\alpha(|x_1|)\right) * \tilde{\gamma},$$

and $(\tilde{x}_2, \tilde{\gamma})$ is a small perturbation about the flat sheet.

Consequently, the equation for the Fourier modes is given by

$$\frac{\mathrm{d}}{\mathrm{d}t}\begin{pmatrix} \hat{\tilde{x}}_2 \\ \hat{\tilde{\gamma}} \end{pmatrix} = \begin{pmatrix} 0 & \frac{\mathrm{i}}{2}\operatorname{sgn}(k) d(k) \\ -\mathrm{i}\frac{\gamma_0^2}{2} k^2 \operatorname{sgn}(k) d(k) & 0 \end{pmatrix} \begin{pmatrix} \hat{\tilde{x}}_2 \\ \hat{\tilde{\gamma}} \end{pmatrix}, \tag{6}$$

where

$$d(k) = \left(1 + \frac{1}{\alpha^2 k^2}\right)^{-1/2} - 1.$$

Observe that in order to calculate the Fourier transform

$$\mathcal{F}(\operatorname{sgn}(x_1) D\Psi^\alpha(|x_1|))(k) = \frac{\mathrm{i}}{2}\operatorname{sgn}(k) d(k),$$

we used the integral representation of the modified Bessel function of the second kind $K_1(x_1) = x_1 \int_1^\infty \mathrm{e}^{-x_1 t}\left(t^2 - 1\right)^{1/2} \mathrm{d}t$ (see, e.g., [58]). The eigenvalues of the coefficient matrix, given in (6), are

$$\lambda(k) = \pm\frac{1}{2}|\gamma_0| |k| \left(1 - \left(1 + \frac{1}{\alpha^2 k^2}\right)^{-1/2}\right). \tag{7}$$

To conclude, the α-regularization mollifies the Kelvin–Helmholtz instability as follows: we have an algebraic decay of the eigenvalues to zero of order $\frac{1}{\alpha^2|k|}$, as $k \to \infty$ (α fixed), while, for $\alpha \to 0$, for fixed k, we recover the eigenvalues of the original BR equations $\pm\frac{1}{2}|\gamma_0||k|$ (see, e.g., [60]).

For the sake of comparison, we observe that for the vortex blob regularization of Krasny [32], where the singular BR kernel, $K(x)$, was replaced with the smoothed kernel

$$K_\delta(x) = K(x)\frac{|x|^2}{|x|^2+\delta^2} = \frac{1}{2\pi}\frac{x^\perp}{|x|^2+\delta^2},$$

the eigenvalues are

$$\lambda(k) = \pm\frac{1}{2}\mathrm{e}^{-\delta k}|\gamma_0||k|$$

with an exponential decay to zero, as $k \to \infty$ ($\delta > 0$ is fixed). As $\delta \to 0$, for fixed k, one recovers again the eigenvalues of the original BR equations.

The behavior of the eigenvalues of the linearized system (6) indicates that high wavenumber perturbations grow exponentially in time with a rate that decays to zero as $k \to \infty$, which is the reason for the well-posedness of the α-regularized model. This is unlike the case for the original BR problem which exhibits the Kelvin–Helmholtz instability. It is worth mentioning that the α-regularization is "closer" to the original system than the vortex blob method at the high wavenumbers, due to the algebraic decay instead of the exponential one in the vortex blob method. This result was also evaluated computationally in [50].

4. Global regularity for BR-α equation

In this section we present the global existence and uniqueness of solutions of the BR-α equation (4) in the appropriate space of functions. We show that initially smooth solutions of (4) remain smooth for all times.

Let us first describe the Hölder space $C^{n,\beta}\left(\Sigma \subset \mathbb{R}; \mathbb{R}^2\right)$, $0 < \beta \le 1$, which is the space of functions $x : \Sigma \subset \mathbb{R} \to \mathbb{R}^2$, with finite norm

$$\|x\|_{C^{n,\beta}(\Sigma)} = \sum_{k=0}^{n}\left|\frac{\mathrm{d}^k}{\mathrm{d}\Gamma^k}x\right|_{C^0(\Sigma)} + \left|\frac{\mathrm{d}^n}{\mathrm{d}\Gamma^n}x\right|_{\beta(\Sigma)},$$

where

$$|x|_{C^0(\Sigma)} = \sup_{\Gamma\in\Sigma}|x(\Gamma)|$$

and $|\cdot|_\beta$ is the Hölder semi-norm

$$|x|_{\beta(\Sigma)} = \sup_{\substack{\Gamma,\Gamma'\in\Sigma\\ \Gamma\ne\Gamma'}}\frac{\left|x(\Gamma)-x\left(\Gamma'\right)\right|}{|\Gamma-\Gamma'|^\beta}.$$

We also use the notation

$$|x|_* = \inf_{\substack{\Gamma,\Gamma'\in\Sigma\\ \Gamma\ne\Gamma'}}\frac{\left|x(\Gamma)-x\left(\Gamma'\right)\right|}{|\Gamma-\Gamma'|}.$$

Next we state our main result.

Theorem 3. *Let $n \ge 1$, $0 < \beta < 1$, $x(\Gamma, 0) = x_0(\Gamma) \in C^{n,\beta}(\Gamma_0, \Gamma_1) \cap \{|x|_* > 0\}$; then for any $T > 0$ there is a unique solution $x \in C^1\left([-T, T]; C^{n,\beta}(\Gamma_0, \Gamma_1) \cap \{|x|_* > 0\}\right)$ of (4).*

In particular, if $x_0 \in C^\infty(\Gamma_0, \Gamma_1) \cap \{|x|_* > 0\}$ then $x \in C^1([-T, T]; C^\infty(\Gamma_0, \Gamma_1) \cap \{|x|_* > 0\})$.

We remark that, although the kernel K^α is a continuous bounded function, its derivatives are unbounded near the origin, and the condition $|x|_* > 0$, which generally means self-avoiding curves, allows us to show the integrability of the relevant terms. Furthermore, it is also worth mentioning that $|x|_*$ being bounded away from zero is similar to the chord arc hypothesis [61], used later in [46,47].

Now we sketch the main steps involved in the proof of Theorem 3. First, we apply the Contraction Mapping Principle to the BR-α equation (4) to prove the short time existence and uniqueness of solutions in the appropriate space of functions. We show that initially $C^{1,\beta}$ smooth solutions of (4) remain $C^{1,\beta}$ smooth for a finite short time. Next, we derive an *a priori* bound for the controlling quantity for continuing the solution for all time. Then we extend the result for higher derivatives. The full details will be reported in a forthcoming paper.

Sketch of the proof. We consider the BR-α equation as an evolution functional equation in the Banach space $C^{n,\beta}$

$$\begin{aligned}&\frac{\partial x}{\partial t}(\Gamma, t) = \int_{\Gamma_0}^{\Gamma_1} K^\alpha\left(x(\Gamma, t) - x\left(\Gamma', t\right)\right)\mathrm{d}\Gamma',\\ &x(\Gamma, 0) = x_0(\Gamma) \in C^{n,\beta} \cap \{|x|_* > 0\}\end{aligned} \tag{8}$$

with $\gamma = 1/|x_\Gamma|$ being the vorticity density along the sheet. Notice that the initial density is well defined for the subset $\{|x|_* > 0\}$.

Step 1. We show the local existence and uniqueness of solutions. To apply the Contraction Mapping Principle to the BR-α equation (8) we first prove the following proposition:

Proposition 4. *Let $1 < M < \infty$, $-\infty < \Gamma_0 < \Gamma_1$, and let S^M be the set*

$$\left\{\Gamma \mapsto x(\Gamma) \in C^{1,\beta}(\Gamma_0, \Gamma_1), |x_\Gamma|_{C^0} < M, |x|_* > \frac{1}{M}\right\}.$$

Then the mapping $x(\Gamma, t) \mapsto$

$$u(x(\Gamma, t), t) = \int_{\Gamma_0}^{\Gamma_1} K^\alpha\left(x(\Gamma, t) - x\left(\Gamma', t\right)\right)\mathrm{d}\Gamma'$$

defines a locally Lipschitz continuous map from S^M into $C^{1,\beta}$.

This implies the local existence and uniqueness of solutions:

Proposition 5. *Given $x_0(\Gamma) \in C^{1,\beta}(\Gamma_0, \Gamma_1) \cap \{|x|_* > 0\}$, there exists $1 < M < \infty$ and a time $T(M)$ such that the system (8) has a unique local solution $x \in C^1((-T(M), T(M)); S^M)$.*

Step 2. The local solutions obtained can be continued in time provided that we have global, in time, bounds on $\frac{1}{|x(\cdot,t)|_*}$

and $|x_\Gamma(\cdot,t)|_\beta$. To control these quantities we need to bound $\int_0^T \|\nabla_x u(x(\cdot,t),t)\|_{L^\infty(\Gamma_0,\Gamma_1)}\,\mathrm{d}t$. We sketch the proof of this bound. We write $\nabla_x u(x(\Gamma,t),t)$ as

$$\begin{aligned}\nabla_x u(x(\Gamma,t),t) &= \int_{\Gamma_0}^{\Gamma_1} \nabla_x K^\alpha\left(x(\Gamma,t)-x\left(\Gamma',t\right)\right)\mathrm{d}\Gamma' \\ &= \int_{E_\varepsilon} + \int_{(\Gamma_0,\Gamma_1)\setminus E_\varepsilon} = I_1 + I_2,\end{aligned}$$

where

$$E_\varepsilon = \left\{\Gamma' \in (\Gamma_0,\Gamma_1) : \frac{\left|x(\Gamma,t)-x\left(\Gamma',t\right)\right|}{\alpha} < \varepsilon\right\},$$

for a fixed small $0 < \varepsilon < 1$, to be further refined later. Let η denote the unique Lagrangian flow map given by Theorem 1. Denote the distance between two points $\eta(x,t)$ and $\eta(x',t)$ by $r(t) = \left|\eta(x,t) - \eta\left(x',t\right)\right|$, where $r(0) = \left|x - x'\right|$.

Then, using the estimate (2.14) of [49], we have

$$\begin{aligned}\left|\frac{\mathrm{d}}{\mathrm{d}t} r(t)\right| &\le \int_{\mathbb{R}^2} \left|K^\alpha(x,y) - K^\alpha\left(x',y\right)\right| |q(y,t)|\,\mathrm{d}y \\ &\le C\frac{1}{\alpha}\varphi\left(\frac{r(t)}{\alpha}\right)\|q\|_{M(\mathbb{R}^2)} \\ &= C\frac{1}{\alpha}\varphi\left(\frac{r(t)}{\alpha}\right)\left\|q^{in}\right\|_{M(\mathbb{R}^2)},\end{aligned}$$

where

$$\varphi(r) = \begin{cases} 0, & r = 0, \\ r(1-\log r), & 0 < r < 1, \\ 1, & r \ge 1. \end{cases}$$

By comparison with the solution of the differential equation

$$\frac{\mathrm{d}}{\mathrm{d}t} r(t) = -C\frac{1}{\alpha}\varphi\left(\frac{r(t)}{\alpha}\right)\left\|q^{in}\right\|_{\mathcal{M}(\mathbb{R}^2)},$$

we can choose $\varepsilon = \varepsilon\left(t, \frac{1}{\alpha}, \left\|q^{in}\right\|_{\mathcal{M}(\mathbb{R}^2)}\right)$ small enough such that, for $\frac{|x(\Gamma,t)-x(\Gamma',t)|}{\alpha} < \varepsilon$,

$$\begin{aligned}&\frac{\left|x(\Gamma,t)-x\left(\Gamma',t\right)\right|}{\alpha} \\ &\quad\ge \left(\frac{\left|x(\Gamma,0)-x\left(\Gamma',0\right)\right|}{\alpha}\right)^{\mathrm{e}^{tC_1}} \mathrm{e}^{1-\mathrm{e}^{tC_1}}, \qquad (9)\end{aligned}$$

where $C_1 = \frac{C}{\alpha^2}\left\|q^{in}\right\|_{\mathcal{M}(\mathbb{R}^2)}$. Now, using also that $|x_0|_*$ is bounded away from zero, we can bound $\frac{|x(\Gamma,t)-x(\Gamma',t)|}{\alpha}$ from below, which in turn implies the bound

$$I_1 \le C\left(t, \frac{1}{\alpha}, \left\|q^{in}\right\|_{\mathcal{M}(\mathbb{R}^2)}, |x_0|_*\right),$$

while to bound I_2, we use the boundedness of $|\nabla_x K^\alpha(x(\Gamma,t), x(\Gamma',t))|$ in $\{\Gamma' \in (\Gamma_0,\Gamma_1) : \frac{|x(\Gamma,t)-x(\Gamma',t)|}{\alpha} \ge \varepsilon\}$. Hence

$$\begin{aligned}&\int_0^T \|\nabla_x u(x(\cdot,t),t)\|_{L^\infty(\Gamma_0,\Gamma_1)}\,\mathrm{d}t \\ &\quad\le C\left(\frac{1}{\alpha}, T, \left\|q^{in}\right\|_{\mathcal{M}(\mathbb{R}^2)}, |x_0|_*\right). \qquad (10)\end{aligned}$$

Now, by the Grönwall inequality the bound (10) provides bounds on $\frac{1}{|x(\cdot,t)|_*}$ and $|x_\Gamma(\cdot,t)|_{C^0}$ on $[0,T]$. The bound on $|x_\Gamma(\cdot,t)|_\beta$ on $[0,T]$ is a consequence of

$$\frac{\mathrm{d}}{\mathrm{d}t} x_\Gamma(\Gamma,t) = \nabla_x u(x(\Gamma,t),t)\cdot x_\Gamma(\Gamma,t),$$

$$|\nabla_x u(x(\cdot,t),t)|_\beta \le C\left(\frac{1}{\alpha}, |x_\Gamma|_{L^\infty}, |x|_*, \Gamma_1 - \Gamma_0\right),$$

(10) and the Grönwall inequality.

This yields global in time existence and uniqueness of $C^{1,\beta}$ solutions of (8).

Step 3. To provide an a priori bound for higher derivatives in terms of lower ones, we show that for $x \in S^M \cap C^{n,\beta}(\Gamma_0,\Gamma_1)$,

$$|u(x(\cdot,t),t)|_{n,\beta} \le C\left(\frac{1}{\alpha}, M, |x(\cdot,t)|_{n-1,\beta}\right)|x(\cdot,t)|_{n,\beta},$$

and hence by the Grönwall inequality and the induction argument, it is enough to control $|x(\cdot,t)|_*$ and $|x_\Gamma(\cdot,t)|_\beta$, to guarantee that $x(\Gamma,t) \in C^{n,\beta}(\Gamma_0,\Gamma_1)$, for all $n \ge 1$ (and consequently in $C^\infty(\Gamma_0,\Gamma_1)$, whenever $x_0 \in C^\infty(\Gamma_0,\Gamma_1) \cap \{|x|_* > 0\}$). $\square$

5. Conclusions

The 2D Euler-α model [1,2,5,55–57] is an inviscid regularization of the Euler equations. In [49] there has been shown the existence of a unique global weak solution of 2D Euler-α equations, when the initial vorticity is in the space of Radon measures on $\mathbb{R}^2$. The Birkhoff–Rott-α equation for the evolution of the 2D vortex sheet is induced by the 2D Euler-α equations, and it is an α-analogue of the Birkhoff–Rott equation, induced by the 2D Euler equations.

The structure of weak solutions of 2D Euler equations, for the vortex sheet initial data with initial vorticity being a Radon measure of a distinguished sign, given by Delort [35–41] is not known, yet the BR equations assume *a priori* that a vortex sheet remains a curve at a later time. In contrast, in the 2D Euler-α case, if the vorticity is initially supported on a curve, it remains supported on a curve for all times; hence the BR-α equation gives an equivalent description of the vortex sheet evolution, as the 2D Euler-α equations.

In this paper we report the global regularity of the BR-α approximation for the 2D vortex sheet evolution. We show that the initially smooth self-avoiding vortex sheet remains smooth for all times, under the condition that the initial density is an integrable function of the vortex curve with respect to the arc-length measure.

Unlike the original BR problem which exhibits the Kelvin–Helmholtz instability, the linearized, about the flat solution, BR-α model has growth rates that decay to zero for large wavenumbers, larger than $O(\alpha)$. This, in turn, is also an indication of the role that the parameter α plays in slowing the process of formation of scales smaller than α. Another indication that α controls the development of small scales, smaller than α, arises from the Lagrangian description of the flow. The lower bound (9) implies that the evolution of small scales, relative to α, at each instant of time, is controlled from below by the initial ratio. That is, for any finite time, the spatial scales smaller than alpha develop at a controlled rate.

The linear stability analysis also implies that the BR-α approximation could be closer to the original BR equation than the existing regularizing methods, such as the vortex blob model, due to the less regular kernel. A numerical study comparing the α and the vortex blob regularizations for planar and axisymmetric vortex filaments and sheets is reported in [50].

The full details of the results reported in this paper will be presented in a forthcoming paper.

Acknowledgments

C.B. would like to thank the Faculty of Mathematics and Computer Science at the Weizmann Institute of Science where this work was initiated for kind hospitality. This work was supported in part by the BSF grant no. 2004271, the ISF grant no. 120/06, and the NSF grants no. DMS-0504619 and no. DMS-0708832.

References

[1] D.D. Holm, J.E. Marsden, T.S. Ratiu, The Euler–Poincaré equations and semidirect products with applications to continuum theories, Adv. Math. 137 (1) (1998) 1–81.

[2] D.D. Holm, J.E. Marsden, T.S. Ratiu, Euler–Poincaré models of ideal fluids with nonlinear dispersion, Phys. Rev. Lett. 80 (19) (1998) 4173–4176.

[3] S. Chen, C. Foias, D.D. Holm, E. Olson, E.S. Titi, S. Wynne, Camassa–Holm equations as a closure model for turbulent channel and pipe flow, Phys. Rev. Lett. 81 (24) (1998) 5338–5341.

[4] S. Chen, C. Foias, D.D. Holm, E. Olson, E.S. Titi, S. Wynne, The Camassa–Holm equations and turbulence, Physica D 133 (1–4) (1999) 49–65.

[5] S. Chen, C. Foias, D.D. Holm, E. Olson, E.S. Titi, S. Wynne, A connection between the Camassa–Holm equations and turbulent flows in channels and pipes, Phys. Fluids 11 (8) (1999) 2343–2353, The International Conference on Turbulence (Los Alamos, NM, 1998).

[6] C. Foias, D.D. Holm, E.S. Titi, The Navier–Stokes-alpha model of fluid turbulence, Physica D 152/153 (2001) 505–519, Advances in nonlinear mathematics and science.

[7] C. Foias, D.D. Holm, E.S. Titi, The three dimensional viscous Camassa–Holm equations, and their relation to the Navier–Stokes equations and turbulence theory, J. Dynam. Differential Equations 14 (1) (2002) 1–35.

[8] D.D. Holm, E.S. Titi, Computational models of turbulence: The LANS-alpha model and the role of global analysis, SIAM News 38(7).

[9] A. Cheskidov, D.D. Holm, E. Olson, E.S. Titi, On a Leray-α model of turbulence, Proc. R. Soc. Lond. Ser. A Math. Phys. Eng. Sci. 461 (2055) (2005) 629–649.

[10] A.A. Ilyin, E. Lunasin, E.S. Titi, A Modified-Leray-α subgrid scale model of turbulence, Nonlinearity 19 (4) (2006) 879–897.

[11] M.I. Vishik, E.S. Titi, V.V. Chepyzhov, Trajectory attractor approximations of the 3D Navier–Stokes system by a Leray-α model, Russian Math. Dokl. 71 (2005) 92–95 (Translated from Russian).

[12] V.V. Chepyzhov, E.S. Titi, M.I. Vishik, On the convergence of solutions of the Leray-α model to the trajectory attractor of the 3D Navier–Stokes system, Discrete Contin. Dyn. Syst. 17 (3) (2007) 481–500.

[13] K. Mohseni, B. Kosović, S. Shkoller, J.E. Marsden, Numerical simulations of the Lagrangian averaged Navier–Stokes equations for homogeneous isotropic turbulence, Phys. Fluids 15 (2) (2003) 524–544.

[14] W. Layton, R. Lewandowski, On a well-posed turbulence model, Discrete Contin. Dyn. Syst. Ser. B 6 (1) (2006) 111–128.

[15] W. Layton, R. Lewandowski, A simple and stable scale-similarity model for large eddy simulation: Energy balance and existence of weak solutions, Appl. Math. Lett. 16 (8) (2003) 1205–1209.

[16] R. Lewandowski, Vorticities in a LES model for 3D periodic turbulent flows, J. Math. Fluid. Mech. 8 (2006) 398–422.

[17] B.J. Geurts, D.D. Holm, Regularization modeling for large-eddy simulation, Phys. Fluids 15 (1) (2003) L13–L16.

[18] B.J. Geurts, D.D. Holm, Leray and LANS-α modelling of turbulent mixing, J. Turbul. 7 (10) (2006) 1–33.

[19] Y. Cao, E. Lunasin, E.S. Titi, Global well-posedness of the three-dimensional viscous and inviscid simplified Bardina turbulence models, Commun. Math. Sci. 4 (4) (2006) 823–848.

[20] J. Bardina, J.H. Ferziger, W.C. Reynolds, Improved subgrid-scale models for large-eddy simulation, Am. Inst. Aeronaut. Astronaut. Paper (1980) 80–1357.

[21] D.D. Holm, B.T. Nadiga, Modeling mesoscale turbulence in the barotropic double-gyre circulation, J. Phys. Oceanogr. 33 (11) (2003) 2355–2365.

[22] C. Cao, D.D. Holm, E.S. Titi, On the Clark-α model of turbulence: global regularity and long-time dynamics, J. Turbul. 6 (2005) Paper 20, 11 pp. (electronic).

[23] R.A. Clark, J.H. Ferziger, W.C. Reynolds, Evaluation of subgrid-scale models using an accurately simulated turbulent flow, J. Fluid Mech. 91 (1) (1979) 1–16.

[24] J.S. Linshiz, E.S. Titi, Analytical study of certain magnetohydrodynamic-alpha models, J. Math. Phys. 48 (6) (2007) 065504, 28.

[25] G. Birkhoff, Helmholtz and Taylor instability, in: Proc. Sympos. Appl. Math., Vol. XIII, American Mathematical Society, Providence, RI, 1962, pp. 55–76.

[26] N. Rott, Diffraction of a weak shock with vortex generation, J. Fluid Mech. 1 (1956) 111–128.

[27] P.G. Saffman, Vortex Dynamics, in: Cambridge Monographs on Mechanics and Applied Mathematics, Cambridge University Press, New York, 1992.

[28] P.G. Saffman, G.R. Baker, Vortex interactions, Ann. Rev. Fluid Mech. 11 (1979) 95–121.

[29] D.W. Moore, The spontaneous appearance of a singularity in the shape of an evolving vortex sheet, Proc. R. Soc. Lond. A 365 (1720) (1979) 105–119.

[30] S.J. Cowley, G.R. Baker, S. Tanveer, On the formation of Moore curvature singularities in vortex sheets, J. Fluid Mech. 378 (2000) 233–267.

[31] D.I. Meiron, G.R. Baker, S.A. Orszag, Analytic structure of vortex sheet dynamics. I. Kelvin–Helmholtz instability, J. Fluid Mech. 114 (1982) 283–298.

[32] R. Krasny, A study of singularity formation in a vortex sheet by the point-vortex approximation, J. Fluid Mech. 167 (1986) 65–93.

[33] J. Duchon, R. Robert, Global vortex sheet solutions of Euler equations in the plane, J. Differential Equations 73 (2) (1988) 215–224.

[34] R.E. Caflisch, O.F. Orellana, Singular solutions and ill-posedness for the evolution of vortex sheets, SIAM J. Math. Anal. 20 (2) (1989) 293–307.

[35] J.-M. Delort, Existence de nappes de tourbillon en dimension deux, J. Amer. Math. Soc. 4 (3) (1991) 553–586.

[36] L.C. Evans, S. Muller, Hardy spaces and the two-dimensional Euler equations with nonnegative vorticity, J. Amer. Math. Soc. 7 (1) (1994) 199–219.

[37] A. Majda, Remarks on weak solutions for vortex sheets with a distinguished sign, Indiana Univ. Math. J 42 (3) (1993) 921–939.

[38] J.G. Liu, Z. Xin, Convergence of vortex methods for weak solutions to the 2D Euler equations with vortex sheet data, Comm. Pure Appl. Math. 48 (6) (1995) 611–628.

[39] S. Schochet, The weak vorticity formulation of the 2D Euler equations and concentration-cancellation, Comm. Partial Differential Equations 20 (1995) 1077–1104.

[40] S. Schochet, Point-vortex method for periodic weak solutions of the 2-D Euler equations, Comm. Pure Appl. Math. 49 (9) (1996) 911–965.

[41] A.J. Majda, A.L. Bertozzi, Vorticity and Incompressible Flow, in: Cambridge Texts in Applied Mathematics, vol. 27, Cambridge University Press, Cambridge, 2002.

[42] M.C. Lopes Filho, H.J. Nussenzveig Lopes, Z. Xin, Existence of vortex sheets with reflection symmetry in two space dimensions, Arch. Ration. Mech. Anal. 158 (3) (2001) 235–257.

[43] D.I. Pullin, On similarity flows containing two-branched vortex sheets, in: Mathematical aspects of vortex dynamics (Leesburg, VA, 1988), SIAM, Philadelphia, PA, 1989, pp. 97–106.
[44] M.C. Lopes Filho, J. Lowengrub, H.J. Nussenzveig Lopes, Y. Zheng, Numerical evidence of nonuniqueness in the evolution of vortex sheets, M2AN Math. Model. Numer. Anal. 40 (2) (2006) 225–237.
[45] M.C. Lopes Filho, H.J. Nussenzveig Lopes, S. Schochet, A criterion for the equivalence of the Birkhoff–Rott and Euler descriptions of vortex sheet evolution, Trans. Amer. Math. Soc. 359 (9) (2007) 4125–4142. (electronic).
[46] S. Wu, Recent progress in mathematical analysis of vortex sheets, in: Proceedings of the International Congress of Mathematicians, Vol. III (Beijing, 2002), Higher Ed. Press, Beijing, 2002, pp. 233–242.
[47] S. Wu, Mathematical analysis of vortex sheets, Comm. Pure Appl. Math. 59 (8) (2006) 1065–1206.
[48] C. Bardos, E.S. Titi, Euler equations of incompressible ideal fluids, UMN 62 (3(375)) (2007) 5–46.
[49] M. Oliver, S. Shkoller, The vortex blob method as a second-grade non-Newtonian fluid, Comm. Partial Differential Equations 26 (1–2) (2001) 295–314.
[50] D.D. Holm, M. Nitsche, V. Putkaradze, Euler-alpha and vortex blob regularization of vortex filament and vortex sheet motion, J. Fluid Mech. 555 (2006) 149–176.
[51] A.J. Chorin, P.J. Bernard, Discretization of a vortex sheet, with an example of roll-up (for elliptically loaded wings), J. Comput. Phys. 13 (1973) 423–429.
[52] R. Krasny, Desingularization of periodic vortex sheet roll-up, J. Comput. Phys. 65 (2) (1986) 292–313.
[53] G.-H. Cottet, P.D. Koumoutsakos, Vortex Methods: Theory and Practice, Cambridge University Press, 2000.
[54] G.R. Baker, L.D. Pham, A comparison of blob methods for vortex sheet roll-up, J. Fluid Mech. 547 (2006) 297–316.
[55] D.D. Holm, Variational principles for Lagrangian-averaged fluid dynamics, J. Phys. A 35 (3) (2002) 679–688.
[56] J.E. Marsden, S. Shkoller, The anisotropic Lagrangian averaged Euler and Navier–Stokes equations, Arch. Ration. Mech. Anal. 166 (1) (2003) 27–46.
[57] P. Constantin, An Eulerian–Lagrangian approach to the Navier–Stokes equations, Comm. Math. Phys. 216 (3) (2001) 663–686.
[58] G.N. Watson, A Treatise on the Theory of Bessel Functions, Cambridge Mathematical Library, Cambridge University Press, Cambridge, 1995, (reprint of the second (1944) edition).
[59] C. Marchioro, M. Pulvirenti, Mathematical Theory of Incompressible Nonviscous Fluids, in: Applied Mathematical Sciences, vol. 96, Springer-Verlag, New York, 1994.
[60] C. Sulem, P.-L. Sulem, C. Bardos, U. Frisch, Finite time analyticity for the two- and three-dimensional Kelvin–Helmholtz instability, Comm. Math. Phys. 80 (4) (1981) 485–516.
[61] G. David, Courbes corde-arc et espaces de Hardy généralisés, Ann. Inst. Fourier (Grenoble) 32 (3) (1982) 227–239. xi.

Available online at www.sciencedirect.com
ScienceDirect
Physica D 237 (2008) 1912–1920
PHYSICA D
www.elsevier.com/locate/physd

3D Euler about a 2D symmetry plane

Miguel D. Bustamante*, Robert M. Kerr

Mathematics Institute, University of Warwick, Coventry CV4 7AL, United Kingdom

Available online 15 February 2008

Abstract

Initial results from new calculations of interacting anti-parallel Euler vortices are presented with the objective of understanding the origins of singular scaling presented by Kerr [R.M. Kerr, Evidence for a singularity of the three-dimensional, incompressible Euler equations, Phys. Fluids 5 (1993) 1725–1746] and the lack thereof by Hou and Li [T.Y. Hou, R. Li, Dynamic depletion of vortex stretching and non-blowup of the 3-D incompressible Euler equations, J. Nonlinear Sci. 16 (2006) 639–664]. Core profiles designed to reproduce the two results are presented, new more robust analysis is proposed, and new criteria for when calculations should be terminated are introduced and compared with classical resolution studies and spectral convergence tests. Most of the analysis is on a $512 \times 128 \times 2048$ mesh, with new analysis on a just completed $1024 \times 256 \times 2048$ used to confirm trends. One might hypothesize that there is a finite-time singularity with enstrophy growth like $\Omega \sim (T_c - t)^{-\gamma_\Omega}$ and vorticity growth like $\|\boldsymbol{\omega}\|_\infty \sim (T_c - t)^{-\gamma}$. The new analysis would then support $\gamma_\Omega \approx 1/2$ and $\gamma > 1$. These represent modifications of the conclusions of Kerr [op. cit.]. Issues that might arise at higher resolution are discussed.

PACS: 47.10.A-; 47.11.Kb; 47.15.ki

Keywords: Euler equations; Fluid singularities; Vortex dynamics

1. Introduction

One definition of solving Euler's 3D incompressible equations [1] is determining whether or not they dynamically generate a finite-time singularity if the initial conditions are smooth, in a bounded domain and have finite energy. The primary analytic constraint that must be satisfied [2] is:

$$\int_0^T \|\boldsymbol{\omega}\|_\infty \mathrm{d}t \to \infty \tag{1}$$

where $\|\boldsymbol{\omega}\|_\infty$ is the maximum of vorticity over all space. To date, [3] remains the only fully 3D simulation of Euler's equations with evidence for a singularity consistent with this and related constraints [4]. Growth of the enstrophy production and stretching along the vorticity, plus collapse of positions, supported this claim [3]. Additional weaker evidence related to blowup in velocity and collapsing scaling functions was presented later [5].

There is only weak numerical evidence supporting these claims [6,7]. In a recent paper, as described in one of the invited talks of this symposium, [8] found evidence that the above scenario failed at late times.

This contribution will first comment on four issues raised at the symposium, then present preliminary new results. The four issues are:

- How should spurious high-wavenumber energy in spectral methods be suppressed?
- What criteria should be used to determine when numerical errors are substantial?
- What effect do the initial conditions have on singular trends? A cleaner initial condition is proposed.
- We introduce a new approach for determining whether there is singular behavior of the primary properties and the associated scaling. This is applied to both new and old data.

All calculations will be in the following domain: $L_x \times L_y \times L_z = 4\pi \times 4\pi \times 2\pi$ with free-slip symmetries in y and z and periodic in x with up to $n_x \times n_y \times n_z = 1024 \times 256 \times 2048$ mesh points. Using these symmetries only one-half of one of the anti-parallel vortices needs to be simulated.

* Corresponding author.
E-mail address: mig_busta@yahoo.com (M.D. Bustamante).

0167-2789/$ - see front matter © 2008 Elsevier B.V. All rights reserved.
doi:10.1016/j.physd.2008.02.007

The "symmetry" plane will be defined as xz free-slip symmetry through the maximum perturbation of the initial vortices and the "dividing" plane will be defined as the xy free-slip symmetry between the vortices.

2. How should spurious high-wavenumber energy in spectral methods be suppressed?

A generic difficulty in applying spectral methods to localized physical space phenomena is the accumulation of spurious high-wavenumber energy that leads to numerical errors.

What is the best approach for eliminating these spurious modes? We have compared the old-fashioned 2/3rds dealiasing versus the recently proposed 36th-power hyperviscous filter [8, 11]. Detailed tests to be described in a later paper show that the latter is better in the sense that for several quantities, such as the peak vorticity, lower resolution calculations follow the high-resolution cases longer. But a combination of the two approaches works even better, and that is what is used here.

Still, caution is required for any of these approaches as the hyperviscosity can dissipate small structures such as the anomalous negative vorticity in the squared-off profile below. Surprisingly the 36th-order hyperviscosity does not appear to produce the ghost vortices that are a known artifact of lower-order schemes.

3. What criteria should be used to determine when numerical errors are substantial?

There are traditionally two approaches to this problem, one emphasizing local quantities such as $\|\boldsymbol{\omega}\|_\infty$, and the other emphasizing global quantities such as the mean square vorticity or enstrophy. We use both.

3.1. Local quantities and resolution

To determine local resolution it is important to check the convergence of local quantities such as:

- The maximum of vorticity $\|\boldsymbol{\omega}\|_\infty$. The location of $\|\boldsymbol{\omega}\|_\infty$ will be defined as $\boldsymbol{x}_\infty$.
- The local stretching of vorticity

$$\alpha = \hat{\boldsymbol{\omega}}_i e_{ij} \hat{\boldsymbol{\omega}}_j \tag{2}$$

where $\hat{\boldsymbol{\omega}} = \boldsymbol{\omega}/|\omega|$ and $e_{ij} = \frac{1}{2}(u_{i,j} + u_{j,i})$.

Following earlier work [3,8], we use the criteria that $\boldsymbol{x}_\infty$ cannot be closer than 6 mesh points from the dividing plane.

3.2. Integral quantities

Examples of integral quantities we could monitor are: energy, circulation (which are in principle conserved), enstrophy and helicity (which are in principle changing).

(i) Energy is robustly conserved by spectral methods even when under-resolved and therefore is not a useful test. Convergence of the energy spectrum [8] is only a partial test because it neglects phase errors.

(ii) Circulation in the upper half of the symmetry plane (i.e., the $z > 0$ half of the xz-plane, which is perpendicular to the primary direction of vorticity y) is conserved. Circulation in the equivalent half of the dividing plane is also conserved. In all of the initial conditions considered here, it is initially zero and ideally should remain so. Therefore, the circulations of the symmetry and dividing planes, $\sigma_y = \int_{z>0} \omega_y(x, 0, z, t)\mathrm{d}x\,\mathrm{d}z$ and $\sigma_z = \int_{y>0} \omega_z(x, y, 0, t)\mathrm{d}x\,\mathrm{d}y$ were monitored.

We have found that serious depletion of σ_y is controlled by n_z and the time this begins is independent of the high-wavenumber filter. Once n_z is set, by convergence of $\|\boldsymbol{\omega}\|_\infty$, we find that there is good convergence if $n_x = n_z/2$ and $n_y = n_z/4$. A later paper will provide more details on these convergence tests. We will violate the condition on n_y at late times due to current memory restrictions.

Without the circulation test, it is difficult to draw conclusions about the late times in [8] where they claim to see divergence from the scaling of Kerr [3].

(iii) Enstrophy Ω grows in time, so one test is to check how it is balanced by its production Ω_p, which we determine directly. The enstrophy and its production are

$$\Omega = \int \mathrm{d}V \omega^2, \qquad \Omega_p = 2\int \mathrm{d}V \omega_i e_{ij} \omega_j. \tag{3}$$

(iv) Helicity grows within the quadrant simulated (not over the full anti-parallel geometry), but its production is determined by pressure which has not been calculated.

4. What is the effect of the initial conditions on the potentially singular behavior?

4.1. Earlier descriptions

As ambiguities in the earlier description of the initial condition of [3] led to differences in the initial condition of Hou and Li [8], the community needs a clear description of a reproducible, clean initial condition that yields the trends of Kerr [3]. Ideally, we want an initial condition whose vorticity is purely positive in the upper half of the symmetry plane, which following Kelvin's theorem will remain positive for all subsequent times. These steps were used [3] to massage the vortex profile in order to achieve this:

(A) The first step in creating the initial profile of the vorticity core is to use an explicit function where the value and all derivatives went smoothly to zero at a given radius. See references in [3] for earlier work that had used a similar profile. To this, a localized perturbation in its position in x was given [9].

(B) The second step is to remove high-wavenumber noise by applying a symmetric high-wavenumber filter of the form: $\exp(-a(k_x^2 + k_y^2 + k_z^2)^2)$. Kerr [10] showed the undesirable side-effects if this is not done. However, it has become apparent that the high-wavenumber filter is not sufficient.

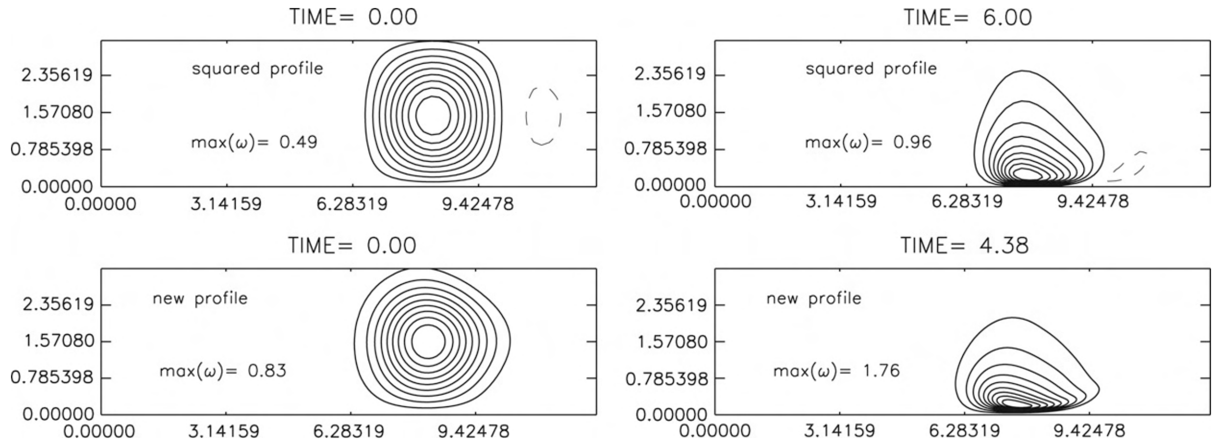

Fig. 1. ω_y in the symmetry plane from two initial conditions for $t = 0$ and for early times with roughly the same growth in $\max(\omega_y)$ in the symmetry plane. The first squared profile is nearly the same as used by [8] using step (A) with $\max(\omega_y) = 0.49$ in the symmetry plane (over all space $\|\boldsymbol{\omega}\|_\infty = \max(|\omega|) = .67$) and for step (B) a squared-off high-wavenumber filter $(\exp(-a(k_x^4 + k_y^4 + k_z^4)))$. Note the large negative vorticity in the lee (right) of the primary vortex as in [8] (Fig. 2) and how this is entrained underneath the primary vortex at $t = 6$, whereupon the hyperviscous filter will dissipate it. In the new profile step (C) is included: adding positive $\omega_y(z)$. In this case $\max(\omega_y) = 0.83$ in the symmetry plane and over all space $\|\boldsymbol{\omega}\|_\infty = 1.05$. There is no anomalous negative vorticity and numerical solutions require less resolution.

4.2. *Effect of a negative region*

The upper frames in Fig. 1 come from a reproduction of the squared-off profile of Hou and Li [8] which follows the procedure above with the exception of using a different high-wavenumber filter. Note the negative region in the lee of the primary vortex and how this is sucked underneath the primary vortex at $t = 6$. The $t = 6$ frame represents the vortices simulated with the 36th-order hyperviscosity [8,11]. For $t > 6$ this secondary vortex is dissipated by the hyperviscosity and circulation is dissipated, meaning these calculations are not faithfully representing the Euler equations. Without the hyperviscosity, numerical noise would dominate as an extra boundary layer needs to be resolved.

4.3. *Final step (C) for purely positive*

What is apparently missing from the previous description [3] is the addition of a mean shear designed to remove the final negative regions in the symmetry plane. This was achieved before [3] as part of an interpolation procedure from a uniform mesh to a Chebyshev mesh. Here it is imposed. Details will appear in a full paper. Initial vorticity in the symmetry plane and a slightly later time ($t = 4.38$) are shown. This is the initial condition for which we have now done up to $1024 \times 256 \times 2048$ calculations to assess the scaling proposed earlier [3].

5. A new approach for determining whether there is singular behavior of the primary properties and the associated scaling

Once reliable data (according to the criteria discussed above) has been obtained, it is common to interpret it in terms of power laws and other simple formulae. For example, assume that

$$f(t) \sim C/(T_c - t)^\gamma. \qquad (4)$$

To properly find all three free parameters (C, T_c and γ) to a set of points requires a minimization procedure.

Kerr [3] avoided this by assuming particularly simple values for γ for several quantities. In particular $\gamma = 1$ was assumed for $\|\boldsymbol{\omega}\|_\infty$, for the maximum of the stretching of the vorticity (2) in the symmetry plane: $\max(\alpha)|_{y=0}$, and for the enstrophy production (3). This procedure was extended to the velocity by assuming that $\gamma_u = 1/2$ for $\sup(|u|)$ [5].

While fits with these assumptions gave consistent results for the singular time T_c, this consistency existed only at late times when resolution was becoming questionable. Analysis of this data by two new methods has shown that the lack of scaling at earlier times is due in part to some of the more restrictive assumptions that were made.

5.1. *Three-parameter fitting*

Our first indication that earlier assumptions [3,5] might be incorrect was obtained by allowing γ to be free. The three parameters (C, T_c and γ) were then obtained as follows: by minimizing the sum of squares of the differences between the logarithm of the data and the logarithm of the fit function, with respect to C and γ, allows one to solve for these two parameters in terms of T_c. Then the sum of squares is further minimized with respect to T_c to obtain all three parameters.

This analysis was applied to $\|\boldsymbol{\omega}\|_\infty$ and Ω_p, the enstrophy production, both of which previously were assumed to have $1/(T_c - t)$ behavior.

It was immediately observed that

- The fitting parameters depended upon the range of times chosen.
- γ in each case was consistently greater than 1.

This would not be inconsistent with known bounds. Recall if power-law behavior is expected for $\|\boldsymbol{\omega}\|_\infty$, (1) only requires that $\gamma \geq 1$.

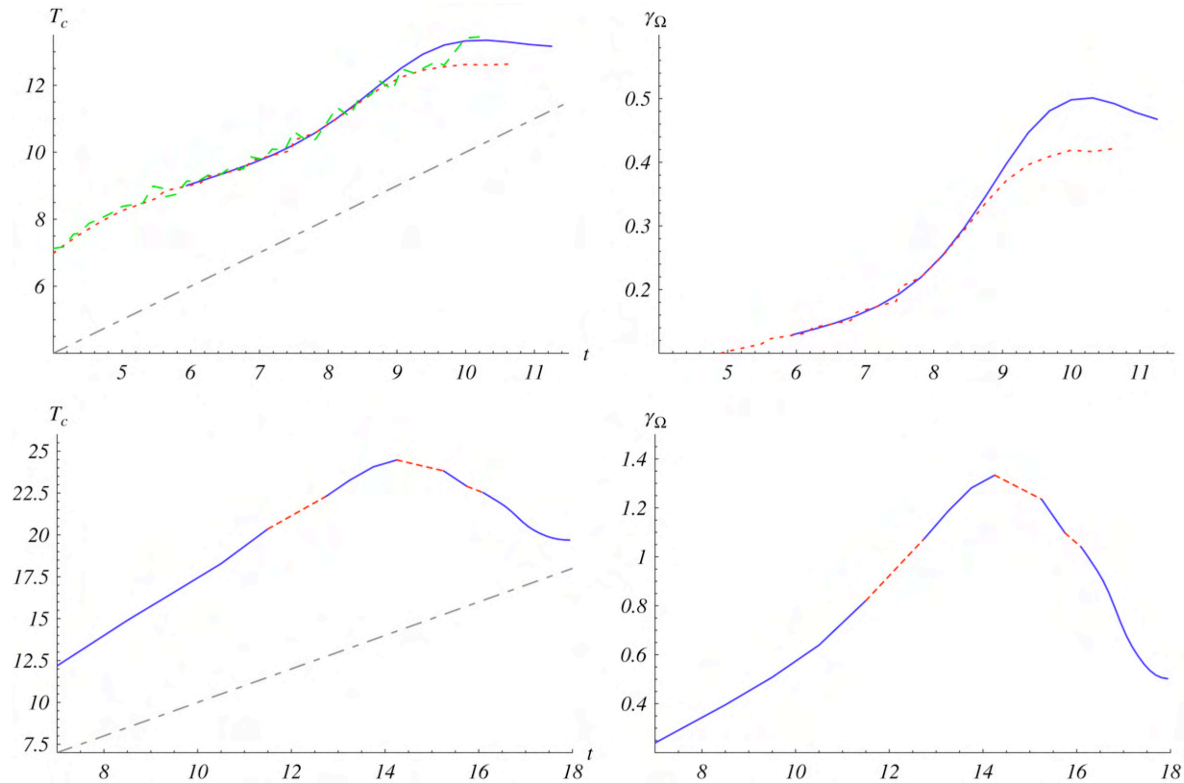

Fig. 2. Upper frames: Resolution study of the predicted singular time T_c and the predicted exponent γ_Ω in the power-law behavior of the total enstrophy Ω using the new data at resolutions: $512 \times 64 \times 2048$ (dashed), $512 \times 128 \times 2048$ (dotted) and $1024 \times 256 \times 2048$ (solid). Lower frames: Predicted T_c and γ_Ω for the Kerr [3] data at the highest resolution (solid). Dashed lines denote gaps in data. In the graphs for the predicted T_c, the dash-dotted diagonal lines denote the $T_c = t$ singularity asymptote.

5.2. Logarithmic time derivatives of enstrophy and $\|\boldsymbol{\omega}\|_\infty$: Instantaneous two-parameter fitting

The original analysis would be possible if there is a secondary quantity which must go as $1/(T_c - t)$ if the primary quantity obeys the power law $1/(T_c - t)^\gamma$. An example of a secondary quantity of that sort is the logarithmic time derivative of the primary quantity, which can be computed if we know independently the quantity $f(t)$ and its time derivative $\dot{f}(t)$.

Therefore we propose a new approach to inferring a singular time and identifying the scaling behavior:

- Find a quantity $f(t)$ whose growth and the growth of its time-derivative can be determined directly. Consider the new function:

$$g(t) = \left(\frac{\mathrm{d}}{\mathrm{d}t}\log f(t)\right)^{-1} = \frac{f}{\dot{f}} = \frac{1}{\gamma}(T_c - t). \tag{5}$$

  Note that the parameter C drops out and the function is linear, so we can predict instantaneous values of γ and T_c by fitting this new function using adjacent points in time.
- Calculating in this manner, using nearest neighbours in time, yields instantaneous predicted singular times $T_c(t)$ and power laws $\gamma(t)$. These instantaneous parameters will generically depend on time.
- See if these converge or relax (as time increases).

Pairs of quantities to which this procedure can be applied are:

- $\|\boldsymbol{\omega}\|_\infty$ and its logarithmic time derivative α_∞ (local stretching at the point $\boldsymbol{x}_\infty$).
- Enstrophy Ω and its production Ω_p (3) where we assume that

$$\Omega \sim \frac{C_\Omega}{(T_c - t)^{\gamma_\Omega}}. \tag{6}$$

- Helicity in the simulated quadrant of space and its production.

This approach is applied to enstrophy and its production on our highest-resolution simulations. As enstrophy and its production are global quantities they converge numerically longer (to $t = 11.25$) than $\|\boldsymbol{\omega}\|_\infty$, for which $\boldsymbol{x}_\infty$ is less than 6 mesh points from the dividing plane for $t > 10$. Running estimates for T_c and γ_Ω are shown in Fig. 2. For the new data (upper frames), the latest data point gives an estimate $T_c \approx 13.16$ and $\gamma_\Omega \approx 0.47$. The bottom frames show the same analysis applied to the data used by [3]. Nearly identical power laws are obtained ($\gamma_\Omega \approx 0.50$), with a predicted singular time $T_c \approx 19.69$, greater than in [3].

One advantage of finding running estimates of T_c is that it can be used to identify cases that are not singular, or would take an unusually long time to become singular. This is done by looking at the instantaneous estimated value of T_c. If T_c continues to increase with time, then there is evidence for regularity. In both the new calculations and for the data from Kerr [3], eventually the estimated T_c decreases and relaxes to

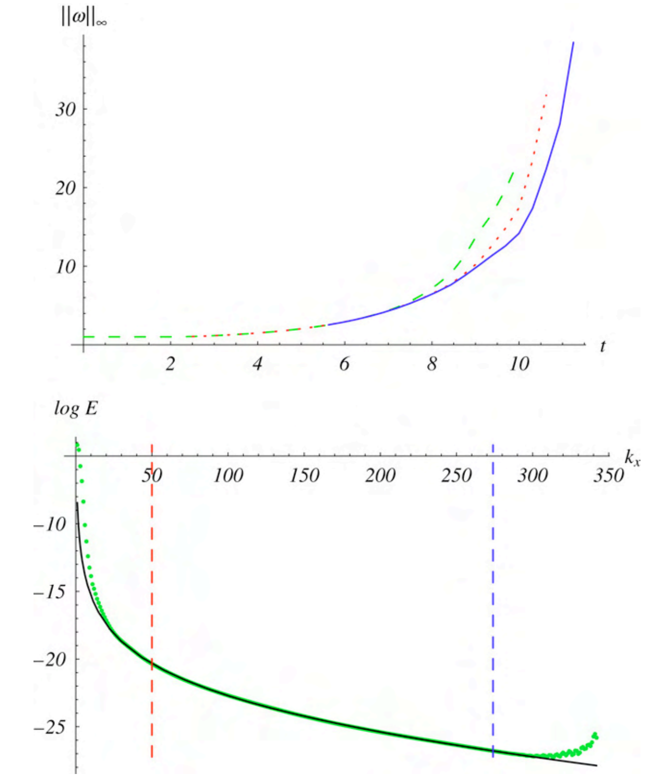

Fig. 3. Top: Resolution study of $\|\omega\|_\infty$, for resolutions $n_x \times n_y \times n_z$ of: $512 \times 64 \times 2048$ (dashed), $512 \times 128 \times 2048$ (dotted) and $1024 \times 256 \times 2048$ (solid). Bottom: Anisotropic energy spectrum (direction k_x) at time $t = 10$ for resolution $1024 \times 256 \times 2048$. Points correspond to numerical data. The solid curve corresponds to the fit of the spectrum according to $\log E(k_x) = C - n\log(k_x) - 2\delta\, k_x$, where the fit interval is defined by the vertical dashed lines.

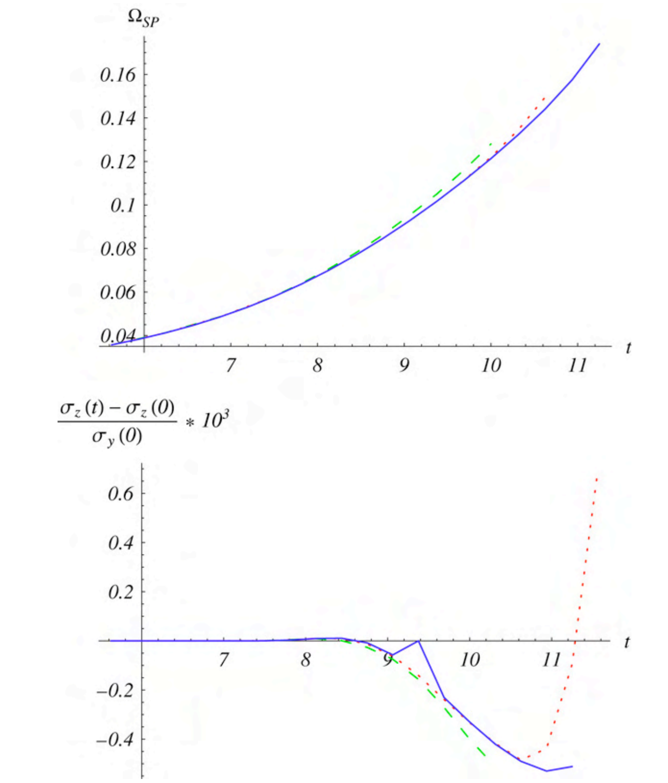

Fig. 4. Resolution study of: the enstrophy in the symmetry plane Ω_{SP} (top); the error in the circulation through the dividing plane σ_z normalized with the initial circulation through the symmetry plane σ_y (bottom), for resolutions $512 \times 64 \times 2048$ (dashed), $512 \times 128 \times 2048$ (dotted) and $1024 \times 256 \times 2048$ (solid).

a finite value. It is quite possible that there is a large pre-factor in front of the power law, which the time dependence of the estimated γ_Ω and C_Ω might be able to shed light on.

This approach assumes smooth values for both quantities in a pair. Unfortunately, we have found that because $\|\boldsymbol{\omega}\|_\infty$ sits on a steep gradient of α, values of α_∞ on the lower resolution mesh were not smooth enough in time to perform this analysis. The analysis will be attempted on the higher resolution $(\|\boldsymbol{\omega}\|_\infty, \alpha_\infty)$ data when that additional analysis of the new data sets is available.

5.3. Convergence studies: Is the evidence for singularity conclusive?

Further tests at higher resolution are needed to support the singular trends seen here. Both current cases (old and new data) could be reliably integrated up to times $t \approx T_c - 2.75$. This would only be the beginning of the asymptotic regime of the potentially singular solution, as is suggested by the late-time behavior of the curves for the predicted singular time T_c in Fig. 2. New calculations in progress should go beyond that barrier and help to test the validity of the hypothesis of finite-time singularity.

In this subsection we show resolution studies with n_z fixed to give a flavor of what will be shown in the next paper (we have also made resolution checks with fixed n_x or n_y and varying the other two, not shown here). The resolution study is a classical tool to validate and find reliability times for the numerical results. Another now widely accepted study that we present is a spectral convergence test (Sulem et al. [12]) used recently by Cichowlas and Brachet (see [13] and the references therein), where the exponential decay of the energy spectrum as a function of the wavenumber is employed to give a criteria for the reliability time. Finally we complement the above classical tests with our newly proposed tests of reliability: conservation of circulation through the symmetry plane and conservation of circulation through the dividing plane.

We consider first the behavior of local quantities, in the sense of Section 3. Fig. 3 (top) is a resolution study of the time dependence of the maximum vorticity; the bottom figure is a $t = 10$ anisotropic energy spectrum $E(k_x, t)$, defined by averaging the Fourier transform $\hat{\mathbf{u}}(\mathbf{k}', t)$ of the velocity field on flat duplicated sheets of width $\Delta k_x = 1$,

$$E(k_x, t) = \frac{1}{2} \sum_{k_x - \Delta k_x/2 < |k_x'| < k_x + \Delta k_x/2} |\hat{\mathbf{u}}(\mathbf{k}', t)|^2.$$

Following [13], we fit: $\log E(k_x) = C - n\log(k_x) - 2\delta\, k_x$ (solid line in the figure). The test consists in monitoring the parameter δ as a function of time. The idea is that δ, being the width in the complex plane of the analyticity strip of the velocity field, should always be numerically resolved, at least by the mesh size. Another way to look at this condition is to ask that the contribution of the exponential term to the change of $\log E(k_x)$

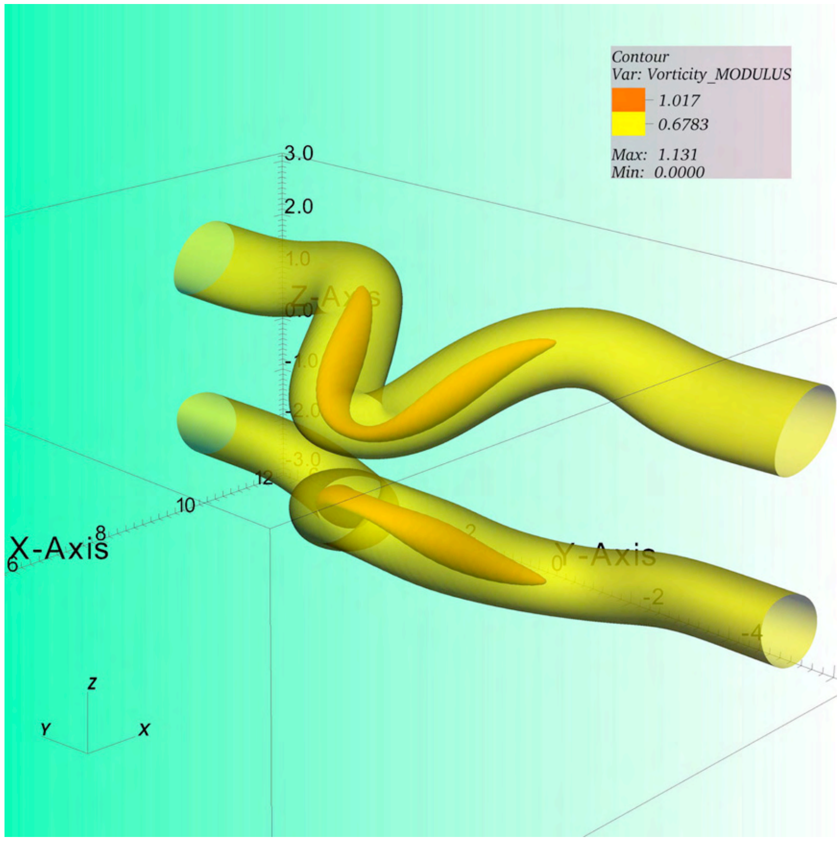

Fig. 5. Euler anti-parallel vortices in full periodic domain near $t = 2.51$. Bright (yellow online) tubes are isosurface contours of vorticity modulus corresponding to 60% of the instantaneous maximum of vorticity modulus. Dark (red online) elongated blobs are isosurfaces corresponding to 90% of the maximum of vorticity modulus.

from the largest to the smallest scale allowed by the numerical resolution, be greater than a prescribed factor. In more explicit terms, we can only fully trust the simulation up until the condition $\delta\, k_x^{\max} \geq 1$ is violated, where $k_x^{\max} = n_x/3$ is the maximum relevant wavenumber of the Fourier representation. Notice that different authors use different factors in the RHS of the last inequality. For our $t = 10$ spectrum in resolution $1024 \times 256 \times 2048$ we obtain $\delta\, k_x^{\max} \approx 1.07$, and therefore our simulation is validated by this method up to $t = 10$. In this way we could extrapolate the convergence of $\|\boldsymbol{\omega}\|_\infty$ up to $t = 10$, whereas a conservative extrapolation based solely on the resolution study in Fig. 3 (top) would see the $1024 \times 256 \times 2048$ computation converged up to $t = 9$.

We consider now the behavior of 2D integral quantities. Due to its 2D character, enstrophy in the symmetry plane $\Omega_{SP} = \int_{y=0} \omega_y^2 \,\mathrm{d}x\,\mathrm{d}z$, shown in Fig. 4 (top), is a more sensitive measure than total enstrophy Ω (Eq. (3), figure not shown), which converges more rapidly than Ω_{SP}. A conservative extrapolation would imply convergence of Ω_{SP} up to times $t \lessapprox 11$.

Fig. 4 (bottom) is a resolution study of the normalized error in the conservation of circulation through the dividing plane σ_z. We observe that, for a given resolution, the numerically induced deviation in σ_z becomes unstable after a certain time. Errors (and fluctuations thereof) less than 10^{-4} are acceptable, as long as they are stable. Then, a reasonable reliability time can be defined for each resolution as the time when the error in σ_z attains its last extremum before the instability takes over. According to this criteria we conclude that the simulation at resolution $512 \times 128 \times 2048$ (dotted line) is converged up to $t \approx 10.7$ and the simulation at resolution $1024 \times 256 \times 2048$ (solid line) converges up to $t \approx 11.25$. In order to display the unstable behavior of the mid-resolution simulation (dotted line), we show data beyond its reliability time.

Finally we return to Fig. 2, considering all three resolutions. For each resolution, T_c has a peak for $t \approx 9 - 10$, and then asymptotes, well within the reliability time for the highest resolution. Similar trends towards convergence appear for γ_Ω. The key question regarding the existence of a finite-time singularity is if the curve for predicted T_c crosses the asymptote $T_c = t$ (dashed-dotted line) in a finite time or not, but we need further tests at higher resolutions (to be shown in a future paper) in order to conclude on these matters.

We have enough resolution to conclude that the power laws are not the ones proposed in [3,5] but not enough resolution to reach definitive conclusions on the singular behavior, since $\|\boldsymbol{\omega}\|_\infty$ does not converge as rapidly as the volumetric quantities studied.

6. Graphics

In this section, 3D isosurface contours of the vorticity modulus are shown, corresponding to the simulation of initially anti-parallel vortices, using a resolution of $512 \times 128 \times 2048$

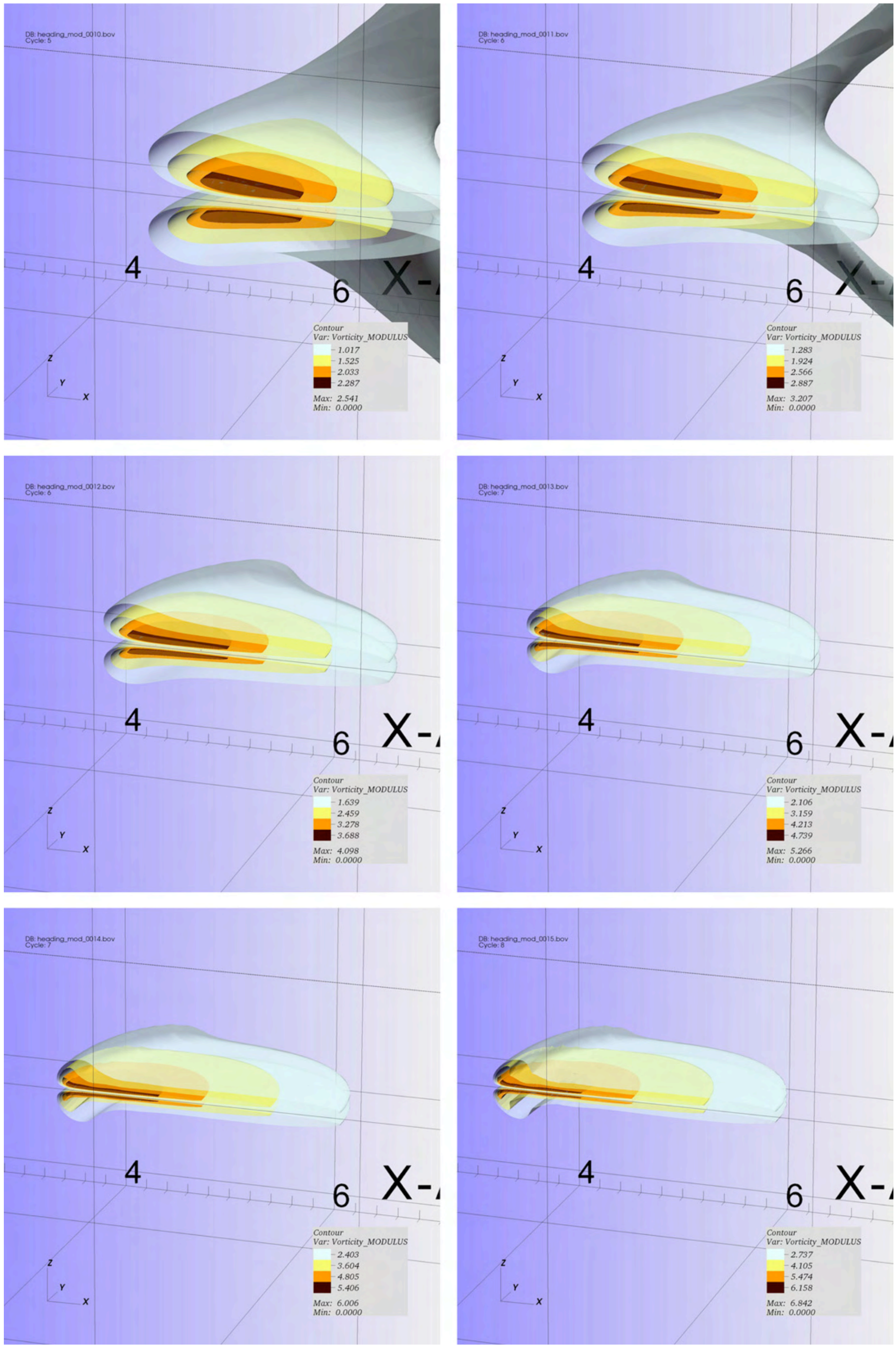

Fig. 6. From left to right, and from top to bottom: six successive, zoomed snapshots of the Euler anti-parallel vortices at times $t = 5.625, 6.25, 6.875, 7.5, 7.8125, 8.125$. The contours are sectioned through the $y = 0$ symmetry plane, to facilitate the view of the structures. The contours are isosurfaces of vorticity modulus corresponding, respectively from outer to inner, to the 40%, 60%, 80% and 90% of the value of the instantaneous maximum vorticity modulus.

in the fundamental quarter of the full domain, corresponding to an effective resolution of $512 \times 256 \times 4096$ in the full domain. For memory-optimizing purposes, the output data used to make the figures has an effective resolution of $512 \times 128 \times 1024$, corresponding to a memory size of 65 MB. The freeware visualization program VisIt has been used to make the plots.

Fig. 5 shows the vortices after some time of evolution in the whole periodic domain. The large tubes are isosurfaces corresponding to 60% of the maximum vorticity modulus. These tubes cross along the periodic Y-Axis and deform notably near the symmetry plane ($y = 0$). The elongated blobs in the interior of the tubes are isosurfaces corresponding to 90% of the maximum vorticity. These isosurfaces are very localized and flattened near the symmetry plane.

Fig. 6 shows successive snapshots at later stages of the flow, of isosurfaces corresponding to the following percentages of the instantaneous value of the maximum vorticity modulus: from outer to inner contours, 40%, 60%, 80% and 90%. Only half of the total domain is shown so that a section of the isosurfaces through the symmetry plane ($y = 0$) is visible. The snapshots are all seen from the same angle and with the same zoom with respect to the fixed box. To read the snapshots going forward in time one advances from left to right and from top to bottom.

The flattening in the z-direction results in structures similar to flattened pillows with some curvature in x (and less in y) that becomes more pronounced at the later times along the cut at the symmetry plane. These empirical observations provide further support for the choice of anisotropic resolution in the simulations.

7. Looking forward

The calculation reported here was the largest possible on the Warwick SGI Altix with our code. In the near future we will have a cluster capable of simulating a $2048 \times 1024 \times 4096$ mesh. We might also use UK national computing resources.

Once our new cluster arrives we anticipate the following calculations:

- Further tests to determine if an initial condition closer to that of Kerr [3] can be obtained.
- After further resolution checks, at least one calculation on a $2048 \times 512 \times 4096$ mesh either on the new profile here or that of Kerr [3].
- At least one modest resolution calculation on the square-off initial condition of Fig. 1.
- Our goal in high-resolution calculations will be to include spectral convergence tests, in particular the analyticity strip method (Sulem et al. [12], see also [13,14] and the references therein) which gives independent evidence of singular/nonsingular behavior of the flow and allows one to extrapolate the convergence of $\|\boldsymbol{\omega}\|_\infty$.
- Convergence of $\|\boldsymbol{\omega}\|_\infty$ and other local quantities should allow us to study regularity bounds from Constantin, Fefferman and Majda [4] and from Deng, Hou and Yu [15].

The finite-time singularity hypothesis of the 3D, incompressible Euler equations, leads to conclusions that are in qualitative agreement with Kerr [3]. However, we have found that the previously proposed scaling laws and estimated singular time must be modified.

One possible outcome which will require further investigation is whether constant circulation is trapped within the collapsing region. If this is confirmed, the two length scaling parameterization proposed [5] cannot be correct.

It is anticipated that in addition to these much higher-resolution anti-parallel calculations, there will soon be new high-resolution calculations of the Kida–Pelz flow (anticipated in these proceedings by the contribution of Grafke et al. [16]) and the Taylor–Green calculations initiated by Brachet et al. [17] will soon be continued by Brachet. If these prove to be singular, and anti-parallel, it is possible that they will reproduce the scalings hinted at here.

Acknowledgments

We acknowledge discussions with C. Bardos, J.D. Gibbon, R. Grauer, T. Hou, S. Kida, R. Morf, K. Ohkitani, E. Titi and other participants in Euler250. We thank U. Frisch and co-workers for organizing this excellent symposium. Support for this work was provided by the Leverhulme Foundation grant F/00 215/AC. Computational support was provided by the Warwick Centre for Scientific Computing.

References

[1] L. Euler, Principia motus fluidorum., Novi Commentarii Acad. Sci. Petropolitanae 6 (1761) 271–311.
[2] J.T. Beale, T. Kato, A. Majda, Remarks on the breakdown of smooth solutions for the $3D$ Euler equations, Commun. Math. Phys. 94 (1984) 61.
[3] R.M. Kerr, Evidence for a singularity of the three-dimensional, incompressible Euler equations, Phys. Fluids 5 (1993) 1725–1746.
[4] P. Constantin, C. Fefferman, A. Majda, Geometric constraints on potentially singular solutions for the 3D Euler equations, Comm. Partial Differential Equations 21 (1996) 559–571.
[5] R.M. Kerr, Velocity and scaling of collapsing Euler vortices, Phys. Fluids 17 (2005) 075103.
[6] R. Grauer, C. Marliani, K. Germaschewski, Adaptive mesh refinement of singular solutions of the incompressible Euler equations, Phys. Rev. Lett. 80 (1998) 4177–4180.
[7] P. Orlandi, G. Carnevale, Nonlinear amplification of vorticity in inviscid interaction of orthogonal Lamb dipoles, Phys. Fluids 19 (2007) 057106.
[8] T.Y. Hou, R. Li, Dynamic depletion of vortex stretching and non-blowup of the 3-D incompressible Euler equations, J. Nonlinear Sci. 16 (2006) 639–664.
[9] R.M. Kerr, F. Hussain, Simulation of vortex reconnection, Physica D 37 (1989) 474–484.
[10] R.M. Kerr, Evidence for a singularity of the three-dimensional incompressible Euler equations, in: G.M. Zaslavsky, M. Tabor, P. Comte (Eds.), Topological Aspects of the Dynamics of Fluids and Plasmas, Proceedings of the NATO-ARW Workshop at the Institute for Theoretical Physics, University of California at Santa Barbara, Kluwer Academic Publishers, Dordrecht, Netherlands, 1992, pp. 309–336.
[11] T.Y. Hou, R. Li, Computing nearly singular solutions using pseudo-spectral methods, J. Comp. Phys. 226 (2007) 379–397.
[12] C. Sulem, P.-L. Sulem, H. Frisch, Tracing complex singularities with spectral methods, J. Comp. Phys. 50 (1983) 138–161.
[13] C. Cichowlas, M.E. Brachet, Evolution of complex singularities in Kida-Pelz and Taylor-Green inviscid flows, Fluid Dynamics Res. 36 (2004) 239–248.

[14] U. Frisch, T. Matsumoto, J. Bec, Singularities of Euler flow? Not out of the blue!, J. Stat. Phys. 113 (2003) 761–781.
[15] J. Deng, T.Y. Hou, X. Yu, Improved geometric condition for non-blowup of the 3D incompressible Euler equation, Commun. Partial Differential Equations 31 (2006) 293–306.
[16] T. Grafke, H. Homann, J. Dreher, R. Grauer, Numerical simulations of possible finite time singularities in the incompressible Euler equations: Comparison of numerical methods 2007 (these Proceedings).
[17] M.E. Brachet, D.I. Meiron, S.A. Orszag, B.G. Nickel, R.H. Morf, U. Frisch, Small-scale structure of the Taylor–Green vortex, J. Fluid Mech. 130 (1983) 411–452.

Available online at www.sciencedirect.com
ScienceDirect
ELSEVIER
Physica D 237 (2008) 1921–1925
PHYSICA D
www.elsevier.com/locate/physd

Growth of anti-parallel vorticity in Euler flows

Stephen Childress*

Applied Mathematics Laboratory, Courant Institute of Mathematical Sciences, New York University, 251 Mercer Street, 10012 NY, United States

Available online 10 March 2008

Abstract

In incompressible Euler flows, vorticity is intensified by line stretching, a process that can come either from the action of shear, or from advection with curvature. Focusing on the latter process, we derive some estimates on the maximal growth of vorticity in axisymmetric flow without swirl, given that vorticity support volume or kinetic energy is fixed. This leads to consideration of locally 2D anti-parallel vortex structures in three dimensions. We exhibit a class of line motions which lead to infinite vorticity in a finite time, with only a finite total line stretching. If the line is replaced by a locally 2D Euler flow, we obtain a class of models of vorticity growth which are similar to the paired vortex structures studied by Pumir and Siggia. We speculate on the mechanisms which can suppress the nonlinear effects necessary for the finite-time singularity exhibited by the moving line problem.

PACS: 47.10.-g; 47.15.ki; 47.32.C-

Keywords: Vorticity growth; Axisymmetric flow without swirl

1. Introduction

The question of the global regularity of three-dimensional solutions of the incompressible Euler equations continues to be of considerable interest to both mathematicians and fluid dynamicists, see e.g. the papers of Constantin, Gibbon, and Hou in this volume. According to the seminal Beale–Majda–Kato criterion, singularity formation must be accompanied by infinite (integral of) maximum vorticity, which in turn requires that some vortex tubes stretch to zero cross-section. The question of global regularity thus depends upon how fast vorticity can grow through line stretching.

In the present note, we re-examine anti-parallel vortex structures as a mechanism for the self-stretching of vorticity. We will also be interested in the existence of Euler flows which maintain quasi-two-dimensionality even as vorticity grows. In a perfect fluid, vortex lines are material and therefore move with the velocity created by the self-same vorticity, as described by the Biot–Savart law. Let us consider a curve $\mathcal{C}(t)$, restricted for simplicity to a plane, moving in the plane with velocity $\mathbf{u}(\zeta_0, t)$. Here ζ_0 is a Lagrangian parameter of the line, here arc length is measured from a reference point at $t = 0$.

Resolving $\mathbf{u}$ into tangential and normal components relative to the curve, a point $\mathbf{x}(\zeta_0, t)$ of $\mathcal{C}$ moves according to

$$\left.\frac{\partial \mathbf{x}}{\partial t}\right|_{\zeta_0} = u(\zeta_0, t)\mathbf{n} + w(\zeta_0, t)\mathbf{t}, \tag{1}$$

where $(\mathbf{n}, \mathbf{b}, \mathbf{t})$ is the orthonormal triad of normal, tangent, and binormal vectors to the curve. As is well known, the equations of motion of the curve can be expressed for given u, w as a pair of equations for the Jacobian $J = \frac{\partial \zeta}{\partial \zeta_0}(\zeta_0, t)$ and the curvature $\kappa(\zeta, t)$, where ζ is the current arc length:

$$\left.\frac{\partial J}{\partial t}\right|_{\zeta_0} = w_\zeta J - J u \kappa, \tag{2}$$

$$\left.\frac{\partial \kappa}{\partial t}\right|_{\zeta_0} - w\kappa_\zeta - \kappa^2 u - u_{\zeta\zeta} = 0. \tag{3}$$

Note that it is derivatives in ζ, not ζ_0, which occur in (3). The two terms on the right of (2) we may call, in order, the *shear* stretching and the *expansive* stretching terms.

Since shear stretching involves the tangential component w, it can be caused by the global vorticity only if the nearby lines

* Tel.: +1 212 998 3000; fax: +1 212 995 4121.
E-mail address: childress@cims.nyu.edu.

0167-2789/$ - see front matter
doi:10.1016/j.physd.2008.02.028

are suitably skew to the line to be stretched. Shear-induced stretching can play a significant role in the amplification of vorticity, as was recognized by Pelz, see e.g. [1]. Expansive stretching is available to locally parallel but curved vortex lines. It is the basis for much of the line stretching in numerical experiments utilizing paired anti-parallel vortex structures, see e.g. [2–4].

We here focus on the intensification of vorticity by expansive stretching. We shall first consider stretching of vorticity in the simplest of 3D Euler flows, namely axisymmetric flow without swirl. In that case we may formulate and solve a maximization problem under global constraints on volume and energy. Next, we set $w = 0$ in (2), (3) and close the system with an equation for u. The resulting equations of motion of a line by its normal are solved, and it is found that finite time singularities, involving only finite total stretching, may occur. If we regard the line as the locus of a locally 2D three-dimensional Euler flow, we make contact with the calculations in [3]. We discuss an attempt to formulate this problem in terms of generalized partial differential equations, and the limitations on growth of vorticity for more general quasi-2D flows. We shall omit most details and refer to [12] for supporting calculations.

2. Axisymmetric flow without swirl

This special class of Euler flows, probably the simplest allowing vortex stretching, is worth considering from the viewpoint established above. How fast can vorticity grow in this class of flows? Does vorticity necessarily become indefinitely large somewhere as $t \to \infty$? What bounds on growth can be given?

Any axisymmetric flow having no swirl has a vorticity field of the form $(0, 0, \omega_\theta(z, r, t))$ in cylindrical polar coordinates z, r, θ. We deal here only with flows in R^3 for which the initial vorticity is contained within a finite volume. Such a flow is known to exist globally in time, and a very direct proof of a bound exponential in time on the maximum vorticity is given in [5]. The proof utilizes the constancy of the volume support of the vorticity in an Euler flow, and also the material invariance of $r^{-1}\omega_\theta(\mathbf{x}, t)$.

The exponential bound is not however sharp; the bound on the growth of vorticity may be improved by making further use of the special geometry. The sustained growth of vorticity must involve continual expansion of a vortex ring. The expansive stretching of this ring must be due to nearby rings. Thus, if we want to find the fastest growth a ring can attain given the initial vorticity field, we can, at each instant in time, assemble the available vorticity in a kind of toroidal "cocoon" about the selected growing ring, termed below the *core ring*. We remark that, for simplicity in constructing the cocoon producing fastest growth of the core ring, we shall in fact allow rings larger than the core, as long as global constraints are met. The core ring itself should be thought of as a "test" vortex tube of small cross-section and circulation.

2.1. Construction of a t^2 bound

Let the initial vorticity have a finite initial support of volume V_0. Suppose that $-c_1 \le \omega_\theta(z, r, 0) \le c_2$ for some positive constants c_1, c_2, and let the region of the support where $\omega_\theta \ge 0$ have volume V_{0+}, that where $\omega_\theta < 0$ have volume $V_{0-} = V_0 - V_{0+}$. We suppose that $r^{-1}|\omega_\theta(\mathbf{x}, 0)| \le C$.

Consider a core ring of radius r at time t, lying on the plane $z = 0$. Taking the z axis as the axis of symmetry, we may assume the ring has radius r at time t, and lies on the plane $z = 0$. It is clear that to maximize the rate of growth at time t of the ring in question, we can take rings of negative vorticity $\omega_\theta = -Cr$ distributed over a volume $V/2$ in $z \ge 0$, and rings of positive vorticity $\omega_\theta = +Cr$ distributed over a volume $V/2$ in $z \le 0$. Indeed, we can have no stronger vorticity and any deviation from an optimal equal partition will be sub-optimal. Note that θ increases counterclockwise looking onto the x, y plane from $z > 0$, so by the right-hand-rule a negative ω_θ in $z > 0$ induces a positive u_r at the core ring.

Consider now the value of u_r induced at the core ring by a ring of radius ρ and cross-sectional area $2\pi\rho \mathrm{d}A$ carrying vorticity $-C\rho$ at height $z = \zeta > 0$. From the Biot–Savart law one finds

$$u_r(r, 0, t) \le \frac{C\rho^2|\zeta|}{4\pi}\left[\int_{-\pi}^{+\pi} H^{-3/2}\mathrm{d}\psi\right]\mathrm{d}A \tag{4}$$

where $H = (r - \rho)^2 + 2r\rho(1 - \cos\psi) + \zeta^2$. Since $1 - \cos\psi \ge k^2\psi^2, ; |\psi| \le \pi,\ k = \sqrt{2}/\pi$, we may make this substitution and carry out the integral with the range extended from $[-\pi, +\pi]$ to $[-\infty, +\infty]$, to obtain

$$u_r(r, 0, t) \le \frac{C|\zeta|\rho^{3/2}}{4\sqrt{r}}((r - \rho)^2 + \zeta^2)^{-1}\mathrm{d}A. \tag{5}$$

We introduce local polar coordinates in the r, z plane, defined by $\rho - r = R\cos\Theta$, $\zeta = R\sin\Theta$. Then, since

$$\begin{aligned} u_r &\le \frac{C|\sin\Theta|(r + R\cos\Theta)^{3/2}\mathrm{d}R\mathrm{d}\Theta}{4\sqrt{r}} \\ &\le \frac{C}{4}|\sin\Theta|(r + R\cos\Theta)(1 + R/r)^{1/2}\mathrm{d}R\mathrm{d}\Theta, \end{aligned} \tag{6}$$

we seek to maximize $U = \int_{\mathcal{A}} f(R, \Theta)\mathrm{d}R\mathrm{d}\Theta$, where

$$f = \frac{C}{4}|\sin\Theta|(r + R\cos\Theta)(1 + R/r)^{1/2}, \tag{7}$$

subject to the volume constraint

$$V = \int_{\mathcal{A}} g(R, \Theta)\mathrm{d}R\mathrm{d}\Theta, \quad g = 2\pi(r + R\cos\Theta)R. \tag{8}$$

Here $\mathcal{A}$ is a set to be determined. It can be shown that $\mathcal{A}$ may be assumed to be mirror symmetric with respect to the plane $z = 0$, and star-like with respect to the core ring.

We may then formulate the optimization problem as the variational problem for the boundary $\mathcal{R}(\Theta)$, $0 \le \Theta \le \pi$, given by

$$\delta\int_0^{\pi}\int_0^{\mathcal{R}}(f(R, \Theta) - \lambda g(R, \Theta))\,\mathrm{d}R\Theta, \tag{9}$$

with scalar multiplier λ.

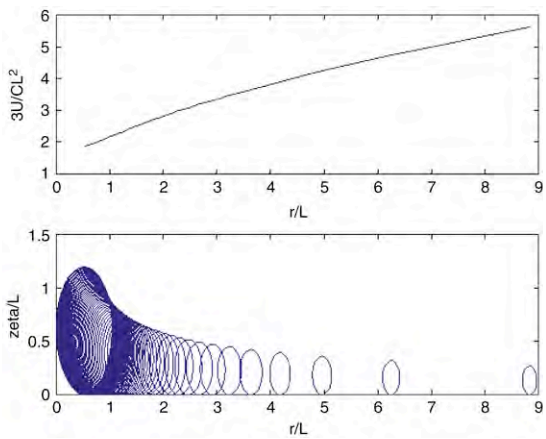

Fig. 1. Top: $\frac{3}{CL^2}\frac{\mathrm{d}r}{\mathrm{d}t}$ (as defined by (10)) versus r/L. Bottom: Cocoon shape for various position of the core ring. The cocoon is mirror symmetric with respect to the r/L line.

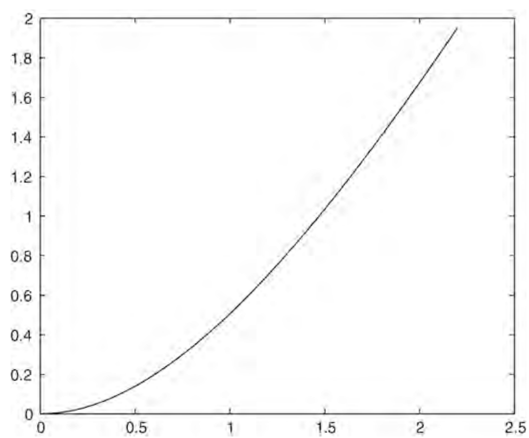

Fig. 2. $zA^{-1}\tau^{\gamma-1}$ versus $xA^{-1}\tau^{\gamma-1}$ for the case $\beta = 2, \gamma = \frac{1}{9}(1+\sqrt{19})$.

This variational problem may be easily solved. The extremal leads to the estimate on growth rate of $r* = r/L$, where $V = 2\pi L^3$, in the form

$$\frac{\mathrm{d}r*}{\mathrm{d}t} \le \sup U \le \frac{CLr*^2}{3}\mathcal{U}(r*). \tag{10}$$

We show this relation in Fig. 1, along with the cocoon boundaries at various values of r/L.

The behavior for large $r*$ leads to an estimate on the vorticity: For axisymmetric flow with initial support volume V and initial vorticity satisfying $|\omega_\theta/r| \le C$, there is a constant C_1 depending only upon V, C such that

$$\sup|\omega_\theta| \le C\left(\frac{C}{8}\sqrt{V}t + C_1\right)^2. \tag{11}$$

Thus vorticity grows no faster than $O(t^2)$ for large time. We remark that the 2D "vortex couple", see [6], p. 535, and also [15], if formed into a toroidal structure, realizes kinematically a sub-optimal cocoon of constant volume.

2.2. Kinetic energy

In terms of basic scaling in r, the cocoon of constant volume is characterized by $J, a, \omega_\theta, U \sim r, 1/\sqrt{r}, r, \sqrt{r}$, a being a transverse dimension, and the kinetic energy is of order $ra^2(\omega_\theta^2 a^2) \sim r$. Thus the kinetic energy of the cocoon of constant volume grows with r. This suggests that a lower estimate of growth can be obtained by requiring that the kinetic energy of the cocoon be fixed.

If constant kinetic energy is imposed as the side constraint instead of constant volume, it can be seen that a, the lateral dimension of the resulting cocoon, must scale as $r^{-3/4}$. The optimizing cocoon for large r then can be shown to yield an $O(t^{4/3})$ growth estimate for ω_θ. The optimizing cocoon shrinks in volume, behaving as $1/\sqrt{r}$, and has a somewhat different shape from the cocoon of constant volume, but remains star-like.

What estimate can be obtained if volume and energy are simultaneously conserved? We have studied this question in a "thin-layer" version of the cocoon construction in the limit $r \to \infty$. Our results suggest that an optimizing cocoon under both volume and energy constraints consists of the cocoon under the energy constraint, with the same estimate on growth, but now having attached to it a filament or filaments (see Section 4) which contain the missing volume but have negligible energy. Thus we conjecture that a $t^{4/3}$ bound on growth is the best available from the cocoon construction. It is likely that the exponent $4/3$ can be reduced by other methods.

Since the Jacobian of the core vortex is proportional to r, and since the speed U of the cocoon is $\sim r^{1/2}$ under constant volume and $\sim r^{1/4}$ under constant energy, we see that the growth is ultimately associated with quasi-2D structures with $J \sim U^2$ and $J \sim U^4$ respectively. Of course these considerations are essentially kinematic and, even in the case of constant energy, need not have any implication for the actual dynamics. On the other hand it is of interest to understand what kind of growth can be realized in three dimensions under similar kinematic constraints by quasi-2D vortex structures. The remainder of this note will deal with this extension to three-dimensional structure.

3. Singular motion of a line by its normal

Motivated by the results just given, we augment the system (2), (3) (with $w = 0$) by

$$J = \alpha'(\zeta_0)(-u)^\beta. \tag{12}$$

Here $\beta \ge 2$, and we assume $u < 0$, i.e. the curve is moving opposite to the direction of $\mathbf{n}$. These assumptions are motivated by the kinematics of propagating, quasi 2D vortex structures, as will be discussed below. With (12) the equations may be reduced to the following equation for u:

$$u_{tt} + (\beta-2)\frac{u_t^2}{u} + \frac{u^2}{\beta\alpha'(\zeta_0)(-u)^\beta}\frac{\partial}{\partial\zeta_0}\frac{1}{\alpha'(\zeta_0)(-u)^\beta}\frac{\partial u}{\partial\zeta_0} = 0. \tag{13}$$

If $\mathcal{C}$ is initially a circle, it will remain a circle for all time. If its radius is $R(t)$ we see easily that $\mathrm{d}R/\mathrm{d}t = cR^{1/\beta}$ for some positive constant c, and so

$$R = \left(c(1-1/\beta)t + R(0)^{\frac{\beta-1}{\beta}}\right)^{\frac{\beta}{\beta-1}}. \tag{14}$$

When the curvature is *not* independent of ζ, more complicated behavior, including finite time singularities may occur. We consider here only solutions of (13) having the similarity form

$$u = -\tau^{-\gamma} A g(\sigma), \quad \sigma = \alpha(\zeta_0)\tau^{-\mu}. \tag{15}$$

Here A is an arbitrary constant, and

$$\tau = -t, \quad t < 0. \tag{16}$$

We take γ for the moment as an arbitrary positive number less than 1. The time of the hypothetical singularity is here stipulated to be $t = 0$. Substituting (15) into (13) we obtain a solution if

$$\mu = (\beta - 1)\gamma + 1. \tag{17}$$

The equation for g can then be integrated once. Applying the conditions $g(0) = 1$ (given the arbitrary constant A), and $g'(0) = 0$ (a symmetry condition), we obtain the following equation for g:

$$\mu\gamma\sigma g^{\beta-1} + \sigma^2\mu^2 g^{\beta-2} g' + \frac{1}{\beta A^{2\beta-2}}\frac{g'}{g^\beta} = 0. \tag{18}$$

A second integration gives

$$\mu\beta A^{2\beta-2}\sigma^2 g^{\frac{2\mu}{\gamma}} + g^{\frac{2}{\gamma}} = 1. \tag{19}$$

Let us regard $\mathcal{C}$ as oriented so that at $\sigma = 0$, $\mathbf{t}$ points in the direction of the positive x-axis. We define θ as the angle made by $\mathbf{t}$ with the z-axis, so that $\kappa = \frac{\partial\theta}{\partial\zeta}$. Then

$$\frac{\partial\theta}{\partial\sigma} = -A^{\beta-1}[g^{\beta-1}\gamma + \mu\sigma g^{\beta-2}g'] = 0, \tag{20}$$

and so, from (18)

$$\theta = -A^{1-\beta}\mu^{-1}\int g^{-\beta}\sigma^{-1}\mathrm{d}g. \tag{21}$$

Here, from (19),

$$\sigma = \frac{A^{1-\beta}}{\sqrt{\mu\beta}} g^{-\mu/\gamma}\sqrt{1-g^{2/\gamma}}. \tag{22}$$

So

$$\theta = \gamma\sqrt{\frac{\beta}{\mu}}\left[\frac{\pi}{2} - \sin^{-1}(g^{1/\gamma})\right]. \tag{23}$$

These formulas allow us to calculate the shape of the curve. At large arc length the curvature tends to zero and the asymptotes make an angle $\pi - 2\theta_\infty$ where

$$\theta_\infty = \frac{\gamma\pi}{2}\sqrt{\frac{\beta}{\mu}}. \tag{24}$$

Note that $\theta_\infty < \pi/2$ if $\gamma < 1$. Setting $\beta = 2$ and requiring that $\theta_\infty = \pi/3$ we find $\gamma = \frac{1}{9}(1+\sqrt{19}) = .5954$. As we shall see, it will be important for us that we take $\gamma > 1/2$. We show in Fig. 2 the shape of $\mathcal{C}$ for $\beta = 2, \gamma = \frac{1}{9}(1+\sqrt{19})$. When $\gamma = 1/2$, $\theta_\infty \approx 52°$. Since $\theta_\infty = \pi/2$ when $\gamma = 1$, we restrict this parameter to the interval $(1/2, 1)$.

The distribution of stretching along $\mathcal{C}$ can be calculated, and the total stretching experienced by the curve between some time $\tau = T > 0$ and $\tau = 0$ demonstrated to be finite if $0 < \gamma < 1$ and $\beta \geq 2$. If we specify $J(\zeta_0, T) = 1$ then $\alpha_0(\zeta_0)$ is determined, and the evolution of J may be calculated. One finds that the stretching is concentrated at the tip as $\tau \to 0$, with $J \to 1$ at points distant from the tip.

If we regard $\mathcal{C}$ as the axis of a circular tube of incompressible fluid, stretching of $\mathcal{C}$ is accompanied by shrinking of the area of the cross section, and assuming this shrinkage is the same in all lateral directions, the radius of the tube will vary in proportion to $1/\sqrt{J}$. Thus the ratio of this radius to the radius of curvature of $\mathcal{C}$ varies as $\kappa/\sqrt{J}$. This is a quantity of order $\tau^{2\gamma-1}$. If $\gamma > 1/2$, The 3D tube has a non-self-similar development since the two radii grow as $\tau^{-\gamma}$ and $\tau^{\gamma-1}$; moreover "local quasi-two-dimensionality" is maintained as $\tau \to 0$. Note that nonexistence of 3D Euler singularities of self-similar form has been established by Chae, see [13].

Of course our interest here is that the "tube" is in fact a locally 2D Euler flow consisting of anti-parallel vortex structures moving according to (12). There are two main problems with such a scenario. First, the 2D propagation of a vortex structure of unchanging form according to (12) does not insure the same for a curved, quasi-2D variant with self-similar cross-sections, because of the failure of conservation of energy. A case in point is the vortex couple already mentioned and discussed in [3]. The result must be what we shall broadly classify as *core deformation*. Because of this deformation, the distribution of vorticity changes, (12) need not be sustained in the 3D problem, and no singularity can be inferred.

Second, the nonuniform stretching of vortex tubes leads to an axial pressure gradient, hence to axial flow within the tubes, and a disruption of area changes occuring during stretching. Some preliminary results, summarized below, suggest that this axial flow is unlikely to be a strong inhibitor of singularity formation, although it cannot be overlooked in a singularity construction involving quasi-2D vortex tubes.

4. Dynamics

The numerical simulations referred to above, as well as more recent ones (see [7–10]) indicate a flattening of the vorticity field and a kind of "tadpole" cross-section not unlike we have described for the cocoon under constraints of volume and energy. It is also interesting that the "vee"-shaped structure of our singular line is similar to some of the proposed singular flows [2]. Our estimates of growth have been essentially kinematic, and cannot address the ultimate dynamical growth. In [3] an attempt was made to calculate what we may refer to here as a "dynamical cocoon", meaning that the asymptotic dynamical evolution of a locally anti-parallel structure, 2D to first approximation, was sought. We have made a similar attempt for structures collapsing according to the moving line, under the working hypothesis that a system could be derived which would either indicate dynamically consistent singularities, or else provide an analytic example of depletion and extinction of the singularity.

Our approach utilized the scalings of the moving line, and contour averaging over closed streamlines of structures similar to the vortex couple [11]. The dominant flow is 2D, and it is assumed that the needed propagating dipole-like solutions exist. To first order, the transverse flow velocities are of order $\tau^{-\gamma}$. The velocity associated with expansive stretching and the shrinking of the cross-section of vortex tubes is smaller, of order $\tau^{1-\gamma}$ (recall $1/2 < \gamma < 1$). Evolution of the structure, including presumably core deformation on a time scale $s \sim -\ln\tau$, is obtained from compatibility conditions on the perturbed 2D system. The result is a system of generalized partial differential equations. A singular flow would be determined as a "fixed point" of the system, steady in the time scale s.

One case that can be calculated approximately is that of two thin anti-parallel vortex tubes. We find, using the model of [14], a system allowing tangential vorticity and velocity to be calculated simultaneously. On the other hand the collapse of the two vortices toward each other under mutual self-induction (see [6], p. 509) provides the core deformation and will presumably arrest the process. As yet we have no examples of a consistent fixed point solution of our system, and the non-existence or existence of the finite-time collapse remains open.

Finally, the Fourier spectrum of a collection of identical singularity forming vortex couples, averaged over orientation and lifetime, yields a $k^{-2/\gamma}$ spectrum for large wavenumber k, indicating a slope between -2 and -4. Such singular flows, should they exist, would have no effect on the $-5/3$ inertial spectrum of turbulence [16].

The ultimate fate of the vorticity in axisymmetric flow without swirl could well be some configuration of thin anti-parallel vortex tubes and we examine now its possible structure. We shall assume that a thin bilayer sheet is attached to a "rim" at position $r \sim t^{4/3}$ representing the cocoon of constant energy. (In the estimates we omit all constants fixed by the initial conditions.) The cocoon originates from some finite radius $r_0 \gg V$, where V is the initial cocoon volume, thereafter sheds volume, forming the sheet. As $t \to \infty$ the cocoon contains negligible volume, is moving with velocity $\sim t^{1/3}$, and has a cross-section of dimension $\sim t^{-1}$. As the sheet is created, it will evolve slowly as a thin vortex layer, but we neglect this evolution. The time rate of change of cocoon volume is $\sim r^{-5/4}$ and this must balance $rHr^{1/4}$ where H is the half-thickness of the bilayer at position r. Thus $H \sim r^{-5/2}$. This shed vorticity carries away the volume at a negligible loss of energy as $r \to \infty$. The maximal sustained growth realizable in this symmetric flow remains an open question. Although such vortices may be rare in fully developed turbulence, general quasi-2D anti-parallel structures and expansive stretching can provide substantial vorticity growth in 3D Euler flows.

The key mechanism for suppression of singularity formation in the structures studied here is a core deformation which can alter the simple kinematic scaling given by (12). An interesting related question, which to our knowledge has not been studied, is the dynamical fate of dipole structures at large distance from the axis in the flow without swirl. Finally, it would be interesting to determine whether or not the flow *with* swirl, involving the additional circulation invariant and having no known bounds on vorticity growth, might be accessible by the methods of this paper.

Acknowledgements

The author has benefited from conversations with Peter Constantin (who suggested the term "cocoon"), Bob Kohn, and Andy Majda. The research reported in this paper was supported by the National Science Foundation under KDI grant DMS-0507615 at New York University.

References

[1] Richard B. Pelz, Symmetry and the hydrodynamic blow-up problem, J. Fluid Mech. 444 (2001) 299–320.
[2] R.M. Kerr, Evidence for a singularity of the three-dimensional incompressible Euler equations, Phys. Fluids A 5 (1993) 1725–1746.
[3] Alain Pumir, Eric D. Siggia, Vortex dynamics and the existence of solutions to the Navier–Stokes equations, Phys. Fluids 30 (1987) 1606–1626.
[4] M.V. Melander, F. Hussain, Cross-linking ot two anti-parallel vortex tubes, Phys. Fluids A 1 (1989) 633–636.
[5] A.J. Majda, A.L. Bertozzi, Vorticity and Incompressible Flow, Cambridge University Press, Cambridge, 2001.
[6] G.K. Batchelor, An Introduction to Fluid Dynamics, Cambridge, 1967.
[7] M. Shelley, DF.I. Meiron, S.A. Orszag, Dynamical aspects of vortex reconnection of perturbed ani-parallel vortex tubes, J. Fluid Mech. 246 (1993) 613–652.
[8] T.Y. Hou, R. Li, Dynamic depletion of vortex stretching and non-blowup of the 3-D incompressible Euler equations, J. Nonlinear Sci. 16 (2006) 639–664.
[9] T.Y. Hou, R. Li, Nonexistence of local self-similar blow-up for the 3-D incompressible Navier–Stokes equations, Discrete Contin. Dyn. Syst. Ser. A 18 (4) (2007) 637–642.
[10] T.Y. Hou, R. Li, Numerical study of nearly singular solutions of the 3-D incompressible euler equations, in: Proceedings of the 2006 Abel Symposium on Computational Mathematics (2006) (in press).
[11] Stephen Childress, Nearly two-dimensional solution of Euler's equations, Phys. Fluids 30 (1987) 944–953.
[12] Stephen Childress, Models of vorticity growth in Euler flows I, Axisymmetric flow without swirl and II, Almost 2-D dynamics, AML reports 05–07 and 06–07, courant institute of mathematical sciences (2007). Available at: http://www.math.nyu.edu/aml/amlreport.html.
[13] Dongho Chae, Nonexistence of self-similar singularities of the 3-D incompressible Euler equations, (2006). Preprint.
[14] T.S. Lundgren, W.T. Ashurst, Area-varying waves on curved vortex tubes with application to vortex breakdown, J. Fluid Mech. 200 (1989) 283–307.
[15] S.A. Chaplygin, On case of vortex motion in fluid, Trans. Sect. Imperial Moscow Soc. Friends Nat. Sci. 11 (N2) (1903) 11–14.
[16] D.D. Holm, Robert Kerr, Transient vortex events in the initial value problem for turbulence, Phys. Rev. Lett. 88 (2002) 244501-1–244501-4.

Available online at www.sciencedirect.com
ScienceDirect
Physica D 237 (2008) 1926–1931
PHYSICA D
www.elsevier.com/locate/physd

Singular, weak and absent: Solutions of the Euler equations

Peter Constantin

Department of Mathematics, The University of Chicago, United States

Available online 15 January 2008

Abstract

We will describe necessary and sufficient conditions for blowup and discuss weak solutions for the incompressible Euler equations. We will also describe a result concerning anomalous dissipation of energy.

PACS: 47.15.ki; 47.32.C-

Keywords: Blowup; Weak solutions

1. Introduction

The incompressible Euler equations are

$$\frac{\partial \boldsymbol{u}}{\partial t} + (\boldsymbol{u} \cdot \nabla)\boldsymbol{u} + \nabla p = 0, \tag{1}$$

$$\nabla \cdot \boldsymbol{u} = 0. \tag{2}$$

We will discuss the case of $x \in \boldsymbol{R}^3$ and require that the velocity decays at infinity fast enough. The curl of u, $\omega = \nabla \times u$ obeys the quadratic vorticity equation,

$$\frac{\partial \omega}{\partial t} + (\boldsymbol{u} \cdot \nabla)\omega = (\omega \cdot \nabla)\boldsymbol{u}. \tag{3}$$

The right-hand side of this equation equals $S\omega$ where $S = \frac{1}{2}\left(\nabla \boldsymbol{u} + (\nabla \boldsymbol{u})^{\mathrm{T}}\right)$ and S can be expressed as a principal-value singular integral

$$(S(x,t))_{ij} = P \cdot V \cdot \int K_{ijk}(\widehat{y})\omega_k(x-y,t)\frac{\mathrm{d}y}{|y|^3} \tag{4}$$

with

$$K_{ijk}(\widehat{y}) = \frac{3}{8\pi}\left(\epsilon_{ipk}\widehat{y}_j + \epsilon_{jpk}\widehat{y}_i\right)\widehat{y}_p \tag{5}$$

and $\widehat{y} = \frac{y}{|y|}$. The integral operator $\omega \mapsto S$ is of classical Calderon–Zygmund type. This means that the equation of evolution for ω is quadratic nonlinear nonlocal. There exist equations of this type that exhibit blowup, the formation of finite time singularities from smooth and localized initial data.

2. Conditions for the absence of blowup

Assuming that the initial data $\boldsymbol{u}_0$ is smooth enough, the Beale–Kato–Majda criterion [1] states that if the time integral of the spatial maximum of vorticity is finite, i.e. if

$$\int_0^T \left(\sup_x |\omega(x,t)|\right) \mathrm{d}t < \infty \tag{6}$$

then the solution is smooth on the time interval $[0, T]$.

2.1. A necessary criterion based on the direction of vorticity

The evolution of $|\omega|$ is given by

$$(\partial_t + u \cdot \nabla)\,|\omega| = \alpha|\omega| \tag{7}$$

with

$$\alpha = (\nabla u)\xi \cdot \xi = S\xi \cdot \xi, \tag{8}$$

$$\xi = \frac{\omega}{|\omega|} \tag{9}$$

and it turns out [2] that

$$\alpha(x,t) = \frac{3}{4\pi} P \cdot V \cdot \int_{\mathbf{R}^3} D(\widehat{y}, \xi(x-y,t), \xi(x,t))|\omega(x-y,t)|\frac{\mathrm{d}y}{|y|^3} \tag{10}$$

E-mail address: const@math.uchicago.edu.

0167-2789/$ - see front matter
doi:10.1016/j.physd.2008.01.006

with

$$D(e_1, e_2, e_3) = (e_1 \cdot e_3)\det(e_1, e_2, e_3). \tag{11}$$

Clearly, if ξ does not vary in space then $\alpha = 0$; this situation is encountered in two space dimensions. In general

$$|D(\widehat{y}, \xi(x-y,t), \xi(x,t))| \\ \le |\xi(x-y,t) \times \xi(x,t)| = |\sin\phi| \tag{12}$$

where ϕ is the angle between the unit vortex line tangent vectors $\xi(x-y,t)$ and $\xi(x,t)$. Some degree of smoothness of the bundle of vortex lines near a potential singularity may result in averting blowup [3]. For simplicity, we will discuss Lipschitz continuous cases, although Hölder continuous cases may be analyzed in a similar fashion. We distinguish between the sine-Lipschitz case (i.e. $\sin\phi$ is locally Lipschitz), when the vortex lines are at worst locally osculating anti-parallel

$$|\xi(x-y,t) \times \xi(x,t)| \le C_a|y|, \quad \text{for } |y| \le r(t) \tag{13}$$

and the Lipschitz case (i.e. ξ is locally Lipschitz) when the vortex lines are at worst locally osculating parallel

$$|\xi(x-y,t) - \xi(x,t)| \le C_p|y|, \quad \text{for } |y| \le r(t). \tag{14}$$

Clearly, Lipschitz implies sine-Lipschitz because

$$|\xi(x-y,t) - \xi(x,t)| \ge |\xi(x-y,t) \times \xi(x,t)|\,. \tag{15}$$

But the other implication is not true in general. In order to analyze the depletion effect due to organized vortex line structure we take a fixed $\rho > 0$, consider $r < \rho$, we take a smooth function $0 \le \chi \le 1$ compactly supported in the unit ball in $\boldsymbol{R}^3$ and define an inner rate of strain S^r as

$$(S^r(x,t))_{ij} \\ = P\cdot V\cdot \int \chi\left(\frac{y}{r}\right) K_{ijk}(\widehat{y})\omega_k(x-y)\frac{\mathrm{d}y}{|y|^3}. \tag{16}$$

Similarly, we define an outer rate of strain S_ρ as

$$(S_\rho(x,t))_{ij} \\ = P\cdot V\cdot \int \left(1-\chi\left(\frac{y}{\rho}\right)\right) K_{ijk}(\widehat{y})\omega_k(x-y)\frac{\mathrm{d}y}{|y|^3} \tag{17}$$

and an intermediate rate of strain as

$$\left(S_r^\rho(x,t)\right)_{ij} \\ = P\cdot V\cdot \int \left(\chi\left(\frac{y}{\rho}\right) - \chi\left(\frac{y}{r}\right)\right) K_{ijk}(\widehat{y})\omega_k(x-y)\frac{\mathrm{d}y}{|y|^3}. \tag{18}$$

This yields a decomposition

$$S = S^r + S_r^\rho + S_\rho. \tag{19}$$

Using (8) we have a corresponding decomposition of the stretching factor:

$$\alpha(x,t) = \alpha^r(x,t) + \alpha_r^\rho(x,t) + \alpha_\rho(x,t). \tag{20}$$

For instance, the inner stretching factor is

$$\alpha^r(x,t) = \frac{3}{4\pi} P\cdot V\cdot \int \chi\left(\frac{y}{r}\right) \\ \times D(\widehat{y}, \xi(x-y,t)\,\xi(x,t))|\omega(x-y,t)|\frac{\mathrm{d}y}{|y|^3}. \tag{21}$$

Now let us make some specific assumptions about the blowup. These are not exhaustive, but exemplify the method of [3] in slightly different circumstances. Our statements will be for the time interval $[0,T)$ and we should think of this being a short time before the blowup, by adjusting $t = 0$ to be just before the suspected blowup time. We assume that there exists a point in space (without loss of generality, this can be $x = 0$) so that the vorticity is going to blow up at $t = T$ somewhere in the neighborhood $B_t = \{x||x| < r(t)\}$ of this point. We do not assume that the vorticity is small outside this region, nor do we assume that the velocity is bounded.

Blowup assumption **A**: We assume that there exists one vortex line that is sine-Lipschitz and stays in B_t, that is,

$$(\mathrm{A}) \begin{cases} \exists q \in B_0 \quad \text{such that } x = X(q,t) \in B_t \text{ for } t \in [0,T), \\ \quad (13) \text{ holds for } x = X(q,t),\ |y| \le r(t), \\ \exists c, \quad 0 < c \le 1, \quad \text{such that} \\ \quad |\omega(X(q,t),t)| \ge c \sup_{z\in\boldsymbol{R}^3} |\omega(z,t)|. \end{cases}$$

Here $X(q,t)$ is the Lagrangian trajectory with initial label q. The assumption is thus that there exists one trajectory carrying a fraction of the maximum vorticity and which has a coherent sine-Lipschitz vortex line field near it at each instance of time, short time before blowup.

From (13) and (21) we obtain with $x = X(q,t)$, for $r \le r(t)$

$$\left|\alpha^r(x,t)\right| \le rC_a \sup_{z\in\boldsymbol{R}^3} |\omega(z,t)|. \tag{22}$$

For the intermediate stretching factor we obtain from (18) and one integration by parts that

$$\left|\alpha_r^\rho(x,t)\right| \le c\frac{U(x,t)}{r} \tag{23}$$

with

$$U(x,t) = \sup_{|x-z|\le\rho} |u(z,t)|. \tag{24}$$

The outer stretching factor is bounded

$$\left|\alpha_\rho(x,t)\right| \le c\rho^{-\frac{3}{2}}\|u_0\|_{L^2}. \tag{25}$$

Denoting

$$U(t) = \sup_x U(x,t), \qquad \Omega(t) = \sup_{z\in\boldsymbol{R}^3} |\omega(z,t)| \tag{26}$$

we can prove using only the Biot–Savart law [4] and the conservation of kinetic energy that

$$U(t) \le c\|\boldsymbol{u}_0\|_{L^2}^{\frac{2}{5}}\Omega(t)^{\frac{3}{5}} \tag{27}$$

holds for $t < T$. This is done by splitting the Biot–Savart integral in an inner integral, where we use $\Omega(t)$, and an outer integral, where we integrate by parts and use $\|u\|_{L^2}$. The inequality (27) then follows by choosing the optimal splitting in order to minimize the bound. Putting together the inequalities

(22), (23) and (25) and using

$$|\omega(X(q,t),t)| \le |\omega_0(q)| \exp \int_0^t |\alpha(X(q,s),s)| \mathrm{d}s \tag{28}$$

we see that if

$$\int_0^T \inf_{r \le r(t)} \left\{ \frac{U(t)}{r} + r C_a \Omega(t) \right\} \mathrm{d}t < \infty \tag{29}$$

then no blowup occurs. For example, let us make the assumption that

$$(T-t)\Omega(t) \le C \tag{30}$$

holds with some constant C. If $r(t) \sim (T-t)^a$, then we have two possibilities. If $a < \frac{1}{5}$ then we may choose $r = \sqrt{\frac{U(t)}{C\Omega(t)}}$ for $T-t$ small, optimizing in (29), and using (27); we see then that no blowup may occur. If $a \ge \frac{1}{5}$, then we have to take $r = r(t)$ in (29) and in that case no blow up occurs if $a < \frac{2}{5}$.

Thus, if the blow up assumption **A** holds and also (30) is valid then $a \ge \frac{2}{5}$ is necessary for blowup. That means that in order for blow up to occur, the vortex lines must become incoherent at distances that are rapidly vanishing.

This kind of argument can yield more restrictive results if more information about the geometry of the vortical region is provided.

There are many results giving criteria for the absence of blowup. In [5] it is shown that simple one-scale selfsimilar blowup is impossible. Absence of squirt singularities is proved in [6]. In [7] a detailed analysis was carried out based on a number of assumptions concerning the geometry of vortex lines and the magnitude of velocity.

2.2. *A sufficient criterion based on the pressure Hessian*

Let

$$\Pi(x,t) = \left(\frac{\partial^2 p}{\partial x_i \, \partial x_j} \right) \tag{31}$$

and consider

$$Q(t) = \{x | \Pi(x,t) > 0\} \tag{32}$$

the region where Π is positive definite. (Note that nondegenerate local minima of $p(x,t)$ are in $Q(t)$.) Then the following is sufficient for blowup:

$$(\mathrm{B}) \begin{cases} \exists a \in Q(0), \quad \text{such that } X(a,t) \in Q(t), \ \forall t \in [0,T] \\ \omega_0(b) = 0, \quad \text{for } |b-a| \text{ small enough}, \\ T\rho(S_0)(a) > 3 \\ \quad \text{where } \rho(S_0) = \text{ is the spectral radius of } S_0. \end{cases}$$

The idea of the proof was used in [8] to prove blowup for distorted Euler equations. We consider the equation obeyed by the rate of strain matrix,

$$D_t S + S^2 + \Pi - \frac{|\omega|^2}{4} P_\omega^\perp = 0 \tag{33}$$

where $D_t = \partial_t + \boldsymbol{u} \cdot \nabla$ and $P_\omega^\perp$ is the matrix that projects a vector onto the plane perpendicular on the direction of ω. The proof of the result is by contradiction. We assume that the solution is smooth up to time T. Then one can find a smooth function ϕ_0 with small support so that

$$\begin{cases} \int_{\boldsymbol{R}^3} |\phi_0(a)|^2 \mathrm{d}a = 1, \\ \int_{\boldsymbol{R}^3} S_0(a)\phi_0(a) \cdot \phi_0(a) \mathrm{d}a < 0, \\ T \left| \int_{\boldsymbol{R}^3} S_0(a)\phi_0(a) \cdot \phi_0(a) \mathrm{d}a \right| > 1, \\ \phi_0 |\omega_0|^2 = 0, \end{cases} \tag{34}$$

and also, if we solve

$$D_t \phi = 0, \quad \phi(a,0) = \phi_0(a) \tag{35}$$

then

$$\operatorname{supp} \phi(t) \subset Q(t) \text{ holds}, \quad \text{for } 0 \le t \le T. \tag{36}$$

We take

$$y(t) = \int S(x,t)\phi(x,t) \cdot \phi(x,t) \mathrm{d}x. \tag{37}$$

This blows up before T:

$$\frac{\mathrm{d}}{\mathrm{d}t} y + y^2 \le 0 \tag{38}$$

because

$$|\omega(x,t)|^2 |\phi(x,t)| = 0, \tag{39}$$

$$\int_{\boldsymbol{R}^3} |\phi(x,t)|^2 \mathrm{d}x = 1 \tag{40}$$

and Cauchy–Schwarz

$$\int_{\boldsymbol{R}^3} |S\phi|^2 \mathrm{d}x \ge y^2(t). \tag{41}$$

3. Weak solutions

The Navier–Stokes equations have global weak solutions in a natural space [9]. The same cannot be said about the Euler equations, but can be said about the surface quasi-geostrophic equations [10,11]. A general methodology for the construction of useful weak solutions does not exist, but the steps are usually: good approximation, integration by parts, weak continuity. Minimal requirements for weak solutions for the Euler equations are that they should be given by a weakly continuous function of time $\boldsymbol{u}(t)$ with values in the space of locally L^2 functions (uniformly, a technical requirement)

$$u \in C_w[0,T; L^2_{\mathrm{loc},u}]$$

such that, for every divergence-free compactly supported smooth function φ

$$\int u(t) \cdot \varphi \mathrm{d}x - \int u_0 \cdot \varphi \mathrm{d}x = \int_0^t \int \operatorname{Trace}\left[(u \otimes u)(\nabla \varphi)\right] \mathrm{d}x \mathrm{d}s$$

holds. The surface quasi-geostrophic equation (QG henceforth)

$$\begin{cases}\partial_t\theta + u\cdot\nabla\theta = 0,\\ u = R^{\perp}\theta\end{cases} \tag{42}$$

has served as a didactic model for 3D Euler equations [2,12]. Here $R = (\nabla)\Lambda^{-1}$ are Riesz operators and $\Lambda = (-\Delta)^{1/2}$ is the Zygmund operator. The equations are in two spatial dimensions and θ is a scalar. Analogous to vortex lines, the iso-θ lines are material, and the "vorticity" equation

$$\partial_t\left(\nabla^{\perp}\theta\right) + u\cdot\nabla\left(\nabla^{\perp}\theta\right) = \left(\nabla^{\perp}\theta\right)\cdot\nabla u \tag{43}$$

has the same stretching term as (3). A criterion like the Beale–Kato–Majda criterion is valid, and the geometric depletion of nonlinearity via the direction of "vorticity" takes place as well. In order to understand why these equations have weak solutions, the easiest route is via Fourier series in the periodic case.

3.1. Weak solutions for QG

For periodic $\theta = \sum_{j\in\mathbf{Z}^2}\widehat{\theta}(j)\mathrm{e}^{\mathrm{i}(j\cdot x)}$, the Eq. (42) is equivalent to an infinite sequence of ordinary differential equations:

$$\frac{\mathrm{d}}{\mathrm{d}t}\widehat{\theta}(l) = \sum_{j+k=l}\left(j^{\perp}\cdot k\right)|j|^{-1}\widehat{\theta}(j)\widehat{\theta}(k). \tag{44}$$

Using the fact that $j^{\perp}\cdot k$ is antisymmetric in j, k while the sum is over a symmetric set of vectorial indices and $\widehat{\theta}(j)\widehat{\theta}(k)$ is symmetric in j, k, it follows that

$$\frac{\mathrm{d}}{\mathrm{d}t}\widehat{\theta}(l) = \sum_{j+k=l}\gamma^{l}_{j,k}\widehat{\theta}(j)\widehat{\theta}(k) \tag{45}$$

where

$$\gamma^{l}_{j,k} = \frac{1}{2}(j^{\perp}\cdot k)\left(\frac{1}{|j|} - \frac{1}{|k|}\right). \tag{46}$$

Now clearly

$$\left|\gamma^{l}_{j,k}\right| \le \frac{|l|^2}{\max\{|j|,|k|\}}. \tag{47}$$

Consequently

$$\|(-\Delta)^{-1}\left[B(\theta_1,\theta_1) - B(\theta_2,\theta_2)\right]\|_w \le C\left(\|\theta_1\|_{L^2} + \|\theta_2\|_{L^2}\right) \times\left\{\|\theta_1-\theta_2\|_w\left(1+\log_+\|\theta_1-\theta_2\|_w\right)\right\} \tag{48}$$

where the weak norm $\|\theta\|_w = \sup_{j\in\mathbf{Z}^2}|\widehat{\theta}(j)|$. We see that the nonlinearity is weakly quasi-Lipschitz, with loss of two derivatives. The loss of derivatives does not impede existence theory for weak solutions. It does however prevent a proof of uniqueness of these weak solutions, and that is still open. The inequality allows a simple strategy of proof of existence of weak solutions. Any approximation procedure that gives long lived solutions and respects the conservation law $\theta \in L^2$ can be used. Then passing to a weakly convergent subsequence we obtain the fact that the weak limit solves weakly the equation, because of the inequality (48) and the strong convergence in $\|\ \|_w$ that follows from weak L^2 convergence. Although the QG equation is two dimensional, the reason for the property that allowed the global weak solutions is structural, not dimensional.

3.2. Littlewood–Paley decomposition and Euler equations

The Littlewood–Paley decomposition is a useful tool. For functions that are sufficiently well behaved at infinity it is enough to look at the so called inhomogeneous decomposition:

$$u = \sum_{j=-1}^{\infty}\Delta_j(u). \tag{49}$$

The operators Δ_j are defined using the Fourier transform $\mathcal{F}$ and have the properties

$$\operatorname{supp}\mathcal{F}(\Delta_j(u)) \subset \left\{\xi;\ |\xi|\in 2^j\left[\frac{1}{2},\frac{5}{4}\right]\right\}$$

$$\Delta_j\Delta_k \ne 0 \Rightarrow |j-k| \le 1,$$

$$\left(\Delta_j + \Delta_{j+1} + \Delta_{j+2}\right)\Delta_{j+1} = \Delta_{j+1}$$

$$\Delta_j\left(S_{k-2}(u)\Delta_k(v)\right) \ne 0 \Rightarrow k\in[j-2, j+2]$$

where $S_k(u) = \sum_{j=-1}^{k}\Delta_j(u)$.

Specifically,

$$\Delta_j = \Psi_j(D) = \Psi_0(2^{-j}D),\quad \Delta_{-1}u = \Phi_{-1}(D)u$$

where Φ_{-1} is radial, nonincreasing, C^{∞} and

$$\begin{cases}\Phi_{-1} = 1, & 0\le r\le a\\ \Phi_{-1} = 0, & r\ge b\\ 0 < a < b < 1\end{cases}$$

$$\Psi_0(r) = \Phi_{-1}(r/2) - \Phi_{-1}(r),\qquad \Psi_j(r) = \Psi_0(2^{-j}r).$$

$$(\Psi(D)u)(x) = (2\pi)^{-n}\int_{\mathbf{R}^n}\mathrm{e}^{\mathrm{i}(x\cdot\xi)}\Psi(\xi)\widehat{u}(\xi)\mathrm{d}\xi$$

$\widehat{u}(\xi) = \mathcal{F}(u)(\xi) = \int_{\mathbf{R}^n}\mathrm{e}^{-\mathrm{i}(x\cdot\xi)}u(x)\mathrm{d}x$ and $a < b < \frac{4}{3}a$ (for instance $a = 1/2, b = 5/8$ works).

The Littlewood decomposition can be used to define inhomogeneous Besov spaces

$$\|u\|_{B^s_{p,q}} = \left\|\left\{2^{sj}\|\Delta_j(u)\|_{L^p}\right\}_j\right\|_{\ell^q(\mathbf{N})}$$

and the space $B^s_{p,c(\mathbf{N})}$ which is the closed subspace of $B^s_{p,\infty}$ formed with functions such that

$$\lim_{j\to\infty}2^{sj}\|\Delta_j(u)\|_{L^p} = 0.$$

In $B^s_{p,q}$, s counts the number of derivatives, p refers to the L^p space and q is an interpolation index.

3.3. Euler weak solutions: Main difficulty

The nonlinearity in the Euler equations is

$$B(u,v) = \mathbf{P}(u\cdot\nabla v) = \Lambda\mathbf{H}(u,v) \tag{50}$$

with $\boldsymbol{P}$ the Leray–Hodge projection on divergence-free functions and

$$[\boldsymbol{H}(u,v)]_i = R_j(u_j v_i) + R_i(R_k R_l(u_k v_l)), \tag{51}$$

and $R_k = \partial_k \Lambda^{-1}$ Riesz transforms. Applying Δ_q we have

$$\Delta_q(B(u,v)) = C_q(u,v) + I_q(u,v) \tag{52}$$

where

$$C_q(u,v) = \sum_{p\geq q-2, |p-p'|\leq 2} \Delta_q(\Lambda \boldsymbol{H}(\Delta_p u, \Delta_{p'} v)) \tag{53}$$

and

$$I_q(u,v) = \sum_{j=-2}^{2} [\Delta_q \Lambda \boldsymbol{H}(S_{q+j-2}u, \Delta_{q+j}v) + \Delta_q \Lambda \boldsymbol{H}(S_{q+j-2}v, \Delta_{q+j}u)] \tag{54}$$

is essentially the Bony paraproduct [13]. For L^2 weak solutions it would be desirable to have a bound of the type

$$\|\Lambda^{-M}(B(u_1,u_1) - B(u_2,u_2))\|_w \leq C\|u_1 - u_2\|_w^a [\|u_1\|_{L^2} + \|u_2\|_{L^2}]^{2-a} \tag{55}$$

with $a > 0$ and $\|f\|_w$ a weak enough norm so that weak convergence in L^2 implies, after localization, strong convergence in the w norm. The number M could be as large as needed. An inequality (55) is true for $I(u,v)$ but not for $C(u,v)$. On the other hand, if one wishes weak solutions with positive derivative exponents, for instance weak solutions in $B^{\frac{1}{3}}_{3,q}$, then $C(u,v)$ has good continuity properties, and $I(u,v)$ does not [14]. The terms I_q, if retained alone, would produce a leaky Galerkin approximation

$$\frac{\partial \Delta_q(u)}{\partial t} = I_q(u,u),$$

and the terms $C_q(u,u)$ an ill-formed shell model

$$\frac{\partial \Delta_q(u)}{\partial t} = C_q(u,u).$$

A description of the regularity of some shell models is given in [15].

3.4. The Onsager conjecture

Although weak solutions with positive smoothness have not been proven to exist (see [16,17] for examples of weak solutions), the subject is important because of the relation to turbulence. The Onsager conjecture [18,19] asserts that kinetic energy is conserved for solutions in C^s with $s > \frac{1}{3}$ and dissipated for rougher solutions, in particular in $C^{\frac{1}{3}}$. The paper [20] proves that if weak solutions belong to $L^3[0,T; B^s_{3,\infty}]$ with $s > \frac{1}{3}$ then they conserve kinetic energy. The paper [21] extended this to spaces in which the fractional derivative D^s (2^{js} in the Littlewood–Paley decomposition) is replaced with any function of $f(D)$ such that $f(D)D^{-\frac{1}{3}} \to \infty$ as $D \to \infty$. This actually follows also from the proof in [20]. More recently, it was shown [14] that weak solutions of the 3D Euler equations in $u \in L^3([0,T], B^{1/3}_{3,c(\boldsymbol{N})})$ conserve kinetic energy. On the other hand, there exist functions in $B^{\frac{1}{3}}_{3\infty}$ that are divergence-free and do not conserve energy in the sense to be made more precise below. Consider the flux

$$\Pi_N := \int_{\boldsymbol{R}^3} \mathrm{Trace}[S_N(u\otimes u)\nabla S_N(u)]\mathrm{d}x. \tag{56}$$

This is the (formal) time derivative

$$\Pi_N = \frac{1}{2}\frac{\mathrm{d}}{\mathrm{d}t}\int_{\boldsymbol{R}^3} |S_N(u(t))|^2\,\mathrm{d}x$$

of the energy contained in $S_N(u)$ when u solves the Euler equation. There exist functions in $B^{1/3}_{3,\infty}$ that are divergence-free and obey $\liminf_{N\to\infty}|\Pi_N| > 0$. On the other hand, if $u \in B^{\frac{1}{3}}_{3,c(\boldsymbol{N})}$ then $\limsup_{N\to\infty}|\Pi_N| = 0$. More specifically, if we let

$$K(j) = \begin{cases} 2^{\frac{2j}{3}}, & j \leq 0; \\ 2^{-\frac{4j}{3}}, & j > 0, \end{cases}$$

and

$$d_j = 2^{j/3}\|\Delta_j(u)\|_3, \quad \text{for } j \geq -1,$$
$$d_j = 0 \quad \text{for } j < -1 d^2 = \{d_j^2\}_j.$$

If $u \in L^2$ then it can be shown that

$$|\Pi_N| \leq C(K * d^2)^{3/2}(N) \tag{57}$$

where $*$ means convolution of sequences. Consequently, of course

$$\limsup_{N\to\infty}|\Pi_N| \leq \limsup_{N\to\infty} d_N^3, \tag{58}$$

but moreover, a strong localization of the flux results from (57).

Acknowledgments

Work partially supported by NSF DMS grant 0504213 and by the ASC Flash Center at the University of Chicago.

References

[1] J.T. Beale, T. Kato, A. Majda, Remarks on the breakdown of smooth solutions for the 3-D Euler equations, Commun. Math. Phys. 94 (1984) 61–66.

[2] P. Constantin, Geometric statistics in turbulence, SIAM Rev. 36 (1994) 73–98.

[3] P. Constantin, C. Fefferman, A. Majda, Geometric constraints on potentially singular solutions for the 3-D Euler equations, Commu. Partial Differential Equations 21 (1996) 559–571.

[4] A. Majda, A. Bertozzi, Vorticity and Incompressible Flow, Cambridge University Press, Cambridge, 2001.

[5] D. Chae, Nonexistence of self-similar singularities for the 3D incompressible Euler equations, Commun. Math. Phys. 273 (2007) 203–215.

[6] D. Cordoba, C. Fefferman, R. de la Llave, On squirt singularities in hydrodynamics, SIAM J. Math. Anal. 36 (2004) 204–213.

[7] J. Deng, T.Y. Hou, X. Yu, Geometric properties and non-blowup for 3-D incompressible Euler flow, Commu. Partial Differential Equations 30 (2005) 225–243.

[8] P. Constantin, Note on loss of regularity for solutions of the 3D incompressible Euler and related equations, Commun. Math. Phys. 106 (1986) 311–326.
[9] J. Leray, Essai sur le mouvement d'un liquide visqueux emplissant l'espace, Acta Math. 63 (1934) 193–248.
[10] S. Resnick, Dynamical problems in nonlinear advective partial differential equations. Ph.D. Thesis, University of Chicago, 1995.
[11] P. Constantin, D. Cordoba, J. Wu, On the critical dissipative quasigeostrophic equation, Indiana U. Math. J. 50 (2001) 97–107.
[12] P. Constantin, A. Majda, E. Tabak, Formation of strong fronts in the 2D quasi-geostrophic thermal active scalar, Nonlinearity 7 (1994) 1495–1533.
[13] J.-M. Bony, Calcul symbolique et propagation des singularités pour les équations aux dérivées partielles non linéaires, Ann. Ecole Norm. Sup. 14 (1981) 209–246.
[14] A. Cheskidov, P. Constantin, S. Friedlander, R. Shvydkoy, Energy conservation and Onsager's conjecture for the Euler equations. arXiv:Math.AP/0704.0759, 2007.
[15] P. Constantin, B. Levant, E. Titi, Regularity of inviscid shell models of turbulence, Phys. Rev. E 75 (1) (2007) 016305.
[16] C. De Lellis, L. Szekelyhidi, The Euler equations as differential inclusions, 2007. Preprint.
[17] A. Shnirelman, On the nonuniqueness of weak solution of the Euler equation, Comm. Pure Appl. Math. 50 (1997) 1261–1286.
[18] L. Onsager, Statistical hydrodynamics, Nuovo Cimento (Supplemento) 6 (1949) 279–287.
[19] G.L. Eyink, Energy dissipation without viscosity in ideal hydrodynamics. I. Fourier analysis and local energy transfer, Phys. D 78 (1994) 222–240.
[20] P. Constantin, W.E.E. Titi, Onsager's conjecture on the energy conservation for solutions of Euler's equation, Commun. Math. Phys. 165 (1994) 207–209.
[21] J. Duchon, R. Robert, Inertial energy dissipation for weak solutions of incompressible Euler and Navier–Stokes equations, Nonlinearity 13 (2000) 249–255.

Available online at www.sciencedirect.com
ScienceDirect
Physica D 237 (2008) 1932–1936
PHYSICA D
www.elsevier.com/locate/physd

Numerical simulations of possible finite time singularities in the incompressible Euler equations: Comparison of numerical methods

Tobias Grafke, Holger Homann, Jürgen Dreher, Rainer Grauer*

Institute for Theoretical Physics I, Ruhr-Universität Bochum, Germany

Available online 17 November 2007

Abstract

The numerical simulation of the 3D incompressible Euler equations is analyzed with respect to different integration methods. The numerical schemes we considered include spectral methods with different strategies for dealiasing and two variants of finite difference methods. Based on this comparison, a Kida–Pelz-like initial condition is integrated using adaptive mesh refinement and estimates on the necessary numerical resolution are given. This estimate is based on analyzing the scaling behavior similar to the procedure in critical phenomena and present simulations are put into perspective.

PACS: 47.10.A-; 47.11.Bc; 47.11.Df; 47.11.Kb; 47.15.ki

Keywords: Finite time singularities; Finite difference/volumes methods; Spectral methods

1. Introduction

The question, whether the incompressible Euler equations develop singularities in finite time starting from smooth initial conditions, remains an outstanding open problem in applied mathematics. Although substantial progress has been made in recent years using a more geometrical viewpoint [1–5], it is not yet clear from numerical simulations, whether the assumptions of the theorems for non-blow up are fulfilled for flows evolving from simple smooth initial conditions. Singular structures, evolving in finite time or simply "fast enough", may play a similar role as shock-like structures in compressible flows, providing structures which dominate energy dissipation even in the non-viscous situation (see Eyink [6–8] and references therein).

In this paper, we study a Kida–Pelz-like flow with different numerical schemes: spectral methods with different strategies of dealiasing (this extends the study of Hou and Li [9] and confirms their results), two finite difference methods and a finite volume method. Studying the structures of vorticity, it turns out that the differences between the various methods of dealiasing are more pronounced than that between the spectral methods and the finite difference/volume methods. This result suggests that resolving the vorticity structures is more important than the order of the numerical scheme. It also justifies the use of finite difference/volume methods in adaptive mesh refinement (AMR) simulations to resolve the vorticity structures.

Using AMR simulations up to an effective resolution of 4096^3 mesh points and comparing the results to lower resolution runs, we observe that the standard way of presenting a $1/|\boldsymbol{\omega}|$ plot in time may lead to misleading conclusions. However, observing normalized plots reveals the issue of numerical resolution in a convincing manner.

2. Numerical schemes

In this section we compare spectral methods with different dealiasing and finite difference/volume methods.

2.1. Spectral methods and dealiasing

We use a standard spectral method where the time stepping is performed with a strongly stable third-order Runge–Kutta method [10] in Fourier space and where non-linearities are

* Corresponding author.
E-mail address: grauer@tp1.rub.de (R. Grauer).

0167-2789/$ - see front matter © 2007 Elsevier B.V. All rights reserved.
doi:10.1016/j.physd.2007.11.006

calculated in real space. On Linux-clusters, the FFTW-library is used whereas the library P3DFFT [11] from the San Diego Supercomputer Center is used on the IBM Regatta series and on BlueGene/L.

We use three ways of dealiasing the spectral data:

1. Spherical mode truncation: this is used in turbulence simulations (Biskamp and Müller [12]). The spherical mode truncation puts a sphere of radius $\frac{N}{2}$ in Fourier space and nullifies all modes outside this sphere.
2. Standard 2/3 rule: same as above, but using a radius of $\frac{2}{3}\frac{N}{2} = \frac{N}{3}$ [13]. This is the most common way of dealiasing spectral data.
3. High-order exponential cut-off: this method was introduced by Hou and Li [9] and consists of introducing a high-order exponential filter function $\rho(k) = \exp(-\alpha(|k|/N)^m)$ with $\alpha = 36$ and $m = 36$.

2.2. *Finite difference/volumes methods*

All the presented finite difference/volume methods are of second order and use the same strongly stable third-order Runge–Kutta method [10] as used in the spectral simulations.

We implemented three different versions of real-space methods:

1. Staggered grid formulation of Harlow and Welsh [14]: Normal components of the velocity are located at their respective cell faces and the pressure is defined at the cell centers. This allows an exact Hodge decomposition such that no pressure oscillations occur. In addition, it conserves momentum and energy and could thus also been seen as a finite volume method.
2. Vorticity formulation for AMR: From our previous AMR studies [15,16] we know that the coarse-fine grid interpolations are very sensitive in the 3D Euler simulations. As in the former simulations we choose to perform all data exchange and interpolation using the vorticity $\boldsymbol{\omega} = \nabla \times \mathbf{u}$. Here, the vorticity is defined at cell centers and we applied a tri-cubic interpolation for coarse-fine grid interpolation. Then, three Poisson equations are solved for the cell-centered vector Potential $\mathbf{A}$ and staggered values for the velocity $\mathbf{u} = \nabla \times \mathbf{A}$ are obtained.
3. Finite volume method: this method is similar to the former but a finite volume method [15,17,18] is used instead of finite differences.

2.3. *Comparison*

We first compare the growth of the maximum vorticity according to the Beale–Kato–Majda result [19,20] for all six numerical methods described above. The initial condition was chosen similar to Kida–Pelz 12 vortices [21–23] with a Gaussian shape for the vorticity distribution. Resolution of all the spectral simulations were 512^3 mesh points (corresponding to the full domain) and in addition the Hou–Li exponential filtering was repeated with 1024^3 mesh points. The finite difference/volume simulations were performed with 512^3 and 1024^3 mesh points. The growth of max $|\boldsymbol{\omega}|$ is shown in Fig. 1.

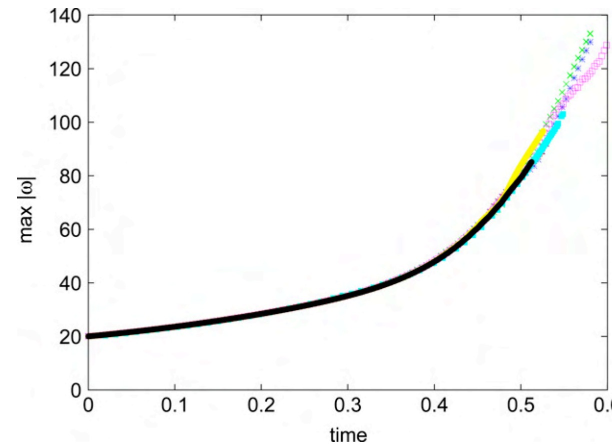

Fig. 1. Growth of max $|\boldsymbol{\omega}|$ for all implemented numerical schemes.

All simulations agree very well up to the time when the flow is underresolved. This is about $t = 0.4$ for the simulations using 512^3 mesh points and $t = 0.47$ for the 1024^3 runs. There is no particular criterion under which the simulation performs better once the simulation is underresolved. The very simple message from this comparison is: you just have to resolve the flow and this is more important than the order of the scheme.

In order to display the differences and similarities of the various numerical methods, we used a "low resolution" simulation with 512^3 mesh points at a late time $t = 0.5$ where the flow is already underresolved. Therefore, we looked at very low levels (5% of the maximum vorticity) as suggested and done by Kerr [24] and Hou and Li [25]. Due to the high symmetry of the flow, only 1/8 of the total configuration is shown in Fig. 2. (To get a better impression for the geometry of the vortices, see Fig. 4, which shows an isosurface of 70% of the peak vorticity.)

The spherical truncation produces highly visible artifacts due to heavy oscillations which grow to substantial values. This is mostly suppressed in the simulation using the classical 2/3 rule and nearly vanishes for the high-order exponential smoothing. Thus our comparison confirms the analysis of Hou and Li [25]. The strong similarity of the real-space methods to the spectral simulation with high-order exponential smoothing is remarkable. This is especially visible in Fig. 3, which shows the energy spectrum for spectral and finite difference/volume methods at time $t = 0.5$. In the spectral schemes, the spherical truncation and the 2/3 rule show strong Gibbs phenomena which is absent in the exponential filtering and the finite difference/volume schemes. The Harlow–Welsh method is slightly more dissipative than the vorticity formulation. From the comparison with the spectral schemes using exponential filtering and 1024^3 mesh points, it is safe to say that the finite difference schemes with an approximately 1.3 times larger resolution in each spatial direction perform equally well as the spectral code with exponential filtering. Thus, our conclusions of this comparison is that the differences in the simulation results caused by the choice of the dealiasing method are larger than the difference to and between the real-space methods. Our finding thus confirms the viewpoint of Orlandi and Carnevale [26] and justifies the use of finite difference/volume methods

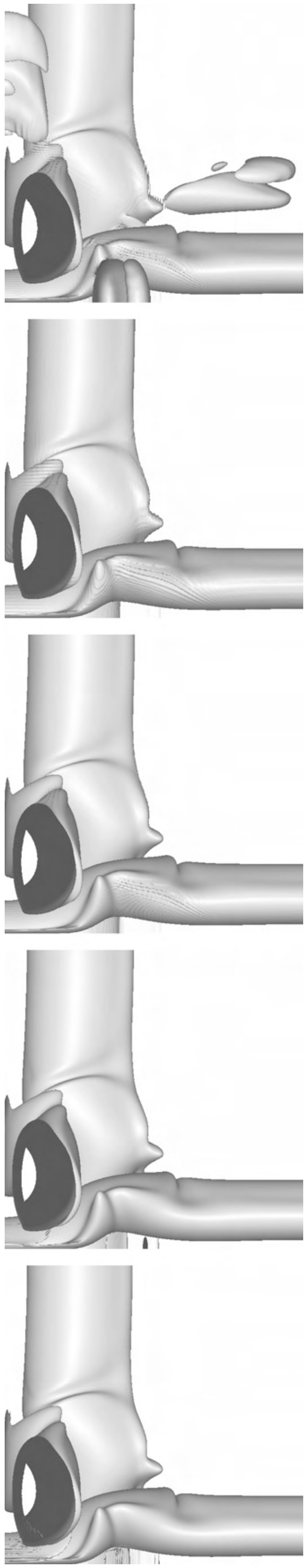

Fig. 2. Isosurface plots of vorticity. From top to bottom: spherical truncation, 2/3 rule, exponential filtering, Harlow–Welsh, vorticity formulation, 512^3 mesh points.

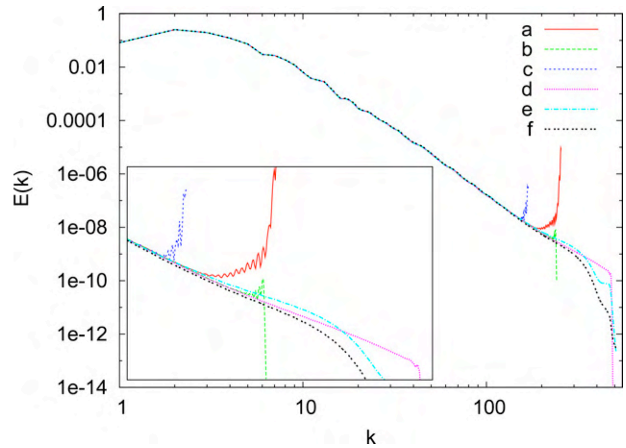

Fig. 3. Energy spectra at time $t = 0.5$ for spectral and finite difference methods: a) spherical model truncation (512^3), (b) high-order exponential cut-off (512^3), (c) 2/3 rule (512^3), (d) high-order exponential cut-off (1024^3), (e) vorticity formulation (1024^3), (f) staggered grid formulation (1024^3).

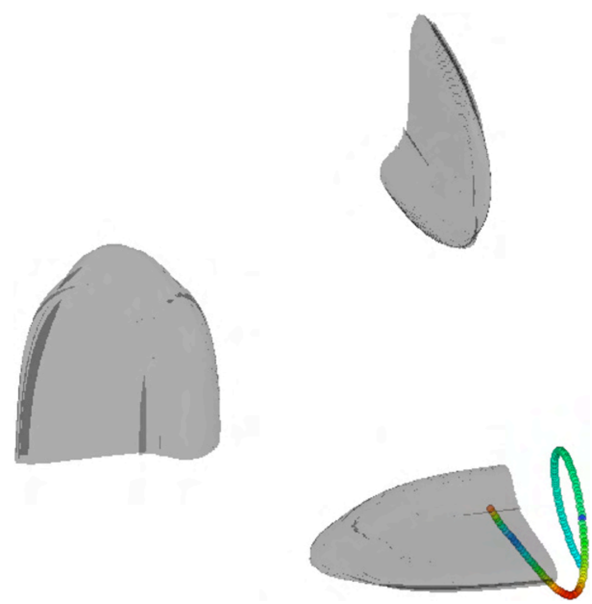

Fig. 4. Isosurface plot of max $|\boldsymbol{\omega}|$ at 70% of maximum vorticity. Shown is also the trajectory of a particle moving to the position of maximum vorticity.

as an integration scheme in an adaptive mesh refinement treatment.

2.4. Lagrangian trajectories

As pointed out in [3,4], the Lagrangian treatment of vorticity amplification is closely related to the local geometric properties – like curvature and torsion – of vortex lines. In Fig. 4 the trajectory of a Lagrangian tracer particle is shown. To obtain this trajectory, we first identified the spatial position of the maximum vorticity at a late time of the simulation and then traced back the actual trajectory. Fig. 5 shows the temporal evolution of vorticity following this trajectory. A tendency to an exponential growth of vorticity along the trajectory is obvious.

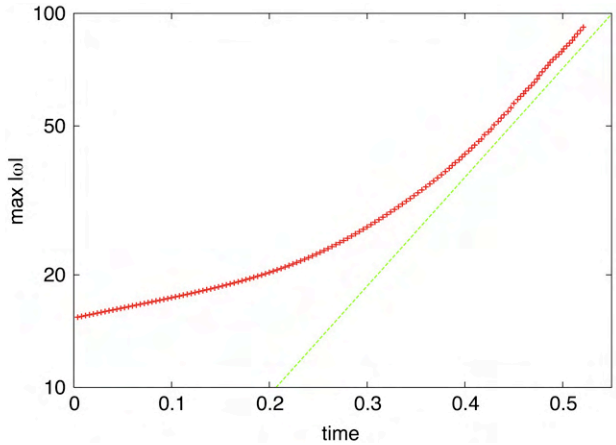

Fig. 5. Growth of vorticity along the Lagrangian trajectory (red) which ends near the point of maximum vorticity and a fitted exponential (green). (For interpretation of the references to colour in this figure legend, the reader is referred to the web version of this article.)

3. Adaptive mesh refinement simulations

3.1. *The framework racoon*

For the adaptive mesh refine calculations, we use our framework *racoon* [27] which is designed for massive parallel computations and scales for hyperbolic systems linearly up to 16 384 processors on BlueGene BG/L. However, for the incompressible Euler equations, the pressure respectively the vector potential are solved using an adaptive multigrid method [28,29] which presently scales only up to 64 processors. Therefore, the present simulations are limited to an effective resolution of 4096^3 mesh points. Parallelization and load balancing are performed using a space-filling Hilbert curve [27].

Using the framework *racoon* and the vorticity formulation, we solve the incompressible Euler equations with an effective resolution of 4096^3 mesh points. Fig. 6 shows a volume rendering of vorticity at the latest time $t = 0.5$ including the adaptive meshes. Memory consumption is quite moderate using less than 80 GBytes.

3.2. *Analyzing the growth of vorticity*

Observing Fig. 7 which shows the time evolution of $1/\max|\boldsymbol{\omega}|$ it is tempting to identify a finite time singularity. However, a more appropriate presentation is obtained by plotting $\max|\boldsymbol{\omega}| \times (t_0 - t)$ where t_0 is the expected singularity time. This quantity should converge to a horizontal line in this plot if a singularity occurs in finite time. The time $t_0 = 0.638$ is chosen in such a way that this scaling is observed in the late phase of the simulation while the numerics are still resolved. This is shown in Fig. 8 and the zoom in the inlet of this figure. Especially the zoom of the late phase of the simulation demonstrates, how sensitive the growth of vorticity depends on the numerical resolution and that conclusions drawn from underresolved simulations must be handled with care.

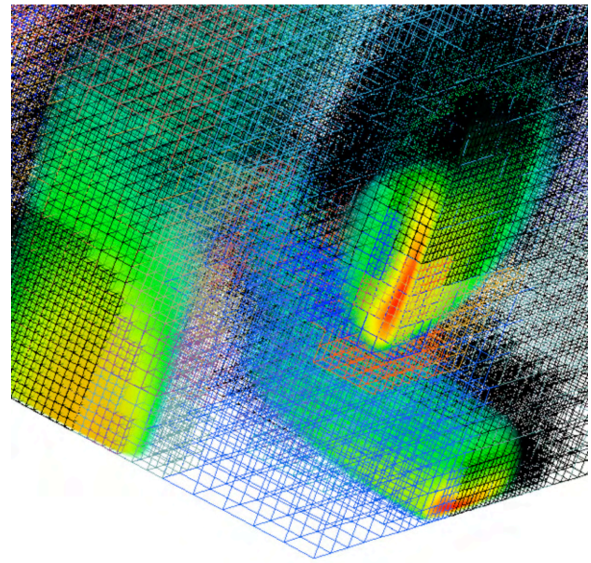

Fig. 6. Volume rendering of vorticity at time $t = 0.5$.

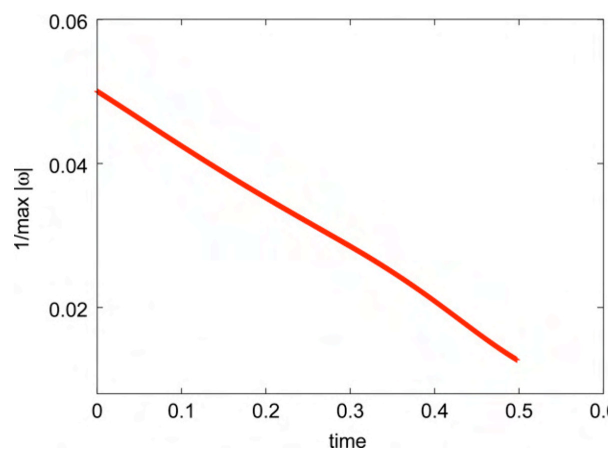

Fig. 7. Temporal evolution of $1/\max|\boldsymbol{\omega}|$.

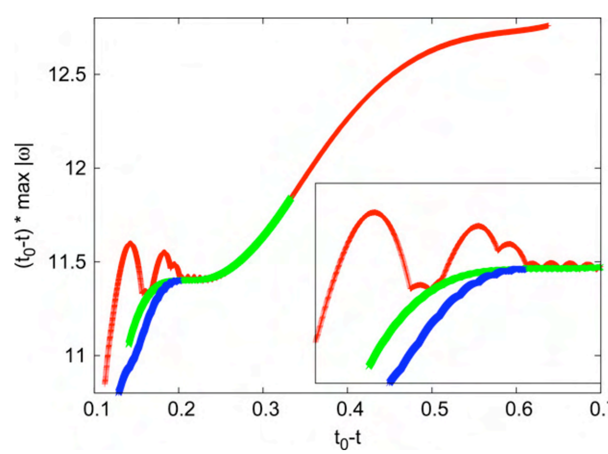

Fig. 8. Scaling of the growth of vorticity. Red: 1024^3 mesh points, Blue: 2048^3 mesh points, Green: 4096^3 mesh points. The inlet shows the late phase of the simulation and highlights the importance of numerical resolution. (For interpretation of the references to colour in this figure legend, the reader is referred to the web version of this article.)

4. Conclusions and outlook

We demonstrated the extreme sensitivity of the growth of vorticity on the numerical resolution. In order to gain further insight into the mechanism of vorticity amplification, future simulations should include the following analysis and diagnostics:

(i) If a finite time singularity is expected, then the blow-up time of vorticity must occur at the same time when the spatial positions of maximum vorticity and maximum strain come together.

(ii) The Lagrangian viewpoint should be analyzed according to Deng, Hou and Xu [4] and Gibbon [3].

(iii) Simulations should use initial conditions including the Kida–Pelz flow [21] and Bob Kerr's orthogonal tubes [30]. However, the shape of the initial vortex tube should be chosen in such a way that vortex shedding will not pollute the vorticity growth. For orthogonal vortex tubes this was achieved by Orlandi and Carnevale [26] starting with Lamb dipoles.

Acknowledgments

R.G. expresses his thanks to Gregory Eyink, John Gibbon, Thomas Hou, Robert Kerr and Miguel D. Bustamante for the fruitful discussion and Uriel Frisch and his coworkers for organizing this conference. Access to the JUMP multiprocessor computer at the FZ Jülich was made available through project HB022. Part of the computations were performed on an Linux-Opteron cluster supported by HBFG-108-291.

References

[1] P. Constantin, C. Fefferman, A.J. Majda, Geometric constraints on potentially singular solutions for the 3-d euler equations, Comm. Partial Differential Equations 21 (1996) 559–571.
[2] J.D. Gibbon, A quaternionic structure in the three dimensional euler and ideal magneto-hydrodynamics equation, Physica D 166 (2002) 17–28.
[3] J.D. Gibbon, The three-dimensional euler equations: Where do we stand?, Physica D 237 (14–17) (2008) 1894–1904.
[4] J. Deng, T.Y. Hou, X. Yu, Geometric properties and non-blowup of 3-d incompressible euler flow, Comm. Partial Differential Equations 30 (2005) 225–243.
[5] J. Deng, T.Y. Hou, X. Yu, Improved geometric conditions for non-blowup of the 3d incompressible euler equation, Comm. Partial Differential Equations 31 (2006) 293— 306.
[6] G.L. Eyink, Energy dissipation without viscosity in ideal hydrodynamics, Physica D 78 (1994) 222–240.
[7] G. Eyink, K.R. Sreenivasan, Onsager and the theory of hydrodynamic turbulence, Rev. Modern Phys. 78 (2006) 87–135.
[8] G. Eyink, Dissipative anomalies in singular Euler flows, Physica D 237 (14–17) (2008) 1956–1968.
[9] T.Y. Hou, R. Li, Computing nearly singular solutions using pseudo-spectral methods, J. Comput. Phys 226 (2007) 379–397.
[10] C. Shu, S. Osher, Efficient implementation of essentially non-oscillatory shock-capturing schemes, J. Comput. Phys. 77 (1988) 439–471.
[11] D. Pekurovsky, P.K. Yeung, D. Donzis, S. Kumar, W. Pfeiffer, G. Chukkapalli, Scalability of a pseudospectral dns turbulence code with 2d domain decomposition on power4+/federation and blue gene systems. www.spscicomp.org/ScicomP12/Presentations/User/Pekurovsky.pdf.
[12] D. Biskamp, W.C. Müller, Decay laws for three-dimensional magnetohydrodynamic turbulence, Phys. Rev. Lett. 83 (1999) 2195.
[13] C. Canuto, M.Y. Hussaini, A. Quarteroni, T.A. Zang, Spectral Methods in Fluid Dynamics, Springer, 1987.
[14] F.H. Harlow, J.E. Welsh, Numerical calculation of time-dependent viscous incompressible flow with free surface, Phys. Fluids 8 (1965) 2182.
[15] R. Grauer, C. Marliani, K. Germaschewski, Adaptive mesh refinement for singular solutions of the incompressible euler equations, Phys. Rev. Lett. 80 (1998) 4177–4180.
[16] R. Grauer, C. Marliani, Current sheet formation in 3d ideal incompressible magnetohydrodynamics, Phys. Rev. Lett. 84 (2000) 4850–4853.
[17] J.B. Bell, P. Colella, H.M. Glaz, A second-order projection method for the incompressible Navier–Stokes equation, J. Comput. Phys. 85 (1989) 257–283.
[18] J.B. Bell, D.L. Marcus, Vorticity intensification and transition to turbulence in the three-dimensional euler equation, Comm. Math. Phys. 147 (1992) 371–394.
[19] J.T. Beale, T. Kato, A. Majda, Remarks on the breakdown of smooth solutions for the 3d euler equations, Comm. Math. Phys. 94 (1984) 61–64.
[20] G. Ponce, Remarks on a paper by J.T. Beale, T. Kato, and A. Majda, Comm. Math. Phys. 98 (1985) 349–353.
[21] S. Kida, Three-dimensional periodic flows with high-symmetry, J. Phys. Soc. Jpn. 54 (1985) 2132–2136.
[22] O.N. Boratav, R.B. Pelz, Direct numerical simulation of transition to turbulence from a high-symmetry initial condition, Phys. Fluids 6 (1994) 2757–2784.
[23] R.B. Pelz, Symmetry and the hydrodynamic blow-up problem, J. Fluid. Mech. 444 (2001) 299–320.
[24] R. Kerr, Computational euler history. arXiv:physics/0607148v2.
[25] T.Y. Hou, R. Li, Dynamic depletion of vortex stretching and non-blowup of the 3-d incompressible euler equations, J. Nonlinear Sci. 16 (2006) 639–664.
[26] P. Orlandi, G.F. Carnevale, Nonlinear amplification of vorticity in inviscid interaction of orthogonal lamb dipoles, Phys. Fluids 19 (2007) 057106.
[27] J. Dreher, R. Grauer, Racoon: A parallel mesh-adaptive framework for hyperbolic conservation laws, Parallel Comput. 31 (2005) 913–932.
[28] A. Brandt, Multi-level adaptive solutions to boundary-value problems, Math. Comput. 31 (1977) 333–390.
[29] M. Barad, P. Colella, A fourth-order accurate local refinement method for poisson's equation, J. Comput. Phys. 1 (2005) 1–18.
[30] R. Kerr, Evidence for a singularity of the three-dimensional, incompressible euler equations, Phys. Fluids A 5 (1993) 1725–1746.

Available online at www.sciencedirect.com
ScienceDirect
Physica D 237 (2008) 1937–1944
PHYSICA D
www.elsevier.com/locate/physd

Blowup or no blowup? The interplay between theory and numerics

Thomas Y. Hou[a,*], Ruo Li[b]

[a] Applied and Computational Math, 217-50, Caltech, Pasadena, CA 91125, USA
[b] LMAM&School of Mathematical Sciences, Peking University, Beijing 100871, China

Available online 25 January 2008

Abstract

The question of whether the 3D incompressible Euler equations can develop a finite time singularity from smooth initial data has been an outstanding open problem in fluid dynamics and mathematics. Recent studies indicate that the local geometric regularity of vortex lines can lead to dynamic depletion of vortex stretching. Guided by the local non-blowup theory, we have performed large scale computations of the 3D Euler equations on some of the most promising blowup candidates. Our results show that there is tremendous dynamic depletion of vortex stretching. The local geometric regularity of vortex lines and the anisotropic solution structure play an important role in depleting the nonlinearity dynamically and thus prevents a finite time blowup.

PACS: 47.32.C-; 47.11.Kb

Keywords: Finite time singularities; 3D Euler equations; Spectral methods

1. Introduction

The question of whether the 3D incompressible Euler equations can develop a finite time singularity from smooth initial data is one of the most outstanding open problems in fluid dynamics and mathematics. This open problem is closely related to the Clay Millennium Open Problem on the 3D Navier–Stokes equations. The understanding of this problem could improve our understanding on the onset of turbulence and the intermittency properties of turbulent flows. A main difficulty in answering this question is the presence of vortex stretching, which gives a formal quadratic nonlinearity in vorticity. There have been many computational efforts in searching for finite time singularities of the 3D Euler equations, see e.g. [2–5,11–13,17,18,21–23]. For a more comprehensive review of this subject, we refer the reader to the book by Majda and Bertozzi [20] and the excellent review article by J. Gibbon in this issue [10].

Computing Euler singularities numerically is an extremely challenging task. First of all, it requires huge computational resources. Tremendous resolutions are required to capture the nearly singular behavior of the Euler equations. Secondly, one has to perform a careful convergence study. It is dangerous to interpret the blowup of an under-resolved computation as an evidence of finite time singularities for the 3D Euler equations. Thirdly, if we believe that the numerical solution we compute leads to a finite time blowup, we need to demonstrate the validation of the asymptotic blowup rate, i.e. is the blowup rate $\|\omega\|_{L^\infty} \approx \frac{C}{(T-t)^\alpha}$ asymptotically valid as $t \to T$? One also needs to check if the blowup rate of the numerical solution is consistent with the Beale–Kato–Majda non-blowup criterion [1] and other non-blowup criteria [7–9]. The interplay between theory and numerics is clearly essential in our search for Euler singularities.

There has been some interesting development in the theoretical understanding of the 3D incompressible Euler equations. It has been shown that the local geometric regularity of vortex lines can play an important role in depleting nonlinear vortex stretching [6–9]. In particular, the recent results obtained by Deng, Hou, and Yu [8,9] show that geometric regularity of vortex lines, even in an extremely localized region containing the maximum vorticity, can lead to depletion of nonlinear vortex stretching, thus avoiding finite

* Corresponding author. Tel.: +1 626 395 4546; fax: +1 626 578 0124.
E-mail address: hou@acm.caltech.edu (T.Y. Hou).

0167-2789/$ - see front matter
doi:10.1016/j.physd.2008.01.018

time singularity formation of the 3D Euler equations. To obtain these results, Deng–Hou–Yu [8,9] explore the connection between the stretching of local vortex lines and the growth of vorticity. In particular, they show that if the vortex lines near the region of maximum vorticity satisfy some local geometric regularity conditions and the maximum velocity field is integrable in time, then no finite time blowup is possible. These localized non-blowup criteria provide stronger constraints on the local geometry of a potential finite time singularity. They can be used to re-examine some of the well-known numerical evidences for finite time singularities of the 3D Euler equations.

2. A brief review

We begin with a brief review on the subject. Due to the formal quadratic nonlinearity in vortex stretching, only short time existence is known for the 3D Euler equations. One of the most well-known results on the 3D Euler equations is due to Beale–Kato–Majda [1] who show that the solution of the 3D Euler equations blows up at T^* if and only if $\int_0^{T^*} \|\boldsymbol{\omega}\|_\infty(t)\,\mathrm{d}t = \infty$, where $\boldsymbol{\omega}$ is vorticity.

There have been some interesting recent theoretical developments. In particular, Constantin–Fefferman–Majda [7] show that local geometric regularity of the unit vorticity vector can lead to depletion of the vortex stretching. Let $\boldsymbol{\xi} = \boldsymbol{\omega}/|\boldsymbol{\omega}|$ be the unit vorticity vector and $\mathbf{u}$ be the velocity field. Roughly speaking, Constantin–Fefferman–Majda show that if (1) $\|\mathbf{u}\|_\infty$ is bounded in a $O(1)$ region containing the maximum vorticity. (2) $\int_0^t \|\nabla\boldsymbol{\xi}\|_\infty^2 \mathrm{d}\tau$ is uniformly bounded for $t < T$, then the solution of the 3D Euler equations remains regular up to $t = T$.

There have been some numerical evidences which suggest a finite time blowup of the 3D Euler equations. One of the most well-known examples is the finite time collapse of two anti-parallel vortex tubes by Kerr [17,18]. In Kerr's computations, he used a pseudo-spectral discretization in the x and y directions, and a Chebyshev discretization in the z direction with resolution of order $512 \times 256 \times 192$. His computations showed that the maximum vorticity blows up like $O((T-t)^{-1})$ with $T = 18.9$. In his subsequent paper [18], Kerr showed that the maximum velocity blows up like $O((T-t)^{-1/2})$ with T being revised to $T = 18.7$. It is worth noting that there is still a considerable gap between the predicted singularity time $T = 18.7$ and the final time $t = 17$ of Kerr's computations which he used as the primary evidence for the finite time singularity.

Kerr's blowup scenario is consistent with the Beale–Kato–Majda non-blowup criterion [1] and the Constantin–Fefferman–Majda non-blowup criterion [7]. But it falls into the critical case of the Deng–Hou–Yu local non-blowup criteria [8,9]. Below we describe the local non-blowup criteria of Deng–Hou–Yu.

3. The local non-blowup criteria of Deng–Hou–Yu [8,9]

Motivated by the result of [7], Deng, Hou, and Yu [8] have obtained a sharper non-blowup condition which uses only very localized information of the vortex lines. Assume that at each time t there exists some vortex line segment L_t on which the local maximum vorticity is comparable to the global maximum vorticity. Further, we denote $L(t)$ as the arclength of L_t, $\mathbf{n}$ the unit normal vector of L_t, and κ the curvature of L_t.

Theorem 1 (*Deng–Hou–Yu [8], 2005*). *Assume that (1) $\max_{L_t}(|\mathbf{u}\cdot\boldsymbol{\xi}| + |\mathbf{u}\cdot\mathbf{n}|) \le C_U(T-t)^{-A}$ with $A < 1$, and (2) $C_L(T-t)^B \le L(t) \le C_0/\max_{L_t}(|\kappa|, |\nabla\cdot\boldsymbol{\xi}|)$ for $0 \le t < T$. Then the solution of the 3D Euler equations remains regular up to $t = T$ if $A + B < 1$.*

In Kerr's computations, the first condition of Theorem 1 is satisfied with $A = 1/2$ if we use $\|\mathbf{u}\|_\infty \le C(T-t)^{-1/2}$ as alleged in [18]. Kerr's computations suggested that κ and $\nabla\cdot\boldsymbol{\xi}$ are bounded by $O((T-t)^{-1/2})$ in the inner region of size $(T-t)^{1/2} \times (T-t)^{1/2} \times (T-t)$ [18]. Moreover, the length of the vortex tube in the inner region is of order $(T-t)^{1/2}$. If we choose a vortex line segment of length $(T-t)^{1/2}$ (i.e. $B = 1/2$), then the second condition is satisfied. However, we violate the condition $A + B < 1$. Thus Kerr's computations fall into the critical case of Theorem 1. In a subsequent paper [9], Deng–Hou–Yu improved the non-blowup condition to include the critical case, $A + B = 1$.

Theorem 2 (*Deng–Hou–Yu [9], 2006*). *Under the same assumptions as Theorem 1, in the case of $A + B = 1$, the solution of the 3D Euler equations remains regular up to $t = T$ if the scaling constants C_U, C_L and C_0 satisfy an algebraic inequality, $f(C_U, C_L, C_0) > 0$.*

We remark that this algebraic inequality can be checked numerically if we obtain a good estimate of these scaling constants. For example, if $C_0 = 0.1$, which seems reasonable since the vortex lines are relatively straight in the inner region, Theorem 2 would imply no blowup up to T if $2C_U < 0.43C_L$. Unfortunately, there was no estimate available for these scaling constants in [17]. One of our original motivations to repeat Kerr's computations using higher resolutions was to obtain a good estimate for these scaling constants.

4. The high resolution 3D Euler computations of Hou and Li [14,15]

In [14,15], we repeat Kerr's computations using two pseudo-spectral methods. The first pseudo-spectral method uses the standard 2/3 dealiasing rule to remove the aliasing error. For the second pseudo-spectral method, we use a novel 36th order Fourier smoothing to remove the aliasing error. For the Fourier smoothing method, we use a Fourier smoother along the x_j direction as follows: $\rho(2k_j/N_j) \equiv \exp(-36(2k_j/N_j)^{36})$, where k_j is the wave number ($|k_j| \le N_j/2$). The time integration is performed by using the classical fourth order Runge–Kutta scheme. Adaptive time stepping is used to satisfy the CFL stability condition with CFL number equal to $\pi/4$. In order to perform a careful resolution study, we use a sequence of resolutions: $768 \times 512 \times 1536$, $1024 \times 768 \times 2048$ and $1536 \times 1024 \times 3072$ in our computations. We compute the solution up to $t = 19$, beyond the alleged singularity time $T = 18.7$ by Kerr [18]. Our computations were performed using

256 parallel processors with maximal memory consumption 120 Gb. The largest number of grid points is close to 5 billions.

As a first step, we demonstrate that the two pseudo-spectral methods can be used to compute a singular solution arbitrarily close to the singularity time. For this purpose, we perform a careful convergence study of the two pseudo-spectral methods in both physical and spectral spaces for the 1D inviscid Burgers equation. The advantage of using the inviscid 1D Burgers equation is that it shares some essential difficulties as the 3D Euler equations, yet we have a semi-analytic formulation for its solution. By using the Newton iterative method, we can obtain an approximate solution to the exact solution up to 13 digits of accuracy. Moreover, we know exactly when a shock singularity will form in time. This enables us to perform a careful convergence study in both the physical space and the spectral space very close to the singularity time.

We have performed a sequence of resolution study with the largest resolution being $N = 16,384$ [15]. Our extensive numerical results demonstrate that the pseudo-spectral method with the high order Fourier smoothing (the Fourier smoothing method for short) gives a much more accurate approximation than the pseudo-spectral method with the 2/3 dealiasing rule (the 2/3 dealiasing method for short). One of the interesting observations is that the unfiltered high frequency coefficients in the Fourier smoothing method approximate accurately the corresponding exact Fourier coefficients. Moreover, we observe that the Fourier smoothing method captures about $12 \sim 15\%$ more effective Fourier modes than the 2/3 dealiasing method in each dimension, see Fig. 1. The gain is even higher for the 3D Euler equations since the number of effective modes in the Fourier smoothing method is higher in three dimensions. Further, we find that the error produced by the Fourier smoothing method is highly localized near the region where the solution is most singular. In fact, the pointwise error decays exponentially fast away from the location of the shock singularities. On the other hand, the error produced by the 2/3 dealiasing method spreads out to the entire domain as we approach the singularity time, see Fig. 2.

Next, we present our high resolution computations for the two anti-parallel vortex tubes [14]. We used the same initial condition whose analytic formula was given by Kerr (see Section III of [17], and also [14] for corrections of some typos in the description of the initial condition in [17]). However, there is some difference between our discretization and Kerr's discretization. We used a pseudo-spectral discretization in all three directions, while Kerr used a pseudo-spectral discretization only in the x and y directions and used a Chebyshev discretization in the z direction. Based on the results of early tests, positive vorticity in the symmetry plane was imposed in the initial condition of Kerr [17]. How this was imposed as the vorticity field was mapped onto the Chebyshev mesh was not documented by Kerr [17]. This has led to some ambiguity in reproducing that initial condition which is being resolved by Kerr's group (private communication).

We first illustrate the dynamic evolution of the vortex tubes. In Figs. 4 and 5, we plot the isosurface of the 3D vortex tubes at $t = 0$ and $t = 6$ respectively. As we can see, the two initial

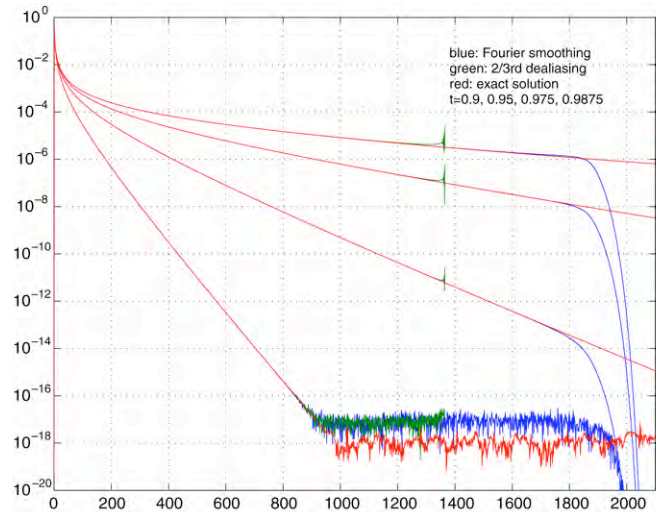

Fig. 1. Spectra comparison on different resolutions at a sequence of moments. The additional modes that kept the Fourier smoothing method higher than the 2/3rd dealiasing method are in fact correct. The initial condition is $u_0(x) = \sin(x)$. The singularity time for this initial condition is $T = 1$.

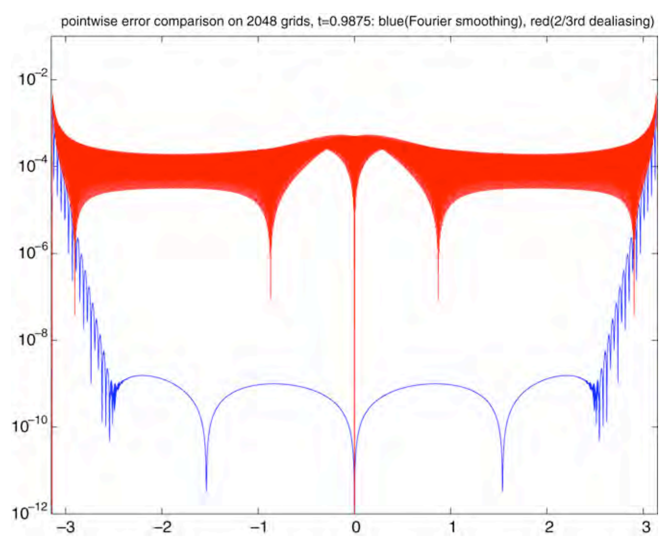

Fig. 2. Pointwise errors of the two pseudo-spectral methods as functions of time using different resolutions. The plot is in a log scale. The error of the 2/3rd dealiasing method (the top curve) is highly oscillatory and spreads out over the entire domain, while the error of the Fourier smoothing method (the bottom curve) is highly localized near the location of the shock singularity.

vortex tubes are very smooth and relatively symmetric. Due to the mutual attraction of the two anti-parallel vortex tubes, the two vortex tubes approach each other and become flattened dynamically. By time $t = 6$, there is already a significant flattening near the center of the tubes. In Fig. 6, we plot the local 3D vortex structure of the upper vortex tube at $t = 17$. By this time, the 3D vortex tube has essentially turned into a thin vortex sheet with rapidly decreasing thickness. The vortex lines become relatively straight. The vortex sheet rolls up near the left edge of the sheet.

We would like to make a few important observations. First of all, the maximum vorticity at later stage of the computation is actually located near the rolled-up region of the vortex sheet

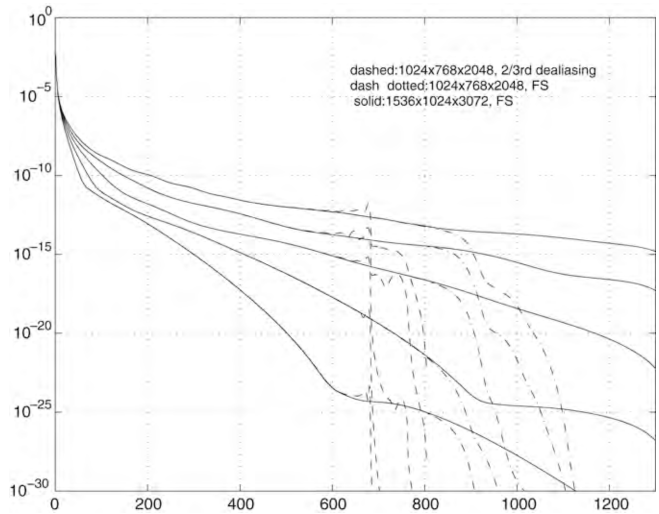

Fig. 3. The energy spectra vs wave numbers. The dashed lines and dash-dotted lines are the energy spectra with the resolution $1024 \times 768 \times 2048$ using the 2/3 dealiasing rule and the Fourier smoothing, respectively. The times for the spectra lines are at $t = 15, 16, 17, 18, 19$ respectively.

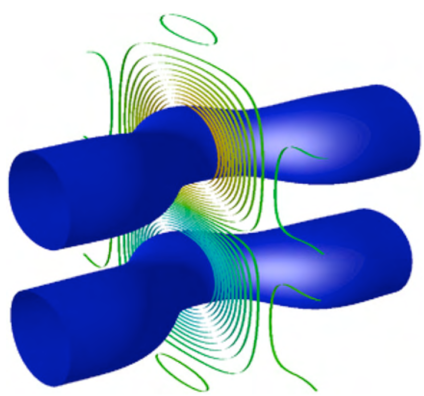

Fig. 4. The 3D view of the vortex tube at $t = 0$.

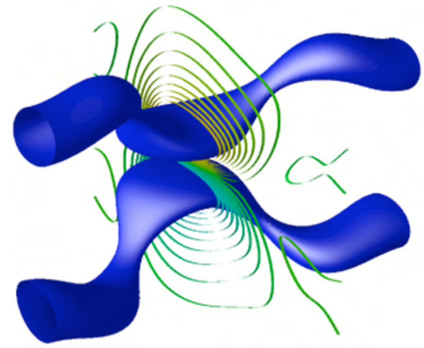

Fig. 5. The 3D view of the vortex tube at $t = 6$.

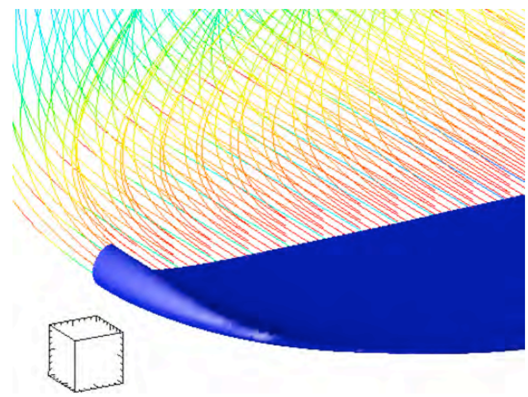

Fig. 6. The local 3D vortex structures and vortex lines around the maximum vorticity at $t = 17$.

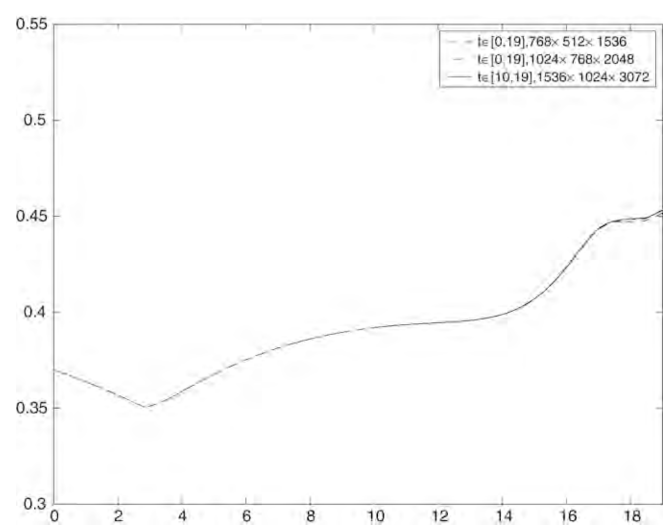

Fig. 7. Maximum velocity $\|\mathbf{u}\|_\infty$ in time using three different resolutions.

and moves away from the bottom of the vortex sheet. Thus the mechanism of strong compression between the two vortex tubes becomes weaker dynamically at later time. Secondly, the location of maximum strain and that of maximum vorticity separate as time increases. Thirdly, the relatively "strong" growth of the maximum velocity between $t = 15$ and $t = 17$ becomes saturated after $t = 17$ when the location of maximum vorticity moves to the rolled-up region, see Fig. 7. All these factors contribute to the dynamic depletion of vortex stretching. The origin of this behavior need to be analyzed in the future study.

We have performed a convergence study for the two numerical methods using a sequence of resolutions. For the Fourier smoothing method, we use the resolutions $768 \times 512 \times 1536$, $1024 \times 768 \times 2048$, and $1536 \times 1024 \times 3072$ respectively. Except for the computation on the largest resolution $1536 \times 1024 \times 3072$, all computations are carried out from $t = 0$ to $t = 19$. The computation on the final resolution $1536 \times 1024 \times 3072$ is started from $t = 10$ with the initial condition given by the computation with the resolution $1024 \times 768 \times 2048$. For the 2/3 dealiasing method, we use the resolutions $512 \times 384 \times 1024$, $768 \times 512 \times 1536$ and $1024 \times 768 \times 2048$ respectively. The computations using these three resolutions are all carried out from $t = 0$ to $t = 19$. See [14,15] for more details.

In Fig. 3, we compare the Fourier spectra of the energy obtained by using the 2/3 dealiasing method with those obtained by the Fourier smoothing method. For a fixed resolution $1024 \times 768 \times 2048$, we can see that the Fourier spectra obtained by the Fourier smoothing method retain more effective

Fourier modes than those obtained by the $2/3$ dealiasing method. This can be seen by comparing the results with the corresponding computations using a higher resolution $1536 \times 1024 \times 3072$ (the solid lines). Moreover, the Fourier smoothing method does not give the spurious oscillations in the Fourier spectra. In comparison, the Fourier spectra obtained by the $2/3$ dealiasing method produce some spurious oscillations near the $2/3$ cut-off point. We would like to emphasize that our Fourier smoothing method conserves the total energy extremely well, at least up to six digits of accuracy. More studies including the convergence of the enstrophy spectra can be found in [14,15].

It is worth emphasizing that a significant portion of those Fourier modes beyond the $2/3$ cut-off position are still accurate for the Fourier smoothing method. This portion of the Fourier modes that go beyond the $2/3$ cut-off point is about $12 \sim 15\%$ of total number of modes in each dimension. For 3D problems, the total number of effective modes in the Fourier smoothing method is about 20% more than that in the $2/3$ dealiasing method. For our largest resolution, we have about 4.8 billions unknowns. An increase of 20% effective Fourier modes represents a very significant increase in the resolution for a large scale computation.

5. Dynamics depletion of vortex stretching

In this section, we present some convincing numerical evidences which show that there is a strong dynamic depletion of vortex stretching due to local geometric regularity of the vortex lines. We first present the result on the growth of the maximum velocity in time, see Fig. 7. The growth rate of the maximum velocity plays a critical role in the non-blowup criteria of Deng–Hou–Yu [8,9]. As we can see from Fig. 7, the maximum velocity remains bounded up to $t = 19$. This is in contrast with the claim in [18] that the maximum velocity blows up like $O((T-t)^{-1/2})$ with $T = 18.7$. We note that the velocity field is smoother than the vorticity field. Thus it is easier to resolve the velocity field than the vorticity field. We observe an excellent agreement between the maximum velocity fields computed by the two largest resolutions. Since the velocity field is bounded, the first condition of Theorem 1 is satisfied by taking $A = 0$. Furthermore, since both $\nabla \cdot \boldsymbol{\xi}$ and κ are bounded by $O((T-t)^{-1/2})$ in the inner region of size $(T-t)^{1/2} \times (T-t)^{1/2} \times (T-t)$ [18], the second condition of Theorem 1 is satisfied with $B = 1/2$ by taking a segment of the vortex line with length $(T-t)^{1/2}$ within this inner region. Thus Theorem 1 can be applied to our computation, which implies that the solution of the 3D Euler equations remains smooth at least up to $T = 19$.

We also study the maximum vorticity as a function of time. The maximum vorticity is found to increase rapidly from the initial value of 0.669 to 23.46 at the final time $t = 19$, a factor of 35 increase from its initial value. Our computations show no sign of finite time blowup of the 3D Euler equations up to $T = 19$, beyond the singularity time predicted by Kerr. The maximum vorticity computed by resolution $1024 \times 768 \times 2048$ agrees very well with that computed by resolution $1536 \times 1024 \times 3072$ up to $t = 17.5$. There is some mild disagreement

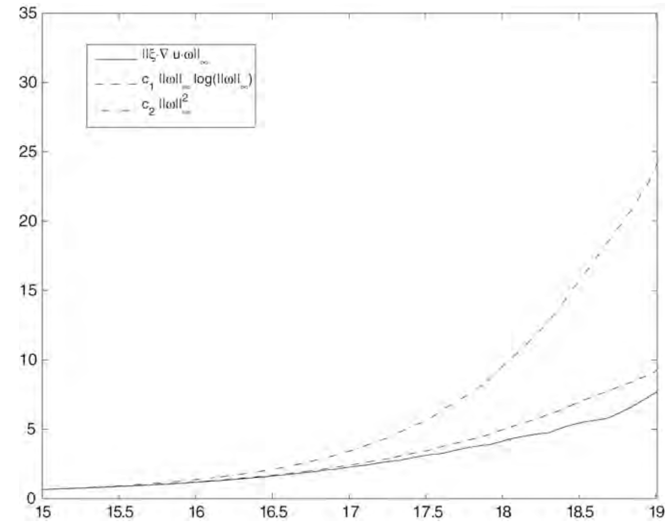

Fig. 8. Study of the vortex stretching term in time, resolution $1536 \times 1024 \times 3072$. The fact $|\boldsymbol{\xi} \cdot \nabla \mathbf{u} \cdot \boldsymbol{\omega}| \le c_1 |\boldsymbol{\omega}| \log |\boldsymbol{\omega}|$ plus $\frac{D}{Dt}|\boldsymbol{\omega}| = \boldsymbol{\xi} \cdot \nabla \mathbf{u} \cdot \boldsymbol{\omega}$ implies $|\boldsymbol{\omega}|$ bounded by doubly exponential..

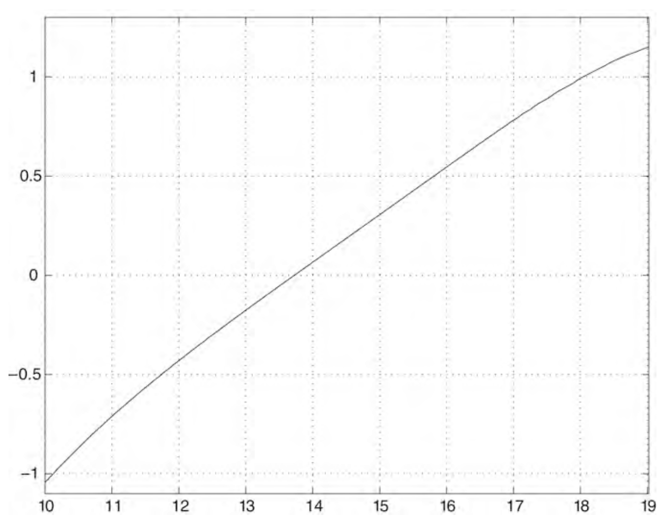

Fig. 9. The plot of $\log \log \|\boldsymbol{\omega}\|_\infty$ vs time, resolution $1536 \times 1024 \times 3072$.

toward the end of the computation. This indicates that a very high space resolution is needed to capture the rapid growth of maximum vorticity at the final stage of the computation.

In order to understand the nature of the dynamic growth in vorticity, we examine the degree of nonlinearity in the vortex stretching term. In Fig. 8, we plot the quantity, $\|\xi \cdot \nabla \mathbf{u} \cdot \boldsymbol{\omega}\|_\infty$, as a function of time. If the maximum vorticity indeed blew up like $O((T-t)^{-1})$, as alleged in [17], this quantity should have been quadratic as a function of maximum vorticity. We find that there is tremendous cancellation in this vortex stretching term. It actually grows slower than $C\|\vec{\omega}\|_\infty \log(\|\vec{\omega}\|_\infty)$, see Fig. 8. It is easy to show that $\|\xi \cdot \nabla \mathbf{u} \cdot \boldsymbol{\omega}\|_\infty \le C\|\vec{\omega}\|_\infty \log(\|\vec{\omega}\|_\infty)$ would imply at most doubly exponential growth in the maximum vorticity. Indeed, as demonstrated by Fig. 9, the maximum vorticity does not grow faster than doubly exponential in time. We have also generated the similar plot by extracting the data

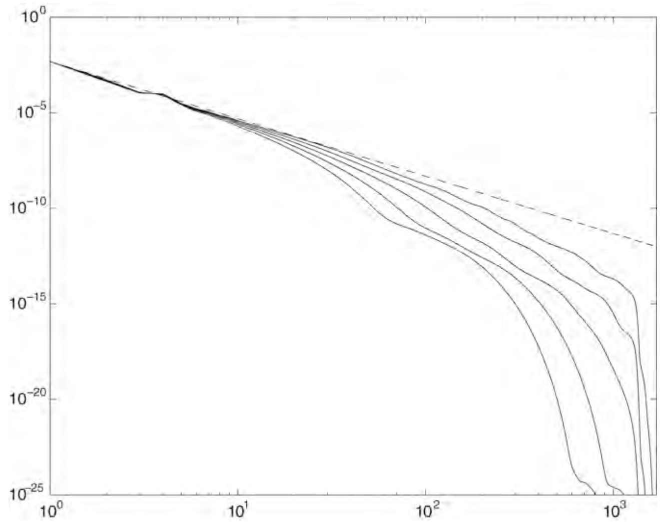

Fig. 10. The energy spectra for velocity at $t = 15, 16, 17, 18, 19$ (from bottom to top) in log–log scale. The dashed line corresponds to k^{-3}.

from Kerr's paper [17]. We find that $\log(\log(\|\boldsymbol{\omega}\|_\infty))$ basically scales linearly with respect to t from $14 \le t \le 17.5$ when his computations are still reasonably resolved. This implies that the maximum vorticity up to $t = 17.5$ in Kerr's computations does not grow faster than doubly exponential in time. This is consistent with our conclusion.

We study the decay rate in the energy spectrum in Fig. 10 at $t = 16, 17, 18, 19$. A finite time blowup of enstrophy would imply that the energy spectrum decays no faster than $|k|^{-3}$. Our computations show that the energy spectrum approaches $|k|^{-3}$ for $|k| \le 100$ as time increases to $t = 19$. This is in qualitative agreement with Kerr's results. Note that there are only less than 100 modes available along the $|k_x|$ or $|k_y|$ direction in Kerr's computations, see Fig. 18 (a)–(b) of [17]. On the other hand, our computations show that the high frequency Fourier spectrum for $100 \le |k| \le 1300$ decays much faster than $|k|^{-3}$, as one can see from Fig. 10. This indicates that there is no blowup in enstrophy.

It is interesting to ask how the vorticity vector aligns with the eigenvectors of the deformation tensor. Recall that the vorticity equations can be written as [20]

$$\frac{\partial}{\partial t}\boldsymbol{\omega} + (\mathbf{u}\cdot\nabla)\boldsymbol{\omega} = S\cdot\boldsymbol{\omega}, \qquad S = \frac{1}{2}(\nabla\mathbf{u} + \nabla^T\mathbf{u}). \tag{1}$$

Let $\lambda_1 < \lambda_2 < \lambda_3$ be the three eigenvalues of S. The incompressibility condition implies that $\lambda_1 + \lambda_2 + \lambda_3 = 0$. If the vorticity vector aligns with the eigenvector corresponding to λ_3, which gives the maximum rate of stretching, then it is very likely that the 3D Euler equations would blow up in a finite time.

In Table 1, we document the alignment information of the vorticity vector around the point of maximum vorticity with resolution $1536 \times 1024 \times 3072$. In this table, θ_i is the angle between the i-th eigenvector of S and the vorticity vector. One can see clearly that for $16 \le t \le 19$ the vorticity vector at the point of maximum vorticity is almost perfectly aligned with the second eigenvector of S. Note that the second eigenvalue, λ_2,

Table 1
The alignment of the vorticity vector and the eigenvectors of S around the point of maximum vorticity with resolution $1536 \times 1024 \times 3072$

Time	$\|\boldsymbol{\omega}\|$	λ_1	θ_1	λ_2	θ_2	λ_3	θ_3
16.012	5.628	−1.508	89.992	0.206	0.007	1.302	89.998
16.515	7.016	−1.864	89.995	0.232	0.010	1.631	89.990
17.013	8.910	−2.322	89.998	0.254	0.006	2.066	89.993
17.515	11.430	−2.630	89.969	0.224	0.085	2.415	89.920
18.011	14.890	−3.625	89.969	0.257	0.036	3.378	89.979
18.516	19.130	−4.501	89.966	0.246	0.036	4.274	89.984
19.014	23.590	−5.477	89.966	0.247	0.034	5.258	89.994

Here, θ_i is the angle between the ith eigenvector of S and the vorticity vector.

is positive and is about 20 times smaller in magnitude than the largest and the smallest eigenvalues. Although the alignment of the vorticity vector with the second eigenvector of the deformation tensor does not rule out a finite time blowup, this alignment is another indication that there is a strong dynamic depletion of vortex stretching.

6. The Kida–Pelz high-symmetry data

Another well-known numerical evidence for finite time Euler singularities is the Kida–Pelz high-symmetry initial data [3,19]. Some people have argued that the singular solution of the 3D Euler equations, if it exists, could be very unstable. A highly symmetric initial condition may have a better chance to produce a finite time singularity. It is also believed that a computer code needs to build in this symmetry property explicitly in order to capture the potentially unstable singular solution. This consideration motivated Boratav and Pelz to perform numerical simulations using a high-symmetry initial condition for the Navier–Stokes equations in [3].

The initial condition that Boratav and Pelz used [3] has the rotational symmetry and the permutation symmetry, which was first introduced by Kida [19]. Their simulations suggested a possible finite time blowup of the maximum vorticity in the limit of infinite Reynolds numbers. However, as they realized later, their simulations were under-resolved at later times when the solution became nearly singular. The vortex structure near the region of maximum vorticity motivated Pelz to construct a vortex filament model to understand this singular behavior. In [21], Pelz presented some numerical evidences which suggest that his filament model develop a self-similar blowup in a finite time. It is interesting to note that Pelz's self singular solution also falls into the critical case of the Deng–Hou–Yu local non-blowup criteria (see Theorem 2). To understand if the same initial condition that led to a finite time blowup in Pelz's filament model would lead to a finite time blowup of the full 3D Euler equations, we decide to repeat Pelz's computations.

Pelz's original filament model was designed for the entire free space. To perform the numerical simulation of the 3D Euler equations in the free space R^3 is very expensive. As a first step, we derive a corresponding periodic filament model. The periodic filament model involves an infinite sum over all the periodic images of the Biot–Savart kernel. This

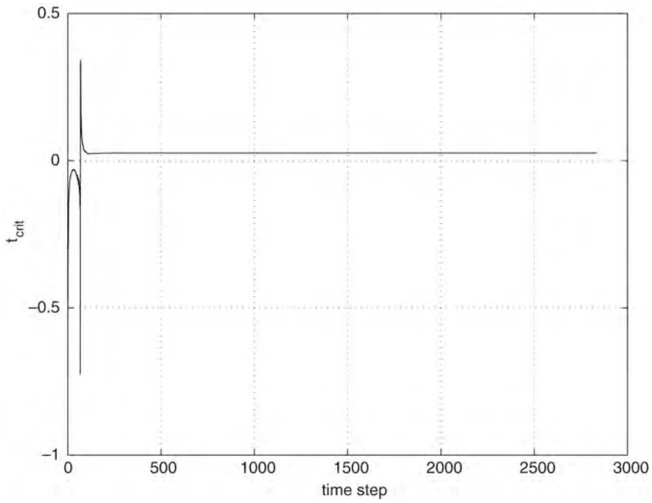

Fig. 11. The validity check of singularity fitting using the asymptotic expression $\|u\|_\infty = \frac{C}{\sqrt{t_{\text{crit}}-t}}$. The figure shows t_{crit} as a function of the computational steps, with $t_{\text{crit}} \to 0.0257874$. Adaptive time stepping is used with the time step chosen to be proportional to the inverse of $\|u\|_\infty$.

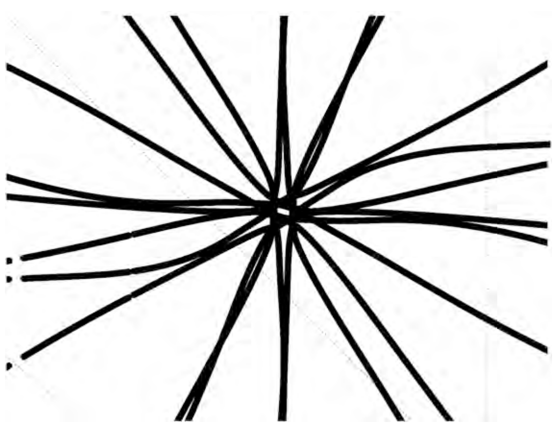

Fig. 12. The locations of the filaments at the end of our computation. The figure gives a closeup view of the filaments around the origin.

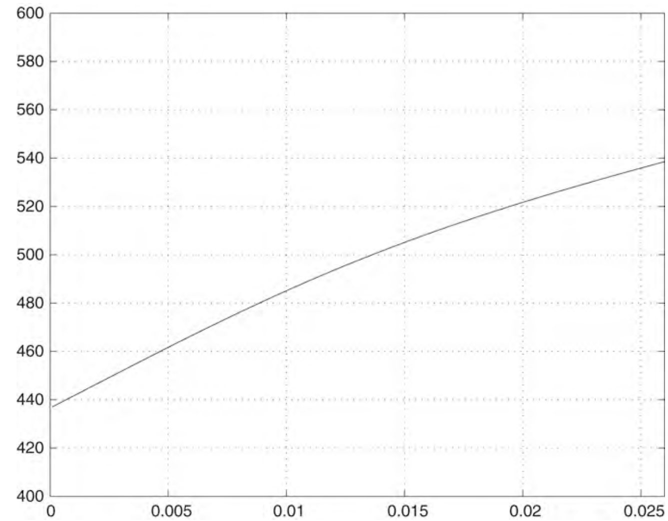

Fig. 13. Maximum vorticity in time of the full Euler equations with two resolutions: 1024^3 (dashed line) vs $N = 2048^4$ (solid line).

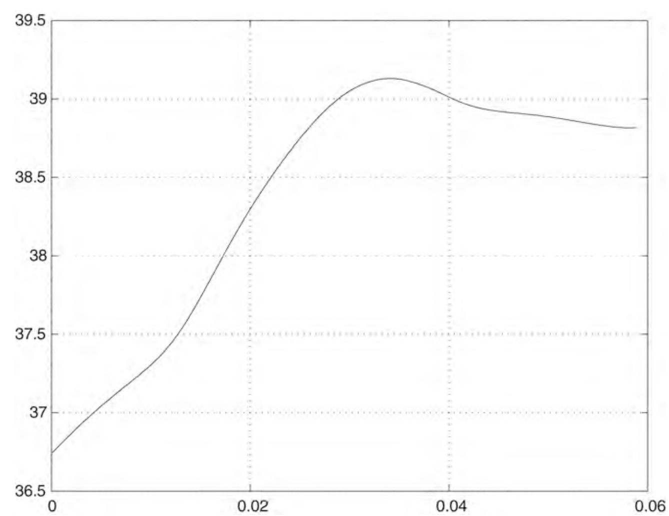

Fig. 14. Maximum velocity in time of the full Euler equations with resolution: 1024^3. The maximum velocity seems to saturate at a later time.

makes the computation of the periodic filament kernel more expensive than the one over the free space. To reduce the computational cost, we apply the Ewald summation formula, which significantly reduces the computational cost.

We solve the periodic filament model using an initial condition which is qualitatively the same as the one used by Pelz [21]. Our numerical computations show that the periodic filament model indeed develops a finite time self-similar singularity around $t = 0.0257874$, see Figs. 11 and 12. However, when we use the same initial condition to solve the full 3D Euler equations, we find that the solution of the 3D Euler equations has a completely different behavior from that of the filament model. We observe no finite time singularity for the 3D Euler equations using the same initial condition. We use a sequence of space resolutions with the two largest resolutions being 1024^3 and 2048^3. More than 100Gb memory is used in our computation on the 2048^3 computations. As we can see from Figs. 13 and 14, the growth of maximum vorticity in time is very mild. The maximum velocity is bounded and becomes saturated around $t = 0.0325$. The 3D isosurface of the vortex tubes at $t = 0.03$ plotted in Fig. 15 also shows that the vortex tubes remain quite regular. We remark that Grauer and his coworkers have recently carried out the full Euler simulation using a simplified Pelz's high-symmetry initial condition which consists of 12 straight parallel bars [13]. They find that the vortex tubes become severely flattened as they approach each other and the growth of maximum vorticity is only exponential in time.

Finally, we remark that we have repeated Boratav's and Pelz's Navier–Stokes computations [3] using the same initial condition, building both the rotational and permutation symmetries of the solution explicitly into our code. Our resolution study shows that their computations are resolved only up to $t = 1.6$ when the growth of the maximum vorticity

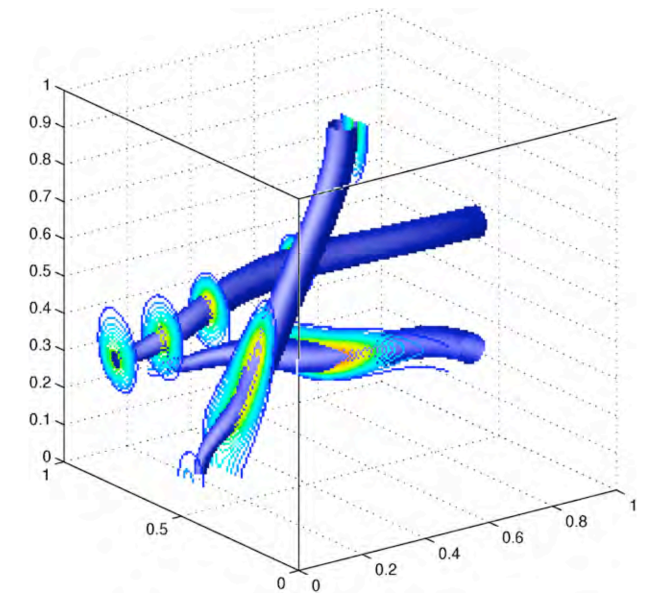

Fig. 15. The 50% isosurface of $|\vec{\omega}|$ at $t = 0.03$. Full 3D Euler equations.

is only exponential in time. The nearly singular growth of maximum vorticity around $t = 2.06$ seems due to under-resolution.

7. Concluding remarks

Our analysis and computations reveal a subtle dynamic depletion of vortex stretching. Sufficient numerical resolution is essential in capturing this dynamic depletion. Our computations for the two anti-parallel vortex tubes' initial data and the high-symmetry initial data show that the velocity is bounded and that the vortex stretching term is bounded by $C\|\omega\|_{L^\infty} \log(\|\omega\|_{L^\infty})$. It is natural to ask if is this dynamic depletion generic? and what is the driving mechanism for this depletion of vortex stretching? Some exciting progress has been made recently in analyzing the dynamic depletion of vortex stretching and nonlinear stability for 3D axisymmetric flows with swirl [16]. The local geometric structure of the solution near the region of maximum vorticity and the anisotropic scaling of the support of maximum vorticity seem to play a key role in the dynamic depletion of vortex stretching.

Acknowledgments

We would like to thank Prof. Lin-Bo Zhang from the Institute of Computational Mathematics and the Center of High Performance Computing in Chinese Academy of Sciences for providing us with the computing resource to perform this large scale computational project. We also thank Prof. Robert Kerr for providing us with his Fortran subroutine that generates initial data. This work was supported in part by NSF under the NSF grants, FRG DMS-0353838, ITR ACI-0204932 and DMS-0713670. Li was subsidized by the National Basic Research Program of China under the grant 2005CB321701.

References

[1] T.J. Beale, T. Kato, A.J. Majda, Remarks on the breakdown of smooth solutions of the 3-D Euler equations, Comm. Math. Phys. 96 (1984) 61–66.
[2] O.N. Boratav, R.B. Pelz, N.J. Zabusky, Reconnection in orthogonally interacting vortex tubes: Direct numerical simulations and quantifications, Phys. Fluids A 4 (1992) 581–605.
[3] O.N. Boratav, R.B. Pelz, Direct numerical simulation of transition to turbulence from a high-symmetry initial condition, Phys. Fluids 6 (1994) 2757–2784.
[4] M.E. Brachet, D.I. Meiron, S.A. Orszag, B.G. Nickel, R.H. Morf, U. Frisch, Small-scale structure of the Taylor-Green vortex, J. Fluid Mech. 130 (1983) 411.
[5] A. Chorin, The evolution of a turbulent vortex, Comm. Math. Phys. 83 (1982) 517.
[6] P. Constantin, Geometric statistics in turbulence, SIAM Rev. 36 (1994) 73.
[7] P. Constantin, C. Fefferman, A.J. Majda, Geometric constraints on potentially singular solutions for the 3-D Euler equation, Commun. PDEs 21 (1996) 559–571.
[8] J. Deng, T.Y. Hou, X. Yu, Geometric properties and non-blowup of 3-D incompressible Euler flow, Commun. PDEs 30 (2005) 225–243.
[9] J. Deng, T.Y. Hou, X. Yu, Improved geometric conditions for non-blowup of 3D incompressible Euler equation, Commun. PDEs 31 (2006) 293–306.
[10] J.D. Gibbon, The three-dimensional Euler equations: Where do we stand?, Physica D 237 (14–17) (2008) 1894–1970.
[11] R. Grauer, T. Sideris, Numerical computation of three dimensional incompressible ideal fluids with swirl, Phys. Rev. Lett. 67 (1991) 3511.
[12] R. Grauer, C. Marliani, K. Germaschewski, Adaptive mesh refinement for singular solutions of the incompressible Euler equations, Phys. Rev. Lett. 80 (1998) 19.
[13] T. Grafke, H. Homann, J. Dreher, R. Grauer, Numerical simulations of possible finite time singularities in the incompressible Euler equations: Comparison of numerical methods, Physica D 237 (14–17) (2008) 1932–1936.
[14] T.Y. Hou, R. Li, Dynamic depletion of vortex stretching and non-blowup of the 3-D incompressible Euler equations, J. Nonlinear Sci. 16 (2006) 639–664.
[15] T.Y. Hou, R. Li, Computing nearly singular solutions using pseudo-spectral methods, J. Comput. Phys. 226 (2007) 379–397.
[16] T.Y. Hou, C. Li, Dynamic stability of the 3D axisymmetric Navier–Stokes equations with swirl, Comm. Pure Appl. Math., published online on August 27, 2007 (doi:10.1002/cpa.20213).
[17] R.M. Kerr, Evidence for a singularity of the three dimensional, incompressible Euler equations, Phys. Fluids 5 (1993) 1725–1746.
[18] R.M. Kerr, Velocity and scaling of collapsing Euler vortices, Phys. Fluids 17 (2005) 075103.
[19] S. Kida, Three-dimensional periodic flows with high symmetry, J. Phys. Soc. Jpn. 54 (1985) 2132.
[20] A.J. Majda, A.L. Bertozzi, Vorticity and Incompressible Flow, Cambridge University Press, Cambridge, 2002.
[21] R.B. Pelz, Locally self-similar, finite-time collapse in a high-symmetry vortex filament model, Phys. Rev. E 55 (1997) 1617–1626.
[22] A. Pumir, E.E. Siggia, Collapsing solutions to the 3-D Euler equations, Phys. Fluids A 2 (1990) 220–241.
[23] M.J. Shelley, D.I. Meiron, S.A. Orszag, Dynamical aspects of vortex reconnection of perturbed anti-parallel vortex tubes, J. Fluid Mech. 246 (1993) 613.

Available online at www.sciencedirect.com
ScienceDirect
Physica D 237 (2008) 1945–1950
PHYSICA D
www.elsevier.com/locate/physd

Complex singularities of solutions of some 1D hydrodynamic models

Dong Li[a,*], Ya.G. Sinai[b,c]

[a] *School of Mathematics, Institute for Advanced Study, Princeton, NJ, USA*
[b] *Mathematics Department, Princeton University, Princeton, NJ, USA*
[c] *Landau Institute of Theoretical Physics, Moscow, Russia*

Available online 3 December 2007

Abstract

We study the complex singularities of solutions of some classes of 1D hydrodynamic models. The method is based on the renormalization group theory. We derive the equation for the corresponding fixed point and study the spectrum of the linearized map near this point. This information allows to describe the initial condition for which blow ups at finite time can occur. We should stress that our solutions having blow ups are complex-valued.

PACS: 47.10.A-; 47.15.ki

Keywords: Renormalization group; Fixed point; Blow up

1. Introduction

In this paper we consider two 1D hydrodynamic models:

model A: $\partial_t \theta + H\theta \cdot \theta_x = \theta_{xx}$

model B: $\partial_t \theta + \frac{1}{2}(H\theta \cdot \theta)_x = \theta_{xx}$,

where $H\theta$ is the usual Hilbert transform of θ:

$$(H\theta)(x) := \frac{1}{\pi} P.V. \int_{-\infty}^{\infty} \frac{\theta(y)}{x-y} \mathrm{d}y.$$

These and related models were considered in many papers. See for example the famous paper by Constantin, Lax and Majda [1] and also the papers by Schochet [7], De Grigorio [2] (see also the book by Majda and Bertozzi [6]). For both the models A and B we shall show that there are solutions with complex singularities. Denote by $\hat{\theta}(k,t)$ the Fourier transform of $\theta(x,t)$. It is easy to see that for model A, $\hat{\theta}(k,t)$ satisfies the equation:

$$\hat{\theta}(k,t) = \mathrm{e}^{-tk^2}\hat{\theta}(k,0) + \int_0^t \mathrm{e}^{-(t-s)k^2} \mathrm{d}s \times \int_{-\infty}^{\infty} \mathrm{sign}(k-k')\hat{\theta}(k-k',s)k'\hat{\theta}(k',s)\mathrm{d}k', \tag{1}$$

where

$$\mathrm{sign}(x) = \begin{cases} 1 & \text{if } k > 0, \\ -1 & \text{if } k < 0. \end{cases}$$

Similarly in the case of model B, the equation for $\hat{\theta}(k,t)$ has the form:

$$\hat{\theta}(k,t) = \mathrm{e}^{-tk^2}\hat{\theta}(k,0) + \frac{1}{2}\int_0^t \mathrm{e}^{-(t-s)k^2} \mathrm{d}s \times \int_{-\infty}^{\infty} \mathrm{sign}(k-k')\hat{\theta}(k-k',s)k\hat{\theta}(k',s)\mathrm{d}k'. \tag{2}$$

For both the models A and B, we choose initial data $\hat{\theta}(k,0)$ which are compactly supported in $(0,\infty)$. From (1) and (2), it follows easily due to the convolutions (in k) the support of $\hat{\theta}(k,t)$ is in the positive half-axis, i.e. $\hat{\theta}(k,t) = 0$, if $k \le 0$. This observation implies that $\hat{\theta}(k,t)$ actually satisfies the following Burgers-type equation written in the mild form:

$$\hat{\theta}(k,t) = \mathrm{e}^{-tk^2}\hat{\theta}(k,0) + \frac{1}{2}\int_0^t \mathrm{e}^{-(t-s)k^2} \mathrm{d}s$$

* Corresponding author. Tel.: +1 609 734 8396.
E-mail addresses: dongli@math.ias.edu (D. Li), sinai@math.princeton.edu (Ya.G. Sinai).

0167-2789/$ - see front matter
doi:10.1016/j.physd.2007.11.015

$$\times \int_{-\infty}^{\infty} \hat{\theta}(k-k',s)k\hat{\theta}(k',s)\mathrm{d}k'. \quad (3)$$

For model A, the derivation of (3) follows by a change of variable and symmetrizing the integral in k'. As in [4,5] we use power series to represent solutions of (3). Let $\hat{\theta}_A(k,0) = A\hat{\theta}(k,0)$, A is a real parameter. The solution $\hat{\theta}_A(k,t)$ of Eq. (3) can be written as the series

$$\hat{\theta}_A(k,t) = A\mathrm{e}^{-tk^2}\hat{\theta}(k,0) + \int_0^t \mathrm{e}^{-(t-s)k^2} \sum_{p>1} A^p g_p(k,s)\mathrm{d}s. \quad (4)$$

Substituting (4) into (3) we get the following system of recurrent relations for the functions g_p:

$$\begin{aligned} g_1(k,s) &= \mathrm{e}^{-sk^2}\hat{\theta}(k,0),\\ g_2(k,s) &= \frac{k}{2}\int_{-\infty}^{\infty} \hat{\theta}(k-k',0)\hat{\theta}(k',0)\mathrm{e}^{-s(k-k')^2-s(k')^2}\mathrm{d}k',\\ g_p(k,s) &= \int_0^s \mathrm{d}s_2 \int_{-\infty}^{\infty} \frac{k}{2}\hat{\theta}(k-k',0)g_{p-1}(k',s_2)\\ &\quad \times \mathrm{e}^{-s(k-k')^2-(s-s_2)(k')^2}\mathrm{d}k' + \sum_{\substack{p_1+p_2=p\\ p_1,p_2>1}} \int_0^s \mathrm{d}s_1 \int_0^s \mathrm{d}s_2\\ &\quad \times \int_{-\infty}^{\infty} g_{p_1}(k-k',s_1)g_{p_2}(k',s_2)\\ &\quad \times \frac{k}{2}\mathrm{e}^{-(s-s_1)(k-k')^2-(s-s_2)(k')^2}\mathrm{d}k'\\ &\quad + \int_0^s \mathrm{d}s_1 \int_{-\infty}^{\infty} \frac{k}{2}\hat{\theta}(k',0)g_{p-1}(k-k',s_1)\\ &\quad \times \mathrm{e}^{-(s-s_1)(k-k')^2-s(k')^2}\mathrm{d}k'. \end{aligned} \quad (5)$$

The same methods as in [8,9] can be used to show that the series (4) converges for small t. It is clear from (5) that the first and last terms are different from the other terms in (5) because they contain explicitly the initial condition.

As in [4,5], our main strategy is to extract the main part of (5). By taking suitable limit transformations we obtain a nonlinear equation whose solution gives the "fixed point" of the renormalization group (see Section 2). In the 1D case considered here, our solutions form a one-parameter family of Gaussian functions. This is much simpler than in the cases considered in [4,5] and in a way exemplifies our approach of constructing blow up solutions. In Section 3 following [4,5] we study the spectrum of the linearized operator. Then by using the same technique as in [4,5] we prove the following results.

Main Theorem. *There exists an open set in the space of 3-parameter families of initial conditions such that for each family from this set there exist the values of parameters so that the solution having the corresponding initial condition develops a blow up at time t_{cr}. If $E(t) = \int_{\mathbb{R}} |\hat{\theta}(k,t)|^2\mathrm{d}k$, $\Omega(t) = \int_{\mathbb{R}} |k|^2|\hat{\theta}(k,t)|^2\mathrm{d}k$ are the energy and the enstrophy of the solution, then $E(t) \approx \frac{1}{(t_{cr}-t)^5}$, $\Omega(t) \approx \frac{1}{(t_{cr}-t)^7}$ as $t \to t_{cr}$.*

2. The derivation of the fixed point equation and the analysis of its solutions

As in [4,5], we take some number k_0 which later will be assumed to be sufficiently large. Then all g_p will be concentrated near the points pk_0. For this reason we write $k = pk_0 + \sqrt{pk_0}Y$. Then instead of k we use the new variable Y which typically takes values $O(1)$. In all integrals over s_1, s_2 in Eq. (5) make another change of variables $s_j = s\left(1 - \frac{\theta_j}{p_j^2}\right)$, $j = 1, 2$. Instead of the integration over k' we introduce Y' such that $k' = p_2k_0 + \sqrt{pk_0}Y'$. Denote $\tilde{g}_r(Y,s) = g_r(rk_0 + \sqrt{rk_0}Y, s)$ and $\gamma = p_1/p$. Then we obtain from (5) a slightly modified recurrent equation:

$$\begin{aligned} \tilde{g}_p(Y,s) &= g_p(pk_0 + \sqrt{pk_0}Y, s)\\ &= (pk_0)^{\frac{3}{2}} \Bigg[\sum_{\substack{p_1+p_2=p\\ p_1,p_2\ge 1}} \int_0^{p_1^2} \mathrm{d}\theta_1 \int_0^{p_2^2} \mathrm{d}\theta_2 \cdot \frac{s^2}{p_1^2 \cdot p_2^2} \cdot \frac{1+\frac{Y}{\sqrt{pk_0}}}{2}\\ &\quad \times \int_{-\infty}^{\infty} \tilde{g}_{p_1}\left(\frac{Y-Y'}{\sqrt{\gamma}}, s\left(1-\frac{\theta_1}{p_1^2}\right)\right)\\ &\quad \times \tilde{g}_{p_2}\left(\frac{Y'}{\sqrt{1-\gamma}}, s\left(1-\frac{\theta_2}{p_2^2}\right)\right)\\ &\quad \times \mathrm{e}^{-s\theta_1\left|k_0+\sqrt{k_0}\frac{Y-Y'}{\sqrt{p\gamma}}\right|^2 - s\theta_2\left|k_0+\sqrt{k_0}\frac{Y'}{\sqrt{p(1-\gamma)}}\right|^2}\mathrm{d}Y' \Bigg]. \end{aligned} \quad (6)$$

This will be our main recurrent relation. It is of some importance that in front of the sum in Eq. (6) we have the factor $p^{3/2}$ and inside the sum the factor $\frac{1}{p_1^2} \cdot \frac{1}{p_2^2}$. As will be clear later the terms corresponding to $p_1 = 1$ or $p_2 = 1$ can be regarded as small remainders. When $p \to \infty$ the recurrent relation (6) takes some limiting form. The main contribution to (6) is from p_1, p_2 of order p. Therefore in the main order of magnitude we can replace the Gaussian terms in (6) by $\mathrm{e}^{-s(\theta_1+\theta_2)|k_0|^2}$, s_1 and s_2 by s and the integration over θ_1, θ_2 and Y' can be done separately. Since Y takes values of $O(1)$, in the main order of magnitude the factor $(1+\frac{Y}{\sqrt{pk_0}})/2$ can be replaced by $1/2$. Thus in the limit $p \to \infty$, instead of (6) we obtain a simpler recurrent relation:

$$\begin{aligned} \tilde{g}_p(Y,s) &= \frac{1}{2k_0^{5/2}} \sum_{\substack{p_1+p_2=p\\ p_1,p_2>\sqrt{p}}} \frac{p^{3/2}}{p_1^2 \cdot p_2^2}\\ &\quad \times \int_{-\infty}^{\infty} \tilde{g}_{p_1}\left(\frac{Y-Y'}{\sqrt{\gamma}}, s\right) \tilde{g}_{p_2}\left(\frac{Y'}{\sqrt{1-\gamma}}, s\right)\mathrm{d}Y'. \end{aligned} \quad (7)$$

As in [4,5] we make the following inductive assumption concerning the form of $\tilde{g}_p(Y,s)$: there exist intervals $S^{(p)} = [S_-^{(p)}, S_+^{(p)}]$, $S^{(p+1)} \subset S^{(p)}$ on the time-axis, functions $Z(s)$, $\Lambda(s)$ defined for $s \in S^{(1)}$ and a positive number σ such that for all $r < p$

$$\tilde{g}_r(Y,s) = Z(s)\Lambda^r(s)r^{\frac{3}{2}}\sqrt{\frac{\sigma}{2\pi}}\mathrm{e}^{-\frac{\sigma}{2}Y^2} \cdot (H(Y) + \delta^{(r)}(Y,s)). \quad (8)$$

We shall derive below the equation for the function H. The main idea of the proof is to carefully organize the inductive procedure so that the remainder terms $\delta^{(r)}$ will tend to zero as

$r \to \infty$. Substituting (8) into (7) and neglecting all remainders $\delta^{(r)}$, we get

$$\tilde{g}_p(Y,s) = \frac{Z(s)^2}{2k_0^{\frac{5}{2}}} \cdot p^{3/2} \cdot \Lambda^p(s) \times \sum_{\gamma=p_1/p} \frac{1}{p} \cdot \int_{-\infty}^{\infty} H\left(\frac{Y-Y'}{\sqrt{\gamma}}\right) \times H\left(\frac{Y'}{\sqrt{1-\gamma}}\right) \sqrt{\frac{\sigma}{2\pi\gamma}} \mathrm{e}^{-\frac{|Y-Y'|^2}{2\gamma}} \times \sqrt{\frac{\sigma}{2\pi(1-\gamma)}} \mathrm{e}^{-\frac{|Y'|^2}{2(1-\gamma)}} \mathrm{d}Y'.$$

Here we do not mention explicitly the dependence of H on s. The last sum looks like the usual Riemannian integral sum and as $p \to \infty$ its limit has the form:

$$H(Y)\sqrt{\frac{\sigma}{2\pi}} \mathrm{e}^{-\frac{Y^2}{2}} = \frac{Z(s)^2}{2k_0^{\frac{5}{2}}} \int_0^1 \mathrm{d}\gamma \int_{-\infty}^{\infty} H\left(\frac{Y-Y'}{\sqrt{\gamma}}\right) \times H\left(\frac{Y'}{\sqrt{1-\gamma}}\right) \sqrt{\frac{\sigma}{2\pi\gamma}} \mathrm{e}^{-\frac{|Y-Y'|^2}{2\gamma}} \sqrt{\frac{\sigma}{2\pi(1-\gamma)}} \mathrm{e}^{-\frac{|Y'|^2}{2(1-\gamma)}} \mathrm{d}Y'.$$

Put $Z(s) = 2k_0^{\frac{5}{2}}$. Then the final equation does not contain k_0 and we have

$$H(Y)\sqrt{\frac{\sigma}{2\pi}} \mathrm{e}^{-\frac{Y^2}{2}} = \int_0^1 \mathrm{d}\gamma \int_{-\infty}^{\infty} H\left(\frac{Y-Y'}{\sqrt{\gamma}}\right) H\left(\frac{Y'}{\sqrt{1-\gamma}}\right) \times \sqrt{\frac{\sigma}{2\pi\gamma}} \mathrm{e}^{-\frac{|Y-Y'|^2}{2\gamma}} \sqrt{\frac{\sigma}{2\pi(1-\gamma)}} \mathrm{e}^{-\frac{|Y'|^2}{2(1-\gamma)}} \mathrm{d}Y'. \tag{9}$$

This equation is the fixed point equation of our renormalization group. Similar but more complicated fixed point equations were derived in [4,5].

The solutions to (9) have natural scaling with respect to the parameter σ. Namely if we solve Eq. (9) for $\sigma = 1$ and denote the corresponding solution by $H(Y)$, then the general solution for arbitrary σ is given by the formula

$$H_\sigma(Y) = \sqrt{\sigma} H(\sqrt{\sigma} Y).$$

Similar scaling relations were also used in [4,5] to find the exact solutions. Thus it is enough to study (9) for the case $\sigma = 1$. As in [4,5] we use expansions over Hermite polynomials:

$$H(Y) = \sum_{m\ge 0} h_m He_m(Y), \tag{10}$$

where $He_m(Y)$ are the Hermite polynomials of degree m with respect to the Gaussian density $\frac{1}{\sqrt{2\pi}}\mathrm{e}^{-\frac{Y^2}{2}}$. Recall the following properties of Hermite polynomials:

1. $He_0(z) = 1$ and $He_1(z) = z$.
2. $zHe_m(z) = He_{m+1}(z) + mHe_{m-1}(z)$, $m > 0$.
3. $\int_{-\infty}^{\infty} He_{m_1}(\frac{Y-Y'}{\sqrt{\gamma}}) \frac{1}{\sqrt{2\pi\gamma}} \mathrm{e}^{-\frac{(Y-Y')^2}{2\gamma}} \frac{1}{\sqrt{2\pi(1-\gamma)}} \mathrm{e}^{-\frac{(Y')^2}{2(1-\gamma)}} He_{m_2}(\frac{Y'}{\sqrt{1-\gamma}}) \mathrm{d}Y' = \gamma^{\frac{m_1}{2}}(1-\gamma)^{\frac{m_2}{2}} He_{m_1+m_2}(Y)\frac{1}{\sqrt{2\pi}}\mathrm{e}^{-\frac{Y^2}{2}}$

Substituting (10) into (9) and using properties 1, 2, 3 above, we obtain recurrent equations for the Hermite coefficients h_m:

$$h_m = \sum_{m_1+m_2=m} \left(\int_0^1 \gamma^{\frac{m_1}{2}}(1-\gamma)^{\frac{m_2}{2}} \mathrm{d}\gamma\right) h_{m_1} h_{m_2}. \tag{11}$$

Clearly the coefficient in (11) is Euler's Beta function. It is not difficult to show that the only solution to (11) is given by

$$h_m = \begin{cases} 1 & \text{if } m = 0, \\ 0 & \text{if } m \ge 1. \end{cases}$$

We formulate this result as the following theorem:

Theorem 2.1. *There exists a unique solution to (9) given by $H_\sigma(Y) = \sqrt{\sigma}$.*

This means that all fixed points of our renormalization group are Gaussian!

3. The linearized equation and the analysis of the spectrum

As in [4,5] our proof is based on the method of Renormalization group. We write

$$\tilde{g}_r(Y,s) \cdot Z(s)^{-1} \cdot \Lambda(s)^{-r} r^{-\frac{3}{2}} \frac{\sqrt{2\pi}}{\sigma} \mathrm{e}^{\frac{Y^2}{2\sigma}} = 1 + \delta^{(r)}(\gamma, Y, s),$$

where $\delta^{(r)}(\gamma,Y,s) = \{\delta_j^{(r)}(\gamma,Y,s),\ 1 \le j \le n\} = \tilde{\delta}^{(p)}(\gamma,Y,s)$, $\gamma = \frac{r}{p}$ and $\gamma \le 1$. It is natural to consider the set of functions $\{\tilde{\delta}^{(p)}(\gamma,Y,s)\}$ as a small perturbation of our fixed point. As we go from p to $p+1$

$$\tilde{\delta}^{(p+1)}(\gamma,Y,s) = \tilde{\delta}^{(p)}\left(\frac{p+1}{p}\gamma, Y, s\right), \quad \gamma \le \frac{p}{p+1}.$$

The formula for $\tilde{\delta}^{(p+1)}(1,Y,s)$ follows from (9):

$$\tilde{\delta}^{(p)}(1,Y,s)\sqrt{\frac{\sigma}{2\pi}} \mathrm{e}^{-\frac{\sigma Y^2}{2}} = \int_0^1 \mathrm{d}\gamma \left(\tilde{\delta}^{(p)}\left(\gamma, \frac{Y-Y'}{\sqrt{\gamma}}, s\right) \times H\left(\frac{Y'}{\sqrt{1-\gamma}}\right) + H\left(\frac{Y-Y'}{\sqrt{\gamma}}\right)\tilde{\delta}^{(p)} \times \left(1-\gamma, \frac{Y'}{\sqrt{1-\gamma}}, s\right)\right) \times \sqrt{\frac{\sigma}{2\pi\gamma}} \mathrm{e}^{-\frac{\sigma(Y-Y')^2}{2\gamma}} \sqrt{\frac{\sigma}{2\pi(1-\gamma)}} \mathrm{e}^{-\frac{\sigma(Y')^2}{2(1-\gamma)}} \mathrm{d}Y'. \tag{12}$$

We did not include in the last expression terms which are quadratic in $\delta^{(p)}$ because in this section we only study the linearized part.

Definition 3.1. A real-valued function $\Phi_\alpha(Y)$ is called an eigenfunction if the function $\Phi_\gamma(\gamma,Y) = \gamma^\alpha \cdot \Phi_\alpha(Y)$ satisfies the equation:

$$\Phi_\alpha(Y)\sqrt{\frac{\sigma}{2\pi}} \mathrm{e}^{-\frac{\sigma Y^2}{2}} = \int_0^1 \mathrm{d}\gamma \int_{-\infty}^{\infty} \left(\gamma^\alpha \Phi_\alpha\left(\frac{Y-Y'}{\sqrt{\gamma}}\right) \times H\left(\frac{Y'}{\sqrt{1-\gamma}}\right) + H\left(\frac{Y-Y'}{\sqrt{\gamma}}\right)(1-\gamma)^\alpha\right.$$

$$\times \Phi_\alpha\left(\frac{Y'}{\sqrt{1-\gamma}}\right)\right) \cdot \mathrm{e}^{-\frac{\sigma(Y-Y')^2}{2\gamma}} \sqrt{\frac{\sigma}{2\pi(1-\gamma)}} \mathrm{e}^{-\frac{\sigma(Y')^2}{2(1-\gamma)}} \mathrm{d}Y'. \tag{13}$$

The meaning of Definition 3.1 is the following. Assume that we have a perturbation proportional to $\delta^{(r)}(Y) = \left(\frac{r}{p}\right)^\alpha \Phi_\alpha(Y)$, $r < p$. If we apply (12) then in the main order of magnitude we shall get $\Phi_\alpha(Y)$.

Below we study in more detail the set of eigenfunctions Φ_α. If $\alpha > 0$, $\alpha = 0$, $\alpha < 0$ then the corresponding eigenfunctions are called unstable, neutral or stable correspondingly. We shall show that there exist the eigenvalue $\alpha = 1$ of multiplicity $\nu_1 = 1$, the eigenvalue $\alpha = 1/2$ of multiplicity $\nu_{1/2} = 1$ and the eigenvalue $\alpha = 0$ of multiplicity $\nu_0 = 1$. All other eigenvalues are stable. In view of the $\sqrt{\sigma}$ scaling mentioned in Section 2, it is enough to consider $\sigma = 1$. Again we expand over Hermite polynomials:

$$\Phi_\alpha(Y) = \sum_{m\geq 0} f_\alpha(m) He_m(Y).$$

Then we come to the following linear recurrent relations:

$$f_\alpha(m) = \sum_{m_1+m_2=m}\left(\int_0^1 \gamma^{\frac{m_1}{2}}(1-\gamma)^{\frac{m_2}{2}+\alpha}\mathrm{d}\gamma\right) h_{m_1} f_\alpha(m_2) + \left(\int_0^1 \gamma^{\frac{m_1}{2}+\alpha}(1-\gamma)^{\frac{m_2}{2}}\mathrm{d}\gamma\right) f_\alpha(m_1) h_{m_2},$$

where h_m are the coefficients of the expansion $H(Y)$. By Theorem 2.1 we have $h_m = \delta_{0m}$ where δ_{0m} is the usual Kronecker delta function. Then we get

$$f_\alpha(m)\cdot\left(1 - 2\int_0^1 \gamma^{\frac{m}{2}+\alpha}\mathrm{d}\gamma\right) = 0. \tag{14}$$

It is not difficult to see that $\alpha = N/2$ for some integer $N \leq 2$. Otherwise all $f_\alpha(m)$ vanish. For any fixed eigenvalue α, we can calculate the explicit expression of the corresponding eigenfunction $f_\alpha(m)$. It is not difficult to find that

$$\alpha = N/2, \quad N = 2, 1, 0, -1, \ldots,$$
$$f_\alpha(m) = Const \cdot \delta_{m,2-2\alpha}.$$

Thus we have the following theorem concerning the spectrum of our linearized operator.

Theorem 3.2. *The spectrum of the linearized operator $\mathcal{A}$ consists of*

$$\mathrm{spec}(\mathcal{A}) = \left\{1, \frac{1}{2}, 0, -\frac{m}{2}, m \geq 1\right\}.$$

All eigenvalues have multiplicity 1. The set of eigenfunctions forms a complete basis in the Gaussian weighted space $L^2(R)$. In fact for eigenvalue α, the corresponding (unnormalized) eigenfunction is $He_{2-2\alpha}(Y)$.

Remark 3.3. Let $\Gamma^{(u)}$ be the unstable subspace generated by all eigenfunctions with eigenvalues $\lambda > 0$, and $\Gamma^{(n)}$ the neutral subspace generated by all eigenfunctions with eigenvalue $\lambda = 0$, $\Gamma^{(s)}$ the stable subspace generated by eigenfunctions with eigenvalue $\lambda < 0$. Then it is clear that $\Gamma^{(u)} = \mathrm{span}\{He_0(Y), He_1(Y)\}$, $\Gamma^{(n)} = \mathrm{span}\{He_2(Y)\}$, $\Gamma^{(s)} = \mathrm{span}\{He_m(Y), m \geq 3\}$.

4. Choice of initial conditions and main steps of the proof

As in [4,5], we take k_0 to be sufficiently large and introduce the neighborhood $A_1 = \{k : |k - k_0| \leq D_1\sqrt{k_0 ln k_0}\}$ where D_1 is also sufficiently large. Our initial conditions will be zero outside A_1. Inside A_1 we take

$$v(k,0) = \frac{1}{\sqrt{2\pi}}\mathrm{e}^{-\frac{Y^2}{2}}\cdot\Big(1 + b_0^{(u)} He_0(Y) + b_1^{(u)} He_1(Y) + b^{(n)} He_2(Y) + \Phi(Y; b_0^{(u)}, b_1^{(u)}, b^{(n)})\Big),$$

where $k = k_0 + \sqrt{k_0}Y$. Recall that the constant 1 is our fixed point with $\sigma = 1$, $He_0(Y)$, $He_1(Y)$ are unstable eigenfunctions and $He_2(Y)$ are neutral eigenfunctions of the linearized group. $b_0^{(u)}, b_1^{(u)}, b^{(n)}$ are our main parameters. We assume that $-\rho_1 \leq b_0^{(u)}, b_1^{(u)}, b^{(n)} \leq \rho_1$ where ρ_1 is a positive constant. Each function $\Phi(Y; b_0^{(u)}, b_1^{(u)}, b^{(n)})$ is small in the sense that

$$\sup_{Y,b} |\Phi(Y; b_0^{(u)}, b_1^{(u)}, b^{(n)})| \leq D_2,$$

$$\sup \|\Phi(Y; \bar{b}_0^{(u)}, \bar{b}_1^{(u)}, \bar{b}^{(n)}) - \Phi(Y; \bar{\bar{b}}_0^{(u)}, \bar{\bar{b}}_1^{(u)}, \bar{\bar{b}}^{(n)})\| \leq D_2(|\bar{b}_0^{(u)} - \bar{\bar{b}}_0^{(u)}| + |\bar{b}_1^{(u)} - \bar{\bar{b}}_1^{(u)}| + |\bar{b}^{(n)} - \bar{\bar{b}}^{(n)}|).$$

We have $l = 3$-parameter families of initial conditions and due to the presence of Φ we have an open set in the space of such families. We now outline the main steps of the proof. More details can be found in [4,5].

`Step 1`: Initial part of the induction procedure. There are several substeps.

`Substep 1`: Assume that for $p < p_0$ and $\forall r < p$,

$$g_r(k,s) = Z\Lambda_r(s) r^{\frac{3}{2}} \frac{1}{\sqrt{2\pi}}\mathrm{e}^{-\frac{Y^2}{2}}(1 + \delta^{(r)}(Y,s)), \tag{15}$$

where Z is a constant to be specified. $\Lambda_r(s)$ is a function of s for each r and $k = rk_0 + \sqrt{rk_0}Y$ with $|Y| \leq D_1\sqrt{ln(rk_0)}$. The values of $g_r(k,s)$ for which $|Y| > D_1\sqrt{ln(rk_0)}$ will be treated as remainders and can be estimated.

`Substep 2`: substitute the Ansatz (15) into (6) and extract the main terms. Then we obtain the recurrent relation for Λ_p:

$$\Lambda_p = \frac{1}{p}\sum_{p_1+p_2=p} \Lambda_{p_1}\Lambda_{p_2}(1 - \mathrm{e}^{-s(p_1 k_0)^2})(1 - \mathrm{e}^{-s(p_2 k_0)^2}).$$

Using the results from [3,10] one can show that the limiting asymptotics of Λ_p is given by

$$\Lambda_p = \Lambda(s)^p(1 + O(p^{-3/2})).$$

`Substep 3`: estimate all the remainders and adjust the parameters b accordingly.

`Step` 2: Procedure for $p > p_0$. Introduce a sequence of numbers $p_m = (1+\epsilon)^m p_0$ where ϵ is sufficiently small. For $p \neq p_m$ no changes are made. At each $p = p_m$ make changes of parameters by the procedure similar to substep 3 in step 1. As a result we can obtain a decreasing sequence of closed intervals for the main parameters b and also for the time interval S. The whole procedure is organized in such a way that $\delta^{(r)} \to 0$ as $r \to \infty$.

5. Formulation of the main result and discussion of the behavior of solutions near the singularity point

Now we give a more detailed formulation of our main theorem.

Theorem 5.1 (*Main Theorem*). *Take a 3-parameter family of initial conditions described in Section 4 and let all constants satisfy the needed inequalities. Then one can find an interval* $S = [S_-, S_+]$, *the functions* $Z(s)$, $\Lambda(s)$, *and the values* $b_0^{(u)}(s)$, $b_1^{(u)}(s)$, $b^{(n)}(s)$ *of parameters such that*
(1) *For* $|Y| \leq D_1\sqrt{pk_0}$,

$$\begin{aligned}\tilde{g}_p(Y,s) &= g_p(pk_0 + \sqrt{pk_0}Y, s)\\ &= Z \cdot \Lambda(s)^p \cdot p^{\frac{3}{2}} \frac{1}{\sqrt{2\pi}} \mathrm{e}^{-\frac{Y^2}{2}} (1 + \delta^{(p)}(Y,s)),\end{aligned}$$

and $\sup_Y |\delta^{(p)}(Y,s)| \to 0$ *as* $p \to \infty$.
(2) *For* $|Y| > D_1\sqrt{pk_0}$, $|\tilde{g}_p(Y,s)| \leq \frac{B_1 \Lambda_p(s)}{p^{\lambda_1}}$ *where* B_1 *and* λ_1 *are constants.*
(3) *The function* $\Lambda(s)$ *is strictly increasing on* S. *Moreover for* $s \in S$, *we have*

$$\Lambda'(s) \geq B > 0,$$

where $B > 0$ *is another constant independent of* s.

The main theorem allows us to study the behavior of our constructed solutions near the blow up point. Consider again our power series:

$$v_A(k,t) = \mathrm{e}^{-tk^2} A v(k,0) + \int_0^t \mathrm{e}^{-(t-s)k^2} \sum_{p>1} A^p g_p(k,s)\mathrm{d}s. \tag{16}$$

Take $t \in [S_-, S_+]$ and find the values of parameters $b_0^{(u)}$, $b_1^{(u)}$, $b^{(n)}$ for which the main theorem holds. Put $A_{cr}(t) = \Lambda^{-1}(t)$. If so then $A^p g_p(k,t)$ is concentrated in the domain whose center is $\kappa^{(0)} p$ and the size is $O(\sqrt{p})$. In this domain it takes values $O(p)$. This immediately implies that at t the energy is infinite.

Consider $t' < t$ and denote $\Delta t = t - t'$. It follows from the properties of $\Lambda(s)$ (see the formulation of the main theorem) that $\Lambda(t')/_{\Lambda(t)} = (1 - B\Delta t + O(\Delta t))$ for some constant $B > 0$. Since $A_{cr}^p \cdot (\Lambda(t'))^p = A_{cr}^p \cdot (\Lambda(t))^p \cdot \left(\Lambda(t')/_{\Lambda(t)}\right)^p = (1 - B\Delta t + o(\Delta t))^p$, it is clear that the terms in (16) with $p \leq O\left(\frac{1}{\Delta t}\right)$ are close to the limiting terms corresponding to t. For $p \gg O\left(\frac{1}{\Delta t}\right)$ the product $A_{cr}^p(\Lambda(t'))^p$ tends exponentially to zero and dominates other terms in the expression for g_p. Therefore for $t' < t$ both the energy and the enstrophy are finite.

In the domain $|k| \leq O\left(\frac{1}{\Delta t}\right)$, the solutions grow as k^2. The extra factor $|k|^{\frac{1}{2}}$ appears because for any k the values of p for which the terms in (16) giving the essential contribution to the solution belong to an interval of size $O(\sqrt{|k|}) = O(\sqrt{p})$. From this argument one can easily derive that $E(t') = \frac{O(1)}{(\Delta t)^5}$ and $\Omega(t') = \frac{O(1)}{(\Delta t)^7}$.

It is interesting to understand the form of the solution at $t = t_{cr}$ in the x-space. Some information can be obtained using (16). Consider the series $g(k,t_{cr}) = \sum_{p>1} A_{cr}^p g_p(k,t_{cr})$. We neglect all remainders δ and take $\tilde{g}_p$ in the form

$$\tilde{g}_r(Y,t_{cr}) = Z(t_{cr})\Lambda^r(t_{cr}) r^{\frac{3}{2}} \frac{1}{\sqrt{2\pi}} \mathrm{e}^{-\frac{Y^2}{2}}.$$

In this way since $A_{cr} = \Lambda(t_{cr})^{-1}$ we have

$$\sum_{p>1} A_{cr}^p g_p(k,t_{cr}) = Z(t_{cr}) \sum_{p>1} p^{\frac{3}{2}} \frac{1}{\sqrt{2\pi}} \times \exp\left\{-\frac{1}{2}\left|\frac{k - pk_0}{\sqrt{pk_0}}\right|^2\right\}.$$

Therefore the Fourier transform of $g(k,t_{cr})$ has the form

$$\begin{aligned}\hat{g}(x,t_{cr}) &= \int_{R^1} \mathrm{e}^{\mathrm{i}\langle x,k\rangle} g(k,t_{cr})\mathrm{d}k\\ &= Z(t_{cr}) \sum_{p>1} p^2 \cdot \frac{1}{\sqrt{k_0}} \mathrm{e}^{\mathrm{i}pk_0x} \cdot \mathrm{e}^{-\frac{1}{2}pk_0x^2}.\end{aligned}$$

This expression shows that for all $x \neq 0$ the function $\hat{g}(x,t_{cr})$ is finite but $\hat{g}(x,t_{cr})$ tends to infinity as $O(\frac{1}{|x|^6})$ as $x \to 0$. The whole energy and enstrophy gets concentrated near $x = 0$. In this sense our solution at t_{cr} is a tornado-like solution as in [4, 5].

Acknowledgements

The authors thank the anonymous referees for their many useful remarks and suggestions. The first author is supported by the NSF Grant DMS 0111298. The second author is supported by the NSF Grant DMS 0600996.

References

[1] P. Constantin, P.D. Lax, A. Majda, A simple one-dimensional model for the three-dimensional vorticity equation, Commun. Pure Appl. Math 38 (1985) 715724.
[2] S. De Grigorio, On a one-dimensional model for the three-dimensional vorticity equation, J. Stat. Phys. 59 (1990) 1251–1263.
[3] D. Li., On a nonlinear recurrent relation. J. Stat. Phy. (in press).
[4] D. Li, Ya.G. Sinai, Blow ups of complex solutions of the 3*D*-Naviers–Stokes system and renormalization group method. J. Eur. Math. Soc. (in press).
[5] D. Li, Ya.G. Sinai, Complex singularities of the Burgers system and renormalization group method, Current Developments in Mathematics, International Press, 2006 (in press).
[6] A.J. Majda, A.L. Bertozzi, Vorticity and Incompressible Flow, Cambridge University Press, 2002.
[7] S. Schochet, Explicit solutions of the viscous model vorticity equation, Commun. Pure Appl. Math. 39 (1986) 531537.

[8] Ya.G. Sinai, Power series for solutions of the Naiver–Stokes system on R^3, J. Stat. Physics 121 (516) (2005) 779–804.
[9] Ya.G. Sinai, Diagrammatic approach to the $3D$-Naiver–Stokes system, Russian Math. Surveys 60 (5) (2005) 47–70.
[10] Ya.G. Sinai, Separating solution of a recurrent equation, Regul. Chaotic Dyn. 12 (5) (2007) 490–501.

Available online at www.sciencedirect.com
ScienceDirect
Physica D 237 (2008) 1951–1955
PHYSICA D
www.elsevier.com/locate/physd

Complex-space singularities of 2D Euler flow in Lagrangian coordinates

Takeshi Matsumoto[a,b,*], Jérémie Bec[b], Uriel Frisch[b]

[a] Department of Physics, Kyoto University, Kitashirakawa Oiwakecho Sakyoku, Kyoto 606-8502, Japan
[b] Labor. Cassiopée, UNSA, CNRS, OCA, BP 4229, 06304 Nice Cedex 4, France

Available online 17 November 2007

Abstract

We show that, for 2D space-periodic incompressible flow, the solution can be evaluated numerically in Lagrangian coordinates with the same accuracy that is achieved in standard Eulerian spectral methods. This allows the determination of complex-space Lagrangian singularities. Lagrangian singularities are found to be closer to the real domain than Eulerian singularities and seem to correspond to fluid particles which escape to (complex) infinity by the current time. Various mathematical conjectures regarding Eulerian/Lagrangian singularities are presented.

PACS: 47.10.A-; 47.15.ki; 47.27.er

Keywords: Complex singularities; Euler equation; Lagrangian frame; Analyticity strip method

1. Introduction

Solutions to the incompressible Euler equation, starting from entire initial data (e.g. trigonometric polynomials), can be analytically continued to the complex space as long as they stay analytic in the real space. Furthermore it is known since the seventies that any singularities in the real space, if they exist, have to be preceded by complex-space singularities [1,2]. In 2D Euler flows, it is known that initial real-space analyticity for periodic solutions is never lost. This was proven in Refs. [3,4] in which it was shown that the distance $\delta(t)$ to the real domain of the nearest complex-space singularity, measured by the exponential falloff of the Fourier amplitude, decreases at large times at most as a double exponential. Actually, already twenty five years ago, spectral simulations with 256^2 Fourier modes indicated that the decrease is more like a simple exponential [5]. Spectral simulations at much higher resolutions, up to 8192^2, which will be published elsewhere also indicate a behavior much closer to a single than to a double exponential.[1] The discrepancy between the simple and the double exponential is generally believed to be due to the phenomenon of *depletion*: the flow organizes itself into ribbon-like vortical structures in which the nonlinearity is almost completely suppressed (the nonlinearity would vanish identically if the flow depended on a single Cartesian coordinate). The same phenomenon also exists in three dimensions and could conceivably prevent finite-time blowup.

In three dimensions the Beale–Kato–Majda (BKM) theorem implies that any blowup must be accompanied by the unboundedness of the modulus of the vorticity in the real domain [7] (see also [8]). In two dimensions, when the initial vorticity is bounded, this is of course ruled out by vorticity conservation. More precisely, it is ruled out in the real domain, but not in the complex domain. Actually, increasing strong numerical evidence has been obtained indicating that the vorticity is infinite at complex singularities [9–11].[2] Such numerical results were obtained only for flows in which the initial stream function is a trigonometric polynomial (the 2D analogues of the famous Taylor–Green flow [12]), which are instances of entire functions, that is, analytic functions that have no singularity at finite complex locations.

* Corresponding author at: Department of Physics, Kyoto University, Kitashirakawa Oiwakecho Sakyoku, Kyoto 606-8502, Japan. Tel.: +81 757533805; fax: +81 757533805.
E-mail address: takeshi@kyoryu.scphys.kyoto-u.ac.jp (T. Matsumoto).

[1] We nevertheless conjecture that by suitable analytic regularization of the flow considered in Ref. [6], long-lasting transients with a double exponential decrease can be achieved.

[2] We have tried but failed to derive such a result from a complex version of the BKM argument.

0167-2789/$ - see front matter © 2007 Elsevier B.V. All rights reserved.
doi:10.1016/j.physd.2007.11.007

The "experimental result" about infinite vorticity along the complex singularities in two dimensions has an important consequence: because the conservation of vorticity along fluid particle trajectories carries over to complex trajectories, (Eulerian) complex locations with infinite vorticity are associated with fluid particles initially at complex infinity; indeed, this is the only place where an entire function can be infinite. We were thus led to investigate the issue of (complex) singularities in Lagrangian coordinates. A Lagrangian singularity is a location at which the (analytic continuation of the) Lagrangian map goes singular. Could it be that for 2D flow there are no (complex) Lagrangian singularities at finite distance? In other words: does the flow in Lagrangian coordinates preserve its initial entire character? A few years ago we performed very accurate numerical simulations, reported here for the first time, and we found strong evidence that the answer is "no". W. Pauls and one of us (TM) [14] then found a very simple counterexample to the preservation of the entire character: the "AB flow" $\psi = \sin x_1 \cos x_2$ is an entire steady solution to the 2D Euler equation in Eulerian coordinates. For this flow, the trajectories of fluid particles can be expressed by elliptic functions and it was shown that, for any real-positive time t, there exist complex-initial locations of fluid particles which are mapped to infinity at time t and which thus are Lagrangian singularities.

There is a considerable renewal of interest in the Lagrangian structure of flows, both from a theoretical and experimental point of view (such issues frequently came up during the Euler conference). It is thus of interest to show that the Lagrangian description of flows can be obtained numerically with an accuracy comparable to that available by spectral methods for the Eulerian description. The present paper is organized as follows. In Section 2 we describe two numerical algorithms, which can be used for Lagrangian integration. In Section 3 we apply this to the identification of complex-Lagrangian singularities. Here, all numerical studies are presented for the (unsteady) 2D flow with the simple initial condition

$$\psi_0 = \cos x_1 + \cos 2x_2, \tag{1}$$

which has been used in Refs. [9–11]; key results are also checked with the flow

$$\psi_0 = \cos x_1 + \cos 2x_2 + \sin(2x_1 - x_2), \tag{2}$$

which has less symmetry than Eq. (1). Some concluding remarks, with emphasis on mathematical conjectures, are presented in Section 4.

2. Numerical solution in Lagrangian coordinates with spectral accuracy

Our goal here is to obtain the velocity field $\boldsymbol{u}$ as a function of the Lagrangian location $\boldsymbol{a}$ and time t. This Lagrangian field will be denoted $\boldsymbol{u}_{\mathrm{L}}(\boldsymbol{a}, t)$.

With simple boundary conditions, e.g. spatial periodicity, the easiest way to obtain high accuracy in a Eulerian simulation is to use a spectral or pseudo-spectral method [13]. For analytic flow, whose Fourier transform decreases exponentially at high wavenumbers, the truncation error will then also decrease exponentially with the resolution.

How does one carry this over to Lagrangian coordinates? In principle one can write an integro-differential equation for the (time-dependent) Lagrangian map $\boldsymbol{a} \mapsto \boldsymbol{x}$. This equation has however nonlinearities with denominators which are not easily handled numerically.

We present here two alternative methods, the spectral particle-tracking method (Section 2.1) and the spectral displacement-Newton method (Section 2.2).

2.1. Particle-tracking method

Obviously, the Lagrangian velocity field can be obtained by composing the Eulerian velocity field $\boldsymbol{u}(\boldsymbol{x}, t)$ with the Lagrangian map $\boldsymbol{x}(\boldsymbol{a}, t)$. The former can be obtained by standard spectral integration. The latter is the solution of the characteristic equation

$$\partial_t \boldsymbol{x}(\boldsymbol{a}, t) = \boldsymbol{u}(\boldsymbol{x}(\boldsymbol{a}, t), t), \qquad \boldsymbol{x}(\boldsymbol{a}, 0) = \boldsymbol{a}. \tag{3}$$

In the tracking method, we select a uniform grid of Lagrangian points and "track" the fluid particles by integrating (3) along all the relevant fluid particle trajectories. This can be done, e.g. using a fourth-order Runge–Kutta method. The problem is that, even if the initial positions coincide with Eulerian collocation points, this usually ceases to hold subsequently. Hence the Eulerian field must be interpolated. In order not to lose the spectral accuracy, the interpolation can be done using the Fourier series representation

$$\boldsymbol{u}(\boldsymbol{x}, t) = \sum_{\boldsymbol{k}} \hat{\boldsymbol{u}}(\boldsymbol{k}, t) \mathrm{e}^{\mathrm{i}\boldsymbol{k}\cdot\boldsymbol{x}}. \tag{4}$$

A difficulty is that, since the relevant $\boldsymbol{x}$'s are not collocation points, the velocities given by (4) cannot be evaluated using fast Fourier transforms but must be calculated "naïvely" in $O(N^4)$ operations if we use an $N \times N$ grid. Furthermore this has to be done at every time step. Since the number of time steps needed to reach a given time t order unity is proportional to the resolution N, this method has a fairly large computational complexity $O(N^5)$ and thus also a significant accumulation of round-off errors. For large values of the resolution N (512 or more) the particle-tracking method is not very practical unless we restrict the Lagrangian grid to being much coarser than the Eulerian grid.

2.2. Displacement-Newton method

This method makes use of the fact that the *inverse Lagrangian map* $\boldsymbol{a}(\boldsymbol{x}, t)$ satisfies, in Eulerian coordinates, the equation

$$\partial_t \boldsymbol{a} + \boldsymbol{u}(\boldsymbol{x}, t) \cdot \nabla \boldsymbol{a} = 0, \tag{5}$$

which just expresses the constancy of the Lagrangian location $\boldsymbol{a}$ under advection by the velocity field. This equation can be solved along with the basic Euler equation, both in Eulerian coordinates. This will however yield a map which still has to be inverted to obtain the direct Lagrangian map.

For periodic boundary conditions the direct and inverse maps are not periodic and it is more convenient to work with the displacement field, here defined as

$$\boldsymbol{d}(\boldsymbol{x},t) \equiv \boldsymbol{a}(\boldsymbol{x},t) - \boldsymbol{x}. \tag{6}$$

It follows from (5) and (6) that the displacement satisfies the following equation in Eulerian coordinates

$$\partial_t \boldsymbol{d}(\boldsymbol{x},t) + (\boldsymbol{u}(\boldsymbol{x},t)\cdot\nabla)\boldsymbol{d}(\boldsymbol{x},t) = -\boldsymbol{u}(\boldsymbol{x},t), \tag{7}$$

with the initial condition $\boldsymbol{d}(\boldsymbol{x},0) = \boldsymbol{0}$. This equation can be solved along with the Euler equation to obtain the displacement in Eulerian coordinates on a uniform grid of $N \times N$ collocation points.

Then comes the difficult step, namely the inversion. For this we define the off-grid displacement, as above, by its Fourier series, extended off-grid and we try to find the $\boldsymbol{x}$ locations associated to a set of Lagrangian collocation points on the regular grid $\boldsymbol{A} = (2\pi i/N, 2\pi j/N)$, $i, j = 0, \dots N-1$. We then determine the direct Lagrangian map $\boldsymbol{x}(\boldsymbol{A},t)$ as the solution of the equation

$$\boldsymbol{d}(\boldsymbol{x},t) = \boldsymbol{A}(\boldsymbol{x},t) - \boldsymbol{x}. \tag{8}$$

First we determine an approximate on-grid solution $\boldsymbol{X}(\boldsymbol{A},t)$ by finding from the inverse map the $\boldsymbol{a}$ point nearest to $\boldsymbol{A}$ and its inverse Lagrangian antecedent $\boldsymbol{X}$. We then set $\boldsymbol{x} = \boldsymbol{X} + \delta\boldsymbol{x}$ and refine the solution of (8) by using a standard-Newton method. This requires the calculation of off-grid values of derivatives, which are again obtained from "naïve" evaluations of the corresponding Fourier series

$$\frac{\partial \boldsymbol{d}}{\partial x_j} = \sum_{\boldsymbol{k}} \mathrm{i}k_j \hat{\boldsymbol{d}}(\boldsymbol{k},t)\mathrm{e}^{\mathrm{i}\boldsymbol{k}\cdot\boldsymbol{x}}, \tag{9}$$

where $\hat{\boldsymbol{d}}(\boldsymbol{k},t)$ are the Fourier coefficients of the displacement (evaluated in Eulerian coordinates). For each stage of the Newton iteration $O(N^4)$ operations are required. The number of stages needed to achieve an accuracy ϵ consistent with double precision is typically five. If the number of output times at which we want to evaluate the Lagrangian velocity field is much smaller than the resolution N, the displacement-Newton method is much faster than particle tracking.

3. Results

We have applied the two methods described in the previous section to the flow with the initial condition (1). The methods give consistent results but the highest resolution (here $N = 512$) is more easily achieved with the displacement-Newton method, which has been used to obtain the results reported here.

The solution of the Euler equation

$$\partial_t \boldsymbol{u} + \boldsymbol{u}\cdot\nabla\boldsymbol{u} = -\nabla p, \quad \nabla\cdot\boldsymbol{u} = 0, \tag{10}$$

together with the displacement equation (7) was obtained by a standard pseudo-spectral method with two-thirds dealiasing and a fourth-order Runge–Kutta temporal integration.

Then we applied the displacement-Newton method (with five iterations) and $\epsilon = 10^{-14}$. The results were checked by computing the Lagrangian vorticity, which should be equal to its initial value for 2D Euler flow, and was indeed found to be so with an accuracy of 10^{-10}.

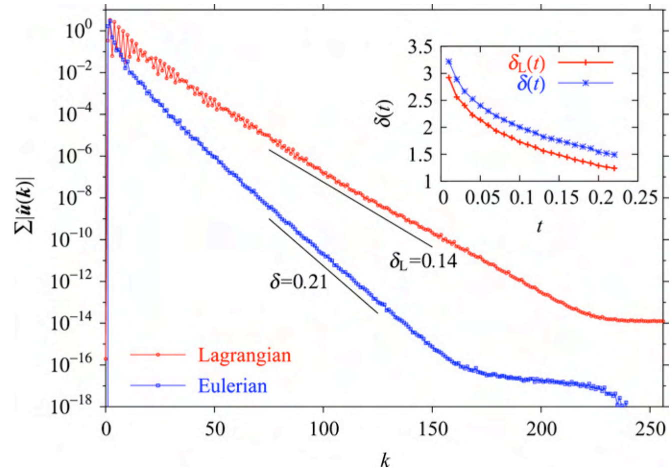

Fig. 1. Shell-summed amplitudes of Eulerian and Lagrangian velocities at time $t = 1.245$ in lin-log coordinates. The initial velocity is given by (1). Inset: time variation (at short times) of the width of the analyticity strip in Eulerian coordinates ($\delta(t)$) and Lagrangian coordinates ($\delta_L(t)$).

In order to locate complex-space singularities for the Lagrangian solution, we applied the tracing method [5]: the Lagrangian solution is represented by its Fourier series

$$\boldsymbol{u}_L(\boldsymbol{a},t) = \sum_{\boldsymbol{k}} \hat{\boldsymbol{u}}_L(\boldsymbol{k},t)\mathrm{e}^{\mathrm{i}\boldsymbol{k}\cdot\boldsymbol{a}}. \tag{11}$$

Then the following asymptotic representation is used for the shell-summed high wavenumber Fourier amplitudes ([10])

$$\sum_{k\le|\boldsymbol{k}|<k+1} |\hat{\boldsymbol{u}}_L(\boldsymbol{k},t)| \simeq C(t)k^{\alpha(t)}\exp[-\delta_L(t)k]. \tag{12}$$

Here $\delta_L(t)$ is the width of the Lagrangian analyticity strip, that is the distance at time t from the real domain of the nearest (Lagrangian) complex-space singularity. The same analysis is applied also to the Eulerian velocity.

Fig. 1 shows the wavenumber dependence of the shell-summed amplitudes for the Eulerian and Lagrangian velocities at the same time, chosen in such a way that there is only a modest range of wavenumbers at high $k \equiv |\boldsymbol{k}|$ at which the rounding errors swamp the (roughly) exponential signal. They both exhibit exponential decay from which the Eulerian $\delta(t)$ and its Lagrangian counterpart $\delta_L(t)$ are measured. It is seen that the Lagrangian δ is significantly smaller than the Eulerian one. Actually, $\delta_L(t) < \delta(t)$ holds for all times $t < 1.245$ (the latest time analyzed). We also checked that the inequality $\delta_L < \delta$ holds for the flow with the initial condition (2) which has less symmetry than (1).

The exponential decay with the wavenumber k of the shell-summed Lagrangian Fourier amplitude is strong evidence that there are singularities of the Lagrangian velocity $\boldsymbol{u}_L(\boldsymbol{a},t)$ at a finite distance from the real domain; thus it cannot be an entire function. We also obtained numerical evidence that the Lagrangian map has the same locations of complex-Lagrangian singularities as the Lagrangian velocity and that the inverse

Lagrangian map has the same locations of complex-Eulerian singularities as the Eulerian velocity. For the very simple Eulerian steady flow investigated in Ref. [14], Lagrangian singularities are mapped to Eulerian (complex) infinity. Is this also the case for the present flow which has nontrivial Eulerian dynamics? Here, the answer appears to be "yes". Specifically, let $\boldsymbol{a}_\star$ be a Lagrangian singular location corresponding to time $t > 0$, say the one closest to the real domain or the one near this position. Does $\boldsymbol{d}(\boldsymbol{a}, t) \equiv \boldsymbol{a} - \boldsymbol{x}(\boldsymbol{a}, t)$ tend to infinity as $\boldsymbol{a} \to \boldsymbol{a}_\star$? In principle we can find the scaling law of any component of $\boldsymbol{d}$ as $\boldsymbol{a} \to \boldsymbol{a}_\star$, if we have sufficiently accurate high-resolution data for the Fourier transform of $\boldsymbol{d}(\boldsymbol{a})$ at high wavenumbers. This is explained in Section 4.2 of Ref. [11]. This requires the determination not only of the exponential decrement δ_{L} but of the exponent of the algebraic prefactor in front of the exponential which controls the nature of the singularity in complex $\boldsymbol{a}$-space. With a resolution of only 512^2, such exponents are rather poorly determined. It is likely that both components of $\boldsymbol{d}(\boldsymbol{a})$ blow up as $s^{-\beta}$ where s is the modulus of $\boldsymbol{a} - \boldsymbol{a}_\star$ and the exponent β is about $3/2$ but with an error bar so large that a negative value cannot be completely ruled out.[3] We shall revisit such issues from a theoretical point of view in the concluding section.

4. Concluding remarks

We have shown that the simple 2D incompressible nonsteady flow with the initial condition (1) has complex singularities not only in Eulerian but also in Lagrangian coordinates. The Lagrangian singularities are significantly closer to the real domain than the Eulerian ones. A possible interpretation of this was given by S. Orszag (private communication 2003): in Eulerian coordinates the buildup of singularities is slowed down by the aforementioned phenomenon of depletion, whereas in Lagrangian coordinates any flow which is nonuniform will keep changing nontrivially, even if it is steady in Eulerian coordinates. To illustrate this we have shown in Fig. 2 the (Eulerian) Laplacian of the vorticity $\nabla^2\omega$ in both Eulerian and Lagrangian coordinates. The former representation displays strongly depleted ribbon-shaped structures, not seen in the latter.

Now we wish to comment on the results concerning the analytic structure in Lagrangian coordinates and on possible generalizations to other 2D flow with space-periodic entire initial data. The most obvious result is that, since the vorticity remains unchanged along fluid particle trajectories in 2D, the Lagrangian vorticity field stays entire for all times and thus is devoid of any singularities other than at complex infinity. The Lagrangian velocity field and the Lagrangian map both have complex singularities (presumably along 1D complex manifolds) and the numerical evidence shows that these are at the same locations. Proving this partially can perhaps be

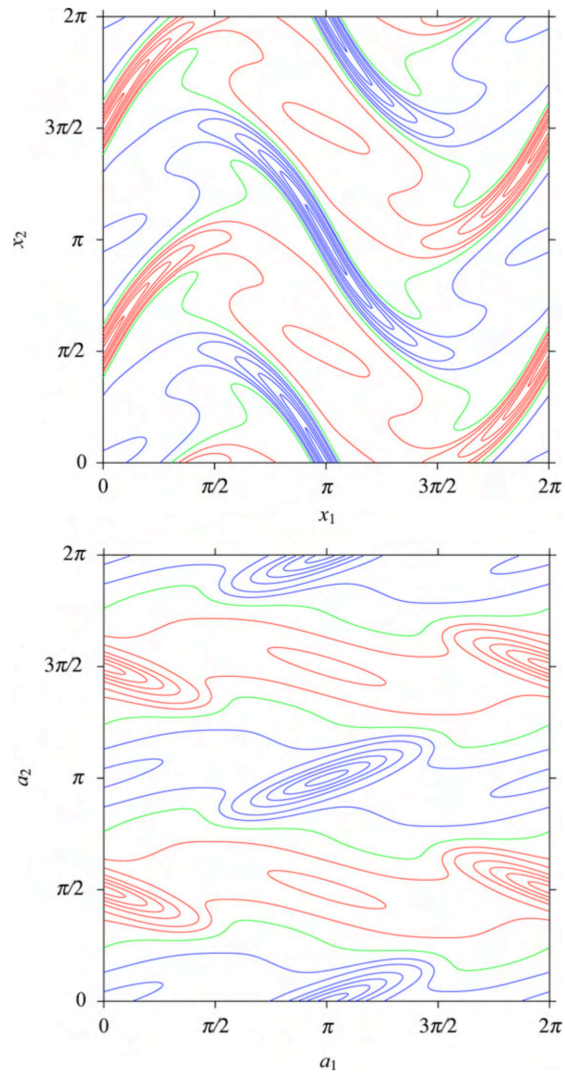

Fig. 2. Contours of the Laplacian of the vorticity shown for the same flow as in Fig. 1, shown at $t = 1.245$. Upper figure: Eulerian coordinates; lower figure: Lagrangian coordinates. For both figures the contour values are $0, \pm 12.5, \pm 25, \pm 50, \pm 75, \pm 100, \pm 125$; red: positive, green: zero, blue: negative. (For interpretation of the references to colour in this figure legend, the reader is referred to the web version of this article.)

done by writing the velocity in terms of the vorticity using the (periodicity-modified) Biot–Savart integral representation and then making the change of variable from Eulerian to Lagrangian coordinates. On the resulting integral, using the fact that the initial vorticity is entire, it may be possible to show that if the Lagrangian map $\boldsymbol{x}(\boldsymbol{a}, t)$ is analytic for some (complex) $\boldsymbol{a}$, the same holds for the Lagrangian velocity.

One of the most striking results reported in Section 3, but one for which the evidence is a bit shaky, is that Lagrangian singularities at time $t > 0$ correspond to fluid particles which at time t escape to infinity. Here are some observations which could be useful for proving this. The idea is to show that there is a contradiction if at time $t > 0$, a Lagrangian singularity $\boldsymbol{a}_\star$ at a finite location is mapped to a point $\boldsymbol{x}_\star$ which is not at infinity. Indeed, if $\boldsymbol{x}_\star$ is at a finite distance, from the fact that the Jacobian of the Lagrangian map is one, it follows that $\boldsymbol{x}_\star$ must

[3] We have applied the same method of analysis to the behavior of $\boldsymbol{d}(\boldsymbol{x})$ when an Eulerian singularity is approached at $\boldsymbol{x}_\star$. The displacement seems again to diverge with an exponent β around $3/2$ (implying also the divergence of the Eulerian vorticity) but the quality of the scaling is again dubious.

be a singularity of the inverse Lagrangian map $\boldsymbol{x} \mapsto \boldsymbol{a}$. The Eulerian vorticity can be obtained by composing the inverse Lagrangian map and the initial (entire) vorticity. Composing a function singular at $\boldsymbol{x}_\star$ with one which is entire does not necessarily yield a singular function. Perhaps with some extra work it can be proved that the Eulerian vorticity is indeed singular at $\boldsymbol{x}_\star$. We already pointed out in the Introduction that for 2D space-periodic initially entire flow there is numerical evidence that the vorticity is infinite at (complex) Eulerian singularities. If this can also be proved, it then follows that $\boldsymbol{a}_\star$ is at infinity and thus we have a contradiction.

The global picture emerging from all this is (tentatively) the following: for entire periodic initial data in 2D, the solutions of the incompressible Euler equation have complex-Eulerian singularities corresponding to fluid particles initially at infinity and Lagrangian singularities corresponding to fluid particles currently at infinity. In both coordinates singularities correspond to some particle escaping to infinity; this mechanism for incompressible fluids is very different from the one operating for the 1D or multi-dimensional *compressible* Burgers equation for which singularities are mostly associated to the vanishing of the Jacobian of the the Lagrangian map (see, e.g., Ref. [15]).

We cannot at present rule out that the same scenario holds in three dimensions but it may not be consistent with real blowup. Of course, there are major differences in 3D; for example, vorticity is not conserved. However, the Lagrangian numerical techniques presented in this paper are easily extended to the 3D case.

Acknowledgments

We are very grateful to W. Pauls for many useful remarks. Thanks are also due to C. Bardos and S. Orszag. TM was supported by the Grant-in-Aid for the 21st Century COE "Center for Diversity and Universality in Physics" from the Japanese Ministry of Education, by the Japanese Ministry of Education Grant-in-Aid for Young Scientists [(B), 15740237, 2003] and by the French Ministry of Education. A part of the numerical calculations was carried out on SX8 at the Yukawa Institute for Theoretical Physics in Kyoto University.

References

[1] S. Benachour, Analyticité des solutions de l'équation d'Euler en trois dimensions, C. R. Acad. Sci. Paris 283 A (1976) 107–110.
[2] S. Benachour, Analyticité des solutions des équations d'Euler, Arch. Ration. Mech. Anal. 71 (1976) 271–299.
[3] E. Hölder, Uber die unbeschränkte Fortsetzbarkeit einer stetigen ebenen Bewegung in einer unbegrenzten inkompressiblen Flüssigkeit, Math. Z. 37 (1933) 727–738.
[4] W. Wolibner, Un theorème sur l'existence du mouvement plan d'un fluide parfait, homogène, incompressible, pendant un temps infiniment long, Math. Z. 37 (1933) 698–726.
[5] C. Sulem, P.-L. Sulem, H. Frisch, Tracing complex singularities with spectral methods, J. Comput. Phys. 50 (1983) 138–161.
[6] H. Bahouri, J.-Y. Chemin, Equations de transport relatives à des champs de vecteurs non-lipschitziens et mécanique des fluides, Arch. Ration. Mech. Anal. 127 (1994) 159–181.
[7] J.T. Beale, T. Kato, A.J. Majda, Remarks on the breakdown of smooth solutions for the 3-D Euler equations, Commun. Math. Phys. 94 (1985) 61–66.
[8] A.J. Majda, A.L. Bertozzi, Vorticity and Incompressible Flow, Cambridge University Press, Cambridge, 2000.
[9] U. Frisch, T. Matsumoto, J. Bec, Singularities of Euler flow? Not out of the blue!, J. Stat. Phys. 113 (2003) 761–781.
[10] T. Matsumoto, J. Bec, U. Frisch, The analytic structure of 2D Euler flow at short times, Fluid Dyn. Res. 36 (2005) 221–237.
[11] W. Pauls, T. Matsumoto, U. Frisch, J. Bec, Nature of complex singularities for the 2D Euler equation, Physica D 219 (2006) 40–59.
[12] G.I. Taylor, A.E. Green, Mechanism of the production of small eddies from large ones, Proc. Roy. Soc. A 158 (1937) 499–521.
[13] D. Gottlieb, S. Orszag, Numerical Analysis of Spectral Methods, SIAM, Philadelphia, 1977.
[14] W. Pauls, T. Matsumoto, Lagrangian singularities of steady two-dimensional flows, Geophys. Astrophys. Fluid Dyn. 99 (2005) 61–75.
[15] J. Bec, K. Khanin, Burgers turbulence, Phys. Rep. 447 (2007) 1–66.

Weak solutions, high Reynolds numbers and statistical mechanics

Available online at www.sciencedirect.com
ScienceDirect
Physica D 237 (2008) 1956–1968
PHYSICA D
www.elsevier.com/locate/physd

Dissipative anomalies in singular Euler flows

Gregory L. Eyink*

Department of Applied Mathematics & Statistics, The Johns Hopkins University, Baltimore, MD 21218, USA
Department of Physics & Astronomy, The Johns Hopkins University, Baltimore, MD 21218, USA

Available online 12 February 2008

Abstract

We discuss Onsager's conjecture that non-vanishing energy dissipation in high-Reynolds-number turbulence is associated to singular (distributional) solutions of the incompressible Euler equations. We carefully explain the physical and mathematical meaning of the conjecture and also review relevant theoretical, experimental and numerical work, emphasizing some of the dramatic successes of Onsager's point of view. Finally, we present several new ideas and results on Lagrangian dynamics of circulations and vortex-lines that we believe will be important for future progress.

PACS: 47.10.A-; 47.27.Ak; 47.27.ef; 47.32.C-

Keywords: Turbulence; Energy dissipation; Euler equations; Coarse-graining

1. Introduction

It is widely accepted that simple molecular fluids are described in the double limit of small Knudsen number *Kn* and small Mach number *Ma* by the incompressible Navier–Stokes equation with kinematic viscosity $\nu > 0$:

$$\partial_t \mathbf{u} + (\mathbf{u} \cdot \nabla)\mathbf{u} = -\nabla p + \nu \triangle \mathbf{u}, \quad \nabla \cdot \mathbf{u} = 0. \tag{1}$$

There are good grounds for this belief. For example, Quastel and Yau [1] have rigorously derived these equations in such a limit for a stochastic lattice-gas model. Their proof shows that the coarse-grained velocity fields in the model must satisfy some Leray solution [2] of (1), *even if* the latter develops singularities at which the velocity field locally becomes infinite. See also the contribution of Saint-Raymond in this volume [3]. There is no apparent limitation on the Reynolds number *Re* in such results. For example, in Kolmogorov's 1941 theory [4] of turbulence $Re = (Ma/Kn)^4$, where $Kn = \ell_{mf}/\eta$ is the Knudsen number based on the Kolmogorov microscale η and the mean-free path ℓ_{mf}, so that $Re \gg 1$ as long as $Kn \ll Ma \ll 1$ [5]. The Navier–Stokes equation (1) is thus expected to describe the dynamics of turbulent fluids at any Reynolds number.

It may be less commonly appreciated that singular solutions of the incompressible Euler equations

$$\partial_t \mathbf{u} + (\mathbf{u} \cdot \nabla)\mathbf{u} = -\nabla p, \quad \nabla \cdot \mathbf{u} = 0 \tag{2}$$

are a good candidate to describe turbulent flow in the asymptotic limit $Re \to \infty$, as first conjectured by Onsager [6]. The present paper reviews this idea, both its physical meaning and its current mathematical status.

2. Empirical foundations

Our story begins with an experimental fact. Energy dissipation $\varepsilon = \nu|\nabla \mathbf{u}|^2$ appears not to vanish in the limit $Re \to \infty$ or $\nu \to 0$, for a variety of turbulent flows. The basis of this statement is empirical: there is still no *a priori* derivation from the Navier–Stokes equation (1). The basic observation was made by the great British fluid-dynamicist, G. I. Taylor, semi-phenomenologically. Discussing turbulent pipe flow in a classic 1935 paper [7], he wrote:

"It has been shown by V. Karman that if the surface stress in a pipe is expressed in the form $\tau = \rho v_\times^2$ then

* Corresponding address: Department of Applied Mathematics & Statistics, The Johns Hopkins University, 3400 N. Charles Street, Baltimore, MD 21218, USA. Tel.: +1 410 516 7201; fax: +1 410 516 7459.
E-mail address: eyink@ams.jhu.edu.

0167-2789/$ - see front matter
doi:10.1016/j.physd.2008.02.005

$$\frac{U_c - U}{v_\times} = f\left(\frac{r}{a}\right), \tag{54}$$

where U_c is the maximum velocity in the middle of the pipe and U is the velocity at radius r. This relationship is associated with the conception that the Reynolds' stresses are proportional to the squares of the turbulent components of velocity. It seems that the rate of dissipation of energy in such a system must be proportional, so far as changes in linear dimensions, velocity, and density are concerned, to $\rho u'^3/l$, where l is some linear dimension defining the scale of the system."

Taylor's claim is that turbulent energy dissipation per unit mass should scale at high Reynolds number, on average, as $\langle\varepsilon\rangle \sim U^3/L$, where U is rms velocity and L is the integral length. This is a remarkable formula, since it is completely independent of molecular viscosity.

Empirically, the formula may be tested by studying the non-dimensional dissipation rate $D(Re) = \langle\varepsilon\rangle/(U^3/L)$, which is a function of Reynolds number $Re = UL/\nu$. Here $\langle\cdot\rangle$ stands for either a space-, time- or spacetime-average, over a finite domain, as employed in experimental studies. If Taylor's observation is correct, then

$$\lim_{Re\to\infty} D(Re) = D_* > 0. \tag{3}$$

Confirmation of (3) was provided in the 1940's by the data of H. L. Dryden on decaying turbulence in wind-tunnels [8]. Although the early tests were fairly crude, later experiments have demonstrated (3) more convincingly. For a compilation of data from various free flows (decaying grid turbulence, jets, wakes, etc.), see [9,11]. The non-vanishing of mean energy dissipation rate is surprising, since there is no reason *a priori* that any of the hydrodynamic energy must be converted to heat as $\nu \to 0$. Perhaps the best checks of (3) have come from numerical simulation of homogeneous, isotropic turbulence in a periodic domain, as summarized by Sreenivasan [12]. The recent numerical study of forced turbulence by Kaneda et al. [13] on a 4096^3 spatial grid has confirmed that $D(Re)$ asymptotes to a constant at high Reynolds numbers. Furthermore, the mean kinetic energy remains bounded in the same limit. This implies that energy is not accumulating in the hydrodynamic modes but, instead, is being transferred to the small-scales where it is efficiently dissipated by viscosity into heat. The experimental situation in wall-bounded flows is more complex. According to classical theories of the "log-layer", the friction velocity u_* (and thus the rms velocity U) are logarithmically decreasing functions of Re for smooth walls and Reynolds-number-independent for rough walls [14]. In an experimental study of Taylor–Couette flow with smooth walls, Cadot et al. [10] have observed distinctly different behaviors in the bulk of the flow and at the boundary. Most of the dissipation was found to occur in a boundary layer at the walls of the apparatus, but this dissipation was a weakly decreasing function of the Reynolds number. On the other hand, the dissipation in the bulk appeared to obey (3) at high Reynolds number.

Summarizing a somewhat complicated experimental picture, we may say that (3) is observed to hold well in a wide range of turbulent flows. Non-vanishing of mean energy dissipation at infinite-Reynolds number was a basic assumption of the Kolmogorov 1941 similarity theory of turbulence [4]. This property is so important – both practically and theoretically – that it is sometimes called the "zeroth law of turbulence" [15].

3. Dissipation and singularities

The Yale chemist, Lars Onsager, was actively interested in the problem of fluid turbulence in the 1940's, and, indeed, rediscovered the Kolmogorov 1941 similarity theory independently of Kolmogorov. For an in-depth historical discussion, see [16]. Onsager was aware of Taylor's estimate of mean turbulent energy dissipation and of Dryden's related experiments. In his only full-length journal article on fluid turbulence in 1949, he drew from these observations a remarkable conclusion [6]:

"It is of some interest to note that in principle, turbulent dissipation as described could take place just as readily without the final assistance by viscosity. In the absence of viscosity, the standard proof of the conservation of energy does not apply, because the velocity field does not remain differentiable! In fact it is possible to show that the velocity field in such "ideal" turbulence cannot obey any LIPSCHITZ condition of the form

$$|\mathbf{v}(\mathbf{r}' + \mathbf{r}) - \mathbf{v}(\mathbf{r}')| < (\text{const.})r^n \tag{26}$$

for any order n greater than $1/3$; otherwise the energy is conserved. Of course, under the circumstances, the ordinary formulation of the laws of motion in terms of differential equations becomes inadequate and must be replaced by a more general description ...."

In this section and the next we shall explicate Onsager's rather concise assertions above.

Perhaps the most physical way to explain these statements is in terms of effective "coarse-grained" equations obtained from the incompressible Navier–Stokes equation, as in [17,18]. Consider a locally space-averaged (low-pass filtered) velocity

$$\overline{\mathbf{u}}_\ell(\mathbf{x}) = \int \mathrm{d}^d r\, G_\ell(\mathbf{r})\mathbf{u}(\mathbf{x}+\mathbf{r}). \tag{4}$$

for an averaging kernel $G_\ell(\mathbf{r}) = \ell^{-d}G(\mathbf{r}/\ell)$ that is non-negative, smooth, and rapidly decaying. Averaging out the small-scales from the Navier–Stokes equation yields effective equations at a continuum of length-scales ℓ:

$$\partial_t\overline{\mathbf{u}}_\ell + \boldsymbol{\nabla}\cdot[\overline{\mathbf{u}}_\ell\overline{\mathbf{u}}_\ell + \boldsymbol{\tau}_\ell] = -\boldsymbol{\nabla}\overline{p}_\ell + \nu\triangle\overline{\mathbf{u}}_\ell, \quad \boldsymbol{\nabla}\cdot\overline{\mathbf{u}}_\ell = 0 \tag{5}$$

where $\boldsymbol{\tau}_\ell$ is the *subscale stress tensor*

$$\boldsymbol{\tau}_\ell = \overline{(\mathbf{u}\otimes\mathbf{u})}_\ell - \overline{\mathbf{u}}_\ell\otimes\overline{\mathbf{u}}_\ell \tag{6}$$

from the eliminated modes. This approach is similar to what in physics is called Wilson–Kadanoff renormalization group (RG) [19]. The same technique is used in Large-Eddy Simulation (LES) of turbulent flow, where a closure equation is employed for the stress tensor $\boldsymbol{\tau}_\ell$ [20].

Simplifications occur in these equations for $Re \gg 1$. An elementary estimate of the viscous diffusion term is

$$\|\nu\triangle\overline{\mathbf{u}}_\ell\|_2 \le (\text{const.})(\nu/\ell^2)\|\mathbf{u}\|_2$$

where $\|\mathbf{u}\|_2^2 = \int_0^T \mathrm{d}t \int \mathrm{d}^d\mathbf{x}\, |\mathbf{u}(\mathbf{x},t)|^2$ is (twice) the time-average kinetic energy. Thus, this term is negligible for small ν or large ℓ and can be dropped, like "irrelevant" terms in RG analysis. Simpler effective equations therefore result for the *inertial-range* of length-scales ℓ:

$$\partial_t \overline{\mathbf{u}}_\ell + \nabla \cdot [\overline{\mathbf{u}}_\ell \overline{\mathbf{u}}_\ell + \boldsymbol{\tau}_\ell] = -\nabla \overline{p}_\ell, \quad \nabla \cdot \overline{\mathbf{u}}_\ell = 0 \tag{7}$$

which retain only the contributions from the nonlinear interactions. Eq. (7) can easily be seen to hold rigorously if the Navier–Stokes solution $\mathbf{u}^\nu$ for viscosity ν converges $\mathbf{u}^\nu \to \mathbf{u}$ in L^2 norm as $\nu \to 0$, i.e. if the residual energy in $\mathbf{u} - \mathbf{u}^\nu$ vanishes. Hereafter we shall consider (7) at fixed, inertial-range length-scales ℓ, from which negligible viscous terms have been dropped.

The large-scale energy balance that follows from (7) is

$$\partial_t e_\ell + \nabla \cdot \mathbf{J}_\ell = -\Pi_\ell$$

where $e_\ell = \frac{1}{2}|\overline{\mathbf{u}}_\ell|^2$ is large-scale energy density per mass,

$$\mathbf{J}_\ell = (e_\ell + \overline{p}_\ell)\overline{\mathbf{u}}_\ell + \overline{\mathbf{u}}_\ell \cdot \boldsymbol{\tau}_\ell$$

is *space transport* of large-scale energy, and

$$\Pi_\ell = -\nabla \overline{\mathbf{u}}_\ell : \boldsymbol{\tau}_\ell \tag{8}$$

is the *rate of work* of the large-scale velocity-gradient against the small-scale stress, or "deformation work" in the terminology of Tennekes and Lumley [14]. Turbulent energy cascade is the dynamical transfer of kinetic energy from large-scales to small-scales via the "energy flux" Π_ℓ through the inertial-range.

A key realization of Onsager was that this energy flux depends only upon *velocity-increments*

$$\delta \mathbf{u}(\mathbf{r}; \mathbf{x}) \equiv \mathbf{u}(\mathbf{x} + \mathbf{r}) - \mathbf{u}(\mathbf{x}).$$

In particular, this holds both for stress

$$\boldsymbol{\tau}_\ell = \int \mathrm{d}^d r\, G_\ell(\mathbf{r}) \delta\mathbf{u}(\mathbf{r}) \otimes \delta\mathbf{u}(\mathbf{r}) - \int \mathrm{d}^d r\, G_\ell(\mathbf{r}) \delta\mathbf{u}(\mathbf{r}) \otimes \int \mathrm{d}^d r\, G_\ell(\mathbf{r}) \delta\mathbf{u}(\mathbf{r})$$

and the velocity-gradient

$$\nabla \overline{\mathbf{u}}_\ell = -(1/\ell) \int \mathrm{d}^d r\, (\nabla G)_\ell(\mathbf{r}) \delta\mathbf{u}(\mathbf{r}).$$

It follows directly from these that

$$\Pi_\ell = O(|\delta u(\ell)|^3/\ell) \tag{9}$$

as a rigorous upper bound, where $\delta u(\ell) = \sup_{r<\ell} |\delta\mathbf{u}(\mathbf{r})|$. This can be regarded as a refinement of the estimate proposed earlier by Taylor and, indeed, is a consequence of the fact that turbulent stress is "proportional to the squares of the turbulent components of velocity".

From the estimate (9), Onsager's assertion about singularities easily follows. Assume that the inertial-range velocity field $\mathbf{u}(t)$ at time t is *Hölder continuous* at point $\mathbf{x}$ with an exponent $0 < \alpha < 1$. Here we follow the standard definition of Hölder–Lipschitz continuity that $\mathbf{u}(t) \in C^\alpha(\mathbf{x})$ iff $|\delta\mathbf{u}(\mathbf{r}; \mathbf{x}, t)| = O(r^\alpha)$. Substituting into estimate (9), one obtains the bound

$$\Pi_\ell(\mathbf{x}, t) = O(\ell^{3\alpha-1}).$$

In particular, $\Pi_\ell(\mathbf{x}, t) \to 0$ as $\ell \to 0$ if $\alpha > 1/3$ and there can then be no asymptotic energy flux to the small-scales where viscosity is effective. The reverse statement is perhaps more interesting: to explain the observed energy dissipation requires $\alpha \leq 1/3$ in the infinite-Reynolds number limit. Onsager's prediction of such (near) singularities in turbulent flow has been well-confirmed by experiment and simulation. For example, see the papers [21,22] where an entire multifractal dimension spectrum of Hölder singularities has been obtained from experiments and simulations, with the most probable exponent $\alpha \simeq 1/3$. The *a priori* prediction of such velocity singularities is striking confirmation of Onsager's views on turbulent energy dissipation.

The singularities predicted by this argument need not be *finite-time inviscid singularities*, however. At fixed positive viscosity ν or large but finite Reynolds number *Re*, a nonzero flux of energy may form for length-scales in the inertial-range $L \gg \ell \gg \eta$, between the integral scale L and the dissipation scale η. If the smallest length-scale $\ell(t)$ down to which flux is constant goes to zero exponentially quickly, for example, then the time τ_{dis} to reach the dissipation scale η will grow weakly (logarithmically) with the Reynolds number. For times $t \ll \tau_{dis}$ no energy will be dissipated by viscosity. Nevertheless, in externally forced turbulence, real singularities down to zero length-scale may be obtained by first allowing the flow to reach steady-state at fixed Reynolds number and then taking subsequently the limit of infinite-Reynolds number. That is, singularities and non-vanishing dissipation may appear in the mathematical limit $t \to \infty$ *first* and $\nu \to 0$ *second*. The situation is different in freely-decaying turbulence. In free decay from smooth initial data, nonzero energy dissipation at finite times for $Re \to \infty$ requires that the time τ_{dis} be *independent* of Reynolds number. Thus, observation of non-vanishing energy dissipation at high Reynolds number in decaying grid-turbulence is consistent with a finite-time inviscid singularity. Of course, this is rather weak evidence for a finite-time singularity, because current experiments can hardly distinguish between a time τ_{dis} which is independent of *Re* and one which grows very slowly, say as $\log(Re)$ or as $\log\log(Re)$.

4. Generalized Euler solutions

We have not yet explained Onsager's assertion about the possibility of energy dissipation "in the absence of viscosity" for "a more general description" of the ideal fluid equations. The effective Eqs. (7) for a length-scale ℓ in the inertial-range are identical to those that would be obtained by coarse-graining not the Navier–Stokes equations but instead the *incompressible Euler equations*

$$\partial_t \mathbf{u} + \nabla \cdot (\mathbf{u}\mathbf{u}) = -\nabla p, \quad \nabla \cdot \mathbf{u} = 0. \tag{10}$$

The above equations with the classical notions of space–time derivatives will not make sense for the singular velocity fields

u considered by Onsager. However, Eq. (10) is meaningful in the sense of distributions, i.e. after smearing with smooth test functions $\varphi(\mathbf{x}, t)$. The effective Eqs. (7) at length-scale ℓ can be obtained (interpreted distributionally in time) by spatial smearing of (10) with the special set of test functions $\varphi_{\mathbf{x},\ell}(\mathbf{x}') = \ell^{-d} G((\mathbf{x}' - \mathbf{x})/\ell)$. In fact, Eq. (10) in the distributional sense is mathematically equivalent to the set of effective Eqs. (7) for all $\ell > 0$. The gist of the matter was well-expressed by Landau & Lifshitz in the 1954 Russian edition of their fluid-dynamics text [23]:

"We therefore conclude that, for the large eddies which are the basis of any turbulent flow, the viscosity is unimportant and may be equated to zero, so that the motion of these eddies obeys Euler's equation. ... The viscosity of the fluid becomes important only for the smallest eddies, whose Reynolds number is comparable with unity."

In RG language, one may regard the Euler equations as "bare" equations obtained in the ultraviolet limit $\ell \to 0$ from the sequence of effective Eqs. (7) at length-scales $\ell > 0$, after having *first* taken the limit $\nu \to 0$.

As realized by Onsager, the Euler equations in this generalized sense do not guarantee conservation of energy. If the Euler solution $\mathbf{u} \in L^3$ in spacetime, then energy balance can be derived distributionally in the form

$$\partial_t \left(\frac{1}{2}|\mathbf{u}|^2\right) + \nabla \cdot \left[\left(\frac{1}{2}|\mathbf{u}|^2 + p\right)\mathbf{u}\right] = -D(\mathbf{u}), \tag{11}$$

where the distribution $D(\mathbf{u})$ need not vanish. It can be defined as the asymptotic energy flux to zero length-scale, $D(\mathbf{u}) = \lim_{\ell\to 0} \Pi_\ell$, with Π_ℓ given by (8). The energy balance (11) was first derived by Duchon and Robert [24], who also obtained the alternative expression

$$D(\mathbf{u}) = \lim_{\ell\to 0} \frac{1}{4\ell} \int \mathrm{d}^d r\, (\nabla G)_\ell(\mathbf{r}) \cdot \left[\delta\mathbf{u}(\mathbf{r})|\delta\mathbf{u}(\mathbf{r})|^2\right]. \tag{12}$$

This is Onsager's *dissipative anomaly*. As was pointed out by Polyakov [25], the violation of naïve conservation laws for Euler solutions due to turbulent cascade is very similar to conservation-law anomalies in quantum field theory, such as the axial-anomaly in quantum electrodynamics (QED).

It is worthwhile to sketch briefly the proof of (11) and (12) from [24], which is based on another form of the large-scale energy balance. Using a smooth point-splitting regularization of the energy density

$$e_\ell^* \equiv \frac{1}{2}\mathbf{u} \cdot \overline{\mathbf{u}}_\ell = \frac{1}{2}\int \mathrm{d}^d r\, G_\ell(\mathbf{r})\, \mathbf{u}(\mathbf{x}, t) \cdot \mathbf{u}(\mathbf{x} + \mathbf{r}, t),$$

one can derive the balance equation

$$\partial_t e_\ell^* + \nabla \cdot \left[e_\ell^* \mathbf{u} + \frac{1}{2}(\overline{p}_\ell \mathbf{u} + p\overline{\mathbf{u}}_\ell) + \frac{1}{2}\left(\overline{(|\mathbf{u}|^2\mathbf{u})}_\ell - \overline{(|\mathbf{u}|^2)}_\ell \mathbf{u}\right)\right] = -D_\ell(\mathbf{u})$$

with

$$D_\ell(\mathbf{u}) = \frac{1}{4\ell}\int \mathrm{d}^d r\, (\nabla G)_\ell(\mathbf{r}) \cdot \left[\delta\mathbf{u}(\mathbf{r})|\delta\mathbf{u}(\mathbf{r})|^2\right].$$

Using the assumption that $\mathbf{u} \in L^3$, it is easy to show that the left-hand side of the above balance equation has the left-hand side of (11) as its distributional limit for $\ell \to 0$. This gives both (11) and (12). These expressions imply immediately Onsager's assertion about Hölder exponent $\alpha > 1/3$. In fact, it follows from the above expression that $D_\ell(\mathbf{u}) = O(\ell^{3\alpha-1})$ if $\mathbf{u}(t) \in C^\alpha$ globally in spacetime. Thus, $D(\mathbf{u}) = 0$ when $\alpha > 1/3$ and the generalized Euler solution must conserve kinetic energy.

There are several interesting historical aspects of the above argument. First, this derivation of the dissipative anomaly in turbulence is quite close to the derivation of the axial-anomaly in QED by a (gauge-invariant) point-splitting regularization, as first given by J. Schwinger in 1951 [26]. Second, it appears that the above argument was Onsager's own proof of his statement about Hölder singularities! The point-split energy balance (in a space-integrated form) was communicated by Onsager to C. C. Lin in a private letter in 1945. See [16] for a reprinting of this letter. Onsager himself never published his proof and considerable time elapsed before his ideas were rediscovered. Sulem and Frisch [27] showed that spectral energy flux $\Pi(k) \to 0$ as $k \to \infty$ for an Euler solution with energy spectral exponent $n > 8/3$. Eyink [28] showed that spectral flux averaged over an octave band must vanish at high-wavenumber if a condition is assumed on Fourier amplitudes somewhat stronger than Hölder continuity with exponent $\alpha > 1/3$. He also showed that Onsager's result is optimal by constructing an instantaneous (single-time) velocity field $\mathbf{u} \in C^{1/3}$ such that $\Pi_\ell \nrightarrow 0$ as $\ell \to 0$. Shortly thereafter, Constantin, E and Titi [17] found the simple argument presented in Section 3, which proved Onsager's original assertion for Hölder continuous velocities. In fact, their argument gave stronger results for **u** merely in a "Besov space", discussed more below, and yielded the Sulem–Frisch result [27] as another corollary.

The paper of Duchon and Robert [24] contained some further important results related to the zero-viscosity limit. It is not hard to see that, if a sequence of Navier–Stokes solutions $\mathbf{u}^\nu$ for viscosities $\nu \to 0$ converges $\mathbf{u}^\nu \to \mathbf{u}$ in L^3 norm, then the limiting **u** is a distributional Euler solution that satisfies the energy balance (11). Furthermore, [24] observed in that case that

$$D(\mathbf{u}) = \lim_{\nu\to 0} \nu|\nabla\mathbf{u}^\nu|^2 \geq 0. \tag{13}$$

Here we have assumed, for simplicity, that the Leray solutions of Navier–Stokes are themselves globally smooth; otherwise, there will be additional dissipation in (13) arising from the Navier–Stokes singularities [24]. The important implication of (13) is the positivity of $D(\mathbf{u})$, which shows that the special Euler solutions obtained as strong L^3 limits of Navier–Stokes solutions will be *dissipative*. Since a positive distribution is a nice (Radon) measure, the limit in (13) implies that the dissipative anomaly $D(\mathbf{u})$ is given by a spacetime measure. This is the multifractal dissipation measure ε extensively studied experimentally at high Reynolds number, e.g. by Meneveau and Sreenivasan [29]. One minor difference is that experimentalists consider instantaneous time-slices. However, it is reasonable for any nice (Borel) set $\Delta \subset \mathbb{R}^3$ to interpret

$$\varepsilon(\Delta, t) = \frac{1}{2\tau} \int_{\Delta} \mathrm{d}^d x' \int_{t-\tau}^{t+\tau} \mathrm{d}t' \; D(\mathbf{u})(\mathbf{x}', t'),$$

taking into account the finite temporal resolution τ of measurements.

There is one last result of Duchon and Robert [24] which deserves to be mentioned. They derived a further expression for the dissipative anomaly, of the form

$$D(\mathbf{u}) = -\frac{3}{4} \lim_{r\to 0} \frac{\langle \delta u_L(\mathbf{r}) |\delta \mathbf{u}(\mathbf{r})|^2 \rangle_{\mathrm{ang}}}{r},$$

where $\delta u_L(\mathbf{r}) = \hat{\mathbf{r}} \cdot \delta \mathbf{u}(\mathbf{r})$ is the longitudinal velocity increment and $\langle \cdot \rangle_{\mathrm{ang}}$ denotes an angular average over the direction $\hat{\mathbf{r}} = \mathbf{r}/r$ of the separation vector $\mathbf{r}$. This result, together with (13), is a generalization of a famous result of Kolmogorov in 1941, the 4/5 th-law [4]. Whereas Kolmogorov proved his result by averaging over ensembles assuming homogeneity and isotropy, the above form of the 4/5th-law is valid for individual realizations and locally in spacetime in the sense of distributions. Actually, the above result is properly a version of the "4/3rd-law" [30], but a bit of further manipulation yields a local version of the 4/5th-law in its standard form [31].

5. Mathematical foundations

As we emphasized at the outset, the basic motivations of our subject are empirical. From the point of view of pure PDE theory, the problem of dissipative Euler solutions remains open. Almost nothing is proved mathematically about existence, uniqueness or regularity of such solutions. We review here the little that is known.

Existence: Shnirelman [32] has constructed an example of a velocity field $\mathbf{u} \in L^2(\mathbb{R}^3 \times \mathbb{R}_+)$ in three-dimensional space (3D) which is a distributional solution of the Euler equations for which the energy $E(t) = \frac{1}{2}\int \mathrm{d}^3 x \, |\mathbf{u}(\mathbf{x}, t)|^2$ is monotone decreasing in time. His construction is related to the notion of a *generalized Euler flow* proposed by Brenier [33–35] to solve the least-action minimization problem with initial and final conditions. Shnirelman's solution lacks the regularity expected of a turbulent velocity field (see below). More importantly, it is *not* obtained from a Leray solution $\mathbf{u}^\nu$ of the Navier–Stokes equation in the limit $\nu \to 0$. In most fluid mechanical contexts, the physically-relevant Euler solutions $\mathbf{u}$ should be obtained as approximations to Navier–Stokes solutions $\mathbf{u}^\nu$ with small but positive viscosities $\nu > 0$. Thus, the existence problem, from the physical point of view, is intimately related to the problem of the zero-viscosity limit. We noted above that a limit $\mathbf{u} = \lim_{\nu\to 0} \mathbf{u}^\nu$ in the strong L^2-norm sense is necessarily a distributional Euler solution. If, furthermore, convergence is in the strong L^3-norm sense, then $\mathbf{u}$ satisfies the energy balance (11) with $D(\mathbf{u}) \geq 0$. The problem is, precisely, that such strong convergence is not known to occur. Zero-viscosity limits of Navier–Stokes solutions have only been shown to exist for weaker notions of convergence that give "Euler solutions" in some still more generalized sense.

For example, DiPerna and Majda [36] have shown that $\mathbf{u}^\nu$ converges weakly (along a suitable subsequence) to a Young measure $P_{\mathbf{x},t}(\mathrm{d}\mathbf{v})$ which is a *measure-valued Euler solution*. Roughly speaking, this means that distributionally in spacetime

$$\partial_t \langle \mathbf{v} \rangle_{\mathbf{x},t} + \nabla \cdot \langle \mathbf{v}\mathbf{v} \rangle_{\mathbf{x},t} = -\nabla p(\mathbf{x}, t)$$

for some distribution p, where $\langle \cdot \rangle_{\mathbf{x},t}$ is average with respect to $P_{\mathbf{x},t}$. If $P_{\mathbf{x},t} = \delta_{\mathbf{u}(\mathbf{x},t)}$ for some $\mathbf{u} \in L^2$, then this reduces to the standard notion of a distributional solution. It is interesting that this concept of Euler solution returns to a "kinetic-theory description," similar to a Boltzmann or Vlasov equation. Brenier [33,35] has discussed relations of DiPerna-Majda solutions with his own notion of a generalized Euler flow. As a second example, we mention the concept of a *dissipative Euler solution* introduced by Lions [37]. He defines $\mathbf{u}$ to be a dissipative solution if $\mathbf{u} \in L^\infty(\mathbb{R}_+, L^2(\mathbb{R}^d)) \cap C(\mathbb{R}_+, L^2_w(\mathbb{R}^d))$, $\nabla \cdot \mathbf{u} = 0$ and if it satisfies the inequality

$$(\mathrm{d}/\mathrm{d}t) \int \mathrm{d}^d x \, \frac{1}{2} |\mathbf{u} - \mathbf{v}|^2 \leq \|\gamma^-(\mathbf{v})\|_\infty \int \mathrm{d}^d x \, |\mathbf{u} - \mathbf{v}|^2 + \int \mathrm{d}^d x \, \mathbf{E}(\mathbf{v}) \cdot (\mathbf{u} - \mathbf{v})$$

for all "nice" $\mathbf{v} \in C(\mathbb{R}_+, L^2(\mathbb{R}^d))$, $\nabla \cdot \mathbf{v} = 0$, where $\gamma^-(\mathbf{v})$ is the most negative eigenvalue of the strain matrix $S_{ij}(\mathbf{v}) = (1/2)(\partial_i v_j + \partial_j v_i)$ and

$$\mathbf{E}(\mathbf{v}) \equiv -\partial_t \mathbf{v} - P^\perp[(\mathbf{v} \cdot \nabla)\mathbf{v}].$$

$P^\perp$ is the Leray projector onto divergence-free fields. Despite the cumbersome formulation, this definition has some desirable properties. Lions proved that "dissipative solutions" can always be obtained as suitable weak limits of Leray solutions $\mathbf{u}^\nu$ as $\nu \to 0$ (along a subsequence). It is a consequence of the definition of dissipative solutions that they coincide with any classical Euler solutions with strain field $\mathbf{S} \in L^1([0, T], L^\infty)$. Furthermore, when such a smooth solution $\mathbf{u}$ of Euler exists, conserving energy, then the solution $\mathbf{u}^\nu$ of the Navier–Stokes equation always converges to $\mathbf{u}$ as $\nu \to 0$ and one has:

$$\lim_{\nu\to 0} \int_0^T \mathrm{d}t \, \nu \|\nabla \mathbf{u}^\nu(t)\|_2^2 = 0. \tag{14}$$

This remark applies to a domain without boundary (torus or infinite-space) but the same result is not known for domains with boundary and no-slip boundary condition on the velocity (see Section IX). As to conjectured distributional Euler solutions that dissipate energy, i.e. satisfying the energy balance (11) with $D(\mathbf{u}) \geq 0$, Duchon and Robert [24] have remarked that these also are "dissipative solutions" in the sense of Lions.

Uniqueness: Distributional Euler solutions, unfortunately, are *not* unique. For example, Scheffer [38] has constructed a two-dimensional (2D) solution $\mathbf{u} \in L^2(\mathbb{R}^2 \times \mathbb{R})$ which he dubbed an "Euler froth" and that has compact support in spacetime. That is, with initial condition $\mathbf{u}_0 = \mathbf{0}$ the solution $\mathbf{u}$ has nontrivial evolution and then comes again to rest in finite time! For the initial condition $\mathbf{u}_0 = \mathbf{0}$ there is a unique classical solution of the 2D Euler equation, which is $\mathbf{u} \equiv \mathbf{0}$ everywhere in spacetime. This is also the unique zero-viscosity limit of the 2D Navier–Stokes solutions $\mathbf{u}^\nu \equiv 0$ with the same initial conditions. However, many other pathological "Euler solutions" in the sense of distributions exist as well. Somewhat simpler examples of this non-uniqueness have been constructed by Shnirelman [39] and by de Lellis and Székelyhidi Jr. [40]. The latter have shown that such weird solutions with compact spacetime support exist with even more regularity, $\mathbf{u}, p \in L^\infty(\mathbb{R}^d \times \mathbb{R})$, for any dimension d.

These examples show that the concept of distributional Euler solution is too general and that there are infinitely many such "solutions" which are physically irrelevant. It is natural to ask whether there is a selection criterion to guarantee uniqueness for generalized solutions. In the case of hyperbolic conservation laws, e.g. Burgers equation and 1D compressible Euler equations, it is known that there are unique distributional (and even measure-valued) solutions of the inviscid equations with appropriate ancillary conditions. For example, adding the 2nd law of thermodynamics as an "entropy condition" leads to a unique class of solutions. Furthermore, these are the same solutions that are obtained by the zero-viscosity limit and by the continuum limit of suitable dissipative numerical schemes. See [41–43]. It is an outstanding problem whether similar selection criteria may be formulated for incompressible Euler solutions and what form such criteria may take. Physical considerations discussed below suggest some intriguing possibilities.

Regularity: Experiments and simulations of high-Reynolds-number turbulence show that scaling laws hold,

$$\langle|\delta\mathbf{u}(\mathbf{r})|^p\rangle^{1/p} \sim r^{\sigma_p},$$

for all $p \geq 1$ and r in the inertial-range $\eta \ll r \ll L$. Whereas Kolmogorov 1941 theory predicts that $\sigma_p = 1/3$ for all p, the measured exponents appear to be monotone decreasing and to lie in the range $0 < \sigma_p < 1$, for experimentally accessible values of p. See [15]. It should be noted that Parisi and Frisch [44] were led by such empirical results to conjecture that turbulent velocity fields for $\nu \to 0$ consist of Euler solutions with Hölder singularities, independent of the suggestions of Onsager based on energy dissipation. Indeed, the observations suggest that Euler solutions relevant to infinite-Reynolds turbulence have $\mathbf{u} \in B_p^{\sigma_p}$, where B_p^s is the so-called *Besov space* consisting of $\mathbf{u} \in L^p$ with

$$\sup_{|\mathbf{r}|<L} \frac{\|\delta\mathbf{u}(\mathbf{r})\|_{L^p}}{|\mathbf{r}|^s} < \infty.$$

See [45] for discussion. (Even if $\langle\cdot\rangle$ is interpreted as an ensemble average, then the observed scaling together with Kolmogorov's continuity theorem [46] imply that Besov regularity holds for individual realizations with probability one; see [45], Theorem 4.) Of course, there may be other explanations of the empirical data. For example, if the relevant Euler solutions are measure-valued, then it is plausible that the observed velocity fields are average values, $\mathbf{u}(\mathbf{x}, t) = \int \mathbf{v} P_{\mathbf{x},t}(\mathrm{d}\mathbf{v})$. But "averaging lemmas" show that $\mathbf{u}(t)$ will then have Besov regularity if $P_{\mathbf{x},t}(\mathrm{d}\mathbf{v}) = f(\mathbf{v}, \mathbf{x}, t)\mathrm{d}\mathbf{v}$ and if the density f and its transport-derivative $(\mathbf{v} \cdot \nabla_\mathbf{x}) f$ have L_p regularity [47,48].

In any case, there is no PDE theory of distributional Euler solutions with $\mathbf{u} \in B_p^s$ for $p \geq 1$, $0 < s < 1$. Such solutions have not been shown even to exist, but only short-time classical solutions in Sobolev or Hölder spaces with much higher degrees of smoothness [49]. Constantin, E, and Titi [17] generalized Onsager's original result to show that distributional Euler solutions with $\mathbf{u} \in B_p^s$ for $p \geq 3$ and $s > 1/3$ (if any exist) will conserve energy. It is very intriguing that experiments and simulations show that $\sigma_p \simeq 1/3$ for $p \simeq 3$. Turbulent solutions of the Euler equations thus appear to have the least degree of singularity consistent with positive dissipation. This suggests that a "generalized energy estimate" may be useful to prove Besov regularity of dissipative Euler solutions, in which *a priori* bounds on total dissipation, $\int_0^T \mathrm{d}t \int \mathrm{d}^d x\, D(\mathbf{u})(\mathbf{x}, t)$, imply the observed regularity.

6. Other turbulent cascades

We have focused so far on the conjectured role of the Euler equations in the 3D energy cascade. However, similar possibilities exist for other turbulent cascade phenomena, as we briefly discuss here.

6.1. 2D enstrophy cascade

Smooth solutions of 2D Euler equations conserve not only energy but also *enstrophy*:

$$\Omega(t) = \frac{1}{2}\int \mathrm{d}^2x\, \omega^2(\mathbf{x}, t),$$

where $\omega = \hat{\mathbf{z}} \cdot (\nabla \times \mathbf{u})$. Just as in 3D where energy cascades from large- to small-scales – a *forward cascade* – it was suggested by Kraichnan [50] and Batchelor [51] that in 2D there can be a forward cascade of enstrophy. In addition, it was predicted by Kraichnan [50] that there can be an *inverse cascade* of energy in 2D, or transfer of energy from small- to large-scales. Here we shall focus mainly on the enstrophy cascade, where there has been more mathematical work, but similar ideas should also apply to the inverse energy cascade. E.g., see [52].

The 2D Euler equation in vorticity form is

$$\partial_t\omega + (\mathbf{u} \cdot \nabla)\omega = 0. \tag{15}$$

When "coarse-grained" at length-scale ℓ it becomes

$$\partial_t\overline{\omega}_\ell + \nabla \cdot [\overline{\mathbf{u}}_\ell\overline{\omega}_\ell + \boldsymbol{\sigma}_\ell] = 0$$

where $\boldsymbol{\sigma}_\ell = \overline{(\mathbf{u}\omega)}_\ell - \overline{\mathbf{u}}_\ell\overline{\omega}_\ell$ is the *turbulent vorticity transport* vector. The large-scale vorticity does not move with the large-scale velocity, but has a relative "drift velocity" $\Delta\mathbf{u}_\ell = \boldsymbol{\sigma}_\ell/\overline{\omega}_\ell$. The large-scale enstrophy density $\eta_\ell = (1/2)|\overline{\omega}_\ell|^2$ satisfies the balance equation:

$$\partial_t\eta_\ell + \nabla \cdot [\eta_\ell\overline{\mathbf{u}}_\ell + \overline{\omega}_\ell\boldsymbol{\sigma}_\ell] = -Z_\ell,$$

with the *enstrophy flux* to small-scales:

$$Z_\ell = -\nabla\overline{\omega}_\ell \cdot \boldsymbol{\sigma}_\ell.$$

Enstrophy suffers "ideal dissipation" when the enstrophy transport $\boldsymbol{\sigma}_\ell$ tends to be down the vorticity-gradient $\nabla\overline{\omega}_\ell$, or $\boldsymbol{\sigma}_\ell \propto -\nabla\overline{\omega}_\ell$, persistently as $\ell \to 0$.

Since the enstrophy flux satisfies "Onsager-type" bounds

$$Z_\ell = O(|\delta u(\ell)/\ell|^3) = O(|\delta\omega(\ell)|^3),$$

very modest smoothness of ω implies $\lim_{\ell\to 0} Z_\ell = 0$. E.g. if the vorticity is Hölder continuous, $\omega \in C^\alpha$ for any small $\alpha > 0$, then enstrophy is conserved. The sharpest results along these lines were obtained by DiPerna and Lions [53]. They defined ω to be a "renormalized solution" of the transport Eq. (15) if it satisfies suitable conservation properties, namely, if

$$\partial_t h(\omega) + (\mathbf{u}\cdot\nabla)h(\omega) = 0$$

in the sense of distributions for all $h \in C^1$, bounded, vanishing near 0. Such renormalized solutions preserve in time the entire vorticity-distribution

$$F(\zeta, t) = \text{area}(\{\mathbf{x} \in \mathbb{R}^2 : |\omega(\mathbf{x}, t)| > \zeta\}).$$

If $\omega \in L^\infty([0, T], L^p(\mathbb{R}^2))$ is a distributional solution of the Euler equations for $p \geq 2$, then it follows from the work of [53] that it is a renormalized solution. In particular, any solution of 2D Euler equations with finite enstrophy must conserve enstrophy. See Lions [37], Eyink [54], Lopes-Filho, Mazzucato & Nussenzveig-Lopes [55].

Note that Kraichnan–Batchelor (KB) theory [50,51] predicts an enstrophy spectrum $\Omega(k) \sim k^{-1}$ (with log-correction) having infinite total enstrophy as $\nu \to 0$. Thus, the above results are consistent with KB-theory. An infinite-enstrophy solution of 2D Euler with $\omega \in B^0_2$ has been constructed as a zero-viscosity limit in [55], with $\lim_{\nu\to 0} \nu|\nabla\omega^\nu|^2 > 0$ but with vanishing nonlinearity. It remains an open problem to construct a 2D Euler solution with nonzero enstrophy flux. Much better PDE results are available for distributional Euler solutions in 2D than in 3D. For example, weak Euler solutions have been shown to exist as zero-viscosity limits of 2D Navier–Stokes solutions for initial data with $\omega_0 \in L^p$, $p > 1$ [56] or even $p = 1$ [57]. 2D Euler solutions are unique if $\omega_0 \in L^\infty$ [58] or if $\omega_0 \in L^p$, $p > 1$ and ω_0 has also some "borderline" Besov regularity [59]. However, none of the classes of 2D Euler solutions that have so far been proved to exist can have non-vanishing enstrophy flux.

6.2. 3D helicity cascade

Smooth solutions of 3D Euler conserve in addition to the energy also the *helicity:*

$$H(t) = \int \mathrm{d}^3x\, \boldsymbol{\omega}(\mathbf{x}, t)\cdot\mathbf{u}(\mathbf{x}, t),$$

with $\boldsymbol{\omega} = \nabla\times\mathbf{u}$, as first noted by Moreau [60]. See also Betchov [61] and Moffatt [62], who emphasized the topological interpretation of the helicity-invariant. According to a theorem of Arnold [63,64], the helicity H of a smooth vorticity field is the average self-linking number of the vortex-lines. Brissaud et al. [65] proposed that in reflection-nonsymmetric turbulence there should be a forward cascade of helicity, coexisting with the forward energy cascade.

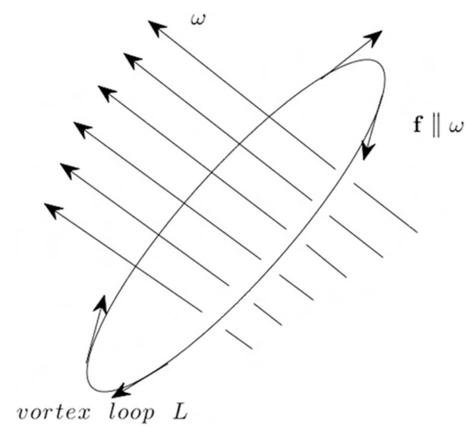

Fig. 1. Helicity generation by force parallel to vorticity.

To explain helicity cascade, we may "coarse-grain" the 3D Euler equations in vorticity formulation, to obtain

$$\partial_t\overline{\boldsymbol{\omega}}_\ell = \nabla\times(\overline{\mathbf{u}}_\ell\times\overline{\boldsymbol{\omega}}_\ell + \mathbf{f}_\ell),$$

where $\mathbf{f}_\ell = -\nabla\cdot\boldsymbol{\tau}_\ell$ is the *turbulent (subscale) force*. From this equation and from (7) follows a balance equation for the large-scale *helicity density* $h_\ell = \overline{\mathbf{u}}_\ell\cdot\overline{\boldsymbol{\omega}}_\ell$:

$$\partial_t h_\ell + \nabla\cdot[h_\ell\overline{\mathbf{u}}_\ell + (\overline{p}_\ell - e_\ell)\overline{\boldsymbol{\omega}}_\ell + \overline{\mathbf{u}}_\ell\times\mathbf{f}_\ell] = -\Lambda_\ell$$

with scale-to-scale *helicity flux*

$$\Lambda_\ell = -2\overline{\boldsymbol{\omega}}_\ell\cdot\mathbf{f}_\ell.$$

The mechanism of transfer of helicity can be understood from Fig. 1. The component of the turbulent force $\mathbf{f}_\ell$ parallel to $\overline{\boldsymbol{\omega}}_\ell$ accelerates fluid about closed vortex loops L, driving a circulation around them. Vorticity-flux is thus created through the vortex loop, corresponding to helicity. For more discussion of such issues, see [66].

The helicity flux Λ_ℓ can easily be shown to satisfy an "Onsager bound"

$$\Lambda_\ell = -2\overline{\boldsymbol{\omega}}_\ell\cdot\mathbf{f}_\ell = O(|\delta u(\ell)|^3/\ell^2).$$

This suggests conservation if $\delta u(\ell) \sim \ell^s$ with $s > 2/3$. Cheskidov et al. [67] have proved that helicity is conserved for any distributional solution of 3D Euler with $\mathbf{u} \in B^s_3 \cap H^{1/2}$ for $s > 2/3$, improving an earlier result of Chae [68]. The additional $H^{1/2}$ condition is imposed so that helicity is guaranteed to exist (but note that this implies an energy spectrum $E(k) \leq Ck^{-2}$, steeper than Kolmogorov's $k^{-5/3}$.) Thus, even more regularity is required for the conservation of helicity than for the conservation of energy. These results are consistent with constant helicity flux coexisting with constant energy flux in a $k^{-5/3}$-type inertial-range, in agreement with numerical studies [69]. Note that [67] in fact proves somewhat sharper results, and also improves slightly upon earlier results for energy conservation in any dimension and enstrophy conservation in 2D.

7. A cascade of circulations?

We have seen in our discussion of helicity cascade that turbulent, subscale forces at length-scale ℓ can generate circulations around closed vortex loops. This raises the possibility that there may be a similar generation of circulation around any advected loop. If the effect is persistent as $\ell \to 0$, it may vitiate the standard Kelvin theorem. This possibility is a bit disconcerting, however, because conservation of circulations and the Helmholtz laws of vortex motion are often believed to be essential for turbulent energy dissipation in 3D! For example, we may quote Onsager from his 1949 paper [6]:

"Two-dimensional convection, which merely redistributes vorticity, cannot account for the rapid dissipation which one observes. However, as pointed out by G.I. Taylor [7], convection in three dimensions will tend to increase the total vorticity. *Since the circulation of a vortex tube is conserved*, the vorticity will increase whenever a vortex tube is stretched. Now it is very reasonable to expect that a vortex-line – or any line which is deformed by the motion of the liquid – will tend to increase in length as a result of more or less haphazard motion. This process tends to make the texture of the motion ever finer, and greatly accelerates the viscous dissipation."

The italics in the quote above are ours and intended to draw attention to the importance of Kelvin's theorem in the argument. This point of view originated, as Onsager states, with Taylor [70,71], who first realized the importance of vortex-line-stretching in the process of generating turbulent energy dissipation.

This motivates us to examine more closely the conservation of circulations. For any initial rectifiable loop C and time t, we may define the *large-scale circulation* $\overline{\Gamma}_\ell(C,t)$ at length-scale ℓ as

$$\overline{\Gamma}_\ell(C,t) = \oint_{\overline{C}_\ell(t)} \overline{\mathbf{u}}_\ell(t)\cdot \mathrm{d}\mathbf{x} = \int_{\overline{S}_\ell(t)} \overline{\boldsymbol{\omega}}_\ell(t)\cdot \mathrm{d}\mathbf{A}. \tag{16}$$

Here $\overline{C}_\ell(t)$ is the loop which coincided with C at the initial time t_0 and was then advected to time t by $\overline{\mathbf{u}}_\ell$, which generates a flow of diffeomorphisms whenever $\mathbf{u} \in L^2$. Correspondingly, $\overline{S}_\ell(t)$ is the advection by $\overline{\mathbf{u}}_\ell$ to time t of a smooth surface S that spanned the initial loop C at time t_0. It is worth remarking that these are the quantities that an experimentalist would consider who wished to test the validity of the Kelvin theorem, by taking measurements of velocity with successively finer resolutions ℓ in space. At a fixed resolution, however, the circulation is *not* conserved but instead the balance holds:

$$(\mathrm{d}/\mathrm{d}t)\overline{\Gamma}_\ell(C,t) = \oint_{\overline{C}_\ell(t)} \mathbf{f}^*_\ell(t)\cdot \mathrm{d}\mathbf{x} \tag{17}$$

where $\mathbf{f}^*_\ell = \overline{(\mathbf{u}\times\boldsymbol{\omega})}_\ell - \overline{\mathbf{u}}_\ell\times\overline{\boldsymbol{\omega}}_\ell$ is the *turbulent vortex-force*. Rather than the latter, one may also employ in the balance (17) the subscale force $\mathbf{f}_\ell = -\nabla\cdot\boldsymbol{\tau}_\ell$ by means of the identity $\mathbf{f}^*_\ell = \mathbf{f}_\ell + \nabla k_\ell$, with $k_\ell = (1/2)\mathrm{Tr}\,\boldsymbol{\tau}_\ell$ the subgrid kinetic energy. The quantity on the right-hand side of the balance (17) defines a *(turbulent) subscale torque*

$$K_\ell(C) = -\oint_C \mathbf{f}^*_\ell\cdot \mathrm{d}\mathbf{x} = -\oint_C \mathbf{f}_\ell\cdot \mathrm{d}\mathbf{x},$$

which drives a circulation around the loop.

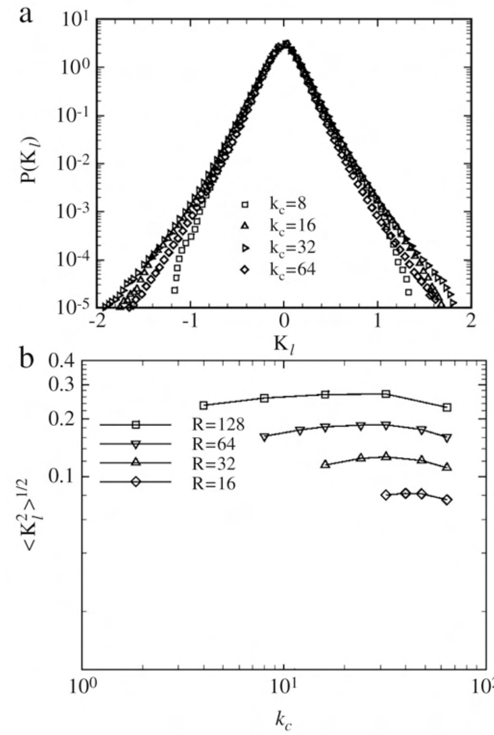

Fig. 2. (a) PDF and (b) RMS of the subscale *loop-torque* $K_\ell(C)$ for square loops C of edge-length 64 in a 1024^3 DNS of forced 3D hydrodynamic turbulence. From [77].

If the velocity is Hölder continuous with exponent α, $\mathbf{u} \in C^\alpha$, and $L(C)$ is the length of C, then it is not hard to derive the rigorous bound

$$|K_\ell(C)| \le (\mathrm{const.})L(C)\ell^{2\alpha-1}. \tag{18}$$

See [72,73]. The key estimate on the vortex-force is that $\mathbf{f}_\ell = O(|\delta u(\ell)|^2/\ell)$. The bound (18) allows violation of the Kelvin Theorem, either if $\alpha \le 1/2$ or if advected loops C are non-rectifiable. Both of these conditions hold in the inertial-range of turbulent flow. As we have already discussed, a spectrum of Hölder singularities is observed in turbulence, with the most probable exponent close to the K41 value $\alpha = 1/3$ [15]. Furthermore, loops $C(t)$ advected by such a rough velocity field are expected to become fractal [74–76], and thus $L(\overline{C}_\ell(t)) \to \infty$ as $\ell \to 0$. Hence, there is every reason to expect that circulations will *not* be conserved – at least in the usual sense – in turbulent flow at infinite-Reynolds number.

The issue is difficult to address mathematically but may be studied in experiment and simulation. In Fig. 2 we present results from a recent numerical study [77]. The statistics of the torques $K_\ell(C)$ were obtained for square loops C with fixed edge-length in the inertial-range of a forced, steady-state simulation of 3D homogeneous turbulence. As shown in Fig. 2, the probability density function (PDF) and root-mean-square (RMS) value of the torques are nearly independent of the effective coarse-graining wavenumber $k_c = 2\pi/\ell$, for k_c in the inertial-range. According to this evidence, the cascade of circulations is persistent in scale! The non-vanishing torques

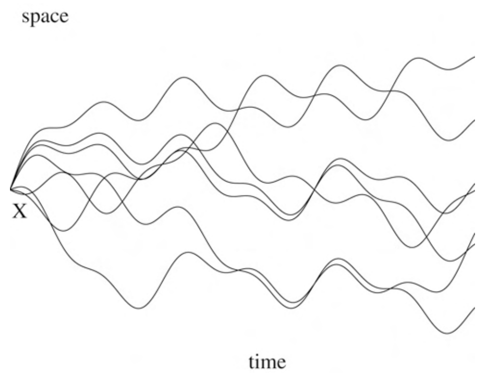

Fig. 3. A random family of non-unique Lagrangian trajectories emanating from a fixed initial point $\mathbf{x}$.

correspond to a turbulent diffusion of vortex-lines out of the loop and a consequent breakdown of the Helmholtz Laws of vortex motion. The subscale force $\mathbf{f}_\ell$ may be decomposed into components longitudinal and transverse to vortex-lines:

$$\mathbf{f}_\ell = \alpha_\ell \overline{\boldsymbol{\omega}}_\ell + (\Delta \mathbf{u}_\ell) \mathbf{x} \overline{\boldsymbol{\omega}}_\ell$$

where

$$\alpha_\ell = \overline{\boldsymbol{\omega}}_\ell \cdot \mathbf{f}_\ell / |\overline{\boldsymbol{\omega}}_\ell|^2, \qquad \Delta \mathbf{u}_\ell = \overline{\boldsymbol{\omega}}_\ell \mathbf{x} \mathbf{f}_\ell / |\overline{\boldsymbol{\omega}}_\ell|^2.$$

We have seen that the longitudinal force is responsible for helicity cascade and is a hydrodynamic analogue of the MHD α-effect [78]. The transverse part corresponds to a "drift" of the vortex-lines, with relative velocity $\Delta\mathbf{u}_\ell$, which diffuses lines out of advected loops moving with velocity $\overline{\mathbf{u}}_\ell$. The transverse force can be interpreted as a *turbulent Magnus force* associated to this drift motion.

8. Spontaneous stochasticity

Note that, formally,

$$\alpha_\ell \sim \Delta \mathbf{u}_\ell \sim \delta u(\ell) \to 0$$

as $\ell \to 0$. For example, in K41 theory, $\delta u(\ell) \sim \ell^{1/3}$. This suggests that there may be some sense in which the Kelvin–Helmholtz results can still be valid in the infinite-Reynolds inertial-range. However, before we can consider this possibility, we must address another complication: Lagrangian trajectories are expected to be non-unique and stochastic for a fixed realization of a rough (Hölder) velocity field! This phenomenon, called *spontaneous stochasticity* [79], is illustrated in Fig. 3. Suppose that Lagrangian particles are started at initial positions sampled from some smooth density ϕ_ρ supported in the ball of radius ρ centered at $\mathbf{x}_0$. Particles advected by the smoothed velocity $\overline{\mathbf{u}}_\ell$ have unique Lagrangian trajectories. However, if one considers first the limit of infinite resolution ($\ell \to 0$) and subsequently the limit of zero particle separation ($\rho \to 0$), then the distribution of Lagrangian histories may converge (weakly) to a nontrivial probability distribution for a *fixed* realization of the velocity $\mathbf{u}$. More formally, this means that for a smooth ϕ_ρ with $\mathrm{supp}\,\phi_\rho \subset B(\mathbf{0}, \rho)$, for bounded, continuous ψ, and for $t \neq t_0$:

$$\lim_{\rho\to 0}\lim_{\ell\to 0} \int \mathrm{d}^d r_0\, \phi_\rho(\mathbf{r}_0)\psi(\overline{\boldsymbol{\xi}}_\ell^{t,t_0}(\mathbf{x}_0+\mathbf{r}_0)) = \int P_{\mathbf{u}}(\mathrm{d}\mathbf{x}, t|\mathbf{x}_0, t_0)\psi(\mathbf{x}). \tag{19}$$

Here $\overline{\boldsymbol{\xi}}_\ell^{t,t_0}$ is the smooth flow generated by $\overline{\mathbf{u}}_\ell$. This phenomenon was discovered by Bernard, Gawędzki and Kupiainen [80] in the Kraichnan model of random advection by a velocity Hölder continuous in space and white-noise in time; see also [81–85]. The stochastic splitting of Lagrangian trajectories was rigorously proved to occur in the Kraichnan model by Le Jan and Raimond [86,87]. The physical mechanism of this non-uniqueness is the famous *Richardson pair-diffusion* in a turbulent flow [88], which allows a pair of Lagrangian particles to separate to a mean-square distance $\Delta x_t^2 \sim t^3$ at time t independent of their initial separation ρ in the inertial-range.

Spontaneous stochasticity is deeply connected with dissipative anomaly for the passive scalar in the Kraichnan model of random advection. This model problem corresponds to the linear stochastic PDE

$$\partial_t \theta^\kappa + (\mathbf{u}\circ\nabla)\theta^\kappa = \kappa \triangle \theta^\kappa, \quad \nabla\cdot\mathbf{u} = 0 \tag{20}$$

where $\mathbf{u}$ is a Gaussian random field, space-homogeneous, zero mean $\langle\mathbf{u}\rangle = \mathbf{0}$, whose increments for $r \ll L$ satisfy

$$\langle \delta\mathbf{u}(\mathbf{r}, t)\cdot\delta\mathbf{u}(\mathbf{r}, t')\rangle \sim D|\mathbf{r}|^{2\alpha}\delta(t-t'), \quad 0 < \alpha < 1.$$

The circle "$\circ$" in the advection term of (20) indicates that the Stratonovich interpretation of the multiplicative noise is employed. See [82] for an extensive review of the physical literature on this model. It is known that there is a dissipative anomaly for the scalar, in the sense that $\lim_{\kappa\to 0}\kappa|\nabla\theta^\kappa|^2 > 0$. Furthermore, as $\kappa \to 0$, $\theta^\kappa \to \theta$ in the sense of distributions to a unique solution of the hyperbolic equation

$$\partial_t\theta + (\mathbf{u}\circ\nabla)\theta = 0, \quad \nabla\cdot\mathbf{u} = 0. \tag{21}$$

This solution has a beautiful stochastic representation as an average over the random ensemble of (backward) Lagrangian characteristics:

$$\theta(\mathbf{x}, t) = \int P_{\mathbf{u}}(\mathrm{d}\mathbf{x}', t'|\mathbf{x}, t)\theta(\mathbf{x}', t'), \quad t > t', \tag{22}$$

where $P_{\mathbf{u}}$ is the distribution defined in (19) [80,83,86]. This representation directly implies by Jensen's inequality that

$$\int \mathrm{d}\mathbf{x}\,|\theta(\mathbf{x}, t)|^2 < \int \mathrm{d}\mathbf{x}\,|\theta(\mathbf{x}, t')|^2$$

for $t > t'$, which shows that the scalar "energy" $\int\theta^2(t)$ decreases monotonically in time. The same solution θ is also obtained by solving the zero-diffusion equation

$$\partial_t\theta^{(\ell)} + (\overline{\mathbf{u}}_\ell\circ\nabla)\theta^{(\ell)} = 0, \quad \nabla\cdot\overline{\mathbf{u}}_\ell = 0, \tag{23}$$

with a regularized velocity $\overline{\mathbf{u}}_\ell$ and then taking the limit $\theta = \lim_{\ell\to 0}\theta^{(\ell)}$. It is important to note that this uniqueness of the dissipative solutions of (21) – obtained as limits of different approximations (20) or (23) – depends upon the assumption of incompressibility of $\mathbf{u}$. If the velocity field is sufficiently compressible, then there are distinct distributional solutions of (21) [and also distinct distributions on Lagrangian histories in (19)] depending upon the limiting procedure adopted [81,83,84, 86,87].

The Kraichnan model (21) is a perfect paradigm for Onsager's vision of generalized "inviscid" solutions of PDE's that sustain turbulent dissipation. There is a unique class of dissipative solutions of (21) for incompressible flow that are robustly obtained by different, physical limiting procedures. The only other case where a comparable mathematical theory has been developed is the "entropy solutions" of hyperbolic conservation laws, such as Burgers equation [41–43]. However, the mechanism of dissipation is quite different in these compressible flow problems, in which Lagrangian particles collide and stick. What is very distinctive about the incompressible version of the Kraichnan model (21) is the "spontaneous stochasticity" or "stochastic splitting" of Lagrangian particles. The irreversibility or arrow of time is introduced in (22) by the stipulation that *future* values of the scalar $\theta(t)$ are represented by averaging *past* values $\theta(t')$ for $t' < t$, rather than the reverse.

It remains a huge challenge to carry over these important insights from the Kraichnan model to the incompressible Euler equation. We mention just one idea that seems to us promising [72,89]. It was pointed out some years ago by the field-theorist Migdal [90] that the incompressible Euler equation in any dimension d can be transformed into an *active scalar equation* but with the scalar defined in the infinite-dimensional *loop-space*. This transformation is obtained by introducing the Eulerian circulations

$$\Gamma_E(C,t) = \oint_C \mathbf{u}(t)\cdot \mathrm{d}\mathbf{x},$$

where – in contrast to (16) – the loop C is fixed in space. It is not difficult to show that these solve

$$\partial_t \Gamma_E(C,t) + \int_0^1 \mathrm{d}s\, u_i(C(s),t)\frac{\delta}{\delta C_i(s)}\Gamma_E(C,t) = 0, \tag{24}$$

which is a functional advection equation in loop-space. Migdal has shown that this equation is an equivalent, independent formulation of the Euler equation, in which the velocity $\mathbf{u}$ can be recovered from the circulations $\Gamma_E(C,t)$ by loop-calculus [90]. In fact, the standard Kelvin theorem is the solution of Midgal's loop equation by the method of characteristics. If we formally apply the same results to (24) that are rigorously demonstrated for the Kraichnan model (21), then we would conjecture that the physical "dissipative" solution of (24) for turbulent flow can be represented as

$$\Gamma_E(C,t) = \int P_{\mathbf{u}}(\mathrm{d}C',t'|C,t)\Gamma_E(C',t'), \quad t > t'. \tag{25}$$

Here $P_{\mathbf{u}}(\mathrm{d}C',t'|C,t)$ should be a stochastic process of material loops advected by $\mathbf{u}$, obtained similarly as (19). Eq. (25) is a generalization of the Kelvin theorem which states that circulations will be conserved *on average* for material loops propagated backward in time. That is, the circulations are "backward martingales" of a generalized Euler flow, roughly in the sense of Brenier [33,35]. It would be very interesting to relate the arrow of time introduced by (25) to that associated with vortex-line-stretching and with positive energy dissipation.

9. Return to pipe flow

We began our story by quoting a passage about energy dissipation in turbulent pipe flow from a paper of G.I. Taylor. As a cautionary remark, we may cite another important observation of Taylor from an earlier paper [91]. This 1932 work is well-known for introducing Taylor's mixing-length theory of vorticity transfer. However, Taylor also derived there an interesting exact result on turbulent pipe flow. To state this result, let us employ curvilinear cylindrical coordinates, with z-coordinate down the pipe axis and with radial coordinate r and azimuthal angle θ. Following Taylor, let us introduce the quantity

$$\Sigma_{r\theta} = u_r\omega_\theta - u_\theta\omega_r - \nu\left[\frac{1}{r}\frac{\partial}{\partial r}(r\omega_\theta) - \frac{1}{r}\frac{\partial\omega_r}{\partial\theta}\right], \tag{26}$$

which describes *vorticity transport* of the azimuthal component of vorticity ω_θ in the radial direction r. The first term in (26) corresponds to advective transport of vorticity, the second to transport by vortex stretching and tilting, and the third term in brackets to viscous diffusion of vorticity. The expression (26) is just the z-component of the nonlinear and viscous terms in the Navier–Stokes equation, $\Sigma_{r\theta} = (\mathbf{u}\times\boldsymbol{\omega} - \nu\nabla\times\boldsymbol{\omega})_z$. It is therefore straightforward to show that its time-average in steady-state, fully-developed turbulence is equal to the mean pressure drop down the pipe [91]:

$$\langle\Sigma_{r\theta}\rangle = \frac{\partial}{\partial z}\langle p\rangle < 0. \tag{27}$$

In fully-developed turbulence in an infinitely long pipe it follows from (27) that $\langle\Sigma_{r\theta}\rangle$ is a *constant*, independent of r,θ and z [14]. This constant flux of mean vorticity corresponds to vortex rings generated at the pipe wall which then shrink and annihilate at the pipe axis. The structure and dynamics of individual vortex-lines in turbulent pipe flow is quite complex, with very random twisting and stretching. However, whatever the details, the mean flux of azimuthal vorticity must be maintained.

Owing to (27), *constant flux of azimuthal vorticity is directly related to turbulent energy dissipation*. Indeed, the energy input into the turbulent fluctuations is provided by the pressure head. Multiplying by the mean mass flux J through the pipe therefore gives the turbulent energy dissipation per length:

$$(1/L_z)\int_{\text{pipe}} \mathrm{d}^3x\,\rho\,\varepsilon = J|\langle\Sigma_{r\theta}\rangle|.$$

This result can be regarded as a classical analogue of the *Josephson–Anderson relation* in quantum superfluids, relating cross-stream transport of vorticity and energy dissipation. See Anderson [92] and Huggins [93], who rediscovered Taylor's result in the quantum setting. The cross-stream motion or "phase slippage" of quantized vortex-lines is widely recognized to be a key mechanism of energy dissipation in quantum superfluids and superconductors [94,95]. This observation may bring a certain unity to the problems of classical and superfluid turbulence; see [96] and the contribution to these proceedings by Barenghi [97].

The lesson to be drawn here is that energy dissipation in realistic inhomogeneous turbulent flows requires not just random line-stretching but also *organized motion of vorticity.* This remark underlines the extreme subtlety of the relation between vortex motion and energy dissipation. The presence of a solid wall or flow boundary can dramatically alter the turbulence dynamics [98]. Onsager's conjecture is very interesting for wall-bounded flows. It is known that a Navier–Stokes solution $\mathbf{u}^\nu$ in a bounded domain can converge to a smooth solution of Euler $\mathbf{u}$ conserving energy, if and only if the viscous energy dissipation vanishes in the limit, in the sense of Eq. (14). In fact, only the energy dissipation in a viscous sublayer of thickness $O(\nu)$ must vanish for this to be true [99] or even just the dissipation from tangential velocity-gradients in a slightly thicker layer [100]. In their Taylor–Couette experiments with smooth walls, Cadot et al. [10] found that the energy dissipation in the boundary layer indeed decreases with Reynolds number but that the energy dissipation in the bulk appears to satisfy Taylor's relation (3) and to be independent of Reynolds number.

10. Conclusion

If Onsager is correct, then inertial-range dynamics of turbulent flow are governed by singular solutions of the Euler fluid equations. Observational evidence and rigorous results are consistent with the idea. We have reviewed much of the relevant mathematical literature, but we hope to have made clear the importance of the problem also to experimentalists and simulators. Onsager's conjecture is not about an esoteric or unphysical mathematical problem but, rather, about the fluid dynamics of turbulence at high Reynolds numbers. The theory makes testable predictions, some of which have not yet been confirmed or disproved. Indeed, the foundations of the subject are empirical, and further laboratory and numerical investigations are necessary to shed light on many difficult and basic questions, still beyond the scope of mathematical analysis. A major open problem, in particular, is how to relate turbulent dissipation of energy, precisely, to the inviscid motion of vortex-lines. Leonhard Euler would doubtless be delighted to see that his equations on their 250th anniversary are of vital interest to the problem of turbulence and remain at the forefront of engineering, physics and mathematics.

Acknowledgments

We would like to thank many people for the discussions on this subject over the years, including H. Aluie, P. Ao, C. Bardos, D. Bernard, S. Chen, M. Chertkov, P. Constantin, J. Duchon, W. E, G. Falkovich, U. Frisch, K. Gawędzki, R.H. Kraichnan, A. Kupiainen, C.D. Levermore, C. Meneveau, R. Robert, K.R. Sreenivasan, E.S. Titi, E. vanden-Eijnden, M. Vergassola & E.T. Vishniac.

References

[1] J. Quastel, H.-T. Yau, Lattice gases, large deviations, and the incompressible Navier–Stokes equations, Ann. of Math. 148 (1998) 51–108.
[2] J. Leray, Essai sur le mouvement d'un liquide visqueux emplissant l'espace, Acta Math. 63 (1934) 193–248.
[3] L. Saint-Raimond, From Boltzmann's kinetic theory to Euler's equations, these Proceedings.
[4] A.N. Kolmogorov, The local structure of turbulence in incompressible viscous fluid for very large Reynolds numbers, Dokl. Akad. Nauk SSSR 30 (1941) 9–13.
[5] S. Corrsin, Outline of some topics in homogeneous turbulent flow, J. Geophys. Res. 64 (1959) 2134–2150.
[6] L. Onsager, Statistical hydrodynamics, Nuovo Cimento 6 (Suppl.) (1949) 279–287.
[7] G.I. Taylor, Statistical theory of turbulence, I, Proc. Roy. Acad. Lond. A 151 (1935) 421–444.
[8] H.L. Dryden, A review of the statistical theory of turbulence, Q. Appl. Math. 1 (1943) 7–42.
[9] K.R. Sreenivasan, On the scaling of the turbulence energy dissipation rate, Phys. Fluids 27 (1984) 1048–1051.
[10] O. Cadot, Y. Couder, A. Daerr, S. Douady, A. Tsinober, Energy injection in closed turbulent flow: Stirring through boundary-layers versus inertial stirring, Phys. Rev. E 56 (1997) 427–433.
[11] B.R. Pearson, P.A. Krogstad, W. van de Water, Measurements of the turbulent energy dissipation rate, Phys. Fluids 14 (2002) 1288–1290.
[12] K.R. Sreenivasan, An update on the energy dissipation rate in isotropic turbulence, Phys. Fluids 10 (1998) 528–529.
[13] Y. Kaneda, T. Ishihara, M. Yokokawa, K. Itakura, A. Uno, Energy dissipation rate and energy spectrum in high resolution direct numerical simulations of turbulence in a periodic box, Phys. Fluids 15 (2003) L21–L24.
[14] H. Tennekes, J.L. Lumley, A First Course in Turbulence, MIT Press, Cambridge, MA, 1972.
[15] U. Frisch, Turbulence: The Legacy of A.N. Kolmogorov, Cambridge University Press, Cambridge, 1995.
[16] G.L. Eyink, K.R. Sreenivasan, Onsager and the theory of hydrodynamic turbulence, Rev. Modern Phys. 78 (2006) 87–135.
[17] P. Constantin, W. E, E.S. Titi, Onsager's conjecture on the energy conservation for solutions of Euler's equation, Commun. Math. Phys. 165 (1994) 207–209.
[18] G.L. Eyink, Local energy flux and the refined similarity hypothesis, J. Stat. Phys. 78 (1995) 335–351.
[19] K.G. Wilson, The renormalization group: Critical phenomena and the Kondo problem, Rev. Modern Phys. 47 (1975) 773–840.
[20] C. Meneveau, J. Katz, Scale-invariance and turbulence models for large-eddy simulation, Ann. Rev. Fluid Mech. 32 (2000) 1–32.
[21] J.F. Muzy, E. Bacry, A. Arneodo, Wavelets and multifractal formalism for singular signals: Application to turbulence data, Phys. Rev. Lett. 67 (1991) 3515–3518.
[22] P. Kestener, A. Arneodo, Generalizing the wavelet-based multifractal formalism to random vector fields: Application to three-dimensional turbulence velocity and vorticity data, Phys. Rev. Lett. 91 (2003) 194501.
[23] L.D. Landau, E.M. Lifshitz, Mekhanika Sploshnykh Sred, Gostekhizdat, Moscow, 1954. English translation: Fluid Mechanics, Pergamon Press, Oxford, 1959.
[24] J. Duchon, R. Robert, Inertial energy dissipation for weak solutions of incompressible Euler and Navier–Stokes equations, Nonlinearity 13 (2000) 249–255.
[25] A.M. Polyakov, The theory of turbulence in two dimensions, Nuclear Phys. B 396 (1993) 367–385.
[26] J. Schwinger, On gauge invariance and vacuum polarization, Phys. Rev. 82 (1951) 664–679.
[27] P.-L. Sulem, U. Frisch, Bounds on energy flux for finite energy turbulence, J. Fluid Mech. 72 (1975) 417–423.
[28] G.L. Eyink, Energy dissipation without viscosity in ideal hydrodynamics, I. Fourier analysis and local energy transfer, Physica D 78 (1994) 222–240.

[29] C. Meneveau, K.R. Sreenivasan, The multifractal nature of turbulent energy dissipation, J. Fluid Mech. 224 (1991) 429–484.
[30] R. Antonia, M. Ould-Rouis, F. Anselmet, Y. Zhu, Analogy between predictions of Kolmogorov and Yaglom, J. Fluid Mech. 332 (1997) 395–409.
[31] G.L. Eyink, Local 4/5-law and energy dissipation anomaly in turbulence, Nonlinearity 16 (2003) 137–145.
[32] A. Shnirelman, Weak solutions with decreasing energy of incompressible Euler equations, Commun. Math. Phys. 210 (2000) 541–603.
[33] Y. Brenier, The least action principle and the related concept of generalized flows for incompressible perfect fluids, J. Amer. Math. Soc. 2 (1989) 225–255.
[34] Y. Brenier, The dual Least Action Problem for an ideal, incompressible fluid, Arch. Ration. Mech. Anal. 122 (1993) 323–351.
[35] Y. Brenier, Topics on hydrodynamics and volume preserving maps, in: Handbook of Mathematical Fluid Dynamics II, North-Holland, Amsterdam, 2003, pp. 55–86.
[36] R.J. DiPerna, A.J. Majda, Oscillations and concentrations in weak solutions of the incompressible fluid equations, Commun. Math. Phys. 108 (1987) 667–689.
[37] P.-L. Lions, Mathematical Topics in Fluid Mechanics, vol. 1, Oxford University Press, Oxford, 1996.
[38] V. Scheffer, An inviscid flow with compact support in space–time, J. Geom. Anal. 3 (1993) 343–401.
[39] A. Shnirelman, On the nonuniqueness of weak solution of the Euler equation, Comm. Pure Appl. Math. 50 (1997) 1261–1286.
[40] C. de Lellis, L. Székelyhidi Jr., 2007, preprint: arXiv:math.AP/0702079.
[41] R. DiPerna, Measure-valued solutions of conservation laws, Arch. Ration. Mech. Anal. 8 (1985) 223–270.
[42] L.C. Evans, Partial Differential Equations, American Mathematical Society, Providence, RI, 1998.
[43] C.M. Dafermos, Entropy for hyperbolic conservation laws, in: A. Greven, G. Keller, G. Warnecke (Eds.), Entropy, in: Princeton Series in Applied Mathematics, Princeton University Press, Princeton, 2003, pp. 107–119.
[44] G. Parisi, U. Frisch, On the singularity structure of fully developed turbulence, in: M. Ghil, R. Benzi, G. Parisi (Eds.), Turbulence and Predictability in Geophysical Fluid Dynamics, Proc. Int. School of Physics Enrico Fermi 1983, North-Holland, Amsterdam, 1985, pp. 84–88.
[45] G.L. Eyink, Besov spaces and the multifractal hypothesis, J. Stat. Phys. 78 (1995) 353–375.
[46] R. Adler, Geometry of Random Fields, Wiley, London, 1981.
[47] F. Golse, P.-L. Lions, B. Perthame, R. Sentis, Regularity of the moments of the solution of a transport equation, J. Funct. Anal. 76 (1988) 110–125.
[48] R. Devore, G. Petrova, The averaging lemma, J. Amer. Math. Soc. 14 (2001) 279–296.
[49] D.G. Ebin, J. Marsden, Groups of diffeomorphisms and the motion of an incompressible fluid, Ann. Math. 92 (1970) 102–163.
[50] R.H. Kraichnan, Inertial ranges in two-dimensional turbulence, Phys. Fluids 10 (1967) 1417–1423.
[51] G.K. Batchelor, Computation of the energy spectrum in homogeneous two-dimensional turbulence, Phys. Fluids 12 (Suppl. II) (1969) 233–239.
[52] D. Bernard, Three-point velocity correlation functions in two-dimensional forced turbulence, Phys. Rev. E 60 (1999) 6184–6187.
[53] R.J. DiPerna, P.-L. Lions, Ordinary differential equations, transport theory and Sobolev spaces, Invent. Math. 98 (1989) 511–547.
[54] G.L. Eyink, Dissipation in turbulent solutions of 2D Euler equations, Nonlinearity 14 (2001) 787–802.
[55] M.C. Lopes-Filho, A.L. Mazzucato, H.J. Nussenzveig-Lopes, Weak solutions, renormalized solutions and enstrophy defects in 2D turbulence, Arch. Ration. Mech. Anal. 179 (2006) 353–387.
[56] R.J. DiPerna, A.J. Majda, Concentrations in regularizations for 2-D incompressible flow, Comm. Pure Appl. Math. XL (1987) 301–345.
[57] G. Wu, P. Zhang, The zero diffusion limit of 2-D Navier–Stokes equations with L^1 initial vorticity, Discrete Contin. Dyn. Syst. 5 (1999) 631–638.
[58] V.I. Yudovich, Nonstationary flow of a perfect incompressible fluid, Zh. Vych. Mat. i Mat. Fiz. 3 (1963) 1032–1066.
[59] M. Vishik, Incompressible flows of an ideal fluid with vorticity in borderline spaces of Besov type, Ann. Ecole Norm. Sup. 32 (1999) 769–812.
[60] J.J. Moreau, Constantes d'un îlot tourbillionnaire en fluide parfait barotrope, C. R. Acad. Sci. Paris 252 (1961) 2810–2812.
[61] R. Betchov, Semi-isotropic turbulence and helicoidal flows, Phys. Fluids 4 (1961) 925–926.
[62] H.K. Moffatt, The degree of knottedness of tangled vortex lines, J. Fluid Mech. 35 (1969) 117–129.
[63] V.I. Arnold, The asymptotic Hopf invariant and its applications, Sel. Math. Sov. 5 (1986) 327–345.
[64] V.I. Arnold, B.A. Khesin, Topological methods in hydrodynamics, in: Applied Mathematical Sciences, vol. 125, Springer-Verlag, New York, 1998.
[65] A. Brissaud, U. Frisch, J. Leorat, M. Lesieur, A. Mazure, Helicity cascades in fully developed isotropic turbulence, Phys. Fluids 16 (1973) 1366–1367.
[66] H. Aluie, G.L. Eyink, E.T. Vishniac, Coarse-grained equations for incompressible MHD plasmas (in press).
[67] A. Cheskidov, P. Constantin, S. Friedlander, R. Shvydkoy, 2007, preprint: arXiv:0704.0759.
[68] D. Chae, Remarks on the helicity of the 3-D incompressible Euler equations, Comm. Math. Phys. 240 (2003) 501–507.
[69] Q. Chen, S. Chen, G.L. Eyink, The joint cascade of energy and helicity in three-dimensional turbulence, Phys. Fluids 15 (2003) 361–374.
[70] G.I. Taylor, A.E. Green, Mechanism of the production of small eddies from larger ones, Proc. Roy. Acad. Lond. A 158 (1937) 499–521.
[71] G.I. Taylor, Production and dissipation of vorticity in a turbulent fluid, Proc. R. Soc. London A 164 (1938) 15–23.
[72] G.L. Eyink, Turbulent cascade of circulations, C. R. Physique 7 (2006) 449–455.
[73] G.L. Eyink, Cascade of circulations in fluid turbulence, Phys. Rev. E 74 (2006) 066302.
[74] E. Villermaux, Y. Gagne, Line dispersion in homogeneous turbulence: Stretching, fractal dimensions and micromixing, Phys. Rev. Lett. 73 (1994) 252–255.
[75] F. Nicolleau, Numerical determination of turbulent fractal dimensions, Phys. Fluids 8 (1996) 2661–2670.
[76] F.C.G.A. Nicolleau, A. Elmaihy, Study of the development of three-dimensional sets of fluid particles and iso-concentration fields using kinematic simulation, J. Fluid Mech. 517 (2004) 229–249.
[77] S. Chen, G.L. Eyink, M. Wan, Z. Xiao, Is the Kelvin theorem valid for high Reynolds number turbulence? Phys. Rev. Lett. 97 (2006) 144505.
[78] U. Frisch, Z.S. She, P.L. Sulem, Large-scale flow driven by the anisotropic kinetic alpha effect, Physica D 28 (1987) 382–392.
[79] M. Chaves, K. Gawędzki, P. Horvai, A. Kupiainen, M. Vergassola, Lagrangian dispersion in Gaussian self-similar velocity ensembles, J. Stat. Phys. 113 (2003) 643–692.
[80] D. Bernard, K. Gawędzki, A. Kupiainen, Slow modes in passive advection, J. Stat. Phys. 90 (1998) 519–569.
[81] K. Gawędzki, M. Vergassola, Phase transition in the passive scalar advection, Physica D 138 (2000) 63–90.
[82] G. Falkovich, K. Gawędzki, M. Vergassola, Particles and fields in fluid turbulence, Rev. Modern Phys. 73 (2001) 913–975.
[83] W. E, E. vanden-Eijnden, Generalized flows, intrinsic stochasticity, and turbulent transport, Proc. Natl. Acad. Sci. 97 (2000) 8200–8205.
[84] W. E, E. Vanden-Eijnden, Turbulent Prandtl number effect on passive scalar advection, Physica D 152–153 (2001) 636–645.
[85] W. E, E. Vanden-Eijnden, A note on generalized flows, Physica D 183 (2003) 159–174.
[86] Y. LeJan, O. Raimond, Integration of Brownian vector fields, Ann. Probab. 30 (2002) 826–873.
[87] Y. LeJan, O. Raimond, Flows, coalescence and noise, Ann. Probab. 32 (2004) 1247–1315.
[88] L.F. Richardson, Atmospheric diffusion shown on a distance-neighbour graph, Proc. R. Soc. Lond. A 110 (1926) 709–737.

[89] G.L. Eyink, Turbulent diffusion of lines and circulations, Phys. Lett. A 368 (2007) 486–490.

[90] A.A. Migdal, 1993, preprints: ArXiv:hep-th/9303130; hep-th/9306152; hep-th/9310088.

[91] G.I. Taylor, The transport of vorticity and heat through fluids in turbulent motion, Proc. Roy. Soc. Lond. A 135 (1932) 685–705.

[92] P.W. Anderson, Considerations on the flow of superfluid helium, Rev. Modern Phys. 38 (1966) 298–310.

[93] E.R. Huggins, Energy dissipation theorem and detailed Josephson equation for ideal incompressible fluids, Phys. Rev. A 1 (1970) 332–337.

[94] W. Zimmerman Jr., Energy transfer and phase slip by quantum vortex motion in superfluid ^{4}He, J. Low Temp. Phys. 93 (1993) 1003–1018.

[95] R.E. Packard, The role of the Josephson–Anderson equation in superfluid helium, Rev. Modern Phys. 70 (1998) 641–651.

[96] E.R. Huggins, Vortex currents in turbulent superfluid and classical fluid channel flow, the Magnus effect, and Goldstone boson fields, J. Low Temp. Phys. 96 (1994) 317–346.

[97] C. Barenghi, These Proceedings.

[98] C. Bardos, What use for the mathematical theory of the Navier–Stokes equations? in: J. Neustupa, P. Penel (Eds.), Mathematical Fluid Mechanics: Recent Results and Open Questions, Birkhäuser, Basel, 2001, pp. 1–26.

[99] T. Kato, Remarks on the zero viscosity limit for non stationary Navier–Stokes flows with boundary, in: S.S. Chern (Ed.), Seminar on Nonlinear Partial Differential Equations, Berkeley, CA, 1983, Springer, NY, 1984, pp. 85–98.

[100] X. Wang, A Kato type theorem on zero viscosity limit of Navier–Stokes flows, Indiana Univ. Math. J. 50 (2001) 223–241.

Available online at www.sciencedirect.com

ScienceDirect

Physica D 237 (2008) 1969–1975

PHYSICA D

www.elsevier.com/locate/physd

Statistical behaviour of isotropic and anisotropic fluctuations in homogeneous turbulence

Luca Biferale[a,b], Alessandra S. Lanotte[c,d,*], Federico Toschi[e,f]

[a] *Department of Physics, University of Tor Vergata, Via della Ricerca Scientifica 1, 00133 Rome, Italy*
[b] *INFN, Sez. Tor Vergata, Via della Ricerca Scientifica 1, 00133 Rome, Italy*
[c] *CNR - Istituto di Scienze dell'Atmosfera e del Clima, Via Fosso del Cavaliere 100, 00133 Rome, Italy*
[d] *INFN, Sez. Lecce, 73100 Lecce, Italy*
[e] *CNR - Istituto per le Applicazioni del Calcolo, Viale del Policlinico 137, 00161 Rome, Italy*
[f] *INFN, Sezione di Ferrara, Via G. Saragat 1, 44100 Ferrara, Italy*

Available online 15 February 2008

Abstract

We review recent progresses on anomalous scaling and universality in anisotropic and homogeneous hydrodynamic turbulent flows. As a central matter, we discuss the validity and the limits of classical ideas of statistical isotropy restoration. Finally, we comment on a still open issue, the observed different scaling behaviour of longitudinal and transverse velocity increment moments in purely statistically isotropic ensemble.

Keywords: Turbulence; Anisotropy; Intermittency

1. Introduction

Statistical restoration of symmetries of the Navier–Stokes equations is at the base of modern theories of turbulence [1]. The presence of geometrical boundaries or obstacles, or the way energy is injected in the flow usually break exact symmetries of the equation of motion. However, for high enough Reynolds number flows, those symmetry properties are supposed to be locally restored in a statistical sense, e.g. only for average quantities. Local homogeneity and local isotropy deserve a particular attention, since they are key features of theoretical approaches to turbulence and transport models. While there has been just a few attempts to make a systematic theory for deviations from statistical homogeneity [2] (see also [3,4] for recent results), it is remarkable that about isotropy restoration, there has been a considerable progress in the last years, as reviewed in Ref. [5]. As a result of this progress, effective data analysis and systematic theoretical studies have been possible, such as to separate isotropic from anisotropic features of turbulent homogeneous statistical fluctuations. Motivation for these researches is related to puzzling experimental and numerical observations, dubbed *persistence of anisotropies*, contradicting classical expectations of recovery of isotropy [6–9]. Persistence of anisotropy accounts for the fact that purely anisotropic adimensional quantities, such as the skewness of velocity gradients transverse to the mean flow do not decay, but remain order $\mathcal{O}(1)$ at very large Reynolds numbers.

On a more general perspective, a proper understanding of scaling behaviours in statistically homogeneous but anisotropic flows is crucial to assess the *universality* of statistical properties of hydrodynamic turbulence [10].

Some crucial steps toward a clear understanding of the statistics of anisotropic fluctuations have been done in the context of Kraichnan models [11–13], simple linear models for passive transport of scalar or vector quantities by homogeneous, isotropic and Gaussian velocity fields, in the presence of large-scale homogeneous but anisotropic forcing [14–18]. While we cannot review these works, it is worth to recall their fundamental results. Isotropic and anisotropic fluctuations can be characterized by different scaling exponents, whose statistical importance is governed by their degree of anisotropy; these exponents are independent of large-scale forcing or

* Corresponding author. Tel.: +39 06 4993 4289.
E-mail address: a.lanotte@isac.cnr.it (A.S. Lanotte).

0167-2789/$ - see front matter © 2008 Elsevier B.V. All rights reserved.
doi:10.1016/j.physd.2008.02.008

boundary conditions, hence universal (see also [19] for a discussion of the case in the presence of an anisotropic and inhomogeneous forcing). The symmetry breaking and peculiar nature of the forcing is revealed in the coefficients appearing in the scaling laws, which are not universal.

In the absence of analytical approaches able to show the validity of these results in the full nonlinear problem, accurate experimental [20–24] and numerical [25–31] measurements become of fundamental importance. Encompassing all results achieved so far, or attempting an historical review of different approaches to homogeneous isotropic – where anisotropic effects are neglected, – and anisotropic turbulence, go beyond our goal and can be found in Ref. [5]. Also we mention that different approaches to anisotropy, mainly focused on large scale flow properties, have been extensively studied in Ref. [32].

Our focus is on small-scale anisotropy. At this purpose, we will first discuss the use of the $SO(3)$ decomposition of statistical observables in terms of their projections on different sectors of the group of rotations in three dimensions [33] (see also Ref. [34] for a rewiew focusing on experimental measurements). The use of $SO(3)$ decomposition, providing a complete basis for angular decomposition, enables us to systematically describe the limits of the idea of *isotropy restoration* at sufficiently small scales (or sufficiently high Reynolds number), as postulated by the Kolmogorov theory [1]. Key working hypothesis, that we will discuss in the sequel, is that forcing has its support at scales much larger than those of the inertial range.

Secondly, we will consider the specific case of large-scale shear flows, for which a theoretical prediction for the dimensional scaling of exponents of velocity increment moments (structure functions) of any order and any degree of anisotropy can be done [35]. Results point to the existence of universal isotropic and anisotropic scaling exponents, deviating from their dimensional values. Anomalous scaling and universality of turbulent fluctuations appear as two concepts intimately related, as highlighted in Kraichnan models.

Finally, we will consider statistically homogeneous and *isotropic* turbulent flows, which can be realized with some degree of accuracy in experiments and in numerics. Compared to strongly anisotropic situations as those encountered in geophysical or plasma applications, they represent a much simpler problem. However, a large number of studies [7,22,36–44] report possible different behaviours for the longitudinal and transverse velocity structure functions in $3D$ flows, for moments high enough. These results contradict our expectations (for second and third moments, analytical constraints resulting from isotropy and incompressibility impose the same scaling to longitudinal and transverse fluctuations). Recent observations will be here reviewed, and commented in the light of the $SO(3)$ decomposition.

The paper is organized as follows. Section 2 recalls the theoretical framework to deal with weak anisotropic fluctuations and the notion of isotropy recovery; this is done by means of the $SO(3)$ decomposition, briefly sketched.

In Section 3, by means of the specific case of homogeneous shear flows, a dimensional argument for the scaling of anisotropic fluctuations is recalled and compared to numerical observations. Last Section 4, before concluding remarks, is devoted to the issue of longitudinal and transverse structure functions scaling in homogeneous isotropic turbulence.

2. Anisotropic hierarchy and the $SO(3)$ decomposition

The starting point of a systematic approach to small-scale anisotropic turbulence is to suppose that both boundary conditions and forcing – which break the invariance under rotation of the Navier–Stokes equations [45], – give a dominant contribution only at large scales, while the transfer of fluctuations from large to small scales is driven by the rotational invariant terms of the equations of motion. This is equivalent to say that anisotropy is only weakly affecting the statistical properties of the turbulent field under exam. Strongly sheared flows constitute a noticeable exception [46,47], as well as magneto-hydrodynamic (MHD) flows in the presence of a mean field for which we still do not have clear evidences [48,49]. However, when the previous hypothesis of large-scale forcing holds, we can study the behaviour of velocity correlation functions in the *inertial range*, at scales $\eta \ll r \ll L$ where η is the dissipation scale and L is the scale of the forcing.

To separate isotropic from anisotropic contributions, it is useful to consider their projections on the irreducible representations of the $SO(3)$ group. As a standard observable, we consider the two-points homogeneous second-order structure function

$$S^{\alpha\beta}(\mathbf{r}) \equiv \left\langle (v_\alpha(\mathbf{r}) - v_\alpha(0))(v_\beta(\mathbf{r}) - v_\beta(0)) \right\rangle .$$

The decomposition of $S^{\alpha\beta}(\mathbf{r})$ in terms of the eigenfunctions of the rotational operator is made by a set of functions labelled with the usual indices $j = 0, 1, \ldots$ and $m = -j, \ldots, +j$, corresponding to the total angular momentum and to the projection of the total angular momentum on a arbitrary direction, respectively.

For scalars quantities, as the longitudinal structure function, $S_L^{(2)}(\mathbf{r}) \equiv \left\langle [(\boldsymbol{v}(\mathbf{r}) - \boldsymbol{v}(0)) \cdot \hat{\boldsymbol{r}}]^2 \right\rangle$, the set of basis functions are the spherical harmonics, $Y_{jm}(\hat{\boldsymbol{r}})$. For a generic pth order tensor, in addition to indices j and m, another index q is necessary, labelling different irreducible representations within each fixed j sector [5,33]. It is easy to show that there are only $q = 1, \ldots, 6$ irreducible representations of the $SO(3)$ group for the space of two-indices symmetrical tensors as $S^{\alpha\beta}(\mathbf{r})$. Accordingly, the second order structure function can be exactly decomposed as

$$S^{\alpha\beta}(\mathbf{r}) \equiv \sum_{q=1}^{6} \sum_{j=0}^{\infty} \sum_{m=-j}^{+j} S^{(2)}_{\mathrm{qjm}}(r) B^{\alpha\beta}_{\mathrm{qjm}}(\hat{\boldsymbol{r}}), \tag{1}$$

where the tensors $B^{\alpha\beta}_{\mathrm{qjm}}(\hat{\boldsymbol{r}})$, defined on the unit sphere, can be seen as a generalization of the spherical harmonics to the tensorial case, and the superscript 2 in the projection $S^{(2)}_{\mathrm{qjm}}(r)$ reminds the order of the analysed correlation function.

In Ref. [33], it has been shown that, if the forcing is at large scales, by projecting the rotational invariant part of the evolution equation for $S^{\alpha\beta}(\mathbf{r})$ on the irreducible representations of the $SO(3)$ group, we obtain a set of dynamic – unclosed – equations for each projection, in each separate sector. The terms of the equations that are not coupled with the forcing, do not depend explicitly on the index m (invariance of Navier–Stokes eqs. with respect to the orientation of the z-axis) and they mix all possible q-representations, for a given j. In other words, if forcing terms are neglected, projections obey separate dynamic equations within each j sector, which corresponds to the *foliation* of the dynamic equation for any correlation in each given sector j of the rotational group [5]. This is a powerful result since, if forcing can be neglected at small scales, it allows to analyse separately the scaling behaviour of isotropic and anisotropic fluctuations in a systematic and quantitative way by studying the behaviour of the projection coefficients $S^{(2)}_{qjm}(r)$, for any degree of anisotropy j.

Moreover, in the limit of infinite Reynolds numbers, Navier–Stokes equations become scaling invariant, sector by sector. It is thus natural to expect the existence of scaling laws characterizing each sector separately, that is:

$$S^{(2)}_{\rm qjm}(r) \sim c^{(2)}_{\rm qjm} r^{\xi^j(2)}, \tag{2}$$

where the coefficients $c^{(2)}_{\rm jmq}$ have to be matched with large-scale boundary conditions and forcing. Decomposition similar to that of Eq. (1) can be generalized to any p-th order tensor, associated to velocity increment moments of order $p > 2$. In principle, nothing prevents the existence of more than one exponent characterizing each separate anisotropic sector, so that the power-law in Eq. (2) has to be considered the dominant term.

When we deal with numerical or experimental data, measuring behaviour of undecomposed velocity increment moments at smaller and smaller scales might not be enough to extract clean results about scaling exponents, even for very large Reynolds number flows. Indeed the presence of anisotropic fluctuations which have not yet decayed even at very small scales, can spoil scaling, thus resulting in a superposition of different power laws.

In particular, measuring scaling properties in each separate sector becomes compulsory if we mean to assess *isotropy recovery* of turbulent statistics. Such a recovery may exist only if, for any moment of given order p, the isotropic scaling exponent is always smaller than the anisotropic ones,

$$\xi^{j=0}(p) < \xi^j(p), \quad \forall j. \tag{3}$$

More generally, a whole hierarchy among the different anisotropic exponents is naturally expected, *within* any order p:

$$\xi^{j=0}(p) \le \xi^{j=1}(p) \le \xi^{j=2}(p) < \cdots, \tag{4}$$

where the exponents $\xi^j(p)$ are supposed to be independent of the (m,q) indices.

In models for passive advection [15,17,18], it has been demonstrated that a similar hierarchy exists, and also that scaling exponents do not show any dependence on the q, m indices. On such basis, we expect that a hierarchy like (4) might exist also in the full hydrodynamic case, and that it is robust at changing large-scale conditions.

The independence of scaling exponents from the m index is given by the arbitrariness in defining the orientation of the coordinate axis in $3D$ space. That from the q index, i.e. from the set of irreducible representations of the rotation group, is much less trivial and with interesting consequences. A dependence on the q index would weaken the whole *foliation* pattern, according to which rotationally invariant properties do not depend on the set of eigenfunctions (with the same rotational properties) chosen to decompose the observables. For example, admitting that projections with different q-indices have different scaling properties could possibly explain the observed different scaling between transverse and longitudinal high-order structure functions in a isotropic statistics ($j = 0$) [22,36,39].

In Ref. [15], it has been shown for the case of passive vector advection that the differential equations for the vector field covariance foliate into independent closed equations for each j sector, which mix different irreducible representations of the $SO(3)$ group, but the scaling exponents do not exhibit any dependence on the q index. We cannot prove that the very same happens for the Navier–Stokes case, although, on a physical ground, we do not see any reason why it should not be like that.

A possible explanation for the observed discrepancy in the scaling exponents of longitudinal and transverse high-order moments might rather be sought in terms of finite Reynolds effects, which prevent from having a unique clear scaling in the inertial range. In this case the differences would become smaller and smaller by going to larger and larger Reynolds numbers. In Section 4, we will come back to this point.

Experimental and numerical measurements often deal with the scaling properties of longitudinal structure functions $S_L^{(p)}(\mathbf{r}) \equiv \langle[(\boldsymbol{v}(\mathbf{r}) - \boldsymbol{v}(0))\cdot\hat{\boldsymbol{r}}]^p\rangle$. As anticipated before, these are scalar objects whose decomposition onto the eigenfunctions of the $SO(3)$ group is particularly simple,

$$S_L^{(p)}(\mathbf{r}) = \sum_{j=0}^{\infty}\sum_{m=-j}^{j} S^{(p)}_{jm}(r) Y_{jm}(\hat{\boldsymbol{r}}). \tag{5}$$

In the sequel, we will consider the scaling behaviour of low order (in p and in j) projections $S^{(p)}_{jm}(r)$.

3. Dimensional prediction for anisotropic fluctuations

A phenomenological theory for dimensional expectation of the scaling exponents of structure functions is important when we try to assess the intermittent behaviour of homogeneous turbulent fluctuations, isotropic as well as anisotropic. Lumley [50] first formulated a dimensional prediction for the scaling exponent of the second order structure function in the sector $j = 2$: $\xi_d^{(j=2)}(p = 2) = 4/3$. In Ref. [35] an argument was given for the dimensional value of scaling exponents of longitudinal structure functions of any order and any degree of anisotropy, which generalizes Lumley's one.

The idea is the following. The overall effect of the large-scale energy pumping and/or boundary conditions is to produce a large-scale anisotropic driving velocity field $\boldsymbol{U}$. This is quite natural and very often encountered in geophysical or laboratory flows. The time evolution equation for the velocity field $\boldsymbol{v}$ can be written as

$$\partial_t v_\alpha + v_\beta \partial_\beta v_\alpha + U_\beta \partial_\beta v_\alpha + v_\beta \partial_\beta U_\alpha = -\partial_\alpha p + \nu \Delta v_\alpha. \quad (6)$$

The major effect of the large-scale field is the instantaneous shear $\mathcal{I}_{\alpha\beta} = \partial_\beta U_\alpha$ which acts as an anisotropic forcing term on small scales, i.e. for scales much smaller than the typical shear-injection scale, $L_S = \sqrt{\epsilon/|\mathcal{I}|^3}$.

To build up a dimensional matching for velocity fluctuations, we first consider the equation of motion for two points quantity $\langle v_\alpha(\boldsymbol{r}) v_\delta(0)\rangle$ in the stationary regime. Inertial and shear-induced contributions can be balanced:

$$\left\langle v_\delta(0) v_\beta(\boldsymbol{r}) \partial_\beta v_\alpha(\boldsymbol{r})\right\rangle \sim \left\langle \mathcal{I}_{\alpha\mu}(\boldsymbol{r}) v_\delta(0) v_\mu(\boldsymbol{r})\right\rangle, \quad (7)$$

to obtain a dimensional estimate of the anisotropic components of the LHS in terms of the RHS shear intensity and of the isotropic part of $\left\langle v(\hat{\boldsymbol{r}}) v(0)\right\rangle$. Similarly for three point quantities and higher order velocity correlation. Since the shear is a large-scale *slow* quantity, a safe estimate is the following:

$$\left\langle \mathcal{I}_{\alpha\mu}(\boldsymbol{r}) v_\delta(0) v_\mu(\boldsymbol{r})\right\rangle \sim D_{\alpha\mu} \left\langle v_\delta(0) v_\mu(\boldsymbol{r})\right\rangle.$$

The $D_{\alpha\beta}$ tensor, associated to the combined probability to have a given shear and a given small scale velocity fluctuation, brings angular momentum only up to $j = 2$. Composition of angular momenta ($j = 2 \oplus j - 2$), then results in the following dimensional matching:

$$S_j^{(p)}(r) \;\sim\; r|D| \cdot S_{j-2}^{(p-1)}(r), \quad (8)$$

where $S_j^{(p)}(r)$ is a shorthand notation of the projection on the j- th sector of the p- th order correlation function previously introduced, neglecting further possible dependencies on q and m indices. In Eq. (8), $|D|$ denotes the typical intensity of the shear term $D_{\alpha\beta}$ in the $j = 2$ sector. For instance, the leading behaviour of the $j = 2$ anisotropic sector of the third-order correlation is: $S_{j=2}^{(3)}(r) \sim r|D| S_{j=0}^{(2)}(r) \sim r^{\xi_d^2(3)}$.

By using a similar argument, we can obtain dimensional predictions for the $j = 2, 4$ sectors of the fourth order structure function. The procedure is easily extended to all orders, leading to the following expression:

$$\xi_d^j(p) = \frac{(p+j)}{3}. \quad (9)$$

Direct numerical simulations (DNS), at moderate Reynolds number $Re_\lambda \sim 100$, of a fully periodic, incompressible flow with a statistically homogeneous but anisotropic large-scale energy injection have been reported in Ref. [27,35]. They can be used to test the validity of the dimensional prediction (9).

In Fig. 1 isotropic and anisotropic fluctuations, which have a signal-to-noise ratio high enough to ensure stable results, are shown. Sectors with odd js are absent due to the parity symmetry of the longitudinal structure functions. We notice a clear foliation in terms of the j index: sectors with the same j but different ms behave very similarly. In Table 1 the best power law fits for structure functions of orders $p = 2, 4, 6$ and sectors $j = 2, 4, 6$ are presented. It is important to notice the presence of a hierarchical organization as assumed in (4), which implies isotropy restoration at sufficiently small scales, and also that there is no saturation for the exponents as a function of the j value. Second, the measured exponents in the sectors $j = 4$ and $j = 6$ are anomalous, i.e. they differ from the dimensional estimate $\xi_d^j(p) = (j+p)/3$. This implies that isotropy is restored at small scales, but subleading anisotropic fluctuations decay slower than predicted by dimensional argument. Such difference with the dimensional scaling has been exploited in Ref. [26] to explain the puzzling results on gradients statistics mentioned in the introduction [6–9]. Persistence of anisotropy can be understood of a combined effect of anisotropy and intermittency, causing anisotropic quantities to decay at high Reynolds at much slower rates that what expected by dimensional predictions (see e.g. Ref. [51]).

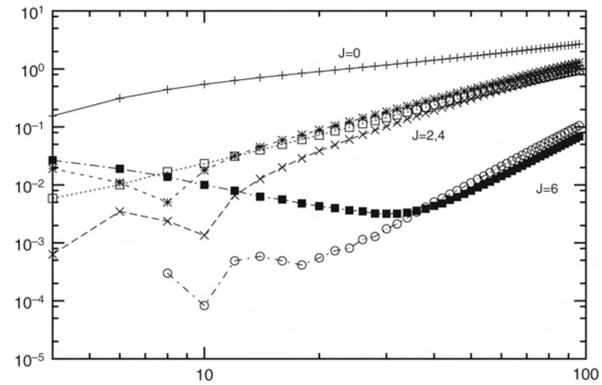

Fig. 1. Log–log plot of the second-order structure function projections $S_{jm}^{(2)}(r)$ versus the scale r, for sectors with a good signal-to-noise ratio. Sectors: $(j,m) = (0,0)$, $(+)$; $(j,m) = (2,2)$, $(\times)$; $(j,m) = (4,0)$, (empty square); $(j,m) = (4,2)$, $(\star)$; $(j,m) = (6,0)$, $(\circ)$; $(j,m) = (6,2)$, (black square). The statistical and numerical noise induced by the $SO(3)$ decomposition is estimated as the threshold where the $j = 6$ sector starts to deviate from the monotonic decreasing behaviour $\sim O(10^{-3})$. This figure is taken from Ref. [27]. Data come from the integration of Navier–Stokes equation for an incompressible flow, solved on a triply periodic box with 256^3 grid points; Taylor scale based Reynolds number is $Re_\lambda \sim 100$.

Moreover, the comparison between new experimental and numerical results [24,29,30] with the data presented in Table 1 suggests that anisotropic fluctuations are indeed universal, i.e. scaling exponents for scales smaller then the typical shear length do not depend on the particular mechanism used to inject anisotropy. A different scenario may emerge if we look at scaling properties for scales larger than the typical shear length, L_S, i.e. where the external forcing mechanism cannot be neglected and therefore the foliation pattern is no longer valid [30,46,47] (consider for example turbulent convection in the Bolgiano regime). If foliation cannot be invoked, all sectors are in principle entangled and scaling properties of isotropic and anisotropic sectors may even become not universal. Further work is needed in this direction, by comparing experiments with different injection mechanisms to better highlight the statistical behaviour at scales $r \gg L_S$.

Table 1
Scaling exponents in the isotropic and anisotropic sectors obtained in Refs. [27,35] by means of DNS

p	$\xi^{j=0}(p)$	$[\xi_d^{j=0}(p)]$	$\xi^{j=2}(p)$	$[\xi_d^{j=2}(p)]$	$\xi^{j=4}(p)$	$[\xi_d^{j=4}(p)]$	$\xi^{j=6}(p)$	$[\xi_d^{j=6}(p)]$
2	0.70 ± 0.2	[0.66]	1.15 ± 0.5	[1.33]	1.65 ± 0.5	[2.00]	3.2 ± 0.2	[2.66]
4	1.28 ± 0.4	[1.33]	1.56 ± 0.5	[2.00]	2.25 ± 0.1	[2.66]	3.1 ± 0.2	[3.33]
6	1.81 ± 0.6	[2.00]	2.07 ± 0.8	[2.33]	2.60 ± 0.1	[3.33]	3.3 ± 0.2	[4.00]

Notice that values for the anisotropic sector $j = 2$, at different order moment order p, are taken from the experiments [21,22]. For the values extracted from the numerical simulation (columns $j = 0, 4, 6$), error bars are estimated on the oscillation of the local slopes. For the experimental data, error bars are given as the mismatch between the two experiments. For all sectors, the dimensional estimates for the scaling exponents $\xi_d^j(p) = (p + j)/3$ are also reported in square brackets.

4. Discussions and open issues

An issue still much debated concerns scaling in purely isotropic ensemble. Velocity tensors can be decomposed, inside the $j = 0$ isotropic sector, in q-different eigenvectors, corresponding for example to purely longitudinal, purely transverse or mixed longitudinal and transverse fluctuations [5]. Purely longitudinal structure functions are given by $S_L^{(p)}(r) \equiv \langle[\delta \boldsymbol{v}(\boldsymbol{r}) \cdot \hat{\boldsymbol{r}}]^p\rangle$; purely transverse structure functions are: $S_T^{(p)}(r) \equiv \langle[\delta \boldsymbol{v}(\boldsymbol{r}_T)]^p\rangle$ (where $\boldsymbol{r}_T \cdot \boldsymbol{v} = 0$). As previously discussed, arguments based on $SO(3)$ decomposition do not distinguish among scaling properties inside a given j sector. If different scaling are observed among transverse and longitudinal fluctuations within the $j = 0$ sector for statistically isotropic flows, new ideas must be presented to explain them. In Fig. 2, we show a comparison between logarithmic local slopes of order $p = 8$ and $p = 4$ in the ESS sense [52,53], of longitudinal and transverse structure functions [36,54]:

$$\zeta(p, r) = \frac{d \log S_{L,T}^{(p)}(r)}{d \log S_{L,T}^{(2)}(r)},$$

for data issuing from two different numerical simulations. This is equal to the ratio of the scaling exponent of the p-th order longitudinal (transverse) structure function to that of the second order longitudinal (transverse) one. The two DNS are *ideally* statistically isotropic since the forcing mechanism is such, and the flow has periodic boundary conditions. Residual anisotropic contribution due to the discretized nature of the numerical grid and to statistical fluctuations in the velocity statistics induced by the forcing, can be quantified and result to be very small in the data shown here. Still, in the inertial range the two datasets agree in showing a detectable difference between the longitudinal and the transverse scaling exponents.

This discrepancy is an open theoretical issue, not explainable using standard symmetry argument in homogeneous and isotropic turbulence [5]. If this is an effect due to finite-Reynolds number or a result which remains true even for most intense turbulent realizations is yet not known (see also [39] for a discussion on this point).

In recent years, many detailed observations about anisotropic turbulence have been collected. These have also given a burst for developing a systematic theory for disentangling isotropic and anisotropic fluctuations in the case of statistically homogeneous turbulent flows. We have now observation of statistical restoration of isotropy in passive transport and hydrodynamic turbulence. However, isotropy is recovered at a slower

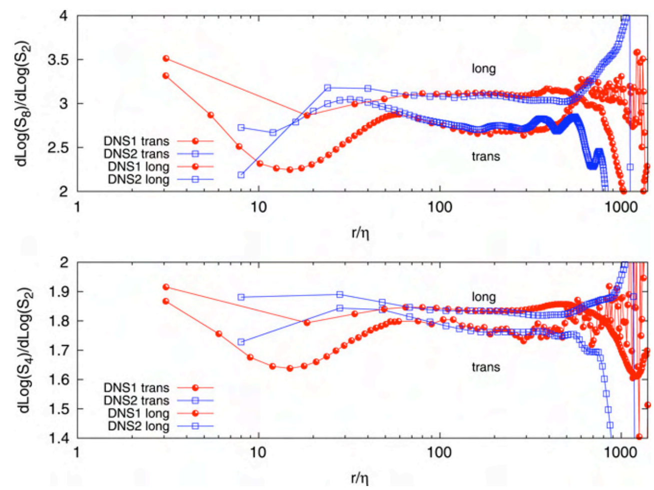

Fig. 2. Top figure: Log-lin plot of the local slopes, in ESS, of the 8th-order longitudinal (top lines) and transverse (bottom lines) structure functions versus the scale r/η, as obtained from DNS data of incompressible turbulence from Ref. [36], (DNS1: circles). These are compared with DNS data obtained for a slightly compressible turbulent flow, as reported in Ref. [54], (DNS2: squares). Bottom figure: The same but for the fourth-order longitudinal and transverse structure functions. Note the good agreement of the two datasets in the inertial range, $r \gg \eta$, where they display the same mismatch between the longitudinal and transverse moments. The discrepancy between DNS1 and DNS2 data close to the dissipative scale, $r/\eta \sim 1$, is due to the fact that the two simulations have different small-scale dissipation mechanisms. DNS1 data refer to an incompressible turbulent flow, with normal viscous dissipation; numerical resolution is 1024^3 grid points and Taylor scale-based Reynolds number is $Re_\lambda \sim 460$. DNS2 data refer to a slightly compressible turbulent flow with Mach number ~ 0.3; numerical resolution is 1856^3 grid points, and estimated Reynolds number is $Re_\lambda \sim 600$. In this run, there are two mechanisms of kinetic energy dissipation. The most important is the transformation of kinetic energy into heat via compressible effects; the second is a numerical smoothing of steep velocity gradients tuned to filter out local numerical instabilities. The latter is important only at scales of the order of the grid spacing.

rate than expected by dimensional argument, due to intermittency. Also, there are evidences that anisotropic exponents, as well as isotropic ones, are anomalous and universal. Numerical and experimental results match with the analytical results obtained in linear model for passive advection, where it has been shown the existence of a hierarchy of exponents depending on the anisotropy degree, as well as the intermittency and universality of these exponents.

Our understanding of anisotropic turbulence is, however, based on the idea that boundary conditions and forcing contribute only at large scales, and do not break rotational invariance at scales in the inertial range. This might not be always true, particularly if we consider the case of MHD turbulence, for which there are observations that anisotropy can grow going at smaller and smaller scales [48]. Similarly, shear flows in the production range or turbulent convection in the Bolgiano regime may posses strong departure from the sort of phenomenology observed within the *foliation* scheme.

Acknowledgments

We acknowledge long-lasting collaboration and discussions with many colleagues, that have contributed to shape our understanding of the problem. In particular, we want to thank I. Arad, A. Celani, C.M. Casciola, I. Daumont, D. Lohse, B. Jacob, I. Mazzitelli, A. Mazzino, I. Procaccia and M. Vergassola. We also thank T. Gotoh and the FLASH center in Chicago, in particular R. Fisher and D. Lamb, for sharing with us the DNS data published in Ref. [36,54], respectively.

References

[1] U. Frisch, Turbulence, in: The Legacy of A.N. Kolmogorov, Cambridge University Press, Cambridge, 1995.
[2] A.S. Monin, A.M. Yaglom, Statistical Fluid Mechanics: Mechanics of Turbulence, vol. 2, MIT Press, 1975.
[3] U. Frisch, J. Bec, E. Aurell, Locally homogeneous turbulence: Is it an inconsistent framework? Phys. Fluids 17 (2005) 081706.
[4] A. Celani, M.M. Afonso, A. Mazzino, Point-source scalar turbulence, J. Fluid Mech. 583 (2007) 189.
[5] L. Biferale, I. Procaccia, Anisotropy in turbulent flows and in turbulent transport, Phys. Rep. 414 (2005) 43.
[6] A. Pumir, B.I. Shraiman, Persistent small scale anisotropy in homogeneous shear flows, Phys. Rev. Lett. 75 (1995) 3114.
[7] X. Shen, Z. Warhaft, The anisotropy of the small scale structure in high Reynolds number (R_{lambda} 1000) turbulent shear flow, Phys. Fluids 12 (2000) 2976.
[8] J. Schumacher, K. Sreenivasan, P.K. Yeung, Derivative moments in turbulent shear flows, Phys. Fluids 15 (2003) 84.
[9] J. Schumacher, Relation between shear parameter and Reynolds number in statistically stationary turbulent shear flows, Phys. Fluids 16 (2004) 3094.
[10] K.R. Sreenivasan, R.A. Antonia, The phenomenology of small-scale turbulence, Annu. Rev. Fluid Mech. 29 (1997) 435.
[11] R.H. Kraichnan, Anomalous scaling of a randomly advected passive scalar, Phys. Rev. Lett. 72 (1994) 1016.
[12] K. Gawędzki, A. Kupiainen, Anomalous scaling of the passive scalar, Phys. Rev. Lett. 75 (1995) 3834.
[13] M. Vergassola, Anomalous scaling for passively advected magnetic fields, Phys. Rev. E 53 (1996) R3021.
[14] A.S. Lanotte, A. Mazzino, Anisotropic nonperturbative zero modes for passively advected magnetic fields, Phys. Rev. E 60 (1999) R3483.
[15] I. Arad, L. Biferale, I. Procaccia, Nonperturbative spectrum of anomalous scaling exponents in the anisotropic sectors of passively advected magnetic fields, Phys. Rev. E 61 (2000) R2654.
[16] I. Arad, V. L'vov, E. Podivilov, I. Procaccia, Anomalous scaling in the anisotropic sectors of the Kraichnan model of passive scalar advection, Phys. Rev. E 62 (2000) 4904.
[17] N.V. Antonov, J. Honkonen, Anomalous scaling in two models of passive scalar advection: Effects of anisotropy and compressibility, Phys. Rev. E 63 (2001) 036302.
[18] I. Arad, I. Procaccia, Spectrum of anisotropic exponents in hydrodynamic systems with pressure, Phys. Rev. E 63 (2001) 056302.
[19] M.M. Afonso, M. Sbragaglia, Inhomogeneous anisotropic passive scalars, J. Turbul. 6 (10) (2005).
[20] I. Arad, B. Dhruva, S. Kurien, V.S. L'vov, I. Procaccia, K.R. Sreenivasan, Extraction of anisotropic contributions in turbulent flows, Phys. Rev. Lett. 81 (1998) 5330.
[21] S. Kurien, K.R. Sreenivasan, Anisotropic scaling contributions to high-order structure functions in high-Reynolds-number turbulence, Phys. Rev. E 62 (2000) 2206.
[22] X. Shen, Z. Warhaft, Longitudinal and transverse structure functions in sheared and unsheared wind-tunnel turbulence, Phys. Fluids 14 (2002) 370.
[23] X. Shen, Z. Warhaft, On the higher order mixed structure functions in laboratory shear flow, Phys. Fluids 14 (2002) 2432.
[24] B. Jacob, L. Biferale, G. Iuso, C.M. Casciola, Anisotropic fluctuations in turbulent shear flows, Phys. Fluids 16 (2004) 4135.
[25] I. Arad, L. Biferale, I. Mazzitelli, I. Procaccia, Disentangling scaling properties in anisotropic and inhomogeneous turbulence, Phys. Rev. Lett. 82 (1999) 5040.
[26] L. Biferale, M. Vergassola, Isotropy vs anisotropy in small-scale turbulence, Phys. Fluids 13 (2001) 2139.
[27] L. Biferale, F. Toschi, Anisotropies in homogeneous turbulence: Hierarchy of scaling exponents and intermittency of the anisotropic sectors, Phys. Rev. Lett. 86 (2001) 4831.
[28] L. Biferale, D. Lohse, I. Mazzitelli, F. Toschi, Probing structures in channel flow through SO(3) and SO(2) decomposition, J. Fluid Mech. 452 (2002) 39.
[29] C.M. Casciola, P. Gualtieri, B. Jacob, R. Piva, Scaling properties in the production range of shear dominated flows, Phys. Rev. Lett. 95 (2005) 024503.
[30] C.M. Casciola, P. Gualtieri, B. Jacob, R. Piva, The residual anisotropy at small scales in high shear turbulence, Phys. Fluids 19 (2007) 101704.
[31] M. Antonelli, A.S. Lanotte, A. Mazzino, Anisotropies and universality of buoyancy-dominated turbulent fluctuations: A large-eddy simulation study, J. Atmos. Sci. 64 (2007) 2642–2656.
[32] C. Cambon, J.F. Scott, Linear and nonlinear models of anisotropic turbulence, Annu. Rev. Fluid Mech. 31 (1999) 1.
[33] I. Arad, V. L'vov, I. Procaccia, Correlation functions in isotropic and anisotropic turbulence: The role of the symmetry group, Phys. Rev. E 59 (1999) 6753.
[34] S. Kurien, K.R. Sreenivasan, Measures of anisotropy and the universal properties of turbulence, in: M. Lesieur, A. Yaglom, F. David (Eds.), Les Houches 2000: New Trends in Turbulence, Springer EDP-Sciences, 2001.
[35] L. Biferale, I. Daumont, A. Lanotte, F. Toschi, Anomalous and dimensional scaling in anisotropic turbulence, Phys. Rev. E 66 (2002) 056306.
[36] T. Gotoh, D. Fukayama, T. Nakano, Velocity field statistics in homogeneous steady turbulence obtained using a high-resolution direct numerical simulation, Phys. Fluids 14 (2002) 1065.
[37] B. Dhruva, Y. Tsuji, K.R. Sreenivasan, Transverse structure functions in high-Reynolds-number turbulence, Phys. Rev. E 56 (1997) R4928.
[38] O.N. Boratav, On longitudinal and lateral moment hierarchy in turbulence, Phys. Fluids 9 (1997) 3120.
[39] S. Chen, K.R. Sreenivasan, M. Nelkin, N. Cao, Refined similarity hypothesis for transverse structure functions in fluid turbulence, Phys. Rev. Lett. 79 (1997) 2253.
[40] O.N. Boratav, R.B. Pelz, Structures and structure functions in the inertial range of turbulence, Phys. Fluids 9 (1997) 1400.
[41] W. Van de Water, J.A. Herweijer, High-order structure functions of turbulence, J. Fluid Mech. 387 (1999) 3.
[42] G. He, G.D. Doolen, S. Chen, Calculations of longitudinal and transverse velocity structure functions using a vortex model of isotropic turbulence, Phys. Fluids 11 (1999) 3743.
[43] T. Zhou, R.A. Antonia, Reynolds number dependence of the small-scale structure of grid turbulence, J. Fluid Mech. 406 (2000) 81.
[44] A. Noullez, G. Wallace, W. Lempert, R.B. Miles, U. Frisch, Transverse velocity increments in turbulent flow using the RELIEF technique, J. Fluid Mech. 339 (1997) 287.
[45] In our derivation, we generally refer to the case of Navier–Stokes turbulence, but similar reasonings apply to the general case of advection-diffusion equations.
[46] F. Toschi, E. Lévêque, G. Ruiz-Chavarria, Shear effects in non-homogeneous turbulence, Phys. Rev. Lett. 85 (7) (2000) 1436.
[47] F. Toschi, G. Amati, S. Succi, R. Benzi, R. Piva, Intermittency and structure functions in channel flow turbulence, Phys. Rev. Lett. 82 (25) (1999) 5044.

[48] D. Biskamp, Magnetohydrodynamic Turbulence, Cambridge University Press, Cambridge, 2003.
[49] W-C. Müller, D. Biskamp, R. Grappin, Statistical anisotropy of magnetohydrodynamic turbulence, Phys. Rev. E 67 (2003) 066302.
[50] J.L. Lumley, Similarity and the turbulent energy spectrum, Phys. Fluids 10 (1967) 855.
[51] A. Celani, A. Lanotte, A. Mazzino, M. Vergassola, Fronts in passive scalar turbulence, Phys. Fluids 13 (2001) 1768.
[52] R. Benzi, S. Ciliberto, R. Tripiccione, C. Baudet, F. Massaioli, S. Succi, Extended self-similarity in turbulent flows, Phys. Rev. E 48 (1993) R29.
[53] R. Benzi, L. Biferale, S. Ciliberto, M.V. Struglia, R. Tripiccione, Generalized scaling in fully developed turbulence, Physica D 96 (1996) 162.
[54] R. Benzi, L. Biferale, R.T. Fisher, L.P. Kadanoff, D.Q. Lamb, F. Toschi, Intermittency and universality in fully-developed inviscid and weakly-compressible turbulent flows. http://arxiv.org/abs/0709.3073. 2007.

Available online at www.sciencedirect.com
ScienceDirect
Physica D 237 (2008) 1976–1981
PHYSICA D
www.elsevier.com/locate/physd

Simpler variational problems for statistical equilibria of the 2D Euler equation and other systems with long range interactions

Freddy Bouchet*

Institut Non Linéaire de Nice, INLN, CNRS, UNSA, 1361 route des lucioles, 06 560 Valbonne - Sophia Antipolis, France

Available online 15 March 2008

Abstract

The Robert–Sommeria–Miller equilibrium statistical mechanics predicts the final organization of two dimensional flows. This powerful theory is difficult to handle practically, due to the complexity associated with an infinite number of constraints. Several alternative simpler variational problems, based on Casimir's or stream function functionals, have been considered recently. We establish the relations between all these variational problems, justifying the use of simpler formulations.

PACS: 05.20.-y; 05.20.Cg; 05.20.Jj; 47.32.-y.; 47.32.C-

Keywords: Two dimensional turbulence; Vortex dynamics; Equilibrium statistical mechanics; Long range interactions; Ensemble inequivalence; Variational problems

We consider the 2D Euler equations, on a domain $\mathcal{D}$

$$\frac{\partial\omega}{\partial t} + \mathbf{v}\cdot\nabla\omega = 0; \quad \mathbf{v} = \mathbf{e}_z \times \nabla\psi; \quad \omega = \Delta\psi \tag{1}$$

where ω is the vorticity, $\mathbf{v}$ the velocity and ψ the stream function (with $\psi = 0$ on $\partial\mathcal{D}$, $\mathcal{D}$ is simply connected).

The equilibrium statistical mechanics of the 2D Euler equation (the Robert–Sommeria–Miller (RSM) theory [1–3]), assuming ergodicity, predicts the final organization of the flow, on a coarse grained level (see [4] for a recent review of Onsager ideas, that inspired the RSM theory, see also [5]). Besides its elegance, this predictive theory is a very interesting and useful scientific tool.

From a mathematical point of view, one has to solve a microcanonical variational problem (MVP): maximizing a mixing entropy $\mathcal{S}[\rho] = -\int_{\mathcal{D}} \mathrm{d}^2x \int \mathrm{d}\sigma \rho \log\rho$, with constraints on energy E and vorticity distribution γ

$$S(E_0,\gamma) = \sup_{\{\rho | N[\rho]=1\}} \{\mathcal{S}[\rho] | E[\overline{\omega}] = E_0, \\ D[\rho] = \gamma\} \text{ (MVP).}$$

$\rho(\mathbf{x},\sigma)$ is normalized ($N[\rho] = 1$, see (6)) and depends on space $\mathbf{x}$ and vorticity σ variables.

The theoretical predictability of RSM theory requires the knowledge of all conserved quantities. The infinite number of Casimir's functionals (this is equivalent to vorticity distribution γ) have then to be considered. This is a huge practical limitation. When faced with real flows, physicists can then either give physical arguments for a given type of distribution γ (modeler approach) or ask whether there exists some distribution γ with RSM equilibria close to the observed flow (inverse problem approach). However, in any case the complexity remains : the class of RSM equilibria is huge.

During recent years, authors have proposed alternative approaches, which led to practical and/or mathematical simplifications in the study of such equilibria. As a first example, Ellis, Haven and Turkington [6] proposed to treat the vorticity distribution canonically (in a canonical statistical ensemble). From a physical point of view, a canonical ensemble for the vorticity distribution would mean that the system is in equilibrium with a bath providing a prior distribution of vorticity. As such a bath does not exist, the physically relevant ensemble remains the one based on the dynamics : the microcanonical one. However, the Ellis–Haven–Turkington approach is extremely interesting as it provides a drastic mathematical and practical simplification to the problem of

* Tel.: +33 04 92 96 73 07.
E-mail address: Freddy.Bouchet@inln.cnrs.fr.

0167-2789/$ - see front matter © 2008 Elsevier B.V. All rights reserved.
doi:10.1016/j.physd.2008.02.029

computing equilibrium states. A second example, largely popularized by Chavanis [7,8], is the maximization of generalized entropies. Both the prior distribution approach of Ellis, Haven and Turkington or its generalized thermodynamics interpretation by Chavanis lead to a second variational problem: the maximization of Casimir's functionals, with energy constraint (CVP)

$$C(E_0, s) = \inf_{\omega} \left\{ \mathcal{C}_s[\omega] = \int_{\mathcal{D}} s(\omega) \mathrm{d}^2 x \,|\, E[\omega] = E_0 \right\} \text{ (CVP)}$$

where $\mathcal{C}_s$ are Casimir's functionals, and s a convex function (Energy-Casimir functionals are used in classical works on nonlinear stability of Euler stationary flows [9,10], and have been used to show the nonlinear stability of some of RSM equilibrium states [2,11]).

Another class of variational problems (SFVP), that involve the stream function only (and not the vorticity), has been considered in relation with the RSM theory

$$D(G) = \inf_{\psi} \left\{ \int_{\mathcal{D}} \mathrm{d}^2 x \left[\frac{1}{2} |\nabla \psi|^2 + G(\psi) \right] \right\} \text{ (SFVP).}$$

Such (SFVP) functionals have been used to prove the existence of solutions to the equation describing critical points of (MVP) [11]. Interestingly, for the Quasi-geostrophic model, in the limit of small Rossby deformation radius, such a SFVP functional is similar to the van der Waals-Cahn Hilliard model which describes phase coexistence in usual thermodynamics [12,13]. This physical analogy has been used to make precise predictions in order to model Jovian vortices [12,14]. Moreover (SFVP) functionals are much more regular than (CVP) functionals and thus also very interesting for mathematical purposes.

When we prescribe appropriate relations between the distribution function γ, the functions s and G, the three previous variational problems have the same critical points. This has been one of the motivations for their use in previous works. However, a clear description of the relations between the stability of these critical points is still missing (is a (CVP) minimizer a RSM equilibria, or does a RSM equilibria minimize (CVP)?). This has led to fuzzy discussions in recent papers. Providing an answer is a very important theoretical issue because, as explained previously, it will lead to deep mathematical simplifications and will provide useful physical analogies.

The aim of this short paper is to establish the relation between these three variational problems. The result is that any minimizer (global or local) of (SFVP) minimizes (CVP) and that any minimizer of (CVP) is a RSM equilibria. The opposite statements are wrong in general. For instance (CVP) minimizers may not minimize (SFVP), but be only saddles. Similarly, RSM equilibria may not minimize (CVP) but be only saddles, even if no explicit example has yet been exhibited.

These results have several interesting consequences:

1. As the ensemble of (CVP) minimizers is a sub-ensemble of the ensemble of RSM equilibria, one cannot claim that (CVP) are more relevant for applications than RSM equilibria (for a different point of view, see for instance [15]).
2. The link between (CVP) and RSM equilibria provides a further justification for studying (CVP).
3. Based on statistical mechanics arguments, when looking at the Euler evolution on a coarse-grained level, it may be natural to expect the RSM entropy to increase. There is however no reason to expect such a property to be true for the Casimir's functional. As explained above, it may also happen that entropy extrema are (CVP) saddles.

In order to simplify the discussion, we keep only the energy constraint at the level of the Casimir functional (CVP). Adding other constraints, such as the circulation [15], or even the microscopic enstrophy, does not change the discussion.

We note that all the discussion can be easily generalized to any system with long range interactions (self-gravitating systems, Vlasov Poisson system) [16].

In the first section, we explain the link between a constrained variational problem and its relaxed version. We explain that any minimizer of the second is a minimizer of the first. In the second section, we present the microcanonical variational problem (MVP). We then introduce a mixed grand canonical ensemble by relaxing the vorticity distribution constraint in the RSM formalism. We prove in the third section that this mixed ensemble is equivalent to (CVP). Similarly, in the last section we prove that the (SFVP) variational problem is equivalent to a relaxed version of (CVP).

1. Relations between constrained and relaxed variational problems

We discuss briefly relations between a constrained variational problem and its relaxed version. This situation appears very often in statistical mechanics when passing from one statistical ensemble to another. We assume that the Lagrange's multipliers rule applies. Let us consider the two variational problems

$$G(C) = \inf_{x} \{ g(x) | c(x) = C \} \quad \text{and}$$

$$H(\gamma) = \inf_{x} \left\{ h_\gamma(x) = g(x) - \gamma c(x) \right\}.$$

G is the constrained variational problem and H is the relaxed one, γ is the Lagrange multiplier (or the dual variable) associated to C. We have the results:

1. $H(\gamma) = \inf_C \{G(C) - \gamma C\}$ and $G(C) \geq \sup_\gamma \{\gamma C + H(\gamma)\}$.
2. If x_m is a minimizer of h_γ then x_m is also a minimizer of $G(C)$ with the constraint $C = c(x_m)$.
3. If x_m is a minimizer of $G(C)$, then it exists a value of γ such that x_m is a critical point of h_γ, but x_m may not be a minimizer of h_γ but just a saddle. Then x_m is a minimizer of h_γ if and only if $G(C) = \sup_\gamma \{H(\gamma) + \gamma C\}$ if and only if $G(C)$ coincides with the convex hull of G in C. In this last situation the two variational problems are called *equivalent*.

Such results are classical. More detailed results in this context may be found in [15]. Situations of ensemble inequivalence have been classified, in relation with phase transitions [17].

Equality in point 1. follows from the remark that

$$H(\gamma) = \inf_C \left\{ \inf_x \{g(x) - \gamma c(x) | c(x) = C\} \right\} = \inf_C \left\{ \inf_x \{g(x) | c(x) = C\} - \gamma C \right\}.$$

We remark that $-H$ is the Legendre–Fenchel transform of G. The inequality of point 1 is then a classical convex analysis result. We have for any value of γ,

$$\begin{aligned} G(C) &= \inf_x \{g(x) | c(x) = C\} \\ &= \inf_x \{g(x) - \gamma c(x) | c(x) = C\} + \gamma C \\ &\geq \inf_x \{g(x) - \gamma c(x)\} + \gamma C = H(\gamma) + \gamma C. \end{aligned} \tag{2}$$

This is a direct proof of the inequality of point 1.

Point 2: for x_m a minimizer of h_γ and x with $c(x) = c(x_m)$, we have $g(x_m) = h_\gamma(x_m) + \gamma c(x_m) \leq h_\gamma(x) + \gamma c(x_m) = g(x)$. This proves 2 First assertion of 3. is Lagrange's multipliers rule. Clearly, x_m is a minimizer of h_γ if and only if equality occurs in (2). It is a classical result of convex analysis that the convex hull of G is the Legendre–Fenchel transform of $-H$. This concludes the proof of 3. Many examples where x_m is a saddle may be found in the literature (see [17], or examples in the context of Euler equation in [18–20]).

2. RSM statistical mechanics

Euler's equations (1) conserve the kinetic energy

$$E[\omega] = \frac{1}{2}\int_{\mathcal{D}} d^2x \, (\nabla\psi)^2 = -\frac{1}{2}\int_{\mathcal{D}} d^2x\,\omega\psi = E_0 \tag{3}$$

and for integrable s, Casimirs' functional

$$\mathcal{C}_s[\omega] = \int_{\mathcal{D}} d^2x\, s(\omega). \tag{4}$$

Let us define $A(\sigma)$ the area of $\mathcal{D}$ with vorticity values lower than σ, and $\gamma(\sigma)$ the vorticity distribution

$$\gamma(\sigma) = \frac{1}{|\mathcal{D}|}\frac{dA}{d\sigma} \quad \text{with } A(\sigma) = \int_{\mathcal{D}} d^2x\, \chi_{\{\omega(\mathbf{x}) \leq \sigma\}}, \tag{5}$$

where χ_B is the characteristic function of the set $B \subset D$, and $|\mathcal{D}|$ is the area of $\mathcal{D}$. As Euler's Eq. (1) is a transport equation by an incompressible flow, $\gamma(\sigma)$ (or equivalently $A(\sigma)$) is conserved by the dynamics. Conservation of distribution $\gamma(\sigma)$ and of all Casimir's functionals (4) is equivalent.

2.1. RSM microcanonical equilibria (MVP)

We present the classical derivation [2] of the microcanonical variational problem which describes RSM equilibria. Such equilibria describe the most probable mixing of the vorticity ω, constrained by the vorticity distribution (5) and energy (3) (other conservation laws could be considered, for instance if the domain D has symmetries).

We make a probabilistic description of the flow. We define $\rho(\sigma, \mathbf{x})$ the local probability that the microscopic vorticity ω takes a value $\omega(\mathbf{x}) = \sigma$ at position $\mathbf{x}$. As ρ is a local probability, it satisfies a local normalization

$$N[\rho](\mathbf{x}) \equiv \int_{-\infty}^{+\infty} d\sigma\rho(\sigma, \mathbf{x}) = 1. \tag{6}$$

The known vorticity distribution (5) imposes

$$D[\rho](\sigma) \equiv \int_{\mathcal{D}} d\mathbf{x}\rho(\sigma, \mathbf{x}) = \gamma(\sigma). \tag{7}$$

We are interested on a locally averaged, coarse-grained description of the flow. The averaged vorticity is

$$\overline{\omega}(\mathbf{x}) = \int_{-\infty}^{+\infty} d\sigma\sigma\rho(\sigma, \mathbf{x}). \tag{8}$$

$\overline{\psi} = \Delta\bar{\omega}$ is the averaged stream function. The energy may be expressed in terms of the averaged vorticity distribution as

$$E[\overline{\omega}] \equiv -\frac{1}{2}\int_{\mathcal{D}} \overline{\psi}\overline{\omega} d\mathbf{x} \simeq E_0. \tag{9}$$

The entropy is a measure of the number of microscopic vorticity fields which are compatible with a distribution ρ. By classical arguments, such a measure is given by the entropy

$$\mathcal{S}[\rho] \equiv -\int_{\mathcal{D}} d^2x \int_{-\infty}^{+\infty} d\sigma\rho\log\rho. \tag{10}$$

The most probable mixing for the potential vorticity is thus given by the probability ρ_{eq} which maximizes the entropy (10), subject to the three constraints (6), (7) and (9). The equilibrium entropy $S(E_0, \gamma)$, the value of the constrained entropy maxima, is then given by the microcanonical variational problem (MVP) (see the introduction).

Using the Lagrange multipliers rule, there exists β and $\alpha(\sigma)$ (the Lagrange parameters associated to the energy and vorticity distribution, respectively) such that the critical points of (MVP) satisfy

$$\rho_{eq}(\mathbf{x}, \sigma) = \frac{1}{z_\alpha(\beta\psi_{eq})}\exp\left[\sigma\beta\psi_{eq} - \alpha(\sigma)\right], \tag{11}$$

where

$$z_\alpha(u) = \int_{-\infty}^{+\infty} d\sigma \exp[\sigma u - \alpha(\sigma)] \quad \text{and}$$

$$f_\alpha(u) = \frac{d}{du}\log z_\alpha. \tag{12}$$

We note that z_α is positive, $\log z_\alpha$ is convex, and thus f_α is strictly increasing.

From (11), using (8), the equilibrium vorticity is

$$\omega_{eq} = f_\alpha(\beta\psi_{eq}) \quad \text{or equivalently} \quad g_\alpha(\omega_{eq}) = \beta\psi_{eq}, \tag{13}$$

where g_α is the inverse of f_α. The actual equilibrium ω_{eq} is the minimizer of the entropy while satisfying the constraints, between all critical points for any possible values of β and α.

We note that solutions to (13) are stationary flows.

2.2. RSM constrained grand canonical ensemble

We consider the statistical equilibrium variational problem (MVP), but we relax the vorticity distribution constraint. This constrained (or mixed) grand canonical variational problem is

$$G(E_0,\alpha)=\inf_{\{\rho|N[\rho]=1\}}\left\{\mathcal{G}_\alpha[\rho]|E\left[\overline{\omega}\right]=E_0\right\}, \tag{14}$$

with the Gibbs potential functional defined as

$$\mathcal{G}_\alpha\left[\rho\right]\equiv-S\left[\rho\right]+\int_{\mathcal{D}}\mathrm{d}^2x\int_{-\infty}^{+\infty}\mathrm{d}\sigma\alpha\left(\sigma\right)\rho\left(\mathbf{x},\sigma\right).$$

In the following section, we prove that (14) is equivalent to the constraint Casimir V.P. (CVP). Using the results of the first section, relating constrained and relaxed variational problems, we can thus conclude that minimizers of (CVP) are RSM equilibria, but the converse is wrong in general, as stated in the introduction.

3. Constrained Casimir (CVP) and grand canonical ensembles are equivalent

3.1. Equivalence

We consider a Casimir's functional (4), where s is assumed to be convex. The critical points of the constrained Casimir variational problem (CVP, see introduction) satisfy

$$\frac{\mathrm{d}s}{\mathrm{d}\omega}\left(\omega_{eq}\right)=\beta\psi_{eq}, \tag{15}$$

where β is the Lagrange's multiplier for the energy. Solutions to this equation are stationary states for the Euler equation. Moreover, with suitable assumptions for the function s, such flows are proved to be nonlinearly stable [9].

This last equation is very similar to the one satisfied by RSM equilibria (13). Indeed let us define s_α the Legendre–Fenchel transform of $\log z_\alpha$

$$s_\alpha\left(\omega\right)=\sup_u\left\{u\omega-\log z_\alpha\left(u\right)\right\}. \tag{16}$$

Then s_α is convex. Moreover, if $\log z_\alpha$ is differentiable, then direct computations lead to

$$s_\alpha\left(\omega\right)=\omega g_\alpha\left(\omega\right)-\log\left(z_\alpha\left(g_\alpha\left(\omega\right)\right)\right) \tag{17}$$

and to $\mathrm{d}s/\mathrm{d}\omega=g_\alpha$. The equilibrium relations (13) and (15) with $s=s_\alpha$, are the same ones. It been observed in the past by a number of authors (see for instance [2]).

Let us prove that (14) and (CVP) are equivalent if $s=s_\alpha$. More precisely, we assume that Lagrange's multipliers rule applies, and we prove that minimizers of both variational problems have the same ω_{eq} and that $C(E_0,s_\alpha)=G(E_0,\alpha)$.

We consider a minimizer ρ_{eq} of (14) and $\omega_{eq}=\int\mathrm{d}\sigma\sigma\rho_{eq}$. Then $E\left[\omega_{eq}\right]=E_0$ and $G(E_0,\alpha)=\mathcal{G}_\alpha\left[\rho_{eq}\right]$. A Lagrange multiplier β then exists such that ρ_{eq} satisfies Eq. (11). Direct computation gives $\rho_{eq}\log\rho_{eq}+\alpha\rho_{eq}=\exp\left(\beta\sigma\psi_{eq}-\alpha\left(\sigma\right)\right)\left[-\log z_\alpha\left(\beta\psi_{eq}\right)+\beta\sigma\psi_{eq}\right]/z_\alpha\left(\beta\psi_{eq}\right)$. Using $\omega_{eq}=\int\mathrm{d}\sigma\sigma\rho_{eq}$, (13) and (17), we obtain

$$\int_{-\infty}^{+\infty}\mathrm{d}\sigma\left(\rho_{eq}\log\rho_{eq}+\alpha\rho_{eq}\right)=-\log z_\alpha\left(\beta\psi_{eq}\right)+\beta\psi_{eq}\omega_{eq}$$
$$=s_\alpha\left(\omega_{eq}\right). \tag{18}$$

From the definitions of $\mathcal{G}$ and $\mathcal{C}$, we obtain $G(E_0,\alpha)=\mathcal{G}_\alpha\left[\rho_{eq}\right]=\mathcal{C}_{s_\alpha}\left[\omega_{eq}\right]$. Now, as C is an infimum, $C_{s_\alpha}\left[\omega_{eq}\right]\geq C(E_0,s_\alpha)$ and

$$G(E_0,\alpha)\geq C(E_0,s_\alpha).$$

We now prove the opposite inequality. Let $\omega_{eq,2}$ be a minimizer of (CVP) with $s=s_\alpha$. Then there exists β_2 such that (15) is satisfied with $\mathrm{d}s_\alpha/\mathrm{d}\omega=g_\alpha$. We then define $\rho_{eq,2}\equiv\exp\left[\sigma\beta_2\psi_{eq,2}-\alpha\left(\sigma\right)\right]/z_\alpha\left(\beta_2\psi_{eq,2}\right)$. Following the same computations as in (18), we conclude that $\mathcal{G}_\alpha\left[\rho_{eq,2}\right]=\mathcal{C}_{s_\alpha}\left[\omega_{eq,2}\right]=C(E_0,s_\alpha)$. Then using that G is an infimum we have $G(E_0,\alpha)\leq C(E_0,s_\alpha)$ and thus

$$G(E_0,\alpha)=C(E_0,s_\alpha).$$

Then $C_{s_\alpha}\left[\omega_{eq}\right]=C(E_0,s_\alpha)=G(E_0,\alpha)=\mathcal{G}_\alpha\left[\rho_{eq,2}\right]$. Thus ω_{eq} and $\rho_{eq,2}$ are minimizers of (CVP) and of (14) respectively. But as such minimizers are in general not unique, ω_{eq} may be different from $\omega_{eq,2}$ and β may be different from β_2.

A formal, but very instructive, alternative way to obtain equivalence between (CVP) and (14) is to note that

$$C_{s_\alpha}\left[\omega\right]=\inf_{\{\rho|N[\rho]=1\}}\left\{\mathcal{G}_\alpha\left[\rho\right]|\int_{-\infty}^{+\infty}\mathrm{d}\sigma\sigma\rho=\omega(\mathbf{x})\right\}. \tag{19}$$

We do not detail the computation. A proof of this result is easy as we minimize a convex functional with linear constraints. Then, from (14), using (19), we obtain

$$\begin{aligned}G(E_0,\alpha)&\\&=\inf_\omega\left\{\inf_{\{\rho|N[\rho]=1\}}\left\{\mathcal{G}_\alpha[\rho]|\int\mathrm{d}\sigma\sigma\rho=\omega(\mathbf{x})\right\}|E\left[\overline{\omega}\right]=E_0\right\}\\&=C(E_0,s_\alpha).\end{aligned}$$

3.2. Second variations and local stability equivalence

In the previous section, we have proved that the constrained Casimir (CVP) and mixed ensemble (14) variational problems are equivalent, for global minimization. Does this equivalence also hold for local minima ? We now prove that the reply is positive.

We say that a critical point ρ_{eq} of the constrained mixed ensemble variational problem (14) is locally stable iff the second variations $\delta^2\mathcal{J}_\alpha$, of the associated free energy $\mathcal{J}_\alpha=\mathcal{G}_\alpha+\beta E$, are positive for perturbations $\delta\rho$ that respect the linearized energy constraints $\int_{\mathcal{D}}\psi_{eq}\delta\omega=0$, where $\delta\omega=\int\mathrm{d}\sigma\sigma\delta\rho$. Similarly, the second variations $\delta^2\mathcal{D}_s$ of the free energy $\mathcal{D}_s=\mathcal{C}_s+\beta E$ define the local stability of the Casimir maximization.

By a direct computation, we have $\delta^2\mathcal{G}_\alpha\left[\delta\rho\right]=-\delta^2\mathcal{S}_\alpha\left[\delta\rho\right]=\int_{\mathcal{D}}\mathrm{d}\mathbf{x}\int\mathrm{d}\sigma\frac{1}{\rho_{eq}}\left(\delta\rho\right)^2$ and $\delta^2\mathcal{C}_{s_\alpha}\left[\delta\omega\right]=\int_{\mathcal{D}}\mathrm{d}\mathbf{x}s''_\alpha\left(\omega_{eq}\right)\left(\delta\omega\right)^2$.

We decompose any $\delta\rho$ as

$$\delta\rho = \delta\rho^{\parallel} + \delta\rho^{\perp} \quad \text{with } \delta\rho^{\parallel} = \frac{\delta\omega}{f'_\alpha}\left(\frac{-z'_\alpha + \sigma z_\alpha}{z_\alpha^2}\right)\exp\left[\sigma\beta\psi_{eq} - \alpha(\sigma)\right].$$

In this expression, the functions f'_α, z_α and z'_α are evaluated at the point $\beta\psi_{eq}$. Using the definition of f_α and of z_α (12), and the fact that $f'_\alpha = \left(-z'^2_\alpha + z_\alpha z''_\alpha\right)/z_\alpha^2$ we easily verify that the above expression is consistent with the relation $\delta\omega = \int \mathrm{d}\sigma\sigma\delta\rho$.

Moreover by lengthy but straightforward computations, we verify that $\int \mathrm{d}\sigma\delta\rho^{\parallel}\delta\rho^{\perp}/\rho_{eq} = 0$. In this sense, the decomposition $\delta\rho = \delta\rho^{\parallel} + \delta\rho^{\perp}$ distinguishes the variations of ρ that are normal to equilibrium relation (11) from the tangential ones.

From $s'_\alpha = g_\alpha$ and using that $(g_\alpha)^{-1} = f_\alpha$, we obtain $s''_\alpha = \left(f'_\alpha\right)^{-1}$. Using this relation we obtain $\int \mathrm{d}\sigma\left(\delta\rho^{\parallel}\right)^2/\rho_{eq} = s''_\alpha\left(\omega_{eq}\right)(\delta\omega)^2$. We thus conclude

$$\delta^2\mathcal{J}_\alpha[\delta\rho] = \int_{\mathcal{D}} \mathrm{d}^2x \int_{-\infty}^{+\infty} \mathrm{d}\sigma \frac{1}{\rho_{eq}}\left(\delta\rho^{\perp}\right)^2 + \delta^2\mathcal{D}_{s_\alpha}[\delta\omega]. \quad (20)$$

To the best of our knowledge, this equality has never been derived before in this context, see [21] in plasma physics (information provided by one of the referee). It may be very useful as second variations are involved in many stability discussions.

From equality (20), it is obvious that the second variations of $\mathcal{J}_\alpha$ are positive iff the second variations of $\mathcal{D}_{s_\alpha}$ are positive. If we also note that perturbations which respect the linearized energy constraint are the same for both functionals, we conclude that the local stabilities of the two variational problems are equivalent.

4. Relation between RSM equilibria and stream function functionals

In this section, we establish the relation between stream function functionals and RSM equilibria. For this we consider the constrained Casimir variational problem (CVP). However, we relax the energy constraint. We thus consider the free energy associated to CVP

$$F(\beta, s) = \inf_{\omega}\left\{\mathcal{F}_s[\omega] = \mathcal{C}_s[\omega] + \beta E[\omega]\right\}. \quad (21)$$

This is an Energy-Casimir functional [9]. As previously explained, minima of this relaxed variational problem are also minimum (CVP). It is thus also a RSM equilibria.

Let $\tilde{G}$ be the Legendre–Fenchel transform of the function s: $\tilde{G}(z) = \sup_y\{zy - s(y)\}$. $\tilde{G}$ is thus convex. Let us define $G_\beta(\psi) = \tilde{G}(\beta\psi)/\beta$. G_β is thus convex for positive β and concave for negative β. In the following, we will show that the variational problem (21) is equivalent to the SFVP

$$D\left(G_\beta\right) = \inf_{\psi}\left\{\mathcal{D}_{G_\beta}[\psi] = \int_{\mathcal{D}} \mathrm{d}^2x\left[|\nabla\psi|^2 + G_\beta(\psi)\right]\right\}.$$

More precisely in the following discussion we prove that

1. $F(\beta, s) = -\beta D(G_\beta)$.
2. If ψ_{eq} is a local minimizer of $\mathcal{D}_{G_\beta}$ then it is a local minimizer of $\mathcal{F}_s$.
3. If we assume that a global minimizer of $\mathcal{D}_{G_\beta}$ exists, then $\omega_{eq} = \Delta\psi_{eq}$ is a global minimizer of $\mathcal{F}_s$ if and only if ψ_{eq} is a global minimizer of $\mathcal{D}_{G_\beta}$.

When $\mathcal{D}_{G_\beta}[\psi]$ and $\mathcal{F}_s[\omega]$ are strictly convex, both variational problems have a single minimizer. As the equations for the critical points of the variational problems coincide, points 2. and 3. above are thus easily verified [11]. Conditions for $\mathcal{D}_{G_\beta}[\psi]$ and $\mathcal{F}_s[\omega]$ to be strictly convex are given, for instance in [11], or [9] for $\mathcal{F}_s[\omega]$. This is obvious for positive temperature $\beta > 0$, as G_β is convex in this case. For negative temperature, G_β is concave. However, if we assume that $\tilde{G}''$ is bounded $0 \le \tilde{G}''(z) \le g$, then it can be proven that $\mathcal{D}_{G_\beta}[\psi]$ is strictly convex for $\beta_c \le \beta \le 0$, with $\beta_c \le \lambda_1/g$, where λ_1 is the opposite of the first eigenvalue of the Laplacian over the domain $\mathcal{D}$ (this follows from the Poincaré inequality, see [9,11]). ($\tilde{G}''$ is actually bounded, for instance if the vorticity distribution $\gamma(\sigma)$ (5) has a compact support, or for the point vortex model). In the following we prove that results 1., 2. and 3. are valid also when $\mathcal{D}_{G_\beta}[\psi]$ and $\mathcal{F}_s[\omega]$ are no longer convex.

In order to prove these results for negative temperature $\beta < 0$, it is sufficient to prove:

(a) $\omega_c = \Delta\psi_c$ is a critical points of $\mathcal{F}_s$ if and only if ψ_c is a critical point of $\mathcal{D}_G$, and then $\mathcal{F}_s[\omega_c] = -\beta\mathcal{D}_{G_\beta}[\psi_c]$.
(b) For any $\omega = \Delta\psi$, $\mathcal{F}_s[\omega] \ge -\beta\mathcal{D}_{G_\beta}[\psi]$.

Point **(a)** has been noticed in [13], and is actually sufficient to prove points 1 and 2. The inequality **(b)** [22] proves that $\mathcal{D}_{G_\beta}$ is a support functional to $\mathcal{F}_s$ [22]. Let us prove points **(a)** and **(b)**. First, the critical points of $\mathcal{F}_s$ and $\mathcal{D}_{G_\beta}$ verify $s'(\omega_c) = \beta\psi_c$ and $\omega_c = G'(\beta\psi_c)$. Now using that G is the Legendre–Fenchel transform of s, if s is differentiable, we have $\left(s'\right)^{-1} = G'$. Thus the critical points of both functionals are the same.

Let us prove point **(b)**

$$\mathcal{F}_s[\omega] = -\int_{\mathcal{D}} \mathrm{d}^2x\left[-s(\omega) + \beta\omega\psi\right] + \int_{\mathcal{D}} \mathrm{d}^2x\frac{\beta}{2}\omega\psi \ge \int_{\mathcal{D}} \mathrm{d}^2x\left[-G(\beta\psi) + \frac{\beta}{2}\omega\psi\right] = -\beta\mathcal{D}_{G_\beta}[\psi]$$

where we have used the definition of G, as the Legendre–Fenchel transform of s, in order to prove the inequality. We now conclude the proof of point **(a)**. A direct computation gives $G(x) = x\left(s'\right)^{-1}(x) - s\left[\left(s'\right)^{-1}(x)\right]$. Thus $G(\beta\psi_c) = \beta\psi_c\omega_c - s(\omega_c)$. This proves that in the preceding inequality, an equality actually occurs for the critical points: $\mathcal{F}_s[\omega_c] = -\beta\mathcal{D}_{G_\beta}[\psi_c]$.

We have thus established the relations between RSM equilibria and the simpler Casimirs (CVP) and stream function (SFVP) variational problems.

Acknowledgments

I warmly thank J. Barré, T. Dauxois, F. Rousset and A. Venaille for helpful comments and discussions. This work was supported by the ANR program STATFLOW (ANR-06-JCJC-0037-01).

References

[1] R. Robert, A maximum-entropy principle for two-dimensional perfect fluid dynamics, J. Stat. Phys. 65 (1991) 531–553.

[2] R. Robert, J. Sommeria, Statistical equililbrium states for two-dimensional flows, J. Fluid Mech. 229 (1991) 291–310.

[3] J. Miller, Statistical mechanics of Euler equations in two dimensions, Phys. Rev. Lett. 65 (17) (1990) 2137–2140.

[4] G.L. Eyink, K.R. Sreenivasan, Onsager and the theory of hydrodynamic turbulence, Rev. Modern Phys. 78 (2006) 87–135.

[5] A.J. Majda, X. Wang, Nonlinear Dynamics and Statistical Theories for Basic Geophysical Flows, Cambridge University Press, 2006.

[6] R.S. Ellis, K. Haven, B. Turkington, Nonequivalent statistical equilibrium ensembles and refined stability theorems for most probable flows, Nonlinearity 15 (2002) 239–255.

[7] P.-H. Chavanis, Generalized thermodynamics and Fokker–Planck equations: Applications to stellar dynamics and two-dimensional turbulence, Phys. Rev. E 68 (3) (2003) 036108.

[8] P.-H. Chavanis, Statistical mechanics of geophysical turbulence: Application to jovian flows and Jupiter's great red spot, Physica D 200 (2005) 257–272.

[9] V.I. Arnold, On an a-priori estimate in the theory of hydrodynamic stability, Izv. Vyssh. Uchebbn. Zaved. Matematika. Engl. transl.: Am. Math. Soc. Trans. 79 (2).

[10] D.D. Holm, J.E. Marsden, T. Ratiu, A. Weinstein, Nonlinear stability of fluid and plasma equilibria, Phys. Rep. 123 (1985) 1–2.

[11] J. Michel, R. Robert, Statistical mechanical theory of the great red spot of jupiter, J. Stat. Phys. 77 (3-4) (1994) 645–666.

[12] F. Bouchet, J. Sommeria, Emergence of intense jets and jupiter's great red spot as maximum entropy structures, J. Fluid Mech. 464 (2002) 165–207.

[13] F. Bouchet, Mécanique statistique des écoulements géophysiques, PHD, Univ. J. Fourier Grenoble, 2001.

[14] F. Bouchet, T. Dumont, Emergence of the great red spot of jupiter from random initial conditions. cond-mat/0305206.

[15] R.S. Ellis, K. Haven, B. Turkington, Large deviation principles and complete equivalence and nonequivalence results for pure and mixed ensembles, J. Stat. Phys. 101 (2000) 999.

[16] T. Dauxois, S. Ruffo, E. Arimondo, M. Wilkens (Eds.), Dynamics and Thermodynamics of Systems With Long Range Interactions, 2002.

[17] F. Bouchet, J. Barré, Classification of phase transitions and ensemble inequivalence, in systems with long range interactions, J. Stat. Phys. 118 (5/6) (2005) 1073–1105.

[18] R.A. Smith, T.M. O'Neil, Nonaxisymmetric thermal equilibria of a cylindrically bounded guiding-center plasma or discrete vortex system, Phys. Fluids B 2 (1990) 2961–2975.

[19] M.K.H. Kiessling, J.L. Lebowitz, The micro-canonical point vortex ensemble: Beyond equivalence, Lett. Math. Phys. 42 (1) (1997) 43–56.

[20] E. Caglioti, P.L. Lions, C. Marchioro, M. Pulvirenti, A special class of stationary flows for two-dimensional euler equations: A statistical mechanics description. Part II, Comm. Math. Phys. 174 (1995) 229–260.

[21] K. Schindler, Physics of Space Plasma Activity, Cambridge University Press, 2006.

[22] G. Wolansky, M. Ghil, Nonlinear stability for saddle solutions of ideal flows and symmetry breaking, Comm. Math. Phys. 193 (1998) 713–736.

Available online at www.sciencedirect.com
ScienceDirect
Physica D 237 (2008) 1982–1988
PHYSICA D
www.elsevier.com/locate/physd

Generalized solutions and hydrostatic approximation of the Euler equations

Yann Brenier*

CNRS, FR 2800 Wolfgang Döblin, Université de Nice, France
Institut für Angewandte Mathematik der Universiät Bonn, Germany

Available online 4 March 2008

Abstract

Solutions to the Euler equations on a 3D domain D_3 (typically the unit cube or the periodic unit cube) can be formally obtained by minimizing the action of an incompressible fluid moving inside D_3 between two given configurations. When these two configurations are very close to each other, classical solutions do exist, as shown by Ebin and Marsden. However, Shnirelman found a class of data (essentially 2D in the sense that they trivially depend on the vertical coordinate) for which there cannot be any classical minimizer. For such data, generalized solutions can be shown to exist, as a substitute for classical solutions. These generalized solutions have unusual features that look highly unphysical (in particular, different fluid parcels can cross at the same point and at the same time), but the pressure field, which does not depend on the vertical coordinate, is well and uniquely defined. In the present paper, we show that these generalized solutions are actually quite conventional in the sense they obey, up to a suitable change of variable, a well-known variant (widely used for geophysical flows) of the 3D Euler equations, for which the vertical acceleration is neglected according to the so-called hydrostatic approximation.

PACS: 47.10.A-; 47.15.ki

Keywords: Incompressible fluids; Euler equations; Hydrostatic approximation; Generalized solutions

1. The Euler equations

A fluid moving inside a 3D compact domain D_3, such as the unit cube or the periodic unit cube, can be described by a time-dependent family $t \to g(t)$ of orientation preserving diffeomorphisms of D_3 giving, at each time t, the position $g(t, a)$ of each fluid parcel of initial position $g(0, a) = a$ in D_3. A fluid is incompressible if and only if, for each t, the map

$a \in D_3 \to g(t, a) \in D_3$

has a unit Jacobian determinant $|\partial_a g(t, a)| = 1$ or, equivalently,

$$\int_{D_3} f(g(t, a))\mathrm{d}a = \int_{D_3} f(a)\mathrm{d}a, \tag{1}$$

for all continuous function f. The fluid obeys the Euler equations if and only if g satisfies:

$$\partial^2_{tt} g(t, a) = -(\nabla p)(t, g(t, a)), \tag{2}$$

for some time-dependent scalar field $p(t, x)$ (called the pressure field), that plays the role of a Lagrange multiplier for the incompressibility condition. Introducing the Eulerian velocity field $u(t, x) \in R^3$, defined by:

$$u(t, g(t, a)) = \partial_t g(t, a), \tag{3}$$

we recover from (2) the more familiar Euler equations written in "Eulerian coordinates" [9]:

$$\partial_t u + (u \cdot \nabla)u + \nabla p = 0, \tag{4}$$

together with the divergence free condition $\nabla \cdot u = 0$. The mathematical analysis of this system of non-linear PDEs is one of the most important and challenging problem in modern analysis (see [10–12] for discussions). As Euler said: "s'il reste des difficultés, ce ne sera pas du côté du méchanique, mais uniquement du côté de l'analytique" [9] (first page of the original edition).

* Corresponding address: CNRS, FR 2800 Wolfgang Döblin, Université de Nice, France.
E-mail address: brenier@math.unice.fr.
URL: http://math1.unice.fr/~brenier/.

0167-2789/$ - see front matter © 2008 Elsevier B.V. All rights reserved.
doi:10.1016/j.physd.2008.02.026

2. The Least Action principle

The Euler equations, written in “Lagrangian coordinates” (2), have a variational interpretation. For smooth g and p, they *exactly* means that, for each time interval $[t_0, t_1]$, the curve $t \to g(t)$ makes stationary the Action

$$\int_{t_0}^{t_1} \int_{D_3} \frac{1}{2} |\partial_t g(t,a)|^2 \, \mathrm{d}a \, \mathrm{d}t, \tag{5}$$

among all smooth curves valued in $SDiff(D_3)$, the class of volume and orientation preserving diffeomorphisms of D_3, that coincide with g at $t = t_0$ and $t = t_1$. This can be seen immediately by varying with respect to both g and p the Lagrangian:

$$\int_{t_0}^{t_1} \int_{D_3} \left(\frac{1}{2} |\partial_t g(t,a)|^2 - p(t, g(t,a)) + p(t,a) \right) \mathrm{d}a \, \mathrm{d}t,$$

that takes into account the incompressibility constraint (1) (obtained by varying p only). In addition, the curve is not only a critical point of the Action but also a minimizer if the time interval is small enough. If D_3 is a convex domain, a sufficient condition for that is:

$$(t_1 - t_0)^2 \sum_{i,j=1,3} \frac{\partial^2 p(t,x)}{\partial x_i \partial x_j} \xi_i \xi_j \le \pi^2 |\xi|^2, \tag{6}$$

for all $t \in [t_0, t_1]$, $x \in D_3$ and $\xi \in R^3$. (This can be shown using the 1D Poincaré inequality.) Thus the Euler equations are governed by the Least Action Principle, as guessed from the very beginning by Euler himself ([9] p. 287 of the original edition): “Cette belle propriété convient admirablement avec le beau principe de la moindre action dont nous devons la découverte à notre Illustre Président, M. de Maupertuis.” Through the Least Action Principle, a remarkable geometric interpretation of the Euler equations has been emphasized by Arnold (see [2,3] for more details): the Euler equations are just the equations of geodesics curves (with constant speed) along the group of all orientation and volume preserving diffeomorphisms $SDiff(D_3)$ for the metric induced by the embedding of the group in the space L^2 of all square integrable maps from D_3 into R^3.

3. The Action Minimization problem

The Least Action Principe suggests a possible (and of course not unique) way to get solutions to the Euler equations. We minimize (5), where $t_0 < t_1$ are fixed and $g(t_0) = h_0$, $g(t_1) = h$ are prescribed in $SDiff(D_3)$. Due to the homogeneity of the Euler equations, we can normalize $t_0 = 0$, $t_1 = 1$ and assume h_0 to be the identity map, so that the only datum is $h \in SDiff(D_3)$. The Action Minimization problem has indeed smooth solutions (which do satisfy the Euler equations) provided that h is sufficiently close to the identity in some suitable norm (typically for the Sobolev norm $H^s(D_3)$ with $s > 5/2$). This has been shown by Ebin and Marsden in [8]. However, in the large, as shown by Shnirelman [15], in the case when D_3 is the unit cube $[0, 1]^3$, there are data h for which the existence of a smooth minimizer is impossible. Shnirelman’s data are of form:

$$h(a) = (H(a_1, a_2), a_3), \quad a = (a_1, a_2, a_3) \in [0, 1]^3, \tag{7}$$

where H belongs to $SDiff([0, 1]^2)$, the set of all area and orientation preserving diffeomorphisms of the unit square $[0, 1]^2$.

They are chosen [15] so that whenever a minimizer g exists, it must have a non-trivial vertical component (i.e. $g_3(t,a) = a_3$ is impossible). (In other words, the Action can be reduced by using some vertical motion between $t = 0$ and $t = 1$. As a matter of fact, this happens for a lot of maps H, since purely horizontal motions are very rigid in comparison with fully 3D motions.) Then, we easily see that for such data H classical minimizers cannot exist. Indeed, any admissible solution $g(t,a)$ with non-trivial vertical component, as well as the corresponding Eulerian velocity field $u(t,x)$ defined by (3), can be rescaled in its vertical component by a positive integer factor n which leads to a strictly lower value of the Action. More precisely, let us define the rescaled space coordinate:

$$x^{(n)} = (x_1, x_2, n x_3 \ \text{ modulo } 1), \quad x = (x_1, x_2, x_3),$$

the rescaled velocity:

$$u^{(n)}(t,x) = (u_1(t, x^{(n)}), u_2(t, x^{(n)}), n^{-1} u_3(t, x^{(n)})),$$

and recover the corresponding $g^{(n)}$ through (3). The remarkable fact is that $g^{(n)}$ is still admissible, with unit Jacobian determinant (because $u^{(n)}$ is still divergence free) and unchanged end point values:

$$g^{(n)}(0,a) = g(0,a) = a,$$
$$g^{(n)}(1,a) = g(1,a) = h(a) = (H(a_1,a_2), a_3)$$

(because h depends trivially on the vertical coordinate), but has a strictly reduced Action, given by:

$$\int \frac{1}{2} \{ \partial_t g_1(t,a)^2 + \partial_t g_2(t,a)^2 + n^{-2} \partial_t g_3(t,a)^2 \} \, \mathrm{d}a \, \mathrm{d}t.$$

Since there is no end to this rescaling process, we conclude that there cannot be a minimizer, at least in a classical sense. (Strictly speaking, there is a flaw in the previous reasoning, since the renormalized flow may loose the smoothness of the original flow. This can be cured in two ways. The first one followed by Shnirelman amounts to slightly mollify the renormalized flow. The second one is to do the construction on the *periodic* unit cube, in which case there is no mollification to do.)

4. The hydrostatic approximation

In the case of Shnirelman’s data, when we try to minimize the Action, we cannot get a classical solution because of the degeneracy of the data in the vertical coordinate, as explained in the previous section. It is therefore natural to minimize instead the renormalized Action obtained by dropping the vertical component of the velocity in definition (5). Then, we expect to get, at least formally, generalized solutions that substitute for the missing classical solutions. More precisely, we are now looking for a solution $t \to g(t)$ still valued in $SDiff([0,1]^3)$, with $g(0,a) = a$, $g(1,a) = h(a) = (H(a_1,a_2),a_3)$, that minimizes:

$$\int_0^1 \int_{[0,1]^3} \{\partial_t g_1(t,a)^2 + \partial_t g_2(t,a)^2\}\,\mathrm{d}a\,\mathrm{d}t, \tag{8}$$

where the vertical component of the velocity has been dropped. The corresponding Lagrangian now reads:

$$\int \left\{ \frac{1}{2}(\partial_t g_1(t,a)^2 + \partial_t g_2(t,a)^2) - p(t,g(t,a)) + p(t,a) \right\} \mathrm{d}a\,\mathrm{d}t.$$

The *formal* optimality equations are just:

$$\partial^2_{tt} g_i(t,a) + (\partial_i p)(t,g(t,a)) = 0, \quad i = 1,2, \tag{9}$$
$$(\partial_3 p)(t,g(t,a)) = 0,$$

in addition to the incompressibility condition (1). Written in Eulerian coordinates, with the velocity field u given by (3), these equations

$$\partial_t u_i(t,a) + (u\cdot\nabla)u_i + \partial_i p = 0, \quad i = 1,2, \tag{10}$$
$$\partial_3 p = 0, \quad \nabla\cdot u = 0, \tag{11}$$

are nothing but the Euler equations where the vertical acceleration is neglected under the so-called "hydrostatic approximation" which is widely used for the modelling of geophysical flows [14]. In particular, the pressure field does not depend on the vertical coordinate.

5. Generalized flows and generalized Euler equations

Although the motion described by the hydrostatic approximation (10) to the Euler equations is fully 3D, the vertical component is actually slaved by the horizontal one. Indeed, we may completely ignore g_3 and still find a self-consistent set of equations for p and the horizontal components (g_1,g_2). To do that, we keep (9), with the boundary conditions at $t = 0$ and $t = 1$:

$$(g_1,g_2)(t=0,a_1,a_2,a_3) = (a_1,a_2), \tag{12}$$
$$(g_1,g_2)(t=1,a_1,a_2,a_3) = H(a_1,a_2),$$

corresponding to a Shnirelman data, and we use the incompressibility condition (1) only for continuous functions $f(a_1,a_2)$ that do not depend on a_3, which leads to:

$$\int_{[0,1]^3} f((g_1,g_2)(t,a_1,a_2,a_3))\mathrm{d}a_1\mathrm{d}a_2\mathrm{d}a_3 = \int_{[0,1]^2} f(a_1,a_2)\mathrm{d}a_1\mathrm{d}a_2. \tag{13}$$

At this point, the full incompressibility condition (1) is not needed to get (p,g_1,g_2) but can be used *a posteriori* to recover the vertical component g_3 from the horizontal component (g_1,g_2). Notice the particular role of a_3 in these equations, which is just an extra parameter without geometrical meaning, and that we may decide now to call ω (just as a random variable valued in a probability space Ω). So the horizontal component of the 3D Euler flow obtained through the hydrostatic approximation, $G = (g_1,g_2)$, can also be seen as a non-classical 2D flow on the horizontal domain $D = [0,1]^2$. This flow does not look conventional at all, since each 2D fluid parcel initially located at $A = (a_1,a_2) \in D$ may split and follow different paths (that are allowed to cross each other!), each of them being labelled by $\omega \in \Omega$:

$$t \in [0,1] \to G(t,A,\omega) \in D, \tag{14}$$

with time boundary conditions:

$$G(t=0,A,\omega) = A, \qquad G(t=1,A,\omega) = H(A). \tag{15}$$

This unusual description of a 2D flow becomes natural once it is understood that G actually is the horizontal projection of a conventional 3D incompressible flow. Indeed, each 2D fluid parcel initially located at $A \in D$ actually corresponds to an entire vertical column of 3D fluid parcels. This column ends up at time $t = 1$ as the vertical column above $H(A)$. However, at each intermediary time $0 < t < 1$, the 3D fluid parcels initially above A do not necessarily form a vertical column but rather a curve in $[0,1]^3$ with horizontal projection given by $\omega \to G(t,A,\omega)$. So the strange behaviour of the 2D "generalized" flow described by G comes naturally from the projection from 3 to 2 dimensions. Also notice that condition (13) can be understood as a generalized incompressibility condition, meaning that the density of the fluid parcels stays uniform on D:

$$\int_{D\times\Omega} f(G(t,A,\omega))\mathrm{d}A\,\mathrm{d}\omega = \int_D f(A)\mathrm{d}A, \tag{16}$$

for all function f continuous on D. In this language, the optimality condition, say (9), becomes a generalized version of the 2D Euler equation:

$$\partial^2_{tt} G(t,A,\omega) + (\nabla p)(t,G(t,A,\omega)) = 0, \tag{17}$$

where $p = p(t,x)$ is a time-dependent function defined on D. Let us finally observe that the renormalized Action (8) can be easily written as:

$$\frac{1}{2}\int_0^1 \mathrm{d}t \int_{D\times\Omega} |\partial_t G(t,A,\omega)|^2 \mathrm{d}A\,\mathrm{d}\omega. \tag{18}$$

So, in this section, we have derived from the hydrostatic approximation of the Euler equations (that comes up in a natural way to deal with Shnirelman's data for the Action Minimization problem), a generalized framework (14) and (16)–(18), that can be used outside of the hydrostatic context and still makes sense for a general d-dimensional domain D, not only the unit square $[0,1]^2$, and without referring to any additional dimension. In particular, D can be taken to be D_3 itself. In addition, time boundary data can be taken in a much more general class than Shnirelman's data as in (15). As a matter of fact, $G(t=0,A,\omega) \in D$ and $G(t=1,A,\omega) \in D$ can be chosen arbitrarily provided they are compatible with the generalized incompressibility condition (16). In particular, we

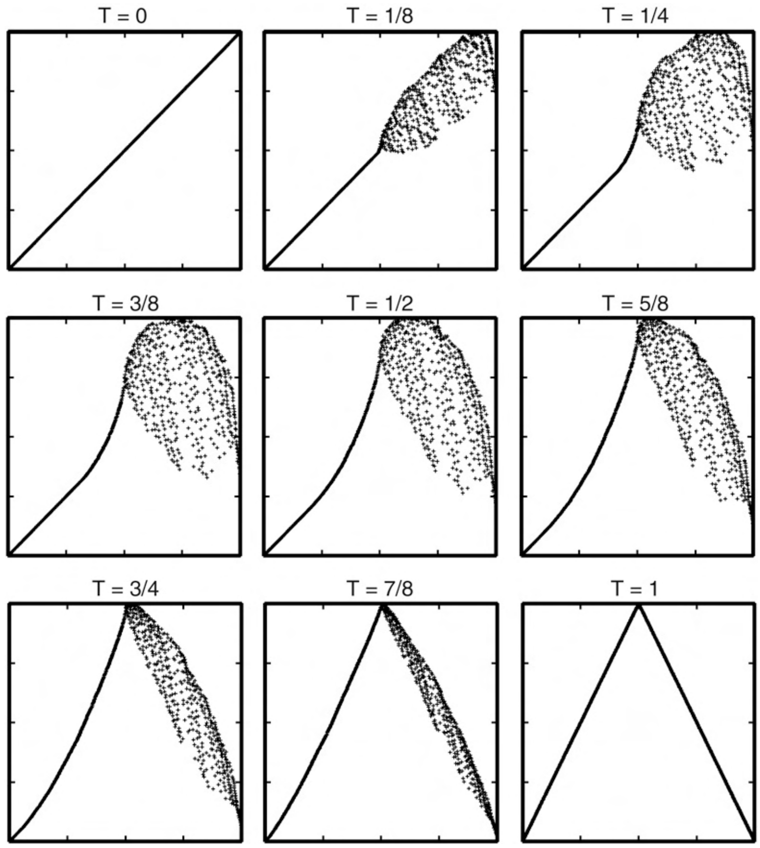

Fig. 1. Approximate geodesic for map 1.

can consider boundary data of type (15), where H is chosen in the class $M(D)$ of all measure preserving map of D, which means that H is just a (Borel) measurable maps that satisfy

$$\int_D f(H(A))\mathrm{d}A = \int_D f(A)\mathrm{d}A, \tag{19}$$

for all function f continuous on D.

6. Mathematical analysis of the Action Minimization problem

So far, we have just made a formal analysis of the Action Minimization problem for Shnirelman's data (7) leading in a natural way to the hydrostatic approximation to the Euler equations, that can rephrased in terms of 2D generalized incompressible flows and generalized 2D Euler equations. A rigorous justification of this formal analysis has been provided in [4,5,16,6,1]. Let us summarize the results obtained in this series of papers. The results are stated either for $D = T^d$ or $D = [0,1]^d$ and $d \geq 1$.

(1) For all generalized data $G(0, A, \omega)$, $G(1, A, \omega)$, there is at least one generalized incompressible flow $G(t, A, \omega)$ that minimizes the generalized Action (18) [4,1].

(2) There is a *unique* pressure gradient $\nabla p(t, x)$ depending only on the data such that the generalized Euler equation (17) is satisfied by G (which is not necessarily unique), in a suitable sense [5]. More precisely, an Eulerian version of the generalized Euler equations has been established in [6]. More recently, Ambrosio and Figalli [1] have shown that (almost surely) each individual trajectories, $t \to \gamma(t) = G(t, A, \omega)$, A and ω being fixed, is a minimizer of the localized Action

$$\int_0^1 \left(\frac{1}{2}|\gamma'(t)|^2 - p(t, \gamma(t))\right) \mathrm{d}t, \tag{20}$$

γ being fixed at time $t = 0$ and $t = 1$. (A key point being that the known regularity of p is sufficient to give sense to this localized Least Action principle.)

(3) In the case $d = 3$, with "deterministic" time boundary data

$$G(t = 0, A, \omega) = A, \qquad G(t = 1, A, \omega) = H(A),$$

where H is a given in $M(D)$ (the class of all measure preserving maps of D, which includes Shnirelman's data), for each generalized solution G and each $\epsilon > 0$, there is a classical incompressible flow $g(t, A)$ such that (i) $g(0, A) = A$, (ii) $g(1, A) - H(A)$ has an L^2 norm less than ϵ, (iii) the classical Action of g (5) differs from the generalized Action of G (18) by less than ϵ. Moreover, the acceleration field $\partial^2_{tt} g \circ g^{-1}$ approaches $-\nabla p$ in the distributional sense as ϵ tends to zero.

The last statement shows that generalized solutions can be approximated by nearly classical solutions to the 3D Euler solutions. In our opinion, all these results provide a full legitimacy to the generalized framework in the mathematical study of the Action Minimization problem for general data H

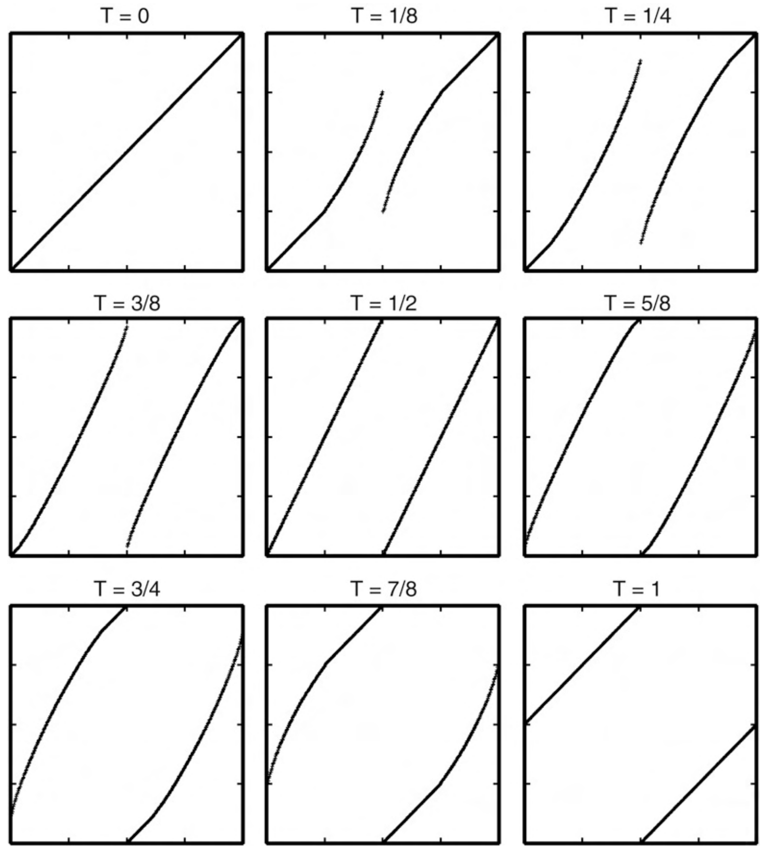

Fig. 2. Approximate geodesic for map 2.

given in $M([0,1]^3)$. In addition, as discussed in the previous sections, in the case of Shnirelman's data, generalized solutions have a clear physical interpretation in terms of hydrostatic approximation to the Euler equations.

7. A numerical scheme

It has been known for a long while that permutations are suitable to approximate volume preserving maps. (See [13,15,7], for example.) This suggests the following strategy to compute approximate solutions to the Action Minimization problem. Hereafter, the computational domain will be $D = [0,1]^d$ (and more specifically $d = 1$ for actual computations). First, we fix two integers N and M. Then, we introduce a uniform time step $1/M$ and we split the unit cube D (up to a set of zero Lebesgue measure) into N^d subcubes, denoted by $D_{N,i}$, for $i = 1, N^d$. The center of mass of each $D_{N,i}$ will be denoted by $x_{N,i}$. To each permutation σ of the N^d first integer, we associate the map H that rigidly moves the subcube $D_{N,i}$ to the subcube $D_{N,\sigma(i)}$, for each $i = 1, N^d$. This map is measure-preserving in the sense of definition (19). We call $P(D)$ the collection of all "permutation maps" obtained this way, for all integers N. The class $M(D)$ of all measure preserving maps of D in the sense of definition (19) can be shown to be the L^2 completion of $P(D)$ for all $d \geq 1$. When $d \geq 2$, $M(D)$ is also the L^2 completion of $SDiff(D)$. (See [13,15,7].) To each sequence of $M+1$ permutations $\sigma_0, \ldots, \sigma_M$, we may associate a "discrete flow" made of the $M+1$ corresponding permutation maps and define a "discrete Action" defined by:

$$\sum_{k=1,M} \sum_{i=1,N^d} |x_{N,\sigma_m(i)} - x_{N,\sigma_{m-1}(i)}|^2. \tag{21}$$

The discrete Action Minimization problem amounts to fix the initial and final permutations and to minimize the discrete Action. Typically the initial permutation is just $\sigma_0(i) = i$ and the final one is chosen so that the corresponding permutation map is an accurate approximation in L^2 of a given measure-preserving map $H \in M(D)$.

8. Numerical results

Let us consider three maps H of the unit cube $D = [0,1]^3$ of the following form:

$$H(a_1, a_2, a_3) = (T(a_1), a_2, a_3) \tag{22}$$

with, successively,

$$T(s) = \min(2s, 2-2s), \quad s \in [0,1],$$
$$T(s) = s + \frac{1}{2} \bmod 1, \quad s \in [0,1],$$
$$T(s) = 1 - s, \quad s \in [0,1].$$

These three maps H clearly belong to the class of measure preserving maps $M(D)$ but certainly not to the class of diffeomorphisms $SDiff(D)$. However, as mentioned earlier, they do belong to the $L^2 closure$ of $SDiff(D)$ and we know that the corresponding generalized solution for the generalized

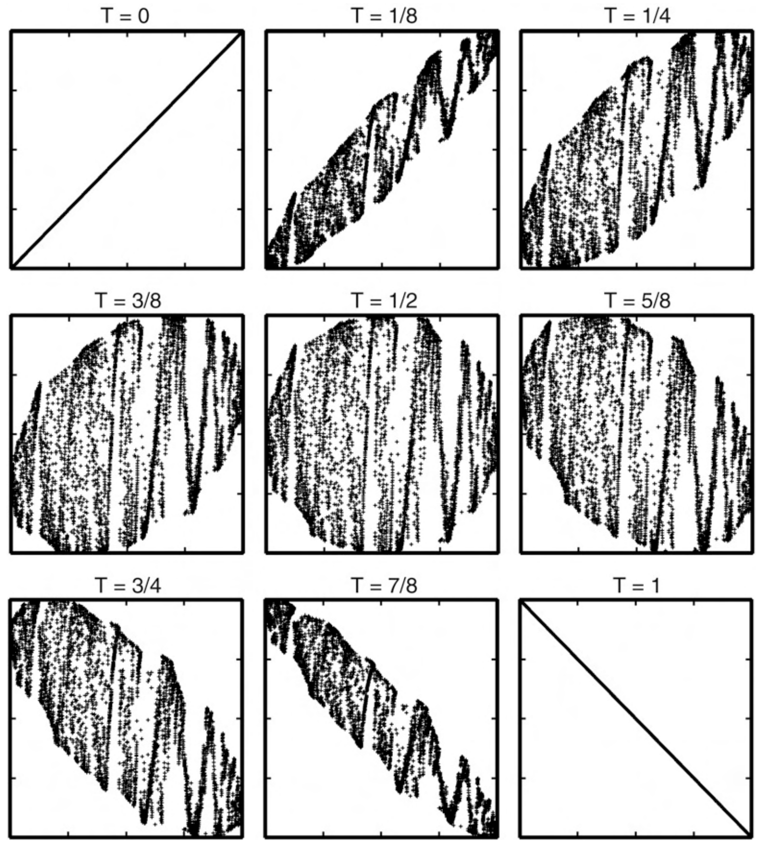

Fig. 3. Approximate geodesic for map 3.

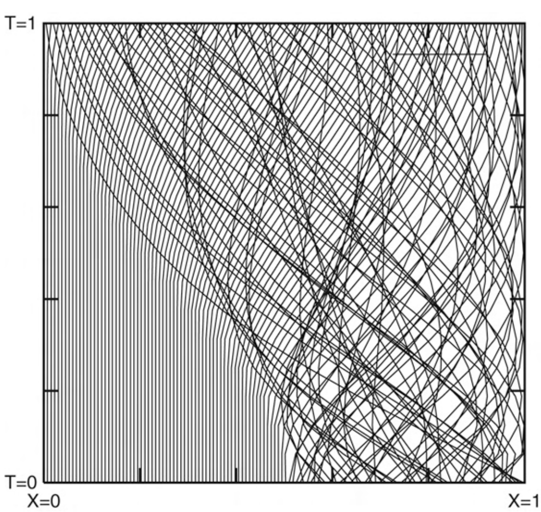

Fig. 4. Trajectories for map 1.

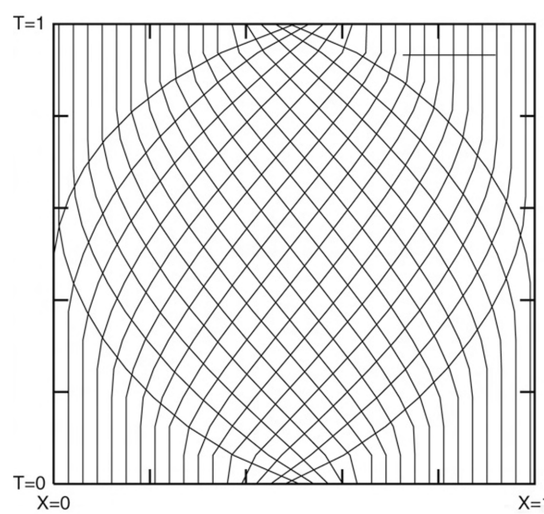

Fig. 5. Trajectories for map 2.

Action Minimization problem describes the limit of nearly solutions to the 3D Euler equations. Therefore, looking for approximate numerical solutions is not meaningless. Since the corresponding T actually belong to $M([0,1])$, the discrete minimization problem can be reduced to one space dimension. Thus, the minimization can be performed very efficiently by using Gauss–Seidel iterations and sorting algorithms. To approximate the first map T, we use the permutation $\sigma(i) = 2i$, for i between 1 and $N/2$, $\sigma(i) = 2N - 2i + 1$, for i between $1 + N/2$ and N. For the second one, $\sigma(i) = N/2 + i$, for i between 1 and $N/2$, $\sigma(i) = i - N/2$, for i between $1 + N/2$ and N. For the third one, $\sigma(i) = N - i + 1$, for i between 1 and $N - 2$, with $\sigma(N) = 2$ and $\sigma(N-1) = 1$. (These two last values are introduced in order to break the symmetry of the algorithm.) Some numerical results are shown at the end of the paper. First, we show (Figs. 1–3), for the three different maps, the successive permutation maps computed at $t = 0$, $t = 1/8$, $t = 1/4$, $t = 3/8$, $t = 1/2$, $t = 5/8$, $t = 3/4$, $t = 7/8$ and $t = 1$. The value of M is 16 and $N = 400$, $N = 100$ and $N = 4000$ respectively. Next, we draw (Figs. 4–6), for the three

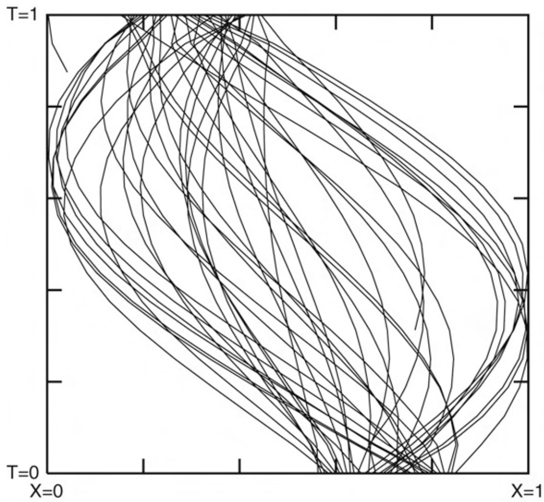

Fig. 6. Selected trajectories for map 3.

different maps, a collection of trajectories (the time axis being vertical, and the space axis being horizontal), obtained by linear interpolation of the discrete trajectories $m \to x_{N,\sigma_{m-1}(i)}$, for a fixed proportion of grid points $i = 1, \ldots, N$. These pictures give a good feeling of the missing dimension(s) encoded by the 1D computation. In particular, for the first map, we see that the particles issued from the right part $[1/2, 1]$ of the unit interval manage to cover the whole unit interval in reverse order through a kind of vortical flow, meanwhile the particles coming from the left also cover the whole interval, but in an order-preserving way through a potential flow. For the second map, we see a kind of two-phase flow, without vorticity. Concerning the third map, for the sake of clarity, we draw trajectories only for the particles initially located in a neighborhood of $x = 3/4$. We see that they form a bundle of trajectories very close at $t = 0$, then diverging and meeting again in a neighborhood of $x = 1/4$ at $t = 1$. At the moment, there is no rigorous convergence analysis of the numerical method. However, for the third map, the exact unique generalized solution is known (see [4]):

$$p(x) = \frac{\pi^2}{2}\left(x - \frac{1}{2}\right)^2, \quad x \in [0, 1],$$
$$G(t, A, \omega) = 1/2 + (A - 1/2)\cos(\pi t) + v(A, \omega)\sin(\pi t),$$
$$v(A, \omega) = \pi\sqrt{\frac{A(1-A)}{2}}\cos(\pi\omega),$$

for $t, A, \omega \in [0, 1]$. We can see that the solution is correctly recovered by the computation. It is striking that a good resolution requires a much more refined mesh in space ($N = 1000$) than in time ($M = 16$).

Acknowledgments

The author is very grateful to the organizers of the Euler 250 Conference, in particular Uriel Frisch, for inviting him to present this paper. This work has been partly supported by the ANR OTARIE grant (ANR BLAN07-2-183172).

References

[1] L. Ambrosio, A. Figalli, Geodesics in the space of measure-preserving maps and plans, CVGMT preprint, Pisa 2007. http://cvgmt.sns.it/cgi/get.cgi/papers/ambfig07/.
[2] V.I. Arnold, Sur la géométrie différentielle des groupes de Lie de dimension infinie et ses applications à l'hydrodynamique des fluides parfaits, Ann. Inst. Fourier 16 (1966) 319–361.
[3] V.I. Arnold, B Khesin, Topological Methods in Hydrodynamics, Springer Verlag, 1998.
[4] Y. Brenier, The least action principle and the related concept of generalized flows for incompressible perfect fluids, J. AMS 2 (1990) 225–255.
[5] Y. Brenier, The Dual Least Action Problem for an Ideal, Incompressible fluid, Arch. Ration. Mech. (1993).
[6] Y. Brenier, Minimal geodesics on groups of volume-preserving maps, Comm. Pure Appl. Math. 52 (1999) 411–452.
[7] Y. Brenier, W. Gangbo, L^p approximation of maps by diffeomorphisms, Calc. Var. Partial Differential Equations 16 (2003) 147–164.
[8] D. Ebin, J. Marsden, Ann. of Math. 92 (1970) 102–163.
[9] L. Euler, Principes généraux du mouvement des fluides, Mémoires de l'académie des sciences de Berlin 11, 274-315, Opera Omnia: Series 2, vol. 12, 1757, 54–91.
[10] P.-L. Lions, Mathematical Topics in Fluid Mechanics. Vol. 1. Incompressible Models, in: Oxford Lecture Series in Mathematics and its Applications, Oxford University Press, New York, 1996.
[11] A. Majda, A. Bertozzi, Vorticity and Incompressible Flow, Cambridge University Press, Cambridge, 2002.
[12] C. Marchioro, M. Pulvirenti, Mathematical Theory of Incompressible Nonviscous Fluids, Springer, New York, 1994.
[13] Y. Neretin, Categories of bistochastic measures and representations of some infinite-dimensional groups, Sb. 183 (1992) 52–76.
[14] J. Pedlosky, Geophysical Fluid Dynamics, Springer, New York, 1979.
[15] A. Shnirelman, On the geometry of the group of diffeomorphisms and the dynamics of an ideal incompressible fluid, Math. Sbornik USSR 56 (1987) 79–105.
[16] A.I. Shnirelman, Generalized fluid flows, their approximation and applications, Geom. Funct. Anal. 4 (1994) 586–620.

Available online at www.sciencedirect.com
ScienceDirect
Physica D 237 (2008) 1989–1992
PHYSICA D
www.elsevier.com/locate/physd

Computational visualization of Shnirelman's compactly supported weak solution

Anne C. Bronzi*, Milton C. Lopes Filho, Helena J. Nussenzveig Lopes

UNICAMP, Brazil

Available online 16 February 2008

Abstract

In [A. Shnirelman, On the non-uniqueness of weak solutions of Euler equations, Comm. Pure Appl. Math. L (1997) 1261–1286], Shnirelman described the construction of a weak solution of the 2D incompressible Euler equations on a torus, with compact support in time. In this article, we use computational tools to obtain an explicit approximation of Shnirelman's flow, with the objective of visualizing its structure. In particular, the construction was based on the use of the 2D inverse energy cascade, and we obtain an illustration on how the inverse cascade is taking place.

PACS: 47.10.A-; 47.15.ki

Keywords: Mathematical formulations; Inviscid flows with vorticity; Finite difference methods

1. Introduction

In [4], Shnirelman constructed a weak solution of the incompressible 2D Euler equations on the torus $\mathbb{T}^2$ which is compactly supported in time. This example is fundamental as it shows that the usual notion of weak solution for the incompressible Euler equations is not strong enough to guarantee uniqueness. Although this is not the first such example, see [3], Shnirelman's construction is both easier and more elementary. The construction is roughly based on the idea of 2D inverse energy cascade. Recently Shnirelman's example was included in a more general abstract construction, see [1], but it is still interesting to understand its specific structure.

Shnirelman's construction proceeds in an infinite sequence of approximating steps, but exploring the first few (three, to be exact), by computational means, can give us a fairly precise idea of the basic structure of the resulting limiting solution. A key ingredient of Shnirelman's construction is the Kolmogorov flow, an oscillatory, highly unstable solution which exhibits spontaneous appearance of oscillation at a large scale from oscillation at a small scale.

To construct the approximate solution of the Euler equations we used the Levy–Tadmor second order central difference scheme in the vorticity formulation of the Euler equations, see [2], together with spectral inversion of the Laplacian.

In Sections 2 and 3 we present the computational approximation of Shnirelman's construction and in Section 4 we use our simulation in order to visualize the inverse cascade.

2. The problem

Consider the 2D incompressible Euler equations on the torus $\mathbb{T}^2$,

$$\begin{cases} \partial_t u + (u \cdot \nabla) u + \nabla p = 0 \\ \operatorname{div} u = 0 \end{cases}$$

here, $u = u(x,t)$ and $p = p(x,t)$ denote, respectively, the velocity field and the pressure, $x \in \mathbb{T}^2$ and $t \in \mathbb{R}$.

We define a weak solution as follows:

Definition 1. A vector field $u = u(x,t) \in L^2_{\text{loc}}(\mathbb{T}^2 \times \mathbb{R}, \mathbb{R}^2)$ is a *weak solution* of the incompressible Euler equations with forcing $f \in \mathcal{D}'$ if, for any test function $\varphi = \varphi(x,t) \in C_c^\infty(\mathbb{T}^2 \times \mathbb{R}, \mathbb{R})$ and $v = v(x,t) \in C_c^\infty(\mathbb{T}^2 \times \mathbb{R}, \mathbb{R}^2)$ such that $\operatorname{div} v = 0$, we have:

$$\int\int -\left[u \cdot \frac{\partial u}{\partial t} + (u \otimes u) \cdot \nabla v\right] \mathrm{d}x\mathrm{d}t = \int\int (f \cdot v) \mathrm{d}x\mathrm{d}t$$

$$\text{and} \quad \int\int -(u \cdot \nabla\varphi) \mathrm{d}x\mathrm{d}t = 0.$$

* Corresponding address: UNICAMP, Sergio Buarque de Holanda, 651, 13083-859 Campinas, Sao Paulo, Brazil. Tel.: +55 16 81166182.
E-mail address: annebronzi@ime.unicamp.br (A.C. Bronzi).

0167-2789/$ - see front matter © 2008 Elsevier B.V. All rights reserved.
doi:10.1016/j.physd.2008.02.013

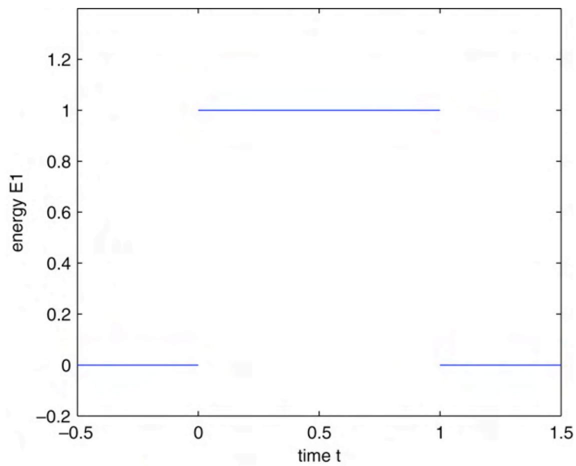

Fig. 1. Energy $E_1(t)$ versus time t for the velocity field u_1 at the first stage of the iteration.

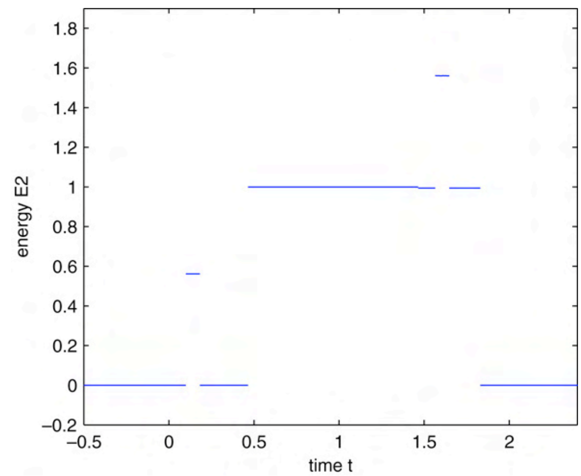

Fig. 2. Energy $E_2(t)$ versus time t for the velocity field u_2 at the second stage of the iteration.

The construction in [4] leads to the following result:

Theorem 1 (*Shnirelman, 1997*). *There exists a weak solution of the Euler equations, $u = u(x,t) \in L^2(\mathbb{T}^2 \times \mathbb{R}, \mathbb{R}^2)$ such that $u(x,t) \equiv 0$, $|t| > C$, for some constant $C > 0$.*

In particular, this theorem implies non-uniqueness of weak solutions of the incompressible 2D Euler equations, in the sense of Definition 1.

3. The construction

The construction is based on the following fact: if $\{u_i\}_i$ is a weak solution of 2D Euler with forcing $\{f_i\}_i$ such that $f_i \rightharpoonup 0$ in $\mathcal{D}'$ and $u_i \to u$ strongly in L^2 then u is a weak solution of 2D Euler without forcing.

We construct a sequence $\{u_i\}_i$ such that u_i is a weak solution of 2D incompressible Euler with forcing f_i, $f_i \rightharpoonup 0$ in $\mathcal{D}'$ and $u_i \to u$ strongly in L^2. In order to construct this sequence we start with an arbitrary non-zero smooth solution of the Euler equations, namely $u_0(x,t)$. We define the first term of the sequence $\{u_i\}_i$ by

$$u_1(x,t) = \begin{cases} u_0(x,t), & |t| < 1 \\ 0, & |t| > 1. \end{cases}$$

In our numerical example we use

$$u_0(x,t) = \frac{u(x,t)}{\|u\|_{L^2}^2},$$

where

$$u(x,t) = \begin{cases} \left(\tanh\left(\frac{15}{\pi}\left(y - \frac{\pi}{2}\right)\right), 0.05\sin(x)\right), & y \le \pi \\ \left(\tanh\left(\frac{15}{\pi}\left(\frac{3\pi}{2} - y\right)\right), 0.05\sin(x)\right), & y > \pi. \end{cases}$$

Fig. 1 describes the numerically computed energy of u_1 as a function of time.

The construction of $u_{i+1}(x,t)$ from $u_i(x,t)$ is made in the following way: If $u_i(x,t)$ is a smooth solution of the Euler equations in the interval $t_{i,j} < t < t_{i,j+1}$, discontinuous at $t = t_{i,j}$, $j = 1, 2, \ldots, J_i$, and such that $u_i(x,t) = 0$ for $t < t_{i,1}$ and $t > t_{i,J_i}$ then $u_i(x,t)$ is a weak solution of the Euler equations with forcing

$$f_i(x,t) = \sum_{j=1}^{J_i} f_{i,j}(x)\delta(t - t_{i,j}).$$

To construct the vector field $u_{i+1}(x,t)$ we insert gaps of size T_i by translating the solution u_i on the interval $(t_{i,j}, t_{i,j+1})$ to the interval $(t_{i,j} + jT_i, t_{i,j+1} + jT_i)$. We will further subdivide the T_i-sized gaps into a finite number of subintervals in which $u_{i+1}(x,t)$ will be a smooth solution of the Euler equations, while it will be discontinuous at the endpoints of these subintervals. Then, $u_{i+1}(x,t)$ will be a weak solution of the Euler equations with forcing

$$f_{i+1}(x,t) = \sum_{j=1}^{J_i} \sum_{p=1}^{p_{ij}} f_{i,j,p}(x)\delta(t - t_{i,j,p}),$$

where

$$f_{i,j,p}(x) = u_{i+1}(x, t_{i,j,p}^{+}) - u_{i+1}(x, t_{i,j,p}^{-}).$$

Note: In place of each pulse $f_{i,j}(x)$ generating the velocity jump at $t = t_{i,j}$, we insert a series of pulses $f_{i,j,p}(x)$ at $t_{i,j,p}$ with the same (delayed) end-result.

The function $u_{i+1}(x,t)$ is constructed independently in each gap, so that the construction is completely described by performing it in the case of a weak solution of the Euler equations with forcing $f(x,t) = f(x)\delta(t - t_0)$, $f(x) = u_+(x) - u_-(x)$, $u_\pm(x) = u(x, t_0^\pm)$.

The construction gives us a vector field $U(x,t)$ such that $f(x,t)$ is changed into a series of pulses having the same net effect as f itself.

It is enough to define the pulses F_j that will be applied at times t_j; then, $U(x, t_j^-) = S_{t_j - t_{j-1}}(U(x, t_{j-1}^+))$ and $U(x, t_j^+) = U(x, t_j^-) + F_j$. Here S_t represents the solution operator of the incompressible Euler equations.

These pulses are chosen so that they converge weakly to 0 in $\mathcal{D}'$ and at the same time they force the solution from

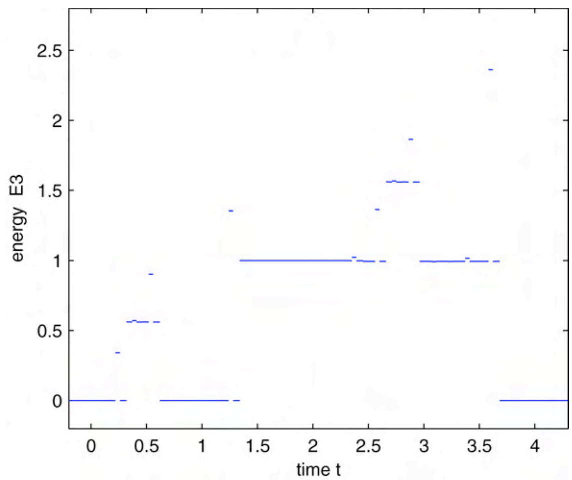

Fig. 3. Energy $E_3(t)$ versus time t for the velocity field u_3 at the third stage of the iteration.

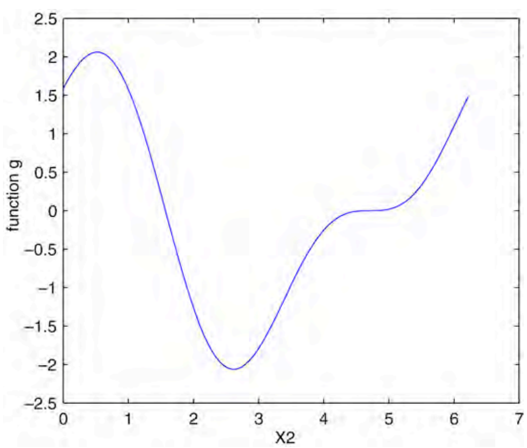

Fig. 4. Graph of $g(x_2) = k^{2\alpha}\frac{1}{8}(\sin 2x_2 + 2\cos x_2)$ versus x_2.

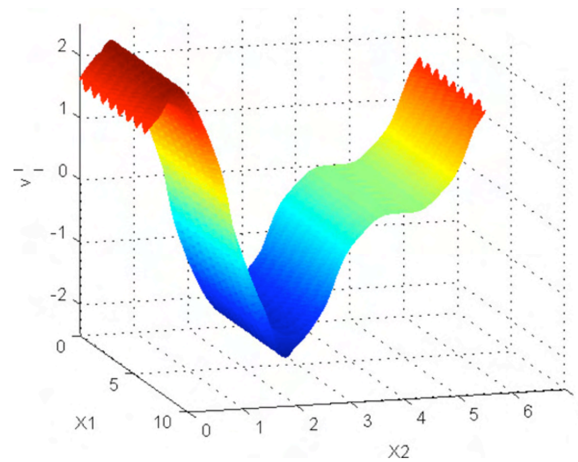

Fig. 5. Graph of v_1^1 versus x_1 and x_2.

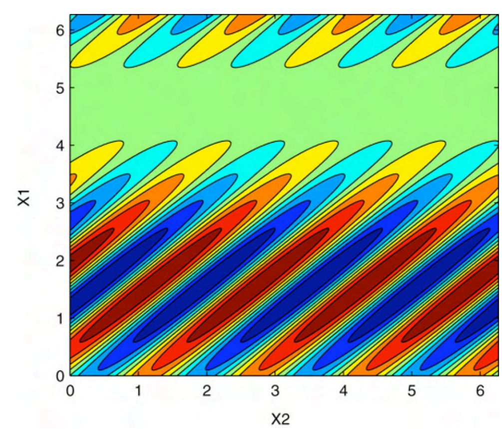

Fig. 6. Level set of the vorticity at $t = 0$.

$u_i(x, t_{i,j}^-)$ to $u_i(x, t_{i,j}^+)$. The inverse cascade, although not explicitly accounted for in the construction, explains how this can actually occur.

Figs. 2 and 3 describe the first and the second steps of the construction.

As expected, from the pictures we can see that when we go from step 1 to step 2, some of the pulses that are inserted have higher energy than the initial pulse. These pulses are actually oscillating vector fields with high frequency and this is their key property as this implies they converge weakly to zero and are still transformed into a non-zero large scale velocity field via the Euler flow.

4. The inverse cascade

The two main tools to make this construction work are: a modulated Kolmogorov flow and a special decomposition theorem for the pulse f.

The modulated Kolmogorov flow is a highly unstable and oscillatory flow which has been extensively used to study inverse energy cascades. Given initial velocity v_0, there exists an asymptotic solution which we truncate, obtaining the approximate Kolmogorov flow $v^N(x,t) = v_0(x) + (t - t_0)v_1(x) + \cdots + (t - t_0)^N v_N(x)$, such that:

$$\frac{\partial v^{(N)}}{\partial t} = A(v^{(N)}, v^{(N)}) + r_N$$
$$v_0(x) = v(x) + w(x),$$
where $A(v, w) = -P[(v \cdot \nabla)w]$,
$$v(x) = \nabla^{\perp}\psi(x), \qquad \psi(x) = k^{-1+\alpha} b(x) \sin(ka \cdot x)$$

and P is an orthogonal projector in $L^2(\mathbb{T}^2, \mathbb{R}^2)$ onto the subspace of divergence-free vector fields.

The second term $v_1(x)$ of the series $v^{(N)}(x,t)$ has the useful property: $v_1(x) = k^{2\alpha}\frac{1}{2}P[(a^{\perp} \cdot \nabla B)a^{\perp}]$ + oscillatory terms with frequency depending on k, where $B(x) = b(x)^2$.

The decomposition result we mentioned before is:

Theorem 2. *Let f be a vector field such that* div $f = 0$ *and $\int f(x)\mathrm{d}x = 0$. Then there exist vectors a_1 and a_2, smooth positive functions $B_1(x)$ and $B_2(x)$, and two pseudo-differential operators Φ_1 and Φ_2 such that $B_j = \Phi_j f$ and we can write*

$$f = \sum_{j=1}^{2} \frac{1}{2} P[(a_j^{\perp} \cdot \nabla B_j)a_j^{\perp}].$$

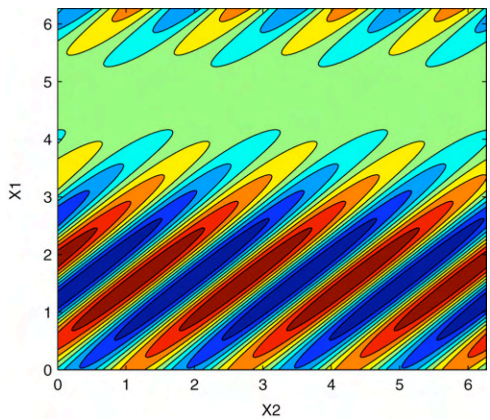

Fig. 7. Level set of the vorticity at $t = 0.15$.

We can implement these operations computationally, and we are able to visualize the spontaneous production of the larger scale from the smaller scale oscillation.

In the construction, Shnirelman used Theorem 2 in order to construct pulses that had inverse cascade behavior, as we will see in the spontaneous period doubling seen in the pictures.

Using v_0 with $w = 0$, we see that the modulated Kolmogorov flow has this period-doubling behavior, and therefore, the pulses defined using Theorem 2 will have this behavior as well.

Let us consider

$$\psi(x) = k^{-1+\alpha} b(x) \sin(ka \cdot x), \text{ where}$$
$$b(x) = \frac{1}{2}(\sin x_2 + 1), \; k = 4, \; \alpha = 2/3 \quad \text{and} \quad a = (1, -1).$$

Thus,

$$B(x) = \frac{1}{4}(\sin^2 x_2 + 2 \sin x_2 + 1) \text{ and}$$
$$\begin{aligned}(v_1^1, v_1^2) &= k^{2\alpha} \frac{1}{2} P[(a^\perp \cdot \nabla B) a^\perp] + \text{oscillatory terms } (k) \\ &= k^{2\alpha} \left(\frac{1}{8}(\sin 2x_2 + 2\cos x_2), 0 \right) \\ &\quad + \text{oscillatory terms } (k).\end{aligned}$$

Fig. 4 describes the function $g(x_2) = k^{2\alpha} \frac{1}{8}(\sin 2x_2 + 2\cos x_2)$ as a function of x_2.

Numerically, we obtain the graph of v_1^1 (as shown in Fig. 5) as a function of (x_1, x_2).

Therefore, v_1 will be the profile in the y-axis of the vorticity of the approximate Kolmogorov flow v.

Figs. 6 and 7 describe the level sets of the vorticity of the approximate Kolmogorov flow v.

Acknowledgments

This research has been supported by FAPESP grant 05/58136-9. The authors would like to thank A. Shnirelman for his helpful suggestions.

References

[1] C. De Lellis, L. Szkelyhidi, The Euler equation as a differential inclusion, Preprint Nr. 07-2007, 2007.

[2] D. Levy, E. Tadmor, Non-oscillatory central schemes for the incompressible 2-D Euler equations, Math. Res. Lett. 4 (1997) 321–340.

[3] V. Scheffer, An inviscid flow with compact support in space-time, J. Geom. Anal. 3 (1993) 343–401.

[4] A. Shnirelman, On the non-uniqueness of weak solutions of Euler equations, Comm. Pure Appl. Math. L (1997) 1261–1286.

Available online at www.sciencedirect.com

ScienceDirect

Physica D 237 (2008) 1993–1997

PHYSICA D

www.elsevier.com/locate/physd

Mixing and coherent structures in 2D viscous flows

H.W. Capel[a], R.A. Pasmanter[b,*]

[a] Inst. Theoretical Physics, University of Amsterdam, Valckenierstraat 65, 1018 XE Amsterdam, The Netherlands
[b] KNMI, P.O. Box 201, 3730 AE, De Bilt, The Netherlands

Available online 29 April 2008

Abstract

We introduce a dynamical description based on a probability density $\phi(\sigma, x, y, t)$ of the vorticity σ in two-dimensional viscous flows such that the average vorticity evolves according to the Navier–Stokes equations. A time-dependent mixing index is defined and the class of probability densities that maximizes this index is studied. The time dependence of the Lagrange multipliers can be chosen in such a way that the masses $m(\sigma, t) := \int \mathrm{d}x\mathrm{d}y\phi(\sigma, x, y, t)$ associated with each vorticity value σ are conserved. When the masses $m(\sigma, t)$ are conserved then (1) the mixing index satisfies an H-theorem and (2) the mixing index is the time-dependent analogue of the entropy employed in the statistical mechanical theory of inviscid 2D flows. In the context of our class of probability densities we also discuss the reconstruction of the probability density of the quasi-stationary coherent structures from the experimentally determined vorticity-stream function relations.

PACS: 47.32.-y; 47.51.+a; 47.27.De; 47.10.ad; 47.10.ab

Keywords: Viscous flows; Two-dimensional flows; Coherent structures; Stochastic dynamics

1. Introduction

When studying the dynamics of two-dimensional fluid motion characterized by a vorticity field $\omega(x, y, t)$ it can be useful to turn to a probabilistic description with distributions $\phi(\sigma, x, y, t)$ for the microscopic vorticity σ such that the average value of σ over these distributions is equal to $\omega(x, y, t)$. The probability distribution represents an ensemble of systems, all the ensemble members satisfy the same constraints. The uncertainties associated with the probability distribution are due to, e.g., the finite experimental precision or to thermal fluctuations. In particular, this can be done in the description of the coherent structures, i.e. the quasi-stationary states (QSS), which are often reached in (numerical) experiments after fast mixing has taken place [5,8,12,19,22]. At high Reynolds' numbers, the vorticity fields $\omega_S(x, y)$ of these QSS's satisfy ω–ψ relations to a good approximation, i.e., $\omega_S(x, y) \simeq \Omega(\psi(x, y))$ where $\psi(x, y)$ is the corresponding stream-function. In other words, the QSS's are approximate stationary solutions of the Euler equation.

A statistical mechanical theory of inviscid two-dimensional steady flows was introduced in [10,11,15–18], an approach that can be traced back to earlier work of Lynden–Bell in 1967 [7]. Some outstanding aspects of this non-dissipative system are: (1) an infinite number of conserved quantities associated with each microscopic-vorticity value σ and (2) non-uniform equilibrium states (the coherent structures) which often correspond to negative-temperature states as already predicted by Onsager's work on point vortices [13]. Theoretical predictions of the statistical mechanics approach to the coherent structures were compared with numerical simulations and with experimental measurements in quasi-two dimensional fluids, e.g., in [2,3, 8,9,19]. However, under standard laboratory conditions fluids are viscous and numerical simulations require the introduction of a non-vanishing (hyper)viscosity in order to avoid some numerical instabilities and other artifacts. In spite of this, in many cases it was found that the agreement between the theoretical predictions based on the statistical mechanics of Miller, Robert and Sommeria (MRS) [10,11,15–18] and (numerical) experiments was better than expected.

* Corresponding author.
E-mail addresses: pasmante@science.uva.nl, pasmante@knmi.nl (R.A. Pasmanter).

0167-2789/$ - see front matter
doi:10.1016/j.physd.2008.04.016

In order to discuss these issues in a more dynamical setting we consider *viscous* flows and propose a family of model evolution equations for the vorticity distribution $\phi(\sigma, x, y, t)$ in Section 2. In Section 3 we discuss the class of time-dependent distributions that maximize a mixing index under certain constraints. In particular, it is shown that the time-dependent Lagrange multipliers appearing in these distributions can be chosen in such a way that the masses associated with each microscopic-vorticity value σ are conserved. When these masses are conserved, the mixing index satisfies an H-theorem. Moreover, the mixing index shows a minimal increase in time [Section 4]. The distribution $\phi_S(\sigma, x, y)$ associated with a given QSS can be obtained, at least in principle, by addressing the reconstruction problem, i.e. how to extract its defining parameters from the QSS's ω–ψ relation. This is discussed in Section 5. In doing so we provide a natural framework for a time-dependent statistical theory connecting an appropriate initial distribution to the QSS distribution associated with the experimental ω–ψ relation and evolving in agreement with the Navier–Stokes equation. The validity of the used assumptions should be tested, for example in numerical simulations.

2. Microscopic viscous models

Let $\phi(\sigma, x, y, t)\mathrm{d}\sigma$ be the probability of finding at time t a microscopic vorticity value in the range $(\sigma, \sigma+\mathrm{d}\sigma)$ at a position (x, y). It should be non-negative and normalized

$$\int \mathrm{d}\sigma \phi(\sigma, x, y, t) = 1. \tag{1}$$

The macroscopic vorticity field is

$$\omega(x, y, t) = \langle \sigma \rangle := \int \mathrm{d}\sigma \sigma \phi(\sigma, x, y, t), \tag{2}$$

in which the pointed brackets denote averages over this distribution, In the inviscid case, the dynamics reduces to the advection of vorticity. Neglecting fluctuations in the velocity field, the time evolution of $\phi(\sigma, x, y, t)$ can be taken to be

$$\frac{\partial \phi(\sigma, x, y, t)}{\partial t} + \vec{v}(x, y, t) \cdot \nabla \phi(\sigma, x, y, t) = 0, \tag{3}$$

where the macroscopic, incompressible velocity field $\vec{v}(x, y, t)$ is related to the macroscopic vorticity $\omega(x, y, t)$ by $\nabla \times \vec{v} = \omega \widetilde{z}$, with $\widetilde{z}$ a unit vector perpendicular to the (x, y)-plane. Extending this to the viscous case the models to be considered are of the form

$$\frac{\partial \phi(\sigma, x, y, t)}{\partial t} + \vec{v}(x, y, t) \cdot \nabla \phi(\sigma, x, y, t) = \nu \Delta \phi + \nu \phi \overline{O}, \tag{4}$$

with ν the fluid viscosity and $\overline{O}$ as yet undefined but constrained by (1) the conservation of the total probabilty $\int \mathrm{d}\sigma \phi(\sigma, x, y, t) = 1$, and by (2) the macroscopic Navier–Stokes equation, i.e.,

$$\frac{\partial \omega(x, y, t)}{\partial t} + \vec{v}(x, y, t) \cdot \nabla \omega(x, y, t) = \nu \Delta \omega(x, y, t) \tag{5}$$

should follow from the microscopic model. These two conditions are equivalent to,

$$\langle \overline{O} \rangle = 0, \quad \text{and} \quad \langle \sigma \overline{O} \rangle = 0. \tag{6}$$

It is convenient to introduce the "masses" $m(\sigma, t)$ associated with each value σ of the microscopic vorticity,

$$m(\sigma, t) := \int \mathrm{d}x\mathrm{d}y \phi(\sigma, x, y, t). \tag{7}$$

In the inviscid case, $\nu = 0$, Eq. (4) has a solution $\phi(\sigma, x, y, t) = \delta(\sigma - \omega(x, y, t))$ therefore $m(\sigma, t)$ is the area occupied by the vorticity field with value σ. As soon as we introduce a diffusion process, as it is implied by Eq. (4) with $\nu \neq 0$, such an identification becomes impossible. In calling $m(\sigma, t)$ a "mass" we stress the analogy between Eq. (4) and an advection–diffusion process of an infinite number of "chemical species", one species for each value σ.

Assuming that there is no leakage of $\phi(\sigma, x, y, t)$ through the boundary, the time derivative of a mass is

$$\frac{\partial m(\sigma, t)}{\partial t} = \nu \int \mathrm{d}x\mathrm{d}y \overline{O} \phi(\sigma, x, y, t). \tag{8}$$

The simplest viscous model satisfying the above requirements is the one with $\overline{O} \equiv 0$. This model is instructive because, while it dissipates energy, it has an infinite number of conserved quantities, i.e., the masses $m(\sigma, t)$. One of the consequences of the conservation laws for $m(\sigma, t)$ is that all the microscopic-vorticity moments $M_n(t) := \int \mathrm{d}\sigma \sigma^n m(\sigma, t)$ are constants of the motion, i.e., $\mathrm{d}M_n/\mathrm{d}t = 0$. In the sequel we shall assume that the conservation of all the microscopic moments M_n implies in turn that the masses $m(\sigma, t)$ are conserved. This is the case if certain technical conditions are satisfied, see e.g., [20]. By contraposition, all even moments of the macroscopic vorticity,

$$\Gamma_{2n}(t) := \int \mathrm{d}x\mathrm{d}y \omega^{2n}(x, y, t), \tag{9}$$

are dissipated since,

$$\frac{\mathrm{d}\Gamma_{2n}}{\mathrm{d}t} = -\nu 2n(2n-1) \int \mathrm{d}x\mathrm{d}y \omega^{2(n-1)} |\nabla \omega|^2 \leq 0. \tag{10}$$

Under appropriate boundary conditions, e.g., periodic ones, the energy $E = 1/2 \int \mathrm{d}x\mathrm{d}y\, v^2 = 1/2 \int \mathrm{d}x\mathrm{d}y \omega \psi$, and its dissipation rate is $\mathrm{d}E/\mathrm{d}t = -\nu \Gamma_2(t)$, where $\psi(x, y, t)$ is the stream-function associated with $\vec{v}(x, y, t)$.

3. Time-dependent extremal distributions

Equations like (4) have been studied extensively; see for example [14] and the references therein. Usually a time-dependent velocity field $\vec{v}(x, y, t)$ leads to chaotic trajectories, namely to the explosive growth of small-scale gradients. These small-scale gradients are then rapidly smoothed out by diffusion, the net result being a very large effective diffusion coefficient, large in comparison to the molecular coefficient ν.

Based on these observations we will consider situations where during a period of time mixing takes place much faster than the changes in the masses $m(\sigma, t)$. In order to quantify this we introduce the degree of mixing of $m(\sigma, t)$, $s(\sigma, t) := -A^{-1} \int dx dy \phi \ln [A\phi/m(\sigma, t)]$, and the corresponding total degree of mixing at time t,

$$S(t) = -A^{-1} \int d\sigma \int dx dy \phi(\sigma, x, y, t) \ln \phi(\sigma, x, y, t) + A^{-1} \int d\sigma m(\sigma, t) \ln \left[A^{-1} m(\sigma, t) \right]. \quad (11)$$

The fast-mixing condition can thus be expressed as,

$$|\partial s(\sigma, t)/\partial t| \gg A^{-1} |\partial m(\sigma, t)/\partial t| . \quad (12)$$

This inequality is satisfied when the masses $m(\sigma, t)$ are conserved, moreover in such a case the second term in (11) is constant in time so that the total degree of mixing $S(t)$ is the time-dependent analogue of the entropy which is used in the MRS statistical mechanics theory and, as shown in the last paragraph of the present section, it satisfies an H-theorem.

Accordingly, in the sequel we investigate the time-dependent distributions $\phi(\sigma, x, y, t)$ that maximize the total vorticity mixing $S(t)$ under the following three constraints: (i) normalization, as in (1), (ii) given values of the masses $m(\sigma, t)$, and (iii) a given distribution first moment $\langle \sigma \rangle = \omega(x, y, t)$ which, by construction, evolves according to the Navier–Stokes equations. Introducing time-dependent Lagrange multipliers $\gamma(x, y, t)$, $\widetilde{\mu}(\sigma, t)$ and $\chi(x, y, t)$ associated to the above-mentioned constraints and denoting the maximizing distribution by $\phi_M(\sigma, x, y, t)$, the vanishing of the first variation of $S(t)$ with respect to ϕ leads to,

$$\phi_M(\sigma, x, y, t) = Z^{-1} \exp [\mu(\sigma, t) + \chi(x, y, t)\sigma] ,$$
$$\text{with} \quad Z(x, y, t) := \int d\sigma \exp [\sigma \chi(x, y, t) + \mu(\sigma, t)] , \quad (13)$$

and $\mu(\sigma, t) := -\widetilde{\mu}(\sigma, t) + \ln A^{-1} m(\sigma, t)$. The functions $\chi(x, y, t)$ and $\mu(\sigma, t)$ will be called the "potentials". Two constraints given by (2) and (7) determine these potentials. For these distributions one has $\phi_M(\sigma, x, y, t) =: \widetilde{\phi}(\sigma, \chi(x, y, t), t)$, therefore the (x, y)-dependence of ω as well as that of the local moments $m_n := \langle \sigma^n \rangle$ and the centered local moments $K_n := \langle (\sigma - \omega)^n \rangle$ is only through $\chi(x, y, t)$, i.e., $K_n(x, y, t) =: \widetilde{K}_n(\chi, t)$, $Z(x, y, t) =: \widetilde{Z}(\chi, t)$, $\omega(x, y, t) =: \widetilde{\Omega}(\chi, t)$, $m_n(x, y, t) =: \widetilde{m}_n(\chi, t)$, and relations like $\partial \widetilde{\Omega}/\partial \chi = \widetilde{K}_2(\chi, t)$ hold.

In the special case of a QSS at time T_S the distribution obtained from the MRS approach is as in Eq. (13) with $\chi(x, y, T_S) = -\beta \psi(x, y, T_S)$ where $\psi(x, y, T_S)$ is the stream function at time T_S and β is associated with an inverse temperature. This distribution is obtained by maximizing $S(T_S)$ under the constraints (i) and (ii) and the constraint that the energy at time T_S has some given value $E(T_S)$. In the MRS inviscid approach the connection with the initial state is made by requiring that the masses at time T_S and the energy at time T_S equal their initial values, therefore the QSS can be predicted from the initial condition. In the context of our present work, for this to be approximately valid the following fast mixing condition should be satisfied,

$$dS(t)/dt \gg E^{-1} (dE/dt) , \quad (14)$$

on top of condition (12).

Assume that at all times the probability density has the form given in (13). Omitting for convenience the subsript M, inserting (13) and (2) in the Navier–Stokes equation (5) and making use of simple algebraic equalities one shows that the time evolution of ϕ_M is given by Eq. (4) with $\overline{O}(\sigma, x, y, t)$ given by,

$$\overline{O}(\sigma, x, y, t) = \left[K_2 + \frac{K_3}{K_2} (\sigma - \omega) - (\sigma - \omega)^2 \right] |\nabla \chi|^2 + \nu^{-1} \left(\frac{\partial \mu}{\partial t} - \left\langle \frac{\partial \mu}{\partial t} \right\rangle \right) - \nu^{-1} \frac{(\sigma - \omega)}{K_2} \left\langle (\sigma - \omega) \frac{\partial \mu}{\partial t} \right\rangle . \quad (15)$$

As one can check, $\langle \overline{O} \rangle = 0$ and $\langle \sigma \overline{O} \rangle = 0$ for all possible time-dependences of $\partial \mu/\partial t$.

From (15) it follows that the simplest viscous model with $\overline{O}(\sigma, x, y, t) \equiv 0$, can be realized only under rather trivial conditions. Indeed, since $\overline{O}(\sigma, x, y, t) \equiv 0$ has to hold for any value of σ, Eq. (15) implies that $\partial \mu/\partial t$ must be quadratic in σ and that $|\nabla \chi|^2$ may be time-dependent but must be (x, y)-independent.

For general $\mu(\sigma, t)$ there is no conservation of the masses $m(\sigma, t)$. However, choosing a suitable time-dependence of $\mu(\sigma, t)$ such that $\int dx dy \, \phi \overline{O} = 0$, ensures the conservation of the masses $m(\sigma, t)$, confer Eq. (8). This condition and Eq. (15) lead to a complicated integro-differential equation for the time-dependence of $\mu(\sigma, t)$. However, using a Taylor expansion $\mu(\sigma, t) = \sum_k \mu_k(t) \sigma^k$, we can derive an infinite set of linear differential equations for the $d\mu_k/dt$. In fact, multiplying Eq. (15) by $\sigma^n \phi(\sigma, x, y, t)$ and integrating it over σ one gets that:

$$\nu \langle \sigma^n \overline{O} \rangle = -\nu |\nabla \chi|^2 h_{n2} + \sum_{k=2}^{\infty} h_{nk} \frac{d\mu_k}{dt} \quad (16)$$

with

$$h_{nk} = m_{k+n} - m_k m_n - K_2^{-1} (m_{n+1} - \omega m_n) (m_{k+1} - \omega m_k) ,$$

where $m_n := \langle \sigma^n \rangle$. The conservation of the moments $M_n = \int dx dy \, m_n$ requires then that $\int dx dy \, \langle \sigma^n \overline{O} \rangle = 0$ and hence (16) becomes,

$$\sum_{k=2}^{\infty} \frac{d\mu_k}{dt} \int dx dy \, h_{nk} = \nu \int dx dy \, h_{n2} |\nabla \chi|^2 . \quad (17)$$

From this infinite set of equations, linear in $d\mu_2/dt$, $d\mu_3/dt, \ldots$, the $d\mu_k/dt$ can, in principle, be solved. The solution describes a *viscous* model with an infinite number of conservation laws. Such a viscous model becomes physically more relevant by making it compatible with a quasi-stationary distribution $\widetilde{\phi}_S(\sigma, \chi)$ corresponding to the $\Omega(\psi)$ relation at time T_S, and with $\chi = -\beta \psi(x, y)$, confer Section 5.

Using Eq. (4) and the conservation of the masses $m(\sigma, t)$ one obtains,

$$\frac{\partial s(\sigma,t)}{\partial t} = \frac{\nu}{A}\int \mathrm{d}x\mathrm{d}y\phi\left[\left|\frac{\nabla\phi}{\phi}\right|^2 - \overline{O}\ln A\phi\right]. \quad (18)$$

When the distribution is of the form given in Eq. (13), using a Taylor expansion for $\mu(\sigma, t)$ one sees that after integration over σ the term containing $\overline{O}$ vanishes, therefore $\mathrm{d}S(t)/\mathrm{d}t$ is non-negative. As shown in Appendix A of Ref. [6] this H-theorem holds *only* for one specific measure of spatial mixing, namely for the one given in (11); see, e.g., Ref. [1,21]. The fast-mixing condition (14), divided by ν becomes then,

$$\frac{1}{A}\int \mathrm{d}x\mathrm{d}y\left\langle|\nabla\ln\phi|^2\right\rangle \gg \frac{1}{E}\int \mathrm{d}x\mathrm{d}y\omega^2. \quad (19)$$

4. Rate of mixing increase

In order to see whether or not this fast-mixing condition (19)is satisfied by the time-dependent distributions $\phi_M(\sigma, x, y, t)$, we derive a lower bound to $\langle|\nabla\ln\phi|^2\rangle$ and we determine the extrema of the l.h.s. of Eq. (19). To this end notice that $\nabla\omega = \langle\sigma\nabla\ln\phi\rangle$ can also be written as $\nabla\omega = \langle(\sigma-\omega)\nabla\ln\phi\rangle$ because $\langle\nabla\ln\phi\rangle = 0$. Applying then the Cauchy–Schwartz inequality to $|\nabla\omega|^2 = |\langle(\sigma-\omega)\nabla\ln\phi\rangle|^2$ leads to $|\nabla\omega|^2 \le \langle(\sigma-\omega)^2\rangle\langle|\nabla\ln\phi|^2\rangle \equiv K_2\langle|\nabla\ln\phi|^2\rangle$, i.e. to the desired lower bound,

$$|\nabla\omega|^2 K_2{}^{-1} \le \left\langle|\nabla\ln\phi|^2\right\rangle. \quad (20)$$

The lower bound on $\langle|\nabla\ln\phi|^2\rangle$ that we have just found means that the fast-mixing condition ((19)) holds whenever

$$\frac{1}{A}\int \mathrm{d}x\mathrm{d}y\frac{|\nabla\omega|^2}{K_2} \gg \frac{1}{E}\int \mathrm{d}x\mathrm{d}y\omega^2.$$

One can show that the family of probability distributions that reach the lower bound in (20) coincides with $\phi_M(\sigma, x, y, t)$ as given by Eq. (13). Here, the input for the determination of the potential functions $\mu(\sigma, t)$ and $\chi(x, y, t)$ are the first and second σ-moments. The details concerning the derivation of this can be found in Appendix B of Ref. [6].

Also the extrema of $\int \mathrm{d}x\mathrm{d}y\langle|\nabla\ln\phi|^2\rangle$ can be investigated taking into account the constraints given by Eqs. (2) and (1). It turns out that in order to obtain sensible solutions, it is necessary to constrain also the distribution's second moment $\langle\sigma^2\rangle$. We find that *all* the extremizer distributions are local *minima* of $\int \mathrm{d}x\mathrm{d}y\langle|\nabla\ln\phi|^2\rangle$ and coincide with $\phi_M(\sigma, x, y, t)$, moreover they all reach the lower bound in (20). The details can be found in Appendix C of Ref. [6].

5. Reconstructing $\mu(\sigma)$ from experimental data

Suppose that in an experiment one is given an initial vorticity field with its corresponding energy E_o and that at a time T_S one finds a quasi-stationary vorticity field $\omega_S(x, y) = \Omega(\psi(x, y))$, with a monotonic $\Omega(\psi)$ and an energy $E_S \le E_o$. As we show below these experimental data can be used in order to determine the potential $\mu(\sigma, T_S)$ occuring in the distribution $\phi_M(\sigma, x, y, T_S)$ as given by Eq. (13) with $\chi = -\beta\psi(x, y, T_S)$. Once the distribution has been reconstructed from the experimental data we can then associate with it a time-dependent distribution function $\phi_M(\sigma, x, y, t)$ as given by Eq. (13) which is a solution of the time-evolution Eq. (4) with suitable initial conditions and such that at time $t = T_S$ one has $\widetilde{\phi}_M(\sigma, \chi(x, y, T_S), T_S) = \widetilde{\phi}_S(\sigma, \chi)$ with $\chi = -\beta\psi$ and with $\mu(\sigma, T_S) = \mu(\sigma)$. The time-dependence of $\mu(\sigma, t)$ is chosen as in Eq. (17) such that all masses $m(\sigma, t)$ are constant in time. Here β can be defined such that $M_2(T_S)$, the microscopic-vorticity second moment of the QSS at time T_S, is equal to Γ_2^0 the enstrophy of the initial vorticity field $\omega_o(x, y)$, i.e.,

$$\beta = -\left(\Gamma_2^0 - \Gamma_2^S\right)^{-1}\int_A \mathrm{d}x\mathrm{d}y\,(\mathrm{d}\Omega/\mathrm{d}\psi) \quad (21)$$

where $\Gamma_2^S = \int \mathrm{d}x\mathrm{d}y\,\omega_S^2(x, y)$ is the enstrophy of the QSS. All the quantities on the r.h.s. of this formula are experimentally accessible.

In order to determine the $\mu(\sigma)$ potential from the experimental $\Omega(\psi)$ use can be made of $\omega = \mathrm{d}\ln\widetilde{Z}(\chi)/\mathrm{d}\chi$, at $\chi = -\beta\psi$, with $\widetilde{Z}(\chi)$ given by (13) and β determined from Eq. (21). Below we illustrate this by considering some examples.

A linear ω–ψ scatter plot at time T_S, $\Omega_l(\psi) = \alpha_1\psi$, with $\alpha_1 > 0$, corresponds to a Gaussian distribution centered on $\alpha_1\psi(x, y)$ and with a width $\alpha_1/|\beta|$, i.e., $\mu(\sigma) = \beta\sigma^2/(2\alpha_1)$. In the present case the expression (21) for β reads, $\beta = -\alpha_1 A/(\Gamma_2^0 - \Gamma_2^S) < 0$. It is worthwhile noticing that a Gaussian distribution with only $\mu_2 \neq 0$ cannot be preserved in the context of the models with conserved masses, i.e. those satisfying Eq. (17).

In the case of nonlinear ω–ψ relations we first notice that, using vanishing boundary conditions at $\sigma = \pm\infty$, one has $\langle\mathrm{d}\mu/\mathrm{d}\sigma\rangle = -\chi(x, y)$. Introducing into this equality the Taylor expansion $\mu(\sigma) = \sum_{k=2}\mu_k\sigma^k$, one gets $\sum_{k=2}k\mu_k m_{k-1}(\chi) = -\chi$. This is a nonlinear equation in χ but since $\widetilde{Z}(\chi)m_n = \mathrm{d}^n[\widetilde{Z}(\chi)]/\mathrm{d}\chi^n$ it is equivalent to a *linear* equation in the partition function $\widetilde{Z}(\chi)$, namely to

$$\sum_{k=2} k\mu_k\frac{\mathrm{d}^{k-1}\widetilde{Z}}{\mathrm{d}\chi^{k-1}} = -\chi\widetilde{Z}. \quad (22)$$

In general, Eq. (22) is of infinite order, however, it can be reduced to finite order when $\mathrm{d}\mu/\mathrm{d}\sigma$ is a rational function. For example if $\mathrm{d}\mu/\mathrm{d}\sigma = -2q^2\sigma/[1 - q^2\sigma^2]$ for $\|q\sigma\| < 1$ and 0 otherwise then $\widetilde{Z}(\chi)$ satisfies a modified Bessel equation, for the details and more examples see Appendix D of Ref. [6].

It is often experimentally found that the ω–ψ plots satisfy $\Omega(-\psi) \simeq -\Omega(\psi)$, or, $\mu(-\sigma) = \mu(\sigma)$. Moreover, in many cases these plots are nearly linear so that, $\widetilde{\Omega}(\chi) = f_1\chi + f_3\chi^3 + f_5\chi^5$, on an interval around $\psi = 0$ or $\chi = 0$, with $|f_{n+2}|\chi^2 < |f_n|$ for odd n and $|\mu_{n+2}| < |\mu_2\mu_n|$ for even n. Inserting the corresponding powers expansions of $\widetilde{Z}(\chi)$ and $\mu(\sigma)$ into (22) allows us to express the $\{\mu_n\}$ in terms of the $\{f_n\}$, i.e., to determine the probability density $\exp\mu(\sigma)$

from the experimentally known scatter-plot $\widetilde{\Omega}(\chi)$. For example, retaining terms up to f_5 and f_3^2 in the Taylor expansion of Eq. (22) one gets that $\mu_{2k} = 0$ for $k > 3$ and, e.g., that

$$\mu_2 = -\frac{1}{2} f_1^{-1} - \frac{3}{2} f_3 f_1^{-3} + \frac{15}{2} f_5 f_1^{-4} - 12 f_3^2 f_1^{-5}.$$

6. Discussion and conclusions

In this paper we exploited the fact that the viscous Navier–Stokes equations are compatible with the conservation of the microscopic vorticity masses. In Sections 3 and 4 we studied the family of maximally mixed states described by the distributions $\phi_M(\sigma, x, y, t)$ given in Eq. (13). These distributions show also a minimal mixing increase among all distributions with the same first and second microscopic moments, $\omega(x, y, t)$ and $\langle \sigma^2 \rangle$. In Section 5 we addressed the problem of how to determine the QSS distribution $\phi_S(\sigma, x, y)$ from an experimental ω–ψ relation observed at a time T_S and β given by Eq. (21). Identifying this $\phi_S(\sigma, x, y)$ with the distribution $\phi_M(\sigma, x, y, T_S)$ of Eq. (13) and using a time-dependent $\mu(\sigma, t)$ satisfying Eq. (17) and such that $\mu(\sigma, T_S) = \mu(\sigma)$ we obtained a dynamical model that conserves the masses, i.e., with $m(\sigma, t) = m(\sigma, t_o)$, and connects the experimental ω–ψ relation found at time T_S with an initial condition $\phi(\sigma, x, y, t_o)$ of the form (13) with an appriopriate $\mu(\sigma, t_o)$, confer Eq. (18). An extra bonus that follows from this methodology is that an H-theorem holds. There are some parallels with the inviscid, statistical mechanics approach of MRS in which the energy is conserved and so are the masses that, in the inviscid case, coincide with the areas occupied by specific vorticity values. In our dynamical models there is no a priori energy conservation and the masses are conserved by imposing Eq. (17). In order to assess the validity of the MRS approach in the case of high-Reynolds' number flows, in Subsection III B of an earlier paper [4], we expressed the quantities

$$\delta_n := \int \mathrm{d}\sigma \int \mathrm{d}x\mathrm{d}y \left[\sigma^n - \omega_S^n(x, y)\right] \phi_S(\sigma, x, y),$$
$$n = 2, 3, \ldots$$

in terms of spatial integrals of certain polynomials in $\Omega(\psi)$ and its derivatives $\{\mathrm{d}^r \Omega / \mathrm{d}\psi^r\}$. We then showed that the so-called yardstick relations $(\delta_n / \Delta\Gamma_n) = 1$, where $\Delta\Gamma_n := \Gamma_n^o - \Gamma_n^S$ are the total change in the n-th moments of the macroscopic vorticity over the time interval $[t_o, T_S]$, are nontrivial checks of the validity of the statistical mechanics approach. Choosing β as in (21) the yardstick relation $\delta_2 / \left(\Gamma_2^0 - \Gamma_2^S\right) = 1$ is automatically satisfied. When all the relations $\delta_n / (\Gamma_n^o - \Gamma_n^S) = 1$ hold then the quasi-stationary state predicted by the MRS approach is in agreement with the experimental ω–ψ relation, moreover, it is also the solution of Eq. (4) at time T_S with conserved total moments M_n and starting from the initial condition $\phi(\sigma, x, y, t_o) = \delta(\sigma - \omega_0(x, y))$. When not all the yardstick relations are satisfied then the MRS approach can only give an approximate prediction of the experimental $\Omega(\psi)$ relation.

References

[1] C. Arndt, Information Measures, Springer, Berlin, 2001.

[2] H. Brands, J. Stulemeyer, R.A. Pasmanter, T.J. Schep, A mean field prediction of the asymptotic state of decaying 2D turbulence, Phys. Fluids 9 (1998) 2815.

[3] H. Brands, P.-H. Chavanis, R.A. Pasmanter, J. Sommeria, Maximum entropy versus minimum enstrophy vortices, Phys. Fluids 11 (1999) 3465.

[4] H.W. Capel, R.A. Pasmanter, Evolution of the vorticity-area density during the formation of coherent structures in two-dimensional flows, Phys. Fluids 12 (2000) 2514.

[5] G.J.F. van Heijst, J.B. Flor, Dipole formations and collisions in a stratified fluid, Nature 340 (1989) 212.

[6] H.W. Capel, R.A. Pasmanter, Mixing and coherent structures in 2D viscous flows, (2007) http://xxx.arxiv.org/abs/physics/0702040.

[7] D. Lynden–Bell, Statistical mechanics of violent relaxation in stellar systems, Mon. Not. R. Astrors. Soc. 136 (1967) 101.

[8] D. Marteau, O. Cardoso, P. Tabeling, Equilibrium states of 2D turbulence: An experimental study, Phys. Rev. E 51 (1995) 5124–5127.

[9] W.H. Matthaeus, W.T. Stribling, D. Martinez, S. Oughton, D. Montgomery, Selective decay and coherent vortices in two-dimensional incompressible turbulence, Phys. Rev. Lett. 66 (1991) 2731 and the references therein.

[10] J. Miller, Statistical mechanics of Euler's equation in two dimensions, Phys. Rev. Lett. 65 (1990) 2137.

[11] J. Miller, P.B. Weichman, M.C. Cross, Statistical mechanics, Euler's equation, and Jupiter's red spot, Phys. Rev. A 45 (1992) 2328.

[12] D. Montgomery, X. Shan, W. Matthaeus, Navier–Stokes relaxation to sinh-Poisson states at finite Reynolds numbers, Phys. Fluids A 5 (1993) 2207.

[13] L. Onsager, Statistical hydrodynamics, Nuovo Cimento (Suppl. 6) (1949) 279–287.

[14] J.M. Ottino, Mixing, chaotic advection and turbulence, Ann. Rev. Fluid Mech. 22 (1990) 207.

[15] R. Robert, Etat d'équilibre statistique pour l'écoulement bidimensionnel d'un fluide parfait, C. R. Acad. Sci. Paris 311 (Série I) (1990) 575.

[16] R. Robert, Maximum entropy principle for two-dimensional Euler equations, J. Stat. Phys. 65 (1991) 531.

[17] R. Robert, J. Sommeria, Relaxation towards a statistical equilibrium state in two-dimensional perfect fluid dynamics, Phys. Rev. Lett. 69 (1992) 2776.

[18] R. Robert, J. Sommeria, Statistical equilibrium states for two dimensional flows, J. Fluid Mech. 229 (1991) 291.

[19] E. Segre, S. Kida, Late states of incompressible 2D decaying vorticity fields, Fluid Dyn. Res. 23 (1998) 89.

[20] J.A. Shohat, J.D. Tamarkin, The problem of moments, Amer. Math. Soc. Math. Surveys (no. 1) (1943).

[21] C. Tsallis, Possible generalization of Boltzmann-Gibbs statistics, J. Stat. Phys. 52 (1988) 479. See also http://tsallis.cat.cbpf.br/biblio.htm.

[22] J.C. McWilliams, The emergence of isolated coherent vortices in turbulent flow, J. Fluid Mech. 146 (1984) 21.

Available online at www.sciencedirect.com
ScienceDirect
Physica D 237 (2008) 1998–2002
PHYSICA D
www.elsevier.com/locate/physd

Statistical mechanics of 2D turbulence with a prior vorticity distribution

Pierre-Henri Chavanis

Laboratoire de Physique Théorique, Université Paul Sabatier, 118 route de Narbonne, 31062 Toulouse, France

Available online 8 March 2008

Abstract

We adapt the formalism of the statistical theory of 2D turbulence to the case where the Casimir constraints are replaced by the specification of a prior vorticity distribution. A phenomenological relaxation equation is obtained for the evolution of the coarse-grained vorticity. This equation monotonically increases a generalized entropic functional (determined by the prior) while conserving circulation and energy. It can be used as a thermodynamical parametrization of forced 2D turbulence, or as a numerical algorithm for constructing (i) arbitrary statistical equilibrium states in the sense of Ellis, Haven and Turkington, (ii) particular statistical equilibrium states in the sense of Miller, Robert and Sommeria, (iii) arbitrary stationary solutions of the 2D Euler equation that are formally nonlinearly dynamically stable according to the Ellis–Haven–Turkington stability criterion refining the Arnold theorems.

PACS: 47.10.A-; 47.15.ki

Keywords: Two-dimensional turbulence; Euler equation; Statistical mechanics; Nonlinear dynamical stability

1. Introduction

Two-dimensional incompressible and inviscid flows are described by the 2D Euler equations

$$\frac{\partial\omega}{\partial t}+\mathbf{u}\cdot\nabla\omega=0,\quad \omega=-\Delta\psi,\ \mathbf{u}=-\mathbf{z}\times\nabla\psi, \tag{1}$$

where ω is the vorticity and ψ the stream-function. The 2D Euler equations are known to develop a complicated mixing process which ultimately leads to the emergence of large-scale coherent structures like jets and vortices. The Jovian atmosphere shows a wide diversity of structures: Jupiter's great red spot, white ovals, brown barges, and so on. One goal of fundamental interest is understanding and predicting the structure and the stability of these quasi-stationary states (QSS). With that purpose, Miller [1] and Robert and Sommeria [2] have proposed a statistical mechanics of the 2D Euler equation (a similar statistical theory had been developed earlier by Lynden-Bell [3] for describing the violent relaxation of collisionless stellar systems governed by the Vlasov equation; see [4] for a description of this analogy). The key idea is to replace the deterministic description of the flow $\omega(\mathbf{r},t)$ by a probabilistic description where $\rho(\mathbf{r},\sigma,t)$ gives the density probability of finding the vorticity level $\omega=\sigma$ in $\mathbf{r}$ at time t. The observed (coarse-grained) vorticity field is then expressed as $\overline{\omega}(\mathbf{r},t)=\int\rho\sigma\,\mathrm{d}\sigma$. To apply the statistical theory, one must first specify the constraints attached to the 2D Euler equation. The circulation $\Gamma=\int\overline{\omega}\mathrm{d}\mathbf{r}$ and the energy $E=\frac{1}{2}\int\overline{\omega}\psi\mathrm{d}\mathbf{r}$ will be called *robust constraints* because they can be expressed in terms of the coarse-grained field $\overline{\omega}$ (the energy of the fluctuations can be neglected). These integrals can be calculated at any time from the coarse-grained field $\overline{\omega}(\mathbf{r},t)$ and they are conserved by the dynamics. By contrast, the Casimir invariants $I_f=\int\overline{f(\omega)}\mathrm{d}\mathbf{r}$, or equivalently the fine-grained moments of the vorticity $\Gamma_{n>1}^{f.g.}=\int\overline{\omega^n}\mathrm{d}\mathbf{r}$, where $\overline{\omega^n}=\int\rho\sigma^n\mathrm{d}\sigma$, will be called *fragile constraints* because they must be expressed in terms of the fine-grained vorticity. Indeed, the moments of the coarse-grained vorticity $\Gamma_{n>1}^{c.g}=\int\overline{\omega}^n\mathrm{d}\mathbf{r}$ are not conserved since $\overline{\omega^n}\neq\overline{\omega}^n$ (part of the coarse-grained moments goes into fine-grained fluctuations). Therefore, the moments $\Gamma_{n>1}^{f.g.}$ must be calculated from the fine-grained field $\omega(\mathbf{r},t)$ or from the initial conditions, i.e. before the vorticity has mixed. Since we often do not know the initial conditions or the fine-grained field, the Casimir invariants often appear as "hidden constraints".

The statistical theory of Miller–Robert–Sommeria (MRS) is based on three assumptions: (i) it is assumed that the evolution

E-mail address: chavanis@irsamc.ups-tlse.fr.

0167-2789/$ - see front matter © 2008 Elsevier B.V. All rights reserved.
doi:10.1016/j.physd.2008.02.027

of the flow is strictly described by the 2D Euler equation (no forcing and no dissipation); (ii) it is assumed that we know the initial conditions (or equivalently the values of all the Casimirs) in detail; (iii) it is assumed that mixing is efficient and that the evolution is ergodic so that the system will reach, at statistical equilibrium, the most probable (most mixed) state. Under these assumptions,[1] the statistical equilibrium state of the 2D Euler equation is obtained by maximizing the mixing entropy

$$S[\rho] = -\int \rho \ln \rho \, \mathrm{d}\mathbf{r}\mathrm{d}\sigma, \tag{2}$$

at fixed energy E and circulation Γ (robust constraints) and fixed fine-grained moments $\Gamma_{n>1}^{f.g.}$ (fragile constraints). We must also account for the normalization condition $\int \rho \mathrm{d}\sigma = 1$. This optimization principle is solved by introducing Lagrange multipliers, writing the first-order variations as [2,5]

$$\delta S - \beta\delta E - \alpha\delta\Gamma - \sum_{n>1}\alpha_n \delta\Gamma_n^{f.g.} - \int \zeta(\mathbf{r})\delta\rho \mathrm{d}\sigma\mathrm{d}\mathbf{r} = 0. \tag{3}$$

In the MRS approach, the conservation of all the Casimirs has to be taken into account. However, in geophysical situations, the flows are forced and dissipated at small scales (due to convection in the Jovian atmosphere) so that the conservation of the Casimirs is destroyed. Ellis, Haven and Turkington [6] have proposed treating these situations by fixing the conjugate variables $\alpha_{n>1}$ instead of the fragile moments $\Gamma_{n>1}^{f.g.}$ (this is essentially a suggestion that has to be tested in practice). If we view the vorticity levels as species of particles, this is similar to fixing the chemical potentials instead of the total number of particles in each species. Therefore, the idea is to treat the fragile constraints *canonically*, whereas the robust constraints are still treated *microcanonically*. A rigorous mathematical formalism has been developed in [7] and a more physical presentation has been given in [8]. In the EHT approach, the relevant thermodynamical potential (grand entropy) is obtained from the mixing entropy (2) by using a Legendre transform with respect to the fragile moments [8]:

$$S_\chi = S - \sum_{n>1}\alpha_n \, \Gamma_n^{f.g.}. \tag{4}$$

Making explicit the fine-grained moments, we obtain the relative (or grand) entropy

$$S_\chi[\rho] = -\int \rho \, \ln\left[\frac{\rho}{\chi(\sigma)}\right] \mathrm{d}\mathbf{r}\mathrm{d}\sigma, \tag{5}$$

where we have defined the *prior vorticity distribution* $\chi(\sigma) \equiv \exp\{-\sum_{n>1}\alpha_n\sigma^n\}$. We shall assume that this function is imposed by the small-scale forcing so it has to be given *a priori* as an input in the theory [6–8].

[1] Some attempts have been proposed for going beyond the assumptions of the statistical theory. For example, Chavanis and Sommeria [5] consider a *strong mixing limit* in which only the first moments of the vorticity are relevant instead of the whole set of Casimirs. They also introduce the concept of *maximum entropy bubbles* (or restricted equilibrium states) for accounting for situations where the evolution of the flow is not ergodic over the whole available domain but only in a subdomain.

2. Equilibrium statistical mechanics with a prior vorticity distribution

When a prior vorticity distribution is given, the statistical equilibrium state is obtained by maximizing the relative (or grand) entropy S_χ at fixed energy E, circulation Γ and normalization condition $\int \rho \mathrm{d}\sigma = 1$ (grand microcanonical ensemble). The conservation of the Casimirs has been replaced by the specification of the prior $\chi(\sigma)$. Writing the first-order variations as $\delta S_\chi - \beta\delta E - \alpha\delta\Gamma - \int \zeta(\mathbf{r})\delta\rho\mathrm{d}\sigma\mathrm{d}\mathbf{r} = 0$, we get the Gibbs state

$$\rho(\mathbf{r},\sigma) = \frac{1}{Z(\mathbf{r})}\chi(\sigma)\mathrm{e}^{-(\beta\psi+\alpha)\sigma}, \tag{6}$$

with $Z = \int_{-\infty}^{+\infty}\chi(\sigma)\mathrm{e}^{-(\beta\psi+\alpha)\sigma}\mathrm{d}\sigma$. This is the product of a universal Boltzmann factor and a non-universal function $\chi(\sigma)$ fixed by the forcing. The coarse-grained vorticity is given by

$$\overline{\omega} = \frac{\int \chi(\sigma)\sigma \mathrm{e}^{-(\beta\psi+\alpha)\sigma}\mathrm{d}\sigma}{\int \chi(\sigma)\mathrm{e}^{-(\beta\psi+\alpha)\sigma}\mathrm{d}\sigma} = F(\beta\psi+\alpha), \tag{7}$$

with $F(\Phi) = -(\ln\hat{\chi})'(\Phi)$, where we have defined $\hat{\chi}(\Phi) = \int_{-\infty}^{+\infty}\chi(\sigma)\mathrm{e}^{-\sigma\Phi}\mathrm{d}\sigma$. It is easy to show that $F'(\Phi) = -\omega_2(\Phi) \leq 0$, where $\omega_2 = \overline{\omega^2} - \overline{\omega}^2 \geq 0$ is the local centered variance of the vorticity. Therefore, $F(\Phi)$ is a decreasing function. Since $\overline{\omega} = f(\psi)$, the statistical theory predicts that the coarse-grained vorticity $\overline{\omega}(\mathbf{r})$ is a *stationary solution* of the 2D Euler equation and that the $\overline{\omega}$–ψ relationship is a *monotonic* function which is increasing at negative temperatures $\beta < 0$ and decreasing at positive temperatures $\beta > 0$. We have $\overline{\omega}'(\psi) = -\beta\omega_2$. We note that the $\overline{\omega}$–ψ relationship predicted by the statistical theory can take a wide diversity of forms (usually non-Boltzmannian) depending on the prior $\chi(\sigma)$. Furthermore, the coarse-grained distribution (7) extremizes a generalized entropy in $\overline{\omega}$-space of the form [9]

$$S[\overline{\omega}] = -\int C(\overline{\omega})\mathrm{d}\mathbf{r}, \tag{8}$$

at fixed circulation and energy (robust constraints). Writing the first-order variations as $\delta S - \beta\delta E - \alpha\delta\Gamma = 0$, leading to

$$C'(\overline{\omega}) = -\beta\psi - \alpha, \tag{9}$$

and comparing with Eq. (7), we find that $C'(x) = -F^{-1}(x)$. Therefore, C is a convex function ($C'' > 0$) determined by the prior $\chi(\sigma)$ encoding the small-scale forcing according to the relation

$$C(\overline{\omega}) = -\int^{\overline{\omega}} F^{-1}(x)\mathrm{d}x = -\int^{\overline{\omega}} [(\ln\hat{\chi})']^{-1}(-x)\mathrm{d}x. \tag{10}$$

We have $\overline{\omega}'(\psi) = -\beta/C''(\overline{\omega})$. Comparing with $\overline{\omega}'(\psi) = -\beta\omega_2$ we find that, at statistical equilibrium,

$$\omega_2 = 1/C''(\overline{\omega}), \tag{11}$$

which links the centered variance of the vorticity to the coarse-grained vorticity and the generalized entropy. It also clearly establishes that $C'' > 0$. On the other hand, the equilibrium coarse-grained vorticity $\overline{\omega}(\mathbf{r})$ maximizes the generalized entropy (8)–(10) at fixed circulation and energy iff $\rho(\mathbf{r},\sigma)$ maximizes S_χ at fixed E, Γ (see Appendix and [6,10]). *Therefore, the maximization of $S[\overline{\omega}]$ at fixed E and Γ is a necessary and sufficient condition of EHT thermodynamical stability.*

The preceding relations are also valid in the MRS approach except that $\chi(\sigma)$ is determined *a posteriori* from the initial conditions by relating the Lagrange multipliers $\alpha_{n>1}$ to the Casimir constraints $\Gamma^{f.g.}_{n>1}$. In this case of freely evolving flows, the generalized entropy (8)–(10) depends on the initial conditions, while in the case of forced flows considered here, it is intrinsically fixed by the prior vorticity distribution. On the other hand, a maximum of $S_\chi[\rho]$ at fixed E and Γ is always a maximum of $S[\rho]$ at fixed E, Γ and $\Gamma^{f.g.}_{n>1}$ (more constrained problem). Therefore, a maximum of the generalized entropy $S[\overline{\omega}]$ at fixed E and Γ determines a statistical equilibrium state from the MRS viewpoint [10]. However, the converse is wrong in the case of "ensemble inequivalence" [11,12] with respect to the conjugate variables $(\Gamma^{f.g.}_{n>1},\alpha_n)$ because a maximum of $S[\rho]$ at fixed E, Γ and $\Gamma^{f.g.}_{n>1}$ is not necessarily a maximum of $S_\chi[\rho]$ at fixed E and Γ. *Therefore, the maximization of $S[\overline{\omega}]$ at fixed E and Γ is a sufficient (but not necessary) condition of MRS thermodynamical stability.*

3. Relaxation towards equilibrium

In the case where a small-scale forcing imposes a prior vorticity distribution $\chi(\sigma)$, it is possible to propose a thermodynamical parametrization of the turbulent flow in the form of a relaxation equation that conserves the circulation and the energy (robust constraints) and that increases the generalized entropy (8)–(10) fixed by the prior. This equation can be obtained from a generalized Maximum Entropy Production Principle (MEPP) in $\overline{\omega}$-space [9]. We write $\omega=\overline{\omega}+\tilde{\omega}$ and take the local average of the 2D Euler equation (1). This yields $D\overline{\omega}/Dt=-\nabla\cdot\overline{\tilde{\omega}\tilde{\mathbf{u}}}\equiv-\nabla\cdot\mathbf{J}$ where $D/Dt=\partial/\partial t+\overline{\mathbf{u}}\cdot\nabla$ is the material derivative and $\mathbf{J}$ is the turbulent current. Then, we determine the optimal current $\mathbf{J}$ which maximizes the rate of entropy production $\dot{S}=-\int C''(\overline{\omega})\mathbf{J}\cdot\nabla\overline{\omega}\mathrm{d}\mathbf{r}$ at fixed energy $\dot{E}=\int\mathbf{J}\cdot\nabla\psi\mathrm{d}\mathbf{r}=0$, assuming that the energy of the fluctuations $\mathbf{J}^2/2\overline{\omega}$ is bounded. According to this phenomenological principle, we find that the coarse-grained vorticity evolves according to [9,8]

$$\frac{\partial\overline{\omega}}{\partial t}+\mathbf{u}\cdot\nabla\overline{\omega}=\nabla\cdot\left\{D\left[\nabla\overline{\omega}+\frac{\beta(t)}{C''(\overline{\omega})}\nabla\psi\right]\right\},\tag{12}$$

$$\beta(t)=-\frac{\int D\nabla\overline{\omega}\cdot\nabla\psi\mathrm{d}\mathbf{r}}{\int D\frac{(\nabla\psi)^2}{C''(\overline{\omega})}\mathrm{d}\mathbf{r}},\quad\overline{\omega}=-\Delta\psi,\tag{13}$$

where $\beta(t)$ is a Lagrange multiplier enforcing the energy constraint $\dot{E}=0$ at any time. It is shown in [9] that these equations increase monotonically the entropy (H-theorem, $\dot{S}\geq 0$) provided that $D>0$. Furthermore, a steady state of (12) is linearly dynamically stable iff it is a (local) entropy maximum at fixed circulation and energy (minima or saddle points of entropy are linearly unstable). Therefore, the relaxation Eqs. (12) and (13) generically converge towards a (local) entropy maximum (if there is no entropy maximum the solutions of the relaxation equations can have a singular behaviour). If there exist several local entropy maxima the selection will depend on a complicated notion of a *basin of attraction*. The diffusion coefficient D is not determined by the MEPP but it can be obtained from a Taylor type argument leading to $D=K\epsilon^2\omega_2^{1/2}$ where ϵ is the coarse-graining mesh size and K is a constant of order unity [8]. Assuming that the relation (11) remains valid out of equilibrium (see Appendix C of [8]), we get the closed expression $D=K\epsilon^2/\sqrt{C''(\overline{\omega})}$. This position dependent diffusion coefficient, related to the strength of the fluctuations, can "freeze" the system in a sub-region of space ("bubble") and account for *incomplete relaxation* and lack of ergodicity [13,4]. The relaxation equation (12) belongs to the class of nonlinear mean field Fokker–Planck equations introduced in [9]. This relaxation equation conserves only the robust constraints (circulation and energy) and increases the generalized entropy (8)–(10) fixed by the prior vorticity distribution $\chi(\sigma)$. It differs from the relaxation equations proposed by Robert and Sommeria [14] for freely evolving flows which conserve all the constraints of the 2D Euler equation (E, Γ and all the Casimirs) and monotonically increase the mixing entropy (2). In Eqs. (12) and (13), the specification of the prior $\chi(\sigma)$ (determined by the small-scale forcing) replaces the specification of the Casimirs (determined by the initial conditions). However, in both models, the robust constraints E and Γ are treated microcanonically (i.e. they are rigorously conserved). The relaxation equations of Robert and Sommeria [14] and Chavanis [9] are essentially phenomenological in nature but they can serve as *numerical algorithms* for computing maximum entropy states. In that context, since we are only interested by the stationary state (not by the dynamics), we can take $D=$ Cst. and drop the advective term in the relaxation equation. Then, Eq. (12) can be used to construct (i) arbitrary EHT statistical equilibria, (ii) a subset of MRS statistical equilibria (see the last paragraph of Section 2).

4. Explicit examples

Let us consider, for illustration, the prior vorticity distribution $\chi(\sigma)$ introduced by Ellis, Haven and Turkington [6] in their model of Jovian vortices. It corresponds to a decentered Gamma distribution

$$\chi(\sigma)=\frac{1}{\Omega_2|\lambda|}R\left[\frac{1}{\Omega_2\lambda}\left(\sigma+\frac{1}{\lambda}\right);\frac{1}{\Omega_2\lambda^2}\right],\tag{14}$$

where $R(z;a)=\Gamma(a)^{-1}z^{a-1}\mathrm{e}^{-z}$ for $z\geq 0$ and $R=0$ otherwise. The scaling of $\chi(\sigma)$ is chosen such that $\langle\sigma\rangle=0$, $\mathrm{var}(\sigma)\equiv\langle\sigma^2\rangle=\Omega_2$ and $\mathrm{skew}(\sigma)\equiv\langle\sigma^3\rangle/\langle\sigma^2\rangle^{3/2}=2\Omega_2^{1/2}\lambda$. We get

$$Z(\Phi)=\hat{\chi}(\Phi)=\frac{\mathrm{e}^{\Phi/\lambda}}{(1+\lambda\Omega_2\Phi)^{1/(\Omega_2\lambda^2)}},\tag{15}$$

$$\overline{\omega}(\Phi)=-(\ln\hat{\chi})'(\Phi)=\frac{-\Omega_2\Phi}{1+\lambda\Omega_2\Phi}.\tag{16}$$

Inverting the relation (16), we obtain

$$-\Phi = \frac{1}{\Omega_2}\frac{\overline{\omega}}{1+\lambda\overline{\omega}} = C'(\overline{\omega}). \tag{17}$$

After integration, we obtain the generalized entropy

$$C(\overline{\omega}) = \frac{1}{\lambda\Omega_2}\left[\overline{\omega} - \frac{1}{\lambda}\ln(1+\lambda\overline{\omega})\right]. \tag{18}$$

In the limit $\lambda \to 0$, the prior is the Gaussian distribution

$$\chi(\sigma) = \frac{1}{\sqrt{2\pi\Omega_2}}\mathrm{e}^{-\frac{\sigma^2}{2\Omega_2}}, \tag{19}$$

and we have $Z(\Phi) = \mathrm{e}^{\frac{1}{2}\Omega_2\Phi^2}$, $\overline{\omega}(\Phi) = -\Omega_2\Phi$, $C(\overline{\omega}) = \frac{\overline{\omega}^2}{2\Omega_2}$. The generalized entropy $S = -\frac{1}{2\Omega_2}\int\overline{\omega}^2\mathrm{d}\mathbf{r}$ associated with a Gaussian prior is proportional (with the opposite sign) to the coarse-grained enstrophy: $S = -\Gamma_2^{c.g.}/(2\Omega_2)$ [9]. This Gaussian prior leads to Fofonoff flows [15] that have oceanic applications.

When the prior is given by Eq. (14), the generalized entropy satisfies $C''(\overline{\omega}) = 1/[\Omega_2(1+\lambda\overline{\omega})^2]$ and we obtain a parametrization of the form

$$\frac{\partial\overline{\omega}}{\partial t} + \mathbf{u}\cdot\nabla\overline{\omega} = \nabla\cdot\left\{D\left[\nabla\overline{\omega} + \beta(t)\Omega_2(1+\lambda\overline{\omega})^2\nabla\psi\right]\right\}, \tag{20}$$

$$\beta(t) = -\frac{\int D\nabla\omega\cdot\nabla\psi d\mathbf{r}}{\int D\Omega_2(1+\lambda\overline{\omega})^2(\nabla\psi)^2\mathrm{d}\mathbf{r}}, \quad D = K\epsilon^2\Omega_2^{1/2}|1+\lambda\overline{\omega}|. \tag{21}$$

For $\lambda = 0$ (Gaussian limit), we get

$$\frac{\partial\overline{\omega}}{\partial t} + \mathbf{u}\cdot\nabla\overline{\omega} = \nabla\cdot\{D[\nabla\overline{\omega} + \beta(t)\Omega_2\nabla\psi]\}, \tag{22}$$

$$\beta(t) = -\frac{\int D\nabla\omega\cdot\nabla\psi\mathrm{d}\mathbf{r}}{\int D\Omega_2(\nabla\psi)^2\mathrm{d}\mathbf{r}}, \quad D = K\epsilon^2\Omega_2^{1/2}. \tag{23}$$

Since D and Ω_2 are uniform, we have $D\overline{\omega}/Dt = D(\Delta\overline{\omega} - \beta(t)\Omega_2\overline{\omega})$ with $\beta(t) = -\Gamma_2^{c.g.}(t)/(2\Omega_2 E) = S(t)/E$ (to arrive at this result, we have used integration by parts in Eq. (23)).

When the prior has two intense peaks $\chi(\sigma) = \delta(\sigma-\sigma_0) + \delta(\sigma-\sigma_1)$, the equilibrium coarse-grained vorticity is

$$\overline{\omega} = \sigma_1 + \frac{\sigma_0 - \sigma_1}{1+\mathrm{e}^{(\sigma_0-\sigma_1)(\beta\psi+\alpha)}}. \tag{24}$$

This is similar to the Fermi–Dirac statistics. Inverting this relation to express $\Phi = \beta\psi + \alpha$ as a function of $\overline{\omega}$ and integrating the resulting expression, we obtain the generalized entropy

$$S[\overline{\omega}] = -\int[p\ln p + (1-p)\ln(1-p)]\mathrm{d}\mathbf{r}, \tag{25}$$

where $\overline{\omega} = p\sigma_0 + (1-p)\sigma_1$. At equilibrium, we have $\omega_2 = 1/C''(\overline{\omega}) = (\sigma_0-\overline{\omega})(\overline{\omega}-\sigma_1)$. For the two-peak distribution, we get a parametrization of the form

$$\frac{\partial\overline{\omega}}{\partial t} + \overline{\mathbf{u}}\cdot\nabla\overline{\omega} = \nabla\cdot[D(\nabla\overline{\omega} + \beta(t)(\sigma_0-\overline{\omega})(\overline{\omega}-\sigma_1)\nabla\psi)], \tag{26}$$

$$\beta(t) = -\frac{\int D\nabla\overline{\omega}\cdot\nabla\psi\mathrm{d}\mathbf{r}}{\int D(\sigma_0-\overline{\omega})(\overline{\omega}-\sigma_1)(\nabla\psi)^2\mathrm{d}\mathbf{r}}, \quad D = K\epsilon^2\omega_2^{1/2}. \tag{27}$$

These are the same equations as in the MRS theory in the two-level case $\omega \in \{\sigma_0, \sigma_1\}$ [1–4]. They amount to maximizing the Fermi–Dirac-like entropy (25) at fixed circulation and energy. This entropy has been used by Bouchet and Sommeria [16] to model Jovian vortices. From the MRS viewpoint, this entropy describes the free merging of a system with two levels of vorticity σ_0 and σ_1, while from the viewpoint developed here, it describes the evolution of a forced system where the forcing has two intense peaks described by the prior $\chi(\sigma) = \delta(\sigma-\sigma_0) + \delta(\sigma-\sigma_1)$ [8]. Other examples of prior vorticity distributions and associated generalized entropies are collected in [9].

5. Nonlinear dynamical stability

Let us consider the Casimir functionals $S[\omega] = -\int C(\omega)\mathrm{d}\mathbf{r}$ where C is any convex function ($C'' > 0$). Since S, E and Γ are individually conserved by the 2D Euler equation, the maximization problem

$$\max_\omega\{S[\omega] \mid E[\omega] = E, \Gamma[\omega] = \Gamma\}, \tag{28}$$

determines a steady state of the 2D Euler equation that is formally nonlinearly dynamically stable [6]. Writing the first variations as $\delta S - \beta\delta E - \alpha\delta\Gamma = 0$, the steady state is characterized by a monotonic relation $\omega = F(\beta\psi+\alpha) = f(\psi)$ where $F(x) = (C')^{-1}(-x)$. Let us introduce the Legendre transform $J = S - \beta E$ and consider the maximization problem

$$\max_\omega\{J[\omega] = S[\omega] - \beta E[\omega] | \Gamma[\omega] = \Gamma\}. \tag{29}$$

If we interpret J as an energy-Casimir functional, the maximization problem (29) corresponds to the Arnold criterion of formal nonlinear dynamical stability. The variational problems (28) and (29) have the same critical points (cancelling the first variations) but not necessarily the same maxima (regarding the second variations). A solution of (29) is always a solution of the more constrained problem (28). However, the reciprocal is wrong. A solution of (28) is not necessarily a solution of (29). The maximization problem (29) and the associated Arnold theorems provide just a *sufficient* condition for nonlinear dynamical stability. The criterion (28) of Ellis, Haven and Turkington is more refined and allows one to construct a larger class of nonlinearly stable steady states. For example, important equilibrium states in the weather layer of Jupiter are nonlinearly dynamically stable according to the refined stability criterion (28) while they do not satisfy the Arnold theorems [6]. The maximization problem (29) determines a *subclass* of solutions of the maximization problem (28). This is similar to a situation of "ensemble inequivalence" with respect to the conjugate variables (E, β) in thermodynamics [11,12]. Indeed, (28) is similar to a criterion of "microcanonical stability" while (29) is similar to a criterion of "canonical stability" in thermodynamics, where S is similar to an entropy and J is similar to a free energy [9]. Canonical stability implies microcanonical stability but the converse is wrong in the case of ensemble inequivalence.[2] Since the relaxation equations (12) and (13) solve the maximization problem (28), they can serve as numerical algorithms for computing nonlinearly dynamically stable stationary solutions of the 2D Euler equation according to the criterion of Ellis, Haven and Turkington. Note that if we fix β, the relaxation equation (12) increases monotonically the "free energy" $J = S - \beta E$ (H-theorem, $\dot{J} \geq 0$) until a (local) maximum of J at fixed Γ is reached [9]. Therefore, we obtain a numerical algorithm that solves the maximization problem (29) and determines a subclass of nonlinearly dynamically stable stationary solutions of the 2D Euler equation corresponding to the Arnold criterion.

6. Conclusion

In this paper, we have shown that the maximization of a functional $S[\omega]$ at fixed circulation Γ and energy E in 2D turbulence can have several interpretations. When S is given by (8)–(10), this maximization problem determines: (i) The whole class of stable EHT statistical equilibria for a given prior vorticity distribution $\chi(\sigma)$ fixed by the small-scale forcing. (ii) A subclass of stable MRS statistical equilibria for initial conditions leading to a vorticity distribution $\chi(\sigma)$ at statistical equilibrium. When S is given by (8) where C is an arbitrary convex function, this maximization problem determines a nonlinearly dynamically stable stationary solution of the 2D Euler equation according to the refined EHT criterion. The next step is to determine whether particular forms of generalized entropies are better adapted than others for describing specific flows and whether they can be regrouped in "classes of equivalence" [9]. For example, the enstrophy functional turns out to be relevant for certain oceanic situations [15] and the Fermi–Dirac-like entropy for Jovian flows [16]. Working with a suitable generalized entropy $S[\omega]$ with only two constraints (Γ, E) is more convenient than working with an infinite set of Casimirs as in the MRS theory. This reduced maximization problem is still very rich because, for any considered form of generalized entropy $S[\omega]$, many bifurcations can take place in the parameter space (E, Γ) [5,6,16].

Appendix. Generalized entropy

We can introduce the generalized entropy $S[\overline{\omega}]$ in the following manner. Initially, we want to determine the vorticity distribution $\rho_*(\mathbf{r}, \sigma)$ which maximizes $S_\chi[\rho]$ with the robust constraints $E[\overline{\omega}] = E$, $\Gamma[\overline{\omega}] = \Gamma$, and the normalization condition $\int \rho\, \mathrm{d}\sigma = 1$. To solve this maximization problem, we can proceed in two steps. *First step:* we determine the distribution $\rho_1(\mathbf{r}, \sigma)$ which maximizes $S_\chi[\rho]$ with the constraints $\int \rho\, \mathrm{d}\sigma = 1$ and a fixed vorticity profile $\int \rho\sigma\, \mathrm{d}\sigma = \overline{\omega}(\mathbf{r})$ (note that fixing $\overline{\omega}$ automatically determines Γ and E). This gives a distribution $\rho_1[\overline{\omega}(\mathbf{r}), \sigma]$ depending on $\overline{\omega}(\mathbf{r})$ and σ. Substituting this distribution in the functional $S_\chi[\rho]$, we obtain a functional $S[\overline{\omega}] \equiv S_\chi[\rho_1]$ of the vorticity $\overline{\omega}$. *Second step:* we determine the vorticity field $\overline{\omega}_*(\mathbf{r})$ which maximizes $S[\overline{\omega}]$ with the constraints $E[\overline{\omega}] = E$ and $\Gamma[\overline{\omega}] = \Gamma$. Finally, we have $\rho_*(\mathbf{r}, \sigma) = \rho_1[\overline{\omega}_*(\mathbf{r}), \sigma]$. Let us be more explicit. The distribution $\rho_1(\mathbf{r}, \sigma)$ that extremizes $S_\chi[\rho]$ with the constraints $\int \rho\, \mathrm{d}\sigma = 1$ and $\int \rho\sigma\, \mathrm{d}\sigma = \overline{\omega}(\mathbf{r})$ satisfies the first-order variations $\delta S_\chi - \int \Phi(\mathbf{r})\delta(\int \rho\sigma \mathrm{d}\sigma)\mathrm{d}\mathbf{r} - \int \zeta(\mathbf{r})\delta(\int \rho \mathrm{d}\sigma)\mathrm{d}\mathbf{r} = 0$, where $\Phi(\mathbf{r})$ and $\zeta(\mathbf{r})$ are Lagrange multipliers. This yields

$$\rho_1(\mathbf{r}, \sigma) = \frac{1}{Z(\mathbf{r})}\chi(\sigma)\mathrm{e}^{-\sigma\Phi(\mathbf{r})}, \tag{A.1}$$

where $Z(\mathbf{r})$ and $\Phi(\mathbf{r})$ are determined by $Z(\mathbf{r}) = \int \chi(\sigma)\mathrm{e}^{-\sigma\Phi(\mathbf{r})}\mathrm{d}\sigma \equiv \hat{\chi}(\Phi)$ and $\overline{\omega}(\mathbf{r}) = \frac{1}{Z(\mathbf{r})}\int \chi(\sigma)\sigma \mathrm{e}^{-\sigma\Phi(\mathbf{r})}\mathrm{d}\sigma = -(\ln\hat{\chi})'(\Phi)$. This critical point is a *maximum* of S_χ with the above-mentioned constraints since $\delta^2 S_\chi = -\int \frac{(\delta\rho)^2}{\rho}\mathrm{d}\mathbf{r}\mathrm{d}\sigma \leq 0$. Then $S_\chi[\rho_1] = \int \rho_1(\sigma\Phi + \ln\hat{\chi})\,\mathrm{d}\mathbf{r}\mathrm{d}\sigma = \int(\overline{\omega}\Phi + \ln\hat{\chi}(\Phi))\,\mathrm{d}\mathbf{r}$. Therefore $S[\overline{\omega}] \equiv S_\chi[\rho_1]$ is given by $S[\overline{\omega}] = -\int C(\overline{\omega})\,\mathrm{d}\mathbf{r}$ with $C(\overline{\omega}) = -\overline{\omega}\Phi - \ln\hat{\chi}(\Phi)$. Now, $\Phi(\mathbf{r})$ is related to $\overline{\omega}(\mathbf{r})$ by $\overline{\omega}(\mathbf{r}) = -(\ln\hat{\chi})'(\Phi)$. This implies that $C'(\overline{\omega}) = -\Phi = -[(\ln\hat{\chi})']^{-1}(-\overline{\omega})$ so

$$C(\overline{\omega}) = -\int^{\overline{\omega}} [(\ln\hat{\chi})']^{-1}(-x)\mathrm{d}x. \tag{A.2}$$

This is precisely the generalized entropy (10). Therefore, $\rho_*(\mathbf{r}, \sigma) = \rho_1[\overline{\omega}_*(\mathbf{r}), \sigma]$ is a maximum of $S_\chi[\rho]$ at fixed E and Γ iff $\overline{\omega}_*(\mathbf{r})$ is a maximum of $S[\overline{\omega}]$ at fixed E and Γ.

References

[1] J. Miller, Phys. Rev. Lett. 65 (1990) 2137.
[2] R. Robert, J. Sommeria, JFM 229 (1991) 291.
[3] D. Lynden-Bell, MNRAS 136 (1967) 101.
[4] P.H. Chavanis, J. Sommeria, R. Robert, Astrophys. J. 471 (1996) 385.
[5] P.H. Chavanis, J. Sommeria, JFM 356 (1998) 259.
[6] R. Ellis, K. Haven, B. Turkington, Nonlinearity 15 (2002) 239.
[7] C. Boucher, R. Ellis, B. Turkington, J. Stat. Phys. 98 (2000) 1235.
[8] P.H. Chavanis, Physica D 200 (2005) 257.
[9] P.H. Chavanis, Phys. Rev. E 68 (2003) 036108.
[10] F. Bouchet, arXiv:0710.5094.
[11] R. Ellis, K. Haven, B. Turkington, J. Stat. Phys. 101 (2000) 935.
[12] F. Bouchet, J. Barré, J. Stat. Phys. 118 (2005) 1073.
[13] R. Robert, C. Rosier, J. Stat. Phys. 86 (1997) 481.
[14] R. Robert, J. Sommeria, PRL 69 (1992) 2776.
[15] N.P. Fofonoff, J. Mar. Res. 13 (1954) 254.
[16] F. Bouchet, J. Sommeria, JFM 464 (2002) 165.

[2] Since the EHT statistical equilibria (with a given prior) satisfy a maximization problem of the form (28) with $C(\overline{\omega})$ given by Eq. (10), they are both thermodynamically stable (with respect to fine-grained perturbations $\delta\rho(\mathbf{r}, \sigma)$) and formally nonlinearly dynamically stable (with respect to coarse-grained perturbations $\delta\overline{\omega}(\mathbf{r})$). Note that the MRS statistical equilibria may not satisfy the nonlinear dynamical stability criterion (28) according to the discussion at the end of Section 2. This intriguing observation demands further investigation.

Available online at www.sciencedirect.com
ScienceDirect
Physica D 237 (2008) 2003–2008
PHYSICA D
www.elsevier.com/locate/physd

Fundamental conditions for N-th-order accurate lattice Boltzmann models

Hudong Chen*, Xiaowen Shan

EXA Corporation, 3 Burlington Woods Drive, Burlington, MA 01803, USA

Available online 23 November 2007

Abstract

In this paper, we theoretically prove a set of fundamental conditions pertaining to discrete velocity sets and corresponding weights. These conditions provide sufficient conditions for *a priori* formulation of lattice Boltzmann models that automatically admit correct hydrodynamic moments up to any given N-th order.

Keywords: Lattice Boltzmann; Hydrodynamic moments

1. Introduction

Lattice Boltzmann methods (LBM) have been recognized as advantageous numerical methods for performing efficient computational fluid dynamics [1,2]. Not only do they offer a new way of describing macroscopic fluid physics, but also they have become practical computational tools and already have been making a substantial impact in real world engineering applications [3]. Furthermore, according to a more recent interpretation, LBM models are special discrete approximations to the continuum Boltzmann kinetic equation [4,5]. Owing to such an underlying kinetic theory origin, the LBM are expected to contain a wider range of fluid flow physics than the conventional hydrodynamic fluid descriptions [6–8,10]. The latter, such as the Euler or the Navier–Stokes equation, rely on various "theoretical" closure approximations for the non-equilibrium effects that are problematic when deviations from local thermodynamic equilibrium are no longer considered small. In addition, due to the fact that the fundamental turbulence modeling is built upon an analogy to regular fluid flows at finite Knudsen numbers, a kinetic theory representation is argued to be more suitable than the classical modeling approach of modified Navier–Stokes equations [22]. However, how much the original range in kinetic theory can be retained depends on the order of accuracy in the LBM models used. Indeed, it has been shown that certain key physical effects beyond the Navier–Stokes equations can be accurately captured using higher order LBM models [5,9].

There have been extensive studies in LBM for more than a decade. However, popularly known LBM models are only accurate in the Navier–Stokes hydrodynamic regime (cf., [12, 14]). That is, physics higher than the Navier–Stokes order is contaminated by numerical artifacts in these LBM models. Furthermore, there has not been progress in systematically deriving higher order accurate LBM models until recently [5]. Originated from the framework of the so called lattice gas automata [15,11], the conventional approach to formulating LBM models is based on a so called "top down" procedure. That is, giving a macroscopic equation such as the Euler or the Navier–Stokes equation, an LBM model may be constructed via an inverse Chapman–Enskog process and a *a posteriori* parameter matching along with various subsequent "corrections" (cf., [13,14,16,17]). But more fundamentally, because such an approach relies on the availability of macroscopic descriptions, it encounters an intrinsic difficulty in extending physics beyond the original macroscopic equations. It is well known that there is no well established and reliable macroscopic equation for deeper non-equilibrium physics beyond the Navier–Stokes regime.

One can theoretically show that the level of non-equilibrium physics is directly associated with the hydrodynamic moments [5]. Specifically, from the representation of the Chapman–Enskog expansion, there exists an apparent hierarchical relationship among hydrodynamic moments at various non-equilibrium levels. That is, n-th-order hydrodynamic

* Corresponding author. Tel.: +1 781 676 8512; fax: +1 781 676 8599.
E-mail address: hudong@exa.com (H. Chen).

0167-2789/$ - see front matter
doi:10.1016/j.physd.2007.11.010

moments at the m-th non-equilibrium level are related to the $(n+1)$-th-order moments at $(m-1)$-th non-equilibrium level. Carrying this hierarchy all the way, we see that in order to ensure the n-th-moment physics at the m-th non-equilibrium level, it requires the equilibrium moments of $(m+n)$-th order to be accurate. In other words, the higher the order of equilibrium hydrodynamic moments captured accurately, the wider the range of non-equilibrium physics that can be described. Indeed, the popularly known lattice Boltzmann models are only accurate up to the second-order equilibrium moment (i.e., the equilibrium momentum flux tensor). As a result, these models only give an approximately correct "level-1" non-equilibrium momentum flux. This is why the conventional LBM models are only applicable to the Navier–Stokes (Newtonian) fluid physics in low Mach number isothermal situations [11–14].

On the basis of the above, we see that the essential requirement for accurately capturing a wider range of physics is directly related to achieving equilibrium hydrodynamic moments to higher orders. Once the higher order moments are accurately realized, the resulting hydrodynamic equations such as Euler, Navier–Stokes and beyond are automatically attained. This is accomplished without the conventional *a posteriori* procedure. As shown in this paper, the above requirement dictates a set of fundamental conditions on the supporting lattice velocity basis in LBM. That is, given an N-th-order moment accuracy requirement, the set of fundamental conditions automatically defines the choice of a discrete lattice velocity set and its corresponding weights for such a purpose.

In this paper, we theoretically derive this set of fundamental conditions for LBM models of N-th order. We prove how the correct hydrodynamic moments up to the corresponding order are realized once the conditions are satisfied.

2. Achieving correct hydrodynamic moments via discrete velocities

According to the standard continuum Boltzmann kinetic theory, an n-th-order equilibrium hydrodynamic moment tensor in D dimensions is defined as

$$\boldsymbol{M}^{(n)}(\boldsymbol{x},t) \equiv \int d^D\boldsymbol{c}\,\underbrace{\boldsymbol{c}\boldsymbol{c}\cdots\boldsymbol{c}}_{n}\,f^{eq}(\boldsymbol{x},\boldsymbol{c},t). \tag{1}$$

Equivalently, it can be expressed in a Cartesian component form as follows:

$$M^{(n)}_{i_1,i_2,\ldots,i_n}(\boldsymbol{x},t) \equiv \int d^D\boldsymbol{c}\, c_{i_1}c_{i_2}\cdots c_{i_n} f^{eq}(\boldsymbol{x},\boldsymbol{c},t) \tag{2}$$

where subscripts $i_1, i_2, \ldots, i_n$ are Cartesian component indices. c_i is the i-th Cartesian component of the microscopic particle velocity $\boldsymbol{c}$. The equilibrium distribution has the standard Maxwell–Boltzmann form

$$f^{eq}(\boldsymbol{x},\boldsymbol{c},t) = \frac{\rho(\boldsymbol{x},t)}{[2\pi\theta(\boldsymbol{x},t)]^{D/2}} \times \exp\left[-\frac{(\boldsymbol{c}-\boldsymbol{u}(\boldsymbol{x},t))^2}{2\theta(\boldsymbol{x},t)}\right] \tag{3}$$

where the macroscopic density, fluid velocity, and temperature are defined, respectively, as

$$\rho(\boldsymbol{x},t) = \int d^D\boldsymbol{c}\; f^{eq}(\boldsymbol{x},\boldsymbol{c},t)$$
$$\rho\boldsymbol{u}(\boldsymbol{x},t) = \int d^D\boldsymbol{c}\,\boldsymbol{c}\,f^{eq}(\boldsymbol{x},\boldsymbol{c},t)$$
$$D\rho\theta(\boldsymbol{x},t) = \int d^D\boldsymbol{c}\;(\boldsymbol{c}-\boldsymbol{u}(\boldsymbol{x},t))^2 f^{eq}(\boldsymbol{x},\boldsymbol{c},t). \tag{4}$$

Apparently, the above three relations correspond to the zeroth-, the first-, and the trace of the second-order hydrodynamic moments. It is well known that these three moments correspond to conservation laws and are invariant under any local collisions.

Notice that the density ρ is an overall multiplier on all moments; without loss of generality for the subsequent analysis, we set it to unity.

Now let us define an analogous hydrodynamic moment expression in terms of summations over discrete velocity values below:

$$\tilde{\boldsymbol{M}}^{(n)}(\boldsymbol{x},t) \equiv \sum_{\alpha=0}^{b}\underbrace{\boldsymbol{c}_\alpha\boldsymbol{c}_\alpha\cdots\boldsymbol{c}_\alpha}_{n}\, f^{eq}_\alpha(\boldsymbol{x},t). \tag{5}$$

Or equivalently, in a Cartesian component form,

$$\tilde{M}^{(n)}_{i_1,i_2\cdots,i_n}(\boldsymbol{x},t) \equiv \sum_{\alpha=0}^{b} c_{\alpha,i_1}c_{\alpha,i_2}\cdots c_{\alpha,i_n} f^{eq}_\alpha(\boldsymbol{x},t). \tag{6}$$

In the above, we have assumed there are $b+1$ discrete D-dimensional vector values in the basis discrete velocity set: $\{\boldsymbol{c}_\alpha : \alpha = 0,\ldots,b\}$. Similarly, we define an analogous equilibrium distribution function:

$$f^{eq}_\alpha(\boldsymbol{x},t) = \bar{w}_\alpha(\theta(\boldsymbol{x},t))\exp\left[-\frac{(\boldsymbol{c}_\alpha-\boldsymbol{u}(\boldsymbol{x},t))^2}{2\theta(\boldsymbol{x},t)}\right] \tag{7}$$

where the macroscopic density, fluid velocity, and temperature are now defined in terms of moment summations instead,

$$1 = \sum_{\alpha=0}^{b} f^{eq}_\alpha(\boldsymbol{x},t)$$
$$\boldsymbol{u}(\boldsymbol{x},t) = \sum_{\alpha=0}^{b}\boldsymbol{c}_\alpha f^{eq}_\alpha(\boldsymbol{x},t)$$
$$D\theta(\boldsymbol{x},t) = \sum_{\alpha=0}^{b}(\boldsymbol{c}_\alpha-\boldsymbol{u})^2 f^{eq}_\alpha(\boldsymbol{x},t). \tag{8}$$

In the above, $\bar{w}_\alpha$ is a weighting factor that is at most dependent on $\theta(\boldsymbol{x},t)$. On the basis of this, we can also re-express the discrete equilibrium distribution (7) in an alternative and simpler form:

$$f^{eq}_\alpha = \bar{w}_\alpha(\theta)\exp\left[-\frac{(\boldsymbol{c}_\alpha-\boldsymbol{u})^2}{2\theta}\right] = w_\alpha(\theta)\exp\left[\frac{\boldsymbol{c}_\alpha\cdot\boldsymbol{u}}{\theta}\right]\exp\left[-\frac{\boldsymbol{u}^2}{2\theta}\right] \tag{9}$$

by defining $w_\alpha(\theta) \equiv \bar{w}_\alpha(\theta)\exp[-\frac{c_\alpha^2}{2\theta}]$. Therefore, the discrete moment definition (6) can be re-expressed as

$$\tilde{M}^{(n)}_{i_1,i_2,\ldots,i_n} \equiv \sum_{\alpha=0}^{b} c_{\alpha,i_1}c_{\alpha,i_2}\cdots c_{\alpha,i_n} w_\alpha(\theta) \times \exp\left[\frac{\boldsymbol{c}_\alpha\cdot\boldsymbol{u}}{\theta}\right]\exp\left[-\frac{\boldsymbol{u}^2}{2\theta}\right]. \tag{10}$$

Having all the basic definitions above specified, we are now ready to prove several fundamental conditions for a lattice velocity basis supporting an n-th-order hydrodynamic moment accuracy and its corresponding form for the discrete equilibrium distribution function. These conditions are set forth for measuring any given lattice in terms of an intrinsic tensor:

$$E^{(n)}_{i_1,\ldots,i_n} \equiv \sum_{\alpha=0}^{b} w_\alpha(\theta)c_{\alpha,i_1}c_{\alpha,i_2}\cdots c_{\alpha,i_n}. \tag{11}$$

Theorem 1. *The discrete moment $\tilde{\boldsymbol{M}}^{(n)}$ is equal to the moment $\boldsymbol{M}^{(n)}$ of the continuum Boltzmann kinetic theory, if the supporting lattice velocity basis satisfies the following conditions:*

$$E^{(n)}_{i_1,i_2,\ldots,i_n} = \begin{cases} \theta^{n/2}\Delta^{(n)}_{i_1,i_2,\ldots,i_n}, & n = 0, 2, 4, \ldots \\ 0, & n = 1, 3, 5, \ldots. \end{cases} \tag{12}$$

In the above, $\Delta^{(n)}_{i_1,i_2,\ldots,i_n}$ is the n-th-order delta function defined as a summation of $n/2$ ($n = even\ integer$) products of simple Kronecker delta functions $\delta_{i_1i_2}\cdots\delta_{i_{n-1}i_n}$ and those from distinctive permutations of its sub-indices [11,18–20]. There are $(n-1)!!$ ($\equiv (n-1)\cdot(n-3)\ldots 3\cdot 1$) distinctive terms in $\Delta^{(n)}_{i_1i_2\ldots i_n}$ in total. For instance, $\Delta^{(2)}_{ij} \equiv \delta_{ij}$, and

$$\Delta^{(4)}_{ijkl} = \delta_{ij}\delta_{kl} + \delta_{ik}\delta_{jl} + \delta_{il}\delta_{jk}$$
$$\Delta^{(6)}_{ijklmn} = \delta_{ij}\Delta^{(4)}_{klmn} + \delta_{ik}\Delta^{(4)}_{lmnj} + \delta_{il}\Delta^{(4)}_{mnjk} + \delta_{im}\Delta^{(4)}_{njkl} + \delta_{in}\Delta^{(4)}_{jklm}. \tag{13}$$

Obviously, a lattice velocity set that satisfies condition (12) for $E^{(n)}$ is n-th-order isotropic.

Proof of Theorem 1. First we prove for the zeroth-order moment, $\tilde{\boldsymbol{M}}^{(0)} = \boldsymbol{M}^{(0)} = 1$. According to (9) we have

$$\begin{aligned}\tilde{\boldsymbol{M}}^{(0)} &= \exp\left[-\frac{\boldsymbol{u}^2}{2\theta}\right]\sum_{\alpha=0}^{b} w_\alpha \exp\left[\frac{\boldsymbol{c}_\alpha\cdot\boldsymbol{u}}{\theta}\right] \\ &= \exp\left[-\frac{\boldsymbol{u}^2}{2\theta}\right]\sum_{l=0}^{\infty}\frac{1}{\theta^l l!}\sum_{\alpha=0}^{b} w_\alpha(\boldsymbol{c}_\alpha\cdot\boldsymbol{u})^l.\end{aligned} \tag{14}$$

If (12) is satisfied, then all odd valued l terms vanish, and the even valued terms become

$$\begin{aligned}\sum_{\alpha=0}^{b} w_\alpha(\boldsymbol{c}_\alpha\cdot\boldsymbol{u})^{2l} &= \theta^l\Delta^{(2l)}\otimes\underbrace{\boldsymbol{u}\boldsymbol{u}\cdots\boldsymbol{u}}_{2l} \\ &= (2l-1)!!\theta^l\boldsymbol{u}^{2l}.\end{aligned} \tag{15}$$

In the above $\otimes$ denotes a scalar product of two tensors. Therefore, (14) reduces to

$$\begin{aligned}\tilde{\boldsymbol{M}}^{(0)} &= \exp\left[-\frac{\boldsymbol{u}^2}{2\theta}\right]\left\{1 + \sum_{l=1}^{\infty}\frac{(2l-1)!!}{(2l)!}\frac{\boldsymbol{u}^{2l}}{\theta^l}\right\} \\ &= \exp\left[-\frac{\boldsymbol{u}^2}{2\theta}\right]\left\{1 + \sum_{l=1}^{\infty}\frac{1}{l!}\frac{\boldsymbol{u}^{2l}}{(2\theta)^l}\right\}\end{aligned} \tag{16}$$

where the identity $(2l-1)!!/(2l)! = 2^{-l}/l!$ is used. Since

$$1 + \sum_{l=1}^{\infty}\frac{1}{l!}\frac{\boldsymbol{u}^{2l}}{(2\theta)^l} = \exp\left[\frac{\boldsymbol{u}^2}{2\theta}\right], \tag{17}$$

substituting this into (16), we have proved that $\tilde{\boldsymbol{M}}^{(0)} = 1$.

Next, we prove $\tilde{\boldsymbol{M}}^{(n)} = \boldsymbol{M}^{(n)}$ for $n > 0$. We start this by defining a partition function in discrete velocity space,

$$\mathcal{Q} \equiv \sum_{\alpha=0}^{b} w_\alpha \exp\left[\frac{\boldsymbol{c}_\alpha\cdot\boldsymbol{u}}{\theta}\right] = \exp\left[\frac{\boldsymbol{u}^2}{2\theta}\right]. \tag{18}$$

Notice that the second equality in the above is a result of the analysis of $\tilde{\boldsymbol{M}}^{(0)} = 1$. Consequently, we show that satisfying the second equality is a sufficient condition for achieving the correct hydrodynamic moment for any integer n. First of all, we have the following general relationship:

$$\begin{aligned}\tilde{\boldsymbol{M}}^{(n)} &= \exp\left[-\frac{\boldsymbol{u}^2}{2\theta}\right]\sum_{\alpha=0}^{b} w_\alpha \underbrace{\boldsymbol{c}_\alpha\boldsymbol{c}_\alpha\cdots\boldsymbol{c}_\alpha}_{n}\exp\left[\frac{\boldsymbol{c}_\alpha\cdot\boldsymbol{u}}{\theta}\right] \\ &= \exp\left[-\frac{\boldsymbol{u}^2}{2\theta}\right]\theta^n\frac{\partial^n}{\partial\boldsymbol{u}^n}\sum_{\alpha=0}^{b} w_\alpha\exp\left[\frac{\boldsymbol{c}_\alpha\cdot\boldsymbol{u}}{\theta}\right] \\ &= \exp\left[-\frac{\boldsymbol{u}^2}{2\theta}\right]\theta^n\frac{\partial^n}{\partial\boldsymbol{u}^n}\mathcal{Q}.\end{aligned} \tag{19}$$

Since $\mathcal{Q} = \exp\left[\boldsymbol{u}^2/2\theta\right]$, then Eq. (19) becomes

$$\tilde{\boldsymbol{M}}^{(n)} = \exp\left[-\frac{\boldsymbol{u}^2}{2\theta}\right]\theta^n\frac{\partial^n}{\partial\boldsymbol{u}^n}\left[\exp\left(\frac{\boldsymbol{u}^2}{2\theta}\right)\right]. \tag{20}$$

In comparison, from the continuum Boltzmann kinetic theory, we have

$$\begin{aligned}\boldsymbol{M}^{(n)} &= \frac{1}{(2\pi\theta)^{D/2}}\int d^D\boldsymbol{c}\ \underbrace{\boldsymbol{c}\cdots\boldsymbol{c}}_{n}\exp\left[-\frac{(\boldsymbol{c}-\boldsymbol{u})^2}{2\theta}\right] \\ &= \mathrm{e}^{-\frac{\boldsymbol{u}^2}{2\theta}}\int d^D\boldsymbol{c}\ \underbrace{\boldsymbol{c}\cdots\boldsymbol{c}}_{n}(2\pi\theta)^{-\frac{D}{2}}\mathrm{e}^{-\frac{\boldsymbol{c}^2}{2\theta}+\frac{\boldsymbol{c}\cdot\boldsymbol{u}}{\theta}} \\ &= \mathrm{e}^{-\frac{\boldsymbol{u}^2}{2\theta}}\theta^n\frac{\partial^n}{\partial\boldsymbol{u}^n}\int d^D\boldsymbol{c}\ (2\pi\theta)^{-\frac{D}{2}}\mathrm{e}^{-\frac{\boldsymbol{c}^2}{2\theta}+\frac{\boldsymbol{c}\cdot\boldsymbol{u}}{\theta}}.\end{aligned} \tag{21}$$

It is easily shown that

$$\int d^D\boldsymbol{c}\ (2\pi\theta)^{-\frac{D}{2}}\mathrm{e}^{-\frac{\boldsymbol{c}^2}{2\theta}+\frac{\boldsymbol{c}\cdot\boldsymbol{u}}{\theta}} = \exp\left[\frac{\boldsymbol{u}^2}{2\theta}\right].$$

Hence, we have shown that (20) and (21) have exactly the same form. Subsequently, we have proved the theorem that $\tilde{\boldsymbol{M}}^{(n)} = \boldsymbol{M}^{(n)}$ for any positive integer n, if condition (12) is satisfied.

It is revealing to check a few obvious representative examples. First of all, the first moment

$$\tilde{\boldsymbol{M}}^{(1)} = \exp\left[-\frac{\boldsymbol{u}^2}{2\theta}\right]\theta\frac{\partial}{\partial\boldsymbol{u}}\exp\left[\frac{\boldsymbol{u}^2}{2\theta}\right] = \boldsymbol{u}.$$

This is simply the fluid momentum or the fluid velocity.

On the other hand, the second moment

$$\tilde{\boldsymbol{M}}^{(2)} = \exp\left[-\frac{\boldsymbol{u}^2}{2\theta}\right]\theta^2\frac{\partial^2}{\partial\boldsymbol{u}^2}\exp\left[\frac{\boldsymbol{u}^2}{2\theta}\right] = \theta\boldsymbol{I} + \boldsymbol{u}\boldsymbol{u}$$

where $\boldsymbol{I}$ is the second-rank unity tensor. Hence the second moment has precisely the same form of the correct hydrodynamic momentum flux tensor. Furthermore, we have

$$\frac{1}{2}\mathrm{Trace}(\tilde{\boldsymbol{M}}^{(2)}) = \frac{D}{2}\theta + \frac{1}{2}\boldsymbol{u}^2$$

which is exactly the hydrodynamic total energy.

3. Moment accuracy for lattices of finite isotropy

In the previous section, we have proved that condition (12) sufficiently ensures that all moments defined via summations over discrete lattice velocity values are equal to that of the continuum Boltzmann kinetic theory. However, such a condition is unnecessarily strong, because it requires the supporting lattice basis to have an infinite isotropy (i.e., $n \to \infty$). Obviously, no lattice velocity set containing a finite number of discrete values is able to meet such a requirement. Hence a realistic goal is finding a relationship between the hydrodynamic moments up to a given finite order and the corresponding isotropy for the supporting lattice velocity basis.

First of all, we notice the existence of a hierarchical relationship among the hydrodynamic moments. On the basis of definition (19), we have

$$\tilde{\boldsymbol{M}}^{(n)} = \exp\left[-\frac{\boldsymbol{u}^2}{2\theta}\right]\left(\theta\frac{\partial}{\partial\boldsymbol{u}}\right)^n \mathcal{Q}. \tag{22}$$

Hence,

$$\begin{aligned}\tilde{\boldsymbol{M}}^{(n+1)} &= \exp\left[-\frac{\boldsymbol{u}^2}{2\theta}\right]\theta\frac{\partial}{\partial\boldsymbol{u}}\left(\theta\frac{\partial}{\partial\boldsymbol{u}}\right)^n \mathcal{Q}\\ &= \exp\left[-\frac{\boldsymbol{u}^2}{2\theta}\right]\theta\frac{\partial}{\partial\boldsymbol{u}}\left[\mathrm{e}^{\frac{\boldsymbol{u}^2}{2\theta}}\mathrm{e}^{-\frac{\boldsymbol{u}^2}{2\theta}}\left(\theta\frac{\partial}{\partial\boldsymbol{u}}\right)^n \mathcal{Q}\right]\\ &= \exp\left[-\frac{\boldsymbol{u}^2}{2\theta}\right]\theta\frac{\partial}{\partial\boldsymbol{u}}\left[\exp\left(\frac{\boldsymbol{u}^2}{2\theta}\right)\tilde{\boldsymbol{M}}^{(n)}\right].\end{aligned}$$

This gives the hierarchical relationship,

$$\tilde{\boldsymbol{M}}^{(n+1)} = \boldsymbol{u}\tilde{\boldsymbol{M}}^{(n)} + \theta\frac{\partial}{\partial\boldsymbol{u}}\tilde{\boldsymbol{M}}^{(n)}. \tag{23}$$

Using the hierarchical relationship (23), all higher order moments are derivable starting from $\tilde{\boldsymbol{M}}^{(0)} = 1$. More importantly, we realize that n-th-order moment $\tilde{\boldsymbol{M}}^{(n)}$ is an n-th-order polynomial in terms of the power of the fluid velocity. That is, the highest power in $\tilde{\boldsymbol{M}}^{(n)}$ is $\boldsymbol{u}^n$. Since hydrodynamic moments up to a finite order only involve a finite power of fluid velocity, we expect that moment accuracy up to a finite order can be achieved by a finite lattice set of adequate isotropy. Having established these properties, we arrive at the next theorem below.

Theorem 2. *If the supporting lattice velocity basis satisfies the following conditions:*

$$E^{(n)}_{i_1,\ldots,i_n} = \begin{cases}\theta^{n/2}\Delta^{(n)}_{i_1,\ldots,i_n}, & n = 0, 2, \ldots, 2N\\ 0, & n = odd\ integer\end{cases} \tag{24}$$

and if the discrete equilibrium distribution function $f^{eq,(N)}_\alpha$ is a truncation of the original exponential form by retaining terms only up to $\boldsymbol{u}^N$, then the discrete moment $\tilde{\boldsymbol{M}}^{(n)}$ is accurate and equal to the moment $\boldsymbol{M}^{(n)}$ of the continuum Boltzmann kinetic theory for any $n \le N$. N is any given finite positive integer.

It is easily recognized that the basis lattice velocity set satisfying the above condition must be $2N$-order isotropic (cf., [11,24]).

Proof of Theorem 2. We start by first examining the standard Maxwell–Boltzmann distribution (3), and express it in an expanded form in powers of fluid velocity $\boldsymbol{u}$. This is very easily accomplished by taking advantage of the following generating function for Hermite series:

$$\exp\left[2tx - t^2\right] = \sum_{n=0}^{\infty}\frac{H_n(x)}{n!}t^n \tag{25}$$

where $H_n(x)$ is the standard n-th-order Hermite polynomial. Let us define the unit vector $\hat{u} \equiv \boldsymbol{u}/|\boldsymbol{u}|$ and $|\boldsymbol{u}| \equiv \sqrt{\sum_{i=1}^D u_i^2}$ as the magnitude, and $\xi \equiv \boldsymbol{c}\cdot\hat{u}/\sqrt{2\theta}$. We can formally express the distribution (3) as

$$\begin{aligned}f^{eq}(\boldsymbol{x},\boldsymbol{c},t) &= \frac{1}{(2\pi\theta)^{\frac{D}{2}}}\exp\left[-\frac{(\boldsymbol{c}-\boldsymbol{u})^2}{2\theta}\right]\\ &= \frac{1}{(2\pi\theta)^{\frac{D}{2}}}\mathrm{e}^{-\frac{c^2}{2\theta}}\exp\left[\frac{\boldsymbol{c}\cdot\boldsymbol{u}}{\theta} - \frac{\boldsymbol{u}^2}{2\theta}\right]\\ &= \frac{1}{(2\pi\theta)^{\frac{D}{2}}}\mathrm{e}^{-\frac{c^2}{2\theta}}\sum_{n=0}^{\infty}\frac{H_n(\xi)}{n!}\left(\frac{\boldsymbol{u}}{\sqrt{2\theta}}\right)^n.\end{aligned} \tag{26}$$

A truncated series $f^{eq,(N)}$ of the above can be defined by simply retaining the terms up to $\boldsymbol{u}^N$. On the basis of the orthogonal property of the Hermite polynomials, namely

$$\int_{-\infty}^{\infty}\mathrm{d}x\ \mathrm{e}^{-x^2}H_m(x)H_n(x) = 0; \quad \forall m \ne n, \tag{27}$$

and because $\boldsymbol{c}$ of power N can be fully represented by Hermite polynomials $\{H_n;\ n = 0,\ldots,N\}$, it is straightforward to see that moments up to N-th order constructed out of f^{eq} are identical to those of $f^{eq,(N)}$, for the higher order terms in f^{eq} give vanishing contributions due to orthogonality.

Next, like in the above, we expand the discrete distribution (9), and keeping terms only up to $\boldsymbol{u}^N$,

$$\begin{aligned}f^{eq,(N)}_\alpha &= w_\alpha\exp\left[\frac{\boldsymbol{c}_\alpha\cdot\boldsymbol{u}}{\theta} - \frac{\boldsymbol{u}^2}{2\theta}\right]\\ &= w_\alpha\sum_{n=0}^{N}\frac{H_n(\xi_\alpha)}{n!}\left(\frac{\boldsymbol{u}}{\sqrt{2\theta}}\right)^n\end{aligned} \tag{28}$$

where $\xi_\alpha \equiv \boldsymbol{c}_\alpha \cdot \hat{u}/\sqrt{2\theta}$. Hence the task of proving Theorem 2 is that of proving that $\tilde{\boldsymbol{M}}^{(n)}$ ($\forall n \le N$) generated by $f_\alpha^{eq,(N)}$ is equal to $\boldsymbol{M}^{(n)}$ from the full Maxwell–Boltzmann distribution f^{eq} or its truncation $f^{eq,(N)}$. According to definition (1), we have

$$\begin{aligned}\boldsymbol{M}^{(n)} &\equiv \int d^D\boldsymbol{c}\ \underbrace{\boldsymbol{c}\cdots\boldsymbol{c}}_{n} f^{eq}(\boldsymbol{x},\boldsymbol{c},t)\\ &= \frac{1}{(2\pi\theta)^{D/2}}\sum_{m=0}^{N}\frac{1}{m!}\left(\frac{\boldsymbol{u}}{\sqrt{2\theta}}\right)^m\\ &\quad\times\int d^D\boldsymbol{c}\ \underbrace{\boldsymbol{c}\cdots\boldsymbol{c}}_{n}\exp\left[-\frac{\boldsymbol{c}^2}{2\theta}\right]H_m(\xi).\end{aligned} \tag{29}$$

On the other hand, according to (5), we have

$$\begin{aligned}\tilde{\boldsymbol{M}}^{(n)} &\equiv \sum_{i=0}^{b}\underbrace{\boldsymbol{c}_\alpha\cdots\boldsymbol{c}_\alpha}_{n} f_\alpha^{eq,(N)}\\ &= \sum_{m=0}^{N}\frac{1}{m!}\left(\frac{\boldsymbol{u}}{\sqrt{2\theta}}\right)^m\sum_{\alpha=0}^{b}\underbrace{\boldsymbol{c}_\alpha\cdots\boldsymbol{c}_\alpha}_{n} w_\alpha H_m(\xi_\alpha).\end{aligned} \tag{30}$$

From (29) and (30), we see that both of these involve Hermite polynomials of orders no greater than N. Furthermore, a given Hermite function $H_n(x)$ is a polynomial of x^m ($m = 0, \ldots, \le n$). Therefore, both $\boldsymbol{M}^{(n)}$ and $\tilde{\boldsymbol{M}}^{(n)}$ involve powers of $\boldsymbol{c}$ (or $\boldsymbol{c}_\alpha$) from 0 up to $n + N$. On the basis of this observation, we see that it is sufficient to prove $\tilde{\boldsymbol{M}}^{(n)} = \boldsymbol{M}^{(n)}$ ($\forall n \le N$), if for all integers $m \le 2N$ the following property is satisfied:

$$\int d^D\boldsymbol{c}\ \frac{\exp[-\boldsymbol{c}^2/2\theta]}{(2\pi\theta)^{D/2}}\underbrace{\boldsymbol{c}\cdots\boldsymbol{c}}_{m} = \sum_{\alpha=0}^{b} w_\alpha \underbrace{\boldsymbol{c}_\alpha\cdots\boldsymbol{c}_\alpha}_{m} \tag{31}$$

$\forall m = 0, \ldots, 2N$.

The result for the discrete summation is already given in the definition of (11) and (24). Hence it is sufficient to just show that this is also true for the continuum integration. In fact, according to the basic Gaussian integral property, we know that

$$\begin{aligned}&\frac{1}{(2\pi\theta)^{D/2}}\int d^D\boldsymbol{c}\exp\left[-\frac{\boldsymbol{c}^2}{2\theta}\right]c_{i_1}c_{i_2}\cdots c_{i_m}\\ &= \begin{cases}\theta^{m/2}\Delta^{(m)}_{i_1,i_2,\ldots,i_m}, & m = 0, 2, 4, \ldots, 2N\\ 0, & m = 1, 3, 5, \ldots, 2N+1.\end{cases}\end{aligned} \tag{32}$$

Consequently, we have proved $\tilde{\boldsymbol{M}}^{(n)} = \boldsymbol{M}^{(n)}$ ($\forall n \le N$), and thus Theorem 2.

It is also worthwhile to note, without repeating the explicit steps of the above, that the same proof applies if the truncation of the exponential form f_α^{eq} is up to $N+1$. Thus, we can retain an extra term in the expanded form.

4. Discussion

In this paper, we have presented and proved a set of fundamental conditions for formulating LBM models. Lattice velocity sets obeying these conditions automatically produce equilibrium moment accuracy to any given N-th order. As demonstrated in [5], non-equilibrium moments are theoretically expressible as spatial and temporal derivatives of equilibrium moments. Therefore, achieving higher order moment accuracy enables accurate description of fluid properties into deeper non-equilibrium regimes [21,22]. This is essential for physical properties at finite Knudsen or Mach numbers that are beyond the Navier–Stokes representation.

To make a more direct comparison with conventional LBM models, we rewrite (28) in a more explicit form (up to $O(u^5)$) below:

$$\begin{aligned}f_\alpha^{eq} = w_\alpha\rho\Bigg[1 &+ \frac{\boldsymbol{c}_\alpha\cdot\boldsymbol{u}}{\theta} + \frac{(\boldsymbol{c}_\alpha\cdot\boldsymbol{u})^2}{2\theta^2} - \frac{\boldsymbol{u}^2}{2\theta} + \frac{(\boldsymbol{c}_\alpha\cdot\boldsymbol{u})^3}{6\theta^3}\\ &- \frac{(\boldsymbol{c}_\alpha\cdot\boldsymbol{u})\boldsymbol{u}^2}{2\theta^2} + \frac{(\boldsymbol{c}_\alpha\cdot\boldsymbol{u})^4}{24\theta^4} - \frac{(\boldsymbol{c}_\alpha\cdot\boldsymbol{u})^2\boldsymbol{u}^2}{4\theta^3} + \frac{\boldsymbol{u}^4}{8\theta^2}\\ &+ \frac{(\boldsymbol{c}_\alpha\cdot\boldsymbol{u})^5}{120\theta^5} - \frac{(\boldsymbol{c}_\alpha\cdot\boldsymbol{u})^3\boldsymbol{u}^2}{12\theta^4} + \frac{(\boldsymbol{c}_\alpha\cdot\boldsymbol{u})\boldsymbol{u}^4}{8\theta^3}\Bigg].\end{aligned} \tag{33}$$

It is immediately recognized that the series for most of the conventional LBM models terminate at $O(u^2)$ or $O(u^3)$. For example, the so called D3Q15 and D3Q19 correspond to the expansion up to $O(u^2)$ [14]. It can be directly verified that their underlying lattice velocity sets only satisfy the fundamental conditions (24) up to $N = 2$, so that the higher order moment terms beyond $O(u^3)$ cannot be accurately supported. Furthermore, in these models, the temperature is fixed at $\theta = 1/3$. An extended 34-velocity model exists [17,23], and its temperature has a range of variation between $1/3$ to $2/3$, and D3Q19 is its reduced limit as $\theta = 1/3$. But the moment accuracy is still $N = 2$.

There are typically two approaches to constructing lattice velocity sets obeying higher order of accuracies ($N > 2$) according to (24). One approach is to rely on relations between discrete rotational symmetry and tensor isotropy [11,24]. For instance, we can start with a lattice velocity set consisting of multiple lattice speeds, namely

$$\mathcal{L} = \mathcal{L}_1 \cup \mathcal{L}_2 \cdots \cup \mathcal{L}_M \tag{34}$$

where each subset is defined as

$$\begin{aligned}&\mathcal{L}_\beta = \{\boldsymbol{c}_{\alpha,\beta};\ i = 0, \ldots, b_\beta\}\\ &\beta = 1, \ldots, M.\end{aligned}$$

All lattice velocities in each subset $\mathcal{L}_\beta$ has the same magnitude, $|\boldsymbol{c}_{\alpha,\beta}| = c_\beta$. This way, the required isotropy can be imposed at each speed level. It has been shown that if such a velocity subset is parity invariant and obeys an n-th-order isotropy ($n =$ *even integer*), then its basic moment tensor has the following form [24]:

$$\boldsymbol{E}^{(n),\beta}_{i_1,i_2,\ldots,i_n} = b_\beta c_\beta^n\frac{(D-2)!!}{(D+n-2)!!}\Delta^{(n)}_{i_1,i_2,\ldots,i_n} \tag{35}$$

and it vanishes for all the odd integer moments. Subsequently, we can assign a weighting factor $w_\beta(\theta)$ for each subset $\mathcal{L}_\beta$, so that the overall condition (24) is achieved by satisfying the following constraint on the weighting factors:

$$\sum_{\beta=1}^{M} b_\beta c_\beta^n \frac{(D-2)!!}{(D+n-2)!!} w_\beta(\theta) = \theta^{n/2} \tag{36}$$

for $n = 0, 2, \ldots, 2N$. There are $2N + 1$ such constraints. Hence, it is necessary to include enough subsets and $w_\beta(\theta)$ ($\beta = 1, \ldots, M \geq N + 1$) in order to have a solution. Using such a procedure, a 59-velocity model in three dimensions is formulated that satisfies (24) up to $N = 3$ with sixth-order tensor isotropy, so that the expansion in (33) can be carried to $O(u^4)$. On the basis of the analysis above and elsewhere [5], such an order of moment accuracy is necessary for getting the correct energy flux in thermal hydrodynamics [25–27]. Another approach is to form the discrete velocity sets via Gaussian quadrature for higher order models [5]. Indeed, (32) defines the precise requirement. The only difference here is that the quadratures need to allow a variable temperature θ. This approach is relatively more straightforward, so that it enables a systematic formulation of higher accurate LBM models to sixth, eighth orders and beyond. There is also a similar work recently by Sbragaglia et al. on how to construct higher order isotropic moments [28].

The formulation described in this paper offers a rigorous measure for evaluating the order of accuracy of a given LBM model. For future convenience, we may simply refer to an LBM model that satisfies condition (24) to N-th order as "$E(N)$-accurate".

Acknowledgments

We dedicate this work to the celebration of 250 years of Euler Equation. We are grateful to Steven Orszag and Raoyang Zhang for valuable discussions. This work is supported in part by the National Science Foundation.

References

[1] R. Benzi, S. Succi, M. Vergassola, Phys. Rep. 222 (1992) 145–197.
[2] S. Chen, G. Doolen, Annu. Rev. Fluid Mech. 30 (1998) 329–364.
[3] H. Chen, et al., Science 301 (2003) 633–636.
[4] X. Shan, X. He, Phys. Rev. Lett. 80 (1998) 65.
[5] X. Shan, X. Yuan, H. Chen, J. Fluid Mech. 550 (2006) 413–441.
[6] C. Cercignani, Theory and Application of the Boltzmann Equation, Elsevier, New York, 1975.
[7] M. Gad-el-Hak, The fluid mechanics of microdevices, the Freeman scholar lecture, J. Fluid Eng.-T. ASME 121 (1999) 5–33.
[8] R. Agarwal, K.-Y. Yun, R. Balakrishnan, Phys. Fluids 13 (10) (2001) 3061.
[9] R. Zhang, X. Shan, H. Chen, Phys. Rev. E 74 (2006) 046703.
[10] H. Chen, S. Orszag, I. Staroselsky, J. Fluid Mech. 574 (2007) 495–505.
[11] S. Wolfram, J. Stat. Phys. 45 (1986) 471–526.
[12] U. Frisch, et al., Complex Syst. 1 (1987) 649–707.
[13] H. Chen, S. Chen, W.H. Matthaeus, Phys. Rev. A 45 (8) (1992) R5339.
[14] Y. Qian, D. d'Humieres, P. Lallemand, Europhys. Lett. 17 (6) (1992) 479.
[15] U. Frisch, B. Hasslacher, Y. Pomeau, Phys. Rev. Lett. 56 (1986) 1505.
[16] F. Alexander, S. Chen, J.D. Sterling, Phys. Rev. E 47 (1993) R2249-52.
[17] H. Chen, C. Teixeira, K. Molvig, Internat. J. Modern Phys. C 9 (8) (1997) 675.
[18] R. Bishop, S. Goldberg, Tensor Analysis on Manifolds, Dover, New York, 1968.
[19] B.K. Vainshtein, Modern Crystallography, Springer, 1981.
[20] R.L.E. Schwarzenberger, N-Dimensional Crystallography, Pitman, 1980.
[21] S. Chapman, T. Cowling, The Mathematical Theory of Non-Uniform Gases, 3rd ed., Cambridge University Press, Cambridge, 1990.
[22] H. Chen, S. Orszag, I. Staroselsky, S. Succi, J. Fluid Mech. 519 (2004) 307.
[23] H. Chen, C. Teixeira, Comp. Phys. Commu. 129 (2000) 21.
[24] H. Chen, I. Goldhirsh, S. Orszag, Discrete rotational symmetry, moment isotropy, and higher order lattice Boltzmann models, J. Sci. Computing (August 2007) (in press).
[25] Y. Chen, H. Ohashi, M. Akiyama, Phys. Rev. E 50 (1994) 2776.
[26] C. Teixeira, H. Chen, D. Freed, Compt. Phys. Commu. 129 (2000) 207.
[27] M. Watari, M. Tsutahara, Phys. Rev. E 70 (2004) 016703.
[28] M. Sbragaglia, R. Benzi, L. Biferale, S. Succi, K. Sugiyama, F. Toschi, Phys. Rev. E 75 (2007) 026702.

Available online at www.sciencedirect.com

ScienceDirect

Physica D 237 (2008) 2009–2014

PHYSICA D

www.elsevier.com/locate/physd

Understanding the different scaling behavior in various shell models proposed for turbulent thermal convection

Emily S.C. Ching[a,b,*], H. Guo[a], W.C. Cheng[a]

[a] *Department of Physics, The Chinese University of Hong Kong, Shatin, New Territories, Hong Kong*
[b] *The Institute of Theoretical Physics, The Chinese University of Hong Kong, Shatin, New Territories, Hong Kong*

Available online 5 January 2008

Abstract

Different scaling behavior has been reported in various shell models proposed for turbulent thermal convection. In this paper, we show that buoyancy is not always relevant to the statistical properties of these shell models even though there is an explicit coupling between velocity and temperature in the equations of motion. When buoyancy is relevant (irrelevant) to the statistical properties, the scaling behavior is Bolgiano–Obukhov (Kolmogorov) plus intermittency corrections. We show that the intermittency corrections of temperature could be solely attributed to fluctuations in the entropy transfer rate when buoyancy is relevant but due to fluctuations in both energy and entropy transfer rates when buoyancy is irrelevant. This difference can be used as a criterion to distinguish whether temperature is behaving as an active or a passive scalar.

PACS: 47.27-i; 47.27te

Keywords: Shell models; Turbulent thermal convection; Scaling behavior

1. Introduction

Turbulent thermal convection is a problem of great research interest (see, for example, [1,2] for a review). One interesting issue is to understand the scaling behavior of the velocity and temperature fluctuations. Turbulent thermal convection is often investigated experimentally in Rayleigh–Bénard convection cells, which are closed cells of fluid heated from below and cooled on the top. Such confined turbulent convective flows are highly inhomogeneous as thermal and viscous boundary layers are formed near the top and bottom of the cell. Scaling laws for the central region of such confined turbulent thermal convection have been put forth and shown to be in good agreement with the existing experimental measurements [3]. On the other hand, shell models focussing on the energy cascade process have been studied intensively and proved to be useful for understanding the scaling behavior of velocity fluctuations in inertia-driven turbulence (see, for example, [4] for a review). It is thus natural to also construct shell models for turbulent thermal convection. Shell models are, by construction, boundary-free and thus shell models for turbulent thermal convection are necessarily models of *homogeneous* turbulent thermal convection. It is known that the presence of boundaries generates coherent structures such as plumes and a large-scale mean flow in confined turbulent thermal convection, and these coherent structures can affect the scaling behavior [3]. Thus, scaling behavior in confined turbulent thermal convection and scaling behavior in homogeneous turbulent thermal convection as studied in shell models can be different.

Several shell models for turbulent thermal convection have been proposed and different scaling behavior reported. Specifically, Bolgiano–Obukhov (BO) scaling [5] plus intermittency corrections has been reported in the shell model constructed by Brandenburg [6] and also in the modified model by Suzuki and Toh [7] for some parameter range. On the other hand, Kolmogorov 1941 (K41) scaling [8] plus intermittency corrections has been reported by Jiang and Liu [9] using a shell model extended from the Gledzer–Ohkitani–Yamada (GOY) model [10],

* Corresponding author at: Department of Physics, The Chinese University of Hong Kong, Shatin, New Territories, Hong Kong.
E-mail address: ching@phy.cuhk.edu.hk (E.S.C. Ching).

0167-2789/$ - see front matter © 2008 Elsevier B.V. All rights reserved.
doi:10.1016/j.physd.2008.01.001

which we shall denote as the GOYT model. In this paper, we show that buoyancy is not always significant and directly relevant to the statistical properties even though there is an explicit coupling between velocity and temperature in the equations of motion in all these shell models. We clarify that the two different types of scaling behavior reported correspond respectively to the case when buoyancy is relevant to the statistical properties and the case when it is not. Specifically, the scaling behavior is BO plus intermittency corrections when buoyancy is relevant, and K41 plus intermittency corrections (as one would expect for temperature behaving as a passive scalar) when buoyancy is irrelevant. We show that the intermittency corrections of temperature could be solely attributed to fluctuations in the entropy transfer rate when buoyancy is relevant but due to fluctuations in both energy and entropy transfer rates when buoyancy is irrelevant. This difference might be used as a criterion to distinguish whether temperature is behaving as an active or a passive scalar.

2. Shell models proposed for turbulent thermal convection

Two classes of shell models have been proposed for studying turbulent thermal convection. The first class consists of the shell model proposed by Brandenburg [6] and its modified versions [7]. The other class consists of the GOYT model, the shell model extended from the GOY model [9] and the SabraT model [11] from the Sabra model [11]. The Sabra model [12] was proposed to eliminate some undesirable periodic oscillations in the GOY model, and have essentially the same scaling behavior as the GOY model. The scaling behavior in the first class of shell models is BO plus corrections in some parameter range while the scaling behavior in the second class of shell models is always K41 plus corrections. In this paper, we focus on two shell models, one from each class. The first one, denoted as the Brandenburg model, is the modified model proposed by Suzuki and Toh [7] without the drag term. The second is the SabraT model.

The basic idea of a shell model is to consider variables in discrete "shells" in Fourier k-space, and construct a set of ordinary differential equations for these variables per shell. For shell models for turbulent thermal convection, there are two variables, the velocity and temperature variables, u_n and θ_n. They can be roughly thought of as the Fourier transforms of the velocity and temperature fields with wavevector $\vec{k}$, whose magnitude satisfies $k_n \le |\vec{k}| \le k_{n+1}$. Here, $k_n = 2^n k_0$ is the wavenumber of the nth shell, with $0 \le n \le N-1$, and $k_0 = 1$ is the wavenumber corresponding to the largest scale in the system. The equations of motion for u_n and θ_n are:

$$\frac{\mathrm{d}u_n}{\mathrm{d}t} = I_u(k_n) - \nu k_n^2 u_n + \alpha g \theta_n \tag{1}$$

$$\frac{\mathrm{d}\theta_n}{\mathrm{d}t} = I_\theta(k_n) - \kappa k_n^2 \theta_n + f_n \tag{2}$$

where f_n is the forcing term acting only on the first few shells. The nonlinear terms $I_u(k_n)$ and $I_\theta(k_n)$ are taken to couple quadratically with the nearest shells and sometimes also the next nearest shells, and are constructed to satisfy two conservation laws of energy and entropy (proportional to $|\theta_n|^2$) in the limit of $\nu \to 0$ and $\kappa \to 0$:

$$\frac{\mathrm{d}}{\mathrm{d}t}\left[\frac{1}{2}\sum_{n=1}^{N}|u_n|^2\right] - \alpha g \sum_{n=1}^{N}\mathrm{Re}\{u_n\theta_n^*\} = 0 \tag{3}$$

$$\frac{\mathrm{d}}{\mathrm{d}t}\left[\frac{1}{2}\sum_{n=1}^{N}|\theta_n|^2\right] = 0. \tag{4}$$

As a result, the nonlinear terms $u_n^* I_u(k_n)$ and $\theta_n^* I_\theta(k_n)$ should have a flux-like form such that the evolution equations of energy and entropy in the nth shell are:

$$\frac{\mathrm{d}}{\mathrm{d}t}\left[\frac{|u_n|^2}{2}\right] = F_u(k_n) - F_u(k_{n+1}) - \nu k_n^2 |u_n|^2 + \alpha g \mathrm{Re}\{u_n\theta_n^*\} \tag{5}$$

$$\frac{\mathrm{d}}{\mathrm{d}t}\left[\frac{|\theta_n|^2}{2}\right] = F_\theta(k_n) - F_\theta(k_{n+1}) - \kappa k_n^2|\theta_n|^2 + f_n\theta_n^*. \tag{6}$$

The fluxes $F_u(k_n)$ and $F_\theta(k_n)$ are respectively the rates of energy and entropy transfer from the $(n-1)$th shell to the nth shell.

In the Brandenburg model, u_n and θ_n are real variables with [6,7]:

$$\begin{aligned} I_u^B(k_n) &= a k_n (u_{n-1}^2 - 2u_n u_{n+1}) \\ &\quad + b k_n (u_n u_{n-1} - 2u_{n+1}^2) \end{aligned} \tag{7}$$

$$\begin{aligned} I_\theta^B(k_n) &= \tilde{a} k_n (u_{n-1}\theta_{n-1} - 2u_n\theta_{n+1}) \\ &\quad + \tilde{b} k_n (u_n\theta_{n-1} - 2u_{n+1}\theta_{n+1}) \end{aligned} \tag{8}$$

$$F_u^B(k_n) = (a u_{n-1} + b u_n) k_n u_{n-1} u_n \tag{9}$$

$$F_\theta^B(k_n) = (\tilde{a} u_{n-1} + \tilde{b} u_n) k_n \theta_{n-1}\theta_n \tag{10}$$

where a, b, $\tilde{a}$ and $\tilde{b}$ are positive parameters. In the SabraT model, u_n and θ_n are complex variables with [11]:

$$\begin{aligned} I_u^S(k_n) &= \mathrm{i} k_n \lambda \left(u_{n+1}^* u_{n+2} - \frac{\delta}{2} u_{n-1}^* u_{n+1} \right. \\ &\quad \left. + \frac{1-\delta}{4} u_{n-1} u_{n-2} \right), \end{aligned} \tag{11}$$

$$\begin{aligned} I_\theta^S(k_n) &= \mathrm{i} k_n (\alpha_1 u_{n+1}^* \theta_{n+2} + \alpha_2 u_{n+2} \theta_{n+1}^* \\ &\quad + \beta_1 u_{n-1}^* \theta_{n+1} - \beta_2 u_{n+1} \theta_{n-1}^* \\ &\quad - \gamma_1 u_{n-1} \theta_{n-2} - \gamma_2 u_{n-2} \theta_{n-1}) \end{aligned} \tag{12}$$

$$\begin{aligned} F_u^S(k_n) &= \lambda \mathrm{Im}[k_{n-1} u_{n-1}^* u_n^* u_{n+1} \\ &\quad + (1-\delta) k_{n-2} u_{n-2}^* u_{n-1}^* u_n] \end{aligned} \tag{13}$$

$$\begin{aligned} F_\theta^S(k_n) &= \mathrm{Im}[\gamma_1 (k_n u_{n-1} \theta_{n-2} \theta_n^* + k_{n+1} u_n \theta_{n-1} \theta_{n+1}^*) \\ &\quad - \beta_2 k_n u_{n+1}^* \theta_{n-1} \theta_n + \gamma_2 k_n u_{n-2} \theta_{n-1} \theta_n^*]. \end{aligned} \tag{14}$$

The parameters $\alpha_{1,2}$, $\beta_{1,2}$ and $\gamma_{1,2}$ are determined by

$$\begin{aligned} &\alpha_1 = 4\tau, \qquad \beta_1 = 1 - \delta - 2\tau, \qquad \gamma_1 = -\tau, \\ &\alpha_2 = 2 - 4\tau, \qquad \beta_2 = 1 - 2\tau, \qquad \gamma_2 = \tau - \frac{1-\delta}{2} \end{aligned} \tag{15}$$

with three free parameters λ, δ and τ. In particular, we fix $\lambda = 2$ and $\tau = 0.7$ and vary δ. The value $\delta = 1$ is the boundary value separating two families of Sabra model: a family of three-dimensional-like models for $0 < \delta < 1$ and a family of two-

Table 1
Values of the parameters used for the results presented

Brandenburg model						
a	b	$\tilde{a}$ and $\tilde{b}$	ν	κ	αg	N
0.01	1	1	5×10^{-17}	5×10^{-15}	1	32
0.31	0.6	1	5×10^{-9}	5×10^{-9}	1	25
SabraT model						
δ	λ	τ	ν	κ	αg	N
0.5	2	0.7	10^{-8}	10^{-8}	1	23
0.8	2	0.7	10^{-8}	10^{-8}	1	23

dimensional-like models for $1 < \delta < 2$. We focus on $0 < \delta < 1$ in this paper.

We study the scaling behavior of the velocity and temperature structure functions, $\langle |u_n|^p \rangle$ and $\langle |\theta_n|^p \rangle$, with scaling exponents ζ_p and ξ_p defined by:

$$\langle |u_n|^p \rangle \sim k_n^{-\zeta_p}; \qquad \langle |\theta_n|^p \rangle \sim k_n^{-\xi_p} \tag{16}$$

where $\langle \ldots \rangle$ denotes a time average. The K41 scaling would be characterized by $\zeta_p = \xi_p = p/3$ while the BO scaling by $\zeta_p = 3p/5$ and $\xi_p = p/5$. In our numerical calculations, we integrate the equations of motion using fourth order Runge–Kutta method with an initial condition of $u_n = \theta_n = 0$ except for a small perturbation of θ_n at intermediate values of n. The Brandenburg model is forced with $f_n = f\delta_{n,0}$ where f is a uniform random noise while the SabraT model is forced with a Gaussian time-correlated noise acting on $n = 3$ and 4 only [12]. For the results presented in this work, we summarize the parameters used in Table 1.

In the Brandenburg model, the scaling behavior depends on the relative magnitudes of the parameters a and b, as reported in earlier studies [6]. When b/a is larger than some critical value of about 2, the scaling exponents ζ_p and ξ_p are given by the BO values plus corrections. The scaling behavior improves with b/a. On the other hand, when b/a is smaller but close to the critical value, the scaling exponents ζ_p and ξ_p are the same as those obtained in the case of passive scalar advection in which the coupling term $\alpha g \theta_n$ with temperature in the velocity equation of motion is replaced by a random forcing at $n = 0$. This indicates that buoyancy does not play a part in the statistical properties in this case and serves only as an effective large-scale forcing. The scaling exponents for $b/a = 100$ and $b/a = 1.94$ are shown respectively in Figs. 1 and 2. For even smaller values of b/a, further away from the critical value, the system is not chaotic, and in most of the shells the solution is given instantaneously by the fixed-point solution of $u_n = Ak_n^{-1/3}$ and $\theta_n = Bk_n^{-1/3}$, which holds exactly in the limit of large N and $\nu = \kappa = \alpha g = 0$.

For the SabraT model, we find that the values of ζ_p remain the same as those in the Sabra model without the coupling term $\alpha g \theta_n$ for all the values of δ studied, again indicating that buoyancy does not play a role in determining the statistical properties in the SabraT model for $0 < \delta < 1$. The precise values of ζ_p depend on δ, as was reported in the GOY

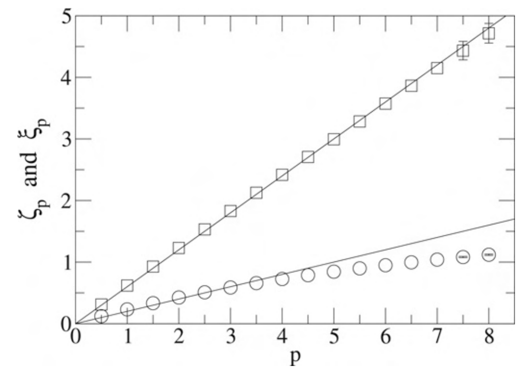

Fig. 1. The scaling exponents ζ_p (squares) and ξ_p (circles) for Brandenburg model with $a = 0.01$ and $b = 1$. The error increases with p and the largest errors are shown. Comparing with the two solid lines of slopes 1/5 and 3/5 shown, it can be seen that the scaling behavior is BO with corrections.

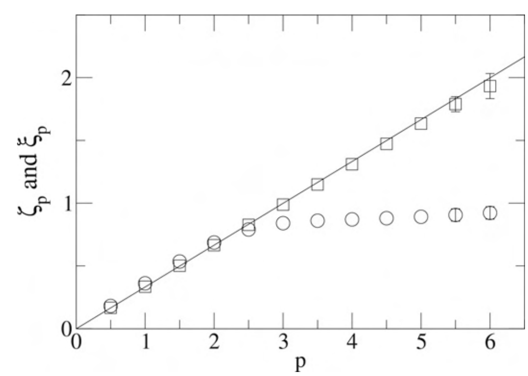

Fig. 2. Same as Fig. 1 for $a = 0.31$ and $b = 0.6$. The solid line shown has slope 1/3.

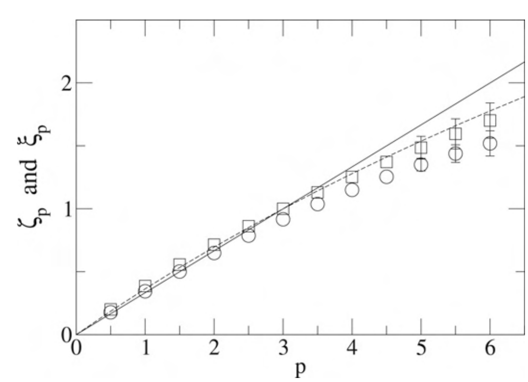

Fig. 3. Same as Fig. 2 for the SabraT model with $\delta = 0.5$. The solid line shown has a slope of 1/3 while the dashed line is the She–Leveque result [14].

model [13]. In Fig. 3, we present the results for ζ_p and ξ_p for $\delta = 0.5$, a conventional value at which the model conserves helicity in the inviscid limit [13]. In this case, the values of ζ_p are well described by the She–Leveque result [14] of $\zeta_p = p/9 + 2[1 - (2/3)^{p/3}]$, as was also reported [9] for the GOYT model with $\delta = 0.5$.

3. The buoyancy scale

In this section, we discuss how to determine whether buoyancy is relevant or not in determining the statistical properties. Consider Eq. (5), which is the energy budget. The

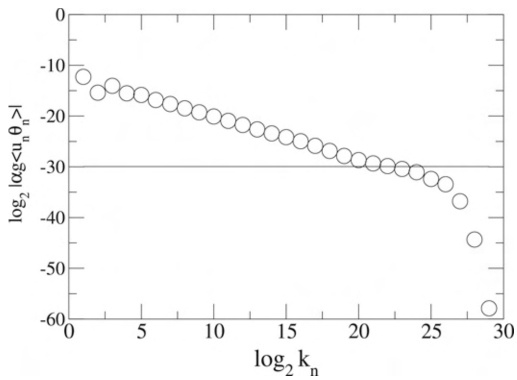

Fig. 4. Comparison of $|\alpha g\langle u_n\theta_n\rangle|$ (circles) with ϵ (solid line) in each shell for the Brandenburg model with a large value of $b/a = 100$.

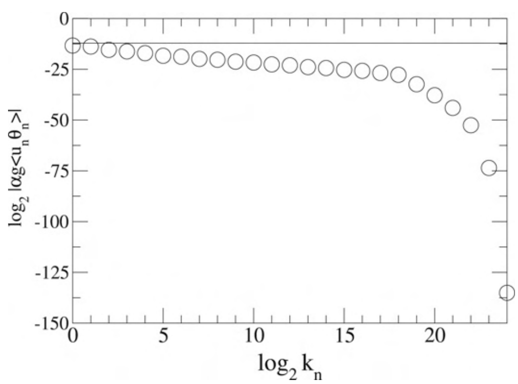

Fig. 5. Same as Fig. 4 for a small value of $b/a \approx 1.9$.

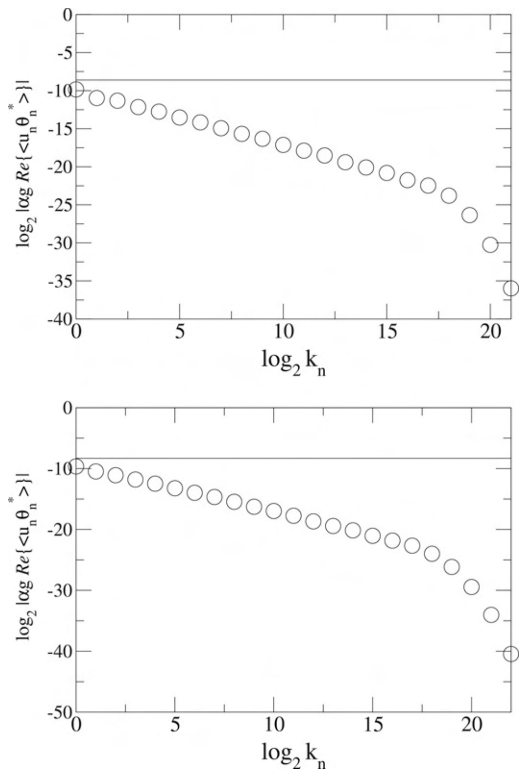

Fig. 6. Comparison of $|\alpha g\langle\mathrm{Re}\{u_n\theta_n^*\}\rangle|$ (circles) with ϵ (solid line) in each shell for the SabraT model with $\delta = 0.5$ in the top panel and $\delta = 0.8$ in the bottom panel.

third term on the right-hand side is the rate of energy dissipation in the nth shell due to viscosity while the last term is the power injected into the nth shell by the buoyancy forces. It is thus reasonable to take buoyancy to be significant in the nth shell if

$$|\alpha g\langle\mathrm{Re}\{u_n\theta_n^*\}\rangle| > \epsilon \tag{17}$$

where $\epsilon \equiv \nu\sum_n k_n^2\langle|u_n|^2\rangle$ is the average energy dissipation rate. We denote the scale at which the equality sign in Eq. (17) holds to be the buoyancy scale k_{n^*}. Hence buoyancy is relevant and significant for $n < n^*$ and irrelevant or insignificant for $n > n^*$. It is easy to show that for u_n and θ_n satisfying exactly K41 or BO scaling, $k_{n^*} = 1/L_B$, where $L_B \equiv \epsilon^{5/4}\chi^{-3/4}(\alpha g)^{-3/2}$ is the Bolgiano length [15] and χ is the average thermal or entropy dissipation rate given by $\chi \equiv \kappa\sum_n k_n^2\langle|\theta_n|^2\rangle$.

As shown in Figs. 4 and 5, we find that Eq. (17) is satisfied for most of the shells only in the Brandenburg model with b/a larger than the critical value. When b/a is smaller than the critical value, buoyancy is insignificant in all except the largest shells. For the SabraT model, we find that buoyancy is insignificant in all except the largest shells for all the values of δ studied. The results for $\delta = 0.5$ and $\delta = 0.8$ are shown in Fig. 6.

One naturally expects different scaling behavior when buoyancy is significant and when it is not. In this sense, it is not puzzling that different scaling behavior was reported in the various shell models proposed. Indeed we find BO scaling plus corrections when buoyancy is significant and K41 scaling plus correction when it is not. The two different scaling behavior can be understood by studying the evolution equations of energy and entropy. In the intermediate range where external forcing is not acting and where energy and entropy dissipation rates are both small, Eqs. (5) and (6) can be approximately written as:

$$F_u(k_n) - F_u(k_{n+1}) + \alpha g\mathrm{Re}\{u_n\theta_n^*\} \approx 0 \tag{18}$$

$$F_\theta(k_n) - F_\theta(k_{n+1}) \approx 0. \tag{19}$$

From Eq. (19), $F_\theta(k_n)$ is independent of k_n in the intermediate range, implying that there is an entropy cascade. From Eq. (18), we see that $\alpha g\mathrm{Re}\{u_n\theta_n^*\}$ is comparable with F_u when buoyancy is significant, and $F_u(k_n) - F_u(k_{n+1}) \approx 0$ when buoyancy is insignificant. Thus when buoyancy is insignificant, there is also an energy cascade as in the usual inertia-driven turbulence.

In the case when buoyancy is significant, there is only the cascade of entropy. As a result, one expects the statistical properties to be controlled by the entropy cascade. Specifically, one expects [16] the statistical properties of u_n and θ_n to be determined solely by F_θ, αg, and k_n:

$$|u_n| = \phi_u(\alpha g)^{2/5}|F_\theta(k_n)|^{1/5}k_n^{-3/5} \tag{20}$$

$$|\theta_n| = \phi_\theta(\alpha g)^{-1/5}|F_\theta(k_n)|^{2/5}k_n^{-1/5} \tag{21}$$

where ϕ_u and ϕ_θ are dimensionless random variables that are independent of k_n and statistically independent of $F_\theta(k_n)$. On the other hand, when buoyancy is insignificant, there is also the energy cascade. Thus one expects the statistical properties of u_n

and θ_n to be determined by F_u, F_θ and k_n:

$$|u_n| = \psi_u |F_u(k_n)|^{1/3} k_n^{-1/3} \tag{22}$$

$$|\theta_n| = \psi_\theta |F_u(k_n)|^{-1/6} |F_\theta(k_n)|^{1/2} k_n^{-1/3} \tag{23}$$

where ψ_u and ψ_θ are dimensionless random variables that are independent of k_n and statistically independent of $F_u(k_n)$ and $F_\theta(k_n)$. Hence we have

$$\langle |u_n|^p \rangle \sim \langle |F_\theta(k_n)|^{p/5} \rangle k_n^{-3p/5} \tag{24}$$

$$\langle |\theta_n|^p \rangle \sim \langle |F_\theta(k_n)|^{2p/5} \rangle k_n^{-p/5} \tag{25}$$

when buoyancy is significant and

$$\langle |u_n|^p \rangle \sim \langle |F_u(k_n)|^{p/3} \rangle k_n^{-p/3} \tag{26}$$

$$\langle |\theta_n|^p \rangle \sim \langle |F_u(k_n)|^{-p/6} |F_\theta(k_n)|^{p/2} \rangle k_n^{-p/3} \tag{27}$$

when it is not. Eqs. (24) and (25), and Eqs. (26) and (27) thus respectively give BO and K41 scaling plus intermittency corrections for the case when buoyancy is significant and when it is not, just as what was found numerically. Moreover, when buoyancy is significant, the intermittency corrections are solely due to fluctuations in F_θ while in the case when buoyancy is insignificant, the intermittency corrections are due to fluctuations in both and F_u and F_θ. We have checked and verified [16] Eqs. (24) and (25).

Our work shows that the mere presence of a coupling term between velocity and temperature in the equations of motion does not automatically imply that buoyancy is significant and affects the statistical properties. This leads to the question: How can one tell whether temperature is behaving as an active or a passive scalar in models for turbulent thermal convection? For shell models, one can use Eq. (17). If Eq. (17) is satisfied in most shells then buoyancy is significant and temperature is active otherwise temperature would behave as a passive scalar. It would also be useful to have some other criterion that involves directly the statistical features of temperature. Eqs. (20) and (21) imply that when buoyancy is significant, the conditional statistics of u_n and θ_n at fixed values of F_θ would have simple BO scaling with no corrections [16]. On the other hand, this is not true when buoyancy is insignificant; instead Eqs. (22) and (23) indicate that the conditional statistics of u_n and θ_n at fixed values of F_θ continue to deviate from simple K41 scaling. Hence one can study the conditional statistics of temperature at fixed values of the entropy transfer rate. If these conditional statistics are described by simple scaling then temperature is behaving as an active scalar. Otherwise if the conditional statistics remain anomalous then temperature is behaving as a passive scalar. To check this idea, we calculate the the conditional temperature structure functions at fixed values of entropy transfer rate and their scaling exponents ξ_p^*:

$$\langle |\theta_n|^p \, | F_\theta = x \rangle \sim k_n^{-\xi_p^*} \tag{28}$$

for the SabraT model the Brandenburg model for both small and large values of b/a. The results of ξ_p^* do not depend on x and are shown in Fig. 7. It can be seen that for Brandenburg model

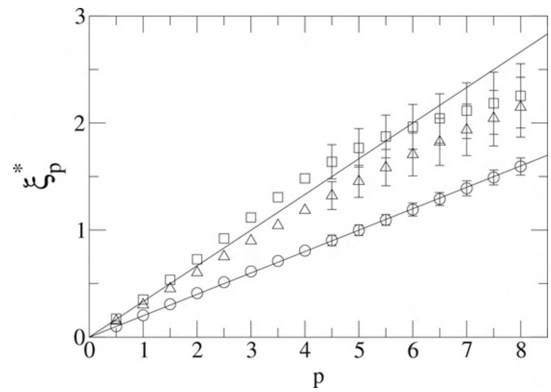

Fig. 7. The scaling exponents ξ_p^* of the conditional temperature structure functions $\langle |\theta_n|^p \, | F_\theta = x \rangle$ for the Brandenburg model with small b/a (squares) and large b/a (circles), and the SabraT model with $\delta = 0.5$ (triangles). The error increases with p and the largest errors are shown. Two solid lines with slopes 1/3 and 1/5 are shown.

with large b/a, ξ_p^* are indeed well described by the BO values of $p/5$. Also, as expected, for both the Brandenburg model with small b/a and the SabraT model, ξ_p^*'s continue to deviate from the K41 values of $p/3$.

4. Conclusions

Various shell models have been proposed for turbulent thermal convection. K41 scaling plus corrections has been reported in most of these models while BO scaling plus intermittency corrections is reported in the Brandenburg model with suitable parameters. In this paper, we have shown that buoyancy is not always significant and relevant to the statistical properties in these shell models even though there is an explicit coupling term with temperature in the equation of motion for velocity. We have further clarified that BO scaling plus corrections would be observed only in the shell models in which buoyancy is significant. For shell models in which buoyancy is insignificant, the statistical properties remain the same as in the case in which the coupling term with temperature is replaced by a large-scale random forcing. We have argued that the statistics properties are controlled solely by the cascade of entropy when buoyancy is significant but controlled by both the cascades of energy and entropy when buoyancy is not significant, and shown how this leads to the two different scaling behavior in the two cases. We have further shown that the intermittency corrections are solely attributed to fluctuations of the entropy transfer rate when buoyancy is significant but are caused by fluctuations of both the energy and entropy transfer rate when buoyancy is insignificant. As a result, the conditional temperature structure functions at fixed entropy transfer rate would have simple scaling when buoyancy is significant but remain anomalous when buoyancy is insignificant. We have demonstrated how this feature can be used as a criterion to distinguish whether temperature is acting as an active or a passive scalar.

Acknowledgments

This work is supported by the Hong Kong Research Grants Council (CUHK 400304 and CA05/06.SC01).

References

[1] E.D. Siggia, Ann. Rev. Fluid Mech. 26 (1994) 137.
[2] L.P. Kadanoff, Phys. Today 54 (8) (2001) 34.
[3] E.S.C. Ching, Phys. Rev. E 75 (2007) 056302.
[4] L. Biferale, Ann. Rev. Fluid Mech. 35 (2003) 441.
[5] R. Bolgiano, J. Geophys. Res. 64 (1959) 2226;
A.M. Obukhov, Dokl. Akad. Nauk. SSSR 125 (1959) 1246.
[6] A. Brandenburg, Phys. Rev. Lett. 69 (1992) 605.
[7] E. Suzuki, S. Toh, Phys. Rev. E 51 (1995) 5628.
[8] A.N. Kolmogorov, C. R. Acad. Sci. URSS 30 (1941) 301.
[9] M.-S. Jiang, S.-D. Liu, Phys. Rev. E 56 (1997) 441.
[10] E.B. Gledzer, Sov. Phys. Dokl. 18 (1973) 216;
K. Ohkitani, M. Yamada, Progr. Theoret. Phys. 89 (1989) 329.
[11] H. Guo, Ph.D. Thesis, The Chinese University of Hong Kong, 2007.
[12] V.S. L'vov, E. Podivilov, A. Pomyalov, I. Procaccia, D. Vandembroucq, Phys. Rev. E 58 (1998) 1811.
[13] L. Kadanoff, D. Lohse, J. Wang, R. Benzi, Phys. Fluids 7 (1995) 617.
[14] Z.S. She, E. Leveque, Phys. Rev. Lett. 72 (1994) 336.
[15] See, for example A.S. Monin, A.Y. Yaglom, Statistical Fluid Mechanics, MIT Press, Cambridge, MA, 1975, Pergamon Press, Oxford, 1987.
[16] E.S.C. Ching, W.C. Cheng, Phys. Rev. E 77 (2008) 015303(R).

Available online at www.sciencedirect.com

ScienceDirect

Physica D 237 (2008) 2015–2019

PHYSICA D

www.elsevier.com/locate/physd

Two-fluid model of the truncated Euler equations

Giorgio Krstulovic*, Marc-Étienne Brachet

Laboratoire de Physique Statistique de l'Ecole Normale Supérieure, Associé au CNRS et aux Universités Paris VI et VII, 24 Rue Lhomond, 75231 Paris, France

Available online 17 November 2007

Abstract

A phenomenological two-fluid model of the (time-reversible) spectrally-truncated $3D$ Euler equation is proposed. The thermalized small scales are first shown to be quasi-normal. The effective viscosity and thermal diffusion are then determined, using EDQNM closure and Monte-Carlo numerical computations. Finally, the model is validated by comparing its dynamics with that of the original truncated Euler equation.

PACS: 47.27.eb; 47.27.em; 47.15.ki

Keywords: Truncated Euler equations; Absolute equilibrium; EDQNM

1. Introduction

It is well known that the (inviscid and conservative) truncated Euler equation admits absolute equilibrium solutions with Gaussian statistics, equipartition of kinetic energy among all Fourier modes and thus an energy spectrum $E(k) \sim k^2$ [1]. Recently, Cichowlas et al. [2,3] observed that the Euler equation, with a very large (several hundreds) spectral truncation wavenumber $k_{\max}$, has long-lasting transients which behave just as those of high Reynolds-number viscous flow; in particular they found an approximately $k^{-5/3}$ inertial range followed by a dissipative range. How is such a behaviour possible? It was found that the highest-k modes thermalize at first, displaying a k^2 spectrum. Progressively the thermalized region extends to lower and lower wavenumbers, eventually covering the whole range of available modes. At intermediate times, when the thermalized regime only extends over the highest wavenumbers, it acts as a thermostat that pumps out the energy of larger-scale modes. Note that similar $k^{-5/3}/k^2$ spectra have already been obtained within the Leith model of hydrodynamic turbulence which is a simple differential closure [4], and earlier similar mixed cascade/thermodynamic states (but with spectra different from $k^{-5/3}/k^2$) were discussed in the wave turbulence literature (e.g. [5]).

The purpose of the present work is to build a quantitative two-fluid model for the relaxation of the $3D$ Euler equation. In Section 2, after a brief recall of basic definitions, the statistics of the thermalized small scales are studied during relaxation. They are shown to be quasi-normal. Our new two-fluid model, involving both an effective viscosity and a thermal diffusion, is introduced in Section 3. The effective diffusion laws are then determined, using an EDQNM closure prediction and direct Monte-Carlo computations. The model is then validated by comparing its predictions with the behaviour of the original truncated Euler equation. Finally Section 4 is our conclusion.

2. Relaxation dynamics of truncated Euler equations

2.1. Basic definitions

The truncated Euler equation (1) are classically obtained [1] by performing a Galerkin truncation ($\hat{v}(k) = 0$ for $\sup_\alpha |k_\alpha| > k_{\max}$) on the Fourier transform $\mathbf{v}(\mathbf{x}, t) = \sum \hat{\mathbf{v}}(\mathbf{k}, t)e^{i\mathbf{k}\cdot\mathbf{x}}$ of a spatially periodic velocity field obeying the (unit density) three-dimensional incompressible Euler equations, $\partial_t \mathbf{v} + (\mathbf{v} \cdot \nabla)\mathbf{v} = -\nabla p, \nabla \cdot \mathbf{v} = 0$. This procedure yields the following finite system of ordinary differentials equations for the complex variables $\hat{\mathbf{v}}(\mathbf{k})$ ($\mathbf{k}$ is a 3 D vector of relative integers (k_1, k_2, k_3) satisfying $\sup_\alpha |k_\alpha| \le k_{\max}$)

$$\partial_t \hat{v}_\alpha(\mathbf{k}, t) = -\frac{i}{2}\mathcal{P}_{\alpha\beta\gamma}(\mathbf{k}) \sum_{\mathbf{p}} \hat{v}_\beta(\mathbf{p}, t)\hat{v}_\gamma(\mathbf{k} - \mathbf{p}, t) \tag{1}$$

* Corresponding author.
E-mail address: krstulov@lps.ens.fr (G. Krstulovic).

0167-2789/$ - see front matter
doi:10.1016/j.physd.2007.11.008

where $\mathcal{P}_{\alpha\beta\gamma} = k_\beta P_{\alpha\gamma} + k_\gamma P_{\alpha\beta}$ with $P_{\alpha\beta} = \delta_{\alpha\beta} - k_\alpha k_\beta / k^2$ and the convolution in (1) is truncated to $\sup_\alpha |k_\alpha| \leq k_{\max}$, $\sup_\alpha |p_\alpha| \leq k_{\max}$ and $\sup_\alpha |k_\alpha - p_\alpha| \leq k_{\max}$.

This time-reversible system exactly conserves the kinetic energy $E = \sum_k E(k,t)$, where the energy spectrum $E(k,t)$ is defined by averaging $\hat{\mathbf{v}}(\mathbf{k}',t)$ on spherical shells of width $\Delta k = 1$,

$$E(k,t) = \frac{1}{2} \sum_{k-\Delta k/2 < |\mathbf{k}'| < k + \Delta k/2} |\hat{\mathbf{v}}(\mathbf{k}',t)|^2. \tag{2}$$

2.2. Small scales statistics

Perhaps the most striking result of Cichowlas et al. [2] was the spontaneous generation of a (time dependent) minimum of the spectrum $E(k,t)$ at wavenumber $k_{\text{th}}(t)$ where the scaling law $E(k,t) = c(t)k^2$ starts. Thus, the energy dissipated from large scales into the time dependent statistical equilibrium is given by

$$E_{\text{th}}(t) = \sum_{k_{\text{th}}(t) < k} E(k,t). \tag{3}$$

In this section we use the so-called Taylor–Green [6] initial condition to (1): the single-mode Fourier transform of $u^{\text{TG}} = \sin x \cos y \cos z$, $v^{\text{TG}} = -u^{\text{TG}}(y,-x,z)$, $w^{\text{TG}} = 0$.

In order to separate the dynamics of large-scale ($k < k_{\text{th}}$) and the statistics of small-scales ($k > k_{\text{th}}$) we define the low- and high-pass filtered fields

$$f^<(\mathbf{r}) = \sum_k F(\mathbf{k}) \hat{f}_{\mathbf{k}} \mathrm{e}^{\mathrm{i}\mathbf{k}\cdot\mathbf{r}} \tag{4}$$

$$f^>(\mathbf{r}) = 1 - f^<(\mathbf{r}) \tag{5}$$

where $f(\mathbf{r})$ is an arbitrary field and $\hat{f}_k$ its Fourier transform; we have chosen $F(\mathbf{k}) = \frac{1}{2}(1 + \tanh[\frac{|k| - k_{\text{th}}}{\Delta k}])$, with $\Delta k = 1/2$.

This filter allows us to define the large-scale velocity field $\mathbf{v}^<$ and the spatially dependent thermalized energy (or heat) associated to quasi-equilibrium. Using the trace of the Reynold's tensor [7], $R_{ij} = \frac{1}{2}(v_i^> v_j^>)^<$, we define the local heat as

$$Q(\mathbf{r}) = \frac{1}{2}\left[(\mathbf{v}^>)^2\right]^<(\mathbf{r}). \tag{6}$$

By construction of the filters, (4) and (5) the heat spatial average is equal to the dissipated energy (3) $\langle Q(r)\rangle = E_{\text{th}}$. Fig. 1a shows a $2D$ cut of the heat Q on the surface $z = \frac{\pi}{2}$, where a cold zone is seen to be present at the centre of the impermeable box ($x = [0,\pi]$, $y = [0,\pi]$, $z = [0,\pi]$). An isosurface of the hottest zones is displayed on Fig. 1b. It is apparent on both figures that $Q(\mathbf{r})$ is not spatially homogeneous.

2.3. Heat diffusion

The simplest quantities to study in order to quantify the evolution of Q, are the spatial average $Q(t) = \langle Q(\mathbf{r},t)\rangle$ and the root mean square variation $\Delta Q = \sqrt{\langle (Q^2 - \langle Q\rangle^2)\rangle}$. These quantities are shown in Fig. 2, where that the mean heat is seen

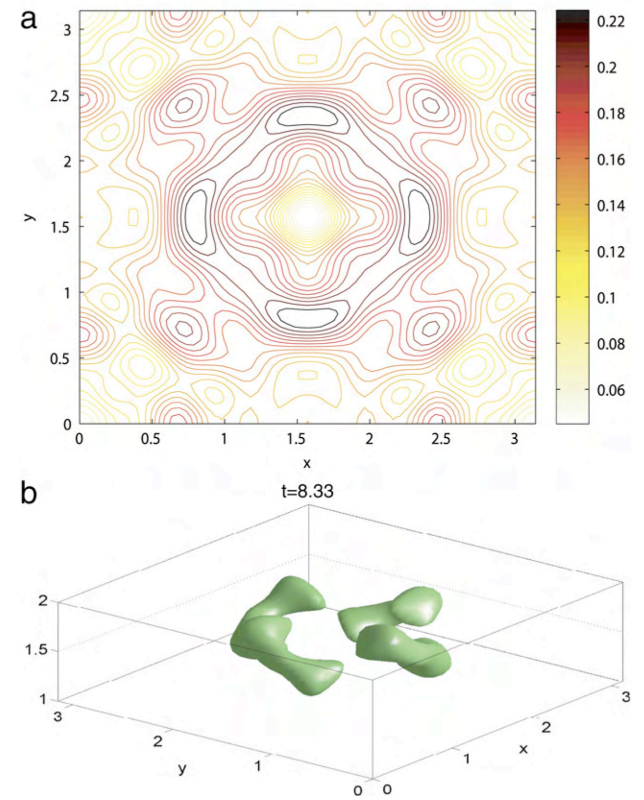

Fig. 1. Cut at $z = \frac{\pi}{2}$ of Q (a) and the isosurface $Q(r) = 0.8Q_{\max} = 0.42$ (b).

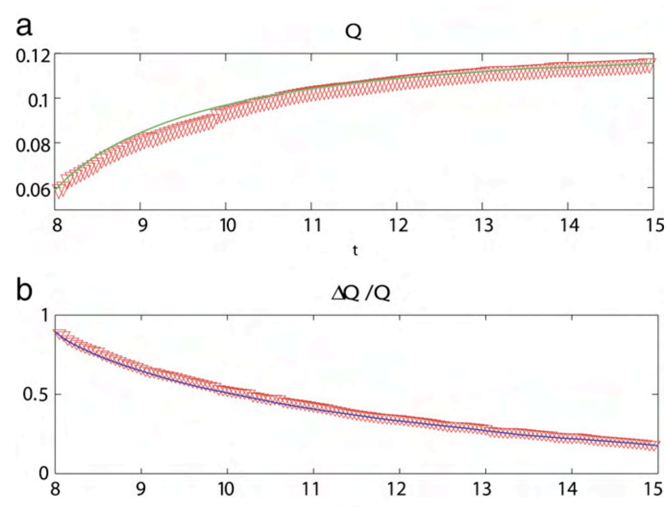

Fig. 2. Plots of $Q(t)$ (a) and $\Delta Q(t)/Q(t)$ (b); solid lines are the results of the two-fluid model (see Section 3).

to increases in time, due to the energy coming from the large eddies, as was shown precedently in [2]. The relative fluctuation $\Delta Q/Q$ is seen to decrease from 0.9 to 0.2.

The next natural question is related to the statistical distribution of the small eddies $v^>$: are they approximately Gaussian, like an absolute equilibrium? A histogram of $v_x^>$ is shown in Fig. 3. As the heat is not homogeneous, we also computed the histogram of the normalized field $\tilde{v}_x^> = v_x^>/\sqrt{Q}$ which seems to better obey Gaussian statistics as can be seen on

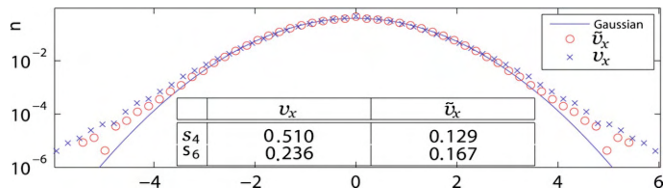

Fig. 3. Histogram of $v_x^>$ and $\tilde{v}_x^>$ and normalized cumulant s_4 and s_6 (odd cumulants vanish because of symmetries).

Fig. 3 and comparing the firsts normalized cumulant $s_n = \frac{c_n}{\sqrt{c_2^n}}$ (c_n is the cumulant of order n) in the table.

3. Two-fluid model

We now introduce our phenomenological two-fluid model of the truncated Euler equation. One of the fluids describes the large scale velocity field and the other represents the thermalized high-wavenumber modes described by a temperature field $T = Q/c$ (c is the specific heat, explicitly given by $c = 8k_{\max}^3$). This model is somewhat analogous to Landau's standard two-fluid model of liquid helium at finite temperature T where there is a natural cut-off wavenumber for thermal excitations: the classical-quantum crossover wavenumber $k_{\max}$ given by $\hbar k_{\max} c_S = k_B T$ (c_S is the sound velocity and k_B Boltzmann's constant). In Landau's model $k_{\max}$ is temperature dependent and the specific heat c is proportional to T^3. In constrast, $k_{\max}$ and the specific heat are constant in our model that reads:

$$\partial_t v_i^< + v_j^< \partial_j v_i^< = -\partial_i \tilde{p} + \partial_j \sigma'_{ij} \tag{7}$$

$$\partial_i v_i^< = 0 \tag{8}$$

$$\partial_t T + v_j^< \partial_j T = \mathcal{D}T + \frac{1}{2c}\left(\partial_j v_i^< + \partial_i v_j^<\right)\sigma'_{ij} \tag{9}$$

where

$$\sigma'_{ij} = \mathcal{F}^{-1}[\nu_{\text{eff}}(k)(ik_i \hat{v}_j^< + ik_j \hat{v}_i^<)] \tag{10}$$

$$\mathcal{D}T = \mathcal{F}^{-1}[-k^2 D_{\text{eff}}(k)\mathcal{F}[T]] \tag{11}$$

and $\mathcal{F}[\cdot]$ denotes the Fourier transform. σ'_{ij} is a generalized form of the standard viscous strain tensor [8]. The precise form of the anomalous diffusion terms ν_{eff} and D_{eff} will be determined below, in Sections 3.1 and 3.2.

The advection terms in Eq. (7) are readily obtained from the Reynolds equations for the filtered velocity by remarking that the diagonal part of the Reynolds stress can, because of incompressibility, be absorbed in the pressure. Eq. (10) represents a simple model of the traceless part of the Reynolds tensor [7]. In the same vein, the advection terms in Eq. (9) are readily obtained together with higher-order moments (see equation (1) of Reference [9]). The dissipation and source terms in (9) are thus simple models of the higher-order moments. It is easy to show that in the present model $\langle \frac{1}{2}\mathbf{v}^{<2} + cT\rangle$ is conserved, corresponding to the energy conservation in the truncated Euler equation.

As the fluctuations $\Delta Q/Q$ are small (see above) we will furthermore assume that ν_{eff} and D_{eff} only depend on $\langle Q\rangle = E_{\text{th}}$. Thus the evolution of the filtered velocity $\mathbf{v}^<$ is independent of the fluctuations ΔQ. As $[E_{\text{th}}] = L^2 T^{-2}$, simple dimensional analysis yields the following form for the function ν_{eff} and D_{eff}:

$$\begin{aligned} \nu_{\text{eff}} &= \frac{\sqrt{E_{\text{th}}}}{k_{\max}} f\left(\frac{k}{k_{\max}}, \frac{k_0}{k_{\max}}\right); \\ D_{\text{eff}} &= \frac{\sqrt{E_{\text{th}}}}{k_{\max}} \Psi\left(\frac{k}{k_{\max}}, \frac{k_0}{k_{\max}}\right) \end{aligned} \tag{12}$$

where $k_0 = 2\pi/L_p$ the smallest nonzero wavenumber (L_p is the periodicity length, 2π in the present simulations).

3.1. EDQNM determination of viscosity

An analytical determination of function ν_{eff} is possible using the eddy-damped quasi-Markovian theory (EDQNM) [10]. It is known that this model well reproduces the dynamics of truncated Euler Equation, including the $k^{-5/3}$ and k^2 scalings and the relaxation to equilibrium [11].

The EDQNM closure furnishes an integro-differential equation for the spectrum $E(k,t)$:

$$\frac{\partial E(k,t)}{\partial t} = T_{NL}(k,t) \tag{13}$$

where the nonlinear transfer T_{NL} is modeled as

$$\begin{aligned} T_{NL}(k,t) = \int\int_\triangle &\Theta_{kpq}(xy+z^3)[k^2 p E(p,t)E(q,t) \\ &- p^3 E(q,t)E(k,t)]\frac{\mathrm{d}p\,\mathrm{d}q}{pq}. \end{aligned} \tag{14}$$

In (14) $\triangle$ is a strip in p, q space such that the three wavevectors $\mathbf{k}$, $\mathbf{p}$, $\mathbf{q}$ form a triangle. x, y, z, are the cosine of the angles opposite to $\mathbf{k}$, $\mathbf{p}$, $\mathbf{q}$. Θ_{kpq} is a characteristic time defined as

$$\Theta_{kpq} = \frac{1 - \exp(-(\eta_k + \eta_p + \eta_q)t)}{\eta_k + \eta_p + \eta_q} \tag{15}$$

and the eddy damped η is defined as

$$\eta_k = \lambda\sqrt{\int_0^k s^2 E(s,t)\mathrm{d}s}. \tag{16}$$

Classically $\lambda = 0.36$ and the truncation is imposed omitting all interactions involving waves numbers larger than $k_{\max}$ in (14).

A simple and important stationary solution of (13) is the absolute equilibrium with equipartition of the kinetic energy and corresponding spectrum $E(k) \sim k^2$.

To compute the EDQNM effective viscosity ν_{eff} we consider an absolute equilibrium with a small perturbation added in the mode of wavenumber k_{pert} and study the relaxation to equilibrium. The corresponding ansatz is $E(p,t) = \frac{3E_{\text{th}}}{k_{\max}^3}p^2 + \gamma(t)\delta(p - k_{\text{pert}})$ and we suppose $E_{\text{th}} \gg \gamma$, so that the total energy is almost constant and equal to E_{th}.

Using the long time limit of (15) and expanding the EDQNM transfer (14) to first order in γ yields for the delta containing part, after a lengthy but straightforward computation:

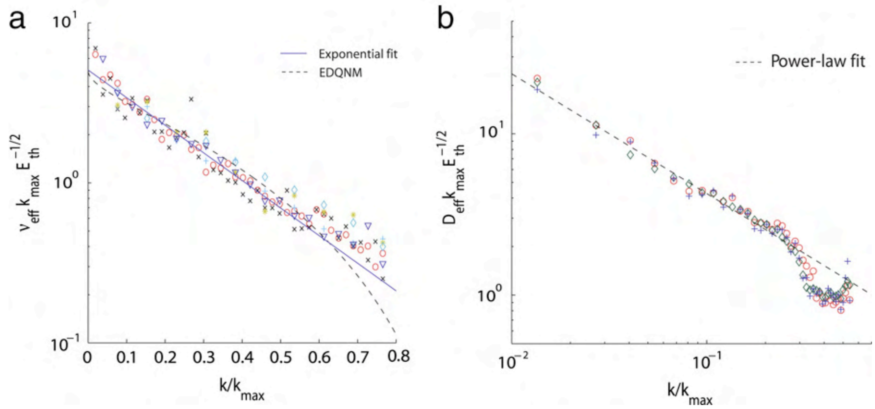

Fig. 4. Effective viscosity ν_{eff} (a) and thermal diffusivity D_{eff} (b) determined by Monte Carlo computations performed at different values of E_{th} and $k_{\max}$ (see text).

$$T_{NL}(k,t) = -\gamma(t)\delta(k - k_{\text{pert}})k^2 \frac{\sqrt{E_{\text{th}}}}{k_{\max}} \frac{\sqrt{30}}{\lambda} I\left(\frac{k}{k_{\max}}\right) \tag{17}$$

where I is given by the explicit integral

$$I(x) = \sqrt{x} \times \int_1^{\frac{2-x}{x}} \int_{-1}^{1} \frac{(p^2-1)(1-q^2)(q^2+p^2(1+2q^2))}{(p^2-q^2)(2^{\frac{5}{2}} + ((p-q)^{\frac{5}{2}} + (p+q)^{\frac{5}{2}}))} \mathrm{d}q\,\mathrm{d}p.$$

Using (13) and (17) and the basic definition of the two-fluid model (7)–(11), we obtain

$$\nu_{\text{eff}}(k) = \frac{\sqrt{E_{\text{th}}}}{k_{\max}} \frac{\sqrt{30}}{2\lambda} I\left(\frac{k}{k_{\max}}\right). \tag{18}$$

The function $f(x = \frac{k}{k_{\max}}, 0)$ in (12) is thus given by

$$f(x,0) = \frac{\sqrt{30}}{2\lambda} I(x). \tag{19}$$

In the limit $x \to 0$, it is simple to show that f has a finite value $f(0,0) = \frac{7}{\sqrt{15}\lambda}$. Thus the EDQNM prediction in the small $k/k_{\max}$ limit is

$$\nu_{\text{eff}} = \frac{\sqrt{E_{\text{th}}}}{k_{\max}} \frac{7}{\sqrt{15}\lambda}, \tag{20}$$

with $\frac{7}{\sqrt{15}\lambda} = 5.021$ for the classic value of $\lambda = 0.36$. This asymptotic value can also be obtained from the EDQNM eddy viscosity expression calculated by Lesieur and Schertzer [12] using an energy spectrum $E(k) \sim k^2$.

3.2. Monte-Carlo determination of viscosity and thermal diffusion

In order to numerically determine the effective viscosity $\nu_{\text{eff}}(k)$ of the two-fluid model, we use a general-periodic code to study the relaxation of an absolute equilibrium perturbed by adding a stationary solution of the Euler equation. We thus consider the initial condition

$$u = \cos kx \sin ky + u_{\text{eq}} \tag{21}$$

$$v = -\sin kx \cos ky + v_{\text{eq}} \tag{22}$$

$$w = w_{\text{eq}} \tag{23}$$

where the (solenoidal and Gaussian) absolute equilibrium velocity field satisfies $\langle u_{\text{eq}}^2 + v_{\text{eq}}^2 + w_{\text{eq}}^2 \rangle = 2E_{\text{th}}$.

The resulting amplitude of the rotation in (21)–(23) is found, after a short transient, to decay exponentially in time. The function $\nu_{\text{eff}}(k)$ is then obtained by finding the halving time τ_k, for which $\hat{v}_\alpha(\mathbf{k}, t_0 + \tau_k) = \hat{v}_\alpha(\mathbf{k}, t_0)/2$, with t_0 chosen larger than the short transient time. The effective dissipation thus reads

$$\nu_{\text{eff}}(k) = \log 2/(k^2 \tau_k). \tag{24}$$

The values of $\nu_{\text{eff}}(k) k_{\max}/\sqrt{E_{\text{th}}}$ are shown in Fig. 4a for different values of $E_{\text{th}}, k, k_{\max}$. A very good agreement with the EDQNM prediction is observed. Note that there is not dependence in the dimensionless parameter $k_0/k_{\max}$ (see Eq. (12)).

An exponential fit of all data in Fig. 4a gives

$$\nu_{\text{eff}} = 5.0723 \frac{\sqrt{E_{\text{th}}}}{k_{\max}} \mathrm{e}^{-3.97k/k_{\max}}. \tag{25}$$

Note that the limit $k/k_{\max} \to 0$ is consistent with the EDQNM prediction (20).

Another simple numerical experiment can be used to characterize the thermal diffusion: the relaxation of a spatially-modulated *pseudo*-equilibrium defined by

$$\left\langle u^2 + v^2 + w^2 \right\rangle = 2E_{\text{th}} + 2\epsilon \cos(kx) \tag{26}$$

with $\epsilon < E_{\text{th}}$.

An x-dependent temperature can be recovered by averaging $u^2 + v^2 + w^2$ over y and z. Numerical integration of the truncated Euler equation with the initial condition (26) produces an amplitude ϵ that decays exponentially, as in the case studied for the determination of effective viscosity. The thermal diffusivity D_{eff} is determined in the same way as in Eq. (24) and the corresponding data are shown in Fig. 4b. A power-law fit gives

$$D_{\text{eff}} = 0.7723 \frac{\sqrt{E_{\text{th}}}}{k_{\max}} (k/k_{\max})^{-0.74}. \tag{27}$$

The negative exponent in (27) is characteristic of hypodiffusive processes.

We can define an effective Prandtl number as the ratio $P_{\text{eff}}(k) = \nu_{\text{eff}}(k)/D_{\text{eff}}(k)$. The Prandtl number is plotted in

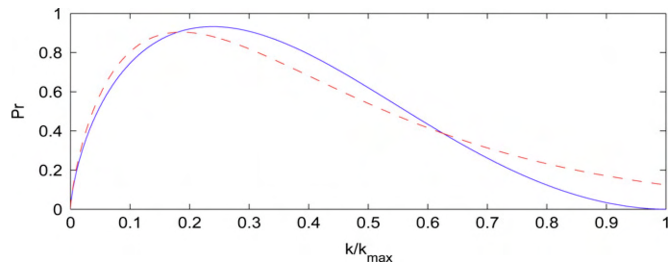

Fig. 5. Effective Prandtl number $P_{\rm eff} = \nu_{\rm eff}/D_{\rm eff}$. (For interpretation of the references to colour in this figure legend, the reader is referred to the web version of this article.)

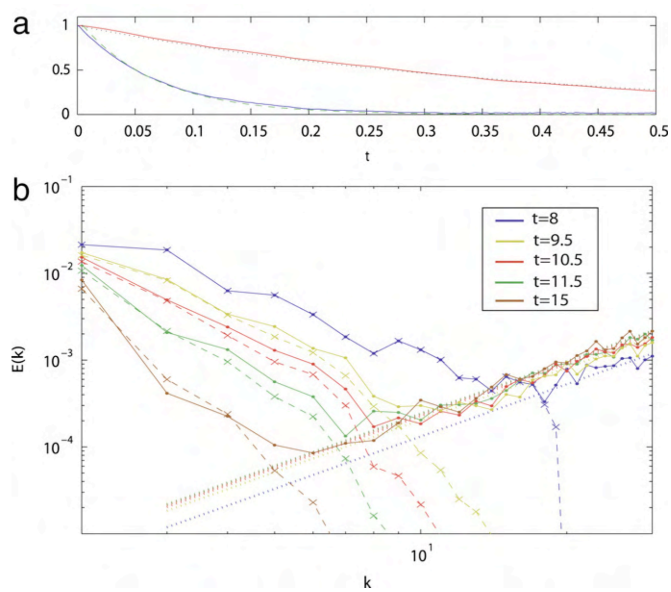

Fig. 6. (a) Time decay of rotation (21) and (22) (upper curve) and temperature modulation (26) (bottom curve). Solid line: truncated Euler equations and dashed line: two-fluid model. (b) Time-evolution of energy spectra, truncated Euler equation: solid lines and two-fluid model: dashed lines. (For interpretation of the references to colour in this figure legend, the reader is referred to the web version of this article.)

Fig. 5, where the solid blue line is obtained using the EDQNM prediction (20) and the fit (27) and the dashed red line is obtained using the fits (25) and (27). Note that the Prandtl vanishes in the the small $k/k_{\rm max}$ limit and verifies $P_{\rm eff} < 1$ for all wavenumbers.

3.3. Validation of the model

In this section, numerical integration of the the two-fluid model equations (7)–(11) are performed using a pseudo-spectral code. Time marching is done using second-order leapfrog finite difference scheme and even and odd time-steps are periodically recoupled by fourth-order Runge–Kutta. The effective viscosity and diffusivity are updated at each time step by resetting $E_{\rm th} = \langle Q \rangle$. The obtained data is compared with that directly produced from the truncated Euler equation.

The time-evolutions resulting from initial data (21) and (22) (in red) and (26) (in blue), both normalized to one and with the same value of $E_{\rm th}$ is displayed on Fig. 6a. Good agreement with the two-fluid model is obtained in both cases and the faster relaxation of the temperature modulation is related to the smallness of $P_{\rm eff} < 1$.

We now compare, the evolution of non-trivial spectra of the truncated Euler equation (1) and the two-fluid model. The truncated Euler equation is integrated using the Taylor–Green initial data. At $t \sim 8$, when a clear scales separation is present, the large-scale fields $\mathbf{v}^{<}$ (see Eq. (4)) and the heat Q (Eq. (6)) are computed and used as initial data for the two-fluid model (7)–(11). The subsequent evolution of the two-fluid model is then compared with that of the truncated Euler equation.

Both spectra, plotted in Fig. 6b, are in good agreement. The straights lines represents the thermalized zone $E(k,t) = c(t)k^2$ in the spectrum of the truncated Euler equation, where $c(t)$ is determined by the condition $\langle Q(t) \rangle = \sum_{k>k_{\rm th}} c(t)k^2$.

The value of $Q(t)$ and $\Delta Q/Q$ are plotted in Fig. 2 (solids lines); the evolution of the fluctuation of the temperature are well reproduced too by the two-fluid model.

4. Conclusion

The thermalized small scales were found to follow a quasi-normal distribution. The effective viscosity was determined, using both EDQNM and Monte Carlo. (Hypo)diffusion of heat was obtained and the effective Prandtl number found to vanish at small $k/k_{\rm max}$. The two-fluid model was found to be in good quantitative agreement with the original truncated Euler equations.

Acknowledgments

We acknowledge useful discussions with A. Pouquet and the support of ECOS, CONICYT and IDRIS.

References

[1] S. Orszag, Statistical theory of turbulence, in: R. Balian, J.L. Peube (Eds.), Les Houches 1973: Fluid Dynamics, Gordon and Breach, New York, 1977.

[2] C. Cichowlas, P. Bonaïti, M. Brachet, Effective dissipation and turbulence in spectrally truncated euler flows, Phys. Rev. Lett. 95 (26) (2005).

[3] C. Cichowlas, Equation d'Euler tronquée: de la dynamique des singularités complexes à la relaxation turbulente, Université Pierre et Marie Curie - Paris VI, 2005.

[4] C. Connaughton, S. Nazarenko, Warm cascades and anomalous scaling in a diffusion model of turbulence, Phys. Rev. Lett. 92 (4) (2004) 044501.

[5] S. Dyachenko, A. Newell, A. Pushkarev, V.E. Zakharov, Optical turbulence: Weak turbulence, condensates and collapsing filaments in the nonlinear Schrödinger equation, Physica D 57 (1992) 96–160.

[6] G.I. Taylor, A.E. Green, Mechanism of the production of small eddies from large ones, Proc. R. Soc. Lond. A 158 (1937) 499–521.

[7] B. Mohammadi, O. Pironneau, Analysis of the $k - \epsilon$ Turbulence Model, John Wiley & Sons, Masson, 1994.

[8] L. Landau, E. Lifchitz, Mécanique des Fluides, MIR, 1971.

[9] B.E. Launder, G.J. Reece, W. Rodi, Progress in the development of a Reynolds-stress turbulence closure, J. Fluid Mech. 68 (1975) 537–566.

[10] S. Orzag, Analytical theories of turbulence, J. Fluid Mech. 41 (363) (1970).

[11] W.J.T. Bos, J.-P. Bertoglio, Dynamics of spectrally truncated inviscid turbulence, Phys. Fluids 18 (2006) 071701.

[12] M. Lesieur, D. Schertzer, Amortissement auto-similaire d'une turbulence à grand nombre de Reynolds, J. Mec. 17 (1978) 609.

Available online at www.sciencedirect.com
ScienceDirect
Physica D 237 (2008) 2020–2027
PHYSICA D
www.elsevier.com/locate/physd

A geometrical study of 3D incompressible Euler flows with Clebsch potentials — a long-lived Euler flow and its power-law energy spectrum

Koji Ohkitani*

Department of Applied Mathematics, The University of Sheffield, Hicks Building, Hounsfield Road, Sheffield S3 7RH, UK

Available online 16 January 2008

Abstract

A simple initial condition for vorticity $\boldsymbol{\omega} = [\sin(y - z), \sin(z - x), \sin(x - y)]$, which has Clebsch potentials, has been identified to lead to a flow evolution with a very weak energy transfer. This allows us to integrate the Euler equations in time longer than commonly expected, to reach a stage at which the total enstrophy attains its peak for the corresponding Navier–Stokes flow. It thereby enables us to study the relationship between the inviscid-limit and totally inviscid behaviours numerically. In spite of small energy dissipation rate, the Navier–Stokes flow shows a power-law spectrum whose exponent is around $-5/3$ and -2. A similar behaviour is also observed for the Euler flow. In physical space, this flow has groups of vorticity layers, which hesitate to roll up.

PACS: 47.27.Jv; 47.32.C-

Keywords: Regularity; Euler equations; Onsager conjecture; Numerical simulation

1. Introduction

The Euler equations for an incompressible flow written down 250 years ago still remain a challenging subject, both mathematically and physically. One of the central problems is the regularity/singularity issue; whether Euler flows of finite total kinetic energy under appropriate boundary conditions develop spontaneous singularity or not. In other words, the problem is to investigate whether the built-in depletion mechanism is sufficiently effective to avoid singularity or not.

For mathematicians, the importance of the problem is self-evident. However, for physicists or engineers the motivation is less obvious. Perhaps the most well-known rationale for studying possible singularity formation in Euler flows is its relevance to the onset or the intermittency phenomena of turbulence.

This is highlighted in the expression for the dissipation rate of total kinetic energy in Navier–Stokes flows:

$$\epsilon = \nu \left\langle |\boldsymbol{\omega}|^2 \right\rangle \to \text{const.} \neq 0$$

in the limit of vanishing viscosity $\nu \to 0$, [22] where the brackets denote a spatial average.

This suggests that fully-developed turbulence may be characterised by singularities, if any, of totally inviscid fluid flows, thereby raising the interest of studying the relationship

$$\nu \equiv 0 \quad \text{vs. } \nu \to 0.$$

Closely related is the Onsager conjecture for $\nu = 0$ [1]. Essentially, it tells us that a blowup in the Euler equations may drop the total kinetic energy and recommends us to study them to characterise fully-developed turbulence.

The outline of this paper will be as follows. We describe our rationale in Section 2, and mathematical formulation in Section 3. We then introduce a condition for geometrical non-degeneracy in Section 4. Numerical results are presented in Sections 5 and 6. Section 7 describes Kida–Pelz initial

* Corresponding address: Department of Applied Mathematics, School of Mathematics and Statistics, The University of Sheffield, Hicks Building, Hounsfield Road, Sheffield S3 7RH, UK. Tel.: +44 114 222 3861; fax: +44 114 222 3739.

E-mail address: K.Ohkitani@sheffield.ac.uk.

0167-2789/$ - see front matter © 2008 Elsevier B.V. All rights reserved.
doi:10.1016/j.physd.2008.01.011

condition briefly, as another example of flows expressed with Clebsch potentials. Section 8 is devoted to summary and outlook. Finally, we review Clebsch's paper briefly in the Appendix A, because this is a conference devoted to historical Euler's legacy and because we will use Clebsch potentials.

2. Inviscid and inviscid-limit behaviours

In view of the results of past numerical simulations of slightly viscous and inviscid flows, it is now apparent that there are at least two time scales involved in the problem.

One time scale t_* for the inviscid case ($\nu = 0$) marks a rapid growth in vorticity, beyond which numerical solutions become under-resolved, possibly leading to a singularity. The other one T_* for the viscous case ($\nu > 0$) is the time when the total enstrophy is peaked, which is to be followed by the development of the Kolmogorov spectrum.

For example, in the well-known two cases, these values are roughly estimated as follows:

- Taylor–Green vortex [2] has $t_* \approx 5$ and $T_* \approx 9$,
- Kida–Pelz high-symmetric flow [3] has $t_* \approx 2$ and $T_* \approx 4$.

In these cases and in many others, the two time scales are widely separate, that is, T_* is larger than t_* from the viewpoint of numerical simulations. If they were about the same, we would be able to investigate the inviscid-limit behaviour $\nu \to 0$ and compare it with the totally inviscid case $\nu = 0$.

Even with decently high spatial resolutions, numerical solutions soon get under-resolved after t_*. To match T_* as small as t_* we would need to lower Reynolds number, resulting out of the fully-developed stage. For this reason, unfortunately we cannot investigate the relationship between inviscid and inviscid-limit behaviours numerically. We are caught between the devil and the deep blue sea.

Then how can we make progress in this difficult problem? As a workaround we may think of going for geometrically the simplest flows and characterise them as thoroughly as possible.

In this work we confine ourselves to a class of flows endowed with Clebsch potentials. Out of these efforts, a particular flow has been identified, in which the energy transfer process is very mild and the relationship between inviscid and inviscid-limit behaviours can be studied numerically. In this simple flow with Clebsch potentials, we find $t_* \approx T_* (\approx 8)$. We do not know if Clebsch potentials play an essential role to have flows with such a property.

3. Mathematical formulation

With standard notations, the incompressible Euler equations have the following form

$$\frac{\partial \mathbf{u}}{\partial t} + (\mathbf{u} \cdot \nabla)\mathbf{u} = -\nabla p, \qquad \nabla \cdot \mathbf{u} = 0. \tag{1}$$

The well-known criterion [4] for the regularity up to T reads

$$\int_0^T \max_{\mathbf{x}} |\boldsymbol{\omega}(\mathbf{x}, t)| \mathrm{d}t < \infty. \tag{2}$$

Alternatively, regularity may be monitored by any advected scalar f subject to the flow

$$\int_0^T \max_{\mathbf{x}} |\nabla f(\mathbf{x}, t)|^2 \mathrm{d}t < \infty, \tag{3}$$

which is due to [5].

The velocity field is said to have Clebsch potentials when it has the following form

$$\mathbf{u} = f\nabla g - \nabla\phi, \tag{4}$$

where f and g are scalar fields defined globally in the domain, except for unphysical singular points. These scalars are called Clebsch potentials, and ϕ is used for solenoidal projection. The corresponding vorticity reads

$$\boldsymbol{\omega} = \nabla f \times \nabla g. \tag{5}$$

It is not necessary, but sufficient to make f and g material. We take $\frac{\mathrm{D}f}{\mathrm{D}t} = \frac{\mathrm{D}g}{\mathrm{D}t} = 0$ for simplicity, where $\mathrm{D}/\mathrm{D}t$ denotes material derivative. Plausibility of using Clebsch potentials is justified in two steps. Kinematically, we recall a result from vector analysis that

$$\boldsymbol{\gamma} = f\nabla g \text{ globally } \Leftrightarrow \boldsymbol{\gamma} \cdot \nabla \times \boldsymbol{\gamma} \equiv 0. \tag{6}$$

This is called Frobenius's condition of integrability. We may take $\boldsymbol{\gamma}$ as the 'impulse' variable, that is, the first term in the expression for velocity $\boldsymbol{\gamma} = \mathbf{u} + \nabla\phi$.

Dynamically, we recall that the helicity density of the impulse $\boldsymbol{\gamma}$ is conserved pointwise in time with the choice of geometric gauge, that is,

$$\frac{\mathrm{D}}{\mathrm{D}t}\boldsymbol{\gamma} \cdot \nabla \times \boldsymbol{\gamma} = 0. \tag{7}$$

Thus, if it vanishes everywhere initially, it will do so all the time as long as smooth solutions persist.

4. Condition for geometrical non-degeneracy

In the above expression for vorticity, we may observe yet another mechanism for nonlinearity depletion. It is most readily seen by considering the minimum rates for possible blowup for vorticity and scalar gradients:

$$\max_{\mathbf{x}} |\boldsymbol{\omega}| = O\left(\frac{1}{T - t}\right), \tag{8}$$

and

$$\max_{\mathbf{x}} |\nabla f|, \max_{\mathbf{x}} |\nabla g| = O\left(\frac{1}{\sqrt{T - t}}\right) \tag{9}$$

the former of which is due to [4] and the latter to [5]. If we plug these into the vorticity expression (5), the rates of blowup on both sides balance, provided that ∇f and ∇g are *not* parallel to each other. In other words, if ∇f tends to be colinear with ∇g we would have a contradiction.

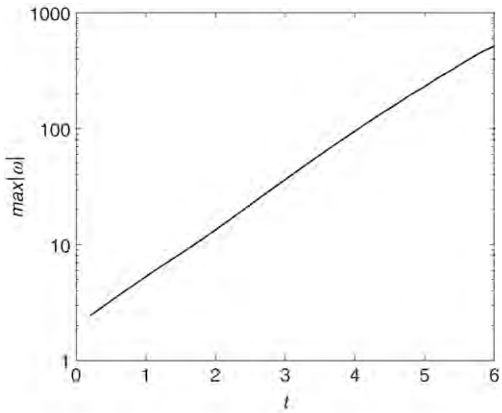

Fig. 1. Time evolution of maximum vorticity.

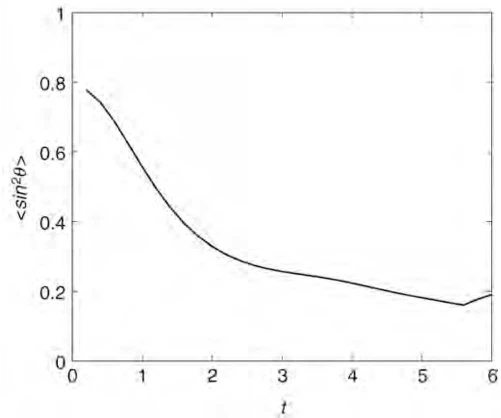

Fig. 2. Time evolution of $\langle \sin^2\theta \rangle$.

5. Numerical results: Euler equations

To test whether the above mechanism is working, we perform a series of numerical simulations. We have two initial conditions in mind; a simple flow with Clebsch potentials and Kida–Pelz high-symmetric flow. We will mainly consider the first case and for the latter we only present a choice of Clebsch potentials and comment on their apparent singularities for comparison.

In practice, by a pseudo-spectral method we solve simultaneously (1) together with

$$\frac{\mathrm{D}f}{\mathrm{D}t} = \frac{\mathrm{D}g}{\mathrm{D}t} = 0. \tag{10}$$

We check $\boldsymbol{\omega} = \nabla f \times \nabla g$ pointwise in space for consistency. The spatial resolution used is 256^3 typically, with the 2/3-dealiasation.

Now we start with the simple initial condition. We consider the following choice of Clebsch potentials

$$f = \sin x + \sin y + \sin z, \qquad g = \cos x + \cos y + \cos z. \tag{11}$$

It is easy to verify that the corresponding vorticity and velocity become

$$\boldsymbol{\omega} = \nabla f \times \nabla g = [\sin(y-z), \sin(z-x), \sin(x-y)], \tag{12}$$

and

$$\mathbf{u} = \left[-\frac{1}{2}(\cos(x-y) + \cos(x-z) + 1), \right.$$
$$-\frac{1}{2}(\cos(y-z) + \cos(y-x) + 1),$$
$$\left. -\frac{1}{2}(\cos(z-x) + \cos(z-y) + 1) \right]. \tag{13}$$

(Note that the constant terms $-\frac{1}{2}$ are included in $\mathbf{u}$ just to make $\mathbf{u} \cdot \boldsymbol{\omega} \equiv 0$. They play no role in dynamics.) First, we plot the growth in maximum vorticity $\max|\boldsymbol{\omega}|$ against time in a semi-linear plot Fig. 1. The straight line shows a clear exponential growth in vorticity.

To check the above-mentioned depletion effect, we monitor

$$\sin^2\theta \equiv \frac{(\nabla f \times \nabla g)^2}{|\nabla f|^2 |\nabla g|^2},$$

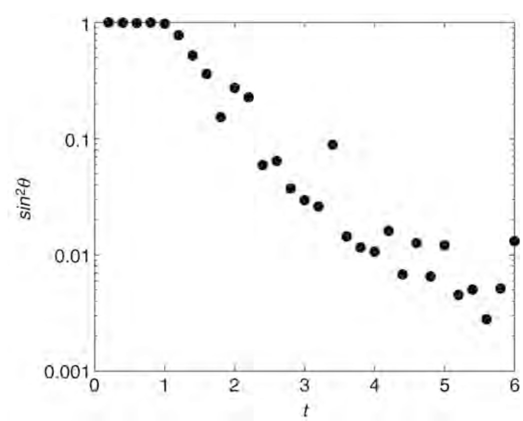

Fig. 3. Time evolution of $\sin^2\theta$ at maximum point of vorticity.

where θ is the angle between the two scalar gradients ∇f and ∇g.

In Fig. 2, we show time evolution of a spatial average $\langle \sin^2\theta \rangle$, which shows a decrease of the angle θ in general. In Fig. 3 evolution of a local value $\sin^2\theta$ evaluated at the maximum point of vorticity is plotted in a log-linear fashion. This shows the angle is shrinking roughly exponential in time. (Some fluctuations are due to a number of different local maxima with the same values.) As far as this initial condition is concerned, the above-mentioned mechanism is actually working to reduce nonlinear effects.

6. Navier–Stokes equations

We consider the Navier–Stokes flows

$$\frac{\partial \mathbf{u}}{\partial t} + (\mathbf{u} \cdot \nabla)\mathbf{u} = -\nabla p + \nu \triangle \mathbf{u}, \qquad \nabla \cdot \mathbf{u} = 0 \tag{14}$$

starting from the same initial condition. We study the time evolution in terms of the enstrophy

$$Q(t) = \left\langle \frac{|\boldsymbol{\omega}|^2}{2} \right\rangle$$

and the energy dissipation rate

$$\epsilon(t) = \nu \left\langle |\boldsymbol{\omega}|^2 \right\rangle.$$

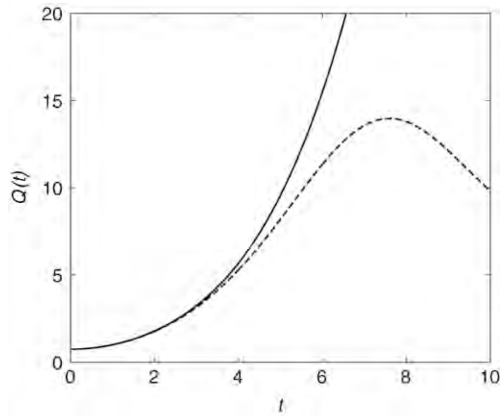

Fig. 4. Time evolution of enstrophy; for $\nu = 0.5 \times 10^{-3}$ (solid) and $\nu = 0$ (dashed).

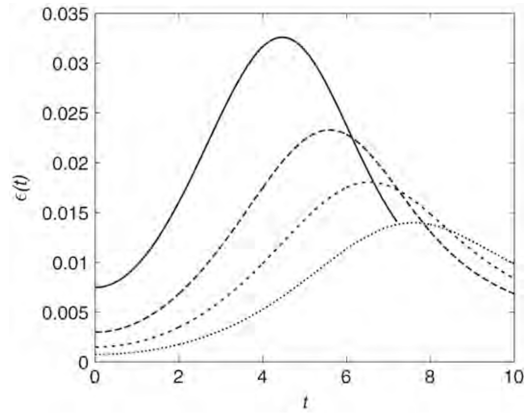

Fig. 5. Time evolution of energy dissipation rate for $\nu = 5.0,\ 2.0,\ 1.0,\ 0.5 \times 10^{-3}$ (solid, dashed, short-dashed and dotted).

The values of kinematic viscosity are chosen as

$$\nu = 5.0,\ 2.0,\ 1.0,\ 0.5 \times 10^{-3}.$$

In Fig. 4 we compare the time evolution of the enstrophy for the inviscid case and the viscous case smallest $\nu = 0.5 \times 10^{-3}$. At around $t = 3$, their difference is noticeable and this Navier–Stokes flow attains the maximum enstrophy around $t = 7$.

We show in Fig. 5 the time evolution of the dissipation rate for the four different values of ν. We show the maximum values of $\epsilon(t)$ against ν in log–log manner Fig. 6. Similarly we show the times of maximum $\epsilon(t)$ against ν in Fig. 7. By using least-squares fitting, we find

$$T_* = B\nu^{-\alpha}, \quad B \approx 1.3,\ \alpha \approx 0.23,$$

and

$$\epsilon_{\max} = A\nu^{\beta}, \quad A \approx 0.23,\ \beta \approx 0.37.$$

These suggest that

$$T_* \to \infty \quad \text{and} \quad \epsilon_{\max} \to 0 \quad \text{as } \nu \to 0.$$

(In Appendix B we compare it with the solution with Burgers's shear layer, which has an infinite amount of total energy.) They are not consistent with what is expected in the phenomenology of turbulence, where ϵ remains independent of ν in the limit.

In Fig. 8, we compare the energy spectrum $E(k)$ for the inviscid and viscous (with $\nu = 0.5 \times 10^{-3}$) cases at $t = 8$. The spectrum shows a short power-law range, whose exponent is around $-5/3$ and -2. It should be noted that the inviscid spectrum also exhibits a short power-law range, which is not markedly different from the Kolmogorov spectrum. However, we refrain from determining the slope in these cases because of the limited range.

In Fig. 9, we show a similar plot at $t = 10$. By plotting the spectrum, in a log-linear manner we have checked that the inviscid flow has a short exponential fall-off, with undulations presumably coming from interferences between vortex structures [9] (see Fig. 11). If we computed an Euler flow that long from general initial data, we would suffer from truncation errors, associated with a turn-up of the higher

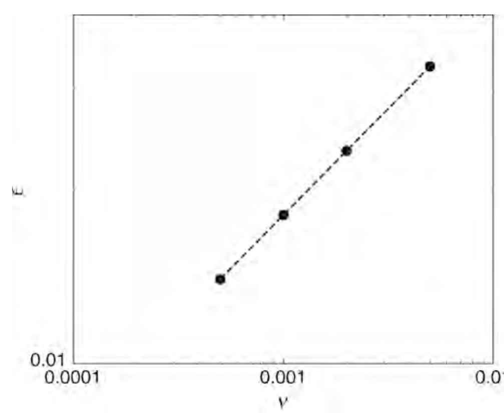

Fig. 6. Viscosity dependence of the maxima of $\epsilon(t)$. The dashed lines shows a least-squares fit, given in the text.

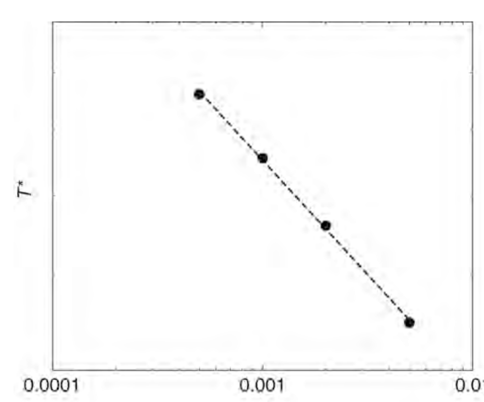

Fig. 7. Viscosity dependence of the times at which $\epsilon(t)$ is peaked. The dashed lines shows a least-squares fit, given in the text.

wavenumber end of the spectrum. In this flow, we see no sign of serious numerical inaccuracy at this stage. Actually, an equipartition part $E(k) \propto k^2$ begins to appear around $t = 14$, or later.

There is a mathematical result which compares an Euler flow with Navier–Stokes flows for a fixed initial condition [6]. If we fix time on a time interval of the regular Euler evolution, the

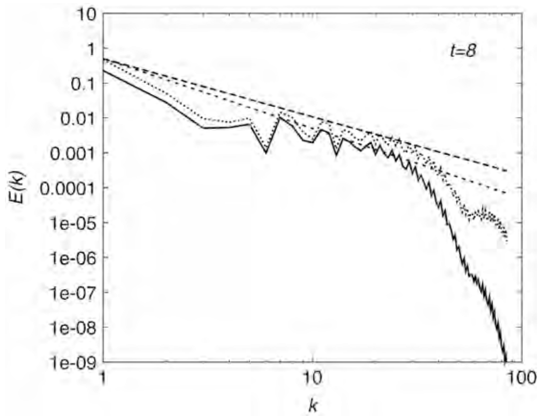

Fig. 8. Energy spectra at $t = 8$ for $\nu = 0.5 \times 10^{-3}$ (solid) and $\nu = 0$ (dotted). The straight lines have a slope of $-5/3$ (solid) and that of -2 (dashed).

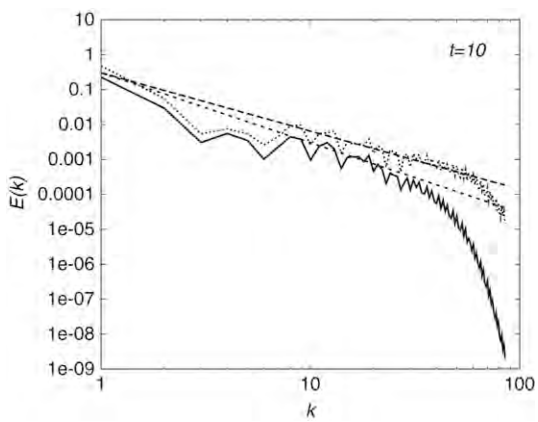

Fig. 9. Energy spectra at $t = 10$ for $\nu =; 0.5 \times 10^{-3}$ (solid) and $\nu = 0$ (dotted). The straight lines have a slope of $-5/3$ (solid) and that of -2 (dashed).

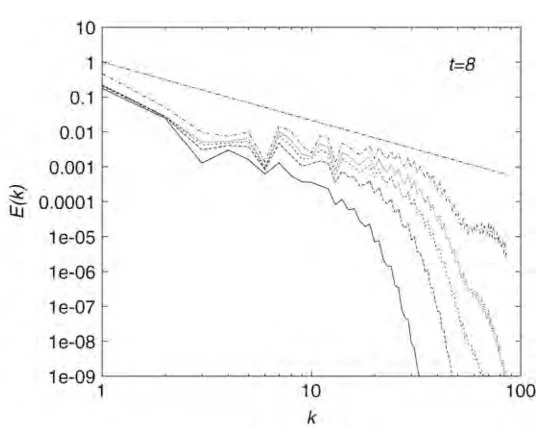

Fig. 10. Energy spectra at $t = 8$ for $\nu = 5.0,\ 2.0,\ 1.0,\ 0.5 \times 10^{-3}, 0$ (solid, dashed, short-dashed, dotted and dash-dotted). The straight line has a slope of $-5/3$.

difference between the Navier–Stokes and Euler flows can be made as small as we wish, by passing ν to zero.

In Fig. 10 we show the energy spectrum for the Euler case and the Navier–Stokes cases with four different values of viscosity. This appears to be consistent with the comparison theorem of [6], that is, for a fixed time t with a regular Euler

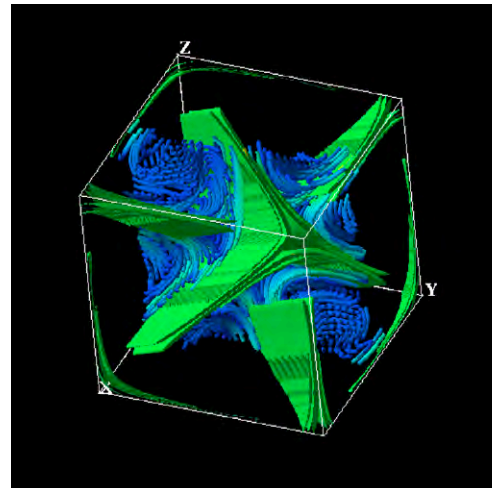

Fig. 11. Iso-surface of vorticity at $t = 8$ for $\nu = 0.5 \times 10^{-3}$ with a threshold $|\boldsymbol{\omega}(\mathbf{x})|^2 = 69.0$, together with vortex lines starting from a plane $x = \pi/2$.

evolution

$E_\nu(k) \to E_0(k)$ as $\nu \to 0$,

where $E_\nu(k)$ denotes an energy spectrum for the case of viscosity ν. However, this does not necessarily imply that $E_0(k) \propto k^{-n}$, even if $E_\nu(k) \propto k^{-n}$ with finite ν, because we are left in the very early stage of evolution $t \ll T_*(\nu)$ when we let $\nu \to 0$ for a fixed t. So, let us assume that $E_0(k) \propto k^{-m}$ for a fixed large t, then we expect its exponent to be shallower than n, that is m ($\leq n$), which is consistent with Fig. 10. We may think of the possible choices, for example, $(n, m) \approx (2, 2), (5/3, 5/3), (2, 5/3)$ but $(n, m) \approx (5/3, 2)$ should be ruled out. Computations at higher resolutions and/or a more sophisticated handling of data analyses (as in [9]) may determine the exponents more convincingly.

It is of interest to study vortical structure in physical space. By visualisations of iso-vorticity surfaces Fig. 11, it turned out that some groups of vorticity layers are situated surrounding the diagonal axis. Unlike usual flow configurations, these vortex layers appear to be stable and get away from being rolled up by Kelvin–Helmholtz instability. This explains at least partially why this flow has a weak energy transfer.

We may summarise the features of this simple flow as follows. It is possible to compute the Euler flow up to a time when the enstrophy of the corresponding Navier–Stokes flow reaches its maximum, that is, $t_* \approx T_*$.

For viscous cases $\nu > 0$, we find:

- a power-law behaviour in $E(k)$ after a maximum of $\epsilon(t)$,
- $T_* \to \infty$ as $\nu \to 0$,
- $\max \epsilon(t) \to 0$ as $\nu \to 0$.

For the inviscid case $\nu = 0$ we find:

- $\max |\boldsymbol{\omega}|$ shows an exponential growth,
- a power-law behaviour in $E(k)$, is observed (to be checked with higher resolution) [23].

If the flow is dominated by a single layer of vorticity, then we would have $E(k) \propto k^{-2}$. It is necessary to perform simulations at higher resolutions to determine the exponent more accurately.

This may serve as an example of a long-lived Euler flow sustaining a power-law spectrum.

7. Kida–Pelz high-symmetric flows

The initial velocity and vorticity of this flow for $(0 \le x, y, z < \pi/2)$ is given by

$$\mathbf{u} = \begin{pmatrix} \sin x(\cos 3y \sin z - \cos y \sin 3z) \\ \sin y(\cos 3z \sin x - \cos z \sin 3x) \\ \sin z(\cos 3x \sin y - \cos x \sin 3y) \end{pmatrix},$$

and

$$\boldsymbol{\omega} = \begin{pmatrix} -2\cos 3x \sin x \sin z + 3\cos x(\sin 3y \sin z + \sin y \sin 3z) \\ -2\cos 3y \sin y \sin x + 3\cos y(\sin 3z \sin x + \sin z \sin 3x) \\ -2\cos 3z \sin z \sin y + 3\cos z(\sin 3x \sin y + \sin x \sin 3y) \end{pmatrix}.$$

It can be checked that $\mathbf{u} \cdot \boldsymbol{\omega} \equiv 0$, so Frobenius's integrability condition is satisfied. We may choose Clebsch potentials for the flow in a closed form, for example, as

$$f = 2\frac{(\cos x)^{3/2}(\cos^2 y - \cos^2 z)}{(\cos y \cos x)^{1/2}},$$
$$g = 2\frac{(\cos y)^{3/2}(\cos^2 z - \cos^2 x)}{(\cos x \cos y)^{1/2}}$$

(details of their derivation are omitted here).

These potentials have singularities at $x = \pi/2$ or $y = \pi/2$. They are unphysical, but they cause difficulties in numerical computations. We need a workaround against apparent singularities in Clebsch potentials to study their behaviour numerically.

We note that Clebsch potentials found for the Taylor–Green vortex have also (milder) singularities [10]:

$$f = \sqrt{2}\cos x\sqrt{|\cos z|}, \qquad g = \sqrt{2}\cos y\sqrt{|\cos z|}\ \mathrm{sgn}(\cos z).$$

They are only in C^0, that is, continuous but non-differentiable on a line $x = \pi/2$.

Presence or absence of such apparent singularities is irrelevant to the tame behaviour observed in the previous section, because we may find flows with reasonable strong energy transfer with smooth Clebsch potentials.

8. Summary and outlook

We have introduced yet another depletion mechanism, that is, colinearity of ∇f and ∇g which may lead to a mild exponential growth in vorticity. We have identified longevity of an inviscid flow with mild energy transfer, thereby demonstrating the coexistence of smooth Euler evolution with a power-law scaling for the slightly viscous case. Thus, as far as this flow is concerned, the most important physical motivation for suspecting singularity has been lost.

We conjecture that the Euler flow starting from the initial condition (5) remains regular all time and that the corresponding Navier–Stokes flows with small but finite viscosity exhibit a power-law energy spectrum. Some comments may be in order regarding the features of this flow. (i) On the relationship between inviscid and inviscid-limit behaviours: if the flow remains regular all time, the comparison theorem [6] should hold any time. The result in Fig. 10. is consistent with this. (ii) The depletion mechanism introduced and discussed in Sections 4 and 5 leads to the tame behaviour. The mechanism is valid for other flows with Clebsch potentials, e.g. the Kida–Pelz vortex (not shown here). It might be useful for characterising and analysing depletion in more details for such flows.

Some of the questions which should be pursued are as follows:

- To check whether inviscid and/or viscous solutions yield $E(k) \propto k^{-n}$, or not $(n \approx 5/3 - 2)$.
- Are solutions which hesitate to roll up (with weak energy transfer) sporadic ?
- What are the implications for more general flows with non-vanishing $\epsilon(t)$ with stronger energy transfer?

This special flow is in a class of flows with Clebsch potentials, which is a small subset of general incompressible flows. We do not know if it is necessary for a flow to be have Clebsch potentials to get stable vortices with weak energy transfer. (We do know that it is not sufficient, because Taylor–Green and Kida–Pelz vortices are counter-examples.)

This flow is quite special and does not represent general features we expect for turbulence. But it is important to discern how different it is from the rest of the general incompressible flows. At least, the following two cases should be distinguished.

(A) All Euler flows remain regular for all time. The difference between this example and more general flows is only quantitative, in that generically vorticity growth in time maybe double exponential, triple exponential, and so on. Global regularity may trivialise Onsager's approach, as we do not know how the Euler equations can characterise developed turbulence.

(B) Some Euler flows remain regular for all time, but others do not, that is, the latter flows go singular in finite time. The difference is qualitative. Onsager conjecture may work literally.

For those people who believe in singularities in the Euler flows, this might appear as an exceptional case of severe depletion. Indeed, the flow we have described may be just one example of the minority in the case (B). It is a rare case of stable vorticity layers with non-trivial vorticity growth. Albeit the evidence heavily depends on numerics, it should be kept in mind that there is at least one flow with finite total energy, which displays such a tame behaviour.

Note

After this numerical work has been completed, it was pointed out to the author by M. Bustamante and E. Titi (private communication) and by an anonymous referee that the flow may be reduced to an essentially 2D system, known as 2.5D flow in [19]. (Equivalently, a class of flows described in p.674 of [20].) On this basis the flow may be proved to remain regular all time. Given that, it may be regarded as an example of 2.5D flows which can be also described by Clebsch potentials. It offers an opportunity to study geometric depletion mechanism, such as the one briefly described here, in detail numerically and theoretically.

Acknowledgments

The author would like to express his cordial thanks to the organisers of the conference, particularly U. Frisch for providing the author with a chance to present this work. The author has been supported by the Royal Society Wolfson Research Merit Award. This work has been partially supported by EPSRC EP/F009267/1. I would like to thank M. Bustamante, S. Childress, D. Dritschel, G. Eyink, A. Gorban, R.M. Kerr, S. Kida, T. Matsumoto, H.K. Moffatt, S. Nazarenko, S. Petrovskiy, C. Tran and C. Vassilicos for the helpful discussions. Part of the simulations have been done on the computing facility at the Research Institute for Mathematical Sciences, Kyoto University.

Appendix A. Clebsch's papers

In 1850s Clebsch published at least two important papers [11,12] in which he developed variational formulations for fluid mechanics. A brief but nice account of these papers may be found in [13]. Note that between these papers, Helmholtz's seminal paper [14] on vortex dynamics appeared in the same Crelle journal.

In [11], a variational principle for stationary case was established. He started off from n-dimensional Euler equations

$$\frac{\partial u_1}{\partial t}+u_1\frac{\partial u_1}{\partial x_1}+u_2\frac{\partial u_1}{\partial x_2}+\cdots+u_n\frac{\partial u_1}{\partial x_n}=-\frac{\partial p}{\partial x_1}, \text{etc} \tag{A.1}$$

with the incompressibility condition

$$\frac{\partial u_1}{\partial x_1}+\frac{\partial u_2}{\partial x_2}+\cdots+\frac{\partial u_n}{\partial x_n}=0. \tag{A.2}$$

He introduced a method of, what may be called *generalised stream functions (or, vector potentials)*. Consider n functions $a_0(x_1,\dots,x_n),\dots,a_{n-1}(x_1,\dots,x_n)$ and form a Jacobian determinant of the form

$$R=\begin{vmatrix} \frac{\partial a_0}{\partial x_1} & \frac{\partial a_0}{\partial x_2} & \cdots & \frac{\partial a_0}{\partial x_n}\\ \frac{\partial a_1}{\partial x_1} & \frac{\partial a_1}{\partial x_2} & \cdots & \frac{\partial a_1}{\partial x_n}\\ \vdots & \vdots & \vdots & \vdots\\ \frac{\partial a_{n-1}}{\partial x_1} & \frac{\partial a_{n-1}}{\partial x_2} & \cdots & \frac{\partial a_{n-1}}{\partial x_n}\end{vmatrix}. \tag{A.3}$$

Expanding it along the first row, we find

$$R=\Delta_1\frac{\partial a_0}{\partial x_1}+\Delta_2\frac{\partial a_0}{\partial x_2}+\cdots+\Delta_n\frac{\partial a_0}{\partial x_n}, \tag{A.4}$$

where Δ_i's are minors. By a theorem of Jacobi, we have

$$\frac{\partial \Delta_1}{\partial x_1}+\frac{\partial \Delta_2}{\partial x_2}+\cdots+\frac{\partial \Delta_n}{\partial x_n}=0. \tag{A.5}$$

On this basis we may identify each minor as a component of an incompressible velocity field

$$\Delta_i=\Delta_i(a_1,a_2,\dots,a_{n-1})\to u_i. \tag{A.6}$$

It should be noted that Δ lies on a hyper-plane $\Pi(a_1,a_2,\dots,a_{n-1})=\text{const}$. Using it, he recast the Euler equations as

$$\frac{\partial \Delta_1}{\partial t}+A_1\frac{\partial a_1}{\partial x_1}+A_2\frac{\partial a_2}{\partial x_1}+\cdots+A_{n-1}\frac{\partial a_{n-1}}{\partial x_1} =-\frac{\partial}{\partial x_1}\left(p+\frac{|\mathbf{u}|^2}{2}\right), \tag{A.7}$$

where

$$A_1\equiv\frac{\partial \Pi}{\partial a_1},\ A_2\equiv\frac{\partial \Pi}{\partial a_2},\dots,\ A_{n-1}\equiv\frac{\partial \Pi}{\partial a_{n-1}}. \tag{A.8}$$

By restricting to a stationary case, he found

$$-\left(p+\frac{|\mathbf{u}|^2}{2}\right)=\Pi(a_1,a_2,\dots,a_{n-1}). \tag{A.9}$$

For example, in the case $n=3$ we have [24]

$$\mathbf{u}=\nabla a_1\times\nabla a_2=\nabla\times(a_1\nabla a_2). \tag{A.10}$$

In particular, if we take $a_1=\psi(x_1,x_2), a_2=x_3$, it reduces to the case in two dimensions,

$$\frac{\mathrm{d}}{\mathrm{d}\psi}\left(p+\frac{|\mathbf{u}|^2}{2}\right)=-\omega,\quad \omega=\omega(\psi). \tag{A.11}$$

In the second paper [12], a variational principle for non-stationary case was treated. He started from $(2n+1)$-dimensional Euler equations [25]

$$\frac{\partial u_0}{\partial t}+u_0\frac{\partial u_0}{\partial x_0}+u_1\frac{\partial u_0}{\partial x_1}+\cdots+u_{2n}\frac{\partial u_0}{\partial x_{2n}}=-\frac{\partial p}{\partial x_0}, \quad \text{etc.} \tag{A.12}$$

and

$$\frac{\partial u_0}{\partial x_0}+\frac{\partial u_1}{\partial x_1}+\cdots+\frac{\partial u_{2n}}{\partial x_{2n}}=0 \tag{A.13}$$

and introduced the following form [26]

$$u_k=\frac{\partial \phi_0}{\partial x_k}+m_1\frac{\partial \phi_1}{\partial x_k}+\cdots+m_n\frac{\partial \phi_n}{\partial x_k}. \tag{A.14}$$

He then derived a famous transformation which bears his name

$$\delta\Pi\equiv-\delta\left(p+\frac{|\mathbf{u}|^2}{2}+\frac{\partial\phi}{\partial t}+m_j\frac{\partial\phi_j}{\partial t}\right) \tag{A.15}$$

$$=\frac{\mathrm{D}m_j}{\mathrm{D}t}\delta\phi_j-\frac{\mathrm{D}\phi_j}{\mathrm{D}t}\delta m_j, \tag{A.16}$$

from which a canonical form of equations are derived

$$\frac{\mathrm{D}m_j}{\mathrm{D}t}=\frac{\delta\Pi}{\delta\phi_j},\qquad \frac{\mathrm{D}\phi_j}{\mathrm{D}t}=-\frac{\delta\Pi}{\delta m_j}. \tag{A.17}$$

See, for example, [15–18] for more about Clebsch potentials.

Appendix B. Burgers shear layer

An example with exponentially increasing vorticity is given by a well-known Burgers layer for an inviscid fluid [21], whose velocity and vorticity read $\mathbf{v} = (u(y,t), -\gamma y, \gamma z)$, $\boldsymbol{\omega} = (0, 0, -\partial_y u)$, where $\gamma (> 0)$ is a constant strain rate. Its vorticity equation

$$\frac{\partial \omega}{\partial t} - \gamma y \frac{\partial \omega}{\partial y} = \gamma \omega$$

is reduced to

$$\frac{\partial \Omega}{\partial T} = 0$$

by $\Omega = \mathrm{e}^{-\gamma t}\omega$, $Y = \mathrm{e}^{\gamma t} y$. Thus we have

$$\omega(y,t) = \mathrm{e}^{\gamma t}\omega_0(\mathrm{e}^{\gamma t} y).$$

It should be noted that this is *not* in L^2 (that is, has infinite energy) unlike the flow presented in this paper. It may be of interest to recall that its volume averaged energy dissipation scales as $\epsilon \propto \sqrt{\nu}$ for a viscous fluid.

References

[1] G.L Eyink, title unknown, these Proceedings.
[2] M.E. Brachet, D.I. Meiron, S.A. Orszag, B.G. Nickel, R.H. Morf, U. Frisch, Small-scale structure of the Taylor–Green vortex, J. Fluid Mech. 130 (1983) 411–452.
[3] O.N. Boratav, R.B. Pelz, Direct numerical simulation of transition to turbulence from a high-symmetry initial condition, Phys. Fluids 6 (1994) 2757–2784.
[4] J.T. Beale, T. Kato, A. Majda, Remarks on the breakdown of smooth solutions for the 3D Euler equations, Comm. Math. Phys. 94 (1984) 61–66.
[5] P. Constantin, An Eulerian–Lagrangian approach for incompressible fluids: Local theory, J. Amer. Math. Soc. 14 (2001) 263–278.
[6] P. Constantin, Note on loss of regularity for solutions of the 3-D incompressible and related equations, Comm. Math. Phys. 104 (1986) 311–326.
[7] C. Cichowlas, P. Bonaiti, F. Debbasch, M. Brachet, Effective dissipation and turbulence in spectrally truncated Euler flows, Phys. Rev. Lett. 95 (2005) 264502.
[8] C. Connaughton, S. Nazarenko, Warm cascades and anomalous scaling in a diffusion model of turbulence, Phys. Rev. Lett. 92 (2004) 044501.
[9] C. Cichowlas, M.-E. Brachet, Evolution of complex singularities in Kida–Pelz and Taylor–Green inviscid flows, Fluid Dyn. Res. 36 (2005) 239–248.
[10] C. Nore, M. Abid, M.E. Brachet, Decaying Kolmogorov turbulence in a model of superflow, Phys. Fluids 9 (1997) 2644–2669.
[11] A. Clebsch, Uber eine allgemeine Transformation der hydrodynamischen Gleichungen, J. Reine Angew. Math. 54 (1857) 293–313 (in German).
[12] A. Clebsch, Uber die Integration der hydrodynamischen Gleichungen, J. Reine Angew. Math. 56 (1859) 1–10 (in German).
[13] W.M. Hicks, Report on Recent Progress in Hydrodynamics—Part I, British Association, 1881.
[14] H. Helmholtz, Uber integrale der hydrodynamischen Gleichungen, welche den wirbelbewegungen entsprechen, J. Reine Angew. Math. 55 (1858) 25–55 (in German).
[15] P. Duhem, Sur les équations de h'hydrodynamique. Commentaire a un mémoire de Clebsch, Ann. Fac. Sci. Univ. Toulouse 3 (1901) 253–279 (in French).
[16] J. Serrin, Mathematical principles of classical fluid mechanics, in: S. Flügge, C. Truesdell (Eds.), Handbuch der Physik, Springer, Berlin, 1959, pp. 125–263.
[17] T.B Benjamin, Impulse, flow force and variational principles, IMA J. Appl. Math. 32 (1984) 3–68.
[18] T. Kambe, Gauge principle and variational formulation for ideal fluids with reference to translational symmetry, Fluid Dyn. Res. 39 (2007) 98–120.
[19] D. Montgomery, L. Turner, Two-and-a-half-dimensional magnetohydrodynamic turbulence, Phys. Fluids 25 (1982) 345–349.
[20] R.J. Diperna, A.J. Majda, Oscillations and concentrations in weak solutions of the incompressible fluid equations, Comm. Math. Phys. 108 (1987) 667–689.
[21] J.M. Burgers, A mathematical model illustrating the theory of turbulence, Adv. Appl. Mech. 1 (1948) 171–199.
[22] This expression is naive as it involves dual limits; small viscosity and large time, which are not interchangeable in general. We will be more specific, where necessary.
[23] The property of this flow should not be confused with 'warm cascade' in which turbulence coexists with a heat bath ($E(k) \propto k^2$ at a higher end of wavenumber) [7,8].
[24] This means that the vector potential has Clebsch potentials $\mathbf{A} = a_1 \nabla a_2 + \nabla \psi$.
[25] For n pairs of Clebsch potentials plus a solenoidal projector.
[26] For such a expression to be valid globally, we need a Frobenius condition of integrability. Thus, actually it restricts us to a very special class of flows.

Available online at www.sciencedirect.com
ScienceDirect
Physica D 237 (2008) 2028–2036
PHYSICA D
www.elsevier.com/locate/physd

From Boltzmann's kinetic theory to Euler's equations

Laure Saint-Raymond*

Département de Mathématiques et Applications, Ecole Normale Supérieure, 45 rue d'Ulm, 75005 Paris, France

Available online 14 December 2007

Abstract

The incompressible Euler equations are obtained as a weak asymptotics of the Boltzmann equation in the fast relaxation limit (the Knudsen number Kn goes to zero), when both the Mach number Ma (defined as the ratio between the bulk velocity and the speed of sound) and the inverse Reynolds number Kn/Ma (which measures the viscosity of the fluid) go to zero.

The entropy method used here consists in deriving some stability inequality which allows us to compare the sequence of solutions of the scaled Boltzmann equation to its expected limit (provided that it is sufficiently smooth). It thus leads to some strong convergence result.

One of the main points to be understood is how to deal with the corrections to the weak limit, i.e. the contributions converging weakly but not strongly to 0 such as the initial layer or the acoustic waves.

PACS: 47.10.A; 47.15.ki

Keywords: Kinetic theory; Hydrodynamic limits; Incompressible Euler equations; Entropy method

The topic of this paper is to discuss the connections between the various models describing the motion of fluids. Actually there is a number of ways to describe that motion, depending on the space and time scales we consider (see Fig. 1).

At the atomic level, the fluid is a large *system of particles* interacting according to repulsive forces. We therefore have a complex system of coupled ordinary differential equations, for which essentially no qualitative behavior can be predicted. However, in general, we are not interested in the exact positions and velocities of all particles, so that a statistical approach is suitable. This is precisely the point of view of *kinetic theory*. Note however that it can be applied only for rarefied gases (in the sense that the size of particles has to be small compared to the mean free path). Now, if we consider typical length scales which are large compared with the mean free path, the collision process is dominating, and local thermodynamic equilibrium is reached almost instantaneously everywhere. The state of the fluid can therefore be described by macroscopic variables such as the pressure, density, and bulk velocity, which are governed by some *hydrodynamic equations*. Considering still larger time and space scales, it should be possible to deal again statistically with the nonlinearity, which should lead to *turbulence models*.

A natural question is therefore to understand the connections between the different levels of modeling, and to get a unified theory of fluids, which is part of the sixth problem proposed by Hilbert on the occasion of the International Congress of Mathematicians held at Paris in 1900 [14]. In the present paper, we will actually focus on the transition from kinetic theory to hydrodynamics, and more precisely from the Boltzmann equation to the incompressible Euler equations. Let us just mention that the derivation of the Boltzmann equation from Newtonian mechanics has been justified by Lanford for short times [17], whereas to our knowledge there is no such rigorous study for the transition from determinist hydrodynamics to turbulence (see [16] for a formal derivation, and [8] for an attempted mathematical approach). Let us also mention the contributions in statistical physics which study directly the transition between stochastic systems of particles and hydrodynamics (see [20] for instance). Actually such direct connections are compulsory to derive real constitutive equations (other than the law of perfect gases).

1. The formal derivation

Our first objective is to explain the formal expansions leading to the incompressible Euler limit. Note that it has

* Tel.: +33 1 44 32 20 36.
E-mail address: Laure.Saint-Raymond@ens.fr.

0167-2789/$ - see front matter © 2007 Elsevier B.V. All rights reserved.
doi:10.1016/j.physd.2007.11.023

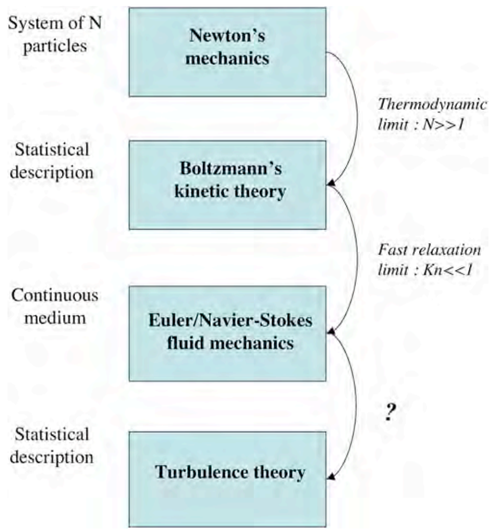

Fig. 1. Description of fluids.

been only recently observed ([1] for time-independent problems and [2,6] for time-dependent problems) that, under convenient scaling, incompressible equations could be directly derived from the Boltzmann equation.

1.1. The Boltzmann equation

Our starting point is the non-dimensional Boltzmann equation, which expresses some balance between the free transport of particles (left-hand side) and the collision process (right-hand side):

$$Ma\partial_t f + v\cdot\nabla_x f = \frac{1}{Kn}Q(f,f) \tag{1}$$

where Ma denotes the Mach number (measuring the compressibility of the fluid) and Kn is the Knudsen number, defined as the ratio between the mean free path and the observation length scale. The operator Q is localized in t and x, and describes elastic binary collisions. Its precise formulation is rather complicated

$$Q(f,f)(v) = \int_{\mathbf{R}^3}\int_{S^2}\left(f(v')f(v_1') - f(v)f(v_1)\right)b\mathrm{d}v_1\mathrm{d}\omega, \tag{2}$$

$$v' = v + (v-v_1)\cdot\omega\omega, \qquad v_1' = v_1 - (v-v_1)\cdot\omega\omega \tag{3}$$

for some nonnegative function $b \equiv b(v - v_1, \omega)$, called the cross-section, giving the statistical repartition of pre-collisional velocities (v', v_1') leading to (v, v_1). This exact formulation will not be useful in what follows of our presentation. What is needed is the physics encoded in this mathematical operator.

As collisions are assumed to be elastic, Q has some symmetry properties leading to the following identities

$$\int Q(f,f)(v)\mathrm{d}v = \int Q(f,f)v_i\mathrm{d}v$$
$$= \int Q(f,f)|v|^2\mathrm{d}v = 0. \tag{4}$$

In particular, integrating the kinetic Eq. (1) against 1, v and $\frac{1}{2}|v|^2$, we recover the local conservations of mass, momentum and energy, or in other words the **first principle of thermodynamics**.

Using the same symmetries, we also obtain

$$D(f) \stackrel{\text{def}}{=} -\int Q(f,f)\ln f(v)\mathrm{d}v \geq 0 \tag{5}$$

and thus the local decay of entropy (note that the mathematical entropy is the opposite of the physical entropy!):

$$Ma\partial_t\int f\ln f\mathrm{d}v + \nabla_x\cdot\int f\ln f(v)v\mathrm{d}v \leq 0. \tag{6}$$

We therefore obtain a Lyapunov functional for the Boltzmann equation, which expresses the irreversibility predicted by the *second principle of thermodynamics*.

Collisions are responsible for that relaxation process. Each elementary process loses some information on the precise microscopic configuration that is realized, so that the global effect of collisions is to increase the uncertainty. The asymptotic distribution, which minimizes the entropy, and cancels the entropy dissipation

$$\int Q(f,f)\ln f(v)\mathrm{d}v = 0 \Leftrightarrow \forall v\in\mathbf{R}^3,\quad Q(f,f)(v) = 0,$$

is the Gaussian having the same mass $R = \int f\mathrm{d}v$, momentum $RU = \int fv\mathrm{d}v$ and energy $\frac{1}{2}R(U^2+3\Theta) = \frac{1}{2}\int f|v|^2\mathrm{d}v$. In other words, the thermodynamic equilibrium obeys *Maxwell's statistics*.

1.2. The incompressible inviscid regime

In the fast relaxation limit, i.e. when the Knudsen number Kn – defined as the ratio between the mean free path and the typical length scale – tends to zero, we thus expect the gas to be at local thermodynamic equilibrium. The distribution f is therefore completely determined by the macroscopic quantities $R = R(t,x)$, $U = U(t,x)$ and $\Theta = \Theta(t,x)$.

Let us first recall that, at leading order with respect to the Knudsen number Kn, the hydrodynamic equations, obtained from the local conservation laws replacing f by the corresponding local Maxwellian

$$\mathcal{M}_{R,U,\Theta} \sim \frac{R(t,x)}{(2\pi\Theta(tx,x))^{3/2}}\exp\left(-\frac{|v-U(t,x)|^2}{2\Theta(t,x)}\right),$$

are, up to terms of order $O(Kn)$,

$$\begin{aligned}
&Ma\partial_t R + \nabla_x\cdot(RU) = 0,\\
&Ma\partial_t(RU) + \nabla_x\cdot(RU\otimes U + R\Theta Id) = 0,\\
&Ma\partial_t\left(\frac{1}{2}RU^2 + \frac{3}{2}R\Theta\right) + \nabla_x\cdot\left(\frac{1}{2}RU^2U + \frac{5}{2}R\Theta U\right) = 0,
\end{aligned} \tag{7}$$

known as the compressible Euler system for perfect gases.

Of course such an asymptotics does not remain relevant if the Mach number Ma also goes to zero in the regime to be considered. The Mach number Ma – defined as the ratio between the bulk velocity of the fluid and the speed of sound – measures indeed the compressibility of the fluid: if $Ma \to 0$ the first equation in (7) is nothing else than the incompressibility constraint $\nabla \cdot (RU) = 0$. The equations of motion are then obtained by a systematic multiscale expansion. Their precise formulation depends further on another important feature of the fluid, namely on its viscosity, which is measured by the Reynolds number Re.

Note that, for perfect gases (i.e. for all gases which can be described by Boltzmann's equation), Von Karmann's relation states

$$Re = \frac{Ma}{Kn}$$

so that all features of the fluid are completely determined by the two non-dimensional parameters Ma and Kn (see [1] for more details).

1.3. *Taking limits as $\varepsilon \to 0$*

In all what follows we are interested in the regimes leading to the incompressible Euler equations. We will thus choose

$$Ma = \varepsilon \to 0,$$

meaning in particular that $U/\sqrt{\Theta} = O(\varepsilon)$, and

$$Kn = \varepsilon^q \quad \text{with } q > 1$$

in order that the Reynolds number $Ma/Kn = \varepsilon^{1-q}$ tends to infinity.

We will further restrict our attention to the homogeneous case, in the sense that the density R and temperature Θ will be assumed to be fluctuations of order ε around their equilibrium values, say without loss of generality around 1. Denoting by ρ, u and θ the fluctuations of mass, momentum and temperature, and plugging the expansions

$$R = 1 + \varepsilon\rho, \qquad U = \varepsilon u, \qquad \Theta = 1 + \varepsilon\theta,$$

in the previous hydrodynamic equation (7), we get at leading order with respect to ε

$$\begin{aligned} &\nabla \cdot u = 0, \\ &\nabla(\rho + \theta) = 0, \end{aligned} \tag{8}$$

which are the macroscopic constraints (incompressibility and Boussinesq relations), then at second order the equations of motion

$$\begin{aligned} &\partial_t u + (u \cdot \nabla_x) u + \nabla p = 0, \\ &\partial_t \theta + \nabla_x \cdot (\theta u) = 0. \end{aligned} \tag{9}$$

where p is the pressure, defined as the Lagrange multiplier associated with the incompressibility constraint $\nabla \cdot u = 0$.

Dealing with the more general case when R and Θ have variations of order 1 is not really more difficult from a formal point of view. We actually get the following asymptotics

$$\begin{aligned} &\nabla(R\Theta) = 0, \\ &\nabla \cdot u = 0, \end{aligned}$$

and

$$\begin{aligned} &\partial_t R + \nabla_x \cdot (Ru) = 0, \\ &\partial_t u + (u \cdot \nabla_x) u + \frac{1}{R} \nabla p = 0. \end{aligned}$$

The point is that the asymptotic analysis would require to control quantities of different sizes (namely $R = O(1)$, $\Theta = O(1)$ and $U = O(\varepsilon)$), and thus to introduce new mathematical tools.

Obtaining full proofs valid in all physical configurations is a major problem due in particular to our limited knowledge concerning the solutions of the 3D Euler equations.

The main difficulty encountered when trying to justify the previous asymptotic process is to determine the limits of nonlinear terms. Indeed the weak compactness inherited from the physical a priori bounds provides some weak convergence, or in other words some convergence in average. In particular, it is not sufficient to study nonlinear terms as shown for instance by the following example

$$\begin{aligned} &\sin\left(\frac{t}{\varepsilon}\right) \rightharpoonup 0, \\ &\left(\sin\left(\frac{t}{\varepsilon}\right)\right)^2 = \frac{1}{2}\left(1 - \cos\left(\frac{2t}{\varepsilon}\right)\right) \rightharpoonup \frac{1}{2}. \end{aligned}$$

From a physical point of view such a phenomenon can be interpreted in terms of interferences. The question is to decide whether or not high frequency waves bring some contribution to low frequency modes.

In order to get a rigorous derivation of the incompressible Euler equations, we will therefore use a stronger notion of convergence.

2. The modulated entropy method

The main idea behind energy and entropy methods is to compare – in some appropriate metrics – the distribution under consideration (for instance the solution to the scaled Boltzmann equation) and its formal asymptotics (here the Gaussian $\mathcal{M}_{1+\varepsilon\rho,\varepsilon u,1+\varepsilon\theta}$ with ρ, u, θ satisfying the homogeneous incompressible Euler equation (8) and (9). Note that such a method requires to describe precisely the asymptotic distribution since the remainder has to converge strongly to zero.

The **first step** is to determine a suitable *functional measuring the stability* of the original system. The convenient quantity here is the scaled relative entropy

$$\frac{1}{\varepsilon^2} H(f_\varepsilon | \mathcal{M}) = \frac{1}{\varepsilon^2} \iint \left(f_\varepsilon \log \frac{f_\varepsilon}{\mathcal{M}} - f_\varepsilon + \mathcal{M} \right) \mathrm{d}v \mathrm{d}x,$$

where $\mathcal{M}$ denotes the centered reduced Gaussian $\mathcal{M} = \mathcal{M}_{1,0,1}$. By Boltzmann's H theorem (6), the relative entropy is indeed a Lyapunov functional for the Boltzmann equation (1). Furthermore it controls the size of the fluctuation

$$\frac{1}{\varepsilon^2} H(f_\varepsilon | \mathcal{M}) \geq 2 \iint \left(\frac{\sqrt{f_\varepsilon} - \sqrt{\mathcal{M}}}{\varepsilon} \right)^2 \mathrm{d}v \mathrm{d}x. \tag{10}$$

The idea of using the relative entropy for this type of asymptotic study goes back to Yau [25] in the framework of the Ginzburg–Landau equation, then to Bardos, Golse and Levermore for the Boltzmann equation [3].

The **second step** is to obtain a *precise approximate solution* f_{app} using some formal analysis. For hydrodynamic limits, the main term of the approximation is given by some asymptotic expansions due to Hilbert [15] in the inviscid case, and to Chapman and Enskog [4] in the viscous case.

Correcting terms are either terms of higher order in the expansion, or terms having rapid variations with respect to time or space variables and thus having no contribution to the mean flow. These fast variations can be oscillations which can be recovered by filtering methods (introduced independently by Schochet [24] and Grenier [11]), or localized phenomena such as boundary and initial layers which require a multiscale treatment (see [5] or [12] for instance).

These correctors depend of course on the scaling to be considered. For instance, in the regime leading to the incompressible Euler equations, and in a spatial domain Ω without boundary, they come both from the acoustic waves (fast oscillating) and from the relaxation layer (rapidly decaying).

The **last step** is to establish some *stability inequality* for the modulated entropy

$$\frac{1}{\varepsilon^2}H(f_\varepsilon|f_{\text{app}}) = \frac{1}{\varepsilon^2}\iint \left(f_\varepsilon \log\frac{f_\varepsilon}{f_{\text{app}}} - f_\varepsilon + f_{\text{app}}\right)\mathrm{d}v\mathrm{d}x.$$

which is the natural quantity to compare the distribution f_ε and its formal asymptotics f_{app} in view of the first step above. The expected convergence result arises then as a direct consequence of that stability inequality provided that the family of initial data converges in the appropriate sense.

Note that this last step contains all the mathematical contribution in the proof of convergence. It uses technical computations and estimates, which depend strongly on the properties of the solutions to the scaled Boltzmann equation, and thus require a deep understanding both of the transport and collision processes.

3. Main results

At the present time the mathematical theory of the Boltzmann equation is not really complete, insofar as there is no global existence and uniqueness result for general initial data with finite mass, energy and entropy. The main difficulty comes from the fact that the nonlinearity is quadratic whereas the functional space determined by the physical a priori estimates is roughly speaking the Orlicz space $L\log L$. In particular, for such functions, the collision term does not even make sense.

We have therefore at our disposal either strong solutions with higher regularity which require smoothness and smallness assumptions on the initial data, or very weak solutions, called renormalized solutions, which are not known to satisfy the kinetic equation in the sense of distributions but verify a family of formally equivalent equations obtained by some truncation process. These renormalized solutions, built by DiPerna and Lions [7], exist globally in time without restriction on the size of the initial data but are not known to be unique, nor to satisfy the local conservations of momentum and energy. Note however that they coincide with the unique classical solution whenever the latter does exist.

Let us then state our main convergence result first in the setting of renormalized solutions, which is the most general framework, then in the setting of classical solutions, for which the asymptotics can be described more precisely. For the sake of simplicity, we restrict our attention to spatial domains Ω without boundary namely the whole space $\mathbf{R}^3$ or the three-dimensional torus $\mathbf{T}^3$. In the regime we consider here, i.e. in the regime leading to the incompressible Euler equations, we then formally expect the approximate solutions to be decomposed as the sum of

- a purely kinetic part (determined by the relaxation process in the initial layer);
- a fast oscillating hydrodynamic part (governed by the acoustic equations);
- a non-oscillating hydrodynamic part (obtained by formal expansion) satisfying the incompressible Euler equations, supplemented by some suitable equation for the temperature.

3.1. In the framework of renormalized solutions

We start by precising a little bit the notion of renormalized solution:

Definition 1. A renormalized solution of the Boltzmann equation (1) is a function $f \in C(\mathbf{R}^+, L^1_{\text{loc}}(\Omega\times\mathbf{R}^3))$ which satisfies in the sense of distributions

$$\mathcal{M}\,(Ma\partial_t + v\cdot\nabla_x)\,\Gamma\left(\frac{f}{\mathcal{M}}\right) = \frac{1}{Kn}\Gamma'\left(\frac{f}{\mathcal{M}}\right)Q(f,f)$$

for any $\Gamma \in C^1(\mathbf{R}^+)$ such that $|\Gamma'(z)| \le C/\sqrt{1+z}$.

Let us then recall that the only requirement for renormalized solutions to exist globally in time is for instance that the initial relative entropy is finite (see [18]):

Proposition. *Assume that the collision cross-section b satisfies Grad's cutoff assumption* [10] *(which holds for instance if particles collide like hard spheres). Given any initial data f^{in} satisfying $H(f^{in}|\mathcal{M}) < +\infty$, there exists a renormalized solution f to the Boltzmann equation* (1) *with initial data f^{in}, satisfying further the entropy inequality*

$$H(f|\mathcal{M})(t) + \frac{1}{MaKn}\int_0^t\int_\Omega D(f)(s,x)\mathrm{d}s\mathrm{d}x \le H(f^{in}|\mathcal{M}).$$

Now if we consider some family of suitably scaled renormalized solutions to the Boltzmann equation, we are able to prove that it satisfies the expected asymptotics in the incompressible Euler limit provided that initial data are well prepared, i.e. in the case when the purely kinetic part, the fast oscillating hydrodynamic part and the non-oscillating part of both the density and temperature vanish asymptotically:

Theorem 1. *Let* (f_ε^{in}) *be a family of nonnegative functions of* $L^1_{\mathrm{loc}}(\Omega \times \mathbf{R}^3)$ *satisfying the scaling condition*

$$\frac{1}{\varepsilon^2} H(f_\varepsilon^{in}|\mathcal{M}) \le C_{in}, \tag{11}$$

and such that

$$\frac{1}{\varepsilon^2} H(f_\varepsilon^{in}|\mathcal{M}_{1,\varepsilon u^{in},1}) \to 0 \quad \text{as } \varepsilon \to 0, \tag{12}$$

for some given divergence-free smooth vector field u^{in}.

Let f_ε *be a family of renormalized solutions to the scaled Boltzmann equation*

$$\begin{aligned} &\varepsilon \partial_t f_\varepsilon + v \cdot \nabla_x f_\varepsilon = \frac{1}{\varepsilon^q} Q(f_\varepsilon, f_\varepsilon),\\ &f_\varepsilon(0,x,v) = f_\varepsilon^{in}(x,v), \end{aligned} \tag{13}$$

where $q > 1$, *meaning in particular that the ratio between the Knudsen number and the Mach number goes to 0.*

Then the family of fluctuations (g_ε) *defined by* $f_\varepsilon = \mathcal{M}(1 + \varepsilon g_\varepsilon)$ *converges (entropically) to* $g = u \cdot v$ *where* u *is the solution to the incompressible Euler equations*

$$\begin{aligned} &\partial_t u + u \cdot \nabla_x u + \nabla_x p = 0, \qquad \nabla_x \cdot u = 0 \quad \text{on } \mathbf{R}^+ \times \Omega,\\ &u(0,x) = u^{in}(x) \quad \text{on } \Omega, \end{aligned} \tag{14}$$

as long as the latter is Lipschitz continuous.

Note that (12) is a very strong assumption on the family of initial data, meaning that "well prepared" has to be understood as follows:

$$g_\varepsilon^{in} = u^{in} \cdot v + o(1)$$

in the sense of entropic convergence.

We thus require that the initial distribution has a *velocity profile* close to the local thermodynamic equilibrium

$$\rho^{in} + u^{in} \cdot v + \theta^{in} \frac{|v|^2 - 3}{2}$$

in order that there is no relaxation layer.

We further ask the asymptotic *initial thermodynamic fields* to satisfy the incompressibility and Boussinesq constraints

$$\nabla \cdot u^{in} = 0, \qquad \nabla(\rho^{in} + \theta^{in}) = 0,$$

which ensures that there is no acoustic wave. We also require that the initial temperature fluctuation (and thus mass fluctuation) is negligible

$$\rho^{in} = \theta^{in} = 0.$$

We therefore expect the temperature fluctuation to remain negligible.

We finally need some *spatial regularity* on the limiting bulk velocity, more precisely we require some Lipschitz continuity.

We are thus able to consider very general initial data (satisfying only the physical estimate (11)), but in the vicinity of a small set of asymptotic distributions.

A natural question is then to know whether or not it is possible to get rid of these restrictions on the asymptotic distribution. In the sketch of proof we will give in Section 4, we will see that the first two assumptions come from the poor understanding of the Boltzmann equation, in particular from the fact that renormalized solutions to the Boltzmann equation are not known to satisfy the local conservation of energy (the heat flux is not even defined), whereas the last assumption concerning the regularity of the limiting distribution is inherent to the modulated entropy method.

Considering solutions to the Boltzmann equation satisfying rigorously the basic physical properties, we expect to *control the energy flux* and extend the convergence result to take into account acoustic waves. In order to also deal with the relaxation layer, we further need to understand the *dissipation mechanism*, which will be done by slight modifications of the method.

On the contrary, relaxing the regularity assumption requires new ideas. The stability in energy and entropy methods is indeed controlled by the Lipschitz norm of the limiting field. In 3D, the incompressible Euler equations are not even known to have weak solutions, so that we do not expect to extend our convergence result for distributions with lower regularity. In return, in 2D, the mathematical theory of the incompressible Euler equations is much better understood and singular solutions such as vortex patches are known to exist globally in time. It should be then relevant to study the hydrodynamic limit of the Boltzmann equation in this setting. By analogy with the compressible Euler equations, we would expect the spatial discontinuities to dissipate entropy, or in other words to create layers where the distribution is far from local thermodynamic equilibrium. The difficulty should be to split the space–time domain according to these layers.

3.2. In the framework of classical solutions

The second result we will state here answers the previous question in the case of smooth limiting fields. Considering a stronger notion of solution for the Boltzmann equation (1), for instance using the classical solutions built by Guo [13], we can prove the convergence to the incompressible Euler equations for general initial data.

We indeed recall that nonlinear energy methods allow us to build global smooth solutions to the Boltzmann equation for smooth small data (see [13]):

Proposition. *Consider the collision cross-section* b *of hard spheres. Given any initial data* f^{in} *satisfying*

$$\left\| (1+|v|)^{1/2} D_x^s \left(\frac{f^{in} - \mathcal{M}}{\sqrt{\mathcal{M}}} \right) \right\|_{L^2(\Omega \times \mathbf{R}^3)} \le \delta \tag{15}$$

for $s \ge 4$ *and* δ *sufficiently small, there exists a unique classical solution* f *to the Boltzmann equation* (1) *with initial data* f^{in} *(such that the previous norm remains bounded for all time). In particular it satisfies the local conservation laws as well as the local entropy inequality.*

Note that, for our asymptotic study, the smallness and regularity assumption (15) is not really a restriction since it does not provide any uniform bound on the sequence of fluctuations

(g_ε^{in}). Actually we even do not need so much regularity. We will only require that the solutions of the Boltzmann equation to be considered satisfy the non-uniform nonlinear estimate

$$\frac{1}{\varepsilon^2}\int \mathcal{M}\left(\frac{f_\varepsilon-\mathcal{M}}{\mathcal{M}}\right)^2 \mathrm{d}v \le \frac{C}{\varepsilon^2} \quad \text{a.e. on } \mathbf{R}^+\times\Omega$$

(to be compared to (10)). The previous proposition just ensures that such solutions exist.

Theorem 2. *Let (f_ε^{in}) be a family of nonnegative functions of $L^1_{\mathrm{loc}}(\Omega\times\mathbf{R}^3)$ satisfying the scaling condition (11)*

$$\frac{1}{\varepsilon^2}H(f_\varepsilon^{in}|\mathcal{M}) \le C_{in}.$$

Let f_ε be some family of solutions to the scaled Boltzmann equation (13) with $q>1$, satisfying further

$$\int \mathcal{M}\left(\frac{f_\varepsilon-\mathcal{M}}{\mathcal{M}}\right)^2 \mathrm{d}v \le C \quad a.e. on\ \mathbf{R}^+\times\Omega. \tag{16}$$

Then, up to the extraction of a subsequence, the family of fluctuations (g_ε) defined by $f_\varepsilon=\mathcal{M}(1+\varepsilon g_\varepsilon)$ converges weakly to $u\cdot v+\frac{1}{2}\theta\left(|v|^2-5\right)$, where (u,θ) is the solution to the incompressible Euler equations

$$\begin{aligned}
&\partial_t u+u\cdot\nabla_x u+\nabla_x p=0, \qquad \nabla_x\cdot u=0 \quad on\ \mathbf{R}^+\times\Omega,\\
&\partial_t\theta+u\cdot\nabla_x\theta=0 \quad on\ \mathbf{R}^+\times\Omega\\
&u(0,x)=Pu^{in}(x), \qquad \theta(0,x)=\frac{1}{5}(3\theta^{in}-2\rho^{in}) \quad on\ \Omega,
\end{aligned} \tag{17}$$

as long as the latter is Lipschitz continuous.

Furthermore the difference $g_\varepsilon-g$ behaves asymptotically in $L^1_{\mathrm{loc}}(\mathrm{d}t\mathrm{d}x, L^1(\mathcal{M}\mathrm{d}v))$ as

$$g_{\mathrm{osc}}\left(\frac{t}{\varepsilon},x,v\right)=(\rho_{\mathrm{osc}},u_{\mathrm{osc}},\theta_{\mathrm{osc}})\left(\frac{t}{\varepsilon},x\right)\cdot\left(1,v,\frac{1}{2}(|v|^2-3)\right)$$

where $(\rho_{\mathrm{osc}},u_{\mathrm{osc}},\theta_{\mathrm{osc}})$ is the fast oscillating part of the solution of the acoustic system (21) stated in Section 5.

Note that the purely kinetic part does not appear in that convergence statement since its contribution to the L^1 norm is negligible. The entropic convergence we will establish is actually stronger.

4. Proof of Theorem 1

Theorem 1 has been established by the author [22], and results from different contributions we will present briefly.

The incompressible Euler limit of the Boltzmann equation has been first investigated by Golse in [9]. He proved the entropic convergence of scaled renormalized solutions for well-prepared data assuming further

(H1) the local conservation of momentum;
(H2) some uniform nonlinear a priori estimate on the fluctuation g_ε giving both a control for large v, and some equiintegrability with respect to x.

Assumption (H1) was removed by Lions and Masmoudi in [19]; their argument uses the local momentum conservation with matrix-valued defect measure satisfied by renormalized solutions of the Boltzmann equation. That this defect measure vanishes in the incompressible Euler limit follows from the strong convergence result to be proved. For the sake of simplicity we will not give the details of this argument below.

Assumption (H2) was removed by the author first in the framework of the BGK equation [21], then in the case of the original Boltzmann equation [22] using refined dissipation estimates. The argument is based on loop estimates instead of a priori estimates, and the conclusion follows from Gronwall's inequality.

4.1. The modulated entropy inequality

In order to establish the stability inequality leading to the entropic convergence stated in Theorem 1, the starting point is the derivation with respect to time of the modulated entropy. For the sake of simplicity, we will omit here the defect measure occurring both in the global entropy inequality and in the local conservation of momentum.

A simple computation based on the entropy inequality and on the local conservations of mass and momentum leads then by integration by parts to

$$\begin{aligned}
&\frac{1}{\varepsilon^2}H(f_\varepsilon|\mathcal{M}_{1,\varepsilon u,1})(t)+\frac{1}{\varepsilon^{q+3}}\int_0^t\int D(f_\varepsilon)(s,x)\mathrm{d}x\mathrm{d}s\\
&\quad\le \frac{1}{\varepsilon^2}H(f_\varepsilon^{in}|\mathcal{M}_{1,\varepsilon u^{in},1})\\
&\qquad+\frac{1}{\varepsilon}\int_0^t\int A(u)\cdot\int(\varepsilon u-v)f_\varepsilon(s,x,v)\mathrm{d}v\mathrm{d}x\mathrm{d}s\\
&\qquad-\frac{1}{\varepsilon^2}\int_0^t\int Du:\int(v-\varepsilon u)^{\otimes 2}f_\varepsilon(s,x,v)\mathrm{d}v\mathrm{d}x\mathrm{d}s
\end{aligned} \tag{18}$$

(note that we consider spatial domains without boundary), where the acceleration operator $A(u)$ is given by

$$A(u)=\partial_t u+u\cdot\nabla_x u.$$

Owing to the assumption on the initial data, the first term on the right-hand side will converge to 0 as $\varepsilon\to 0$.

The convergence of the second term will be given (up to the extraction of a subsequence) by the weak compactness on $\frac{1}{\varepsilon}(\sqrt{f_\varepsilon}-\sqrt{\mathcal{M}})$ (see (10)) coming from the uniform entropy bound.

The difficulty is thus to control the last term, referred to as the flux term. Actually we are not able to obtain directly some convergence. In such an inviscid regime, the entropy dissipation does not control the transport term $v\cdot\nabla_x g_\varepsilon$, and thus does not provide any additional regularity on the bulk velocity. This lack of strong compactness is also the reason why weak solutions to the 3D incompressible Euler equations are not known to exist.

4.2. Control of the flux term

The method consists then in introducing a suitable decomposition of the momentum flux, and estimating each term in that decomposition either by the modulated entropy, or by the entropy dissipation, to get

$$-\frac{1}{2\varepsilon^2}\int_0^t \iint \nabla_x u : \int (v-\varepsilon u)^{\otimes 2} f_\varepsilon(s,x,v)\mathrm{d}v\mathrm{d}x\mathrm{d}s$$
$$\leq \frac{C}{\varepsilon^2}\int_0^t \|Du\|_{L^2\cap L^\infty(\Omega)} H(f_\varepsilon|\mathcal{M}_{1,\varepsilon u,1})(s)\mathrm{d}s + o(1). \quad (19)$$

The main idea behind this result is that the local thermodynamic equilibrium $\mathcal{M}_{f_\varepsilon}$ is expected to give a good approximation of the distribution f_ε in the fast relaxation limit, at least if the moments remain bounded. Now, for Maxwellian distributions, the flux term can be computed explicitly in terms of the moments

$$\int (v-\varepsilon u)^{\otimes 2}\mathcal{M}_{f_\varepsilon}\mathrm{d}v$$
$$= (1+\varepsilon\rho_\varepsilon)\left(\varepsilon^2(u_\varepsilon-u)^{\otimes 2} + \frac{1+\varepsilon\theta_\varepsilon}{3} Id\right)$$

and estimated by the modulated entropy

$$\frac{1}{2}(1+\varepsilon\rho_\varepsilon)|u_\varepsilon-u|^2 \leq \frac{1}{\varepsilon^2}H(f_\varepsilon|\mathcal{M}_{1,\varepsilon u,1})$$

(the trace part of the matrix has no contribution since the test velocity field is divergence-free.)

The first difficulty to apply this strategy is to obtain a control on the relaxation to local Maxwellians. Indeed, in the case of the Boltzmann equation, the entropy production is not known to measure the distance between f_ε and $\mathcal{M}_{f_\varepsilon}$. We cannot give here the details of the argument which is rather technical. Let us just mention that the suitable decomposition looks like some linearized Chapman–Enskog's expansion:

$$g_\varepsilon = \Pi_\perp g_\varepsilon + \left(\rho_\varepsilon + u_\varepsilon\cdot v + \theta_\varepsilon\frac{|v|^2-3}{2}\right),$$
$$\rho_\varepsilon = \int \mathcal{M}g_\varepsilon \mathrm{d}v, \qquad u_\varepsilon = \int \mathcal{M}g_\varepsilon v\mathrm{d}v,$$
$$\theta_\varepsilon = \int \mathcal{M}g_\varepsilon\frac{|v|^2-3}{2}\mathrm{d}v,$$

where $\Pi_\perp$ denotes the orthogonal projection parallel to the kernel of the linearized collision operator. (Note that, as g_ε is not in L^2, we need to introduce some renormalized fluctuation). The first term is then controlled by the entropy dissipation while the second one can easily be estimated in terms of the modulated entropy.

A second difficulty to be addressed is related to cases where moments are far from their asymptotic values (i.e. when they become very large pointwise or when the macroscopic density or temperature vanish). In that case, the flux term is estimated directly by the modulated entropy, using both the Young and Bienaymé–Chebyshev inequalities.

4.3. Convergence

Combining (18) and (19), we then conclude by Gronwall's lemma:

$$\frac{1}{\varepsilon^2}H(f_\varepsilon|\mathcal{M}_{1,\varepsilon u,1})(t)$$
$$\leq \frac{1}{\varepsilon^2}H(f_\varepsilon^{in}|\mathcal{M}_{1,\varepsilon u^{in},1})\exp\left(\int_0^t \|Du\|_{L^2\cap L^\infty}\mathrm{d}s\right)$$
$$+\frac{1}{\varepsilon}\int_0^t\int A(u)\cdot\int(\varepsilon u-v)f_\varepsilon(s,x,v)\mathrm{d}v\mathrm{d}x$$
$$\times\exp\left(\int_s^t \|Du\|_{L^2\cap L^\infty}\mathrm{d}\sigma\right)\mathrm{d}s$$
$$+\int_0^t o(1)\exp\left(\int_s^t \|Du\|_{L^2\cap L^\infty}\mathrm{d}\sigma\right)\mathrm{d}s.$$

If u is Lipschitz continuous, the first term on the right-hand side converges to 0 by the assumption (12) on the initial data.

The weak convergence on $\frac{1}{\varepsilon}(f_\varepsilon-\mathcal{M})$ inherited from the uniform entropy bound (11) ensures that there exists some $\bar{u}$ such that, up to the extraction of a subsequence,

$$\frac{1}{\varepsilon}\int(\varepsilon u-v)f_\varepsilon\mathrm{d}v \rightharpoonup (u-\bar{u}).$$

Taking limits in the local conservation of mass, we then get the incompressibility constraint $\nabla_x\cdot\bar{u}=0$. As u is the solution to the incompressible Euler equations, we have $A(u)=-\nabla_x p$. Integrating by parts, we conclude that the second term also converges to 0.

We thus get the entropic convergence for all $t\geq 0$

$$\frac{1}{\varepsilon^2}H(f_\varepsilon|\mathcal{M}_{1,\varepsilon u,1})(t)\to 0.$$

(For the details we refer to [22]).

5. Proof of Theorem 2

Theorem 2 requires some improvements in the relative entropy method developed in [23]. The main idea is that, in domains where the distribution is expected to present rapid variations, the formal hydrodynamic approximation is not relevant, and that correctors have to be added in order to obtain the convenient asymptotics.

The point is indeed to obtain a refined description of the asymptotics taking into account both the relaxation in the initial layer and the acoustic waves.

5.1. Description of acoustic waves

Since acoustic waves only contribute to the hydrodynamic part of the distribution, relaxing the constraints on the initial thermodynamic fields does not require strong modifications of the method.

Outside from the initial layer, the strategy consists then in modulating the entropy by any fluctuation of Maxwellian, meaning that we assume neither the incompressibility constraint nor the Boussinesq constraint on the test functions. We define the approximate solution f_{app} by

$$\log f_{\mathrm{app}} = -\frac{3}{2}\log(2\pi)+\varepsilon\left(\rho-\frac{3}{2}\theta\right)-\frac{1}{2}\mathrm{e}^{-\varepsilon\theta}|v-\varepsilon u|^2.$$

We then expect the *modulated entropy inequality* to differ from the usual one by some penalization arising in the acceleration operator. More precisely, (18) has to be replaced by

$$\frac{1}{\varepsilon^2}H(f_\varepsilon|f_{\text{app}})(t)+\frac{1}{\varepsilon^{q+3}}\int_0^t\iint D(f_\varepsilon)\mathrm{d}s\mathrm{d}x$$
$$\le \frac{1}{\varepsilon^2}H(f_\varepsilon^{in}|f_{\text{app}}^{in})+\frac{1}{\varepsilon^2}\int_0^t\int \partial_t\exp(\varepsilon\rho)\mathrm{d}x\mathrm{d}s$$
$$+\frac{1}{\varepsilon}\int_0^t\iint f_\varepsilon\left(1,\mathrm{e}^{-\varepsilon\theta}(v-\varepsilon u),\frac{1}{2}\left(\frac{|v-\varepsilon u|^2}{\mathrm{e}^{\varepsilon\theta}}-3\right)\right)\cdot\mathbf{A}_\varepsilon(\rho,u,\theta)\mathrm{d}v\mathrm{d}x\mathrm{d}s$$
$$+\frac{1}{\varepsilon^2}\int_0^t\iint f_\varepsilon\left(D_xu:\Phi_\varepsilon+\mathrm{e}^{\frac{1}{2}\varepsilon\theta}D_x\theta\cdot\Psi_\varepsilon\right)\mathrm{d}x\mathrm{d}v\mathrm{d}s \quad (20)$$

denoting by $\mathbf{A}_\varepsilon(\rho,u,\theta)$ the (five components) generalized acceleration operator, and by Φ_ε and Ψ_ε the kinetic momentum and energy fluxes — which are scaled translated variants of

$$\Phi=\left(v^{\otimes 2}-\frac{1}{3}|v|^2Id\right),$$
$$\Psi=\frac{1}{2}v\left(|v|^2-5\right).$$

Note that such an inequality is established only for solutions to the Boltzmann equation satisfying the local conservations of mass, momentum and energy.

The difficult point is to build some suitable *approximate solutions* f_{app}, or in other words some family $(\rho_{\text{app}},u_{\text{app}},\theta_{\text{app}})$ of smooth thermodynamic fields satisfying approximately $\mathbf{A}_\varepsilon(\rho_{\text{app}},u_{\text{app}},\theta_{\text{app}})=0$, i.e. the acoustic system

$$\begin{pmatrix}\partial_t\rho+u\cdot\nabla_x\rho+\frac{1}{\varepsilon}\nabla_x\cdot u\\ \partial_tu+u\cdot\nabla_xu+\theta\nabla_x\left(\rho-\frac{3}{2}\theta\right)+\frac{1}{\varepsilon}\nabla_x(\rho+\theta)\\ \partial_t\theta+u\cdot\nabla_x\theta+\frac{2}{3\varepsilon}\nabla_x\cdot u\end{pmatrix}=0. \quad (21)$$

Such a construction is done by a filtering method (see [24] or [11] for instance).

Let us first rewrite the previous system (21) on $(\rho_{\text{app}},u_{\text{app}},\theta_{\text{app}})\stackrel{\text{def}}{=}V_{\text{app}}$ in a more abstract way:

$$\partial_tV+\frac{1}{\varepsilon}LV+Q(V,V)=0$$

where Q describes the nonlinear part of the system, and L is the linear penalization defined by

$$L:(\rho,u,\theta)\mapsto\left(\nabla_x\cdot u,\nabla_x(\rho+\theta),\frac{2}{3}\nabla_x\cdot u\right).$$

The first step is to conjugate the system by the semi-group generated by the linear penalization L

$$\partial_t\left(\exp\left(\frac{tL}{\varepsilon}\right)V\right)+\exp\left(\frac{tL}{\varepsilon}\right)Q(V,V)=0,$$

or equivalently

$$\partial_t\tilde V+\exp\left(\frac{tL}{\varepsilon}\right)Q\left(\exp\left(-\frac{tL}{\varepsilon}\right)\tilde V,\exp\left(-\frac{tL}{\varepsilon}\right)\tilde V\right)=0.$$

The first-order approximation, i.e. the envelope equation, is then obtained by taking limits in that filtered system:

$$\partial_t\tilde V_0+\tilde Q(\tilde V_0,\tilde V_0)=0$$

where $\tilde Q$ is defined as some projection of Q on the resonant modes of the linear penalization L.

Nevertheless, because of the high frequency oscillations, we do not expect the error in the first-order approximation to converge strongly to 0. We therefore have to add some correctors (i.e. the second- and third-order approximations) in order to establish the convenient convergence statement :

$$\left\|V_{\text{app}}-\exp\left(-\frac{tL}{\varepsilon}\right)(\tilde V_0+\varepsilon\tilde V_1+\varepsilon^2\tilde V_2)\right\|_{L^2}\to 0.$$

The conclusion of the proof follows from the same arguments as in the previous case, i.e. from *Gronwall's lemma*, except that the control of the energy flux (which is a third moment in v) requires some additional estimate, for instance (16). (For the details we refer to [23]).

5.2. *Description of the Knudsen layer*

In the initial layer, the purely kinetic part of the fluctuation is expected to be of order $O(1)$ and to converge to 0 exponentially in time. In order to take into account the relaxation process in the relative entropy method, one thus has to construct a refined approximation f_{app}, and then to introduce it in the modulated entropy inequality (20). This requires in particular to also modulate the entropy dissipation.

The *modulated entropy inequality* becomes indeed

$$\frac{1}{\varepsilon^2}H(f_\varepsilon|f_{\text{app}})(t)+\frac{1}{\varepsilon^{q+3}}\int_0^t\iint D(f_\varepsilon|f_{\text{app}})\mathrm{d}s\mathrm{d}x \quad (22)$$
$$\le\frac{1}{\varepsilon^2}H(f_\varepsilon^{in}|f_{\text{app}}^{in})$$
$$-\frac{1}{\varepsilon}\int_0^t\iint\gamma_\varepsilon\left(\partial_tf_{\text{app}}-\frac{1}{\varepsilon^{q+1}}Q(f_{\text{app}},f_{\text{app}})+\frac{1}{\varepsilon}v\cdot\nabla_xf_{\text{app}}\right)\mathrm{d}v\mathrm{d}x\mathrm{d}s$$
$$+\frac{1}{4\varepsilon^{q+1}}\int_0^t\iint\iint\left(f'_{\text{app}}f'_{\text{app}1}-f_{\text{app}}f_{\text{app}1}\right)\times\left(\gamma_\varepsilon\gamma_{\varepsilon1}-\gamma'_\varepsilon\gamma'_{\varepsilon1}\right)\mathrm{d}v\mathrm{d}v_1\mathrm{d}\omega\mathrm{d}x\mathrm{d}s$$

denoting by γ_ε the modulated fluctuation defined by $f_\varepsilon=f_{\text{app}}(1+\varepsilon\gamma_\varepsilon)$ and by $D(f_\varepsilon|f_{\text{app}})$ the modulated entropy dissipation. Note that the integrand defining the modulated entropy dissipation is always nonnegative, which is crucial to get some stability.

It remains then to build a suitable *approximate solution* f_{app}. Let us recall that, in the initial layer, the dominating process is expected to be the relaxation, so that the transport can be neglected in first approximation. We thus solve the homogeneous equation

$$\partial_tf_{\text{app}}=\frac{1}{\varepsilon^{q+1}}Q(f_{\text{app}},f_{\text{app}})$$

using a fixed-point argument in some functional space with exponential time decay.

Up to some spatial regularization of the initial data and truncation of large velocities, we are then able to prove that the second term on the right-hand side of (22) converge to 0, provided that $t = o(\varepsilon)$.

The conclusion is again based on some *Gronwall's type argument*. The point is to prove that the $L^2_x(L^{p'}(f_{\mathrm{app}}\mathrm{d}v))$ norm of γ_ε is controlled by the square root of the modulated entropy, and to obtain a uniform bound on

$$\chi_\varepsilon(t) = \frac{1}{\varepsilon^{q+1}} \int_0^t \|f'_{\mathrm{app}} f'_{\mathrm{app}1} - f_{\mathrm{app}} f_{\mathrm{app}1}\|_{L^\infty_x(L^p_{v,v_1,\omega})} \mathrm{d}s.$$

We then obtain, for any $\tau_\varepsilon \ll \varepsilon$,

$$\frac{1}{\varepsilon^2} H(f_\varepsilon | f_{\mathrm{app}})(\tau_\varepsilon) \le \frac{1}{\varepsilon^2} H(f_\varepsilon^{in} | f_{\mathrm{app}}^{in}) \exp(\chi_\varepsilon(\tau_\varepsilon)) + o(1).$$

This concludes the proof inside the initial layer.

It remains then to put together both estimates (inside and outside the initial layer) using the fact that the local thermodynamic equilibrium is a good approximation in entropic sense, provided that $\tau_\varepsilon \gg \varepsilon^{q+1}$.

(For the details we refer again to [23]).

References

[1] K. Aoki, Y. Sone, Steady gas flows past bodies at small Knudsen numbers — Boltzmann and hydrodynamic systems, Trans. Theory Stat. Phys. 16 (1987) 189–199.
[2] C. Bardos, F. Golse, C.D. Levermore, Fluid dynamic limits of kinetic equations. I. Formal derivations, J. Stat. Phys. 63 (1991) 323–344.
[3] C. Bardos, F. Golse, C.D. Levermore, Fluid dynamic limits of the Boltzmann equation II: Convergence proofs, Commun. Pure Appl. Math. 46 (1993) 667–753.
[4] S. Chapman, T.G. Cowling, The Mathematical Theory of Non-Uniform Gases: An Account of the Kinetic Theory of Viscosity, Thermal Conduction, and Diffusion in Gases, Cambridge University Press, New York, 1960.
[5] F. Coron, F. Golse, C. Sulem, A classification of well-posed kinetic layer problems, Comm. Pure Appl. Math. 41 (1988) 409–435.
[6] A. De Masi, R. Esposito, J.L. Lebowitz, Incompressible Navier–Stokes and Euler limits of the Boltzmann equation, Comm. Pure Appl. Math. 42 (1989) 1189–1214.
[7] R.J. DiPerna, P.-L. Lions, On the Cauchy problem for the Boltzmann equation: Global existence and weak stability results, Ann. of Math. 130 (1990) 321–366.
[8] I. Gallagher, L. Saint-Raymond, B. Texier, Towards a mathematical understanding of weak turbulence (in preparation).
[9] F. Golse, The Boltzmann equation and its hydrodynamic limits, in: L. Desvillettes, B. Perthame (Eds.), Kinetic Equations and Asymptotic Theory, Editions scientifiques et médicales Elsevier, Paris, 2000.
[10] H. Grad, Asymptotic theory of the Boltzmann equation II, in: Rarefied Gas Dynamics, in: Proc. of the 3rd Intern. Sympos. Palais de l'UNESCO, Paris, 1962, pp. 26–59.
[11] E. Grenier, Quelques limites singulires oscillantes, in: Séminaire sur les Equations aux Dérivées Partielles, Ecole Polytech., Palaiseau, 1995, Exp No XXI.
[12] E. Grenier, N. Masmoudi, Ekman layers of rotating fluids, the case of well prepared initial data, Comm. Partial Differential Equations 22 (1997) 953–975.
[13] Y. Guo, The Boltzmann equation in the whole space, Indiana Univ. Math. J. 53 (2004) 1081–1094.
[14] D. Hilbert, Sur les problèmes futurs des mathématiques. Les 23 problèmes, Translated from the 1900 German original by M.L. Laugel and revised by the author, Les Grands Classiques Gauthier-Villars, Editions Jacques Gabay, Sceaux, 1990.
[15] D. Hilbert, Begründung der kinetischen Gastheorie, Math. Ann. 72 (1912) 562–577.
[16] E. Landauer, D.B. Spalding, Lectures in Mathematical Models of Turbulence, Academic Press, London, 1972.
[17] O.E. Lanford, Time Evolution of Large Classical Systems, in: Lect. Notes in Physics, vol. 38, Springer Verlag, 1975.
[18] P.-L. Lions, Conditions at infinity for Boltzmann's equation, Comm. Partial Differential Equations 19 (1994) 335–367.
[19] P.-L. Lions, N. Masmoudi, From Boltzmann equation to the Navier–Stokes and Euler equation, Arch. Ration. Mech. Anal. 158 (2001) 173–193.
[20] J. Quastel, H.-T. Yau, Lattice gases, large deviations, and the incompressible Navier–Stokes equations, Ann. of Math. 148 (1998) 51–108.
[21] L. Saint-Raymond, From the BGK model to the Navier–Stokes equations, Ann. Sci. École Norm. Sup. 36 (2003) 271–317.
[22] L. Saint-Raymond, Convergence of solutions to the Boltzmann equation in the incompressible Euler limit, Arch. Ration. Mech. Anal. 166 (2003) 47–80.
[23] L. Saint-Raymond, Hydrodynamic limits: Some improvements of the relative entropy method, Ann. IHP (2008) (in press).
[24] S. Schochet, Fast singular limits of hyperbolic PDEs, J. Differential Equations 114 (1994) 476–512.
[25] H.T. Yau, Relative entropy and hydrodynamics of Ginzburg–Landau models, Lett. Math. Phys. 22 (1991) 63–80.

Lagrangian description and mixing

Available online at www.sciencedirect.com
ScienceDirect
Physica D 237 (2008) 2037–2050
PHYSICA D
www.elsevier.com/locate/physd

Stochastic suspensions of heavy particles

Jérémie Bec[a,*], Massimo Cencini[b,c], Rafaela Hillerbrand[d], Konstantin Turitsyn[e,f]

[a] Laboratoire Cassiopée, Observatoire de la Côte d'Azur, CNRS, Université de Nice Sophia-Antipolis, Bd. de l'Observatoire, 06300 Nice, France
[b] SMC INFM-CNR c/o Dip. di Fisica Università di Roma "La Sapienza", Piazzale A. Moro 2, 00185 Roma, Italy
[c] CNR, Istituto dei Sistemi Complessi, Via dei Taurini 19, 00185 Roma, Italy
[d] The Future of Humanity Institute, University of Oxford, Suite 8, Littlegate House 16/17, St Ebbe's Street, Oxford, OX1 1PT, United Kingdom
[e] James Franck Institute, University of Chicago, Chicago, IL 60637, USA
[f] Landau Institute for Theoretical Physics, Moscow, Kosygina 2, 119334, Russia

Available online 29 February 2008

Abstract

Turbulent suspensions of heavy particles in incompressible flows have gained much attention in recent years. A large amount of work focused on the impact that the inertia and the dissipative dynamics of the particles have on their dynamic and statistical properties. Substantial progress followed from the study of suspensions in model flows which, although much simpler, reproduce most of the important mechanisms observed in real turbulence. This paper presents recent developments made on the relative motion of a pair of particles suspended in time-uncorrelated and spatially self-similar Gaussian flows. This review is complemented by new results. By introducing a time-dependent Stokes number, it is demonstrated that inertial particle relative dispersion recovers asymptotically Richardson's diffusion associated to simple tracers. A perturbative (homogeneization) technique is used in the small-Stokes-number asymptotics and leads to interpreting first-order corrections to tracer dynamics in terms of an effective drift. This expansion implies that the correlation dimension deficit behaves linearly as a function of the Stokes number. The validity and the accuracy of this prediction is confirmed by numerical simulations.

PACS: 47.27.-i; 47.51.+a; 47.55.-t

Keywords: Stochastic flows; Inertial particles; Kraichnan model; Lyapunov exponent

1. Introduction

The current understanding of passive turbulent transport profited significantly from studies of the advection by random fields. In particular, flows belonging to the so-called *Kraichnan ensemble* – i. e. spatially self-similar Gaussian velocity fields with no time correlation – which was first introduced in the late 1960s by Kraichnan [1], led in the mid-1990s to a first analytical description of anomalous scaling in turbulence (see [2] for a review). More recently, much work is devoted to a generalization of this passive advection to heavy particles that, conversely to tracers, do not follow the flow exactly but lag behind it due to their inertia. The particle dynamics is thus dissipative even if the carrier flow is incompressible. This paper provides an overview of several recent results on the dynamics of very heavy particles suspended in random flows belonging to the Kraichnan ensemble.

The recent shift of focus to the transport of heavy particles is motivated by the fact that in many natural and industrial flows finite-size and mass effects of the suspended particles cannot be neglected. Important applications encompass rain formation [3–5] and suspensions of biological organisms in the ocean [6–8]. For practical purposes, the formation of particle clusters due to inertia is of central importance as the presence of such inhomogeneities significantly enhances interactions between the suspended particles. However, detailed and reliable predictions on collision or reaction rates, which are crucial to many applications, are still missing.

Two mechanisms compete in the formation of clusters. First, particles much denser than the fluid are ejected from the eddies of the carrier flow and concentrate in the strain-dominated

* Corresponding author.
E-mail address: jeremie.bec@oca.eu (J. Bec).

0167-2789/$ - see front matter © 2008 Elsevier B.V. All rights reserved.
doi:10.1016/j.physd.2008.02.022

regions [9]. Second, the dissipative dynamics leads the particle trajectories to converge onto a fractal, dynamically evolving attractor [10,11]. In many studies, a carrier velocity field with no time correlation – and thus no persistent structures – is used to isolate the latter effect. As interactions between three or more particles are usually subdominant, most of the interesting features of monodisperse suspensions can be captured by focusing on the relative motion of two particles separated by $\boldsymbol{R}$:

$$\ddot{\boldsymbol{R}} = -\frac{1}{\tau}\left[\dot{\boldsymbol{R}} - \delta\boldsymbol{u}(\boldsymbol{R}, t)\right], \tag{1}$$

where dots denote time derivatives and τ the particle response time. The fluid velocity difference $\delta\boldsymbol{u}$ is a Gaussian vector field with correlation

$$\left\langle \delta u^i(\boldsymbol{r}, t)\, \delta u^j(\boldsymbol{r}', t')\right\rangle = 2\, b^{ij}(\boldsymbol{r} - \boldsymbol{r}')\, \delta(t - t'). \tag{2}$$

In order to model turbulent flows, the tensorial structure of the spatial correlation $b^{ij}(\boldsymbol{r})$ is chosen to ensure incompressibility, isotropy and scale invariance, namely

$$b^{ij}(\boldsymbol{r}) = D_1\, r^{2h}[(d - 1 + 2h)\, \delta^{ij} - 2h\, r^i r^j / r^2], \tag{3}$$

where h relates to the Hölder exponent of the fluid velocity field and D_1 measures the intensity of its fluctuations. In particular, $h = 1$ corresponds to a spatially differentiable velocity field, mimicking the dissipative range of a turbulent flow, while $h < 1$ models rough flows as in the inertial range of turbulence. In this paper we mostly focus on space dimensions $d = 1$ and $d = 2$; extensions to higher dimensions are just sketched.

The above depicted model flow has the advantage that the particle dynamics is a Markov process. In particular, Gaussianity and δ-correlation in time of the fluid velocity field imply that the probability density $p(\boldsymbol{r}, \boldsymbol{v}, t|\boldsymbol{r}_0, \boldsymbol{v}_0, t_0)$ of finding the particles at separation $\boldsymbol{R}(t) = \boldsymbol{r}$ and with relative velocity $\dot{\boldsymbol{R}}(t) = \boldsymbol{v}$ at time t, when $\boldsymbol{R}(t_0) = \boldsymbol{r}_0$ and $\dot{\boldsymbol{R}}(t_0) = \boldsymbol{v}_0$ is a solution of the Fokker–Planck equation

$$\partial_t p + \sum_i \left(\partial_r^i - \frac{1}{\tau}\partial_v^i\right)\left(v^i\, p\right) - \sum_{i,j} \frac{b^{ij}(\boldsymbol{r})}{\tau^2}\, \partial_v^i \partial_v^j\, p = 0, \tag{4}$$

with the initial condition $p(\boldsymbol{r}, \boldsymbol{v}, t_0) = \delta(\boldsymbol{r} - \boldsymbol{r}_0)\, \delta(\boldsymbol{v} - \boldsymbol{v}_0)$. To maintain a statistical steady state, the Fokker–Planck equation (4) as well as the stochastic differential equation (1) should be supplemented by boundary conditions, here chosen to be reflective at a given distance L.

For smooth flows ($h = 1$), the intensity of inertia is generally measured by the *Stokes number St*, defined as the ratio between the particle response time τ and the fluid characteristic time scale. For $St \to 0$, particles recover the incompressible dynamics of tracers. In the opposite limit where St is very large, inertia effects dominate and the dynamics approaches that of free particles. In the above depicted model, the Stokes number is defined by nondimensionalizing τ by the typical fluid velocity gradient, i.e. $St = D_1\tau$. Note that by rescaling the physical time by τ, it is straightforward to recognize that the dynamics depends solely on St.

Similarly it can be checked that in rough flows ($h < 1$) – with an additional rescaling of the distances by a factor $(D_1\tau)^{1/(2-2h)}$ – the dynamics of a particle pair at a distance r only depends on the *local Stokes number* $St(r) = D_1\tau/r^{2(1-h)}$. This dimensionless quantity, first introduced in [12] and later used in [13], is a generalization of the Stokes number to cases in which the fluid turnover times depend on the observation scale. At large scales, $St(r) \to 0$ and inertia becomes negligible. Particle dynamics thus approaches that of tracers. At small scales, $St(r) \to \infty$ and the particle and fluid motions decorrelate, so that the inertial particles move ballistically. In both the large and small Stokes number asymptotics, particles distribute uniformly in space, while inhomogeneities are expected at intermediate values of $St(r)$.

The paper is organized as follows. In Section 2, an approach originally proposed in [14] is used to reduce the dynamics of the particle separation to a system of three stochastic equations with additive noises. This formulation is useful for both numerical and analytical purposes, particularly when studying the statistical properties of particle pairs. In Section 3, we introduce the correlation dimension to quantify clustering as well as the approaching rate which measures collisions. Numerical results for these quantities are reported. In Section 4 we introduce the notion of time-dependent Stokes number which makes particularly transparent the interpretation of the behaviour of the long-time separation between particles. We show how Richardson dispersion, as for tracers, is recovered in the long-time asymptotics. Section 5 briefly summarizes some exact results that can be obtained for the one-dimensional case. Sections 6 and 7 are dedicated to the small and large Stokes number asymptotics, respectively. In particular, the former presents an original perturbative approach which turned out to predict, in agreement with numerical computations, the behaviour of the correlation dimension that characterizes particle clusters. Finally, Section 8 encompasses conclusions, open questions and discusses the relevance of the considered model for real suspensions in turbulent flows.

2. Reduced dynamics for the two-point motion

In this Section we focus on planar suspensions ($d = 2$). Following the approach proposed in [14] and with the notation $R = |\boldsymbol{R}|$, the change of variables

$$\sigma_1 = (L/R)^{1+h}\boldsymbol{R}\cdot\dot{\boldsymbol{R}}/L^2, \tag{5}$$

$$\sigma_2 = (L/R)^{1+h}|\boldsymbol{R}\wedge\dot{\boldsymbol{R}}|/L^2, \tag{6}$$

$$\rho = (R/L)^{1-h}, \tag{7}$$

is introduced to reduce the original system of $2d = 4$ stochastic equations to the following one of only three equations:

$$\dot{\sigma}_1 = -\sigma_1/\tau - \left[h\sigma_1^2 - \sigma_2^2\right]/\rho + \sqrt{C}\,\eta_1, \tag{8}$$

$$\dot{\sigma}_2 = -\sigma_2/\tau - (1+h)\sigma_1\sigma_2/\rho + \sqrt{(1+2h)C}\,\eta_2, \tag{9}$$

$$\dot{\rho} = (1-h)\,\sigma_1, \tag{10}$$

where $C = 2D_1/(\tau L^{1-h})^2$ and η_i denote two independent white noises. Reflective boundary conditions at $R = L$ in

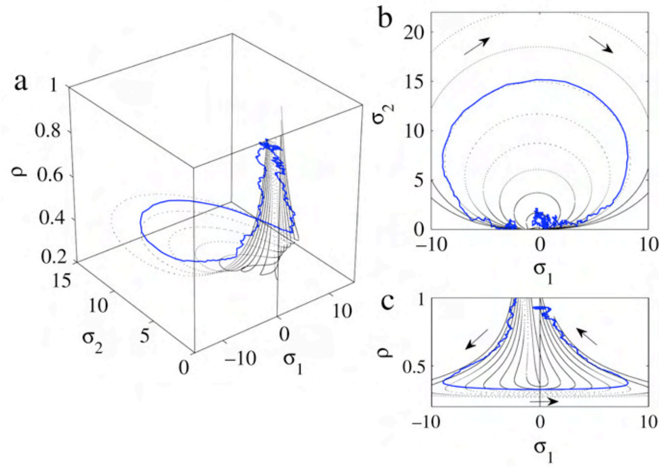

Fig. 1. Sketch of the reduced dynamics (8)–(10) for $h = 0.7$. The dotted lines represent the drift. The solid line depicts a random trajectory with $St(L) = 1$. (a) full $(\sigma_1, \sigma_2, \rho)$-space, (b) projection on $\rho = 0$ plane, and (c) on the $\sigma_2 = 0$ plane.

physical space imply reflection at $\rho = 1$. Note that σ_1 and σ_2 are proportional to the longitudinal and to the transversal relative velocities between the two particles. In the smooth case ($h = 1$), we have $\rho = 1$ and Eqs. (8) and (9) decouple from (10). The particle separation R then evolves as

$$\dot{R} = \sigma_1(t)R. \tag{11}$$

Besides this simple evolution and the reduction of the number of variables from $2d$ to only three, the change of variables $\{\boldsymbol{R}, \dot{\boldsymbol{R}}\} \mapsto \{\rho, \sigma_1, \sigma_2\}$ has several other advantages. For instance the noise, which is multiplicative in the original dynamics (1), becomes additive in the reduced system (8)–(10). However, this simplification is counterbalanced by the presence of nonlinear drift terms. Note that in dimensions higher than two, there is an additional term $\propto 1/\sigma_2$, which is due to the Itô formula [15,16].

Fig. 1 sketches the deterministic drift and shows a typical trajectory in the reduced space. This dynamics can be qualitatively described as follows. The line $\sigma_1 = \sigma_2 = 0$ acts as a stable fixed line for the drift. Hence a typical trajectory spends a long time diffusing around it, until the noise realization becomes strong enough to let the trajectory escape from the vicinity of this line. Whenever this happens with a positive longitudinal relative velocity ($\sigma_1 > 0$), the trajectory is pulled back to the stable line by the quadratic terms in the drift. Conversely, if $\sigma_1 < 0$ and $h\sigma_1^2 + \sigma_1\rho - \sigma_2^2 < 0$, the drift pushes the trajectory towards larger negative values of σ_1. Then the particles get closer to each other and ρ decreases, until the quadratic terms in Eqs. (8) and (9) become dominant. The trajectory then loops back in the (σ_1, σ_2)-plane, approaching the stable line from its right. It is during these loops that the interparticle distance R becomes substantially small. The loops thus provide the main mechanisms for cluster formation.

2.1. *Velocity statistics*

Numerical simulations show that the probability density function (pdf) of the longitudinal relative velocity σ_1 displays

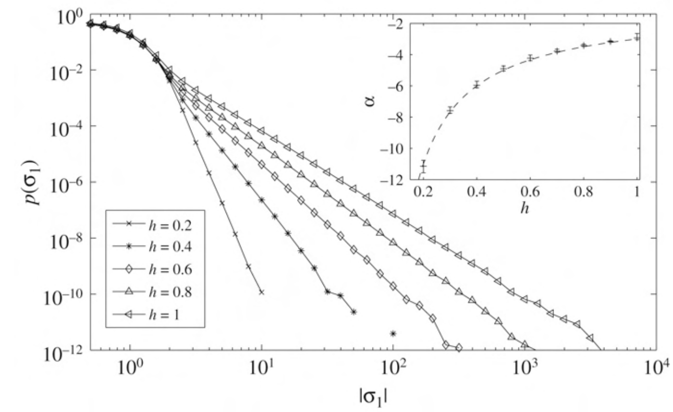

Fig. 2. Log–log plot of the pdf of σ_1 for $St(L) = 1$ for five values of the fluid Hölder exponent h. Power-law tails are always observed, $p(\sigma) \propto |\sigma|^{-\alpha}$. Inset: exponent α versus h; the dashed line is the theoretical prediction $\alpha = 1 + 2/h$.

algebraic tails at large positive and negative values (see Fig. 2). As will become clear in the sequel, these power-law tails are a signature of the above-mentioned large loops. Let us consider the cumulative probability $P^{<}(\sigma) = \Pr(\sigma_1 < \sigma)$ for $\sigma \ll -1$. This quantity can be estimated as the product of (i) the probability to start a sufficiently large loop in the (σ_1, σ_2)-plane that reaches values smaller than σ and (ii) the fraction of time spent by the trajectory at $\sigma_1 < \sigma$. Within a distance of the order of unity from the line $\sigma_1 = \sigma_2 = 0$, the quadratic terms in the drift are subdominant and can be disregarded. Then σ_1 and σ_2 can be approximated by two independent Ornstein–Uhlenbeck processes. Conversely, at sufficiently large distances from that line, only the quadratic terms in the drift contribute and the noises are negligible.

Within this simplified dynamics, a loop is initiated at a time t_0 for which $\sigma_1(t_0) < -1$ and $\sigma_2(t_0) \ll |\sigma_1(t_0)|$. Once these conditions are fulfilled, the trajectory performs a loop in the (σ_1, σ_2)-plane and both $|\sigma_1(t)|$ and $\sigma_2(t)$ become very large. The maximum distance from the stable line, which gives an estimate of the loop radius, is reached when σ_2 is of the order of $|\sigma_1|$. Let t^* denote the time when this happens, i.e. $\sigma_2(t^*)/|\sigma_1(t^*)| = O(1)$. When neglecting the noise, this condition leads to the following estimate for the loop radius:

$$|\sigma_1(t^*)| \propto [\,\sigma_1(t_0) + \rho(t_0)/\tau]\, |\tau\sigma_1(t_0)|^h\, (\tau\sigma_2(t_0))^{-h}, \tag{12}$$

see [13] for details. In order to reach velocity differences such that $\sigma_1 < \sigma \ll -1$, the radius of the loop has to be larger than $|\sigma|$. From (12) this implies that $\sigma_2(t_0)$ has to be smaller than $|\sigma|^{-1/h}$. In order to evaluate contribution (i), we have to estimate the probability to have $\sigma_1(t_0) \lesssim -1$ and $\sigma_2(t_0) < |\sigma|^{-1/h}$ from the dynamics in the vicinity of the origin. Approximating the two velocity differences σ_1 and σ_2 by independent Ornstein–Uhlenbeck processes close to the line $\sigma_1 = \sigma_2 = 0$, the first condition gives an order-unity contribution, while the second has a probability $\propto |\sigma|^{-1/h}$. For estimating (ii), we neglect the noise in the dynamics far from the stable line. The probability is then given by the fraction of time spent at $\sigma_1 < \sigma$ which is proportional to $\sigma_2(t_0) \propto |\sigma|^{-1/h}$. Put together, the two contributions yield $P^{<}(x) \propto |\sigma|^{-2/h}$ when

$\sigma \ll -1$. Thus the negative tail of the pdf of σ_1 behaves as $\propto |\sigma|^{-\alpha}$, with $\alpha = 1 + 2/h$.

During the large loops, the trajectories equally reach large *positive* values of σ_1 and of σ_2. Again the fraction of time spent at both σ_1 and σ_2 larger than $\sigma \gg 1$ can be estimated as $\sigma^{-1/h}$. Hence, the pdf of both longitudinal σ_1 and transversal σ_2 velocity differences have algebraic left and right tails with exponent α. Both tails are depicted in Fig. 2, where the inset shows that the numerical measurements are in good agreement with the predicted value of α. The relation between α and the Hölder exponent h implies in particular that $\alpha = 3$ in the smooth case, while it increases with decreasing h. Moreover, it follows straightforwardly from (8) to (10) that during the loops $\rho(t) \propto \rho(t_0)^h$ when $\rho(t_0) \ll 1$. Hence it becomes less and less probable to reach smaller values of ρ as h decreases. In other words, particle clustering should be very strong for smooth flows and become weaker when the flow roughness is increased. This prediction is confirmed by the numerical studies presented in the next section.

Finally it should be pointed out that although the change of variables (5)–(7) can be applied equally in three dimensions, the above analysis does not carry over to higher dimensions. First, as already pointed out, an additional drift term arises. This Itô-term renders a straightforward derivation of an analytical solution for the deterministic drift impossible. Second, for higher dimensions the fixed point of the reduced dynamics is located far from the origin, see [16]. Hence the approximations made above for $d = 2$ are not applicable. Careful numerical studies are needed to understand whether or not algebraic tails are also present in higher dimensions.

3. Correlation dimension and approaching rate

Particle clustering is often quantified by the *radial distribution function* $g(r)$, which is defined as the ratio between the number of particles inside a thin shell of radius r centred on a given particle and the number which would be in this shell if the particles were uniformly distributed. This quantity enters models for the collision kernel [17]. Following [10,13,16,18], we consider a different, but related way to characterize particle clustering. Instead of the radial distribution function we evaluate the *correlation dimension* $\mathcal{D}_2$ of the set formed by the particles. This dimension is widely used in dissipative dynamic system theory and in fractal geometry (see, e.g. [19,20]). It is defined as the exponent of the power-law behaviour at small scales of the probability $P_2(r)$ of finding two particles at a distance $R < r$:

$$\mathcal{D}_2 = \lim_{r\to 0} d_2(r), \qquad d_2(r) = \frac{\mathrm{d}\ln P_2(r)}{\mathrm{d}\ln r}, \tag{13}$$

where the logarithmic derivative $d_2(r)$ is called the *local correlation dimension*. $\mathcal{D}_2$ relates to the radial distribution function via $\ln g(r)/\ln r \to \mathcal{D}_2 - d$ for $r \to 0$. For uniformly distributed particles, $\mathcal{D}_2 = d$, so that $g(r) = \mathrm{O}(1)$. On the contrary, when particles cluster on a fractal set, $\mathcal{D}_2 < d$ and $g(r)$ diverges for $r \to 0$. This was also found numerically in [17].

Depending on whether the carrier flow is spatially smooth ($h = 1$) or rough ($h < 1$), $\mathcal{D}_2$ and $d_2(r)$ behave differently. In the former case, random dynamic system theory [21] suggests that within the $2 \times d$ position-velocity phase space, particles converge onto a multifractal set with correlation dimension $0 < \overline{\mathcal{D}}_2 < 2d$. Here $\overline{\mathcal{D}}_2$ denotes the correlation dimension in the full phase space. It is defined in complete analogy to $\mathcal{D}_2$ through the scaling behavior of the probability $\overline{P}_2(r)$ to find two particles at a distance less than r in phase space:

$$\overline{P}_2(r) \sim r^{\overline{\mathcal{D}}_2} \quad \text{for } r \to 0. \tag{14}$$

The distance r is now computed by using the phase-space Euclidean norm $\sqrt{|\boldsymbol{R}|^2 + |\boldsymbol{V}/D_1|^2}$; $\boldsymbol{V}$ is normalized by the typical fluid velocity gradient D_1 for dimensional reasons. The physical-space correlation dimension $\mathcal{D}_2$ is actually the dimension of the projection of the set from the full phase space onto the position space, and it is also expected to be fractal (see Section 7 for details on the relation between $\overline{\mathcal{D}}_2$ and $\mathcal{D}_2$). We focus in this section on quantifying clustering in position space and hence consider only $\mathcal{D}_2$ and $d_2(r)$.

Balkovsky et al. argued in [43] that particles do not form fractal sets in nonsmooth flows because the correlation function of the particle density field should be a stretched exponential. Clustering and inhomogeneities are hence not quantified by a fractal dimension but by the detailed scale dependence of $d_2(r)$. However, as discussed in the Introduction, one expects the statistical properties of two particles separated by a distance r in a flow with Hölder exponent h to depend on the local Stokes number $St(r) = D_1\tau/r^{2(1-h)}$ only, which for smooth flows degenerates to a scale independent number, $St(r) = St = D_1\tau$. In rough flows, at scales small enough, particles move ballistically and distribute homogeneously as the Lagrangian motion is too fast for the particles to follow ($St(r) \to \infty$ as $r \to 0$) and hence $\mathcal{D}_2 = d$ for *all* particle response times τ. However, information on the inhomogeneities of the particle distribution at larger scales can still be obtained through the scale dependence of the local correlation dimension $d_2(r)$ defined in (13).

The relevance of the local Stokes number and of the local correlation dimension is confirmed by numerical experiments of planar suspensions. Simulations were performed by directly integrating the reduced system described in the previous section. Fig. 3 shows $d_2(r)$ as a function of $St(r)$ for various values of h. The curves obtained with different values of the response time τ collapse onto the same h-dependent master curve once the scale dependency is reabsorbed by using $St(r)$. In the plot, only scales far from the boundaries were considered, as otherwise the self-similarity of the fluid flow is broken. The data for $h = 1$ estimate the limit of $d_2(r)$ as $r \to 0$, and so correspond to the value of the correlation dimension $\mathcal{D}_2$. As anticipated in the previous section, Fig. 3 also shows that clustering is weakening when the roughness of the fluid velocity increases (i.e. when h decreases). In particular, $\min_r\{d_2(r)\}$ gets closer to d, i.e. particles approach the uniform distribution as $h \to 0$. Finally notice that for $St(r) \to 0$, i.e. at large scales in rough flows, $d_2(r) \to d$ as well. This is due to the

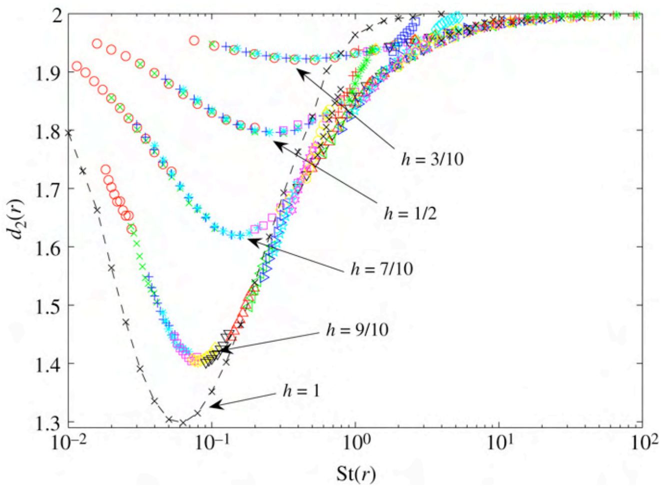

Fig. 3. Local correlation dimension $d_2(r)$ versus the scale-dependent Stokes number $St(r) = D_1\tau/r^{2(1-h)}$ for two-dimensional flows with different h. Symbols denote different particle response times τ. For $h = 1$, $\mathcal{D}_2 = d_2(r \to 0)$ is displayed and $St(r) = St = D_1\tau$.

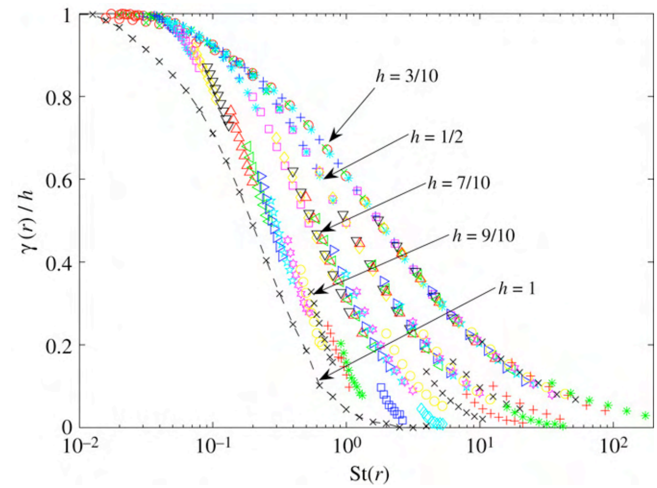

Fig. 4. Ratio between the local Hölder exponent $\gamma(r)$ of the particle velocity and that of the fluid h versus $St(r)$. The symbols in each curve refer to different values of the particle response time τ. As in Fig. 3, for $h = 1$, the small-scale limiting value Γ is depicted.

fact that at these scales the Lagrangian motion becomes much slower than the relaxation time of the particles. The particles thus recover the tracer limit and distribute homogeneously. As we will see in Section 6 the local dimension $d_2(r)$ tends linearly to the space dimension d when $St(r) \to 0$ with a factor whose dependence on h and d can be obtained analytically by perturbative methods.

The radial distribution function and hence the correlation dimension give only partial information on the rate at which particles collide. Indeed, in order to evaluate the collision rate, one needs to know not only the probability that the particles are close to each other, but also their typical velocity difference. Here, following [18], we study the approaching rate $\kappa(r)$ defined as the flux of particles that are separated by a distance less than r and approach each other, i.e.

$$\kappa(r) = \langle \dot{\boldsymbol{R}} \cdot \boldsymbol{R}/|\boldsymbol{R}|\, \Theta(-\dot{\boldsymbol{R}} \cdot \boldsymbol{R}/|\boldsymbol{R}|)\, \Theta(r - |\boldsymbol{R}|)\rangle, \tag{15}$$

where Θ denotes the Heaviside function and the average is defined on the Lagrangian trajectories. As detailed in [18], $\kappa(r)$ is related to the binary collision rate in the framework of the so-called *ghost collision scheme* [23]. Within this approach collision events are counted while allowing particles to overlap instead of scattering. At small separations, $\kappa(r)$ behaves as a power law. This algebraic behaviour allows defining a *local Hölder exponent* $\gamma(r)$ for the particle velocities

$$\gamma(r) = \frac{\ln \kappa(r)}{\ln r} - d_2(r). \tag{16}$$

In the above definition the contribution from clustering, accounted for by the local correlation dimension $d_2(r)$, is removed. The local Hölder exponent $\gamma(r)$, similarly to $d_2(r)$, tends to a finite limit Γ as $r \to 0$ which, for particles suspended in a smooth flow ($h = 1$), depends nontrivially on the Stokes number.

Fig. 4 shows numerical estimations of $\gamma(r)/h$ as a function of $St(r)$ for various values of h. In the smooth case ($h = 1$), the limit value Γ decreases from $\Gamma = 1$ for $St = 0$, which corresponds to a differentiable particle velocity field, to $\Gamma = 0$ for $St \to \infty$, which means that particles move with uncorrelated velocities [16]. The fact that $\Gamma < 1$ is due to the contribution of caustics appearing in the particle velocity field [24,26,25,15,18] (see Section 5 for a discussion in $d = 1$). Similarly, in nonsmooth flows $\gamma(r)$ is asymptotically equal to the fluid Hölder exponent h at large scales ($St(r) \to 0$), and approaches 0 at very small scales ($St(r) \to \infty$). Therefore, all the relevant information is entailed in the intermediate behaviour of $\gamma(r)$. The latter should only depend on the fluid Hölder exponent and on the local Stokes number, as confirmed by the collapse observed in Fig. 4. Note that the transition from $\gamma(r) = h$ to $\gamma(r) = 0$ shifts towards larger values of the local Stokes number and broadens as h decreases. The fact that $\gamma(r) = h$ for $r \to \infty$ implies that the particles should asymptotically experience Richardson diffusion just as tracers (see Section 4 for details). For comments on how the findings reported in this section translate to realistic turbulent flows, we refer the reader to Section 8.

4. Stretching rate and relative dispersion

This section is devoted to the study of the behaviour of the distance $R(t)$ between two particles at intermediate times t such that $R(0) \ll R(t) \ll L$. For convenience, we drop the reflective boundary condition at $R = L$ and consider particles evolving in an unbounded domain.

We first consider a differentiable fluid velocity field ($h = 1$). In this case, the time evolution of the distance $R(t)$ is given by (11), so that

$$R(t) = R(0)\, \exp\left[\int_0^t \sigma_1(t')\, \mathrm{d}t'\right] \tag{17}$$

and the particle separation can be measured by the *stretching rate* $\mu(t) \equiv (1/t)\ln[R(t)/R(0)]$. It is assumed that the reduced dynamics (8)–(10) is ergodic. There is currently no rigorous proof of ergodicity. However, such an assumption relies on

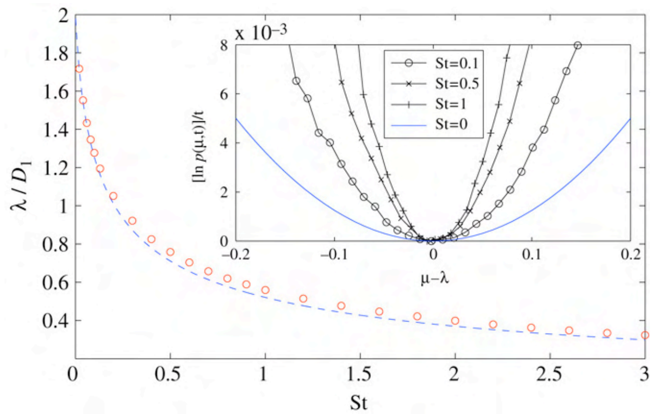

Fig. 5. Lyapunov exponent λ versus St: the circles are the numerical measurements while the dashed line corresponds to Eq. (20). Inset: rate function H associated to the large deviations of the stretching rate μ for three values of St; the solid line corresponds to H for tracers for, whose analytic expression is known (see, e.g. [2]).

numerical evidence and on the following phenomenological argument. The deterministic loops described in Section 2 are randomly initiated by the near-origin behaviour of the system, providing a mechanism of rapid memory loss that might ensure ergodicity. With this assumption, the time averages converge to ensemble averages, so that

$$\mu(t) = \frac{1}{t}\int_0^t \sigma_1(t')\,\mathrm{d}t' \to \langle\sigma_1\rangle \quad \text{as } t \to \infty. \tag{18}$$

In other words, the distance between particles asymptotically behaves as $R(t) = R(0)\exp(t\lambda)$, where $\lambda = \langle\sigma_1\rangle$ is a nonrandom quantity referred to as the *Lyapunov exponent*. A positive Lyapunov exponent implies that the particle dynamics is chaotic [19].

Fig. 5 shows numerical measurements of the Lyapunov exponent λ. The exponent remains positive for all values of the Stokes number. This means in particular that particles suspended in incompressible flow cannot experience *strong clustering*, which consists in the convergence of all trajectories together to form point clusters. This contrasts with the case of compressible flows where, for suitable values of St and of the compressibility, negative Lyapunov exponents are observed [24]. A first attempt to derive an analytical expression for $\lambda(St)$ was proposed by Piterbarg [14]. His approach is based on studying the Laplace transform $\varphi(p)$ of the distribution of the complex random variable $z = \sigma_1 + \mathrm{i}\sigma_2$, i.e. $\varphi(p,t) = \langle\exp(-pz(t))\rangle$ which satisfies

$$\partial_t\varphi = -(p/\tau)\,\partial_p\varphi + p\,\partial_p^2\varphi - (2D_1/\tau)p^2\varphi. \tag{19}$$

If $\varphi(p,t)$ reaches a steady state at large times, one can infer an analytic expression for the asymptotic solution $\varphi_\infty(p)$ by requiring that the right-hand side of (19) vanishes. It is then straightforward to deduce that the Lyapunov exponent satisfies $\lambda = -\lim_{p\to 0}\Re\{\partial_p\varphi_\infty\}$. This implies

$$\lambda = -\frac{D_1}{2St}\Re\left\{1 + \frac{\mathrm{Ai}'(x)}{\sqrt{x}\,\mathrm{Ai}(x)}\right\},$$
$$x = (16\,St)^{-2/3}, \tag{20}$$

where Ai and Ai′ designate the Airy function of the first kind and its derivative respectively. This prediction is compared to the numerical measurements in Fig. 5. As stressed in [25], there is evidence that the moments $\varphi(p,t)$ do not converge to a steady state, but rather diverge at large times. This might explain the discrepancies observed in Fig. 5. However, the numerical precision is not high enough to test the presence of corrections to the analytical expression (20).

At large but finite time t, the distance between the two particles is measured by the *stretching rate* $\mu(t) = (1/t)\ln[R(t)/R(0)]$. This quantity becomes more and more sharply distributed around the Lyapunov exponent λ as t increases. More precisely, it obeys a large deviation principle and its pdf $p(\mu,t)$ takes the asymptotic form (see, e.g. [2])

$$\frac{1}{t}\ln p(\mu,t) \sim -H(\mu), \tag{21}$$

where H is a positive convex function attaining its minimum in $\mu = \lambda$, in particular $H(\lambda) = 0$. The *rate function* H measures the large fluctuations of μ, which are important to quantify particle clustering. Rate functions obtained from numerical experiments are represented in Fig. 5 for various values of the Stokes number. The function becomes less and less broad when St increases, a phenomenon that can be quantified in the limit $St \to \infty$ as discussed in Section 7. Note that the same qualitative behaviour is also observed for heavy particles suspended in homogeneous isotropic flow [27].

We now turn to the case of particles suspended in nondifferentiable flows ($h < 1$). As we dropped the boundary condition, the initial interparticle distance $R(0)$ is the only relevant length scale. By using $R(0)$ instead of L in the change of variables (5)–(7), the problem of relative dispersion is expressed solely in terms of the Hölder exponent h and of a time-dependent Stokes number which can be defined in terms of the local Stokes number as $St_t = D_1\tau/[R(t)]^{2(1-h)}$. In particular, the evolution of $R(t)$ directly follows from its initial value St_0. From the evolution equation (10) for the reduced separation $\rho(t) = [R(t)/R(0)]^{1-h}$, we obtain

$$\rho(t) = 1 + (1-h)\int_0^t \sigma_1(t')\,\mathrm{d}t', \tag{22}$$

where $\rho(\in[0,\infty))$ typically increases with time. The time-dependent Stokes number $St_t = D_1\tau/R^{2(1-h)} = St_0/\rho^2$, which measures the effect of inertia when the particles are at a distance $R(t)$, decreases with time. Hence, conversely to the case of differentiable carrier flow, σ_1 is not a stationary process and the integral in (22) does not tend to $t\langle\sigma_1\rangle$.

Hereafter, we confine the discussion to the case $St_0 \gg 1$ because it contains a richer physics than smaller St_0. As observed from Fig. 6, we can distinguish two regimes in the time behavior of $\rho(t)$. At first the particle separation evolves ballistically, i.e. $R(t) \propto t$, meaning that the time-dependent Stokes number St_t decreases as $t^{-2/(1-h)}$ (see inset of Fig. 6) and reaches order-unity values for $t \approx \tau$. During this phase, the time growth of ρ is accelerated or slowed down and ultimately reaches a diffusive behaviour $\propto t^{1/2}$. This corresponds to the limit of tracers, which is approached when $St_t \ll 1$. At this

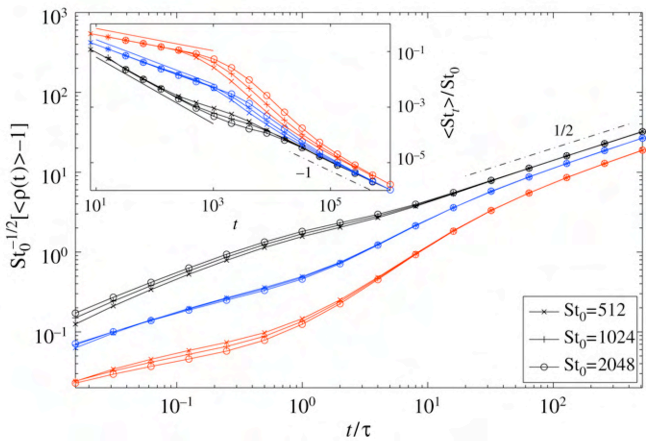

Fig. 6. Time evolution of the average rescaled separation $\langle(\rho(t)-\rho(0))\rangle$ for different initial Stokes numbers St_0, and $h = 0.4$, 0.6, and 0.8 (from top to bottom). Inset: long-time behaviour of the time-dependent Stokes number $St_t = D_1\tau/\rho^2(t)$ for different St_0 and the same three values of h (now from bottom to the top). The segments on the left indicate the slopes $-2/(1-h)$ corresponding to the regime of ballistic separation.

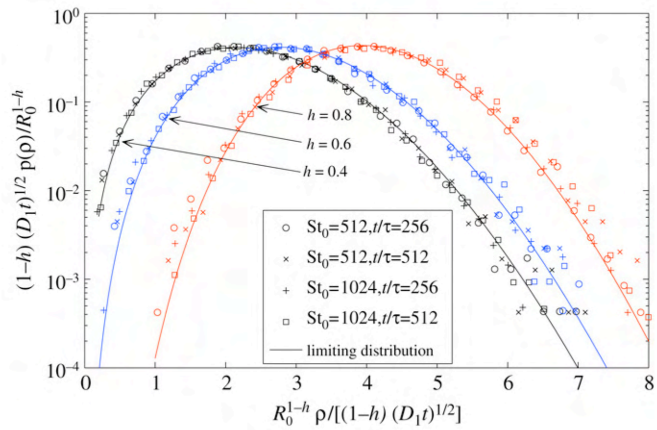

Fig. 7. Pdf of the rescaled separation $\rho(t)$ for various combinations of St_0 and large times t. The solid lines represent the limiting distribution given by (23) with $A = 1/4$.

stage, the interparticle distance behaves as $R(t) \propto t^{1/2(1-h)}$ and, consequently, the St_t decreases as $1/t$ (see Fig. 6).

The convergence to tracer diffusion in the limit of large distances R gives an original way to interpret Richardson's law for delta-correlated velocity fields in terms of the asymptotic behaviour of the reduced variables (5)–(7). When ρ is large, the quadratic terms in the drift of Eq. (8) can be neglected and σ_1 behaves as an Ornstein–Uhlenbeck process with response time τ. However, when σ_1 becomes of the order of $\rho/(h\tau)$, the quadratic terms cease to be negligible and they push the trajectory back to $\sigma_1 > 0$. This process happens on time scales that are of the order of unity and thus much smaller than the time scales relevant for large-scale dispersion. Hence the dynamics of $\sigma_1(t)$ can be approximated as an Ornstein–Uhlenbeck process with reflective boundary condition on $\sigma_1 = \rho/(h\tau)$. This implies that ρ has a diffusive behaviour. More specifically, numerical simulations (see Fig. 7) show that the pdf of ρ behaves as

$$p(\rho, t) \propto \rho^{\nu} t^{-(\nu+1)/2} \exp\left[-A\rho^2/t\right], \tag{23}$$

where $\nu = (1+h)/(1-h)$ and A is a positive constant. At large times and consequently large distances $St_t \to 0$, the tracer limit is fully recovered as confirmed by expressing the above relation in terms of the physical distance $R = \rho^{1/(1-h)}$. Indeed it becomes identical to the law that governs the separation of tracers in a Kraichnan flow [28]. However, a direct derivation of (23) in terms of the ρ and $\boldsymbol{\sigma}$ dynamics is still lacking.

5. Exact results in one dimension

A number of analytical results were derived for one-dimensional flows [29–31]. Although such flows are always compressible, their study helps improving the intuition for the dynamics of inertial particles in higher-dimensional random flows. In particular, several results on caustic formation hold also in two-dimensional (incompressible) flows because the typical velocity fluctuations, which lead to caustic formation, are effectively one-dimensional.

Here, we focus on one-dimensional smooth flows, for which the equations analogous to (8)–(10) reduce to

$$\dot{\sigma} = -\sigma/\tau - \sigma^2 + \sqrt{C}\,\eta(t), \tag{24}$$

$$\dot{R} = \sigma R, \tag{25}$$

where $\sigma = V/R$ and, as in (8)–(10), $C = 2D_1/\tau^2$. The quadratic term in (24) implies that σ can escape to $-\infty$ with a finite probability. These events are the one-dimensional counterpart of the loops described in Section 2 and correspond to the formation of caustics: particle trajectories intersect with a finite relative velocity. Note that the equation for σ decouples from the equation for R, so that it can be studied separately. Stationary statistics of σ can be described by the pdf $P(\sigma)$ which obeys the one-dimensional Fokker–Planck equation

$$\left[\partial_\sigma \left(\sigma/\tau + \sigma^2\right) + (C/2)\,\partial_\sigma^2\right] P(\sigma) = 0. \tag{26}$$

This equation can be rewritten as $\partial_\sigma J(\sigma) = 0$, where $J(\sigma) = (\sigma/\tau + \sigma^2)P(\sigma) + CP'(\sigma)/2$ is a probability flux in the σ-space. Eq. (26) is supplied by the boundary conditions $J(+\infty) = J(-\infty)$, which are required to resolve escapes to infinity and thus caustic formations. Indeed such events correspond to particle crossings during which $R \to 0$ and V remains finite, so that $\sigma = V/R$ changes sign. Hence, all particles escaping to $\sigma = +\infty$ reappear at $\sigma = -\infty$. The stationary solutions of Eq. (26) satisfying such a boundary condition corresponds to a constant flux J and can be written as

$$P(\sigma) = \frac{2|J|}{C} \mathrm{e}^{-2U(\sigma)/C} \int_{-\infty}^{\sigma} \mathrm{d}\sigma' \mathrm{e}^{2U(\sigma')/C}, \tag{27}$$

where $U(\sigma) = \sigma^3/3 + \sigma^2/2\tau$. Note that as in two dimensions, $P(\sigma)$ has power-law tails. The argument presented in Section 2 can actually be straightforwardly applied with the difference that there is no loop anymore but just escapes to infinity occurring with a probability that is independent of σ. This leads to $P(\sigma) \propto |\sigma|^{-2}$ for $|\sigma| \to \infty$ (the exponent is actually $-(1 + 1/h)$ in the general case of Hölder-continuous carrier flows).

Using the constant-flux solution (27), one can derive the Lyapunov exponent $\lambda = \langle\sigma\rangle$. As shown in [30], its value nontrivially depends on the Stokes number. For $St = D_1\tau \ll 1$, it is negative and behaves like $\lambda \simeq -D_1$ while for $St \gg 1$ it becomes positive and its value is given by the asymptotic expression $\lambda \simeq D_1 St^{-2/3}\sqrt{3}\,12^{5/6}\Gamma(5/6)/(24\sqrt{\pi}) > 0$. There exists a critical value of the Stokes number (≈ 0.827) for which the Lyapunov exponent changes its sign. This phenomenon of sign-changing has been dubbed *path coalescence transition* by Wilkinson and Mehlig in [30]. It is closely related to the aggregation-disorder transition discussed in [29]. The sign of the Lyapunov exponent determines how the distance between two initially close particles evolves with time. It turns out that the answer depends on the particle size: small particles (with small-enough Stokes numbers) tend to approach each other, while large particles (with large Stokes numbers) get separated by the flow.

Another important phenomenon which was extensively studied within the one-dimensional model is the formation of caustics. The average rate of caustics formation is given by the absolute value of the probability flux J. For large values of the Stokes number it can be written as $|J| \simeq D_1 St^{-2/3}\Gamma(5/6)12^{5/6}/(8\pi^{3/2})$, while for small Stokes it becomes exponentially small $|J| \sim D_1(2\pi St)^{-1}\exp[-1/(6St)]$. The formation of caustics is a stochastic process, whose properties can be described by the pdf of the caustic formation time T. In [31] it is shown that for $St \ll 1$ this pdf can be estimated as $P(T) \propto \exp[-1/(6St)]$ for $\tau \ll T \ll \tau\exp[1/(6St)]$ and $P(T) \propto \exp\left[-w/(3CT^3)\right]$, with $w = \Gamma(1/4)^8/96\pi^2$ (Γ denoting the Gamma function here), for $T \ll \tau$. The exponential factor $\exp[-1/(6St)]$ which characterizes the small rate of caustic formations for $St \ll 1$ can be easily explained if we formally consider Eq. (24) as a Langevin equation for a particle which is driven by the thermal noise $\eta(t)$ and evolves in the potential $U(\sigma)$. In this case, the rate of caustic formation is given by the probability for the particle to tunnel through the potential barrier in $U(\sigma)$. Such probability can be estimated as $\exp[-1/(6St)]$. For large Stokes numbers, the barrier disappears and the rate of caustic formation is not exponentially damped anymore.

6. Small Stokes number asymptotics

This section reports some asymptotic results related to the limit of small particle inertia. The first part summarizes the approach developed by Mehlig, Wilkinson, and collaborators for differentiable flows ($h = 1$). In analogy to the WKB approximation in quantum mechanics (see, e.g. [32]), the authors construct perturbatively the steady solution to the Fokker–Planck equation associated to the reduced system (8) and (9). In the second part of this section original results are reported where the particle dynamics is approximated as the advection by a synthetic flow comprising an effective compressible drift which accounts for leading-order corrections due to particle inertia.

Mehlig and Wilkinson proposed in [24] (see also [33]) to approach the limit of small Stokes numbers in terms of the variables $x_1 = (\tau/D_1)^{1/2}\sigma_1$ and $x_2 = (\tau/3D_1)^{1/2}\sigma_2$. From Eqs. (8) and (9), their time evolution follows to satisfy

$$\dot{x}_1 = -x_1 - \varepsilon\left[x_1^2 - 3x_2^2\right] + \sqrt{2}\,\eta_1(s), \tag{28}$$

$$\dot{x}_2 = -x_2 - 2\varepsilon x_1 x_2 + \sqrt{2}\,\eta_2(s), \tag{29}$$

where $\varepsilon = \sqrt{St}$, dots denote derivatives with respect to the rescaled time $s = t/\tau$ and η_1 and η_2 are independent white noises. The evolution equations (28) and (29) can be written in vectorial form, namely $\dot{\boldsymbol{x}} = -\boldsymbol{x} + \varepsilon\mathbf{V}(\boldsymbol{x}) + \sqrt{2}\,\boldsymbol{\eta}$, where $\boldsymbol{x} = (x_1, x_2)$, $\boldsymbol{\eta} = (\eta_1, \eta_2)$ and $\mathbf{V}$ denotes the quadratic drift. The steady-state probability density $p(\boldsymbol{x})$ is a solution to the stationary Fokker–Planck equation

$$\nabla_{\boldsymbol{x}}^2 p + \nabla_{\boldsymbol{x}}\cdot(\boldsymbol{x}p) = \varepsilon\nabla_{\boldsymbol{x}}\cdot[\mathbf{V}(\boldsymbol{x})p]. \tag{30}$$

The next step consists in writing perturbatively the probability density of $\boldsymbol{x}$ as $p(\boldsymbol{x}) = \exp(-|\boldsymbol{x}|^2/4)\,(Q_0 + \varepsilon Q_1 + \varepsilon^2 Q_2 + \cdots)$. The functions Q_k satisfy the recursion relation $\mathcal{H}_0 Q_{k+1} = \mathcal{H}_1 Q_k$, where

$$\mathcal{H}_0 = 1 + \nabla_{\boldsymbol{x}}^2 - |\boldsymbol{x}|^2/4, \tag{31}$$

$$\mathcal{H}_1 = \nabla_{\boldsymbol{x}}\cdot\mathbf{V}(\boldsymbol{x}) + \boldsymbol{x}\cdot\mathbf{V}(\boldsymbol{x})/2. \tag{32}$$

The operator $\mathcal{H}_0$ is the Hamiltonian of an isotropic two-dimensional quantum harmonic oscillator. This suggests introducing creation and annihilation operators and to expand the functions Q_k in terms of the eigenstates of the harmonic oscillator (see [24,33] for details).

This approach yields a perturbative expansion of the Lyapunov exponent [24]

$$\lambda = D_1\langle x_1\rangle/\varepsilon = 2D_1\sum_{k\geq 0} a_k\varepsilon^{2k} = 2D_1\sum_{k\geq 0} a_k St^k, \tag{33}$$

where the coefficients a_k satisfy the recurrence relation

$$a_{k+1} = 4(4-3k)a_k - 2\sum_{\ell=0}^{k} a_\ell a_{k-\ell}, \tag{34}$$

with $a_0 = 1$. For large k, these coefficients behave as $a_k \sim (-12)^k k!$, so that the series (33) diverges no matter how small the value of ε (and thus of St). Hence the sum representation of λ makes sense as an approximation only if truncated at an index $k_\star$ for which $|a_k St^k|$ attains its minimum. For small values of St, $k_\star \sim 1/(12St)$ and the error of the asymptotic approximation is of the order of the smallest term, namely $\sim |a_{k_\star} St^{k_\star}| \sim \exp[-1/(12St)]$. This approach was refined by Wilkinson et al. [33] adopting an approach based on Padé–Borel summation, which was found to yield satisfactory results.

The nonanalyticity of $\lambda(St)$ at $St = 0$ is interpreted in [24] as a drawback of the perturbative approach. Indeed the quadratic terms in (28) and (29) are not negligible for all values of x_1 and x_2: When $|\boldsymbol{x}|$ becomes larger than ε^{-1} they are actually dominant and the trajectory performs a loop in the $\boldsymbol{x}$ (or $\boldsymbol{\sigma}$) plane (see Section 2). When $St = \varepsilon^2$ is small, the probability to initiate such a loop is given by the tail of the distribution governing scales $|\boldsymbol{x}| \ll \varepsilon^{-1}$, and is hence $\propto \exp[-1/(6\varepsilon^2)]$, which coincides with the one-dimensional result discussed in previous section, confirming the relevance of $d = 1$ physics to the formation of caustics in higher dimension. Taking into account this correction due to *caustics*, i.e. the contribution of events when the particles approach very close to each other keeping a finite velocity difference, Mehlig and Wilkinson proposed to write the Lyapunov exponent as

$$\lambda/D_1 \sim B\, St^{-1}\mathrm{e}^{-1/(6St)} + 2\sum_{k=0}^{k_\star} a_k St^k, \tag{35}$$

where B is a positive constant. We finish this summary by stressing that this approach equally applies to the case of compressible carrier flows [24], and was extended to three dimensions where it yields a prediction on the St-dependence of the three largest Lyapunov exponents [33].

The above perturbative approach can be generalized to small particles evolving in rough flows. For small (local) Stokes numbers, the characteristic time scales of velocity evolution are much smaller compared to the temporal scales associated to the dynamics of the particle separation. Therefore, we can obtain the effective equation for the evolution of particle separation by averaging over the fast velocity difference variables. The systematic mathematical strategy of such an averaging was proposed in [34] in the context of stochastic climate models. This strategy is closely related to the Nakajima–Zwanzig technique which was developed to study similar problems arising in damping theory [35,36]. Applications of this technique to the elimination of fast variables in Fokker–Planck equations are discussed in [37,38]. In this framework we can derive an expansion for the Fokker–Planck type operator entering into the equation for the slow-variable probability distribution function. In our case, this leads to a closed equation for the pdf of the particle separation R. This equation can be used to determine the local correlation dimension $d_2(r)$ for $St(r) \ll 1$. We present here only the general idea and the main results; details of the calculations will be reported elsewhere.

To carry out the above-mentioned procedure the joint position-velocity pdf $p(\boldsymbol{r}, \boldsymbol{v})$ is approximated by

$$p(\boldsymbol{r}, \boldsymbol{v}) \simeq p(\boldsymbol{r}) P_{\boldsymbol{r}}(\boldsymbol{v}) + \tilde{p}(\boldsymbol{r}, \boldsymbol{v}), \tag{36}$$

where $\tilde{p}(\boldsymbol{r}, \boldsymbol{v})$ denotes subleading terms which are $\mathrm{O}(St)$; $P_{\boldsymbol{r}}(\boldsymbol{v})$ is the stationary distribution associated to the fast velocity variables and satisfies the Fokker–Planck equation

$$\hat{L}_0\, P_{\boldsymbol{r}}(\boldsymbol{v}) \equiv -\left[\frac{1}{\tau}\partial_v^i v^i + \frac{b^{ij}(\boldsymbol{r})}{\tau^2}\partial_v^i\partial_v^j\right] P_{\boldsymbol{r}}(\boldsymbol{v}) = 0, \tag{37}$$

with the normalization condition $\int \mathrm{d}\boldsymbol{v}\, P_{\boldsymbol{r}}(\boldsymbol{v}) = 1$. Without loss of generality, it is assumed that the subleading terms $\tilde{p}(\boldsymbol{r}, \boldsymbol{v})$ in the approximation (36) do not contribute to the normalization condition, so that $\int \mathrm{d}\boldsymbol{v}\, p(\boldsymbol{r}, \boldsymbol{v}) = p(\boldsymbol{r})$. The effective equation for $p(\boldsymbol{r})$ can be derived by introducing the expansion $p(\boldsymbol{r}) = \sum_{k=0}^{\infty} St^{k/2} p_k(\boldsymbol{r})$. This expansion, which enters the definition (36), is then substituted into (4) and all terms of the same order in St are collected. Note that the operator $\hat{L}_1 = \partial_r^i v^i$ entering Eq. (4) is smaller than the other operators by a factor $St^{1/2}$. The chain of equations for $p_k(\mathbf{r})$ has a solvability condition that results in the following effective equation for $p(\boldsymbol{r})$:

$$\left(\hat{M}_1 + \hat{M}_2 + \cdots\right) p(\boldsymbol{r}) = 0, \tag{38}$$

where the operators $\hat{M}_k$ can be written as

$$\hat{M}_k\, p(\boldsymbol{r}) = \int \mathrm{d}\boldsymbol{v}\, \left(\hat{L}_1 \hat{L}_0^{-1}\right)^k \hat{L}_1\, p(\boldsymbol{r})\, P_{\boldsymbol{r}}(\boldsymbol{v}). \tag{39}$$

$\hat{L}_0^{-1}$ denotes here the inverse of $\hat{L}_0$, i.e. the Green function obtained from (37) with the right-hand side replaced by a δ-function. This operator is defined in such a way that $\int \mathrm{d}\boldsymbol{v}\, \hat{L}_0^{-1} f(\boldsymbol{v}) = 0$ for any function $f(\boldsymbol{v})$ satisfying $\int \mathrm{d}\boldsymbol{v}\, f(\boldsymbol{v}) = 0$. One can check that the leading-order operator is $\hat{M}_1 = \partial_r^i b^{ij}(\boldsymbol{r})\partial_r^j$ which, as expected, corresponds to turbulent diffusion. Indeed the dynamics of tracers is recovered when $St \to 0$. The pdf $p(\boldsymbol{r})$ which solves the equation $\hat{M}_1 p(\boldsymbol{r}) = 0$ is simply the uniform distribution. To measure particle clustering, which can be estimated, for instance, by the local correlation dimension $d_2(r)$ (see Section 3), we have to calculate the next order operators. It can be easily checked that all operators $\hat{M}_k$ of even order k are zero. The first nonvanishing correction to $\hat{M}_1$ is thus given by the third-order operator $\hat{M}_3$. When interested in the stationary distribution only, the terms which enter this operator and which are associated to transients can be disregarded and we can write

$$\hat{M}_3 \cdot = \partial_r^i [V^i \cdot], \quad \text{with}$$

$$V^i = -\frac{1}{2}\left(\partial_r^k \partial_r^l b^{ij}\right)\left(\partial_r^j b^{kl}\right). \tag{40}$$

The operator $\hat{M}_3$ can be interpreted as an effective drift in $\boldsymbol{r}$-space and, for the Kraichnan model, represented as $V^i = -2(d^2 - 1)(d - 2 + 4h)h^2 St^2(r) r^i$. The functional form of this drift implies that the first nonvanishing corrections to the uniform distribution are proportional to $St(r)$. Indeed, for isotropic flows one can look for a solution $p(\boldsymbol{r})$, which depends only on the modulus r of its argument. In this case Eq. (38) becomes an ordinary differential equation of Fokker–Planck type. Looking for a nonflux solution we readily obtain the desired $p(r)$. In rough flows ($h < 1$), we have $\ln p(\boldsymbol{r}) \sim [(d+1)(d-2+2h)h^2/(1-h)]\, St(r)$ and the local correlation dimension behaves as

$$d_2(r) \simeq d - \frac{2d(d+1)(d-2+4h)h^2}{d-2+2h} St(r). \tag{41}$$

Note that the second term on the right-hand side of the above expression disappears for $h \to 0$, confirming once again the finding of the previous sections about the decrease of clustering going from smooth to rough flows. For differentiable carrier flows ($h = 1$), the distribution has algebraic tails: $\ln p(\boldsymbol{r}) \sim -2(d+1)(d+2) St \ln r$, and hence the correlation dimension behaves as

$$\mathcal{D}_2 = d - 2(d+1)(d+2)\, St + \mathrm{O}(St^2). \tag{42}$$

The dimension deficit $d - \mathcal{D}_2$ is equal to $24St$ for two-dimensional flows and to $d - \mathcal{D}_2 = 40St$ for three-dimensional

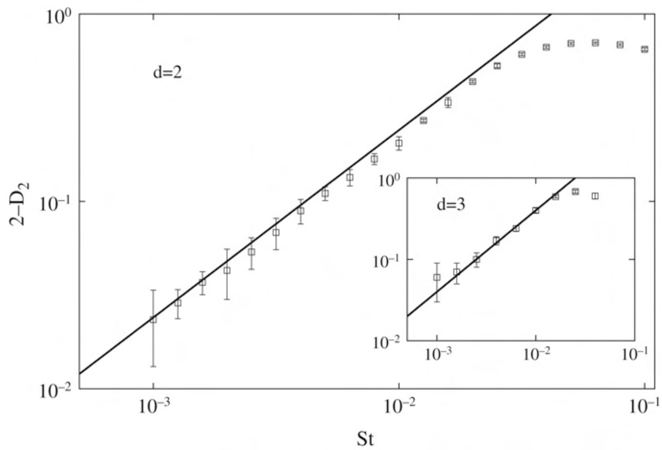

Fig. 8. Dimensional deficit $2-\mathcal{D}_2$ versus St in $d=2$ for smooth flows ($h=1$). Inset: same for $d=3$. Points represent numerical results and the straight line corresponds to the perturbative predictions given by (42) for $d=2$ and 3 respectively.

ones. The latter result is in agreement with the dimension deficit of the Lyapunov dimension reported by Wilkinson et al. in [33].

Testing with high accuracy the prediction obtained for rough flows requires a large numerical investment that is beyond the scope of the current work. It was, however, checked that there is no detectable disagreement between (41) and the results reported in Section 3. For smooth flows, the leading-order behaviour (42) obtained above for the dimension deficit is in very good agreement with numerical simulations in two and three dimensions, as can be seen from Fig. 8. To conclude this section we notice that in time-correlated random smooth flows, as well as in developed turbulence, the dimension deficit has been shown to be $\propto St^2$ [5,11,39,40]. Therefore, including temporal correlations seems to be crucial to reproduce the details of the small-Stokes statistics of turbulent suspensions.

7. Large Stokes number asymptotics

Particles with huge inertia ($St \gg 1$) take an infinite time to relax to the velocity of the carrier fluid. They become therefore uncorrelated with the underlying flow and evolve with ballistic dynamics, moving freely and maintaining, almost unchanged, their initial velocities. This limit is particularly appealing for deriving asymptotic theories [16]. In this section, we focus on two aspects, namely the problem of the recovery of homogeneous/uniform distribution for $St \gg 1$ and the problem of the asymptotic scaling for the statistics of the particle separation and of the velocity differences.

7.1. Saturation of the correlation dimension

Ballistic particles injected homogeneously and uniformly remain so [41]. Hence for the correlation dimension associated with their distribution (13) we have $\mathcal{D}_2 = d$. This result follows directly from the Fokker–Planck equation (4), which can be seen as an advection-diffusion equation in phase space. The effective flow is compressible because of the term $-\partial_v v/\tau$ but, in the limit $St \to \infty$, it becomes negligible and the equation reduces to diffusion plus advection by an incompressible flow. The resulting stationary pdf is thus uniform in phase space and hence in its projection in position space. Moreover, as particle velocities and fluid flow are uncorrelated and consequently the particles are not correlated with each other, the exponent Γ which characterizes the small-scale behaviour of the approaching rate (see Section 3) vanishes. Thus $\mathcal{D}_2 \to d$ and $\Gamma \to 0$ for $St \to \infty$.

This asymptotic regime can be achieved *via* two possible scenarios: (a) asymptotic convergence of $\mathcal{D}_2$ to d, and (b) saturation of $\mathcal{D}_2$ to d for Stokes numbers above a critical value $St^\dagger$. In what follows, we provide evidence for (b), limiting the discussion to two-dimensional smooth flows.

Let us first discuss a phenomenological argument in favor of saturation. As already noted in Section 3, their dissipative dynamics yields the phase-space trajectories of the particles to converge onto a random, dynamically evolving attractor, which is typically characterized by a multifractal measure [19,20]. In our setting, this measure is the phase-space correlation dimension defined in Eq. (14). Ballistic motion for $St \gg 1$ corresponds to $\overline{\mathcal{D}}_2 \to 2d$, therefore a critical Stokes number $St^\dagger$ exists such that $\overline{\mathcal{D}}_2(St^\dagger) = d$. The particles' spatial distribution is obtained by projecting the $(2\times d)$-dimensional phase space onto the d-dimensional physical space. It is tempting to apply a rigorous result on the projection of random fractal sets [22,42] stating that for *almost all* projections, the correlation dimension of the projected set is related to that of the unprojected one *via* the relation

$$\mathcal{D}_2 = \min\{d, \overline{\mathcal{D}}_2\}. \qquad (43)$$

Having $\overline{\mathcal{D}}_2(St^\dagger) = d$ with the above expression implies that $\mathcal{D}_2(St) = d$ for all $St \geq St^\dagger$. Unfortunately, there is *a priori* no reason for assuming some kind of isotropy in phase space which justifies the validity of (43). We thus proceed numerically.

As Eq. (43) requires the isotropy of the set, we have tested whether this applies to our case. The correlation dimension of different two-dimensional projections was evaluated through the computation of the probabilities $P_2^{\alpha,\beta}(r)$ of having two particles at a distance less than r using the norm $\Delta^2_{\alpha,\beta} = \delta^2_\alpha + \delta^2_\beta$, with $\alpha, \beta = X, Y, V_X/D_1, V_Y/D_1$, and δ_α denoting the coordinate-α separation between the two particles. Note that $\alpha = X$ and $\beta = Y$ corresponds to the spatial correlation dimension discussed so far. Fig. 9 shows the logarithmic derivatives $(\mathrm{d}\ln P_2^{\alpha,\beta}(r))/(\mathrm{d}\ln r)$ for various α, β and three different values St. All curves collapse within error-bars, confirming that the projection is rather typical and thus strengthening the argument in favour of saturation. However, as can be seen in Fig. 9, the logarithmic derivatives on the different projections are curved, indicating behaviours different from the expected power law. It is therefore difficult to decide whether or not the saturation occurs. As discussed in [44], one can understand the curvature of the local slopes with the presence of subdominant terms, e.g. with the superposition of two power laws $P_2(r) \simeq Ar^a + Br^b$. In our case, we can expect that

$$P_2(r) = Ar^{\overline{\mathcal{D}}_2} + Br^d, \qquad (44)$$

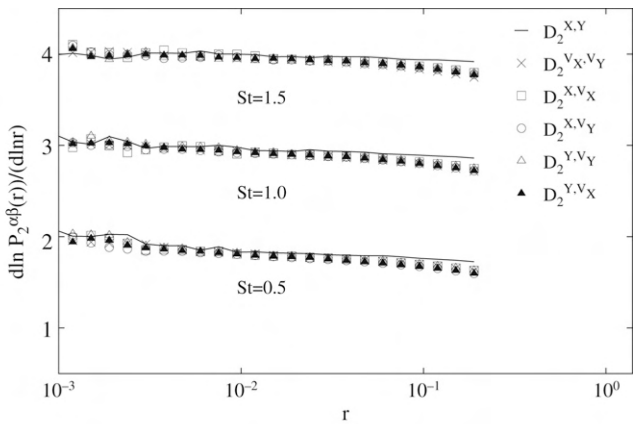

Fig. 9. Logarithmic derivative $(\mathrm{d}\ln P_2^{\alpha,\beta}(r))/(\mathrm{d}\ln r)$ for different projections α, β for $St = 0.5$, $St = 1$ (shifted up by a factor 1), and $St = 1.5$ (shifted up by a factor 2). A small mismatch in the scaling range can observed for large r (this is unavoidable as positions and velocities involve different scales).

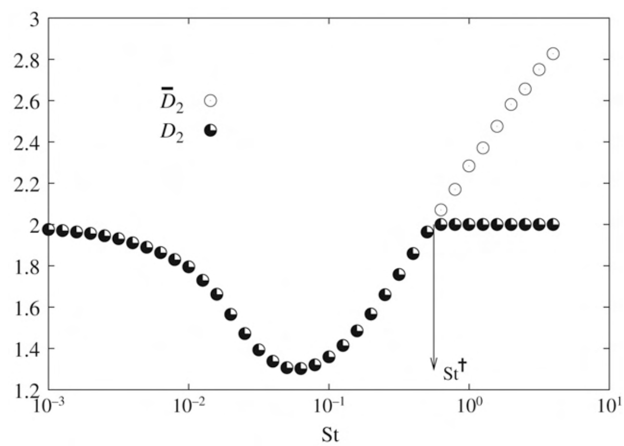

Fig. 10. Physical space $\mathcal{D}_2$, and phase-space $\overline{\mathcal{D}}_2$ correlation dimensions versus St as obtained by using (44) for fitting the exponents. Errors are of the order of the size of the symbol. The arrow indicates the estimated location of $St^\dagger$.

where d and $\overline{\mathcal{D}}_2$ are the only dimensions entering the problem [16]. For $\overline{\mathcal{D}}_2 < d$, the second power law can be interpret also as the contribution of caustics [26,18]: With nonzero probability, particles may be very close to each other with quite different velocities, see Section 5. Once projected onto physical space, caustics appear as spots of uncorrelated particles, and hence, the correlation dimension is locally $\mathcal{D}_2 = d$. The validity of (44) as well as of the projection formula (43) was confirmed in Ref. [16].

Fig. 10 summarizes the results depicted above. In particular, $\overline{\mathcal{D}}_2$ clearly displays a crossover to values larger than d for $St > St^\dagger \approx 0.6$. $\mathcal{D}_2$, once properly estimated by using (43), displays the saturation to $d = 2$ above $St^\dagger$, at which the large Stokes asymptotics starts, at least for the particle distribution.

Let us comment briefly on the implication of saturation on the behaviour of the approaching rate which, in the limit $St \to \infty$, is characterized by the exponent $\Gamma \to 0$. Similarly to $\mathcal{D}_2$, deviations of Γ from its limiting value cannot be determined by scaling arguments. Saturation of $\mathcal{D}_2$ would, however, affect Γ. This is related to the dominant contribution of caustics which might imply also the saturation of Γ to 0 for sufficiently large

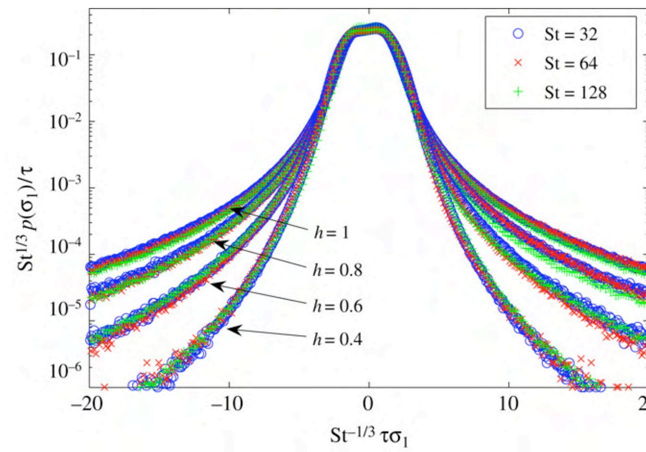

Fig. 11. Pdf of the non-dimensional longitudinal velocity difference σ_1 at large values St (symbols are for different values) for various values of h.

Stokes numbers. Though numerical experiments confirm this scenario [16], saturation cannot be studied with as much detail as for $\mathcal{D}_2$. At present, there is no simple phenomenological argument for the subleading terms as for $\mathcal{D}_2$.

7.2. Scaling arguments

The limit of large values of the Stokes number can be approached by assuming $\tau \to \infty$ and keeping $C = 2D_1/(\tau L^{1-h})^2$ constant. The dynamics (8) and (9) for the relative velocity differences can then be approximated by

$$\dot{\sigma}_1 \simeq -\left(h\sigma_1^2 - \sigma_2^2\right)/\rho + \sqrt{C}\,\eta_1, \tag{45}$$

$$\dot{\sigma}_2 \simeq -(h+1)\sigma_1\sigma_2/\rho + \sqrt{(1+2h)C}\,\eta_2\,. \tag{46}$$

For a given exponent h, the limiting dynamics depends solely on C while – after nondimensionalizing time and relative velocities by τ – the general dynamics depends on $St(L)$ only (see the Introduction). This congruence, which was first used in [45] for determining the large-St behavior of the Lyapunov exponent, allows to derive scaling arguments of various other quantities characterizing two-particle dynamics.

Let us detail this for the distribution of the longitudinal velocity difference σ_1. It is clear from the above considerations that for fixed h and $\sigma_1 \gg (1/\tau)$ the following relation holds:

$$\tau\,\tilde{p}(\tau\sigma_1; St) \simeq p(\sigma_1; C). \tag{47}$$

Differentiating with respect to D_1 and τ gives a necessary condition for such a behaviour: p must satisfy

$$p + \sigma_1\partial_{\sigma_1} p + 3C\,\partial_C\, p = 0, \tag{48}$$

which itself implies $p(\sigma_1; C) = C^{-1/3} f(C^{-1/3}\sigma_1)$, so that

$$p(\sigma_1) \simeq St^{-1/3}\tau f(St^{-1/3}\tau\sigma_1) \quad \text{for } St \gg 1. \tag{49}$$

As shown in Fig. 11 this asymptotic scaling behaviour can be observed numerically. As a consequence of (49), for differentiable carrier flows ($h = 1$) the Lyapunov exponent

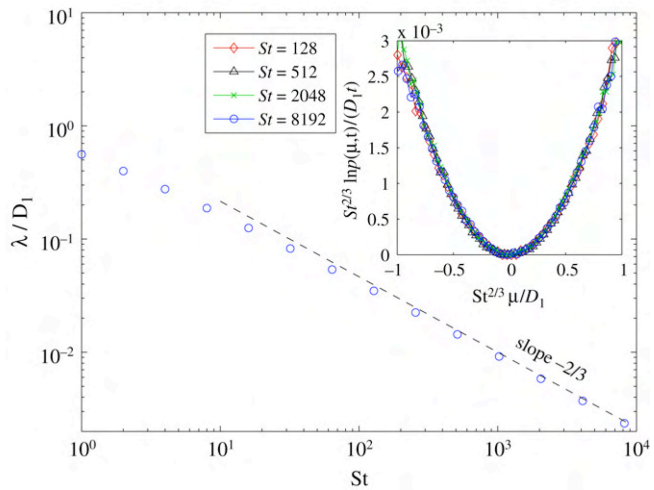

Fig. 12. Lyapunov exponent λ versus St. The dashed line is the asymptotic prediction (50). Inset: rate function $H(\mu)$ for various large values of St.

$\lambda = \langle\sigma_1\rangle$, which measures the asymptotic growth rate of the interparticle distance (see Section 4), behaves as

$$\lambda \simeq c D_1 St^{-2/3} \quad \text{for } St \gg 1, \tag{50}$$

where c is a parameter-independent positive constant. Note that the original derivation [45] of this law applies also to compressible carrier flows, so the constant c depends on the compressibility of the fluid velocity field. It is shown in [16] that this result also holds in three dimensions. Its confirmation by numerical simulations is illustrated in Fig. 12.

The scaling argument described above can be carried forward to the fluctuations of the stretching rate $\mu(t) = (1/t)\ln[R(t)/R(0)]$. As we have seen in Section 4, for large times the distribution of μ obeys the large deviation principle (21). It can be shown (see [16] for details) that the associated rate function $H(\mu) = \lim_{t\to\infty}(1/t)\ln p(\mu, t)$ satisfies

$$H(\mu) \simeq D_1 St^{-2/3} h(St^{2/3}\mu/D_1) \quad \text{for } St \gg 1. \tag{51}$$

This scaling is confirmed numerically (inset of Fig. 12).

We finally comment on how the stretching rate fluctuations change with St. Taylor expansion of H around its minimum together with the scaling behaviour (51) shows that the standard deviation of the stretching rate is of the order of $St^{-1/3}/\sqrt{t}$. For a given time t, the stretching rate μ distributes more and more sharply around λ when St increases. This behaviour was anticipated by the numerical measurements reported in Section 4 and is observed in direct numerical simulations of heavy particles in homogeneous isotropic flows [27].

8. Remarks and conclusions

Before concluding this paper the results discussed so far are commented in the light of what is known about real turbulent suspensions, which are relevant to most applications. Let us start by recalling the main features of turbulent flows. Turbulence is a multiscale phenomenon [46] which spans length scales ranging from a large (energy injection) scale L to the very small (dissipative) scale η, often called the Kolmogorov scale. This hierarchy of length scales is associated with a hierarchy of time scales: from the large-scale eddy turnover time τ_L to the Kolmogorov time τ_η. Both ratios L/η and τ_L/τ_η increase with the Reynolds number Re of the turbulent flow. Therefore, in general settings, no separation of time scales can be invoked to simplify the motion of suspended particles. However, in two circumstances simplifications are possible, namely:

(i) For particles with a response time τ much greater than τ_L, the fluid velocity seen by the particle can be approximated by a random flow belonging to the Kraichnan ensemble, as discussed in this paper. Then a Hölder exponent $h = 1$ or $h < 1$ is chosen to study the dissipative or inertial scales of turbulence, respectively.

(ii) For intermediate response times $\tau_\eta \ll \tau \ll \tau_L$, at least for single or two-particle motions, the fluid velocity seen by the particles can be approximated by an anisotropic generalization of the Kraichnan model [47].

In both asymptotics, the Kraichnan model and its generalization allow for predictions on single- and two-particle properties, many of them were discussed throughout this paper. In the following we discuss them in the context of turbulent suspensions. We focus mostly on two-particle properties at dissipative and inertial scales.

Dissipative range. At such small scales, particles form (multi)fractal clusters, which can be quantitatively characterized by the St-dependence of the correlation dimension $\mathcal{D}_2$ or, equivalently, of the dimensional deficit $d - \mathcal{D}_2$ (in turbulence one can define $St = \tau/\tau_\eta$). Numerical studies [10,50] show that the qualitative St-dependence of $\mathcal{D}_2$ is similar to that observed in the Kraichnan model. Despite such similarities, it is likely that in turbulence, ejection from vortical regions play, at least for small St, an important role [50]. This can clearly not be accounted for in Kraichnan flows, as δ-correlated flows have no persistent structures. The absence of time correlations certainly affects also the scaling behaviour when $St \ll 1$ of the dimension deficit: while in turbulence [5,40] and time-correlated stochastic flows [11,39] it is observed that $d - \mathcal{D}_2 \propto St^2$, we have shown here that the behaviour is linear in St. These discrepancies originate from the fact that white-in-time carrier flows are valid approximations of turbulence only for $St \gg 1$.

Another question concerns the relative dispersion of a particle pair. In the dissipative range, the velocity field is smooth, so that particles separate exponentially with a rate given by the largest Lyapunov exponent λ. If $\tau \gg \tau_L$ the results presented in previous sections should apply, i.e. $\lambda \propto St^{-2/3}$. For $\tau_\eta \ll \tau \ll \tau_L$, the anisotropic generalization of the Kraichnan model predicts $\lambda \propto St^{-5/6}$ [47]. However, the measurements of Lyapunov exponents made up to now (see e.g. [27]) do not involve high-enough Stokes and Reynolds numbers to test the validity of these predictions in turbulent flows

Inertial range. As shown in this paper, for rough Kraichnan-type carrier flows, particles also form clusters which are, however, not fractal as they were in the dissipative range. This seems to be in qualitative agreement with the observations made in the inertial range of turbulence: Inhomogeneities have been found in $2d$ turbulence in the inverse cascade regime [48, 49] as well as in 3d turbulence [50,51]. However, while in the Kraichnan case the particle distribution depends on the local Stokes number $St(r)$ only, this does not seem to be the case in turbulence, at least for $St(r) \ll 1$ as studied in [50] (which in turbulence is defined by $St(r) = \tau/\tau_r$, τ_r being the characteristic turbulent time scale associated to the scale r). In turbulent flows, for small values of $St(r)$ a different rescaling related to that of the acceleration (and hence pressure) field has been found [50]. However such discrepancies do not question the relevance of the Kraichnan model to turbulent flows as it is expected to be a good approximation only for scales r such that $\tau_r \ll \tau$, i.e. $St(r) \gg 1$. Experiments or direct numerical simulations with high Re and St are thus needed to actually test the validity of the dynamic scaling in terms of $St(r)$ and to reproduce an equivalent of Fig. 3 for turbulent flows. As far as particle separation is concerned, we have seen in Section 4 that at very long times, and thus for separations r such that $\tau \ll \tau_r$ one should expect to observe Richardson dispersion. For intermediate times at which the separation is such that $\tau_\eta \ll \tau_r \ll \tau$, it is predicted in [47] that an intermediate asymptotic regime may emerge with the typical particle separation r growing as t^9, i.e. much faster than Richardson diffusion. On the numerical and experimental side, we are not aware of any results on the relative dispersion of two heavy particles in the inertial range. Testing the above predictions can be probably done only in experiments where Re can be very high.

In summary, this paper reviewed most of current understanding of heavy particle suspensions in Kraichnan-like stochastic flows. In particular, we examined in details two-particle statistics both in smooth and rough velocity fields. Numerical simulations, validated by analytics originally derived in this paper, show that particle clustering is more efficient for smooth than rough flows, and can be characterized in terms of the local Stokes number. Detailed predictions can be done in the very small and very large Stokes number asymptotics. In the former we provided an analytical expression for the dimensional deficit for any value of the fluid Hölder exponent. More specifically, it is shown that the departure from a uniform distribution is linear in the Stokes number, a result which is confirmed by numerics. As for the evolution of the relative separation of particle pairs at small separations, a well-verified asymptotic behaviour for the Lyapunov exponent is discussed. At larger scales, by converting the scale-dependent Stokes number into a time-dependent one, we provided an original way to account for the recovering of tracer-like Richardson diffusion. Finally, the relevance of these results, together with other predictions obtained in recent years from Kraichnan-like models of heavy particle suspensions, to particles in turbulent flows has been discussed.

To conclude this work we suggest two different directions for further investigations. First, most of the predictions related to the large-Stokes asymptotics lack numerical or experimental evidence in fluid flows with high Reynolds numbers and particles with huge inertia. Second, it is now definitely clear that an important challenge for the near future is to understand whether or not some of the techniques developed for suspensions in random time-uncorrelated flows can be generalized/extended to time-correlated flows. For instance, a quantitative understanding of the small-Stokes-number asymptotics in models that are closer to turbulence would be of great interest to many applications. A first step in this direction has been recently attempted in [52].

Acknowledgments

We acknowledge useful discussions with S. Musacchio and M. Wilkinson. Part of this work was done while K.T. was visiting Lab. Cassiopée in the framework of the ENS-Landau exchange programme. J.B. was partially supported by ANR "DSPET" BLAN07-1_192604.

References

[1] R.H. Kraichnan, Small-scale structure of a scalar field convected by turbulence, Phys. Fluids 11 (1968) 945–953.
[2] G. Falkovich, K. Gawędzki, M. Vergassola, Particles and fields in fluid turbulence, Rev. Modern Phys. 73 (2001) 913–975.
[3] H. Pruppacher, J. Klett, Microphysics of Clouds and Precipitation, Kluwer Academic Publishers, Dordrecht, 1996.
[4] M.B. Pinsky, A.P. Khain, Turbulence effects on droplet growth and size distribution in clouds— a review, J. Aerosol. Sci. 28 (1997) 1177–1214.
[5] G. Falkovich, A. Fouxon, M.G. Stepanov, Acceleration of rain initiation by cloud turbulence, Nature 419 (2002) 151–154.
[6] B.J. Rothschild, T.R. Osborn, Small-scale turbulence and plankton contact rates, J. Plankton Res. 10 (1988) 465–474.
[7] S. Sundby, P. Fossum, Feeding conditions of Arcto-Norwegian cod larvae compared with the Rothschild–Osborn theory on small-scale turbulence and plankton contact rates, J. Plankton Res. 12 (1990) 1153–1162.
[8] J. Mann, S. Ott, H.L. Pécseli, J. Trulsen, Predator–prey encounters in turbulent waters, Phys. Rev. E 65 (2002) 026304.
[9] J.K. Eaton, J.R. Fessler, Preferential concentration of particles by turbulence, Int. J. Multiphase Flow 20 (1994) 169–209.
[10] R.C. Hogan, J.N. Cuzzi, Stokes and Reynolds number dependence of preferential particle concentration in simulated three-dimensional turbulence, Phys. Fluids 13 (2001) 2938–2945.
[11] J. Bec, Fractal clustering of inertial particles in random flows, Phys. Fluids 15 (2003) L81–L84.
[12] G. Falkovich, A. Fouxon, M. Stepanov, in: A. Gyr, W. Kinzelbach (Eds.), Sedimentation and Sediment Transport, Kluwer Academic Publishers, Dordrecht, 2003, pp. 155–158.
[13] J. Bec, M. Cencini, R. Hillerbrand, Clustering of heavy particles in random self-similar flow, Phys. Rev. E 75 (2007) 025301.
[14] L.I. Piterbarg, The top Lyapunov exponent for stochastic flow modeling the upper ocean turbulence, SIAM J. Appl. Math. 62 (2002) 777–800.
[15] K. Duncan, B. Mehlig, S. Östlund, M. Wilkinson, Clustering by mixing flows, Phys. Rev. Lett. 95 (2005) 240602.
[16] J. Bec, M. Cencini, R. Hillerbrand, Heavy particles in incompressible flows: The large Stokes number asymptotics, Physica D 226 (2007) 11–22.
[17] W.C. Reade, L.R. Collins, Effect of preferential concentration on turbulent collision rates, Phys. Fluids 12 (2000) 2530–2540.
[18] J. Bec, A. Celani, M. Cencini, S. Musacchio, Clustering and collisions of heavy particles in random smooth flows, Phys. Fluids 17 (2005) 073301.
[19] J.-P. Eckmann, D. Ruelle, Ergodic theory of chaos and strange attractors, Rev. Modern Phys. 57 (1985) 617–656.
[20] G. Paladin, A. Vulpiani, Anomalous scaling laws in multifractal objects, Phys. Rep. 156 (1987) 147–225.
[21] L. Arnold, Random Dynamical Systems, Springer Monographs in Mathematics, Berlin, New York, 2003.
[22] T.D. Sauer, J.A. Yorke, Are the dimensions of a set and its image equal under typical smooth functions? Ergodic Theory Dynam. Syst. 17 (1997) 941–956.

[23] L.-P. Wang, A.S. Wexler, Y. Zhou, On the collision rate of small particles in isotropic turbulence. Part I. Zero-inertia case, Phys. Fluids 10 (1998) 266–276;
Y. Zhou, L.-P. Wang, A.S. Wexler, On the collision rate of small particles in isotropic turbulence. Part II. Finite-inertia case, Phys. Fluids 10 (1998) 1206–1216.
[24] B. Mehlig, M. Wilkinson, Coagulation by random velocity fields as a Kramers problem, Phys. Rev. Lett. 92 (2004) 250602.
[25] B. Mehlig, M. Wilkinson, K. Duncan, T. Weber, M. Ljunggren, Aggregation of inertial particles in random flows, Phys. Rev. E 72 (2005) 051104.
[26] M. Wilkinson, B. Mehlig, Caustics in turbulent aerosols, Europhys. Lett. 71 (2005) 186–192.
[27] J. Bec, L. Biferale, G. Boffetta, M. Cencini, S. Musacchio, F. Toschi, Lyapunov exponents of heavy particles in turbulence, Phys. Fluids 18 (2006) 091702.
[28] K. Gawędzki, M. Vergassola, Phase transition in the passive scaler advection, Physica D 138 (2000) 63–90.
[29] J.M. Deutsch, Aggregation-disorder transition induced by random forces, J. Phys. A 18 (1985) 1449–1456.
[30] M. Wilkinson, B. Mehlig, Path coalescence transition and its applications, Phys. Rev. E 68 (2003) 040101.
[31] S. Derevyanko, G. Falkovich, K. Turitsyn, S. Turitsyn, Lagrangian and Eulerian descriptions of inertial particles in random flows, J. Turbul. 8 (1) (2007) 1–18.
[32] R. Liboff, Introductory Quantum Mechanics, Addison-Wesley, 2003.
[33] M. Wilkinson, B. Mehlig, S. Östlund, K.P. Duncan, Unmixing in random flows. Preprint nlin.CD/0612061, 2006.
[34] A. Majda, I. Timofeyev, E. Vanden Eijnden, A mathematical framework for stochastic climate models, Comm. Pure Appl. Math. 54 (2001) 891–974.
[35] S. Nakajima, On quantum theory of transport phenomena: Steady diffusion, Progr. Theoret. Phys. 20 (1958) 948–959.
[36] R. Zwanzig, Ensemble method in the theory of universality, J. Chem. Phys. 33 (1960) 1338–1341.
[37] H. Risken, The Fokker–Planck Equation, Springer-Verlag, Berlin, 1989.
[38] S. Chaturvedi, F. Shibata, Time-convolutionless operator formalism for elimination of fast variables. Applications to Brownian motion, Zeit. Phys. B 35 (1979) 297–308.
[39] L.I. Zaichik, V. Alipchenkov, Pair dispersion and preferential concentration of particles in isotropic turbulence, Phys. Fluids 15 (2003) 1776–1787.
[40] G. Falkovich, A. Pumir, Intermittent distribution of heavy particles in a turbulent flow, Phys. Fluids 16 (2004) L47–L50.
[41] H. Sigurgeirsson, A.M. Stuart, A model for preferential concentration, Phys. Fluids 14 (2002) 4352–4361.
[42] B. Hunt, V. Kaloshin, How projections affect the dimension spectrum of fractal measures, Nonlinearity 10 (1997) 1031–1046.
[43] E. Balkovsky, G. Falkovich, A. Fouxon, Intermittent distribution of inertial particles in turbulent flows, Phys. Rev. Lett. 86 (2001) 2790–2793.
[44] L. Biferale, M. Cencini, A. Lanotte, M. Sbragaglia, F. Toschi, Anomalous scaling and universality in hydrodynamic systems with power-law forcing, New J. Phys. 6 (2004) 37.
[45] P. Horvai, Lyapunov exponent for inertial particles in the 2D Kraichnan model as a problem of Anderson localization with complex valued potential, Preprint nlin.CD/0511023, 2005.
[46] U. Frisch, Turbulence: The Legacy of A.N. Kolmogorov, Cambridge University Press, Cambridge UK, 1995.
[47] I. Fouxon, P. Horvai, Single and two-particle motion of heavy particles in turbulence, Preprint arXiv:0704.3893, 2007.
[48] G. Boffetta, F. De Lillo, A. Gamba, Large scale inhomogeneity of inertial particles in turbulent flow, Phys. Fluids 16 (2004) L20–L23.
[49] L. Chen, S. Goto, J.C. Vassilicos, Turbulent clustering of stagnation points and inertial particles, J. Fluid Mech. 553 (2006) 143–154.
[50] J. Bec, L. Biferale, M. Cencini, A. Lanotte, S. Musacchio, F. Toschi, Heavy particle concentration in turbulence at dissipative and inertial scales, Phys. Rev. Lett. 98 (2007) 084502.
[51] H. Yoshimoto, S. Goto, Self-similar clustering of inertial particles in homogeneous turbulence, J. Fluid Mech. 577 (2007) 275–286.
[52] G. Falkovich, S. Musacchio, L. Piterbarg, M. Vucelja, Inertial particles driven by a telegraph noise, Phys. Rev. E 76 (2007) 026313.

Available online at www.sciencedirect.com
ScienceDirect
ELSEVIER
Physica D 237 (2008) 2051–2055
PHYSICA D
www.elsevier.com/locate/physd

Thomson's Heptagon: A case of bifurcation at infinity

Stefanella Boatto[a,*], Carles Simó[b]

[a] *Departamento de Matemática Aplicada, Instituto de Matemática, Universidade Federal de Rio de Janeiro, Caixa Postal 68530, Ilha do Fundão, Rio de Janeiro, RJ, CEP 21945-970, Brazil*

[b] *Dept. de Matemàtica Aplicada i Anàlisi, Universitat de Barcelona, Gran Via de les Corts Catalanes 585, Barcelona 08007, Spain*

Available online 15 March 2008

Abstract

Vortex modeling has a long history. Descartes (1644) used it as a model for the solar systems. J. J. Thomsom (1883) used it as a model for the atom. We consider point-vortex systems, which can be regarded as "discrete" solutions of the Euler equation. Their dynamics is described by a Hamiltonian system of equations. We are interested in polygonal configurations and how their stability depends upon various dynamical variables. In the plane a polygon with seven vortices has been shown to be a special boundary case: polygons with $N < 7$ vortices are (linearly and nonlinearly) stable while polygons with $N > 7$ vortices are unstable. Why should $N = 7$ be special? Celestial Mechanics helped us to simplify a problem that has been studied for over a century, and to show that the case of Thomson's Heptagon is actually a case of bifurcation at infinity. This becomes particularly clear when considering the corresponding problem of a ring on a sphere with two polar vortices of variable intensities Γ_{N} and Γ_{S}, at the North and South Pole, respectively.

PACS: 47.10.Df; 47.10.Fg

Keywords: Point-vortex dynamics; Hamiltonian systems; Relative equilibria; Stability

1. Introduction

In 1883, when searching for a model for the atom, J.J. Thomson came to study the linear stability of polygonal configurations of N identical point-vortices in the plane. In his analysis he reached the conclusion that a ring of six or fewer vortices was stable, while for seven vortices he erroneously concluded that the ring was slightly unstable [11]. Fifty years later, in 1931, Havelock [6] succeeded in solving the ring linear analysis in full generality and showed that Thomson's Heptagon was *neutrally* stable. In 1999, Cabral and Schmidt [4] performed a nonlinear stability analysis for polygonal configurations with a central vortex (see Fig. 1(a)). Recently, in 2003, Kurakin and Yudovich [9] also provided a proof that the heptagon is nonlinearly stable. Then the "biblical" question arises: why should $N = 7$ be anything special? Why is seven the border-line between stability and instability in the plane? What is happening for rings of vortices, say, on a sphere? In this article we show that the case of Thomson's Heptagon is actually a case of bifurcation at infinity! People were looking at the problem in a reduced parameter space — i.e. for a special value of an extra parameter at infinity. This is particularly clear when considering the problem of a ring of vortices on a sphere with two polar vortices of variable intensities, Γ_N and Γ_S, at the North and South Pole, respectively.

2. Equations of motion

Let us consider a non-rotating sphere of radius R. The position of a point-vortex on the surface of the sphere is specified by means of the usual spherical coordinates (ϕ, θ), where $\theta \in [0, \pi]$ is the co-latitude and $\phi \in [0, 2\pi]$ the longitude. It has already been shown in the literature (see for example [1,2,7,8]) that on a sphere the dynamics of N point vortices of strengths $\Gamma_1, \ldots, \Gamma_N$ is given by the Hamiltonian system of equations

$$\dot{q}_\alpha = -\frac{\partial H}{\partial p_\alpha}, \quad \dot{p}_\alpha = \frac{\partial H}{\partial q_\alpha}, \quad \alpha = 1, \ldots, N, \tag{1}$$

* Corresponding author. Tel.: +55 21 22878744; fax: +55 21 22901095.
E-mail address: lella@im.ufrj.br (S. Boatto).

0167-2789/$ - see front matter © 2008 Elsevier B.V. All rights reserved.
doi:10.1016/j.physd.2008.02.030

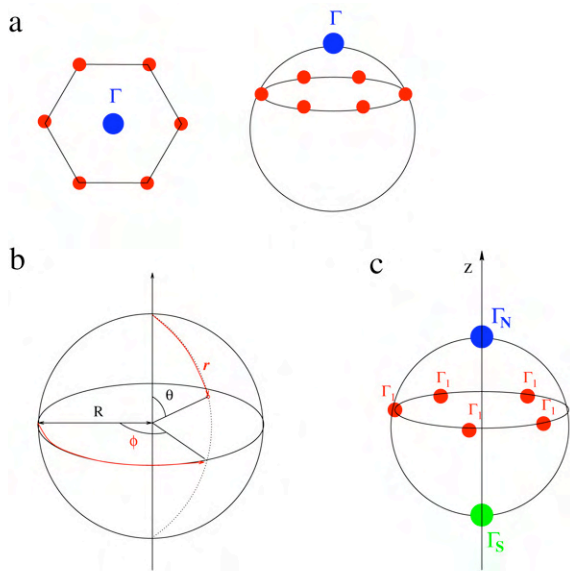

Fig. 1. (a) In the plane and on a sphere, a configuration of a ring of identical vortices with a central vortex of vorticity Γ. (b) A point on the sphere of radius R can be localized by specifying its longitude φ and its co-latitude θ. (c) Configuration of a ring and two polar vortices on a sphere.

where $q_\alpha = \phi_\alpha$ and $p_\alpha = \Gamma_\alpha R^2(\cos\theta_\alpha - 1)$ are the canonical variables associated to the αth vortex, and H is the autonomous Hamiltonian

$$H(q_1, \dots, q_N, p_1, \dots, p_N) = c \sum_{\alpha<\beta} \Gamma_\alpha \Gamma_\beta \ln(1 - d_{\alpha\beta}), \tag{2}$$

with $c = -1/4\pi$ and $d_{\alpha\beta} = \left(1 + \frac{p_\alpha}{R^2\Gamma_\alpha}\right)\left(1 + \frac{p_\beta}{R^2\Gamma_\alpha}\right) + \sqrt{\frac{p_\alpha}{R^2\Gamma_\alpha}\frac{p_\beta}{R^2\Gamma_\beta}\left(2 + \frac{p_\alpha}{R^2\Gamma_\alpha}\right)\left(2 + \frac{p_\beta}{R^2\Gamma_\beta}\right)}\cos(q_\alpha - q_\beta)$.

3. A ring of identical vortices

Now let us focus our attention on the case of the unit sphere, $R = 1$, and a vortex configuration consisting of one latitudinal ring of N identical vortices, say of vorticity $\Gamma_1 = \dots = \Gamma_N = 1$, i.e.

$$q_\alpha(0) = \frac{2\pi(\alpha - 1)}{N}, \qquad p_\alpha(0) = \cos\theta_o - 1 \tag{3}$$

and two polar vortices of vorticity Γ_{N} and Γ_{S}, respectively, held fixed at each pole, as shown in Fig. 1(c). The Hamiltonian of the vortex system is $H = H_o + H_{FP}$, where

$$H_{FP} = c\Gamma_{\mathrm{N}} \sum_{\beta=1}^{N} \ln(-p_\beta) + c\Gamma_{\mathrm{S}} \sum_{\beta=1}^{N} \ln(2 + p_\beta)$$

is the part describing the interaction of the polar vortices with each vortex in the ring, and H_o is as H in (2), the Hamiltonian describing the interaction of the vortices of the ring. It has been shown (see [3,10]) that the dynamics of such a configuration is a rigid rotation – i.e. in *relative equilibrium* –

$$q_\alpha(t) = \nu t + q_\alpha(0), \qquad p_\alpha(t) = z_o - 1, \tag{4}$$

where $z_o = \cos\theta_o$, $\nu = c\left[\frac{z_o}{\rho_o^2}(N-1) + \frac{\Gamma_{\mathrm{N}}}{1-z_o} - \frac{\Gamma_{\mathrm{S}}}{1+z_o}\right]$ is the rotational frequency deduced in [3] and $\rho_o = \sqrt{1 - z_o^2}$. Now the following question naturally arises:

How does the stability (linear and non linear) of such a configuration depend upon N, z_o, Γ_N e Γ_S ?

To tackle this question we begin by rewriting the system (1) as

$$\frac{\mathrm{d}X}{\mathrm{d}t} = J\nabla_X H,$$

where $X = (q_1, \dots, q_N, p_1, \dots, p_N)$, $J = \left(\begin{array}{c|c} O & -\mathbb{I} \\ \hline \mathbb{I} & O \end{array}\right)$ and $\nabla_X = \left(\frac{\partial}{\partial q_1}, \dots, \frac{\partial}{\partial q_N}, \frac{\partial}{\partial p_1}, \dots, \frac{\partial}{\partial p_N}\right)$. It is clear that exchanging the values of Γ_{N} and Γ_{S} is equivalent to exchanging z_o with $-z_o$. Hence, it will be enough to discuss the behaviour for fixed values of Γ_{S} and let Γ_{N} and z_o vary. Then we do the following (see for details Boatto and Simó [3]):

(i) Change of reference frame: we view the dynamics in a frame co-rotating with the relative equilibrium configuration. In the co-rotating reference system, the Hamiltonian takes the form

$$\tilde{H} = H + \nu M,$$

where $M = N + \sum_{\alpha=1}^{N} p_\alpha$ is the momentum of the system — associated with the invariance under translations of the Hamiltonian H along the parallels of the sphere. The relative equilibrium becomes an equilibrium, X^*, in the new reference system, and standard techniques can be used to study its stability.

The relevant equation to be studied is therefore

$$\frac{\mathrm{d}\Delta X}{\mathrm{d}t} = JS\,\Delta X \tag{5}$$

where $X = X^* + \Delta X$, and S is the Hessian of $\tilde{H}$ evaluated at the equilibrium X^*. For *linear stability* we study the eigenvalues of the matrix JS (spectral stability), while for *nonlinear stability* we make use of Dirichlet's Criterion, i.e. we study the definiteness of the Hessian S [4,5]:

Theorem 3.1 (*Dirichlet's Criterion*). *Let X^* be an equilibrium of an autonomous system of ordinary differential equations*

$$\frac{\mathrm{d}X}{\mathrm{d}t} = f(X), \qquad X \in \Omega \subset \mathbb{R}^{2N}, \tag{6}$$

that is, $f(X^*) = 0$. If there exists a positive (or negative) definite integral $\boldsymbol{\Psi}$ of the system (6) in a neighbourhood of the equilibrium X^*, then X^* is stable.

Notice that in our case the system is Hamiltonian and the Hamiltonian is time independent, then $\tilde{H}$ is a first integral. Near the equilibrium X^* (3), $\tilde{H}$ can be expanded as

$$\tilde{H}(X) = \tilde{H}(X^*) + \nabla\tilde{H}(X^*)\cdot\Delta X + \frac{1}{2}\Delta X S \Delta X + \cdots \tag{7}$$

where the linear term disappears due to the fact that $\nabla\tilde{H}(X^*) = 0$. Then we refer to the Hamiltonian as being (positive or negative) definite at X^* if the quadratic form $\Delta X^{\mathrm{T}} S \Delta X$ is, i.e. if the Hessian S is. Notice that since the Hessian S is a symmetric matrix then it is diagonalizable, i.e. there exists an orthogonal matrix C such that $C^{\mathrm{T}} SC = D$, where $D = \mathrm{diag}(\lambda_1, \ldots, \lambda_{2N})$ is a diagonal matrix. Furthermore the matrix C can be chosen to leave invariant the symplectic form (equivalently $J = C^{\mathrm{T}} JC$). Then by the canonical change of variables $Y = C^{\mathrm{T}} X$ Eq. (5) becomes

$$\frac{\mathrm{d}\Delta Y}{\mathrm{d}t} = JD\,\Delta Y, \tag{8}$$

where $Y = (\tilde{q}_1, \ldots, \tilde{q}_N, \tilde{p}_1, \ldots, \tilde{p}_N)$ and $(\tilde{q}_j, \tilde{p}_j)$, $j = 1, \ldots, N$, are pairs of conjugate variables. Eq. (8) can be rewritten as

$$\frac{\mathrm{d}^2 \Delta\tilde{q}_j}{\mathrm{d}t^2} = -\lambda_j \lambda_{j+N} \Delta\tilde{q}_j, \quad j = 1, \ldots, N.$$

Then we have linear stability if

$$\Lambda_j = \lambda_j \lambda_{j+N} > 0 \tag{9}$$

for all $j = 1, \ldots, N$, with the exception of the zero eigenvalues due to symmetries of H.

(ii) As deduced in [3] the Hessian S of $\tilde{H}$ has the structure

$$S = \left(\begin{array}{c|c} Q & \mathbf{O} \\ \hline \mathbf{O} & P \end{array}\right) \tag{10}$$

where the matrices Q and P are of the form

$$Q = c(-s\mathbb{I} + A), \qquad P = c\frac{1}{\rho_o^4}((t_1 - \tilde{t}_1)\mathbb{I} - A), \tag{11}$$

$$t_1 = s - (N-1)(1 + z_o^2), \qquad \tilde{t}_1 = \rho_o^4(\Gamma_{\mathrm{N}}\eta^2 + \Gamma_{\mathrm{S}}\tilde{\eta}^2),$$

$$\eta = \frac{1}{1 - z_o}, \qquad \tilde{\eta} = \frac{1}{1 + z_o}, \qquad s = \frac{N^2 - 1}{6},$$

and A is a symmetric circulant matrix with first row

$$a_1 = 0, \quad \text{and} \quad a_j = \frac{1}{1 - \cos(2\pi(j-1)/N)} = a_{N-j+2},$$

$j = 1, \ldots, N$, and has minimum and maximum eigenvalues

$$\lambda_{A_{\min}} = -\frac{1}{24}[2N^2 + 1 + 3(-1)^N], \qquad \lambda_{A_{\max}} = s. \tag{12}$$

It follows that Q has a zero eigenvalue, to be denoted as λ_{Q_1} and the other ones are positive (since $c < 0$).

(iii) As Q and P are linear combinations of $\mathbb{I}$ and A, they diagonalize in the same basis as A. Let $\lambda_{Q_j}, \lambda_{P_j}$ be the respective eigenvalues. Hence, we can diagonalize JS and its eigenvalues are

$$\lambda_{JS_j} = \sqrt{\lambda_{Q_j}\lambda_{P_j}}, \qquad \lambda_{JS_{j+N}} = -\sqrt{\lambda_{Q_j}\lambda_{P_j}},$$

$j = 1, \ldots, N$. Then the single zero eigenvalue λ_{Q_1} of S corresponds to a double two eigenvalue equal to zero of JS, i.e. $\lambda_{JS_1} = \lambda_{JS_{N+1}} = 0$.

Then following the procedure described above (see [3] for details) we consider a symplectic change of variables which diagonalizes the Hessian. It is enough to use, both for the q and the p variables, the eigenbasis of A.

As stated above the nonzero eigenvalues of Q are positive. It follows from Eqs. (11) and (12) that

$$\lambda_{P\,min} = -\frac{c}{\rho_o^4}\left\{-\frac{1}{24}[2N^2 + 1 + 3(-1)^N] - \frac{N^2-1}{6} \right.$$
$$\left. + (N-1)(1 + z_o^2) + \Gamma_{\mathrm{N}}(1 + z_o)^2 + \Gamma_{\mathrm{S}}(1 - z_o)^2 \right\}. \tag{13}$$

Linear stability is assured when $\lambda_{P\,\min} > 0$.

Then what about nonlinear stability?

It follows from the discussion above and from Dirichlet's Criterion, Theorem 3.1, that nonlinear stability is assured when the minimum eigenvalue of P is positive [3], as well!

Theorem 3.2 (*Spherical Case*). *The equilibrium X^* (3) is (linearly and nonlinearly) stable if*

$$\lambda_{P\,\min} > 0,$$

i.e. if

$$-(N-2)^2 - \delta + 4(N-1)z_o^2 + 4(1 + z_o)^2\Gamma_{\mathrm{N}}$$
$$+ 4(1 - z_o)^2\Gamma_{\mathrm{S}} > 0, \tag{14}$$

where $\delta = 0$ for N even, $\delta = 1$ for N odd. It is linearly unstable if the inequality in (14) is reversed.

Remarks. (1) From the above theorem we guarantee stability if

$$\Gamma_{\mathrm{N}} > \frac{(N-2)^2 + \delta - 4(N-1)z_o^2 - 4(1 - z_o)^2\Gamma_{\mathrm{S}}}{4(1 + z_o)^2}$$

with δ defined as before.

(2) When $\Gamma_{\mathrm{N}} > 0$ and $\Gamma_{\mathrm{S}} > 0$, notice the stabilizing influence of the polar vortices – i.e. of the factor $4(1 + z_o)^2\Gamma_{\mathrm{N}} + 4\Gamma_{\mathrm{S}}(1 - z_o)^2$ in the equations of the theorem above.

(3) Concerning stability in the critical case $\lambda_{P\,\min} = 0$, it is necessary to carry out a computation of higher order terms in the Normal Form of the Hamiltonian around the fixed point, as done in [4] for the planar case, $N = 7$.

(4) Notice $\theta = \sqrt{K}r$ where r is the geodesic distance from the north pole and $K = 1/\sqrt{R}$ is the curvature of the sphere. Then fixing r, we recover the planar case (see Fig. 1) by considering $K \to 0$ (as fully discussed in [2]), obtaining

$$\lim_{K \to 0} p_\alpha = -\frac{r_\alpha^2}{2}.$$

In a similar way we can recover the planar case by letting z_0 tend to 1. The previous theorem reduces to the case already studied by Cabral and Schmidt [4].

Corollary 3.3 (*Planar Limit*). *The equilibrium* $X^* = \left(0, \frac{2\pi}{N}, \ldots, \frac{2\pi(N-1)}{N}, -\frac{r_o^2}{2}, \ldots, -\frac{r_o^2}{2}\right)$ *is (linearly and nonlinearly) stable if the vorticity strength of the center vortex verifies*

$$\Gamma_{\mathrm{N}} > \frac{(N-2)^2 + \delta - 4(N-1)}{16}, \tag{15}$$

where $\delta = 0$ for N even, $\delta = 1$ for N odd. It is linearly unstable if the inequality is reversed.

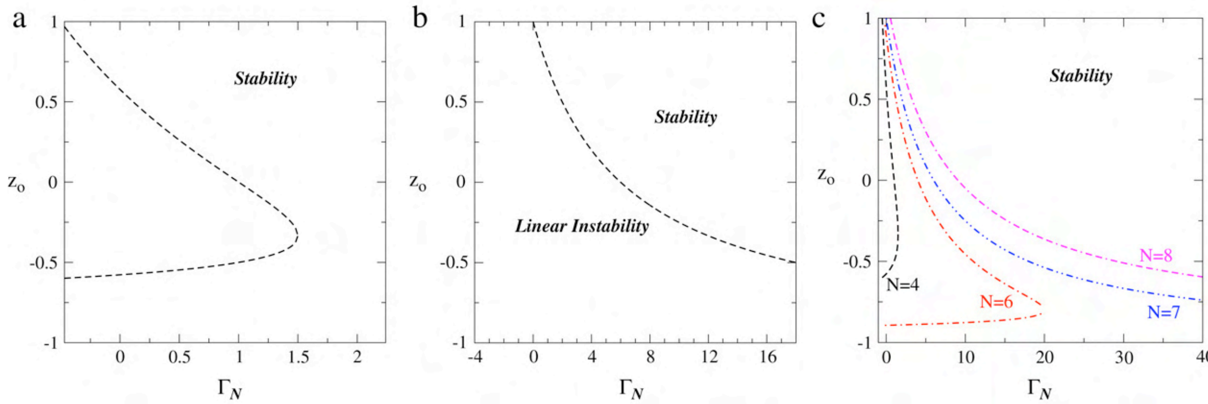

Fig. 2. $\Gamma_{\rm S} = 0$. Regions of stability and of linear instability for (a) $N = 4$, (b) $N = 7$ and (c) $N = 4, 6, 7, 8$.

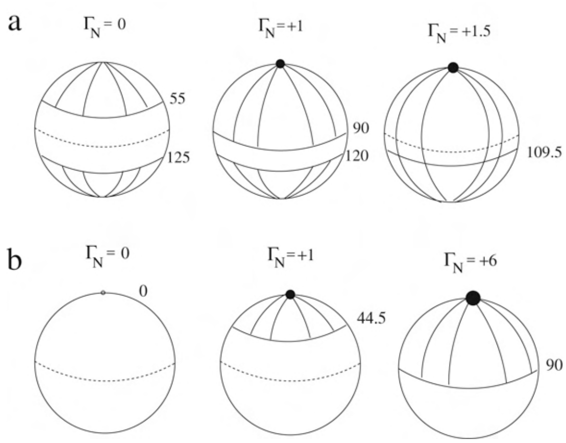

Fig. 3. $\Gamma_{\rm S} = 0$. Stability region of a ring of N identical vortices with a vortex of vorticity $\Gamma_{\rm N}$ held fixed at the North Pole. Notice how the stability band increases with $\Gamma_{\rm N}$. (a) for $N = 4$; (b) for $N = 7$.

A complete discussion about the planar limit is given in [2].

What is the relevance of having two polar vortices?

As shown in Figs. 2 and 3 when $\Gamma_S = 0$, the stability region for $N < 7$ is quite different from the one of the case $N \geq 7$. In the case $N < 7$ both polar cups exhibit a stability region, and the region grows with the increasing of the value of Γ_N (see Fig. 2(a)–(c)) and Fig. 3(a)). More specifically, for a given $N < 7$ there is a particular value of Γ_N above which the stability region is the whole sphere! The situation is quite different for $N \geq 7$. As Γ_N increases the stability region around the north polar cup increases (see Fig. 2(b)–(c)) and Fig. 3(b)), but never reaches the south pole!

Now when $\Gamma_S \neq 0$ things are quite different! Let us illustrate this with an example. Consider the case of a ring of eight vortices, i.e. $N = 8$, and let us see how the presence of a southern polar vortex could extend the assured stability region — and equivalently reduce the linear instability region. In Fig. 4 the curves delimiting the stability region are given for different values of the strength of the southern polar vortex, $\Gamma_{\rm S}$. In particular, notice that if the value of $\Gamma_{\rm S}$ is above the critical one (i.e. $\Gamma_{\rm S} > \Gamma_{\rm S}^* = 1/2$) the stability region can extend to the southern polar region for negative values of $\Gamma_{\rm N}$, as well. Analogously, in the case of a ring of four vortices, i.e. $N = 4$, if the southern polar vortex has a strength $\Gamma_{\rm S} < \Gamma_{\rm S}^* = -1/2$,

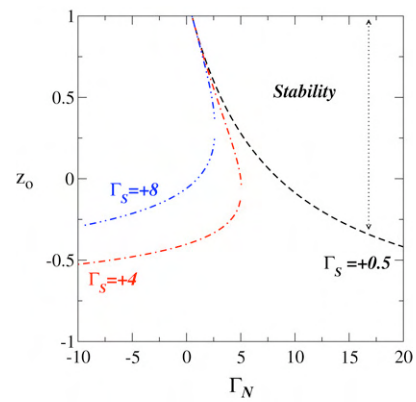

Fig. 4. For $N = 8$, different stability regions for different values of $\Gamma_{\rm S} \geq \tilde{\Gamma}_{\rm S}^*$.

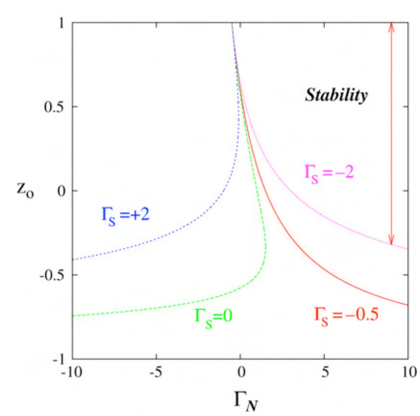

Fig. 5. For $N = 4$, different stability regions for different values of $\Gamma_{\rm S} \geq \Gamma_{\rm S}^*$.

the assured stability region does not include a neighbourhood of the south pole, see Fig. 5. As one last comment, we want to point out that for fixed N and $\Gamma_{\rm S} > \Gamma_{\rm S}^*$, a turning point bounds the values of $\Gamma_{\rm N}$ for which there exists some range of stability in the z_o variable. The location of the turning point is given by

$$-16\Gamma_{\rm N}\Gamma_{\rm S} + (\Gamma_{\rm N} + \Gamma_{\rm S})(N^2 - 8N + 8 + \delta) \\ + (N-1)((N-2)^2 + \delta) = 0,$$

provided $|\Gamma_{\rm N} - \Gamma_{\rm S}| < |N - 1 + \Gamma_{\rm N} + \Gamma_{\rm S}|$, which is the required condition to have then $|z_o| < 1$. From the above relation we have at the turning point

$$\Gamma_{\mathrm{N}} = \frac{\Gamma_{\mathrm{S}}(N^2 - 8N + 8 + \delta) + ((N-1)((N-2)^2 + \delta))}{16\Gamma_{\mathrm{S}} - (N^2 - 8N + 8 + \delta)}.$$

One checks, for instance, the values $\Gamma_{\mathrm{N}} = 71/14$, $\Gamma_{\mathrm{N}} = 79/30$ in Fig. 4 for $N = 8$ and $\Gamma_{\mathrm{S}} = 4$, $\Gamma_{\mathrm{S}} = 8$, respectively, and the values $\Gamma_{\mathrm{N}} = 1.5$, $\Gamma_{\mathrm{N}} = -0.1$ for $\Gamma_{\mathrm{S}} = 0$, $\Gamma_{\mathrm{S}} = 2$, respectively, in Fig. 5.

4. Conclusions

On a sphere, we investigated the linear and nonlinear stability of a latitudinal polygonal ring of identical point-vortices, in the presence of two fixed polar vortices. The purpose of our study was to show the full symmetry of the stability problem. In fact as already widely discussed in the literature for over a century (see [4,6,9,11]), in the planar case it would appear that a ring of seven vortices is a special case. When considering a ring of vortices with a central vortex (as in Fig. 1(a)) the stability behaviour is quite different for rings with more or less than seven vortices. The Thomson Heptagon appears as a mysterious boundary case! In this article we showed that on the sphere – that can be thought as the plane plus the point at infinity – when letting Γ_{S} vary we are accordingly setting new boundary values for N. In particular our study gives the critical value of Γ_{S}^* for all N, i.e.

$$\Gamma_{\mathrm{S}}^* = (N^2 - 8N + 8 - \delta)/16,$$

where $\delta = 0$ for N even, $\delta = 1$ for N odd. To obtain this critical value it is enough to replace $>$ by $=$ in (14) and let z_o tend to -1. To illustrate this more clearly in Fig. 4 we showed that for $\Gamma_{\mathrm{S}}^* = 1/2$ the boundary value for N is 8. In other words, $N = 7$ is a special boundary case only for $\Gamma_{\mathrm{S}}^* = 0$, and the planar setting can be viewed as a case of bifurcation at infinity!

Acknowledgments

The authors would like to thank Alain Chenciner and Jair Koiller for many helpful discussions. C.S. has been supported by grants MTM2006-05849/Consolider (Spain) and CIRIT 2005 SGR-1028 (Catalonia).

References

[1] H. Aref, P.K. Newton, M.A. Stremler, T. Tokieda, D.L. Vainchtein, Vortex crystals, Adv. Appl. Math. 39 (2003).
[2] S. Boatto, Curvature perturbations and stability of a ring of vortices, Discrete Continuous Dynam. Syst. (2007) (in press).
[3] S. Boatto, C. Simó, Stability of latitudinal vortex rings with polar vortices, preprint, 2004. http://www.ma.utexas.edu/mp_arc/a/04-67.
[4] H.E. Cabral, D.S. Schmidt, Stability of relative equilibria in the problem of $N + 1$ vortices, SIAM J. Math. Anal. 31 (2) (1999/00) 231–250.
[5] G. Lejeune, Dirichlet, Werke, vol. 2, Berlin, pp. 5–8, 1897.
[6] T.H. Havelock, The stability of motion of rectilinear vortices in ring formation, Philos. Mag. S. 7 11 (70) (1931) 617–633.
[7] R. Kidambi, P.K. Newton, Motion of three point vortices on a sphere, Physica D 116 (1998) 143–175.
[8] Y. Kimura, Vortex motion on surfaces with constant curvature, Proc. R. Soc. Lond. A 455 (1999) 245–259.
[9] L.G. Kurakin, V.I. Yudovich, The stability of stationary rotation of a regular vortex polygon, Chaos 12 (3) (2002) 574–595.
[10] C. Lim, J. Montaldi, M. Roberts, Relative equilibria of point vortices on the sphere, Physica D 148 (2001) 97–135.
[11] J.J. Thomson, A Treatise on the Motion of Vortex Rings, Macmillian, New York, 1883. Adam Prize Essay; Electricity and Matter, Westmister Archibald Constable & Co., Ltd, 1904.

Available online at www.sciencedirect.com
ScienceDirect
Physica D 237 (2008) 2056–2061
PHYSICA D
www.elsevier.com/locate/physd

Topology of stirring in two-dimensional turbulence: Point vortex in a time-dependent ambient strain

Michał Branicki

School of Mathematics, University of Bristol, University Walk, Bristol, BS8 1TW, UK

Available online 4 March 2008

Abstract

We analyse the Lagrangian geometry of a time-dependent flow in the neighbourhood of a coherent vortex which is assumed to be a member of a vortex cluster collectively ruling the dynamics in the late stages of decaying two-dimensional turbulence. In order to gain insight into the highly inhomogeneous transport of a passive tracer in such vortex-dominated flows, we consider an idealised kinematic model of a local flow around a single coherent vortex in the cluster at distances much smaller than the distance to its nearest neighbour. We focus, in particular, on flow configurations which lead to a vigorous stirring and a subsequent escape of a passive tracer from the neighbourhood of the vortex. Here, the central vortex is approximated by a point vortex but the analytical arguments can be modified to cater for more realistic vorticity distributions. The principal axes of an irrotational ambient strain, which represents the combined, leading-order influence of its neighbours, are assumed to rotate with constant angular velocity and the strain-rate varies harmonically in time. The Lagrangian structure of the flow near the vortex is analysed by utilising the Hamiltonian formalism and employing appropriate perturbation methods. It is shown that sufficiently near the vortex there exist KAM-like tori which confine regions of purely chaotic tracer trajectories to the neighbourhood of the vortex. We emphasise, however, that there can exist certain 'open' flow geometries which lead to eventual 'leakage' of the tracer from 'sufficiently distant' regions of vigorous stirring to the outer flow. Such local flow configurations can be regarded as a prototype of the 'mixers' in decaying 2D turbulence.

Keywords: Stirring; Inhomogeneous transport; Coherent vortex; Open flow geometry; Decaying two-dimensional turbulence; Hamiltonian perturbation methods

1. Introduction

The flow in the late stages of the decaying two-dimensional turbulence is dominated by a relatively small number of strong coherent vortices whose lifetimes are much longer than the characteristic time scale of the nonlinear turbulent interactions [13,3,5].The analysis of velocity distributions show that these coherent structures destroy the self-similarity and the dynamical homogeneity of the transport dynamics at intermediate scales in the inertial range for active and passive tracers [2]. Even though it is known, based on the (local) tracer-gradient dynamics, that the passive tracer variance evolves from large to small scales the most rapidly within the robust 'elliptic' cores of the coherent vortices, many aspects of this process, and in particular differences between the passive and active case, remain unclear [1]. For example, in the Eulerian framework, the usually close-to-axisymmetric vortex cores are known to be robust to perturbations so that the vorticity filaments are stripped only from their edges during close interactions [14]. If then the passive tracer is vigorously redistributed within the vortex core, what mechanisms are responsible for allowing it (or not) to escape to the outer flow?

Leaving the more intricate problem of active tracer dynamics aside, we approach the issue of passive scalar transport in the absence of diffusion (i.e. stirring) from the Lagrangian point of view, which lends itself to a variety of techniques from Dynamical Systems. This approach has been successfully used in the past in fluid dynamical considerations [16]; some of the most important results include the existence of KAM-like invariants, representing kinematical barriers to transport in time-periodic flows [10], robustness of Smale horseshoes [7] generating regions of chaotic fluid–particle trajectories, or lobe dynamics [19].

In the following sections, we study a simple kinematic model of a flow dominated by a nearly conservative mutual

E-mail address: m.branicki@bristol.ac.uk.

0167-2789/$ - see front matter
doi:10.1016/j.physd.2008.02.021

advection of coherent vortices, and assume that except for their brief and relatively infrequent interactions these structures move like interacting point vortices. Such idealised models were used successfully in the past in different contexts (see, for example, [13]). Here, we are particularly interested in the role each such a vortex plays in affecting the stirring (and motions) over extended regions of space. In particular, based on the robustness of hyperbolic sets, we establish the necessary conditions for existence of unbounded trajectories in the model flow, localised around the chosen vortex, leading to (locally) open-flow configurations. Other models of local transport, considering primarily stirring in bounded, chaotic regions in flows derived from time-periodic generalisations of the Kida's solutions, were also studied [15,8]. Here, we also assume that the flow field is periodic in time which, while simplifying the analysis, reveals some interesting mechanisms for generation of non-trivial geometric templates for transport due to the central vortex. We note that, while introducing the time-dependence in this fashion may seem somewhat artificial, it proved to be very revealing in the past (see, for example, [4,18,20]). A more realistic model, allowing for aperiodic time dependence and a non-singular vorticity distribution, will be discussed in a future publication. The more general treatment requires the use of lobe dynamics and geometric analysis of time-dependent invariant manifolds of the so-called Distinguished Hyperbolic Trajectories (the DHTs are also present in the time-periodic case but they are not necessary for the analysis) in the flow which 'spread the influence' of the DHTs globally throughout the flow (see, for example, [12] for a review).

2. Equations of the kinematic model

Consider an instantaneous flow, at a point (x, y) in Cartesian coordinates, due to a cluster of $N+1$ point vortices located at $(x_i, y_i), i = 1, \ldots, N+1$ and characterised by circulations Γ_i respectively. Provided that $(x, y) \neq (x_i, y_i)$, the corresponding vector field can be written as

$$\left.\begin{aligned} U(x, y) &= -\frac{1}{2\pi}\sum_{i=1}^{N+1}\frac{\Gamma_i\cdot(y-y_i)}{(y-y_i)^2+(x-x_i)^2},\\ V(x, y) &= \frac{1}{2\pi}\sum_{i=1}^{N+1}\frac{\Gamma_i\cdot(x-x_i)}{(y-y_i)^2+(x-x_i)^2},\end{aligned}\right\} \tag{1}$$

where a positive circulation is assumed for a counter-clockwise rotating vortex. The flow in a neighbourhood of, say, the $(N+1)$-st vortex due to the remaining N vortices can be easily derived by shifting the origin to the vortex (i.e. $x = x_{N+1} + \tilde{x}$, $y = y_{N+1} + \tilde{y}$) and summing (1) up to to the first $i = N$ terms.

A useful linearisation around the chosen vortex can be obtained by first transforming (1) to the polar coordinates (i.e. $x = \varrho\cos\varphi$, $y = \varrho\sin\varphi$) and then using the multipole expansion, which leads to the following representation of the velocity field

$$U(\varrho,\varphi) = -\frac{1}{2\pi}\sum_{i=1}^{N}\frac{\Gamma_i}{\delta_i}\left(\frac{\varrho}{\delta_i}\sin\varphi - \sin\phi_i\right)$$
$$\times\sum_{k=0}^{\infty}\sum_{l=0}^{\infty}\left(\frac{\varrho}{\delta_i}\right)^{k+l}P_l\left(\cos(\varphi-\phi_i)\right)P_k\left(\cos(\varphi-\phi_i)\right), \tag{2}$$

$$V(\varrho,\varphi) = \frac{1}{2\pi}\sum_{i=1}^{N}\frac{\Gamma_i}{\delta_i}\left(\frac{\varrho}{\delta_i}\cos\varphi - \cos\phi_i\right)$$
$$\times\sum_{k=0}^{\infty}\sum_{l=0}^{\infty}\left(\frac{\varrho}{\delta_i}\right)^{k+l}P_l\left(\cos(\varphi-\phi_i)\right)P_k\left(\cos(\varphi-\phi_i)\right); \tag{3}$$

here $(x_i, y_i) = (\delta_i\cos\phi_i, \delta_i\sin\phi_i)$ and P_l denotes the Legendre polynomial of the lth order. Denoting the distance to the nearest neighbour by $\delta_{\min} = \min\{\delta_i\} \neq 0$, we can now linearise the flow in the region $\varrho/\delta_{\min} \ll 1$ as follows:

$$\begin{aligned} U \sim{}& \sum_{i=1}^{N}\frac{\Gamma_i\sin\phi_i}{2\pi\delta_i} + \varrho\cos\varphi\sum_{i=1}^{N}\frac{\Gamma_i\sin 2\phi_i}{2\pi\delta_i^2}\\ &-\varrho\sin\varphi\sum_{i=1}^{N}\frac{\Gamma_i\cos 2\phi_i}{2\pi\delta_i^2} + \mathcal{O}\left(\varrho^2/\delta_{\min}^2\right),\end{aligned} \tag{4}$$

$$\begin{aligned} V \sim{}& -\sum_{i=1}^{N}\frac{\Gamma_i\cos\phi_i}{2\pi\delta_i} - \varrho\cos\varphi\sum_{i=1}^{N}\frac{\Gamma_i\cos 2\phi_i}{2\pi\delta_i^2}\\ &-\varrho\sin\varphi\sum_{i=1}^{N}\frac{\Gamma_i\sin 2\phi_i}{2\pi\delta_i^2} + \mathcal{O}\left(\varrho^2/\delta_{\min}^2\right).\end{aligned} \tag{5}$$

Clearly, the ϱ^0 terms in (4) and (5) correspond to a uniform field driving the vortex core. The ϱ^1 terms represent the first order approximation to the deformation field which can be transformed back to the Cartesian coordinates in the form

$$\begin{bmatrix}U^1\\V^1\end{bmatrix} = \begin{bmatrix}\alpha & -\beta\\-\beta & -\alpha\end{bmatrix}\begin{bmatrix}x\\y\end{bmatrix}, \qquad \begin{aligned}\alpha &= \sum_{i=1}^{N}\Gamma_i\sin 2\phi_i/2\pi\delta_i^2,\\ \beta &= \sum_{i=1}^{N}\Gamma_i\cos 2\phi_i/2\pi\delta_i^2.\end{aligned} \tag{6}$$

The flow given by (6) can be identified as an irrotational strain with (orthogonal) principal axes rotated with respect to $\hat{\mathbf{e}}_x$ by an angle $\theta = \operatorname{atan}(\beta/\alpha)$ and amplitude $\mathcal{A} = (\alpha^2+\beta^2)^{1/2}$. Evolution of the vortex cluster implies that both the amplitude and orientation of the ambient strain vary in time (since $\delta_i = \delta_i(t)$, $\phi_i = \phi_i(t)$). We model it simply by assuming that the strain axes rotate with constant angular velocity λ, and that the strain amplitude depends harmonically on time,

$$\hat{\mathcal{S}}\,s_{\omega,\Delta}(t) = \hat{\mathcal{S}}\frac{\Delta+\cos(\omega t)}{\Delta+1}. \tag{7}$$

We stress, however, that as long as the vortex model remains axisymmetric and the strain is linear and time-periodic, similar analysis to that discussed below can be carried out.

If we now choose as a unit of time $T = 1/\hat{\mathcal{S}}$ and unit of length $L = (\Gamma/2\pi\hat{\mathcal{S}})^{1/2}$, the local (non-dimensionalised) flow around a point vortex in the frame of reference rotating with the axes of the strain can be written as

$$\begin{bmatrix}\dot{x}\\\dot{y}\end{bmatrix} = \frac{1}{\left(x^2+y^2\right)}\begin{bmatrix}-y\\x\end{bmatrix} + \begin{bmatrix}-s_{\Omega,\Delta} & \Lambda\\-\Lambda & s_{\Omega,\Delta}\end{bmatrix}\begin{bmatrix}x\\y\end{bmatrix}, \tag{8}$$

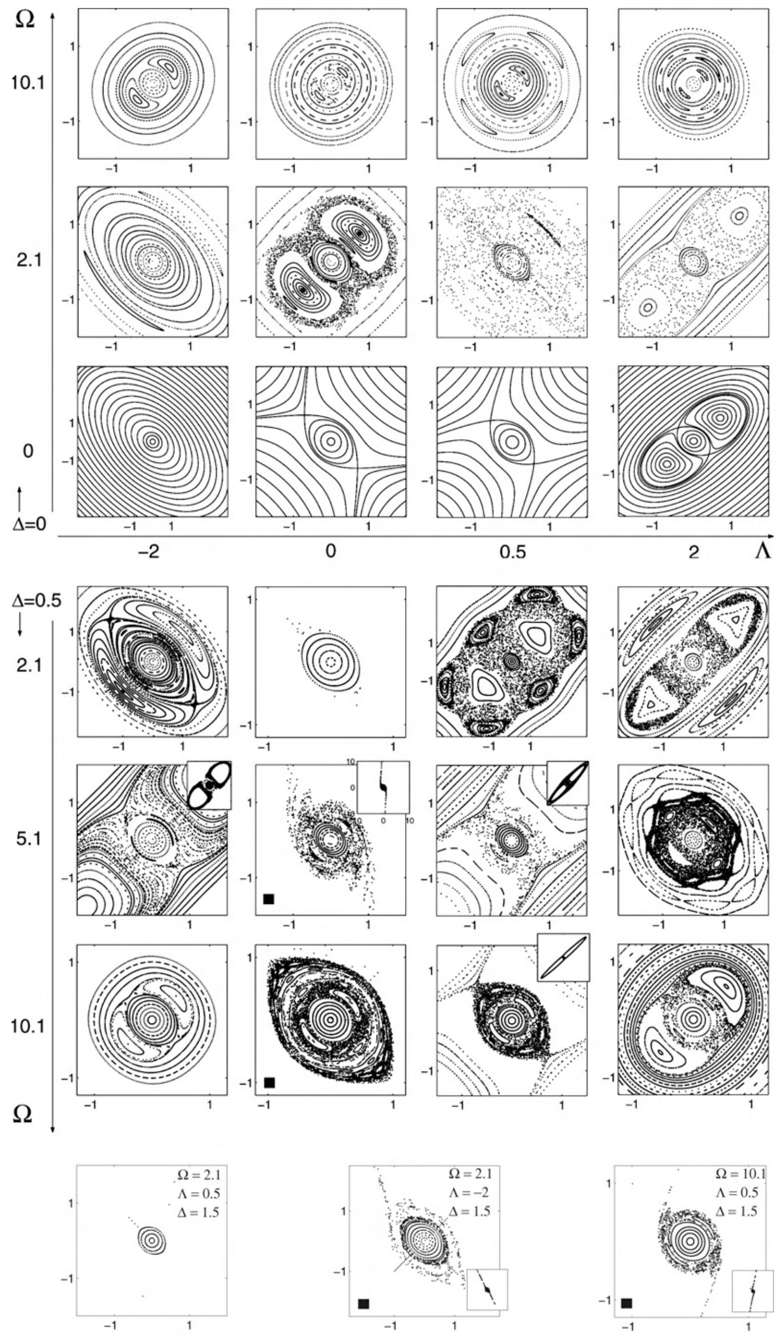

Fig. 1. Examples of Poincaré sections for advection by the flow (9) in the frame rotating with the strain axes for different values of the system parameters (Ω, Λ, Δ). Note in particular the examples of 'open' flow configurations, which are characterised by the existence of a set of initial conditions (of non-zero measure) giving rise to trajectories which evolve in the area of vigorous stirring for a finite time and then escape to the outer flow (see the insets marked with black squares). The condition for existence of such configurations is given by (18).

where now $\Omega^{-1} = \hat{\mathcal{S}}/\omega$ is the dimensionless frequency of oscillations of the strain amplitude, and $\Lambda = \lambda/\hat{\mathcal{S}}$ is the angular velocity of the strain axes. Finally, the system (8) can be re-written in polar coordinates as

$$\left.\begin{aligned} \dot{\varrho} &= -s_{\Omega,\Delta}\,\varrho\cos 2\varphi, \\ \dot{\varphi} &= s_{\Omega,\Delta}\sin 2\varphi - \Lambda + 1/\varrho^2, \end{aligned}\right\} \tag{9}$$

which will prove useful in analysis presented in Section 4.

3. Lagrangian vs. Eulerian viewpoints

It is instructive to analyse first the structure of the system (9) in the steady case (i.e. $s_{\Omega,\Delta} = \text{const.}$) depending on the system parameters. One can easily deduce that the fixed points of (9) lie symmetrically with respect to the origin on one of the diagonal lines inclined at $\pm 45°$ to the strain axes. Because of the inherent symmetry in the model, there is always an elliptic fixed point at the centre, which is also the only stagnation point in the flow for $\Lambda < -1$. For $-1 < \Lambda < 1$ there are additionally two hyperbolic fixed points located at

$$\varrho_{1,2}^{\text{hyp}} = (\Lambda + 1)^{-1/2}, \quad \varphi_1 = -\pi/4, \quad \varphi_2 = 3\pi/4, \tag{10}$$

and the system trajectories trace out the familiar cat's eye pattern (see Fig. 1 for $\Omega = 0$) where the two heteroclinic connections confine the recirculating flow to the neighbourhood of the origin. For $\Lambda > 1$ two more elliptic fixed points are present in the flow, and are located at

$$\varrho_{1,2}^{\text{ell}} = (\Lambda - 1)^{-1/2}, \quad \varphi_1 = \pi/4, \quad \varphi_2 = -3\pi/4. \tag{11}$$

In this case, there are four distinct regions in the flow which all contain bounded periodic trajectories (in the rotating frame of reference). These regions are separated by invariant manifolds of the hyperbolic fixed points which implies that tracer particles located initially in different regions do not mix.

The above scenario can be dramatically altered when the strain amplitude, $s_{\Omega,\Delta}$, becomes time-dependent (i.e. when $\Omega \neq 0$) so that the location of instantaneous stagnation points of the vector field (9) (referred to hereafter as ISPs) changes in time. It is important to recognise that the ISPs are frame-dependent, Eulerian objects and that for $\Omega \neq 0$ their paths in the extended phase space (spanned in this case by two space coordinates and time) are no longer trajectories of the system (9). One can easily deduce that the ISPs must lie on the same diagonal lines as in the steady case but now their distance to the origin is given by

$$\begin{cases} \varrho_{1,2}^{\text{hyp}}(t) = (\Lambda + s_{\Omega,\Delta}(t))^{-1/2} & \text{if } \Lambda > -s_{\Omega,\Delta}, \\ \varrho_{1,2}^{\text{ell}}(t) = (\Lambda - s_{\Omega,\Delta}(t))^{-1/2} & \text{if } \Lambda > \ \ s_{\Omega,\Delta}. \end{cases} \tag{12}$$

Apart from vector fields that vary slowly in time, the 'Eulerian snapshots', given by the instantaneous streamline patterns, bear little correspondence to the actual structure of trajectories in the system's phase space which, for time-periodic flows, can be studied by means of the two-dimensional, area-preserving Poincaré map.

A few examples of such a mapping, shown in Fig. 1 for a different system parameter values, give a flavour of the complexity introduced into the trajectory structure by the simple time-periodic strain variations. In a generic case, the time-dependence introduces a wealth of chaotic regions which are often separated (in two dimensions) by robust KAM-like invariants. If all contours of these invariants are closed, the spatial extent of the mixing by the vortex is limited. If, however, such invariants do not exist at sufficiently large distances from the origin or have an 'open' topology (see Fig. 2b), there can exist a set of initial conditions of non-zero measure which yields trajectories that reside in a region of vigorous stirring near the vortex for a finite time and then escape to the outer flow (see the insets in Fig. 1 marked by black squares).

It can be shown, using the Kruskal's averaging method [9], that when all trajectories of the time-dependent ambient strain are periodic (for example $\Delta = \Lambda = 0$), there exist adiabatic invariants in the nonlinear system (9) which prevent the tracer from escaping from the neighbourhood of the vortex [6].

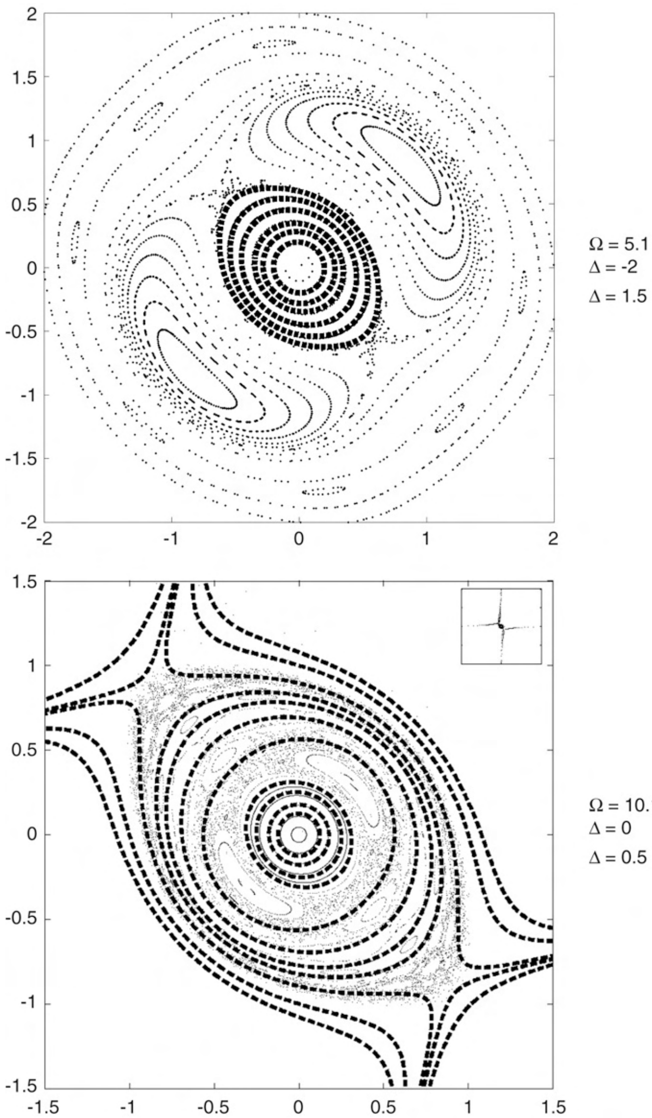

Fig. 2. Comparison between the numerically computed, nearly-integrable structure of Lagrangian fluid trajectories of the flow (9) at times $t_n = 2\pi n/\Omega$ (dots), and the contours of an approximate invariant (26) derived using time-dependent Hamiltonian perturbation method (thick dashed lines). The perturbation method is formally valid only near the vortex centre. The first example (top) shows a flow with no unbounded trajectories. In the second example, even the 'open' invariant structure at $\rho \sim \mathcal{O}(1)$ is surprisingly well approximated.

The problem of finding such an adiabatic invariant structure becomes formidable in less degenerate cases and we defer such analysis to a future publication. Instead, we note that sufficiently far away from the origin, the flow due to the vortex can be regarded as a perturbation to the base flow given by the time-dependent ambient strain (the last term in (8)), which is fully characterised by the fundamental solution matrix

$$\Phi(t, t_0) = \begin{bmatrix} \cosh\tilde{\sigma} - (\tilde{s}/\tilde{\sigma})\sinh\tilde{\sigma} & -(\tilde{\lambda}/\tilde{\sigma})\sinh\tilde{\sigma} \\ (\tilde{\lambda}/\tilde{\sigma})\sinh\tilde{\sigma} & \cosh\tilde{\sigma} + (\tilde{s}/\tilde{\sigma})\sinh\tilde{\sigma} \end{bmatrix}, \tag{13}$$

where

$$\tilde{s} = \int_{t_0}^{t} s(t')\mathrm{d}t', \quad \tilde{\lambda} = \int_{t_0}^{t} \Lambda(t')\mathrm{d}t', \quad \tilde{\sigma} = \sqrt{\tilde{s}^2 - \tilde{\Lambda}^2}. \qquad (14)$$

Using (13), we can relatively easily check for the existence of unbounded hyperbolic trajectories in the unperturbed system (8). (Hyperbolic trajectories and their invariant manifolds bear similarities to non-degenerate saddle fixed points (and their manifolds) in the sense of how nearby trajectories behave in the frame of reference moving with the hyperbolic trajectory [21].) Due to the robustness of hyperbolic structures (see [17] and references therein), we can deduce that for any hyperbolic trajectory of (13) satisfying

$$\| \boldsymbol{\Phi}(t, t_0)\mathbf{x}_0 \| \gg 1, \quad \forall\, t \in [t_0,\ \infty), \qquad (15)$$

there exists a 'perturbed' analogue in the flow (9). Based on the form of (13), we can easily see that in order for a trajectory of the unperturbed linear flow to be unbounded and hyperbolic, there must exist a time t^* such that

$$\Re[\sigma] \neq 0,\ \Re[\mathrm{d}\sigma/\mathrm{d}t] > 0, \quad \forall t > t^*, \ \wedge \ \mathcal{L}_{1,2} \neq 0, \qquad (16)$$

where the Lyapunov exponents, $\mathcal{L}_{1,2}$, are defined in the standard way as the logarithms of the eigenvalues of

$$\mathcal{M} = \lim_{(t-t_0)\to\infty} (\boldsymbol{\Phi}^{\mathrm{T}}(t, t_0)\,\boldsymbol{\Phi}(t, t_0))^{1/2(t-t_0)}. \qquad (17)$$

In the case of our model, the conditions (16) reduce to

$$\begin{cases} \Delta^2 - \Lambda^2(\Delta+1)^2 > 0 & \text{if } \Omega \neq 0, \\ \Lambda^2 < 1 & \text{if } \Omega = 0. \end{cases} \qquad (18)$$

It should be noted, however, that the criterion (18), remains rather formal in the sense that we do not specify explicitly the set of initial conditions that satisfies (15); this becomes particularly tricky for $\Omega \to 0$ when, due to the unbounded oscillatory character of the unperturbed strain trajectories, even distant trajectories may return close to the origin.

4. 'Near-field' structure

As seen from Poincaré sections shown in Fig. 1, the structure of the system trajectories near the origin resembles that of a nearly-integrable Hamiltonian system, and the KAM-like invariants prevent the tracer trapped too close to the vortex core from escaping. Consequently, even in the open flow configurations discussed in the previous section only trajectories starting sufficiently far away from the origin can be stripped away from the vortex. In order to gain more insight into the geometry of those impenetrable mixing barriers, we can determine an approximate (integrable) phase-space structure near the vortex by employing the Hamiltonian perturbation theory, which we outline here only briefly (see [11] for more details). We note that the system (9) can be re-written in the Hamiltonian form, i.e.

$$\dot{J} = -\partial H/\partial\theta, \qquad \dot{\theta} = \partial H/\partial J, \qquad (19)$$

with the Hamiltonian written in the 'perturbed' form

$$\begin{aligned} H(J,\theta,t) &= H^0(J) + \epsilon H^1(J,\theta,t) \\ &= -\frac{1}{2}\ln J + J\Lambda + \epsilon J s_{\Omega,\Lambda} \sin 2\theta, \end{aligned} \qquad (20)$$

where $J = \varrho^2/2$, and $\theta = -\varphi$. The first term in (20) corresponds to the Hamiltonian of the point-vortex flow and the remaining terms represent the Hamiltonian of the time-dependent strain. We note that sufficiently near the origin, i.e. $J \ll 1$, the 'non-rotating' part of the ambient strain can be treated as a perturbation, which is non-uniform in space. We emphasize this fact by introducing an 'ordering' parameter, ϵ, which will be later set to unity. The perturbation H^1 is periodic in t, with period $T = 2\pi/\Omega$ and with period 2π in θ, and can be expanded in the Fourier series as

$$H^1 = \sum_{lm} \hat{H}^1_{lm}(J)\mathrm{e}^{\mathrm{i}(l\theta + m\Omega t)}. \qquad (21)$$

It can be shown (see [11]) that for the perturbed, non-autonomous, one-degree-of-freedom Hamiltonian system (20), there exists a 'nearby' integrable Hamiltonian system given by

$$\bar{H}(\bar{J}(J,\theta)) = H^0(J) + \epsilon\langle H^1\rangle_{\theta,t}, \qquad (22)$$

where $\langle\cdot\rangle_{\theta,t}$ denotes a 'fast-variable' average over the 'fast' manifold (torus in this case). The new invariant, $\bar{J}(J,\theta,t)$, is obtained by seeking a near-identity generating function

$$S(\bar{J},\theta) = \bar{J}\theta + \epsilon S_1(\bar{J},\theta,t) + O(\epsilon^2), \qquad (23)$$

which, when combined with (22), enables determination of S_1 (up to $\mathcal{O}(\epsilon)$) in the form

$$S_1 = i \sum_{\substack{lm \\ l=m\neq \mathbf{0}}} \frac{H^1_{lm}(J)}{l\omega(J) + m\Omega}\mathrm{e}^{\mathrm{i}(l\theta + m\Omega t)}, \qquad (24)$$

and subsequently yields the new invariant in the form

$$\bar{J} = J - \epsilon\frac{\partial S_1(J,\theta,t)}{\partial\theta}. \qquad (25)$$

In the particular case when the perturbing Hamiltonian, H^1, is given by the last term of (20), the new invariant (25) can be written as

$$\bar{J} = J + \frac{\epsilon J}{\Delta+1}\left[\frac{\Delta\sin(2\theta)}{\omega(J)} + \frac{\sin(2\theta+\Omega t)}{2\omega(J)+\Omega} + \frac{\sin(2\theta-\Omega t)}{2\omega(J)-\Omega}\right], \qquad (26)$$

where $\omega(J) = \partial H^0/\partial J = -1/(2J) + \Lambda$, is the winding frequency on the unperturbed torus. The approximation (26) is obviously valid away from the resonances given by $\omega(J) = \pm\Omega/2$ and $\omega(J) = 0$.

We compare contours of (26) with results based on direct integration of the system (9) in Fig. 2 again by computing the Poincaré sections. The contours of the new invariant clearly are a very good approximation to the integrable structure near the origin. It is often the case that approximations obtained via perturbation techniques are a surprisingly good approximation well beyond the range of their formal applicability. One can observe a similar effect here: the integrable structure is often reasonably well approximated even at distances $\varrho \sim \mathcal{O}(1)$ although the chaotic separatrix layers are obviously missed by the approximation. Note in particular the open contours of the new invariant in Fig. 2b which allow trajectories in the outermost nearly-chaotic band to eventually escape.

5. Conclusions

We studied the Lagrangian structure of a simple, time-periodic model flow in an attempt to elucidate the mechanisms responsible for stirring of a passive scalar around strong, coherent vortices in advection-dominated flows. We showed, using time-dependent Hamiltonian perturbation method, that the chaotic regions located sufficiently near the centre of the vortex are bounded by KAM-like invariants which serve as barriers to mixing, trapping tracer particles originating near the vortex. However, there exist flow configurations where, even in the absence of close interactions with neighbouring vortices, some tracer is stripped off the vortex after a transient period of being vigorously stirred in its neighbourhood. This framework can be easily extended to more realistic models of the vortex core, as long as it remains axisymmetric and the ambient strain is time-periodic. Further analysis is clearly needed in order to investigate the consequences of aperiodic time dependence.

Acknowledgments

I am grateful to Konrad Bajer (University of Warsaw) for many stimulating discussions and guidance when he first drew my attention to the problem as a supervisor of my M.Sc. thesis [6], concerned with similar issues.

References

[1] A. Babiano, A. Provenzale, Coherent vortices and tracer cascades in two-dimensional turbulence, J. Fluid Mech. 574 (2007) 429–448.
[2] A. Babiano, T. Dubos, On the contribution of coherent vortices to the two-dimensional inverse energy cascade, J. Fluid Mech. 529 (2005) 97–115.
[3] R. Benzi, S. Patarnello, P. Santangelo, Self-similar coherent structures in two-dimensional decaying turbulence, J. Phys. A 21 (1988) 1221.
[4] A.S. Bower, A simple kinematic mechanism for mixing fluid parcels across a meandering jet, J. Phys. Oceanogr. 21 (1991) 173–180.
[5] M Brachet, M. Meneguzzi, H. Politano, P. Sulem, The dynamics of freely decaying two-dimensional turbulence, J. Fluid Mech. 194 (1988) 333.
[6] M. Branicki (supervisor K. Bajer), Flow kinematics near a point vortex in a time-dependent strain, M.Sc. Thesis, Warsaw University, 2001.
[7] W.L. Chien, H. Rising, J.M. Ottino, Laminar mixing and chaotic mixing in several cavity flows, J. Fluid Mech. 170 (1986) 355–377.
[8] K. Ide, S. Wiggins, The dynamics of elliptically shaped regions of uniform vorticity in time-periodic,linear external velocity fields, Fluid Dynam. Res. 15 (1995) 205–235.
[9] M. Kruskal, Asymptotic theory of Hamiltonian and other systems with all solutions nearly periodic, J. Math. Phys. 3 (1962) 806–828.
[10] H.A. Kusch, J.M. Ottino, Experiments on mixing in continuous chaotic flows, J. Fluid. Mech. 236 (1992) 319–348.
[11] A.J. Lichtenberg, M.A. Lieberman, Regular and stochastic motion, in: Applied Mathematical Sciences, vol. 38, Springer-Verlag, 1983.
[12] A.M. Mancho, D. Small, S. Wiggins, A tutorial on dynamical systems concepts applied to Lagrangian transport in oceanic flows defined as finite time data sets: Theoretical and computational issues, Phys. Rep. 437 (2006) 55–124.
[13] J. McWilliams, The emergence of isolated coherent vortices in turbulent flow, J. Fluid Mech. 146 (1984) 21–43.
[14] M.V. Melander, J.C. McWilliams, N.J. Zabusky, Axisymmetrization and vorticity-gradient intensification of an isolated two-dimensional vortex through filamentation, J. Fluid Mech. 178 (1987) 137.
[15] L.M. Polvani, J. Wisdom, On chaotic flow around the Kida vortex, in: H.K. Moffatt, A. Tsinober (Eds.), Topological Fluid Mechanics, Cambridge University Press, 1990, pp. 34–44.
[16] J. Ottino, The Kinematics of Mixing: Stretching, Chaos, and Transport, Cambridge University Press, 1989.
[17] V.A. Pliss, G.R. Sell, Robustness of exponential dichotomies in infinite-dimensional dynamical systems, J. Dynam. Differential Equations 11 (3) (1999) 471–513.
[18] A.C. Poje, G. Haller, Geometry of cross-stream mixing in a double-gyre ocean model, J. Phys. Oceanogr. 29 (1999) 1649–1665.
[19] V. Rom-Kedar, A Leonard, S. Wiggins, An analytical study of transport, mixing, and chaos in an unsteady vortical flow, J. Fluid Mech. 214 (1990) 347–394.
[20] R.M. Samelson, Fluid exchange across a meandering jet, J. Phys. Oceanogr. 22 (4) (1992) 431–440.
[21] S. Wiggins, Introduction to Applied Nonlinear Dynamical Systems and Chaos, Springer, New York, 2003.

Available online at www.sciencedirect.com
ScienceDirect
ELSEVIER
Physica D 237 (2008) 2062–2066
PHYSICA D
www.elsevier.com/locate/physd

Spectral energetics of quasi-static MHD turbulence

Paolo Burattini*, Maxime Kinet, Daniele Carati, Bernard Knaepen

Université Libre de Bruxelles, Physique Statistique et des Plasmas, Brussels, Belgium

Available online 17 January 2008

Abstract

Some spectral properties of homogeneous magnetohydrodynamic (MHD) turbulence are reported. The incompressible fluid is electrically conducting and subject to a uniform magnetic field of different intensities. The flow evolution is studied by solving directly in a periodic cubic box the Navier–Stokes equations with the addition of the Lorentz term. This is modeled according to the quasi-static approximation, given the low value of the magnetic Reynolds number. 2D spectra of the kinetic energy highlight the region of the Fourier space that is the most affected by Joule dissipation, and how the anisotropy varies with respect to the direction of application of the magnetic field. Distributions of the nonlinear transfer indicate that, at small scales, the flux of energy is both radial and angular. The degree of locality of the transfer in both directions is of comparable degree, when the Lorentz force is large.

PACS: 47.65.-d; 47.27.Gs

Keywords: MHD turbulence; Homogeneous turbulence; Liquid metal flow

1. Introduction

While isotropic turbulence has been extensively studied in the past, to date homogeneous anisotropic turbulence remains far less explored. In practice, there are a number of ways in which this condition can be realised. One is by imposing a rigid rotation on a turbulent flow (e.g. [9]). A second example is provided by the motion of a conductive fluid under the effect of an imposed magnetic field **B**. If, in particular, the fluctuations of the magnetic field induced by the fluid are small relative to **B** (that is, the magnetic Reynolds number is very low), the Lorentz force acting on the fluid becomes proportional to the velocity — an approximation referred to as the quasi-static. In this context, the flow of an incompressible fluid is described by the Navier–Stokes equation with an additional term

$$\partial_t \mathbf{u} + (\mathbf{u} \cdot \nabla)\mathbf{u} = -\frac{1}{\rho}\nabla p + \nu \Delta \mathbf{u} - \frac{\sigma B_0^2}{\rho}\Delta^{-1}\partial_{33}\mathbf{u} \tag{1}$$

$$\nabla \cdot \mathbf{u} = 0, \tag{2}$$

where $\mathbf{u} = (u_1, u_2, u_3)$ is the velocity, ρ the fluid density, p the hydrodynamic plus magnetic pressure, σ the electrical conductivity, and B_0 the intensity of the magnetic field (assumed constant, uniform, and directed along the direction x_3). In (1), Δ^{-1} is the formal inverse of the Laplacian operator, e.g. [13]. The flow that develops under these conditions is encountered in very different contexts, such as metal production and semiconductor crystal growth. Another application concerns the cooling blankets of the future nuclear fusion reactor ITER. In them, the lithium surrounding the annular ring of plasma is subject to an intense confining magnetic field. The ability to predict the laminar or turbulent state of the lithium, as this flows in the blankets, has a crucial importance in the design of the reactor.

As observed in previous work [1,7], because of the Lorentz term turbulence becomes anisotropic and locally axisymmetric (that is, locally invariant under rotation about a preferred axis). This could be anticipated from the expression of the Lorentz force, which is proportional to the gradient of **u** along the direction of application of **B**, see (1). Recent numerical results [16] showed that this anisotropy is rather uniform throughout the scales. Further, the net effect of B_0 is to increase the dissipation of the velocity fluctuations. The experiment

* Corresponding author. Tel.: +32 0 2 650 5777; fax: +32 0 2 650 5824.
E-mail address: paolo.burattini@ulb.ac.be (P. Burattini).

0167-2789/$ - see front matter © 2008 Elsevier B.V. All rights reserved.
doi:10.1016/j.physd.2008.01.009

of Alemany et al. [1], who performed measurements in the wake of a grid moving in a column of still mercury, indicated that the power law decay of the turbulent kinetic energy was accelerated, in the presence of the magnetic field. The recent large-eddy simulations of Knaepen and Moin [8] confirmed this behaviour. In addition, these authors visualised the tendency towards two-dimensionality of the flow, for large values of B_0. The numerical study of Zikanov and Thess [18] also addressed the effect of the magnetic field on the velocity, with a view to clarifying the intermittent transition between two- and three-dimensionality. That analysis has been later extended to the inviscid case [15]. Ikeda and Kaneda [6] (IK hereafter) considered in detail the velocity spectrum tensor and derived scaling laws, after assuming that **B** only produced small perturbations at large wavenumbers with respect to the isotropic, nonmagnetic case. The theoretical prediction was found in agreement with data obtained from direct numerical simulations (DNS).

Comparatively, more results are available for full MHD turbulence (that is, for large values of magnetic Reynolds number). Matthaeus et al. [10] analysed 2D energy spectra and found that the anisotropy was larger for the velocity components perpendicular to the magnetic field. Carati et al. [4] examined the nonlinear transfers between the magnetic and velocity fields, by performing a DNS. They concluded that the cross-interactions between **B** and **u** were nonlocal, contrary to the direct inner interactions.

Despite the growing interest in the dynamic of liquid metals, basic information is still unavailable regarding, for example, detailed spectral distributions of the terms in the kinetic energy equation and their scaling properties. This knowledge would be invaluable in the modelling of unbounded MHD flows, and perhaps for the bulk region (i.e., away from the walls) of bounded flows. As an aside, notice that numerical simulations have a crucial role in quasi-static MHD, since performing experiments with liquid metals is both complex and dangerous.

2. Numerical method

Homogeneous MHD turbulence is simulated in a periodic box with a pseudo-spectral DNS code. The Navier–Stokes equation is combined with the Lorentz force, according to the quasi-static approximation [7]. The nonlinear term is evaluated in real space, after backward Fourier transforming the velocity field; aliasing errors are removed using phase-shifting [14]. Time advancement is performed with a third-order, low-storage, Runge–Kutta time integration scheme [17]. The computational domain is cubic (with a side of 2π), discretised by 256^3 Fourier modes, and the maximum significant wavenumber is $k_{\max} = 128$. Forcing is applied at low wavenumber, in the range $1.5 \le k \le 3.1$, so that a stationary state is achieved. This is characterised by a Taylor-microscale Reynolds number $R_\lambda = u_1'\lambda/\nu = 92$ [u_1' is the fluctuation rms of u_1, $\lambda = u_1(15\nu/\epsilon)^{1/2}$ is the Taylor-microscale, $\nu = 0.006$ is the kinematic viscosity], when $B_0 = 0$. After the magnetic field is applied, a transient follows, before the statistical quantities settle on new values. This state is described in the remainder. The intensity of the magnetic effect is quantified by the interaction parameter

$$N = \frac{\sigma B_0^2}{\rho} \frac{L}{u_1'} \tag{3}$$

where $L = (\pi/2u_1'^2) \int_0^{k_{\max}} E(k)/k\mathrm{d}k$ is the integral length scale and $E(k)$ is the 3D energy spectrum (see below). Three values of N (=1, 3, 5) are considered, in addition to the nonmagnetic case $N = 0$; in the following, results will be given mainly for $N = 1$ and 3, for brevity. Note that the ratio L/u_1' (the eddy turn-over time, which here is estimated just before B_0 is applied), depends only on the large scales. Therefore it inevitably reflects the type of forcing used. This should be kept in mind when comparing results in the literature.

3. Results

Some insight into the flow dynamics can be obtained from the kinetic energy equation in spectral space

$$F(\mathbf{k}) = T(\mathbf{k}) - 2\nu k^2 E(\mathbf{k}) - \underbrace{\frac{\sigma B_0^2}{\rho} \cos^2(\theta) E(\mathbf{k})}_{D_J(\mathbf{k})}, \tag{4}$$

where $\mathbf{k}$ is the wavenumber vector of magnitude k, $F(\mathbf{k})$ the forcing term, $T(\mathbf{k})$ the nonlinear transfer, $E(\mathbf{k})$ half the trace of the velocity spectrum tensor $\Phi_{ij}(\mathbf{k})$ [2], and θ the angle between $\mathbf{k}$ and $\mathbf{B} = B_0\mathbf{e}_3$. The turbulent kinetic energy is dissipated because of the joint effect of viscous $\epsilon_\nu = 2\nu \int k^2 E(\mathbf{k})\mathrm{d}\mathbf{k}$ and Joule dissipation $\epsilon_J = \int D_J(\mathbf{k})\mathrm{d}\mathbf{k}$. The latter is dominant over the former, in the present cases — the ratio ϵ_J/ϵ_ν is 2.9 for $N = 1$, and becomes 7.0 and 8.3 for $N = 3$ and 5, respectively. IK reported a ratio of 2.5, for $N = 1$.

3.1. Kinetic energy and dissipation spectra

As in isotropic turbulence, $E(\mathbf{k})$ is first averaged over thin spherical shells. The 3D spectra E_s (henceforth, the subscript s if for shell averaging) in Fig. 1 show that, at large N, Joule dissipation reduces drastically the turbulent energy at small scales. The inset of the figure displays the distributions compensated by $k^{5/3}$, in order to highlight the possible presence of the Kolmogorov inertial range. With the exception, perhaps, of the nonmagnetic case, no plateau is discernible.

In order to retain the angular information linked to the axisymmetry, the kinetic energy equation is averaged over thin spherical rings whose centre lies on the $\mathbf{e}_3$ axis, see Fig. 2. Eq. (4) is therefore rewritten as

$$F_r\left(k_\perp, k_\parallel\right) = T_r\left(k_\perp, k_\parallel\right) - 2\nu k^2 E_r\left(k_\perp, k_\parallel\right) - \frac{\sigma B_0^2}{\rho} \cos^2(\theta)\, E_r\left(k_\perp, k_\parallel\right), \tag{5}$$

where the subscript r if for ring averaging, and $k_\perp = k\sin(\theta)$, $k_\parallel = k\cos(\theta)$. In the following, 2D quantities, which are function of $\left(k_\perp, k_\parallel\right)$, are plotted after dividing by $\sin(\theta)$ (and are thus denoted by an asterisk). In this manner, for the isotropic

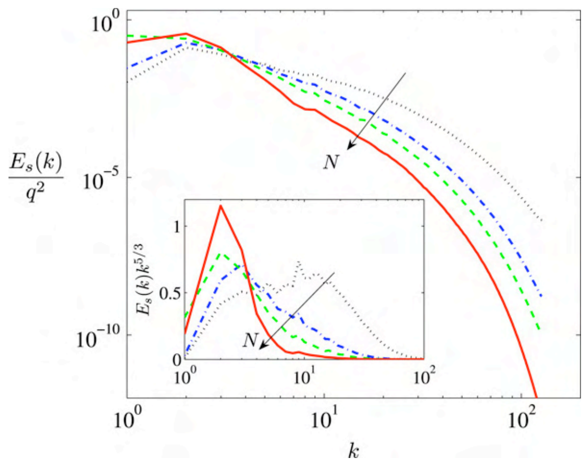

Fig. 1. Contours of the 3D spectra of $E(\mathbf{k})$ normalised by the total energy $q^2 = u_1'^2 + u_2'^2 + u_3'^2$. $\cdots$, $N = 0$; $\cdot-$, $N = 1$; $--$, $N = 3$; — $N = 5$. Inset: compensated spectra (line styles are as in main figure body).

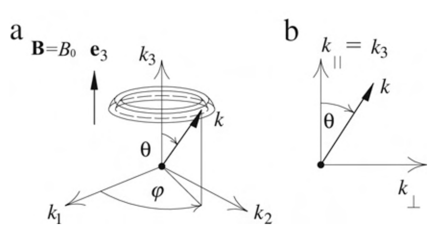

Fig. 2. Spherical ring averaging. (a) Cartesian and polar spherical coordinate systems, with representation of one ring and direction of application of the magnetic field. (b) Reduced coordinate system.

case, the distributions retain only the k-dependence (i.e. the iso-contours are arcs). This is done to highlight any θ-dependence due only to the anisotropy.

Distributions of the turbulent kinetic energy E_r^* are plotted in Figs. 3–5. For $N = 0$, the contours are, to a close approximation, arcs of a circle — i.e. there is no dependence on θ. A comparison between the profiles for $N = 0$ and $N = 1$ and 5 indicates that Joule dissipation attenuates the energy in a region close to the $k_\|$ axis, while in the proximity of $k_\perp$ the contours still follow a circular profile. For the largest value of N, the region where E_r^* is depleted approaches the shape of a wedge [11]. Similar results, obtained by experiments, are presented in [3].

More detailed information about the scaling of the velocity spectra can be obtained, if, following the proposal of IK, the two spectral quantities

$$E_a(\mathbf{k}) = \frac{k^2 + k_\|^2}{k^2 - k_\|^2}\Phi_{33}(\mathbf{k}) - \Phi_{11}(\mathbf{k}) - \Phi_{22}(\mathbf{k}) \tag{6}$$

$$E_b(\mathbf{k}) = \frac{k_\|^2}{k^2 - k_\|^2}\Phi_{33}(\mathbf{k}) + \Phi_{11}(\mathbf{k}) + \Phi_{22}(\mathbf{k}) \tag{7}$$

are defined. According to IK, these quantities represent the first-order deviations from the isotropic turbulence spectrum, in the case where the interaction parameter is small (or, for large values of N, at sufficiently high wavenumbers). Based on a Kolmogorov scaling argument, IK advocate that (6) and

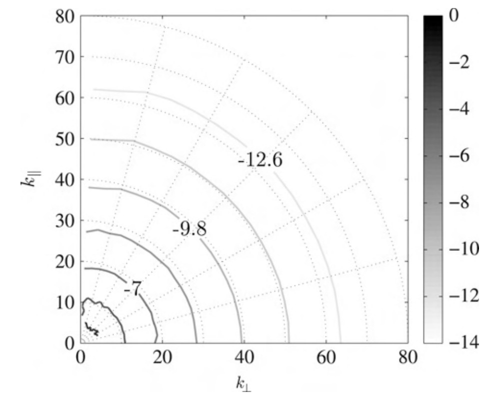

Fig. 3. Contours of $\log(E_r^*(k_\perp, k_\|))$, $N = 0$ (hereafter, iso-contours of 2D distributions are equally spaced).

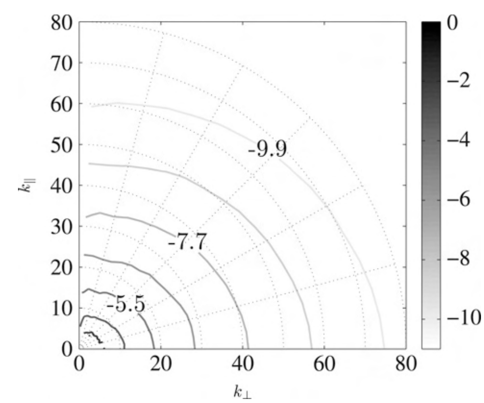

Fig. 4. Contours of $\log(E_r^*(k_\perp, k_\|))$, $N = 1$.

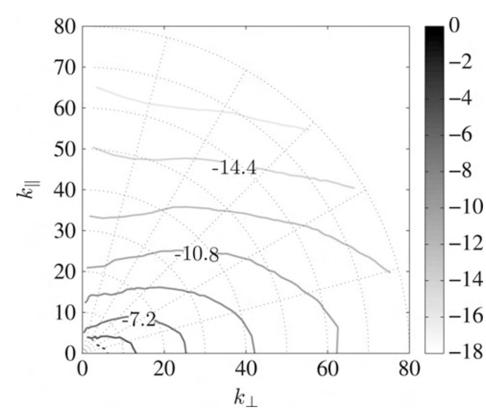

Fig. 5. Contours of $\log(E_r^*(k_\perp, k_\|))$, $N = 5$.

(7) should follow a $k^{-7/3}$ power law, when averaged over thin shells. The present profiles of $E_{as}(k)$ and $E_{bs}(k)$, Fig. 6, display this power law, for $k < 20$, in agreement with the numerical data of IK. However, such support of the theoretical analysis is somewhat surprising, if one recalls that the 3D spectra do not show any convincing Kolmogorov scaling in the same wavenumber range (even for $N = 1$, see Fig. 1). As seen in Fig. 7, for larger values of N, the $k^{-7/3}$ scaling is clearly violated, which is commensurate with the fact that ϵ_J is much larger than ϵ_ν. Therefore the effect of the Lorentz term cannot any longer be considered as a mere perturbation.

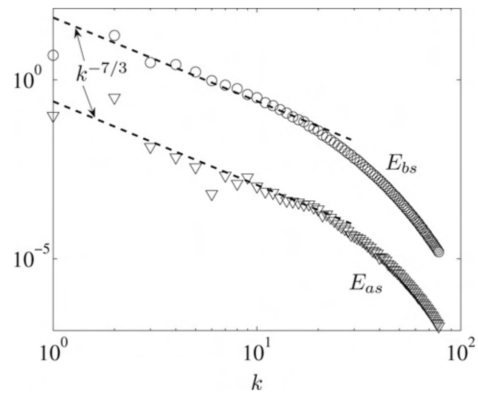

Fig. 6. Spectra $E_{as}(k)$, $E_{bs}(k)$, $N = 1$.

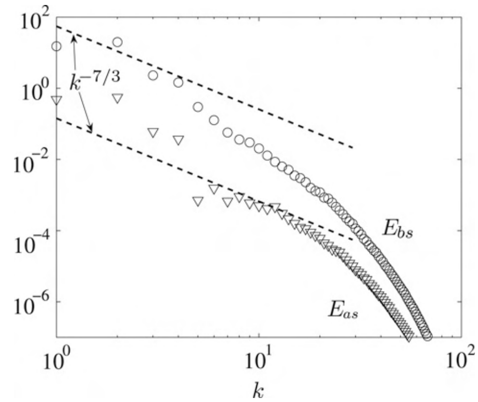

Fig. 7. Spectra $E_{as}(k)$, $E_{bs}(k)$, $N = 5$.

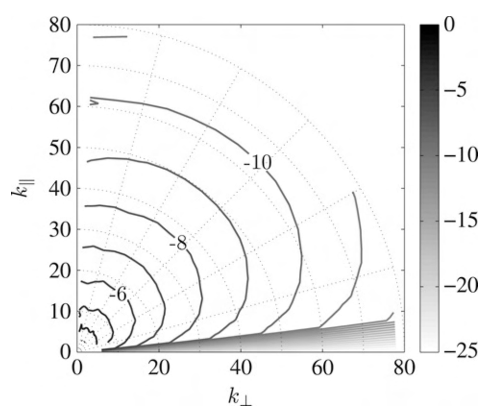

Fig. 8. Contours of $\log(D^*_{Jr}(k_\perp, k_\parallel))$, $N = 1$.

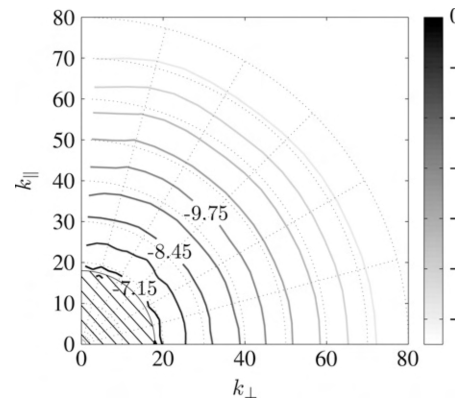

Fig. 9. Contours of $\log(T^*_r(k_\perp, k_\parallel))$, $N = 0$. (To increase the dynamic range, in this figure and the next, the hatched area is excluded from the plot.)

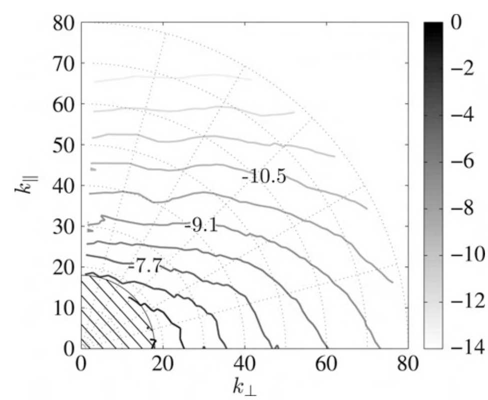

Fig. 10. Contours of $\log(T^*_r(k_\perp, k_\parallel))$, $N = 3$.

The Joule dissipation spectrum D^*_{Jr} for $N = 1$ (Fig. 8) reflects closely the contours of E^*_r (Fig. 4), at least at small values of θ. However, when the angle approaches 90°, the magnetic dissipation vanishes, see (5).

3.2. Nonlinear transfer

Distributions of T^*_r are shown in Figs. 9 and 10. At small k, the transfer is negative and rather large in absolute value. This region, where the effect of forcing is dominant, is excluded from the plots. At large k, the contours for $N = 0$ are independent of θ, as expected. For $N = 3$, the shape of the attenuation of the nonlinear transfer resembles that of energy distribution. Therefore, T^*_r has a gradient not only in the radial but also in the angular direction.

The locality of the energy transfers can be assessed by decomposing the convolution integral in the expression of the nonlinear transfer (e.g. [12])

$$T(\mathbf{k}) = k_l P_{jk}(\mathbf{k}) \Re \left\{ \mathrm{i}\hat{u}_j(\mathbf{k}) \int \hat{u}^*_k(\mathbf{p}) \hat{u}^*_l(\mathbf{k}-\mathbf{p}) \,\mathrm{d}\mathbf{p} \right\}. \quad (8)$$

In (8), $\hat{u}_j$ is the j-component of the velocity, the hat represents the Fourier transform, $\Re$ the real part, the asterisk complex conjugate (here only), and $P_{jk}(\mathbf{k}) = \delta_{jk} - k_j k_k / k^2$ is the projector tensor (with δ_{jk} the Kronecker symbol). By dividing in rings the domain of integration over $\mathbf{p}$, one obtains detailed functions $T^*_{pr}(p, \psi, k, \theta)$, which are a measure of the transfer between a first ring identified by the pair (p, ψ) and a second ring localised at (k, θ). This procedure represents a direct extension of that of Domaradzki and Rogallo [5] (see also [2]). Profiles of $T^*_{pr}(p, \psi)_{p=k}$ and $T^*_{pr}(p, \psi)_{\psi=\theta}$ for $N = 3$ and at $k = 30, \theta = \pi/4$ are shown in Fig. 11. (Other locations in the same area display the same features.) These quantities can be interpreted, by extension of the spherical case, as radial and angular transfers. In the absence of the magnetic field, there is only radial transfer, from small to large values of k (not shown). As N increases, the gradient of the energy in the angular direction yields a second transfer, from large to small

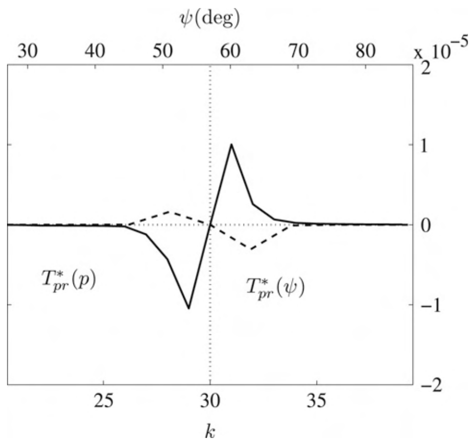

Fig. 11. Detailed transfer T^*_{pr} at $k = 30, \theta = \pi/4, N = 3$.

values of the angle ψ. Note that the two detailed transfers have comparable intensity and degree of locality in wavenumber space.

4. Conclusions

Some properties of the turbulent flow developing in liquid metals, subject to a uniform magnetic field, have been reported. By analysing the terms of the kinetic energy equation obtained from direct numerical simulations, it has been found that the effect of Joule dissipation is localised in the vicinity of the axis of application of the magnetic field. For unity value of the interaction parameter N, a scaling law of the velocity fluctuation spectra has been verified. However, for the range of scales resolved by the present simulations, this scaling appears ineffective at higher values of N. The nonlinear transfer has been computed and was found to be a function of the angle with respect to the magnetic field. Detailed energy transfers arise not only between velocity fluctuations of different sizes but also of different orientations. Both detailed transfers are rather local, in wavenumber space.

Acknowledgments

This work, conducted as part of the award (Modelling and simulation of turbulent conductive flows in the limit of low magnetic Reynolds number) made under the European Heads of Research Councils and European Science Foundation EURYI (European Young Investigator) Awards scheme, was supported by funds from the Participating Organisations of EURYI and the EC Sixth Framework Programme. Financial support from the Communauté Française de Belgique (ARC 02/07-283) and from the contract of association EURATOM-Belgian state is also gratefully acknowledged. The content of the publication is the sole responsibility of the authors and it does not necessarily represent the views of the Commission or its services. MK and DC are supported by FRIA and FRS-FNRS Belgium.

References

[1] A. Alemany, R. Moreau, P.L. Sulem, U. Frisch, Influence of an external magnetic field on homogeneous MHD turbulence, J. de Mécanique 18 (1979) 277–313.

[2] G.K. Batchelor, The Theory of Homogeneous Turbulence, Cambridge University Press, Cambridge, 1953.

[3] P. Caperan, A. Alemany, Homogeneous low-magnetic-Reynolds-number MHD turbulence — Study of the transition to the quasi-two-dimensional phase and characterization of its anisotropy, J. de Mécanique 4 (1985) 175–200.

[4] D. Carati, O. Debliquy, B. Knaepen, B. Teaca, M. Verma, Energy transfers in forced MHD turbulence, J. Turbul. 7 (51) (2006) 1–12.

[5] J.A. Domaradzki, R.S. Rogallo, Local energy transfer and nonlocal interactions in homogeneous, isotropic turbulence, Phys. Fluids 2 (1990) 413–426.

[6] T. Ishida, Y. Kaneda, Small-scale anisotropy in magnetohydrodynamic turbulence under a strong uniform magnetic field, Phys. Fluids 19 (075104) (2007) 1–10.

[7] B. Knaepen, S. Kassinos, D. Carati, Magnetohydrodynamic turbulence at moderate magnetic Reynolds number, J. Fluid Mech. 513 (2004) 199–220.

[8] B. Knaepen, P. Moin, Large-eddy simulation of conductive flows at low magnetic Reynolds number, Phys. Fluids 16 (2004) 1255–1261.

[9] J. Mathieu, J. Scott, An Introduction to Turbulent Flow, Cambridge University Press, Cambridge, 2000.

[10] W.H. Matthaeus, S. Ghosh, S. Oughton, D.A. Roberts, Anisotropic three-dimensional MHD turbulence, J. Geophys. Res. 101 (1996) 7619–7630.

[11] R. Moreau, Magnetohydrodynamics, Kluwer Academic, Dordrecht, 1990.

[12] S.B. Pope, Turbulent Flows, Cambridge University Press, Cambridge, 2000.

[13] P.H. Roberts, An Introduction to Magnetohydrodynamics, Elsevier, New York, 1967.

[14] R.S. Rogallo, Numerical experiments in homogeneous turbulence, NASA Tech. Memo. TM 81315 (1981).

[15] A. Thess, O. Zikanov, Transition from two-dimensional to three-dimensional magnetohydrodynamic turbulence, J. Fluid Mech. 579 (2007) 383–412.

[16] A. Vorobev, O. Zikanov, P.A. Davidson, B. Knaepen, Anisotropy of magnetohydrodynamic turbulence at low magnetic Reynolds number, Phys. Fluids 17 (125105) (2005) 1–12.

[17] J.H. Williamson, Low-storage Runge–Kutta schemes, J. Comput. Phys. 35 (1980) 48–56.

[18] O. Zikanov, A. Thess, Direct numerical simulation of forced MHD turbulence at low magnetic Reynolds number, J. Fluid Mech. 358 (1998) 299–333.

Available online at www.sciencedirect.com

ScienceDirect

Physica D 237 (2008) 2067–2071

PHYSICA D

www.elsevier.com/locate/physd

Variational formulation of the motion of an ideal fluid on the basis of gauge principle

Tsutomu Kambe*

IDS, Higashi-yama 2-11-3, Meguro-ku, Tokyo 153-0043, Japan
Chern Institute of Mathematics, Nankai University, China[1]

Available online 25 September 2007

Abstract

On the basis of gauge principle in the field theory, a new variational formulation is presented for flows of an ideal fluid. The fluid is defined thermodynamically by mass density and entropy density, and its flow fields are characterized by symmetries of translation and rotation. A structure of rotation symmetry is equipped with a Lagrangian Λ_A including vorticity, in addition to Lagrangians of translation symmetry. From the action principle, Euler's equation of motion is derived. In addition, the equations of continuity and entropy are derived from the variations. Equations of conserved currents are deduced as the Noether theorem in the space of Lagrangian coordinate $\boldsymbol{a}$. It is shown that, with the translation symmetry alone, there is freedom in the transformation between the Lagrangian $\boldsymbol{a}$-space and Eulerian $\boldsymbol{x}$-space. The Lagrangian Λ_A provides non-trivial topology of vorticity field and yields a source term of the helicity. The vorticity equation is derived as an equation of the gauge field. The present formulation provides a basis on which the transformation between the $\boldsymbol{a}$ space and the $\boldsymbol{x}$ space is determined uniquely.

Keywords: Variational formulation; Gauge principle; Euler's equation; Helicity; Chern–Simons term

1. Introduction

In the historical paper '*General laws of the motion of fluids*' [1], Leonhard Euler verified that his equation of motion can describe rotational flows. The same theme is investigated in this paper under a modern view. *Fluid mechanics* is understood to be a field theory in Newtonian mechanics that has Galilean symmetry. It is covariant under transformations of the Galilei group. The gauge principle [19–21] requires a physical system under investigation to have a *symmetry*, *i.e.* a gauge invariance with respect to a certain group of transformations. Following this principle, the gauge symmetry of flow fields is studied in [2] and [3] with respect to both translational and rotational transformations. The formulation started from a Galilei-invariant Lagrangian of a system of *point masses* which is known to have *global* gauge symmetries with respect to both translation and rotation [4]. It was then extended to flows of a fluid, a continuous material characterized with mass density and entropy density. In addition to the global symmetry, *local* gauge invariance of a Lagrangian is required for such a continuous field. Symmetries imply conservation laws. Equations of conserved currents are deduced as the Noether theorem.

Thus, the convective derivative of fluid mechanics, *i.e.* the Lagrange derivative, is identified as the *covariant derivative*, which is a building block in the framework of gauge theory. Based on this, appropriate Lagrangians are defined for motion of an ideal fluid. Euler's equation of motion is derived from the action principle. In most traditional formulations, the continuity equation and entropy equation are given as constraints for the variations, while in this new formulation those equations were derived from the action principle. In the previous study [5,6] of rotational symmetry of the velocity field $\boldsymbol{v}(\boldsymbol{x})$, it is found that the vorticity $\boldsymbol{\omega} = \nabla \times \boldsymbol{v}$ is the gauge field associated with the rotational symmetry of velocity.

A new structure of the rotational symmetry was given in [3] by the following Lagrangian:

* Corresponding address: IDS, Higashi-yama 2-11-3, Meguro-ku, Tokyo 153-0043, Japan. Tel.: +81 3 3792 2904; fax: +81 3 3792 2859.
E-mail address: kambe@ruby.dti.ne.jp.
URL: http://www.purple.dti.ne.jp/kambe/.

[1] Visiting Professor.

0167-2789/$ - see front matter
doi:10.1016/j.physd.2007.09.020

$$\Lambda_A = -\int_M \langle \mathcal{L}_W \boldsymbol{A}, \boldsymbol{\omega} \rangle \, \mathrm{d}^3\boldsymbol{x},$$

where $\boldsymbol{A}$ is a vector potential and $\mathcal{L}_W \boldsymbol{A} = \partial_t \boldsymbol{A} + v^k \partial_k \boldsymbol{A} + A_k \nabla v^k$. This is derived from a representation characteristic of a *topological* term known in the gauge theory. This yields a non-vanishing rotational component of the velocity field, and provides a source term of helicity. This is closely related to the Chern–Simons term, describing non-trivial topology of vorticity field, *i.e.* mutual linking of vorticity lines. The vorticity equation is derived as an equation for the gauge field.

With regard to the variational formulation of fluid flows, the papers [7] and [8] are among the earliest to have influenced current formulations. Their variations are carried out in two ways: *i.e.* a Lagrangian approach and an Eulerian approach. In both approaches, the equation of continuity and the condition of isentropy are added as constraint conditions on the variations by means of Lagrange multipliers. The Lagrangian approach is also taken by [9]. In this relativistic formulation those equation are derived from the equations of current conservation. Several action principles to describe relativistic fluid dynamics have appeared in the past (see [9, Section 4.2] for a list of some of them).

In the Lagrangian approach, the Euler–Lagrange equation results in an equation equivalent to Euler's equation of motion in which the acceleration term is represented as the second time derivative of position coordinates of the Lagrangian representation. In this formulation, however, there is a certain degree of freedom in the relation between the Lagrangian particle coordinates and Eulerian space coordinates. Namely, the relation between them is determined only up to an unknown rotation. In the second approach referred to as the *Eulerian* description, the action principle of an ideal fluid results in potential flows with vanishing helicity, if the fluid is *homentropic* [2]. However, as noted in the beginning, it should be possible to have rotational flows even in such a homentropic fluid. Gauge theory for fluid flows provides a crucial key to resolve these issues. It was also shown in [2] that a general solution in the translational symmetry alone is equivalent to the classical Clebsch solution [10]. A new formulation on the basis of the Clebsch parametrization is carried out in [11] and [12] aiming at its extension to supersymmetric and non-Abelian fluid mechanics.

It is interesting to note the gauge invariances known in the theory of electromagnetism and fluid flows. There is an invariance under a gauge transformation of electromagnetic potentials consisting of a scalar potential ϕ and a vector potential $\boldsymbol{A}$. An analogous invariance is pointed out in [2] for a gauge transformation of a velocity potential ϕ of irrotational flows of an ideal fluid, where the velocity is represented as $\boldsymbol{v} = \nabla\phi$. It is shown in [7] (cited in [3]) that gauge invariance is not restricted to the potential flows, but also there is known to be an invariance in the rotational flow of *Clebsch representation*.

2. Equations in *a*-space

2.1. Lagrangian

Let us consider a variational formulation with a Lagrangian represented with the particle coordinate $\boldsymbol{a} = (a^1, a^2, a^3) = (a, b, c)$ (*i.e. Lagrangian* coordinates). Independent variables are denoted with a^μ where μ or a greek letter suffix take $= 0, 1, 2, 3$ with a^0 the time variable written also as $\tau \ (= t)$: $a^\mu = (\tau, a^1, a^2, a^3)$. Corresponding physical space coordinate $\boldsymbol{x} = (x, y, z)$ (*Eulerian* coordinates) are written also as $x^\mu = (t, x^1, x^2, x^3)$. The letter τ is used (instead of t) in combination with the particle coordinates a^k. Physical space position of a particle $\boldsymbol{a}$ is expressed by $X^k(a^\mu) = X^k(\tau, \boldsymbol{a})$, or $X^k = (X, Y, Z)$. Its velocity is given by $v^k = \partial_\tau X^k$, also written as X^k_τ.

The Lagrangian coordinates (a, b, c) are defined such that an infinitesimal three-element $\mathrm{d}^3\boldsymbol{a} = \mathrm{d}a\,\mathrm{d}b\,\mathrm{d}c$ denotes a mass element $\mathrm{d}m$ of an infinitesimal volume $\mathrm{d}^3\boldsymbol{x} = \mathrm{d}x\,\mathrm{d}y\,\mathrm{d}z$ of the $\boldsymbol{x}$-space. The mass element $\mathrm{d}m$ should be invariant during the motion:

$$\partial_\tau(\mathrm{d}m) \equiv \partial_\tau(\mathrm{d}^3\boldsymbol{a}) = 0. \tag{1}$$

The mass-density ρ is defined by the equation $\mathrm{d}^3\boldsymbol{a} = \rho\,\mathrm{d}^3\boldsymbol{x}$. With using a Jacobian determinant J of the transformation $X^k = X^k(a^l)$ from $\boldsymbol{a}$-space to $\boldsymbol{X}$-space ($k, l = 1, 2, 3$), we have

$$\rho = \frac{1}{J}, \quad J = \frac{\partial(X^1, X^2, X^3)}{\partial(a^1, a^2, a^3)} = \frac{\partial(X, Y, Z)}{\partial(a, b, c)}. \tag{2}$$

In an ideal fluid, there is no dissipation of kinetic energy into heat, by definition. According to thermodynamics for the entropy s (per unit mass) and temperature T, we have $T\delta s = 0$ if there is no heat production. Namely the entropy s does not depend on τ. Then, the change of internal energy ϵ (per unit mass) is related to the density change $\delta\rho$ alone by

$$\delta\epsilon = (\delta\epsilon)_s = \frac{p}{\rho^2}\,\delta\rho, \quad \left(\frac{\partial\epsilon}{\partial\rho}\right)_s = \frac{p}{\rho^2}, \quad \delta h = \frac{1}{\rho}\delta p, \tag{3}$$

where p is the fluid pressure, $h = \epsilon + p/\rho$ the enthalpy, and $(\,\cdot\,)_s$ denotes s being fixed. However, the entropy s may not be uniform and may depend on $\boldsymbol{a}$ by initial conditions. Hence, $s = s(\boldsymbol{a})$, or equivalently,

$$\partial_\tau s = 0. \tag{4}$$

The total Lagrangian is defined by

$$\Lambda_{\mathrm{T}} = \int_{M_a} \frac{1}{2} X^k_\tau X^k_\tau \mathrm{d}^3\boldsymbol{a} - \int_{M_a} \epsilon(\rho, s)\mathrm{d}^3\boldsymbol{a}, \tag{5}$$

[3], where M_a is a space of fluid under investigation, and $X^k_\tau = X^k_0 = v^k$ is the velocity. The internal energy $\epsilon(\rho, s)$ of the second term depends on ρ (which in turn depends on $X^k_l = \partial X^k/\partial a^l$ by (2)) and the entropy $s(\boldsymbol{a})$.

An action I is defined by the integral: $I = \int \Lambda_{\mathrm{T}} \mathrm{d}\tau$:

$$I = \int L(X^k_\mu)\,\mathrm{d}^4 a, \quad \mathrm{d}^4 a = \mathrm{d}\tau\,\mathrm{d}^3\boldsymbol{a}, \tag{6}$$

$$L(X^k_\mu) = \frac{1}{2} X^k_0 X^k_0 - \epsilon(X^k_l, a^k). \tag{7}$$

2.2. Noether's theorem

The Euler–Lagrange equation associated with the Lagrangian (7) is given by

$$\frac{\partial}{\partial a^\mu}\left(\frac{\partial L}{\partial X^k_\mu}\right) - \frac{\partial L}{\partial X^k} = \partial_\mu \left(\frac{\partial L}{\partial X^k_\mu}\right) - \frac{\partial L}{\partial X^k} = 0. \tag{8}$$

Energy–momentum tensor T^ν_μ is defined by

$$T^\nu_\mu \equiv X^k_\mu \left(\frac{\partial L}{\partial X^k_\nu}\right) - L\delta^\nu_\mu, \tag{9}$$

[7], where $k = 1, 2, 3$. As long as (8) is satisfied together with an assumption of τ-independence of L (*i.e.* $\partial_\tau L = 0$), it can be verified [3] that we have a conservation equation $\partial_\nu T^\nu_\mu = 0$ (where $\partial_\mu = \partial/\partial a^\mu$). This is the Noether theorem [13,19].

For $\mu \neq 0\,(x^\mu = \alpha)$, the conservation law $\partial_\nu T^\nu_\mu = 0$ reduces to the momentum equations:

$$\partial_\tau V_\alpha + \partial_\alpha F = 0 \quad (V_\alpha \equiv X_\alpha X_\tau + Y_\alpha Y_\tau + Z_\alpha Z_\tau), \tag{10}$$

[7], where $F = -\frac{1}{2} v^2 + h$. Two other equations are obtained with α replaced by cyclic permutation of (a, b, c). Integrating this with respect to τ between 0 and t, we find the Weber's transformation [14, Art.15]:

$$V_\alpha(\tau) \equiv X_\alpha X_\tau + Y_\alpha Y_\tau + Z_\alpha Z_\tau = V_\alpha(0) - \partial_\alpha \chi, \tag{11}$$
$$\chi = \int_0^t F\,\mathrm{d}\tau = \int_0^t \left(-\frac{1}{2} v^2 + h\right)\mathrm{d}\tau.$$

The V_α of (10) is a transformed velocity in the $\boldsymbol{a}$-space (Section 5.1). Its time evolution is given by (11) for a given initial value of $V_\alpha(0, \boldsymbol{a})$ and $h(0, \boldsymbol{a})$ at $\boldsymbol{a} = \boldsymbol{x}$.

With $\mu = 0$, we have the energy equation:

$$\partial_\tau H + \partial_a \left[p\frac{\partial(X, Y, Z)}{\partial(\tau, b, c)}\right] + \partial_b \left[p\frac{\partial(X, Y, Z)}{\partial(a, \tau, c)}\right] + \partial_c \left[p\frac{\partial(X, Y, Z)}{\partial(a, b, \tau)}\right] = 0 \tag{12}$$

where $H = \frac{1}{2} v^2 + \epsilon$. The Eq. (10) reduces to the equation for the acceleration $\mathcal{A}_\alpha(\tau, \boldsymbol{a})$:

$$\mathcal{A}_\alpha \equiv X_\alpha X_{\tau\tau} + Y_\alpha Y_{\tau\tau} + Z_\alpha Z_{\tau\tau} = -\frac{1}{\rho}\partial_\alpha p, \tag{13}$$

which is known as the Lagrangian form of the equation of motion [14, Art.13]. This can be transformed to

$$X_{\tau\tau} = -\frac{1}{\rho}\partial_x p, \quad \partial_x p = \frac{\partial\alpha}{\partial x}\frac{\partial p}{\partial\alpha} \tag{14}$$

[3]. Since $X_{\tau\tau}$ is the x-acceleration of the particle $\boldsymbol{a}$, this is the form equivalent to the x-component of Euler's equation of motion (25). The y and z components can be obtained analogously.

2.3. Arbitrariness in the transformation

There is an arbitrariness in the transformation from the $\boldsymbol{a}$-space to the $\boldsymbol{x}$-space with respect to Eq. (13). Its middle-side expression is a form of scalar product of two vectors in the $\boldsymbol{x}$-space: the particle acceleration $(X_{\tau\tau}, Y_{\tau\tau}, Z_{\tau\tau})$ and the direction vector $(X_\alpha, Y_\alpha, Z_\alpha)$ of the α-axis in the $\boldsymbol{a}$-space.

Putting it in a different way, Eq. (13) is invariant with respect to orthogonal rotational transformations of a displacement vector $\Delta\boldsymbol{X} = (\Delta X, \Delta Y, \Delta Z)$ of a particle in the $\boldsymbol{x}$-space. In fact, suppose that a vector $\Delta\boldsymbol{X}$ satisfies Eq. (13). Then, another vector $\overline{\Delta\boldsymbol{X}} = R\,\Delta\boldsymbol{X}$ obtained by an orthogonal transformation R satisfies the same equation, since any orthogonal matrix satisfies $RR^{\mathrm{T}} = I$ (unit matrix) where R^{T} denotes the transposed matrix of R so that the vector $\Delta\boldsymbol{X}$ is not uniquely determined. The same freedom can be said to the velocity $V_\alpha(\tau, \boldsymbol{a})$ of (11) as well.

These imply that a certain machinery must be equipped in order to fix this arbitrariness within the framework of rotational symmetry. This will be considered later. Note that the density ρ is not changed by the orthogonal transformation.

3. Equations in $\boldsymbol{x}$-space

3.1. Action in Eulerian representation

The Eulerian description is represented by the independent variables (t, x, y, z). Local gauge symmetries of fluid flows are investigated in detail in [2,3]. The time derivative ∂_τ is equivalent to the convective derivative D_t:

$$\partial_\tau = \mathrm{D}_t, \quad \mathrm{D}_t \equiv \partial_t + u\partial_x + v\partial_y + w\partial_z = \partial_t + \boldsymbol{v}\cdot\nabla. \tag{15}$$

The operator D_t is verified to be gauge-invariant. The velocity field $\boldsymbol{v}(\boldsymbol{x}, t)$ is defined by the particle velocity:

$$\boldsymbol{v}(\boldsymbol{x}, t) = \partial_\tau \boldsymbol{X} = \mathrm{D}_t \boldsymbol{x}. \tag{16}$$

The acceleration field $\mathcal{A}(\boldsymbol{x}, t)$ is also defined by

$$\mathcal{A}(\boldsymbol{x}, t) = \partial_\tau{}^2 \boldsymbol{X} = \mathrm{D}_t \boldsymbol{v} = (\partial_t + v^k\partial_k)\boldsymbol{v}. \tag{17}$$

As noted previously, the mass $\mathrm{d}^3\boldsymbol{a}(\boldsymbol{a})$ and the entropy $s = s(\boldsymbol{a})$ satisfy (1) and (4). In view of these properties, we can define the following two Lagrangians:

$$L_\phi = -\int_M \partial_\tau\phi\,\mathrm{d}^3\boldsymbol{a}, \quad L_\psi = -\int_M s\,\partial_\tau\psi\,\mathrm{d}^3\boldsymbol{a}, \tag{18}$$

where $\phi(\boldsymbol{a}, \tau)$ and $\psi(\boldsymbol{a}, \tau)$ are scalar fields associated with mass and entropy, respectively. By adding L_ϕ and L_ψ to Λ_{T} of (5), the total Lagrangian is given by

$$\Lambda^*_{\mathrm{T}} = \Lambda_{\mathrm{T}} - \int \partial_\tau\phi\,\mathrm{d}^3\boldsymbol{a} - \int s\,\partial_\tau\psi\,\mathrm{d}^3\boldsymbol{a}. \tag{19}$$

The action is defined by $I = \int_{\tau_1}^{\tau_2} \Lambda^*_{\mathrm{T}}\mathrm{d}\tau$, where the integral $I_\phi = \int \mathrm{d}\tau \int \partial_\tau\phi\,\mathrm{d}^3\boldsymbol{a}$ can be integrated with respect to τ and expressed as $\int[\phi]\mathrm{d}^3\boldsymbol{a}$, where $[\phi] = \phi|_{\tau_2} - \phi|_{\tau_1}$ is the difference of ϕ at the end times τ_2 and τ_1 and hence independent of $\tau \in (\tau_1, \tau_2)$. Likewise, the last integral can be expressed as

$I_\psi = \int[\psi]s\,\mathrm{d}^3\boldsymbol{a}$, because s is independent of τ. This means that the gauge potentials ϕ and ψ do not appear in the equation of motion obtained through variations of the action I for $\tau \in (\tau_1, \tau_2)$.

However, it soon becomes clear that these are nontrivial in the expressions of the $\boldsymbol{x}$-space, because they are rewritten as $L_\phi = -\int_M \rho\, \mathrm{D}_t\phi\, \mathrm{d}^3\boldsymbol{x}$, and $L_\psi = -\int_M \rho s\, \mathrm{D}_t\psi\, \mathrm{d}^3\boldsymbol{x}$ by using the relations $\mathrm{d}^3\boldsymbol{a} = \rho\, \mathrm{d}^3\boldsymbol{x}$ and $\partial_\tau = \mathrm{D}_t$.

In the $\boldsymbol{x}$-space, the total Lagrangian can be written as $\Lambda^*_{\mathrm{T}} = \int_M \mathcal{L}(\boldsymbol{v}, \rho, s, \phi, \psi)\, \mathrm{d}^3\boldsymbol{x}$, where

$$\mathcal{L} \equiv \frac{1}{2}\rho\, v^k v^k - \rho\epsilon(\rho, s) - \rho \mathrm{D}_t\phi - \rho s \mathrm{D}_t\psi \tag{20}$$

[22]. This is proposed as a *possible* form of Lagrangian in the $\boldsymbol{x}$-space (but an additional term will be added later). The action is defined by $I = \int \mathcal{L}(\boldsymbol{v}, \rho, s, \phi, \psi)\, \mathrm{d}^4x$, where $\mathrm{d}^4x = \mathrm{d}t\, \mathrm{d}^3\boldsymbol{x}$. However, the action principle results in the potential flow represented by $\boldsymbol{v} = \mathrm{grad}(\phi + s_0\psi)$ when the fluid has a uniform entropy s_0 (see [2]).

3.2. Outcomes of variations

We require invariance of the action I with respect to variations. First, consider the following infinitesimal transformation: $\boldsymbol{x}'(\boldsymbol{x}, t) = \boldsymbol{x} + \boldsymbol{\xi}(\boldsymbol{x}, t)$. The volume element $\mathrm{d}^3\boldsymbol{x}$ is changed to $\mathrm{d}^3\boldsymbol{x}' = (1 + \partial_k\xi^k)\mathrm{d}^3\boldsymbol{x}$, up to the first order terms. Hence the variation of volume is given by $\Delta(\mathrm{d}^3\boldsymbol{x}) = \partial_k\xi^k\, \mathrm{d}^3\boldsymbol{x}$, while the variations of density, velocity and entropy are $\Delta\rho = -\rho\, \partial_k\xi^k$, $\Delta\boldsymbol{v} = \mathrm{D}_t\boldsymbol{\xi}$, and $\Delta s = 0$. Under these together with (1) and (4) (with keeping ϕ and ψ fixed), the variation of I is given by

$$\Delta I = \int \mathrm{d}^4x \left[\frac{\partial L}{\partial \boldsymbol{v}}\Delta\boldsymbol{v} + \frac{\partial L}{\partial \rho}\Delta\rho + \frac{\partial L}{\partial s}\Delta s + L\partial_k\xi^k\right].$$

This is required to vanish for arbitrary variation of ξ^k, which results in the Euler–Lagrange equation:

$$\frac{\partial}{\partial t}\left(\frac{\partial L}{\partial v^k}\right) + \frac{\partial}{\partial x^l}\left(v^l\frac{\partial L}{\partial v^k}\right) + \frac{\partial}{\partial x^k}\left(L - \rho\frac{\partial L}{\partial \rho}\right) = 0. \tag{21}$$

Similarly, invariance of I with respect to arbitrary variations of ϕ and ψ (denoted by $\Delta\phi$ and $\Delta\psi$) leads to

$$\Delta\phi : \partial_t\rho + \nabla\cdot(\rho\boldsymbol{v}) = 0 \text{ (continuity equation)}, \tag{22}$$

$$\Delta\psi : \partial_t(\rho s) + \nabla\cdot(\rho s\boldsymbol{v}) = 0. \tag{23}$$

3.3. Noether's theorem in Eulerian representation

Associated with (21), one can define the momentum density m_k and momentum–flux tensor M_k^l by

$$m_k = \frac{\partial L}{\partial v^k}, \quad M_k^l = v^l\frac{\partial L}{\partial v^k} + \left(L - \rho\frac{\partial L}{\partial \rho}\right)\delta_k^l. \tag{24}$$

From (7), we obtain $m_k = \rho v_k$ and $M_k^l = \rho v_k v^l + p\,\delta_k^l$, where $v_k = v^k$ in the present Euclidean space. The Eq. (21) can be written in the form of momentum conservation, $\partial_t(\rho v^k) + \partial_l(\rho v^l v^k) + \partial_k p = 0$ ($\partial_k = \partial/\partial x^k$). Using (22), this equation can be reduced to the following Euler's equation of motion:

$$\partial_t v^k + (v^l\partial_l)v^k = -\frac{1}{\rho}\,\partial_k\, p \quad (= -\partial_k\, h). \tag{25}$$

The Eq. (14) is equivalent to this equation.

The energy Eq. (12) can be transformed to the following equation of energy conservation:

$$\partial_t\left[\rho\left(\frac{1}{2}v^2 + \epsilon\right)\right] + \partial_k\left[\rho v^k\left(\frac{1}{2}v^2 + h\right)\right] = 0.$$

4. Rotation symmetry

A topological structure of vorticity field is now considered with respect to the rotational symmetry. The related gauge group is the rotation group $SO(3)$. An infinitesimal rotation is described by the Lie algebra $\mathbf{so}(3)$ of three dimensions, which is non-Abelian.

From the study of the rotational gauge transformation [3], it is found that the covariant derivative ∇_t, velocity $\boldsymbol{v}$ and acceleration $\mathcal{A}$ are represented as

$$\nabla_t = \partial_t + (\boldsymbol{v}\cdot\nabla), \tag{26}$$

$$\boldsymbol{v} = \nabla_t\boldsymbol{x} = (\partial_t + (\boldsymbol{v}\cdot\nabla))\boldsymbol{x}, \tag{27}$$

$$\mathcal{A} = \nabla_t\boldsymbol{v} = \partial_t\boldsymbol{v} + (\boldsymbol{v}\cdot\nabla)\,\boldsymbol{v} \tag{28}$$

$$\nabla_t\boldsymbol{v} = \partial_t\boldsymbol{v} + \mathrm{grad}\left(\frac{1}{2}v^2\right) + \boldsymbol{\omega}\times\boldsymbol{v}. \tag{29}$$

It is verified that the last expression of $\nabla_t\boldsymbol{v} = \partial_t\boldsymbol{v} + \nabla(\frac{1}{2}v^2) + \boldsymbol{\omega}\times\boldsymbol{v}$ not only satisfies the rotational gauge-invariance, but also expresses that $\boldsymbol{\omega}$ is the gauge field of the rotational symmetry. In addition, it satisfies the covariance requirement with respect to Galilean transformation from one reference frame $(t, \boldsymbol{x}, \boldsymbol{v})$ to another $(t_*, \boldsymbol{x}_*, \boldsymbol{v}_*)$ moving with a uniform relative velocity $\boldsymbol{U}$, where $t_* = t$, $\boldsymbol{x}_* = \boldsymbol{x} - \boldsymbol{U}t$ and $\boldsymbol{v}_* = \boldsymbol{v} - \boldsymbol{U}$. Namely, we have the covariance $\nabla_t\boldsymbol{v} = (\nabla_t\boldsymbol{v})_*$.

5. Lagrangian associated with rotation symmetry

Associated with the rotation symmetry, an additional Lagrangian is to be defined according to the gauge principle. It is important to observe from Section 3.1 that, in the Lagrangian (19), the integrands of the last two integrals are of the form $\partial_\tau(\cdot)$. The action is defined by $I = \int\int[\Lambda_{\mathrm{T}} + \partial_\tau(\cdot)]\,\mathrm{d}\tau\mathrm{d}^3\boldsymbol{a}$. This property is regarded as the simplest representation of topology in the gauge theory [16–19]. In the context of rotational flows, it is known that the helicity (or Hopf invariant, [15]) describes non-trivial topology of vorticity field, *i.e.* mutual linking of vorticity lines. This is closely related with the Chern–Simons term (without third-order term) in the gauge theory. This term lives in one dimension lower than the original four space–time (x^μ) of the action I because a topological term in the action is expressed in a form of total divergence $(\partial_\mu F^\mu)$ and characterizes topologically non-trivial structures of the gauge field.

However, we learn here from the formulation of Section 3.1 and look for a τ-independent field directly.

5.1. Lagrangian Λ_A and helicity

The τ-independent field can be found immediately from Eq. (10). Taking the curl of this equation with respect to the coordinates (a, b, c), we obtain

$$\nabla_a \times \partial_\tau \boldsymbol{V}_a = \partial_\tau (\nabla_a \times \boldsymbol{V}_a) = 0, \tag{30}$$

where $\nabla_a = (\partial_a, \partial_b, \partial_c)$. Hence, one may write as $\nabla_a \times \boldsymbol{V}_a = \boldsymbol{\Omega}_a(\boldsymbol{a})$ [7].

The vector $\boldsymbol{V}_a$ is a transformed form of the velocity $\boldsymbol{v} = (X_\tau, Y_\tau, Z_\tau) = (u, v, w)$ into the $\boldsymbol{a}$-space. This is seen on the basis of a 1-form V^1 defined by

$$V^1 = V_a\,\mathrm{d}a + V_b\,\mathrm{d}b + V_c\,\mathrm{d}c \tag{31}$$

$$= u\,\mathrm{d}x + v\,\mathrm{d}y + w\,\mathrm{d}z \tag{32}$$

where $V_a = ux_a + vy_a + wz_a$, $x_a = \partial X/\partial a$, $u = X_\tau$, *etc.* Its differential $\mathrm{d}V^1$ gives a 2-form $\Omega^2 = \mathrm{d}V^1$:

$$\begin{aligned}\Omega^2 &= \Omega_a \mathrm{d}b \wedge \mathrm{d}c + \Omega_b \mathrm{d}c \wedge \mathrm{d}a + \Omega_c \mathrm{d}a \wedge \mathrm{d}b \\ &= \omega_x \mathrm{d}y \wedge \mathrm{d}z + \omega_y \mathrm{d}z \wedge \mathrm{d}x + \omega_z \mathrm{d}x \wedge \mathrm{d}y,\end{aligned} \tag{33}$$

where $(\Omega_a, \Omega_b, \Omega_c) = \boldsymbol{\Omega}_a$, and $\nabla \times \boldsymbol{v} = (\omega_x, \omega_y, \omega_z) = \boldsymbol{\omega}$ is the vorticity. Thus, it is seen that $\boldsymbol{\Omega}_a$ is the vorticity transformed to the $\boldsymbol{a}$-space. The Eq. (30) is transformed into the τ-derivative of the 2-form Ω^2, $\mathcal{L}_{\partial_\tau}\Omega^2 = 0$ (understood as the Lie derivative).

Next, let us introduce a gauge-potential vector $\boldsymbol{A}_a = (\overline{A}_a, \overline{A}_b, \overline{A}_c)$ in the $\boldsymbol{a}$-space, and define its 1-form A^1 by $A^1 = \overline{A}_a\,\mathrm{d}a + \overline{A}_b\,\mathrm{d}b + \overline{A}_c\,\mathrm{d}c = \overline{A}_x\,\mathrm{d}x + \overline{A}_y\,\mathrm{d}y + \overline{A}_z\,\mathrm{d}z$. Thus, it is proposed that a *possible* type of Lagrangian is

$$\Lambda_A = -\int_M \langle \partial_\tau \boldsymbol{A}_a, \boldsymbol{\Omega}_a \rangle\,\mathrm{d}^3\boldsymbol{a} = \int_M \langle \boldsymbol{A},\ E_W[\boldsymbol{\omega}]\,\rangle\,\mathrm{d}^3\boldsymbol{x},$$

where $E_W[\boldsymbol{\omega}] \equiv \partial_t \boldsymbol{\omega} + (\boldsymbol{v}\cdot\nabla)\boldsymbol{\omega} - (\boldsymbol{\omega}\cdot\nabla)\boldsymbol{v} + (\nabla\cdot\boldsymbol{v})\boldsymbol{\omega}$.

New results were deduced from this Lagrangian in [3]: (i) the velocity $\boldsymbol{v}$ includes a new rotational term, (ii) the vorticity equation is derived from the variation of $\boldsymbol{A}$:

$$E_W[\boldsymbol{\omega}] = \partial_t \boldsymbol{\omega} + (\boldsymbol{v}\cdot\nabla)\boldsymbol{\omega} - (\boldsymbol{\omega}\cdot\nabla)\boldsymbol{v} + (\nabla\cdot\boldsymbol{v})\boldsymbol{\omega} = 0,$$

and (iii) we have non-vanishing helicity H, where

$$H = \int_V \boldsymbol{\omega}\cdot\boldsymbol{v}\mathrm{d}^3\boldsymbol{x} = \int_V \boldsymbol{\omega}\cdot\frac{E_W[\mathrm{curl}\boldsymbol{A}]}{\rho}\mathrm{d}^3\boldsymbol{x}.$$

5.2. Uniqueness of transformation

Transformation from the Lagrangian $\boldsymbol{a}$ space to Eulerian $\boldsymbol{x}(\boldsymbol{a})$ space is determined locally by nine components of the matrix $\partial x^k/\partial a^l$. However, in the previous solution considered in Section 2.3, we had three relations (11) between $\boldsymbol{v} = (X_\tau, Y_\tau, Z_\tau)$ and (V_a, V_b, V_c), and another three relations (13) between $\mathcal{A} = (X_{\tau\tau}, Y_{\tau\tau}, Z_{\tau\tau})$ and $(\mathcal{A}_a, \mathcal{A}_b, \mathcal{A}_c)$. The remaining three conditions are given by Eq. (33) connecting $\boldsymbol{\omega} = (\omega_x, \omega_y, \omega_z)$ and $\boldsymbol{\Omega}_a(\boldsymbol{a}) = (\Omega_a, \Omega_b, \Omega_c)$. For example, Ω_a is determined by

$$\begin{aligned}\Omega_a &= \omega_x\,(\partial_b y\,\partial_c z - \partial_c y\,\partial_b z) + \omega_y\,(\partial_b z\,\partial_c x - \partial_c z\,\partial_b x) \\ &\quad + \omega_z\,(\partial_b x\,\partial_c y - \partial_c x\,\partial_b y).\end{aligned} \tag{34}$$

There are three vectors (velocity, acceleration and vorticity) determined by evolution equations subject to initial conditions in each space of $\boldsymbol{x}$ and $\boldsymbol{a}$ coordinates. Transformation relations of the three vectors suffice to determine the nine matrix elements $\partial x^k/\partial a^l$ locally. Thus, the transformation between the Lagrangian $\boldsymbol{a}$ space and Eulerian $\boldsymbol{x}(\boldsymbol{a})$ space is determined uniquely [3].

6. Summary and discussion

Following the scenario of the gauge principle of field theory, it is found that the variational principle of fluid motions can be reformulated successfully in terms of covariant derivatives and Lagrangians defined appropriately. The present variational formulation is self-consistent and comprehensively describes flows of an ideal fluid.

In the improved formulation taking account of the rotational symmetry with additional equations of (33), the transformation relations of the three vectors (velocity, acceleration and vorticity) suffice to determine the nine matrix elements $\partial x^k/\partial a^l$ locally. Thus, the transformation between the Lagrangian $\boldsymbol{a}$ space and Eulerian $\boldsymbol{x}(\boldsymbol{a})$ space is determined uniquely.

References

[1] L. Euler, Principes généraux du mouvement des fluides, MASB 11 (1755) 274–315 (printed in 1757). Also in Opera omnia, Ser. 2, 12, 54–91. E226.
[2] T. Kambe, Fluid Dyn. Res. 39 (2007) 98–120.
[3] T. Kambe, Fluid Dyn. Res. (2007) (in press). Preprint. TK2007b http://www.purple.dti.ne.jp/kambe/.
[4] L.D. Landau, E.M. Lifshitz, Mechanics, 3rd ed., Pergamon Press, 1976.
[5] T. Kambe, Fluid Dyn. Res. 32 (2003) 193–199.
[6] T. Kambe, Acta Mech. Sinica 19 (2003) 437–452.
[7] C. Eckart, Phys. Fluids 3 (1960) 421;
C. Eckart, Phys. Rev. 54 (1938) 920.
[8] J.W. Herivel, Proc. Camb. Phil. Soc. 51 (1955) 344–349.
[9] D.E. Soper, Classical Field Theory, John Wiley, 1976.
[10] A. Clebsch, J. Reine Angew. Math. 56 (1859) 1.
[11] R. Jackiw, Lectures on Fluid Mechanics, Springer, 2002.
[12] R. Jackiw, V.P. Nair, S.-Y. Pi, A.P. Polychronakos, J. Phys. A 37 (2004) R327–R432. [hep-ph/0407101].
[13] E. Noether, Invariant variations problem, Klg-Ges. Wiss. Nach. Göttingen, Math. Physik Kl, 2 (1918) 235.
[14] H. Lamb, Hydrodynamics, Cambridge University Press, Cambridge, 1932.
[15] V.I. Arnold, B. Khesin, Topological Methods in Hydrodynamics, Springer, 1998.
[16] S.S. Chern, Complex Manifolds without Potential Theory, 2nd ed., Springer-Verlag, Berlin, 1979.
[17] R. Jackiw, Chern–Simons terms and cocycles in physics and mathematics, in: Fradkin Festschrift, Adam Hilger, Bristol, 1985.
[18] S. Desser, R. Jackiw, S. Templeton, Ann. Phys. 140 (1982) 372–411.
[19] S. Weinberg, The Quantum Theory of Fields, vol. I, Cambridge University Press, 1995, vol. II (1996).
[20] T. Frankel, The Geometry of Physics. An Introduction, Cambridge University Press, 1997.
[21] I.J.R. Aitchison, A.J.G. Hey, Gauge Theories in Particle Physics, Adam Hilger, Bristol, 1982.
[22] Roman Jackiw [11] arrived at the same form, but with a different approach using Lagrange multipliers for constraint conditions, in order to extend it to the relativistic case, *e.g.* Eqs. (2.56) of [11] and (1.2.68) of [12].

Available online at www.sciencedirect.com
ScienceDirect
Physica D 237 (2008) 2072–2077
PHYSICA D
www.elsevier.com/locate/physd

Poisson geometry and first integrals of geostrophic equations

Boris Khesin, Paul Lee*

Department of Mathematics, University of Toronto, ON M5S 2E4, Canada

Available online 10 March 2008

Abstract

We describe first integrals of geostrophic equations, which are similar to the enstrophy invariants of the Euler equation for an ideal incompressible fluid. We explain the geometry behind this similarity, give several equivalent definitions of the Poisson structure on the space of smooth densities on a symplectic manifold, and show how it can be obtained via the Hamiltonian reduction from a symplectic structure on the diffeomorphism group.

PACS: 47.10.Df; 02.20.Tw

Keywords: Geostrophic equations; Enstrophy invariants; Poisson structure; Wasserstein space; Hamiltonian reduction; Diffeomorphism group

1. Introduction

The Euler equation of an ideal incompressible m-dimensional fluid has a peculiar set of invariants: in addition to the energy conservation, the Euler equation has the helicity-type invariant in any odd m, and an infinite number of enstrophy-type invariants in any even m. Furthermore, these invariants are Casimir functions, which implies that they are invariants of the Euler equation for any choice of a Riemannian metric on the manifold filled by the fluid.

In this paper we show how the same enstrophy-type invariants appear in semi-geostrophic equations. These invariants are related to the Poisson geometry of the corresponding space of densities. Namely, for any Poisson manifold M the space of densities on M is also Poisson. The reason is that the space of functions on M forms a Lie algebra with respect to the Poisson bracket, while densities are objects dual to functions, so their space forms a dual Lie algebra. Thus this dual space gets equipped with the linear Kirillov-Kostant (or Lie-Poisson) structure, see [1,7,11]. We show that this Poisson structure has several equivalent descriptions and relate it to the symplectic geometry of the diffeomorphism group of the manifold. In this paper we explore the role of Casimirs and the corresponding group actions in the Poisson geometry of these infinite-dimensional spaces.

Recall that Poisson manifolds are foliated by symplectic leaves, and Casimir functions are functions constant on symplectic leaves. Equivalently, Casimir functions are those Hamiltonians which correspond to everywhere vanishing Hamiltonian vector fields on a Poisson manifold. They are constants of motion for any Hamiltonian flow on the manifold. For instance, the hydrodynamic Euler equation on an odd-dimensional manifold has a helicity-type Casimir, which generalizes the 3-dimensional helicity integral

$$I(v) = \int_M (v, \operatorname{curl} v) \mathrm{d}\mu.$$

For an even-dimensional manifold M ($m = 2n$) the Euler equation has an infinite number of enstrophy-type invariants:

$$I_h(v) = \int_M h\left(\frac{(\operatorname{curl} v)^n}{\mathrm{d}\mu}\right) \mathrm{d}\mu,$$

where $\operatorname{curl} v$ is the vorticity 2-form for the velocity field v on $2n$-dimensional manifold M and h is any function $\mathbb{R} \to \mathbb{R}$, see [9,10]. The latter integral turns out to be similar to Casimir functions found on the space of densities on both even- and odd-dimensional manifold, as we discuss below.

We should mention that the information on Casimir functions is useful for the study of the stability of Hamiltonian

* Corresponding author. Tel.: +1 4163355047.
E-mail addresses: khesin@math.toronto.edu (B. Khesin), plee@math.toronto.edu (P. Lee).

0167-2789/$ - see front matter © 2008 Elsevier B.V. All rights reserved.
doi:10.1016/j.physd.2008.03.001

flows, e.g. via the energy-Casimir method. Note that the existence of an infinite number of Casimirs for a given Hamiltonian system does not mean its complete integrability. These invariants merely single out the symplectic leaf where the dynamics takes place, but do not specify the dynamics along this leaf, cf. [2].

Below we also describe explicitly two natural Hamiltonian reductions leading to the Poisson structure on densities. A Hamiltonian reduction is a two-step procedure for reducing the dimension of a Hamiltonian system with symmetry: restriction to a given level set of first integrals, and taking the quotient along the symmetry group action. We prove that the Poisson structure on densities can be obtained by the reduction from the symplectic structure considered in [4]. More precisely, let $\mathcal{M}ap$ be the space of all maps from a manifold M equipped with a volume form μ to a symplectic manifold N. The symplectic structure on $\mathcal{M}ap$ is given by averaging the pullbacks of the one on N against the volume form μ, see [4]. In Section 3 we describe what this general construction gives for diffeomorphism groups of symplectic manifolds and densities on them.

2. The Poisson structures on the density spaces and their Casimirs

Let M be a compact Poisson manifold with a Poisson bracket $\{,\}$, and let Dens be the set of smooth volume forms on M with total integral 1. (The set Dens can be given a smooth topology and regarded as an infinite-dimensional smooth manifold, see [6]. It is also a dense subset in the L^2-Wasserstein space of Borel probability measures on M.) Any smooth function f on M defines a linear functional on Dens whose value at a point $\mathrm{d}\nu \in$ Dens is given by the formula

$$F_f(\mathrm{d}\nu) := \int_M f\,\mathrm{d}\nu.$$

(For a noncompact M, e.g. for $M = \mathbb{R}^n$, we can consider functions f with compact support.)

Definition 2.1. Let $\mathcal{P} = \{F_f : \text{Dens} \to \mathbb{R} \mid f \in C^\infty(M)\}$ be the set of linear functionals F_f. Define the bracket on $\mathcal{P}$ by

$$\{F_f, F_g\}_{\text{Dens}}(\mathrm{d}\nu) := F_{\{f,g\}}(\mathrm{d}\nu) = \int_M \{f,g\}\,\mathrm{d}\nu.$$

Proposition 2.2 (*See e.g. [7,11]*).

1. *The bracket $\{,\}_{Dens}$ defines a Poisson structure on the density space Dens.*
2. *The symplectic leaves on Dens are orbits of the natural action of the group of Hamiltonian diffeomorphisms on densities on M.*

As we discussed in Introduction, the Poisson structure on the density space comes from the Poisson structure on the underlying manifold, as the Poisson–Lie structure on the dual of the Lie algebra of Hamiltonian functions on M. The statement (2) is proved in [7] for a symplectic M, but the proof extends verbatim to a general Poisson manifold M, provided that the group of Hamiltonian diffeomorphisms is understood as that generated by flows of Hamiltonian fields on M.

2.1. The symplectic case

First consider in more detail the case of a *symplectic* manifold M of dimension $2n$. Let ω be a symplectic structure on M, which generates the Poisson bracket $\{\ ,\ \}$. Note that in this case the Liouville form ω^n can be regarded as a natural choice for a reference density $\mathrm{d}\mu = \omega^n$.

Proposition 2.3. *The Poisson bracket $\{,\}_{Dens}$ admits infinitely many functionally independent Casimirs. Namely, for any function $h : \mathbb{R} \to \mathbb{R}$, the functional on Dens defined by*

$$C_h(\mathrm{d}\nu) := \int_M h\left(\frac{\mathrm{d}\nu}{\omega^n}\right)\omega^n$$

is a Casimir, i.e. it is constant on symplectic leaves of this bracket in the density space Dens.

Proof. Since the symplectic leaves of the Poisson structure $\{,\}_{\text{Dens}}$ are orbits of the action of Hamiltonian flows on the smooth Wasserstein space Dens, it suffices to check that the functions C_h are invariant under this action. Now we have:

$$\begin{aligned} C_h(\phi^*\mathrm{d}\nu) &= \int_M h\left(\frac{\phi^*\mathrm{d}\nu}{\omega^n}\right)\omega^n \\ &= \int_M h\left(\frac{\phi^*\mathrm{d}\nu}{\phi^*\omega^n}\right)\phi^*\omega^n \\ &= C_h(\mathrm{d}\nu), \end{aligned}$$

where the last identity follows from the change of variable formula, and the second one follows from conservation of ω under the Hamiltonian action: $\phi^*\omega = \omega$. □

Geometrically, these Casimirs capture all moments of the relative density $\mathrm{d}\nu$ with respect to the reference density $\mathrm{d}\mu$. The ratio function $\theta = \mathrm{d}\nu/\mathrm{d}\mu$ is preserved by any Hamiltonian flow, and hence so are all its moments over the manifold M.

Remark 2.4. Similar Casimirs arise in the case of the Euler equation

$$\partial_t v + v \cdot \nabla v = -\nabla p$$

for a divergence-free vector field v on any even-dimensional Riemannian manifold M with volume form $\mathrm{d}\mu$. Namely, one considers the vorticity 2-form $\mathrm{d}u$ for the 1-form u which is related to the vector field v by means of the metric on M. Then for any function $h : \mathbb{R} \to \mathbb{R}$, the functional on vorticities defined by

$$I_h(\mathrm{d}u) = \int_M h\left(\frac{(\mathrm{d}u)^n}{\mathrm{d}\mu}\right)\mathrm{d}\mu$$

is a Casimir for the action of diffeomorphisms preserving the "reference density" $\mathrm{d}\mu$, see [9,10] and introduction. These Casimirs also measure relative density of the generalized vorticity $(\mathrm{d}u)^n$, which is frozen into the ideal fluid, with respect to the volume form $\mathrm{d}\mu$.

Conjecturally, a complete set of Casimirs is encoded in the (Morse) graph with measure, associated to the function θ on M. Its vertices correspond to critical points of θ on M, and the edges correspond to pairs of critical points which can be connected via nonsingular levels, while $\mathrm{d}\theta$ defines the measure on the graph. This construction has been used for regular vorticity function in the 2D Euler equation (cf. [2]), and is applicable to symplectic leaves in the density space for any dimension.

Example 2.5. Consider the following semi-geostrophic equation in (a domain of) $\mathbb{R}^2$:

$$\partial_t v_g + v \cdot \nabla v_g + Jv + \nabla f = 0,$$

where J is the 90°-rotation operator on $\mathbb{R}^2$, v is a divergence-free velocity field, v_g is the geostrophic velocity field "defined by" the relation $\nabla f = J v_g$ for a potential f in the domain, see [3]. (This system is obtained from the two-dimensional Euler equation in the rotating frame, where we assume the Coriolis force to be constant in the domain, and make the semi-geostrophic approximation, see e.g. [8].)

Introduce the new potential $\tilde{f}(t,x) := |x|^2/2 + f(t,x)$. Consider the map $\phi_t(x) = \nabla \tilde{f}(t, \varphi_t(x))$, where φ_t is the flow of the divergence-free vector field $v(t,\cdot)$ solving the above semi-geostrophic equation, and assume that ϕ_t is a diffeomorphism for t in some interval. Then the family ϕ_t descends to the following Hamiltonian system on the density space by tracing how it pushes the reference density $\mathrm{d}\mu$. Namely, the form $\mathrm{d}\nu_t := (\phi_t)_*\mathrm{d}\mu$ satisfies the Hamiltonian system on the space Dens with respect to the Poisson structure $\{,\}_{\mathrm{Dens}}$ and the Hamiltonian H^{Dens} given by

$$H^{\mathrm{Dens}}(\mathrm{d}\nu) = -\mathrm{Wass}^2(\mathrm{d}\mu, \mathrm{d}\nu)/2,$$

where *Wass* is the Wasserstein L^2-distance on Dens.

The relative density $\mathrm{d}\nu/\mathrm{d}\mu$ discussed in Proposition 2.3 becomes

$$\theta := \frac{\phi_*\mathrm{d}\mu}{\mathrm{d}\mu} = \frac{(\nabla\tilde{f})_*\mathrm{d}\mu}{\mathrm{d}\mu} = \det(\mathrm{Hess}\,\tilde{f}) = \det(I + \mathrm{Hess}\,f),$$

where Hess f is the Hessian matrix of the function f. The latter expression for θ is known as the potential vorticity in the semi-geostrophic equation, and is known to be frozen into semi-geostrophic flow, similar to the standard vorticity of an ideal two-dimensional fluid, see [8].

Thus Proposition 2.3 is a generalization of the Casimir property of the potential vorticity to higher dimensions and to other Riemannian metrics. Its frozenness property is shown to be related to the geometry of the underlying Poisson structure $\{,\}_{\mathrm{Dens}}$ on the density space, rather than to the the specific Hamiltonian equation.

2.2. *The Poisson case*

Assume now that M is a *Poisson* manifold whose symplectic leaves are of codimension ≥ 1, and $\lambda : M \to \mathbb{R}$ is a smooth nonconstant Casimir function on M. It turns out that in this case symplectic leaves of the Poisson bracket $\{,\}_{\mathrm{Dens}}$ still have infinite codimension in Dens, similar to the case of a symplectic M.

Proposition 2.6. *The Poisson bracket $\{,\}_{Dens}$ admits infinitely many functionally independent Casimirs. Namely, for any function $h : \mathbb{R} \to \mathbb{R}$, the functional*

$$C_{h,\lambda}(\mathrm{d}\nu) := \int_M (h \circ \lambda)\mathrm{d}\nu$$

is a Casimir on the density space Dens.

Proof. We check that the functionals $C_{h,\lambda}$ are invariant under the Hamiltonian action:

$$\begin{aligned} C_{h,\lambda}(\phi^*\mathrm{d}\nu) &= \int_M (h\circ\lambda)(x)\phi^*\mathrm{d}\nu(x) \\ &= \int_M (h\circ\lambda)(\phi(x))\phi^*\mathrm{d}\nu(x) \\ &= C_{h,\lambda}(\mathrm{d}\nu), \end{aligned}$$

where we used the Casimir property of λ on M: $\lambda(\phi(x)) = \lambda(x)$ for a Hamiltonian diffeomorphism ϕ. $\square$

Note that for symplectic leaves of codimension 1 on M, one can think of invariants $C_{h,\lambda}$ as measuring the relative volume for the volume form $d\lambda \wedge \omega^n$ with respect to the reference density $\mathrm{d}\mu$, where ω stands for symplectic structure on the leaves in M. This, in turn, is similar to the helicity-type invariants for the Euler equation on odd-dimensional manifolds, with the important distinction, though, that for the density space Dens one has not only one, but an infinite number of Casimirs regardless of the dimension of the manifold M.

3. Symplectic structure on the diffeomorphism group of a symplectic manifold

Let (M,ω) be a $2n$-dimensional symplectic manifold and let $\mathcal{D}$ be the space of all orientation preserving diffeomorphisms of M. This is an infinite-dimensional Lie group with the Lie algebra $\mathfrak{X}$ of all smooth vector fields on the manifold M. The tangent space to the group $\mathcal{D}$ at a point ϕ consists of right translations of vector fields to ϕ: $T_\phi\mathcal{D} = \{X \circ \phi \mid X \in \mathfrak{X}\}$. Fix the reference volume form $\mathrm{d}\mu = \omega^n$ on M.

Definition 3.1. The diffeomorphism group $\mathcal{D}$ can be equipped with the following natural symplectic form $W^{\mathcal{D}}$: given two tangent vectors $X\circ\phi$ and $Y\circ\phi$ at $\phi\in\mathcal{D}$ we set

$$W^{\mathcal{D}}(X\circ\phi, Y\circ\phi) := \int_M \omega(X\circ\phi(x), Y\circ\phi(x))\mathrm{d}\mu(x)$$
$$= \int_M \omega(X,Y)(\phi^{-1})^*\mathrm{d}\mu = \int_M \omega(X,Y)\phi_*\mathrm{d}\mu.$$

As before, let Dens be the (smooth Wasserstein) space of all volume forms on the manifold M with total integral 1. The tangent space to this infinite-dimensional manifold Dens at a point $\mathrm{d}\nu$ consists of smooth $2n$-forms on the manifold M with zero integral. Denote the tangent bundle of the smooth Wasserstein space by T Dens.

Consider the natural projection $\pi : \mathcal{D} \to \mathrm{Dens}$ of diffeomorphisms into the volume forms on M, according to how the diffeomorphisms move the reference density $\mathrm{d}\mu$: $\pi(\phi) = \phi_*(\mathrm{d}\mu)$. This way the diffeomorphism group $\mathcal{D}$ can be regarded as the total space of the principal bundle over the base Dens with the structure group $\mathcal{D}_\mu$ of all diffeomorphisms preserving the volume form $\mathrm{d}\mu$.

Theorem 3.2. *The symplectic structure $W^{\mathcal{D}}$ on the diffeomorphism group $\mathcal{D}$ descends to the Poisson structure $\{\,,\}_{Dens}$ on the Wasserstein space Dens.*

Proof. The symplectic form $W^{\mathcal{D}}$ is invariant under the $\mathcal{D}_\mu$-action of volume-preserving diffeomorphisms and hence under the map π it descends to a certain Poisson structure on the density space Dens. We would like to show that the corresponding quotient Poisson structure coincides with $\{\,,\}_{\mathrm{Dens}}$.

Let $f : M \to \mathbb{R}$ be a function on the manifold M and $F_f(\mathrm{d}\nu) = \int_M f\,\mathrm{d}\nu$ the corresponding linear functional on Dens. Consider the pullback $\bar{F}_f := \pi^* F_f$ of this functional F_f to the diffeomorphism group $\mathcal{D}$ by the map π. Explicitly it is given by

$$\bar{F}_f(\phi) = \int_M f\,\mathrm{d}\nu = \int_M f\,\phi_*(\mathrm{d}\mu) = \int_M (f\circ\phi)(\mathrm{d}\mu).$$

Let X_f be the Hamiltonian vector field for the Hamiltonian function f on the symplectic manifold (M,ω) and let $X_f^{\mathcal{D}}$ be the Hamiltonian vector field of the pullback functional $\bar{F}_f$ on $(\mathcal{D}, W^{\mathcal{D}})$, the diffeomorphism group $\mathcal{D}$ equipped with the symplectic structure $W^{\mathcal{D}}$.

Lemma 3.3. *The Hamiltonian vector fields X_f on (M,ω) and $X_f^{\mathcal{D}}$ on $(\mathcal{D}, W^{\mathcal{D}})$ are related in the following way:*

$$X_f^{\mathcal{D}}(\phi) = X_f\circ\phi.$$

Proof. By the definition of the Hamiltonian field $X_{\bar{F}_f}$ at a point $\phi\in\mathcal{D}$,

$$W^{\mathcal{D}}(X_f^{\mathcal{D}}(\phi), Y\circ\phi) = \langle d\bar{F}_f, Y\circ\phi\rangle$$

for any vector field $Y\in\mathfrak{X}$. On the other hand, by employing the definition of the pullback and changing the variable, we rewrite the latter expression as follows:

$$\int_M \langle \mathrm{d}f_{\phi(x)}, Y\circ\phi(x)\rangle\,\mathrm{d}\mu(x) = \int_M \langle \mathrm{d}f_x, Y(x)\rangle\,\phi_*(\mathrm{d}\mu)(x).$$

Now by the definition of the Hamiltonian field X_f on M this is equal to

$$\int_M \omega(X_f(x), Y(x))\phi_*(\mathrm{d}\mu)(x) = \int_M \omega(X_f\circ\phi, Y\circ\phi)(\mathrm{d}\mu),$$

which completes the proof of the lemma, due to arbitrariness of the field Y. □

Returning to the proof of the theorem, we are going to compute the Poisson bracket of the pullback functions $\bar{F}_f$ and $\bar{F}_g$. By the definition, the value of the Poisson bracket $\{,\}^{\mathcal{D}}$, which is dual to the symplectic structure $W^{\mathcal{D}}$ on the diffeomorphism group, for these two functions is

$$\{\bar{F}_f, \bar{F}_g\}^{\mathcal{D}}(\phi) = W^{\mathcal{D}}(X_{\bar{F}_f}(\phi), X_{\bar{F}_g}(\phi)).$$

By using the lemma above and the change of variable, the right-hand side above becomes

$$\begin{aligned}\int_M \omega(X_f\circ\phi, X_g\circ\phi)\mathrm{d}\mu &= \int_M \omega(X_f, X_g)\phi_*(\mathrm{d}\mu)\\ &= \int_M \{f,g\}\,\phi_*(\mathrm{d}\mu)\\ &= \int_M \{f,g\}\,\mathrm{d}\nu,\end{aligned}$$

as required. □

Remark 3.4. This symplectic structure $W^{\mathcal{D}}$ on the diffeomorphism group can be viewed as a particular case of that considered in [4]. More generally, let S be a compact manifold with a fixed volume form $d\sigma$, while (M,ω) is a symplectic manifold. The space $\mathcal{M}ap$ of all maps $\rho : S\to M$ (of some fixed homotopy class) has a natural symplectic structure. Namely, the tangent space to $\mathcal{M}ap$ at a point $\rho\in\mathcal{M}ap$ is the space of sections of the bundle $\rho^*(TM)$ over S and the symplectic structure is

$$\Omega_f(v,w) := \int_M \rho^*\omega(v,w)d\sigma$$

for a pair of sections v, w of $\rho^*(TM)$. The group of volume-preserving diffeomorphisms of S defines a symplectic group action on $\mathcal{M}ap$. Donaldson considers in [4] the corresponding moment map and the Hamiltonian reduction of the space $\mathcal{M}ap$ under this group action. In our case, the two manifolds S and M coincide, while the volume form $d\sigma$ is the symplectic volume form $\mathrm{d}\mu = \omega^n$. Then the diffeomorphism group $\mathcal{D}$ is an open subset of $\mathcal{M}ap$ with the symplectic structure described above, and we consider the action of the subgroup $\mathcal{D}_\mu$ of volume-preserving diffeomorphisms on it.

Remark 3.5. The same Poisson structure on Dens was also defined in [1] in slightly different terms, cf. [7]. For a symplectic manifold (M,ω) we fix a Riemannian metric $\langle,\rangle$ and an almost complex structure J compatible with the metric: $\omega(u,v) = \langle u, Jv\rangle$. Let f be a function on the manifold M and ∇f its gradient with respect to the metric $\langle,\rangle$. The Hamiltonian field on M for the Hamiltonian f is $X_f = J\nabla f$.

Consider the distribution τ on the smooth Wasserstein space defined at a point $\mathrm{d}\nu\in$ Dens by all possible infinitesimal shifts of $\mathrm{d}\nu$ by Hamiltonian fields: $\tau_\nu := \{L_{X_f}\mathrm{d}\nu \mid f\in C^\infty(M)\}$, where L denotes the Lie derivative along a vector field on M. Define a 2-form on the distribution τ by

$$\omega^\tau(L_{X_f}\mathrm{d}\nu, L_{X_g}\mathrm{d}\nu) = \int_M \omega(\nabla f, \nabla g)\mathrm{d}\nu.$$

In [1] it is shown that the distribution τ_ν is integrable on the smooth Wasserstein space, and this 2-form is a well-defined symplectic structure on the integral leaves of this distribution. One can see that these leaves are exactly the symplectic leaves of the Poisson structure $\{\,,\}_{\mathrm{Dens}}$ on the density space, while the symplectic structure ω^τ is dual to the Poisson structure discussed above:

$$\omega^\tau(L_{X_f}\mathrm{d}\nu, L_{X_g}\mathrm{d}\nu) = \int_M \omega(X_f, X_g)\mathrm{d}\nu = \{F_f, F_g\}_{\mathrm{Dens}}(\mathrm{d}\nu).$$

4. The two-dimensional case and geostrophic equations

4.1. The Noether theorem for an extra symmetry on the plane

Return to the two-dimensional M and consider the smooth density space Dens for $M = \mathbb{R}^2$ with the standard symplectic structure $\omega = dx_1 \wedge dx_2$. This induces the Poisson structure on Dens, as described above. There is the natural $SO(2)$-action by rotations on densities: $\mathrm{d}\nu \mapsto \varphi_*(\mathrm{d}\nu)$, where $\mathrm{d}\nu \in$ Dens is a measure and $\varphi \in SO(2)$.

Recall that for the standard measure ω, the semi-geostrophic equation is the Hamiltonian equation on Dens with the Hamiltonian function $H(\mathrm{d}\nu) = -\mathrm{Wass}^2(\omega, \mathrm{d}\nu)/2$, where Wass is the Wasserstein distance on densities.

Proposition 4.1. *The functional $K(\mathrm{d}\nu) := \int_{\mathbb{R}^2} |x|^2\, \mathrm{d}\nu$ is a first integral of the semi-geostrophic equation.*

Proof. First we note that the $SO(2)$-action is Hamiltonian with the Hamiltonian function given by the functional $K(\mathrm{d}\nu)$ on Dens. Indeed, take the generator of the rotation group with the Hamiltonian $\kappa(x) = |x|^2$ on $\mathbb{R}^2$. Then the corresponding action on densities in Dens is generated by the field with Hamiltonian $K(\mathrm{d}\nu) := \int_{\mathbb{R}^2} \kappa\, \mathrm{d}\nu = \int_{\mathbb{R}^2} |x|^2\, \mathrm{d}\nu$, while the corresponding action on diffeomorphisms in $\mathcal{D}$ is generated by the Hamiltonian $\bar{K} = \pi^* K$, cf. Lemma 3.3.

Next, we see that the Wasserstein distance $H(\mathrm{d}\nu)$ from any measure $\mathrm{d}\nu$ to the standard measure ω is $SO(2)$-invariant, since so is ω. Thus the $SO(2)$-action is a symmetry of the function $H(\mathrm{d}\nu) = -\mathrm{Wass}^2(\omega, \mathrm{d}\nu)/2$, i.e. the Hamiltonians H and K are in involution on the density space Dens with respect to the Poisson structure $\{,\}_{\mathrm{Dens}}$. In particular, $K(\mathrm{d}\nu)$ is a conserved quantity for the semi-geostrophic equation. □

This proposition naturally generalizes to any dimension: If the Hamiltonian field with a Hamiltonian function κ generates an isometry of M^{2n}, and the reference density $\mathrm{d}\mu = \omega^n$ is invariant with respect to this isometry, then the Hamiltonian field for $H(\mathrm{d}\nu) = -\mathrm{Wass}^2(\mathrm{d}\mu, \mathrm{d}\nu)/2$ on Dens has the first integral $K(\mathrm{d}\nu) := \int_M \kappa\, \mathrm{d}\nu$.

4.2. More Hamiltonian reductions to the density space

Consider the case of a two-dimensional manifold M in more detail. In this section we would like to compare the symplectic geometry of the diffeomorphism group $\mathcal{D}(M)$ with that of the cotangent bundle $T^*\mathcal{D}_\mu(M)$ of the group of area-preserving diffeomorphisms of the surface M.

As we discussed above, the group $\mathcal{D}$ for an oriented surface (or, for any symplectic manifold) M can be equipped with a symplectic structure, which descends to the Poisson structure on Dens under the projection $\pi : \mathcal{D} \to$ Dens, or, more precisely, under the Hamiltonian reduction with respect to the $\mathcal{D}_\mu$-action. Note that the space Dens is a convex subset in the space $\Omega^2(M)$ of 2-forms on M: Dens $= \{\mathrm{d}\nu \in \Omega^2(M) \mid \mathrm{d}\nu > 0, \int_M \mathrm{d}\nu = 1\}$.

Now consider the group $\mathcal{D}_\mu$ and its cotangent bundle $T^*\mathcal{D}_\mu$. Identify $T^*\mathcal{D}_\mu \simeq \mathcal{D}_\mu \times \mathfrak{X}_\mu^*$ by means of right translations on the group. Note that the Lie algebra $\mathfrak{X}_\mu$ consists of divergence-free vector fields on the surface M. Such fields are described locally by their Hamiltonian (or, stream) functions. First we assume that M is a two-dimensional sphere S^2, so that the fields are globally Hamiltonian. Then the algebra $\mathfrak{X}_\mu$ can be viewed as the Poisson algebra $C_0^\infty(M)$ of functions with zero mean on M (with respect to the reference density $\mathrm{d}\mu = \omega$). The corresponding (smooth) dual space $\mathfrak{X}_\mu^*(M) = \Omega_0^2(M)$ consists of smooth 2-forms on M with zero total integral.

By shifting this dual space to the reference density $\mathrm{d}\mu$ we can regard the (smooth) density space Dens as a convex subset in $\Omega_0^2(M)$:

$$\mathrm{Dens} = \{\mathrm{d}\mu + d\bar{\nu} \mid \mathrm{d}\mu + d\bar{\nu} > 0, d\bar{\nu} \in \Omega_0^2(M)\} \subset \mathrm{d}\mu + \Omega_0^2(M).$$

After this shift to the reference density $\mathrm{d}\mu$ the diffeomorphism group $\mathcal{D} \simeq \mathcal{D}_\mu \times$ Dens becomes a subset in the cotangent bundle $T^*\mathcal{D}_\mu \simeq \mathcal{D}_\mu \times \Omega_0^2$.

Recall that the cotangent bundle $T^*\mathcal{D}_\mu$ has a natural symplectic structure (denoted later by W^{T^*}), which descends to the Poisson–Lie structure on the dual Lie algebra $\mathfrak{X}_\mu^* \simeq \Omega_0^2$. The latter is exactly the Poisson structure $\{\ ,\ \}_{\mathrm{Dens}}$ upon restriction to the density space Dens $\subset \Omega_0^2$.

Conjecture 4.2. *The natural symplectic structure W^{T^*} on the cotangent bundle $T^*\mathcal{D}_\mu$ coincides with the symplectic structure $W^{\mathcal{D}}$ on the diffeomorphism group $\mathcal{D}$, understood as a subset of $T^*\mathcal{D}_\mu$ via the identification described above.*

In other words, not only coincide the Poisson structures on the density space Dens understood by itself or as a part of the dual $\mathfrak{X}_\mu^*$, but presumably so do the corresponding symplectic structures before the Hamiltonian reduction. We note that the convex subset Dens of positive densities is preserved under the diffeomorphism action on Ω_0^2, so the Poisson structure on Ω_0^2 can indeed be restricted to this subset.

In the case of a general surface M, divergence-free fields on M may have multivalued Hamiltonians: $\mathfrak{X}_\mu(M) = C_0^\infty(M) \oplus H_1(M)$. Respectively, the dual space $\mathfrak{X}_\mu^*(M)$ is a finite-dimensional extension of $\Omega_0^2(M)$, since $\mathcal{D}_\mu^*(M) \simeq \Omega^1(M)/d\Omega^0(M) \simeq \Omega_0^2(M) \oplus H^1(M)$. Now the density space Dens(M) can be understood as a convex subset in a plane of finite codimension in the dual space $\mathfrak{X}_\mu^*(M)$.

Note also that for a higher-dimensional symplectic M, there is a natural map from the dual $\mathfrak{X}_\mu^* \simeq \Omega^1(M)/d\Omega^0(M) \simeq \Omega_0^2(M) \oplus H^1(M)$ to the space $\Omega^{2n}(M)$ of $2n$-forms: $\rho : [u] \mapsto (\mathrm{d}u)^n$, where $[u] \in \mathfrak{X}_\mu^*$ is a 1-form u modulo addition of an exact 1-form on M. This map commutes with the natural $\mathcal{D}_\mu$-action of volume-preserving diffeomorphisms on forms, which explains the common origin of the Casimirs on the space Dens of volume forms and on the dual space $\mathfrak{X}_\mu^*$.

Finally, we note that the Euler equation of an ideal fluid on the two-dimensional M is the Hamiltonian equation on Ω_0^2 with respect to the Poisson–Lie structure $\{\ ,\ \}_{\mathrm{Dens}}$ whose Hamiltonian function is the *energy* quadratic form on Ω_0^2. It is interesting to compare this with (the projection of) the semi-geostrophic equation, where the Hamiltonian function is $H^{\mathrm{Dens}}(\mathrm{d}\nu) = -\mathrm{Wass}^2(\mathrm{d}\mu, \mathrm{d}\nu)/2$, the square of the Wasserstein distance on Dens $\subset \mathrm{d}\mu + \Omega_0^2$. This shift of the quadratic form to the reference density $\mathrm{d}\mu$ is similar to the shift observed in the infinite conductivity equation, and in the f-plane and β-plane geostrophic equations, see [2,5,12].

Before the Hamiltonian reduction, the semi-geostrophic equation is a Hamiltonian system on the diffeomorphism group with respect to the symplectic structure $W^{\mathcal{D}}$ and the Hamiltonian function $H^{\mathcal{D}}$ evaluating how far our diffeomorphism is from being area-preserving:

$$H^{\mathcal{D}}(\phi) = \frac{1}{2}\mathrm{dist}^2(\phi, \mathcal{D}_\mu),$$

where *dist* is the distance in the “flat” L^2-type metric on the diffeomorphism group $\mathcal{D}$ from $\phi \in \mathcal{D}$ to the subgroup $\mathcal{D}_\mu$ of diffeomorphisms preserving the standard area form $\omega = \mathrm{d}\mu$ on $\mathbb{R}^2$, see [3]. This Hamiltonian is invariant under the action of the group $\mathcal{D}_\mu$ of area-preserving diffeomorphisms, and so it descends to the above semi-geostrophic Hamiltonian system on the density space Dens.

Acknowledgments

We are grateful to W. Gangbo, D. Goldman, and R. McCann for useful discussions. We are also indebted to the organizers of the conference “Euler Equations: 250 years on” in Aussois and the workshop “Optimal Transportation, and Applications to Geophysics and Geometry” in Edinburgh for a stimulating working atmosphere and hospitality. This research was partially supported by an NSERC research grant.

References

[1] L. Ambrosio, W. Gangbo, Hamiltonian ODE’s in the Wasserstein space of probability measures, Comm. Pure Appl. Math. LXI (2008) 0018–0053.
[2] V. Arnold, B. Khesin, Topological Methods in Hydrodynamics, in: Applied Math. Series, vol. 125, Springer-Verlag, 1998, pp. 374+xv.
[3] Y. Brenier, A geometric presentation of the semi-geostrophic equations, Preprint 1996, pp. 11.
[4] S.K. Donaldson, Moment maps and diffeomorphisms, Asian J. Math. 3 (1) (1999) 1–16.
[5] D.D. Holm, V. Zeitlin, Hamilton’s principle for quasigeostrophic motion, Phys. Fluids 10 (4) (1998) 800–806.
[6] A. Kriegl, P. Michor, The Convenient Setting of Global Analysis, Mathematical Surveys and Monographs, vol. 53, American Mathematical Society, Providence, RI, 1997.
[7] J. Lott, Some geometric calculations on Wasserstein space, Comm. Math. Phys. 277 (2008) 423–437.
[8] R. McCann, A. Oberman, Exact semi-geostrophic flows in an elliptical ocean basin, Nonlinearity 17 (2004) 1891–1922.
[9] V. Ovsienko, B. Khesin, Yu. Chekanov, Integrals of the Euler equations in multidimensional hydrodynamics and superconductivity, Zap. Nauchn. Sem. Leningrad. Otdel. Mat. Inst. Steklov. (LOMI) 172 (1989) 105–113. English transl. in J. Soviet Math. 59 (5) (1992), 1096–1101.
[10] D. Serre, Invariants et dégénérescence symplectique de l’équation d’Euler des fluides parfaits incompressibles, C. R. Acad. Sci. Paris Sér. I Math. 298 (14) (1984) 349–352.
[11] A. Weinstein, Hamiltonian structure for drift waves and geostrophic flow, Phys. Fluids 26 (2) (1983) 388–390.
[12] V. Zeitlin, R.A. Pasmanter, On the differential geometry approach to geophysical flows, Phys. Lett. A 189 (1–2) (1994) 59–63.

Available online at www.sciencedirect.com
ScienceDirect
Physica D 237 (2008) 2078–2083
PHYSICA D
www.elsevier.com/locate/physd

Chaotic motion of the N-vortex problem on a sphere: II. Saddle centers in three-degree-of-freedom Hamiltonians

Takashi Sakajo[a,*], Kazuyuki Yagasaki[b]

[a] *Department of Mathematics, Hokkaido University, Sapporo 060-0810, Japan*
[b] *Department of Mechanical and Systems Engineering, Gifu University, Gifu 501-1193, Japan*

Available online 7 February 2008

Abstract

This paper deals with complicated behavior in the $N = 8n$ vortex problem on a sphere, which is reduced to three-degree-of-freedom Hamiltonian systems. In the reduced Hamiltonians, the polygonal ring configuration of the point vortices becomes a saddle-center equilibrium which has two hyperbolic and four center directions in some parameter regions. Near the saddle center, there exists a normally hyperbolic, locally invariant manifold including a Cantor set of *whiskered tori*. For $N = 8$ we numerically compute the stable and unstable manifolds of the locally invariant manifold with the assistance of the center manifold technique, and show that they intersect transversely and complicated dynamics may occur. Direct numerical simulations are also given to demonstrate our numerical analysis.

Keywords: Point vortex; Flows on sphere; Chaos; Saddle centers

1. Introduction

We consider the motion of N point vortices with the unit strength on a sphere. Their equations of motion are derived from the two-dimensional incompressible Euler equations on the sphere by assuming that the vorticity is concentrated at discrete points (Θ_m, Ψ_m), $m = 1, \ldots, N$, in the spherical coordinates. They can be written in a Hamiltonian system with N degrees of freedom [15]:

$$\dot{q}_m = \frac{\partial H}{\partial p_m}, \qquad \dot{p}_m = -\frac{\partial H}{\partial q_m}, \tag{1}$$

where $(q_m, p_m) = (\Psi_m, \cos\Theta_m)$ are the symplectic variables. The Hamiltonian H is given by

$$H = -\frac{\Gamma_\mathrm{n}}{4\pi}\sum_{m=1}^{N}\log(1-\cos\Theta_m) - \frac{\Gamma_\mathrm{s}}{4\pi}\sum_{m=1}^{N}\log(1+\cos\Theta_m) - \frac{1}{4\pi}\sum_{m=1}^{N}\sum_{m<j}^{N}\log(1-\cos\gamma_{mj}), \tag{2}$$

in which γ_{mj} denotes the central angle between the mth and jth point vortices such that $\cos\gamma_{mj} = \cos\Theta_m\cos\Theta_j - \sin\Theta_m\sin\Theta_j\cos(\Psi_m - \Psi_j)$. The parameters Γ_n and Γ_s represent the strengths of the point vortices fixed at the north and the south poles of the sphere, which are introduced to take into account the local contribution of rotation of the sphere locally. The N-*vortex problem* on the sphere has been extensively studied when N is small. For instance, the integrable 3-vortex problem and an integrable 4-vortex problem were discussed in detail [11,19,23]. See [1,15] for further references on this topic.

Now, we focus on the evolution of the polygonal ring configuration, called the N-*ring*, where the point vortices are equally spaced along a line of latitude when N is not small. The configuration is of significance since such coherent vortex structure is often observed in numerical simulations on planetary flows [17,20]. The N-ring, $\Theta_m = \theta_0$ and $\Psi_m = 2\pi m/N$, is a relative equilibrium of (1) rotating with a constant speed in the longitudinal direction. Such relative configurations with special symmetries were investigated in a systematic way [12] and its stability has been investigated very well [3,4,21]. Here we are interested in how the N-ring evolves when it becomes unstable. In general, it is difficult to describe the

* Corresponding author. Fax: +81 11 727 3705.
E-mail address: sakajo@math.sci.hokudai.ac.jp (T. Sakajo).

0167-2789/$ - see front matter © 2008 Elsevier B.V. All rights reserved.
doi:10.1016/j.physd.2008.02.001

evolution of many point vortices since the degree of freedom of the system is quite large. However, the Hamiltonian system (1) can often be reduced to a lower-dimensional system in a systematic way [22].

For $N = 5n, 6n$ with $n \in \mathbb{N}$, using the reduction method, we obtain a two-degree-of-freedom Hamiltonian system that has a saddle-center equilibrium with two hyperbolic and two center directions for some regions of $\Gamma_\mathrm{n} = \Gamma_\mathrm{s}$. Near the saddle center there is a one-parameter family of periodic orbits by the Lyapunov center theorem [13], and their stable and unstable manifolds may intersect transversely so that horseshoe-type chaotic dynamics occurs. We applied a global perturbation technique [27] for $N = 6$ and used a numerical technique [30] for $N = 5, 6$ to detect such transverse intersections [24]. These treatments can also be performed for the general cases of $N = 5n, 6n$.

In the present paper, as a sequel to the previous work [24], we study complicated dynamics of the $N = 8n$ vortex problem when the N-ring is a saddle center. We first reduce (1) to a three-degree-of-freedom Hamiltonian system. Near the saddle center, instead of a one-parameter family of periodic orbits, there is a normally hyperbolic, locally invariant manifold including a Cantor set of *whiskered tori*, and its stable and unstable manifolds may also intersect, so that complicated dynamics can occur [29] (see also Section II). An analytical technique similar to that of [27] was also developed to treat this situation in [29] but is not applicable in our case. So we use the numerical technique of [30] with assistance of the center manifold technique [8] to show numerically that such intersection really occurs.

This paper is organized as follows: In Section 2, we apply the reduction method of [22] to (1) for $N = 8n$ and discuss complicated dynamics resulting from intersection between the stable and unstable manifolds of the locally invariant manifold. In Section 3, we introduce some symplectic transformations to make the problem amenable to our analysis. In Section 4 we describe the center manifold calculation and numerical technique to compute the stable and unstable manifolds of the locally invariant manifold. In Section 5 we perform the numerical analysis for $N = 8$ and give direct numerical simulations that support our analytical results relying on numerics. We conclude with a summary and comments in Section 6.

2. Invariant dynamical systems in the $N = 8n$ vortex problem

Linear stability analysis of the N-ring [21] gives the explicit representation of the eigenvalues. Let $\lambda_m^\pm$, $m = 0, \dots, N$, denote the eigenvalues for the N-ring equilibrium. Suppose that N is even and set $N = 2M$. Since $\lambda_0^\pm = 0$ and $\lambda_m^\pm = \lambda_{N-m}^\pm$, we see that $\lambda_M^\pm$ are simple and $\lambda_m^\pm$ are double for $m = 1, \dots, M-1$. Since $\left(\lambda_i^\pm\right)^2 < \left(\lambda_j^\pm\right)^2$ for $1 \le i < j \le M$, we have $\left(\lambda_k^\pm\right)^2 < 0 < \left(\lambda_{k+1}^\pm\right)^2$ for some k so that $\lambda_m^\pm$ are neutrally stable for $m \le k$ and λ_m^+ (resp. λ_m^-) is unstable (resp. stable) for $m > k$.

We define two transformations for the configuration $(\Theta_1, \dots, \Theta_N, \Psi_1, \dots, \Psi_N) \in \mathbb{P}_N = [0, \pi]^N \times (\mathbb{R}/2\pi\mathbb{Z})^N$. The first transformation rotates the point vortices by the degree $2\pi p/N$, which is denoted by $\sigma_p : (\Theta_1, \dots, \Theta_N, \Psi_1, \dots, \Psi_N) \mapsto (\Theta_1', \dots, \Theta_N', \Psi_1', \dots, \Psi_N')$, where $\Theta_m' = \Theta_{N-p+m}$, $\Psi_m' = \Psi_{N-p+m} + 2\pi p/N$ for $m = 1, \dots, p$ and $\Theta_m' = \Theta_{m-p}$, $\Psi_m' = \Psi_{m-p} + 2\pi p/N$ for $m = p+1, \dots, N$. The second one is the pole reversal transformation that reverses the north and the south poles around the x-axis; For $N = 2M$, it is given by $\pi_\mathrm{e} : (\Theta_1, \dots, \Theta_N, \Psi_1, \dots, \Psi_N) \mapsto (\Theta_1'', \dots, \Theta_N'', \Psi_1'', \dots, \Psi_N'')$, where $\Theta_1'' = \pi - \Theta_1$, $\Psi_1'' = \Psi_1$, $\Theta_m'' = \pi - \Theta_{N-m+2}$ and $\Psi_m'' = 2\pi + 2\Psi_1 - \Psi_{N-m+2}$ for $m \ne 1$.

Let $\boldsymbol{\phi}_m^\pm$, $m = 1, \dots, M-1$, be the linear independent eigenvectors to $\lambda_m^\pm$, which were also given explicitly in [21]. Then we have the following result [22].

Proposition 1. *Let $N = 2M = pq\,(p, q \in \mathbb{N})$ and let $\Gamma_\mathrm{n} = \Gamma_\mathrm{s}$. If $\sigma_p\pi_\mathrm{e}\boldsymbol{X}(0) = \boldsymbol{X}(0)$ for $\boldsymbol{X} \in \mathbb{P}_N$, then $\sigma_p\pi_\mathrm{e}\boldsymbol{X}(t) = \boldsymbol{X}(t)$ for $t \ge 0$. Furthermore, the set of*

$$\boldsymbol{X} = \boldsymbol{X}_\mathrm{e} + \sum_k \left(b_k^+ \boldsymbol{\phi}_{kq}^+ + b_k^- \boldsymbol{\phi}_{kq}^- \right), \qquad b_k^\pm \in \mathbb{R}, \tag{3}$$

is invariant with respect to $\sigma_p\pi_\mathrm{e}$, where $\boldsymbol{X}_\mathrm{e}$ represents the N-ring at the equator.

Note that the dimension of the vector space (3) is $[(M-1)/q]$ since the number of eigenvectors $\boldsymbol{\phi}_m^\pm$ is $M-1$, where $[r]$ denotes the maximum integer that is less than or equals to r. Henceforth we set $\Gamma_\mathrm{n} = \Gamma_\mathrm{s} = \Gamma$.

Applying Proposition 1 to the case of $N = 8n$, i.e. $p = 8$, $q = n$ and $M = 4n$, we obtain a reduced Hamiltonian system with three degrees of freedom in which $\lambda_n^\pm$, $\lambda_{2n}^\pm$ and $\lambda_{3n}^\pm$ are eigenvalues for an equilibrium corresponding the N-ring. Moreover, for a certain region of Γ, we have $\left(\lambda_n^\pm\right)^2 < \left(\lambda_{2n}^\pm\right)^2 < 0 < \left(\lambda_{3n}^\pm\right)^2$ so that the equilibrium becomes a saddle center since $\lambda_{3n}^\pm$ are real with $\lambda_{3n}^- < 0 < \lambda_{3n}^+$ while $\lambda_n^\pm$ and $\lambda_{2n}^\pm$ are purely imaginary.

In this situation, we can apply a slight modification of discussions given in [29]. The saddle center has a four-dimensional center manifold, which we regard as a normally hyperbolic, locally invariant manifold $\mathscr{M}$ having five-dimensional stable and unstable manifolds $W^{\mathrm{s,u}}(\mathscr{M})$. Here "normal hyperbolicity" means that the expansion and contraction rates of the flow normal to $\mathscr{M}$ dominate those tangent to $\mathscr{M}$. We also say that $\mathscr{M}$ is "locally invariant" if any trajectory starting in $\mathscr{M}$ remains in $\mathscr{M}$ or escapes $\mathscr{M}$ through its boundary $\partial\mathscr{M}$. See, e.g., [26] for the details of these concepts. Using the normal form of Graff [7] and applying the KAM theorem [14] (see also [18]), we can show that there exists a Cantor set of invariant tori near the saddle center. Each invariant torus $\mathscr{T}$ is *whiskered* and has three-dimensional stable and unstable manifolds $W^\mathrm{s}(\mathscr{T})$ and $W^\mathrm{u}(\mathscr{T})$, which are contained by $W^\mathrm{s}(\mathscr{M})$ and $W^\mathrm{u}(\mathscr{M})$, respectively.

Suppose that $W^\mathrm{s}(\mathscr{M})$ and $W^\mathrm{u}(\mathscr{M})$ intersect transversely. Then for any $K > 2$, there may be a *transition chain* of K

whiskered tori, $\mathscr{T}_j$, $j = 1, \dots, K$, on $\mathscr{M}$ near the saddle center, such that $W^{\mathrm{u}}(\mathscr{T}_j)$ intersects $W^{\mathrm{s}}(\mathscr{T}_{j+1})$ for $j = 1, \dots, K-1$. It follows that there exist trajectories starting near $\mathscr{T}_1$, passing near $\mathscr{T}_j$, $j = 2, \dots, K-1$, in turn and arriving near $\mathscr{T}_K$: "diffusion motions" occur. Moreover, there may be a pair of distinct *heteroclinic cycles*, $\{\mathscr{T}_0, \mathscr{T}_1^j, \dots, \mathscr{T}_{K_j}^j, \mathscr{T}_0\}$ with $K_j \geq 1$, $j = 1, 2$ among the transition chains. So we can find trajectories which start in a neighborhood of $\mathscr{T}_0$ and return there repeatedly after they pass near $\mathscr{T}_1^1, \dots, \mathscr{T}_{K_1}^1$ or near $\mathscr{T}_1^2, \dots, \mathscr{T}_{K_2}^2$. These trajectories can be assigned the symbols '1' or '2' depending whether they pass near $\mathscr{T}_1^1, \dots, \mathscr{T}_{K_1}^1$ or near $\mathscr{T}_1^2, \dots, \mathscr{T}_{K_2}^2$. Thus, they can be characterized by the Bernoulli shift and hence chaotic dynamics occurs. This also implies that chaotic drift of trajectories occurs in the center directions of the saddle center. See [29] for more details.

Thus, the transverse intersection between $W^{\mathrm{s}}(\mathscr{M})$ and $W^{\mathrm{u}}(\mathscr{M})$ indicates complicated dynamics. We especially note that the complicated motions are not confined to a small neighborhood of the saddle center. In the following, we focus on a special case of $N = 8$ and numerically show the occurrence of such intersection in the reduced system since the analytical technique of [29] is not applicable. Before that, as in [24], we modify the reduced system by symplectic transformations so that it becomes amenable to our analysis, in the next section.

3. Symplectic transformations for $N = 8$

Since σ_8 is the identity map for $N = 8$ so that $\sigma_8 \pi_{\mathrm{e}} = \pi_{\mathrm{e}}$, we reduce the system (1) via Proposition 1 to a π_{e}-invariant three-degree-of-freedom Hamiltonian system whose phase space (3) is represented by

$$\boldsymbol{X} = \boldsymbol{X}_{\mathrm{e}} + \sum_{k=1}^{3} (b_k^+ \boldsymbol{\phi}_k^+ + b_k^- \boldsymbol{\phi}_k^-), \quad b_{1,2,3}^{\pm} \in \mathbb{R}. \tag{4}$$

As in [24], introducing the generating function

$$W(P_m, q_m) = P_1 q_1 + \sum_{m=2}^{8} P_m (q_m - q_{m-1}), \tag{5}$$

we define a symplectic transformation $(q_m, p_m) \mapsto (Q_m, P_m)$. It follows directly from the definition of π_{e} that π_{e}-invariant orbits satisfy

$$\begin{aligned} &q_1 = 0, \qquad q_5 = \pi, \qquad q_m + q_{10-m} = 2\pi, \\ &p_1 = p_5 = 0, \qquad p_m + p_{10-m} = 0 \end{aligned} \tag{6}$$

for $m = 2, 3, 4$. Since in the symplectic transformation generated by (5)

$$\begin{aligned} &q_2 = 2\pi - Q_3 - Q_4 - Q_5, \qquad q_3 = 2\pi - Q_4 - Q_5, \\ &q_4 = 2\pi - Q_5, \qquad p_2 = -P_3, \qquad p_3 = P_3 - P_4, \\ &p_4 = P_4 - P_5, \end{aligned} \tag{7}$$

the reduced Hamiltonian system is represented by (Q_m, P_m) with $m = 3, 4, 5$ and the 8-ring becomes $Q_m = \pi/4$ and $P_m = 0$.

We further introduce the symplectic transformation

$$\begin{aligned} Q_3 &= \frac{1}{4}(\pi + (1+\sqrt{2})x_1 + 2y_1 + (1-\sqrt{2})y_2), \\ Q_4 &= \frac{1}{4}(\pi - (1+\sqrt{2})x_1 + 2y_1 - (1-\sqrt{2})y_2), \\ Q_5 &= \frac{1}{4}(\pi + x_1 - 2y_1 + y_2), \\ P_3 &= x_2 + y_3 + y_4, \\ P_4 &= (1-\sqrt{2})x_2 + y_3 + (1+\sqrt{2})y_4, \\ P_5 &= (2-\sqrt{2})x_2 + (2+\sqrt{2})y_4, \end{aligned} \tag{8}$$

so that the 8-ring becomes the origin O and the eigenspaces for the saddle and center eigenvalues correspond to the $\boldsymbol{x}$-plane and $\boldsymbol{y}$-hyperplane, respectively. Thus, we finally obtain the Hamiltonian system

$$\dot{\boldsymbol{x}} = J_1 \mathrm{D}_x H(\boldsymbol{x}, \boldsymbol{y}), \qquad \dot{\boldsymbol{y}} = J_2 \mathrm{D}_y H(\boldsymbol{x}, \boldsymbol{y}), \tag{9}$$

where J_m is the $2m \times 2m$ symplectic matrix,

$$J_m = \begin{pmatrix} 0 & \mathrm{id}_m \\ -\mathrm{id}_m & 0 \end{pmatrix}$$

with id_m the $m \times m$ identity matrix. The expression of $H(\boldsymbol{x}, \boldsymbol{y})$ is easily obtained by substituting (7) and (8) into (2) under the constraints (6), but it is too lengthy to present in the paper.

Let us assume that $5/2 \leq \Gamma \leq 4$. Then the 8-ring corresponds to a saddle-center equilibrium in (9) since $(\lambda_1^{\pm})^2 < (\lambda_2^{\pm})^2 < 0 < (\lambda_3^{\pm})^2$. Moreover, there exists an unstable direction associated with $\lambda_4^+ > 0$ and normal to the invariant space (4). However, we expect that solutions of the full system (1) starting near the invariant space must repeatedly return near it by the Poincaré recurrence theorem [2] and hence some of them exhibit chaotic motions.

4. Numerical computation of $W^{\mathrm{s,u}}(\mathscr{M})$

Now we describe our approach for numerical computation of $W^{\mathrm{s,u}}(\mathscr{M})$ in (9) when $\mathscr{M}$ is in a small neighborhood of O. Other methods for such computation are also available [10,25], but ours is simpler and easier to perform since neither Fourier series nor normal form calculations are necessary.

We begin with a standard asymptotic expansion method [8] to compute the center manifold of the saddle center at the origin approximately up to $\mathscr{O}(|\boldsymbol{y}|^3)$ as

$$\mathscr{M} = \{(\boldsymbol{x}, \boldsymbol{y}) \in \mathbb{R}^2 \times \mathbb{R}^4 \mid \boldsymbol{x} = \boldsymbol{h}(\boldsymbol{y})\}, \tag{10}$$

where $\boldsymbol{h}(\boldsymbol{y}) = (h_1(\boldsymbol{y}), h_2(\boldsymbol{y}))^{\mathrm{T}}$ with

$$\begin{aligned} h_1(\boldsymbol{y}) &= b_{1100}^{(1)} y_1 y_2 + b_{0011}^{(1)} y_3 y_4 + b_{0300}^{(1)} y_2^3 + b_{2100}^{(1)} y_1^2 y_2 \\ &\quad + b_{0120}^{(1)} y_2 y_3^2 + b_{0102}^{(1)} y_2 y_4^2 + b_{1011}^{(1)} y_1 y_3 y_4, \\ h_2(\boldsymbol{y}) &= b_{1001}^{(2)} y_1 y_4 + b_{0110}^{(2)} y_2 y_3 + b_{0003}^{(2)} y_4^3 + b_{2001}^{(2)} y_1^2 y_4 \\ &\quad + b_{0201}^{(2)} y_2^2 y_4 + b_{0021}^{(2)} y_3^2 y_4 + b_{1110}^{(2)} y_1 y_2 y_3. \end{aligned} \tag{11}$$

(see Appendix for the coefficients in (11)). Thus, we can approximate (9) near the origin as

$$\dot{\boldsymbol{\xi}} = \boldsymbol{J}_1 \mathrm{D}_x^2 H_4(\boldsymbol{h}(\boldsymbol{y}), \boldsymbol{y}) \boldsymbol{\xi}, \qquad \dot{\boldsymbol{y}} = \boldsymbol{J}_2 \mathrm{D}_y H_4(\boldsymbol{h}(\boldsymbol{y}), \boldsymbol{y}), \tag{12}$$

where $H_4(\boldsymbol{x}, \boldsymbol{y})$ is the fourth-order polynomial approximation of the Hamiltonian $H(\boldsymbol{x}, \boldsymbol{y})$ and $\xi = \boldsymbol{x} - \boldsymbol{h}(\boldsymbol{y})$.

Using the numerical technique of [30] with assistance of the approximation (12), we compute the unstable manifold $W^{\mathrm{u}}(\mathscr{M})$ as follows. We first numerically solve (12) on a time-interval $[-T, 0]$ to obtain a small trajectory $\bar{\boldsymbol{y}}(t)$ on $\mathscr{M}$ near the origin O and its one-dimensional unstable subspace $E^{\mathrm{u}} \subset \mathbb{R}^2$ for $\bar{\boldsymbol{y}}(t)$ at $t = 0$ such that $\boldsymbol{\xi}(t) \to \boldsymbol{0}$ as $t \to -\infty$ if $\boldsymbol{\xi}(0) \in E^{\mathrm{u}}$. Let $\boldsymbol{e}^{\mathrm{u}}$ be a unit vector spanning E^{u}, which is approximated as

$$\boldsymbol{e}^{\mathrm{u}} \approx \boldsymbol{\xi}(\boldsymbol{0})/|\boldsymbol{\xi}(\boldsymbol{0})|, \qquad \boldsymbol{\xi}(\bar{T}) = \boldsymbol{\xi}_0 \tag{13}$$

if $\bar{T}$ is large and $(\boldsymbol{\xi}_0, \boldsymbol{0})$ is the unstable eigenvector of O in (9), as shown in [30]. We compute a trajectory $(\boldsymbol{x}^{\mathrm{u}}(t), \boldsymbol{y}^{\mathrm{u}}(t))$ on $W^{\mathrm{u}}(\mathscr{M})$ by solving (9) under the boundary conditions

$$\begin{aligned} &\boldsymbol{x}^{\mathrm{u}}(0) - \boldsymbol{h}(\boldsymbol{y}^{\mathrm{u}}(0)) = \varepsilon_{\mathrm{u}} \boldsymbol{e}^{\mathrm{u}}, \qquad \boldsymbol{y}^{\mathrm{u}}(0) = \bar{\boldsymbol{y}}(0), \\ &\quad (\boldsymbol{x}^{\mathrm{u}}(T_{\mathrm{u}}), \boldsymbol{y}^{\mathrm{u}}(T_{\mathrm{u}})) = (\boldsymbol{x}_0^{\mathrm{u}}, \boldsymbol{y}_0^{\mathrm{u}}), \end{aligned} \tag{14}$$

where $\varepsilon_{\mathrm{u}} \ll 1$ and T_{u} are positive constants, and $(\boldsymbol{x}_0^{\mathrm{u}}, \boldsymbol{y}_0^{\mathrm{u}}) \in \mathbb{R}^2 \times \mathbb{R}^4$ represents an approximate point on $W^{\mathrm{u}}(\mathscr{M})$. Thus, numerical continuation of the solutions $(\boldsymbol{\xi}(t), \bar{\boldsymbol{y}}(t))$ and $(\boldsymbol{x}^{\mathrm{u}}(t), \boldsymbol{y}^{\mathrm{u}}(t))$ for the boundary value problem (9), (12) and (14) gives $W^{\mathrm{u}}(\mathscr{M})$. Similarly, we compute $W^{\mathrm{s}}(\mathscr{M})$ by continuing a solution $(\xi(t), \bar{\boldsymbol{y}}(t))$ of (12) on $[0, \bar{T}]$ and a solution $(\boldsymbol{x}^{\mathrm{s}}(t), \boldsymbol{y}^{\mathrm{s}}(t))$ of (9) satisfying the boundary conditions

$$\begin{aligned} &\boldsymbol{x}^{\mathrm{s}}(0) - \boldsymbol{h}(\boldsymbol{y}^{\mathrm{s}}(0)) = \varepsilon_{\mathrm{s}} \boldsymbol{e}^{\mathrm{s}}, \qquad \boldsymbol{y}^{\mathrm{s}}(0) = \bar{\boldsymbol{y}}(0), \\ &\quad (\boldsymbol{x}^{\mathrm{s}}(-T_{\mathrm{s}}), \boldsymbol{y}^{\mathrm{s}}(-T_{\mathrm{s}})) = (\boldsymbol{x}_0^{\mathrm{s}}, \boldsymbol{y}_0^{\mathrm{s}}), \end{aligned} \tag{15}$$

where $\boldsymbol{e}^{\mathrm{s}} \in \mathbb{R}^2$ is a unit vector spanning the one-dimensional stable subspace $E^{\mathrm{s}} \subset \mathbb{R}^2$ for $\bar{\boldsymbol{y}}(t)$ at $t = 0$ such that $\boldsymbol{\xi}(t) \to \boldsymbol{0}$ as $t \to \infty$ if $\boldsymbol{\xi}(0) \in E^{\mathrm{s}}$, where $\varepsilon_s \ll 1$ and T_{s} are positive constants, and $(\boldsymbol{x}_0^{\mathrm{s}}, \boldsymbol{y}_0^{\mathrm{s}}) \in \mathbb{R}^2 \times \mathbb{R}^4$ represents an approximate point on $W^{\mathrm{s}}(\mathscr{M})$. Note that as in (13), $\boldsymbol{e}^{\mathrm{s}}$ is approximated as

$$\boldsymbol{e}^{\mathrm{s}} \approx \boldsymbol{\xi}(\boldsymbol{0})/|\boldsymbol{\xi}(\boldsymbol{0})|, \qquad \boldsymbol{\xi}(-\bar{T}) = \boldsymbol{\xi}_0 \tag{16}$$

if $\bar{T}$ is large and $(\boldsymbol{\xi}_0, \boldsymbol{0})$ is the stable eigenvector of O in (9).

To carry out the above computations of continuation, we use the computer tool "AUTO97" [6]. As the starting ones for the continuation, we take solutions of the linearized system for (12) at the origin (with $\bar{T}$ and $T_{\mathrm{s,u}}$ small), as in [24]. In the continuation $\bar{T}$, $T_{\mathrm{s,u}}$, $\boldsymbol{x}_0^{\mathrm{s,u}}$, $\boldsymbol{y}_0^{\mathrm{s,u}}$ or $\bar{\boldsymbol{y}}(\pm\bar{T})$ are chosen as the free parameters.

5. Numerical results

Using the method of Section 4, we compute the stable and unstable manifolds $W^{\mathrm{s,u}}(\mathscr{M})$ in the reduced three-degree-of-freedom Hamiltonian system (9) for $N = 8$. Fig. 1 shows an example of the numerical results for $\Gamma = 3$ and $\Delta H = H - H(\boldsymbol{0}, \boldsymbol{0}) = 5 \times 10^{-3}$. We see that these manifolds intersect transversely so that complicated dynamics may occur in (9), as described in Section 2.

To demonstrate the occurrence of such complicated dynamics, we carry out direct numerical simulations using an approach similar to that of [24] and a computer software named "Dynamics" [16] with an adoption of a code named "DOP853" [9]. The code is based on the explicit Runge–Kutta method of order 8 by Dormand and Prince [5], a fifth-order error estimator with third-order correction is utilized and a dense output of order 7 is included. A small tolerance of 10^{-8} is chosen in the computations so that the numerical results are very accurate although the method is not symplectic. Below we set $\Gamma = 3$ and $\Delta H = 5 \times 10^{-3}$ as in Fig. 1, and often use the Poincaré map for the section $\{y_4 = 0, \dot{y}_4 > 0\}$.

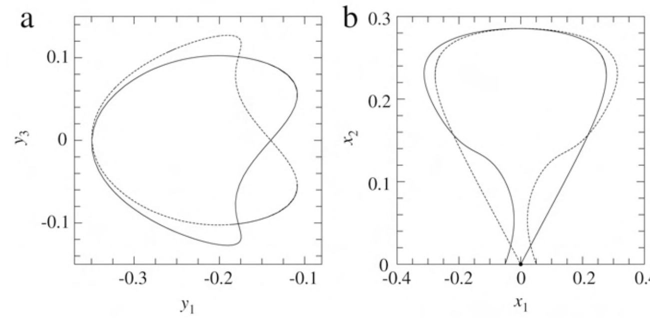

Fig. 1. Intersection of the unstable and stable manifolds $W^{\mathrm{s,u}}(\mathscr{M})$ with the section $\{x_1 = y_2 = y_4 = 0\}$ or $\{y_2 = y_3 = y_4 = 0\}$ for $\Gamma = 3$ on the energy level $\Delta H = 5 \times 10^{-3}$: (a) Their projections onto the (y_1, y_3)-plane; (b) onto the $\boldsymbol{x}$-plane. The solid and broken lines represent the stable and unstable manifolds, respectively. In plate (b), '•' represents the saddle center at the origin.

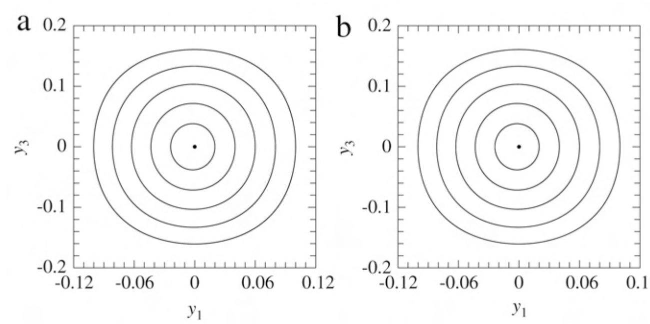

Fig. 2. Approximately computed orbits of the Poincaré map on the locally invariant manifold $\mathscr{M}$. The fourth-order approximate and exact Hamiltonian are used in plates (a) and (b), respectively.

Fig. 2 shows approximately computed orbits of the Poincaré map on $\mathscr{M}$. Here the fourth-order approximate and exact Hamiltonian are used in Fig. 2(a) and (b), respectively, while the third-order approximation is used for $\mathscr{M}$ in both figures. We see that both results are almost the same and that all the computed orbits construct invariant tori. This also implies that our approximations made for computation of $W^{\mathrm{s,u}}(\mathscr{M})$ are appropriate.

Fig. 3 shows a numerically computed orbit of the Poincaré map starting at $(\boldsymbol{x}, \boldsymbol{y}) = (0.001, 0, 0.0861491, 0, 0.1, 0)$. Its projection onto the $\boldsymbol{x}$-plane is plotted with 20 000 points in Fig. 3(a), and its projection onto the (y_1, y_3)-plane when it enters a neighborhood of $\mathscr{M}$, $\{|\boldsymbol{x} - \boldsymbol{h}(\boldsymbol{y})| < 0.01\}$, is plotted with 60 points in Fig. 3(b), where different symbols are used for every 20 visits. Note that the points of Fig. 3(a) are confined to some region since the energy level set is bounded. We observe that the orbit does not only exhibit a chaotic motion but also randomly drifts in the center directions of the saddle center, as described in Section 2. A numerical observation of such

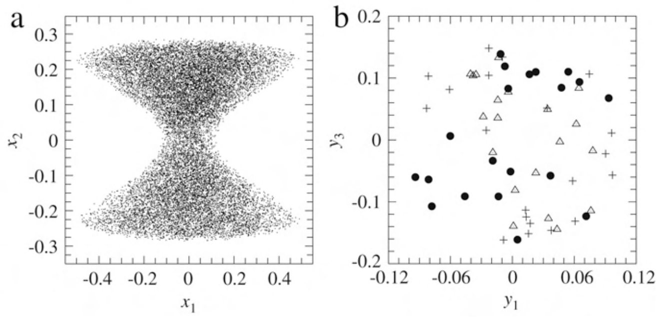

Fig. 3. Orbit of the Poincaré map: (a) Its projections onto the $\boldsymbol{x}$-plane; (b) onto the (y_1, y_3)-plane when it enters a neighborhood of $\mathscr{M}$. In plate (b), '+' represents for 1st–20th visits, '•' for 21st–40th, and '△' for 41st–60th.

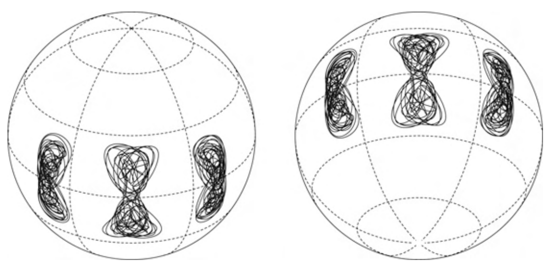

Fig. 4. Chaotic motion of the eight point vortices in the π_e invariant system, which corresponds to the orbit in Fig. 3.

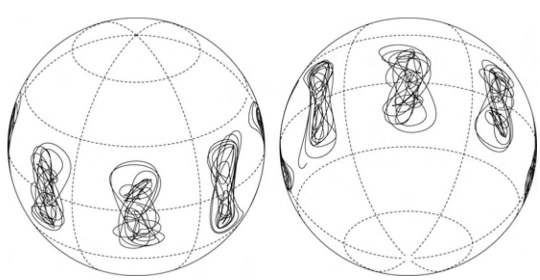

Fig. 5. Chaotic motion of the eight point vortices in the full system (1).

behavior in a three-degree-of-freedom Hamiltonian system was reported in [28] earlier.

Fig. 4 shows a chaotic motion of the eight point vortices on the sphere, which is obtained by a solution of the reduced system (9) and corresponds to the orbits in Fig. 3. For comparison, we show a chaotic motion of the full system (1) without the π_e-symmetry in Fig. 5. Although the invariant space (4) is unstable, we see that the chaotic trajectory in the full system evolves like that in the reduced system, as predicted by the Poincaré recurrence theorem [2] (see Section 3 and also Section 7 of [24]).

6. Conclusions

In this paper we have revealed that complicated dynamics exists in the $N = 8n$ vortex problem on a sphere. Our numerical analysis with assistance of the center manifold technique showed that the stable and unstable manifolds of a locally invariant manifold including a Cantor set of whiskered tori near the saddle-center N-ring equilibrium intersect transversely in the reduced Hamiltonian system. We gave numerical simulation results to demonstrate that complicated behavior resulting from such intersection occurs in the Euler flow as well as in the reduced system. Thus, our dynamical systems approach sheds light on the new interesting feature of the important fluid problem, as in [24]. Finally, we remark that our treatment is also valid for $N = 7n$ as well as $N = 8n$ although the necessary center manifold calculations are tedious, and that the numerical technique is applicable to a large class of Hamiltonian systems with saddle centers.

Acknowledgments

T.S. is partially supported by the Japan Society for the Promotion of Science (JSPS), Grant-in-Aid for Young Scientists (A) #17684002 and Grant-in-Aid for Exploratory Science, # 19654014. K.Y. is partially supported by the JSPS, Grant-in-Aid for Scientific Research (C) #18560056.

Appendix. Coefficients of (11)

Let

$$\beta_1 = 16\Gamma^2 - 54\Gamma - 45,$$
$$\beta_2 = 128\Gamma^4 - 1232\Gamma^3 + 1140\Gamma^2 + 6300\Gamma + 3375,$$
$$\beta_3 = 256\Gamma^4 - 2304\Gamma^3 + 7740\Gamma^2 - 8100\Gamma - 10125,$$
$$\beta_4 = 8(2\Gamma - 15)\beta_3.$$

The second-order coefficients are given by

$$b^{(1)}_{1100} = -\frac{4\Gamma^2 + 60\Gamma - 279}{4\beta_1},$$
$$b^{(1)}_{0011} = -\frac{2(4\Gamma^3 - 60\Gamma^2 + 171\Gamma + 45)}{\beta_1},$$
$$b^{(2)}_{1001} = \frac{5(4\Gamma^2 - 36\Gamma + 9)}{4\beta_1},\quad b^{(2)}_{0110} = \frac{5(4\Gamma^2 - 24\Gamma + 99)}{16\beta_1};$$

and the third-order coefficients are given by

$$\begin{aligned}
b^{(1)}_{0300} &= -\frac{1}{1536\beta_2}(176\Gamma^4 - 26684\Gamma^3 + 88560\Gamma^2 \\
&\quad - 145215\Gamma + 788400),\\
b^{(1)}_{2100} &= \frac{1}{\beta_4}(328\Gamma^5 - 12528\Gamma^4 + 98154\Gamma^3 \\
&\quad - 254880\Gamma^2 - 151875\Gamma + 1245375),\\
b^{(1)}_{0120} &= -\frac{1}{\beta_4}(432\Gamma^6 - 2376\Gamma^5 - 28588\Gamma^4 + 431550\Gamma^3 \\
&\quad - 2477700\Gamma^2 + 6773625\Gamma - 7948125),\\
b^{(1)}_{0102} &= \frac{1}{16\beta_2}(80\Gamma^5 - 356\Gamma^4 + 11976\Gamma^3 - 81633\Gamma^2 \\
&\quad + 111150\Gamma + 83700),\\
b^{(1)}_{1011} &= \frac{1}{\beta_3}(136\Gamma^5 - 1464\Gamma^4 + 8658\Gamma^3 - 21942\Gamma^2 \\
&\quad + 36855\Gamma - 46575),\\
b^{(2)}_{0003} &= \frac{5}{16\beta_2}(16\Gamma^5 + 44\Gamma^4 + 2840\Gamma^3 - 12813\Gamma^2 \\
&\quad - 10350\Gamma + 2700),
\end{aligned}$$

$$b_{2001}^{(2)} = -\frac{1}{\beta_4}(1304\Gamma^5 - 8736\Gamma^4 + 8190\Gamma^3 + 143100\Gamma^2 - 658125\Gamma + 151875),$$

$$b_{0201}^{(2)} = \frac{15(16\Gamma^4 + 1228\Gamma^3 - 7216\Gamma^2 + 18915\Gamma - 18000)}{512\beta_2},$$

$$b_{0021}^{(2)} = \frac{1}{\beta_4}(656\Gamma^6 - 20664\Gamma^5 + 185100\Gamma^4 - 757710\Gamma^3 + 1479600\Gamma^2 - 1387125\Gamma + 1366875),$$

$$b_{1110}^{(2)} = \frac{1384\Gamma^4 - 8568\Gamma^3 - 342\Gamma^2 + 196830\Gamma - 431325}{32\beta_3}.$$

References

[1] H. Aref, P.K. Newton, M.A. Stremler, T. Tokieda, D.L. Vainchtein, Vortex crystals, in: E. van der Giessen, H. Aref (Eds.), Advances in Applied Mechanics, vol. 39, 2003, pp. 2–81.

[2] V.I. Arnold, Mathematical Methods of Classical Mechanics, 2nd. ed., Springer, New York, 1989.

[3] S. Boatto, H.E. Cabral, Nonlinear stability of a latitudinal ring of point-vortices on a nonrotating sphere, SIAM J. Appl. Math. 64 (2003) 216–230.

[4] H.E. Cabral, K.R. Meyer, D.S. Schmidt, Stability and bifurcation of the $N + 1$ vortex problem on sphere, Regul. Chaotic Dyn. 8 (2003) 259–282.

[5] J.R. Dormand, P.J. Prince, Practical Runge–Kutta processes, SIAM J. Sci. Stat. Comput. 10 (1989) 977–989.

[6] E. Doedel, A.R. Champneys, T.F. Fairgrieve, Y.A. Kuznetsov, B. Sandstede, X. Wang, AUTO97: Continuation and Bifurcation Software for Ordinary Differential Equations (with HomCont), 1997. Available by anonymous ftp from ftp.cs.concordia.ca, directory pub/doedel/auto.

[7] S.M. Graff, On the conservation of hyperbolic invariant tori for Hamiltonian systems, J. Differential Equations 15 (1974) 1–69.

[8] J. Guckenheimer, P. Holmes, Nonlinear Oscillations, Dynamical Systems, and Bifurcations of Vector Fields, Springer, New York, 1983.

[9] E. Hairer, S.P. Nørsett, G. Wanner, Solving Ordinary Differential equation (I), 2nd ed., Springer, Berlin, 1993.

[10] A. Jorba, Numerical computation of the normal behaviour of invariant curves of n-dimensional maps, Nonlinearity 14 (2001) 943–976.

[11] R. Kidambi, P.K. Newton, Motion of three point vortices on a sphere, Physica D 116 (1998) 95–134.

[12] C.C. Lim, J. Montaldi, M. Roberts, Relative equilibria of point vortices on the sphere, Physica D 148 (2001) 97–135.

[13] K.R. Meyer, G.R. Hall, Introduction to Hamiltonian Dynamical Systems and the N-Body Problem, Springer, New York, 1992.

[14] J. Moser, Stable and Random Motions in Dynamical Systems, Princeton Univ. Press, 1973.

[15] P.K. Newton, The N-vortex problem, Analytical techniques, Springer, New York, 2001.

[16] H.E. Nusse, J.A. Yorke, Dynamics: Numerical Explorations, 2nd ed., Springer, New York, 1997.

[17] L.M. Polvani, D.G. Dritschel, Wave and vortex dynamics on the surface of a sphere, J. Fluid Mech. 255 (1993) 35–64.

[18] J. Pöschel, Über invariant Tori in Differenzierbaren Hamiltonschen Systemen, in: Bonn Math. Schr, 120, Universität Bonn, Bonn, 1980.

[19] T. Sakajo, The motion of three point vortices on a sphere, Japan J. Indust. Appl. Math. 16 (1999) 321–347.

[20] T. Sakajo, Motion of a vortex sheet on a sphere with pole vortices, Phys. Fluids 16 (2004) 717–727.

[21] T. Sakajo, Transition of global dynamics of a polygonal vortex ring on a sphere with pole vortices, Physica D 196 (2004) 243–264.

[22] T. Sakajo, Invariant dynamical systems embedded in the N-vortex problem on a sphere with pole vortices, Physica D 217 (2006) 142–152; Physica D 225 (2007) 235–236 (erratum).

[23] T. Sakajo, Integrable four-vortex motion on sphere with zero moment of vorticity, Phys. Fluids 19 (2007) 017019.

[24] T. Sakajo, K. Yagasaki, Chaotic motion of the N-vortex problem on a sphere: I. Saddle centers in two-degree-of-freedom Hamiltonian, J. Nonlinear Sci. (2008), doi:10.1007/s00332-008-9019-9.

[25] H. Waalkens, A. Burbanks, S. Wiggins, A computational procedure to detect a new type of high-dimensional chaotic saddle and its application to the 3D Hill's problem, J. Phys. A 37 (2004) L257–L265.

[26] S. Wiggins, Normally Hyperbolic Invariant Manifolds in Dynamical Systems, Springer, New York, 1994.

[27] K. Yagasaki, Horseshoe in two-degree-of-freedom Hamiltonian systems with saddle-centers, Arch. Ration. Mech. Anal. 154 (2000) 275–296.

[28] K. Yagasaki, Numerical evidence of fast diffusion in a three-degree-of-freedom Hamiltonian system with a saddle-center, Phys. Lett. A 301 (2002) 45–52.

[29] K. Yagasaki, Homoclinic and heteroclinic orbits to invariant tori in multi-degree-of-freedom Hamiltonian systems with saddle-centers, Nonlinearity 18 (2005) 1331–1350.

[30] K. Yagasaki, Numerical computation of stable and unstable manifolds of normally hyperbolic invariant manifolds (in preparation).

Available online at www.sciencedirect.com
ScienceDirect
Physica D 237 (2008) 2084–2089
PHYSICA D
www.elsevier.com/locate/physd

Acceleration of heavy and light particles in turbulence: Comparison between experiments and direct numerical simulations

R. Volk[a,*], E. Calzavarini[b], G. Verhille[a], D. Lohse[b], N. Mordant[c], J.-F. Pinton[a], F. Toschi[d,e]

[a] *Laboratoire de Physique, de l'École normale supérieure de Lyon, CNRS UMR5672, 46 Allée d'Italie, 69007 Lyon, France*
[b] *Faculty of Science, J.M. Burgers Centre for Fluid Dynamics, and Impact-Institute, University of Twente, 7500 AE Enschede, The Netherlands*
[c] *Laboratoire de Physique, Statistique de l'École normale supérieure de Paris, CNRS UMR8550, 24 rue Lhomond, 75005 Paris, France*
[d] *Istituto per le Applicazioni del Calcolo CNR, Viale del Policlinico 137, 00161 Roma, Italy*
[e] *INFN, Sezione di Ferrara, Via G. Saragat 1, I-44100 Ferrara, Italy*

Available online 24 January 2008

Abstract

We compare experimental data and numerical simulations for the dynamics of inertial particles with finite density in turbulence. In the experiment, bubbles and solid particles are optically tracked in a turbulent flow of water using an Extended Laser Doppler Velocimetry technique. The probability density functions (PDF) of particle accelerations and their auto-correlation in time are computed. Numerical results are obtained from a direct numerical simulation in which a suspension of passive pointwise particles is tracked, with the same finite density and the same response time as in the experiment. We observe a good agreement for both the variance of acceleration and the autocorrelation time scale of the dynamics; small discrepancies on the shape of the acceleration PDF are observed. We discuss the effects induced by the finite size of the particles, not taken into account in the present numerical simulations.

PACS: 47.27.Jv; 47.27.Gs; 02.50.-r

Keywords: Inertial particles; Lagrangian acceleration; Lagrangian turbulence

1. Introduction

Understanding the transport of inertial particles with finite density, such as sediments, neutrally buoyant particles or bubbles in turbulent flows of water is of practical interest for both industrial engineering or environmental problems. In a turbulent flow, the mismatch in density between the particles and the fluid causes light particles to be trapped in high vortical regions while heavy particles are ejected form vortex cores and concentrate in high strain regions [1]. As particles with different buoyancy tend to concentrate in different regions of the flow, they are expected to exhibit different dynamic behaviours. In recent years, significant progress has been made in the limit of infinitely heavy, pointwise particles [2,3], and numerical simulations have received experimental support [4,5]. In case of infinitely light particles (*bubbles*): the result of the numerical simulations on particle distributions and on fluid velocity spectra [6–8] agree in various aspects with experimental findings [9–12] although direct comparison between experiments and numerical simulations for the acceleration PDF and correlation of the particles has not been investigated in the past.

Indeed, in spite of the growing resolution of Direct Numerical Simulations (DNS) of the Navier-Stokes equations at high Reynolds numbers, it remains a challenge to resolve the motion of realistic inertial particles: some degree of modelization is necessary. The equation of motion of finite size, finite density particles moving in a turbulent flow, is not precisely known, and a comparison with experimental data can help in refining the models and extending their range of validity.

Several experimental techniques have been developed for measuring the velocity of particles along their trajectories. The optical tracking method developed in the Cornell group

* Corresponding author. Tel.: +33 472728472; fax: +33 472728080.
E-mail address: romain.volk@ens-lyon.fr (R. Volk).

0167-2789/$ - see front matter
doi:10.1016/j.physd.2008.01.016

has revealed that fluid particles experience extremely intense accelerations [13], while individual particles have been tracked for time durations of the order of the flow integral time scale using an acoustic technique [14]. Because of the very fast decrease of the acoustic scattering cross-section with the scatterer's size, this method is limited to particles with diameter of the order of the wavelength, *i.e.* inertial range sizes [15, 23]. The principle of the acoustic technique is completely analogous to laser Doppler velocimetry (LDV), provided that expanded light beams are used (an arrangement we call E-LDV hereafter). The advantage of E-LDV, compared to acoustics, is that the much smaller wavelength of light allows a better resolution in space and also the use of smaller tracer particles. The principle of the measurement technique is reported in [16], where its performance has been compared and validated against silicon-strip tracking [13,17] of neutrally buoyant Lagrangian tracers. We focus here on the dynamics of inertial particles *i.e.* particles whose density differ from that of the fluid. We report the first comparison between experimental measurements of acceleration of particles having a relative density in the range 10^{-3} (air bubbles) to 1.4 (PMMA) in the same highly turbulent flow, and numerical results obtained by tracking pointwise particles with finite density in a direct numerical simulation of isotropic homogeneous turbulence [18,19].

Numerical simulations are performed by means of standard pseudo-spectral methods, where particular care has been used in keeping a good resolution at the dissipative scales. The numerical code for integrating the evolution of the Eulerian field and the Lagrangian tracing of particles is the same as described in [7,8,25]. A thorough validation of the numerical approach, included the Lagrangian evolution of the tracers has recently been performed against experimental measurements [26]. The numerical integration of tracers has, with respect to experiments, the clear advantage of a uniform, well controlled geometry and very large statistics; on the opposite, the resolution can be limited to small Reynolds numbers. For what concerns the treatment of realistic particles, i.e. particles with a density mismatch and a "finite" size, the best modelization to use is not clear and one of the main goals of this manuscript is indeed to compare state-of-the-art Lagrangian data against numerical results from a current modelization.

2. Experimental setup and results

The Laser Doppler technique is based on the same principle as the ultrasound Doppler method which has good tracking performance of individual Lagrangian tracers [14,23]. In order to access dissipative scales, and in particular for acceleration measurements, we adapt the technique from ultrasound to laser light: the gain is of a factor 1000 in wavelength so that one expects to detect micron-sized particles. For a Lagrangian measurement, one has to be able to follow the particle motion to get information about its dynamics in time. For this, wide Laser beams are needed to illuminate the particle on a significant fraction of its path. The optical setup is an extension of the well known laser Doppler velocimetry technique; Fig. 1. A Laser beam is split into two beams; each is then expanded by

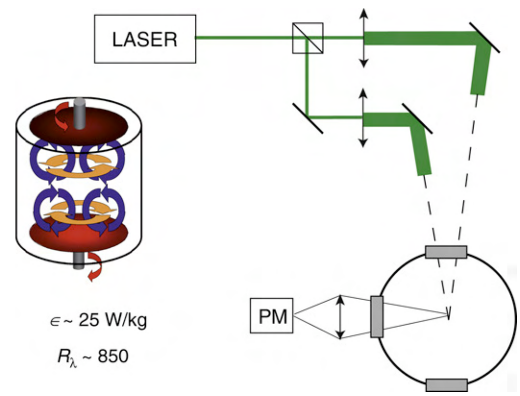

Fig. 1. Experimental setup. (Top left): schematics of the von Kármán flow in water – side view. (Top right): principle of the Laser-Doppler Velocimetry using wide beams (ELDV) – top view of the experiment. PM: location of the photmultipler which detects scattering light modulation as a particle crosses the interference pattern created at the intersection of the laser beams.

a telescope so that their diameter is about 5 mm. Then the two beams intersect in the flow where they create an array of interference fringes. As a particle crosses the fringes, the scattered light is modulated at a frequency directly proportional to the component of the velocity perpendicular to the fringes. It yields a measurement of one component of the particle velocity. In practice, we use a CW YAG laser of wave length 532 nm with 1.2 W maximum output power. In order to get the sign of the velocity we use acousto-optic modulators (AOM) to shift the frequency of the beams so that the fringes are actually travelling at a constant speed. The angle of the two beams is tuned to impose a 60 microns inter-fringe so that the frequency shift between the beams (100 kHz) corresponds to 6 m/s. As the beams are not focused, the inter-fringe remains constant across the measurement volume whose size is about $5 \times 5 \times 10$ mm^3. It is imaged on a photomultiplier whose output is recorded using a National Instrument PXI-NI5621 digitizer at rate 1 MHz.

The flow is of the Von Kármán kind as in several previous experiments using acoustics [14] or optical techniques [13]. Water fills a cylindrical container of internal diameter 15 cm, length 20 cm. It is driven by two disks of diameter 10 cm, fitted with blades in order to increase steering. The rotation rate is fixed at values up to 10 Hz. For the measurements reported here, the Taylor-based Reynolds number reaches up to 850 at a maximum dissipation rate ϵ equal to 25 W/kg. We study three types of particles: neutrally buoyant polystyrene particles with size 31 microns and density 1.06, PMMA particles with size 43 microns and density 1.4 and air bubbles with a size of about 150 microns. The mean size of the bubbles, measured optically by imaging the measurement volume on a CCD, is imposed by the balance between the interfacial surface tension σ and the turbulent fluctuations of pressure. This fragmentation process is known to lead to a well defined and stationary size distribution [20] with a typical diameter $D \propto (\sigma/\rho_f)^{3/5}\epsilon^{-2/5}$, ρ_f being the density of the fluid.

The signal processing step is crucial as both time and frequency – (*i.e.* velocity) – resolutions rely on its performance. Frequency demodulation is achieved using the same algorithm as in the acoustic Doppler technique. It is a approximated

Table 1
(top) Parameters of the particles in the von Kármán flow at $R_\lambda = 850$ ($\eta = (\nu^3/\epsilon)^{1/4} = 17$ µm and $\tau_\eta = \sqrt{\nu/\epsilon} = 0.26\ 10^{-3}$ s)

Experiment					
Particle	Radius a	$\beta = \frac{3\rho_f}{\rho_f+2\rho_p}$	$St = \frac{\tau_p}{\tau_\eta}$	a_0	$a_0/a_{0,T}$
Tracers	15.5 µm	0.96	0.24	6.4 ± 1	1
Neutral	125 µm	0.96	16	2.2 ± 1	0.34
Heavy	20.5 µm	0.79	0.58	4.3 ± 1	0.67
Bubble	75 µm	2.99	1.85	26 ± 5	4.06
Numerics					
Particle	Radius a	$\beta = \frac{3\rho_f}{\rho_f+2\rho_p}$	$St = \frac{\tau_p}{\tau_\eta}$	a_0	$a_0/a_{0,T}$
Tracers	–	1	0.31	2.85 ± 0.07	1
Neutral	–	1	4.1	2.94 ± 0.07	1.03
Heavy	–	0.75	1.03	2.63 ± 0.12	0.92
Bubble	–	3	1.64	25.9 ± 0.46	9.08

ρ_p and ρ_f are the densities of the particles and fluid, and $\tau_p = a^2/(3\beta\nu)$ is the stokes response time of the particles. The Taylor-based turbulent Reynolds number is computed as $R_\lambda = \sqrt{15u_{\rm rms}^4/\epsilon\nu}$ measuring the one-component root-mean-square velocity, $u_{\rm rms}$, with the E-LDV system and ϵ by monitoring the power consumption of the motors. The nondimensional constant a_0 is derived from the Heisenberg–Yaglom relationship. The last column compares the value for the inertial particle to the one obtained for the Lagrangian tracer (which is denoted by the subscript T). (bottom) Same as above: parameters of the particles tracked in the DNS of homogeneous isotropic turbulence at $R_\lambda = 180$. Out of the numerically analysed 64 parameter combinations (β, St), we have picked those which were close to the experimental values for (β, St).

maximum likelihood method coupled with a Kalman filter [21]: a parametric estimator assumes that the signal is made of a modulated complex exponential and Gaussian noise. The amplitude of the recorded signal and the modulation frequencies are assumed to be slowly evolving compared to the duration of the time window used to estimate the instantaneous frequency. Here the time window is about 30 µs long and sets the time resolution of the algorithm. Outputs of the algorithm are the instantaneous frequency, the amplitude of the modulation and a confidence estimate which is used to eliminate unreliable detections. Afterwards, the acceleration of the particle is computed by differentiation of the velocity output. Note that measurements are performed only when a particle moves within the (limited) measurement volume so that after processing, the data consists in a collection of sequences with variable lengths. For all the measurements, the acceleration variance is computed using the same procedure as in [17]: it is obtained for several widths of the smoothing kernel used in the differentiation of the velocity signal and then interpolated to zero filter width.

For small neutrally buoyant particles, *i.e.* Lagrangian tracers, our data is in excellent agreement with the high-speed imaging measurements performed by the Cornell group [13,16,17]. When the variance of the acceleration is normalized by the Heisenberg–Yaglom scaling: $\langle a^2\rangle = a_0\epsilon^{3/2}\nu^{-1/2}$ (ϵ being the energy dissipation rate per unit mass and $\nu = 1.3\cdot 10^{-6}$ m^2 s^{-1} the kinematic viscosity of the fluid), both experiments yields the same values for the nondimensional constant a_0 ($a_0 = 6.4\pm 1$ at $R_\lambda = 850$ for the E-LDV compared to 6.2 ± 0.4 for the Cornell data at $R_\lambda = 690$).

We have applied our technique to compare the dynamics of Lagrangian tracers to the one of heavier or lighter particles (see Table 1 for numbers). We first compute the velocity root-mean-square value $u_{\rm rms}$ for the three cases: the values are $\{1.1, 1.2, 1.0\} \pm 0.1$ m.s^{-1} at $R_\lambda = 850$ for the tracers, heavy (PMMA spheres), and light particles (bubbles). Within error bars, the large scale dynamics seems to be unaffected by changes in the particle inertia. The acceleration distribution and autocorrelation in the three cases are shown respectively in Fig. 2 (top) and Fig. 3 (top). The acceleration PDFs are quite similar for moderate acceleration values (below about $10\,a_{\rm rms}$), as also observed in low Reynolds number numerical simulations [22]. However, the probability of very large accelerations seems to be reduced in the case of inertial particles as compared to Lagrangian tracers. The normalized acceleration variance a_0 varies very significantly: it is reduced to 4.3 ± 1 for heavier particles while it is increased to 26 ± 5 for bubbles. The correlation functions also show significant changes with inertia: the characteristic time of decay is longer for heavy particles and shorter for bubbles compared to tracers. We measure $\tau_{\rm corr}/\tau_\eta = \{0.5, 0.9, 0.25\}$ respectively for tracers, heavy and light particles, with the correlation time defined as the half-width at mid-amplitude of the correlation function. We thus observe important changes in the dynamics, even if the distribution of acceleration weakly changes with inertia.

Note that in our setup the Kolmogorov length is about $\eta = 17$ µm at $R_\lambda = 850$, so that the bubble size is about $10\,\eta$ and therefore may not be considered as a point particle. Thus, one may wonder if the bubble dynamics is not altered by spatial filtering as recently demonstrated for particles with diameters in the inertia range [23]. To check, we have compared the dynamics of large neutrally buoyant particles with diameter 250 µm to the one of Lagrangian tracers. The results is shown in Fig. 2 together with the other particles: the effect of the particle size on the PDF is found to be weak as the curve nicely superimposes with the ones for inertial particles. However, the size effect is clear when comparing either the coefficient a_0 (reduced to 2.2), or the autocorrelation functions. One observes that the correlation time of the large particles is twice that

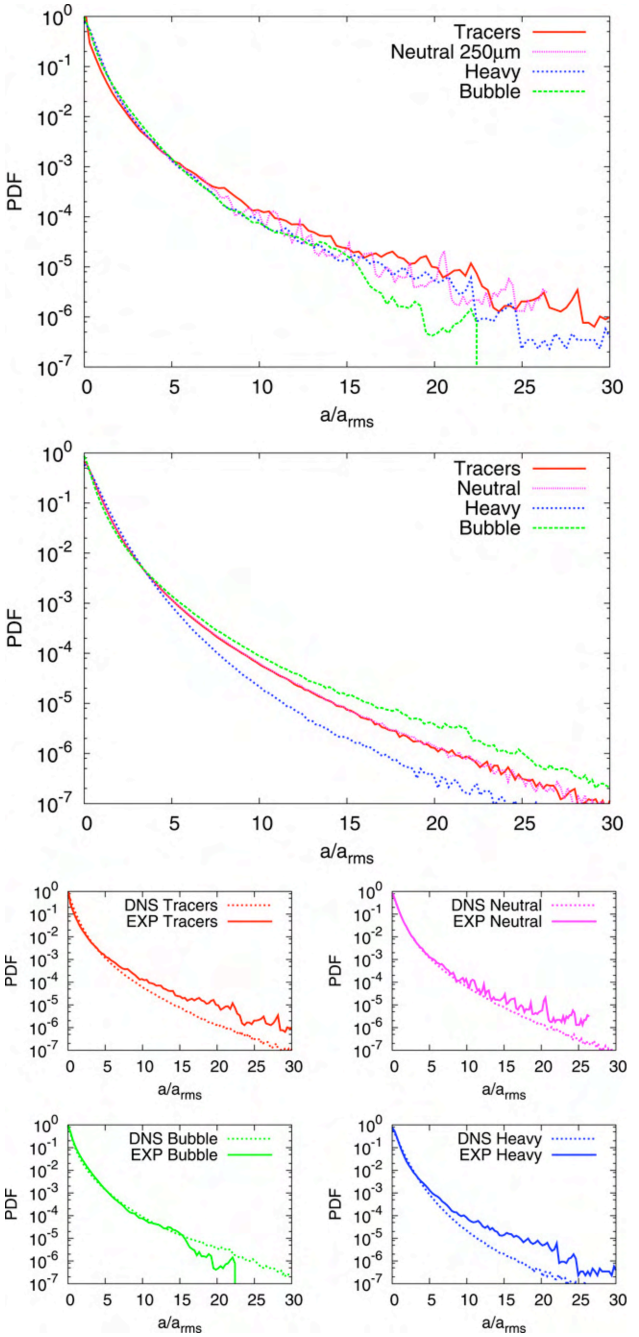

Fig. 2. Probability distribution function of accelerations, normalized to the variance of the data sets. (top) Data from experiment at $R_\lambda = 850$. (middle) DNS of homogeneous isotropic turbulence at $R_\lambda = 180$. (bottom) Comparison of experimental measurements and DNS results.

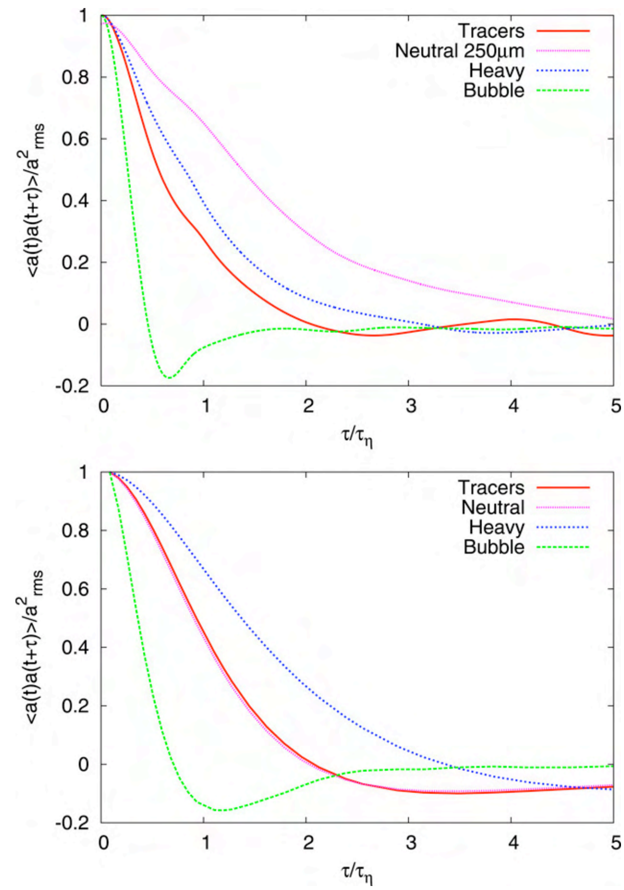

Fig. 3. Autocorrelation coefficients of the accelerations: (top) Data from experiments at $R_\lambda = 850$. (bottom) Data from DNS of homogeneous isotropic turbulence at $R_\lambda = 180$ For the (β, St) values we refer to Table 1.

for the tracers. We conclude that the bubbles size may have a leading effect on the acceleration variance, and that the value of a_0 reported here probably underestimates the one that would be measured for smaller bubbles (with diameters closer to the Kolmogorov scale).

3. Comparison with numerical simulations

We compare the experimental data with the results from a direct numerical simulation [18,19] where a passive suspension of pointwise particles with finite density are tracked in a homogeneous isotropic turbulent flow. The dynamics of the particles is computed in the most simplified form of the equation of motion, *i.e.* assuming that the particles are spherical, nondeformable, smaller than the Kolmogorov length scale of the flow, and that their Reynolds number is small [24]. When we retain only the Stokes drag force and the added mass effect, the equation of motion then reads

$$\frac{\mathrm{d}\mathbf{v}_p}{\mathrm{d}t} = \beta \frac{D\mathbf{u}}{Dt} + \frac{1}{\tau_p}\left(\mathbf{u} - \mathbf{v}_p\right), \qquad (1)$$

where $\mathbf{v}_p = \dot{x}(t)$ is the particle velocity, $\mathbf{u}(x(t), t)$ the velocity of the fluid at the location of the particle described by the Navier–Stokes equation, while $\beta = 3\rho_f/(\rho_f + 2\rho_p)$ accounts for the added mass effect and and $\tau_p = a^2/(3\beta\nu)$ is the Stokes response time for a particle of radius a. When made dimensionless by the Kolmogorov dissipative scales $(\tau_\eta, \eta, u_\eta)$ Eq. (1) reads

$$\mathbf{a} \equiv \frac{\mathrm{d}\mathbf{v}_p}{\mathrm{d}t} = \beta \frac{D\mathbf{u}}{Dt} + \frac{1}{St}\left(\mathbf{u} - \mathbf{v}_p\right), \qquad (2)$$

with the particle acceleration $\mathbf{a}$ now expressed in the Heisenberg–Yaglom units. Thus, at a given Reynolds number, the particles dynamics only depends on the values of the two dimensionless parameters β and $St = \tau_p/\tau_\eta$ This is generally different from the case of infinite inertia of the particles ($\beta = 0$) and finite response time τ_p, which has been formerly addressed in several numerical and theoretical studies [2], and for which instead only the Stokes number St matters. It is also different from the pure bubble case ($\beta = 3$) for which the particle indeed has no inertia but only added mass [6–8]. We performed numerical simulation at $Re_\lambda = 180$ (grid resolution 512^3), in which many particles, characterized by different pairs, (β, St) (specifically 64 different sets of $O(10^5)$ particles) were numerically integrated by means of Eq. (1). Particles do not have feedback on the flow field.

In order to compare the numerical results with the experimental data, three types of particles (tracers, heavy and bubbles) with different inertia and Stokes number have been studied. The values for both β and St have been chosen close to the ones of the particles used for the E-LDV (see Table 1). The evolution of the normalized acceleration variance shows the same trend in experiments and numerics: a_0 is reduced from the tracer value 2.85 to 2.63 for heavier particles and increased to 26 for bubbles (Table 1). This seems to be a robust trend in the DNS. To emphasize this, in Fig. 4 we show the behaviour of $\sqrt{a_0}$, i.e. the root-mean-square value of the particle acceleration normalized by the Heisenberg–Yaglom scaling, in a wide range of the (β, St) parameter space from a less turbulent DNS ($Re_\lambda = 75$) which has a very large number of (β, St) pairs. Results from the $Re_\lambda = 180$, not shown here, are qualitatively similar. Note again that no significant Reynolds number dependence of the probability distribution was found in Ref. [16].

The acceleration distribution behavior and its comparison with the experiment is reported in Fig. 2. In the numerics we observe that the probability of very large accelerations is reduced for the heavier particles as compared with tracers, while it is increased for the bubbles. This feature,seems not to be present in the experimental results. Furthermore, we notice that for the three types of particles, the acceleration PDFs, rescaled by the *rms* acceleration, is close to the experiments. Experimental ones have always longer tails, reflecting the more intermittent nature of the turbulent flow, which has a larger Reynolds number ($Re_{\lambda,\mathrm{EXP}} = 850$ vs. $Re_{\lambda,\mathrm{DNS}} = 180$). We also observe a qualitative agreement for the changes in the acceleration autocorrelation functions when changing inertia, Fig. 3. One measures $\tau_{\mathrm{corr}}/\tau_\eta = \{0.95,\ 1.35,\ 0.25\}$ respectively for tracers, heavy and light particles. Just as observed for the experiments, the dynamics is faster for the bubbles while heavier particles decorrelate slower than fluid tracers. The Re_λ difference is more pronounced here than in the PDFs (see Ref. [16]) and prevent a more detailed comparison.

4. Discussion

While solving a simplified version for the equation of motion, the numerics reproduce qualitatively the effect of the particles' inertia on their dynamics. In particular, the dependence of the acceleration autocorrelation on the particle inertia is nicely reproduced, see Fig. 3. However, also some discrepancies become visible, though not yet completely conclusive, as a better resolution and statistics of both the experiments and the numerics would be important for firmer conclusions. Nevertheless, in this section we shall have a closer look at the differences and propose some explanations.

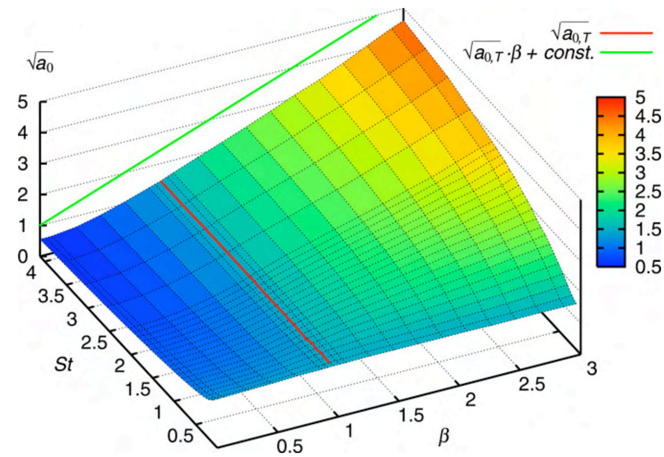

Fig. 4. Behaviour of the normalized *root-mean-square* acceleration $\sqrt{a_0} = (\langle a^2\rangle\epsilon^{-3/2}\nu^{1/2})^{1/2}$ as a function of both St and β for a $Re_\lambda = 75$ DNS. Isocontour for $\sqrt{a_{0,T}}$ (red) and the line $\sqrt{a_{0,T}}\cdot\beta + const.$ (green) are also reported. Note that a_0 does not depend on St for neutral ($\beta = 1$) particles. While it is always reduced/enhanced for heavy/light particles. For large particles ($St \simeq 4.1$) we find $\sqrt{a_0} \simeq \beta\sqrt{a_{0,T}}$. (For interpretation of the references to colour in this figure legend, the reader is referred to the web version of this article.)

First of all, there is only qualitative agreement on the ratio $a_{0,H}/a_{0,T}$. It is larger for the experiment than for the numerics. Moreover, the tails of the numerical PDF of the bubble acceleration seem to be enhanced as compared to those for tracer acceleration. Vice versa, the tails of the numerical PDF of the particle acceleration seem to be reduced as compared to those for tracer acceleration.

What is the origin of the difference between the experiments and the numerics? First of all the Taylor–Reynolds numbers are different, but Ref. [16] suggests an at most weak dependence of the acceleration PDFs on the Reynolds number; a finding that is supported by a comparison of our numerical simulations at $Re_\lambda = 185$ and $Re_\lambda = 75$.

Next, in the numerical simulations we disregarded the lift and the gravitational force. While this presumably has little effect on heavy particles and tracer, it does modify the dynamics of the bubbles. In Refs. [7,8] we had shown by comparison of numerical simulations for point bubbles with and without lift, that without lift the bubble accumulation inside the vortices is more pronounced, i.e. bubbles without lift are more exposed to the small-scale fluctuations, which clearly will contribute to the pronounced tails of the numerically found acceleration PDF, see Fig. 3, bottom.

Next, also the two-way coupling of the particles (i.e., the back-reaction of the particles on the flow due to their buoyancy difference) has been neglected in the simulations of this paper. As e.g. shown in Refs. [7,8] for bubbles and in Ref. [27] for particles, it has an effect on the turbulent energy spectrum and thus also on the acceleration statistics. However, as in the present experiments the particle and bubble concentrations are very low, the two-way coupling effect on the spectra should hardly be detectable.

The final difference between numerics and experiments we will discuss here – and presumably the most relevant one – is the finite size of the particles in the experiments as compared to the numerics which is based on effective forces on a point particle. Although the heavy particles are not large as compared to η, this clearly holds for the bubbles and the 250 μm diameter neutral particles. Indeed, Fig. 3 shows how the finite size of these particles smears out the acceleration autocorrelation, as compared to the tracer case. Also the ratio $a_{0,N}/a_{0,T}$ for large neutral particles is only 0.34, which demonstrates that the size of large particles has a large effect on their acceleration variance. This type of spatial filtering, which also lowers the PDF of large neutral particles in the experiment, is not related to a temporal filtering of the particle based on its response time. This is clearly visible in Fig. 2 (middle) where one can see that two neutral particles ($\beta = 1$) with different response times (different St or τ_p) have the same acceleration PDF, with same a_0, and same autocorrelation function. Thus this size effect, which is not taken into account in the point-particle-based numerical simulations, presumably is responsible for both the relatively small value of $a_{0,B}/a_{0,T}$ measured for bubbles, and the change in the shape of the PDF.

To conclude, we have reported acceleration measurements of inertial particles using extended Laser Doppler velocimetry and have compared the experimental data to DNS simulations of the motion of pointwise particles with finite density. We have observed a qualitative agreement between experiments and numerics in the shape of the PDF and of the autocorrelation function. We have given arguments for the small discrepancies. An experimental study of the motion of bubbles with smaller sizes is needed for a better comparison with the numerical simulations. Also numerical simulations keeping into account the finite size of particles would presumably improve the agreement between experiments and numerical data and detailed comparisons as the one presented in this paper help to reveal the limitations of point-particle models. Obviously, going beyond point-particles is extremely challenging in numerical simulations. A first step in this direction has e.g. been taken by Prosperetti and coworkers with their *Physalis* method [28] which presently is extended towards turbulent flows [29].

Acknowledgements

RV, GV, NM and JFP are indebted to Artem Petrosian for his help in setting-up up the optics of the experiment, and to Mickael Bourgoin for many fruitful discussions. We are grateful to Massimo Cencini, who contributed to the numerical study. This work was partially funded by the Region Rhône-Alpes, under Emergence Contract No. 0501551301, and by ANR contract #192604. We thank the CASPUR (Rome-ITALY), CINECA (Bologna-ITALY) and SARA (Amsterdam, The Netherlands) for computing time and technical support.

References

[1] S. Sundaram, L.R. Collins, J. Fluid Mech. 379 (1999) 105.
[2] J. Bec, M. Cencini, R. Hillerbrand, Physica D 226 (2007) 11; J. Bec, L. Biferale, M. Cencini, A. Lanotte, S. Musacchio, F. Toschi, Phys. Rev. Lett. 98 (2007) 084502.
[3] M. Cencini, J. Bec, L. Biferale, G. Boffetta, A. Celani, A.S. Lanotte, S. Musacchio, F. Toschi, J. Turb. 7 (36) (2006) 1–17.
[4] J.R. Fessler, J.D. Kulick, J.K. Eaton, Phys. Fluids 6 (1994) 3742–3749.
[5] S. Ayyalasomayajula, A. Gylfason, L.R. Collins, E. Bodenschatz, Z. Warhaft, Phys. Rev. Let. 97 (2006) 144507.
[6] L. Wang, M.R. Maxey, Appl. Sci. Res. 51 (1993) 291–296.
[7] I. Mazzitelli, D. Lohse, F. Toschi, Phys. Fluids 15 (2003) L5–L8.
[8] I. Mazzitelli, D. Lohse, F. Toschi, J. Fluid Mech. 488 (2003) 283–313.
[9] J.M. Rensen, S. Luther, D. Lohse, J. Fluid Mech. 538 (2005) 153–187.
[10] T.H. van den Berg, S. Luther, I. Mazzitelli, J. Rensen, F. Toschi, D. Lohse, J. Turb. 7 (2006) 1–12.
[11] T.H. van den Berg, S. Luther, D. Lohse, Phys. Fluids 18 (2006) 038103.
[12] E. Calzavarini, T.H. van den Berg, S. Luther, F. Toschi, D. Lohse, Quantifying microbubble clustering in turbulent flow from single-point measurements, Phys. Fluids (2008) (in press). arXiv:0607255.
[13] G.A. Voth, A. La Porta, A.M. Crawford, J. Alexander, E. Bodenschatz, J. Fluid Mech 469 (2002) 121.
[14] N. Mordant, et al., Phys. Rev. Lett. 87 (21) (2001) 214501; N. Mordant, P. Metz, O. Michel, J.-F. Pinton, Rev. Sci. Instr. 76 (2005) 025105.
[15] N. Mordant, E. Lévêque, J.-F. Pinton, New J. Phys. 6 (2004) 116.
[16] R. Volk, N. Mordant, G. Verhille, J.-F. Pinton, Laser Doppler measurement of inertial particle and bubble accelerations in turbulence, Eur. Phys. Lett. (2008) (in press). arXiv:0708.3350.
[17] N. Mordant, A.M. Crawford, E. Bodenschatz, Physica D 193 (2004) 245; N. Mordant, A.M. Crawford, E. Bodenschatz, Phys. Rev. Lett. 94 (2004) 024501.
[18] E. Calzavarini, M. Kerscher, D. Lohse, F. Toschi, Dimensionality and morphology of particle and bubble clusters in turbulent flow, J. Fluid Mech. (2007) (submitted for publication). Arxiv:nlin.CD/0710.1705.
[19] E. Calzavarini, M. Cencini, D. Lohse, F. Toschi, Quantifying turbulence induced segregation of inertial particles, Phys. Rev. Lett. (2008) (submitted for publication). arXiv:0802.0607.
[20] C. Martinez-Bazá, J.-L. Montañés, J.C. Lasheras, J. Fluid Mech. 401 (1999) 183–207.
[21] N. Mordant, O. Michel, J.-F. Pinton, J. Acoust. Soc. Am. 112 (2002) 108–119.
[22] I.M. Mazzitelli, D. Lohse, New J. Phys. 6 (2004) 203.
[23] N. Qureshi, M. Bourgoin, C. Baudet, A. Cartellier, Y. Gagne, Phys. Rev. Lett. arXiv:0706.3042 (in press).
[24] M.R. Maxey, J. Riley, Phys. Fluids 26 (1983) 883.
[25] L. Biferale, G. Boffetta, A. Celani, B. Devenish, A. Lanotte, F. Toschi, Phys. Rev. Lett. 93 (2004) 064502.
[26] L. Biferale, E. Bodenschatz, M. Cencini, A.S. Lanotte, N.T. Ouellette, F. Toschi, H. Xu, arXiv:0708.0311, 2007.
[27] M. Boivin, O. Simonin, K.D. Squires, J. Fluid Mech. 375 (1998) 235–263.
[28] Z. Zhang, A. Prosperetti, J. Comput. Phys. 210 (2005) 292–324; J. Appl. Mech. - Transactions of the ASME 70 (2003) 64–74.
[29] A. Naso, A. Prosperetti, Proceedings of ICMF 2007, Leipzig (D) July 9-13, 2007.

Available online at www.sciencedirect.com
ScienceDirect
Physica D 237 (2008) 2090–2094
PHYSICA D
www.elsevier.com/locate/physd

Lagrangian investigation of two-dimensional decaying turbulence

Michael Wilczek*, Oliver Kamps, Rudolf Friedrich

Institute for Theoretical Physics, University of Münster, Wilhelm-Klemm-Street 9, 48149 Münster, Germany

Available online 17 January 2008

Abstract

We present a numerical investigation of two-dimensional decaying turbulence in the Lagrangian framework. Focusing on single particle statistics, we investigate Lagrangian trajectories in a freely evolving turbulent velocity field. The dynamical evolution of the tracer particles is strongly dominated by the emergence and evolution of coherent structures. For a statistical analysis we focus on the Lagrangian acceleration as a central quantity. For more geometrical aspects we investigate the curvature along the trajectories. We find strong signatures for the self-similar universal behavior.

PACS: 47.10.-g; 47.27.-i; 47.27.De

Keywords: Turbulence; Lagrangian turbulence; Two-dimensional turbulence; Decaying turbulence; Dynamical systems

1. Introduction

Beyond its importance for geophysical and astrophysical applications two-dimensional turbulence often serves as a paradigm of a complex, self-organizing system. Despite its spatio-temporal complexity freely decaying two-dimensional turbulence exhibits a stunning degree of coherence. The dynamical evolution of the turbulent vorticity field is dominated by the emergence, coalescence and nonlinear interaction of circular and spiral-like vortices (see e.g. [1] and the references therein).

During the decay process these coherent structures tend to organize in a self-similar way [2–5], for example the temporal evolution of their density, the mean absolute value of the circulation and the mean vortex radius follow power-laws [4], indicating that the decay process might display some degree of universality.

The Lagrangian frame of reference offers a natural access to the description of turbulent flows. However, results on the Lagrangian description of two-dimensional turbulence are sparse. Hence we are led to study the evolution of tracer particles in the two-dimensional decaying system. We find, as expected, that their evolution is strongly dominated by the coherent vortices.

Regarding a statistical analysis we focus on the acceleration as well as on the curvature along the trajectories. We find strong evidence for a self-similar temporal evolution of some of the quantities.

The system under consideration is governed by the nonlinear effects of vortex interaction and merging as well as by viscous forces. Thus please note that our results cannot be referred to in the framework of the universal decay theory proposed by Carnevale et al. [4,5] as we operate in a different parameter range, where the viscosity cannot be neglected.

The remainder of this article is structured as follows. After summarizing the details on numerical issues and simulation parameters we procede to a qualitative discussion of trajectories. We then present the statistical results of the Lagrangian acceleration and curvature.

2. Numerics and simulation details

We solve the two-dimensional vorticity equation

$$\frac{\partial \omega}{\partial t}(\mathbf{x}, t) + (\mathbf{u}(\mathbf{x}, t) \cdot \nabla)\omega(\mathbf{x}, t) = \nu \Delta\omega(\mathbf{x}, t) \tag{1}$$

by means of a standard pseudospectral code on a 1024^2 grid with periodic boundary conditions. Table 1 sums up the major

* Corresponding author. Tel.: +49 251 8334914.
E-mail address: mwilczek@uni-muenster.de (M. Wilczek).

0167-2789/$ - see front matter © 2008 Elsevier B.V. All rights reserved.
doi:10.1016/j.physd.2008.01.013

Table 1
Major simulation parameters. Number of grid points N^2, box length L, viscosity ν, initial Reynolds number $Re_i = \frac{2\pi\, u_{\mathrm{rms}}}{\nu}$, timestep $\mathrm{d}t$, total simulation time T, number of tracer particles per realization N_{tra} and total number of realizations N_{re}

N^2	L	ν	Re_i	$\mathrm{d}t$	T	N_{tra}	N_{re}
1024^2	2π	0.0004	12 500	0.0005	25	16 384	40

simulation parameters. We suppress the aliasing errors by a spherical mode truncation according to Orszag's famous two-thirds rule. To obtain reliable statistical results we immerse approximately 16 000 tracer particles into the flow and follow them throughout the decay process. The Eulerian fields are interpolated by a bicubic scheme. The acceleration is explicitly calculated each timestep by evaluating the right-hand side of the Navier–Stokes equation. The resulting field is then interpolated at the particle positions.

In order to increase the statistical quality we additionally perform an ensemble average over forty independent realizations of the flow (about 19 gigabytes of Lagrangian tracer data, $\mathcal{O}(1600)$ hours of cpu time). The initial conditions are obtained from a forced turbulence simulation that has reached statistical equilibrium in the following manner. A master field from such a forced simulation is taken and forty copies are made. For each copy a forced simulation with a duration of about five large eddy turnover times is performed with a differently initialized random number generator for the forcing (see [6] for details on the forcing). We thereby gain forty statistically independent initial conditions for the subsequent decaying turbulence runs. We would like to stress that by the large amount of ensemble realizations we achieve an extraordinarily high statistical quality. One additional run with doubled total simulation time was performed for checking and visualization purposes. For a more detailed description of the numerical issues see Reference [6].

The initial conditions exhibit a clear inertial range according to Kolmogorov's predictions in the inverse energy cascade regime as depicted in Fig. 1 (here, no ensemble average was performed). The time-resolved energy spectrum reveals that the initial inertial range scaling is quickly destroyed as the high modes get damped out. Simultaneously energy is transported into the low modes by nonlinear mode interaction of the inverse energy cascade. Due to our broadband $k^{-5/3}$ initial condition from the forced turbulence simulations the temporal evolution of our energy spectrum deviates from the classically expected Batchelor–Kraichnan scaling. However, the choice of the present initial condition is physically sound as the relaxation from the stationary state in the inverse cascade regime to thermodynamical equilibrium is in the focus of our studies. In physical space the temporal evolution of the energy spectrum is mirrored by the decay of small-scaled structures and the emergence of bigger coherent vortices as depicted in Fig. 2.

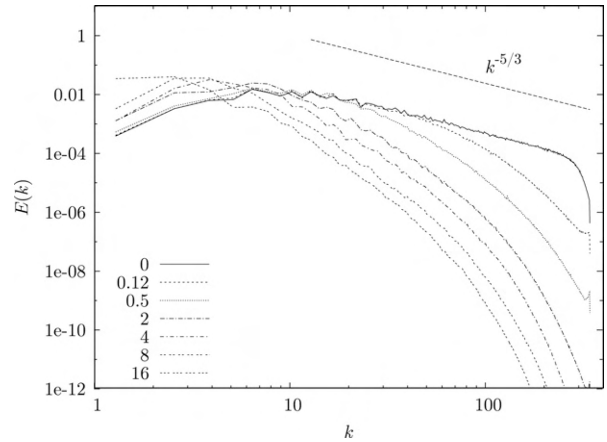

Fig. 1. Temporal evolution of the energy spectrum for $t \in [0, 16]$. High modes get damped out while the energy contained in the low modes increases. The $k^{-5/3}$ slope indicates the slope of the initial condition.

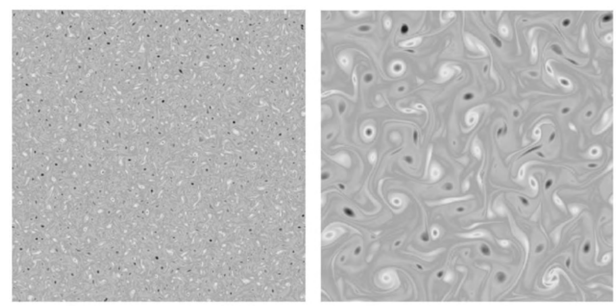

Fig. 2. Vorticity field for $t = 0.3$ and $t = 4$. The number of vortices decreases due to vortex coalescence and destruction.

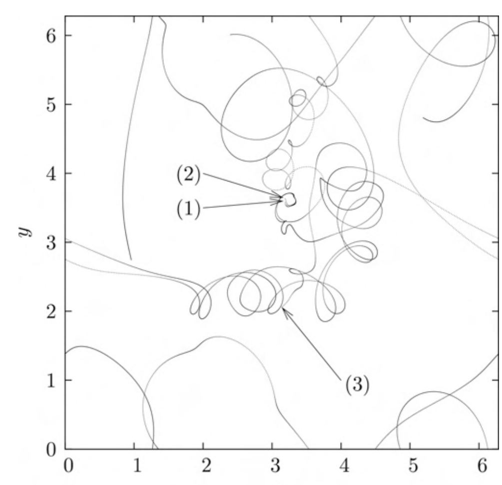

Fig. 3. Typical particle paths in decaying turbulence. The spiraling motion indicates vortex trapping events. The numbers denote the initial position of the three particles.

3. Trajectories

Turning now to a Lagrangian description of the turbulent field, Fig. 3 shows some sample trajectories. As characteristic for a turbulent chaotic system two initially neighboring trajectories ((1) and (2)) separate quickly as they get caught into the velocity field of different vortices. The spiraling motion of the particles indicates that vortex trapping is generic for particles in two-dimensional decaying turbulence. As the vortices merge into bigger structures the radius of the spiral

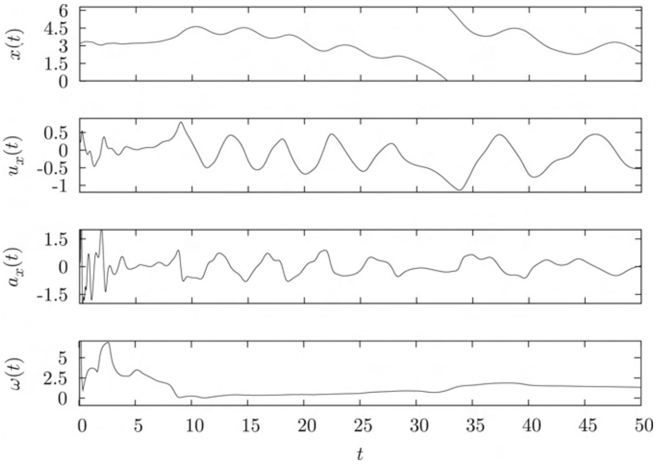

Fig. 4. Time-resolved trajectory in decaying turbulence. Vortex trapping results in an oscillating behavior of the components of position, velocity and acceleration.

motion increases on average over time. We postpone a more quantitative discussion of this point to the following section.

While the chaotic advection can significantly increase the pair separation also the opposite takes places. For example trajectory (1) and trajectory (3) subsequently enter the velocity fields of the same vortex leading to a sticking effect; As these two particles are mainly influenced by the velocity field of a single emerging vortex, they stay close for a comparably long time although they started from far separated places in the turbulent field.

Fig. 4 shows the time-resolved trajectory (1). After the initial emergence of medium-scaled vortices from the rather rough and unstructured initial vorticity all the components of space, velocity and acceleration show the signatures of vortex trapping by their oscillating behavior. The strength and also the frequency of the oscillations decrease throughout the decay process as the coherent structures increase in size and the velocity field gets smoother and damped because of the viscous effects. All these observations show that Lagrangian particle dynamics is strongly dominated by the motion in single coherent structures. Please note that the oscillatory behavior shows up clearly in the time-interval [10 : 30] when large-scale structures already have emerged. However, from Fig. 3 it is evident that a spiraling motion of the tracer particles is generic from the very beginning of the decay process.

4. Statistical results

After this rather qualitative discussion let us now turn to the central statistical observable of this work. The Lagrangian acceleration of a particle initially located at $\mathbf{y}$ is defined by

$$\mathbf{a}(t, \mathbf{y}) = \ddot{\mathbf{X}}(t, \mathbf{y}) = [-\nabla p(\mathbf{x}, t) + \nu \Delta \mathbf{u}(\mathbf{x}, t)]_{\mathbf{x}=\mathbf{X}(t,\mathbf{y})}. \quad (2)$$

For a more detailed dynamical description this acceleration can be decomposed into an acceleration parallel to the current velocity and an acceleration perpendicular to the current velocity. With $\mathbf{u}_\parallel = \mathbf{u}/|\mathbf{u}|$ and $\mathbf{u}_\perp = (-u_y, u_x)/|\mathbf{u}|$ the decomposition reads

$$\mathbf{a}(t, \mathbf{y}) = a_\parallel(t, \mathbf{y})\mathbf{u}_\parallel(t, \mathbf{y}) + a_\perp(t, \mathbf{y})\mathbf{u}_\perp(t, \mathbf{y}), \quad (3)$$

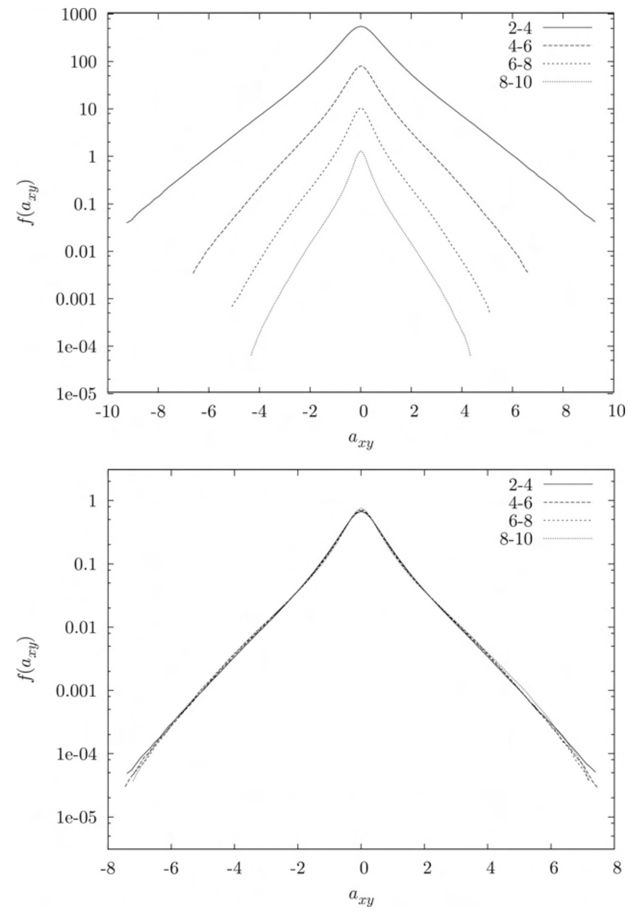

Fig. 5. Time-resolved acceleration pdf. The upper figure shows the acceleration pdf's for different times vertically shifted. The lower figure shows the same pdf's normalized by their standard deviation resulting in a collapse of the curves. Time-windows over which averaging is performed are indicated.

thereby defining

$$a_\parallel = \mathbf{a} \cdot \mathbf{u}_\parallel \quad \text{and} \quad a_\perp = \mathbf{a} \cdot \mathbf{u}_\perp. \quad (4)$$

Let us start with the time-resolved pdf $f(a_{xy})$ of a single component of the acceleration, which is depicted in Fig. 5. Owing to the statistical isotropy of the flow we improve our statistics by averaging over both spatial directions (which is indicated by the subscript xy). The time-resolved acceleration pdf's clearly exhibit large deviations from a Gaussian distribution as expected from the intermittent nature of turbulent acceleration (intermittent in the sense of classical dynamical systems theory). They exhibit almost exponential tails. However, when normalized by their standard deviation all of the curves collapse over the selected time interval thereby indicating a universal temporal evolution of the pdf. This view is supported by Fig. 6 which shows the time-resolved moments of the acceleration pdf. By inspection of this figure the scaling regime roughly can be estimated as the time interval for $t \in [0.1, 10]$. Note that this choice is rather conservative. The size of this time interval will surely depend on physical parameters like viscosity or initial Reynolds number. Additionally statistical issues might matter; as the turbulence decays the number of vortices rapidly drops. Consequently there are fewer and fewer coherent structures

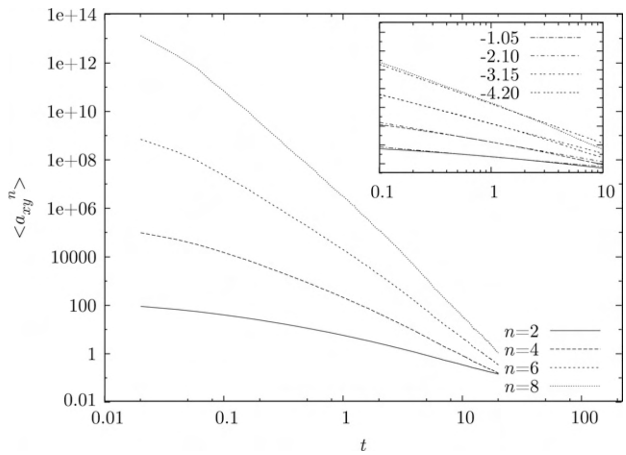

Fig. 6. Time-resolved moments of the acceleration pdf. The moments clearly show power-law behavior. The inset shows a comparison with power-law functions. The algebraic exponents are displayed.

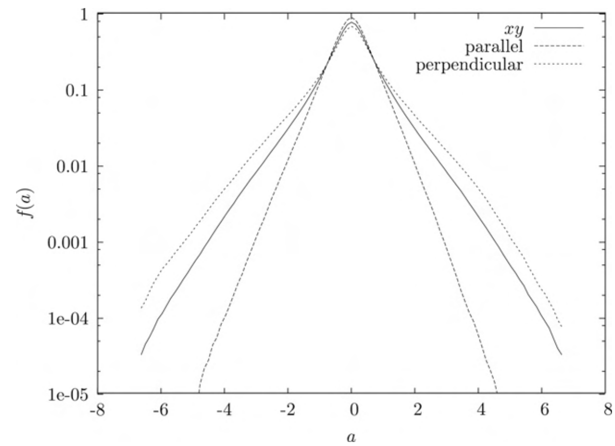

Fig. 7. Pdf's of the acceleration components a_{xy}, $a_{\parallel}$ and $a_{\perp}$ for the time-window 4–6. In comparison with a_{xy} the perpendicular component exhibits more pronounced tails while the parallel component shows less pronounced tails.

contributing to the overall statistics resulting in a decreasing statistical quality.

Fig. 6 also shows a comparison with power-law functions $\langle a^n_{xy} \rangle \sim t^{\zeta_n}$ with the exponents ζ_n. The numerical values roughly suggest $\zeta_{2n} \sim n\zeta_2$ for the selected moments as necessarily required for a self-similar evolution of the pdf's. We do not claim these exponents to be universal for all turbulent flows as they should depend on the Reynolds number, the type of numerical viscosity applied in the simulation and on the exact initial condition. For a detailed investigation of the impact of different initial conditions on the decay process see [7]. The detection of this scaling range in the moments of the Lagrangian acceleration pdf is one of the main results in the present work.

We now proceed to a discussion of the parallel and perpendicular component of the acceleration. Fig. 7 shows a comparison of the pdf's of the acceleration components a_{xy}, $a_{\parallel}$ and $a_{\perp}$ for a single time-window. One can see that the perpendicular component is slightly more intermittent than the xy-averaged component. However, the parallel component clearly exhibits less fat tails than the other two components. This difference remains when the pdf's are rescaled to their standard deviation (not depicted) indicating that the three components have a fundamentally differing functional form. These observations presented for a single time interval hold throughout the whole scaling interval. The physical interpretation of these results is quite straightforward. The fact that the perpendicular component of the acceleration exhibits a larger flatness than the parallel one shows that the spiraling motion in the vortices is a major contributor to the intermittent nature of the turbulent acceleration. Hence this can be regarded as statistical evidence for the dynamical importance of vortices regarding Lagrangian dynamics.

We checked that also the pdf's of the components $a_{\parallel}$ and $a_{\perp}$ collapse over the selected interval when normalized by their standard deviation (not depicted) and hence also the moments show a power-law behavior. This is exemplified in Fig. 8, where the second, fourth and sixth moment of the corresponding pdf's are shown. This inspection reveals that the moments show nearly identical temporal scaling behavior, i.e. $\langle a^n_{xy} \rangle = c_{xy} t^{\zeta_n}$,

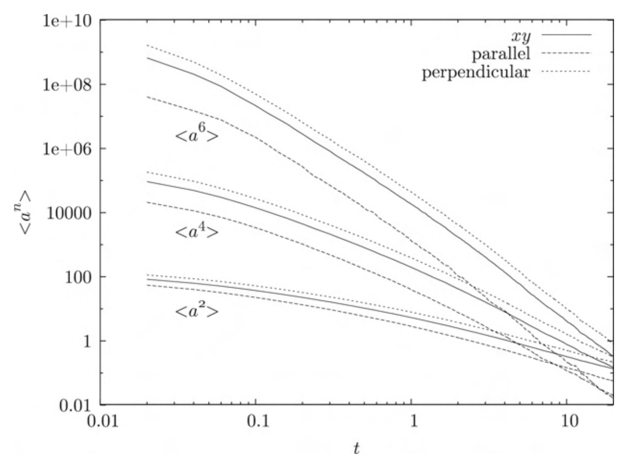

Fig. 8. Temporal scaling for the second, fourth and sixth moments of the pdf's of the acceleration components a_{xy}, $a_{\parallel}$ and $a_{\perp}$. While the scaling exponents seem to be almost identical the moments differ by a multiplicative factor.

$\langle a^n_{\parallel} \rangle = c_{\parallel} t^{\zeta_n}$ and $\langle a^n_{\perp} \rangle = c_{\perp} t^{\zeta_n}$ with identical ζ_n, but differ by their prefactors c_{xy}, $c_{\parallel}$ and $c_{\perp}$. That means the differing functional form can be traced back to a differing weighting for each moment. The emerging picture is quite interesting: while the functional form of each of these pdf's seems to be determined by an initial weighting factor for each moment, their temporal behavior is universal.

To close this section let us turn to more geometrical properties of the trajectories. We investigate the curvature of the trajectories defined by

$$\kappa(t, \mathbf{y}) = \frac{|a_{\perp}(t, \mathbf{y})|}{\mathbf{u}^2(t, \mathbf{y})}. \tag{5}$$

Fig. 9 shows the mean curvature, averaged over all trajectories. Although this quantity is extremely fluctuating, that is because of the $1/\mathbf{u}^2$ dependence, the average trend of a decreasing curvature is clearly visible. As the curvature is proportional to the inverse of the spiral radius, the emergence of bigger and bigger coherent structures therefore on average leads to increasing spiral radii of the trajectories. This is the statistical

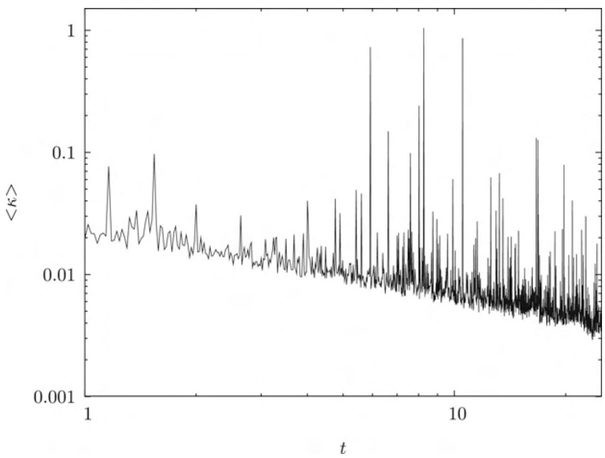

Fig. 9. Log–log plot of the mean curvature as a function of time. The increasing spiral radii of the trajectories result in a decaying curvature.

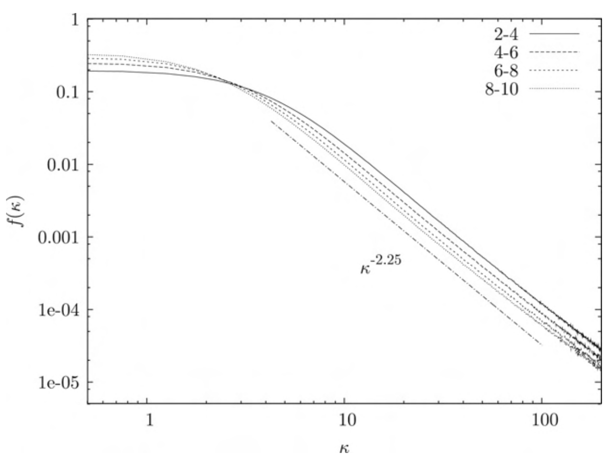

Fig. 10. Log–log plot of the time-resolved curvature pdf. The pdf's show an algebraic decay with an exponent close to −2.25.

approval for the qualitative discussion of the trajectories in the preceding section. The time-resolved pdf of the curvature contains even more information and is shown in Fig. 10. The time-resolved pdf's are fairly similar to each other. However, the probability for a high curvature (a small spiral radius) decreases over time, as expected for coalescing and growing vortices. Interestingly, all of the pdf's show an extraordinarily clear algebraic decay with an exponent close to −2.25.

5. Summary

To sum up, we presented a detailed investigation of two-dimensional decaying turbulence in the Lagrangian frame of reference. Our results reveal that the Lagrangian dynamics in this system is strongly influenced by long periods in which the tracer particles are mainly influenced by the velocity field of single coherent structures. The spiraling motion of the particles is a consequence.

We focused on the Lagrangian acceleration as a central statistical quantity finding that the turbulent fields tend to organize in a self-similar way. Hence we are able to identify a time interval where a self-similar scaling of the acceleration pdf's and corresponding moments holds. A decomposition of the acceleration into components parallel and perpendicular to the velocity reveals that the non-Gaussian nature of the acceleration is partly due to the centripetal accelerations caused by the coherent structures. Closely connected to the acceleration is the curvature of the trajectory, adding a more geometrical point of view. We found the mean curvature decaying algebraically in time, consistent with the qualitative picture drawn in the first sections. The time-resolved pdf's of the curvature show a clear power-law behavior.

Our investigation gives evidence that the two-dimensional decaying Lagrangian turbulence is dominated by self-similar scaling laws, even when viscosity is not negligible.

Acknowledgements

OK would like to thank Tom Bauer for the help with the Condor grid computing software and the Morfeus GRID. Computational resources were allocated by the Morfeus GRID at the Westfälische Wilhelms-Universität Münster, with the use of Condor [8].

References

[1] P. Tabeling, Two-dimensional turbulence: a physicist approach, Phys. Rep. 362 (2002) 1–62.
[2] R. Benzi, S. Patarnello, P. Santangelo, Self-similar coherent structures in two-dimensional decaying turbulence, J. Phys. A 21 (5) (1988) 1221–1237.
[3] J.-P. Laval, P.-H. Chavanis, B. Dubrulle, C. Sire, Scaling laws and vortex profiles in two-dimensional decaying turbulence, Phys. Rev. E 63 (6) (2001) 065301.
[4] G.F. Carnevale, J.C. McWilliams, Y. Pomeau, J.B. Weiss, W.R. Young, Evolution of vortex statistics in two-dimensional turbulence, Phys. Rev. Lett. 66 (21) (1991) 2735–2737.
[5] J.B. Weiss, J.C. McWilliams, Temporal scaling behavior of decaying two-dimensional turbulence, Phys. Fluids 5 (1993) 608–621.
[6] O. Kamps, R. Friedrich, Lagrangian statistics in forced two-dimensional turbulence, arXiv.org:0710.1739 (2007).
[7] L.J.A. van Bokhoven, R.R. Trieling, H.J.H. Clercx, G.J.F. van Heijst, Influence of initial conditions on decaying two-dimensional turbulence, Phys. Fluids 19 (4) (2007) 046601.
[8] M.J. Litzkow, M. Livny, M.W. Mutka, Condor-a hunter of idle workstations, in: Proc. 8th Int. Conf. on Distributed Computing Systems (1988) 104–111.

Available online at www.sciencedirect.com
ScienceDirect
Physica D 237 (2008) 2095–2100
PHYSICA D
www.elsevier.com/locate/physd

Motion of inertial particles with size larger than Kolmogorov scale in turbulent flows

Haitao Xu[a,b], Eberhard Bodenschatz[a,b,c,d,e,*]

[a] International Collaboration for Turbulence Research
[b] Max Planck Institute for Dynamics and Self-Organization, D-37077 Göttingen, Germany
[c] Laboratory of Atomic and Solid State Physics, Cornell University, Ithaca, NY 14853, USA
[d] Sibley School of Mechanical and Aerospace Engineering, Cornell University, Ithaca, NY 14853, USA
[e] Inst. for Nonlinear Dynamics, U. Göttingen, D-37073 Göttingen, Germany

Available online 15 May 2008

Abstract

We report experimental results on the motion of tracer and non-tracer particles in intense turbulent water flows between counter-rotating disks measured by three-dimensional Lagrangian particle tracking. The sizes of the non-tracer particles were in the range of $\eta < d_p \ll L$, where η is the Kolmogorov length scale and L is the integral scale. We propose a modified Stokes number that takes into account the effects from finite particle size and inertia. We compare results from tracers and from two types of particles (heavy+small, approx. neutrally bouyant+large) for which the conventional Stokes numbers differ by a factor of ≈8% and the modified Stokes numbers by ≈60%. The conventional Stokes numbers of the particles investigated were in the range of 0.7 and 1.5, while the modified Stokes numbers were smaller between 0.1 to 0.3. We observed that the tails of the measured acceleration PDFs were slightly narrower compared to tracer particles with the heavier+smaller particles showing a larger effect. The measured Lagrangian acceleration correlations of the large particles were approximately the same as that of the tracer particles. This suggests that trajectories of large particles are not biased towards the low-vorticity, high-straining region as was observed previously in the case of small, very heavy particles. These findings are also supported by the measurements of the local slopes of the fourth order Lagrangian structure functions.

PACS: 47.27.Gs; 47.27.Jv; 47.80.Fg

Keywords: Lagrangian particle tracking; Turbulence experiment; Non-tracer particles

1. Introduction

The effect of inertia on the motion of particles in a fluid flow is characterized by the Stokes number $St \equiv \tau_p/\tau_f$, where τ_p is the time scale for the particle to react to the flow and τ_f is the time scale of the fluid flow. For small particles in turbulence, if the particle size d_p is smaller than the Kolmogorov length-scale η, the Stokes number based on the particle viscous relaxation time τ_v and the Kolmogorov time-scale τ_η is usually used. It can be written as $St_K \equiv \tau_v/\tau_\eta = (1/18)(\rho_p/\rho_f)(d_p/\eta)^2$, where ρ_p is the material density of the particles and ρ_f is the density of the fluid. Small and neutrally buoyant particles with $St_K \ll 1$ follow the fluid flow faithfully and are often used as tracers in particle image velocimetry and particle tracking experiments [1]. Small and heavy particles with $St_K \approx 1$ are known to be ejected out of the high-vorticity regions and to be accumulated in the straining regions. This phenomenon is known as preferential concentration [2–7]. It has been much investigated recently as it is closely related to the formation of rain from minute water droplets in clouds [8,9]. The motions of particles with densities similar to that of the fluid, but sizes larger than the Kolmogorov length scale have not seen the same rigorous studies as the dynamics of small particles. Therefore, it is fair to say that the dynamics of large particles

* Corresponding author at: Max Planck Institute for Dynamics and Self-Organization, D-37077 Göttingen, Germany.
E-mail addresses: haitao.xu@ds.mpg.de (H. Xu), eberhard.bodenschatz@ds.mpg.de (E. Bodenschatz).

0167-2789/$ - see front matter
doi:10.1016/j.physd.2008.04.022

Table 1
Parameters of the experiments

R_λ	u'(m/s)	ε(m^2/s^3)	L (mm)	η (μm)	τ_η (ms)	N_f (frames/τ_η)	meas. vol. (η^3)	Δx(μm/pix)
370	0.16	0.072	57	61	3.7	75	$160 \times 160 \times 160$	40
460	0.25	0.28	56	43	1.9	69	$240 \times 240 \times 240$	40

u' is the root-mean-square velocity. ε is the turbulent energy dissipation rate per unit mass. $L \equiv u'^3/\varepsilon$ is the integral length scale. $\eta \equiv (\nu^3/\varepsilon)^{1/4}$ and $\tau_\eta \equiv (\nu/\varepsilon)^{1/2}$ are the Kolmogorov length and time scales, respectively, where ν is the kinematic viscosity of the fluid. N_f is the frame rate of the cameras, in frames per τ_η. The measurement volume is nearly a cube in the center of the tank, and its lateral size is given in the units of the Kolmogorov length scale η. Δx is the spatial discretization of the recording system. The spatial uncertainty of the position measurements is roughly $0.1\Delta x$.

in turbulent flows still needs to be understood. This problem is not only of academic interest,but also of practical importance in nature and technology. In biological systems, such as the zooplankton in ocean, the size of the "particles" are often larger than the Kolmogorov scale at typical conditions [10]. In storms the debris carried by the wind is also often larger than the Kolmogorov scale of the turbulence. In many measurements of turbulent flows, especially at high Reynolds numbers, it is often unavoidable to use particles with $d_p > \eta$ as tracers [11–13].

Very recently, there have been measurements of the accelerations of large particles in turbulence using the acoustic doppler technique [14,15]. The findings were in agreement with earlier measurements using an optical particle tracking technique [12]. In a paper in the same volume of these proceedings, recent measurements employing the extended laser doppler technique are compared with results from numerical simulations [16]. There, it is concluded that even the most advanced state-of-the-art numerical simulations may not capture, in an accurate and efficient way, the size effect of the "large" particles in turbulence. Therefore, detailed information can currently only be obtained from experiments.

Here, we present three-dimensional Lagrangian particle tracking measurements of the motion of larger-than-η particles in intense turbulent flows with Taylor micro-scale Reynolds numbers in the range $370 \leq R_\lambda \leq 460$ and compare the results with those from tracer particles. We report the effect of particle size on the acceleration probability density functions (PDF) and the Lagrangian acceleration correlations. The measured Lagrangian acceleration correlations of the large particles were found to be close to that of the tracer particles. This suggests that the particle trajectories of large particles are not biased towards the low-vorticity, high-straining region as was observed previously in numerical simulations in the case of small, very heavy particles [6,7]. These findings are also supported by the measurements of the local slopes of the fourth order Lagrangian structure functions. We also found that large particles are not uniformly distributed in our turbulence, with the clustering possibly caused by stagnation points of the flow. However, at this time, the detailed mechanisms are unclear. Further experiments in flows with different generating mechanisms are needed to improve the understanding of this clustering phenomenon.

2. Experiment

We carried out three-dimensional Lagrangian Particle Tracking experiments in a von Kármán water flow between counter rotating disks. The relevant parameters of the flow and the experiments are shown in Table 1. All measurements were done in an apparatus similar to that described earlier in Ref. [12]. The main differences were that the propellers were larger in size (40 mm in diameter) and the AC driving motors were more powerful (7.5 kW each). The particles were illuminated by high-power Nd:YAG lasers, and three cameras at different viewing angles were used to record the motion of the tracer particles in the center of the apparatus. The measurement volume was approximately a cube of size $\sim$ (10 mm)^3. Phantom v7.2 cameras from Vision Research Inc. were used, which were capable of recording at 37,000 frames per second at a resolution of 256×256 pixels. We first processed the images and tracked the particles in three-dimensional space using a predictive algorithm to obtain the Lagrangian trajectories [17]. The image intensities of particles often fluctuate due to many unfavorable factors in the recording system, including the fluctuations in laser intensity, the uneven sensitivity of the physical pixels in the camera sensor array, and the electronic and thermal noise. In the data analysis, when the image intensity of a particle was below a chosen threshold, the tracking algorithm lost that particle and treated later particle tracks as a new trajectory. Consequently, the raw trajectories contained many short segments that in fact belonged to the same trajectory. Since the velocities of these broken trajectory segments are correlated, the continuation of both velocity and position can be used to connect these segments. We report here the results from longer trajectories obtained from applying a modified predictive tracking algorithm that is able to connect particle tracks across missing segments in the six-dimensional coordinate/velocities space [18]. To obtain the velocities and accelerations, the measured particle positions were first smoothed with a Gaussian filter and subsequently differentiated, as described in Ref. [19].

We used three types of particles in the experiments. The first type were approximately neutrally buoyant, polystyrene particles with a mean diameter of 26 μm, which behave as passive tracers in our flows. The second type were also polystyrene particles, but with a mean diameter of 220 μm, much larger than the Kolmogorov length scale of the flow. The third type of particles were glass spheres with a diameter of 138 μm and a density of 2.5 times that of water. The parameters of these particles are summarized in Table 2. The conventional Stokes number St_K is defined as

$$St_K \equiv \frac{\tau_v}{\tau_\eta} = \frac{1}{18}\left(\frac{\rho_p}{\rho_f}\right)\left(\frac{d_p}{\eta}\right)^2, \tag{1}$$

Table 2
Parameters of the particles used in the experiments

R_λ	d_p (μm)	ρ_p (g/cm^3)	$\langle a^2\rangle^{1/2}$ (m/s^2)	τ_v (ms)	St_K	τ_d (ms)	St_d	Re_p	τ_p (ms)	St_p
370	26 ± 4	1.06	8.9 ± 0.9	0.04	0.01					
–	220 ± 27	1.06	8.7 ± 1.7	2.85	0.76	8.8	0.33	35	1.0	0.11
–	138 ± 13	2.5	9.0 ± 1.8	2.65	0.70	6.4	0.41	22	1.1	0.18
460	26 ± 4	1.06	31 ± 3	0.04	0.02					
–	220 ± 27	1.06	30 ± 6	2.85	1.5	5.6	0.51	55	0.8	0.15
–	138 ± 13	2.5	33 ± 6	2.65	1.4	4.1	0.65	35	0.9	0.23

d_p and ρ_p are the diameter and the material density of the particles. $\tau_v \equiv (1/18)(\rho_p/\rho_f)(d_p^2/\nu)$ is the viscous relaxation time. $St_K \equiv \tau_v/\tau_\eta$ is the Stokes number based on the Kolmogorov time scale. $\tau_d \equiv (d_p^2/\varepsilon)^{1/3}$ is the turbulence dynamic time at the scale of the particle diameter. $St_d \equiv \tau_v/\tau_d$ is the Stokes number based on the turbulence dynamic time scale. $Re_p \equiv d_p u'/\nu$ is the particle Reynolds number based on the local turbulence velocity at the scale of the particle diameter. $\tau_p \equiv \tau_v/C_f$ is the particle relaxation time scale taking into account the finite inertia of the particles, $C_f = C_D Re/24$ is the increase of drag due to the finite Reynolds number effect and C_D is the usual drag coefficient. $St_p \equiv \tau_p/\tau_d$ is the Stokes number that characterizes the response of large particles in turbulent flows.

where the viscous relaxation time of the particle is

$$\tau_v \equiv \frac{1}{18}\left(\frac{\rho_p}{\rho_f}\right)\frac{d_p^2}{\nu}. \tag{2}$$

In the definition of the traditional Stokes number, it is assumed that the dynamics of a particle in a turbulent flow is described by a flow time scale – the Kolmogorov time scale τ_η and a particle response time scale – the viscous relaxation time τ_v. These choices of time scales are appropriate for particles with sizes smaller than the Kolmogorov length scale η. For particles with sizes larger than the Kolmogorov length scale, the relevant flow time scale is not the Kolmogorov time scale, but the turbulent dynamic time at the scale of the particle size, i.e.

$$\tau_d \equiv \left(\frac{d_p^2}{\varepsilon}\right)^{1/3}. \tag{3}$$

Using this time scale, we can define another Stokes number as[1]

$$St_d \equiv \frac{\tau_v}{\tau_d} = \frac{1}{18}\left(\frac{\rho_p}{\rho_f}\right)\left(\frac{d_p}{\eta}\right)^{4/3}, \tag{4}$$

which is notably smaller than St_K given by Eq. (1) for particles with size larger than η.

A further complication to the definition of Stokes number is that the use of the viscous relaxation time as the particle time scale implies that the particle Reynolds number is vanishingly small, which is not true for particles with sizes larger than η and hence the finite Reynolds number correction is needed. Following [28], we define the particle Reynolds number based on the fluctuation velocity of the turbulent flow,

$$Re_p \equiv \frac{u' d_p}{\nu}. \tag{5}$$

The drag force on particles with small, but finite Reynolds numbers are characterized by the drag coefficient as [20]

$$C_D = \frac{24}{Re_p}\left(1 + 0.1315 Re_p^n\right), \tag{6}$$

where the exponent n also depends on Re_p:

$$n = 0.82 - 0.05 \log_{10} Re_p. \tag{7}$$

The characteristic time scale for particles with finite Reynolds numbers are related to the viscous time scale as

$$\tau_p = \tau_v \frac{24}{Re_p C_D} = \frac{\tau_v}{1 + 0.1315 Re_p^n}. \tag{8}$$

We note that this particle response time can be formally derived by considering a particle, initially at rest, being carried by a uniform flow. The relevance of τ_p for particles in a turbulent flow is, on the other hand, an open question, as we will discuss later.

In the limit of $Re_p \to 0$, the drag coefficient given by Eq. (6) recovers the Stokes drag law $C_D = 24/Re_p$ and the particle time scale τ_p is the same as τ_v.

With these choices for the relevant time scales, we define a modified Stokes number as

$$St_p \equiv \frac{\tau_p}{\tau_d} = \frac{1}{18}\left(\frac{\rho_p}{\rho_f}\right)\frac{(d_p/\eta)^{4/3}}{1 + 0.1315 Re_p^n}. \tag{9}$$

3. Result

First, we examine the effect of the size on particle acceleration. The measured PDFs of the normalized acceleration $a^+ \equiv a/\langle a^2\rangle^{1/2}$ are plotted in Fig. 1. Due to technical reasons, for the large particles the total number of samples were much less than that for the tracer particles. In order to make an accurate comparison of the PDFs, we restrict our attention only to events with probability larger than 10^{-5} and normalize the PDFs for the particles accordingly. The normalized PDFs of the large particles are close to the ones of the tracer particles. This is in agreement with previous particle tracking measurements [12, 19] and more recent doppler measurements [14,15]. However, the following difference can be observed: At both Reynolds numbers, the tails of the acceleration PDFs of the large particles are suppressed slightly compared to that of the tracer particles. This is consistent with our earlier measurements [12]. The effect of suppression increases at larger Reynolds numbers, or equivalently, at larger Stokes numbers. It might be argued that

[1] After the completion of the current work, the authors received the preprint of Ref. [10], in which a modified Stokes number as in Eq. (4) was also independently proposed.

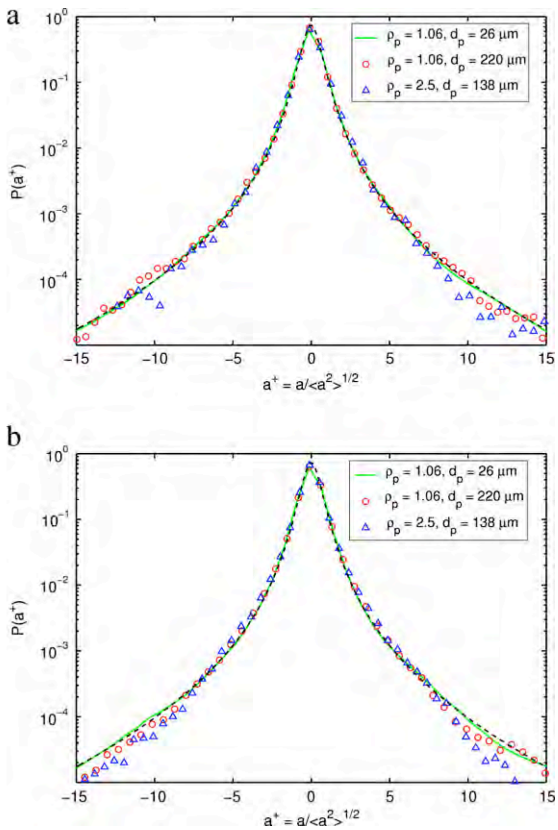

Fig. 1. PDF of the normalized acceleration $a^+ \equiv a/\langle a^2\rangle^{1/2}$. (a) In the $R_\lambda = 370$ experiment; (b) In the $R_\lambda = 460$ experiment. The dashed lines are from the previous measurements using silicon-strip detectors in a similar apparatus at $R_\lambda = 690$ [19]. The solid lines, the circles, and the triangles are the results from the tracer particles, the large polystyrene particles, and the glass particles, respectively.

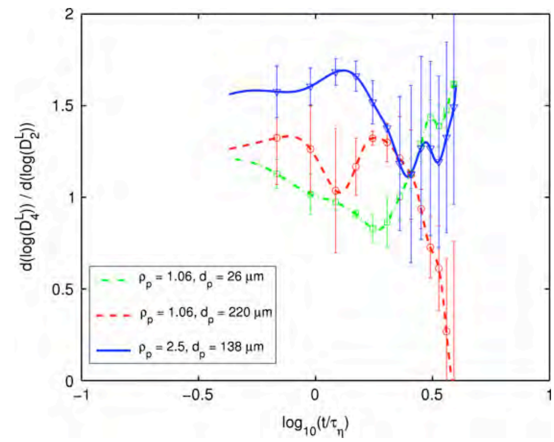

Fig. 2. Local slopes of the 4-th order Lagrangian velocity structure functions measured with different particles in the $R_\lambda = 370$ experiment. The dash-dotted, dashed, and solid lines are the results with the tracer particles, the large polystyrene particles, and the glass particles, respectively. The error bars are estimated from the scattering of measurements in three different directions.

the modified Stokes number St_p is more appropriate in characterizing the effect of the large particles: The glass particles, which have a larger St_p than the larger polystyrene particles, show a stronger effect on acceleration, but the conventional Stokes numbers St_K for the glass particles are smaller than the polystyrene particles at both Reynolds numbers. Of course, these arguments are based on small differences between the PDFs. Since the differences in both the traditional Stokes number St_K or the corrected Stokes number St_p are very small, the relevance of St_K might not be completely ruled out. Further experiments with a systematic study using different particles and various flow conditions are required to answer this question.

On the other hand, the effect of the large particles on acceleration is smaller compared to the heavy, but small, point-like particles. Recent numerical simulations [7] and experiments [21] showed that for the heavy, point-like particles, the effect is very pronounced even at $St_K \approx 0.1$, which is smaller than most of the St_p in the current experiment. In addition, we note that the measured acceleration variances in the current experiments are nearly the same for three different types of particles at the same Reynolds number, in agreement with previous measurements reported in Ref. [12], where the decrease in acceleration variance is notable only for particles with size $d_p/\eta > 7$. The recent measurements by Qureshi et al. [14] seem to suggest that the decrease in acceleration occurs at $d_p/\eta > 10$. This is also in contrast to the observations of large reduction of acceleration variance with heavy particles [7]. There, it was shown in numerical simulations that at small Stokes numbers, the main effect on acceleration is due to the preferential concentration of particles in the straining region. Therefore, the differences between heavy particles and large particles suggest that the large particles are not centrifuged out of the high-vorticity regions as it is the case for the heavy particles [7]. The effect on acceleration is then mainly due to the filtering of violent, fast events due to the finite response time of these particles.

This can also be tested by the local slopes of the higher order Lagrangian velocity structure functions $D_n^L(\tau) \equiv \langle [u(t+\tau) - u(t)]^n \rangle$, measured using the Extended Self-Similarity (ESS) ansatz. It is known that these are very sensitive to Stokes number [22]: the ESS local slope for the tracer particles displays the so-called “bottleneck” at time lags of a few τ_η, which is mainly due to the high-acceleration events, while the “bottleneck” is significantly suppressed in the ESS local slope for point-like, inertial particles, even when the Stokes number (St_k for the point-like particles used in simulations) is as small as 0.16. Fig. 2 shows the ESS local slopes of the fourth-order Lagrangian structure functions measured from our experiments using the different particles. The large particles suppress the magnitudes of the “bottleneck” in the ESS local slopes, similar to the effect of the point-particles observed in numerical simulations [22]. Moreover, the suppressed “bottleneck” regions were shifted towards larger time-lags. As shown in a recent work [23], over-filtering the velocities of tracer particles produces this combination of suppression and shift. The effects on the ESS local slope mainly come from the “filtering” by the large sizes of these particles, rather than from the effect of selecting preferential flow regions. This is in agreement with the observed effects on acceleration PDFs discussed above and acceleration correlations described below. In addition, the effect of the glass particles are more pronounced compared to the larger, but lighter polystyrene particles, which again supports the choice of using St_p over St_K.

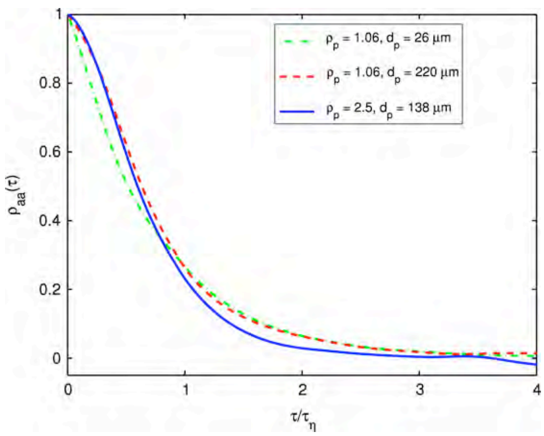

Fig. 3. Lagrangian correlation of acceleration measured with different particles in the $R_\lambda = 460$ experiment. The dash-dotted, dashed, and solid lines are the results with the tracer particles, the large polystyrene particles, and the glass particles, respectively.

Another quantity that we measured is the Lagrangian acceleration correlation, which is known to have a characteristic time scale of approximately $2.2\tau_\eta$ [24,25] in a wide range of Reynolds numbers. In all our experiments, the particle time scale τ_p is always smaller than the Kolmogorov time scale τ_η. Therefore, the effect of the particles on the Lagrangian acceleration correlation is expected to be small. As shown in Fig. 3, the measured acceleration correlations of the large particles are almost indistinguishable, within experimental uncertainty, from that of tracer particles, except at very small time lags, where the finite particle response time would result in higher correlations of Lagrangian acceleration.

In an effort to determine whether the particles are uniformly distributed in space, we also measured the radial distribution functions [6]. We observed an increase of the radial distribution functions for the two types of large particles at separations smaller than $15 \sim 20\eta$. The volume fractions of the particles used in our flow were very small (less than 10^{-4} in all cases). This increase of the radial distribution function can not be explained by the excluded volume effect alone as in the packing of hard spheres [26]. Judging from the acceleration PDFs, there is no strong evidence that the large particles are preferentially distributed in the low-vorticity, high-strain rate regions as in the case of point-like, heavy particles [7]. The precise mechanism of this increase of the radial distribution function is currently not known and will be an interesting problem for further studies. A possible candidate is the hydrodynamical interactions between particles. We note that the particle Reynolds numbers are much larger than unity. In a steady flow, there will be wakes forming behind the particles [27] at these Reynolds numbers.

Another possible reason for the increase of the radial distribution of the large particles are the stagnation points in the turbulent flow. We find evidence that the large particles are found more likely in the center of the apparatus, where a statistical stagnation point resides, while the small, tracer particles distribute uniformly in the volume measured. More detailed investigations are currently being carried out.

4. Conclusion

We measured the accelerations and Lagrangian velocities of particles with sizes larger than the Kolmogorov length scales in intense turbulent flows. We propose a modified Stokes number to characterize the effect of particle size and inertia. The modified Stokes number includes a correction due to particle Reynolds number. The measured acceleration PDFs of the large particles deviate slightly from that of tracer particles, with the tails being weakly suppressed. The measured Lagrangian acceleration correlations of the larger particles are close to that of the tracer particles, which indicates that the large particles were sampling the same flow region as the tracer particles did. The effect of particle size may thus be attributed to the filtering of the turbulence at the scale of the particles, which are captured by the modified Stokes number. These findings are also supported by the measurement of the ESS local slopes of the fourth-order Lagrangian velocity structure functions. We also observed that the large particles were not distributed uniformly in out flows. Although the experiments suggest that the stagnation points of the turbulence cause this effect, the precise mechanism of this inhomogeneity remains an open problem for further studies.

Acknowledgments

We appreciate helpful discussions during this work with J. Bec, M. Bourgoin, M. Cencini, L. Collins, A. Lanotte, R. Shaw, F. Toschi, and Z. Warhaft. We thank F. Schmitt for sending us the preprint of Ref. [10] before publication. This work was carried out in cooperation with the International Collaboration for Turbulence Research and was supported by the Max Planck Society and by the NSF under Grants No. PHY-9988755 and No. PHY-0216406.

References

[1] R.J. Adrian, Particle-imaging techniques for experimental fluid mechanics, Annu. Rev. Fluid Mech. 23 (1991) 261–304.
[2] M.R. Maxey, The gravitational settling of aerosol particles in homogeneous turbulence and random flow fields, J. Fluid Mech. 174 (1987) 441–465.
[3] P.D. Squires, J.K. Eaton, Preferential concentration of particles by turbulence, Phys. Fluids A 3 (1991) 1169–1178.
[4] L.-P. Wang, M.R. Maxey, Settling velocity and concentration distribution of heavy particles in homogenous isotropic turbulence, J. Fluid Mech. 256 (1993) 27–68.
[5] J.R. Fessler, J.D. Kulick, J.K. Eaton, Preferential concentration of heavy particles in a turbulent channel flow, Phys. Fluids 6 (1994) 3742–3749.
[6] S. Sundaram, L.R. Collins, Collision statistics in an isotropic particle-laden turbulent suspension. Part 1. Direct numerical simulations, J. Fluid Mech. 335 (1997) 75–109.
[7] J. Bec, L. Biferale, G. Boffetta, A. Celani, M. Cencini, A. Lanotte, S. Musacchio, F. Toschi, Acceleration statistics of heavy particles in turbulence, J. Fluid Mech. 550 (2006) 349–358.
[8] G. Falkovich, A. Fouxon, M.G. Stepanov, Acceleration of rain initiation by cloud turbulence, Nature 419 (2002) 151–154.
[9] R.A. Shaw, Particle-turbulence interactions in atmospheric clouds, Annu. Rev. Fluid Mech. 35 (2003) 183–227.
[10] F.C. Schmitt, L. Seuront, Intermittent turbulence and copepod dynamics: Increase in encounter rates through preferential concentration, J. Mar. Sys. 70 (2008) 263–272.

[11] A. La Porta, G.A. Voth, A.M. Crawford, J. Alexander, E. Bodenschatz, Fluid particle accelerations in fully developed turbulence, Nature 409 (2001) 1017–1019.

[12] G.A. Voth, A. La Porta, A.M. Crawford, J. Alexander, E. Bodenschatz, Measurement of particle accelerations in fully developed turbulence, J. Fluid Mech. 469 (2002) 121–160.

[13] N. Mordant, P. Metz, O. Michel, J.-F. Pinton, Measurement of Lagrangian velocity in fully developed turbulence, Phys. Rev. Lett. 87 (2001) 214501.

[14] N.M. Qureshi, M. Bourgoin, C. Baudet, A. Cartellier, Y. Gagne, Turbulent transport of material particles: An experimental study of finite size effects, Phys. Rev. Lett. 99 (2007) 184502.

[15] R. Volk, N. Mordant, G. Verhille, J.-F. Pinton, Laser doppler measurement of inertial particle and bubble accelerations in turbulence, Europhys. Lett. 81 (2008) 34002.

[16] R. Volk, E. Calzavarini, G. Verhille, D. Lohse, N. Mordant, J.-F. Pinton, F. Toschi, Acceleration of heavy and light particles in turbulence: Comparison between experiments and direct numerical simulations, Physica D 237 (14–17) (2008) 2084–2089.

[17] N.T. Ouellette, H. Xu, E. Bodenschatz, A quantitative study of three-dimensional Lagrangian particle tracking algorithms, Exp. Fluids 40 (2006) 301–313.

[18] H. Xu, Tracking lagrangian trajectories in position-velocity space, Meas. Sci. Tech. 19 (2008) (in press).

[19] N. Mordant, A.M. Crawford, E. Bodenschatz, Experimental Lagrangian acceleration probability density function measurement, Physica D 193 (2004) 245–251.

[20] R. Clift, J.R. Grace, M.E. Weber, Bubbles, Drops, and Particles, Academic Press, New York, NY, 1978.

[21] S. Ayyalasomayajula, A. Gylfason, L.R. Collins, E. Bodenschatz, Z. Warhaft, Lagrangian measurements of inertial particle accelerations in grid generated wind tunnel turbulence, Phys. Rev. Lett. 97 (2006) 144507.

[22] J. Bec, L. Biferale, M. Cencini, A. Lanotte, F. Toschi, Effects of vortex filaments on the velocity of tracers and heavy particles in turbulence, Phys. Fluids 18 (2006) 081702.

[23] L. Biferale, E. Bodenschatz, M. Cencini, A. Lanotte, N.T. Ouellette, F. Toschi, H. Xu, Lagrangian structure functions in turbulence: A quantitative comparison between experiment and direct numerical simulation, Phys. Fluids 20 (2008), in press (doi:10.1063/1.2930672).

[24] P.K. Yeung, S.B. Pope, Lagrangian statistics from direct numerical simulations of isotropic turbulence, J. Fluid Mech. 207 (1989) 531–586.

[25] N. Mordant, A.M. Crawford, E. Bodenschatz, Three-dimensional structure of the Lagrangian acceleration in turbulent flows, Phys. Rev. Lett. 93 (2004) 214501.

[26] S. Torquato, Nearest-neighbor statistics for packings of hard spheres and disks, Phys. Rev. E 51 (1995) 3170–3182.

[27] M.D. van Dyke, An Album of Fluid Motion, Parabolic Press, Stanford, CA, 1982.

[28] A.M. Wood, W. Hwang, J.K. Eaton, Preferential concentration of particles in homogeneous and isotropic turbulence, Int. J. Multiphase Flow 31 (2005) 1220–1230.

Geophysical and astrophysical fluid dynamics

Available online at www.sciencedirect.com
ScienceDirect
Physica D 237 (2008) 2101–2110
PHYSICA D
www.elsevier.com/locate/physd

Euler equations in geophysics and astrophysics

F.H. Busse*

Institute of Physics, University of Bayreuth, D-95440, Bayreuth, Germany

Available online 2 February 2008

Abstract

The use of Euler equations in Geophysics and Astrophysics is reviewed. Recent developments and new applications are emphasized. Examples are buoyancy columns in rotating fluids, possible preference for axisymmetric inertial convection at low Prandtl numbers, resonance properties of precessing spheroidal fluid filled cavities, and the possible absence of turbulence in rotating shear flows in the limit of high Reynolds numbers.

PACS: 47.10.A-; 47.15.ki; 47.20.Bp; 47.20.Qr; 47.32.-y; 97.10.Gz; 97.10.Kc; 97.25.Za

Keywords: Euler equations; Rotating fluids; Thermal Rossby waves; Inertial convection; Rotating stars; Precessing spheroids; Absence of turbulence; Bimodal convection

1. Introduction

Euler equations as well as their dissipative equivalent, the Navier–Stokes equations, have been applied to a large variety of problems in geophysics and astrophysics and through their use an impressive progress in the understanding of dynamical processes occurring in nature has been achieved. One of the not yet fully understood aspects of these applications is the close similarity between dynamical phenomena observed in the atmosphere and oceans and their pendants in laboratory experiments. This is surprising since the latter usually exhibit laminar flows, while their natural equivalents are fully turbulent. We shall return to this point at the end of this paper.

Fluid dynamics in geophysics and astrophysics is governed by actions of Coriolis and buoyancy forces. Euler equations for incompressible fluids seem to have even more applications in a rotating system than in a non-rotating system. This is caused by the property that in rotating fluids viscous dissipation is confined to thin layers attached to the solid boundaries, called Ekman layers, or to shear layers parallel to the axis of rotation, called Stewartson layers. The description of fluid flows can thus be simplified considerably in that the Euler equations govern the dynamics in the bulk of the fluid, while modifications caused by viscous friction can be treated as perturbations. We refer to Greenspan's [1] book for details on the various ways in which problems can be solved through expansions in powers of the Ekman number E. This parameter is defined with the kinematic viscosity ν of the fluid, the angular velocity Ω of rotation, and a typical length scale h of the system in the direction of the axis of rotation, $E = \nu/\Omega h^2$. E is usually rather small, say of the order 10^{-3} or less, in laboratory experiments with rotating fluids.

A second property of rotating systems that facilitates the description of dynamical processes on the basis of dissipationless equations is the possible balance between Coriolis and buoyancy forces. In contrast to non-rotating systems where simple equilibria can only be obtained when the hydrostatic balance, $\nabla\rho \times \nabla\Phi = 0$, is satisfied, a much wider variety of equilibria can be attained in rotating fluids in the form of the thermal wind balance,

$$2\boldsymbol{\Omega} \cdot \nabla\boldsymbol{v} = \nabla\rho \times \nabla\Phi. \quad (1)$$

Here $\boldsymbol{v}$ is the velocity field, ρ denotes the density distribution of the fluid and Φ is the potential of the force acting on it. Some examples for relationship (1) will be mentioned in the following.

Since the applications of Euler equations in geophysics and astrophysics go back nearly as far as their first publication in 1757, it is impossible to review all of them in a short article.

* Tel.: +49 0921 55 3329; fax: +49 0921 55 5820.
E-mail address: busse@uni-bayreuth.de.

0167-2789/$ - see front matter
doi:10.1016/j.physd.2008.01.024

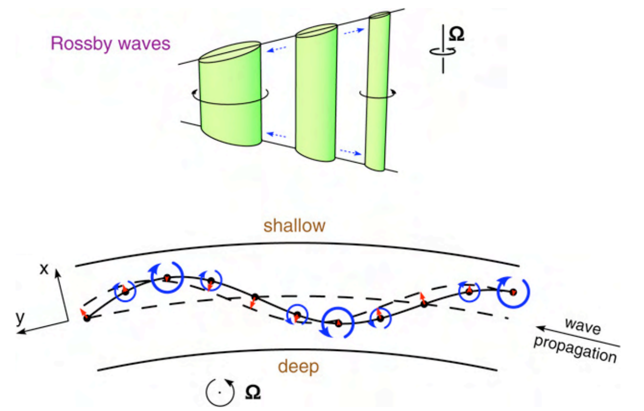

Fig. 1. Sketches for the dynamics of Rossby waves.

The use of Euler equations flourished in the 19th century when water waves were studied and the theory of the action of tides and of precession on rotating fluids was developed. A good access to these and other applications can be found in Lamb's [2] "Hydrodynamics". Modern books on geophysical and astrophysical fluid dynamics are those of (in alphabetical order) Cushman-Roisin [3], Ghil and Childress [4], Gill [5], McWilliams [6], Pedlosky [7], and Tassoul [8]. Most of these books deal with problems in shallow fluid layers such as those posed by the dynamics of oceans and of the atmosphere.

In the present paper we shall focus the attention on more general configurations which are applicable to the dynamics of the deep interiors of planets and stars. Some recent developments will be reviewed which are not yet well known and indeed are yet unpublished in parts. Magnetohydrodynamic applications will not be considered in this paper. For these we refer to the recent volume [9] and the book by Rüdiger and Hollerbach [10].

2. Thermal Rossby waves

The basic theorem of rotating fluid dynamics is the Proudman–Taylor theorem which states that steady small amplitude motions of a barotropic rotating fluid do not vary in the direction of the axis of rotation when viscous effects can be neglected. "Small amplitude" means in this connection that the vorticity of the motion is negligible in comparison to the rotation rate of the system. The Proudman–Taylor condition is a consequence of the complete balance between Coriolis force and pressure gradient. This balance is also called geostrophic balance since it holds in good approximation for the large scale motions in the Earth's atmosphere.

Two-dimensional fluid motions cannot often be accommodated in physical reality and motions are thus forced to become time dependent. In the simplest cases the motions assume the form of propagating Rossby waves. As indicated in Fig. 1, Rossby waves can be understood on the basis of the conservation of angular momentum. When a column of fluid (aligned with the axis of rotation) moves into a shallower place it becomes compressed and, because of the conservation of mass, its moment of inertia increases. To conserve angular momentum its rotation relative to an inertial system must decrease. Relative to the rotating system it thus acquires anticyclonic vorticity. The opposite process happens when the column moves into a deeper place where it gets stretched in the direction of the axis of rotation and acquires cyclonic vorticity.

In the annular fluid layer of Fig. 1 the depth decreases with increasing distance from the axis. A sinusoidal displacement of the initially static fluid columns leads to a flow structure in the form of vortices which tend to move the columns to new positions as indicated by the dashed line in the lower plot of the figure, i.e. the initial sinusoidal displacement propagates as a wave in the prograde direction. A retrograde propagation relative to the sense of rotation will be obtained when the depth of the annular layer increases with distance from the axis.

A dispersion relation for Rossby waves can be derived when the linearized Euler equations relative to a system rotating with the constant angular velocity $\boldsymbol{\Omega}$ are considered,

$$\frac{\partial}{\partial t}\boldsymbol{v} + 2\,\boldsymbol{\Omega}\times\boldsymbol{v} = -\nabla\pi, \tag{2a}$$

$$\nabla\cdot\boldsymbol{v} = 0. \tag{2b}$$

Assuming the small-gap limit of the annulus configuration we introduce a cartesian system of coordinates with the x-, y- and z-coordinates in the radial, azimuthal and axial directions, respectively. The velocity field can then be written in the form

$$\boldsymbol{v} = \nabla\psi(x,y)\times\boldsymbol{k}\exp\{\mathrm{i}\omega t\} + \cdots, \tag{3}$$

where $\boldsymbol{k}$ is the unit vector in the z-direction and the dots indicate higher-order contributions since the deviation from the Proudman–Taylor condition are assumed to be small. By taking the z-component of the curl of Eq. (2a) we obtain

$$-\mathrm{i}\omega\Delta_2\psi - 2\Omega\boldsymbol{k}\cdot\nabla v_z = 0 \tag{4}$$

where the two-dimensional Laplacian $\Delta_2 \equiv \frac{\partial^2}{\partial x^2} + \frac{\partial^2}{\partial y^2}$ has been introduced. After averaging Eq. (4) over the height h of the annulus and using the boundary conditions,

$$v_z \pm \eta\frac{\partial}{\partial y}\psi = 0 \quad \text{at } z = \pm h/2, \tag{5}$$

we find

$$-\mathrm{i}\omega\Delta_2\psi + \frac{4\Omega\eta}{h}\frac{\partial}{\partial y}\psi = 0. \tag{6}$$

The small parameter η is the tangent of the angle χ between the top boundary and the equatorial plane of the annulus. For simplicity the latter has been assumed as a plane of symmetry of the configuration as is also indicated in Fig. 2. The analysis of asymmetric configurations proceeds analogously since only the variation of the height in the direction of the axis of rotation matters.

A solution of Eq. (6) is easily obtained,

$$\psi(x,y) = \cos(\pi x/d)\exp\{\mathrm{i}\alpha y\}$$

$$\text{corresponding to } \omega = -\frac{4\Omega\eta\alpha}{h(\alpha^2 + (\pi/d)^2)}, \tag{7}$$

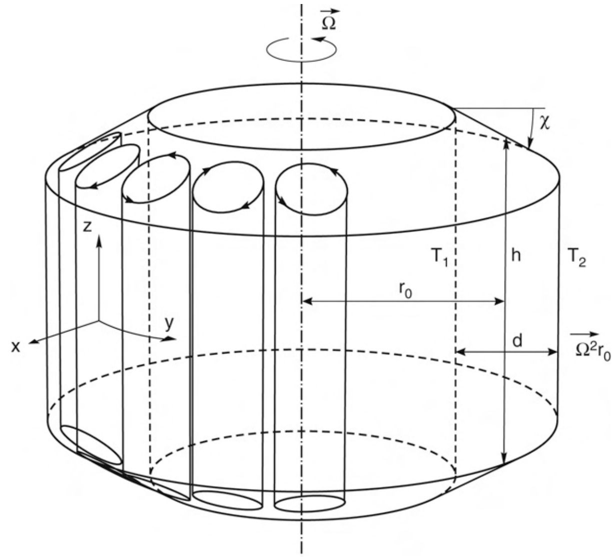

Fig. 2. Geometrical configuration of the rotating annulus.

which satisfies the boundary condition that the normal component of the velocity field vanishes at the side walls, $x = \pm d/2$, of the annulus.

Thermal Rossby waves are generated as growing disturbances when a temperature difference, $T_2 - T_1$, and a gravity force are applied in the x-direction such that a basic state with an unstable density stratification is obtained. The geometrical configuration is sketched in Fig. 2. In the experimental realization of the problem [11] the centrifugal force $\Omega^2 r_0$ is used as gravity and the temperature gradient must point outward in order to create the unstable density stratification. For geophysical applications one may think of the opposite directions for gravity and temperature gradient, but the mathematical problem is the same in both cases.

It is convenient to use a dimensionless description through the introduction of d as length scale, d^2/ν as time scale, and $(T_2 - T_1)/P$ as temperature scale where the Prandtl number P is defined as the ratio between kinematic viscosity ν and thermal diffusivity κ. The dimensionless equations for the streamfunction ψ and for the deviation Θ of the temperature from its static distribution assume the form

$$-\mathrm{i}\omega\Delta_2\psi + \eta^*\frac{\partial}{\partial y}\psi = R\frac{\partial}{\partial y}\Theta, \tag{8a}$$

$$\mathrm{i}\omega P\Theta + \frac{\partial}{\partial y}\psi = 0, \tag{8b}$$

where the Rayleigh number R and the dimensionless rotation parameter η^* are defined by

$$R = \frac{\gamma(T_2 - T_1)\Omega^2 r_0 d^3}{\nu\kappa}, \qquad \eta^* = \frac{4\Omega\eta d^3}{\nu h}. \tag{9}$$

Here γ denotes the coefficient of thermal expansion. In keeping with the philosophy of the Euler equations we have neglected the thermal diffusion term in the linearized heat equation (8b). Since the laboratory version of the problem has been chosen the higher temperature T_2 is assumed at the outer wall of the annulus. The solution for ψ of Eq. (8) has the same form as that of Eq. (6) while the expressions for Θ and ω are given by

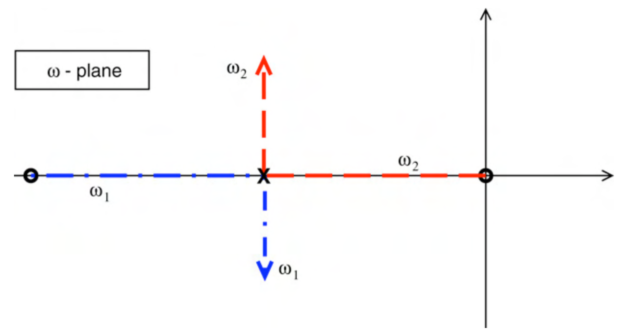

Fig. 3. Move in the complex ω-plane of the eigenvalues ω_1 and ω_2 with increasing R from their position at $R = 0$.

$$\Theta = -\frac{\alpha\psi}{\omega P}\exp\{\mathrm{i}\omega t\} = -\cos(\pi x/d)\frac{\alpha}{\omega P}\exp\{\mathrm{i}\alpha y + \mathrm{i}\omega t\} \tag{10}$$

corresponding to

$$\omega_{1,2} = -\frac{\eta^*\alpha}{2(\alpha^2+\pi^2)} \pm \sqrt{\frac{(\alpha\eta^*)^2}{4(\pi^2+\alpha^2)^2} - \frac{R\alpha^2}{P(\pi^2+\alpha^2)}}. \tag{11}$$

In the limit $0 \le R \ll \eta^{*2}P/(\pi^2+\alpha^2)$ we recover the angular frequency of Rossby waves and in addition find the dispersion relation for a slow mode,

$$\omega_1 = -\frac{\eta^*\alpha}{(\alpha^2+\pi^2)}, \qquad \omega_2 = -\frac{R\alpha}{P\eta^*}. \tag{12}$$

In the case of the slow mode described by ω_2 the part of the Coriolis force that is not balanced by the pressure gradient is balanced by the buoyancy column Θ. As R increases the frequencies ω_1 and ω_2 move along the negative real axis in the complex ω-plane as indicated in Fig. 3. When R exceeds $\eta^{*2}P/4(\pi^2+\alpha^2)$, ω_1 acquires a negative imaginary part indicating a growing instability, called the thermal Rossby wave, while ω_2 corresponds to a decaying mode.

When dissipative terms are added in Eq. (8) all modes will decay except, possibly, the thermal Rossby wave. The critical value R_c of the Rayleigh number for the onset of the latter cannot be determined from Eq. (8) since it would correspond to an infinite α. When viscous friction and thermal diffusion are taken into account [12,13] the onset of thermal Rossby waves in the presence of stress-free walls is described by

$$R_c = \eta_P^{\frac{4}{3}}(3 + \pi^2\eta_P^{-\frac{2}{3}} + \cdots), \qquad \alpha_c = \eta_P^{\frac{1}{3}}(1+\cdots),$$
$$\omega_c = -\sqrt{2}\eta_P^{\frac{2}{3}}(1+\cdots)/P \quad \text{with } \eta_P \equiv \frac{\eta^* P}{\sqrt{2}(1+P)}. \tag{13}$$

This result describes in good approximation the onset of convection not only in rotating annuli, but in rotating fluid spheres as well [12] since only the azimuthal length scale described by α is important and the boundaries in the radial (i.e. perpendicular to the axis) direction do not enter the expressions in first approximation. For a more detailed discussion of the relationship between the analytical result (13) and numerical solutions for convection in rotating spheres see the recent review [14] where also the relevance of the convection flows for the generation of planetary magnetic fields is discussed.

Here we want to return to the slow mode with its nearly stagnant buoyancy column. While it is damped in the simple annulus model, it becomes physically relevant when more than one source of buoyancy is admitted. In the Earth's core chemical buoyancy is released in the form of light elements in the neighborhood of the growing solid inner core and joins the thermal buoyancy in driving convection in the liquid outer core. This situation can be modeled in the rotating annulus configuration when a compositional gradient, $(C_2 - C_1)/d$, is added to the thermal gradient. A compositional Rayleigh number, C_R, can be defined in analogy to the definition (9) of R by replacing $\gamma(T_2 - T_1)$ by $\gamma_C(C_2 - C_1)$. The diffusion equation for the light elements is identical to the heat equation except that the Laplace operator is multiplied by the factor $1/L$ where L is the Lewis number. The latter denotes the ratio between thermal and compositional diffusivities and is assumed to be very large. In the limit $\frac{|C_R|\alpha}{P\eta^*} \ll 1$ the angular frequency of the slow mode and the corresponding value of the Rayleigh number R are given by [15],

$$\omega = -\frac{\alpha C_R}{P\eta^*}, \qquad R_c \approx \frac{(\pi^2+\alpha^2)^3}{\alpha^2} - \frac{P\omega^2(\pi^2+\alpha^2)}{\alpha^2}. \quad (14)$$

Since the last term can be neglected in the comparison with the preceding term, we recover the critical Rayleigh number for the onset of Rayleigh–Bénard convection in the absence of rotation! The buoyancy provided by the compositional gradient just serves to counteract the yet unbalanced portion of the Coriolis force. Note that this balance works independently of the sign of C_R. Please also note that the factor C_R/P is missing in the second term on the right-hand side in Eq. (13b) of [15].

3. Inertial waves and inertial convection

Inertial oscillations and waves represent an important class of solutions of the Euler equations in a rotating system. Axisymmetric solutions in containers that are symmetric with respect to the axis of rotation assume the form of standing oscillations, while non-axisymmetric solutions propagate in the form of waves. In contrast to Rossby waves which can be regarded as the quasi geostrophic subset of inertial waves and which propagate only in a single azimuthal direction, non-axisymmetric inertial waves may propagate in both azimuthal directions, albeit with different speeds. For an introduction to the theory of inertial waves we refer to Greenspan's [1] book. Among more recent results we like to mention the simplified representations of inertial waves in rotating spheres [16] and spheroids [17]. The theory of inertial oscillations is not only valid for incompressible fluids, but holds for barotropic fluids as well [18] and thus can be applied to the Sun and other stars. An unambiguous observational evidence for stellar inertial waves has not yet been obtained, however.

Slight modifications of inertial waves through the introduction of buoyancy and dissipative effects can lead to instabilities just as in the case of thermal Rossby waves. This property has been used by Zhang [19] and by Busse and Simitev [20] to obtain analytical solutions describing the onset of non-axisymmetric thermal convection in rotating spheres heated from within in the presence of a stress-free outer boundary. The corresponding problem with a no-slip outer boundary has been treated by Zhang [21]. We briefly study this problem here and describe some new results for axisymmetric inertial convection.

We consider a homogeneously heated, self-gravitating fluid sphere rotating with the constant angular velocity Ω about an axis fixed in space. A static state thus exists with the temperature distribution $T_S = T_0 - \beta r_0^2 r^2/2$ and the gravity field given by $\boldsymbol{g} = -\gamma_g r_0 \boldsymbol{r}$ where $\boldsymbol{r}$ is the position vector with respect to the center of the sphere and r is its length measured in fractions of the radius r_0 of the sphere. In addition to the length r_0, the time r_0^2/ν and the temperature $\nu^2/\gamma_g\gamma r_0^4$ are used as scales for the dimensionless description of the problem. The density is assumed to be constant except in the gravity term where its temperature dependence given by $\gamma \equiv -(\mathrm{d}\varrho/\mathrm{d}T)/\varrho = \text{const.}$ is taken into account. The basic equations of motion and the heat equation for the deviation Θ from the static temperature distribution are thus given by

$$\partial_t \boldsymbol{v} + \tau \boldsymbol{k} \times \boldsymbol{v} + \nabla\pi = \Theta \boldsymbol{r} + \nabla^2 \boldsymbol{v}, \quad (15a)$$

$$\nabla \cdot \boldsymbol{v} = 0, \quad (15b)$$

$$0 = R\boldsymbol{r} \cdot \boldsymbol{v} + \nabla^2\Theta - P\partial_t\Theta, \quad (15c)$$

where the Rayleigh number R, the Coriolis parameter τ and the Prandtl number P are defined by

$$R = \frac{\gamma\gamma_g\beta r_0^6}{\nu\kappa}, \qquad \tau = \frac{2\Omega r_0^2}{\nu}, \qquad P = \frac{\nu}{\kappa}. \quad (16)$$

We have neglected the nonlinear terms $\boldsymbol{v}\cdot\nabla\boldsymbol{v}$ and $\boldsymbol{v}\cdot\nabla\Theta$ in Eq. (15) since we restrict the attention to the problem of the onset of convection in the form of small disturbances. In the limit of high τ the right-hand sides of Eq. (15) can be neglected and the equation for inertial waves is obtained. For the description of inertial wave solutions $\boldsymbol{v}_0$ we use the general representation in terms of poloidal and toroidal components for the solenoidal field $\boldsymbol{v}_0$,

$$\boldsymbol{v}_0 = \nabla \times (\nabla(f\exp\{\mathrm{i}m\phi + \mathrm{i}\omega t\}) \times \boldsymbol{r}) + \nabla(g\exp\{\mathrm{i}m\phi + \mathrm{i}\omega t\}) \times \boldsymbol{r}, \quad (17)$$

where a spherical system of coordinates r, θ, ϕ has been introduced and f, g are functions of r and θ. By multiplying the (curl)^2 and the curl of the inertial wave equation by $\boldsymbol{r}$ we obtain two equations for f and g,

$$[\mathrm{i}\omega\mathcal{L}_2 - \mathrm{i}m\tau]\nabla^2 f - \tau\mathcal{Q}g = 0, \quad (18a)$$

$$[\mathrm{i}\omega\mathcal{L}_2 - \mathrm{i}m\tau]g + \tau\mathcal{Q}f = 0, \quad (18b)$$

where the operators $\mathcal{L}_2$ and $\mathcal{Q}$ are defined by

$$\mathcal{L}_2 \equiv (\sin\theta)^{-1}\partial_\theta(\sin\theta\partial_\theta) - m^2, \quad (19a)$$

$$\mathcal{Q} \equiv r\cos\theta\nabla^2 - (\mathcal{L}_2 + r\partial_r)(\cos\theta\partial_r - r^{-1}\sin\theta\partial_\theta). \quad (19b)$$

The only boundary condition to be satisfied by solutions of Eq. (18) is $f = 0$ at $r = 1$.

In the axisymmetric case $m = 0$ simple solutions of Eq. (18) can be found such as

$$f = P_1(r - r^3), \quad g = 2ir^2\tau P_2/3\omega \quad \text{with } \omega = \pm\frac{\tau}{\sqrt{5}}, \tag{20a}$$

$$f = P_2(r^2 - r^4),$$
$$g = i\tau\left(P_3\frac{4}{5}r^3 - 3P_1\left(r - \frac{7}{5}r^3\right)\right)\Big/\omega$$
$$\text{with} \quad \omega = \pm\tau\sqrt{\frac{3}{7}}, \tag{20b}$$

$$f = P_1\left(r - \frac{14}{5}r^3 + \frac{9}{5}r^5\right) + P_3(r^3 - r^5)\left(\frac{1}{5} - \frac{\omega^2}{\tau^2}\right)\frac{7}{3},$$
$$g = i\left(P_2\left(\frac{28}{3}r^2 - 12r^4\right)\frac{\omega}{\tau} + P_4r^4\left(\frac{2\tau}{5\omega} - \frac{2\omega}{\tau}\right)\right)$$
$$\text{with } \omega = \pm\tau\sqrt{\frac{1}{3} \pm \sqrt{\frac{4}{63}}}, \tag{20c}$$

where the functions $P_n = P_n(\cos\theta)$ are the Legendre polynomials. A typical property of inertial modes with $m = 0$ is that solutions always exist with both signs of ω such that they can be realized in the form of standing oscillations. This property contrasts with that of non-axisymmetric modes which always propagate in either the prograde or the retrograde direction, but with different speeds.

In order to solve the full Eq. (15) by the perturbation approach we first obtain an expression for Θ. Restricting attention to the limit $P\tau \ll 1$, but allowing for either a fixed temperature, $\Theta = 0$ at $r = 1$ (case A), or a thermally insulating boundary, $\partial\Theta/\partial r = 0$ at $r = 1$ (case B), we obtain

$$\Theta = P_l(\cos\theta)\exp\{i\omega t\}h_l(r), \tag{21}$$

with

$$h_l(r) = l(l+1)R\left(\frac{r^{l+4}}{(l+5)(l+4) - (l+1)l} - \frac{r^{l+2}}{(l+3)(l+2) - (l+1)l} - cr^l\right), \tag{22}$$

where the coefficient c is given by

$$c = \begin{cases} \dfrac{1}{(l+5)(l+4) - (l+1)l} - \dfrac{1}{(l+3)(l+2) - (l+1)l}, \\ \dfrac{(l+4)/l}{(l+5)(l+4) - (l+1)l} - \dfrac{(l+2)/l}{(l+3)(l+2) - (l+1)l}, \end{cases} \tag{23}$$

in the cases A and B, respectively. The expressions (22) and (23) apply only for $l = 1$ and $l = 2$, i.e. for solutions (20a) and (20b). For solution (20c) and all other axisymmetric inertial oscillations more complex expressions must be expected.

When the perturbation expansion $\boldsymbol{v} = \boldsymbol{v}_0 + \boldsymbol{v}_1 + \cdots$ is inserted into Eq. (15a) it must be taken into account that the perturbation $\boldsymbol{v}_1$ consists of two parts, $\boldsymbol{v}_1 = \boldsymbol{v}_i + \boldsymbol{v}_b$ where $\boldsymbol{v}_i$ denotes the perturbation of the interior flow, while $\boldsymbol{v}_b$ is the Ekman boundary flow which is required because $\boldsymbol{v}_0$ does not satisfy the viscous boundary condition. Assuming a stress-free boundary we require

$$\boldsymbol{r}\cdot\nabla(\boldsymbol{r}\times(\boldsymbol{v}_0 + \boldsymbol{v}_b)/r^2) = 0 \quad \text{at } r = 1. \tag{24}$$

The solvability condition for the equation for $\boldsymbol{v}_1$ is obtained by multiplying it with $\boldsymbol{v}_0^*$ and averaging it over the fluid sphere,

$$0 = \langle\Theta\boldsymbol{r}\cdot\boldsymbol{v}_0^*\rangle + \langle\boldsymbol{v}_0^*\cdot\nabla^2(\boldsymbol{v}_0 + \boldsymbol{v}_b)\rangle, \tag{25}$$

where the brackets $\langle\cdots\rangle$ indicate the average over the fluid sphere and the $*$ indicates the complex conjugate. We have also anticipated that there is no perturbation contribution to the frequency since all terms in Eq. (25) are real. In the evaluation of the integrals in Eq. (25) the remarkable result that $\langle\boldsymbol{v}_0^*\cdot\nabla^2\boldsymbol{v}_0\rangle = 0$ holds for all inertial oscillations in rotating spheroidal cavities [17] can be used. Otherwise the evaluation proceeds as in Section 2 of [20] and yields in the case of solution (20a) the analytical expression

$$R = \frac{44\cdot(7\cdot5\cdot3)^2}{173 \mp 99} \approx 4169.4 \pm 2386.0, \tag{26}$$

where the upper sign applies in the case A and the lower sign in case B. For solution (20b) higher values of R are found in both cases and the same must be expected for all other axisymmetric solutions. Since the values (26) are only slightly larger than those obtained in [20] for non-axisymmetric inertial convection with $m = 1$ in the cases A and B, respectively, a close competition of the latter mode and convection in the form of the inertial oscillation (20a) must be expected at the onset of convection for sufficiently small values of $P\tau$. Indeed, numerical computations indicate that for intervals around $P\tau = 20$ and $P\tau = 5$ in the cases A and B, respectively, the axisymmetric mode sets in at a lower value of the Rayleigh number than all non-axisymmetric ones.

The axisymmetric convection described by the inertial wave (20a) corresponds to a flow along the axis of rotation from south to north in one phase of the cycle with a return flow along the surface which owing to the Coriolis force yields a retrograde (prograde) zonal flow in the northern (southern) hemisphere. The Coriolis force acting on this zonal flow in turn causes a reversal of the meridional circulation with the flow along the axis directed from north to south in the second half of the cycle. It will be of interest to find out whether such oscillations are realized in rotating stars.

4. Solutions of nonlinear Euler equations

4.1. Baroclinic rotating stars

Ever since von Zeipel [22] formulated his famous theorem that a hydrostatic equilibrium in rotating stars is not possible, the state of motion in axisymmetric rotating stars has been of considerable concern to astrophysicists. Vogt [23], Eddington [24], and later Sweet [25] assumed that low amplitude meridional circulations are realized, but it soon became apparent that those motions break down through the advection of angular momentum [26,8,27]. An alternative resolution of von Zeipel's paradox has been proposed by Schwarzschild [28], Roxburgh [29], and others who demonstrated that for a particular differential rotation which depends only on the distance from the center the basic equations of stellar structure could be satisfied without meridional circulations. It seems unlikely, however, that such a special differential rotation could be attained from arbitrary initial angular momentum distributions. Here we want to draw attention to more general solutions of the Euler equations that can accommodate angular momentum distributions with arbitrary dependences on the distance from the axis.

To demonstrate the essential points we consider an idealized star with most of its mass concentrated in the core and its energy flux $\boldsymbol{F}$ dependent only on the temperature distribution such that

$$\Phi = -g_0 r_0^2/r \quad \text{and} \quad \boldsymbol{F} = f(T)\nabla T \tag{27}$$

can be assumed where r_0 is the radius of the star and g_0 is its surface gravity. In the absence of motion in an inertial system the hydrostatic equilibrium,

$$T = T^{(0)}(r), \qquad p = p^{(0)}(r), \qquad \rho = \rho^{(0)}(r), \tag{28}$$

is possible. In particular, it can be assumed that the boundary condition $T = \rho = 0$ for $p = 0$ is satisfied. Since we assume an ideal gas, $p/\rho = R_g T$ where R_g is the gas constant, solution (28) satisfies the relationship

$$\frac{1}{R_g T^{(0)}}\nabla\Phi = -\frac{1}{p^{(0)}}\nabla p^{(0)} = p^{(0)}\nabla\frac{1}{p^{(0)}}. \tag{29}$$

We anticipate that in the presence of a motion of the form $\boldsymbol{v} = \omega(r,\theta)\boldsymbol{k}\times\boldsymbol{r}$ with $\theta = \arccos(\boldsymbol{r}\cdot\boldsymbol{k}/r)$, where $\boldsymbol{k}$ denotes a constant unit vector, the thermodynamic variables can be written in the form

$$\begin{aligned} &T = T^{(0)}(r), \qquad p = p^{(0)} + p^{(1)}, \\ &\rho = (p^{(0)} + p^{(1)})/R_g T^{(0)}, \end{aligned} \tag{30}$$

where $p^{(1)}$ is not necessarily small in comparison to $p^{(0)}$. The nonlinear equation of motion now assumes the form

$$\begin{aligned} \rho\omega^2(\boldsymbol{k}\times\boldsymbol{r})\times\boldsymbol{k} &= \nabla p^{(1)} + \frac{p^{(1)}}{R_g T^{(0)}}\nabla\Phi \\ &= p^{(0)}\nabla\frac{p^{(1)}}{p^{(0)}} = p^{(0)}\nabla\frac{p^{(1)}+p^{(0)}}{p^{(0)}}, \end{aligned} \tag{31}$$

from which

$$\omega^2(\boldsymbol{k}\times\boldsymbol{r})\times\boldsymbol{k}/R_g T^{(0)} = \nabla\ln\frac{p^{(1)}+p^{(0)}}{p^{(0)}}, \tag{32}$$

follows. Necessary and sufficient for a solution $p^{(1)}$ of Eq. (31) is thus

$$\omega^2 = G(r\sin\theta)R_g T^{(0)}(r), \tag{33}$$

where the arbitrary function G is sufficient to accommodate all axisymmetric angular momentum distributions [27]. In the special case of a constant function G a purely r-dependent angular velocity ω is obtained as proposed by Schwarzschild [28] and Roxburgh [29].

In Fig. 4 a sketch for an example of the solution (33) is shown. Typically, the ellipticity of the isopycnals exceeds that of the isobars which in turn exceeds that of the isotherms.

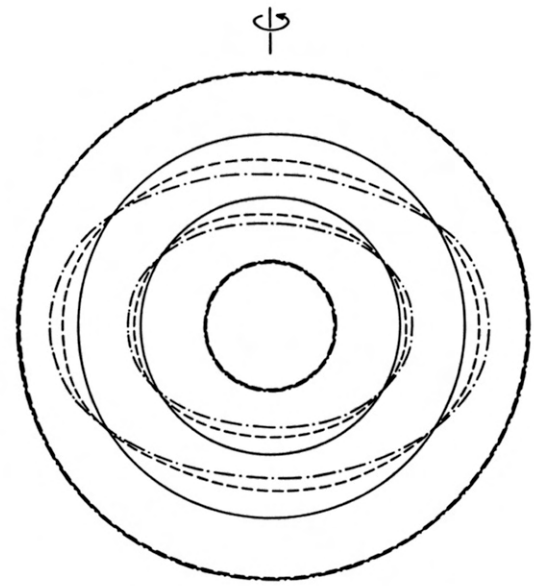

Fig. 4. Simple model of a rotating baroclinic star. Surfaces of constant temperature (solid lines), of constant pressure (dashed lines) and constant density (dash-dotted lines) are shown.

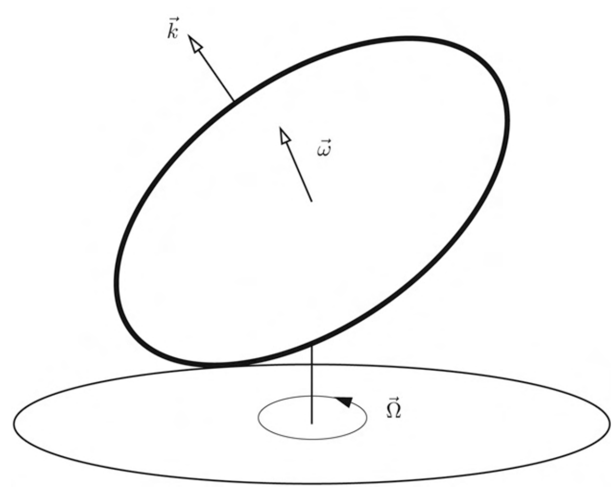

Fig. 5. Geometrical configuration of the precessing spheroidal cavity.

4.2. Flow in a precessing spheroidal cavity

The flow in a precessing spheroidal cavity is of considerable geophysical interest since it applies to the liquid core of the Earth. The solar–lunar precession of the Earth's axis of rotation about the normal of the ecliptic plane with a period of 25 700 years is a result of the torques exerted by Sun and Moon on the equatorial bulge of the Earth. The ellipsoidal flattening of the Earth's figure caused by the centrifugal potential is about 1/300. Owing to its higher density the ellipticity of the iron core is lower than that of the Earth's mantle. Hence the precessional torques exerted on the latter by Sun and Moon are larger than those acting on the core. There is thus an unbalanced precessional torque exerted by the mantle on the core. This situation can be modeled by a fluid filled spheroidal cavity rotating about its figure axis in a system that is rotating about a different axis as indicated in Fig. 5.

The Euler equations relative to the frame of reference precessing with the angular velocity $\boldsymbol{\Omega}$ (mantle frame) are given by

$$\partial_t \boldsymbol{v} + \boldsymbol{v} \cdot \nabla \boldsymbol{v} + 2\Omega \times \boldsymbol{v} + \nabla \pi = 0, \tag{34a}$$

$$\nabla \cdot \boldsymbol{v} = 0. \tag{34b}$$

The normal component of the velocity must vanish at the boundary of the spheroidal cavity,

$$\boldsymbol{v} \cdot (\boldsymbol{r} + \zeta \boldsymbol{k} \boldsymbol{r} \cdot \boldsymbol{k}) = 0 \quad \text{at} \quad |\boldsymbol{r}|^2 + \zeta |\boldsymbol{k} \cdot \boldsymbol{r}|^2 = 1, \tag{35}$$

where we have introduced the equatorial radius a of the cavity as length scale and where the parameter ζ is related to the ellipticity $\eta = (a - c)/a$ through $\zeta = \eta(2 - \eta)/(1 - \eta)^2$. The unit vector $\boldsymbol{k}$ indicates the figure axis of the cavity.

Sloudsky [30] and later independently Poincaré [31] derived a steady solution with constant vorticity for the problem (34) and (35),

$$\boldsymbol{v} = \boldsymbol{\omega} \times \boldsymbol{r} + \nabla \Psi \quad \text{with} \tag{36a}$$

$$\boldsymbol{\omega} = \boldsymbol{k} \cdot \boldsymbol{\omega} \left(\boldsymbol{k} + \boldsymbol{k} \times (\boldsymbol{\Omega} \times \boldsymbol{k}) \frac{2 + \zeta}{\zeta \boldsymbol{k} \cdot \boldsymbol{\omega} + 2\boldsymbol{k} \cdot \boldsymbol{\Omega}(1 + \zeta)} \right), \tag{36b}$$

$$\Psi = \frac{\zeta \boldsymbol{k} \cdot \boldsymbol{r}\, (\boldsymbol{\Omega} \times \boldsymbol{k}) \cdot \boldsymbol{r}\, \boldsymbol{k} \cdot \boldsymbol{\omega}}{\zeta \boldsymbol{k} \cdot \boldsymbol{\omega} + 2\boldsymbol{k} \cdot \boldsymbol{\Omega}(1 + \zeta)}. \tag{36c}$$

There are two difficulties with this solution which occur also in other applications of the Euler equations:

- The vorticity component in the direction of $\boldsymbol{k}$ remains undetermined.
- The assumption of a constant vorticity vector in the interior may not be correct, even in the limit of vanishing viscosity.

The first of these difficulties can be resolved when the viscous Ekman layer is added to the solution (36). According to the analysis of Busse [32] the expression (36b) becomes

$$\boldsymbol{\omega} = \omega^2 \Bigg(\boldsymbol{k} + \boldsymbol{k} \times \frac{\boldsymbol{\Omega} 2.62\sqrt{E\omega} + (\boldsymbol{\Omega} \times \boldsymbol{k})(\eta\omega^2 + \boldsymbol{k} \cdot \boldsymbol{\Omega} + 0.259\sqrt{E/\omega})}{(2.62\sqrt{E\omega})^2 + (\eta\omega^2 + \boldsymbol{k} \cdot \boldsymbol{\Omega} + 0.259\sqrt{E/\omega})^2} \Bigg) \tag{37}$$

where $E = \nu/(a^2\omega_c)$ is the Ekman number. In addition to the length scale a we are using $1/\omega_c$ as time scale where ω_c is the angular velocity of the cavity. It has also been assumed that E, η, and $|\boldsymbol{\Omega}|$ are small quantities. Expression (37) agrees with the corresponding expression derived earlier by Stewartson and Roberts [33], but is correct in the order $\epsilon^2 \equiv 1 - \omega^2$ instead of only in the order ϵ. In the limit $E \to 0$ and for small η and $|\boldsymbol{\Omega}|$ expression (37) agrees with expression (36b) with the implication $\omega^2 = \boldsymbol{k} \cdot \boldsymbol{\omega}$.

The assumption of a constant vorticity vector in the limit of vanishing viscosity has been established by the Prandtl–Batchelor theorem [34] in the case of a steady two-dimensional vortex, but this theorem cannot be extended to three-dimensional configurations in rotating systems even if the flow is essentially two-dimensional. In general tangential discontinuities and even divergences must be expected since they are admitted by the Euler equations. An example is the deviation from the Sloudsky–Poincaré solution (36) caused by the presence of the no-slip boundary as has been demonstrated by Busse [32]. In this latter paper it is shown that the flow of finite amplitude in the Ekman boundary layer causes a cylindrical shear layer in the interior of the precessing cavity at the distance $\sqrt{3}/2$ from the axis determined by $\boldsymbol{\omega}$ in the case of the sphere with the radius 1. This singularity is caused by the fact that the thickness of the Ekman boundary layer diverges like $\sqrt{E/|\boldsymbol{k} \cdot \boldsymbol{r} - \omega|}$ at the critical latitudes given by $\boldsymbol{k} \cdot \boldsymbol{r} = \omega$. In the case of a precessing sphere with $|\boldsymbol{k} - \boldsymbol{\omega}| \ll 1$ these latitudes are located at $\pm 30°$. A theoretical profile in the limit $E \to 0$ together with a profile measured in the experiment of Malkus [35] and a profile obtained by Noir et al. [36] in a numerical simulation with $E = 10^{-6}$ are shown in Fig. 6. A visualization of the shear layer in the case of an oblate spheroid can be seen in Fig. 7. To achieve a closer correspondence between the asymptotic profile and the other curves shown in Fig. 6 higher-order terms in the description of the Ekman layer near its divergence need to be taken into account in the asymptotic analysis.

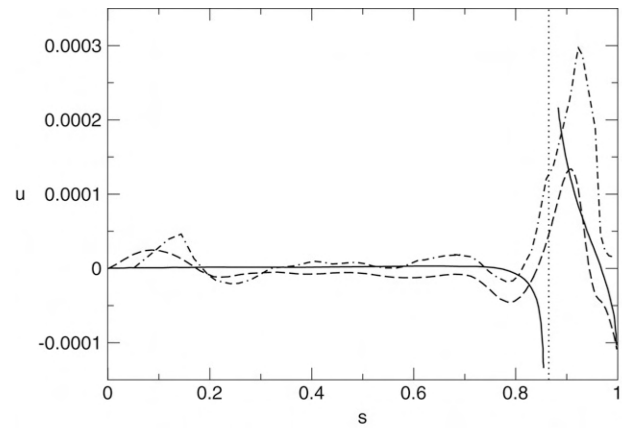

Fig. 6. Differential rotation in a precessing nearly spherical cavity as a function of the distance from the axis. Results of the asymptotic analysis [32] (solid lines) and from a numerical simulation for $E = 10^{-6}$ [36] (dashed line) are compared with the experimental measurement of Malkus [35] (dash-dotted line). The dotted line indicates the cylindrical surface intersecting the boundary at the critical latitudes.

The divergence of the Ekman layer at the critical latitudes also causes the excitation of inertial waves [37] which in turn spawn oscillatory internal shear layers which are oblique with respect to the rotation axis of the fluid [38,39]; see also [40, 41]. With increasing amplitude of precession nonlinear effects of these shear layers give rise to interior differential rotations that are much more complex than that exhibited in Fig. 7; see, for example, the experimental photographs of [42].

Of special interest is the possibility of a resonance in expression (37) when $\boldsymbol{\Omega} \cdot \boldsymbol{k}$ is negative such that the denominator can approach zero in the limit $E \to 0$. Such a resonance represents the excitation of the inertial spin-over mode. But this inertial mode depends on the rotation vector of the fluid, not on the prescribed rotation of the container. Owing to the implicit nature of expression (37) for $\boldsymbol{\omega}$ there does not exist a simple linear resonance. Instead a complex nonlinear relationship in

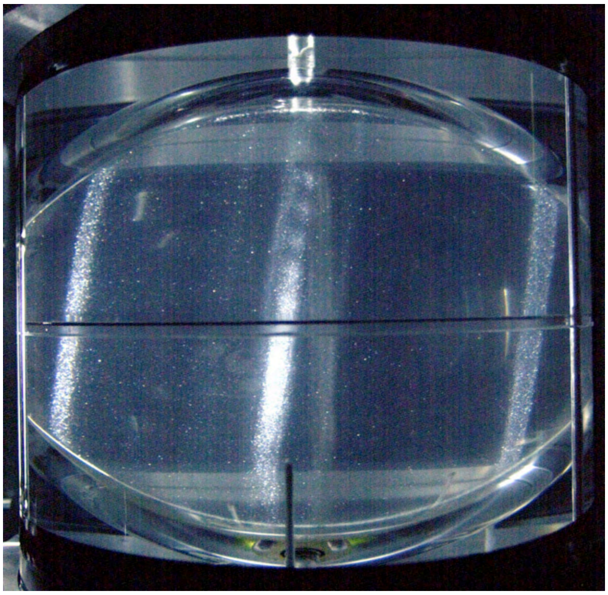

Fig. 7. Cylindrical shear layer in the precessing spherical cavity of the experiment of [43]. The shear becomes visible through the alignment of tiny flat particles. This photograph has been provided by the authors of [37]. A modified version of the figure has been published in [37].

the dependence of $\boldsymbol{\omega}$ admitting multiple solutions exist in the neighborhood of $\boldsymbol{\Omega} \cdot \boldsymbol{k} \approx -\eta$ as has been shown by Noir et al. [43]. These authors have investigated the resonance also experimentally and have found that expression (37) describes the measurements quite well even when the perturbation parameter ϵ approaches the order unity as shown in Figs. 7 and 9 of [43]. This is much beyond the range of small ϵ for which expression (37) had been derived originally. For a related discussion with respect to the experiments of Malkus [35] see [44].

5. The possible absence of turbulence in some shear flows for $Re \to \infty$

One of the most discussed problems in astrophysical fluid dynamics is the problem of turbulence in accretion disks. In the outer parts of the latter, where the electrical conductivity is too low for the Lorentz force to play a significant role, hydrodynamically generated turbulence is expected to be responsible for an efficient outward transport of angular momentum. This problem has focused the attention on the onset of turbulence in flows between two coaxial cylinders with radii r_1 and r_2 with $r_1 < r_2$ and associated constant angular velocities Ω_1 and Ω_2 with $\Omega_1 > \Omega_2 > 0$. According to Rayleigh's criterion the basic solution $\Omega(r)$ depending solely on the distance r from the axis is unstable with respect to axisymmetric disturbances when the condition

$$\frac{\mathrm{d}(r^2\Omega)}{\mathrm{d}r} < 0 \tag{38}$$

is satisfied. In the small-gap limit this criterion can be written in the form

$$\tau < Re \tag{39}$$

where the definitions

$$Re = \frac{(\Omega_1 - \Omega_2)d(r_2 + r_1)}{2\nu}, \qquad \tau = \frac{(\Omega_1 + \Omega_2)d^2}{\nu} \tag{40}$$

have been introduced with the gap width $d = r_2 - r_1$. Criterion (39) can be stated in a simple way: When shear vorticity and global vorticity have opposite signs, the former must exceed the latter in magnitude for instability.

Linear analysis of the stability with respect to infinitesimal disturbances confirms criterions (38) and (39) for instability at least for large values of Re. For lower values viscosity contributes a stabilizing influence such that the criterion for onset of infinitesimal disturbances in the small-gap limit becomes

$$Re > \frac{Re_E^2}{4\tau} + \tau \tag{41}$$

where R_E is the energy stability limit for plane Couette flow [45,46], $R_E = 2\sqrt{1708}$. Here the value 1708 refers to the well known critical value of the Rayleigh number for the onset of Rayleigh–Bénard convection in a horizontal fluid layer heated from below with no-slip boundaries. Experimental observations and numerical simulations based on the nonlinear Navier–Stokes equations agree with criterion (41) for the onset of instability – even if disturbances of finite amplitude are admitted – unless τ becomes small in comparison to R_E [47–49]. This does not exclude, however, the possibility of the existence of yet unrealized turbulent states of flow when the right-hand side of criterion (41) exceeds Re while τ is sufficiently large, say $\tau \gtrsim R_E/2$ is satisfied. A recent paper on bounds for the momentum transport in rotating systems considers this question [50].

It is a common notion among fluid dynamicists that all shear flows become turbulent provided the Reynolds number is sufficiently large and disturbances of finite amplitude are admitted. The absence of any turbulent flow under stationary conditions in the regime

$$-R_E \le Re \le \frac{Re_E^2}{4\tau} + \tau \tag{42}$$

as proposed in [50] contradicts this notion since Re can become arbitrarily large provided that τ becomes even larger. The proof for this proposal is incomplete, however, and is actually restricted to the neighborhood of $\tau = Re_E/2$ at which point the right-hand side of inequality (42) becomes equal to Re_E. If the proposal is correct, however, as is suggested by the presently available experimental and numerical evidence, then angular velocity distributions $\Omega(r)$ with $\mathrm{d}\Omega/\mathrm{d}r \le 0$ satisfying

$$\frac{\mathrm{d}(r^2\Omega)}{\mathrm{d}r} \ge 0 \tag{43}$$

are absolutely stable. Since the Keplerian velocity field in accretion disks is governed by the balance between

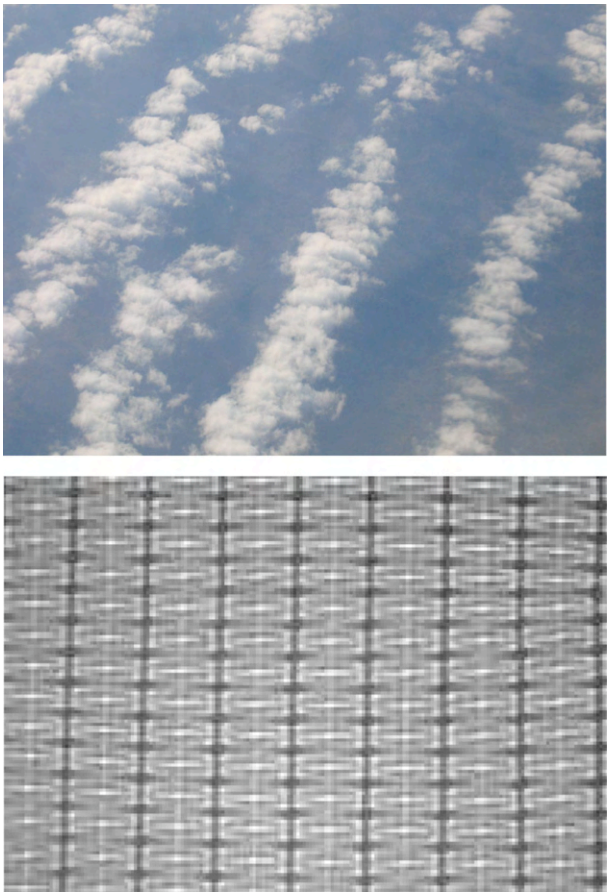

Fig. 8. Bimodal pattern in a cloud street (top, as seen from an airplane) and shadowgraph image of bimodal convection in a laboratory experiment (bottom, dark areas indicate rising hotter liquid, while bright areas indicate descending colder liquid; for further details see [56]).

gravitational attraction and the centripetal force, $\Omega^2 r \backsim 1/r^2$, it satisfies (43) and accretion disks cannot be turbulent under the idealized conditions considered here. In terms of the small-gap limit, $Re \approx d^2\nu^{-1}r|\mathrm{d}\Omega/\mathrm{d}r| \approx \Omega 3d^2/2\nu \approx 3\tau/4$ grows only in proportion to $3\tau/4$ asymptotically and thus cannot give rise to turbulence according to criterion (42).

Of course, hydrodynamic turbulence in accretion disks could be generated through additional effects such as a stable density stratification in the direction normal to the disk. Theoretical analyses [51–53] confirmed by recent experimental work [54] support this idea in that they demonstrate that in a Taylor–Couette system an axisymmetric density gradient in the direction of gravity exerts a destabilizing influence on the onset of instability such that Rayleigh's criterion (38) is violated.

6. Bimodal convection in geophysics

In order to illustrate the close similarity between laboratory flows and corresponding observed geophysical phenomena we choose the case of bimodal convection since it is not as well known as other examples such as von Karman vortex streets in the wake of some oceanic islands, Kelvin–Helmholtz waves in the atmosphere, or cloud patterns corresponding to convection rolls and hexagonal cells. Bimodal convection originates from an instability of convection rolls and is driven by the buoyancy stored in the thermal boundary layers associated with a convecting fluid layer [55]. It has been studied experimentally by Busse & Whitehead [56] and its finite amplitude properties have been analyzed numerically by Frick et al. [57]. A laboratory shadowgraph image is shown in Fig. 8 together with an observed example of bimodal structures in a cloud street. Another observational example can be found in the recent review [58]. This agreement between a laboratory convection pattern and an atmospheric phenomenon is remarkable in that bimodal convection is generated through a secondary bifurcation in contrast to the other examples mentioned above which correspond to primary bifurcations.

Since bimodal convection is usually observed only in fluids with a Prandtl number P in excess of the order 10, it may be surprising to observe this phenomenon in the atmosphere as air is characterized by a Prandtl number of only 0.7. It must be kept in mind, however, that the condensation of water vapor not only acts as a convenient indicator of upward motions, but also influences the thermodynamics of the convecting layer. The latent heat liberated through the condensation of water droplets causes an increase in the specific heat of the fluid which in turn lowers the effective thermal diffusivity. Since P is defined as the ratio of kinematic viscosity to thermal diffusivity it assumes a high value for convection in the presence of clouds.

Another case of bimodal convection may be found in the Earth's mantle. Convection cells involving the whole mantle are believed to be responsible for plate tectonics, i.e. for the motion of crustal plates in the outermost region of the "solid" Earth. Secondary motions beneath the plates appear to occur in many places as has been pointed out by Richter [59] and others. As in the case of laboratory bimodal convection (see Fig. 8) the smaller secondary convection rolls are always oriented at right angles to the larger primary convection rolls. In this way the stabilizing effect of the shear of the primary convection rolls on the secondary rolls is minimized. In the case of the Earth's mantle additional influences on convection arise, of course, from the presence of the olivine–spinel and the spinel–perovskite phase transitions at the depths of 400 km and 660 km, respectively.

7. Concluding remarks

In this review we have pointed out a few solutions of the Euler equations which have been of recent interest in the field of geophysical and astrophysical fluid dynamics. These simple solutions can be realized in laboratory experiments and also be applied to large scale fluid dynamical phenomena in geophysics and astrophysics. The fact that the latter systems are usually in a turbulent state of motion does not seem to affect the usefulness of the laminar solutions. Since the interaction of the large scale components of the velocity and buoyancy fields occurs rather independently of the influence of the small scale motions, the latter can roughly be taken into account as diffusive effects. From this point of view it is not surprising that the employment of eddy diffusivities has been quite successful in describing the effects of turbulence in geophysical and astrophysical systems.

Acknowledgments

The help of Drs. R. Simitev and T. Pöschel in creating the figures is gratefully acknowledged.

References

[1] H.P. Greenspan, The Theory of Rotating Fluids, Cambridge University Press, 1968.

[2] H. Lamb, Hydrodynamics, Dover Publications, 1945.

[3] B. Cushman-Roisin, Introduction to Geophysical Fluid Dynamics, Prentice-Hall, 1994.

[4] M. Ghil, S. Childress, Topics in geophysical fluid dynamics, in: Dynamo Theory and Climate Dynamics, Springer Verlag, 1987.

[5] A.E. Gill, Atmosphere-Ocean Dynamics, Academic Press, 1982.

[6] J.C. McWilliams, Fundamentals of Geophysical Fluid Dynamics, Cambridge University Press, 2007.

[7] J. Pedlosky, Geophysical Fluid Dynamics, 2nd ed., Springer Verlag, 1987.

[8] J.-L. Tassoul, Theory of Rotating Stars, Princeton University Press, 1968.

[9] E. Dormy, A.M. Soward (Eds.), Mathematical Aspects of Natural Dynamos, CRC Press, Taylor & Francis Group, 2007.

[10] G. Rüdiger, R. Hollerbach, The Magnetic Universe, Wiley-VHC, Weinheim, 2004.

[11] F.H. Busse, C.R. Carrigan, Laboratory simulation of thermal convection in rotating planets and stars, Science 191 (1976) 81–83.

[12] F.H. Busse, Thermal instabilities in rapidly rotating systems, J. Fluid Mech. 44 (1970) 441–460.

[13] F.H. Busse, Asymptotic theory of convection in a rotating, cylindrical annulus, J. Fluid Mech. 173 (1986) 545–556.

[14] F.H. Busse, Convective flows in rapidly rotating spheres and their dynamo action, Phys. Fluids 14 (2002) 1301–1314.

[15] F.H. Busse, Is low Rayleigh number convection possible in the Earth's core? Geophys. Res. Letts. 29 (2002) GLO149597.

[16] K. Zhang, P. Earnshaw, X. Liao, F.H. Busse, On inertial waves in a rotating fluid sphere, J. Fluid Mech. 437 (2001) 103–119.

[17] K. Zhang, X. Liao, P. Earnshaw, On inertial waves in a rapidly rotating spheroid, J. Fluid Mech. 504 (2004) 1–40.

[18] F.H. Busse, K. Zhang, X. Liao, On slow inertial waves in the solar convection zone, Astrophys. J. 631 (2005) L171–L174.

[19] K. Zhang, On coupling between the Poincaré equation and the heat equation, J. Fluid Mech. 268 (1994) 211–229.

[20] F.H. Busse, R. Simitev, Inertial convection in rotating fluid spheres, J. Fluid Mech. 498 (2004) 23–30.

[21] K. Zhang, On coupling between the Poincaré equation and the heat equation: No-slip boundary condition, J. Fluid Mech. 284 (1995) 239–256.

[22] H. von Zeipel, Probleme der Astronomie (Festschrift für H. von Seeliger), Springer-Verlag, Berlin, 1924, pp. 144–152.

[23] H. Vogt, Zum Strahlungsgleichgewicht der Sterne, Astron. Nachr. 223 (1925) 229–232.

[24] A.S. Eddington, Circulating currents in rotating stars, The Observatory 48 (1925) 73–75.

[25] P.A. Sweet, The importance of rotation in stellar evolution, Month. Not. Roy. Astron. Soc. 110 (1950) 548–558.

[26] G. Randers, Large-scale motions in stars, Astrophys. J. 94 (1941) 109–123.

[27] F.H. Busse, On the problem of stellar rotation, Astrophys. J. 259 (1982) 759–766.

[28] M. Schwarzschild, On stellar rotation. II, Astrophys. J. 106 (1947) 427–456.

[29] I.W. Roxburgh, On stellar rotation: I. The rotation of upper main-sequence stars, Month. Not. Roy. Astron. Soc. 128 (1964) 157–171.

[30] T. Sloudsky, De la rotation de la terre supposée a son intérieur, Bull. Soc. Impér. Natur. 9 (1895) 285–318.

[31] H. Poincaré, Sur la précession des corps déformables, Bull. Astr. 25 (1910) 321–356.

[32] F.H. Busse, Steady fluid flow in a precessing spheroidal shell, J. Fluid Mech. 33 (1968) 739–751.

[33] K. Stewartson, P.H. Roberts, On the motion of a liquid in a spheroidal cavity of a precessing rigid body, J. Fluid Mech. 17 (1963) 1–20.

[34] G.K. Batchelor, Steady laminar flow with closed streamlines at large Reynolds numbers, J. Fluid Mech. 1 (1956) 177–190.

[35] W.V.R. Malkus, Precession of the Earth as the cause of geomagnetism, Science 160 (1968) 259–264.

[36] J. Noir, D. Jault, P. Cardin, Numerical study of the motions within a slowly precessing sphere at low Ekman number, J. Fluid Mech. 437 (2001) 283–299.

[37] J. Noir, D. Brito, K. Aldridge, P. Cardin, Experimental evidence of inertial waves in a precessing spheroidal cavity, Geophys. Res. Lett. 28 (2001) 3785–3788.

[38] R.R. Kerswell, On the internal shear layers spawned by the critical regions in oscillatory Ekman boundary layers, J. Fluid Mech. 289 (1995) 311–325.

[39] R. Hollerbach, R.R. Kerswell, Oscillatory internal shear layers in rotating and precessing flows, J. Fluid Mech. 289 (1995) 327–339.

[40] A. Tilgner, Driven inertial oscillations in spherical shells, Phys. Rev. E 59 (1999) 1789–1794.

[41] M. Rieutord, B. Georgeot, L. Valdettaro, Inertial waves in a rotating spherical shell: Attractors and asymptotic spectrum, J. Fluid Mech. 435 (2001) 103–144.

[42] J. Vanyo, P. Wilde, P. Cardin, P. Olson, Experiments on precessing flows in the Earth's liquid core, Geophys. J. Int. 121 (1995) 136–142.

[43] J. Noir, P. Cardin, D. Jault, J.-P. Masson, Experimental evidence of non-linear resonance effects between retrograde precession and the tilt-over mode within a spheroid, Geophys. J. Int. 154 (2003) 407–416.

[44] S. Lorenzani, A. Tilgner, Inertial instabilities of fluid flow in precessing spheroidal shells, J. Fluid Mech. 492 (2003) 363–379.

[45] F.H. Busse, Über notwendige und hinreichende Kriterien für die Stabilität von Strömungen, ZAMM 50 (1970) T173–T174.

[46] F.H. Busse, A Property of the Energy Stability Limit for Plane Parallel Shear Flow, Arch. Ration. Mech. Anal. 47 (1972) 28–35.

[47] B. Dubrulle, O. Dauchot, F. Daviaud, P:-Y. Longaretti, D. Richard, J.-P. Zahn, Stability and turbulent transport in rotating shear flows: Prescription from analysis of cylindrical and plane Couette flows data, Phys. Fluids 17 (2005) 095103.

[48] H. Ji, M. Burin, E. Schartman, J. Goodman, Hydrodynamic turbulence cannot transport angular momentum effectively in astrophysical disks, Nature 444 (2006) 343–346.

[49] F. Rincon, G.I. Ogilvie, C. Cossu, On self-sustaining processes in Rayleigh-stable rotating plane Couette flows and subcritical transition to turbulence in accretion disks, Astron. Astrophys. 463 (2007) 817–832.

[50] F.H. Busse, Bounds on the momentum transport by turbulent shear flow in rotating systems, J. Fluid Mech. 583 (2007) 303–311.

[51] M.J. Molemaker, J.C. McWilliams, I. Yavneh, Instability and equilibration of centrifugally stable stratified Taylor–Couette flow, Phys. Rev. Lett. 86 (2001) 5270–5273.

[52] I. Yavneh, J.C. McWilliams, M.J. Molemaker, Non-axisymmetric instability of centrifugally stable stratified Taylor–Couette flow, J. Fluid Mech. 448 (2001) 1–21.

[53] D. Shalybkov, G. Rüdiger, Stability of density-stratified viscous Taylor–Couette flows, Astron. Astrophys. 438 (2005) 411–417.

[54] M. Le Bars, P. Le Gal, Experimental analysis of the stratorotational instability in a cylindrical Couette flow, Phys. Rev. Lett. 99 (2007) 064502.

[55] F.H. Busse, On the stability of two-dimensional convection in a layer heated from below, J. Math. Phys. 46 (1967) 140–150.

[56] F.H. Busse, J. Whitehead, Instabilities of convection rolls in a high-Prandtl number fluid, J. Fluid Mech. 47 (1971) 305–320.

[57] H. Frick, F.H. Busse, R.M. Clever, Steady three-dimensional convection at high Prandtl numbers, J. Fluid Mech. 127 (1983) 141–153.

[58] F.H. Busse, The Sequence-of-bifurcations approach towards understanding turbulent fluid flow, Surv. Geophys. 24 (2003) 269–288.

[59] F.M. Richter, Convection and the large-scale circulation of the mantle, J. Geophys. Res. 78 (1973) 8735–8745.

Available online at www.sciencedirect.com

ScienceDirect

Physica D 237 (2008) 2111–2126

PHYSICA D

www.elsevier.com/locate/physd

Climate dynamics and fluid mechanics: Natural variability and related uncertainties

Michael Ghil[a,b,c,d,*], Mickaël D. Chekroun[d], Eric Simonnet[e]

[a] Département Terre-Atmosphère-Océan and Laboratoire de Météorologie Dynamique (CNRS and IPSL), École Normale Supérieure, 75231 Paris Cedex 05, France

[b] Department of Atmospheric Sciences, University of California, Los Angeles, CA 90095-1565, USA

[c] Institute of Geophysics and Planetary Physics, University of California, Los Angeles, CA 90095-1565, USA

[d] Environmental Research and Teaching Institute, École Normale Supérieure, 75231 Paris Cedex 05, France

[e] Institut Non Linéaire de Nice (INLN)-UNSA, UMR 6618 CNRS, 1361, route des Lucioles 06560 Valbonne, France

Available online 1 April 2008

Abstract

The purpose of this review-and-research paper is twofold: (i) to review the role played in climate dynamics by fluid-dynamical models; and (ii) to contribute to the understanding and reduction of the uncertainties in future climate-change projections. To illustrate the first point, we review recent theoretical advances in studying the wind-driven circulation of the oceans. In doing so, we concentrate on the large-scale, wind-driven flow of the mid-latitude oceans, which is dominated by the presence of a larger, anticyclonic and a smaller, cyclonic gyre. The two gyres share the eastward extension of western boundary currents, such as the Gulf Stream or Kuroshio, and are induced by the shear in the winds that cross the respective ocean basins. The boundary currents and eastward jets carry substantial amounts of heat and momentum, and thus contribute in a crucial way to Earth's climate, and to changes therein.

Changes in this double-gyre circulation occur from year to year and decade to decade. We study this low-frequency variability of the wind-driven, double-gyre circulation in mid-latitude ocean basins, via the bifurcation sequence that leads from steady states through periodic solutions and on to the chaotic, irregular flows documented in the observations. This sequence involves local, pitchfork and Hopf bifurcations, as well as global, homoclinic ones.

The natural climate variability induced by the low-frequency variability of the ocean circulation is but one of the causes of uncertainties in climate projections. The range of these uncertainties has barely decreased, or even increased, over the last three decades. Another major cause of such uncertainties could reside in the structural instability – in the classical, topological sense – of the equations governing climate dynamics, including but not restricted to those of atmospheric and ocean dynamics.

We propose a novel approach to understand, and possibly reduce, these uncertainties, based on the concepts and methods of random dynamical systems theory. The idea is to compare the climate simulations of distinct general circulation models (GCMs) used in climate projections, by applying stochastic-conjugacy methods and thus perform a stochastic classification of GCM families. This approach is particularly appropriate given recent interest in stochastic parametrization of subgrid-scale processes in GCMs.

As a very first step in this direction, we study the behavior of the Arnol'd family of circle maps in the presence of noise. The maps' fine-grained resonant landscape is smoothed by the noise, thus permitting their coarse-grained classification.

Keywords: Climate change; Physical oceanography; Dynamical systems; Bifurcations; Structural stochastic stability; Arnol'd tongues

1. Introduction

Charney et al. [1] were the first to attempt a consensus estimate of the equilibrium sensitivity of climate to changes in atmospheric CO_2 concentrations. The result was the now famous range for an increase of 1.5–4.5 K in global near-surface air temperatures, given a doubling of CO_2 concentration.

As the relatively new science of climate dynamics evolved through the 1980s and 1990s, it became quite clear – from observational data, both instrumental and paleoclimatic, as well as model studies – that Earth's climate never was and is

* Corresponding author at: Département Terre-Atmosphère-Océan and Laboratoire de Météorologie Dynamique (CNRS and IPSL), École Normale Supérieure, 75231 Paris Cedex 05, France. Tel.: +33 310 206 2285.

E-mail address: ghil@lmd.ens.fr (M. Ghil).

0167-2789/$ - see front matter © 2008 Elsevier B.V. All rights reserved.
doi:10.1016/j.physd.2008.03.036

unlikely to ever be in equilibrium. The three successive IPCC reports (1991 [2], 1996, and 2001 [3]) concentrated therefore, in addition to estimates of equilibrium sensitivity, on estimates of climate change over the 21st century, based on several scenarios of CO_2 increase over this time interval, and using up to 18 general circulation models (GCMs) in the fourth IPCC Assessment Report (AR4) [4].

The GCM results of temperature increase over the coming 100 years have stubbornly resisted any narrowing of the range of estimates, with results for T_s in 2100 as low as 1.4 K or as high as 5.8 K, according to the Third Assessment Report. The hope in the research leading up to the AR4 was that a set of suitably defined "better GCMs" would exhibit a narrower range of year-2100 estimates, but this does not seem to have been the case.

The difficulty in narrowing the range of estimates for either equilibrium sensitivity of climate or for end-of-the-century temperatures is clearly connected to the complexity of the climate system, the multiplicity and nonlinearity of the processes and feedbacks it contains, and the obstacles to a faithful representation of these processes and feedbacks in GCMs. The practice of the science and engineering of GCMs over several decades has amply demonstrated that any addition or change in the model's "parametrizations" – *i.e.*, of the representation of subgrid-scale processes in terms of the model's explicit, large-scale variables – may result in noticeable changes in the model solutions' behavior.

As an illustration, Fig. 1 shows the sensitivity of an atmospheric GCM, which does not include a dynamical ocean, to changes in its model parameters. Several thousand simulations were performed as part of the "climate*prediction*.net" experiment [6], using perturbations in several parameters of the Hadley Centre's HadAM3 model [7], coupled to a passive, mixed-layer ocean model. The lower panel of Fig. 1 clearly illustrates a wide range of responses to CO_2 doubling, from about -1 K to about 8 K [8].

The last IPCC report [4] has investigated climate change as a result of various scenarios of CO_2 increase for a set of 18 distinct GCMs. The best estimate of the temperature increase at the end of the 21st century from AR4 is about 4.0 °C for the worst scenario of greenhouse-gas increase, namely A1F1, this scenario envisages, roughly speaking, a future world with a very rapid economic growth. The likely range of end-of-century increase in global temperatures is of 2.4–6.4 °C in this case, and comparably large ranges of uncertainties obtain for all the other scenarios as well [4]. The consequences of these scientific uncertainties for the ethical quandaries arising in the socio-economic and political decision-making process involved in adaptation to and mitigation of climate changes are discussed in [5].

An essential contributor to this range of uncertainty is natural climate variability [9] of the coupled ocean-atmosphere system. As mentioned already in [10], most GCM simulations do not exhibit the observed interdecadal variability of the oceans' buoyancy-driven, *thermohaline* circulation [11]. This circulation corresponds to a slow, pole-to-pole motion of the oceans' main water masses, also referred to as the *overturning*

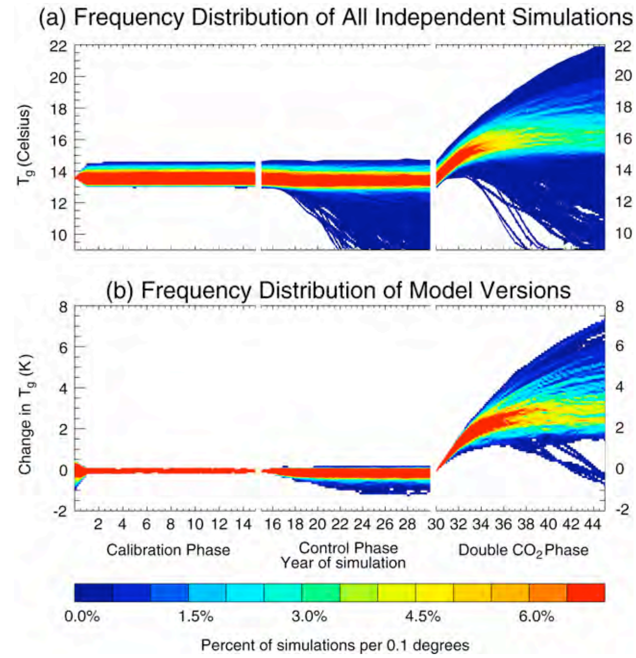

Fig. 1. Frequency distributions of global mean, annual mean, near-surface temperature (T_g) for (a) 2017 GCM simulations, and doubled CO_2; and for (b) a subset of 414 stable simulations, without substantial climate drift.

circulation. Cold and denser waters sink in the subpolar North Atlantic and lighter waters rise over much wider areas of the lower and southern latitudes.

Another striking example of low-frequency, interannual-and-interdecadal variability is provided by the near-surface, *wind-driven ocean circulation* [11,12]. Key features of this circulation are described at length in Section 2. The influence of strong thermal fronts – like the Gulf Stream in the North Atlantic or the Kuroshio in the North Pacific – on the mid-latitude atmosphere above is severely underestimated. Typical spatial resolutions in the century-scale GCM simulations of [2–4,6–8] are of the order of 100 km at best, whereas resolutions of 20 km and less would be needed to really capture the strong mid-latitude ocean-atmosphere coupling just above the oceanic fronts [13,14].

An important additional source of uncertainty comes from the difficulty to correctly parametrize global and regional effects of clouds and their highly complex small-scale physics. This difficulty is particularly critical in the tropics, where large-scale features such as the El-Niño/Southern Oscillation and the Madden–Julian oscillation are strongly coupled with convective phenomena [15–17].

The purpose of this paper is twofold. First, we describe in Section 2 the most recent theoretical results regarding the internal variability of the mid-latitude wind-driven circulation, viewed as a problem in nonlinear fluid mechanics. These results rely to a large extent on the deterministic theory of dynamical systems [18,19]. Second, we address in Section 3 the more general issue of uncertainties in climate change projections. Here we rely on concepts and methods from random dynamical systems theory [20] to help understand and possibly reduce

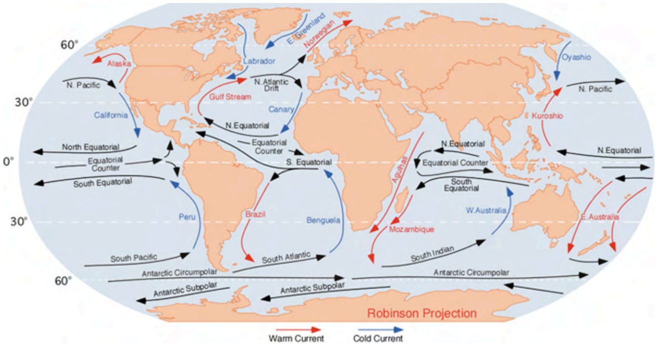

Fig. 2. A map of the main oceanic currents: warm currents in red and cold ones in blue, from http://www.physicalgeography.net..

these uncertainties. Much of the material in the latter section is new; it is supplemented by rigorous mathematical definitions and results in Appendices A and B. A summary and an outlook on future work follow in Section 4.

2. Natural variability of the wind-driven ocean circulation

2.1. Observations

To a first approximation, the main near-surface currents in the oceans are driven by the mean effect of the winds. The trade winds near the equator blow mainly from east to west and are called also the tropical easterlies. In mid-latitudes, the dominant winds are the prevailing westerlies, and towards the poles the winds are easterly again. Three of the strongest near-surface, mid-and-high-latitude currents are the Antarctic Circumpolar Current, the Gulf Stream in the North Atlantic, and the Kuroshio Extension off Japan. The Antarctic Circumpolar Current, sometimes called the Westwind Drift, circles eastward around Antarctica; see Fig. 2.

The Gulf Stream is an oceanic jet with a strong influence on the climate of eastern North America and of western Europe. Actually, the Gulf Stream is part of a larger, gyre-like current system, which includes the North Atlantic Drift, the Canary Current and the North Equatorial Current. It is also coupled with the pole-to-pole overturning circulation. From Mexico's Yucatan Peninsula, the Gulf Stream flows north through the Florida Straits and along the East Coast of the United States. Near Cape Hatteras, it detaches from the coast and begins to drift off into the North Atlantic towards the Grand Banks near Newfoundland.

The Coriolis force is responsible for the so-called Ekman transport, which deflects water masses orthogonally to the near-surface wind direction and to the right [21–23]. In the North Atlantic, this Ekman transport creates a divergence and a convergence of near-surface water masses, respectively, resulting in the formation of two oceanic gyres: a smaller, cyclonic one in subpolar latitudes, the other larger and anticyclonic in the subtropics. This type of *double-gyre* circulation characterizes all mid-latitude ocean basins, including the South Atlantic, as well as the North and South Pacific.

The double-gyre circulation is intensified as the currents approach the East Coast of North America due to the β-effect.

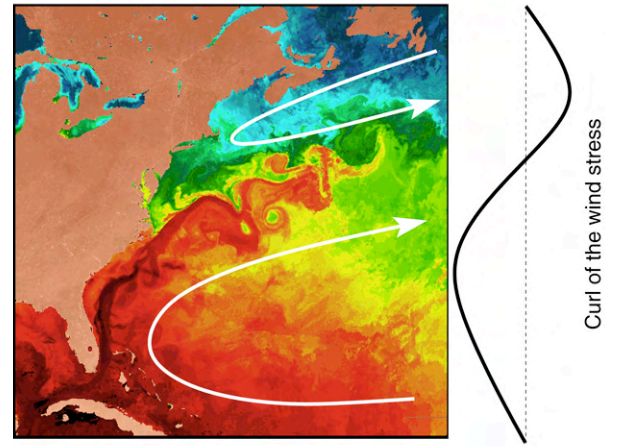

Fig. 3. A satellite image of the sea surface temperature (SST) over the northwestern North Atlantic (US National Oceanic and Atmospheric Administration), together with a sketch of the associated double-gyre circulation (white arrows). An idealized view of the amount of potential vorticity injected into the ocean circulation by the trade winds, westerlies and polar easterlies is shown to the right.

This effect arises primarily from the variation of the Coriolis force with latitude, while the oceans' bottom topography also contributes to it. The former, planetary β-effect is of crucial importance in geophysical flows and induces free Rossby waves propagating westward [21–23].

The currents along the western shores of the North Atlantic and of the other mid-latitude ocean basins exhibit boundary-layer characteristics and are commonly called western boundary currents (WBCs). The northward-flowing Gulf Stream and the southward-flowing Labrador Current extension meet near Cape Hatteras and yield a strong eastward jet. The formation of this jet and of the intense recirculation vortices near the western boundary, to either side of the jet, is mostly driven by internal, nonlinear effects.

Fig. 3 illustrates how these large-scale wind-driven oceanic flows self-organize, as well as the resulting eastward jet. Different spatial and time scales contribute to this self-organization, mesoscales eddies playing the role of the synoptic-scale systems in the atmosphere. Warm and cold rings last for several months up to a year and have a size of about 100 km; two cold rings are clearly visible in Fig. 3. Meanders involve larger spatial scales, up to 1000 km, and are associated with interannual variability. The characteristic scale of the jet and gyres is of several thousand kilometers and they exhibit their own intrinsic dynamics on time scales of several years to possibly several decades.

A striking feature of the wind-driven circulation is the existence of two well-known North-Atlantic oscillations, with a period of about 7 and 14 years, respectively. Data analysis of various climatic variables, such as sea surface temperature (SST) over the North Atlantic or sea level pressure (SLP) over western Europe [24–26] and local surface air temperatures in Central England [27], as well as of proxy records, such as tree rings in Britain, travertine concretions in southeastern France [28], and Nile floods over the last millennium or so [29], all exhibit strikingly robust oscillatory behavior with a 7-yr period and, to a lesser extent, with a 14-yr period. Variations in the path and intensity of the Gulf Stream are most likely to exert a major influence on the climate in this part of the world [30]. This is why theoretical studies of the low-frequency variability of the double-gyre circulation are important.

Given the complexity of the processes involved, climate studies have been most successful when using not just a single model but a full hierarchy of models, from the simplest "toy" models to the most detailed GCMs [17]. In the following, we describe one of the simplest models of the hierarchy used in studying this problem.

2.2. A simple model of the double-gyre circulation

The simplest model that includes many of the mechanisms described above is governed by the barotropic *quasi-geostrophic* (QG) equations. The term geostrophic refers to the fact that large-scale rotating flows tend to run parallel to, rather than perpendicular to constant-pressure contours; in the oceans, these contours are associated with the deviation from rest of the surfaces of equal water mass, due to Ekman pumping. Geostrophic balance implies in particular that the flow is divergence-free. The term barotropic, as opposed to baroclinic, has a slightly different meaning in geophysical fluid dynamics than in engineering fluid mechanics: it means that the model describes a single fluid layer of constant density and therefore the solutions do not depend on depth [21–23].

We consider an idealized, rectangular basin geometry and simplified forcing that mimics the distribution of vorticity contribution by the winds, as sketched to the right of Fig. 3. In our idealized model, the amounts of subpolar and subtropical vorticity injected into the basin are equal and the rectangular domain $\Omega = (0, L_x) \times (0, L_y)$ is symmetric about the axis of zero wind stress curl. The barotropic two-dimensional (2-D) QG equations in this idealized setting are:

$$q_t + J(\psi, q) - \nu \Delta^2 \psi + \mu \Delta \psi = -\tau \sin \frac{2\pi y}{L_y}, \quad q = \Delta\psi - \lambda_R^{-2}\psi + \beta y. \tag{1}$$

Here q and ψ are the potential vorticity and streamfunction, respectively, and the Jacobian J corresponds to the advection of potential vorticity by the flow, $J(\psi, q) = \psi_x q_y - \psi_y q_x = \mathbf{u} \cdot \nabla q$, where $\mathbf{u} = (-\psi_y, \psi_x)$, x points east and y points north. The physical parameters are the strength of the planetary vorticity gradient β, the Rossby radius of deformation λ_R^{-2}, the eddy-viscosity coefficient ν, the bottom friction coefficient μ, and the wind-stress intensity τ. We use here free-slip boundary conditions $\psi = \Delta^2\psi = 0$; the qualitative results described below do not depend on the particular choice of homogeneous boundary conditions.

We consider (1) as an infinite-dimensional dynamical system and study its bifurcation sets as the parameters change. Two key parameters are the wind stress intensity τ and the eddy viscosity ν. An important property of (1) is its mirror symmetry in the $y = L_y/2$ axis. This symmetry can be expressed as invariance with respect to the discrete $\mathbb{Z}_2$ group $\mathcal{S}$:

$$\mathcal{S}[\psi(x, y)] = -\psi(x, L_y - y); \tag{2}$$

any solution of (1) is thus accompanied by its mirror-conjugated solution. Hence, in generic terms, the prevailing bifurcations are of either the symmetry-breaking or the saddle-node or the Hopf type.

2.3. Bifurcations in the double-gyre problem

The historical development of a comprehensive nonlinear theory of the double-gyre circulation is interesting on its own, having seen substantial progress in the last 15 years. One can distinguish four main steps.

2.3.1. Symmetry-breaking bifurcations

The first step was to realize that the first generic bifurcation of this QG model was a genuine pitchfork bifurcation that breaks the system's symmetry as the nonlinearity becomes large enough [31–33]. The situation is shown in Fig. 4. When the forcing is weak or the dissipation is large, there is only one steady solution, which is antisymmetric with respect to the mid-axis of the basin. This solution exhibits two large gyres, along with their typical, β-induced WBCs. Away from the western boundary, such a near-linear solution (not shown) is dominated by *Sverdrup* balance between wind stress curl and the meridional mass transport [21,34].

As the wind stress increases, the near-linear Sverdrup solution develops an eastward jet along the mid-axis, which penetrates farther into the domain. This more intense, and hence more nonlinear solution is still antisymmetric about the mid-axis, but loses its stability for some critical value of the wind-stress intensity (indicated by "Pitchfork" in Fig. 4).

A pair of mirror-symmetric solutions emerges and is characterized by a rather different vorticity distribution; the streamfunction fields associated with the two stable steady-state branches are plotted to the upper-left and right of Fig. 4. In particular, the jet in such a solution exhibits a large meander, reminiscent of the one seen in Fig. 3 just downstream of Cape Hatteras; note that the colors in Fig. 4 have been chosen to facilitate the comparison with Fig. 3. These asymmetric flows are characterized by one gyre being stronger in intensity than the other and therefore the jet is deflected either to the southeast or to the northeast.

2.3.2. Gyre modes

The next step was taken in part concurrently with [31,32] and in part shortly after [35–37] the first one. It involved the study of time-periodic instabilities through Hopf bifurcation from either an antisymmetric or an asymmetric steady flow. Some of these studies concentrated on the wind-driven circulation formulated for the stand-alone, single gyre [37,38]. The idea was to develop a full generic picture of the time-dependent behavior of the solutions in more turbulent regimes, by classifying the various instabilities in a comprehensive way. However, it quickly appeared that one kind of asymmetric instabilities, called *gyre modes* [32,35], was prevalent across the full hierarchy of models of the double-gyre circulation; furthermore, these instabilities trigger the lowest nonzero frequency present in these models.

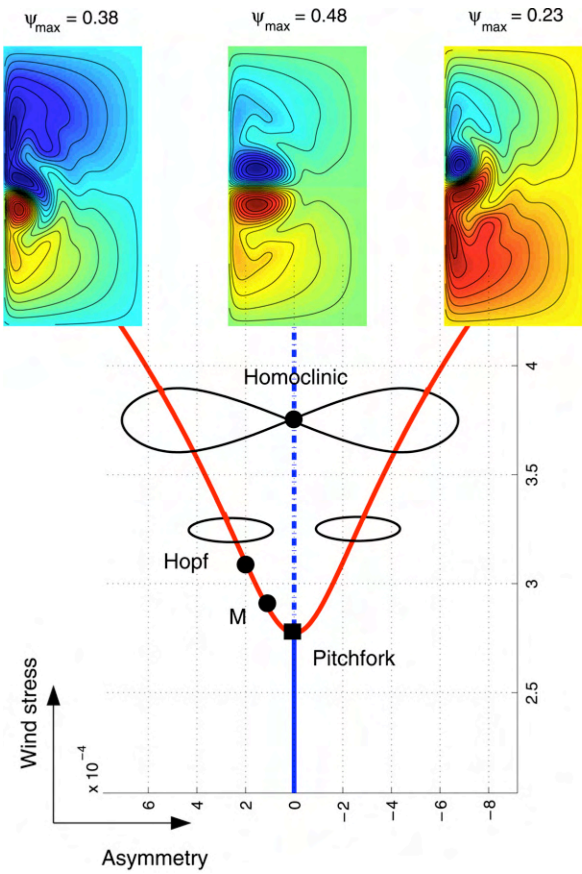

Fig. 4. Generic bifurcation diagram for the barotropic QG model of the double-gyre problem: the asymmetry of the solution is plotted versus the intensity of the wind stress τ. The streamfunction field is plotted for a steady-state solution associated with each of the three branches; positive values in red and negative ones in blue (after [46]).

These modes always appear *after* the first pitchfork bifurcation, and it took several years to really understand their genesis: gyre modes arise as two eigenvalues merge — one is associated with a symmetric eigenfunction and responsible for the pitchfork bifurcation, the other is associated with an antisymmetric eigenfunction [39]; this merging is marked by M in Fig. 4.

Such a phenomenon is not a bifurcation *stricto sensu*: one has topological C^0 equivalence before and after the eigenvalue merging, but not from the C^1 point of view. We recall here that functions are C^k if they and their inverses are k times continuously differentiable. Still, this phenomenon is quite common in small-dimensional dynamical systems with symmetry, as exemplified by the unfolding of codimension-2 bifurcations of Bogdanov-Takens type [19]. In particular, the fact that gyre modes trigger the lowest-frequency of the model is due to the frequency of these modes growing quadratically from zero until nonlinear saturation. Of course, these modes, in turn, become unstable shortly after the merging, through a Hopf bifurcation, indicated by "Hopf" in Fig. 4.

2.3.3. Global bifurcations

The importance of these gyre modes was further confirmed recently through an even more puzzling discovery. Several authors realized, independently of each other, that the low-frequency dynamics of their respective double-gyre models was driven by intense relaxation oscillations of the jet [40–46]. These relaxation oscillations, already described in [32,35], were now attributed to *homoclinic* bifurcations, with a global character in phase space [19,22]. In effect, the QG model reviewed here undergoes a genuine homoclinic bifurcation (see Fig. 4), which is generic across the full hierarchy of double-gyre models. Moreover, this global bifurcation is associated with chaotic behavior of the flow due to the Shilnikov phenomenon [43,46], which induces horseshoes in phase space.

The connection between such homoclinic bifurcations and gyre modes was not immediately obvious, but Simonnet et al. [46] emphasized that the two were part of a single, global dynamical phenomenon. The homoclinic bifurcation indeed results from the unfolding of the gyre modes' limit cycles. This familiar dynamical scenario is again well illustrated by the unfolding of a codimension-2 Bogdanov-Takens bifurcation, where the homoclinic orbits emerge naturally. We deal, once more, with the lowest-frequency modes, since homoclinic orbits have an infinite period. Due to the genericity of this phenomenon, it was natural to hypothesize that the gyre-mode mechanism, in this broader, global-bifurcation context, gave rise to the observed 7-yr and 14-yr North-Atlantic oscillations. Although this hypothesis may appear a little farfetched, in view of the simplicity of the double-gyre models analyzed in detail so far, it poses an interesting question.

2.3.4. Quantization and open questions

The chaotic dynamics observed in the QG models after the homoclinic bifurcation is eventually destroyed as the nonlinearity and the resolution both increase. As one expects the real oceans to be in a far more turbulent regime than those studied so far, some authors proposed different mechanisms for low-frequency variability in fully turbulent flow regimes [47,48]. It turns out, though, that – just as gyre modes could be reconciled with homoclinic-driven dynamics, – the latter can also be reconciled with eddy-driven dynamics, via the so-called *quantization* of the low-frequency dynamics [49].

Primeau [50] showed that, in large basins comparable in size with the North Atlantic, there is not only one but a set of successive pitchfork bifurcations. One supercritical pitchfork bifurcation, associated with the destabilization of antisymmetric flows, is followed generically by a subcritical one, associated this time with a stabilization of antisymmetric flows (modulo high-frequency instabilities) [49]. As a matter of fact, this phenomenon appears to be a consequence of the spectral behavior of the 2-D Euler equations [51], and hence of the closely related barotropic QG model in bounded domains.

Remarkably, this scenario repeats itself as the nonlinearity increases, but now higher wavenumbers are involved in physical space. Simonnet [49] showed that this was also the case for gyre modes and the corresponding dynamics induced by global bifurcations: the low-frequency dynamics is quantized as the jet stream extends further eastward into the basin, due to the increased forcing and nonlinearity. Fig. 5 illustrates this situation: two families of regimes can

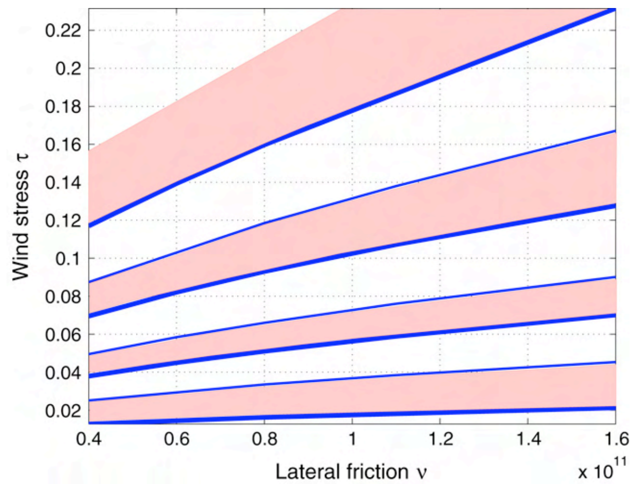

Fig. 5. Two-parameter plane, with the wind-stress intensity τ *vs.* the eddy-viscosity coefficient ν: the curves indicate the locations of supercritical and subcritical pitchfork bifurcations. Each band is associated with a different wavenumber and timescale (from [49]).

be identified, the colored bands correspond to (supercritical) regimes driven by the gyre modes, the others to (subcritical) regimes driven by the eddies. Note that this scenario is also robust to perturbing the problem's symmetry.

The successive-bifurcation theory appears therewith to be fairly complete for barotropic, single-layer models of the double-gyre circulation. This theory also provides a self-consistent, plausible explanation for the climatically important 7-year and 14-year oscillations of the oceanic circulation and the related atmospheric phenomena in and around the North-Atlantic basin [11,12,24–29,45,46]. The dominant 7- and 14-year modes of this theory also survive perturbation by seasonal-cycle changes in the intensity and meridional position of the westerly winds [52].

In baroclinic models, with two or more active layers of different density, baroclinic instabilities [11,14,21–23,30,38,45,47,48] surely play a fundamental role, as they do in the observed dynamics of the oceans. However, it is not known to what extent baroclinic instabilities can destroy gyre-mode dynamics. The difficulty lies in a deeper understanding of the so-called *rectification* process [53], which arises from the nonzero mean effect of the baroclinic component of the flow.

Roughly speaking, rectification drives the dynamics far away from any steady states. In this situation, dynamical systems theory cannot be used as an explanation of complex, observed behavior resulting from successive bifurcations that are rooted in a simple steady state. Other tools from statistical mechanics and nonequilibrium thermodynamics should, therefore, be considered [54–57]. Combining these tools with those of the successive-bifurcation approach may eventually lead to a more general and complete physical characterization of gyre modes in realistic models.

3. Climate-change projections and random dynamical systems (RDSs)

As discussed in Section 1, the climate system's natural variability and the difficulties in parametrizing subgrid-scale processes are not the only causes for the uncertainties in projecting future climate evolution. In this section, we address more generally these uncertainties and present a novel approach for treating them. To do so, we start with some simple ideas about deterministic *vs.* stochastic modeling.

3.1. Background and motivation

Many physical phenomena can be modeled by deterministic evolution equations. Dynamical systems theory is essentially a geometric approach for studying the asymptotic, long-term properties of solutions to such equations in phase space. Pioneered by Poincaré [58], this theory took great strides over the last fifty years. To apply the theory in a reliable manner to a set of complex physical phenomena, one needs a criterion to evaluate the *robustness* of a given model within a class of dynamical systems. Such a criterion should help us deal with the inescapable uncertainties in model formulation, whether due to incomplete knowledge of the governing laws or inaccuracies in determining model parameters.

In this context, Andronov and Pontryagin [59] took a major step toward classifying dynamical systems, by introducing the concept of *structural stability*. Structural stability means that a small, continuous perturbation of a given system preserves its dynamics up to a *homeomorphism*, *i.e.*, up to a one-to-one continuous change of variables that transforms the phase portrait of our system into that of the nearby system; thus fixed points go into fixed points, limit cycles into limit cycles, etc. Closely related is the notion of *hyperbolicity* introduced by Smale [60]. A system is hyperbolic if, (very) loosely speaking, its limit set can be continuously decomposed into invariant sets that are either contracting or expanding; see [61] for more rigorous definitions.

A very simple example is the phase portrait in the neighborhood of a fixed point of saddle type. In this case, the Hartman-Grobman theorem states that the dynamics in this neighborhood is structurally stable. The converse statement, *i.e.* whether structural stability implies hyperbolicity, is still an open question; the equivalence between structural stability and hyperbolicity has only been shown in the C^1 case, under certain technical conditions [62–65]. Bifurcation theory is well grounded in the setting of hyperbolic dynamics. Problems with hyperbolicity and bifurcations arise, however, when one deals with more complicated limit sets.

Hyperbolicity was introduced initially to help pursue the "dynamicist's dream" of finding, in the abstract space of all possible dynamical systems, an open and dense set consisting of structurally stable ones. Being open and dense, roughly speaking, means that any possible dynamical system can be approximated by systems taken from this set, while systems in its complement are negligible in a suitable sense.

Smale conjectured that hyperbolic systems form an open and dense set in the space of all C^1 dynamical systems. If this conjecture were true then hyperbolicity would be typical of all dynamics. Unfortunately, though, this conjecture is only true for one-dimensional dynamics and flows on disks and surfaces [66]. Smale [67] himself found several counterexamples to his conjecture. Newhouse [68] was able to generate open sets of nonhyperbolic diffeomorphisms using homoclinic tangencies. For the physicist, it is even more striking that the famous Lorenz attractor [69] is structurally unstable. Families of Lorenz attractors, classified by topological type, are not even countable [70,71]. In each of these examples, we observe chaotic behavior in a nonhyperbolic situation, *i.e. nonhyperbolic chaos.*

Nonhyperbolic chaos appears, therefore, to be a severe obstacle to any "easy" classification of dynamic behavior. As mentioned by Palis [65], Kolmogorov already suggested at the end of the sixties that "the global study of dynamical systems could not go very far without the use of new additional mathematical tools, like probabilistic ones". Once more, Kolmogorov showed prophetic insight, and nowadays the concept of *stochastic stability* is an important tool in the study of genericity and robustness for dynamical systems. To replace the failed program of classifying dynamical systems based on structural stability and hyperbolicity, Palis [65] formulated the following *global conjecture*: systems having only finitely many attractors (*i.e.* periodic or chaotic sinks) – such that (i) the union of their basins has full Lebesgue measure; and (ii) each is stochastically stable in their basins of attraction – are dense in the $C^r, r \geq 1$ topology. A system is stochastically stable if its Sinai–Ruelle–Bowen (SRB) measure [72] is stable with respect to stochastic perturbations, and the SRB measure is given by $\lim_{n\to\infty} \frac{1}{n}\sum_i \delta_{z_i}$, with z_i being the successive iterates of the dynamics. This measure is obtained intuitively by allowing the entire phase space to flow onto the attractor [73].

Stochastic stability is fundamentally based on ergodic theory. We would like to consider a more geometric approach, which can provide a coarser, more robust classification of GCMs and their climate-change projections. In this section, we propose such an approach, based on concepts from the rapidly growing field of random dynamical systems (RDSs), as developed by Arnold [20] and his "Bremen group", among others. RDS theory describes the behavior of dynamical systems subject to external stochastic forcing; its tools have been developed to help study the geometric properties of stochastic differential equations (SDEs). In some sense, RDS theory is the stochastic counterpart of the geometric theory of ordinary differential equations (ODEs). This approach provides a rigorous mathematical framework for a stochastic form of robustness, while the more traditional, topological concepts do not seem to be appropriate.

3.2. RDSs, random attractors, and robust classification

Stochastic parametrizations for GCMs aim at compensating for our lack of detailed knowledge on small spatial scales in the best way possible [74–79]. The underlying assumption is that the associated time scales are also much shorter than the scales of interest and, therefore, the lag correlation of the phenomena being parametrized is negligibly small. Stochastic parametrizations thus essentially transform a deterministic autonomous system into a nonautonomous one, subject to random forcing.

Explicit time dependence in a dynamical system immediately raises a technical difficulty. Indeed, the classical notion of attractor is not always relevant, since any object in phase space is "moving" with time and the natural concept of forward asymptotics is meaningless. One needs therefore another notion of attractor. In the deterministic nonautonomous framework, the appropriate notion is that of a *pullback attractor* [80], which we present below. The closely related notion of *random attractor* in the stochastic framework is also explained briefly below, with further details given in Appendix A.

3.2.1. Framework and objectives

Before defining the notion of pullback attractor, let us recall some basic facts about nonautonomous dynamical systems. Consider the ODE

$$\dot{x} = f(t, x) \tag{3}$$

on a vector space X; this space could even be infinite-dimensional, if we were dealing with partial or functional differential equations, as is often the case in fluid-flow and climate problems. Rigorously speaking, we cannot associate a dynamical system acting on X with a nonautonomous ODE; nevertheless, in the case of unique solvability of the initial-value problem, we can introduce a two-parameter family of operators $\{S(t,s)\}_{t\geq s}$ acting on X, with s and t real, such that $S(t,s)x(s) = x(t)$ for $t \geq s$, where $x(t)$ is the solution of the Cauchy problem with initial data $x(s)$. This family of operators satisfies $S(s,s) = \mathrm{Id}_X$ and $S(t,\tau) \circ S(\tau,s) = S(t,s)$ for all $t \geq \tau \geq s$, and all real s. This family of operators is called a "process" by Sell [81]. It extends the classical notion of the resolvent of a nonautonomous linear ODE to the nonlinear setting.

We can now define the pullback attractor as simply the family of invariant sets $\{\mathcal{A}(t)\}$ that satisfy for every real t and all x_0 in X:

$$\lim_{s\to-\infty} \mathrm{dist}\,(S(t,s)x_0, \mathcal{A}(t)) = 0. \tag{4}$$

"Pullback" attraction does not involve running time backwards; it corresponds instead to the idea of measurements being performed at present time t in an experiment that was started at some time $s < t$ in the past: the experiment has been running for long enough, and we are thus looking now at an "attracting state". Note that there exists several ways of defining a pullback attractor — the one retained here is a local one (*cf.* [80] and references therein); see [82] for further information on nonautonomous dynamical systems in general.

In the stochastic context, noise forcing is modeled by a stationary stochastic process. If the deterministic dynamical system of interest is coupled to this stochastic process in a reasonable way – to be expressed below by the "cocycle property" – then random pullback attractors may appear. These pullback attractors will exist for almost each sample path of the driving stochastic process, so that the same probability distribution governs both sample paths and their corresponding pullback attractors. A more detailed explanation is given in Appendix A.

Roughly speaking, this concept of *random attractor* provides a geometric framework for the description of asymptotic regimes in the context of stochastic dynamics. To compare different stochastic systems in terms of their random attractors that evolve in time, it would be nice to be able to identify the common underlying geometric structures via a random change of variables. This identification is achieved through the concept of *stochastic equivalence* that is developed in Appendix A, and it is central in obtaining a coarser and more robust classification than in the purely deterministic context.

Returning now to our main objective, suppose for instance that one is presented with results from two distinct GCMs, say two probability distributions functions (PDFs) of the temperature or precipitation in a given area. These two PDFs are generated, typically, by an ensemble of each GCM's simulations, as described in the introduction, and they are likely to differ in their spatial pattern. To ascertain the physical significance of this discrepancy, one needs to know how each GCM result varies as either a parametrization or a parameter value are changed.

In order to consider the difficult question of why GCM responses to CO_2 doubling might differ, one idea is to investigate the structure of the space of all GCMs. We mean therewith the space of all deterministic GCMs, when their stochastic parametrizations are switched off. We know, by now, from experience with GCM results over several decades – including the four IPCC assessment reports [2–4] and the climate*prediction*.net exercise [6–8] – that there is enormous scatter in this space; see also [84,85]. Our question, therefore, is: can we achieve a more robust classification of GCMs when stochastic parametrizations are used and for a given level of the noise?

As mentioned in Section 3.1, such a classification is not feasible by restricting ourself to deterministic systems and topological concepts. As one switches on stochastic parametrizations [74–79], the situation might change, and hopefully improve, dramatically: as the noise level becomes large enough, the models' deterministic behavior may be completely destroyed, and all the results could cluster into one huge, diffuse clump. We would like, therefore, to investigate how a classification based on stochastic equivalence evolves as the level of the noise or the stochastic parametrizations change. As the noise tends to zero, do we recover the "granularity" of the set of all deterministic dynamical systems? This idea is schematically represented in Fig. 6: for a given level of the noise, we expect the space of all GCMs to be decomposed into a possibly finite number of classes. Within one of these classes, all the GCMs are topologically equivalent in the stochastic sense defined above; see Eq. (A.2).

Serious difficulties might arise in this program, due to the presence of nonhyperbolic chaos in climate models. Several studies have pointed out that the characteristics of nonhyperbolic chaos in the presence of noise may depend on its intensity and statistics [86–89].

Such issues, however, go well beyond the setting of this paper and are left for further investigation. Much more modestly, we will study here whether, in certain very simple

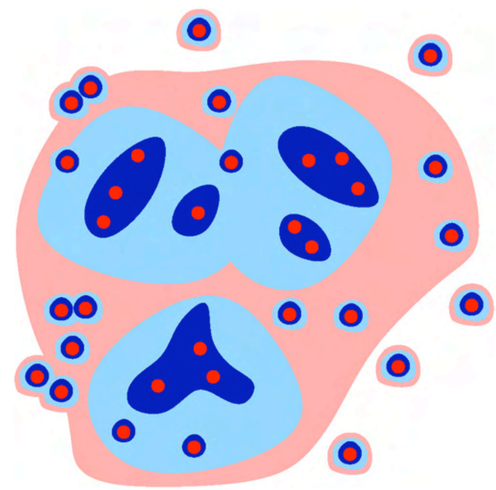

Fig. 6. A conjectural view of stochastic classification for GCMs, using the concept of random attractors. Each point in red represents a GCM in which stochastic parametrizations are switched off, while each gray area represents a cluster of stochastically equivalent GCMs for a given level of the noise.

cases, the conjectural view of Fig. 6 might be relevant for some dynamical systems that are "metaphors" of climate dynamics. The following subsection is dedicated to the study of such a metaphorical object, namely the Arnol'd circle map.

3.2.2. *The stochastically perturbed circle map*

To go beyond our pictorial view of stochastic classification for GCMs in Fig. 6, we study now the effect of noise on a family of diffeomorphisms of the circle. This toy model exhibits two features of interest for our purpose. The first one is that the two-parameter family $\{F_{\tau,\epsilon}\}$ defined by Eq. (5) below exhibits an infinite number of topological classes [18]. The second feature of interest is the frequency-locking behavior observed in many field of physics in general [90–92] and in some El-Niño/Southern-Oscillation (ENSO) models in particular [93–99]. Studying noise effects on these two features has, therefore, physical and mathematical, as well as climatological relevance.

Many physical and biological systems exhibit interference effects due to competing periodicities. One such effect is mode locking, which is due to nonlinear interaction between an "internal" frequency ω_i of the system and an "external" frequency ω_e. In the ENSO case, the external periodicity is the seasonal cycle. A simple model for systems with two competing periodicities is the well-known Arnol'd family of circle maps

$$x_{n+1} = F_{\tau,\epsilon}(x_n) := x_n + \tau - \epsilon \sin(2\pi x_n) \bmod 1, \tag{5}$$

where basically $\tau := \omega_i/\omega_e$ and ϵ parameterizes the magnitude of nonlinear effects; the map (5) is often called the *standard circle map* [18].

These maps also represent frequency locking near a bifurcation of Neimark-Sacker type (*e.g.* [100], p. 434); here the parameter τ is typically interpreted as the novel (internal) frequency involved in the bifurcation and ϵ corresponds to the nonlinearity near the bifurcation.

Such nonlinear coupling between two oscillators gives rise to a characteristic pattern, in the plane of ϵ *vs.* τ, called Arnol'd tongues. We computed this pattern numerically for the family

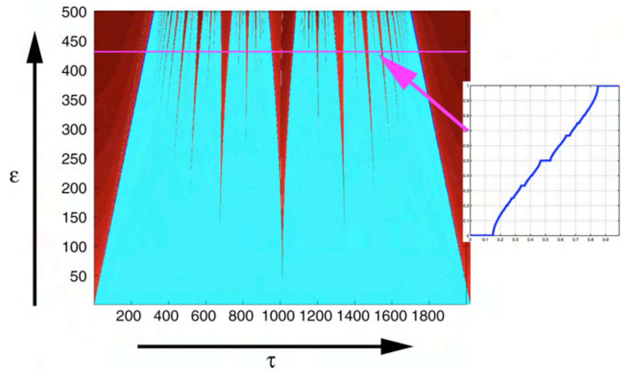

Fig. 7. Arnol'd tongues for the family of diffeomorphisms of the circle; units for τ and ϵ are 5×10^{-4} and 10^{-4} respectively. Devil's staircase in the cross-section to the right.

of Eq. (5), together with a cross-section at a fixed value of ϵ; see Fig. 7. This cross-section exhibits the so-called Devil's staircase, with "steps" on which the *rotation number* [58] is constant within each Arnol'd tongue; the rotation number measures the average rotation per iterate of (5).

For $\epsilon = 0$, two types of phenomena occur: either τ is rational and in this case the dynamics is periodic with period q, where $\tau = p/q$, or τ is irrational and the iterates $\{x_n\}$ fill the whole circle densely. As ϵ increases, an Arnol'd tongue of increasing width grows out of each $\tau = p/q$ on the abscissa $\epsilon = 0$. It follows that, in this very simple case, such an Arnol'd tongue corresponds to hyperbolic dynamics that is robust to perturbations, as verified by linearizing the map at the periodic point; the rotation number is then rational and equal to p/q.

The set of all these tongues is dense within the whole circle map family, while the Lebesgue measure of this set, at given ϵ, tends to zero as ϵ goes to zero. On the contrary, if a point in the (τ, ϵ)-plane does not belong to an Arnol'd tongue, the rotation number for those parameter values is irrational and the dynamics is nonhyperbolic; the latter fact follows, for instance, from a theorem of Denjoy [101] showing that such dynamics is smoothly equivalent to an irrational rotation. The probability to observe nonhyperbolic dynamics tends therewith to unity as ϵ goes to zero. One has, therefore, a countably infinite number of distinct topological classes, namely the Arnol'd tongues p/q, and an uncoutably infinite number of maps with irrational rotation numbers.

What happens when noise is added in Eq. (5)? We consider here the case of additive forcing by a noise process obtained via sampling at each iterate n a random variable with uniform density and intensity σ. Experiments with colored, rather than white noise and multiplicative, rather than additive noise led to the same qualitative results. The results for additive white noise are shown in Fig. 8 for three different levels of noise intensity σ.

As expected, only the largest tongues survive the presence of the noise; in particular, there is only a finite number of surviving tongues, shown in red in Fig. 8. Within such a surviving tongue, the random attractor $\mathcal{A}(\omega)$ is a random periodic cycle of period q (not shown). In the blue region outside the Arnol'd tongues, the random attractor is a fixed but random point $\mathcal{A}(\omega) = \{a(\omega)\}$: if one starts a numerical simulation for a fixed realization of the noise ω, all initial data x converge to the same fixed point a, say.

We illustrate this remarkable property in Fig. 9 in the case of a random fixed point, for given ϵ and τ. The Lyapunov exponent for the three distinct trajectories shown in the figure is strictly negative and the trajectories are exponentially attracted to the single random fixed point $a(\omega)$, the realization of the driving system $\theta(\omega)$ being the same for all the trajectories; see Appendices A and B. Kaijser [102] provided rigorous results on this type of synchronization phenomenon, but in a totally different conceptual setting. Interestingly, as the noise intensity increases, the Lyapunov exponent becomes more negative, so that the synchronization occurs even more rapidly, given a fixed realization ω.

This clustering behavior of trajectories with different initial data is in fact well known for flows on the circle [103]. In our example, this phenomenon in phase space is related to a smoothing of the Devil's staircase in parameter space, the latter cannot be solely explained by the former. Indeed, we show in Appendix B that for different irrational numbers and a sufficiently high noise level, the corresponding stochastic dynamics are stochastically equivalent, an equivalence that results in the smoothing of certain steps of the Devil's staircase.

As shown in the lower panel of Fig. 8, there is also a direct relationship between the random dynamics and the support of the PDF on the circle. For a given noise level, this support can either be the union of a finite number of disjoint intervals (red and blue curves) or it can fill the whole circle (black curve). The random attractor is, accordingly, either a random periodic orbit, with the disjoint intervals being visited in succession, or a random fixed point; this PDF behavior characterizes the level of the noise needed to destroy a given tongue.

An exact definition of random fixed point and random periodic orbit is given in Appendix B, where we provide a rigorous justification of the numerical results in Figs. 7–9. This theoretical analysis helps clarify the interaction between noise and nonlinear dynamics in the context of the GCM classification problem we are interested in.

4. Concluding remarks

We recall that Section 2 dealt with the natural, interannual and interdecadal variability of the ocean's wind-driven circulation. The oceans' internal variability is an important source of uncertainty in past-climate reconstructions and future-climate projections [9–12]. In Section 3 and Appendices A and B, we dealt more generally with the problem of structural instability as a possible cause for the stubborn tendency of the range of uncertainties in climate change projections to increase, rather than diminish over the last three decades [1–4]; see again Fig. 1. We summarize here the main results of the two sections in succession, and outline several open problems.

The wind-driven double-gyre circulation dominates the near-surface flow in the oceans' mid-latitude basins. Particular attention was paid to the North Atlantic and North Pacific, traversed by the best-known oceanic jets, namely the Gulf

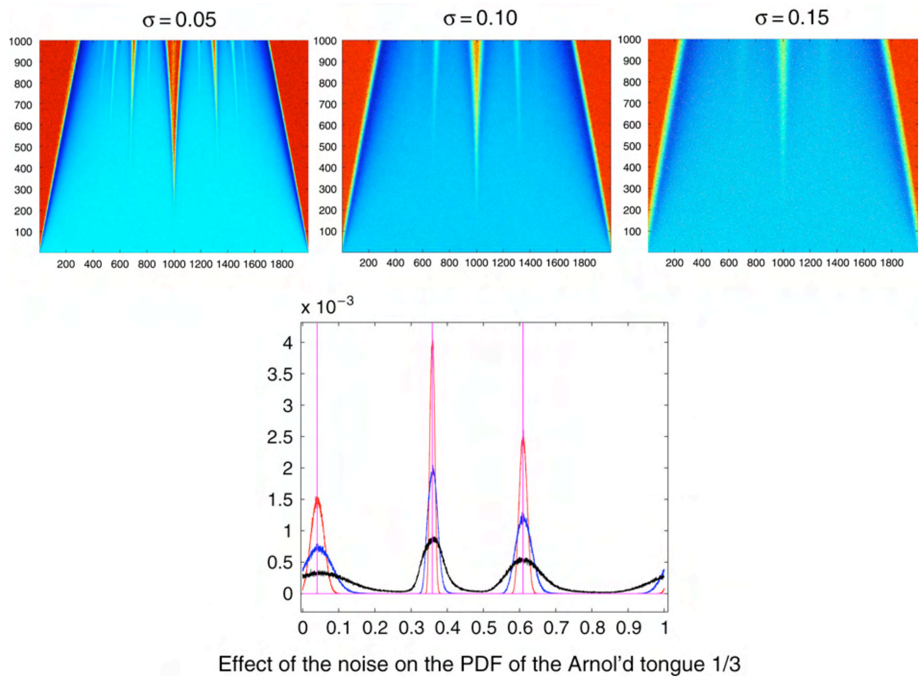

Fig. 8. Arnol'd tongues in the presence of additive noise with different noise amplitudes σ. Upper panels: Arnol'd tongues for $\sigma = 0.05, 0.10$ and 0.15; lower panel: PDF for $\epsilon = 0.9$ and the three σ-values in the upper panels: $\sigma = 0.05$ (red curve), $\sigma = 0.10$ (blue curve), and $\sigma = 0.15$ (black curve).

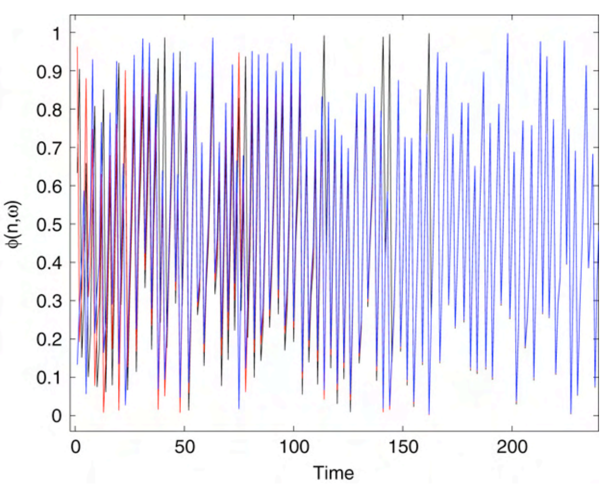

Fig. 9. Synchronization by additive noise: three distinct trajectories (in blue, red and black) of $x_{n+1} = F_{\tau,\epsilon;\omega}(x_n)$, with $F_{\tau,\epsilon;\omega}$ given by (B.1); the three trajectories start from three initial points on the circle, but are driven by the same realization ω of the noise, and thus converge to the same random fixed point $a(\omega)$, which is moving with time. The parameters are $\epsilon = 0.5$, $\tau = 0.283$ and $\sigma = 0.3$, and the corresponding Lyapunov exponent is $\lambda \simeq -0.0104$.

Stream and the Kuroshio Extension (see Fig. 2). The wind-driven circulation exhibits very rich internal dynamics and multiscale behavior associated with turbulent mesoscales (see Fig. 3). Aside from the intrinsic interest of this problem in physical oceanography, these major oceanic currents help regulate the climate of the adjacent continents, while their low-frequency variability affects past, present and future global climate.

Thanks in part to the systematic use of dynamical systems theory, a comprehensive understanding of simple, barotropic, quasi-geostrophic (QG) models of the double-gyre circulation has been achieved over the last two decades, and was reviewed in Section 2 here. In particular, the importance of symmetry-breaking and homoclinic bifurcations (see Fig. 4) in explaining the observed low-frequency variability has been validated across a wide hierarchy of models, including models with much more comprehensive physical formulation, more realistic geometry, and greater resolution in the horizontal and vertical [11,12]. This successive-bifurcation theory also provides a self-consistent explanation for the climatically important 7-year and 14-year oscillations of the oceanic circulation and the related atmospheric phenomena in and around the North-Atlantic basin [11,12,24–29,45,46].

The next challenge in physical oceanography is to reconcile the points of view of dynamical systems theory and statistical mechanics in describing the interaction between the largest scales of motion and geostrophic mesoscale turbulence, which is fully captured in baroclinic QG models. We emphasize that the complexity of these models of the double-gyre circulation is intermediate between high-end GCMs and simple "toy" models; these models offer, therefore, an ideal laboratory to test our ideas. In particular, stochastic parametrizations of the rectification process, absent in barotropic QG models, could be studied using some of the concepts and tools from RDS theory presented here. Note that the RDS approach has already been used in the context of stochastic partial differential equations, in particular for showing the existence of random attractors, as well as stable, unstable and inertial manifolds. Thus RDS concepts and tools are not restricted to finite-dimensional systems [104–106].

In Section 3, we have addressed the range-of-uncertainty problem for IPCC-class GCM simulations (see Fig. 1) by considering them as stochastically perturbed dynamical systems. This approach is consonant with recent interest for stochastic parametrizations in the high-end modeling-and-simulation community [74–79]. Rigorous mathematical results from the dynamical systems literature suggest that – in the absence of stochastic ingredients – GCMs as well as simpler models, found on the lower rungs of the modeling hierarchy [17], are bound to differ from each other in their results.

This sensitivity follows from the fact that, among deterministic dynamical systems, those that are hyperbolic are essentially the only ones that are also structurally stable, at least in the C^1 case [62–65]. Thus, because hyperbolic systems are not dense in the set of smooth deterministic ones [67], we are led to conclude that the topological, structural-stability approach does not guarantee deterministic-model robustness, in spite of its many valuable contributions so far. Related issues for GCM modeling were emphasized recently by Mitchell [83], Held [84] and McWilliams [85].

We have gone one step further and considered model robustness in the presence of stochastic terms; such terms could represent either parametrizations of unresolved processes in GCMs or stochastic components of natural or anthropogenic forcing, such as volcanic eruptions or fluctuations in greenhouse gas or aerosol emissions. Despite the obvious gap between idealized models and high-end simulations, we have brought to bear random dynamical systems (RDS) theory [20] on the former.

In this framework, we have considered a robustness criterion that could replace structural stability, through the concept of stochastic conjugacy (see Figs. A.1 and A.2). We have shown, for a stochastically perturbed Arnol'd family of circle maps, that noise can enhance model robustness. More precisely, this circle map family exhibits structurally stable, as well as structurally unstable behavior. When noise is added, the entire family exhibits *stochastic* structural stability, based on the stochastic-conjugacy concept, even in those regions of parameter space where deterministic structural instability occurs for vanishing noise (see Figs. 7 and 8).

Clearly the hope that noise can smooth the very highly structured pattern of distinct behavior types for climate models, across the full hierarchy, has to be tempered by a number of caveats. First, serious questions remain at the fundamental, mathematical level about the behavior of nonhyperbolic chaotic attractors in the presence of noise [86–88]. Likewise, the case of driving by nonergodic noise is being actively studied [107–109].

Second, the presence of certain manifestations of a Devil's staircase has been documented across the full hierarchy of ENSO models [17,93–99], as well as in certain observations [17,99]. Interestingly, both GCMs and observations only exhibit a few, broad steps of the staircase, such as $4:1 = 4$ yr, $4:2 = 2$ yr, and $4:3 \cong 16$ months. Does this result actually support the idea that nature and its detailed models always provide sufficient noise to achieve considerable smoothing of the much finer structure apparent in simpler models? Be that as it may, we need a much better understanding of how different types of noise – additive and multiplicative, white and colored – act across even a partial hierarchy of models, say from the simplest ones, like those studied in Section 3, to the intermediate ones considered in Section 2.

Third, one needs to connect more closely the nature of a stochastic parametrization and its effects on the model's behavior in phase-parameter space. As shown in Appendix B, not all types of noise are equal with respect to these effects. We are thus left with a rich, and hopefully fruitful, set of questions, which we expect to pursue in future work.

Acknowledgements

It is a pleasure to thank the organizers and participants of the Conference on the "*Euler Equations: 250 Years On*" and, more than all, Uriel Frisch, for a stimulating and altogether pleasant experience. We are grateful to I.M. Held, J.C. McWilliams, J.D. Neelin and I. Zaliapin for many useful discussions and their continuing interest in the questions studied here. A. Sobolevskiĭ, E. Tziperman and an anonymous reviewer have provided constructive criticism and stimulating remarks that helped improve the presentation. This study was supported by the US Department of Energy grant DE-FG02-07ER64439 from its Climate Change Prediction Program, and by the European Commission's No. 12975 (NEST) project "Extreme Events: Causes and Consequences (E2-C2)".

Appendix A. RDSs and random attractors

We present here briefly the mathematical concepts and tools of random dynamical systems, random attractors and stochastic equivalence. We shall use the concept of pullback attractor introduced in Section 3.2.1 to define the closely related notion of a random attractor, but need first to define an RDS. We denote by $\mathbb{T}$ the set $\mathbb{Z}$, for maps, or $\mathbb{R}$, for flows. Let $(X, \mathcal{B})$ be a measurable phase space, and $(\Omega, \mathcal{F}, \mathbb{P}, (\theta(t))_{t\in\mathbb{T}})$ be a *metric* dynamical system *i.e.* a flow in the probability space $(\Omega, \mathcal{F}, \mathbb{P})$, such that $(t, \omega) \mapsto \theta(t)\omega$ is measurable and $\theta(t) : \Omega \to \Omega$ is measure preserving, *i.e.* $\theta(t)\mathbb{P} = \mathbb{P}$.

Let $\varphi : \mathbb{T}\times\Omega\times X \to X$, $(t, \omega, x) \mapsto \varphi(t, \omega)x$, be a mapping with the two following properties:

(R_1) : $\varphi(0, \omega) = \mathrm{Id}_X$, and
(R_2) (the cocycle property): For all $s, t \in \mathbb{T}$ and all $\omega \in \Omega$,

$$\varphi(t + s, \omega) = \varphi(t, \theta(s)\omega) \circ \varphi(s, \omega).$$

If φ is measurable, it is called a *measurable* RDS over θ. If, in addition, X is a topological space (respectively a Banach space), and φ satisfies $(t, \omega) \mapsto \varphi(t, \omega)x$ continuous (resp. C^k, $1 \le k \le \infty$) for all $(t, \omega) \in \mathbb{T}\times\Omega$, then φ is called a *continuous* (resp. C^k) RDS over the flow θ. If so, then

$$(\omega, x) \mapsto \Theta(t)(x, \omega) := (\theta(t)\omega, \varphi(t, \omega)x), \tag{A.1}$$

is a (measurable) flow on $\Omega \times X$, and is called the *skew-product* of θ and φ. In the sequel, we shall use the terms "RDS" or "cocycle" synonymously.

The choice of the so-called *driving system* θ is a crucial step in this set-up; it is mostly dictated by the fact that the coupling

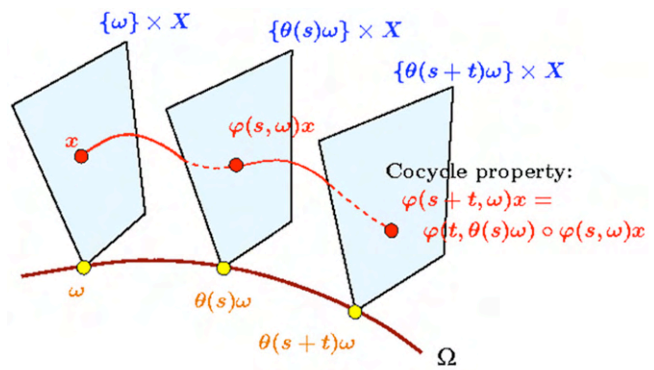

Fig. A.1. Random dynamical systems (RDS) viewed as a flow on the bundle $X \times \Omega =$ "dynamical space" $\times$ "probability space". For a given state x and realization ω, the RDS φ is such that $\Theta(t)(x, \omega) = (\theta(t)\omega, \varphi(t, \omega)x)$ is a flow on the bundle.

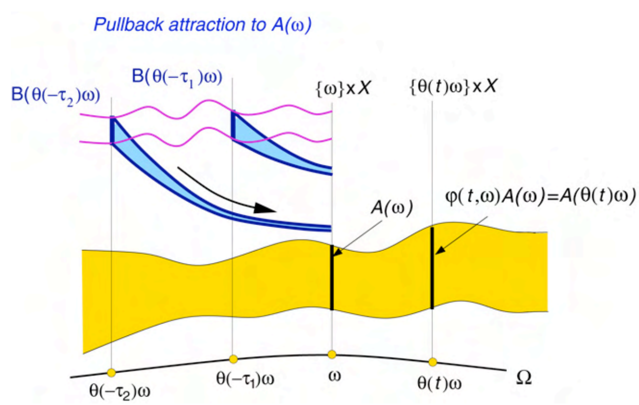

Fig. A.2. Schematic diagram of a random attractor $\mathcal{A}(\omega)$, where $\omega \in \Omega$ is a fixed realization of the noise. To be attracting, for every set B of X in a family $\mathfrak{B}$ of such sets, one must have $\lim_{t\to+\infty} \mathrm{dist}(B(\theta(-t)\omega), \mathcal{A}(\omega)) = 0$ with $B(\theta(-t)\omega) := \varphi(t, \theta(-t)\omega)B$; to be invariant, one must have $\varphi(t, \omega)\mathcal{A}(\omega) = \mathcal{A}(\theta(t)\omega)$. This definition depends strongly on $\mathfrak{B}$; see [112] for more details.

between the stationary driving and the deterministic dynamics should respect the time invariance of the former, as illustrated in Fig. A.1. The driving system θ also plays an important role in establishing *stochastic conjugacy* [110] and hence the kind of classification we aim at.

The concept of *random attractor* is a natural and straightforward extension of the definition of pullback attractor (4), in which Sell's [81] process is replaced by a cocycle, *cf.* Fig. A.1, and the attractor $\mathcal{A}$ now depends on the realization ω of the noise, so that we have a family of random attractors $\mathcal{A}(\omega)$, *cf.* Fig. A.2. Roughly speaking, for a fixed realization of the noise, one "rewinds" the noise back to $t \to -\infty$ and lets the experiment evolve (forward in time) towards a possibly attracting set $\mathcal{A}(\omega)$; the driving system θ enables one to do this rewinding without changing the statistics, cf. Figs. A.1 and A.2.

Other notions of attractor can be defined in the stochastic context, in particular based on the original SDE; see [111] or [112] for a discussion on this topic. The present definition, though, will serve us well.

Having defined RDSs and random attractors, we now introduce the notion of *stochastic equivalence* or *conjugacy*, in order to rigourously compare two RDSs; it is defined as follows: two cocycles $\varphi_1(\omega, t)$ and $\varphi_2(\omega, t)$ are conjugated if and only if there exists a random homeomorphism $h \in \mathrm{Homeo}(X)$ and an invariant set such that $h(\omega)(0) = 0$ and

$$\varphi_1(\omega, t) = h(\theta(t)\omega)^{-1} \circ \varphi_2(\omega, t) \circ h(\omega). \tag{A.2}$$

Stochastic equivalence extends classic topological conjugacy to the bundle space $X \times \Omega$, stating that there exists a one-to-one, stochastic change of variables that continuously transforms the phase portrait of one sample system in X into that of any other such system.

Appendix B. Coarse-graining of the circle map family

We provide here a rigorous justification of the numerical results obtained in Section 3.2.2 on the topological classification of the family of Arnol'd circle maps in the presence of noise. Consider the following random family of diffeomorphisms:

$$F_{\tau,\epsilon;\omega}(x) := x + \tau + \sigma\omega - \epsilon \sin(2\pi x) \mod 1, \tag{B.1}$$

for $x \in \mathbb{S}^1$, ϵ a real parameter in $(0, 1)$, and ω a random parameter distributed in the compact interval $I = [-1/2, 1/2]$ with fixed distribution ν and noise intensity σ. We denote by $F_{\tau,\epsilon}$ the corresponding deterministic family of diffeomorphisms when the noise is switched off, $\sigma = 0$.

In the RDS framework, we need to specify the metric dynamical system modeling the noise. We choose here the interval σI as the base for the probability space Ω and define the flow θ simply as mapping the point ω into its successor in a sequence of realizations of the noise. One could also use an irrational rotation on Ω for instance; in either case, ergodicity is ensured.

For the sake of simplicity, we omit for the moment the dependence on τ and ϵ. In discrete time, with $\mathbb{T} = \mathbb{Z}$, we define a map $\phi : \mathbb{T} \times \Omega \times \mathbb{S}^1 \to \mathbb{S}^1$, $(n, \omega, x) \mapsto \phi(n, \omega)x$, such that

$$\phi(n, \omega) := \begin{cases} F_{\theta^{n-1}\omega} \circ \cdots \circ F_{\omega}, & n \geq 1, \\ \mathrm{Id}_{\mathbb{S}^1}, & n = 0, \\ F^{-1}_{\theta^n\omega} \circ \cdots \circ F^{-1}_{\theta^{-1}\omega}, & n \leq -1. \end{cases} \tag{B.2}$$

One can prove easily that this ϕ satisfies the cocycle property and is in fact a C^∞ RDS on $\mathbb{S}^1$ over θ.

The pair of mappings $\Theta := (\theta, \phi)$ is the corresponding skew-product (A.1), and it defines a flow on $\Omega \times \mathbb{S}^1$ by the relation:

$$(\omega, x) \mapsto \Theta(n)(\omega, x) := (\theta^n\omega, \phi(n, \omega)x). \tag{B.3}$$

A stationary measure m on $\mathbb{S}^1$ under the random diffeomorphism $F_{\tau,\epsilon;\omega}$ yields a Θ-invariant measure $\mu := m \times \nu$, *i.e.* $\Theta_n\mu = \mu$; explicitly,

$$\int_{\Omega\times\mathbb{S}^1} f(\omega, x)\mu(\mathrm{d}\omega, \mathrm{d}x) = \int_{\Omega\times\mathbb{S}^1} f(\theta_n\omega, \phi(n, \omega)x)\mu(\mathrm{d}\omega, \mathrm{d}x) \tag{B.4}$$

for all $n \in \mathbb{T}$ and $f \in L^1(\Omega \times \mathbb{S}^1, \mu)$.

Let us recall the following important proposition [113] concerning the stationary measures obtained from the random family $\{F_{\tau,\epsilon;\omega}\}$.

Theorem 1. *The random circle diffeomorphism $F_{\tau,\epsilon;\omega}$ has a unique stationary measure $m_{\tau,\epsilon}$. The support of $m_{\tau,\epsilon}$ consists either of q mutually disjoint intervals or of the entire circle $\mathbb{S}^1$. The density function $\phi_{\tau,\epsilon}$ is in $C^\infty(\mathbb{S}^1)$ and depends C^∞ on τ. The invariant measure μ is ergodic. If the support of m is connected, then it is mixing and so is μ.*

Mixing for m means that, for any bounded function $f : \mathbb{S}^1 \to \mathbb{R}$, and for an arbitrary initial point $x_0 \in \mathbb{S}^1$, $\mathbb{E} f(\phi(n,\omega)x_0)$ tends to $\int_{\mathbb{S}^1} f(x)m(\mathrm{d}x)$ as $n \to +\infty$; see [114] for more on random attractors and mixing.

For deterministic diffeomorphisms of the circle, the rotation number measures the average rotation per iterate of $F_{\tau,\epsilon}$. In the presence of noise, one can still define a rotation number for $F_{\tau,\epsilon;\omega}$, namely

$$\rho_{\tau,\epsilon;\omega}(x) = \lim_{k\to\infty} \frac{\tilde{F}^k_{\tau,\epsilon;\omega}(x) - x}{k}, \tag{B.5}$$

where $\tilde{F}$ denotes the lift of a map F, acting on $\mathbb{S}^1$ modulo 1, to a map acting on $\mathbb{R}$. For fixed τ and ϵ, we can then show that $\rho_{\tau,\epsilon;\omega}$ exists for ν-almost all ω and is a constant; this constant $\rho_{\tau;\omega}$ is independent of x and ω [113]. Furthermore, $\tau \to \rho_{\tau,\epsilon}$ is C^∞ for each ϵ, which is not true in the deterministic case with $\sigma = 0$; see again [113].

Theorem 1 has a natural geometric counterpart in terms of random attractors, as confirmed through our numerical study; see again Fig. 8. More precisely, we introduce also the following definitions of *random fixed point* and *random periodic orbit*; these definitions differ somewhat from those given in [113].

Definition 1. A random fixed point is a measurable map $a : \Omega \to \mathbb{S}^1$ for which

$$\phi(1,\omega)a(\omega) = a(\theta(\omega)), \tag{B.6}$$

for ν-almost all $\omega \in \Omega$, *i.e.* such that $\Omega \times a(\Omega)$ is an invariant set for the flow given by the skew-product Θ. A random periodic orbit of period q is likewise an invariant set with cardinality q in fibers $\mathbb{S}^1 \times \{\omega\}$ for ν-almost all ω.

With these definitions, the following results of [113] still hold.

Theorem 2. *For a random diffeomorphism $F_{\tau,\epsilon;\omega}$ of the circle $\mathbb{S}^1$, with a stationary measure m supported on a union E of q disjoint intervals, the corresponding skew-product Θ restricted to E has precisely one attracting random periodic orbit and one repelling random periodic orbit.*

Attraction in the preceding theorem means that $\lim_{n\to\infty} |F^n_\omega(x) - F^n_\omega(a(\omega))| = 0$, for a set of initial data $(x,\omega) \in \mathbb{S}^1 \times \Omega$ with positive $\lambda \times \nu$-measure, in the case of a random attracting fixed point; here λ is Lebesgue measure on $\mathbb{S}^1$ and the extension to a random periodic orbit is obvious.

Using these two theorems and rigorous results on random point attractors [112], we can show that (i) if the support of the stationary measure is the whole circle (black curve in Fig. 8), then there exists one random fixed point which is pullback attracting; and (ii) if the support consists of q disjoint intervals, then the random attractor is a random periodic orbit of period q (red and blue curves).

Having explained how the connectedness of the PDF support at different noise levels is related to the nature of the random attractor, we now turn to an explanation of the "disappearance" of the smaller steps in the Devil's staircase, as the noise level increases. To do so, we consider the Lyapunov spectrum of an RDS, which still relies on the Oseledets [115] *multiplicative ergodic theorem* (MET).

To state an MET for RDS on manifolds, we differentiate $\phi(n,\omega)$ at $x \in \mathbb{S}^1$, and obtain the linear map

$$T\phi(n,\omega,x) : T_x M \to T_{\phi(n,\omega)x} M, \tag{B.7}$$

where $T\phi$ is a continuous linear cocycle on the tangent bundle TM of the manifold M over the skew-product flow Θ. If the flow ϕ possesses an ergodic invariant measure μ such that the required integrability condition for applying the MET is verified with respect to μ, then the MET holds for ϕ over M [116].

Because of Theorem 1 here, we can apply the MET to our problem and conclude that a unique Lyapunov exponent exists for the *linearization* of each diffeomorphism belonging to our family of random diffeomorphisms, and that this exponent is independent of the realization of the noise. We show next how to use the Lyapunov spectrum in studying the stochastic equivalence classes of a given RDS family, along with its driving system θ. This last aspect of the classification problem is outlined for linear hyperbolic cocycles.

Cong [117] has shown that, even in the linear context, the main difference with respect to the deterministic case is that the classification depends strongly on the properties of θ, which is directly linked to the system noise and its modeling. For instance, if θ is an irrational rotation on $\mathbb{S}^1$, one can construct infinitely many classes of hyperbolic cocycles that are not pairwise topologically equivalent, by playing essentially with the orientations of the cocyles, *i.e.* reversing between clockwise and anticlockwise rotation on $\mathbb{S}^1$. As we shall see, such difficulties can be avoided in the case of noisy Arnol'd tongues, especially for additive noise. Related issues still form an active research area in RDS theory; see [116] for a brief survey.

A key ingredient for the linear classification is the notion of *coboundary*, which we recall herewith.

Definition 2. A measurable set $K \subset \Omega$ is called a *coboundary* if there exists a set $H \in \mathcal{F}$ such that $K = H\triangle\theta H$, where $H\triangle\theta H$ denotes the symmetric difference of H and θH.

Let A and B be two linear random maps on $\mathbb{R}^d$, and denote by deg $A(\omega)$ and deg $B(\omega)$ the degrees of the maps $A(\omega)$ and $B(\omega)$ with respect to a chosen random orientation. These degrees are just the sign of the determinant of the corresponding random matrices, and equal -1 or 1; see [110,117] for details.

Consider the two linear hyperbolic cocycles Φ_A and Φ_B, associated with the maps A and B, and the following subset of Ω:

$$C_{AB} = \{\omega \in \Omega |\deg A(\omega) \cdot \deg B(\omega) = -1\}; \tag{B.8}$$

C_{AB} is just the set of all $\omega \in \Omega$ for which the degrees of the two linear maps $A(\omega)$ and $B(\omega)$ differ.

The main theorem for the classification of our diffeomorphisms of $\mathbb{S}^1$ follows [117].

Theorem 3. *Two one-dimensional linear hyperbolic cocycles Φ_A and Φ_B are conjugate if and only if the following conditions hold:*

(i) *sign λ_A = sign λ_B, and*
(ii) *the associated set C_{AB} is a coboundary.*

Here λ_A and λ_B indicate the Lyapunov exponents of Φ_A and Φ_B, respectively.

Before applying this result, let us explain heuristically how a Devil's staircase step that corresponds to a rational rotation number can be "destroyed" by a sufficiently intense noise. Consider the period-1 locked state in the deterministic setting. At the beginning of this step, a pair of fixed points is created, one stable and the other unstable. As the bifurcation parameter is increased, these two points move away from each other, until they are π radians apart. Increasing the parameter further causes the fixed points to continue moving along, until they finally meet again and are annihilated in a *saddle-node bifurcation*, thus signaling the end of the locking interval.

When noise is added, we have to distinguish between a "strongly locked" regime, where the stable and unstable fixed points are nearly π radians apart, and a "weakly locked" regime, where these two fixed points are close to each other. In both regimes, the relaxation time in the vicinity of the stable point represents an important time scale of the problem. In the strongly locked regime, this is the only time scale of interest. In the weakly locked regime, though, the process of escaping across the unstable fixed point is non-negligible and the associated escape time becomes the second time scale of interest. From these heuristic considerations it follows that the distinction between strong and weak locking depends on the strength of the external noise.

If we consider period-T locked states, with $T \geq 2$, the same kind of reasoning can be applied to the stable and unstable T-cycle. We conclude therefore, for a fixed $\epsilon > 0$, that the narrower Devil's staircase steps are the least robust, while the wider ones are the most robust.

The fact that a locked case becomes unlocked when noise is growing implies in particular that the rotation number $\rho_{\tau,\epsilon}$ becomes *irrational* for a sufficiently high noise level. According to Theorem 2.1 of [102], the Lyapunov exponent is strictly *negative* in this case almost surely. Moreover, by reinterpreting other results of Kaijser [102] in our RDS framework, we can show that the random attractor is in fact a random fixed point; this, in turn, allows us to conclude that the corresponding linearized cocycle at this random fixed point is hyperbolic. Next, by using the Hartman-Grobman theorem for RDSs [118–120], we can conjugate the nonlinear cocycle with its linearization; in fact, Theorem 3.1 of [119] says that this conjugacy is global.

Consider now two linearized cocycles Φ_A and Φ_B, at one and the same or at two distinct random fixed points of the family of random diffeomorphisms, for the same noise intensity, and denote by $A(\omega)$ and $B(\omega)$ the random linear parts of the cocycles Φ_A and Φ_B respectively; it follows from our model of noisy circle maps that C_{AB} is empty. Indeed, the noise being additive, the random orientation is preserved for different parameter values. But θ is assumed to be ergodic, and so we have that $\Omega\Delta\theta\Omega$ is empty and, therefore, C_{AB} is a coboundary. Therewith, Theorem 3 can be applied to obtain the desired result for the problem considered here: with an appropriate amount of noise, two deterministic diffeomorphisms that are not topologically equivalent can fall into the same topological stochastic class! The numerical results of Section 3.2 are entirely in agreement with this assertion.

Note that the set C_{AB} could differ from a coboundary, if the noise occurred additively in the phase of the nonlinear term, for instance. Here we see the importance of noise modeling in obtaining the conjectural view of Fig. 6 for a family of dynamical systems in general.

It follows, in particular, that the exact nature of the stochastic parametrizations in a family of GCMs does matter. It's not enough to follow the trend by devising and implementing such parametrizations: one should test that a given parametrization, once found to be suitable in other respects, does improve the proximity, in an appropriate sense, between climate simulations within the family of GCMs for which it has been been developed.

References

[1] J. Charney, et al., Carbon Dioxide and Climate: A Scientific Assessment, National Academies Press, Washington, DC, 1979.
[2] J.T. Houghton, G.J. Jenkins, J.J. Ephraums (Eds.), Climate Change, The IPCC Scientific Assessment, Cambridge Univ. Press, Cambridge, MA, 1991, p. 365.
[3] J.T. Houghton, Y. Ding, D.J. Griggs, M. Noguer, P.J. van der Linden, X. Dai, K. Maskell, C.A. Johnson (Eds.), Climate Change 2001: The Scientific Basis. Contribution of Working Group I to the Third Assessment Report of the Intergovernmental Panel on Climate Change (IPCC), Cambridge University Press, Cambridge, UK, 2001, p. 944.
[4] S. Solomon, D. Qin, M. Manning, Z. Chen, M. Marquis, K.B. Averyt, M. Tignor, H.L. Miller (Eds.), Climate Change 2007: The Physical Science Basis. Contribution of Working Group I to the Fourth Assessment Report of the IPCC, Cambridge University Press, Cambridge, UK and New York, NY, USA, 2007.
[5] R. Hillerbrand, M. Ghil, Anthropogenic climate change: Scientific uncertainties and moral dilemmas, Physica D 237 (14–17) (2008) 2132–2138.
[6] M.R. Allen, Do-it-yourself climate prediction, Nature 401 (1999) 627.
[7] V.D. Pope, M. Gallani, P.R. Rowntree, R.A. Stratton, The impact of new physical parameterisations in the Hadley Centre climate model - HadAM3, Clim. Dyn. 16 (2000) 123–146.
[8] D.A. Stainforth, et al., Uncertainty in predictions of the climate response to rising levels of greenhouse gases, Nature 433 (2005) 403–406.
[9] D.G. Martinson, K. Bryan, M. Ghil, et al. (Eds.), National Research Council, Natural Climate Variability on Decade-to-Century Time Scales, National Academies Press, Washington, DC, 1995, p. 630.
[10] M. Ghil, Hilbert problems for the geosciences in the 21st century, Nonlin. Proc. Geophys. 8 (2001) 211–222.

[11] H.A. Dijkstra, M. Ghil, Low-frequency variability of the large-scale ocean circulation: A dynamical systems approach, Rev. Geophys. 43 (2005) RG3002. doi:10.1029/2002RG000122.
[12] H.A. Dijkstra, Nonlinear Physical Oceanography: A Dynamical Systems Approach to the Large Scale Ocean Circulation and El Niño, 2nd ed., Springer, 2005, p. 532.
[13] Y. Feliks, M. Ghil, E. Simonnet, Low-frequency variability in the mid-latitude atmosphere induced by an oceanic thermal front, J. Atmos. Sci. 61 (2004) 961–981.
[14] Y. Feliks, M. Ghil, E. Simonnet, Low-frequency variability in the mid-latitude baroclinic atmosphere induced by an oceanic thermal front, J. Atmos. Sci. 64 (2007) 97–116.
[15] R.A. Madden, P.R. Julian, Observations of the 40–50-day tropical oscillations — a review, Monthly Weather Rev. 122 (5) (1994) 814–837.
[16] J.D. Neelin, D.S. Battisti, A.C. Hirst, F.-F. Jin, Y. Wakata, T. Yamagata, S. Zebiak, ENSO theory, J. Geophys. Res. 103 (C7) (1998) 14261–14290.
[17] M. Ghil, A.W. Robertson, Solving problems with GCMs: General circulation models and their role in the climate modeling hierarchy, in: D. Randall (Ed.), General Circulation Model Development: Past, Present and Future, Academic Press, San Diego, 2000, pp. 285–325.
[18] V.I. Arnol'd, Geometrical Methods in the Theory of Differential Equations, Springer, 1983, p. 334.
[19] J. Guckenheimer, P. Holmes, Nonlinear Oscillations, Dynamical Systems and Bifurcations of Vector Fields, 2nd ed., Springer-Verlag, 1991, p. 453.
[20] L. Arnold, Random Dynamical Systems, Springer-Verlag, 1998, p. 616.
[21] A.E. Gill, Atmosphere-Ocean Dynamics, Academic Press, 1982, p. 662.
[22] M. Ghil, S. Childress, Topics in Geophysical Fluid Dynamics: Atmospheric Dynamics, Dynamo Theory, and Climate Dynamics, Springer-Verlag, Berlin, Heidelberg, New York, 1987, p. 512.
[23] J. Pedlosky, Geophysical Fluid Dynamics, 2nd ed., Springer-Verlag, 1987, p. 710.
[24] V. Moron, R. Vautard, M. Ghil, Trends, interdecadal and interannual oscillations in global sea-surface temperatures, Clim. Dyn. 14 (1998) 545–569.
[25] C. Wunsch, The interpretation of short climate records, with comments on the North Atlantic and Southern Oscillations, Bull. Am. Meteorol. Soc. 80 (1999) 245–255.
[26] E.D. Da Costa, A.C. Colin de Verdière, The 7.7 year North Atlantic oscillation, Q. J. R. Meteorol. Soc. 128 (2004) 797–818.
[27] G. Plaut, M. Ghil, R. Vautard, Interannual and interdecadal variability in 335 years of Central England temperatures, Science 268 (1995) 710–713.
[28] M. Dubar, Approche climatique de la période romaine dans l'est du Var : recherche et analyse des composantes périodiques sur un concrétionnement centennal (Ier-IIe siècle apr. J.-C.) de l'aqueduc de Fréjus, Archeoscience 30 (2006) 163–171.
[29] D. Kondrashov, Y. Feliks, M. Ghil, Oscillatory modes of extended Nile River records (A.D. 622–1922), Geophys. Res. Lett. 32 (2005) L10702. doi:10.1029/2004GL022156.
[30] H. Stommel, The Gulf Stream: A Physical and Dynamical Description, 2nd ed., Cambridge Univ. Press, London, 1965, p. 248.
[31] S. Jiang, F.F. Jin, M. Ghil, The nonlinear behavior of western boundary currents in a wind-driven, double-gyre, shallow-water model, in: Ninth Conf. Atmos. & Oceanic Waves and Stability (San Antonio, TX), American Meterorological Society, Boston, Mass, 1993, pp. 64–67.
[32] S. Jiang, F.F. Jin, M. Ghil, Multiple equilibria, periodic, and aperiodic solutions in a wind-driven, double-gyre, shallow-water model, J. Phys. Oceanogr. 25 (1995) 764–786.
[33] P. Cessi, G.R. Ierley, Symmetry-breaking multiple equilibria in quasigeostrophic, wind-driven flows, J. Phys. Oceanogr. 25 (6) (1995) 1196–1205.
[34] H.U. Sverdrup, Wind-driven currents in a baroclinic ocean; with application to the equatorial currents of the eastern Pacific, Proc. Natl. Acad. Sci. USA 33 (1947) 318–326.
[35] S. Speich, H.A. Dijkstra, M. Ghil, Successive bifurcations in a shallow-water model applied to the wind-driven ocean circulation, Nonl. Proc. Geophys. 2 (1995) 241–268.
[36] H.A. Dijkstra, C.A. Katsman, Temporal variability of the wind-driven quasi-geostrophic double gyre ocean circulation: Basic bifurcation diagrams, Geophys. Astrophys. Fluid Dyn. 85 (1997) 195–232.
[37] V.A. Sheremet, G.R. Ierley, V.M. Kamenkovitch, Eigenanalysis of the two-dimensional wind-driven ocean circulation problem, J. Mar. Res. 55 (1997) 57–92.
[38] J. Pedlosky, Ocean Circulation Theory, Springer, New York, 1996.
[39] E. Simonnet, H.A. Dijkstra, Spontaneous generation of low-frequency modes of variability in the wind-driven ocean circulation, J. Phys. Oceanogr. 32 (2002) 1747–1762.
[40] E. Simonnet, R. Temam, S. Wang, M. Ghil, K. Ide, Successive bifurcations in a shallow-water ocean model, in: 16th Intl. Conf. Numerical Methods in Fluid Dynamics, in: Lecture Notes in Physics, vol. 515, Springer-Verlag, 1995, pp. 225–230.
[41] S.P. Meacham, Low-frequency variability in the wind-driven circulation, J. Phys. Oceanogr. 30 (2000) 269–293.
[42] K.I. Chang, K. Ide, M. Ghil, C.-C.A. Lai, Transition to aperiodic variability in a wind-driven double-gyre circulation model, J. Phys. Oceanogr. 31 (2001) 1260–1286.
[43] N.T. Nadiga, B.P. Luce, Global bifurcation of Shilnikov type in a double-gyre ocean model, J. Phys. Oceanogr. 31 (2001) 2669–2690.
[44] E. Simonnet, M. Ghil, K. Ide, R. Temam, S. Wang, Low-frequency variability in shallow-water models of the wind-driven ocean circulation. Part I: Steady-state solutions, J. Phys. Oceanogr. 33 (2003) 712–728.
[45] E. Simonnet, M. Ghil, K. Ide, R. Temam, S. Wang, Low-frequency variability in shallow-water models of the wind-driven ocean circulation. Part II: Time-dependent solutions, Oceanogr. 33 (2003) 729–752.
[46] E. Simonnet, M. Ghil, H.A. Dijkstra, Homoclinic bifurcations in the quasi-geostrophic double-gyre circulation, J. Mar. Res. 63 (2005) 931–956.
[47] P. Berloff, A. Hogg, W. Dewar, The turbulent oscillator: A mechanism of low-frequency variability of the wind-driven ocean gyres, J. Phys. Oceanogr. 37 (2007) 2363–2386.
[48] S. Kravtsov, P. Berloff, W.K. Dewar, M. Ghil, J.C. McWilliams, Dynamical origin of low-frequency variability in a highly nonlinear mid-latitude coupled model, J. Climate 19 (2007) 6391–6408.
[49] E. Simonnet, Quantization of the low-frequency variability of the double-gyre circulation, J. Phys. Oceanogr. 35 (2005) 2268–2290.
[50] F.W. Primeau, Multiple equilibria and low-frequency variability of the wind-driven ocean circulation, J. Phys. Oceanogr. 32 (2002) 2236–2256.
[51] E. Simonnet, On the unstable discrete spectrum of the linearized 2-D Euler equations in bounded domains, Physica D, sub judice.
[52] L. Sushama, M. Ghil, K. Ide, Spatio-temporal variability in a mid-latitude ocean basin subject to periodic wind forcing, Atmosphere-Ocean 45 (2007) 227–250. doi:10.3137/ao.450404.
[53] C.A. Katsman, H.A. Dijkstra, S.S. Drijfhout, The rectification of the wind-driven ocean circulation due to its instabilities, J. Mar. Res. 56 (1998) 559–587.
[54] R. Robert, J. Sommeria, Statistical equilibrium states for two-dimensional flows, J. Fluid. Mech. 229 (1991) 291–310.
[55] L.N. Trefethen, A. Trefethen, S.C. Reddy, T.A. Driscoll, Hydrodynamic stability without eigenvalues, Science 261 (1993) 578–584.
[56] F. Bouchet, J. Sommeria, Emergence of intense jets and Jupiter's great red spot as maximum entropy structures, J. Fluid. Mech. 464 (2002) 465–207.
[57] B.F. Farrel, P.J. Ioannou, Structural stability of turbulent jets, J. Atmos. Sci. 60 (2003) 2101–2118.
[58] H. Poincaré, Sur les équations de la dynamique et le problème des trois corps, Acta Math. 13 (1890) 1–270.
[59] A.A. Andronov, L.S. Pontryagin, Systèmes grossiers, Dokl. Akad. Nauk. SSSR 14 (5) (1937) 247–250.
[60] S. Smale, Differentiable dynamical systems, Bull. Amer. Math. Soc. 73 (1967) 199–206.
[61] A. Katok, B. Haselblatt, Introduction to the Modern Theroy of Dynamical Systems, in: Encycl. Math. Appl., vol. 54, Cambridge Univ. Press, 1995, p. 822.
[62] J. Robbin, A structural stability theorem, Ann. Math. 94 (1971) 447–449.
[63] C. Robinson, Structural stability of C^1 diffeomorphisms, J. Differential Equations 22 (1976) 28–73.

[64] R. Mañé, A proof of the C^1-stability conjecture, Publ. Math, I.H.E.S. 66 (1987) 161–210.
[65] J. Palis, A global perspective for non-conservative dynamics, Ann. I.H. Poincaré 22 (2005) 485–507.
[66] M. Peixoto, Structural stability on two-dimensional manifolds, Topology 1 (1962) 101–110.
[67] S. Smale, Structurally stable systems are not dense, Amer. J. Math. 88 (2) (1966) 491–496.
[68] S. Newhouse, The abundance of wild hyperbolic sets and nonsmooth stable sets for diffeomorphisms, Publ. Math. I.H.E.S. 50 (1979) 101–150.
[69] E.N. Lorenz, Deterministic nonperiodic flow, J. Atmos. Sci. 20 (1963) 130–141.
[70] J. Guckenheimer, R.F. Williams, Structural stability of Lorenz attractors, Publ. Math. I.H.E.S. 50 (1979) 59–72.
[71] R.F. Williams, The structure of Lorenz attractors, Publ. Math. I.H.E.S. 50 (1979) 73–99.
[72] Y. Sinai, Gibbs measures in ergodic theory, Russian Math. Surveys 27 (1972) 21–69.
[73] J.P. Eckmann, D. Ruelle, Ergodic theory of chaos and strange attractors, Rev. Modern Phys. 57 (1985) 617–656; Rev. Modern Phys. 57 (1985) 1115 (addendum).
[74] J.W.B. Lin, J.D. Neelin, Influence of a stochastic moist convective parameterization on tropical climate variability, Geophys. Res. Lett. 27 (2000) 3691–3694.
[75] J.W.B. Lin, J.D. Neelin, Considerations for stochastic convective parameterization, J. Atmos. Sci. 59 (2002) 959–975.
[76] J.W.B. Lin, J.D. Neelin, Toward stochastic deep convective parameterization in general circulation models, Geophys. Res. Lett. 30 (2003) 1162. doi:10.1029/2002GL016203.
[77] T.N. Palmer, The prediction of uncertainty in weather and climate forecasting, Rep. Prog. Phys. 63 (2000) 71–116.
[78] T. Jung, T.N. Palmer, G.J. Shutts, Geophys. Res. Lett. 32 (2005) Art. No. L23811.
[79] B. Stevens, Y. Zhang, M. Ghil, Stochastic effects in the representation of stratocumulus-topped mixed layers, in: Proc. ECMWF Workshop on Representation of Sub-Grid Processes Using Stochastic-Dynamic Models, 6–8 June 2005, Shinfield Park, Reading, UK, pp. 79–90.
[80] J.A. Langa, J.C. Robinson, A. Suarez, Stability, instability, and bifurcation phenomena in non-autonomous differential equations, Nonlinearity 15 (2002) 887–903.
[81] G. Sell, Non-autonomous differential equations and dynamical systems, Trans. Amer. Math. Soc. 127 (1967) 241–283.
[82] A. Berger, S. Siegmund, On the gap between random dynamical systems and continuous skew products, J. Dyn. Diff. Eq. 15 (2003) 237–279.
[83] J.F.B. Mitchell, Can we believe predictions of climate change? Quart. J. Roy. Meteorol. Soc. (Part A) 130 (2004) 2341–2360.
[84] I.M. Held, The gap between simulation and understanding in climate modeling, Bull. Amer. Meteo. Soc. 86 (2005) 1609–1614.
[85] J.C. McWilliams, Irreducible imprecision in atmospheric and oceanic simulations, PNAS 104 (21) (2007) 8709–8713.
[86] V.S. Anishchenko, T.E. Vadivasova, A.S. Kopeikin, J. Kurths, G.I. Strelkova, Effect of noise on the relaxation to an invariant probability measure of nonhyperbolic chaotic attractors, Phys. Rev. Lett. 87 (5) (2001) 054101-1–054101-4.
[87] V.S. Anishchenko, T.E. Vadivasova, A.S. Kopeikin, G.I. Strelkova, J. Kurths, Influence of noise on statistical properties of nonhyperbolic attractors, Phys. Rev. E 62 (2000) 7886.
[88] V.S. Anishchenko, T.E. Vadivasova, A.S. Kopeikin, G.I. Strelkova, J. Kurths, Peculiarities of the relaxation to an invariant probability measure of nonhyperbolic chaotic attractors in the presence of noise, Phys. Rev. E 65 (3) (2002) 036206.
[89] C. Grebogi, H. Kantz, A. Prasad, Y.C. Lai, E. Sinde, Unexpected robustness-against-noise of a class of nonhyperbolic chaotic attractors, Phys. Rev. E 65 (2002) 026209-1–026209-18.
[90] M.J. Feigenbaum, L.P. Kadanoff, S.J. Shenker, Quasiperiodicity in dissipative systems: A renormalization group analysis, Physica D 5 (1982) 370–386.
[91] P. Bak, R. Bruinsma, One-dimensional Ising model and the complete devil's staircase, Phys. Rev. Lett. 49 (1982) 249–251.
[92] P. Bak, The devil's staircase, Phys. Today 39 (12) (1986) 38–45.
[93] F.-F. Jin, J.D. Neelin, M. Ghil, El Niño on the Devil's Staircase: Annual subharmonic steps to chaos, Science 264 (1994) 70–72.
[94] F.-F. Jin, J.D. Neelin, M. Ghil, El Niño/Southern Oscillation and the annual cycle: Subharmonic frequency locking and aperiodicity, Physica D 98 (1996) 442–465.
[95] E. Tziperman, L. Stone, M. Cane, H. Jarosh, El Niño chaos: Overlapping of resonances between the seasonal cycle and the Pacific ocean-atmosphere oscillator, Science 264 (1994) 72–74.
[96] E. Tziperman, M.A. Cane, S.E. Zebiak, Irregularity and locking to the seasonal cycle in an ENSO prediction model as explained by the quasi-periodicity route to chaos, J. Atmos. Sci. 50 (1995) 293–306.
[97] P. Chang, L. Ji, H. Li, M. Flugel, Chaotic dynamics versus stochastic processes in El Niño-Southern Oscillation in coupled ocean-atmosphere models, Physica D 98 (1996) 301–320.
[98] A. Saunders, M. Ghil, A Boolean delay equation model of ENSO variability, Physica D 160 (2001) 54–78.
[99] M. Ghil, I. Zaliapin, S. Thompson, A delay differential model of ENSO variability: Parametric instability and the distribution of extremes, Nonlin. Proc. Geophys. 15 (2008) 1–17.
[100] Yu.A. Kuznetsov, Elements of Applied Bifurcation Theory, 3rd ed., Springer-Verlag, New York, 2004, p. 631.
[101] A. Denjoy, Sur les courbes définies par les équations différentielles à la surface du tore, J. Math. Pure Appl. 11 (IV) (1932) 333–375.
[102] T. Kaijser, On stochastic perturbations of iterations of circle maps, Physica D 68 (1993) 201–231.
[103] P.E. Kloeden, E. Platen, Numerical Solution of Stochastic Differential Equations, Springer, Berlin, 1992, p. 632.
[104] T. Caraballo, J.A. Langa, J.C. Robinson, A stochastic pitchfork bifurcation in a reaction-diffusion equation, Proc. R. Soc. Lond. A 457 (2001) 2041–2061.
[105] J. Duan, K. Lu, B. Schmalfuss, Smooth stable and unstable manifolds for stochastic evolutionary equations, J. Dyn. Diff. Eq. 16 (2004) 949–972.
[106] J. Duan, K. Lu, B. Schmalfuss, Invariant manifolds for stochastic partial differential equations, Ann. Probab. 31 (2003) 2109–2135.
[107] L. Arnold, K. Xu, Normal forms for random differential equations, J. Differential Equations 116 (1995) 484–503.
[108] L. Arnold, P. Imkeller, Normal forms for stochastic differential equations, Probab. Theory Related Fields 110 (4) (1998) 559–588.
[109] W. Li, K. Lu, Sternberg theorems for random dynamical systems, Comm. Pure Appl. Math. 58 (2005) 941–988.
[110] N.D. Cong, Topological Dynamics of Random Dynamical Systems, in: Oxford Mathematical Monographs, Clarendon Press, Oxford, 1997, p. 212.
[111] H. Crauel, F. Flandoli, Attractors for random dynamical systems, Scuola Normale Superiore Pisa 148 (1992), Technical Report.
[112] H. Crauel, A uniformly exponential attractor which is not a pullback attractor, Arch. Math. 78 (2002) 329–336.
[113] H. Zmarrou, A.J. Homburg, Bifurcations of stationary measures of random diffeomorphisms, Ergodic Theory Dynam. Systems 27 (2007) 1651–1692.
[114] S. Kuksin, A. Shirikyan, On random attractors for mixing-type systems, Funct. Anal. Appl. 38 (1) (2004) 34–46.
[115] V.I. Oseledets, A multiplicative ergodic theorem. Lyapunov characteristic numbers for dynamical systems, Trans. Moscow Math. Soc. 19 (1968) 197–231.
[116] L. Arnold, Trends and open problems in the theory of random dynamical systems, in: L. Accardi, C.C. Heyde (Eds.), Probability Towards 2000, in: Springer Lecture Notes in Statistics, vol. 128, 1998, pp. 34–46.
[117] N.D. Cong, Topological classification of linear hyperbolic cocycles, J. Dyn. Diff. Eq. 8 (1996) 427–467.
[118] T. Wanner, Linearization of random dynamical systems, in: C.K.R.T. Jonesm, U. Kirchgraber, H.O. Walther (Eds.), Dynamics Reported, vol. 4, Springer, Berlin, Heidelberg, New York, 1995, pp. 203–269.
[119] E.A. Coayla-Teran, P.R.C. Ruffino, Random versions of Hartman-Grobman theorems, Preprint IMECC, UNICAMP, No. 27/01, 2001.
[120] E.A. Coayla-Teran, S.A. Mohammed, P.R.C. Ruffino, Hartman-Grobman theorems along hyperbolic stationary trajectories, Discrete Contin. Dyn. Syst. A 17 (2) (2007) 281–292.

Available online at www.sciencedirect.com
ScienceDirect
Physica D 237 (2008) 2127–2131
PHYSICA D
www.elsevier.com/locate/physd

Rogue waves in oceanic turbulence

Francesco Fedele*

School of Civil & Environmental Engineering, Georgia Institute of Technology, Savannah Georgia, USA

Available online 31 January 2008

Abstract

A stochastic model of wave groups is presented to explain the occurrence of exceptionally large waves, usually referred to as rogue waves. The model leads to the description of the non-Gaussian statistics of large waves in oceanic turbulence and to a new asymptotic distribution of their crest heights in a form that generalizes the Tayfun model. The new model explains the unusually large crests observed in flume experiments of narrow-band waves. However, comparisons with realistic oceanic measurements gathered in the North Sea during an intense storm indicate that the generalized model agrees with the original Tayfun distribution.

PACS: 92.10.Hm; 91.30.Fn

Keywords: Rogue wave; Weak wave turbulence; Wave group; Non-Gaussian; Crest statistics

1. Introduction

Rogue waves are extreme events with potentially devastating effects on offshore structures and ships. A rogue wave observed at the Draupner platform in the North Sea during a storm in January, 1995 provides evidence that such waves can occur in the open ocean. Theoretical models offer various physical mechanisms that can produce such focusing of wave energy in a small area of the ocean. When nonlinearities are negligible, ocean waves are usually modeled as Gaussian seas, as a linear superimposition of a large number of elementary waves with amplitudes related to a given spectrum and random phases. In this case, large waves occur due to the dynamics of a large stochastic wave group evolving linearly in accordance with both the Slepian model [1] and the theory of quasi-determinism of Boccotti [2]. Moreover, crests and troughs are both Rayleigh-distributed. If second-order nonlinearities are dominant, then the sea surface displays sharper narrower crests and shallower more rounded troughs. As a result, the skewness of surface elevations is positive [3], and wave crests are distributed according to the Tayfun model [4–7]. If, however, elementary waves also exchange energy nonlinearly via third-order four-wave resonances, narrow-band wave trains can undergo intense modulational instability enhancing the occurrence of larger waves [5,8] and, as a result, the distribution of crest heights can deviate from the Tayfun model. This is confirmed by both the wave-flume experiments in [6] and the numerical simulations of the Dysthe equation [7], a special case of the Zakharov equation [9] governing the dynamics of weakly nonlinear water waves. The unusually large wave crests observed in both the latter experiments and simulations are explained reasonably well by a Gram–Charlier approximation of the crest distribution recently proposed in [5]. This model stems from the general Hermite series expansion of random variables [3], and it relates to the physics of ocean waves only through various statistics such as the skewness and kurtosis of surface displacements. Could such type of Gram–Charlier models for crests proceed directly from the basic equations governing the ocean dynamics without assuming a priori that the associated statistical structure is in the form of a Gram–Charlier expansion in Hermite polynomials ? This paper will explore this query by formulating a new stochastic model of wave groups, describing the non-Gaussian statistics of large waves under conditions referred to as oceanic or wave turbulence (WT). The latter state defines the chaotic behavior of a sea of weakly nonlinear-coupled dispersive wave trains evolving in accordance with the Zakharov equation [9]. An

* Tel.: +1 902 966 6785.
E-mail address: francesco.fedele@gtsav.gatech.edu.

0167-2789/$ - see front matter © 2008 Elsevier B.V. All rights reserved.
doi:10.1016/j.physd.2008.01.022

initial Gaussian field is weakly modulated as nonlinearities develop in time, leading to intermittency in the turbulent signal due to the formation of sparse but intense coherent structures. Large wave crests observed during these localized events may explain the occurrence of rogue waves in open ocean. By exploiting the weak nature of the nonlinear interactions of $O(\mu^2)$, with μ defined as a small parameter for wave steepness, large crests are identified as those waves riding on top of large groups. In fact, for time scales much larger than the typical wave period T_L, but much less than the nonlinear time scale $T_{NL} \sim O(\mu^{-2})$, waves traveling in groups evolve mainly due to the faster non-resonant second-order interactions while the slower third-order resonant interactions modify and intensify their amplitudes. Thus, the initial deviations from Gaussianity observed in the statistical structure of large waves are revealed before turbulence becomes strong and thus the WT theory breaks down.

Herein, the WT theory is briefly reviewed first. Then, some salient features of the concept of stochastic wave groups relevant to WT are discussed, leading to a generalization of the Tayfun model for the statistical distribution of crest heights over large waves. Finally, comparisons with the lab data, numerical simulations and wave measurements collected in the North Sea are presented.

2. Oceanic turbulence

Consider weakly nonlinear random waves propagating in water of uniform depth d in accordance with the Zakharov equation for WT [9]. Define $\mathbf{x} = (x, y)$ as the horizontal position vector on a plane coincident with the water mean level, t the time, $\mathbf{k}$ as the horizontal wave-number vector, and ω is the angular frequency related to k via $gk \tanh kd = \omega^2$, with $k = |\mathbf{k}|$. Drawing upon [11], the sea surface displacement ζ from the mean sea level is given, correct to $O(\mu^2)$, by

$$\zeta = \zeta_1 + \zeta_2, \tag{1}$$

where the component ζ_1, that accounts for four-wave resonant interactions, is given by

$$\zeta_1 = \int b_1(t) \mathrm{e}^{\mathrm{i}(\boldsymbol{\theta}_1 - \Omega_1 t)} \mathrm{d}\mathbf{k}_1 + c.c. \tag{2}$$

with $\boldsymbol{\theta}_1 = \mathbf{k}_1 \cdot \mathbf{x} - \omega_1 t$ and $b_1(t) = b(\mathbf{k}_1, t)$ a complex amplitude whose perturbation expansion in small μ is given, correct to $O(\mu^2)$, by [11]

$$b_1(t) = B_1(1 + \mathrm{i}\mu^2 \Omega_1 t) - 2\mu^2 g \left[\mathcal{G}(t; B) - \mathcal{G}(0; B)\right], \tag{3}$$

where

$$\Omega_1 = 2\omega_1 \int W_{12}^{12} |A_2|^2 \, d\mathbf{k}_2$$

is the renormalization frequency arising from the nonlinear frequency shift due to self-interactions, and

$$\mathcal{G}(t; B) = \int W_{34}^{12} \sqrt{\frac{\omega_1}{\omega_2\omega_3\omega_4}} \bar{B}_2 B_3 B_4 \delta_{34}^{12} \frac{\exp\left(-i\omega_{34}^{12} t\right)}{\omega_{34}^{12}} \mathrm{d}\mathbf{k}_{234},$$

is a function of the initial amplitudes $B_1 = B(\mathbf{k}_1)$ at $t = 0$, W_{34}^{12} is the four-wave interaction kernel, $\omega_{34}^{12} = \omega_1 + \omega_2 - \omega_3 - \omega_4$, $\delta_{34}^{12} = \delta(\mathbf{k}_1 + \mathbf{k}_2 - \mathbf{k}_3 - \mathbf{k}_4)$, and $\bar{B}$ is the complex conjugate of B. The correction ζ_2 due to non-resonant interactions is given by

$$\zeta_2 = \int b_1 b_2 \left[A_{12}^{+} \mathrm{e}^{\mathrm{i}(\boldsymbol{\theta}_1 + \boldsymbol{\theta}_2)} + A_{12}^{-} \mathrm{e}^{\mathrm{i}(\boldsymbol{\theta}_1 - \boldsymbol{\theta}_2)}\right] \mathrm{d}\mathbf{k}_{12} + c.c. \tag{4}$$

where $A_{12}^{\pm} = A^{\pm}(\mathbf{k}_1, \mathbf{k}_2)$ are interaction coefficients [10]. Clearly $\langle\zeta\rangle = 0$ and the variance $\langle\zeta^2\rangle = \sigma^2$, where $\langle\cdot\rangle$ stands for expected value.

3. Large crests in Gaussian seas

Neglect both resonant and non-resonant interactions so that ζ_1 is Gaussian. Further, assume that a large wave crest of amplitude h is recorded at $\mathbf{x} = \mathbf{x}_0$ and $t = t_0$. Boccotti [2] shows that as $h/\sigma \to \infty$, with probability approaching 1, the large crest occurs when a well-defined wave group ζ_c passes through $\mathbf{x}_0$. The surface displacement of ζ_c around $\mathbf{x} = \mathbf{x}_0 + \mathbf{X}$ and $t = t_0 + T$ is asymptotically described by the following conditional process

$$\zeta_c = \{\zeta_1(\mathbf{X}, T) | \zeta_1(\mathbf{0}, 0) = h\} = \zeta_{\text{det}} + \mathcal{R}_\zeta, \tag{5}$$

as the sum of a deterministic part ζ_{det} previously derived in [1,2], and given by

$$\zeta_{\text{det}} = \langle\zeta_1(\mathbf{X}, T) | \zeta_1(\mathbf{0}, 0) = h\rangle = h \frac{\Psi}{\sigma^2},$$

and a random residual $\mathcal{R}_\zeta$ that can be explicitly expressed as (see [12] and also Appendix for details)

$$\mathcal{R}_\zeta(\mathbf{X}, T) = \frac{\Delta}{\sigma^2} \frac{-\psi^* \ \Psi(\mathbf{X}, T) + \Psi(\mathbf{X}, T - T^*)}{1 - \psi^{*2}} + O(h^{-1}),$$

where Δ is a random variable of $O(h^0)$, and Ψ is the space–time covariance of ζ_1 given by

$$\Psi(\mathbf{X}, T) = \int S_1 \cos(\mathbf{k}_1 \cdot \boldsymbol{X} - \omega_1 T) \mathrm{d}\mathbf{k}_1,$$

with $S(\mathbf{k}_1)$ = the wave-spectral density with bandwidth ν, and $\psi^* \equiv \psi(T^*)/\psi(0)$ with T^* being the abscissa of the first local minimum of the time covariance $\psi(T) = \Psi(\mathbf{0}, T)$. Since h and Δ are random variables, ζ_c identifies a *stochastic wave group* which evolves linearly through a wave background represented by the residual $\mathcal{R}_\zeta$. The largest crest occurs as waves, growing from the tail of the group, reach its apex [2]. The dimensionless variables $\xi = h/\sigma$ and $\tilde{\Delta} = \Delta/\sigma$ are stochastically independent, as $\xi \to \infty$. Moreover, ξ is Rayleigh-distributed and $\tilde{\Delta}$ is Gaussian with zero mean and variance $1 - \psi^{*2}$. In the following, it will be useful to express ζ_c in the form

$$\zeta_c = \int \tilde{B}_1 \mathrm{e}^{\mathrm{i}\boldsymbol{\theta}_1} \mathrm{d}\mathbf{k}_1 + c.c. \tag{6}$$

where

$$\tilde{B}_1 = \left(h - \Delta \frac{-\psi^* + \mathrm{e}^{\mathrm{i}\omega_1 T^*}}{1 - \psi^{*2}}\right) \frac{S_1}{2\sigma^2} \mathrm{e}^{-\mathrm{i}(\mathbf{k}_1 \cdot \mathbf{x}_0 - \omega_1 t_0)}, \tag{7}$$

with $S_1 = S(\mathbf{k}_1)$. Hereafter, the concept of stochastic wave groups is exploited to explain the occurrence of large waves and the associated crest statistics in WT.

4. Large crests in oceanic turbulence

Consider the nonlinear surface ζ. Because of both the fast non-resonant and slow resonant interactions, crest statistics deviate from being Gaussian. Such deviations can be quantified by drawing upon [13,14]. So, assuming that a large crest of amplitude h_{nl} is recorded at $\mathbf{x} = \mathbf{x}_0$ and $t = t_0$, ζ surrounding that crest locally around $\mathbf{x} = \mathbf{x}_0 + \mathbf{X}$ and $t = t_0 + T$ is given by the nonlinear conditional process

$$\zeta_{nc} = \{\zeta(\mathbf{X}, T) | \zeta(\mathbf{0}, 0) = h_{nl}\}. \tag{8}$$

If the waves were Gaussian, ζ_{nc} would be identical to the wave group ζ_c in (5). For nonlinear waves, does ζ_{nc} still represent a group forming a large crest with amplitude h_{nl}? The answer to this question is given by exploiting the weakly nature of the nonlinear interactions of ζ. First, ignore four-wave resonances in (1). Then, ζ_1 is Gaussian and ζ is homogeneous in space and time, but non-Gaussian. Under these conditions, the crest statistics deviate from the Rayleigh distribution, but they are well described by the Tayfun distribution [4,5,12]. For long-crested narrow-band waves in deep water, as the spectral bandwidth $\nu \to 0$, ζ assumes the simple form [4,5]

$$\zeta = \zeta_1 + \frac{\mu}{2\sigma}\left(\zeta_1^2 - \hat{\zeta}_1^2\right) + O(\nu), \tag{9}$$

where the component ζ_2 is explicitly identified in terms of ζ_1, $\mu = \lambda_3/3$ is related to the skewness coefficient $\lambda_3 = \langle \zeta^3 \rangle / \sigma^3$, and $\hat{\zeta}_1$ denotes the Hilbert transform of ζ_1 with respect to time. From (9) it is clear that the component ζ_2 is phase-coupled to the extremes of the Gaussian ζ_1. So, a large crest of ζ with amplitude h_{nl} occurs simultaneously when ζ_1 itself is at a large crest with an amplitude, say h [14]. Thus, the conditional process (8) is equivalent to the simpler process

$$\zeta_{nc} = \{\zeta | \zeta_1 = \zeta_c\}, \tag{10}$$

which explicitly follows, by replacing ζ_1 in (9) with ζ_c of (6), as

$$\zeta_{nc} = \zeta_c + \frac{\mu}{2\sigma}\left(\zeta_c^2 - \hat{\zeta}_c^2\right). \tag{11}$$

The amplitude h_{nl} of the largest crest of ζ_{nc} occurs at $\mathbf{x} = \mathbf{x}_0$ and $t = t_0$, i.e. $\mathbf{X} = \mathbf{0}$ and $T = 0$, when $\zeta_c = h$ and $\hat{\zeta}_c = 0$, and it is given in the *Tayfun form* as

$$\xi_{\max} = \xi + \frac{\mu}{2}\xi^2, \tag{12}$$

where $\xi_{\max} = h_{nl}/\sigma$ [12]. Thus, the Tayfun (T) model for the exceedance of the crest height $\xi_{\max}$ readily follows from the Rayleigh distribution of ξ as [4]

$$\Pr\{\xi_{\max} > \lambda\} = \exp\left(-\frac{\xi_0^2}{2}\right), \tag{13}$$

where ξ_0 satisfies the quadratic equation

$$\xi_0 + \frac{\mu}{2}\xi_0^2 = \lambda. \tag{14}$$

For $T_L \ll t_0 \ll T_{NL} \sim O(\mu^{-2})$, third-order resonant interactions develop and the wave field becomes nonstationary in time but still homogeneous in space. Moreover, the crest statistics deviates from the Tayfun model because the latter is based on the particular non-resonant form (9) of the generic ζ in (1). The deviations from the second-order theory can be still quantified by exploiting the space–time evolution of wave groups. In fact, the new group ζ_{nc} in (10) arising from the four-wave resonances of narrow-band waves is given by

$$\zeta_{nc} = \zeta_d + \frac{\mu}{2\sigma}\left(\zeta_d^2 - \hat{\zeta}_d^2\right), \tag{15}$$

where ζ_d originates from the modulation of the group ζ_c in (6) from pure resonant interactions. An explicit expression for ζ_d stems from ζ_1 in (2) by replacing the initial values B_1 of the associated complex amplitude $b_1(t)$ in (3) with those values $\tilde{B}_1$ of ζ_c in (7), that is

$$\zeta_d = \int e^{i(\boldsymbol{\theta}_1 - \Omega_1 t)} \left\{\tilde{B}_1(1 + i\mu^2\Omega_1 t) - 2\mu^2\left[\mathcal{G}(t; \tilde{B}) - \mathcal{G}(0; \tilde{B})\right]\right\} d\mathbf{k}_1 + c.c. \tag{16}$$

By a direct inspection of both (15) and (16) one can show that the nonlinear group ζ_{nc} still focuses at $\mathbf{x} = \mathbf{x}_0$ and $t = t_0$ for $t_0 \ll T_{NL}$ with the largest crest amplitude $\xi_{\max}$ given by

$$\xi_{\max} = \xi + \frac{\mu}{2}\xi^2 + \mathcal{I}(t_0)\xi^3 + \mathcal{A}(t_0)\xi^2\tilde{\Delta} + \mathcal{B}(t_0)\xi\tilde{\Delta}^2, \tag{17}$$

where $O(\tilde{\Delta}^3, \mu^3)$ terms have been neglected and the dependence on $\mathbf{x}_0$ drops out because the field is homogeneous in space but nonstationary in time. Moreover $\mathcal{I}$, $\mathcal{A}$ and $\mathcal{B}$ are multidimensional integrals in $(\mathbf{k}_2, \mathbf{k}_3, \mathbf{k}_4)$ space. In particular,

$$\mathcal{I} = \int Q_{34}^{12} S_2 S_3 S_4 \, d\mathbf{k}_{234},$$

with

$$Q_{34}^{12} = \frac{\mu^2 g}{2m_0^2} W_{34}^{12} \sqrt{\frac{\omega_1}{\omega_2\omega_3\omega_4}} \delta_{34}^{12} \frac{1 - \cos\left(\omega_{34}^{12} t_0\right)}{\omega_{34}^{12}},$$

and in the narrow-band limit, as $\nu \to 0$,

$$\mathcal{A} \approx O(\nu), \qquad \mathcal{B} = -3\mathcal{I}\Big/\left(1 - \psi^{*2}\right) + O(\nu).$$

Drawing upon [8], the coefficient $\mathcal{I}$ relates to the fourth-order cumulant $\lambda_{40} = \mu_4 - 3$ of the wave surface as $\lambda_{40} = 24\mathcal{I}$, μ_4 being the kurtosis. The probability of exceedance for the nonlinear wave-crest height $\xi_{\max}$ is given by

$$\Pr\{\xi_{\max} > \lambda\} = \int_{-\infty}^{\infty} \Pr\left\{\xi > \xi^*(\lambda) \middle| \tilde{\Delta}\right\} p_{\tilde{\Delta}} d\tilde{\Delta}, \tag{18}$$

where $p_{\tilde{\Delta}}$ is the Gaussian density of $\tilde{\Delta}$, ξ is Rayleigh-distributed and its associated threshold ξ^* satisfies $\xi_{\max} = \lambda$ in (17). Further, correct to $O(\nu)$, ξ^* can be Taylor-expanded in terms of $\tilde{\Delta}$ starting from $\xi = \xi_0$ of (14) as

$$\xi^* = \xi_0 - \frac{\lambda_{40}}{24}\left(\xi_0^3 - \frac{3\xi_0\tilde{\Delta}^2}{1 - \psi^{*2}}\right) + O(\tilde{\Delta}^3).$$

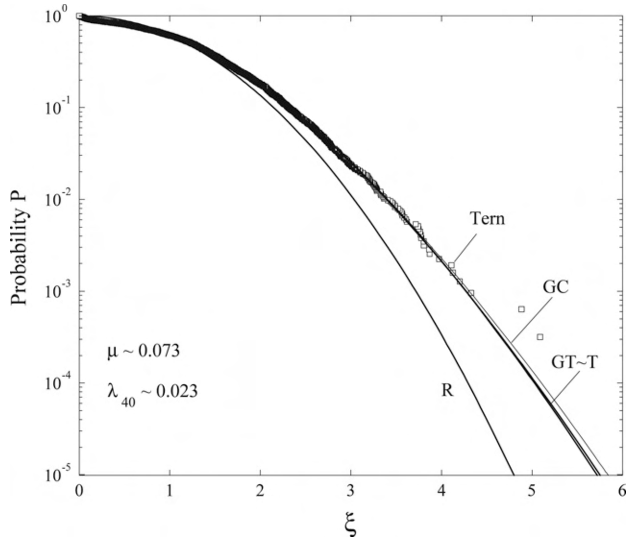

Fig. 1. Crest exceedances from Tern in comparison with the Tayfun, generalized Tayfun and Gram–Charlier models. Labels: R=Rayleigh, T = Tayfun (μ), GT= generalized Tayfun (μ, λ_{40}), GC= Gram–Charlier.

Ignoring terms of $O(\tilde{\Delta}^3)$ in the integration of (18) yields the probability of exceedance for $\xi_{\max}$ as

$$\Pr\{\xi_{\max} > \lambda\} = \exp\left(-\frac{1}{2}\xi_0^2\right)\left[1 + \frac{\lambda_{40}}{24}\lambda^2\left(\lambda^2 - 3\right)\right],$$

correct to $O(\mu^2)$. We shall refer to this asymptotic result, as the generalized Tayfun (GT) distribution, which is very similar to the Gram–Charlier (GC) approximation proposed in [5], viz.

$$\Pr\{\xi_{\max} > \lambda\} = \exp\left(-\frac{1}{2}\xi_0^2\right)\left[1 + \frac{\lambda_{40}}{24}\lambda^2\left(\lambda^2 - 4\right)\right].$$

Note that for directional broadband waves, wave-number quadruplets are in perfect resonance, i.e. $\omega_{34}^{12} = 0$, and the Tayfun model is recovered from both the GT and GC models since $\lambda_{40} = 0$.

5. Comparisons

The data to be considered for comparisons here comprise 9 h of measurements gathered during a severe storm in January, 1993 with a Marex radar from the Tern platform located in the northern North Sea in 167 m water depth. This data set is hereafter simply referred to as Tern. Tern represents storm seas under fairly steady conditions with broadband spectra characterized with $\sigma = 3.024$ m, spectral bandwidth $\nu = 0.629$ and $\lambda_3 = 0.174$. A stable estimate of the steepness μ in terms of spectral properties is given by $\mu_a = \mu_m\left(1 - \nu + \nu^2\right)$ [12]. In Fig. 1, the empirical distribution from Tern is compared with the T ($\mu \simeq \mu_a = 0.073$), GT ($\mu \simeq \mu_a = 0.073$, $\lambda_{40} \simeq 0.023$) and GC models respectively. It is observed that both the GT and GC models do not appear to improve significantly the predictions derived from the simpler T model. For most practical applications, the differences between the models appear insignificant, falling within a band of 1%–2%. Consider now the case of unidirectional narrow-band waves. The trend of the experimental wave-flume data of Fig. 2 in [6] is reproduced and shown in Fig. 2 here together with

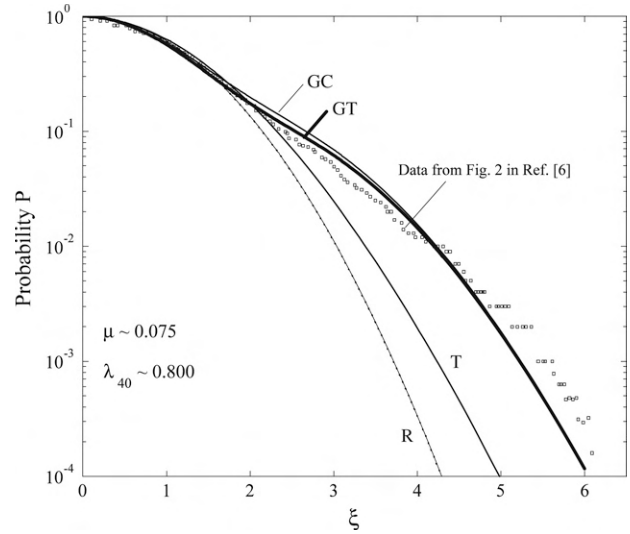

Fig. 2. Crest-height distribution from wave-flume experiments (Fig. 2 in [6]) in comparison with the Tayfun, generalized Tayfun and Gram–Charlier models. Labels are as for Fig. 1.

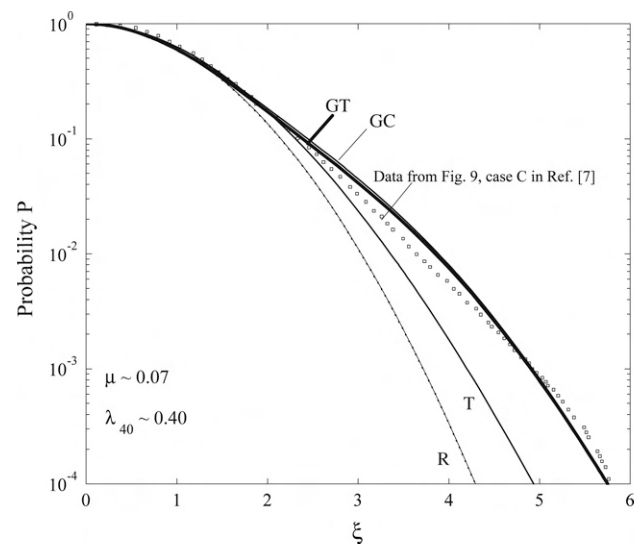

Fig. 3. Crest exceedances from numerical simulations (Fig. 9, case C in [7]) in comparison with the Tayfun, generalized Tayfun and Gram–Charlier models. Labels are as for Fig. 1.

the predictions based on GT, GC ($\mu \simeq 0.075$, $\lambda_{40} \simeq 0.80$) and T ($\mu \simeq 0.075$) models. The original T model tends to underestimate the data whereas both the GT and GC models appear to explain data qualitatively well. The latter models also describe well the crest-height distribution from Fig. 9 (case C) of [7] obtained from numerical simulations of the Dysthe equation, reproduced and shown in Fig. 3 in comparison with the GT, GC ($\mu \simeq 0.07$, $\lambda_{40} \simeq 0.40$) and T ($\mu \simeq 0.07$) models.

6. Conclusions

A generalized Tayfun model for the statistics of crest heights over large waves in oceanic turbulence is proposed. The new crest model can explain the deviations from the Tayfun distribution observed in flume experiments of narrow-band waves. However, for realistic oceanic sea states the differences between the predictions of the new model and the Tayfun distribution appear negligible.

Acknowledgments

The author thanks M. Aziz Tayfun for useful comments and discussions and George Forristall for the data utilized in the paper.

Appendix

The wave profile $\eta_c(T)$ at $\mathbf{X} = \mathbf{0}$ is expressed in terms of an $O(h)$ contribution $\eta_{\det}(T) = \zeta_{\det}(\mathbf{0}, T)$ and the random residual $r(T) = \mathcal{R}_\zeta(\mathbf{0}, T)$ of $O(h^0)$ as

$$\eta_c(T) = \eta_{\det}(T) + r(T),$$

where $\eta_{\det}(T) = \zeta_{\det}(\mathbf{0}, T) = h\psi(T)/\sigma^2$. Drawing upon [15], the effects of the residual $r(T)$ on η_c are now determined. Specifically, as $h/\sigma \to \infty$, with probability approaching 1, the surface profile locally near a large crest tends to assume the shape given by $\eta_{\det}(T)$ [1,2]. The latter represents a wave profile with a crest of amplitude h at time $T = 0$ followed by the absolute minimum of amplitude $\eta_{\det}(T^*)$ at $T = T^*$, with T^* being the abscissa of the first local minimum of $\psi(T)$. For large values of h, the wave trough of the profile $\eta_c(T)$ following the crest of amplitude h shall now occur at time $T = T^* + u$, with u being random. As $h/\sigma \to \infty$, a crest of amplitude h that occurs at $T = 0$, is followed after a time lag $T^* + u$ by a trough, and $\eta_c(T)$ and its first time derivative $\dot{\eta}_c(T)$ at $T = T^*$ attain values given, correct to $O\left(h^0\right)$, by

$$\eta_c(T^*) = \eta_{\det}(T^*) + \Delta, \qquad \dot{\eta}_c(T^*) = -\ddot{\eta}_{\det}(T^*)u.$$

For linear Gaussian functions, an approximation to $\eta_c(T)$ satisfying the preceding conditions exactly is given by

$$\eta_c(T) = \eta_{\det}(T) + \frac{\Delta}{\sigma^2}\frac{-\psi(T)\psi(T^*)/\sigma^2 + \psi(T - T^*)}{1 - \psi(T^*)^2/\sigma^4},$$

where u drops out ignoring terms of $O(h^{-1})$. The straightforward extension of the above time formulation to the space–time domain leads to (5).

References

[1] G. Lindgren, Local maxima of Gaussian fields, Ark. Mat. 10 (1972) 195–218.
[2] P. Boccotti, Wave Mechanics for Ocean Engineering, Elsevier Science, Oxford, 2000.
[3] M.S. Longuet-Higgins, The effects of non-linearities on statistical distributions in the theory of sea waves, J. Fluid Mech. 17 (1963) 459–480.
[4] M.A. Tayfun, Narrow-band nonlinear sea waves, J. Geophys. Res. 85 (C3) (1980) 1548–1552.
[5] A. Tayfun, F. Fedele, Wave-height distributions and nonlinear effects, Ocean Eng. 34 (2007) 1631–1634.
[6] M. Onorato, A.M. Osborne, M. Serio, L. Cavaleri, C. Brandini, C.T. Stansberg, Extreme waves, modulational instability and second order theory: Wave flume experiments on irregular waves, Eur. J. Mech. B-Fluids 25 (2006) 586–601.
[7] H. Socquet-Juglard, K. Dysthe, K. Trulsen, H.E. Krogstad, J. Liu, Probability distributions of surface gravity waves during spectral changes, J. Fluid Mech. 542 (2005) 195–216.
[8] Peter A.E.M. Janssen, Nonlinear four-wave interactions and freak waves, J. Phys. Oceanogr. 33 (4) (2003) 863–884.
[9] V.E. Zakharov, Statistical theory of gravity and capillary waves on the surface of a finite-depth fluid, Eur. J. Mech. B-fluids 18 (3) (1999) 327–344.
[10] J.N. Sharma, R.G. Dean, Development and evaluation of a procedure for simulating a random directional second order sea surface and associated wave forces, Ocean Engineering Report no. 20, University of Delaware, 1979.
[11] Y. Choi, Y.V. Lvov, S. Nazarenko, B. Pokorni, Anomalous probability of large amplitudes in wave turbulence, Phys. Lett. A 339 (2005) 361–369.
[12] F. Fedele, M.A. Tayfun, On nonlinear wave groups and crest statistics, J. Fluid Mech. (under review).
[13] F. Fedele, Extreme events in nonlinear random seas, ASME J. Offshore Mech. Arc. Eng. 128 (1) (2006) 11–16.
[14] F. Fedele, F. Arena, Weakly nonlinear statistics of high non-linear random waves, Phys. Fluids 17 (1) (2005) 026601.
[15] P. Boccotti, On mechanics of irregular gravity waves, Atti Accad. Naz. Lincei Memorie VIII 19 (1989) 111–170.

Available online at www.sciencedirect.com
ScienceDirect
Physica D 237 (2008) 2132–2138
PHYSICA D
www.elsevier.com/locate/physd

Anthropogenic climate change: Scientific uncertainties and moral dilemmas

Rafaela Hillerbrand[a,*], Michael Ghil[b,c]

[a] The Future of Humanity Institute, University of Oxford, Suite 8, Littlegate House 16/17, St Ebbe's Street, Oxford, OX1 1PT, United Kingdom
[b] Geosciences Department and Environmental Research and Teaching Institute, Ecole Normale Supérieure, 75231 Paris Cedex 05, France
[c] Department of Atmospheric and Oceanic Sciences and Institute of Geophysics and Planetary Physics, University of California at Los Angeles, Los Angeles, CA 90095-1565, USA

Available online 21 February 2008

Abstract

This paper considers the role of scientific expertise and moral reasoning in the decision making process involved in climate-change issues. It points to an unresolved moral dilemma that lies at the heart of this decision making, namely how to balance duties towards future generations against duties towards our contemporaries. At present, the prevailing moral and political discourses shy away from addressing this dilemma and evade responsibility by falsely drawing normative conclusions from the predictions of climate models alone.

We argue that such moral dilemmas are best addressed in the framework of Expected Utility Theory. A crucial issue is to adequately incorporate into this framework the uncertainties associated with the predicted consequences of climate change on the well-being of future generations. The uncertainties that need to be considered include those usually associated with climate modeling and prediction, but also moral and general epistemic ones. This paper suggests a way to correctly incorporate all the relevant uncertainties into the decision making process.

PACS: 92.60.Ry; 92.70.Gt

Keywords: Climate change; Impact models; Precautionary principle; Expected Utility Theory

1. Introduction

Significant and enduring anthropogenic impact on climate is not a peculiarity of our time. Man is part of the biosphere and as such always did and always will influence the climate system, a system that comprises, apart from the atmosphere and hydrosphere, also the bio, litho and cryosphere. Slash-and-burn agriculture, changes in farming practices, building development or regulation of inland waters have modified the back-scattering of radiation by Earth's surface and the near-surface atmospheric winds [1,2]. The shift from nomadism to farming several thousands of years ago resulted in vast clearings and thus had a significant and sustained influence on regional climate.

The converse influence that climate exerts on man, particularly via atmospheric conditions and weather, has been acknowledged for a long time, too. The European revolutions of 1789 and 1848, no doubt a result of long-lasting social, political and economic circumstances, were also affected by continued years of bad weather, bad crops, and high corn prices [3]. Recent research suggests that a possibly worldwide drought in the 10th century was the catalyst for the demise of the Tang Dynasty in China, as well as of the Mayan civilization in Central America [4].

The increased use of fossil fuels, started at the beginning of the industrial revolution, has led to rapid increase in greenhouse emissions since World War II. In particular, atmospheric concentrations of carbon dioxide, the most abundant and hence best-known anthropogenic greenhouse gas, have increased measurably and significantly over the last few decades [5]. The so-called "greenhouse effect" of trapping outgoing thermal radiation in the lower atmosphere yields, in all likelihood, an anthropogenic climate change of global extent and unprecedented consequences, for decades to come.

The present paper does not aim at an overview of the currently available predictions on the future state of the climate system, their relative merit or their shortcomings [5].

* Corresponding author.
E-mail address: rafaela.hillerbrand@philosophy.ox.ac.uk (R. Hillerbrand).

0167-2789/$ - see front matter © 2008 Elsevier B.V. All rights reserved.
doi:10.1016/j.physd.2008.02.015

We aim instead at describing the role of science within the debate on adaptation and mitigation, and at complementing an understanding of the scientific uncertainties [6] with an introduction to the epistemic, i.e. knowledge-theoretical, uncertainties. By bringing these issues to the attention of the scientific community, we hope to improve communication between this community, the broader public, and decision makers.

We choose to evaluate the state of the climate system only in terms of its value for humans (or other sentient beings). Section 2 points out that this choice implies one cannot base a normative – i.e. prescriptive rather than purely descriptive or empirical – evaluation of the consequences of climate change on the scientific predictions of the system's future state alone: putting adaptation and mitigation issues into the broader context of competing needs and limited resources raises moral problems that cannot be easily dismissed. Section 3 suggests addressing the moral dilemmas raised in Section 2 within the framework of Expected Utility Theory (EUT) [7,8]. The EUT approach, however, depends sensitively on the predicted impacts of climate change on people's well-being, which are still highly uncertain, and may have to remain so for a long time.

Section 4 argues that not all of these uncertainties can be properly quantified. Intrinsic obstacles to communicating certain types of scientific uncertainties to broader audiences might exist. Each scientific community has its own language (or jargon) and translation between these languages, and between either one of them and the common language of educated lay people, poses possibly unsurmountable difficulties. Already the difficulty of communicating between climate dynamicists and welfare economists has been noted by many participants in the emerging dialog between these two communities. Section 5 draws conclusions about the role of science in the normative evaluation of anthropogenic climate change.

2. Jumping to conclusions

Large segments of the media, in Europe and elsewhere, presuppose a clear moral obligation to mitigate the socio-economic consequences of climate change. Likewise, most related moral-philosophical considerations focus on questions like how to distribute the costs of mitigation, while considering principles of fairness. The moral obligation to mitigate is rarely discussed; for noteworthy exceptions see [9–11]. At first glance, the sole questions remaining open as regards climate change thus seem to be of a political or scientific nature.

In contrast, we argue here that there are as yet unresolved ethical questions regarding our obligation to mitigate climate change, questions that precede the practical ones discussed in the current literature and media. If there is a moral obligation to preserve the climate in its present state, where does it stem from? Addressing this question seems inevitable in determining what our moral duties as regards climate may reasonably be. Moreover, formulating explicitly the reasons behind what is perceived by many, but not all, as a moral obligation should help in convincing the sceptics.

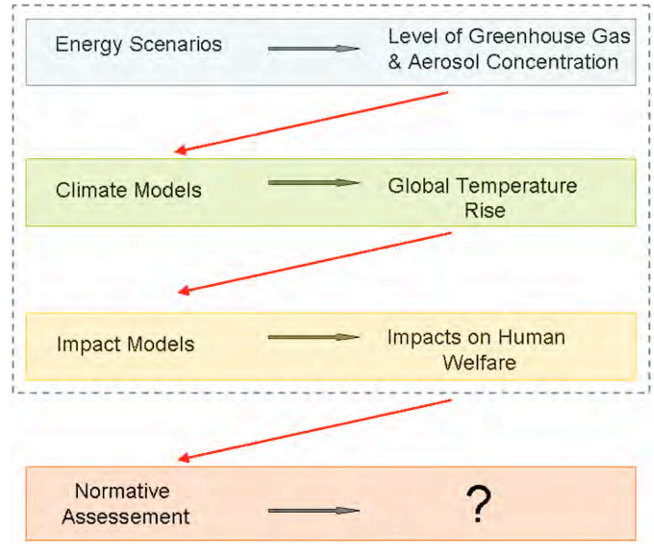

Fig. 1. Estimating the impacts of anthropogenic emissions of greenhouse gases on the living conditions of future generations. The short straight arrows (double arrow, grey) correspond to "yields the output", while long oblique (heavy arrow, red) arrows correspond to "is input for". The dashed rectangle indicates the combination of scientific prognoses that, as a whole, serve as an input for a political or moral evaluation, on the last line.

Let us suppose a moral obligation to take into account the well-being of future generations in the same way as our own and that of our fellow human beings. Obviously this calls for environmentally sound actions in order to not deprive posterity of adequate resources. But, as usual, the devil is in the details: What exactly does this mean in the case of the climate system?

If we value the climate system only because of its value for future generations (or for other sentient beings), a mere rise in global mean temperature is not morally relevant per se, as illustrated in Fig. 1. What matters is the effects of this change in mean temperature and other climatic variables on the living conditions of present and future human beings. These effects are far from straightforward. The so-called *impact models* estimate the direct and indirect influences of climate change on the expectancy and quality of human life. The most advanced of these welfare-economic models determine the monetary costs arising in a broad range of market sectors, as well as in non-market sectors, such as the costs arising from changes in human mortality or in biodiversity [12–14].

Still, these models fail to adequately account for many aspects of human suffering possibly caused by climate change, as they evaluate the impact of climate change on human welfare purely in monetary terms [9,12]. Money can be lent, exchanged, traded or it can carry an interest; many factors which (co-) determine an individual's welfare cannot. Moreover, future losses are discounted at a fairly arbitrary rate. Of course, any realistic analysis has to take into account that future generations might have means and possibilities to adapt to the consequences of climate changes, maybe even of severe ones. The single discount rate currently used is not, however, connected to predictions on the capacity to adapt or mitigate. Furthermore, welfare-economic analysis commonly ignores costs stemming from psychological afflictions that are hard or even impossible to monetarize. Finally, almost all impact models in use so far ignore economic variability, e.g. business cycles and major crashes, and the genuine coupling of this variability to climate dynamics [15,16].

Yet, for the time being, we have to accept these modeling shortcomings – just as we have to deal not only with the various shortcomings of present climate models but also with those of other predictions, e.g. on weather, earthquakes, or stock market prices. These shortcomings introduce uncertainties into the model outputs, which then have to be taken into consideration, along with those of climate-change predictions and of the energy scenarios.

In practice, the distribution of the various tasks in determining the effects of anthropogenic greenhouse gas emissions is not as clear-cut as sketched in Fig. 1. Economic models are frequently mistaken as moral assessments, although they clearly do not constitute evaluations on moral grounds. Basic modeling assumptions – like discounting future losses or evaluating the harm in purely monetary terms, etc. – cannot be morally justified, although they might be reasonable assumptions for estimating the economic impact of climate change. But even if we accept these assumptions as reasonable for the time being, the economic models still do not qualify as a "first-order approximation" to a normative assessment, whether moral or political.

In determining what it means to act rightly or wrongly, in moral terms, a cost-benefit analysis of one action always has to include an evaluation of alternative actions. Climate change and its mitigation cannot be treated as the only issue at hand: epidemics caused by other factors, industrial and agricultural pollution endangering air and water quality, educational opportunities, poverty, discrimination etc., are matters of legitimate concern as well. Existing cost-benefit analyses, even those few that try to avoid the above-mentioned shortcomings of economic models [9], fail to put the analysis of climate change into the requisite broader context.

Societies (or other subjects) are able to part only with a certain amount of money or other resources for predominantly altruistic goals, of which the mitigation of major changes in future climate is only one. Investing in the mitigation of climate-change effects means forgoing other investments, e.g. the reduction of world poverty, towards which we have a moral obligation. For example, on the one hand, the Stern report [12] famously mentions 1% of global gross domestic product (GDP) as the sum needed to avoid major hazards that may arise from climate change. This amounts to an investment of US $ 450 billion per year, if we base the calculation on the current GDP value. On the other hand, current estimates of the money needed to provide 80% of rural populations in Africa with access to water and sanitation by 2015 amounts to only US $ 1.3 billion per annum [17].

The trade-off between investment into the mitigation of and adaption to climate-change effects and investment in safe water supply in developing countries, for example, is currently not included in the moral or political evaluation of climate change. Political reasoning seems to shy away from the trade-off. The moral discourse contents itself with an *ex post* justification of established public opinion. As a result, the discussion is cut short and moral obligations are derived already on the level of merely discussing climate-model predictions.

This preempting of the moral debate is not only at variance with sound decision making. Putting the cart before the horse, i.e. presupposing a moral obligation before all the steps of the cost-benefit analysis have been carried out, also seems to adversely affect the science itself. As Pielke [18], p. 406, notes in this context: "In many instances science, particularly environmental science, has become little more than a mechanics of marketing competing political agendas, and scientists have become leading members of the advertising campaigns".

The heated debate that followed the publication of Lomborg's book [19], as well as many of the current discussions on various 'scientific' blogs [20], illustrate how scientific reasoning is, mostly implicitly, accused of being but a political instrument for the wrong side [21].

3. Balancing costs and benefits

Reasoning about morally right or wrong actions becomes significantly more difficult when their consequences affect also future generations. Quite often, various moral duties cannot be honored simultaneously; thus there might arise a conflict between preventing future harm from climate change and fulfilling our duties to currently living humans. Philosophers refer to such situations as *moral dilemmas*. Such dilemmas are not restricted to climate-change issues, but they do become quite critical in this case. Should we invest in educating women in developing countries now or invest in some of the less promising sources of alternative energy? Shall our concerted actions aim at reducing the number of currently ongoing wars or at preventing future flood damages? Such questions are clearly bothersome but still cannot be dismissed easily: has alleviating current suffering priority over mitigating future losses about whose extent legitimate uncertainties might exist?

Having posed the moral dilemma in this way, it seems natural to approach its solution by pursuing a more complete cost-benefit analysis. In such an analysis, costs and benefits have to reflect the impact of alternative courses of action on human well-being, current and future. In this broader setting, the morally correct action is the one that maximizes overall human welfare. This approach can be seen as a variant of utilitarian ethics, dating back to Bentham and Mill [22]. These early thinkers identified well-being boldly with happiness; modern utilitarianists replace the concept of happiness by the general term welfare and refer to the fulfillment of the individual's preferences.

The individual preference function $U_i : X \to \mathbb{R}$, reflects the preference of person i in the distribution X of some goods, with the preference function going from $-\infty$ to $+\infty$, i.e. it can be any real number U_i in $\mathbb{R}$. Note that 'goods' are to be understood here in a very general way, not restricted to material goods but also including mental states, being free from pain, etc. The utilitarian or welfare-ethical principle then amounts to maximizing the welfare function $U = \sum_i \lambda_i U_i$, where the sum is over all individuals which are affected by the action under consideration and λ_i is some arbitrary weighting factor. In this setting, the utilitarian principle of procedural justice, Bentham's famous "Everybody to count for one, nobody for more than one" becomes "$\lambda_i = \lambda_j$ for all i, j".

The utilitarian approach has the advantage that it generalizes in a straightforward manner to actions for which the outcomes are not known with certainty, but only known to occur with some likelihood; e.g. the exact number of class-5 hurricanes at the end of this century that would result from a given greenhouse-gas emission scenario. In this probabilistic generalization, one maximizes the *mean expected welfare*, rather than the deterministic welfare function above. In the welfare-economic and philosophical literature, this approach is referred to as Expected Utility Theory (EUT).

Applying EUT to climate-change issues is not straightforward, since assigning actual likelihood values to expected impacts on human welfare is often difficult or even impossible with the current state of knowledge; see Section 4 for a discussion of this issue and [6] and the references therein for the underlying uncertainties in climate-change estimates. Another problem with this approach, which has been addressed extensively within the philosophical and economic literature, regards the very existence of an individual welfare function U_i. It seems odd to assign cardinal values to individual harms and benefits in order to make them accessible to interpersonal comparisons [23].

In the context of intergenerational ethics, another problem becomes quite arduous, namely that of assigning preferences to future generations: are theirs going to be necessarily the same as ours? More likely not! J.H. Ausubel [24] gives an amusing example of how the unknown preferences of posterity challenge cost-benefit analysis for climate-change issues: "One hundred years ago icebergs were a major climatic threat impeding travel between North America and Europe. 1513 lives ended when the British liner Titanic collided with one on 14 April 1912. 50 years later jets overflew liners. Anticipating the solution to the iceberg danger required understanding not only the rates and paths on which icebergs travel but the ways humans travel, too."

In fact, ascribing our own preferences to future generations clearly contradicts the above-mentioned utilitarian principle of procedural justice; see [25] for a possible way of avoiding such problems.

In approaching climate-change issues from a moral point of view, we have chosen here an *anthropocentric consequentialism*: There are no *a priori* obligations, and any action has to be evaluated as to how it promotes overall human welfare. To defend this approach within an intergenerational ethics discourse, we begin with a defense of consequentialism.

Modern normative ethics are frequently classified as either *consequentialist* or *deontological*. The latter focuses on the rightness or wrongness of actions themselves, as opposed to the rightness or wrongness of the consequences of those actions. Kant's categorical imperative is a paradigm of a deontological principle. The utilitarian approach discussed above is rooted in consequentialist ethics, as the actions are evaluated solely on the basis of their impact on human welfare. As previously mentioned, one advantage of the consequentialist approach is that it generalizes to actions with highly uncertain outcomes, while this is not possible for deontological approaches [26]. Moreover, Patzig [27] and others have argued that, in handling moral dilemmas, consequentialist approaches are superior to deontological ones [28,29].

Various environmentalists have criticized valuing the environment solely as a basic resource for humanity, as done in the present paper. Movements like "deep ecology" [30] or "land ethics" [31] recently attracted considerable attention in environmental arguments. Their positions are genuinely non-anthropocentric: either nature as a whole or parts of (nonhuman) nature are assigned some moral value. Hence the whole ecosystems or even the climate system have to be valued for their own sake, i.e. not merely due to their value for a sentient being. Note that by 'non-anthropocentric', we refer here to approaches that assign actual moral values to plants or inanimate matter; while we do not pursue this avenue in this paper, the welfare-based approach can be generalized to other sentient beings in a straightforward manner.

Most of the proposed non-anthropocentric approaches in the literature have difficulties in dealing with moral dilemmas [32]. This is not a crucial shortcoming of such approaches, though, as a hierarchical value structure could solve this problem.

A key shortcoming of non-anthropocentric approaches, however, is that they contradict Occam's razor: a larger number of premises is needed in arguing for physiocentricism or holism, and these added premises cannot be justified any further [32]. Keeping the number of such metaphysical assumptions as low as possible is particularly important within environmental ethics, for the following reason: In order to become effective, norms that, for example, rule the emissions of greenhouse gases have to be implemented on a global scale and by future generations as well. The metaphysical background shared by different cultures – or, within one culture, over several generations – seems rather limited. The assumptions of a welfare-based approach are the most likely to be shared by people from different cultural backgrounds.

4. Communicating epistemic uncertainties

Determining the ultimate impacts of present and future greenhouse gas emissions necessitates a multifaceted interplay of various disciplines, as sketched in Fig. 1. The suggested welfare-based approach to climate-change issues – in which the morally correct action is that which maximizes overall human welfare – is seriously called into question by the lack of reliable probability estimates. The requisite estimates range from the various anthropogenic impacts on the climate system to the consequences of these impacts on human welfare. As stressed in [5], even the probability distribution estimates for future mean temperatures or other climatic variables require considerable refinement; this holds true all the more for the estimated probabilities of specific consequences, for example, of the influence of climate change on farming in Africa and its implications on migration [12].

One refers to actions for which there are no reliable probability estimates in terms of objective frequencies of occurrence as "actions under (epistemic) uncertainty." This is opposed to "actions under risk," for which all outcomes of a given action can be assigned some frequency of occurrence. This classification of *risk* and *uncertainty* became popular in discussing the civilian use of nuclear power and is now commonly used within technology assessment.

For actions under uncertainty, it has been suggested to fall back on non-probabilistic decision models. The most popular model of this type is the *minimax rule*, i.e. minimizing the maximal harm that can be expected; within environmental ethics or political decision making, this rule is known as the 'precautionary principle'. Note that the use of this phrase is fraught with ambiguity: within a juridical context in general or in European Union legislation in particular, the notion is fairly vague [33]. Hence we prefer to use the term as used within ethics and popularized by H. Jonas [34], namely: if we cannot exclude with certainty that an action, like the release of greenhouse gases, has the potential to cause severe or irreversible harm – to present or future generations – it is to be abandoned.

This principle, however, raises several difficulties [35], the central problem being that, in almost all practical cases, acting as well as not acting might yield unacceptable consequences. Unless a morally relevant distinction between act and omission exists, the precautionary principle therefore is incomplete, and thus is inadequate for actual decision making processes. Hence, despite the lack of probability estimates for the impact of climate change on the well-being of future generations, we have to proceed along the lines of EUT. Applying EUT to decisions under uncertainty requires supplementing the frequencies that are already available for some of the predicted consequences of climate change with subjective probabilities for other consequences. While economists are familiar with such subjective probabilities, natural scientists, including climate dynamicists, are generally quite sceptical about their use.

Note in particular that what is referred to as uncertainties within climate science [6,37,36] differs from the epistemic uncertainties as defined above. To be more precise, the uncertainties that climatologists discuss do not involve a need for subjective probabilities. Uncertainties like the range of the predicted temperatures for the end of this century, for example, are only one aspect of the uncertainties that decision making has to deal with. In particular, the uncertainties with which decision making struggles most are those that are not quantified as yet. A very broad or highly skewed probability distribution is awkward, as one needs to discuss issues related to risk-averseness. Such uncertainties, though, do not challenge the foundations of the proposed EUT approach.

Reducing the uncertainties faced by the various IPCC working groups can be associated with the various rectangles in Fig. 1. Each group so far has proceeded within the methodology of a specific field of knowledge [5,38]. For the climate dynamics addressed within Working Group I, methods for reducing uncertainties in prediction have advanced significantly of late [6,39]. The same holds true for the economical analyses within Working Group II. Quantitative methods for how to determine not only objective occurrence frequencies, but also reliable subjective probabilities were provided. These methods include, for example, the use of decision markets [40] or the implementation of Delphi methods, in which several experts provide subjective probability estimates that are refined in a multi-level process [41]. Also other quantitative tools for decision making were put forward [42].

Despite this progress, not all epistemic uncertainties can be quantified in a simple figure, like the width of a probability distribution or the area of a Schneider–Moss plot [43], say. Such plots have been used to yield ostensibly a quantification of the subjective reliability a researcher assigns to a theory, an observation, or the consensus within the field for the model results that underlie a specific prediction. Still, in estimating the reliability of a physical or economic model there always remain factors that are hard to communicate. For example, the outputs of a statistical analysis will always depend on the specific experimental paradigm, the accepted practice, and the general research experience within the field; these factors cannot be defined in lay language in a straightforward way, but must be learned by working in the field.

Scientists in a given field tend to assign so-called "higher-order beliefs" to all these factors, i.e. beliefs that express their confidence in the underlying theory, the methodology used, the researcher or group who carried out the work, etc. These higher-order beliefs, however, are only very rarely quantifiable themselves in terms of a subjective probability. Schneider–Moss plots [43], for example, presuppose that subjective beliefs can be expressed in cardinal numbers.

Hence the communication of uncertainties is, at least in part, limited to a scientific community — physical or economical, say. A scientific community is thus an instance of a Wittgensteinian language community: "the term '*language-game*' is meant to bring into prominence the fact that the *speaking* of a language is part of an activity [...]". As an example of a language-game, Wittgenstein himself refers to "presenting the results of an experiment in tables and diagrams" [44]. Assessing the reliability of climate-change predictions seems, at least to some extent, something that is learnt by the practice of carrying out and verifying such predictions.

5. Concluding remarks

The preceding discussion suggests an antithetic conclusion as regards the role of science in political and moral decision making: (i) A partial delegation of responsibility by the decision makers to the scientists, i.e. mainly climatologists and economists, is absolutely necessary, while (ii) at the same time, the climate-change debate demands a somewhat more restricted role of scientific prognoses than the one they currently play in the public debate. We discuss now the two terms of this antithesis in succession.

(i) Non-quantified epistemic uncertainties – whether contingent or necessary – hamper the proper communication of the actual degree of reliability of predicting anthropogenic impacts on the climate system. These uncertainties are wedded to specific model outputs, whether climatic or impact models. The respective modelers thus seem to have the high ground insofar as they can best assess those uncertainties that remain unquantified, at least for the moment.

A cost-benefit analysis depends sensitively on these uncertainties. This sensitivity implies, first, that performing such an analysis rests on the shoulders of the scientists. Second, it calls for more interdisciplinary work: It is the output of impact models that is needed for cost-benefit analysis; in this output, however, the uncertainties from the predicted concentration of greenhouse gases and from climate models, for instance, are compounded, linearly [37] or nonlinearly [6].

The proposed strengthening of the role of the sciences clearly does not imply a blind trust in scientific outcomes. First, it is the decision makers who set the rules for how to perform the cost-benefit analysis; see item (ii) below. Second, taking uncertainties seriously implies scrutinizing closely the scientific methodology. Shifting the actual performance of cost-benefit analysis to the sciences just acknowledges that neither political decision making nor moral evaluation are the place for a critical evaluation of scientific methodology. This is the task of the scientific community itself, together with an exterior watchdog consisting of, for example, the sociology and philosophy of science. Although currently this watchdog seems to lag behind the scientific progress, there already exist some interesting accounts on the "science of climate change," seen from the outside. The practice of welfare-economic analysis, however, is still insufficiently elucidated.

(ii) Saying that the cost-benefit analysis has to be performed on the basis of criteria from outside the sciences merely acknowledges the fact that the decision to choose among several ways of reacting to or anticipating climate changes invokes genuine moral values that science can – and indeed should – be neutral about. As it presumes such a value judgement, the oft-used term "catastrophe" has no place within the scientific debate on climate change.

The decision for or against a reduction or mitigation of predicted climate-change impacts is always a decision for or against the promotion of other investments, e.g. in water supply or education for developing countries. In current political decision making, scientific prognoses, however, act as "fig leaves" [45] that hide the actual decision making process and the normative assumptions on which it rests. Scientific, i.e. climatological or economical, prognoses as regards climate change or any other topic, taken on their own, give no sufficient reasons for acting or not acting, this way or the other.

Acknowledgments

It is a pleasure to thank the organizers and participants of the Conference on the "*Euler Equations: 250 Years On*" and, more than all, Uriel Frisch and Andrei Sobolevskii, for a very stimulating experience. We are grateful to our colleagues Peter Taylor and Nick Shackel for constructive input on the issues discussed herein. This study was supported by the U.S. Department of Energy grant DE-FG02-07ER64439 from the Climate Change Prediction Program, and by the European Commission's No. 12975 (NEST) project "Extreme Events: Causes and Consequences (E2-C2)."

References

[1] F.T. Mackenzie, A. Lerman, L.M. Ver, Recent past and future of the global carbon cycle, in: L.C. Gerhard, W.E. Harrison, B.M. Hanson (Eds.), Geological Perspectives of Global Climate Change, in: AAPG Studies in Geology, 47, Tulsa, OK, 2001, pp. 51–82.
[2] R.C. Wilson, S.A. Drury, J.L. Chapman, The Great Ice Age. Climate Change and Life, Routledge, London, New York, 2000.
[3] E. Le Roy Ladurie, Histoire humaine et comparée du climat II. Disettes et révolutions, Fayard, Paris, 2006, pp. 1740–1860.
[4] G. Yancheva, N.R. Nowaczyk, J. Mingram, P. Dulski, G. Schettler, J.F.W. Negendank, J. Liu, D.M. Sigman, L.C. Peterson, F.H. Haug, Influence of the intertropical convergence zone on the East Asian monsoon, Nature 445 (2007) 74–77.
[5] S. Solomon, D. Qin, M. Manning, Z. Chen, M. Marquis, K.B. Averyt, M. Tignor, H.L. Miller (Eds.), Climate Change 2007: The Physical Science Basis. Contribution of WG I to the 4th Assessment Report of the IPCC, Cambridge University Press, Cambridge, New York, 2007.
[6] M. Ghil, M.D. Chekroun, E. Simonnet, Climate dynamics and fluid mechanics: Natural variability and related uncertainties, Physica D (2008) (in this issue).
[7] R.D. Luce, H. Raiffa, Games and Decisions, J. Wiley, New York, 1957.
[8] L.J. Savage, The Foundations of Statistics, J. Wiley, New York, 1954.
[9] C. Lumer, The Greenhouse. A Welfare Assessment and Some Morals, University Press of America, Lanham, Md., New York, Oxford, 2002.
[10] S.O. Hanson, M. Johannesson, Decision-theoretic approaches to global climate change, in: G. Fermann (Ed.), International Politics of Climate Change, Scandinavian University Press, Stockholm, 1997, pp. 153–178.
[11] S.M. Gardiner, A Perfect moral storm: Climate change, intergenerational ethics and the problem of moral corruption, Environmental Values 15 (2006) 397–413.
[12] N. Stern, The Economics of Climate Change, in: The Stern Review, Cambridge University Press, Cambridge, 2007.
[13] R.S.J. Tol, Estimates of the damage costs of climate change. Part II: Dynamic estimates, Environmental & Resource Economics 21 (2002) 135–160.
[14] W.D. Nordhaus, J.G. Boyer, Warming the World: The Economics of the Greenhouse Effect, MIT Press, Cambridge, MA, 2000.
[15] S. Hallegatte, M. Ghil, P. Dumas, J.-C. Hourcade, Business cycles, bifurcations and chaos in a neo-classical model with investment dynamics, J. Econ. Behavior & Organization (2007) (in press). http://dx.doi.org/10.1016/j.jebo.2007.05.001.
[16] S. Hallegatte, J.-C. Hourcade, P. Dumas, Why economic dynamics matter in assessing climate change damages: Illustration on extreme events, Ecological Economics 62 (2) (2007) 330–340.
[17] P. Martinez Austria, P. van Hofwegen (Eds.), Synthesis of the 4th World Water Forum, Mexico City, 2006.
[18] R.A. Pielke Jr., When scientists politicize science: Making sense of controversy over the sceptical environmentalist, Environmental Science & Policy 7 (2004) 405–417.
[19] B. Lomborg, The Sceptical Environmentalist. Measuring the Real State of the World, Cambridge University Press, Cambridge, 2001.
[20] http://www.realclimate.org.
[21] N. Oreskes, Science and public policy. What's proof got to do with it? Environmental Science & Policy 7 (5) (2004) 369–383.
[22] J.St. Mill, Utilitarianism, in: M. Robson (Ed.), John Stuart Mill. A Selection of His Works, Bobbs-Merrill Educational Publishing, Indianapolis, 1982, pp. 149–228.
[23] A.M. Feldman, Welfare Economics and Social Choice Theory, Kluwer–Nijhoff Publishing, Boston, The Hague, London, 1980.
[24] J.H. Ausubel, Technical progress in climate change, Energy Policy 23 (1995) 411–416.

[25] R. Hillerbrand, Technik, Ökologie und Ethik. Ein normativ-ethischer Grundlagendiskurs über den Umgang mit Wissenschaft, Technik und Umwelt, Mentis, Paderborn, 2005.
[26] R. Nozick, Anarchy, State, and Utopia, Basic Books, New York, 1974.
[27] G. Patzig, Die Begründbarkeit moralischer Forderungen, in: G. Patzig (Ed.), Gesammelte Schriften 1, Wallstein Verlag, Göttingen, 1994, pp. 44–71.
[28] W.K. Frankena, Ethics, Englewood Cliffs, NJ, Prentice Hall, 1970.
[29] R.M. Hare, Sorting out Ethics, Oxford University Press, Oxford, 2000.
[30] W. Devall, G. Sessions, Deep Ecology: Living as if Nature Mattered, G. M. Smith, Salt Lake City, 1985.
[31] H.D. Thoreau, Walden and Other Writings, Elibron Classics, Chestnut Hill, MA, 2004.
[32] A. Krebs, Ethics of Nature. A Map, de Gruyter, Berlin, New York, 1999.
[33] United Nations Framework Convention on Climate Change, UNFCC, Kyoto Protocol to the United Nations Framework on Climate Change, http://unfccc.int/resource/docs/convkp/kpeng.pdf, 1998.
[34] H. Jonas, The Imperative of Responsibility: In Search of an Ethics for the Technological Age, The University of Chicago Press, Chicago, 1984.
[35] S. Clarke, Future technologies, dystopic futures and the precautionary principle, Ethics & Information Technology 7 (2005) 121–126.
[36] S. Bony, J.L. Dufresne, R. Colman, V.M. Kattsov, R.P. Allan, C.S. Bretherton, A. Hall, S. Hallegatte, M.M. Holland, W. Ingram, D.A. Randall, B.J. Soden, G. Tselioudis, M.J. Webb, How well do we understand and evaluate climate change feedback processes? J. Clim. 19 (2006) 3445–3482.
[37] G.H. Roe, M.B. Baker, Why is climate sensitivity so unpredictable? Science 318 (2007) 629–632.
[38] J. Giles, When doubt is a sure thing, Nature 418 (2002) 476–478.
[39] M. Collins, S. Knight (Eds.), Ensembles and probabilities: A new era in the prediction of climate change, Phil. Trans. R. Soc. A 365 (1857), 1955–2191.
[40] R. Hanson, The policy analysis market: A thwarted experiment in the use of prediction market for public policy, Innovations 2 (2007) 73–88.
[41] S. Cunliffe, Forecasting risks in the tourism industry using the Delphi technique, Tourism 50 (1) (2002) 31–41.
[42] R.H. Socolow, S.H. Lam, Good enough tools for global warming policy making, Phil. Trans. R. Soc. A 365 (2007) 897–934.
[43] R.H. Moss, S.H. Schneider, in: R. Pachauri, T. Taniguchi, K. Tanaka (Eds.), Guidance Papers on the Cross Cutting Issues of the Third Assessment Report of the IPCC, World Meteorol. Org., Geneva, 2000, pp. 33–51.
[44] L. Wittgenstein, Philosophical Investigations, Blackwell Publishers, Oxford, 2001.
[45] O.H. Pilkey, L. Pilkey-Jarvis, Useless Arithmetic. Why Environmental Scientists Can't Predict the Future, Columbia University Press, New York, Chichester, West Sussex, 2007.

Available online at www.sciencedirect.com

ScienceDirect

Physica D 237 (2008) 2139–2144

PHYSICA D

www.elsevier.com/locate/physd

Lagrangian reconstruction of cosmic velocity fields

Guilhem Lavaux*

Institut d'Astrophysique de Paris, 98bis Bd Arago, 75015Paris, France
Université Paris 6, France
Université Paris 11, France

Available online 21 February 2008

Abstract

We discuss a Lagrangian reconstruction method of the velocity field from galaxy redshift catalog that takes its root in the Euler equation. This results in a "functional" of the velocity field which must be minimized. This is helped by an algorithm solving the minimization of cost-flow problems. The results obtained by applying this method to cosmological problems are shown and boundary effects happening in real observational cases are then discussed. Finally, a statistical model of the errors made by the reconstruction method is proposed.

PACS: 47.10.A-; 47.15.km; 47.11.Fg; 95.35.+d; 98.62.Py

Keywords: Cosmology; Velocity field reconstruction; Numerical method; Statistics

1. Introduction

Cosmologists are highly interested in studying galaxy peculiar velocities. Indeed, their study is a direct way to measure the dynamical state of a system and would thus permit to better understand the dark matter distribution in our local Universe. The main difficulty is that measured velocities are only available sparsely and hence does not provide a good probe of the matter distribution. One must then devise an algorithm that is able to predict, under fair hypotheses, galaxy peculiar velocities from their present positions, which are their sky coordinates and their redshift, and compare the result to the measurement. Jim Peebles [1] first tried to do full orbit reconstruction by evolving the present system back in time. This method proved to be quite accurate for very small volume and number of objects. However, whenever one tries to reconstruct orbits of a large number of galaxies, the method fails because the number of plausible solution is blowing up. A simplification of this problem is presented: 3D galaxy positions are assumed to be known and a simpler gravitational dynamic model is going to be assumed. We will also assume that the dynamics of galaxies is mostly driven by collisionless dark matter particles.

This proceeding is organized as follows. In Section 2, we recall the principal result of the reconstruction method developed in [2] (see also the companion paper [3]). The method requires to use a special fast algorithm to solve the problem. This algorithm is presented in Section 3. The method is then applied to a dark matter distribution obtained from a cosmological simulation and the reconstructed velocities are checked against the simulated ones (Section 4). Finally, a discussion on problems with bad boundary conditions, as usually met in observational cosmology, is quickly discussed in Section 5.

2. Velocity reconstruction theory

The theory of velocity reconstruction in cosmology is detailed in [3]. We recall here the main results. To reconstruct the peculiar velocity field one must first compute the displacement field of dark matter particles by solving a Monge–Ampère equation (Eq. (16) of [3]). We achieve that by minimizing Eq. (17) of [3] in its simplified form using the "Auction" algorithm, with σ the pairing map and μ the mass of each particles of the mesh:

$$S_\sigma = \mu \sum_{i=0}^{N} \left(\mathbf{x}_i - \mathbf{q}_{\sigma(i)}\right)^2, \tag{1}$$

* Corresponding address: Institut d'Astrophysique de Paris, 98bis Bd Arago, 75015Paris, France. Tel.: +33 1 44 32 81 34; fax: +33 1 44 32 80 01.
E-mail address: lavaux@iap.fr.

0167-2789/$ - see front matter © 2008 Elsevier B.V. All rights reserved.
doi:10.1016/j.physd.2008.02.016

The minimization is conducted over σ. We recall also the Zel'dovich approximation (Eq. 12 of [3]) for the velocity field is taking the following form:

$$\mathbf{v}(\mathbf{x}_i) = \beta\left(\mathbf{x}_i - \mathbf{q}_i\right), \tag{2}$$

where β is the linear growth factor, which is well approximated by $\beta \simeq \Omega_{\rm m}^{9/5}$ when it is computed at redshift $z = 0$.

3. Minimization algorithm

Direct minimization of Eq. (1) is a computationally difficult problem [time complexity $O(N!)$]. Fortunately, there exist better alternatives that have been developed for solving minimal cost-flow problems and that can be adapted to our minimal transportation problem. In particular, we are going to use the "Auction" algorithm developed in [4]. The time complexity of this algorithm is of the order of $O(n^{2.25})$ by direct performance measurement, with n the particle density.[1] The exact constant hidden in $O(n^{2.25})$ depends a lot on the difficulty of the assignment problem, which means it is catalog dependent.

3.1. Auction algorithm

The algorithm tries to evolve the pairing map σ between $\mathbf{x}_i$ and $\mathbf{q}_j$ such that when the function is stationary between two consequent iterations it corresponds to minimizing the given total association cost. Particles located at different Eulerian positions x_i compete against each other for Lagrangian positions q_j. Minimization of the total association cost S_σ is achieved by studying the dual problem of minimization of association penalties p_j. In [4] it is shown that

$$\min_\sigma S_\sigma = \max_{p_j;\, j=1,\ldots,n} \left\{ \sum_j p_j + \sum_i r_i \right\}, \tag{3}$$

with $a_{i,j} = \mu(\mathbf{x}_i - \mathbf{q}_j)^2$, the cost of associating $\mathbf{x}_i$ to $\mathbf{q}_j$ and $r_i = \min_j(a_{i,j} + p_j)$. Once the set $\{p_j\}$ is determined by the above maximization, the map σ is simply given by:

$$\sigma(i) = \arg\min_j \left\{a_{i,j} + p_j\right\}. \tag{4}$$

Effectively, $\{p_j\}$ is computed iteratively by the algorithm. Each iteration is composed of two parts. During the first one, we obtain a set of best assignment $\mathcal{A}(j)$ for each particle $\mathbf{q}_j$ by minimizing all possible r_i. Then, we link $\mathbf{x}_{i_j^*}$ to $\mathbf{q}_j$ with i_j^* being the particle having the minimal $r_{i_j^*}$ in the set $\mathcal{A}(j)$. We also have a reverse mapping for this link that we write j_i^*. Finally, the penalty p_j is updated such that

$$p_j \to \tilde{p}_j = a_{i_j^*,j} + w_{i_j^*} - \epsilon, \tag{5}$$

with $\epsilon > 0$ and

$$w_i = \min_{j \neq j_i^*}\left(a_{i,j} + p_j\right). \tag{6}$$

[1] This number is obtained for a given simulation, and particles randomly until the desired average density is obtained. The worst case of this algorithm is actually $O(N^3)$, if one makes a dense search on purely random data.

The solution found is the same as for $\epsilon = 0$ provided $\epsilon < \epsilon_0/N$, with

$$\epsilon_0 = \min_{\{i,j\}/a_{i,j}\neq 0} a_{i,j}. \tag{7}$$

The time complexity depends quite a lot on the way ϵ is scaled down from its initial value to the ϵ_0/N. Numerical experiments have shown that trying to converge in about 5 iterations and starting from $\epsilon/\epsilon_0 \simeq N/2$ seems to give a faster convergence.

3.2. Implementation

We developed a C++ multi-threaded (shared memory parallelism) and MPI version of the "Auction" algorithm, it will be available later as a multi-purpose library for cost-flow problems at the address http://www.iap.fr/users/lavaux/. Besides doing a full minimization over all $\mathbf{q}_j$ for a given $\mathbf{x}_i$ ("dense" mode), it also supports a "sparse" mode that solves a partial minimization problem: for a given $\mathbf{x}_i$, it only minimizes over a subset of $\{\mathbf{q}_j\}$ such that $\|\mathbf{x}_i - \mathbf{q}_j\|_\infty < R$, where R is a parameter given at the initialization to the algorithm. This allows us to reduce drastically the computing time while giving the same result provided that R is not too small (typically $R = 40$ h^{-1} Mpc for a ΛCDM Universe). On a Dual-core AMD Athlon64 4800+, the SMP implementation (dense mode) takes 50 min to assign 79,000 particles. It has successfully reconstructed a 128^3 dense mesh in a month in the sparse mode. The MPI version of the corresponding algorithm is only performant for larger number of particles (typically $N \gtrsim 500{,}000$). Most of the time is, at the moment, spent at computing $\min_j\left(a_{i,j} + p_j\right)$ as the cost values are only kept in a minimalistic cache. Precomputing the costs is also not feasible because of the excessive amount of memory that would be needed to store all costs for all (i, j) pairs. We also consider to implement a general purpose totally asynchronous implementation in the near future.

4. Application to cosmology: Test on cosmological simulation

To check that the dark matter dynamical model is working, we are testing it against a 128^3 N-body sample [5] which was generated with the public version of the N-body code HYDRA [6] to simulate collisionless structure formation in a standard ΛCDM cosmology. The volume of the simulation is 200^3 h^{-3} Mpc^3. The mean matter density is $\Omega_{\rm m} = 0.30$ and the cosmological constant is $\Omega_\Lambda = 0.70$. The Hubble constant is $H_0 = 65$ km s^{-1} Mpc and the normalization of the density fluctuations in a sphere of radius 8 h^{-1} Mpc is $\sigma_8 = 0.99$.

Haloes of dark matter particles are identified using a friend-of-friend algorithm with a traditional value of the linking parameter $l = 0.2$ times the mean particle separation. A limit of 5 linked particles is put to bind particles into a halo. The particles left unbound by this criterion were kept in a set called the "background field". All objects are kept in a mock catalog called *FullMock*. We have run a reconstruction on FullMock using a MAK mesh with 128^3 elements. Each object of FullMock was given a number of elements $\mathbf{x}_i$ equal

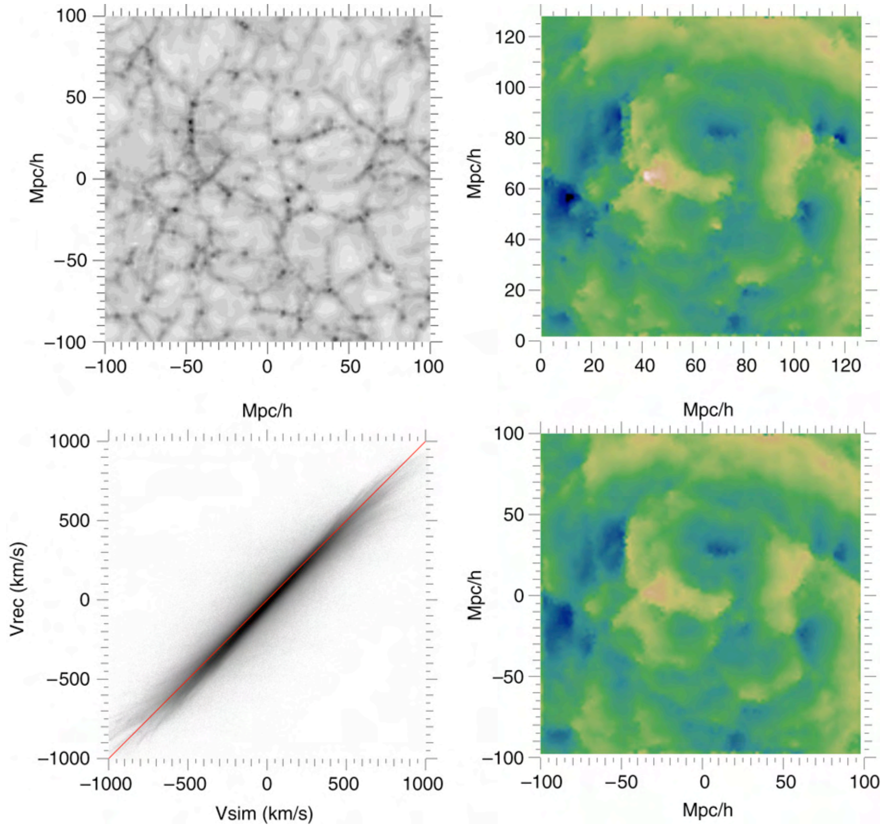

Fig. 1. *Application to Cosmology — Top left*: A slice of the density field of the ΛCDM simulation that is used for the tests (shades of gray indicate logarithm of the mass density). *Top right*: Adaptively smoothed line-of-sight component of the velocity field in the same slice. *Bottom right*: MAK reconstructed line-of-sight component of the velocity field of the same slice. Linear color scale: dark (blue, color online) = -1000 km s^{-1}, white = $+1000$ km s^{-1}. *Bottom left*: Scatter plot between reconstructed and simulated velocities for objects identified in the simulation. Shades of gray show levels of the logarithm of the point density.

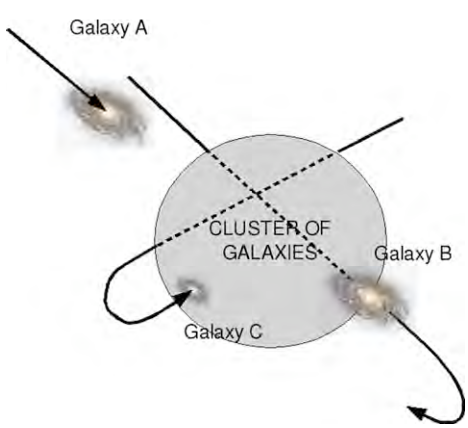

Fig. 2. Cosmology / Multi-streaming regions — This figure illustrates the different problems that may occur for a halo of dark matter particles near a cluster of galaxies. Galaxy A is in the region of first infall. The displacement field will be well reconstructed. Galaxy B is coming from the same direction as Galaxy A but has already gone through the center of the cluster and is decelerating. In that case, its displacement is badly reconstructed as, most likely, MAK predicts that the matter composing Galaxy B is coming from the region opposite to Galaxy A's region. Galaxy C is also wrongly reconstructed.

to the number of particles of the original simulation which has been bound into this object. We distributed the $\mathbf{q}_j$ mesh elements regularly on a cubic grid of the same physical size as the simulation box. Finally we computed the convex mapping σ corresponding to the MAK problem with the help of the algorithm described in Section 3. The velocities for each particle were computed using the Zel'dovich approximation Eq. (2), using the same cosmology as the simulation to compute β.

Fig. 1 summarizes the results obtained using the MAK method on the reconstructed velocities. The individual object velocities, in the bottom-left panel, are exceptionally well reconstructed. Visual inspection of the line-of-sight component of the velocity field in the two right panels shows nearly no discrepancy except in regions with really high velocities. In these regions, the dynamics is highly nonlinear, which means that the convex hypothesis is not valid anymore. This problem arises on a typical cosmological scale of at most a few Mpc around large clusters. Indeed, in those regions the fluid description of dark matter particles completely fails because the mass tracers may have already crossed the center of the gravitational attractor and are currently falling back to the center, as illustrated in Fig. 2. This renders the displacement field reconstruction dubious in those cases.

5. Application to cosmology: Boundary problems

One does not necessarily know the Lagrangian domain $\mathbf{q}$ on which the MAK reconstruction must be computed. This is the case for real cosmological observations and one must use some empirical prescription to attenuate the boundary effects on reconstructed velocities. This scheme is helped by the

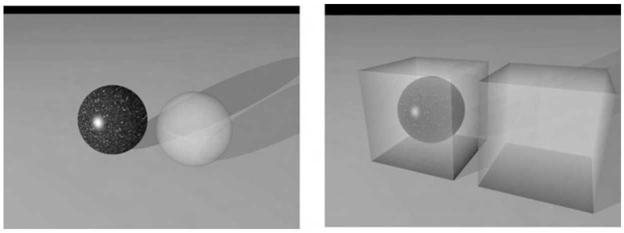

Fig. 3. *Cosmology / Boundary problems* — *Left panel:* Illustration of the NaiveDom approach to handle boundary problems while doing a reconstruction. The dark starry ball illustrates the current dark matter distribution as inferred from galaxy catalogs. The whitish transparent ball is the assumed initial volume for the dark matter that has fallen in present structures. *Right panel:* Same as left panel but this illustrates the PaddedDom approach.

overall homogeneity of the Universe above scales larger than 200 h^{-1} Mpc. We propose thus to check two schemes to handle boundary effects:

- A naive approach would be to assume that the piece of Universe considered has not changed its volume sufficiently between initial time and the current time. This means that we may assume that if we select a ball of matter, in the Universe, centered on us, all the mass that is inside this ball is coming from the same homogeneous ball in the Universe as it was at decoupling time. We call this approach *NaiveDom*. It is equivalent to say that tidal field effects are totally negligible on the considered scale.
- An alternative approach is not to make an assumption on the exact shape but on the low amount of fluctuation on the boundary. Consequently, if one selects the same ball of matter in the present Universe, it is fair under this approximation to pad the matter distribution using homogeneously distributed particles. One may then build the mapping between the "padded piece of Universe" and an initial completely homogeneous set of particles. We call this approach *PaddedDom*.

These two ways of handling boundary effects are illustrated in Fig. 3 and the results are presented in Fig. 4.

As expected, boundaries are badly reconstructed in PaddedDom and NaiveDom. However at the center of the spherical cut, the velocity field seems correctly reconstructed by visual comparison to the velocity field computed from the simulation. Looking carefully at the result using NaiveDom indicates that there is likely a systematic error near the center (the dark region is deeper in color and more extended than in the two other figures). This is probably due to stronger boundary effects that are not correctly attenuated by the NaiveDom scheme (a detailed quantitative analysis of boundary artefacts are given in [7]). Empirically, we found that a buffer zone of, at least, about 20 h^{-1} Mpc is needed to reduce boundary effects with a PaddedDom reconstruction scheme.

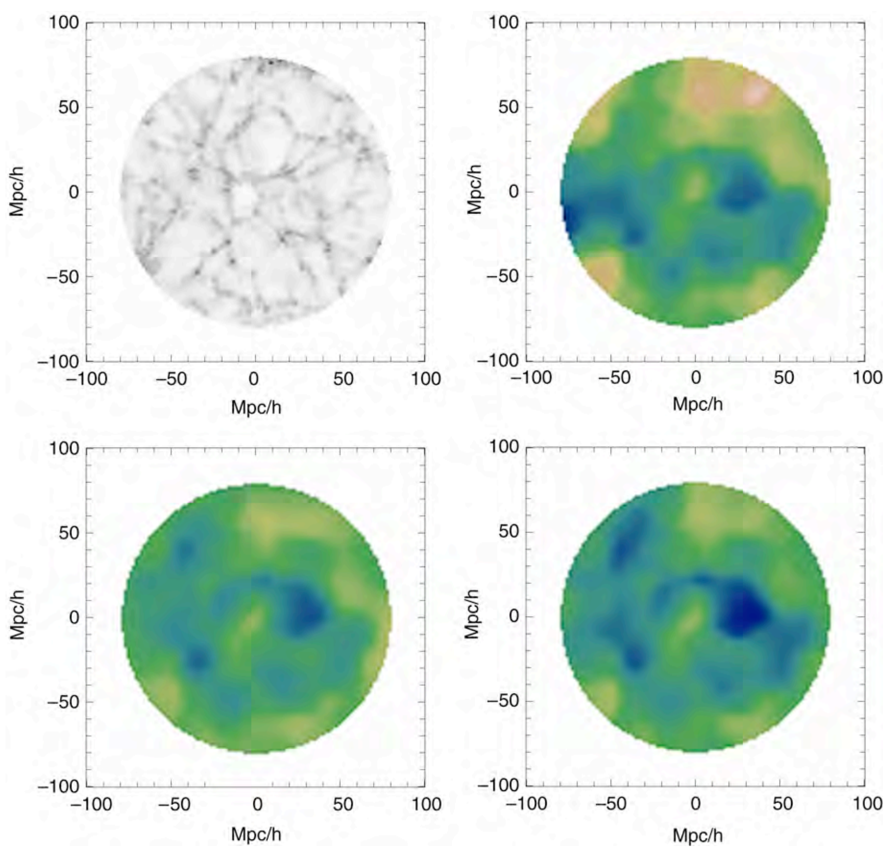

Fig. 4. *Cosmology / Boundary problems* — Outer boundary problems while doing reconstruction on finite volume catalog. Color scale is the same everywhere: dark (blue, color online) = −1000 km s^{-1}, white = +1000 km s^{-1}. *Top left*: Density field of the mock catalog (log scale). *Top right*: Simulated velocity field, smoothed with a 5 h^{-1} Mpc Gaussian window. *Low left*: PaddedDom velocity field, smoothed equally. *Low right*: NaiveDom velocity field, smoothed equally.

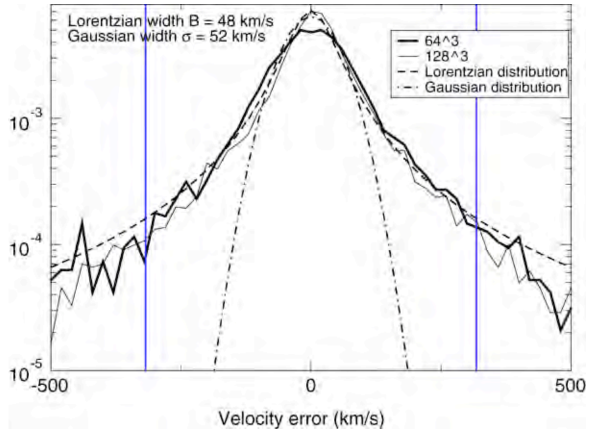

Fig. 5. Error in the reconstruction — This plot displays the probability distribution of the quantity $v_{\mathrm{r,rec}} - v_{\mathrm{r,sim}}$, where $v_{\mathrm{r,rec}}$ and $v_{\mathrm{r,sim}}$ are the line-of-sight reconstructed and simulated velocities, respectively, after choosing an observer at the center of the simulation box. The dashed and dot-dashed curves give the best fit of a Gaussian and a Lorentzian distribution, respectively.

6. Statistical analysis of errors in the reconstruction

The measurement of the slope between velocities and reconstructed displacements should give an estimation of Ω_{m}. However, building a reliable estimator of this slope without the statistical model of errors made both at the observation and the reconstruction level may produce unacceptable bias. We propose to show how to use models on reconstruction errors to make a Bayesian analysis of the reconstructed velocities. We will focus here on errors made during a reconstruction and assume that the observed peculiar velocities v are equal to their true velocities. A more detailed discussion can be found in [7].

Using simulations, we have measured the distribution of reconstruction errors, for each object i of a catalog of galaxy, $\{e_i\}$ defined as

$$e = v_{\mathrm{r}} - \beta\psi_{\mathrm{r,rec}}, \tag{8}$$

with $\beta = 0.51$ for the studied simulation (corresponding to $\Omega_m = 0.30$), v_{r} the line-of-sight component of the simulated velocity of the considered, $\psi_{\mathrm{r,rec}}$ the reconstructed radial displacement. The result is given in Fig. 5. We have tried to fit a histogram of the errors $\{e_i\}$ by both a Gaussian function of width B

$$f_G(e) \propto \exp\left(-\frac{e^2}{B^2}\right) \tag{9}$$

and a Lorentzian function

$$f_L(e) \propto \frac{1}{1+\frac{e^2}{B^2}}. \tag{10}$$

We obtained approximately the same width B for the two fits (which is expected from the second-order development of both functions), however it is striking that f_L is a much better approximation than f_G to the observed error distribution.

We equate the probability of getting an error e on the true velocity v_{r} for an object of the catalog to $f_L(e)$. We also assume now that the distribution of velocities in the object sample is, for a sufficiently large volume, Gaussian with a width σ_v:

$$P(v_{\mathrm{r}}|\sigma_v) \propto \exp\left(-\frac{v_{\mathrm{r}}^2}{2\sigma_v^2}\right). \tag{11}$$

Now we can build the joint probability of getting v_{r}, $\psi_{\mathrm{r,rec}}$ and β:

$$\begin{aligned} &P(v_{\mathrm{r}}, \psi_{\mathrm{r,rec}}, \beta|B, \sigma_v) \\ &\quad\propto P(e(v_{\mathrm{r}}, \psi_{\mathrm{r,rec}})|B, \sigma_v)P(v_{\mathrm{r}}|B, \sigma_v)P(\psi_{\mathrm{r,rec}}|B, \sigma_v) \\ &\quad\propto P(\psi_{\mathrm{r,rec}}|B, \sigma_v)\frac{\exp\left(-\frac{v_{\mathrm{r}}^2}{2\sigma_v^2}\right)}{1+\left(\frac{v_{\mathrm{r}}-\beta\psi_{\mathrm{r,rec}}}{B}\right)^2}, \end{aligned} \tag{12}$$

where the constant of proportionality eventually depends on B, σ_v and β. Using the theorem of Bayes, it is now possible to compute the conditional probability that the true velocity of some object is v_{r} given that the reconstructed displacement is $\psi_{\mathrm{r,rec}}$:

$$\begin{aligned} &P(v_{\mathrm{r}}|\psi_{\mathrm{r,rec}}, \beta, B, \sigma_v) \\ &\quad= \frac{\mathrm{e}^{-\frac{v_r^2}{2\sigma_v^2}}\left(1+\left(\frac{\beta_*\psi_r-\alpha_*v_r+\gamma_*}{B_v}\right)^2\right)^{-1}}{\int_{v=-\infty}^{+\infty}\mathrm{e}^{-\frac{v^2}{2\sigma_v^2}}\left(1+\left(\frac{\beta_*\psi_r-\alpha_*v+\gamma_*}{B_v}\right)^2\right)^{-1}\mathrm{d}v}. \end{aligned} \tag{13}$$

To obtain the total likelihood $\mathfrak{L}(\beta)$ to observe true velocities $\{v_{i,\mathrm{r}}\}$ given that the reconstructed displacements are $\{\psi_{i,\mathrm{r,rec}}\}$, one may assume the statistical independence of the $(v_{i,\mathrm{r}}, \psi_{i,\mathrm{r,rec}})$ duets. With this assumption, $\mathfrak{L}$ is simply

$$\mathfrak{L}(\beta) = \prod_i P(v_{i,\mathrm{r}}|\psi_{i,\mathrm{r,rec},\beta,B,\sigma_v}). \tag{14}$$

Using that approach we have made measurements in finite volume mock catalogs. For example, with a PaddedDom reconstruction, one measure $\Omega_{\mathrm{m}} = 0.34$ with this approach (for an effective $\Omega_{\mathrm{m}} = 0.35$ in this catalog), whereas a naive measurement would yield $\Omega_{\mathrm{m}} \simeq 0.26$.

7. Conclusion

We presented a method to predict velocities of galaxies from their current position. To solve this problem, we implemented a fast algorithm invented by Dimitri Bertsekas [4] and applied the method to a pure dark matter simulation. It happens that the reconstructed velocities are impressively accurate on large scales (Section 4). However, the solution is only approximate in regions where multi-streaming occurs.

We proposed two methods for partially correcting boundary effects (Section 5) and showed how boundary effects affect the reconstructed velocity field. We preferred the PaddedDom reconstruction scheme as it seems to give overall better results. Empirically we found that a buffer zone of 20 h^{-1} Mpc is needed before obtaining a reconstructed velocity field correlated with the one given by the simulation.

At last, we proposed a Bayesian model (Section 6) to account for reconstruction errors while estimating the slope between the reconstructed displacements and the true velocities of objects in a galaxy catalog.

We would like to continue this work by improving the padding schemes to have even less boundary effects and make full use of available data in astronomy. We are also working on an improved algorithm that is able to take into account in a better way the nonlinearities that are introduced in the velocity field due to gravitational effects occurring along particle trajectories. This new algorithm will try to fully solve the Euler–Poisson problem.[2]

Acknowledgement

This work is partially supported by the ANR grant BLAN07-2_183172 (project OTARIE).

References

[1] P.J.E. Peebles, Tracing galaxy orbits back in time, Astophys. J. Lett. 344 (1989) L53–L56.
[2] Y. Brenier, U. Frisch, M. Hénon, G. Loeper, S. Matarrese, R. Mohayaee, A. Sobolevskiĭ, Reconstruction of the early Universe as a convex optimization problem, Monthly Notices R. Astronom. Soc. 346 (2003) 501–524.
[3] R. Mohayaee, A. Sobolevskiĭ, The Monge–Ampère–Kantorovich approach to reconstruction in cosmology, These Proceedings.
[4] D.P. Bertsekas, A Distributed Algorithm for the Assignment Problem, MIT Press, Cambridge, MA, 1979.
[5] R. Mohayaee, H. Mathis, S. Colombi, J. Silk, Reconstruction of primordial density fields, Monthly Notices R. Astronom. Soc. 365 (2006) 939–959.
[6] H.M.P. Couchman, P.A. Thomas, F.R. Pearce, Hydra: An adaptive-mesh implementation of P 3M-SPH, Astrophys. J. 452 (1995) 797.
[7] G. Lavaux, R. Mohayaee, S. Colombi, R.B. Tully, F. Bernardeau, J. Silk, Observational biases in Lagrangian reconstructions of cosmic velocity fields, ArXiv e-prints 707.

[2] G. Lavaux & G. Loeper, work in progress.

Available online at www.sciencedirect.com
ScienceDirect
Physica D 237 (2008) 2145–2150
PHYSICA D
www.elsevier.com/locate/physd

The Monge–Ampère–Kantorovich approach to reconstruction in cosmology

Roya Mohayaee[a], Andreĭ Sobolevskiĭ[b,c,d,*]

[a] *Institut d'Astrophysique de Paris, CNRS UMR 7095, 75014 Paris, France*
[b] *Physics Department, M. V. Lomonossov Moscow State University, 119992 Moscow, Russia*
[c] *International Institute for Earthquake Prediction Theory and Mathematical Geophysics, 117997 Moscow, Russia*
[d] *Laboratoire J.-V. Poncelet, CNRS UMI 2615, 119002 Moscow, Russia*

Available online 16 January 2008

Abstract

Motion of a continuous fluid can be decomposed into an "incompressible" rearrangement, which preserves the volume of each infinitesimal fluid element, and a gradient map that transfers fluid elements in a way unaffected by any pressure or elasticity (the *polar decomposition* of Y. Brenier). The Euler equation describes a system whose kinematics is dominated by incompressible rearrangement. The opposite limit, in which the incompressible component is negligible, corresponds to the Zel'dovich approximation, a model of motion of self-gravitating fluid in cosmology.

We present a method of approximate reconstruction of the large-scale proper motions of matter in the Universe from the present-day mass density field. The method is based on recovering the corresponding gradient transfer map. We discuss its algorithmics, tests of the method against mock cosmological catalogues, and its application to observational data, which results in tight constraints on the mean mass density Ω_m and age of the Universe.

PACS: 95.35.+d; 95.75.Pq; 98.62.Py; 98.65.Dx

Keywords: Dark matter; Proper motions of galaxies; Reconstruction; Convex optimization

1. Introduction

In the spectrum of possible models of fluid motion, the Euler equation of incompressible fluid constitutes an extreme. As was shown by Y. Brenier [1,2], any Lagrangian motion of fluid admits a *polar factorization* into a composition of an "incompressible" rearrangement, which preserves the volume of each infinitesimal fluid element, and an "absolutely compressible" transfer, which displaces fluid elements to their final locations prescribed by the gradient of a suitable convex potential, while expanding or contracting them in a way unaffected by any pressure or elasticity. Decomposing a fluid motion into a sequence of small time steps and factoring out the compressible transfer from the inertial fluid motion at each step yields a difference scheme for the incompressible Euler equation [3].

In this article we show how the opposite approach, in which only the compressible transfer is retained, can be applied to solving the problem of reconstructing peculiar motions and velocities of dark matter elements in cosmology. We also discuss the algorithmics of this method, which gives an explicit discrete approximation to polar decomposition and can also be applied to model incompressible fluid as suggested in [3].

Recall that on scales from several to a few dozen of h^{-1} Mpc the large-scale structure of the Universe is primarily determined by the distribution of the dark matter. This distribution can be described by the mass density field and by the large-scale component of the peculiar velocity field,[1] controlled by dark matter itself via gravitational interaction. The dark

* Corresponding author at: Physics Department, M. V. Lomonossov Moscow State University, 119992 Moscow, Russia. Tel.: +7 499 2425366.
E-mail addresses: mohayaee@iap.fr (R. Mohayaee), sobolevski@phys.msu.ru (A. Sobolevskiĭ).

[1] The cosmological flow of dark matter is conveniently decomposed into the uniform Hubble expansion and the residual, or *peculiar*, motion.

0167-2789/$ - see front matter © 2008 Elsevier B.V. All rights reserved.
doi:10.1016/j.physd.2008.01.007

matter distribution is traced by galaxies, whose positions and luminosities are presently summarized in extensive surveys [4–6]. On large scales luminosities of galaxies allow to determine their masses, from which the mass density of the dark matter environment can be estimated using well-established techniques [7,8].

It is appropriate to consider the reconstruction of the field of peculiar velocities as part of the more complex problem of reconstructing the full dynamical history of a particular patch of the Universe. Several approximate methods have been proposed to this end, of which we mention here two. The *Numerical Action Method*, based on looking for minimum or saddle-point solutions for a variational principle involving motion of discrete galaxies, was introduced by P.J.E. Peebles in the late 1980s [9]; its modern state is addressed in the present volume by A. Nusser [15]. In this paper we concentrate on the *Monge–Ampère–Kantorovich* method introduced in [10] (hereafter the *MAK method*), specifically highlighting the structural relationship between the MAK method and the variational approach to the Euler equation of incompressible fluid [11].

In Section 2 the mathematical setting of the MAK reconstruction is derived by the application of the Zel'dovich approximation to a suitable variational formulation of dark matter dynamics, which leads to the Monge–Kantorovich mass transfer problem and the Monge–Ampère equation. In Section 3 we discuss the algorithmics of solving the discretized Monge–Kantorovich problem, which gives as a byproduct an algorithm of polar decomposition for maps between discrete finite point sets. In Section 4 we show that the MAK method performs very well when tested against direct numerical simulations of the cosmological evolution and review the recent applications of the MAK method to real observational data, which yielded new tight constraints on the value of the mean mass density of the Universe. A detailed treatment of implementation and testing the MAK method against N-body simulations is presented in the companion paper by G. Lavaux in the present volume [20]. The paper is finished with a discussion and conclusions.

2. Dynamics of cold dark matter and the Zel'dovich approximation

The most widely accepted explanation of the large-scale structure seen in galaxy surveys is that it results from small primordial fluctuations that grew under gravitational self-interaction of collisionless cold dark matter particles in an expanding universe (see, e.g., [12] and the references therein). The relevant equations of motion are the Euler–Poisson equations written here for a flat, matter-dominated Einstein–de Sitter universe (for a more general case see, e.g., [13]):

$$\partial_\tau \boldsymbol{v} + (\boldsymbol{v}\cdot\nabla_{\boldsymbol{x}}\boldsymbol{v}) = -\frac{3}{2\tau}(\boldsymbol{v} + \nabla_{\boldsymbol{x}}\phi), \tag{1}$$

$$\partial_\tau \rho + \nabla_{\boldsymbol{x}}\cdot(\rho\boldsymbol{v}) = 0, \tag{2}$$

$$\nabla^2_{\boldsymbol{x}}\phi = \frac{1}{\tau}(\rho - 1). \tag{3}$$

Here $\boldsymbol{v}(\boldsymbol{x},\tau)$ denotes the velocity, $\rho(\boldsymbol{x},\tau)$ denotes the density (normalized so that the background density is unity) and $\phi(\boldsymbol{x},\tau)$ is a gravitational potential. All quantities are expressed in comoving spatial coordinates $\boldsymbol{x}$ and linear growth factor τ, which is used as the time variable; in particular, $\boldsymbol{v}$ is the Lagrangian τ-time derivative of the comoving coordinate of a fluid element. A non-technical explanation of the meaning of these variables and a derivation of Eqs. (1)–(3) in the Newtonian approximation can be found, e.g., in [14]; see also [15] in the present volume, where the growth factor is denoted by a.

The right-hand sides of the Euler and Poisson equations (1) and (3) contain denominators proportional to τ. Hence, it suffices for the problem not to be singular as $\tau \to 0$ that

$$\boldsymbol{v}(\boldsymbol{x},0) + \nabla_{\boldsymbol{x}}\phi(\boldsymbol{x},0) = 0, \qquad \rho(\boldsymbol{x},0) = 1. \tag{4}$$

Note that the density contrast $\rho - 1$ vanishes initially, but the gravitational potential and the velocity, as defined here, stay finite thanks to our choice of the linear growth factor as the time variable. Eq. (4) provides initial conditions at $\tau = 0$; at the present time $\tau = \tau_0$ the density is prescribed by a galaxy survey as explained above:

$$\rho(\boldsymbol{x},\tau_0) = \rho_0(\boldsymbol{x}). \tag{5}$$

In parallel with the Euler equation of incompressible fluid, Eq. (1) can be considered as the Euler–Lagrange equation for a suitable action [16,14]:

$$\mathcal{I}_\alpha = \frac{1}{2}\int_0^{\tau_0} \mathrm{d}\tau \int \mathrm{d}\boldsymbol{x}\cdot\tau^\alpha(\rho|\boldsymbol{v}|^2 + \alpha|\nabla_{\boldsymbol{x}}\phi|^2), \tag{6}$$

where $\alpha = \frac{3}{2}$ for the flat Universe and minimization is performed under the constraints expressed by Eqs. (2)–(5). Note that the term containing $|\nabla_{\boldsymbol{x}}\phi|^2$ may be seen as a penalization for the nonuniformity of the mass distribution, which corresponds to the lack of incompressibility of the fluid; enhancing this penalization infinitely would suppress the "absolutely compressible" transfer of fluid elements, thus recovering the incompressible Euler equation.

However, according to Eq. (4) the rotational component of the initial velocity field vanishes, which strongly suppresses the "incompressible" mode of the fluid motion at early times. Based on this observation, Ya.B. Zel'dovich proposed [17] an opposite approximation in which $\alpha \to 0$. In this approximation Eq. (1) assumes the form

$$\partial_\tau\boldsymbol{v} + (\boldsymbol{v}\cdot\nabla_{\boldsymbol{x}})\boldsymbol{v} = 0. \tag{7}$$

Much as the incompressible Euler system, the study of the Zel'dovich approximation benefits from the Lagrangian approach. Let $\boldsymbol{x}(\boldsymbol{q},\tau)$ be the comoving coordinate at time τ of a fluid particle that was initially located at $\boldsymbol{q}$: $\boldsymbol{x}(\boldsymbol{q},0) = \boldsymbol{q}$. Then

$$\rho(\boldsymbol{x}(\boldsymbol{q},\tau),\tau) = (\det(\partial\boldsymbol{x}/\partial\boldsymbol{q}))^{-1}, \tag{8}$$

$$\boldsymbol{v}(\boldsymbol{x}(\boldsymbol{q},\tau),\tau) = \partial_\tau\boldsymbol{x}(\boldsymbol{q},\tau), \tag{9}$$

where the τ derivative is taken as $\boldsymbol{q}$ is fixed. As observed by Zel'dovich, in these new variables the nonlinear equation (7) assumes a linear form

$$\partial_\tau^2 \boldsymbol{x} = 0. \tag{10}$$

Moreover Eq. (2) is satisfied automatically, and the action becomes

$$\mathcal{I}_0 = \frac{1}{2}\int_0^{\tau_0} \mathrm{d}\tau \int \mathrm{d}\boldsymbol{q}\, |\partial_\tau \boldsymbol{x}(\boldsymbol{q},\tau)|^2 = \frac{1}{2\tau_0}\int \mathrm{d}\boldsymbol{q}\, |\boldsymbol{x}_0(\boldsymbol{q}) - \boldsymbol{q}|^2. \tag{11}$$

Here we denote $\boldsymbol{x}_0(\boldsymbol{q}) = \boldsymbol{x}(\boldsymbol{q},\tau_0)$ and use the fact that action minimizing trajectories of fluid elements, determined by Eq. (10), are given by

$$\boldsymbol{x}(\boldsymbol{q},\tau) = \boldsymbol{q} + (\tau/\tau_0)(\boldsymbol{x}_0(\boldsymbol{q}) - \boldsymbol{q}). \tag{12}$$

Note that according to the first condition (4), $\boldsymbol{v}(\boldsymbol{q},0) = (1/\tau_0)(\boldsymbol{x}_0(\boldsymbol{q}) - \boldsymbol{q}) = \nabla_{\boldsymbol{q}}\bar{\Phi}(\boldsymbol{q})$ and the Lagrangian map (12) remains curl-free for all $\tau > 0$: $\boldsymbol{x}(\boldsymbol{q},\tau) = \boldsymbol{q} + \tau\nabla_{\boldsymbol{q}}\bar{\Phi}(\boldsymbol{q}) = \nabla_{\boldsymbol{q}}\Phi(\boldsymbol{q},\tau)$ with $\Phi(\boldsymbol{q},\tau) = |\boldsymbol{q}|^2/2 + \tau\bar{\Phi}(\boldsymbol{q})$; thus the "incompressible" rotational component of the fluid motion is indeed fully suppressed.

To find the motion of the fluid in the Zel'dovich approximation it is necessary to minimize the action (11) under the constraint provided by the representation of density (8) and the boundary conditions (4) and (5):

$$\det(\partial \boldsymbol{x}_0(\boldsymbol{q})/\partial \boldsymbol{q}) = 1/\rho(\boldsymbol{x}_0(\boldsymbol{q})). \tag{13}$$

In optimization theory this problem is called the *Monge–Kantorovich problem*. Equivalently, one can solve the *Monge–Ampère equation* that follows from (13) for the function $\Phi_0(\boldsymbol{q}) = \Phi(\boldsymbol{q},\tau_0)$ such that $\boldsymbol{x}_0(\boldsymbol{q}) = \nabla_{\boldsymbol{q}}\Phi_0(\boldsymbol{q})$:

$$\det(\partial^2\Phi_0(\boldsymbol{q})/\partial q_i \partial q_j) = 1/\rho_0(\nabla_{\boldsymbol{q}}\Phi_0(\boldsymbol{q})). \tag{14}$$

At large scales the Lagrangian map $\boldsymbol{x}_0(\boldsymbol{q})$ in cosmology is free from *multistreaming* (the presence of several streams of dark matter at the same spatial location). Under this assumption the potential $\Phi_0(\boldsymbol{q})$ is necessarily convex,[2] and the Legendre transform

$$\Psi_0(\boldsymbol{x}) = \max_{\boldsymbol{q}}(\boldsymbol{q}\cdot\boldsymbol{x} - \Phi_0(\boldsymbol{q})), \tag{15}$$

where the maximum is attained at $\boldsymbol{q}$ such that $\boldsymbol{x} = \nabla_{\boldsymbol{q}}\Phi_0(\boldsymbol{q})$, gives (14) a simpler form

$$\det(\partial^2\Psi_0(\boldsymbol{x})/\partial x_i \partial x_j) = \rho_0(\boldsymbol{x}). \tag{16}$$

The *Monge–Ampère–Kantorovich (MAK) method*, introduced in [10], consists in solving either of these two problems for $\boldsymbol{x}_0(\boldsymbol{q})$ and using Eqs. (9) and (12) to approximately recover the present field $\boldsymbol{v}(\boldsymbol{x},\tau_0)$ of peculiar velocities.

3. Algorithmics of solving the Monge–Kantorovich problem and the discrete polar decomposition

To solve the Monge–Kantorovich problem numerically we discretize the initial and final distributions of mass into collections of Dirac point masses: all initial point masses $(\mu,\boldsymbol{q}_i)$ are assumed to lie on a regular grid and be equal, whereas the masses $(m_j,\boldsymbol{x}_j)$ discretizing the present distribution $\rho_0(\boldsymbol{x})$ typically come from a galaxy survey. The discretized action functional (11) assumes the form

$$\frac{1}{2}\sum_{i,j}\gamma_{ij}|\boldsymbol{x}_j - \boldsymbol{q}_i|^2, \tag{17}$$

where $\gamma_{ij} \geq 0$ denotes the amount of mass transferred from $\boldsymbol{q}_i$ to $\boldsymbol{x}_j$ and mass conservation implies for all i, j

$$\sum_k \gamma_{kj} = m_j, \quad \sum_l \gamma_{il} = \mu. \tag{18}$$

In practice we choose all m_j to be integer multiples of the elementary mass μ, which guarantees that all γ_{ij} assume only values 0 or μ.

Observe that the unknowns γ_{ij} enter into the problem of minimizing (17) under constraints (18) linearly. Problems of this form are called *linear programs* and can be efficiently solved by various optimization methods, see, e.g., [18]. Often the original, *primal* formulation of a linear program is treated simultaneously with a *(Lagrange) dual* formulation, which is another linear program; such algorithms are called *primal–dual* algorithms. For the linear program at hand the dual formulation is to maximize

$$-\mu\sum_i \phi_i - \sum_j \psi_j m_j \tag{19}$$

under the constraints

$$\frac{1}{2}|\boldsymbol{x}_j - \boldsymbol{q}_i|^2 + \phi_i + \psi_j \geq 0 \quad \text{for all } i, j. \tag{20}$$

Here ϕ_i, ψ_j are Lagrange multipliers for constraints (18); the duality comes from the following representation of the (coinciding) optimal values of the two problems:

$$\min_{\gamma_{ij}\geq 0}\max_{\phi_i,\psi_j}\left(\frac{1}{2}\sum_{i,j}\gamma_{ij}|\boldsymbol{x}_j - \boldsymbol{q}_i|^2 + \sum_i \phi_i\left(\sum_j \gamma_{ij} - \mu\right) + \sum_j \psi_j\left(\sum_i \gamma_{ij} - m_j\right)\right),$$

where taking max or min leads to the primal or dual problem respectively. The coincidence of the optimal values implies that $\bar{\gamma}_{ij}$, $\bar{\phi}_i$, $\bar{\psi}_j$ solve the respective problems if and only if

$$\sum_{i,j}\bar{\gamma}_{ij}\left(\frac{1}{2}|\boldsymbol{x}_j - \boldsymbol{q}_i|^2 + \bar{\phi}_i + \bar{\psi}_j\right) = 0. \tag{21}$$

In view of the nonnegativity conditions this means that for each pair (i, j) either $\bar{\gamma}_{ij} = 0$ or constraint (20) is satisfied with equality (and then $\bar{\gamma}_{ij} = \mu$). For all other values of $\gamma_{ij} \geq 0$ and ϕ_i, ψ_j that satisfy constraints (18) and (20), the left-hand side of (21) is strictly positive and thus the value of (17) is strictly greater than that of (19); such γ_{ij}, η_i, ψ_j cannot be solutions to the respective optimization problems.

A typical primal–dual algorithm starts with a set of values of ϕ_i, ψ_j for which all inequalities (20) hold and proceeds in

[2] Convexity of the function $\Phi(\boldsymbol{q},\tau) = |\boldsymbol{q}|^2/2 + \tau\Phi_0(\boldsymbol{q})$ holds at $\tau = 0$ and must be preserved for $\tau > 0$ if no multistreaming occurs.

a series of steps. At each step a constraint of the form (20) is found that is, in a certain sense, the easiest to be turned into equality, values of the corresponding ϕ_i and ψ_j are updated accordingly, and the γ_{ij} is set to μ. An algorithm stops when the number of equalities in (20) equals the number of masses $(\mu, \boldsymbol{q}_i)$, so that (21) is satisfied.

We found the *auction algorithm* of D. Bertsekas [19] (see also [20]) to be a particularly efficient primal–dual algorithm for the huge data sets arising from the cosmological application. The search for the constraint (20) that is to be satisfied with equality at each step may be performed very efficiently using a specially developed geometrical search routine, which is based on suitably modified routines of the ANN library [21]. Further details of this numerical implementation of the MAK method are given in [14] and in our forthcoming publication with M. Hénon. A new implementation in a parallel computing environment is reported in the companion paper of G. Lavaux [20].

We finally show why the solution of the Monge–Kantorovich problem in the discrete case gives a discrete analogue of polar decomposition. Let a discrete "map" γ^* between two sets of points $(\mu, \boldsymbol{q}_i)$ and $(m_j, \boldsymbol{x}_j)$ be given such that $m_j = \sum_i \gamma^*_{ij}$ and γ^*_{ij} take only values 0 and μ. Solving the corresponding Monge–Kantorovich problem will give a discrete analogue γ_{ij} of the gradient transfer. To see this observe that for $\Phi_i = \frac{1}{2}|\boldsymbol{q}_i|^2 + \phi_i$, $\Psi_j = \frac{1}{2}|\boldsymbol{x}_j|^2 + \psi_j$ equality in (20) means that

$$\Psi_j = \max_k (\boldsymbol{q}_k \cdot \boldsymbol{x}_j - \Phi_k) \tag{22}$$

(cf. (15)), i.e., the map sending $\boldsymbol{q}_i$ to $\boldsymbol{x}_j$ is a discrete analogue of the gradient map $\boldsymbol{x}(\boldsymbol{q}) = \nabla_{\boldsymbol{q}} \Phi(\boldsymbol{q})$ of the previous section. The corresponding discrete analogue of "incompressible" rearrangement is a permutation of $(\mu, \boldsymbol{q}_i)$ that for any j sends the set of points i such that $\gamma^*_{ij} > 0$ to the set of points i' such that $\gamma_{i'j} > 0$; if furthermore $m_j = \mu$ for all j, both sets are singletons and the permutation is recovered uniquely.

In the MAK method we are interested in the "gradient" part of the Lagrangian map sending elements of dark matter to their present positions, whereas in the difference scheme for the Euler equation proposed by Y. Brenier in [3] it is the permutation part that is retained.

Finally note that an alternative approaches to solve the Monge–Kantorovich problem, based on direct numerical resolution of Eqs. (2) and (7), was proposed in [22].

4. Testing and application of the MAK method to cosmological reconstruction

The validity of the MAK method depends on the quality of the Zel'dovich approximation, which is hard to establish rigorously. To be able to apply the method to real-world data we have instead to rely on extensive numerical tests.

We report here a test of the MAK method against an N-body simulation with over 2×10^6 particles [23]. The N-body simulation had the following characteristics: 128^3 particles were assembled in a cubic box of $200\,h^{-1}$ Mpc, giving the mean inter-particle separation of $1.5\,h^{-1}$ Mpc; the initial conditions

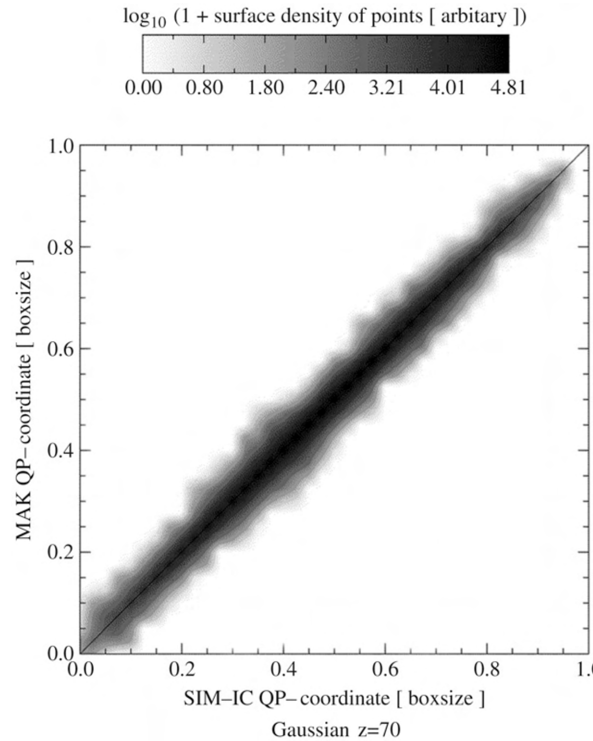

Fig. 1. Scatter plot of the MAK-reconstructed initial coordinates of particles versus their true initial coordinates for a sample of an N-body simulation with 128^3 particles in a cubic box of size $200\,h^{-1}$ Mpc; ideal reconstruction would correspond to the diagonal. A "quasi-periodic (QP) projection" coordinate $\tilde{q} = (q_1 + q_2\sqrt{2} + q_3\sqrt{3})/(1 + \sqrt{2} + \sqrt{3})$ is used with $0 \le q_i \le 1$, where 1 corresponds to the (rescaled) box size. The QP projection maps a regular grid in the unit cube into the unit segment such that $\tilde{q}$ images of no two grid points coincide. Shown is the decimal logarithm of the local density of points plus 1; the resolution in QP coordinates is 1/256, the Lagrangian mesh spacing is 1/128.

Table 1
MAK reconstruction: percentage of successfully reconstructed initial positions at different scales (measured in units of mesh size in a box of 128^3 grid points)

Scale	0[a]	≤1	≤2	≤3	≤4	≤5
%	18%	41%	54%	66%	74%	81%

[a] Exact reconstruction.

for the velocity field $\boldsymbol{v}(\boldsymbol{q}, 0)$ were taken Gaussian; the density parameter was chosen to be $\Omega_m = 0.3$, the Hubble parameter to be $h = 0.65$, the normalization of the initial power-spectrum $\sigma_8 = 0.99$, and the mass of a single particle in this simulation was $M = 3.2 \times 10^{11} h^{-1} M_\odot$ where $M_\odot$ is the solar mass.

The scatter plot in Fig. 1 demonstrates the performance of the MAK method in finding Lagrangian positions of the particles. At the scales that were probed, positions of about 20% of particles are reconstructed exactly (for detailed data see Table 1). This low rate is due to large multistreaming at such small scales; at larger scales where mean inter-particle separation is about $6\,h^{-1}$ Mpc (up to 3 meshes), the MAK reconstruction gives the Lagrangian positions of two thirds of the particles exactly. At the moment of its implementation in 2006 this reconstruction of 128^3 particles was unprecedented and broke a computational barrier for

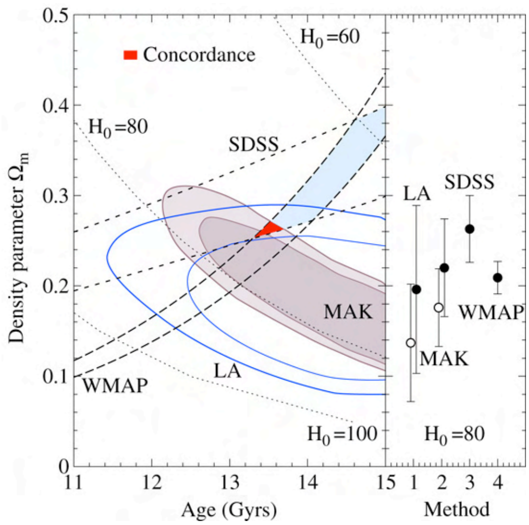

Fig. 2. Constraints on the mean mass density and the age of the Universe obtained by applying reconstruction techniques to real observational data. Left pane: solid contours mark σ and 2σ confidence levels for the MAK reconstruction (shaded) and the least-action (LA) reconstruction (unfilled). Shaded also is the confluence of the constraints on density and age parameters from *WMAP* [24] of $\Omega_m h^2 = 0.134$ and from SDSS [6] of $\Omega_m h = 0.21$. The 2σ concordance region of the four methods is filled. Right pane: density parameter estimates for $H_0 = 80$. For details see [25].

cosmological reconstruction schemes; more detailed tests of the MAK reconstruction of the same scale are reported by G. Lavaux [20] in the present volume.

We now turn to applications of the MAK reconstruction to real observational data. The MAK reconstruction of the peculiar velocities depends on the mean density of the Universe (the parameter Ω_m), the age of the Universe τ_0 ($\tau_0 \sim 1/H_0$ where $H_0 = 100 \times h$ is the Hubble parameter), and the mass-luminosity relation. Assuming certain values of these parameters, one can estimate the peculiar velocities of the galaxies as ratios of their displacements to τ_0. Optimizing the matching between these velocities and the observed velocities of a few test galaxies, one can then constrain the parameters of the reconstruction.

This procedure is illustrated in Fig. 2, taken from [25]. The catalog of galaxies $(m_j, \boldsymbol{x}_j)$ that is used here is a 40% augmentation of the Nearby Galaxies Catalog, now including 3300 galaxies within 3000 km s^{-1} [4]. This depth is more than twice the distance of the dominant component, the Virgo cluster, and the completion to this depth in the current catalog compares favourably with other all-sky surveys. The second observational component is an extended catalog of galaxy distances (or radial component of peculiar velocities). In this catalog, there are over 1400 galaxies with distance measures within the 3000 km s^{-1} volume; over 400 of these are derived by high quality observational techniques that give accurate estimates of the radial components of peculiar velocities. The important feature of Fig. 2 is that the MAK contours are transversal to contours provided by other methods, which largely reduces the degeneracy of constraints in the parameter space.

5. Conclusion

According to the polar decomposition theorem of Y. Brenier [1,2], kinematics of continuous fluid motion can be decomposed into “incompressible” rearrangement and “infinitely compressible” gradient transfer. The Euler equation describes a system whose kinematics is dominated by incompressible motion. In this paper we show that the opposite limit, in which the incompressible component is negligible, corresponds to the Zel’dovich approximation, a physically meaningful model of motion of self-gravitating fluid arising in cosmology.

This result enables us to approximately reconstruct peculiar motion of matter elements in the Universe from information on their present-day distribution, without any knowledge of the velocity field; indeed, the latter itself can be recovered from the reconstructed Lagrangian map. The viability of this method is established by testing it against a large-scale direct N-body simulation of cosmological evolution; when applied to real observational data, the method allows to get very tight constraints on the values of the mean mass density and the age of the Universe.

Another of our contribution is an efficient numerical method decomposing a given displacement field into “incompressible” and “infinitely compressible” parts. This method is not limited to cosmological reconstruction but can also be used for modelling the dynamics of incompressible fluid as suggested by Y. Brenier in [3].

Acknowledgments

This work is partially supported by the ANR grant BLAN07–2_183172 (project OTARIE). AS acknowledges the support of the French Ministry of Education and the joint RFBR/CNRS grant 05–01–02807.

References

[1] Y. Brenier, Décomposition polaire et réarrangement monotone des champs de vecteurs, C. R. Acad. Sci. Paris Sér. I Math. 305 (19) (1987) 805–808.

[2] Y. Brenier, Polar factorization and monotone rearrangement of vector-valued functions, Commun. Pure Appl. Math. 44 (4) (1991) 375–417.

[3] Y. Brenier, A combinatorial algorithm for the Euler equations of incompressible flows, Comput. Methods Appl. Mech. Engrg. 75 (1–3) (1989) 325–332.

[4] R.B. Tully, Nearby Galaxies Catalog, Cambridge University Press, Cambridge and New York, 1988.

[5] J. Peacock, S. Cole, P. Norberg, C. Baugh, J. Bland-Hawthorn, T. Bridges, R. Cannon, M. Colless, C. Collins, W. Couch, et al., A measurement of the cosmological mass density from clustering in the 2dF Galaxy Redshift Survey, Nature 410 (2001) 169–173.

[6] M. Tegmark, M.A. Strauss, M.R. Blanton, K. Abazajian, S. Dodelson, H. Sandvik, X. Wang, D.H. Weinberg, I. Zehavi, N.A. Bahcall, F. Hoyle, D. Schlegel, R. Scoccimarro, M.S. Vogeley, A. Berlind, T. Budavari, A. Connolly, D.J. Eisenstein, D. Finkbeiner, J.A. Frieman, J.E. Gunn, L. Hui, B. Jain, D. Johnston, S. Kent, H. Lin, R. Nakajima, R.C. Nichol, J.P. Ostriker, A. Pope, R. Scranton, U. Seljak, R.K. Sheth, A. Stebbins, A.S. Szalay, I. Szapudi, Y. Xu, J. Annis, J. Brinkmann, S. Burles, F.J. Castander, I. Csabai, J. Loveday, M. Doi, M. Fukugita, B. Gillespie, G. Hennessy, D.W. Hogg, Ž. Ivezić, G.R. Knapp, D.Q. Lamb, B.C. Lee, R.H. Lupton, T.A. McKay, P. Kunszt, J.A. Munn, L. O’Connell, J. Peoples,

J.R. Pier, M. Richmond, C. Rockosi, D.P. Schneider, C. Stoughton, D.L. Tucker, D.E. vanden Berk, B. Yanny, D.G. York, Cosmological parameters from SDSS and WMAP, Phys. Rev. D 69 (10) (2004) 103501.
[7] N. Kaiser, On the spatial correlations of Abell clusters, Astrophys. J. 284 (1984) L9–L12.
[8] N. Bahcall, R. Cen, R. Davé, J. Ostriker, Q. Yu, The mass-to-light function: antibias and Omega m, Astrophys. J. 541 (1) (2000) 1–9.
[9] P.J.E. Peebles, Tracing galaxy orbits back in time, Astrophys. J. 344 (1989) L53–L56.
[10] U. Frisch, S. Matarrese, R. Mohayaee, A. Sobolevski, A reconstruction of the initial conditions of the Universe by optimal mass transportation, Nature 417 (2002) 260–262.
[11] Y. Brenier, Generalized solutions and hydrostatic approximation of the Euler equations, these Proceedings.
[12] F. Bernardeau, S. Colombi, E. Gaztañaga, R. Scoccimarro, Large-scale structure of the universe and cosmological perturbation theory, Phys. Rep. 367 (1–3) (2002) 1–248.
[13] P. Catelan, F. Lucchin, S. Matarrese, L. Moscardini, Eulerian perturbation theory in non-flat universes: second-order approximation, Monthly Notices R. Astronom. Soc. 276 (1995) 39–56.
[14] Y. Brenier, U. Frisch, M. Hénon, G. Loeper, S. Matarrese, R. Mohayaee, A. Sobolevskiĭ, Reconstruction of the early Universe as a convex optimization problem, Monthly Notices R. Astronom. Soc. 346 (2003) 501–524.
[15] A. Nusser, Boundary-value problems in cosmological dynamics, these Proceedings.
[16] M. Giavalisco, B. Mancinelli, P.J. Mancinelli, A. Yahil, A generalized Zel'dovich approximation to gravitational instability, Astrophys. J. 411 (1993) 9–15.
[17] Y.B. Zel'dovich, Gravitational instability: an approximate theory for large density perturbations, Astronom. Astrophys. 5 (1970) 84–89.
[18] C.H. Papadimitriou, K. Steiglitz, Combinatorial Optimization: Algorithms and Complexity, Prentice-Hall Inc., Englewood Cliffs, NJ, 1982.
[19] D.P. Bertsekas, Auction algorithms for network flow problems: A tutorial introduction, Comput. Optim. Appl. 1 (1) (1992) 7–66.
[20] G. Lavaux, Lagrangian reconstruction of cosmic velocity fields, these Proceedings.
[21] D.M. Mount, S. Arya, ANN: A library for approximate nearest neighbor searching (Apr 2005). URL: http://www.cs.umd.edu/˜mount/ANN/
[22] J.D. Benamou, Y. Brenier, A computational fluid mechanics solution to the Monge–Kantorovich mass transfer problem, Numer. Math. 84 (3) (2000) 375–393.
[23] R. Mohayaee, H. Mathis, S. Colombi, J. Silk, Reconstruction of primordial density fields, Monthly Notices R. Astronom. Soc. 365 (3) (2006) 939–959.
[24] D.N. Spergel, L. Verde, H.V. Peiris, E. Komatsu, M.R. Nolta, C.L. Bennett, M. Halpern, G. Hinshaw, N. Jarosik, A. Kogut, M. Limon, S.S. Meyer, L. Page, G.S. Tucker, J.L. Weiland, E. Wollack, E.L. Wright, First year Wilkinson Microwave Anisotropy Probe (WMAP) observations: Determination of cosmological parameters (2003). arXiv:astro-ph/0302209.
[25] R. Mohayaee, R.B. Tully, The cosmological mean density and its local variations probed by peculiar velocities, Astrophys. J. 635 (2005) L113–L116.

Available online at www.sciencedirect.com
ScienceDirect
Physica D 237 (2008) 2151–2157
PHYSICA D
www.elsevier.com/locate/physd

Wavelets meet Burgulence: CVS-filtered Burgers equation

Romain Nguyen van yen[a,*], Marie Farge[a], Dmitry Kolomenskiy[b], Kai Schneider[b], Nick Kingsbury[c]

[a] LMD–CNRS, École Normale Supérieure, Paris, France
[b] M2P2–CNRS & CMI, Université de Provence, Marseille, France
[c] Signal Processing Group, Department of Engineering, Cambridge University, UK

Available online 16 February 2008

Abstract

Numerical experiments with the one-dimensional inviscid Burgers equation show that filtering the solution at each time step in a way similar to CVS (Coherent Vortex Simulation) gives the solution of the viscous Burgers equation. The CVS filter used here is based on a complex-valued translation-invariant wavelet representation of the velocity, from which one selects the wavelet coefficients having modulus larger than a threshold whose value is iteratively estimated. The flow evolution is computed from either deterministic or random initial conditions, considering both white noise and Brownian motion.

PACS: 47.27.Eq

Keywords: Burgers equation; Wavelets; Coherent vortex simulation

1. Introduction

The fully-developed turbulent regime is described by solutions of the Navier–Stokes equations for two or three-dimensional incompressible fluids, in the limit where the kinematic viscosity becomes very small. By analogy, Burgulence is described by the solutions of Burgers equations for a one–dimensional fluid in the same limit, as first proposed by Burgers [3] and advocated by von Neumann [19]. This toy model for turbulence has been extensively used since then [1,13,15,21,23]; Frisch and Bec have proposed to name it: *Burgulence* [11].

We consider the one-dimensional Burgers equation in a periodic domain of support $x \in [-1, 1]$, which describes the space–time evolution of the velocity $u(x, t)$ of a one-dimensional fluid flow:

$$\partial_t u + \frac{1}{2}\partial_x u^2 = \nu \partial_{xx} u, \tag{1}$$

supplemented with a suitable initial condition and where ν denotes the kinematic viscosity. The solutions of (1) can be computed analytically using the Cole–Hopf transformation [4,6,14]. When $\nu \rightarrow 0$ the solutions of the viscous Burgers equation approach weak solutions of the inviscid problem. The uniqueness of these solutions stems from the condition that shocks have negative jumps, which guarantees energy dissipation. For Burgers equation, this condition is equivalent to an entropy condition [12,17,18,20].

The wavelet representation has been proposed for studying turbulence [7], since it preserves both the spatial and spectral structure of the flow by realizing an optimal compromise in regard of the uncertainty principle. We have found that projecting the vorticity field onto a wavelet basis, and retaining only the strongest coefficients, extracts the coherent structures out of fully-developed turbulent flows [8,9]. We have then proposed a computational method for solving the Navier–Stokes equations in wavelet space [8]. We have shown that extracting the coherent contribution at each time step preserves the nonlinear dynamics, whatever its scale of activity, while discarding the incoherent contribution corresponds to turbulent dissipation [22]. This is the principle of the CVS (Coherent Vortex Simulation) method we have proposed [8,10].

The aim of the present paper is to apply the CVS filter to the inviscid Burgers equation and check if this is equivalent

* Corresponding author.
E-mail addresses: rnguyen@lmd.ens.fr (R. Nguyen van yen), farge@lmd.ens.fr (M. Farge).

0167-2789/$ - see front matter © 2008 Elsevier B.V. All rights reserved.
doi:10.1016/j.physd.2008.02.011

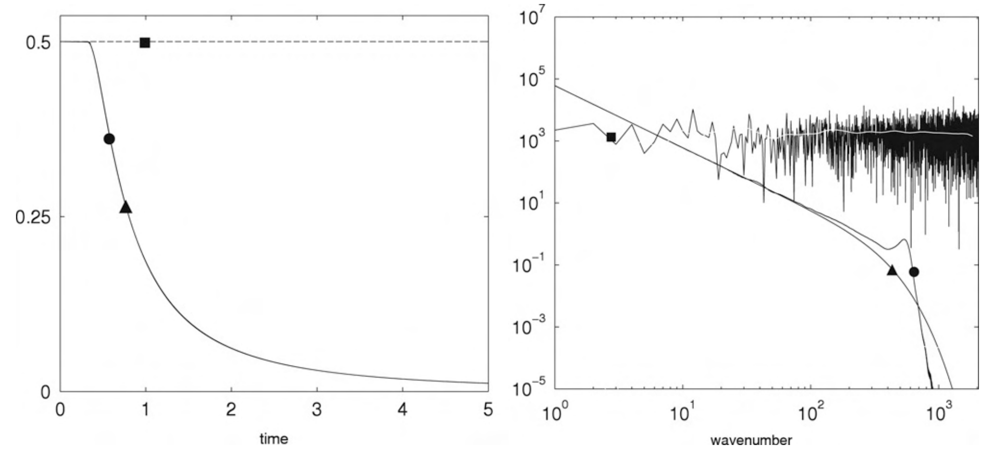

Fig. 1. Deterministic initial conditions. Left: Time evolution of energy. Right: Energy spectrum at $t = 5$. We compare the Galerkin-truncated inviscid (square), viscous (triangle) and CVS-filtered inviscid (circle) cases. We observe that for the inviscid case (right) the wavelet spectrum (white line) better exhibits the energy equipartition than the Fourier spectrum (black line).

to solving the viscous Burgers equation. The outline is the following. First we recall the principle of CVS filtering and its extension using complex-valued translation-invariant wavelets. The numerical scheme is described briefly and the main part presents results of several numerical experiments, considering either deterministic or random initial conditions. Finally, we draw conclusions and propose some perspectives.

2. Numerical method

The Burgers equation (1) is discretized on N grid points using a Fourier spectral collocation methods,

$$\frac{\partial U}{\partial t} + \frac{1}{3} D_N(U^2) + \frac{1}{3} U \cdot D_N(U) - \nu D_N^2(U) = 0, \tag{2}$$

where U approximates $(u(x_0, t), u(x_1, t), \ldots, u(x_{N-1}, t))$, D_N stands for the Fourier collocation differentiation and $\cdot$ is the pointwise product of two vectors. The discretization of the nonlinear term in (2) is chosen in order to conserve the kinetic energy $E = \frac{1}{2} \int_{-1}^{1} u^2(x, t)\mathrm{d}x$ when $\nu = 0$ [5]. For time integration a fourth-order Runge–Kutta scheme is used.

At each time step we filter the solution using the CVS method, which we now recall briefly. Given orthogonal wavelets (ψ_{ji}) and the associated scaling function at the largest scale φ, the velocity can be expanded into

$$u(x) = \langle u \mid \varphi \rangle \varphi(x) + \sum_{j=0}^{J-1} \sum_{i=1}^{2^j} \langle u \mid \psi_{ji} \rangle \psi_{ji}(x), \tag{3}$$

where j is the scale index, i is the position index and the inner product is $\langle a \mid b \rangle = \int_{-1}^{1} a(x) \cdot b^*(x)\mathrm{d}x$ with b^* denoting the complex conjugate of b. Since location in orthogonal wavelet space is sampled on a dyadic grid, this representation breaks the local translation invariance of (1) which may impair the stability of the numerical scheme. Therefore we prefer using, instead of real-valued wavelets, complex valued wavelets [16] which very closely preserve translation invariance. In this case, (3) still holds as long as we replace the right-hand side by its real part.

The CVS filter then consists in discarding the wavelet coefficients whose modulus is below a threshold T. In addition, wavelet coefficients at the finest scale are systematically filtered out to avoid aliasing errors. The resulting velocity u_T is a nonlinear approximation of u.

Because the velocity field decays in time, the threshold has to be estimated at each time step in a self-consistent way. To do this, we follow the iterative method introduced in [2], which consists in imposing the ratio between the standard deviation of the discarded wavelet coefficients and the threshold itself,

$$T^2 = \frac{5}{N_T} \sum_{j=0}^{J-1} \sum_{i=1}^{2^j} |\widetilde{u}_{ji}|^2 H(T - |\widetilde{u}_{ji}|), \tag{4}$$

where H is the Heaviside step function and N_T is the number of wavelet coefficients below the threshold. The solution of (4) is determined numerically using a fixed point iterative procedure [2], initialized with $T_0 = 5E/N$, where E is the total energy.

3. Deterministic initial condition

We consider Burgers equation (1) with the deterministic initial condition $u(t = 0, x) = -\sin(\pi x)$. We begin by comparing three computations: a Galerkin-truncated inviscid case ($\nu = 0$), a viscous case ($\nu = 10^{-4}$), and an inviscid case with the CVS filter applied at each time step. The solutions are computed up to time $t = 5$, using $N = 4096$ grid points.

By computing in the Galerkin-truncated inviscid case ($\nu = 0$), we check that our numerical scheme conserves energy (Fig. 1, left) as theoretically predicted. We observe that the final solution at $t = 5$ exhibits energy equipartition (Fig. 1, right) with a Gaussian velocity PDF, as expected. Note that the white line in Fig. 1 (right) corresponds to the wavelet energy spectrum, *i.e.*, the squared modulus of the wavelet coefficients computed with a complex-valued Morlet wavelet. It better exhibits the k^0 scaling, characteristic of the energy equipartition, than the highly oscillatory Fourier energy spectrum (black line). This illustrates the fact that the wavelet energy spectrum is more stable than the Fourier energy

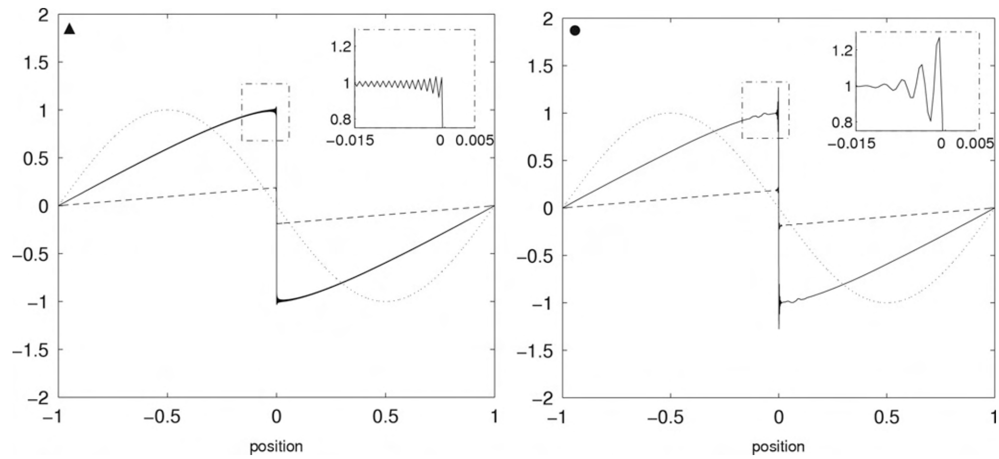

Fig. 2. Deterministic initial conditions. Snapshots of velocity for the viscous (left) and the CVS-Filtered inviscid (right) cases at $t = 0$ (dotted line), $t = 0.5$ (solid line) and $t = 5$ (dashed line). The insets show a zoom of the shock at $t = 0.5$.

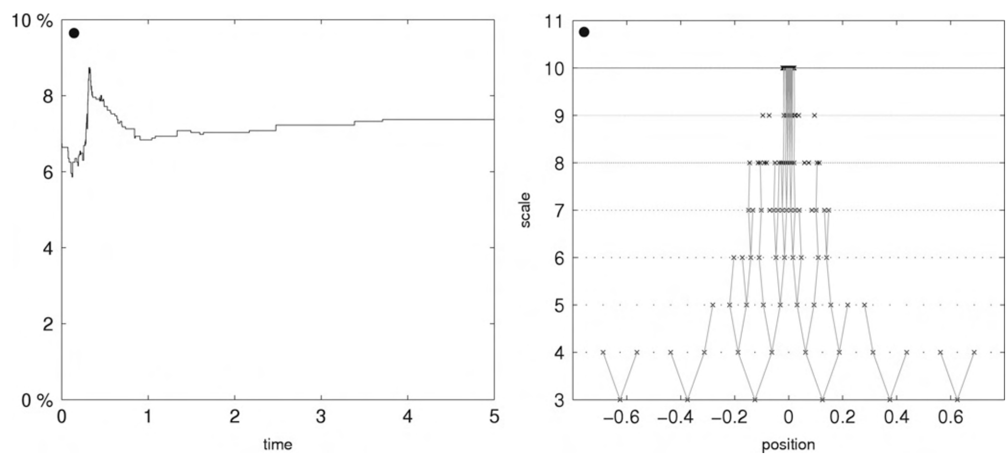

Fig. 3. Deterministic initial conditions. Left: Time evolution of the percentage of wavelet coefficients retained after filtering. Right: Dyadic tree of the wavelet coefficients which are retained after filtering at $t = 5$. The crosses indicate the $7\%N$ retained wavelet coefficients, while the small dots correspond to the $93\%N$ discarded wavelet coefficients. The scale varies from coarse to fine, up the vertical axis.

spectrum when we analyse only one realization of a stochastic process [7].

For the viscous and CVS-filtered inviscid cases, the energy remains basically constant until the shock forms at $t = 1/\pi$, but then decays with a t^{-2} law. In Fig. 1 (right) the energy spectra of the viscous and CVS-filtered inviscid cases exhibit a power law behaviour with slope -2.

Fig. 2 shows the velocity at three time instants for the viscous and CVS-filtered inviscid cases. The CVS-filtered inviscid solution follows the same dynamics as the viscous one, except for the small overshoot we observe at $x = 0$ after the shock has formed. This Gibbs phenomenon is stronger but less oscillatory for the CVS-filtered inviscid case than for the viscous case (see the insets in Fig. 2).

The time evolution of the percentage of retained wavelet coefficients is presented in Fig. 3 (left). It shows that, with only relatively few coefficients (about $7\%N$), we are able to track the nonlinear dynamics of the flow and this number remains almost constant after the shock formation. At $t = 5$, the retained wavelet coefficients are located around $x = 0$, the position of the shock, and span all scales there, as illustrated in Fig. 3 (right).

We now show that, when N increases, the filtered solutions converge towards the entropy solution u_{ref} which solves the Burgers equation in the inviscid limit. For comparison, we also consider viscous solutions with viscosity depending on N ($\nu = 0.4096N^{-1}$), which are known to converge to u_{ref} everywhere, except at $x = 0$. The entropy solution u_{ref} is directly calculated using the method of characteristics.

First, we consider a global error estimate, the relative mean square error, defined as

$$\epsilon_N(t) = \frac{\|u - u_{\mathrm{ref}}\|_2^2}{\|u_{\mathrm{ref}}\|_2^2}. \tag{5}$$

On Fig. 4(left) we plot $\epsilon_N(t)$ for $N = 4096$. The error for the CVS-filtered inviscid case is larger but saturates after $t \simeq 2$. In contrast, the error for the viscous case keeps increasing because the finite viscosity smooths the shock away. Considering now $t = 5$ and varying N, we find that for both the viscous

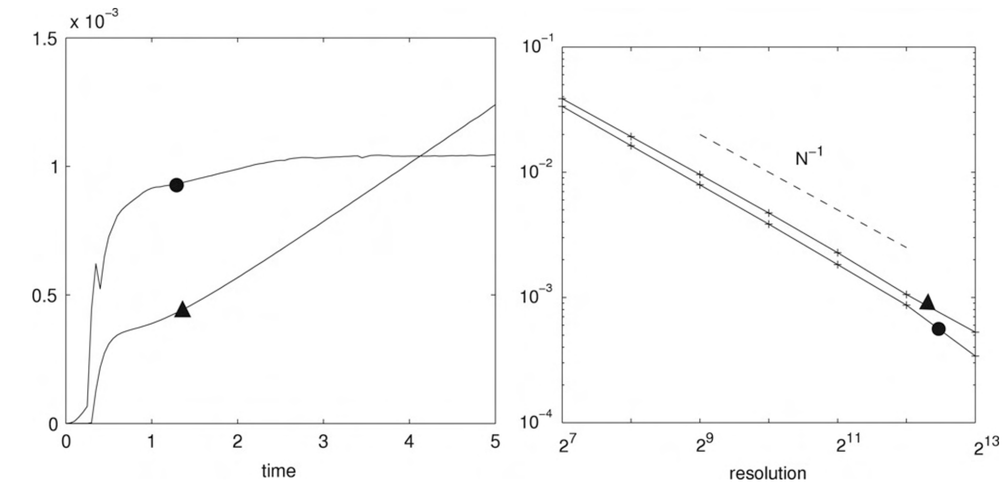

Fig. 4. Deterministic initial conditions. Left: Time evolution of the relative mean squared error ϵ_N at $N = 4096$. Right: Relative mean squared error ϵ_N at $t = 5$ for different numerical resolutions, $N = 128$ to $N = 8192$. We compare the viscous (triangle) and CVS-filtered inviscid (circle) cases.

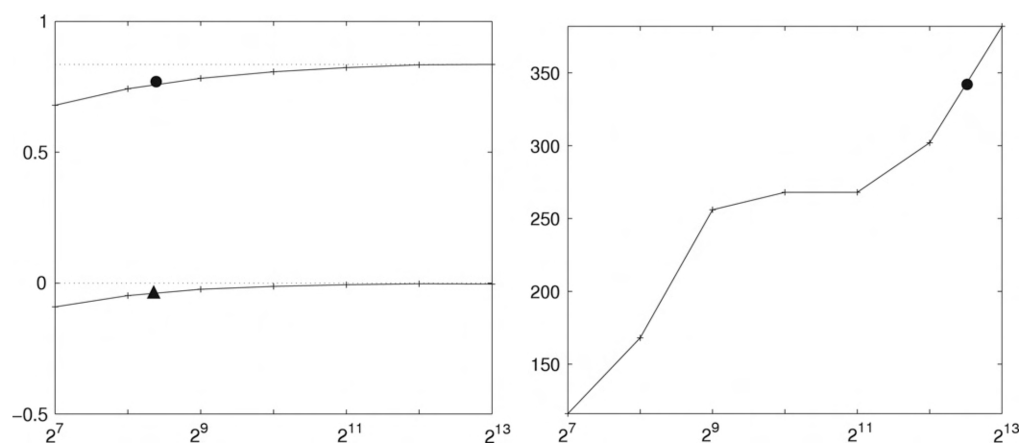

Fig. 5. Deterministic initial conditions. Error on the relative total variation ϵ'_N (left), and number of retained wavelet coefficients (right), as functions of N at $t = 5$, for the viscous (triangle) and CVS-filtered inviscid (circle) solutions.

and CVS-filtered inviscid cases ϵ_N decreases as N^{-1} (Fig. 4, right).

We now study the behaviour of the oscillations in the neighbourhood of the shock when the resolution N is increased. The total variation of a function f on $[-1, 1]$ is defined by:

$$\|f\|_{TV} = \int_{-1}^{1} |\partial_x f| \mathrm{d}x. \tag{6}$$

To detect the presence of spurious oscillations, we compute the relative error on the total variation.

$$\epsilon'_N(t) = \frac{\|u(x,t)\|_{TV} - \|u_{\mathrm{ref}}(x,t)\|_{TV}}{\|u_{\mathrm{ref}}(x,t)\|_{TV}}, \tag{7}$$

which is plotted as a function of N for $t = 5$ on Fig. 5 (left). For the viscous case, ϵ'_N is negative and converges towards zero when N increases. For the CVS-filtered inviscid case, ϵ'_N tends to a finite positive value close to 0.84. The overshoot that could be seen on Fig. 2 persists but becomes more and more localized around the singularity when N increases, thus ensuring mean square convergence.

Let us end this section by a short discussion on the evolution of the compression rate when N increases. Fig. 5 (right) shows that the number of retained wavelet coefficients increases roughly logarithmically as a function of N. As a consequence, notice that for the filtered solution the relative mean square error $\epsilon_N(t)$, if it is considered as a function of the number of retained coefficients only, converges to zero exponentially fast. However, to experience this promising rate of convergence in practice, we should compute the evolution of u using only the wavelet coefficients whose modulus remains above the threshold.

4. Random initial condition

In the previous section we demonstrated that the CVS-filtered inviscid Burgers equation exhibits an evolution similar to that of the viscous Burgers equation. We now would like to check if this is still verified in the context of *Burgulence* for both white noise [1] and Brownian motion [21].

4.1. White-noise initial condition

We take as initial velocity one realization of a Gaussian white noise computed at resolution $N = 4096$, which corresponds to a random non-intermittent initial condition.

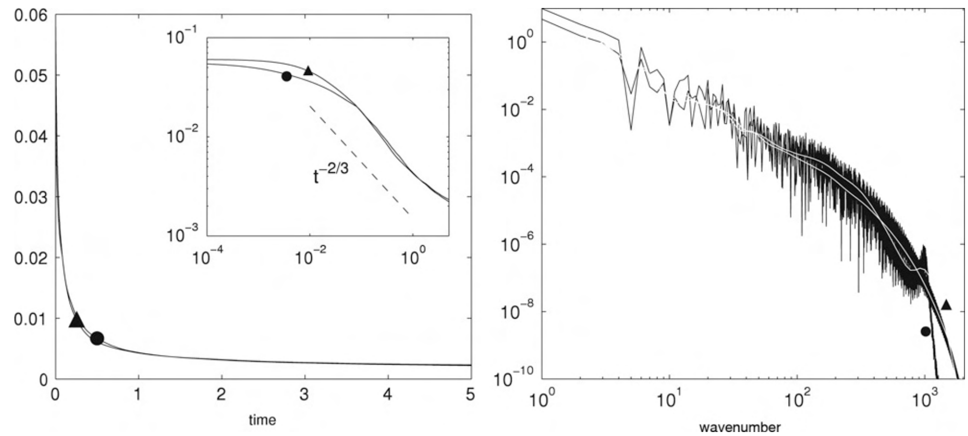

Fig. 6. White noise initial conditions. Left: Time evolution of energy. The inset shows the $t^{-2/3}$ decay in log–log coordinates. Right: energy spectrum at $t = 5$. We compare the viscous (triangle) and CVS-filtered inviscid (circle) simulations. We observe that the wavelet spectrum (white lines) better exhibits the k^{-2} scaling of energy than the Fourier spectrum (black lines).

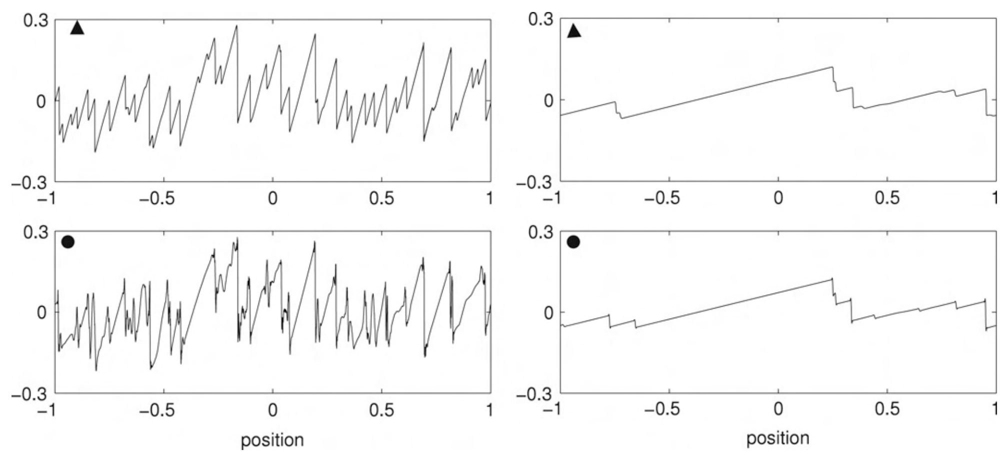

Fig. 7. White noise initial conditions. Snapshots of velocity at $t = 0.3$ (left) and $t = 5$ (right). Top: viscous equation with $\nu = 2 \times 10^{-5}$. Bottom: CVS-filtered inviscid equation.

Since the CVS filter removes the non-intermittent noisy contributions, if applied to a Gaussian white noise the latter would be completely filtered out. Therefore we first integrate the viscous equation with $\nu = 2 \times 10^{-5}$ without filtering, and wait until the flow intermittency has sufficiently developed before applying the filter. To check the flow intermittency we monitor the flatness of the velocity gradient until it reaches the value 20, which happens at $t = 0.017$ for the realization described here. Then, we reset $t = 0$ and integrate up to $t = 5$, both the viscous equation with $\nu = 2 \times 10^{-5}$, and the CVS-filtered inviscid equation.

In Fig. 6 (left) we show that the energy, for both the CVS-filtered inviscid solution and the viscous solution, decays with a $t^{-2/3}$ law, as found by Burgers [4,21]. In Fig. 6 (right) we observe at $t = 5$ that both energy spectra present the same k^{-2} scaling. Notice that the two white lines in Fig. 6 (right) correspond to the wavelet energy spectrum, which better exhibits the k^{-2} scaling of the energy than the highly oscillatory Fourier energy spectrum (black lines).

Finally, we show on Fig. 7 that the viscous and CVS-filtered inviscid solutions are almost identical in physical space, presenting a typical sawtooth profile as first noticed by Burgers [4].

4.2. Brownian motion initial condition

We use the same resolution $N = 4096$ as above, but only the initial condition changes. Since we have chosen periodic boundary conditions we approximate the Brownian motion by the Fourier series:

$$u(x, 0) = \mathrm{Re}\left(\sum_k \widehat{u_k} \mathrm{e}^{ikx}\right) \tag{8}$$

where $k = -\frac{N}{2} + 1, -\frac{N}{2}, \ldots, \frac{N}{2} - 1$. We set $\widehat{u_0} = 0$ and, for $k \neq 0$, we take for $\widehat{u_k}$ a complex Gaussian random variable with standard deviation $1/|k|$.

The solution for the viscous case is computed with $\nu = 1.2 \times 10^{-4}$. For the CVS-filtered inviscid case, as we did for the white noise initial condition, we do not filter before enough intermittency has developed. We thus integrate the viscous equation with $\nu = 1.2 \times 10^{-4}$ for 0.05 time units and then switch viscosity off. This procedure provides the initial velocity which, by construction, is the same for both methods (Fig. 8).

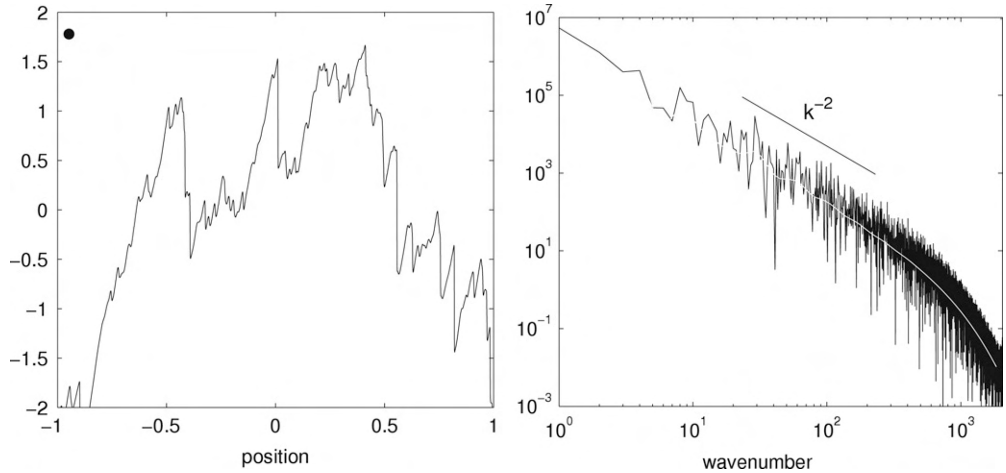

Fig. 8. Brownian initial condition. Velocity at $t = 0$ (left), its Fourier energy spectrum (right, black line) and its wavelet energy spectrum (right, white line).

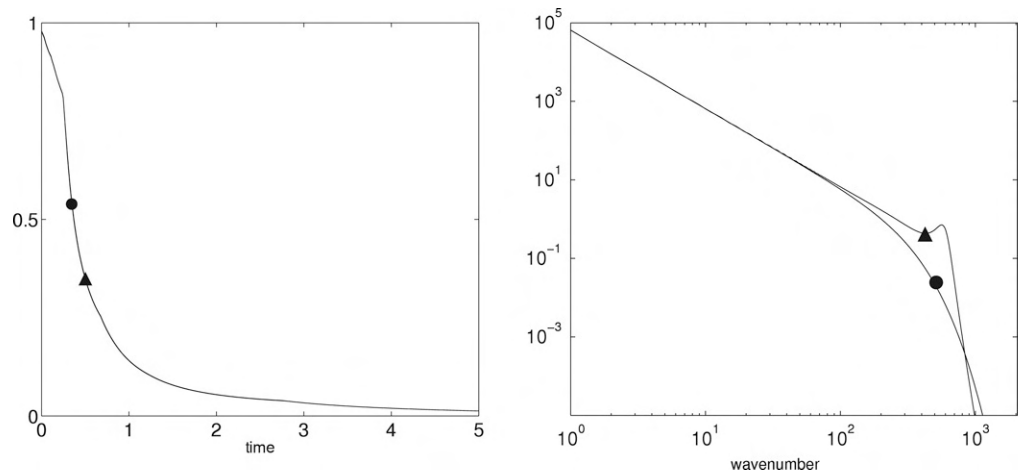

Fig. 9. Brownian initial condition. Left: Time evolution of energy. Right: wavelet energy spectrum at $t = 5$. We compare the viscous (triangle) and CVS-filtered inviscid (circle) cases.

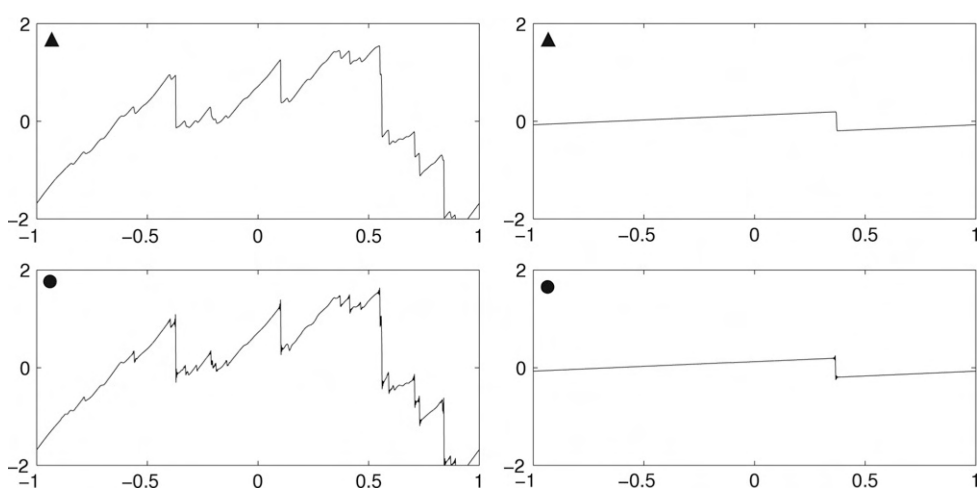

Fig. 10. Brownian initial conditions. Snapshots of velocity at $t = 0.1$ (left) and $t = 5$ (right). Top: viscous equation with $\nu = 1.2 \times 10^{-4}$. Bottom: CVS-filtered inviscid equation.

The energy decay matches well between the CVS-filtered inviscid and the viscous solutions (Fig. 9, left). A k^{-2} power spectrum is also obtained for both at $t = 5$ (Fig. 9, right).

At $t = 0.1$ numerous small shocks are present in the viscous solution (Fig. 10, top left). All of them are correctly reproduced by the CVS-filtered inviscid solution (Fig. 10, bottom left).

At $t = 5$ the single remaining shock, which is still resolved in the viscous solution (Fig. 10, top right), is correctly reproduced in the CVS-filtered inviscid solution (Fig. 10, bottom right).

5. Conclusion

We have shown that CVS filtering at each time step the solution of the inviscid Burgers equation gives the same evolution as the viscous Burgers equation, for both deterministic and random initial conditions. As our contribution to Euler equations' 250th anniversary and Euler's 300th birthday, we conjecture that CVS filtering the Euler equation may be equivalent to solving the Navier–Stokes equations in the fully-developed turbulent regime, *i.e.*, when dissipation has become independent of viscosity. We predict that the retained wavelet coefficients would preserve Euler's nonlinear dynamics, while discarding the weaker wavelet coefficients would model turbulent dissipation and give Navier–Stokes solutions. Since in the fully-developed turbulent regime turbulent dissipation strongly dominates molecular dissipation, there is no reason to model turbulent dissipation by a Laplace operator anymore. Indeed, turbulent dissipation is a property of the flow, while molecular dissipation is a property of the fluid and may no more play a role when turbulence is fully-developed. We think that in this regime the CVS filter could be a better way to model dissipation, replacing global by local smoothing, while preserving nonlinear interactions. In this paper we have chosen the simplest toy model to test this conjecture, although Burgers' equation, in contrast to Euler's equation, is neither chaotic nor produces randomness. Therefore we conjecture that the CVS-filter would work better for Euler/Navier–Stokes than for Burgers, since CVS is based on denoising which is justified when there is chaos and randomness.

Acknowledgments

We thank Uriel Frisch, Margarete Domingues, Claude Bardos, François Dubois and two anonymous referees for their useful comments. We acknowledge financial support from the ANR under contract M2TFP (Méthodes Multi-échelles pour la Turbulence Fluide et Plasma) and from the Association CEA-Euratom under contract V.3258.006. NK thanks the Universite de Provence for supporting his stay in Marseille. MF is grateful to the Fellows of Trinity College, Cambridge (UK), in particular Keith Moffatt, for their kind hospitality while revising this paper.

References

[1] M. Avellaneda, W.E. , Commun. Math. Phys. 172 (1995) 13–38.
[2] A. Azzalini, M. Farge, K. Schneider, Appl. Comput. Harmon. Anal. 18 (2) (2005) 177–185.
[3] J.M. Burgers, Verh. KNAW, Afd. Natuurkunde, XVII 2 (1939) 1–53.
[4] J.M. Burgers, Proc. KNAW B, LVII 1 (1954) 45–72.
[5] C. Canuto, M.Y. Hussaini, A. Quarteroni, T.A. Zang, Spectral Methods in Fluid Dynamics, Springer-Verlag, 1988.
[6] J.D. Cole, Q. Appl. Math. 9 (1951) 225.
[7] M. Farge, Ann. Rev. Fluid Mech. 24 (1992) 395–457.
[8] M. Farge, K. Schneider, N. Kevlahan, Phys. Fluids 11 (8) (1999) 2187–2201.
[9] M. Farge, G. Pellegrino, K. Schneider, Phys. Rev. Lett. 87 (5) (2001) 45011–45014.
[10] M. Farge, K. Schneider, Flow, Turb. Combus. 66 (4) (2001) 393–426.
[11] U. Frisch, J. Bec, New trends in turbulence, in: M. Lesieur, A. Yaglom, F. David (Eds.), in: Les Houches 2000, vol. 74, Springer, 2002, p. 341.
[12] P. Germain, R. Bader, Note technique ONERA, OA no 1/1711-1, May 1953.
[13] S.N. Gurbatov, S.I. Simdyankin, E. Aurell, U. Frisch, G. Tóth, J. Fluid Mech. 344 (1997) 339–374.
[14] E. Hopf, Comm. Pure Appl. Math. 3 (1950) 201.
[15] S. Kida, J. Fluid Mech. 79 (1997) 337–377.
[16] N. Kingsbury, Appl. Comput. Harmon. Anal. 10 (3) (2001) 234–253.
[17] S.N. Kruzhkov, Math. USSR Sb. 10 (2) (1970) 217–243; Amer. Math. Transl. Ser. 2 26, 95–172.
[18] P.-D. Lax, Comm. Pure Appl. Math. 7 (1954) 159–193.
[19] J. von Neumann, in: A.H. Taub (Ed.), Collected Works, vol. 5, Pergamon, 1961, pp. 437–471.
[20] O. Oleinik, Usp. Mat. Nauk 12 (3) (1957) 3–73; Amer. Math. Transl. Ser. 2 26, 95–172.
[21] Z.S. She, E. Aurell, U. Frisch, Commun. Math. Phys. 148 (1992) 623–641.
[22] K. Schneider, M. Farge, G. Pellegrino, M. Rogers, J. Fluid Mech. 534 (2005) 39–66.
[23] M. Vergassola, B. Dubrulle, U. Frisch, A. Noullez, Astron. Astrophys. 289 (1994) 325–356.

Available online at www.sciencedirect.com

ScienceDirect

Physica D 237 (2008) 2158–2161

PHYSICA D

www.elsevier.com/locate/physd

Boundary-value problems in cosmological dynamics

Adi Nusser

Physics Department - Technion, Haifa 32000, Israel

Available online 26 February 2008

Abstract

The dynamics of cosmological gravitating system is governed by the Euler and the Poisson equations. Tiny fluctuations near the big bang singularity are amplified by gravitational instability into the observed structure today. Given the current distribution of galaxies and assuming initial homogeneity, dynamic reconstruction methods have been developed to derive the cosmic density and velocity fields back in time. The reconstruction method described here is based on a least action principle formulation of the dynamics of collisionless particles (representing galaxies). Two observational data sets will be considered. The first is the distribution of galaxies which is assumed to be an fair tracer of the mass density field of the dark matter. The second set is measurements of the peculiar velocities (deviations from pure Hubble flow) of galaxies. Given the first data set, the reconstruction method recovers the associated velocity field which can then be compared with the second data set. This comparison constrains the nature of the dark matter and the relation between mass and light in the Universe.

PACS: 95.35.+d

Keywords: Cosmology; Dark matter; Large scale structure

1. Introduction

Cosmology is concerned with observing and modelling the universe on large scales: from our own Milky Way, other galaxies, galaxy clusters, super clusters up to the largest scales as probed by measurements of the cosmic microwave background radiation (CMB). These observations span a huge range of scales and all strongly suggest that: (1) the dominant form of matter is dark (a factor of six in mass over the normal baryonic matter), (2) the clustering amplitude decreases with scale, and (3) structure forms by gravitational amplification of tiny initial fluctuations. These are some of the main component of the standard paradigm in cosmology. Violation of any of them or all of them is consistent with only a very limited set of observations, if any. Cosmology has had a great impact on other fields of physics and science in general. The bare existence of the gravitationally dominant dark matter has stimulated scientists' (and others') vivid imagination for a few decades now. Abundance and masses of nonstandard particles have been constrained from the observed clustering pattern alone. In addition to gravity, hydrodynamic processes can greatly influence the formation and evolution of galaxies, groups and clusters of galaxies. Hydrodynamic effects, however, play a minor role in shaping the observed distribution of galaxies on scales a few times larger than the size of galaxy clusters. Therefore, gravitational instability theory directly relates the present-day large-scale structure to the initial density field and provides the framework within which the observations are analyzed and interpreted. Gravitational instability is a nonlinear process. Analytical solutions exist only for configurations with special symmetry, and approximate tools are limited to moderate density contrasts. So, numerical methods are necessary for a full understanding of the observed large scale structure of the universe. There are two complementary numerical approaches. The first approach relies on N-body techniques designed to solve an initial value problem in which the evolution of a self-gravitating system of massive particles is determined by numerical integration of the Newtonian differential equations. Combined with semi-analytical models of galaxy formation, N-body simulations have become an essential tool for comparing the predictions of cosmological models with the observed properties of galaxies. Because the exact initial conditions are unknown, comparisons

E-mail address: adi@physics.technion.ac.il.

0167-2789/$ - see front matter © 2008 Elsevier B.V. All rights reserved.
doi:10.1016/j.physd.2008.02.018

between simulations and observations are mainly concerned with general statistical properties. The second approach aims at finding the past orbits of mass tracers (galaxies) from their observed present-day distribution. The orbits must be such that the initial spatial distribution is homogeneous. This approach is very useful for direct comparisons between different types of observations of the large-scale structure. Most common are the velocity–velocity (hereafter v–v) comparisons between the observed peculiar velocities of galaxies and the velocity field inferred from the galaxy distribution in redshift surveys. This type of analysis yield the cosmological mass density parameter Ω_m. Any systematic mismatch between the fields serves as an indication to the nature of galaxy formation and/or the origin of galaxy intrinsic scaling relations used to measure the distances, provided that errors in the calibration have been properly corrected for. This second approach also allows to perform back-in-time reconstructions of the density field on scales $\sim 5\ \mathrm{h}^{-1}$ Mpc [3].

Finding the orbits that satisfy initial homogeneity and match the present-day distribution of mass tracers is a boundary value problem. This problem naturally lends itself to an application of Hamilton's variational principle where the orbits of the objects are found by searching for stationary variations of the action subject to the boundary conditions. The use of the Principle of Least Action in a cosmological frame-work has been pioneered by Peebles [6] and has long been restricted to small systems such as the Local Group [7] and the Local Supercluster [8]. Early applications to large galaxy redshift surveys have been hampered by the computational cost of handling the relatively large number of objects. Subsequent numerical applications speeded up the method and allowed the reconstruction of the orbits of $\sim 10^3$ particles [8]. However, it was only recently that the improvement of the minimization techniques and the use of efficient gravity solvers made it possible to deal with more than 10^4 objects [5], comparable to the number of objects contained in the largest all-sky galaxy catalogues.

2. Cosmological dynamics

For the background cosmology we work with a Friedmann-Robertson-Walker Universe. In this uniform background, the physical distance, r, between two points is $r \propto a(t)$ where $a(t)$ is the scale factor. We consider a matter dominated universe with mean density $\bar{\rho} = \Omega\rho_c$ with $\rho_c = 3H^2/8\pi G$. For a $\Omega = 1$, we get a critical density flat universe with $a \sim t^{2/3}$. The Universe is geometrically hyperbolic for $\Omega < 1$ and spherical for $\Omega > 1$. Current observations indicate that the Universe contains a cosmological constant which makes it flat even though $\Omega \approx 0.3$ [9]. Apart from the dependence of a on t the presence of a cosmological constant has very little effect on our description here. In particular, the equations of motion of perturbations remain correct. We further define, $H(t) = \dot{a}/a$ is the Hubble function, and denote the comoving coordinate of a patch of matter by $\boldsymbol{x} = \boldsymbol{r}/a$. The fluctuations are described by the density contrast $\delta(\boldsymbol{x}, t) = \rho(\boldsymbol{x}, t)/\bar{\rho}(t) - 1$ and the comoving velocity by $\boldsymbol{v} = \mathrm{d}\boldsymbol{x}/\mathrm{d}t$. Also, let $D(t)$ be the linear density growing mode normalized to unity at the present epoch, and $f(\Omega_m) = \mathrm{d}\ln D/\mathrm{d}\ln a \approx \Omega_m^{0.6}$. The equations governing the evolution of fluctuations in a collisionless mass component in an expanding Universe are, The Euler equation,

$$\frac{\mathrm{d}\boldsymbol{v}}{\mathrm{d}t} + 2H\boldsymbol{v} + \boldsymbol{v}\cdot\nabla\boldsymbol{v} = -\nabla\varphi_g, \tag{1}$$

the continuity,

$$\frac{\partial\delta}{\partial t} + \nabla\cdot(1+\delta)\boldsymbol{v} = 0 \tag{2}$$

and the Poisson equation,

$$\nabla^2\varphi_g = 4\pi G\bar{\rho}\delta. \tag{3}$$

The term $2H\boldsymbol{v}$ in the Euler equation is due to the expansion of the cosmological background. The source term in the Poisson equation represents density fluctuations above the mean background density.

2.1. Linear gravitational instability

Neglecting the non-linear terms $\boldsymbol{v}\cdot\nabla\boldsymbol{v}$ and $\nabla\cdot\delta\boldsymbol{v}$, the equations of motion reduce to

$$\delta = -\frac{1}{f(\Omega)H}\nabla\cdot\boldsymbol{v} \tag{4}$$

and

$$\ddot{\delta} + 2H\dot{\delta} = \frac{3}{2}H^2\Omega\delta, \tag{5}$$

where an over-dot indicates a partial time derivative. For a critical density Universe ($\Omega = 1$ and $H = 2/3t$), the Eq. (5) gives $\delta_1 \propto t^{2/3}$ and $\delta_2 \propto t^{-1}$, as the growing and decaying solutions, respectively. A few things to note. First, without the term $2H\dot{\delta}$ the solutions would be exponential functions rather than power laws in time. Second, even in the linear regime, the decaying mode prevents a full recovery of the initial conditions, at $t \approx 0$ near the big bang cosmological singularity. Indeed, recovering this mode requires a precise knowledge of the present δ and $\dot{\delta}$ (or $\boldsymbol{v}$), in order to prevent a blow-up as $t \to 0$.

The relation (4) has a simple interpretation. Since $H \sim 1/t$ and $t\nabla^2\phi_g \sim -\delta$, it gives the intuitive relation $\boldsymbol{v} \sim -\nabla\phi_g t$ between the acceleration, $-\nabla\phi_g$ and velocity. The relation has played a prominent role in the analysis of large scale structure. The density contrast $\delta(\boldsymbol{x})$ as estimated form the distribution of galaxies, could be used in this relation to obtain the associated peculiar velocity $\boldsymbol{v}(\boldsymbol{x})$. This velocity fields could be compared with the actual observed velocities of galaxies. A good agreement between the fields yields the cosmological density parameter, Ω, and also a confirmation of the gravitational instability mechanism for structure formation. But, perhaps more interestingly, any mismatch between the fields could be an indication of a strange mode of galaxy/structure formation the result of which is a galaxy distribution different from that of the dark matter.

2.2. Nonlinear cosmological dynamics

Linear theory is valid only when the fluctuations are small. We describe here some nonlinear methods which can be used for a variety of purposes, e.g. recovery of the initial conditions, estimating $\boldsymbol{v}$ from the galaxy distribution and constraining the masses of galactic halos. Here we focus on the estimation of $\boldsymbol{v}$. One can use numerical simulations of nonlinear gravity to calibrate semi-analytical nonlinear generalizations to (4). The approach is useful as it provides partial differential equations which can be solved for $\boldsymbol{v}$ for a given source term, δ. Nevertheless, such generalizations are usually statistical in nature. In the following, we will describe a more rigorous and accurate approach.

We switch to a Lagrangian description for a system of N equal mass particles in an expanding universe. Each particle represents a patch of matter which, for practical purposes, could be a galaxy. The equations of motion are ($i = 1 \cdots N$),

$$\frac{\mathrm{d}\boldsymbol{v}_i}{\mathrm{d}t} + 2H\boldsymbol{v}_i = \boldsymbol{g}_i, \tag{6}$$

where $\boldsymbol{g} = -\nabla\phi_g$ and is given by

$$\boldsymbol{g}(\boldsymbol{x}) = -\frac{G}{a^3}\sum_i \frac{\boldsymbol{x}-\boldsymbol{x}_i}{|\boldsymbol{x}-\boldsymbol{x}_i|^3} + \frac{4}{3}G\bar{\rho}a\boldsymbol{x}. \tag{7}$$

The equations can be derived from the action,

$$S = \int_0^{t_0} \mathrm{d}t \sum_i \left\{ \frac{a^2}{2}\boldsymbol{v}_i^2 + \frac{G}{a}\left[\sum_{j<i}\frac{1}{|\boldsymbol{x}_i-\boldsymbol{x}_j|} + \frac{2\pi}{3}\bar{\rho}a^3\boldsymbol{x}_i^2\right]\right\} \tag{8}$$

under stationary first variations of the orbits that leave $\boldsymbol{x}$ fixed at the present epoch and satisfy the constraint $t^{1/3}\boldsymbol{v} \to$ const as $t \to 0$ [1,5,6]. The second condition on the velocities guarantees homogeneity near the big bang singularity $t \to 0$, preventing a blow up of the solutions. We expand the orbits in a time-dependent base functions $q_n(t)$ in the form,

$$\boldsymbol{x}_i(t) = \boldsymbol{x}_{i,0} + \sum_{n=1}^{n_{\max}} q_n(t)\boldsymbol{C}_{i,n}, \tag{9}$$

where $\boldsymbol{x}_{i,0}$ is the position of the particle i at the present epoch, and the vectors $\boldsymbol{C}_{i,n}$ are the expansion coefficients with respect to which the action is varied, i.e. they satisfy $\partial S/\partial\boldsymbol{C}_{i,n} = 0$. The base functions q_n are chosen such that the boundary conditions are satisfied.

Our strategy is to find orbits that are as close as possible to the Hubble flow. Therefore, we search for the minimum of the action and do not look for stationary points which might describe oscillatory behaviour of the orbits. To find the coefficients $\boldsymbol{C}_{i,n}$ that minimize the action, we use the Conjugate Gradient Method (CGM) which is fast and easy to implement. The gravitational force $\boldsymbol{g}$ and its potential are computed using the TREECODE gravity solver. The time integration in the expression for the action is done using the Gaussian quadrature method with 10 points at the time abscissa. The CGM requires an initial guess for $\boldsymbol{C}_{i,n}$. We will use the term FAM, for Fast Action Method, to refer to the reconstruction method described here. In the standard FAM application we compute the initial guess using the linear theory relation between the velocity and mass distribution. The minimum of the action proved to be rather insensitive to the choice of initial guess for $\boldsymbol{C}_{i,n}$, as we have checked by running FAM experiments with initial $\boldsymbol{C}_{i,n}$ both set to zero and to random numbers with appropriate variance. Besides the initial set of $\boldsymbol{C}_{i,n}$, the other free parameters are the softening used by the gravity solver and the tolerance parameter that sets the convergence of the CGM method. The success of the least action reconstruction method is illustrated in Fig. 1.

3. Discussion

The rapid rotation of galactic disks revealed the existence of dark matter halos which engulf the luminous component. The measured virial motions of galaxies in clusters of galaxies also require a gravitationally dominant dark component. Away from bound systems of galaxies and galaxy clusters, field galaxies show coherent flow pattern which deviates from a pure Hubble expansion. This coherent velocity field is a direct probe of the large-scale dark matter distribution in as much as rotational speeds and virial motions are a measure of the dark matter in galaxies and clusters. Indeed, the cosmic gravitational field responsible for the motions of galaxies, mainly depends on the gravitationally dominant mass density field of the dark matter. The actual distribution of galaxies may well be quite different from the dark matter distribution. Recent analysis of the galaxy surveys, however, reveal a good match between the statistical properties of the galaxy distribution and the corresponding properties for the dark matter as inferred from numerical simulations of dark matter evolution in the universe. This is encouraging, but there may still be significant deviations between the distribution of the dark and luminous components, which are not reflected in statistical comparisons. The only way to detect such deviations is via direct detailed comparisons between the measured velocities of galaxies and velocities estimated from the galaxy distribution. These comparisons have been done in the linear regime. The overall agreement between the fields is impressive, but minor persisting mismatch is detected in some regions in the local volume. It is possible that nonlinear analysis based on the least action principle could mitigate some of the disagreement. This remains to be seen. The least action principle could also be used to recover the initial conditions, allowing us to answer one of the fundamental question of whether or not initial fluctuations were gaussian [4].

The program is not without flaws. Many physical effects need to be addressed in detail. Most pressing is incorporating the assembly (or merging) history of galaxies. Galaxies reside in dark matter halos which form in a hierarchical manner from small to large. Thus our own Milky Way galaxy, for example, is likely to have had a major merging activity some 8 Gyr ago. All reconstruction methods assume that galaxies are point tracers of the mass density field and do not account for merging effects.

For a discussion of an alternative approach to cosmological reconstruction, see [2].

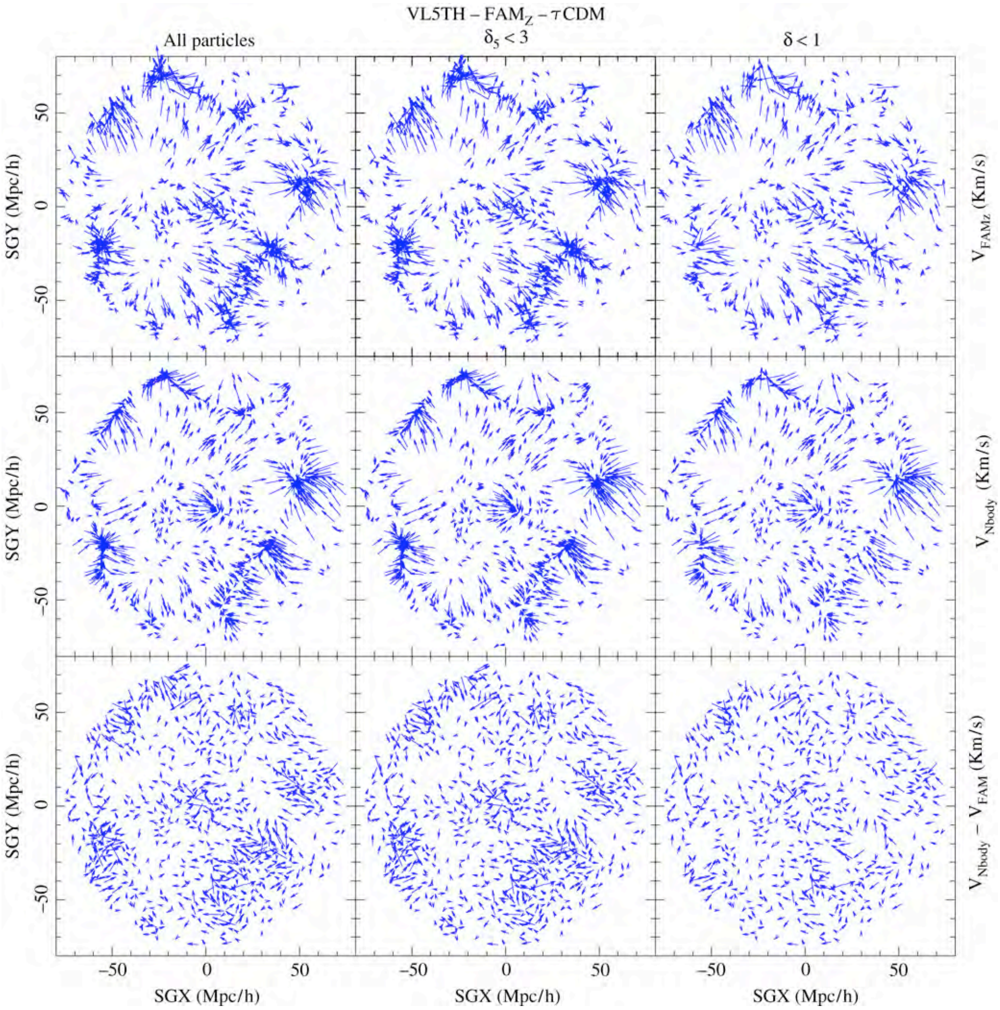

Fig. 1. Maps of 2D-projected peculiar velocities for points residing in a slice of thickness 6 h^{-1} Mpc cut through a simulated catalogue. The length of the vectors is drawn in units of 1 h^{-1} Mpc = 50 Km s^{-1}. The top row shows the least action predicted velocities (labelled FAMz). N-body velocities are shown in the middle row. The velocity residuals, $\mathbf{v}_{\rm Nbody} - \mathbf{v}_{\rm FAMz}$, are displayed on the bottom. The maps shown in the panels to the left hand side refer to all the points in the slice while only the velocities of points with moderate density contrast are plotted in the central and right columns.

Acknowledgments

I wish to express my thanks to the organizers of this exceptional conference.

References

[1] S.D. Phelps, V. Desjacques, A. Nusser, E.J. Shaya, MNRAS 370 (2006) 1361.
[2] R. Mohayee, A. Sobolevskii, These Proceedings.
[3] U. Frisch, S. Matarrese, R. Mohayaee, A. Sobolevski, Nature 417 (2002) 260.
[4] A. Nusser, A. Dekel, A. Yahil, Astrophys. J. 449 (1995) 439.
[5] A. Nusser, E. Branchini, MNRAS 313 (2000) 587.
[6] P.J.E. Peebles, Astrophys. J. 344 (1989) 53.
[7] P.J.E. Peebles, Astrophys. J. 429 (1994) 43.
[8] E.J. Shaya, P.J.E. Peebles, R.B. Tully, Astrophys. J. 454 (1995) 15.
[9] A.D.N. Spergel, Astrophys. J. D 170 (2007) 377.

Available online at www.sciencedirect.com
ScienceDirect
Physica D 237 (2008) 2162–2166
PHYSICA D
www.elsevier.com/locate/physd

On axisymmetric intrusive gravity currents: The approach to self-similarity solutions of the shallow-water equations in a stratified ambient

T. Zemach*, M. Ungarish

Department of Computer Science, Technion, Haifa 32000, Israel

Available online 31 January 2008

Abstract

The axisymmetric intrusion of a fixed volume of fluid, which is released from rest and then propagates radially at the neutral buoyancy level in a deep linearly stratified ambient fluid is investigated. The SW equations representing the high-Reynolds number motion are used. For the long-time motion an analytical similarity solution indicates propagation with $t^{1/3}$, but the shape is peculiar: the intrusion propagates like a ring and the inner domain contains a thin tail of clear ambient fluid. To avoid accumulation of numerical errors the problem was reformulated in terms of new variables and solved by finite-difference scheme. It is shown that the initial-value problem tends to the similarity prediction. Comparison with the non-stratified case is presented. It was found that for the non-stratified case there is a similar "tail-ring" stage of propagation, however this stage is only a transient to a different self-similar shape.

PACS: 47.10.A-; 47.15.ki

Keywords: Intrusion; Axisymmetric; Stratified

1. Introduction

Intrusive gravity currents are formed when a given volume of fluid of constant density ρ_c and kinematic viscosity ν is released from the lock of height h_0 into a vertically stratified ambient of density ρ_a at the level of a neutral buoyancy. The typical system configuration is sketched in Fig. 1. The propagation starts from rest in a region of radial dimension r_0 about the axis and the velocity has no lateral (azimuthal) component. We assume that the density of the ambient fluid varies linearly over the full depth of the container and that the Reynolds number Re of the flow is large.

The previous investigations (e.g. Hoult [2], Grundy and Rottman [1]) were concerned mainly with the axisymmetric gravity currents released from behind a lock into a non-stratified homogeneous ambient. The recent investigations of axisymmetric intrusions released from behind a lock into a linearly stratified ambient were presented by Ungarish and Zemach [6]. They showed that for the large time developed motion an analytical similarity solution exists. The self-similarity result indicates radial propagation with $t^{1/3}$, but the shape is peculiar: the intruding fluid propagates like a ring with a fixed ratio of inner to outer radii. Inside the inner radius of

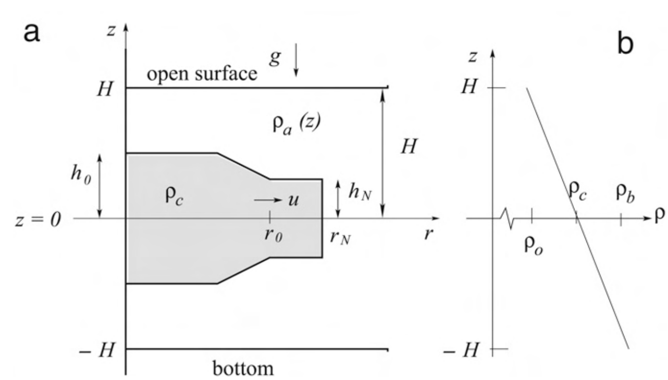

Fig. 1. Schematic description of the system (a) the geometry; (b) density profile in the ambient. In the dimensionless form, the horizontal lengths are scaled with r_0 and the vertical lengths with h_0. The subscripts denote: N — nose (or front); a — ambient; b — bottom; c — current (intrusion); o — open surface.

* Corresponding author.
E-mail address: tamart@cs.technion.ac.il (T. Zemach).

0167-2789/$ - see front matter © 2008 Elsevier B.V. All rights reserved.
doi:10.1016/j.physd.2008.01.020

the ring there is a thin "tail" — residual layer of mixed fluid, whose thickness decreases as t^{-2}. To confirm this analytical approach, Ungarish and Zemach [6] have solved the shallow-water (SW) initial-value problem by a finite-difference scheme for $0 \le t \le 10$. They showed that after an initial propagation to about 2.5 times the initial radius, at $t \approx 5$, the intrusion approaches a self-similar behavior.

The "tail-ring" form similarity solution of the axisymmetric stratified problem is unique and it is different from the similarity solution of the non-stratified axisymmetric problem. As it is shown by Ungarish and Zemach [5] quite soon after the release, at $t \approx 8$, the axisymmetric non-stratified current takes the form which reminds the stratified current "tail-ring" form. However according to Grundy and Rottman [1] the similarity solution for this case is different and if so, the "tail-ring" stage of propagation is finite and an additional stage between the "tail-ring" and the similarity solution stages should occur.

This behavior of the non-stratified current indicates that the stage of stratified current should also be carefully investigated numerically for long periods. However, as for the non-stratified case, large times after release the current becomes very thin and the solution of the standard SW problem by numerical methods is expected to contain a large numerical error. To overcome this loss of accuracy the problem should be reformulated.

In the present paper we attempt to confirm numerically the similarity solutions for the large time limits. For this purpose, the problem is reformulated in terms of long-time variables. The comparison with the non-stratified case is also discussed.

2. Formulation and SW approximations

We use the SW one-layer axisymmetric inviscid model (see Ungarish [3]). The ambient fluid is in the domain $-H \le z \le H$ and is stably linearly stratified (see Fig. 1). The density increases linearly from ρ_o at $z = H$ to ρ_b at $z = -H$. In the ambient fluid domain we assume that $u = v = w = 0$ and hence the fluid is in purely hydrostatic balance. The motion is assumed to take place in the intruding layer of fluid only, $0 \le r \le r_N$ and $-h \le z \le h$. The subscript N denotes the nose (front) of the intrusion. The density ρ_c of the intrusion is constant and is defined to be $\rho_c = \frac{1}{2}(\rho_b + \rho_0)$. The initial flow-field configuration is symmetric with respect to the horizontal plane $z = 0$. The following SW approximations are concerned with the inviscid and Boussinesq limits. In this case, the initial symmetry is expected to prevail also during the time-dependent propagation. It is therefore sufficient to consider the flow in the domain $0 \le z$.

We note that the buoyancy frequency of the unperturbed ambient is constant and given by

$$\mathcal{N} = \left(\frac{g'}{H}\right)^{1/2}, \tag{2.1}$$

where $g' = \frac{\rho_c - \rho_o}{\rho_o} g$ and g is the gravitational acceleration.

The dimensional variables (denoted here by asterisks) are scaled as follows

$$\left\{r^*, z^*, h^*, H^*, t^*, u^*, p^*\right\} = \left\{r_0 r, h_0 z, h_0 h, h_0 H, T_{\rm ref} t, U_{\rm ref} u, \rho_o U_{\rm ref}^2 p\right\}, \tag{2.2}$$

where $U_{\rm ref} = \mathcal{N} h_0$, $T_{\rm ref} = \frac{r_0}{U_{\rm ref}}$; r_0 and h_0 are the initial length and half-thickness of the intrusion, $U_{\rm ref}$ is the typical inertial velocity of propagation on the nose and $T_{\rm ref}$ is a typical time period for longitudinal propagation over a typical distance r_0. The typical Reynolds number is large and defined by $Re = \frac{U_{\rm ref} h_0}{\nu}$, where ν is the kinematic viscosity.

We emphasize that hereafter the variables r, z, u, t, h, H, p are in dimensionless form unless stated otherwise.

2.1. The governing equations

The equations of motion were formulated by Ungarish and Zemach [6]. The shallow-water equations can be expressed in dimensionless form for the dense fluid variables: the height $h(r, t)$ and the averaged longitudinal velocity $u(r, t)$. Using these dependent variables, the continuity and momentum equations can be expressed as:

$$\begin{cases} h_t + (hu)_r = -\dfrac{uh}{r} \\ u_t + hh_r + uu_r = 0. \end{cases} \tag{2.3}$$

The appropriate boundary conditions are: (1) the no-flow condition $u(0, t) = 0$ at the center; (2) kinematic condition at the nose $\frac{\mathrm{d}}{\mathrm{d}t} r_N = u(r_N, t)$; (3) the boundary condition for the velocity at the nose

$$u(r_N, t) = \frac{Fr}{\sqrt{2}} h_N, \tag{2.4}$$

where the Froude number, Fr is in the range: $1 \le Fr \le \sqrt{2}$. A more rigorous justification of the nose condition is presented by Ungarish [3], Ungarish [4] and Ungarish and Zemach [6]. The initial conditions are

$$\begin{aligned} &r_N(0) = 1; \\ &u(r, 0) = 0, \quad 0 \le r < 1; \\ &h(r, 0) = \begin{cases} 1, & \text{for the cylinder;} \\ \sqrt{1 - r^2}, & \text{for the ellipsoid;} \end{cases} \quad 0 \le r < 1. \end{aligned} \tag{2.5}$$

2.2. Similarity solution

According Ungarish and Zemach [6], for a deep intrusion (Fr is constant) and large values of t, the above-mentioned system of Eq. (2.3) with appropriate boundary conditions is satisfied by the following self-similarity solution:

$$\begin{aligned} &r_N(t) = K(t + \gamma)^{1/3}; \\ &h(y, t) = \frac{1}{3} K(t + \gamma)^{-2/3} \cdot \sqrt{2}(y^2 - y_1^2)^{1/2}; \\ &u(y, t) = \frac{1}{3} K(t + \gamma)^{-2/3} y \end{aligned} \tag{2.6}$$

where $y = \frac{r}{r_N(t)}$ is stretched radial coordinate which maps the radial domain $[0, r_N(t)]$ into $[0, 1]$; $y_1 = \sqrt{1 - \frac{1}{Fr^2}}$; K is a positive constant given by:

$$K = 3Fr\left(\frac{V_0}{3\sqrt{2}}\right)^{1/3}, \tag{2.7}$$

where V_0 is the constant volume of the upper part of the intrusion (per unit azimuthal angle) and is equal to 0.5 for the standard initial cylinder and to $1/3$ for an initial ellipsoid. The constant $\gamma \approx -1.53$ for the cylinder and -1.63 for the ellipsoid.

The solution (2.6) is valid only in the $y_1 \le y \le 1$ domain, where the intruding fluid propagates like a ring with a fixed ratio of inner and outer radii. We will call this region the "ring region". Inside the inner radius of the ring there is a thin "tail" — residual layer of mixed fluid, whose thickness decreases like t^{-2}.

The behavior of the thin tail region in the domain $0 \le y \le y_1$ is given by the analytical expression

$$h(r,t) = \frac{C_1}{(t+C_2)^2}; \qquad u(r,t) = \frac{1}{t+C_2}r, \tag{2.8}$$

where for $Fr = 1.19$, $C_1 = 1.194$ and $C_2 = 0.194$ for the cylinder and $C_1 = 1.946$ and $C_2 = 0.815$ for the ellipsoid.

To patch these two regions we derive the analytical expression of their meeting point y_M by the assumption that the height is continuous at y_M:

$$y_M^2(t) = \frac{9}{2}\frac{C_1^2}{K^2}\frac{(t+\gamma)^{4/3}}{(t+C_2)^4} + y_1^2. \tag{2.9}$$

A short calculation shows that (1) for $Fr > 1$ the long-time solution conserves its "tail-ring" form; The case $Fr = 1$ is different from the rest since for this case $y_1 = 0$ and the "intrusion tail" region vanishes. (2) the value of y_M is always greater than y_1 and (3) $\lim_{t\to\infty} y_M = y_1$.

2.3. Numerical solutions

We follow the method used by Grundy and Rottman [1] for the non-stratified problem. Here we develop the appropriate solution for the stratified intrusion. The original system of Eq. (2.3) with appropriate boundary and initial conditions is reformulated here in terms of the new independent variables

$$y = \frac{r}{r_N}, \quad (0 \le y \le 1); \qquad T = \frac{1}{3}\ln(t), \quad T \ge 0 \tag{2.10}$$

and the dependent variables R, H and U, defined by

$$\begin{aligned} r_N(t) &= Kt^{1/3}R(T);\\ h(r,t) &= \frac{1}{3}Kt^{-2/3}H(y,T);\\ u(r,t) &= \frac{1}{3}Kt^{-2/3}U(y,T), \end{aligned} \tag{2.11}$$

where K is given by (2.7).

The original equations were subjected to the correspond become:

$$\begin{cases} H_T + \dfrac{1}{R}(HU)_y - y(1+\dfrac{R'}{R})H_y = 2H - \dfrac{1}{R}\dfrac{HU}{y},\\ (UH)_T + \dfrac{1}{R}(U^2H)_y - y(1+\dfrac{R'}{R})(UH)_y\\ \quad = 4UH - \dfrac{1}{R}\dfrac{U^2H}{y} - \dfrac{1}{R}H^2H_y. \end{cases} \tag{2.12}$$

The boundary conditions are:

$$\begin{aligned} &U(0,T) = 0;\\ &R(T) + R'(T) = U(1,T);\\ &U(1,T) = \frac{Fr}{\sqrt{2}}H(1,T). \end{aligned} \tag{2.13}$$

The appropriate initial conditions (2.5) at $T = 0$ ($T = 0$ corresponds to $t = 1$) are:

$$\begin{aligned} &H(y,0) = \begin{cases} \dfrac{3}{K}, & \text{for the cylinder;}\\ \dfrac{3}{K}\sqrt{1-y^2}, & \text{for the ellipsoid;} \end{cases}\\ &U(y,0) = 0;\\ &R(0) = \frac{1}{K}. \end{aligned} \tag{2.14}$$

The system (2.12)–(2.14) is solved numerically by a finite-difference McCormack scheme. The boundary conditions for H at $y = 1$ and $y = 0$ are calculated for each new time step from the balances on the characteristics $C_{\pm}$.

The choice of variables keeps the independent variables (2.10) within reasonably moderate ranges, $0 \le y \le 1$ and $0 \le T$ and the dependent variables were found to be in the range $0 \le H < 2$, $0 \le U \le 2.5$, $0.6 \le R \le 1.1$. The dependent variables can be compared directly with the similarity forms (2.6). For this comparison moderate values of T can be used (since $T = 2$ corresponds to $t = e^6 \approx 403$).

3. Results and comparisons

The comparison between the SW numerical solution and analytical similarity solution for $Fr = 1.19$ and cylindrical initial configuration is shown in Fig. 2.

Fig. 2(a)–(b) are plots of $H(y,T)$ and $U(y,T)$ at several values of T. The similarity "ring" solution is shown as a bold solid line. Fig. 2 shows that at the initial phase of propagation ($T \le 1$), the shape resembles the behavior of the dam-break problem, however at $T \approx 1$ the similarity "tail-ring" form is already obtained. By the time $T \approx 2$ ($t \approx e^6$) the numerical solution is very close to the analytical similarity solution. For $T > 2$ this numerical solution changes very slowly and actually coincides with the numerical solution at $T \approx 2$, except, to a very small region near $y = y_1$.

Fig. 2(c) shows that the front position $R(T)$ (solid line) approaches the similarity result 1 (bold dashed curve). The comparison between the analytical and numerical results for the

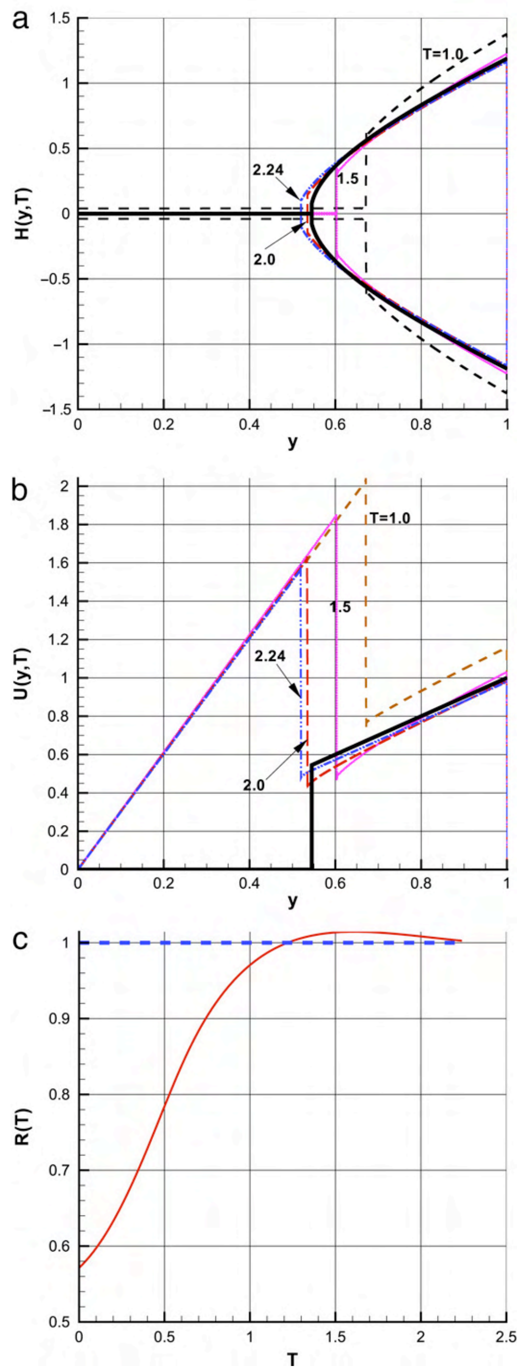

Fig. 2. Stratified axisymmetric intrusion for cylindrical initial configuration: comparison between the similarity and numerical solutions for $Fr = 1.19$. (a), (b): Computed height and velocity profiles $H(y, T)$ and $U(y, T)$ vs. $T = 1.0, 1.5, 2.0, 2.24$ ($t \approx 19.9, 88.8, 396.1, 812.0$). (c): the computed transformed front position $R(T)$. The bold solid curve is the similarity solution (2.6).

position of the meeting point y_M is shown in Fig. 3 for $Fr = 1.19$. The numerical values of y_M were calculated according to the location of the velocity jump. The function y_M decreases with T and its numerical value tends to approach $y \approx 0.52$ when $T \to \infty$. The comparison shows that the numerical results confirms the analytical estimate (2.9) and deviates from it by about 3%. However, running the simulation to longer

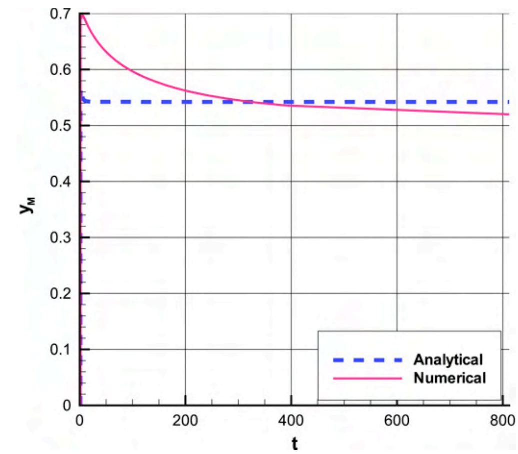

Fig. 3. Comparison between the analytical expression (2.9) and numerical result for the position of patching point y_M.

times probably would show that the solution oscillates about the similarity solution.

To strengthen the insights into the propagation of a deep intrusion, we also considered the release of an initial ellipsoid volume of mixed fluid, i.e. $h = \sqrt{1 - r^2}$ for $0 \leq r \leq 1$ at $t = 1$. The results show that the essential propagation is similar to that of the previous cylindrical problem. The initial spread is slightly delayed by the fact that the height of the nose must develop from zero, but the tendency to the similarity shape at $T > 1.6$ is evident.

The comparison with non-stratified results (see Grundy and Rottman [1]) shows that in both, the stratified and non-stratified cases, a "tail-ring" shape appears at about $t = 2$ and in both cases, the thickness of the tail decreases like t^{-2}. However, for the stratified problem the length of the tail increases (the patching point between the tail and the ring, y_M, is near $\approx y_1$ and hence $r_M = y_M r_N(t)$ increases). On the other hand, for the non-stratified case, the length of the tail decreases till the patching point $r_{M_{NS}} = y_{M_{NS}} r_N(t)$ approaches zero and the "tail" disappears. Thus, for the non-stratified case, the "tail-ring" form appears only for a finite period of time during the developing of the similarity solution.

4. Conclusions

The propagation of an axisymmetric intrusion of a fixed volume released from a lock at the neutral buoyancy level in a stratified ambient was considered. We used a new analysis, based on a one-layer SW closed formulation. The previous SW results presented by Ungarish and Zemach [6] show that after an initial propagation to about 2.5 times the initial radius, the intrusion tends to a self-similar behavior with an unique "tail-ring" form. On the other hand, analysis of the non-stratified intrusion shows that for this case there also is a stage of propagation when the intrusion has a "tail-ring" form, but the analytical similarity solution for this case is quite different and a tail in the very long-time behavior is unacceptable. Our investigation elucidated the details of the approach to similarity in these cases. To verify the similarity analytical prediction long time after release, the SW problem was reformulated in terms of new variables to avoid accumulation of numerical errors. Predictions were obtained for realistic cylindric and elliptic lock geometries, initial and boundary conditions. Various values of the Froude number were used in the domain $1 \leq Fr < \sqrt{2}$. We note that, for the Boussinesq currents considered here such values of Fr are only physically possible.

The "tail-ring" form of the current, obtained from the numerical solution of the rescaled SW problem, is in good agreement with the analytical expression of the similarity solution (for both the cylindrical and elliptical initial geometry of the current).

The comparison of the results obtained for the stratified intrusion with the classical non-stratified case shows that in the latter case the "tail-ring" shape appears only as a transient stage of propagation. The similarity behavior of the current in this case is quite different from the former one without the "tail-ring" behavior.

The similarity solutions considered here can be applied to the study of various effects of axisymmetric intrusions, such as energy transfers and stability.

After a spread to a relatively large radius the intrusion is expected to become very thin and slow. At this stage, in a real fluid, the effects of viscosity, mixing and wave influence are expected to become dominant. This requires a separate investigation.

To our best knowledge, there are presently no experimental verification of the flow discussed in our work. The lack of experimental data prevents sharper conclusions about the insights provided by the present theory. We hope that the present study will provide the background, guidelines and the motivation for the laboratory experiments on this problem.

Acknowledgment

The research was supported by E. and J. Bishop Research Fund of the Technion.

References

[1] R.E. Grundy, J.W. Rottman, J. Fluid Mech. 156 (1985) 39–53.
[2] D. Hoult, Annu. Rev. Fluid Mech. 2 (1972) 341–368.
[3] M. Ungarish, J. Fluid Mech. 535 (2005) 287–323.
[4] M. Ungarish, J. Fluid Mech. 548 (2006) 49–68.
[5] M. Ungarish, T. Zemach, J. Fluid Mech. 481 (2002) 37–66.
[6] M. Ungarish, T. Zemach, EJMB 26 (2007) (2007) 220–235.

Boundaries and vortical structures

Available online at www.sciencedirect.com
ScienceDirect
Physica D 237 (2008) 2167–2183
PHYSICA D
www.elsevier.com/locate/physd

The state of the art in hydrodynamic turbulence: Past successes and future challenges

Itamar Procaccia[a,*], K.R. Sreenivasan[b]

[a] Department of Chemical Physics, The Weizmann Institute of Science, Rehovot 76100, Israel
[b] International Centre for Theoretical Physics, Strada Costiera 11, 34014 Trieste, Italy

Available online 6 February 2008

Abstract

We present a personal view of the state of the art in turbulence research. We summarize first the main achievements of the recent past, and then point ahead to the main challenges that remain for experimental and theoretical efforts.

Keywords: Anomalous scaling; Anisotropic and wall turbulence; Drag reduction; Convective and superfluid turbulence

1. Introduction

"The problem of turbulence" is often hailed as one of the last open problems of classical physics. In fact, there is no single "problem of turbulence"; rather, there are many inter-related problems, some of which have seen significant progress in recent years, and some are still open and inviting further research. The aim of this short review is to explain where fundamental progress has been made and where, in the opinion of the present writers, there are opportunities for further research.

There are many ways to set a fluid into turbulent motion. Examples include creating a large pressure gradient in a channel or a pipe, pulling a grid through a fluid, moving one or more boundaries to create a high shear and forcing a high thermal gradient. Customarily the vigor of forcing is measured by the Reynolds number Re, defined as $Re \equiv UL/\nu$ where L is the scale of the forcing, U is the characteristic velocity of the fluid at that same scale, and ν is the kinematic viscosity. The higher the Reynolds number the larger is the range of scales involved in the turbulent motion, roughly from the scale L itself (known as the "outer" or "integral" scale) down to the so-called "viscous" scale η which decreases as $Re^{-3/4}$ [1]. For large Re a turbulent flow exhibits an erratic dependence of the velocity field on the position in the fluid and on time. For this reason it is universally accepted that a statistical description of turbulence is called for, such that the objects of interest are almost invariably mean quantities (over time, space or an ensemble, depending on the application), fluctuations about the mean quantities, and correlation functions defined by these fluctuations; precise definitions will be given below. The crucial scientific questions thus deal typically with the universality of the statistical objects, universality with respect to the change of the fluid, or universality with respect to the change of forcing mechanisms. We will see that this universality issue binds together the various aspects of turbulence to be discussed below into a common quest – the quest for understanding those aspects of the phenomenon that transcend particular examples. We will strive to underline instances when this quest has been successful and when doubts remain.

The structure of this review is as follows: in Section 2 we discuss the statistical theory of homogeneous and isotropic turbulence and focus on the anomalous scaling exponents of correlation functions. For a part of the community this represented *the* important open problem in turbulence, and indeed great progress has been achieved here. In Section 3 we address homogeneous but anisotropic turbulence and present recent progress in understanding how to extract information about isotropic statistical objects, and how to characterize the anisotropic contributions. Section 4 deals with wall-bounded turbulence where both isotropy and homogeneity are lost (this

* Corresponding author.
E-mail address: itamar.procaccia@weizmann.ac.il (I. Procaccia).

0167-2789/$ - see front matter
doi:10.1016/j.physd.2008.01.025

being the norm in practice, rather than the exception). We focus on the controversial issue of the log versus power-laws, clarifying the scaling assumptions underlying each of these approaches and replacing them by a universal scaling function; we show that this achieves an excellent modeling of channel or pipe flows. In Section 5 we consider turbulence with additives (like polymers or bubbles) and review the progress in understanding drag reduction by such additives. Section 6 discusses problems in thermal convection, with emphasis on recent work. Finally, Section 7 provides a selective account of the problems that have come to the fore in superfluid turbulence, sometimes bearing directly on its classical counterpart. The article concludes with a summary of the outlook.

2. Anomalous scaling in homogeneous and isotropic turbulence

A riddle of central interest for more than half a century to the theorist and the experimentalist alike concerns the numerical values of the scaling exponents that characterize the correlation and structure functions in homogeneous and isotropic turbulence. Before stating the problem one should note again that strictly homogeneous and isotropic state of a turbulent flow is not achievable in experiments; typically the same forcing mechanism that creates the turbulent flow is also responsible for breaking homogeneity or isotropy. Nevertheless, some reasonable approximations have been created in the laboratory. To get an even closer approximation, one has to resort to numerical simulations. For a long time, the Reynolds number of simulations was limited by numerical resolution and by storage capabilities, but this situation has improved tremendously in the past few years. Indeed, as an idealized state of turbulence which incorporates the essentials of the nonlinear transfer of energy among scales, homogeneous and isotropic turbulence has gained a time-honored status in the history of turbulence research, since its introduction by Taylor [2].

Consider then the velocity field $\boldsymbol{u}(\boldsymbol{r}, t)$ which satisfies the Navier–Stokes equations

$$\frac{\partial \boldsymbol{u}}{\partial t} + \boldsymbol{u} \cdot \nabla \boldsymbol{u} = -\nabla p + \nu \nabla^2 \boldsymbol{u} + \boldsymbol{f}, \tag{1}$$

where p is the pressure and $\boldsymbol{f}$ the (isotropic and homogeneous) forcing that creates the (isotropic and homogeneous) turbulent flow. Defining by $\langle \dots \rangle$ an average over time, we realize that $\langle \boldsymbol{u} \rangle = 0$ everywhere in this flow. On the other hand, correlations of $\boldsymbol{u}$ are of interest, and we define the so-called "unfused" nth-order correlation function $\boldsymbol{T}_n$ as

$$\boldsymbol{T}_n(\boldsymbol{r}_1, t_1, \boldsymbol{r}_2, t_2, \dots \boldsymbol{r}_n, t_n) \equiv \langle \boldsymbol{u}(\boldsymbol{r}_1, t_1) \boldsymbol{u}(\boldsymbol{r}_2, t_2) \dots \boldsymbol{u}(\boldsymbol{r}_n, t_n) \rangle. \tag{2}$$

When all the times t_i are the same, $t_i = t$, we get the equal-time correlation function $\boldsymbol{F}_n(\boldsymbol{r}_1, \boldsymbol{r}_2, \dots \boldsymbol{r}_n)$ which, for a forcing that is stationary in time, is a time-independent function of the $n(n-1)/2$ distances between the points of measurements, due to homogeneity. An even more contracted object is the so-called "longitudinal structure function" S_n,

$$S_n(R) \equiv \langle \{[\boldsymbol{u}(\boldsymbol{r} + \boldsymbol{R}, t) - \boldsymbol{u}(\boldsymbol{r}, t)] \cdot \boldsymbol{R}/R\}^n \rangle, \tag{3}$$

which can be obtained by sums and differences of correlation functions $\boldsymbol{F}_n$, together with some fusion of coordinates [3]. On the basis of evidence from experiments and simulations, it has been stipulated (although never proven) that S_n is a homogeneous function of its arguments when the distance R is within the so-called "inertial range" $\eta \ll R \ll L$ in the sense that

$$S_n(\lambda R) = \lambda^{\zeta_n} S_n(R). \tag{4}$$

A central question concerns the numerical values of the "scaling exponents" ζ_n and their universality with respect to the nature of the forcing f. Even if we set aside questions about the form of $S_n(R)$, the question on exponents poses serious difficulties since it is impossible to derive a closed-form theory for the general structure function S_n, since any such theory involves higher-order unfused correlation functions with integrations over the time variable [4,5].

A closely related question with lesser theoretical difficulties pertains to other fields that couple to the velocity field, with the "passive scalar" case drawing most attention during the nineties. A passive scalar $\phi(\boldsymbol{r}, t)$ is a field that is advected by a turbulent velocity which itself is unaffected by it. For example,

$$\frac{\partial \phi}{\partial t} + \boldsymbol{u} \cdot \nabla \phi = \kappa \nabla^2 \phi + f. \tag{5}$$

If $\boldsymbol{u}$ and f are homogeneous and isotropic, and $Re \to \infty$ and $\kappa \to 0$, the structure functions $\mathcal{S}_n \equiv \langle [\phi(\boldsymbol{r} + \boldsymbol{R}) - \phi(\boldsymbol{r})]^n \rangle$ are stipulated to be homogeneous functions of their arguments with scaling exponents ξ_n.

Dimensional considerations predict $\zeta_n = \xi_n = n/3$, with $\zeta_3 = 1$ being an exact result from fluid mechanics, going back to Kolmogorov [6]. Experimental and simulations data deviated from these predictions (except, of course, for $n = 3$), and a hot pursuit for an example where these exponents could be calculated theoretically was inevitable. The first example that yielded to analysis was the Kraichnan model [7], in which $\boldsymbol{u}$ is not a generic velocity field, but rather a random Gaussian field whose second-order structure function scales with a scaling exponent ζ_2 as in Eq. (4), but is δ-correlated in time. This feature of the advecting field leads to a great theoretical simplification, not as much as to provide a closed-form theory for $\mathcal{S}_n$, but enough to allow a derivation of a differential equation for the simultaneous $2n$th-order correlation function $\mathcal{F}_{2n} = \langle \phi(\boldsymbol{r}_1) \dots \phi(\boldsymbol{r}_{2n}) \rangle$, having the symbolic form [7]

$$\mathcal{O}\mathcal{F}_{2n} = RHS(\mathcal{F}_{2n-2}). \tag{6}$$

Guessing the scaling exponent of $\mathcal{F}_{2n}$ by power counting and balancing the LHS against the RHS yields dimensional scaling estimates which, in this case, are $\xi_{2n} = (2 - \zeta_2)n$. The crucial observation, however, is that the differential equation (6) possesses, in addition to the inhomogeneous solution that can be guessed by power counting, also homogeneous solutions of the equation $\mathcal{O}\mathcal{F}_{2n} = 0$ [8–10]. These "zero modes" are homogeneous functions of their arguments but their exponent cannot be guessed from power counting; the scaling exponents are anomalous – i.e., $\xi_{2n} < (2-\zeta_2)n$ – and therefore dominant at small scales. As the scaling exponents appear in power-laws of the type $(r/\Lambda)^{\xi}$, Λ being some typical outer scale and $r \ll \Lambda$, the larger the exponent, the faster the decay of the contribution as the scale r diminishes. The exponents could be computed in perturbation theory around $\zeta_2 = 0$, demonstrating for the first time that dimensional scaling exponents are not the solution to the problem. For a further review see [11].

An appealing interpretation of the physical mechanism for anomalous exponents of the Kraichnan model was presented in the framework of the Lagrangian formulation [12]. In this formulation an nth-order correlation function results from averaging over all the Lagrangian trajectories of groups of n fluid points that started somewhere at $t = -\infty$ and ended their trajectories at points $\boldsymbol{r}_1 \ldots \boldsymbol{r}_n$ at time $t = 0$. Analyzing this dynamics revealed that the Richardson diffusion of these groups did not contribute to anomalous scaling. Rather, it is the dynamics of the shapes (triangles for 3 points, tetrahedra for 4 points, etc.) that is responsible for the anomaly. In fact, the anomalous scaling exponents could be related to eigenvalues of operators made from the shape-to-shape transition probability [13]. The zero modes discussed above are *distributions over the space of shapes* that remain invariant to the dynamics [14]. It appears that these findings of the importance of shapes rather than scales in determining anomalous exponents is a new contribution to the plethora of anomalous exponents in field theory, and it would be surprising if other examples where shapes rather than scales are crucial will not appear in other corners of field theory, classical as well as quantum-mechanical.

The finding of distributions that remain invariant to the dynamics meant that there must be such distributions in the Eulerian frame as well, since the change from Lagrangian to Eulerian is just a smooth change of coordinates. Indeed this was the case; and this provided the clue to generalizing the results of the non-generic Kraichnan model to the generic case represented by Eq. (5) with a generic velocity field that stems from the Navier–Stokes equations. The central comment is that the decaying passive scalar problem, i.e. Eq. (5) with $f = 0$, is a linear problem for which one can always define a propagator from $\mathcal{F}_n$ at $t = 0$ (i.e. $\langle \phi(\boldsymbol{r}_1, t=0) \cdots \phi(\boldsymbol{r}_n, t=0) \rangle$) to the same object at time t (note that for the decaying problem this is no longer a stationary quantity) [15]. This propagator possesses eigenfunctions of eigenvalue 1 which are homogeneous functions of their arguments, characterized by anomalous exponents. They are the analogs of zero modes of the Kraichnan model, and are responsible for anomalous exponents in the generic case [16,17]. Thus the general statement that can be made is that the anomaly for the passive scalar, generic or otherwise, is due to the existence of "statistically preserved structures"; the structures can change in every single experiment, but remain invariant on the average. This is a novel notion that pertains to nonequilibrium systems without a known analog in equilibrium problems.

At present it is still unclear whether the insight gained from linear models might have direct relevance to the nonlinear velocity problem itself. Some positive indications in this direction can be found in [18], but much more needs to be done before firm conclusions can be drawn.

3. Statistical theory of anisotropic homogeneous turbulence

As mentioned above, the agents that produce turbulence tend to destroy its homogeneity and isotropy. In this section we are concerned about the loss of isotropy and review the extensive work that has been done to come to grips with this issue in a systematic fashion. Since this subject has been reviewed extensively [19], we limit this section to only a few essential comments.

The need for rethinking the issue of loss of isotropy was underlined by the appearance of several papers where anisotropic flows were analyzed disregarding anisotropy, and exponents were extracted from data assuming that the inertial range scales were isotropic. The results were confusing: scaling exponents varied from experiment to experiment, and from one position in the flow to another. If this were indeed the case, the notion of universality in turbulence would fail irreversibly. In fact, it can now be shown that all these worrisome results can be attributed to anisotropic contributions in the inertial range, as explained below.

The basic idea in dealing with anisotropy is that the equations of fluid mechanics are invariant to all rotations. Of course, these equations are also nonlinear, and therefore one cannot foliate them into the sectors of the SO(3) symmetry group. The equations for correlation functions are, however, linear (though forming an infinite hierarchy). Thus by expanding the correlation functions in the irreducible representations of the symmetry group, one gets a set of equations that are valid sector by sector [20]. The irreducible representations of the SO(3) symmetry group are organized by two quantum numbers j, m with $j = 0, 1, 2, \ldots$ and $m = -j, -j+1, \ldots j$. It turns out that the m components are mixed by the equations of motion, but the j components are not. Accordingly one can show that an n-point correlation function admits the expansion

$$\boldsymbol{F}_n(\boldsymbol{r}_1, \boldsymbol{r}_2, \ldots \boldsymbol{r}_n) = \sum_{qjm} A_{qjm}(r_1, r_2, \ldots, r_n) \times \boldsymbol{B}_{qjm}(\hat{\mathbf{r}}_1, \hat{\mathbf{r}}_2 \ldots \hat{\mathbf{r}}_n), \tag{7}$$

where $\hat{\mathbf{r}}$ is a unit vector in the direction of $\boldsymbol{r}$, and A_{qjm} is a homogeneous function of the scalar $r_1 \ldots r_n$,

$$A_{qjm}(\lambda r_1, \lambda r_2, \ldots, \lambda r_n) = \lambda^{\zeta_n^{(j)}} A_{qjm}(r_1, r_2, \ldots, r_n). \tag{8}$$

Here $\zeta_n^{(j)}$ is the scaling exponent characterizing the j-sector of the symmetry group for the nth-order correlation function. $\boldsymbol{B}_{qjm}(\hat{\mathbf{r}}_1, \hat{\mathbf{r}}_2 \ldots \hat{\mathbf{r}}_n)$ are the n-rank tensorial irreducible representations of the SO(3) symmetry group, and the index q in Eq. (7) is due to the fact that higher-order tensors have more than one irreducible representation with the same j, m [20].

It was shown that this property of the nth-order correlation functions is inherited by the structure functions as well [21]. Since these are scalar functions of a vector argument they get expanded in standard spherical harmonics $\phi_{jm}(\hat{\mathbf{R}})$

$$S_n(\boldsymbol{R}) = \sum_{jm} a_{jm}(r)\phi_{jm}(\hat{\mathbf{R}}), \tag{9}$$

with

$$a_{jm}(\lambda r) = \lambda^{\zeta_n^{(j)}} a_{jm}(r). \tag{10}$$

The main issue for research was the numerical values of this plethora of scaling exponents.

Of considerable help in organizing the scaling exponents in the various sectors of the symmetry group were the Kraichnan model and related models (like the passive vector model with pressure), where the exponents could be computed analytically in the Eulerian frame in any sector of the symmetry group. The central quantitative result of the Eulerian calculation is the expression for the scaling exponent $\xi_j^{(n)}$ which is associated with the scaling behavior of the nth-order correlation function (or structure function) of the scalar field in the jth sector of the symmetry group. In other words, this is the scaling exponent of the projection of the correlation function on the jth irreducible representation of the SO(d) symmetry group, d being the space dimension, with n and j taking on even values only, $n = 0, 2, \ldots$ and $j = 0, 2, \ldots$ [23]:

$$\xi_j^{(n)} = n - \epsilon\left[\frac{n(n+d)}{2(d+2)} - \frac{(d+1)j(j+d-2)}{2(d+2)(d-1)}\right] + O(\epsilon^2). \tag{11}$$

The result is valid for any even $j \le n$, and to $O(\epsilon)$. In the isotropic sector ($j = 0$) we recover the result of [8]. It is noteworthy that for higher values of j the discrete spectrum is a strictly increasing function of j. This is important, since it shows that for diminishing scales the higher-order scaling exponents become irrelevant, and for sufficiently small scales only the isotropic contribution survives. Recall that the scaling exponents appear in power-laws of the type $(r/\Lambda)^{\xi}$ with Λ a typical outer scale and $r \ll \Lambda$; the larger the exponent, the faster the decay of the contribution as the scale r diminishes. This is precisely how the isotropization of small scales takes place, with the higher-order exponents describing the rate of isotropization. Nevertheless, for intermediate scales or for finite values of the Reynolds and Peclet numbers, the lower-lying scaling exponents will appear in all the measured quantities, and understanding their role and disentangling their various contributions cannot be avoided.

For Navier–Stokes turbulence the exponents cannot be computed analytically, but the results obtained from experiments [21] and simulations [22] indicate that the picture obtained for the Kraichnan model repeats itself. The isotropic sector is always leading (in the sense that scaling exponents belonging to higher sector are numerically larger). There is growing evidence of universality of scaling exponents in all the sectors, but this issue is far from being settled, and more experiments and simulations are necessary to provide decisive evidence. It is noteworthy that the issue of universality of the exponents in the isotropic sector is here expanded many-fold into all the sectors of the symmetry group, and is certainly worth further study.

4. Wall-bounded turbulence

Turbulent flows of highest relevance for engineering application possess neither isotropy nor homogeneity. For example, turbulent flows in channels and pipes are strongly anisotropic and inhomogeneous; indeed, in a stationary plane channel flow with a constant pressure gradient $p' \equiv -\mathrm{d}p/\mathrm{d}x$ the only component of the mean velocity $\boldsymbol{V}$, the streamwise component $V_x \equiv V$, depends strongly on the wall normal direction z; the derivatives of V_x with respect to z and the second-order quantities such as mean-square-fluctuations similarly depend only on z. A long-standing challenge is the description of the **profiles** of the mean velocity and second-order fluctuations throughout the channel or pipe at relatively high but finite Reynolds numbers.

To understand the issue, focus on a channel of width $2L$ between its parallel walls, where the incompressible fluid velocity $\boldsymbol{U}(\boldsymbol{r}, t)$ is decomposed into its mean (i.e., average over time) and a fluctuating part

$$\boldsymbol{U}(\boldsymbol{r}, t) = \boldsymbol{V}(\boldsymbol{r}) + \boldsymbol{u}(\boldsymbol{r}, t), \quad \boldsymbol{V}(\boldsymbol{r}) \equiv \langle \boldsymbol{U}(\boldsymbol{r}, t)\rangle. \tag{12}$$

Near the wall, the mean velocity profiles for different Reynolds numbers exhibit data collapse once presented in wall units. Here in "data collapse" we mean that data obtained at different experimental conditions can be collapsed on the same curve by re-plotting in different units (see Fig. 4 for example). The 'wall units' are obtained by defining the Reynolds number Re_τ, the normalized distance from the wall z^+ and the normalized mean velocity $V^+(z^+)$ (for channels) by

$$Re_\tau \equiv L\sqrt{p'L}/\nu, \qquad z^+ \equiv zRe_\tau/L, \qquad V^+ \equiv V/\sqrt{p'L}.$$

The classical theory of Prandtl and von Kármán for infinitely large Re_τ is based on dimensional reasoning and on the assumption that *the single characteristic scale in the problem is proportional to the distance from the (nearest) wall* (see below for details). It leads to the celebrated von Kármán log-law [1]

$$V^+(z^+) = \kappa^{-1}\ln(z^+) + B\,, \tag{13}$$

which serves as a basis for the parametrization of turbulent flows near a wall in many engineering applications. On the face of it, this law agrees with the data (see, e.g. Fig. 1) for relatively large z^+, say for $z^+ > 100$, giving $\kappa \sim 0.4$ and $B \sim 5$. The range of validly of the log-law is definitely restricted by the requirement $\zeta \ll 1$, where $\zeta \equiv z/L$ (channel) or $\zeta \equiv r/R$ (pipe of radius R). For $\zeta \sim 1$ the global geometry becomes important leading to unavoidable deviations of $V^+(\zeta)$ from the log-law (13), known as *the wake*.

The problem is that for finite Re_τ the corrections to the log-law (13) are in powers of $\varepsilon \equiv 1/\ln Re_\tau$ [24,25] and definitely cannot be neglected for the currently largest available direct numerical simulation (DNS) of channel flows ($Re_\tau = 2003$ [26,27] or $\varepsilon \approx 0.13$). Even for Re_τ approaching 500,000 as in the Princeton superpipe experiment [28], $\varepsilon \approx 0.08$. This opens a Pandora box with various possibilities to revise the log-law (13) and to replace it, as was suggested in [24], by a power-law

$$V^+(z^+) = C(Re_\tau)(z^+)^{\gamma(Re_\tau)} . \tag{14}$$

Here both the coefficients $C(Re_\tau)$ and the exponents $\gamma(Re_\tau)$ were represented as asymptotic series expansions in ε. The relative complexity of this proposition compared to the simplicity of Eq. (13) resulted in a mixed response in the fluid mechanics community [29], leading to a controversy. Various attempts [24,28–32] to validate the log-law (13) or the alternative power-law (14) were based on extensive analysis of experimental data used to fit the velocity profiles as a formal expansion in inverse powers of ε or as composite expansions in both z^+ and ζ.

Recently a complementary approach to this issue was proposed on the basis of experience with critical phenomena where one employs scaling functions rather than scaling laws [33]. The essence of this approach is the realization that a characteristic scale, say $\widetilde{\ell}$, may depend on the position in the flow. The simple scaling assumption near the wall, $\widetilde{\ell}^+ = \kappa z^+$, leads to the log-law (13). The alternative suggestion of [24], $\widetilde{\ell}^+ \propto (z^+)^{\alpha(Re_\tau)}$, leads to alternative power-law (14). But there is no physical reason why $\widetilde{\ell}$ should behave in either manner. Instead, it was shown that $\widetilde{\ell}/L$ should depend on $\zeta = z/L$, approaching $\kappa\zeta$ in the limit $\zeta \to 0$ (in accordance with the classical thinking). However, for $\zeta \sim 1$, $\widetilde{\ell}$ should saturate at some level below κL due to the effect of the other wall. We recall now the recent analysis of DNS data that provides a strong support to this idea, allowing one to get, within the traditional (second-order) closure procedure, a quantitative description of the following three quantities: the mean shear, $S(z) = \mathrm{d}V(z)/\mathrm{d}z$, the kinetic energy density (per unit mass), $K(z) \equiv \langle |\boldsymbol{u}|^2\rangle/2$, and the tangential Reynolds stress, $W(z) \equiv -\langle u_x u_z\rangle$. This is achieved in the entire flow and in a wide region of Re_τ, using only three Re_τ-independent parameters.

The first relation between these objects follows from the Navier–Stokes equation for the mean velocity. The resulting equation is exact, being the mechanical balance between the momentum generated at distance z from the wall, i.e. $p'(L - z)$, and the momentum transferred to the wall by kinematic viscosity and turbulent transport. In physical and wall units it has the form

$$\nu S + W = p'(L - z) \Rightarrow S^+ + W^+ = 1 - \zeta. \tag{15}$$

Neglecting the turbulent diffusion of energy (known to be relatively small in the log-law region), one gets a second relation as a local balance between the turbulent energy generated by the mean flow at a rate SW, and the dissipation at a rate $\varepsilon_K \equiv \nu\langle|\nabla u|^2\rangle$: $\varepsilon_K \approx SW$. For stationary conditions ε_K equals the energy flux toward smaller scales from the outer scale of turbulence, $\widetilde{\ell}_K$. Thus, the flux is estimated as $\gamma_K(z)K(z)$, where $\gamma_K(z)$ is the typical eddy turnover inverse time, estimated as $\sqrt{K(z)}/\widetilde{\ell}_K(z)$. This gives rise to the other (now approximate) relations:

$$S^+W^+ \approx \varepsilon_K^+, \quad \varepsilon_K^+ = \gamma_K^+ K^+ = K^+\sqrt{K^+}/\widetilde{\ell}_K^+. \tag{16}$$

The third required relationship can be obtained from the Navier Stokes equation, similar to Eq. (16), as the local balance between the rate of Reynolds stress production $\approx SK$ and its dissipation ε_W: $\varepsilon_W \approx SK$. The main contribution to ε_W comes from the so-called Return-to-Isotropy process and can be estimated [34], similarly to ε_K, as $\gamma_W\, W$ with $\gamma_W = \sqrt{K}/\widetilde{\ell}_W$, involving yet another length scale $\widetilde{\ell}_W$ which is of the same order of magnitude as ℓ_K. Thus one has, similarly to Eq. (16),

$$S^+K^+ \approx \varepsilon_W^+, \qquad \varepsilon_W^+ = \gamma_W^+ W^+ = W^+\sqrt{K^+}/\widetilde{\ell}_W^+. \tag{17}$$

Now we show that the source of ambiguity is the assumption that the length scales can be determined *a priori* as $\ell_{K,W}^+ \propto (z^+)^\alpha$ with $\alpha = 1$ or $\alpha \neq 1$. In reality we have another characteristic length scale, i.e. L, that also should enter the picture when $\zeta = z/L$ is not very small. The actual dependence $\widetilde{\ell}_W$ and $\widetilde{\ell}_K$ on z and L can be found from the data. Consider first $\widetilde{\ell}_W$, defined by Eq. (17), and introduce a new scale $\ell_W \equiv \widetilde{\ell}_W r_W(z^+)/\kappa_W$ such that

$$\ell_W^+ \equiv \frac{W^+(z^+, Re_\tau)\, r_W(z^+)}{\kappa_W S^+(z^+, Re_\tau)\sqrt{K^+(z^+, Re_\tau)}} . \tag{18}$$

Here, $r_W(z^+)$ is a universal i.e. Re_τ-independent dimensionless *function* of z^+, chosen such that new scale $\ell_W/L = \ell_W^+/Re_\tau$ becomes a Re_τ-independent function of only one variable $\zeta = (z/L) = (z^+/Re_\tau)$. The dimensionless constant $\kappa_W \approx 0.20$ is chosen to ensure that $\lim_{z\ll L} \ell_W^+(\zeta) = z^+$. Note that if r_W were a constant, ℓ_W would have started near the wall quadratically, i.e. as $z \times z^+$. Later ℓ_W^+ would have become $\propto z^+$ for $50 \ll z^+ \ll Re_\tau$ [34]. Thus to normalize it to slope 1 we need the function $r_W(z^+)$ that behaves as $1/z^+$ for $z^+ \ll 50$ and approaches unity (under a proper choice of κ_W) for $z^+ \gg 50$. A choice that leads to good data collapse is

$$r_W(z^+) = \left[1 + \left(\ell_{\mathrm{buf}}^+/z^+\right)^6\right]^{1/6} , \quad \ell_{\mathrm{buf}}^+ \approx 49, \tag{19}$$

where ℓ_{buf}^+ is a Re_τ-independent length that plays a role of the crossover scale (in wall units) between the buffer and log regions. The quality of the data collapse for this scaling function is demonstrated in Fig. 2.

The second length scale, $\widetilde{\ell}_K^+$, is determined by Eq. (16):

$$\widetilde{\ell}_K^+ \equiv \frac{(K^+(z^+, Re_\tau))^{3/2}}{\varepsilon_K^+(z^+, Re_\tau)} = \kappa_K \ell_K^+, \quad \kappa_K \approx 3.7. \tag{20}$$

In Fig. 2 we demonstrate that this simple scaling function leads to good data collapse everywhere except perhaps in the viscous layer. We will see below that this has only negligible effects on our results.

Solution and velocity profiles: Solving Eqs. (16) and (17) and accounting for Eqs. (18) and (20) we find

$$W^+ = \left(\kappa S^+ \ell^+\right)^2 r_W^{-3/2}, \tag{21}$$

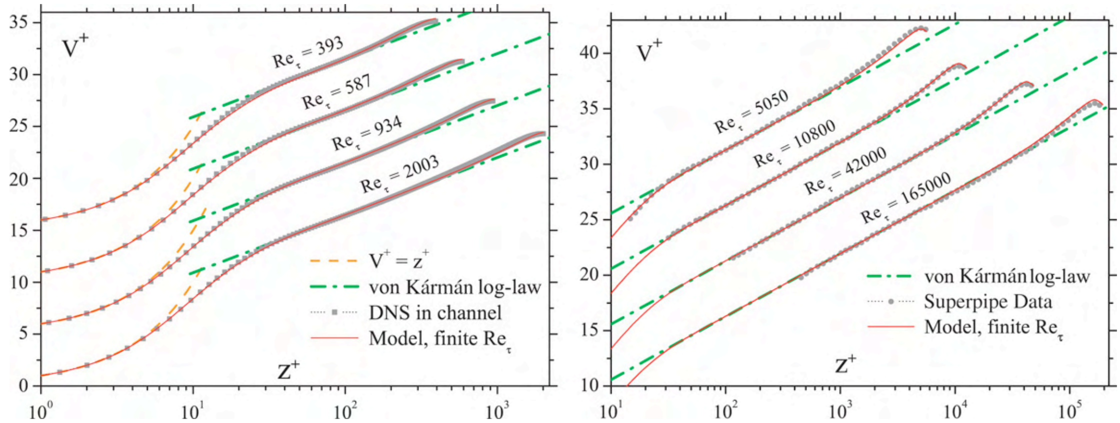

Fig. 1. Color online. Comparison of the theoretical mean velocity profiles (red solid lines) at different values of Re_τ with the DNS data for the channel flow [26,27] (left panel, grey squares; model with $\ell_{\text{buf}} = 49$, $\kappa = 0.415$, $\ell_s = 0.311$) and with the experimental superpipe data [28] (right panel, grey circles; model with $\ell_{\text{buf}} = 46$, $\kappa = 0.405$, $\ell_s = 0.275$). In orange dashed line we plot the viscous solution $V^+ = z^+$. In green dashed dotted line we present the von Kármán log-law. Note that the theoretical predictions with three Re_τ-independent parameters fits the data throughout the channel and pipe, from the viscous scale, through the buffer layer, the log-layer and the wake. For clarity different plots are shifted vertically by five units.

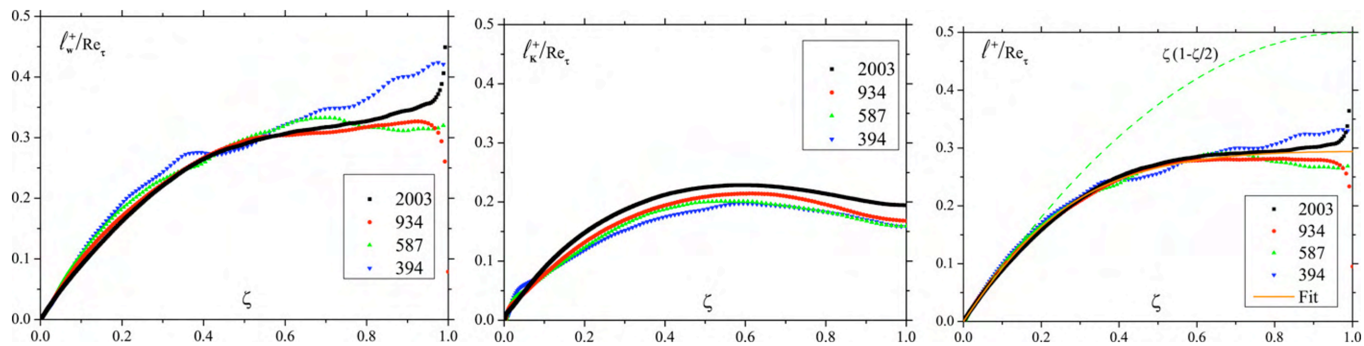

Fig. 2. Color online. The scaling function $\ell_W^+(\zeta)/Re_\tau$ (left panel), $\ell_K^+(\zeta)/Re_\tau$ (middle panel) and the final scaling function $\ell^+(\zeta)$ (right panel), as a function of $\zeta \equiv z/L$, for four different values of Re_τ, computed from the DNS data [26,27]. Note that the data collapse everywhere except at $\zeta \to 1$ where $W^+ \sim S^+ \ll 1$ and accuracy is lost. The green dash line represents $\tilde{\zeta} = \zeta\,(1 - \zeta/2)$ with a saturation level 0.5; in orange solid line we show the fitted function Eq. (24) with $\ell_{\text{sat}} = 0.311$.

where we have defined the von Kármán constant and the crucial scaling function $\ell^+(\zeta)$ as

$$\kappa \equiv (\kappa_W^3 \kappa_K)^{1/4} \approx 0.415, \qquad \ell^+ \equiv [\ell_W^{+\,3}(\zeta)\,\ell_K^+(\zeta)]^{1/4}. \quad (22)$$

The convincing data collapse for the resulting function $\ell^+(\zeta)/Re_\tau$ is shown in Fig. 2, rightmost panel. Substituting Eq. (21) in Eq. (15) we find a quadratic equation for S with the solution

$$S^+ = \frac{\sqrt{1 + (1-\zeta)[2\kappa\ell^+(\zeta)]^2/r_W(z^+)^{3/2}} - 1}{2[\kappa\ell^+(\zeta)]^2/r_W(z^+)^{3/2}}. \quad (23)$$

To integrate this equation and find the mean velocity profile for any value of Re_τ we need to determine the scaling function $\ell^+(\zeta)$ from the data. A careful analysis of the DNS data allows us to find a good *one-parameter* fit for $\ell^+(\zeta)$,

$$\frac{\ell^+(\zeta)}{Re_\tau} = \ell_s \left\{ 1 - \exp\left[-\frac{\tilde{\zeta}}{\ell_s} \left(1 + \frac{\tilde{\zeta}}{2\ell_s} \right) \right] \right\}, \quad (24)$$

where $\tilde{\zeta} \equiv \zeta(1 - \zeta/2)$ and $\ell_s \approx 0.311$. The quality of the fit is obvious from the continuous line in the rightmost panel of Fig. 2.

Finally the theory for the mean velocity contains three parameters, namely ℓ_s together with ℓ_{buff}^+ and κ. We demonstrate now that with these three parameters we can determine the mean velocity profile for any value Re_τ, throughout the channel, including the viscous layer, the buffer layer, the log-law region and the wake. Examples of the integration of Eq. (23) are shown in Fig. 1. We trust that, irrespective of the reader's own preference to the log-law or the power-law, he would agree that these fits are very good. It remains now to estimate, using (23), the conditions under which we expect to see a log-law and those when deviations due to finite Re_τ would seem important. In addition, our theory yields the kinetic energy and Reynolds stress profiles which are in qualitative agreement with the DNS data; for W profiles see Fig. 3.

To show that the present approach is quite general, we apply it now to the experimental data that were at the center of the controversy [24], i.e., the Princeton superpipe data [28]. In Fig. 1 right panel we show the mean velocity profiles measured in the superpipe compared with our prediction using *the same scaling function* $\ell^+(\zeta)$. Note that the data spans values of Re_τ from 5050 to 165,000, and the fits with only three Re_τ-

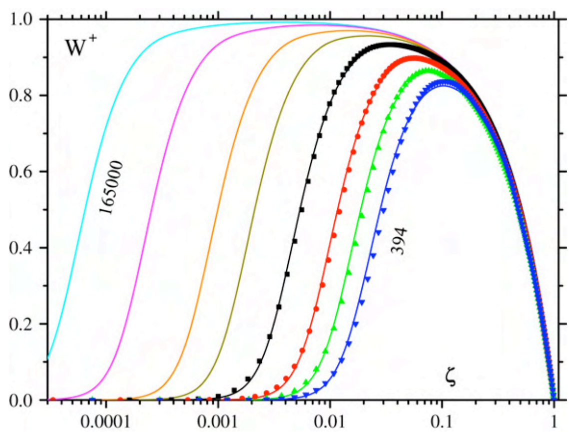

Fig. 3. The Reynolds stress profiles (solid lines) at Re_τ from 394 to 2003 (in channel) and from 5050 to 165,000 (in pipe) in comparison with available DNS data (dots) for the channel.

independent constants are excellent. Note the 2% difference in the value of κ between the DNS and the experimental data; we do not know at this point whether this stems from inaccuracies in the DNS or the experimental data, or whether turbulent flows in different geometries have different values of κ. While the latter is theoretically questionable, we cannot exclude this possibility until a better understanding of how to compute κ from first principles is achieved.

So far we discussed turbulent channel and pipe flows and demonstrated the existence and usefulness of a scaling function $\ell^+(\zeta)$ which allows us to get the profiles of the mean velocities for all values of Re_τ and throughout the channel. While this function begins near the wall as z^+, it saturates later, and its full functional dependence on ζ is crucial for finding the correct mean velocity profiles. The approach also allows us to delineate the accuracy of the log-law presentation, which depends on z^+ and the value of Re_τ. For asymptotically large Re_τ the region of the log-law can be very large, but nevertheless it breaks down near the mid channel and near the buffer layer, where corrections were presented.

The future challenge is to apply this idea to other examples of wall-bounded flows, including time-developing boundary layers, turbulent flows with temperature gradients or laden with particles. There may be more typical "lengths" in such systems, and it is very likely that turning these lengths into scaling functions will provide new insights and better models for a variety of engineering applications. Such efforts are not entirely new; see, for example, [35].

5. Drag reduction by additives

One severe technological problem with turbulent flows is that they cost a lot to maintain; the drag that the fluid exerts on the wall increases significantly when turbulence sets in. It is therefore important that there exist additives, in particular polymers and bubbles, that can reduce this drag significantly. Over the last few years there has been great progress in understanding these phenomena, and here we provide a short review of this progress.

5.1. Drag reduction by polymers

The addition of few tens of parts per million (by weight) of long-chain polymers to turbulent fluid flows in channels or pipes can bring about a reduction of the friction drag by up to 80% [36–39]. This phenomenon of "drag reduction" is well documented and is used in technological applications from fire engines (allowing a water jet to reach high floors) to oil pipes. In spite of a large amount of experimental and simulations data, the fundamental mechanism for drag reduction has remained under debate for a long time [39–41]. In such wall-bounded turbulence, the drag is caused by momentum dissipation at the walls. For Newtonian flows (in which the kinematic viscosity is constant) the momentum flux is dominated by the so-called Reynolds stress, leading to the logarithmic (von-Kármán) dependence of the mean velocity on the distance from the wall [34]. However, with polymers, the drag reduction entails a change in the von-Kármán log-law such that a much higher mean velocity is achieved. In particular, for high concentrations of polymers, a regime of maximum drag reduction is attained (the "MDR asymptote"), independent of the chemical identity of the polymer [37], see Fig. 4. During the last few years the fundamental mechanism for this phenomenon was elucidated: while momentum is produced at a fixed rate by the forcing, polymer stretching results in a suppression of the momentum flux from the bulk to the wall. Accordingly the mean velocity in the channel must increase. It was shown that polymer stretching results in an effective viscosity that increases linearly with the distance from the wall. The MDR asymptote is consistent with the largest possible such linear increase in viscosity for which turbulent solutions still exist. In other words, the MDR is an edge solution separating turbulent from laminar flows. This insight allowed one to derive the MDR as a new logarithmic law for the mean velocity with a slope that fits existing numerical and experimental data. The law is universal, explaining the MDR asymptote.

5.2. Short review of the theory

The riddle of drag reduction can be introduced by a juxtaposition of the effect of polymers with respect to the universal Newtonian law (13). In the presence of long chain polymers the mean velocity profile $V^+(y^+)$ (for a fixed value of p' and channel geometry) changes dramatically. For sufficiently large concentration of polymers $V^+(y^+)$ saturates to a new (universal, polymer independent) "law of the wall" [37],

$$V^+(y^+) = {\kappa_V}^{-1} \ln\left(e\,\kappa_V y^+\right) \quad \text{for } y^+ \gtrsim 10. \tag{25}$$

This law, which was discovered experimentally by Virk (and hence the notation κ_V), is also claimed to be universal, independent of the Newtonian fluid and the nature of the polymer additive, including flexible and rigid polymers [38]. Previous to our work in this network, the numerical value of the coefficient κ_V was known only from experiments, ${\kappa_V}^{-1} \approx 11.7$, giving a phenomenological MDR law in the form [37]

$$V^+(y^+) = 11.7 \ln y^+ - 17. \tag{26}$$

For smaller concentration of polymers the situation is as shown in Fig. 4. The Newtonian law of the wall (13) is the black solid line for $y^+ \gtrsim 30$. The MDR asymptote (25) is the dashed red line. For intermediate concentrations the mean velocity profile starts along the asymptotic law (25), and then crosses over to the so-called "Newtonian plug" with a Newtonian logarithmic slope identical to the inverse of von-Kármán's constant. The region of values of y^+ in which the asymptotic law (25) prevails was termed "the elastic sublayer" [37]. The relative increase of the mean velocity (for a given p') due to the existence of the new law of the wall (25) *is* the phenomenon of drag reduction. Thus the main theoretical challenge is to understand the origin of the new law (25), and in particular its universality, or independence of the polymer used. A secondary challenge is to understand the concentration-dependent cross over back to the Newtonian plug. In our work we argue that the phenomenon can be understood mainly by the influence of the polymer stretching on the y^+-dependent effective viscosity. The latter becomes a crucial agent in carrying the momentum flux from the bulk of the channel to the walls (where the momentum is dissipated by friction). In the Newtonian case the viscosity has a negligible role in carrying the momentum flux; this difference gives rise to the change of Eq. (13) in favor of Eq. (25) which we derive below.

The equations of motion of polymer solutions are written in the FENE-P approximation [42,43] by coupling the fluid velocity $\boldsymbol{u}(\boldsymbol{r},t)$ to the tensor field of "polymer conformation tensor" $\boldsymbol{R}(\boldsymbol{r},t)$. The latter is made from the "end-to-end" separation vector as $R_{\alpha\beta}(\boldsymbol{r},t) \equiv \langle r_\alpha r_\beta\rangle$, and it satisfies the equation of motion

$$\begin{aligned}\frac{\partial R_{\alpha\beta}}{\partial t} + (u_\gamma \nabla_\gamma) R_{\alpha\beta} &= \frac{\partial u_\alpha}{\partial r_\gamma} R_{\gamma\beta} + R_{\alpha\gamma}\frac{\partial u_\beta}{\partial r_\gamma} \\ &\quad - \frac{1}{\tau}\left[P(\boldsymbol{r},t)R_{\alpha\beta} - \rho_0^2\delta_{\alpha\beta}\right],\\ P(\boldsymbol{r},t) &= (\rho_m^2-\rho_0^2)/(\rho_m^2 - R_{\gamma\gamma}) \end{aligned} \tag{27}$$

ρ_m^2 and ρ_0^2 refer to the maximal and the equilibrium values of the trace $R_{\gamma\gamma}$. In most applications $\rho_m \gg \rho_0$

$$P(r,t) \approx (1/(1-\alpha R_{\gamma\gamma})),$$

where $\alpha = \rho_m^{-2}$. The equation for the fluid velocity field gains a new stress tensor:

$$\frac{\partial u_\alpha}{\partial t} + (u_\gamma\nabla_\gamma)u_\alpha = -\nabla_\alpha p + \nu_s\nabla^2 u_\alpha + \nabla_\gamma T_{\alpha\gamma} \tag{28}$$

$$T_{\alpha\beta}(r,t) = \frac{\nu_p}{\tau}\left[\frac{P(r,t)}{\rho_0^2}R_{\alpha\beta}(r,t) - \delta_{\alpha\beta}\right]. \tag{29}$$

Here ν_s is the viscosity of the neat fluid, and ν_p is a viscosity parameter which is related to the concentration of the polymer, i.e. $\nu_p/\nu_s \sim c_p$.

We shall use the approximation

$$T_{\alpha\beta} \sim \frac{\nu_p}{\tau}\frac{P}{\rho_0^2}R_{\alpha\beta}.$$

Armed with the equation for the viscoelastic medium we establish the mechanism of drag reduction following the standard strategy of Reynolds. Eq. (15) changes now to another exact relation [44] between the objects S and W which includes the effect of the polymers:

$$W + \nu S + \frac{\nu_p}{\tau}\langle P R_{xy}\rangle(y) = p'(L-y). \tag{30}$$

On the RHS of this equation we see the production of momentum flux due to the pressure gradient; on the LHS we have the Reynolds stress, the Newtonian viscous contribution to the momentum flux, and the polymer contribution to the momentum flux. A second relation between $S(y)$, $W(y)$, $K(y)$ and $\boldsymbol{R}(y)$ is obtained from the energy balance. In Newtonian fluids the energy is created by the large scale motions at a rate of $W(y)S(y)$. It is cascaded down the scales by a flux of energy, and is finally dissipated at a rate ϵ, where $\epsilon = \nu\langle|\nabla u|^2\rangle$. In viscoelastic flows one has an additional contribution due to the polymers. Our calculation [44] showed that the energy balance equation takes the form:

$$a\nu\frac{K}{y^2} + b\frac{K^{3/2}}{y} + \frac{A^2\nu_p}{2\tau^2}\langle P\rangle^2(\langle R_{yy}\rangle + \langle R_{zz}\rangle) = WS. \tag{31}$$

We note that contrary to Eq. (30) which is exact, Eq. (31) is not exact. We expect it, however, to yield good order of magnitude estimates as is demonstrated below. Finally, we quote the experimental fact [37] that outside the viscous boundary layer

$$\frac{W(y)}{K(y)} = \begin{cases} c_N^2, & \text{for Newtonian flow,}\\ c_V^2, & \text{for viscoelastic flow.}\end{cases} \tag{32}$$

The coefficients c_N and c_V are bounded from above by unity. (The proof is $|c| \equiv |W|/K \le 2|\langle u_x u_y\rangle|/\langle u_x^2 + u_y^2\rangle \le 1$, because $(u_x \pm u_y)^2 \ge 0$.)

To proceed, one needs to estimate the various components of the polymer conformation tensor. This was done in [45] with the final result that for c_p large (where $P \approx 1$), and Deborah number $\mathrm{De} \equiv \tau S(y) \gg 1$ the conformation tensor is highly anisotropic,

$$\boldsymbol{R}(y) \simeq R^{yy}(y)\begin{pmatrix} 2\mathrm{De}^2(y) & \mathrm{De}(y) & 0\\ \mathrm{De}(y) & 1 & 0\\ 0 & 0 & C(y)\end{pmatrix}.$$

The important conclusion is that the term proportional to $\langle R_{yy}\rangle$ in Eq. (31) can be written as $\nu_p\langle\mathcal{R}_{yy}\rangle(y)S(y)$. Defining the "effective viscosity" $\nu(y)$ according to

$$\nu(y) = \nu_0 + \nu_p\langle\mathcal{R}_{yy}\rangle(y). \tag{33}$$

The momentum balance equation attains the form

$$\nu(y)S(y) + W(y) = p'L. \tag{34}$$

It was shown in [44] that also the energy balance equation can be rewritten with the very same effective viscosity, i.e.,

$$\nu(y)\left(\frac{a}{y}\right)^2 K(y) + \frac{b\sqrt{K(y)}}{y}K(y) = W(y)S(y). \tag{35}$$

In the MDR region the first term on the RHS in Eqs. (34) and (35) dominate; from the first equation $\nu(y) \sim 1/S(y)$. Put in Eq. (35) this leads to $S(y) \sim 1/y$, which translates to the new logarithmic law which is the MDR. We will determine the actual slope momentarily. At this point one needs to stress that this results means that $\nu(y)$ must be proportional to y in the MDR regime. This linear dependence of the effective viscosity is one of the central discoveries of our approach. Translated back, it predicts that $\langle R_{yy}\rangle \sim y$ outside the boundary layer. This prediction is well supported by numerical simulations.

The crucial new insight that explained the universality of the MDR and furnished the basis for its calculation is that the MDR is a marginal flow state of wall-bounded turbulence: attempting to increase $S(y)$ beyond the MDR results in the collapse of the turbulent solutions in favor of a stable laminar solution $W = 0$. As such, the MDR is universal by definition, and the only question is whether a polymeric (or other additive) can supply the particular effective viscosity $\nu(y)$ that drives Eqs. (34) and (35) to attain the marginal solution that maximizes the velocity profile. We predict that the same marginal state will exist in numerical solutions of the Navier–Stokes equations furnished with a y-dependent viscosity $\nu(y)$. There will be no turbulent solutions with velocity profiles higher than the MDR.

To see this explicitly, we first rewrite the balance equations in wall units. For constant viscosity (i.e. $\nu(y) \equiv \nu_0$), Eqs. (34) and (35) form a closed set of equations for $S^+ \equiv S\nu_0/(P'L)$ and $W^+ \equiv W/\sqrt{P'L}$ in terms of two dimensionless constant $\delta^+ \equiv a\sqrt{K/W}$ (the thickness of the viscous boundary layer) and $\kappa_{\rm K} \equiv b/c_V^3$ (the von Kármán constant). Newtonian experiments and simulations agree well with a fit using $\delta^+ \sim 6$ and $\kappa_{\rm K} \sim 0.436$ (see the black continuous line in Fig. 4 which shows the mean velocity profile using these very constants). Once the effective viscosity $\nu(y)$ is no longer constant we expect c_V to change and consequently the two dimensionless constants will change as well. We will denote the new constants as Δ and $\kappa_{\rm C}$ respectively. Clearly one must require that for $\nu(y)/\nu_0 \to 1$, $\Delta \to \delta^+$ and $\kappa_{\rm C} \to \kappa_{\rm K}$. The balance equations are now written as

$$\nu^+(y^+)S^+(y^+) + W^+(y^+) = 1, \tag{36}$$

$$\nu^+(y^+)\frac{\Delta^2}{y^{+2}} + \frac{\sqrt{W^+}}{\kappa_{\rm C}\, y^+} = S^+. \tag{37}$$

where $\nu^+(y^+) \equiv \nu(y^+)/\nu_0$. Substituting now S^+ from Eq. (36) into Eq. (37) leads to a quadratic equation for $\sqrt{W^+}$. This equation has as a zero solution for W^+ (laminar solution) as long as $\nu^+(y^+)\Delta/y^+ = 1$. Turbulent solutions are possible only when $\nu^+(y^+)\Delta/y^+ < 1$. Thus at the edge of existence of turbulent solutions we find $\nu^+ \propto y^+$ for $y^+ \gg 1$. This is not surprising, since it was observed already in previous work that the MDR solution is consistent with an effective viscosity which is asymptotically linear in y^+ [46,47]. It is therefore sufficient to seek the edge solution of the velocity profile with respect to linear viscosity profiles, and we rewrite Eqs. (36) and (37) with an effective viscosity that depends linearly on y^+ outside the boundary layer of thickness δ^+:

$$[1 + \alpha(y^+ - \delta^+)]S^+ + W^+ = 1\ , \tag{38}$$

$$[1 + \alpha(y^+ - \delta^+)]\frac{\Delta^2(\alpha)}{y^{+2}} + \frac{\sqrt{W^+}}{\kappa_{\rm C}\, y^+} = S^+\ . \tag{39}$$

We now endow Δ with an explicit dependence on the slope of the effective viscosity $\nu^+(y)$, $\Delta = \Delta(\alpha)$. Since drag reduction must involve a decrease in W, we expect the ratio a^2K/W to depend on α, with the constraint that $\Delta(\alpha) \to \delta^+$ when $\alpha \to 0$. Although Δ, δ^+ and α are all dimensionless quantities, physically Δ and δ^+ represent (viscous) length scales (for the linear viscosity profile and for the Newtonian case, respectively) while α^{-1} is the scale associated to the slope of the linear viscosity profile. It follows that $\alpha\delta^+$ is dimensionless even in the original physical units. It is thus natural to present $\Delta(\alpha)$ in terms of a dimensionless scaling function $f(x)$,

$$\Delta(\alpha) = \delta^+ f(\alpha\delta^+). \tag{40}$$

Obviously, $f(0) = 1$. In [48] it was shown that the balance equations (38) and (39) (with the prescribed form of the effective viscosity profile) have a nontrivial symmetry that leaves them invariant under rescaling of the wall units. This symmetry dictates the function $\Delta(\alpha)$ in the form

$$\Delta(\alpha) = \frac{\delta^+}{1 - \alpha\delta^+}. \tag{41}$$

Armed with this knowledge we can now find the maximal possible velocity far away from the wall, $y^+ \gg \delta^+$. There the balance equations simplify to

$$\alpha y^+ S^+ + W^+ = 1, \tag{42}$$

$$\alpha\Delta^2(\alpha) + \sqrt{W^+}/\kappa_{\rm C} = y^+ S^+. \tag{43}$$

These equations have the y^+-independent solution for $\sqrt{W^+}$ and y^+S^+:

$$\sqrt{W^+} = -\frac{\alpha}{2\kappa_{\rm C}} + \sqrt{\left(\frac{\alpha}{2\kappa_{\rm C}}\right)^2 + 1 - \alpha^2\Delta^2(\alpha)},$$
$$y^+S^+ = \alpha\Delta^2(\alpha) + \sqrt{W^+}/\kappa_{\rm C}. \tag{44}$$

By using Eq. (44) (see Fig. 5), we obtain that the edge solution ($W^+ \to 0$) corresponds to the supremum of y^+S^+, which happens precisely when $\alpha = 1/\Delta(\alpha)$. Using Eq. (41) we find the solution $\alpha = \alpha_m = 1/2\delta^+$. Then $y^+S^+ = \Delta(\alpha_m)$, giving $\kappa_{\rm V}^{-1} = 2\delta^+$. Using the estimate $\delta^+ \approx 6$ we get the final prediction for the MDR. Using Eq. (25) with $\kappa_{\rm V}^{-1} = 12$, we get

$$V^+(y^+) \approx 12 \ln y^+ - 17.8. \tag{45}$$

This result is in close agreement with the empirical law (26) proposed by Virk. The value of the intercept on the RHS of Eq. (45) follows from Eq. (25) which is based on matching the viscous solution to the MDR log-law in [46]. Note that the numbers appearing in Virk's law correspond to $\delta^+ = 5.85$, which is well within the error bar on the value of this Newtonian parameter. Note that we can easily predict where the asymptotic law turns into the viscous layer upon the approach to the wall.

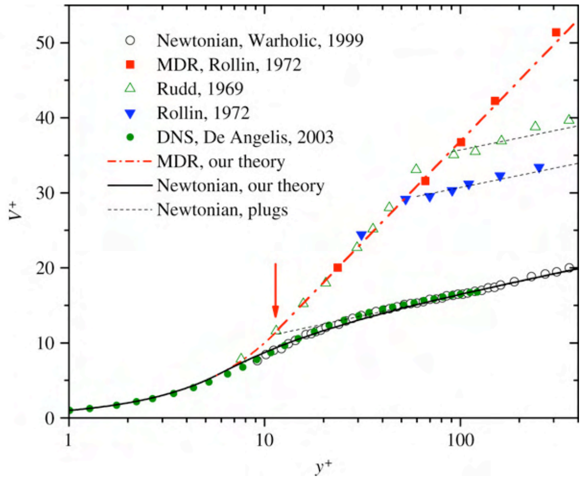

Fig. 4. Mean normalized velocity profiles as a function of the normalized distance from the wall during drag reduction. The data points from numerical simulations (green circles) [52] and the experimental points (open circles) [53] represent the Newtonian results. The black solid line is the universal Newtonian line which for large y^+ agrees with von-Kármán's logarithmic law of the wall (13). The red data points (squares) [54] represent the Maximum Drag Reduction (MDR) asymptote. The dashed red curve represents our theory for the profile which for large y^+ agrees with the universal law (25). The blue filled triangles [54] and green open triangles [55] represent the cross over, for intermediate concentrations of the polymer, from the MDR asymptote to the Newtonian plug. Our theory is not detailed enough to capture this cross over properly. (For interpretation of the references to colour in this figure legend, the reader is referred to the web version of this article.)

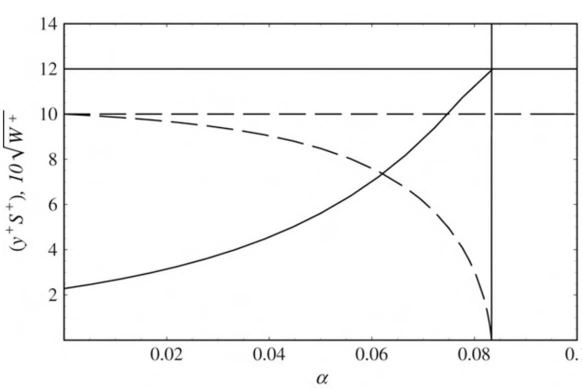

Fig. 5. The solution for $10\sqrt{W^+}$ (dashed line) and y^+S^+ (solid line) in the asymptotic region $y^+ \gg \delta^+$, as a function of α. The vertical solid line $\alpha = 1/2\delta^+ = 1/12$ which is the edge of turbulent solutions; Since $\sqrt{W^+}$ changes sign here, to the right of this line there are only laminar states. The horizontal solid line indicates the highest attainable value of the slope of the MDR logarithmic law $1/\kappa_V = 12$.

We can consider an infinitesimal W^+ and solve Eqs. (36) and (37) for S^+ and the viscosity profile. The result, as before, is $\nu^+(y) = \Delta(\alpha_m)y^+$. Since the effective viscosity cannot fall bellow the Newtonian limit $\nu^+ = 1$ we see that the MDR cannot go below $y^+ = \Delta(\alpha_m) = 2\delta^+$. We thus expect an extension of the viscous layer by a factor of 2, in very good agreement with the experimental data.

5.3. Non-universal aspects of drag reduction by polymers

When the concentration of polymers is not large enough, or when the Reynolds number is too low, the MDR is attained only up to some value of y^+ that depends in a non-universal manner on the Reynolds number and on the nature of the polymer [49]. These non-universal turn-backs to the so-called "Newtonian plug" can be understood theoretically, and we refer the reader to [44,50] for further details.

5.4. Drag reduction by micro-bubbles

Finally, we should mention that drag reduction by polymers is not the solution for many technologically pressing problems, the most prominent of which is the locomotion of ships. Here a more promising possibility is the drag reduction by bubbles, a subject that is much less developed than drag reduction by polymers. For some recent papers on this subject, see, for example [51] and the references therein; we stress that this subject is far from being exhausted by these papers, and expect more work to appear in the near future.

6. Thermal convection

Convection in Nature often occurs in conjunction with other physical effects such as rotation, magnetic field and particulate matter, so the knowledge of the subject is relevant to several closely related fields. The complexity of the underlying equations has precluded much analytical progress for circumstances of practical interest, and the demands of computing power are such that routine simulations have not yet been possible. Thus, the progress in the field has depended more on input from experiment, which has limitations of its own in terms of accessible parameter ranges. The progress in the subject, such as it is, has been possible only through strong interactions among theory, experiment and simulation. This is as it should be.

The paradigm for thermal convection is the Rayleigh–Bénard problem in which a thin fluid layer of infinite lateral extent is contained between two isothermal surfaces with the bottom surface maintained slightly hotter. When the expansion coefficient is positive (as is the case usually), an instability develops because the hot fluid from below rises to the top and the colder fluid from above sinks to the bottom. The applied driving force is measured in terms of a Rayleigh number, Ra,

$$Ra = g\alpha \Delta T H^3/\nu\kappa, \tag{46}$$

which emerges [56] as the appropriate non-dimensional measure of the imposed temperature difference across the fluid layer. Here, g is the acceleration due to gravity, H is the vertical distance between the top and bottom plates, α, ν and κ are, respectively, the isobaric thermal expansion coefficient, the kinematic viscosity and the thermal diffusivity of the fluid. Physically, the Rayleigh number measures the ratio of the rate of potential energy release due to buoyancy to the rate of its dissipation due to thermal and viscous diffusion.

The second important parameter is the Prandtl number

$$Pr = \nu/\kappa, \tag{47}$$

which is the ratio of time scales due to thermal diffusion ($\tau_\theta = H^2/\kappa$) and momentum diffusion ($\tau_\nu = H^2/\nu$), and

Table 1
Values of the combination of fluid properties $\alpha/\nu\kappa$ for air, water and helium [66]; SVP = saturated vapor pressure

Fluid	T (K)	P (Bar)	$\alpha/\nu\kappa$
Air	293	1	0.12
Water	293	1	14
Helium I	2.2	SVP	2.3×10^5
Helium II	1.8	SVP	–
Helium gas	5.25	2.36	6×10^9
Helium gas	4.4	2×10^{-4}	6×10^{-3}

determines the ratio of viscous and thermal boundary layers on the solid surfaces. With increasing Ra the dynamical state of the Rayleigh–Bénard system goes from a uniform and parallel roll pattern at the onset ($Ra \sim 10^3$) to turbulent state beyond Ra of 10^8, say.

For purposes of theoretical simplification, it is customary to assume that the thermal driving does not affect the pressure or the incompressibility condition, and that its only effect is to introduce buoyancy. This is the Boussinesq approximation. How closely the theoretical results correspond to observations depends on how closely the experiments obey the Boussinesq approximation. It is also not clear if small deviations from the ideal boundary conditions produce only small effects.

6.1. *Experiments using cryogenic helium*

Since many examples of convection occur at very high Rayleigh numbers [57], it is of interest to understand the heat transport characteristics in that limit. It is also necessary to be able to cover a large range of Ra in order to discover the applicable scaling laws. Cryogenic helium has been used successfully for the purpose. Though experiments in conventional fluids have been valuable [58,59], the Rayleigh number has been pushed to the limit only through the use of cryogenic helium. The same properties that make helium a suitable fluid for convection studies also makes it suitable for creating flows with very high Reynolds numbers [60].

Historically, a small "superfluid wind tunnel" was constructed [61] with the idea of exploiting the superfluid properties of helium II for obtaining very high Reynolds numbers. Potential flow was observed for low velocities, with no measurable lift on a pair of fly wings hanging in the tunnel, but the inevitable appearance of quantized vortices (see Section 7 on superfluid turbulence) altered that picture for higher flow speeds. Threlfall [62] recognized the advantages of using low temperature helium gas to study high-Ra convection. The later work by Libchaber and co-workers [63] brought broader awareness to the potential of helium. The work of Refs. [64,65] is a natural culmination of this cumulative effort. It is regrettable, though understandable, that the drive towards higher Rayleigh numbers has occurred in all these experiments at the sacrifice of the lateral extent of the apparatus (so the connection to the ideal Rayleigh–Bénard problem needs some justification).

The specific advantage of using helium for convection is the huge value of the combination $\alpha/\nu\kappa$ near the critical point. This can generate large Ra (see Table 1). For a fluid layer some 10 m tall and a reasonable temperature difference of 0.5 K, Rayleigh numbers of the order 10^{21} are possible. Table 1 also shows that $\alpha/\nu\kappa$ is quite small at pressures and temperatures sufficiently far away from the critical value. In fact, the range shown in the table covers a factor of 10^{12}, so any experiment of fixed size H can yield about 12 decades of the control parameter Ra by this means alone. However, if H is chosen to be large enough, this entire range of Ra can be shifted to a regime of developed turbulence where well-articulated scaling relations might be observed. This tunability is essentially impossible for air and water, especially because one cannot use more than modest temperature difference to increase Ra (due to the attendant non-Boussinesq effects, Section 6.3). For other advantages of using helium, see [66].

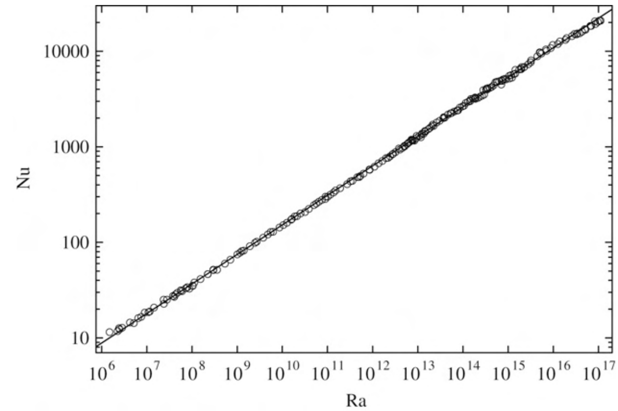

Fig. 6. Log–log plot of the Nusselt number versus Rayleigh number. The line through the data is a least-square fit over the entire Ra range, and represents a d log Nu/d log Ra slope of 0.32.

6.2. *The scaling of the heat transport*

The heat transport in convection is usually expressed in terms of the Nusselt number Nu

$$Nu = \frac{q}{q_{cond}} = \frac{qH}{k_f \Delta T}, \tag{48}$$

where q is the total heat flux, q_{cond} is the heat flux in the absence of convection, given by Fourier's law, and k_f is the thermal conductivity of the fluid. Nu represents the ratio of the effective thermal conductivity of the fluid due to its turbulent motion to its molecular value. One goal of convection research is to determine the functional relation $Nu = f(Ra, Pr)$. This relation is at least as fundamental as the skin friction relation in isothermal flows.

Fig. 6, reproduced from Ref. [66], illustrates the enormous range of Ra and Nu that is possible in low temperature experiments of modest physical size (1 m height). The Nusselt numbers have been corrected here for sidewall conduction and also for finite thermal conductivity of the plates (and both corrections are small, see [66]). That Nusselt numbers attain values as high as 10^4 in these measurements is a testimony to the great practical importance of turbulence.

We have shown this figure partly because it represents the highest Ra achieved so far under laboratory conditions and also the largest range of Ra in the turbulent scaling regime, both of which represent the fulfilment of the promise of cryogenic helium gas. The average power-law exponent over 11 decades is 0.32, close to $1/3$. We show this figure also because one might have hoped that such an unusual straight line spanning many decades in Ra might have a finality to it. Perhaps it does. However, experiments of Chavanne et al. [65], and by Niemela and Sreenivasan [67] for a different aspect ratio, have found a scaling exponent rising beyond $1/3$ towards the very highest Ra. The plausible conclusions of Niemela and Sreenivasan [67,68] were that those data corresponded to large non-Boussinesq conditions and to variable Prandtl number (which occur when one operates close to the critical point), but it is important to test these plausible conclusions directly. We shall momentarily discuss the current work in this direction. If we ignore the apparently non-Boussinesq regime, it has been argued in Refs. [67,68] that the scaling exponent from existing data is most likely consistent with a value close to $1/3$.

As already mentioned, computations have not yet approached experiments in terms of high Ra, but their advantage is that Pr can be held constant and the Boussinesq approximation can be enforced strictly. The available computational ability has recently been pushed by Amati et al. [69], who have reached Rayleigh numbers of 2×10^{14}. Even though this number is still about three orders of magnitude lower than the highest experimental value, it has become quite competitive with respect to many other experiments. This work suggests that the one-third exponent is quite likely, reinforcing the conclusion of Refs. [67,68]. Computational simulations have also explored the effects of finite conductivity, sidewall conduction and non-Boussinesq effects [70,71].

In spite of the limitations of Ra attainable in simulations, much of the details we know about boundary layers and fluctuations come from them. If one were to desire more of simulations (apart from nudging the ranges of Rayleigh and Prandtl numbers), it is that they should test the limits of resolution better. Direct knowledge of the velocity is most desirable in understanding the dynamics of plumes and boundary layers, and also the importance of the mean wind. Experiments in convection have limited themselves to measuring the mean wind and temperature at a few points, but not the spatial structures. The conventional techniques of velocity measurements and flow visualization are fraught with difficulties when considered for thermal convection in cryogenic helium, as has been discussed in [66].

We should now comment on the contributions of the theory to the heat transport problem. Two limiting cases for the scaling of Nu have been considered. The first scenario imagines that the global flux of heat is determined by processes occurring in the two thermal boundary layers at the top and bottom of the heated fluid layer. Then the intervening fluid, being fully turbulent and "randomized", acts as a thermal short circuit and therefore its precise nature is immaterial to the heat flux. We can then determine by dimensional arguments the relation to be $Nu \sim Ra^{1/3}$ [72]. This scaling assumes that the heat flux has no dependence on H. In the limit in which molecular properties are deemed irrelevant in determining heat transport – that is, when boundary layers cease to exist – an exponent of $1/2$ (modulo logarithmic corrections) has been worked out phenomenologically [73]. There has been an alternative theory [63] that obtains the $2/7$th scaling through intermediate asymptotics, but this aspect of the experimental result that motivated the work has not been sustained by more recent work.

The upperbound theory, though quite old (see Refs. [72,74]), has been taken to new levels through the efforts of Constantin and Doering (e.g., Ref. [75]), as well as by others more recently, and has contributed the following valuable hints on the heat transport law:

1. *Arbitrary Prandtl number:* $Nu < Ra^{1/2}$ uniformly in Prandtl number, Pr [75]. This result rules out dependencies such as $Pr^{1/2}$ [76,77] and $Pr^{-1/4}$ [73]. In particular, [73] was written when the boundary layer structure was understood much less than now, and there is a need to reconstruct its arguments afresh, in particular for the reassessment of the Rayleigh number at which the so-called "ultimate regime" with an exponent of $1/2$ is supposed to prevail for Prandtl numbers of the order unity.
2. *Large but finite Prandtl numbers:* The largeness of the Prandtl number is prescribed by the condition $Pr > cRa$, where c is a constant of the order unity. Under this condition, the upperbound is given by $Nu \le Ra^{1/3}(\ln Ra)^{2/3}$ [78]. For higher Rayleigh numbers the upperbound is still given by (1) above.
3. *Infinite Prandtl number:* The latest result due to Doering et al. [79], is $Nu \le CRa^{1/3}(\ln Ra)^{1/3}$. Robust calculations by Ireley et al. [80], which still seem to fall short of mathematical proof, is $Nu \le aRa^{1/3}$, where a is a constant of the order unity.

Thus, as far as the upperbound theory is concerned, the $Ra^{1/2}$ result is permissible for Prandtl numbers of the order unity, though some semi-analytical results on Prandtl number dependencies are ruled out as noted in (1) above. Simulations suggest that the Nusselt number is independent of the Prandtl number above values of the order unity, so it is possible that the infinite Prandtl number limit already operates for unity values. The half-power seems likely when there are no boundary layers (such as in vertical pipes with no bottom and top boundaries), but there is also the continuing (though dwindling) hope of finding this behavior for "very large" Rayleigh numbers in a closed container. Exactly how large is "very large"? The notion that boundary layers will become irrelevant at very high Rayleigh numbers seems misconstrued to us.

Finally, we mention the effect of rough surfaces on the global heat transfer rate [81,82] and the presence of a weakly organized mean wind [83–86]. The studies just mentioned have added to our understanding of turbulent convection. The wind phenomenon has had a rather broad reach; e.g., quantitative observations of occasional reversals of the mean wind flow direction have been related to simple models of self-organized criticality [87]. Furthermore, the lifetimes of the metastable states of the bi-directional mean flow have intriguing analogies with reversals of the Earth's magnetic field polarity, a phenomena arising from turbulent convection within the outer core [88]; there is also a quantitative statistical analogy with the lifetime of solar flare activity driven by turbulent convection in the Sun's outer layer [89]. This latter conclusion may indicate the existence of an underlying universality class, or a more direct physical similarity in the convective processes that lead to reshuffling of the magnetic footprints and to flare extinction.

6.3. Non-Boussinesq effects

One possible constraint for the Boussinesq condition to hold is that the fractional change in density across the layer,

$$\frac{\Delta\rho}{\rho} = \alpha\Delta T, \tag{49}$$

must be small. On the basis of a comparison to the Boussinesq problem at the onset of convection, it is generally assumed that values of $\alpha\Delta T < 0.2$, or less than 20% variation of density across the flow thickness, is acceptable. In the experiments this criterion is indeed satisfied up to very high values of Ra (up to 10^{15} for one set of data [67] and up to 10^{16} for another [64]), although there is no assurance that asymmetries of this magnitude are irrelevant at such high Ra. In fact, a more stringent requirement by a factor of 4 was adopted in Ref. [67].

Owing to the importance of non-Boussinesq effects, as discussed in Ref. [67], recent attention has been focused on them. An early exploration was by Wu and Libchaber [90], who reported top-bottom asymmetry in boundary layers as a main characteristic of non-Boussinesq effects, and observed, with increasing Ra, a reduction in the ratio of temperature drop across top boundary layer to that across the bottom boundary layer. Velocity profiles measured in a follow-up paper [91], at lower Ra, using glycerol, also showed an asymmetry. Ahlers and collaborators [92] showed that non-Boussinesq effects depend on the fluid, as one could readily expect. For water, Nu showed a modest decrease with increase in ΔT. For ethane, they found larger Nu than in the Boussinesq case, nearly 10% higher when $\alpha\Delta T = 0.2$.

As there are many possible non-Boussinesq effects and their relative importance depends on the fluid and its operating conditions, it is difficult to study these effects systematically in experiments. A numerical computation by [93] in two dimensions, using glycerol as the working fluid, showed that effects on Nu were marginal, with some decrease in Nu with $\alpha\Delta T$ for $Ra > 10^7$. In [71], these effects have been explored in three-dimensional convection, also computationally. The finding is that – at least for conditions corresponding to cryogenic helium gas at moderate Rayleigh numbers – while viscosity plays an important role in diminishing the movement of plumes to the interior of convection, it is the coefficient of thermal expansion that affects heat transport most.

6.4. Whither helium experiments?

While thermal convection has been studied for quite some time, the recent surge of interest – even in theory and simulations – has been triggered by helium experiments. Indeed, these experiments were ahead of theory and simulations about two decades ago. Since then, theory has been making its presence felt slowly and simulations have been making considerable inroads. Experiments have surely extended the parameter ranges, but, just as surely, they have not kept up the pace of sophistication. A major step in the understanding of the problem will occur only if accompanied by major improvement in experimental sophistication. It is therefore useful to take stock of the situation briefly. It is perhaps useful even to raise the question as to whether the promise of helium is realizable in its entirety anytime soon.

It has been recognized abundantly that the problem is with instrumentation and with probes of the desired temporal and spatial resolution. It is not clear to us that smaller probes based on the principles of standard thermal anemometry are the solution to the problem, part of which is that the use of helium raises the Reynolds number of the probe itself to higher values than in conventional fluids, leading to unfavorable (and poorly understood) heat transfer characteristics.

In thermal convection flows, where some direct knowledge of the velocity would be most desirable even at scales much larger than the Kolmogorov length, the use of hot and cold wires is further complicated by the fact that they require a steady flow – and the mean wind is effective only near the boundaries and also becomes weaker with Ra. Complications arise because the probe is sensitive simultaneously to temperature and velocity fluctuations in the environment.

Even if single-point measurements were successful, the need to measure the entire velocity field in a turbulent flow remains to be addressed. While a number of hot wires at several points can be used to obtain some spatial information, there is a limit to how far this procedure can be escalated. Particle Image Velocimetry (PIV) has been applied recently to liquid helium grid turbulence at 4.2 K [94,95], in counterflow turbulence [96] and in helium II turbulence [97]. However, the information has been obtained only in the form of two-dimensional sections, and time evolution of the flow cannot be assessed because of constraints of data acquisition. The PIV images do little justice to the three-dimensionality of the flow and to the enormous range of scales present at high Rayleigh numbers.

Particle selection and injection remain a fundamental hurdle for PIV measurements at low temperatures. Liquid helium has a relatively low density, and this makes it harder to find suitably buoyant particles that are also not too large. The use of hydrogen particles that match the density of helium has been the most promising step in this direction [97], but refined control of the particle generation is needed to render the technique routinely usable.

The seeding of helium gas for thermal convection experiments is probably even more difficult owing to the large variation of the density, and its nominally small value, which at best is less than half that of the liquid phase. As noted above, the liquid flow can be seeded to some level of adequacy but the price to pay is that the large range of Rayleigh numbers is attainable only in the gaseous phase.

Flow visualization can focus experimental – and even theoretical – efforts, and yet this domain has not been well developed for cryogenic helium. We believe that there is a huge pay-off here because most existing flow visualizations in water and other room-temperature fluids are at low to moderate Rayleigh numbers, and the intuition that one derives from low Ra cannot easily be extended to high Ra. There are no technological barriers to perfecting the present efforts – only one of integrating various components together. We may also remark that it is not easy to test new particles in the actual low temperature environment. In experimental phase, White et al. [94] had resorted to testing in a pressurized SF_6 environment, where the density could be matched to that of liquid helium.

Where density gradients exist in the flow, visualization can occur in the absence of tracer particles, using shadowgraphy (which depends on the density gradient) or schlieren technique (which depends on the second derivative of the density). It has been demonstrated [98] that shadowgraphy can be used in helium I to visualize even weak flows near the convective onset. A light beam reflected from the cell displays intensity variations resulting from the convergence or divergence due to gradients in refractive index. Note that the technique does not give local information, but can be used to visualize only global flows. In the case of large apparatus, installing an optically transparent and thermally conducting plates is a nontrivial task.

For the case of turbulence under isothermal conditions, it would be possible to use helium 3 as a marker for shadowgraphs.

Scattering of ultrasound is another method that can in principle be used for velocity measurements in helium. It can be used in the gas phase which makes it a plausible candidate for cryogenic convection experiments. However, there would be substantial problems in achieving sufficiently high signal-to-noise ratio resulting from a mismatch of acoustic impedance between the sound transducers and the helium. The work in this direction [99,100] has not yet been adopted for cryogenic helium.

In summary, one part of the promise of helium (namely large values and ranges of the control parameters) has been delivered; flows with huge values of Ra and Re have indeed been generated in laboratory-sized apparatus. However, the second part of the promise (of being able to develop versatile techniques for precise measurements of velocity and vorticity) has lagged behind substantially, despite some impressive efforts. This is the aspect that needs financial investment and intellectual focus.

Once the instrumentation issues are clearer, we need to seriously consider an experiment that can combine moderate aspect ratio (say, 4) with high Ra, constant Pr, and Boussinesq conditions. Such an experiment is probably not without considerable technical difficulties. A large scale low temperature apparatus could be constructed, say at a facility like CERN or BNL, where there is adequate refrigeration capacity. Having a horizontal dimension of, say, 5 m or more would probably require some type of segmentation of the plates with multiplexing of the heating and temperature control. Fundamentally, this is no more complicated than the mirror arrays used in astrophysical observation. The bottom plate, which has a constant heat flux condition imposed, can be arbitrarily thick since it can be supported from below. The temperature control of the plate would probably be more difficult. Estimates for the cooling power required for cells of the size just mentioned seem well within the capacity of the existing refrigeration plants [66].

7. Superfluid turbulence

We now review some phenomenological aspects of liquid helium below the lambda point, called helium II. Helium II has a normal component and a superfluid component whose relative fractions depend on the temperature. The superfluid is frictionless at low flow velocities but enters, beyond a critical velocity, a state in which thin vortex lines are formed spontaneously. These line vortices align themselves with the axis of rotation if the container as a whole rotates, but otherwise form self-sustained tangles. The vortex lines move about in the background of elementary excitations or "quasi-particles" (which, in fact, form the normal component). The vortices scatter the excitations when there is relative velocity between them, thus generating the so-called mutual friction [101]. It was recognized by Onsager [102] that quantum mechanics constrains the circulation around the vortices to be $n\kappa/m$, where κ is Planck's constant and m is the mass of the helium atom; the integer $n = 1$ normally. However, the irrotational flow away from the core of the vortices, whose diameter is estimated to be of the order of an angstrom, is thought to be classical [103]. The motion produced by a vortex tangle, which can be quite complex because of the tangle's complex geometry, is called superfluid turbulence [104,105].

7.1. The $-5/3$ law and analogies to classical turbulence

One of the recent findings [106] is that turbulence in helium II has the Kolmogorov form for the spectral density with a well-defined $-5/3$ power, independent of whether the fraction of the superfluid is negligible or dominant. This result may not seem surprising if one takes the view that any nonlinearly interacting dissipative system of many scales will behave similarly to the classical Kolmogorov turbulence in the inertial range [1]: What is needed is merely the existence of mechanisms of excitation at some large scale and dissipation at the small scale, with no further detail mattering in the inertial range. However, several problems come to the fore when one examines possible scenarios for these mechanisms.

First the dissipation mechanism: Feynman [103] proposed a scenario by which vortex reconnections generate smaller and smaller loops in a cascade-like fashion, carrying energy away from larger scales. Vinen [107] suggested that the short wavelength Kelvin waves, which are created presumably by impulses associated with the reconnection of vortices, act as mediators of dissipation. For temperatures of 1 K and above, the Kelvin waves are damped out by the background excitations thus providing the dissipation mechanism. For lower temperatures, for which the normal fluid is negligible, the energy is radiated away as sound at sufficiently small wavelengths. There is follow-up work on the Kelvin-wave mechanism for dissipation and on the nature of energy spectrum at very high wavenumbers (e.g., [108–110]; see also [105,111]) but the details are not yet fully understood. In particular, for energy loss by radiation to be effective, one needs very high velocities and short wavelengths: Modest motion of vortices will not do. Higher velocities are possible very close to the vortex core because of the inverse power-law of the potential velocity field – and also because of reconnection events, which produce cusp-like local structures with sharply repelling velocities.

Regarding the forcing scale, in experiments with a pull-through grid in helium II [112], it is conceivable that the forcing is produced very similarly to that in classical turbulence, and is related to the mesh length and the time of evolution of the turbulence. In simulations, on the other hand, the forcing scale cannot be defined unambiguously. For instance, in the important foray into superfluid turbulence that was made by Schwarz [113], it appears at first sight that the forcing scale was the size of the computational box, as also in the case of the simulations of the Taylor–Green problem by Nore et al. [114] and Araki et al. [115]. However, it appears that reconnections play an important role in determining this scale (or range of scales).

As another perspective on the same issue, the occurrence of the $-5/3$ spectrum in superfluid turbulence may be regarded as surprising if one takes the stand that the key mechanism for energy transfer across scales in hydrodynamic turbulence, namely vortex stretching, is absent in superfluid turbulence: No intensification and break-up due to vortex stretching is possible. It is the vortex break-up due to reconnections, not vortex stretching, that appears to be the key to the spectral distribution here. If this is true, it is interesting to speculate about the central importance attached to vortex stretching in classical turbulence.

To be sure, one should look closely at the veracity of claims about the $-5/3$ power-law. Our view is that the available evidence is too fragile to sustain the claim on the existence of the $-5/3$ spectrum in experiment or simulations. In experiments, the only real piece of evidence comes from [106], but at least to us it is not exactly clear what is being measured at the low end of the temperature (below 1 K), despite a good assessment in [104]. At slightly higher temperatures than 1 K, for which the available evidence for the $-5/3$ law also comes from [106], the data concern different fractions of superfluid and normal helium making it hard to disentangle the two. The measurements of [112], though intrinsically exciting in addition to having instigated the recent interest in the problem, are only indirectly supportive of the $-5/3$ law. Here, one measures the decay of superfluid vorticity (with certain caveats which are partially resolved by [116]) and notes that the behavior is similar to that of the classical vorticity. From this one can compute the energy dissipation rate and infer the classical Kolmogorov spectrum.

In simulations of superfluid turbulence, the result is unconvincing because the computational box size is still small. Here, we make a strong case for pushing the computational size to those that are currently the norm for classical turbulence.

Our conclusion is *not* that the $-5/3$ power is ruled out, but that the evidence is soft at present; one needs to produce more direct and convincing evidence.

There is another interesting wrinkle. If one assumes that the wavelength of the Kelvin waves which dissipate or radiate the energy are very small compared to the Kolmogorov scale, it is plausible to infer the spectral amplitude of fluctuations of superfluid velocity in the sub-Kolmogorov range. Presumably, the only relevant parameter in that range is the strain rate at the Kolmogorov scale, quite like the situation of the passive scalar spectrum at high Schmidt numbers. It then follows from dimensional reasoning that one should expect a -1 power for the spectrum in that region (see also [110]). On the other hand, decay data of superfluid vorticity were analyzed in [117] to suggest that the energy spectrum is consistent with a -3 power-law. This behavior is poorly understood at present.

7.2. *Visualization of quantized vortex lines*

An exciting development of recent few years is the visualization of quantized vortices and their reconnection using small neutral particles [97,118]. These particles are made by the *in situ* freezing of mixtures of hydrogen and helium. While these visualization studies have confirmed some interesting aspects of quantized vortices such as rings and reconnections, the particles are still too large compared with the diameter of the vortices (by a factor of about 10^4). Thus, while it is easy to convince oneself that the particles get attracted to vortex cores and decorate them, it is obvious that the particles are not always passive. One can calculate conditions under which the inertia of the particles has marginal influence on vortex lines, but there is no controlled means to ensure that this happens always: One would have to devise smaller particles before one can be confident of the fine details.

7.3. *Concluding remarks on superfluid turbulence*

At least in the initial stages when the study of superfluid turbulence was brought closer to classical turbulence community, one of the hopes was that it might be possible to create enormous Reynolds numbers in modest-sized facilities using helium II. However, it has turned out that the situation is no better than what is possible with helium I. The bottleneck is that the superfluid vorticity introduces an effective kinematic viscosity which is of the same order as the kinematic viscosity of helium I [104,111,112]. There indeed is a lot to learn and understand about superfluid turbulence as a subject of intrinsic interest. It is also likely that such knowledge offers new insights on classical turbulence.

A new direction of superfluid turbulence concerns helium 3 at much colder temperatures [119].

8. Final remarks

If we are interested in discovering laws underlying systems with many strongly interacting degrees of freedom and are far from equilibrium, it is important to begin with a study a few of them with the same rigor and control for which particle physics, say, is well known. We can probably make the case that hydrodynamic turbulence, which arises in flowing fluids, is an ideal paradigm. Our first point is that the dynamical equations for the motion of fluids are known to great accuracy, which means that understanding their analytic structure can greatly supplement experimental queries; in just the same way, computer simulations – even if they require much investment of time and money – can be far more useful here than for many other problems of the condensed phase, in which the interaction potential among microscopic parts is often simply an educated guess. The stochasticity of turbulence (and of all systems that are driven hard) means that one may discern only laws that concern statistical behavior. If we are fortunate, these laws are universal in some well-understood sense. This is the way we regard the "problem of turbulence".

While we have not yet reached a state when we can declare victory (perhaps that may never happen in a strict sense), the "problem of turbulence" is being slowly chipped away by understanding, albeit partially, its several aspects. This review has touched a few aspects of the problem in which considerable progress has been made recently. There is, of course, much to do, and one needs to understand the richness of the problem and possess the discipline and focus needed to make a dent in one of its nontrivial aspects.

Acknowledgements

This work was supported in part by the US-Israel Binational Science Foundation. Section 6 has had significant input from Dr. J.J. Niemela.

References

[1] A.S. Monin, A.M. Yaglom, Statistical Fluid Mechanics, vol. II, MIT Press, 1971. Indeed, smaller scales than η are usually present because of intermittency, but we shall not consider this aspect here.
[2] G.I. Taylor, Proc. Roy. Soc. A 151 (1935) 421.
[3] V.S. L'vov, I. Procaccia, Phys. Rev. Lett. 76 (1996) 2896.
[4] V.I. Belinicher, V.S. L'vov, A. Pomyalov, I. Procaccia, J. Stat. Phys. 93 (1998) 797.
[5] V.S. L'vov, I. Procaccia, Phys. Rev. E 62 (2000) 8037.
[6] A.N. Kolmogorov, Dokl. Akad. Nauk. USSR 32 (1941) 16.
[7] R.H. Kraichnan, Phys. Fluids 11 (1968) 946.
[8] K. Gawedzki, A. Kupiainen, Phys. Rev. Lett. 75 (1995) 3608.
[9] M. Chertkov, G. Falkovich, I. Kolokolov, V. Lebedev, Phys. Rev. E 52 (1995) 4924.
[10] A. Pumir, B.I. Shraiman, E.D. Siggia, Phys. Rev. E 55 (1997) R1263.
[11] G. Falkovich, K. Gawedzk, M. Vergassola, Rev. Modern Phys. 73 (2001) 913.
[12] O. Gat, I. Procaccia, R. Zeitak, Phys. Rev. Lett. 80 (1998) 5536.
[13] I. Arad, I. Procaccia, Anomalous scaling in passive scalar advection and lagrangian shape dynamics, in: T. Kambe, (Ed.), IUTAM Symposium, 2001 pp. 175–184.
[14] A. Celani, M. Vergassola, Phys. Rev. Lett. 86 (2001) 424.
[15] I. Arad, L. Biferale, A. Celani, I. Procaccia, M. Vergassola, Phys. Rev. Lett. 87 (2001) 164502.
[16] Y. Cohen, T. Gilbert, I. Procaccia, Phys. Rev. E. 65 (2002) 026314.
[17] Y. Cohen, A. Pomyalov, I. Procaccia, Phys. Rev. E. 68 (2003) 036303.
[18] L. Angheluta, R. Benzi, L. Biferale, I. Procaccia, Phys. Rev. Lett. 97 (2006) 160601.
[19] S. Kurien, K.R. Sreenivasan, Measures of anisotropy and the universal properties of turbulence, in: New Trends in Turbulence, NATO Advanced Study Institute, Les Houches, Springer and EDP-Sciences, 2001, pp. 53–111;
L. Biferale, I. Procaccia, Phys. Rep. 414 (2–3) (2005) 43–164.
[20] I. Arad, V.S. L'vov, I. Procaccia, Phys. Rev. E 59 (1999) 6753.
[21] I. Arad, B. Dhruva, S. Kurien, V.S. L'vov, I. Procaccia, K.R. Sreenivasan, Phys. Rev. Lett. 81 (1998) 5330.
[22] I. Arad, L. Biferale, I. Mazzitelli, I. Procaccia, Phys. Rev. Lett. 82 (1999) 5040.
[23] I. Arad, V.S. L'vov, E. Podivilov, I. Procaccia, Phys. Rev. E 62 (2000) 4904.
[24] G.I. Barenblatt, J. Fluid Mech. 249 (1993) 513;
G.I. Barenblatt, A.J. Chorin, Phys. Fluids 10 (1998) 1043.
[25] K.R. Sreenivasan, A. Bershadskii, J. Fluid Mech. 554 (2006) 477.
[26] R.G. Moser, J. Kim, N.N. Mansour, Phys. Fluids 11 (1999) 943. DNS data at: http://www.tam.uiuc.edu/Faculty/Moser/channel.
[27] S. Hoyas, J. Jimenez, Phys. Fluids 18 (2006) 011702. DNS data at: http://torroja.dmt.upm.es/ftp/channels/.
[28] B.J. McKeon, J. Li, W. Jiang, J.F. Morrison, A.J. Smits, J. Fluid Mech. 501 (2004) 135. The data at: http://gasdyn.princeton.edu/data/e248/mckeon_data.html.
[29] A.J. Smits, M.V. Zagarola, Phys. Fluids 10 (1998) 1045;
M.V. Zagarola, A.E. Perry, A.J. Smits, Phys. Fluids 9 (1997) 2094;
M.V. Zagarola, A.J. Smits, Phys. Rev. Lett. 78 (1997) 239.
[30] W.K. George, Phil. Trans. R. Soc. A 365 (2007) 789.
[31] R.L. Panton, Phil. Trans. R. Soc. A 365 (2007) 733.
[32] P. Monkewitz, K.A. Chauhan, H.M. Nagib, Phys. Fluids (in press).
[33] V.S. L'vov, I Procaccia, O. Rudenko, Phys. Rev. Lett. (submitted for publication).
[34] S.B. Pope, Turbulent Flows, Cambridge, 2000.
[35] A.M.O. Smith, T. Cebeci, Douglas Aircraft Division Report DAC 33735, 1967.
[36] B.A. Toms, Proc. Internat. Congr. Rheology Amsterdam, vol. 2, North Holland, 1949, pp. 0.135–0.141.
[37] P.S. Virk, AIChE J. 21 (1975) 625.
[38] P.S. Virk, D.C. Sherma, D.L. Wagger, AIChE J. 43 (1997) 3257.
[39] K.R. Sreenivasan, C.M. White, J. Fluid Mech. 409 (2000) 149.
[40] J.L. Lumley, Annu. Rev. Fluid Mech. 1 (1969) 367.
[41] P.-G. de Gennes, Introduction to Polymer Dynamics, Cambridge, 1990.
[42] R.B. Bird, C.F. Curtiss, R.C. Armstrong, O. Hassager, Dynamics of Polymeric Fluids, vol. 2, Wiley, NY, 1987.
[43] A.N. Beris, B.J. Edwards, Thermodynamics of Flowing Systems with Internal Microstructure, Oxford University Press, NY, 1994.
[44] R. Benzi, E. De Angelis, V.S. L'vov, I. Procaccia, V. Tiberkevich, J. Fluid Mech. 551 (2006) 185.
[45] V.S. L'vov, A. Pomyalov, I. Procaccia, V. Tiberkevich, Phys. Rev. E 71 (2005) 016305.
[46] V.S. L'vov, A. Pomyalov, I. Procaccia, V. Tiberkevich, Phys. Rev. Lett. 92 (2004) 244503.
[47] E. De Angelis, C. Casciola, V.S. L'vov, A. Pomyalov, I. Procaccia, V. Tiberkevich, Phys. Rev. E 70 (2004) 055301.
[48] R. Benzi, E. deAngelis, V.S. L'vov, I. Procaccia, Phys. Rev. Lett. 95 (2005) 194502.
[49] H.J. Choi, S.T. Lim, P.-Y. Lai, C.K. Chan, Phys. Rev. Lett. 89 (2002) 088302.
[50] R. Benzi, V.S. L'vov, I. Procaccia, V. Tiberkevich, Europhys. Lett. 68 (2004) 825.
[51] T.S. Lo, V.S. L'vov, I. Procaccia, Phys. Rev. E 73 (2006) 036308.
[52] E. De Angelis, C.M. Casciola, V.S. L'vov, R. Piva, I. Procaccia, Phys. Rev. E 67 (2003) 056312.
[53] M.D. Warholic, H. Massah, T.J. Hanratty, Exp. Fluids 27 (1999) 461.
[54] A. Rollin, F.A. Seyer, Canad. J. Chem. Eng. 50 (1972) 714–718.
[55] M.J. Rudd, Nature 224 (1969) 587.
[56] D.J. Tritton, Physical Fluid Dynamics, Oxford, 1998.
[57] K.R. Sreenivasan, R.J. Donnelly, Adv. Appl. Mech. 37 (2001) 239–276.
[58] R.J. Goldstein, H.D. Chiang, D.L. See, J. Fluid Mech. 213 (1990) 111.

[59] G. Ahlers, Phys. Rev. E. 63 (2001) art. no. 015303;
E. Brown, A. Nikolaenko, D. Funfschilling, G. Ahlers, Phys. Fluids 17 (2005) 075108.
[60] B.J. McKeon, C.J. Swanson, M.V. Zagarola, R.J. Donnelly, A.J. Smits, J. Fluid Mech. 511 (2004) 41.
[61] P.P. Craig, J.R. Pellam, Phys. Rev. 108 (1957) 1109.
[62] D.C. Threlfall, J. Fluid. Mech. 67 (1975) 17.
[63] B. Castaing, G. Gunaratne, F. Heslot, L. Kadanoff, A. Libchaber, S. Thomae, X.-Z. Wu, S. Zaleski, G. Zanetti, J. Fluid Mech. 204 (1989) 1.
[64] J.J. Niemela, L. Skrbek, K.R. Sreenivasan, R.J. Donnelly, Nature 404 (2000) 837.
[65] X. Chavanne, F. Chilla, B. Chabaud, B. Castaing, B. Hebral, Phys. Fluids 13 (2001) 1300.
[66] J.J. Niemela, K.R. Sreenivasan, J. Low Temp. Phys. 143 (2006) 163.
[67] J.J. Niemela, K.R. Sreenivasan, J. Fluid Mech. 481 (2003) 355.
[68] J.J. Niemela, K.R. Sreenivasan, J. Fluid Mech. 557 (2006) 411.
[69] G. Amati, K. Koal, F. Massaioli, K.R. Sreenivasan, R. Verzicco, Phys. Fluids 17 (2005) 121710.
[70] R. Verzicco, J. Fluid Mech. 473 (2002) 201;
R. Verzicco, Phys. Fluids 16 (2004) 1965.
[71] A. Sameen, R. Verzicco, K.R. Sreenivasan, Phys. Scr. (submitted for publication).
[72] W.V.R. Malkus, Proc. Roy. Soc. Lond. A 225 (1954) 196;
W.V.R. Malkus, Stud. Appl. Math. 107 (2001) 325.
[73] R.H. Kraichnan, Phys. Fluids 5 (1962) 1374.
[74] L.N. Howard, in: H. Gortler (Ed.), Proc. 11th Intern. Cong. Appl. Mech., Springer, Berlin, 1966, p. 1109; Annu. Rev. Fluid Mech. 4 (1972) 473.
[75] P. Constantin, C.R. Doering, J. Stat. Phys. 94 (1999) 159.
[76] E.M. Spiegel, Ann. Rev. Astron. Astrophys. 9 (1971) 323.
[77] S. Grossmann, D. Lohse, Phys. Rev. Lett. 86 (2001) 3316.
[78] X. Wang, Bound on vertical heat transport at large Prandtl numbers, 2007, preprint.
[79] C.R. Doering, F. Otto, M.G. Rezikoff, J. Fluid Mech. 560 (2006) 229–241.
[80] G.R. Ireley, R.R. Kerswell, S.C. Plasting, J. Fluid Mech. 560 (2006) 159–227.
[81] Y.B. Du, P. Tong, Phys. Rev. Lett. 81 (1998) 987.
[82] P. Roche, B. Castaing, B. Chabaud, B. Hebral, J. Sommeria, Euro. Phys. J. 24 (2001) 405.
[83] J.J. Niemela, L. Skrbek, K.R. Sreenivasan, R.J. Donnelly, J. Fluid Mech. 449 (2001) 169.
[84] K.R. Sreenivasan, A. Bershadskii, J.J. Niemela, Phys. Rev. E 65 (2002) 056306.
[85] X.L. Qui, P. Tong, Phys. Rev. E 64 (2002) 036304.
[86] E. Villermaux, Phys. Rev. Lett. 75 (1995) 4618.
[87] K.R. Sreenivasan, A. Bershadskii, J.J. Niemela, Physica A 340 (2004) 574.
[88] G.A. Glatzmaier, R.C. Coe, L. Hongre, P.H. Roberts, Nature 401 (1999) 885.
[89] A. Bershadskii, J.J. Niemela, K.R. Sreenivasan, Phys. Lett. A 331 (2004) 15.
[90] X.-Z. Wu, A. Libchaber, Phys. Rev. A 43 (1991) 2833–2839.
[91] J. Zhang, S. Childress, A. Libchaber, Phys. Fluids 10 (1998) 1534–1536.
[92] G. Ahlers, E. Brown, F.F. Araujo, D. Funschilling, S. Grossmann, D. Lohse, J. Fluid Mech. 569 (2006) 409–445;
G. Ahlers, F.F. Araujo, D. Funschilling, S. Grossmann, D. Lohse, Phy. Rev. Lett. 98 (2007) 054501.
[93] K. Sugiyama, E. Calzavarini, S. Grossmann, D. Lohse, Europhys. Lett. 80 (2007) 34002.
[94] C.M. White, A.N. Karpetis, K.R. Sreenivasan, J. Fluid Mech. 452 (2002) 189.
[95] R.J. Donnelly, A.N. Karpetis, J.J. Niemela, K.R. Sreenivasan, W.F. Vinen, C.M. White, J. Low Temp. Phys. 126 (2002) 327.
[96] T. Zhang, S.W. Van Sciver, J. Low Temp. Phys. 138 (2005) 865.
[97] G.P. Bewley, D.P. Lathrop, K.R. Sreenivasan, Nature 441 (2006) 588.
[98] A.L. Woodcraft, P.G.J. Lucas, R.G. Matley, W.Y.T. Wong, in: R.J. Donnelly, K.R. Sreenivasan (Eds.), Ultra-High Reynolds Number Flows, 1999, p. 436;
R.G. Matley, W.Y.T. Wong, M.S. Thurlow, P.G.J. Lucas, M.J. Lees, O.J. Griffiths, A.L. Woodcraft, Phys. Rev. E 63 (2001) 045301.
[99] S. Siefer, V. Steinberg, Phys. Fluids 16 (2004) 1587.
[100] C. Baudet, S. Ciliberto, J.-F. Pinton, Phys. Rev. Lett. 67 (1991) 193.
[101] H.E. Hall, W.F. Vinen, Proc. Roy. Soc. A 238 (1956) 204.
[102] L. Onsager, Nuovo Cimento Suppl. 6 (1949) 249. Discussion on the paper by C.J. Gorter.
[103] R.P. Feynman, Prog. Low Temp. Phys., 1, North-Holland, 1955, p. 17.
[104] W.F. Vinen, J.J. Niemela, J. Low Temp. Phys. 128 (2002) 167.
[105] W.F. Vinen, R.J. Donnelly, Phys. Today 43 (2007) 43.
[106] J. Maurer, Tabeling, Europhys. Lett. 43 (1998) 29.
[107] W.F. Winen, Phys. Rev. B 61 (2000) 1410.
[108] V.S. L'vov, S.V. Nazarenko, O. Rudenko, Phys. Rev. B 76 (2007) 024520.
[109] V.B. Eltsov, A.I. Golov, R. de Graaf, R. Hänninen, M. Krusis, V.S. L'vov, R.E. Solntsev. arXiv:0708.1095v1[cond-mat.soft], 8 August 2007.
[110] E. Kozik, B. Svistunov. arXiv:cond-mat/0703047v3[cond-mat.other], 24 October 2007.
[111] P.M. Walmsley, A.I. Golov, H.E. Hall, A.A. Levchenko, W.F. Vinen. arXiv:0710.1033v2[cond-mat.other], 31 October 2007.
[112] S.R. Stalp, L. Skrbek, R.J. Donnelly, Phys. Rev. Lett. 82 (1999) 4831;
L. Skrbek, J.J. Niemela, R.J. Donnelly, Phys. Rev. Lett. 85 (2000) 4831;
S.R. Stalp, J.J. Niemela, W.F. Winen, R.J. Donnelly, Phys. Fluids 14 (2002) 1377.
[113] K.W. Schwarz, Phys. Rev. B 31 (1985) 5782; Phys. Rev. B 38 (1988) 2398.
[114] C. Nore, M. Abid, M.E. Brachet, Phys. Rev. Lett. 78 (1997) 3896.
[115] T. Araki, M. Tsubota, S.K. Nemirovskii, Phys. Rev. Lett. 89 (2002) 145301.
[116] T.V. Chagovets, A.V. Gordeev, L. Skrbek, Phys. Rev. E 76 (2007) 027301.
[117] L. Skrbek, J.J. Niemela, K.R. Sreenivasan, Phys. Rev. E 64 067301.
[118] G.P. Bewley, M.S. Paoletti, K.R. Sreenivasan, D.P. Lathrop, 2007 (submitted for publication).
[119] L. Skrbek, JETP Lett. 80 (2004) 474.

Available online at www.sciencedirect.com
ScienceDirect
Physica D 237 (2008) 2184–2189
PHYSICA D
www.elsevier.com/locate/physd

Aeroacoustic study of a forward facing step using linearized Euler equations

Irfan Ali[a,*], Stefan Becker[a], Jens Utzmann[b], Claus-Dieter Munz[b]

[a] *Institute of Fluid Mechanics, University of Erlangen-Nuremberg, D-91058 Erlangen, Germany*
[b] *Institute of Aerodynamics and Gasdynamics, University of Stuttgart, D-70550 Stuttgart, Germany*

Available online 14 December 2007

Abstract

We present a hybrid approach for computational aeroacoustics in the time domain. The flow field is computed using large eddy simulation and coupled to the acoustic propagation solver based on linearized Euler equations. Coupling in the time domain avoids storage of large flow field volume data, avoiding the slow hard disk access rate and hence speeding up the computation. Acoustic sources are calculated on the fine fluid grid and interpolated conservatively onto the coarse acoustic grid. The problem studied is flow-induced noise from flow over a forward facing step and the Reynolds number based on the height of the step ($H = 12$ mm) is $Re_H \approx 8000$. The sound pressure levels obtained compare well with the published results.

PACS: 47.27.ep; 43.28.Gq; 43.28.Ra; 43.58.Ta

Keywords: Aeroacoustics; Large eddy simulation; Linearized Euler equation; MpCCI

1. Introduction

Some of the causes of aerodynamically generated noise in the transportation industry are geometries similar to the forward facing step (FFS). These geometries occur due to deliberate design features and are often due to manufacturing imperfections, which could be power supply units on top of high-speed trains, wings of aeroplanes or wiper blades in automobiles. Several numerical and experimental studies are available in the fluid dynamics literature [1–3], which show that the flow physics in FFS is highly complex and is not clearly understood for such a simple geometry. In a recent paper by Largeau and Moriniere [4], it was further mentioned that large discrepancies exist in published data on the recirculation bubble length on the step. Flow over FFS is two-dimensional below the critical Reynolds number of $Re_{\text{critical}} < 135$ [2]; with increasing Reynolds number the flow becomes turbulent and three-dimensional. Experimental aeroacoustic investigations carried out by Becker et al. [5,6] showed that the broad-band noise generated by a step ($H = 12$ mm) is present between 1 and 8 kHz for $8000 < Re_H < 24\,000$.

The turbulent structures present in the flow are responsible for the radiated acoustic energy, which itself is a minute fraction of the turbulent kinetic energy (TKE). Furthermore, acoustic generation in fluid simulation is non-linear and its propagation is linear, which can be described with the help of linear numerical solvers. The disparity of scales results in the prevalence of hybrid methods for computational aeroacoustics (CAA), employing different numerical methods for fluid and acoustic simulation. Direct computation of sound has been tried [7,8], but is not applicable for complex geometries and the industrially relevant Reynolds numbers. Linearized Euler equations (LEE) have been successfully used in a hybrid approach for jet noise [9], vortex–blade interaction [10] and cavity flow [11]. In this present study, the turbulent flow was simulated with a finite-volume (FV) code using a large eddy simulation (LES), which has been widely used in CAA [11] and the noise propagation is computed with LEE in the time domain.

* Corresponding author. Tel.: +49 9131 8529508; fax: +49 9131 8529503.
E-mail address: irfan@lstm.uni-erlangen.de (I. Ali).
URL: http://www.lstm.uni-erlangen.de/~irfan (I. Ali).

0167-2789/$ - see front matter
doi:10.1016/j.physd.2007.12.002

2. Numerical method

2.1. Flow simulation

The flow field is computed with LES using our in-house incompressible finite-volume code FASTEST-3D [12]. The underlying numerical scheme is based on a procedure described by Perić [13], consisting of a fully conservative second-order FV space discretization with a collocated arrangement of variables on non-orthogonal grids. For the time discretization, an implicit second-order scheme is employed, while a non-linear multi-grid scheme, in which the pressure correction method acts as a smoother on the different grid levels, is used for convergence acceleration. In DNS, all the relevant scales of turbulence have to be directly computed, whereas in a RANS calculation, all the relevant scales of turbulence need to be modeled. In LES, the flow field is decomposed into a large-scale or grid scale (GS) component and a sub grid scale (SGS) component, given for a field variable ϕ as, $\phi = \underbrace{\bar{\phi}}_{\text{GS}} + \underbrace{\phi'}_{\text{SGS}}$.

The GS component is obtained by filtering the entire domain using a grid filter function, G and $\bar{\Delta}$, the filter width which defines the smallest resolved scale:

$$\bar{\phi}(\boldsymbol{x}, t) = \iiint_{-\infty}^{\infty} \phi(\boldsymbol{x} - \boldsymbol{s}, t) G(\boldsymbol{x}, \boldsymbol{s}; \bar{\Delta}) \mathrm{d}\boldsymbol{s}. \tag{1}$$

The filtering operation removes the SGS turbulence from the Navier–Stokes equations. The resulting governing equations are then solved directly for the GS turbulent motions, while the effect of the SGSs is computed using an SGS model, such as the classical Smagorinsky model [14] as used in this work. In this model the, eddy viscosity is written as a function of the density ρ, a length scale l and the magnitude of the resolved strain rate tensor $|\bar{S}_{ij}|$. The governing equations for LES can be given as below, where the continuity equation is $\frac{\partial \bar{U}}{\partial x_i} = 0$ and the momentum equation is given as:

$$\rho \left(\frac{\partial \bar{U}_j}{\partial t} + U_i \frac{\partial \bar{U}_j}{\partial x_i} \right) = -\frac{\partial \bar{P}}{\partial x_j} - \frac{\partial \bar{\tau}_{ij}}{\partial x_i} - \frac{\partial \tau_{ij}^{\text{SGS}}}{\partial x_i}. \tag{2}$$

The SGS τ^{SGS} is divided into the isotropic and the anisotropic part as $\tau_j^{\text{SGS}} = \underbrace{\tau_{ij}}_{\text{anisotropic}} + \underbrace{\frac{1}{3}\delta_{ij}\tau_{kk}^{\text{SGS}}}_{\text{isotropic}}$. The anisotropic part of the Reynolds stress tensor is given as a function of the eddy viscosity and the strain rate tensor $\tau_{ij} = -2\mu_t \bar{S}_{ij}$. Similar to the eddy viscosity, the turbulent eddy viscosity is written as a function of the GS variables, characteristic length scale, $l_c = C_s \bar{\Delta}$ and some characteristic velocity $U_c = l_c |\bar{S}_{ij}|$, where C_s is called the Smagorinsky constant, giving $\mu_t = \rho l_c^2 |\bar{S}_{ij}|$. The C_s depends on the Reynolds number and the flow configuration and needs special attention close to the wall. The van Driest-damping function [15] is used which is defined as

$$l_c = C_s \bar{\Delta} \left\{ 1 - \exp\left[\left(\frac{-z^+}{A+} \right)^{\gamma_1} \right] \right\}^{\gamma_2} \tag{3}$$

where the dimensionless distance from the wall is $z^+ = z u_\tau / \nu$

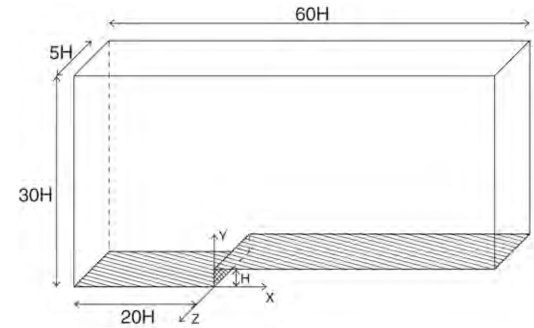

Fig. 1. Numerical domain for FFS simulation.

and the wall shear stress velocity is $u_\tau = \sqrt{\tau_w / \rho}$, and the constants are given as $A^+ = 25$, $\gamma_1 = 3$ and $\gamma_2 = 0.5$.

In the model used, $C_s = 0.1$ and $\bar{\Delta} = (\Delta x \Delta y \Delta z)^{\frac{1}{3}}$, where Δ is the grid size in the respective direction. The FV code used is block structured and parallel based on domain decomposition. The fluid computational domain for the FFS consists of 12 blocks with refinement at the step as shown in Fig. 1 to resolve the boundary layer, where H is the height of the step. The fine grid consists of $360 \times 100 \times 40$ control volumes. The stretching factor from the wall was taken to be 1.05. The height of the numerical domain is 30 H, width 5 H and length 60 H as used by Moon et al. [16]. For the simulation the fluid was taken as air at 25 °C. The inlet profile is provided based on the experiments performed by Becker et al. [5] ($U_0 = 10$ m/s), giving a $Re_H = 7816$. The low Mach number justifies the use of an incompressible flow solver for acoustic source calculation [17]. The outlet boundary has a convective exit condition and the remaining boundaries are slip walls. A time step of $\Delta t_f = 1.5 \times 10^{-6}$ s is used.

Fig. 2 shows the vortex structures present over the step and the grid around the step. At different planes over the step, the velocity is compared with experiments as shown in Fig. 3. The instantaneous pressure data on the wall of the step were monitored to carry out frequency analysis as shown in Fig. 4. PSD was calculated using 194 718 time steps, averaged over 4 equal timeseries, giving a resolution of around 1 Hz. The positions shown are relative to the position of the step i.e. −10, −5, 15, 30 and 50 mm, where at position 0 mm is the step. The monitoring points lie on the center plane of the simulation domain at $Z = 2.5$ H. A broad-band spectrum is seen in the points after the step. The PSD spectrum shows roughly a slope of −1 up to 2 kHz, which rapidly decays afterwards. A broadened peak of a tonal component at 165 Hz is seen, with higher modes of it being more dominant in monitoring points before the step.

2.2. Fluid–acoustic coupling

Acoustic sources are coupled from the fluid computation to the acoustic propagation solver in time domain. We use the assumption that it is a one-sided coupling as in the low Reynolds number flows, i.e. the acoustic field has negligible influence on the fluid field. The source terms are coupled along with the mean flow from the fluid simulation using the

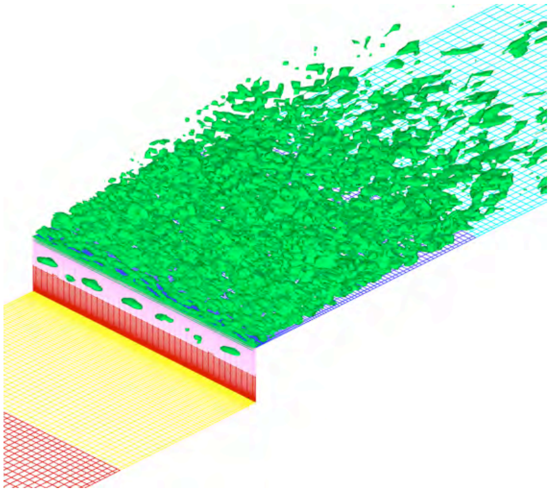

Fig. 2. Instantaneous eddy structures (Q-criteria) over the step, showing the grid and blocking around the step.

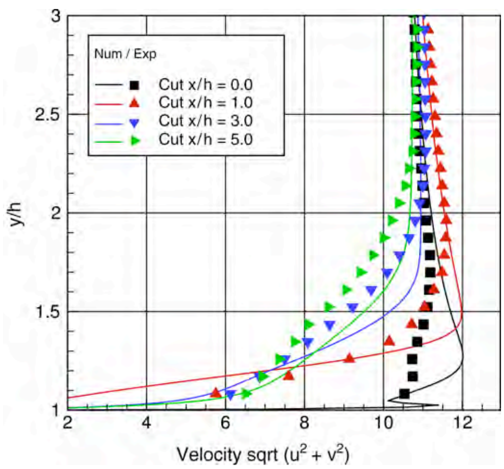

Fig. 3. Comparison of velocity profiles.

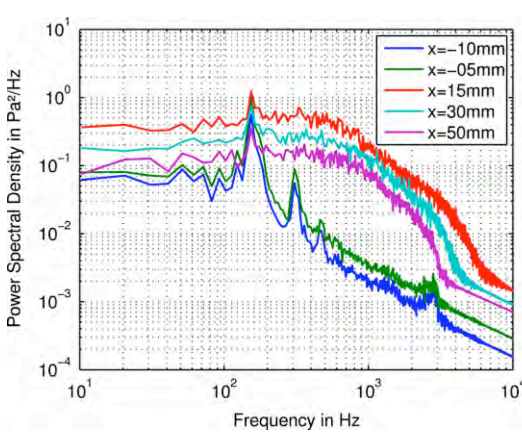

Fig. 4. PSD based on monitoring points on the step.

MpCCI [18] library. MpCCI is based on MPI and communication between the solvers is as per MPI protocols and also supports message transfer between parallel codes. The topologies of the meshes on both sides are provided and the bilinear interpolation coefficients are generated at the very beginning of the simulation. With the completion of this initialization phase, simulation proceeds and after each fluid simulation time step the source terms are coupled to the acoustic solver. A detailed overview of the coupling was published by Ali et al. [19].

2.3. Acoustic simulation

One of the early theoretical references to the use of LEE in aeroacoustics was by Goldstein [20]. In computational context LEE were first used in a simplified form with global linearization followed later by local linearization based on the mean flow values. Early references can be found in unsteady turbomachinery aerodynamics such as in cascades of airfoils, where it is natural to look at flow linearized about a uniform state in the work of Hall [21] and Clark [22]. Kerrebrock [23] investigated the propagation of small disturbances in a duct with swirling flow and used the normal mode analysis applied directly to LEE, and showed the presence of nearly-convected shear-like disturbances and pressure waves. In-jet noise references can be found in the work of Maestrello et al. [24], Mankbadi et al. [9] and by Hardin and Pope [25] on low Mach number aeroacoustics. Tam [26] showed that the aeroacoustics problems are linear and supported the use of LEE. Further improvements came with the development of suitable boundary conditions as proposed by Giles [27] and Hu [28]. During the last few years, with increasing computational resources, there has been ever-increasing focus on LEE and very promising results have been obtained, as in the work of Bailly et al. [29]. The governing equations for the acoustic field are the LEE which are solved using the ADER-DG method as proposed by Dumbser and Munz [30, 31] and implemented in an unstructured two-dimensional code Hydsol. The Euler equations in primitive variables are given as follows [32]:

$$\begin{aligned}
&\frac{\partial \rho}{\partial t} + u\frac{\partial \rho}{\partial x} + \rho\frac{\partial u}{\partial x} + v\frac{\partial \rho}{\partial y} + \rho\frac{\partial v}{\partial y} = 0\\
&\frac{\partial u}{\partial t} + u\frac{\partial u}{\partial x} + v\frac{\partial u}{\partial y} + \frac{1}{\rho}\frac{\partial p}{\partial x} = 0\\
&\frac{\partial v}{\partial t} + u\frac{\partial v}{\partial x} + v\frac{\partial v}{\partial y} + \frac{1}{\rho}\frac{\partial p}{\partial y} = 0\\
&\frac{\partial p}{\partial t} + \gamma p\frac{\partial u}{\partial x} + u\frac{\partial p}{\partial x} + \gamma p\frac{\partial v}{\partial y} + v\frac{\partial p}{\partial y} = 0.
\end{aligned} \tag{4}$$

In the low Reynolds number aeroacoustics, changes in the perturbation quantities are much smaller than their reference values. The acoustic pressure p' is many orders of magnitude smaller than the stagnation pressure p_0. Computing small differences in large numbers on the computer leads to cancellation and hence are negligible. Thus the primitive variables are linearized around a stationary field and only the perturbations are computed. The unknown values are decomposed into a stationary mean value and a perturbation component:

$$u_p = u_q = \begin{pmatrix} \rho_0 + \rho' \\ u_0 + u' \\ v_0 + v' \\ p_0 + p' \end{pmatrix} = \underbrace{\begin{pmatrix} \rho_0 \\ u_0 \\ v_0 \\ p_0 \end{pmatrix}}_{u_{p0}} + \underbrace{\begin{pmatrix} \rho' \\ u' \\ v' \\ p' \end{pmatrix}}_{u'_p}.$$

Under the approximation that for the matrix elements only the mean values are considered:

$$A_{pq}(u_{p0} + u'_p) \approx A_{pq}(u_{p0}) \quad \text{and}$$
$$B_{pq}(u_{p0} + u'_p) \approx B_{pq}(u_{p0})$$

we obtain

$$\frac{\partial u'_p}{\partial t} + A_{pq}(u_{p0})\frac{\partial u'_q}{\partial x} + B_{pq}(u_{p0})\frac{\partial u'_q}{\partial y}$$
$$= -\frac{\partial u_{p0}}{\partial t} - A_{pq}(u_{p0})\frac{\partial u_{q0}}{\partial x} - B_{pq}(u_{p0})\frac{\partial u_{q0}}{\partial y}. \tag{5}$$

The mean values u_{p0} of the original unknown vector u_p now are source terms on the right-hand side of the equation. For a good approximation, the right-hand side can be reduced to a time derivative vector including only the pressure derivative as source term. The LEE in two dimensions can finally be written as

$$\frac{\partial u_p}{\partial t} + A_{pq}\frac{\partial u_q}{\partial x} + B_{pq}\frac{\partial u_q}{\partial y} = S \tag{6}$$

with $u_p = u_q = (\rho', u', v', p')^T$ are the fluctuation quantities, the Jacobians of the fluxes are A_{pq} and B_{pq}, where the linearization performed about the mean flow is denoted by subscript 0. $S = (0, 0, 0, -\frac{\partial p}{\partial t})$ is the source term for the current LEE implementation as suggested by Ewert and Schröder [33] for low Mach number and incompressible flows. A_{pq} and B_{pq} are given by

$$\begin{pmatrix} u_0 & \rho_0 & 0 & 0 \\ 0 & u_0 & 0 & \frac{1}{\rho_0} \\ 0 & 0 & u_0 & 0 \\ 0 & \gamma p_0 & 0 & u_0 \end{pmatrix} \quad \text{and} \quad \begin{pmatrix} v_0 & 0 & \rho_0 & 0 \\ 0 & v_0 & 0 & 0 \\ 0 & 0 & v_0 & \frac{1}{\rho_0} \\ 0 & 0 & \gamma p_0 & v_0 \end{pmatrix}$$

respectively, where a suitable numerical flux F_p^h must be introduced for the surface integral.

ADER-DG schemes are really of arbitrary high order of accuracy in space and time on structured and unstructured grids. The very compact ADER-DG formulation does not need a reconstruction and thus provides the possibility of achieving arbitrary high order of accuracy in space and time even on unstructured grids, which should be useful for accurate noise propagation in the time domain around complex obstacles or in complex geometries. ADER-DG schemes are quadrature-free finite elements which perform time integration in single step and are ideal for parallelization. The two-dimensional acoustic grid consists of a semicircle with the step bottom point at its center and radius 5 m. For the directivity analysis, monitoring points were created at radius of 1, 2 and 3 m. The acoustic grid consisted of 130 006 control volumes, with which all final acoustic simulations were carried out. The minimal wall spacing was 10 times larger than the hydrodynamic value. For the simulations, the fluid was assumed to be air at 25 °C, as in the LES. The simulation was run for 36 900 iterations with $\Delta t_a = 1.5 \times 10^{-6}$ s, giving a physical simulation time of 0.055 s. The time step chosen corresponds to a CFL = 0.73 for the acoustic fine grid, based on the minimal element size $\Delta x = 1.157 \times 10^{-3}$ m. The resolution of the Fourier transformed signal is 19.2 Hz, which is relatively high and could be improved by longer simulation runs. Fig. 5 shows the time series of the monitoring point located at 40° from the step at a distance of 1 m. In Fig. 6, its FFT is shown with a broadband signal between 1 and 5 kHz, as expected.

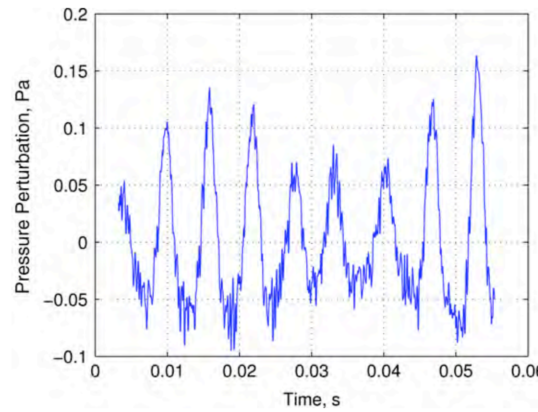

Fig. 5. Time series of acoustic pressure at a 1 m distance at 40° from the step.

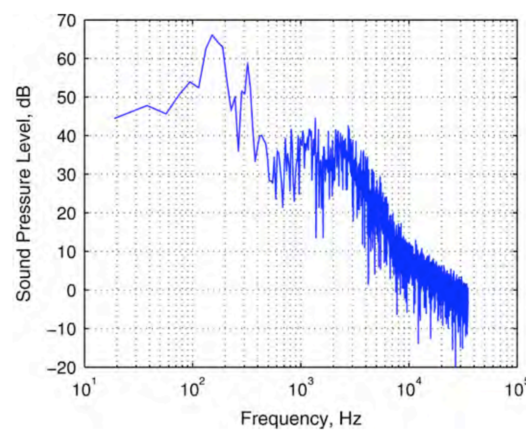

Fig. 6. FFT of acoustic pressure at a 1 m distance at 40° from the step.

3. Results and discussion

The coupling of the acoustic sources from Eq. (6) from the fluid computation to the acoustic code is very critical to the computation. This leads to a large dependence of the results on the computational grids both on the fluid and acoustic sides as already mentioned in Section 2.2. The computational effort is very high, needed for higher resolution of the acoustic results and requiring a longer simulation physical time.

In the current implementation, p' calculated is larger than in [5]. This can be attributed to the two-dimensional acoustic field calculation with normalization for the three-dimensional, and also to the lower order of discretization used in the

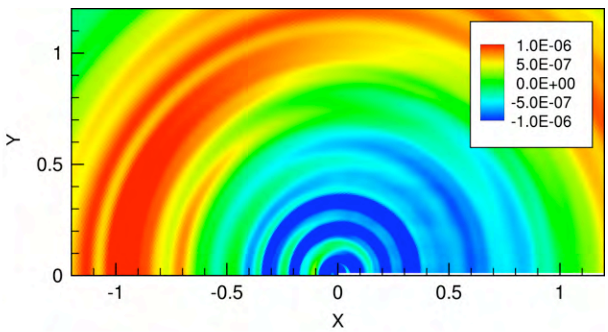

Fig. 7. Instantaneous acoustic pressure field, step at the origin.

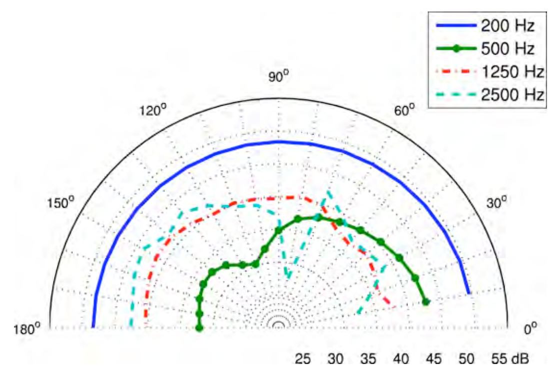

Fig. 8. Directivity map with the step located at the origin.

acoustic computation, which again is dependent on the current implementation of the fluid–acoustic coupling. Fig. 7 shows the instantaneous pressure fluctuation field ($\Delta p' = p - p_0$). Using the time series of p' at the monitoring points in the acoustic grid at a fixed radius, directivity plots are generated. At an observer location 1 m from the step, for 200 Hz a prominent monopole and for 500 Hz a dipole nature are observed, with the dipole aligned in the flow direction, as seen in Fig. 8. It is seen that directivities at higher frequencies show a multi-polar nature. These results are in good qualitative agreement with work by Moon et al. [16].

4. Conclusion

Investigations on flow-induced noise from a forward facing step were performed using LES and LEE. The coupling occurs in the time domain, avoiding storage of large LES volume data. Improvement in the source term evaluation is needed to smooth out large flow field fluctuations present in a well-refined LES. The coupling strategy was evaluated and the acoustic source generation mechanism was studied. There is good qualitative agreement of the results with published numerical and experimental data. The developed tool can be used in aeroacoustic optimization studies.

Acknowledgments

This research was supported by Bayerische Forschungsstiftung (BFS). We are grateful to Mr. Hahn of the Dept. of Sensors, University of Erlangen, Germany, for providing us the experimental data for the comparisons. We also acknowledge the help of Prof. Moon of the University of Seoul, Korea in giving insight into the physics of the problem.

References

[1] D. Wilhelm, C. Härtel, L. Kleiser, Computational analysis of the two-dimensional transition in forward-facing step flow, J. Fluid Mech. 489 (2003) 1–27.
[2] H. Stürer, Investigation of separation on a forward facing step, Ph.D. Thesis 13132, ETH Zürich, 1999.
[3] Y. Addad, D. Laurence, C. Talotte, M.C. Jacob, Large Eddy simulation of a forward–backward facing step for acoustic source identification, Int. J. Heat Fluid Flow 24 (2003) 562–571.
[4] J.F. Largeau, V. Moriniere, Wall pressure fluctuations and topology in separated flows over a forward-facing step, Exp. Fluids 42 (2007) 21–40.
[5] S. Becker, M. Escobar, M. Hahn, I. Ali, M. Kaltenbacher, B. Basel, M. Grünewald, Experimental and numerical investigation of the flow induced noise from a forward facing step, in: 11th AIAA/CEAS Aeroacoustics Conference, vol. 2005–3006, 2005.
[6] C. Hahn, S. Becker, I. Ali, M. Escobar, M. Kaltenbacher, New results in numerical and experimental fluid mechanics VI, in: Ch. Investigation of Flow Induced Sound Radiated by a Forward Facing Step, in: Notes on Numerical Fluid Mechanics and Multidisciplinary Design, vol. 96, Springer, 2007, pp. 438–445.
[7] T. Colonius, A.J. Basu, C.W. Rowley, Numerical investigation of the flow past a cavity, in: 5th AIAA/CEAS Aeroacoustics Conference, vol. 99–1912, Greater Seattle, Washington, 1999.
[8] X. Gloerfelt, C. Bailly, D. Juvé, Direct computation of the noise radiated by a subsonic cavity flow and application of integral methods, J. Sound Vibr. 266 (2003) 119–146.
[9] R.R. Mankbadi, R. Hixon, S.-H. Shih, L.A. Povinelli, On the use of linearized Euler equations in the prediction of jet noise, Technical Memorandum AIAA-95-0505, NASA, Reno, Nevada, 9 January 1995.
[10] G.S. Djambazov, C.-H. Lai, K.A. Pericleous, On the coupling of Navier–Stokes and linearized Euler equations for aeroacoustic simulation, Comput. Vis. Sci. 3 (2000) 9–12.
[11] C. Wagner, T. Hüttl, P. Sagaut (Eds.), Large-Eddy Simulation for Aeroacoustics, in: Cambridge Aerospace Series, Cambridge University Press, 2007.
[12] F. Durst, M. Schäfer, A parallel block-structured multigrid method for the prediction of incompressible flows, Internat. J. Numer. Methods Fluids 22 (1996) 549–565.
[13] M. Perić, A finite volume method for the prediction of three-dimensional flow in complex ducts, Ph.D. Thesis, University of London, 1985.
[14] J. Smagorinsky, General circulation experiments with the primitive equations, Monthly Weather Rev. 91 (3) (1963) 99–164.
[15] E.R. van Driest, On turbulent flow near a wall, J. Aeronaut. Sci. 23 (11) (1956) 1007–1011.
[16] Y.M. Bae, M.H. Cho, Y.J. Moon, S. Becker, Investigation of flow-induced noise from a forward facing step, in: 19th Symposium of Japan CFD, Tokyo, 2005.
[17] M. Wang, B.J. Freund, K.S. Lele, Computational prediction of flow-generated sound, Annu. Rev. Fluid Mech. 38 (2006) 482–512.
[18] MpCCI Technical Manual, MpCCI 3.0.4, 3rd ed., Frauenhofer–Institute SCAI, 6 June 2005.
[19] I. Ali, M. Escobar, M. Kaltenbacher, S. Becker, Time domain computation of flow induced sound, Comput. Fluids, 2007, in press, (doi:10.1016/j.compfluid.2007.02.011).
[20] E.M. Goldstein, Aeroacoustics, McGraw-Hill, 1976.
[21] K.C. Hall, A linearized euler analysis of unsteady flows in turbomachinery, Tech. Rep., Gas Turbine Laboratory, MIT, June 1987.
[22] C.K. Hall, W.S. Clark, Linearized Euler predictions of unsteady aerodynamics loads in cascades, AIAA J. 31 (3) (1993) 540–550.
[23] J.L. Kerrebrock, Small disturbances in turbomachine annuli with swirl, AIAA J. 15 (6) (1977) 794–803.
[24] L. Maestrello, A. Bayliss, E. Turkel, On the interaction between a sound pulse with the shear layer on an axisymmetric jet, Tech. Rep. 79-31, Institute of Computer Application in Science and Engineering, NASA Langley, 19 December 1979.

[25] J.C. Hardin, D.S. Pope, An acoustic/viscous splitting technique for computational aeroacoustics, Theor. Comput. Fluid Dynamics 6 (1994) 323–340.
[26] K.W.C. Tam, Computational aeroacoustics: Issues and methods, AIAA J. 33 (10) (1995) 1788–1796.
[27] M.B. Giles, Nonreflecting boundary conditions for Euler equation calculations, AIAA J. 28 (12) (1990) 2050–2058.
[28] Q.F. Hu, On absorbing boundary conditions for linearized Euler equations by a perfectly matched layer, Tech. Rep. 95-70, ICASE, NASA Langley Research Center, October 1995.
[29] C. Bailly, C. Bogey, D. Juvé, Computation of flow noise using source terms in linearized Euler's equations, AIAA J. 40 (2) (2000) 235–242.
[30] M. Dumbser, Arbitrary high order schemes for the solution of hyperbolic conservation laws in complex domains, Ph.D. Thesis, Institut für Aerodynamik und Gasdynamik, Universität Stuttgart, Shaker Verlag, Aachen, 2005.
[31] M. Dumbser, C.-D. Munz, Building blocks for arbitrary high order discontinuous Galerkin schemes, J. Sci. Comput. 27 (1–3) (2006) 215–230.
[32] C. Bailly, D. Juvé, Numerical solutions of acoustic propagation problems using linearized Euler equations, AIAA J. 38 (1) (2000) 22–29.
[33] R. Ewert, W. Schröder, Acoustic perturbation equations based on flow decomposition via source filtering, J. Comput. Phys. 188 (2003) 365–398.

Available online at www.sciencedirect.com
ScienceDirect
Physica D 237 (2008) 2190–2194
PHYSICA D
www.elsevier.com/locate/physd

Passive scalar statistics in a turbulent channel with local time-periodic blowing/suction at walls

Guillermo Araya[a,*], Stefano Leonardi[b], Luciano Castillo[a]

[a] Department of Mechanical, Aeronautical and Nuclear Eng., Rensselaer Polytechnic Institute, Troy, NY, 12180, USA
[b] Department of Mechanical Eng., University of Puerto Rico, Mayaguez, PR, 00680, USA

Available online 26 April 2008

Abstract

Direct Numerical Simulations (DNS) of an incompressible turbulent channel flow with local forcing at the walls are performed. Time-periodic blowing/suction is applied by means of narrow spanwise slots located at the lower and upper walls in $x/L_x = 0$ (where L_x is the channel length). The normal perturbing velocity is varied sinusoidailly in time at several perturbing frequencies between $0.16 < \overline{f} < 1.6$ and at a fixed amplitude of $A_o = 0.2$. The temperature field is also computed and assumed to be a passive scalar. The Reynolds number of the unperturbed case is $Re_\tau = 394$ and the Prandtl number is $Pr = 0.71$. It is concluded that the forcing frequency of $\overline{f} = 0.64$ or $f^+ = 0.044$ produces the largest local increase of the skin friction in the region $0.1 < x/L_x < 0.3$, followed by the highest augmentation of the Stanton number. Furthermore, budgets of the passive-scalar variance and wall-normal turbulent heat fluxes at this frequency demonstrate a significant enhancement of the molecular diffusion at the wall and pressure-related terms, respectively. The latter confirms the importance of pressure fluctuations on the transport of passive scalars and redistribution of energy.

PACS: 47.27.De; 47.27.E-; 47.27.ek; 47.27.nd

Keywords: DNS; Local forcing; Passive scalar

1. Introduction

One of the most important characteristics of the near-wall region in turbulent channel flows is the presence of coherent structures [1]. These structures play a key role in the turbulence production, dissipation and transport phenomena in wall-bounded flows. In fact, there have been many attempts to control near-wall turbulence by managing such coherent structures [2]. Among all the techniques employed so far, local forcing is a simple and efficient active approach, which consists of perturbing the flow by a steady or time-periodic velocity (i.e., blowing and/or suction) applied in a confined zone of the wall. Park et al. [3,4] performed experiments in a wind tunnel to analyze the flow structures behind the point, at which a local time-periodic blowing/suction perturbation is applied on a flat plate, by considering integer multiples of the bursting frequency found by Tardu [5]. They showed that, by increasing the forcing frequency, a local reduction in the skin friction, up to 75%, was obtained and significant changes in the downstream structures were observed. Additionally, time-periodic blowing from a spanwise slot was numerically (DNS) investigated by Kim and Sung [6] in an evolving boundary layer at three different forcing frequencies. They obtained maximal increase of the skin friction and streamwise vorticity fluctuations at an optimal blowing frequency of $f^+ = 0.035$ downstream of the maximum drag reduction location. Furthermore, the budget analysis of the Reynolds stresses indicated that the greatest augmentation of the pressure–strain term occurred at this frequency. Investigations of the influence of local forcing on turbulent heat transfer are rather scarce. Rhee and Sung [7] numerically predicted the enhancement of heat transfer in a locally forced turbulent, separated and reattaching flow over a backward-facing step. Several forcing frequencies were employed in simulations at a fixed amplitude, namely, 3% of the streamwise time-mean centerline velocity at the inlet, U_∞.

* Corresponding author.
E-mail address: araya@mailaps.org (G. Araya).

0167-2789/$ - see front matter
doi:10.1016/j.physd.2008.04.011

They obtained a maximal increase of 40% in the peak value of the Stanton number, S_t, at a dimensionless frequency of $fH/U_\infty = 0.275$, where H is the height of the backward-facing step. Kong et al. [8] performed a DNS of a spatially evolving boundary layer and found a significant dissimilarity between the Stanton number and the friction coefficient, due to the pressure gradient generated by uniform blowing or suction.

According to Mosyak and Hetsroni [1], coherent structures exhibit their dynamics through the bursting process, defined by alternating sweeps and ejections in the near-wall region. In addition, Hussain [9] includes the following comments on coherent motions: *If the coherent structure plays a key role in the transport phenomena in a boundary layer, then excitation at the bursting frequency should alter the bursting event and thus the overall characteristics of the boundary layer*. Despite advances in the understanding of near-wall structures, the effect of unsteady excitation on coherent structures and energy transport among turbulence components has not been elucidated completely yet. Motivated by the previous statement, we will explore the effects of several blowing/suction frequencies (selected as integer multiples of the bursting frequency) on the temperature field and thermal correlation budgets of a turbulent channel flow.

2. Numerical details

The non-dimensional governing equations, i.e. continuity, momentum and passive-scalar transport, for an incompressible flow are given below:

$$\frac{\partial U_i}{\partial \bar{x}_i} = 0; \tag{1}$$

$$\frac{\partial U_i}{\partial \bar{t}} + \frac{\partial U_i U_j}{\partial \bar{x}_j} = -\frac{\partial P}{\partial \bar{x}_i} + \frac{1}{Re_h}\frac{\partial^2 U_i}{\partial \bar{x}_j^2}; \tag{2}$$

$$\frac{\partial \Theta}{\partial \bar{t}} + \frac{\partial \left(\Theta U_j\right)}{\partial \bar{x}_j} = \frac{1}{Re_h Pr}\frac{\partial^2 \Theta}{\partial \bar{x}_j^2}. \tag{3}$$

The instantaneous temperature is normalized by the lower wall (hot) and upper wall (cold) temperatures. Isothermal conditions are assumed at each wall.

The equations of motion have been discretized in an orthogonal coordinate system using a staggered central second-order finite-difference scheme. The discretized system is advanced in time by using a fractional-step method, with viscous terms treated implicitly and convective terms explicitly. More details about the numerical procedure are given by Orlandi [10].

2.1. Boundary conditions and input forcing parameters

A mean parabolic velocity profile with random fluctuations is used as an initial condition in the entire domain. The molecular Prandtl number, Pr, is 0.71 and the Reynolds number is 394, $Re_\tau = hu_\tau/\nu$, where u_τ is the friction velocity of the unforced channel and ν the kinematic viscosity. The temperature difference between both walls is assumed small;

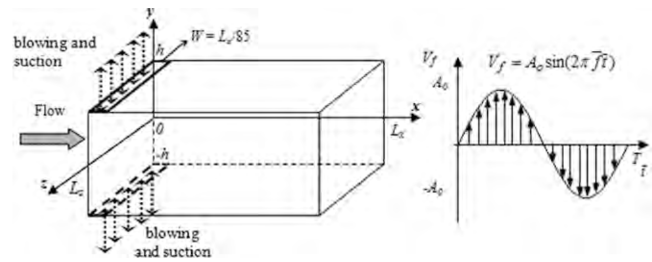

Fig. 1. Schematic of the channel with local forcing.

therefore, buoyancy effects and the temperature dependence of material properties are negligible. The perturbing flow does not contain the scalar and the walls are very thin; hence, heat conduction in the solid is neglected. Periodic boundary conditions are used along the spanwise and streamwise directions. Moreover, local forcing is modeled as a vertical velocity, V_f, (i.e. blowing and suction) with a time sinusoidal behavior imposed at both walls in thin slots of length, L_z, and width, $W = L_x/85$, as shown in Fig. 1. Normal perturbing velocities are in phase at both walls in order to preserve mass in the computational box. The forcing frequencies are normalized by the half height, h, and the centerline laminar velocity, U_C, of the channel (i.e. $\overline{f} = ft_o$, where $t_o = h/U_C$). Integer multiples of the bursting frequency found in [5,1] are used in this paper. Thus, the bursting frequency is around 0.011 when normalized as $f^+ = ft_i$, where $t_i = \upsilon/u_\tau^2$. This value corresponds to $\overline{f} = 0.16$ according to our non-dimensionalization. Furthermore, five forcing frequencies are considered in the present study (i.e. $\overline{f} = 0.16, 0.32, 0.64, 1.28$ and 1.6), which correspond to one, two, four, eight and ten integer multiples of the bursting frequency. The forcing amplitude, $A_o = V_{f\,\max}/U_C$, is fixed at 0.2, where $V_{f\,\max}$ is the maximum normal perturbing velocity.

3. Numerical simulations

Fig. 1 shows the computational domain with the following dimensions: $L_z = \pi h$, $L_y = 2h$ and $L_x = 2\pi h$. A grid-independence test is performed and details are given in Araya et al. [11]. Two mesh configurations are tested: $161 \times 177 \times 257$ and $257 \times 193 \times 257$, which represent numbers of points along the spanwise, normal and streamwise directions, respectively. Fig. 2 depicts thermal fluctuation profiles at $\overline{f} = 0.64$ for both mesh configurations at two x-locations and normalized by the unforced friction temperature, $T_\tau = q_w/[\rho C_p u_\tau]$. It can be observed that predictions of the coarser mesh ($161 \times 177 \times 257$) almost overlap the results from the finer grid ($257 \times 193 \times 257$); therefore, the first configuration is selected for further analyses in this paper. The mesh resolution is: $\Delta z^+ = 7.7$, $\Delta y^+_{\min} = 0.1$, $\Delta y^+_{\max} = 12$ and $\Delta x^+ = 9.7$. The Courant, Friedrichs, Levy (CFL) parameter remains constant during simulations (but is modified according to the frequency) and the time step range is $\Delta t^+ \approx 0.046 - 0.28$.

3.1. Analysis of time-mean components

The friction coefficient is time-spanwise averaged and shown for different frequencies in Fig. 3 in terms of the

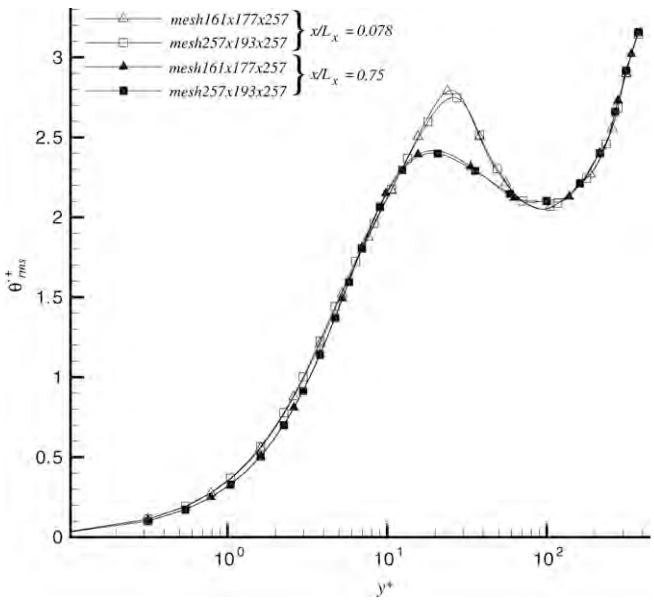

Fig. 2. Thermal fluctuations in wall units.

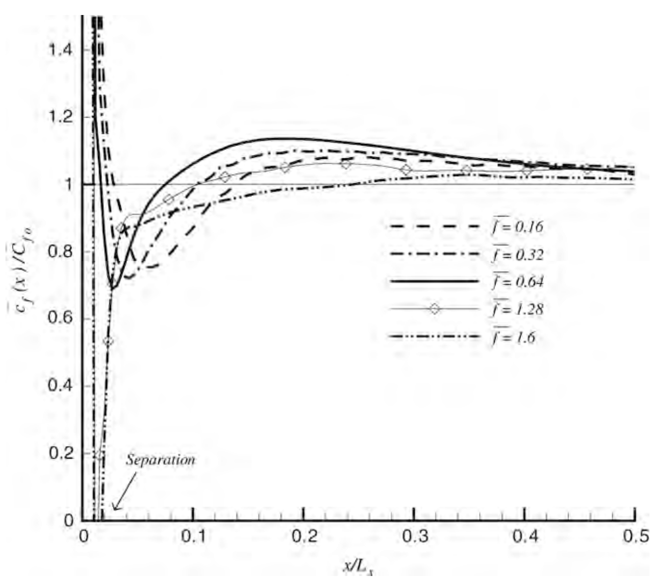

Fig. 3. Relative friction coefficient.

calculated unforced value, $\overline{C}_{fo}$. Flow perturbation is more pronounced over and at the adjacent downstream zone of the local forcing slot, which results in large velocity gradients and, consequently, large skin-friction coefficients. Downstream, the friction coefficients of the forced cases reach a minimum local value. In essence, local forcing creates a spanwise vortex that generates a reverse flow in the near wall region and reduces the velocity gradient. Thus, an overshoot is attained afterwards, as observed in Fig. 3. Finally, the skin friction tends toward the unforced channel value. It is also observed in Fig. 3 that, as the frequency increases, the maximum local drag reduction also increases and the location moves upstream. This is because the diameter of the spanwise vortex [3], created by local forcing, is inversely proportional to the frequency. Furthermore, if the frequency is augmented beyond a certain value (i.e. $\overline{f} = 1.28$), negative streamwise velocities with small zones of separated

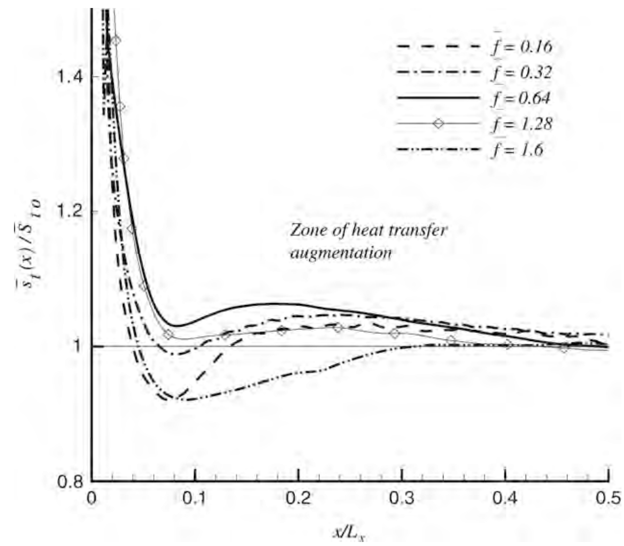

Fig. 4. Relative Stanton number.

flow around $x/L_x = 0.02$ begin to develop as the reverse flow becomes more intense.

It is interesting to highlight the observed similarity between the present friction coefficient behavior and the results from Kim and Sung [6] in their figure 10. In their study, time-periodic blowing was applied in a spatially evolving boundary layer at three different frequencies, namely, $f^+ = 0.01, 0.035$ and 0.08, by considering two inlet Reynolds numbers, $Re_\theta = 300$ and 670. They stated that points of maximum local drag reduction also moved upstream as the frequency was augmented and the downstream overshoot of the friction coefficient was most prominent at $f^+ = 0.035$. In the present simulations, the results of Fig. 3 also show a maximum overshoot of the friction coefficient around $x/L_x = 0.18$ at a similar dimensionless frequency of $\overline{f} = 0.64$ or $f^+ = 0.044$.

Fig. 4 depicts the time-spanwise averaged Stanton number along the channel in terms of the computed unforced value, $\overline{S}_{to}$. In the immediate downstream vicinity of the slot, the perturbation induced on the flow is more evident; this significantly increases the wall heat flux and the Stanton number (up to 50%). Afterwards, the ratio $\overline{S}_t/\overline{S}_{to}$ displays a behavior similar to that of the friction coefficient. However, the undershoots and overshoots become less pronounced, particularly as the frequency increases. This dissimilarity between the momentum and scalar transport [8] arises mainly because of the existence of a large streamwise pressure gradient and pressure fluctuations, at walls in the vicinity of slots, provoked by blowing/suction. Finally, a zone of heat-transfer enhancement, between $0.1 < x/L_x < 0.3$, is observed in Fig. 4 at a specific frequency of $\overline{f} = 0.64$. Hence, thermal energy budgets are examined in the following sections for that condition.

3.2. Budgets of the scalar variance and wall-normal turbulent heat flux for the unperturbed channel

Budgets of the temperature correlations of the unforced channel are computed and compared with other simulations

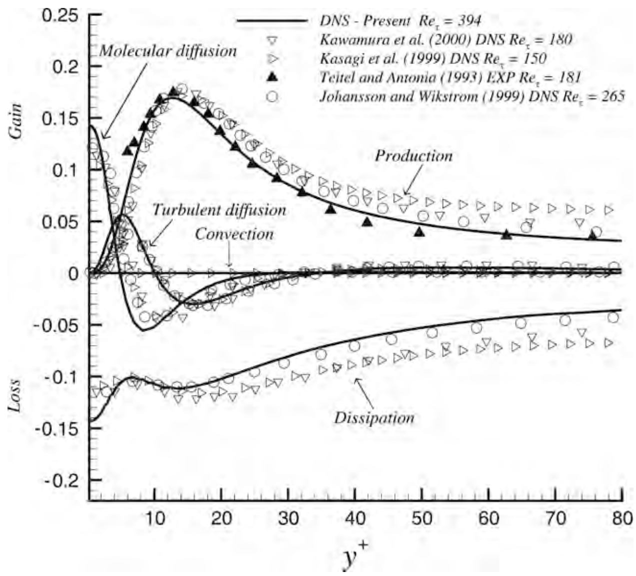

Fig. 5. Budget of the temperature variance, $\overline{\theta'^{+2}}/2$.

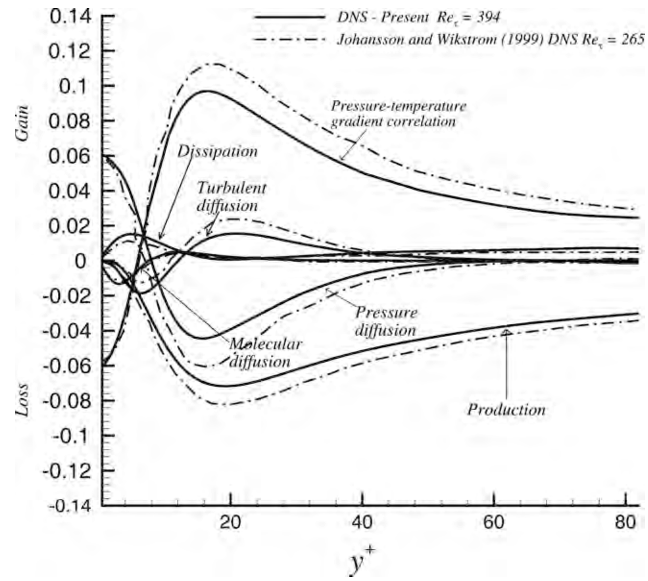

Fig. 6. Budget of wall-normal turbulent heat fluxes, $\overline{v'^{+}\theta'^{+}}$.

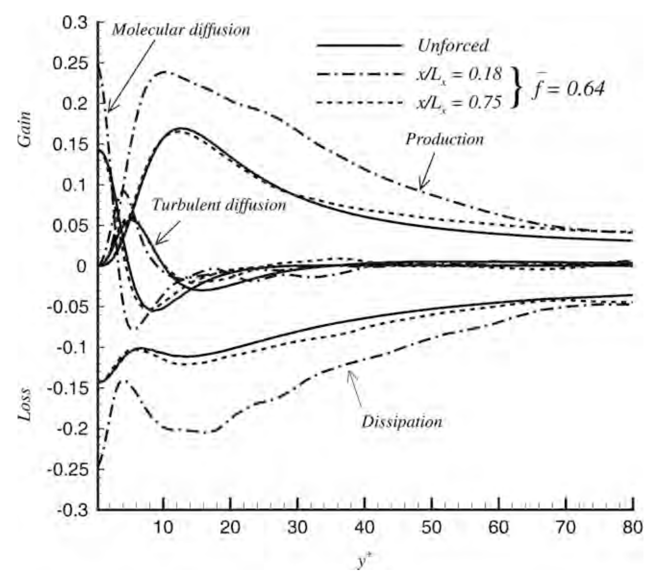

Fig. 7. Budget of temperature variance $\overline{\theta'^{+2}}/2$.

and experimental data. The time-spanwise averaged transport equations of temperature variance, $\overline{\theta'^2}/2$, and wall-normal turbulent heat fluxes, $\overline{v'^{+}\theta'^{+}}$, are derived in Sumitani and Kasagi [12]. It is concluded that major contributions to different terms are given by the y-derivatives; the x-derivatives affect mostly peak values of the production and dissipation terms. All terms, including those of forced cases, have been normalized by $u_\tau^2 T_\tau^2/\nu$. The convection term is almost negligible as can be seen in Fig. 5, in accordance with Kasagi and Iida [13]. Moreover, the thermal-production component, $-\overline{v'^{+}\theta'^{+}}\frac{\partial \bar{\Theta}^{+}}{\partial y^{+}}$, shows a maximum value at $y^+ \approx 13$ in the buffer zone. The theoretical maximum value of 0.1775 for production computed in Teitel and Antonia [14], by assuming a molecular Prandtl number of 0.71, is confirmed as seen in Fig. 5. Notice that present computations of thermal production agree fairly well with experimental data from [14]. In addition, good agreement is observed with DNS data from Johansson and Wikström [15] at $Re_\tau = 265$. However, some discrepancies are observed with the computations given in Kawamura et al. [16] and Kasagi and Iida [13] at lower values of Re_τ than those used in the present simulations. In particular, differences are observed in the production and dissipation terms in the region $y^+ > 20$; these may arise from Reynolds number effects. Fig. 6 shows the wall-normal turbulent heat flux budget together with DNS results from Johansson and Wikström [15]. Fairly good agreement is obtained in the near-wall region; however, some differences are found in the buffer layer, where maximum values are observed. Again, this feature may arise because of some Reynolds number dependence. However, the y-locations of the maxima do not change significantly with Re_τ.

3.3. Budgets of the scalar variance and wall-normal turbulent heat flux for the forced channel

Budgets of thermal correlations ($\overline{\theta'^{+2}}/2$ and $\overline{v'^{+}\theta'^{+}}$) at the characteristic frequency, $\overline{f} = 0.64$, are plotted in Figs. 7–9 for $x/L_x = 0.18$ and for $x/L_x = 0.75$. The first location corresponds to the point where the maximum Stanton number was achieved; and the second location is selected far downstream from the slot. The most noticeable changes occur in the zone very close to the wall, namely, $0 < y^+ < 50$. Beyond this region, the different budget terms of the forced cases tend to the unforced channel values as expected.

Fig. 7 exhibits the budget of the temperature variance $\overline{\theta'^{+}}/2$ versus y^+ at $\overline{f} = 0.64$. For $x/L_x = 0.18$, molecular diffusion and dissipation undergo a significant augmentation (up to 60%) mostly in the near wall region. In the buffer layer, $10 < y^+ < 30$, all peak values experience a considerable enhancement, particularly for production and dissipation. Furthermore, locations of maxima are pushed to the wall; this corresponds to the zone of streamwise vortex centers. Profiles for $x/L_x = 0.75$ and unperturbed curves almost overlap, confirming that the flow has recovered its undisturbed features by this streamwise location. Figs. 8 and 9 show the budget of

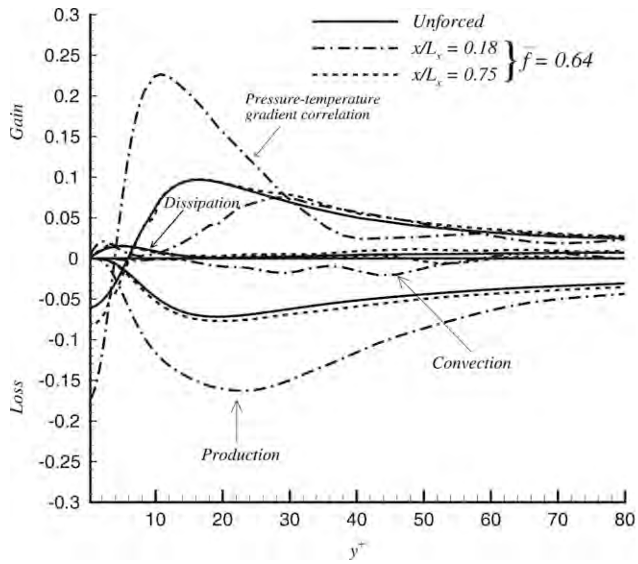

Fig. 8. Budget of wall-normal turbulent heat fluxes, $\overline{v'^+\theta'^+}$: pressure–temperature gradient correlation, dissipation, production and convection.

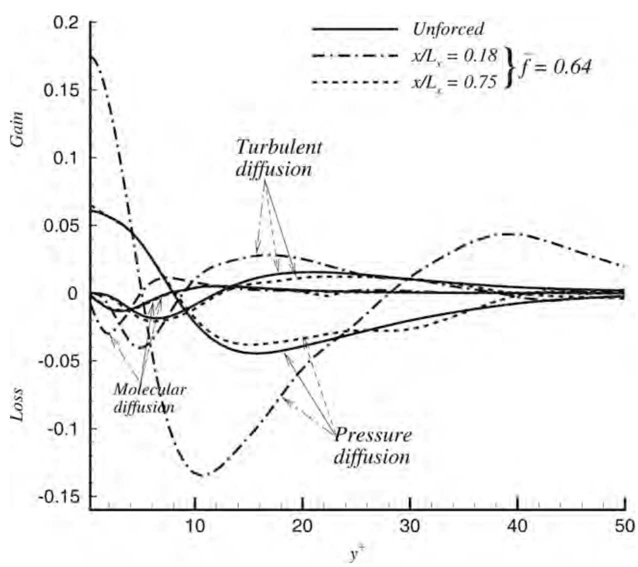

Fig. 9. Budget of wall-normal turbulent heat fluxes, $\overline{v'^+\theta'^+}$: turbulent, molecular and pressure diffusion terms.

wall-normal turbulent heat fluxes. For clarity, terms have been split in two plots. According to Fig. 8, the pressure–temperature gradient correlation term is dominant at $x/L_x = 0.18$, which indicates the important role that pressure fluctuations play in the turbulent thermal transport. Its peak values, i.e. at the wall and in the buffer layer, are more than twice as large as those of the corresponding unforced maxima. To a similar extent, the production of $\overline{v'^+\theta'^+}$ is also intensified in the buffer layer. The convection of $\overline{v'^+\theta'^+}$ is significant in the region $20 < y^+ < 50$ for $x/L_x = 0.18$; and it is found that the major contribution comes from the streamwise convection. In Fig. 9, the different diffusion terms of $\overline{v'^+\theta'^+}$ are shown. The pressure diffusion is significantly increased by local forcing; this confirms the key role of pressure fluctuations in the normal heat-transfer component. The maximum of the pressure diffusion term at $y^+ \approx 10$ for $x/L_x = 0.18$ is approximately 3 times higher than that of the unforced channel. Note also that the transport of wall-normal turbulent heat fluxes (or the turbulent-diffusion term) is enhanced by local forcing, with local increases up to 100%, as observed in its peak values. Finally, the trend of the $\overline{v'^+\theta'^+}$ budget at $x/L_x = 0.75$ resembles the unperturbed channel-flow profiles.

4. Conclusion

Based on extensive DNS, a numerical analysis of the influence of local forcing on the molecular heat transfer and scalar fluctuations in a turbulent channel flow is performed. Maximum local increases of the Stanton number are obtained at a characteristic forcing frequency of $\overline{f} = 0.64$ or $f^+ = 0.044$. The budget analysis of the temperature variance and wall-normal turbulent heat fluxes indicates, in general, an increase of all terms in the zone of Stanton number augmentation, principally, very close to the wall (i.e., $0 < y^+ < 50$). In particular, molecular diffusion and dissipation of the temperature variance experience a remarkable enhancement at the wall with peaks up to 1.7 times larger than their unperturbed values. On the other hand, the budgets of wall-normal turbulent heat fluxes show clear evidence of the key role of pressure fluctuations in the energy exchange and redistribution among the components.

References

[1] A. Mosyak, G. Hetsroni, Visual study of bursting using infrared technique, Exp. Fluids 37 (2004) 40–46.
[2] M. Gad-el-Hak, Flow Control: Passive, Active, and Reactive Flow Management, New York Cambridge University Press, Cambridge, 2000.
[3] S. Park, I. Lee, H. Sung, Effect of local forcing on a turbulent boundary layer, Exp. Fluids 31 (2001) 384–393.
[4] Y. Park, S. Park, H. Sung, Measurement of local forcing on a turbulent boundary layer using PIV, Exp. Fluids 34 (2003) 697–707.
[5] S. Tardu, Near wall turbulence control by local time periodical blowing, Exp. Thermal Fluid Sci. 16 (1998) 41–53.
[6] K. Kim, H. Sung, Effects of unsteady blowing through a spanwise slot on a turbulent boundary layer, J. Fluid Mech. 557 (2006) 423–450.
[7] G. Rhee, H. Sung, Enhancement of heat transfer in turbulent separated and reattaching flow by local forcing, Numer. Heat Transfer, Part A 37 (2000) 733–753.
[8] H. Kong, H. Choi, J. Lee, Dissimilarity between the velocity and temperature fields in a perturbed turbulent thermal boundary layer, Phys. Fluids 13 (5) (2001) 1466–1479.
[9] A. Hussain, Coherent structures—reality and myth, Phys. Fluids 26 (10) (1983) 2816–2850.
[10] P. Orlandi, Fluid Flow Phenomena: A Numerical Toolkit, Kluwer, Dordrecht, 2000.
[11] G. Araya, S. Leonardi, L. Castillo, Numerical assessment of local forcing on the heat transfer in a turbulent channel flow, Phys. Fluids, (2008) (in press).
[12] Y. Sumitani, N. Kasagi, Direct numerical simulation of turbulent transport with uniform wall injection and suction, AIAA J. 33 (7) (1995) 1220–1228.
[13] N. Kasagi, O. Iida, Progress in DNS of turbulent heat transfer, in: Proc. of the 5th ASME/JSME Thermal Engineering Joint Conference, 1999.
[14] M. Teitel, R.A. Antonia, Heat-transfer in fully-developed turbulent channel flow—comparison between experiment and direct numerical simulations, Int. J. Heat Mass Transfer 36 (6) (1993) 1701–1706.
[15] A. Johansson, P. Wikström, DNS and modelling of passive scalar transport in turbulent channel flow with a focus on scalar dissipation rate modelling, Flow, Turbulence and Combustion 63 (1999) 223–245.
[16] H. Kawamura, H. Abe, K. Shingai, DNS of turbulence and heat transport in a channel flow with different *Re* and *Pr* numbers and boundary conditions, Turbulence, Heat Mass Transfer 3 (2000) 15–32.

Available online at www.sciencedirect.com
ScienceDirect
Physica D 237 (2008) 2195–2202
PHYSICA D
www.elsevier.com/locate/physd

Is the Reynolds number infinite in superfluid turbulence?

Carlo F. Barenghi*

School of Mathematics and Statistics, Newcastle University, Newcastle upon Tyne NE1 7RU, UK

Available online 16 January 2008

Abstract

Superfluidity, the hallmark property of quantum fluids (e.g. liquid helium, atomic Bose–Einstein condensates, neutron stars), is characterised by the absence of viscosity. At temperatures which are low enough that thermal excitations can be neglected, liquid helium can be considered a perfect superfluid, and one would expect that superfluid turbulence were dissipationless because the Reynolds number is infinite. On the contrary, experiments show that helium turbulence decays, even at these low temperatures. The solution of this apparent puzzle lies in subtle but crucial differences between a superfluid and a classical Euler fluid.

PACS: 67.40.Vs; 47.27.-i; 03.75.Lm; 67.57.Fg

Keywords: Superfluid helium; Euler; Vortices; Turbulence

1. Introduction

The motivation behind this article is the relation between the concept of inviscid, incompressible Euler fluid (as in traditional textbooks of fluid mechanics) and superfluid helium. This relation is particularly intriguing in view of recent experiments [1,2] concerning the nature of turbulent dissipation near absolute zero. A second motivation is that research in superfluidity, quantised vorticity and turbulence [3] has gone beyond the traditional context of liquid helium (the two isotopes ^{4}He and ^{3}He) and now includes ultra-cold atomic gases [4] and neutron stars [5]. Clearly the three physics communities which are involved (condensed matter physics, atomic physics and astrophysics) should benefit from more contact with classical fluid mechanics. The third motivation is the recognition of the great potential of cryogenics helium to produce turbulence at very large Reynolds numbers [6] and Rayleigh numbers [7], which is making classical fluid mechanicists interested in issues of turbulence at very low temperatures. An example of the successful interaction between classical fluid mechanicists and low temperature physicists is the recent application of the classical Particle Image Velocimetry method in liquid helium [8,9].

Since the best known superfluid is still the common isotope ^{4}He, most of the following considerations will refer directly to it, unless stated otherwise. Helium is a gas at room temperature. To turn it into a liquid it is necessary to cool it down to approximately 4 K degrees above absolute zero. Upon further cooling a phase transition occurs at the critical temperature $T_c = 2.1768$ K (at saturated vapour pressure), marking the onset of Bose–Einstein condensation [10]. Below T_c liquid helium is a quantum fluid called helium II. Its strange properties are well described by the two-fluid model of Landau and Tisza [11]. According to this model, helium II is the intimate mixture of two-fluid components, the normal fluid and the superfluid. The normal fluid consists of thermal excitations (similar to phonons in a solid) which carry the entire entropy and viscosity of the liquid. The superfluid is related to the Bose–Einstein condensate [10] and has zero entropy and viscosity. Hereafter, for the sake of simplicity, I shall ignore the difference between the superfluid fraction and the condensate. The feature which is crucial in our problem is that the normal-fluid fraction decreases very rapidly with temperature, and below 1 K, at temperatures which can be easily reached experimentally, helium II can be considered a pure superfluid. The normal fluid can be neglected in the case of ^{3}He too; although the critical temperature T_c for the onset of superfluidity is much lower (few mK) than in ^{4}He,

* Tel.: +44 191 222 7307; fax: +44 191 222 8020.
E-mail address: C.F.Barenghi@ncl.ac.uk.

0167-2789/$ - see front matter © 2008 Elsevier B.V. All rights reserved.
doi:10.1016/j.physd.2008.01.010

turbulence experiments can be performed at very small values of T/T_c [12].

In classical fluid dynamics the ratio of the magnitudes of inertial and viscous forces acting on a fluid is the Reynolds number $Re = UD/\nu$, where D and U are the characteristic length scale and velocity scale of the flow and ν is the kinematic viscosity of the fluid. If $Re \gg 1$ inertial forces dominate and the flow is turbulent. Thus Re measures the intensity of the turbulence. The kinematic viscosity of liquid helium is almost two orders of magnitude less than water's, so it is relatively easy to make liquid helium turbulent.

The issue which we address is what happens at temperatures so small that helium II is a pure superfluid. Since a superfluid has zero viscosity, the Reynolds number of helium II flow is infinite and one would expect a form of dissipationless turbulence. On the contrary, experiments [1,2] show that turbulence decays, even at temperatures as low as few mK, which is puzzling. The natural question is: what is the ultimate energy sink near absolute zero? To answer the question and to solve the puzzle we must identify subtle but crucial differences between a superfluid and a classical Euler fluid.

2. The NLSE

Quantum mechanics constrains the rotational motion of the superfluid to vortex lines [13]. To understand the superfluid vortex structure it is convenient to consider the nonlinear Schroedinger equation (NLSE) for a weakly-interacting Bose–Einstein condensate [14]:

$$\mathrm{i}\hbar\frac{\partial\psi}{\partial t} = -\frac{\hbar^2}{2m}\nabla^2\psi + V_0|\psi|^2\psi - E_0\psi, \tag{1}$$

where $\psi = \psi(\mathbf{x}, t)$ is the macroscopic single-particle wavefunction, V_0 the (delta-function repulsive) potential of interaction between the bosons, m the mass of one boson, E_0 the energy increase upon addition of a boson, h Planck's constant and $\hbar = h/(2\pi)$ The total energy of the condensate, defined as

$$E_{\mathrm{tot}} = \frac{\hbar^2}{2m}\int|\nabla\psi|^2\mathrm{d}^3x + \frac{V_0}{2}\int|\psi|^4\mathrm{d}^3x, \tag{2}$$

is a constant of motion. In the case of a trapped atomic condensate, a term of the form $V_{\mathrm{ext}}\psi$ must be added to the right-hand side of Eq. (1), where V_{ext} is a confining harmonic potential [10].

In using the NLSE model one should keep in mind that the NLSE has quantitative predicting power in the case of atomic Bose–Einstein condensates, but is only a qualitative model of helium II. The reason is that helium II is a liquid, not a weakly-interacting gas; as far as our discussion is concerned, however, the difference should not be essential. Our aim is to compare vortex lines solutions of the NLSE model with vortex lines solutions of the classical incompressible Euler equations

$$\frac{\partial\mathbf{v}_s}{\partial t} + (\mathbf{v}_s\cdot\nabla)\mathbf{v}_s = -\frac{1}{\rho_s}\nabla p, \quad \nabla\cdot\mathbf{v}_s = 0. \tag{3}$$

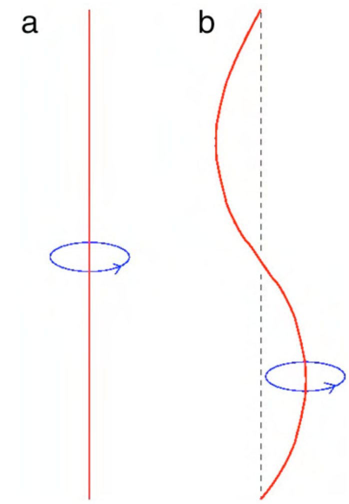

Fig. 1. Straight vortex line (a) and Kelvin wave (b).

3. Fluid dynamics interpretation of the NLSE

The fluid dynamics interpretation of the NLSE is based on the Madelung transformation $\psi = R\mathrm{e}^{\mathrm{i}S}$ where R and S are the amplitude and the phase of ψ. Substitution into Eq. (1) yields the following classical continuity equation for the superfluid density $\rho_s = mR^2$:

$$\frac{\partial\rho_s}{\partial t} + \nabla\cdot(\rho_s\mathbf{v}_s) = 0, \tag{4}$$

and the following (quasi) Euler equation for the superfluid velocity $\mathbf{v}_s = (\hbar/m)\nabla S$:

$$\rho_s\left(\frac{\partial v_{sj}}{\partial t} + v_{sk}\frac{\partial v_{sj}}{\partial x_k}\right) = -\frac{\partial p}{\partial x_j} + \frac{\partial\Sigma_{jk}}{\partial x_k}, \tag{5}$$

where v_{sj} is the jth component of $\mathbf{v}_s$. The pressure, p, and the quantum stress, Σ_{jk}, are defined as

$$p = \frac{V_0}{2m^2}\rho_s^2, \qquad \Sigma_{jk} = \left(\frac{\hbar}{2m}\right)^2\rho_s\frac{\partial^2\ln\rho_s}{\partial x_j\partial x_k}. \tag{6}$$

Note that without the quantum stresses term, Eq. (5) would be the classical Euler equation (3).

4. Vortex lines and vortex tangles

The solution of the NLSE which corresponds to a vortex aligned along the z-axis, as in Fig. 1(a), is obtained by letting $S = \phi$ in cylindrical coordinates (r, ϕ, z). The resulting velocity is

$$\mathbf{v}_s = \frac{\hbar}{mr}\hat{\boldsymbol{\phi}}, \tag{7}$$

where $\hat{\boldsymbol{\phi}}$ is the unit vector along the ϕ direction. This is the textbook velocity field of a vortex line in a classical Euler fluid, shown in Fig. 2. As we shall see in Fig. 4, the corresponding density is zero on the axis of the vortex.

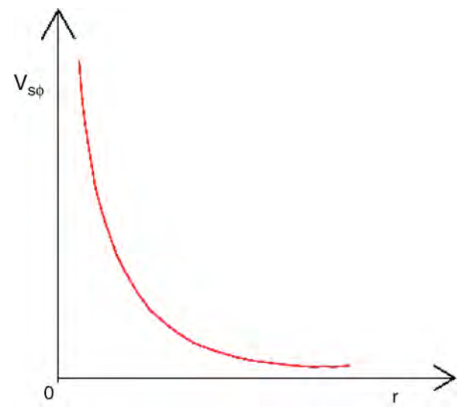

Fig. 2. Superfluid velocity field around a vortex line.

Let C be any path of integration around the vortex line. Then the circulation Γ around C is

$$\Gamma = \oint_C \mathbf{v}_s \cdot \mathbf{d}\boldsymbol{\ell} = \kappa, \tag{8}$$

where the constant $\kappa = h/m \approx 10^{-3}$ cm^2/s is called the quantum of circulation. Since $\nabla \times \nabla S = 0$, a superfluid vortex line has zero vorticity but finite circulation: the core is a microscopic hole, surrounded by a macroscopic region of potential flow.

A sinusoidal, or, more in general, a helical displacement of the vortex line away from the straight position is called Kelvin wave, as shown in Fig. 1(b). The wave rotates with angular frequency $\omega \sim \kappa k^2$, where k is the wavenumber and $\lambda = 2\pi/k$ the wavelength.

5. Turbulence

Vortex systems can be laminar or turbulent. If the vessel which contains helium II rotates at constant angular velocity Ω (larger than some small critical value), the superfluid breaks into vortex lines which are aligned along the axis of rotation [13] forming a lattice of areal density $n = 2\Omega/\kappa$. Essentially the superfluid mimics the classical vorticity 2Ω of a rotating Euler fluid by making n vortices (per unit area) carrying one quantum of circulation each.

Disordered systems of vortex lines are easily created by making the helium turbulent, This can be done, for example, by imposing a heat flow [15,16] or by agitating the liquid helium with towed grids [17], rotating propellers [18,19], vibrating grids [1,2] or wires [20]. Numerical simulations indicate that superfluid turbulence manifests itself as a disordered tangle of vortex filaments, as shown in Fig. 3. The intensity of the turbulence is usually characterised by the vortex line density L (vortex length per unit volume). The quantity $\delta = L^{-1/2}$ is the average distance between the vortex lines in the tangle.

The nature of superfluid turbulence and its similarities with classical turbulence is a problem which is attracting attention, as reviewed by Vinen and Niemela [21]. The particular aspect which is relevant to our problem is the experimental observation that turbulence generated at very low temperatures decays [1,2] or diffuses away [20], which is at first surprising, given that

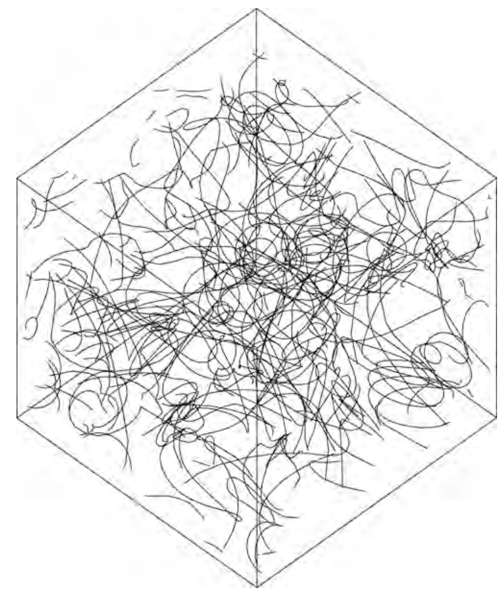

Fig. 3. Tangle of vortex filaments in a periodic box computed using the approach of Schwarz.

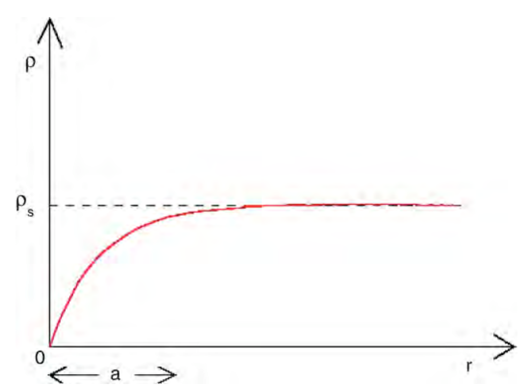

Fig. 4. Superfluid density near a vortex line.

the superfluid is usually interpreted as an inviscid Euler fluid. To understand these experiments, it is necessary to understand the difference between a superfluid and a classical Euler fluid, expressed by the last term of Eq. (5).

6. Euler fluid vs superfluid

In the classical Euler case we are free to assume that the fluid's density is constant. In the NLSE model the density near the vortex must be determined self-consistently by solving the NLSE for the amplitude of ψ. The result is shown in Fig. 4. The density drops from its bulk value (away from the vortex) to zero (on the axis of the vortex) over a characteristic distance $a \approx 10^{-8}$ cm called the vortex core radius; this quantity is of the order of the superfluid healing length $\xi = \hbar/\sqrt{mE_0}$. Fig. 4 shows that the superfluid vortex core is hollow, and the presence of a vortex makes a region of liquid helium to become multiply-connected. This means that the diverging velocity field, $v_{s\phi} \rightarrow \infty$ for $r \rightarrow 0$ predicted by Eq. (7) is not a problem, because, in the same limit, $\rho_s \rightarrow 0$, whereas the classical Euler model of a vortex line breaks down on the axis.

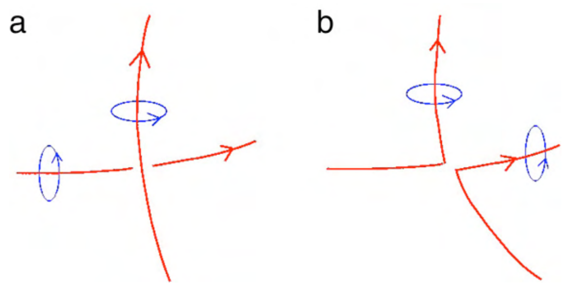

Fig. 5. Schematic vortex reconnection.

In general, the total circulation Γ around an arbitrary region is preserved by the evolution until a vortex line crosses C, which causes a change of Γ by one quantum κ. Note that the classical Kelvin's theorem that Γ is constant does not apply because when the vortex meets C the density becomes zero. Thus, although both the classical Euler fluid and the superfluid conserve the total energy, there is an important difference: in the classical Euler case the circulation cannot change and the topology of the flow is determined by the initial condition. In the NLSE case, on the contrary, vortex reconnections are possible (see Fig. 5), as first demonstrated by Koplik and Levine [22], and the topology can change while conserving the total energy. The existence of vortex reconnections in a classical viscous fluid is well known [23,24]. However, whereas in the Navier–Stokes equation reconnections are controlled by the viscosity and dissipate energy, in the NLSE reconnections are controlled by the quantum stress and maintain the total energy constant.

A striking consequence of the ability of superfluid vortices to reconnect is the following. Consider a vortex tangle initially confined within a region of radius R in infinite space. The tangle consists of a number of vortex loops of any size and orientation. If the loops obeyed ordinary Euler dynamics, the initial linkage between the loops could not change, because helicity, hence the linking number, must be conserved. On the contrary, superfluid vortex loops can reconnect and undergo the following unusual process of diffusion in space [25]. Suppose that a vortex reconnection creates a vortex loop which is smaller than the average distance δ between loops, is located near the boundary of the tangle and has circulation such that its translational velocity points out of the tangle. The small loop can escape to infinity with very little probability of being re-absorbed into the tangle by another vortex reconnection, because its speed is inversely proportional to its size and most other loops are larger and slower. Once the small loop has escaped, the total vortex length of the tangle has been reduced, hence the typical spacing of loops has increased, which favours the escape of a second loop, and so on. In this way the tangle evaporates into loops, thus spreading in space. This scenario [25] is consistent with what is seen in the experiments [20].

Vortex nucleation is another phenomenon which is possible in a superfluid but not in a classical Euler fluid. Typically nucleation occurs near a boundary where $\psi \to 0$, for example in the equatorial region of a rapidly moving ion [26,27], or at the edge of a trapped condensate [28] or at an intense rarefaction sound pulse [29] or at a dark soliton [30].

Vortex reconnections are special events which arise from the presence of the quantum stress Eq. (6), the term which makes Eq. (5) to differ from Eq. (3). Let D be the typical length scale of a flow. The ratio of the pressure term and the quantum stress term scales as $\hbar^2/(mE_0D^2)$ and becomes unity only if $D \sim \xi$. Thus the quantum stress term is important only at scales smaller than the vortex core radius, Away from vortices ρ_s is constant and Eq. (5) reduces to the classical Euler equation. The smallest macroscopic flow scale D in a superfluid vortex tangle is of the order of the average distance $\delta \approx L^{-1/2}$ between vortex lines; typical experimental values are $\delta \approx 10^{-3}$–10^{-4} cm, orders of magnitude bigger than $a \approx 10^{-8}$ cm. We conclude that, apart from vortex reconnecting events, in most of the fluid and at most times the quantum stress term in Eq. (5) is negligible, and the superfluid obeys classical Euler dynamics.

This consideration justifies the vortex filament approach to superfluid turbulence of Schwarz [31]. He modelled superfluid vortices as space curves of infinitesimal thickness which move under the velocity field which each line induces upon each other. Let $\mathbf{x}$ be a point along a filament and $\mathbf{x}'$ the derivative with respect to arclength. In the absence of the normal fluid, the velocity of the vortex at $\mathbf{x}$ is given by the Biot–Savart integral

$$\frac{\mathrm{d}\mathbf{x}}{\mathrm{d}t} = -\frac{\kappa}{4\pi}\oint \frac{(\mathbf{x}-\mathbf{z})}{|\mathbf{x}-\mathbf{z}|^3} \times \mathbf{dz}, \tag{9}$$

which expresses Euler's dynamics in integral form. A convenient approximation to Eq. (9) which is often used is the Local Induction Approximation (LIA), $\mathrm{d}\mathbf{x}/\mathrm{d}t \approx \beta \mathbf{x}' \times \mathbf{x}''$ where $\beta = \kappa/(4\pi)\ln(1/(|\mathbf{x}''|a))$. To implement Schwarz's approach, the computer code must introduce vortex reconnections when two vortex lines come sufficiently close to each other.

7. Dissipation of kinetic energy at absolute zero

Using the NLSE model, Nore et al. [32], made a discovery which shed light onto the nature of dissipation at absolute zero. They computed the temporal evolution of an arbitrary vortex configuration (a Taylor–Green flow) which evolved into a vortex tangle, and noticed that, while the total energy remained constant, incompressible kinetic energy was transformed into compressible sound energy. They also found that the energy spectrum is consistent with the $k^{-5/3}$ classical Kolmogorov spectrum observed experimentally [18] above and below T_c. Further work using both the vortex filament model [33] and the NLSE [34] gave spectra consistent with the classical Kolmogorov law.

7.1. Sound radiation by vortex motion

Generation of sound by vortex motion is a known classical effect. In the case of quantised vorticity, the effect can be accurately investigated in the controlled experimental conditions of trapped Bose–Einstein condensates. In particular, Parker et al. [35] suggested to add a Gaussian dimple at the bottom of the harmonic trapping potential. By tuning the depth of the dimple, the sound which is radiated by the vortices can escape the dimple, whereas the vortices remain trapped in it;

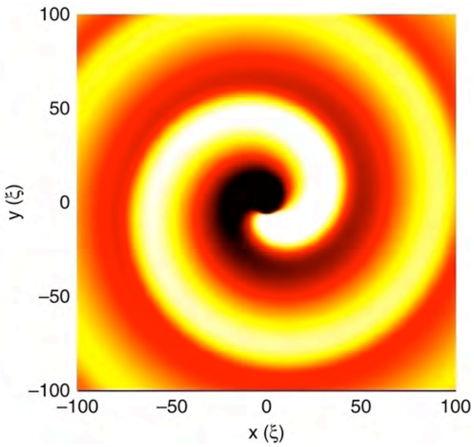

Fig. 6. Density waves created by an a single vortex which orbits a dimple trap (x and y coordinates are in units of ξ).

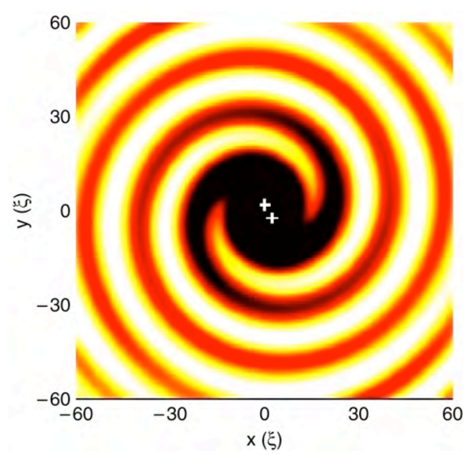

Fig. 7. Density waves created by a vortex–vortex pair.

this allowed Parker et al. to relate the vortex acceleration to the sound energy. Fig. 6 shows the dipolar radiation pattern generated by an off-centre vortex which moves along an orbit in the dimple; the quadrupolar pattern emitted by a corotating vortex–vortex pair is shown in Fig. 7.

Fig. 8 shows a two-dimensional vortex–antivortex pair which travels towards an isolated vortex [36]. The vortex pair is deflected, and the sound which is generated by the interaction is visible as a density ripple. After the interaction, the separation between the two vortices of the pair is reduced because some kinetic energy was turned into sound energy.

In three dimensions, sound radiation can be emitted by rotating Kelvin waves [37]. The power which is radiate per unit length by a co-rotating vortex–vortex pair separated by the distance ℓ is proportional to ℓ^{-6}. Taking $\ell \sim \delta$ (where δ is the average intervortex spacing deduced from the observed vortex line density L) we find that sound radiation by moving vortices cannot account for the observed decay of superfluid turbulence [21]: a much shorter length scale is necessary to radiate enough sound and explain the measurements.

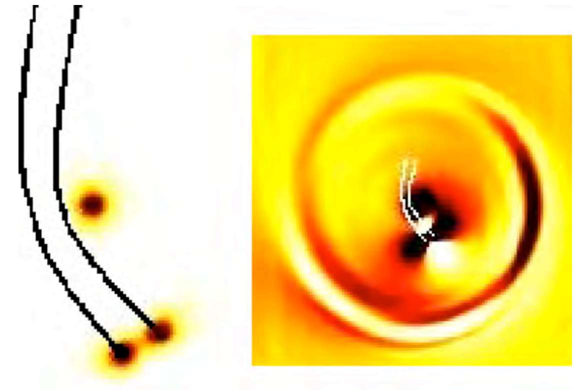

Fig. 8. Left: interaction of vortex–antivortex pair (coming from the top of the figure) with a third vortex. Right: corresponding density wave; the trajectory of the vortex pair is superimposed.

7.2. The Kelvin wave cascade

A mechanism to transfer energy towards small scales is the reconnection-driven cascade of smaller and smaller loops, eventually to thermal excitations [38], proposed by Feynman [39], later demonstrated numerically [40] and also modelled by a master-equation approach [41]. Here I shall describe other recently discovered mechanisms which can create very short length scales. The first is the Kelvin wave cascade [42]. Fig. 9 shows that when vortex lines collide and reconnect, the resulting reconnection cusps generate large amplitude Kelvin waves (compared to the wavelength) which interact with each other and create further Kelvin waves of shorter and shorter wavelength. At temperatures above 1 K the friction with thermal excitations would damp out the Kelvin waves, feeding energy into the normal fluid, but in the low temperature regime this energy sink does not exist. Kinetic energy is thus shifted to higher and higher wavenumbers k as in the energy spectrum shown in Fig. 10, until k is large enough that sound can be efficiently radiated away. The Kelvin wave cascade is thus similar to the Richardson cascade of classical Kolmogorov turbulence. The important difference is that the energy sink is acoustic for the Kelvin cascade and viscous for the Richardson cascade. Studying the Kelvin wave cascade numerically, it is important to realize that the LIA is not suitable because it conserves length, not energy (like the exact Biot–Savart law). There are still many open questions on the Kelvin wave cascade; current work attempts to determine the precise power law of the Kelvin cascade energy spectrum [43–45] and what happens in the transition regime [46,47] between the Richardson cascade ($k \ll 1/\delta$) and the Kelvin wave cascade ($k \gg 1/\delta$).

7.3. Reconnection pulses

Another more direct mechanism to turn kinetic energy into sound energy was found by Leadbeater et al. [48] by studying the collision of vortex rings in the NLSE model, see Fig. 11. They found that at the point of reconnection a rarefaction pulse is created, expanding in size and becoming more shallow as it moves away. Fig. 12 shows density profiles of the same pulse at

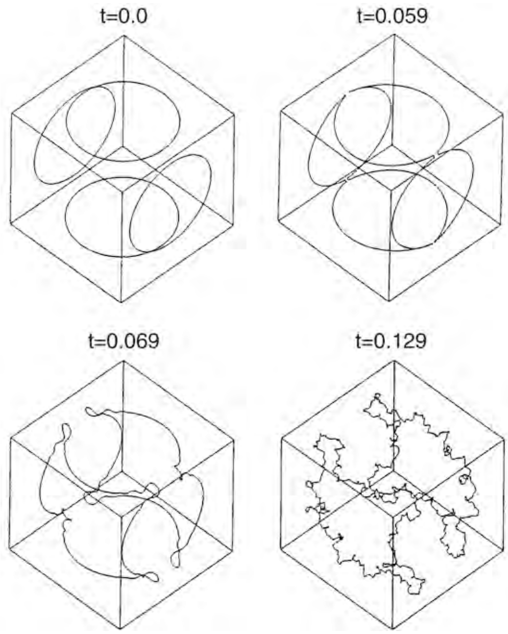

Fig. 9. Collision of four vortex rings. $t = 0$: initially the rings are set to travel against each other; $t = 0.59$: cusps created by the vortex reconnections; $t = 0.069$: the cusps relax and launch large amplitude Kelvin waves along the vortices. $t = 0.129$: generation of Kelvin waves of larger and larger wavenumber.

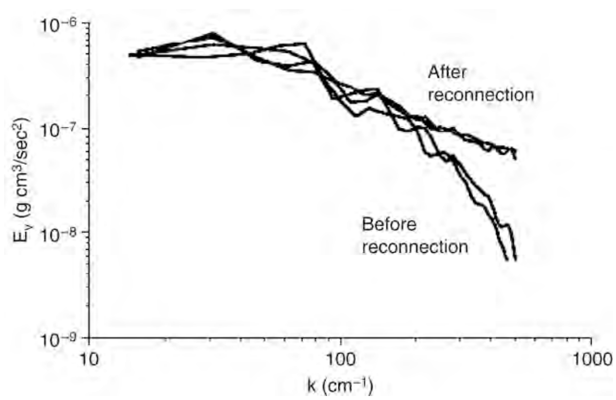

Fig. 10. Energy spectrum before the collision of the four vortex rings of the previous figure, and after the collision. Note the saturated energy spectrum.

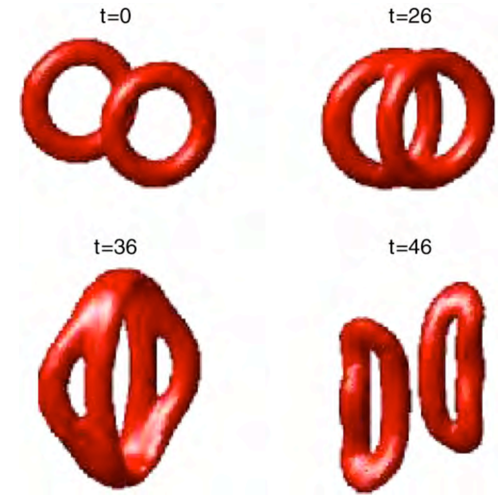

Fig. 11. Collision of vortex rings in the NLSE model. The time sequence shows the interaction of two rings, which are initially slightly offset with respect to each other.

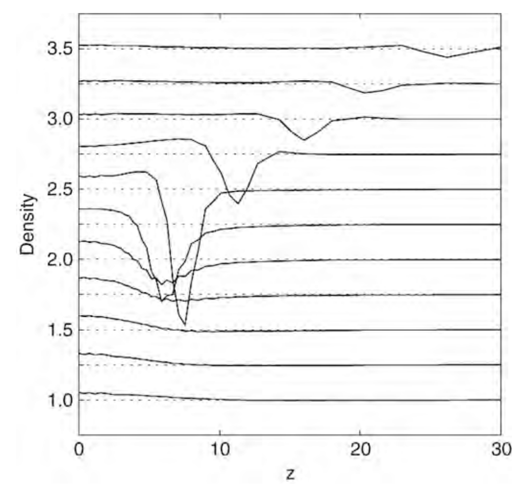

Fig. 12. Density along the z-axis for a collision of two vortex rings initially offset with respect to each other. The eleven curves correspond to different times. Just before the reconnection (bottom curve) the density is uniform except for a slight increase near the origin indicating the approaching rings. At the reconnection a rarefaction pulse is created in which the depth drops to zero. As the pulse moves away, the depth decreases.

different times following the vortex reconnection. Immediately after the reconnection the pulse is short (few times the healing length ξ) and intense (the density drops to zero). Later the pulse spreads out and becomes more shallow as it moves away. The kinetic energy which is transformed into sound energy of the pulse depends on the initial impact parameters, and it is maximum if the two rings collide head-on and destroy each other.

Calculations involving a small number of interacting vortex rings [49] show that in general the Kelvin wave cascade and the rarefaction pulses are present at the same time. Fig. 13 shows that the total vortex length, which can be taken as a proxy for total kinetic energy, decreases with time. The sudden drops in length are caused by the creation of rarefaction pulses, and the oscillations are due to Kelvin waves. The relative importance of the Kelvin wave cascade and the rarefaction pulses depends on the vortex line density L and how the vortex reconnection rate scales with L [50].

8. Conclusions

The vortex filaments shown in Fig. 3 are similar to coherent vortex structures computed in classical turbulence [51,52]. The similarity of superfluid turbulence to classical turbulence seems to go beyond pictures: the same laws of vortex dynamics are present, and the same $k^{-5/3}$ Kolmogorov spectrum is observed. In many respects superfluid turbulence is simpler than classical turbulence: superfluid vortices are discrete filaments with the same circulation and the same microscopic core structure, whereas in classical turbulence vorticity is continuous and eddies can be of any size and strength; moreover, the flow around each superfluid vortex line is potential, whereas in

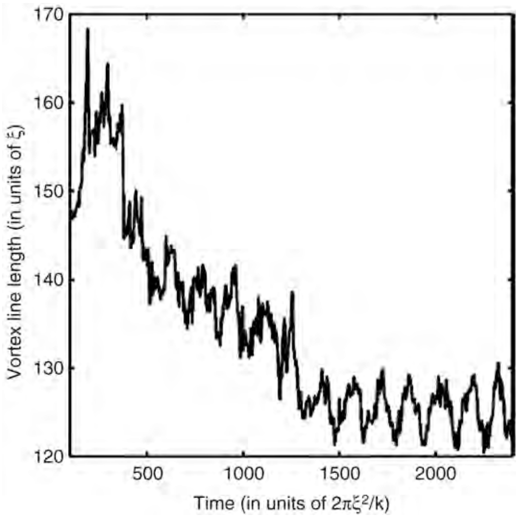

Fig. 13. Total vortex length (which can be interpreted as measure of kinetic energy) vs time for the interaction of a small number of vortex rings.

classical turbulence eddies have arbitrary rotation curves; finally, the superfluid is inviscid, whereas a classical fluid is viscous.

The classical theory of homogeneous, isotropic turbulence deals with incompressible fluids. In superfluid turbulence density changes are relevant only when one considers effects at length scales of the order of the vortex core radius (e.g., vortex reconnections) or at length scales bigger than the vortex core but still much smaller than the average intervortex distance δ (eg sound emission by Kelvin waves). At length scales larger than δ, superfluid turbulence can be considered incompressible. Indeed, for $k \ll 1/\delta$, superfluid turbulence and classical turbulence seem to obey the same Kolmogorov spectrum (although numerical calculations with better resolution are needed). It is the nature of the energy sink at high wavenumbers which is very different: viscous for the classical fluid and acoustic for the quantum fluid.

In conclusion, the NLSE can be interpreted as a way to regularise the Euler equation, removing the singularities on the axes of vortices and allowing the vortices to reconnect. Superfluid turbulence at very low temperatures can be interpreted as the turbulence of an incompressible, reconnecting Euler fluid, in which the energy sink at very small scales is acoustic.

The solution of our puzzle is that, although the superfluid has zero viscosity, the Reynolds number is infinite only nominally. Dissipation exists even in the limit of absolute zero: organised kinetic energy can be turned into disorganised sound energy. Vortex reconnections are the key to understand the puzzle, because they trigger both the Kelvin wave cascade and rarefaction pulses.

The approach of Schwarz is convenient because it allows the calculation of more intense vortex tangles than the NLSE, but it is incompressible, so it does not include the acoustic loss of kinetic energy which is crucial at low T. However, the finite discretisation along the filaments introduces a small, unavoidable energy sink. Future work should calibrate this numerical dissipation (particularly during vortex reconnections) against results obtained using the NLSE, in order to create a more realistic model of superfluid turbulence.

Acknowledgments

I am grateful to W.F. Vinen for stimulating discussions. This work is supported by EPSRC grants GR/T08876/01 and EP/D040892/1.

References

[1] S.I. Davis, P.C. Hendry, P.V.E. McClintock, Decay of quantised vorticity in superfluid He-4 at mK temperatures, Physica B 280 (2000) 43–44.
[2] D.I. Bradley, D.O. Clubb, S.N. Fisher, A.M. Guenault, R.P. Haley, C.J. Matthews, G.R. Pickett, V. Tsepelin, K. Zaki, Decay of pure quantum turbulence in superfluid He-3-B, Phys. Rev. Lett. 96 (2006) 035301.
[3] C.F. Barenghi, R.J. Donnelly, W.F. Vinen (Eds.), Quantized Vortex Dynamics And Superfluid Turbulence, Springer Verlag, 2001.
[4] N.G. Parker, B. Jackson, A.M. Martin, C.S. Adams, Vortices in Bose–Einstein condensates. arXiv:0704.0146, 2007.
[5] N. Andersson, Modelling the dynamics of superfluid neutron stars, Astrophys. Space Sci. 308 (2007) 395–402.
[6] R.J. Donnelly, Ultra-High Reynolds Number Flows Using Cryogenic Helium: An Overview, in: R.J. Donnelly, K.R. Sreenivasan (Eds.), Ultra-High Reynolds And Rayleigh Number Flows, Springer Verlag, 1998, pp. 1–28.
[7] J.J. Niemela, L. Skrbek, K.R. Sreenivasan, R.J Donnelly, Turbulent convection at very high Rayleigh numbers, Nature 406 (2000) 439–439.
[8] T. Zhang, S.W. Van Sciver, Nature Phys. 1 (2005) 36–38.
[9] G.P. Bewley, D.P. Lathrop, K.R. Sreenivasan, Superfluid helium: visualization of quantized vortices, Nature 441 (2006) 588–588.
[10] C.J. Pethick, H. Smith, Bose-Einstein Condensation in Dilute Gases, Cambridge University Press, Cambridge, 2001.
[11] L.D. Landau, E.M. Lifschitz, Fluid Mechanics, Pergamon Press, 1987.
[12] A.P. Finne, T. Araki, R. Blaauwgeers, V.B. Eltsov, N.B. Kopnin, M. Krusius, L. Skrbek, M. Tsubota, G.E. Volovik, An intrinsic velocity-independent criterion for superfluid turbulence, Nature 424 (2003) 1022–1025.
[13] R.J. Donnelly, Quantized Vortices in Helium II, Cambridge University Press, Cambridge, 1991.
[14] P.H. Roberts, N.G. Berloff, The nonlinear Schroedinger equation as a model of superfluidity, in: C.F. Barenghi, R.J. Donnelly, W.F. Vinen (Eds.), Quantized Vortex Dynamics and Superfluid Turbulence, Springer Verlag, 2001, pp. 235–257.
[15] W.F. Vinen, Mutual friction in a heat current in liquid helium II. Experiments in steady heat currents, Proc. Roy. Soc. A 240 (1957) 114–127.
[16] C.F. Barenghi, A.V. Gordeev, L. Skrbek, Depolarization of decaying counterflow turbulence in He II, Phys. Rev. E 74 (2006) 026309.
[17] M.R. Smith, R.J. Donnelly, N. Goldenfeld, W.F. Vinen, Decay of vorticity in homogeneous turbulence, Phys. Rev. Lett. 71 (1993) 2583–2586.
[18] J. Maurer, P. Tabeling, Local investigation of superfluid turbulence, Europhys. Lett. 43 (1998) 29–34.
[19] P.E. Roche, P. Diribarne, T. Didelot, O. Francais, L. Rousseau, H. Willaime, Vortex density spectrum of quantum turbulence, Europhys. Lett. 77 (2007). Art. No. 66002 2007.
[20] S.N. Fisher, A.J. Hale, A.M. Guenault, G.R. Pickett, Generation and detection of quantum turbulence in Superfluid He-3B, Phys. Rev. Lett. 86 (2001) 244–247.
[21] W.F. Vinen, J.J. Niemela, Quantum turbulence, J. Low Temp. Phys. 128 (2002) 167–231; J. Low. Temp. Phys. 129 (2002) 213 (erratum).
[22] J. Koplik, H. Levine, Vortex reconnection in superfluid helium, Phys. Rev. Lett. 71 (1993) 1375–1378.
[23] A.K.M. Hussain, Coherent structures in turbulence, J. Fluid Mech. 173 (1986) 303–356.

[24] M.V. Melander, F. Hussain, Cross linking of 2 antiparallel vortex tubes, Phys. Fluids A 1 (1989) 633–639.
[25] C.F. Barenghi, D.C. Samuels, Evaporation of a packet of quantized vorticity, Phys. Rev. Lett. 89 (2002) 155302–155305.
[26] T. Winiecki, C.S. Adams, Motion of an object through a quantum fluid, Europhys. Lett. 52 (2000) 257–263.
[27] T. Frisch, Y. Pomeau, S. Rica, Transition to dissipation in a model of superflow, Phys. Rev. Lett. 69 (1992) 1644–1648.
[28] M. Tsubota, K. Kasamatsu, M. Ueda, Vortex lattice formation in a rotating Bose–Einstein condensate, Phys. Rev. A 65 (2002) 0236031–0236034.
[29] N.G. Berloff, C.F. Barenghi, Vortex nucleation by collapsing bubbles in Bose–Einstein condensates, Phys. Rev. Lett. 93 (2004) 090401–090404.
[30] B.P. Anderson, P.C. Haljan, C.A. Regal, D.L. Feder, L.A. Collins, C.W. Clark, E.A. Cornell, Watching dark solitons decay into vortex rings in a Bose-Einstein condensate, Phys. Rev. Lett. 86 (2001) 2926–2929.
[31] K.W. Schwarz, Three-dimensional vortex dynamics in superfluid 4He: Homogeneous superfluid turbulence, Phys. Rev. B 38 (1988) 2398–2417.
[32] C. Nore, M. Abid, M.E. Brachet, Kolmogorov turbulence in low temperature superflows, Phys. Rev. Lett. 78 (1997) 3896–3899.
[33] T. Araki, M. Tsubota, S.K. Nemirovskii, Energy spectrum of superfluid turbulence with no normal-fluid component, Phys. Rev. Lett. 89 (2002) 145301–145303.
[34] M. Kobayashi, M. Tsubota, Kolmogorov spectrum of superfluid turbulence: Numerical analysis of the Gross–Pitaevksii equation with a small-scale dissipation, Phys. Rev. Lett. 94 (2005) 065302–065305.
[35] N.G. Parker, N.P. Proukakis, C.F. Barenghi, C.S. Adams, Controlled vortex sound interaction in Bose-Einstein condensates, Phys. Rev. Lett. 92 (2004) 160403–160406.
[36] C.F. Barenghi, N.G. Parker, N.P. Proukakis, C.S. Adams, Decay of quantized vorticity by sound emission, J. Low Temp. Phys. 138 (2005) 629–634.
[37] W.F. Vinen, Decay of superfluid turbulence at a very low temperature: The radiation of sound from a Kelvin wave on a quantized vortex, Phys. Rev. B 64 (2001) 134520–134523.
[38] D.C. Samuels, C.F. Barenghi, Vortex heating in superfluid helium at low temperatures, Phys. Rev. Lett. 81 (1998) 4381–4384.
[39] R.P. Feynman, Application of quantum mechanics to liquid helium, in: C.J. Gorter (Ed.), Progress in Low Temperature Physics, vol. I, North-Holland, Amsterdam, 1955, pp. 17–53.
[40] M. Tsubota, T. Araki, S.K. Nemirovskii, Dynamics of vortex tangle without mutual friction in superfluid ^{4}He, Phys. Rev. B 62 (2000) 11751–11762.
[41] S.K. Nemirovskii, Evolution of a network of vortex loops in He II: Exact solution of the rate equation, Phys. Rev. Lett. 96 (2006) 015301–015304.
[42] D. Kivotides, J.C. Vassilicos, D.C. Samuels, C.F. Barenghi, Kelvin wave cascade in superfluid turbulence, Phys. Rev. Lett. 86 (2001) 3080–3083.
[43] W.F. Vinen, M. Tsubota, A. Mitani, Kelvin-wave cascade on a vortex in superfluid He-4 at a very low temperature, Phys. Rev. Lett. 91 (2003) 135301–135304.
[44] E. Kozik, B. Svistunov, Kelvin-wave cascade and decay of superfluid turbulence, Phys. Rev. Lett. 92 (2004) 035301–035304.
[45] S. Nazarenko, Kelvin wave turbulence generated by vortex reconnections, JETP Lett. 84 (2007) 585–587.
[46] E. Kozik, B. Svistunov, Kolmogorov and Kelvin wave cascade in superfluid turbulence at $T = 0$: What is in between? arXiv:condmat/0703047, 2007.
[47] V.S. L'vov, S. Nazarenko, O. Rudenko, Bottleneck crossover between classical and quantum turbulence, Phys. Rev. B 76 (2007) 024520–024529.
[48] M. Leadbeater, T. Winiecki, D.C. Samuels, C.F. Barenghi, C.S. Adams, Sound emission due to superfluid vortex reconnections, Phys. Rev. Lett. 86 (2001) 1410–1413.
[49] M. Leadbeater, D.C. Samuels, C.F. Barenghi, C.S. Adams, Decay of superfluid vortices due to Kelvin wave radiation, Phys. Rev. A 67 (2002) 015601.
[50] C.F. Barenghi, D.C. Samuels, Scaling laws of vortex reconnections, J. Low Temp. Phys. 36 (2004) 281.
[51] A. Vincent, M. Meneguzzi, The dynamics of vorticity tubes in homogeneous turbulence, J. Fluid Mech. 258 (1994) 245–254.
[52] M. Farge, G. Pellegrino, K. Schneider, Coherent vortex extraction in 3D turbulent flows using orthogonal wavelets, Phys. Rev. Lett. 87 (2001) 0545011–0545014.

Available online at www.sciencedirect.com
ScienceDirect
Physica D 237 (2008) 2203–2209
PHYSICA D
www.elsevier.com/locate/physd

On cylindrically converging shock waves shaped by obstacles

Veronica Eliasson[a,b,*], William D. Henshaw[c], Daniel Appelö[c]

[a] KTH Mechanics, KTH, SE-100 44 Stockholm, Sweden
[b] Department of Mechanical Engineering, University of California, Berkeley, CA 94720, USA
[c] Lawrence Livermore National Laboratory, Livermore, CA 94551, USA

Available online 8 December 2007

Abstract

Motivated by recent experiments, numerical simulations of cylindrically converging shock waves were performed. The converging shocks impinged upon a set of 0–16 regularly space obstacles. For more than two obstacles the resulting diffracted shock fronts formed polygonal shaped patterns near the point of focus. The maximum pressure and temperature as a function of the number of obstacles were studied. The self-similar behavior of cylindrical, triangular and square-shaped shocks was also investigated.

PACS: 47.10.ab; 47.40Nm

Keywords: Converging shock; Mach reflection; Regular reflection; Adaptive mesh refinement; Overlapping structured grids

1. Introduction

Converging shock waves can be found in a broad range of situations, from astronomical size events like supernovae collapse, to microscopic events such as sono-luminescence when tiny bubbles collapse so strongly as to produce light. Shock waves are an effective method to generate high temperatures and pressures for experimental and engineering purposes and thus remain an area of continued research.

Over the years many experiments have been performed on cylindrically converging shock waves (see e.g. [1,2]). It is common to use annular shock tubes to create and study converging shock waves. The converging shocks are often visualized by either schlieren photographs or interferograms taken during the focusing process. These methods give a measure of the shock position and shape development as a function of time. With these techniques it is not possible to measure other quantities, like temperatures and pressures. In a recent paper Eliasson et al. [3] presented experimental results on the light emission occurring at the focal point for converging shock waves of different shapes. By analyzing the response from a photomultiplier tube, Eliasson et al. found that the amount of emitted light depended on the shape of the converging shock wave. In [3] only a small number of obstacles were considered, which resulted in polygons with a small number of sides.

In this paper we present numerical simulations of the experimental setup used in [3]. We consider cylindrically converging shock waves shaped by 0–16 obstacles, yielding 17 different configurations. From monitoring the maximum pressure and temperature as the shocks converge, we find that a small number of obstacles gives a low maximum pressure and temperature, compared to the case with no obstacles. This is consistent with the amount of light observed in [3] for zero, one, three and four obstacles. However, as we increase the number of obstacles we see a gradual increase in the maximum pressure and temperature; this is somewhat surprising since a greater portion of the initial cylindrical shock is reflected by the obstacles. The present model, the Euler equations for an ideal gas, does not take real gas and ionization effects into account, thus it is not possible to make detailed predictions on light production. Our numerical results suggest that further experiments for more than four obstacles would be of great interest.

* Corresponding author at: KTH Mechanics, KTH, SE-100 44 Stockholm, Sweden.
E-mail address: veronica@mech.kth.se (V. Eliasson).

0167-2789/$ - see front matter © 2007 Elsevier B.V. All rights reserved.
doi:10.1016/j.physd.2007.11.021

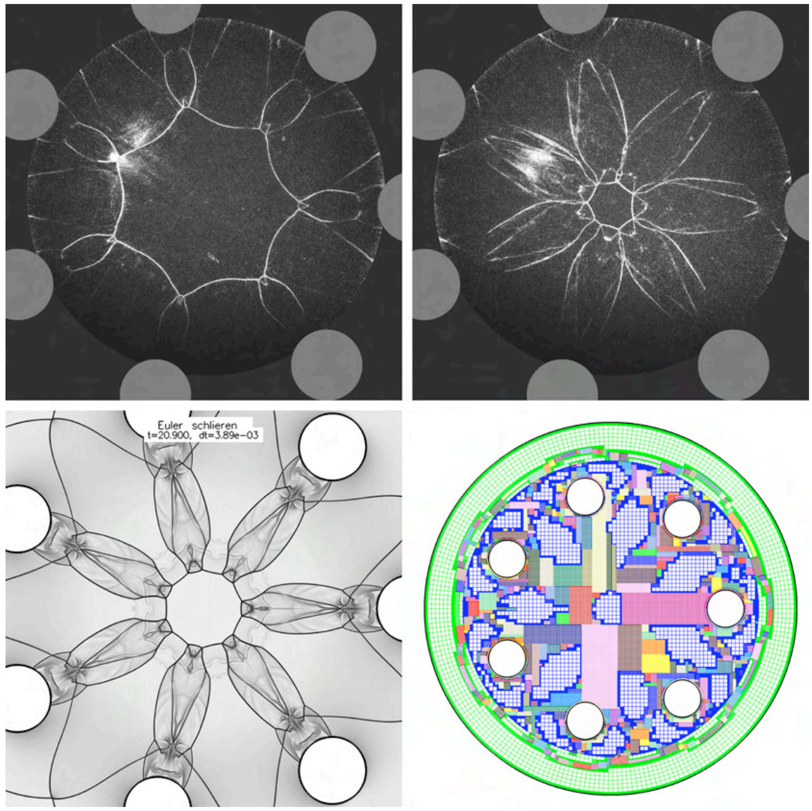

Fig. 1. Experimental and numerical schlieren photographs of a converging polygonal shock wave. Top: experimental results for seven obstacles. Lower left: numerical results. Lower right: an AMR grid with two levels of refinement adapted to the shock structures (every eighth line is plotted).

Converging shock waves of different polygonal shapes have been studied for example in [4,5]. For a polygonal shock the regions of high curvature, such as corners, generally travel faster than the planar parts. This leads to a reconfiguration of the shape of the shock wave during the focusing process. For example, a square-shaped shock wave will transform into an octagon and then back to a square again. This process repeats as the shock focuses provided there are no other disturbances to interrupt it.

In this work we use the method suggested and tested in experiments by Eliasson et al., [4] to produce converging polygonal shock waves. The numerical simulations were performed using a state of the art adaptive mesh refinement (AMR) flow solver. Disturbances in the form of cylindrical obstacles were introduced in front of an initially cylindrical converging shock. The obstacles used to shape the shock are not small. Therefore it takes some time for the shock front to reach the asymptotic state described by the theory of Schwendeman and Whitham [5]. From our highly resolved numerical simulations we find that only at the very final stage of the convergence does a shock perturbed by four obstacles become square-shaped. At this stage, the mean radius of the shock is well described by Guderley's [6] self-similar solution, giving a base solution around which geometrical shock dynamics [5] can be utilized. The fact that the polygonal shape of the shock is attained only at the final stage, where characteristic length scales (the sides of the polygon) are very small compared to the initial scales (the diameter of initial shock), means that the numerical simulations become quite challenging.

2. Numerical method and experiments

The Euler equations of gas dynamics are solved numerically using a high-order accurate Godunov method [7,8]. The geometry is discretized with overlapping structured grids. The initial grids for the geometry are constructed with the overlapping grid generator that comes with the Overture software package. Adaptive mesh refinement is used to dynamically track the shocks and contacts. The refinement meshes are automatically created every few time steps, based on an estimate of the error. For further details please refer to [7,8] where the accuracy and convergence rates of the numerical method are carefully validated, and where solutions computed using different grids are compared. The basic conclusions are that excellent results are obtained with the scheme. The software, along with references describing the approach can be found at http://www.llnl.gov/casc/Overture. The initial conditions in front of the shock are set to be a gas at pressure $p = 13.33$ kPa (100 Torr) and at room temperature $T = 294$ K, where $\gamma = 1.4$, $R_g = 287.06$ J/kg K and $p = \rho R_g T$. The shock front is given an initial shock Mach number of $M = 2.4$. The state behind the shock is determined by the standard shock relations. The diameter of the computational domain is set to 150 mm.

The following cases were simulated: an initially cylindrical shock wave perturbed by 0–16 obstacles (cylinders with a

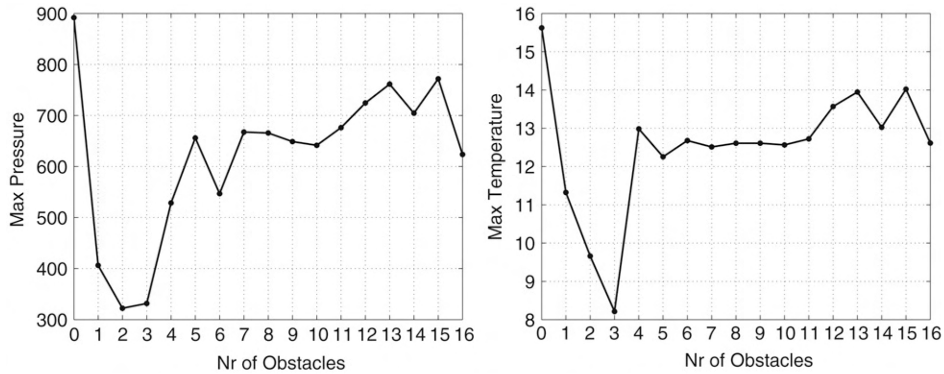

Fig. 2. Maximum pressure and temperature near the focal point as a function of the number of cylinders.

diameter of 15 mm) placed in a symmetrical pattern at a radial distance of 46.25 mm from the focal point (see Fig. 1). The boundary conditions on the cylinders are modeled by slip wall conditions. Supersonic outflow boundary conditions are imposed at the perimeter of the computational domain.

In a first set of simulations we compute solutions with 0–16 obstacles to study how quantities like the maximum pressure and temperature vary with the number of obstacles. For these computations the initial grid is composed of a Cartesian background grid (covering most of the domain), an annular perimeter grid and embedded cylindrical grids around each obstacle. The annular grids have a cell size adjusted to the (non-refined) Cartesian grid which has a grid-spacing of 0.2 mm. We use two levels of AMR with a refinement ratio of four yielding a smallest grid size of 50 μm. The main features of the flow are very similar when computed using a coarser base mesh or fewer levels of refinement. However, additional fine scale features appear as the mesh is refined.

In a second set of experiments, we use an initial grid with a Cartesian grid-spacing of 0.5 mm but with four levels of AMR with refinement ratio four, yielding a smallest grid size of 7.8125 μm. With this setup, we limit our simulations to the cases with zero, three and four obstacles and focus on the asymptotic behavior of the converging shocks.

2.1. *Maximum pressure and temperature as a function of the number of cylinders*

The pressure and temperature near the focal point were measured for all 17 cases. Fig. 2 shows the maximum pressure and temperature as a function of the number of cylinders. Fig. 7 shows the numerically computed schlieren images for some of these cases. The results show that the undisturbed cylindrical shock gives the highest pressure and temperature near the focal point. This should be expected, since in all other cases part of the flow is reflected by the obstacles and never reaches the focal point. For a small number of cylinders (one to six) the maximum values are low. This is most likely caused by the fact that all parts of the shock front do not reach the focal point at the same time and hence the focusing effect is lost (see Fig. 7). Higher pressure and temperatures are obtained for the cases with a larger number of obstacles (seven to thirteen).

Table 1
Self-similarity exponents for converging cylindrical shock waves

	Self-similar exponent
Present results (zero obstacles)	0.844
Present results (four obstacles)	0.835
Guderley (1942) [6]	0.834
Butler (1954)	0.835217
Stanyukovich (1960)	0.834
Welsh (1967)	0.835323
Mishkin & Fujimoto (1978)	0.828
Nakamura (1983)	0.8342, $M_s = 4.0$
	0.8345, $M_s = 10.0$
de Neef & Nechtman[a] (1978)	0.835 ± 0.003
Kleine[a] (1985)	$0.832 + 0.028, -0.043$
Takayama[a] (1986)	0.831 ± 0.002

[a] Experiments.

2.2. *Comparison with Guderley's self-similar solution*

Guderley [6] derived a self-similar solution for the radius of the converging shock wave as a function of time, which can be expressed as

$$R = \xi_0 \, (t_c - t)^{\alpha} \, . \tag{1}$$

Here α is the self-similar power law exponent, R is the radius of the converging shock wave, t is the time, t_c is the time when the shock wave arrives at the center of convergence and ξ_0 is a constant. Guderley found the self-similar power law exponent for cylindrical shock waves to be $\alpha = 0.834$ and this has been confirmed by many other investigations (see Table 1).

In this study we investigate when the converging shocks shaped by obstacles are described by Guderely's solution. We fit data from the numerical experiments to Eq. (1) in order to find the similarity exponent, α. We do this for the three cases of a cylinder, a triangle and a square-shaped shock.

Zero Obstacles. To test the accuracy of the numerical algorithms we first consider an unperturbed converging shock and extract the distance between the shock front and the focal point. Starting at time 20 we save solutions every 0.02 time units until time 22.46. For each of the saved solutions we find the position along rays starting at the focal point, where the pressure is half of its global maximum. Precisely, we use rays along the positive and negative x and y axis and the four diagonals in between. We fit the extracted data to Eq. (1) by

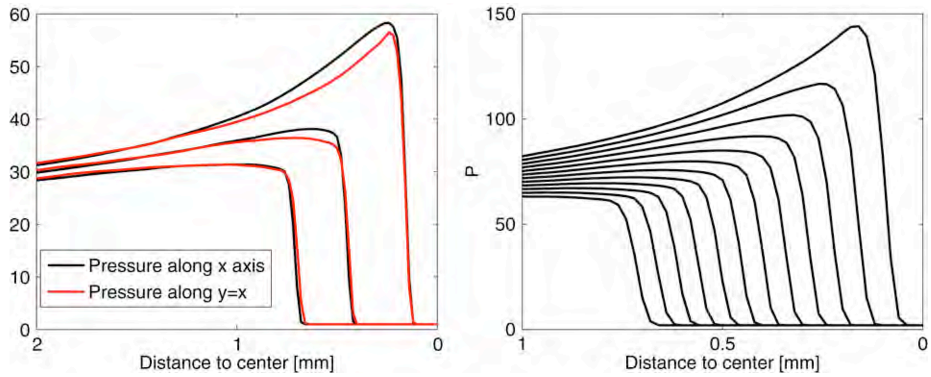

Fig. 3. The case with zero obstacles. Left: the solution along the negative x axis and the line $y = x, x > 0$, at times 22.28, 22.38, 22.48. The difference between the solutions increases as the shock sharpens up. Right: the value of the pressure averaged along the positive and negative x and y axes at times 22.34–22.56 with time spacing 0.02. Note that the shock is accelerating.

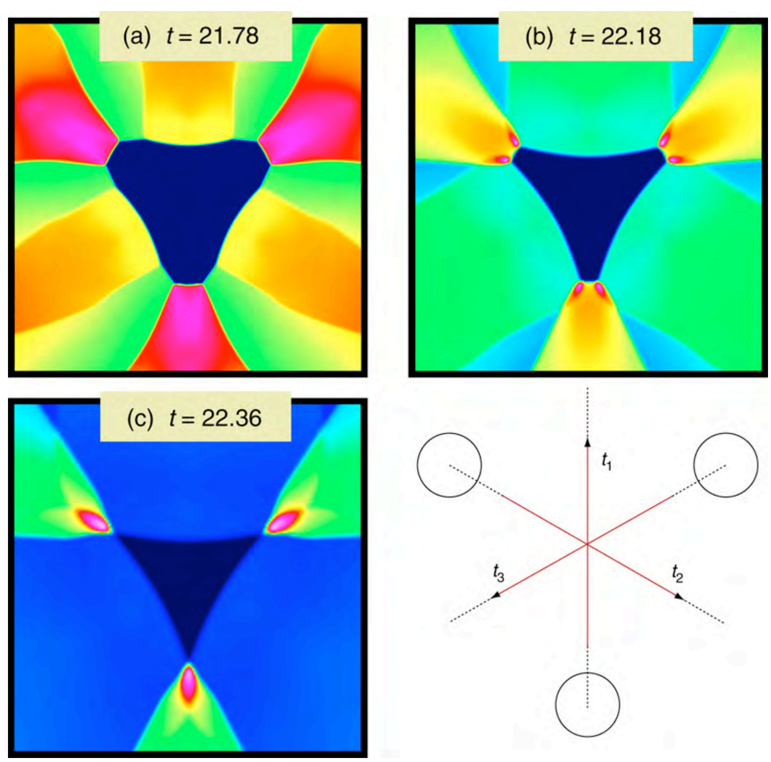

Fig. 4. Contours of the pressure for three obstacles showing the formation of the triangular converging shock.

minimizing $\sum_i |R(t_i) - \xi_0 (t_c - t_i)^\alpha|^2$, thus finding α, t_c and ξ_0. Here $R(t_i)$ is taken as the average of the data from the eight rays at time t_i. The value of the self-similar power law exponent, $\alpha = 0.844$, agrees well with other values in the literature (see Table 1). Note that for the rays used here, the anisotropy in the solution due to grid effects is largest (see Fig. 3), thus the errors in the results obtained using these values are likely maximized.

Three Obstacles. The triangular shape was generated by placing three obstacles in an equilateral triangular pattern. Close to the focal point, the shock wave assumes a triangular shape and the similarity exponent can be found. The shock front just before the triangular shape appears is shown in Fig. 4(a)–(b). The plane sides develop as soon as the reflected part of the shock, originating from the reflection off the cylinder, has passed the whole side of the triangle. In Fig. 4(a) the reflected shock is still interacting with the sides of the triangle. In (b), the reflected shocks have passed the sides of the triangle and in (c) a triangle-shaped shock is observed. Once the triangle-shaped shock has formed it remains for the duration of the focusing process since the plane sides undergo regular reflection; this is consistent with results in [9]. For this experiment the self-similar exponent was computed from solution data along the three lines shown in Fig. 4(d). The pressure, averaged along the three lines, is plotted in Fig. 5. Referring to Fig. 5, there is a significant difference in the profile of the pressure in the regions to the left and right of the focal point at the origin; we therefore make two fits to the data. Using the averaged values of the solutions at times 22.34–22.56 we get a self-similar exponent $\alpha = 1.155$ for the data to the left and $\alpha = 0.977$ to the data on the right. The fact the similarity

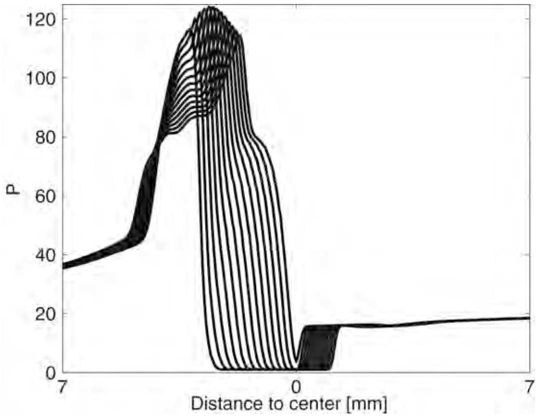

Fig. 5. The value of the pressure with three obstacles averaged along the lines t_1, t_2, t_3 of Fig. 4. The solutions are displayed at times 22.28–22.5 with time spacing 0.02. The solution to the left of the origin corresponds to the part of the lines t_1, t_2, t_3 closest to the obstacles.

exponent is not exactly equal to unity probably results from the sides not being perfectly plane until the very last stages of the focusing process (see Fig. 4(c)).

Four Obstacles. A square-shaped shock was obtained by perturbing a cylindrical shock with four obstacles placed in a square formation (see Fig. 6). A square-shaped shock undergoes Mach reflection if the shock Mach number is larger than 1.24, [9], as is the case here. This means that when two plane sides meet in a corner, a new shock (the Mach stem) is created. The Mach stem travels faster than the adjacent plane sides and will consume these; repeating for the rest of the focusing process. In the present setup, the Mach stem will form along the lines s_2 and s_4 (see Fig. 6(d)) and expand outwards towards the lines s_1 and s_3. When adjacent stems meet the square has turned 45 degrees. Because of this reconfiguration process it is impractical to detect the location of the shock along rays. Instead we compute the area of the domain where the pressure is within 5% of its quiescent state. Assuming the area to be proportional to the square of the mean radius, we can use the square root of the area instead of R to find α from (1). Using solutions from the final stages, corresponding to times 21.96–22.7 (with a time step of 0.02), we obtain a self-similar exponent $\alpha = 0.835$. This is in agreement with the theory in [5]. It should be noted that in general the computed value of the self-similar exponent depends slightly on the data set used. In particular for the case of four obstacles, there is a tendency for the computed value of α to be somewhat larger when solutions at earlier times are included.

3. Conclusions

The shape of the shock front and the diffraction pattern behind the shock in the numerical simulations agree well with the experimental results in [4]. The maximum pressure and temperature near the focal point were computed using 0–16 cylindrical obstacles. The highest maximum pressure and temperature occurred with zero obstacles. With a small number of obstacles (one to six) the maximum pressure and temperature were lower than with a large number of obstacles (seven to

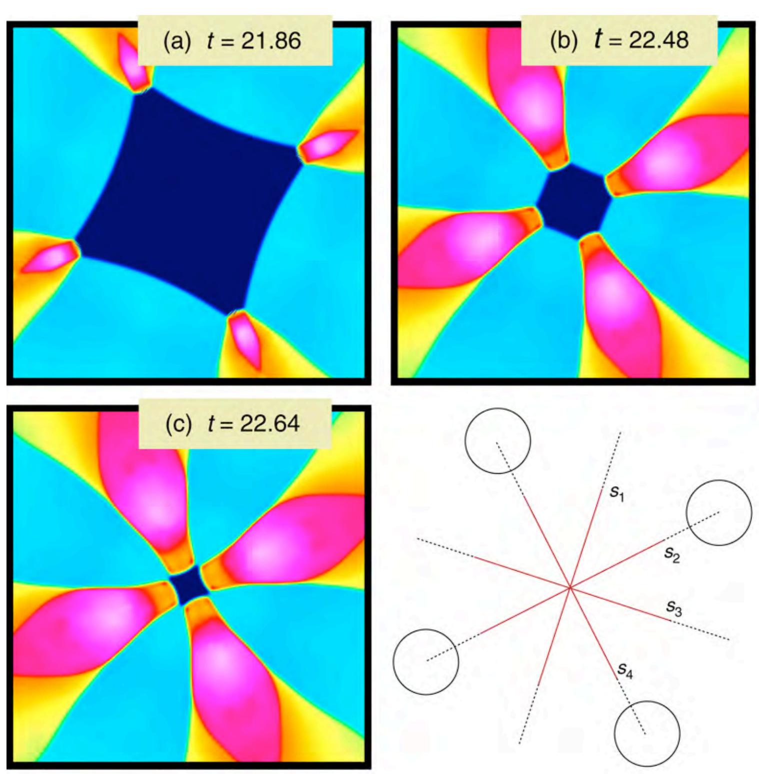

Fig. 6. Contours of the pressure for four obstacles. The square shaped shock front periodically reforms, rotated by 45 degrees.

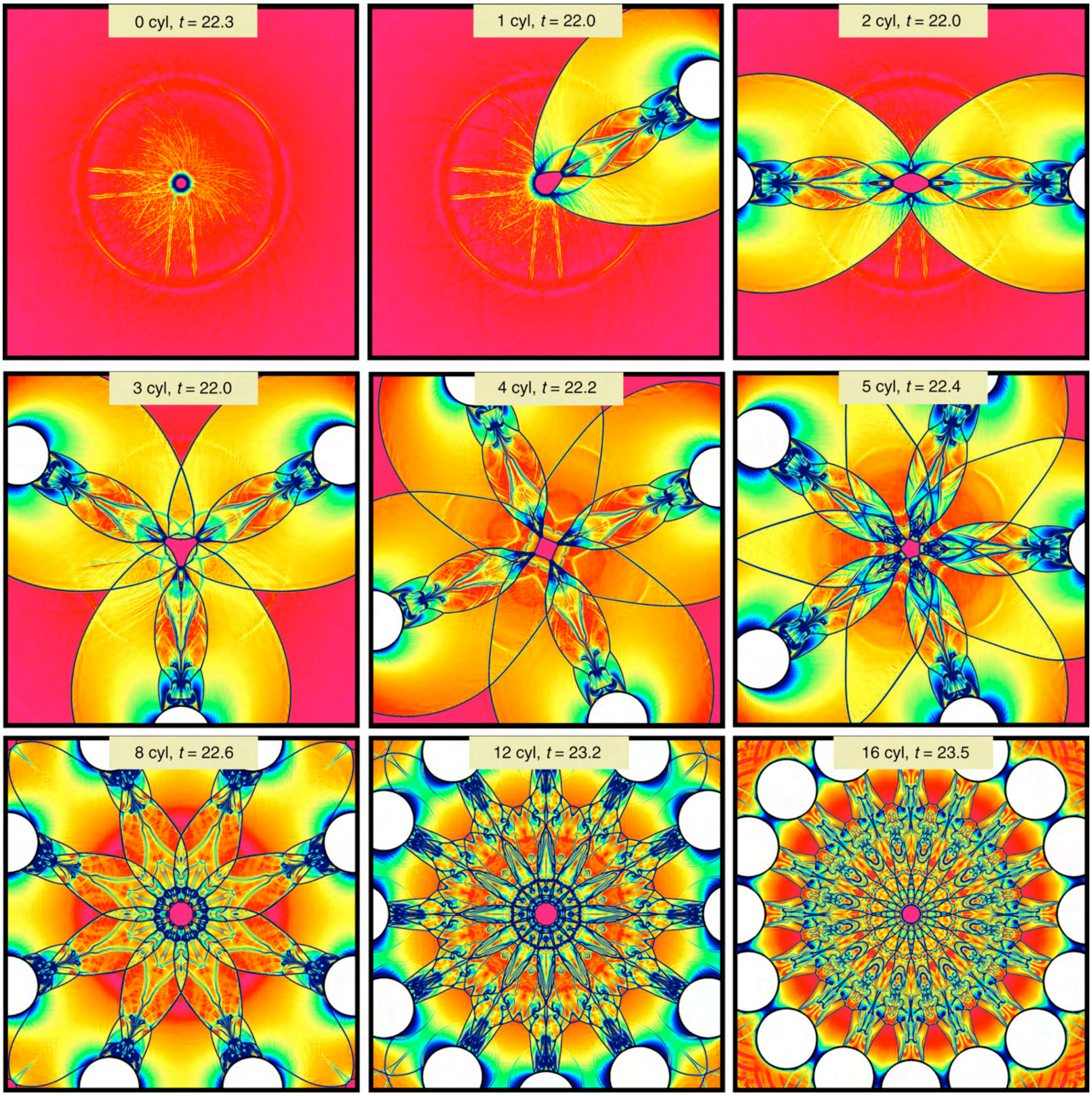

Fig. 7. Numerically computed schlieren images for a converging shock diffracted by 0, 1, 2, 3, 4, 5, 8, 12 and 16 cylindrical obstacles. The dominant portion of the shock is located near the focal point. This part of the shock front is far from circular in cases 1–5, whereas it is close to circular in cases 8–16.

sixteen). During the final stages of the focusing process, a self-similar solution is obtained for the triangular and the square-shaped shock. The triangle-shaped shock undergoes regular reflection and the same shape remains during the focusing process. For the triangle, the self-similar exponent depends on the direction in which the location of the shock front is measured. For the two directions measured here the exponents were $\alpha = 0.977$ and $\alpha = 1.155$, compared to the expected value of 1. The square-shaped shock undergoes Mach reflection and the self-similar exponent was found to be $\alpha = 0.835$, in agreement with other published results.

Acknowledgments

V.E. thanks Professor A.J. Szeri at the Department of Mechanical Engineering, UC Berkeley, for hosting her visit and providing computational resources. V.E. was supported by KTH Mechanics, Stiftelsens Bengt Ingeströms Stipendiefond and Helge Ax:son Johnsons Stiftelse. The authors acknowledge valuable discussions with Professor D.W. Schwendeman.

The third author's work was performed under the auspices of the U.S. Department of Energy by University of California, Lawrence Livermore National Laboratory under Contract W-7405-Eng-48.

References

[1] K. Takayama, H. Kleine, H. Grönig, Exp. Fluids 5 (1987) 315.
[2] M. Watanabe, O. Onodera, K. Takayama, Shock Waves @ Marseille IV, 1995.
[3] V. Eliasson, N. Apazidis, N. Tillmark, A.J. Szeri, Phys. Fluids 19 (2007) 106106.

[4] V. Eliasson, N. Apazidis, N. Tillmark, M.B. Lesser, Shock Waves 15 (2006) 205.
[5] D.W. Schwendeman, G.B. Whitham, Proc. R. Soc. Lond. A413 (1987) 297.
[6] G. Guderley, Luftfahrtforsch 19 (1942) 302.
[7] W.D. Henshaw, D.W. Schwendeman, J. Comput. Phys. 191 (2003) 420.
[8] W.D. Henshaw, D.W. Schwendeman, J. Comput. Phys. (ISSN: 0021-9991) 216 (2006) 744.
[9] S.I. Betelu, D.G. Aronson, Phys. Rev. Lett. 87 (2001) 074501.

Available online at www.sciencedirect.com

ScienceDirect

Physica D 237 (2008) 2210–2217

PHYSICA D

www.elsevier.com/locate/physd

Kinematic variational principle for motion of vortex rings

Y. Fukumoto[a,*], H.K. Moffatt[b]

[a] Graduate School of Mathematics and Mathematical Research Center for Industrial Technology, Kyushu University 33, Fukuoka 812-8581, Japan
[b] Department of Applied Mathematics and Theoretical Physics, Centre for Mathematical Science, University of Cambridge, Wilberforce Road, Cambridge CB3 0WA, UK

Available online 12 February 2008

Abstract

We show how the ideas of topology and variational principle, opened up by Euler, facilitate the calculation of motion of vortex rings. Kelvin–Benjamin's principle, as generalised to three dimensions, states that a steady distribution of vorticity, relative to a moving frame, is the state that maximizes the total kinetic energy, under the constraint of constant hydrodynamic impulse, on an iso-vortical sheet. By adapting this principle, combined with an asymptotic solution of the Euler equations, we make an extension of Fraenkel–Saffman's formula for the translation velocity of an axisymmetric vortex ring to third order in a small parameter, the ratio of the core radius to the ring radius. Saffman's formula for a viscous vortex ring is also extended to third order.

PACS: 47.10.A-; 47.10.ad; 47.15.ki; 47.32.C-

Keywords: Vortex ring; Translation velocity; Variational principle; Iso-vortical sheet

1. Introduction

Euler opened up the field of topology when he presented the solution to the Königsberg bridge problem in 1735 [1]. As "geometry of position" in the title signifies, Euler envisaged a new type of geometric problem in which distance is not relevant. In 1750, he discovered the polyhedral theorem on the Euler characteristic, a summation of alternately signed numbers of vertices, edges and faces of a polyhedron [2]. This theorem stands as the cornerstone of topology. Almost at the same time, the Euler equations for fluid flows were born.

Euler's 1757 paper [3] certainly overcame the limitation to irrotational velocity field, posed by Bernoulli, and accommodated vorticity. However a century passed before Helmholtz discovered the key to the heart of vortex motion that the vortex lines are frozen into the fluid [4]. Helmholtz' theorem implied that link and knot types of vortex lines remain unchanged throughout the flow evolution. This implication, along with the invariance of circulation, sparked, in Scotland, the construction of atom models by knotted vortex tubes. Inspired by the vortex atom theory, Tait attempted classification of knot and link types [5]. It took another century for the helicity to be discovered [6–9]. This topological invariant is tied with linkage and knottedness of vortex filaments [9]. More precisely, the helicity embodies the Călugăreanu invariant [10], a summation of the writhe and the twist, of a twisted flux tube [11].

The study of the motion of vortex rings started simultaneously with the birth of the field of vortex dynamics [4]. Extending Helmholtz' analysis, Kelvin obtained the formula for velocity of an axisymmetric vortex ring, steadily translating in an inviscid incompressible fluid of infinite extent, for a distribution of vorticity, in the core, proportional to the distance from the axis of symmetry. The assumption is made that the ring is very thin:

$$\varepsilon = \sigma/R_0 \ll 1, \tag{1}$$

where σ is the core radius and R_0 is the ring radius. The formula allowing for an arbitrary distribution of vorticity was found by Fraenkel [12] and Saffman [13] (see also Ref. [14]) as

$$U_0 = \frac{\Gamma}{4\pi R_0}\left\{\log\left(\frac{8R_0}{\sigma}\right) + A - \frac{1}{2}\right\}, \tag{2}$$

* Corresponding author. Tel.: +81 92 642 2762; fax: +81 92 642 2779.
E-mail address: yasuhide@math.kyushu-u.ac.jp (Y. Fukumoto).

0167-2789/$ - see front matter
doi:10.1016/j.physd.2008.02.003

where Γ is the circulation and

$$A = \lim_{r\to\infty}\left\{\frac{4\pi^2}{\Gamma^2}\int_0^r r' v_0(r')^2 \mathrm{d}r' - \log\left(\frac{r}{\sigma}\right)\right\}, \tag{3}$$

with $v_0(r)$ being the local velocity of circulatory motion of the fluid around the toroidal center circle, as a function only of the local distance r from the circle. In the absence of viscosity, $v_0(r)$ and therefore the local vorticity field may be arbitrary functions of r.

Viscosity acts to diffuse vorticity, and the motion ceases to be steady. For a vortex ring with its toroidal vorticity $\zeta(r,t)$ 'δ-function' concentrated on the circle of radius R_0, at a virtual instant,

$$\zeta(r,0) = \Gamma\delta(\rho - R_0)\delta(z - Z) \quad \text{at } t = 0, \tag{4}$$

with $r^2 = (\rho - R_0)^2 + (z - Z)^2$, it suffices to substitute, into (3), the Oseen diffusing vortex

$$\zeta_0 = \frac{\Gamma}{4\pi\nu t}\mathrm{e}^{-r^2/4\nu t}, \qquad v_0 = \frac{\Gamma}{2\pi r}\left(1 - \mathrm{e}^{-r^2/4\nu t}\right), \tag{5}$$

where ν is the kinematic viscosity and t is the time measured from the instant at which the core is infinitely thin. With this form, (2) supplemented by (3) becomes

$$U_0 = \frac{\Gamma}{4\pi R_0}\left\{\log\left(\frac{8R_0}{2\sqrt{\nu t}}\right) - \frac{1}{2}(1 - \gamma + \log 2)\right\}, \tag{6}$$

where $\gamma = 0.57721566\cdots$ is Euler's constant. Comparison with the result of numerical simulation of the axisymmetric Navier–Stokes equations [15] illustrates that validity of Saffman's formula (6) is limited to very small times ($\nu t/R_0^2 \ll 1$) [16].

Vortex rings observed in nature are not necessarily thin. Kelvin's formula is an asymptotic solution to $O(\varepsilon)$ for vorticity linear in the distance from the symmetric axis. Dyson [17] accomplished its extension to $O(\varepsilon^3)$ [18]. For this distribution, evidence is available that Dyson's formula fits rather well with the speed of Hill's spherical vortex, the fat limit of Fraenkel–Norbury's family of vortex rings [19]. This unexpected agreement stimulates us to pursue a higher-order correction to (2).

The method of matched asymptotic expansions has been previously developed for a systematic treatment of motion of slender vortex tubes [14,20], and was extended to second order in ε [21]. Derivation of the correction to Fraenkel–Saffman's formula (2) requests us to enter into the third order. A flood of nonlinear terms of a higher order in the Navier–Stokes equations makes our mathematical handling out of control. It was shown that the radius of the circle of vorticity centroid grows linearly in time due to the action of vorticity [22], but reduction of the expression for the speed of a vortex ring remains yet to be attained. The method of Lamb–Saffman–Rott–Cantwell [23,13,24] provides an efficient means.

We show how topological ideas help to bring in a further simplification. It is well known that a stationary configuration of vorticity, embedded in an inviscid incompressible fluid, is realizable as an extremal of energy on an iso-vortical sheet [25–27]. An iso-vortical sheet comprises volume-preserving diffeomorphisms, or smooth maps of fluid particles, with vorticity frozen into the fluid. For a moving state, this conditional variational principle should be augmented by a constraint. Benjamin [28] put forward a variational principle that an axisymmetric vortex ring moving steadily in an inviscid incompressible fluid is realizable as the maximum state of the kinetic energy H on an iso-vortical sheet, subject to the constraint of constant hydrodynamic impulse

$$\boldsymbol{P} = \frac{1}{2}\iiint \boldsymbol{x}\times\boldsymbol{\omega}\,\mathrm{d}V. \tag{7}$$

When translated into three dimensions, Kelvin–Benjamin's principle reads

$$\delta H - \boldsymbol{U}\cdot\delta\boldsymbol{P} = 0, \tag{8}$$

where the velocity $\boldsymbol{U}$ of the region plays the role of the Lagrangian multipliers.

An iso-vortical sheet is infinite dimensional. A family of solutions of the Euler equations include several parameters. By posing some relations on these parameters, we can maintain the solutions on a single iso-vortical sheet, and, when restricted to this family, the dimension of an iso-vortical sheet is reduced to finite. Thus the traveling speed of a vortex ring may be calculable through (8). This is indeed the case for the first-order velocity formula as listed in the book [29]. The principle (8) has a wider applicability as exemplified by a vortex ring governed by the Gross–Pitaevskii equation [30]. In this paper, we adapt this variational principle to deduce the $O(\varepsilon^3)$ correction to the traveling speed. At large Reynolds numbers, the viscosity plays a secondary role only of selecting vorticity profile, and the inviscid formula is applicable to give the correction term to Saffman's formula (6).

We begin with the general variational formulation in three dimensions (Section 2). After a statement of asymptotic expansions of the flow field, the kinetic energy and the impulse (Section 3), we recall the outer and inner solutions [22] in Sections 4 and 5 respectively. Thereafter, we calculate, in Section 6, the energy and the impulse to $O(\varepsilon^2)$ and present, in Section 7, a recipe for implementing (8) to produce the $O(\varepsilon^3)$ correction to Fraenkel–Saffman's formula (2) and Saffman's formula (6) for the traveling speed of vortex rings. It is highly probable that a vortex ring obeying the Euler equations is a maximum-energy state [28,31]. The upper bound of energy, if available, guarantees the existence of this extremal, and is furnished by a topological invariant [32]. Appendix gives a concise description for viewing this invariant as a variant of the helicity [33].

2. Variational principle

Roberts [34] proved the above principle for an axisymmetric vortex ring steadily translating in an inviscid fluid. Below, we extend this principle to three dimensions to gain an insight into the variational structure.

Under the assumption that the fluid is incompressible, we can introduce the vector potential $\boldsymbol{A}$ for the velocity field $\boldsymbol{u}$ ($\boldsymbol{u} = \nabla \times \boldsymbol{A}$). We assume that the vorticity $\boldsymbol{\omega} = \nabla \times \boldsymbol{u}$ is localised in some finite region in such a way that the velocity decreases sufficiently rapidly. These assumptions admit a representation of the total kinetic energy H of the fluid, filling an unbounded space, as

$$H = \frac{1}{2}\iiint \boldsymbol{u}^2 \mathrm{d}V = \frac{1}{2}\iiint \boldsymbol{\omega}\cdot\boldsymbol{A}\,\mathrm{d}V, \tag{9}$$

where the density of fluid is set to be unity.

We confine ourselves to steady motion, with constant speed $\boldsymbol{U}$, of a region with vorticity and assume that the flow is stationary in a frame moving with $\boldsymbol{U}$. It is expedient to partition the velocity $\boldsymbol{u}$ as $\boldsymbol{u} = \bar{\boldsymbol{u}} + \boldsymbol{U}$. By the assumption that the relative velocity $\bar{\boldsymbol{u}}$ is steady, it obeys

$$\nabla \times (\bar{\boldsymbol{u}} \times \boldsymbol{\omega}) = 0. \tag{10}$$

Consequently, there exists a globally defined spatial function $h(\boldsymbol{x})$ such that

$$\bar{\boldsymbol{u}} \times \boldsymbol{\omega} = \nabla h. \tag{11}$$

Suppose that fluid particles undergo an infinitesimal displacement $\delta\xi$ while preserving the volume of an arbitrary fluid element:

$$\boldsymbol{x} \to \tilde{\boldsymbol{x}} = \boldsymbol{x} + \delta\xi(\boldsymbol{x})\,; \qquad \nabla\cdot\delta\xi = 0. \tag{12}$$

We impose the condition that the flux of vorticity through an arbitrary material surface be unchanged throughout the process of the displacement. Its local representation is [26,27,32]

$$\delta\boldsymbol{\omega} = \nabla \times (\delta\xi \times \boldsymbol{\omega})\,. \tag{13}$$

In keeping with the above, we decompose the vector potential $\boldsymbol{A}(\boldsymbol{x})$ as $\boldsymbol{A} = \bar{\boldsymbol{A}} - \boldsymbol{x}\times\boldsymbol{U}/2$. Using the definition $\bar{\boldsymbol{u}} = \nabla \times \bar{\boldsymbol{A}}$, we can deduce, from (11) and (13),

$$\bar{\boldsymbol{A}}\cdot\delta\boldsymbol{\omega} = -\nabla\cdot\left\{h\delta\xi + \bar{\boldsymbol{A}}\times(\delta\xi\times\boldsymbol{\omega})\right\}. \tag{14}$$

The variation δH of the kinetic energy, subjected to the variation of fluid-particle positions (12), is calculated as

$$\begin{aligned}\delta H &= \iiint \boldsymbol{A}\cdot\delta\boldsymbol{\omega}\,\mathrm{d}V = \boldsymbol{U}\cdot\left(\frac{1}{2}\iiint \boldsymbol{x}\times\delta\boldsymbol{\omega}\,\mathrm{d}V\right)\\ &\quad - \iint \left\{h\delta\xi + \bar{\boldsymbol{A}}\times(\delta\xi\times\boldsymbol{\omega})\right\}\cdot\boldsymbol{n}\,\mathrm{d}A. \end{aligned}\tag{15}$$

The surface integral is taken over the closed surface receding to infinity that bounds the whole region. The second term of the surface integral vanishes under the assumption that the vorticity $|\boldsymbol{\omega}|$ decays sufficiently rapidly with distance $|\boldsymbol{x}|$, say exponentially in $|\boldsymbol{x}|$. Under the same assumption, h approaches a constant h_∞ at large distances $|\boldsymbol{x}|$, and the first term of the surface integral vanishes, with the aid of the Gauss theorem, owing to (12). Consequently, we are left only with the volume integral in (15). The variation of the hydrodynamic impulse (7) is

$$\delta\boldsymbol{P} = \frac{1}{2}\iiint \boldsymbol{x}\times\delta\boldsymbol{\omega}\,\mathrm{d}V. \tag{16}$$

With this form, (15) is reckoned upon as the variational principle (8) for the translation speed $\boldsymbol{U}$ of the vortex region.

A steadily moving vortex ring would be the maximal of the energy [28,31]. For a compact distribution of vorticity of an axisymmetric vortex ring, an upper bound on the energy is supplied by the topological invariant (A.8), with fluid density $\rho_\mathrm{f} = 1$, which guarantees the existence of the solution for vortex rings. By Poincaré's inequality, the energy (9) is bounded above as $\int \boldsymbol{u}^2\mathrm{d}V \le C\int \boldsymbol{\omega}^2\mathrm{d}V$ for some constant C. Introduce cylindrical coordinates (ρ, ϕ, z) with the z-axis coincident with the axis of symmetry and ρ being the distance from the symmetric axis, Supposing that the vorticity $\boldsymbol{\omega} = \zeta\boldsymbol{e}_\phi$, with $\boldsymbol{e}_\phi$ being the unit vector in the ϕ-direction, is confined to a compact region $\mathcal{A}$ in the meridional plane, the enstrophy is shown to be bounded above in the following way [32]:

$$\begin{aligned}\int_{\mathcal{A}} \zeta^2\rho\mathrm{d}\rho\mathrm{d}z &= \int_{\mathcal{A}}\left(\frac{\zeta}{\rho}\right)^2\rho^2\rho\mathrm{d}\rho\mathrm{d}z\\ &\le \left\{\int_{\mathcal{A}}\left(\frac{\zeta}{\rho}\right)^4\rho\mathrm{d}\rho\mathrm{d}z\int_{\mathcal{A}}\rho^4\rho\mathrm{d}\rho\mathrm{d}z\right\}^{1/2} = \text{const.}\end{aligned}\tag{17}$$

The similar would hold true for a continuous, but localised, distribution of vorticity.

3. Asymptotic expansions of energy and impulse

We confine ourselves to steady motion of axisymmetric vortex rings with vorticity $\boldsymbol{\omega}$ in the toroidal directions. The vector potential $\boldsymbol{A} = -\psi(\rho, z, t)/\rho\boldsymbol{e}_\phi$ possesses azimuthal components only. The scalar field ψ is named the Stokes streamfunction.

We build the solution of the Euler equations in the form of a power series in the small parameter ε, inside and around the core. To this end, it is advantageous to employ the local moving cylindrical coordinates (r, θ), on the meridional plane, with the origin maintained in the core. We nondimensionalize the variables in terms of the circulation Γ, the typical ring radius R_0 and the core radius σ. Attached with an asterisk, the nondimensional variables look like

$$\begin{aligned}&r^* = r/\varepsilon R_0, \qquad t^* = t\Big/\frac{R_0^2}{\Gamma}, \qquad \psi^* = \frac{\psi}{\Gamma R_0},\\ &\zeta^* = \zeta\Big/\frac{\Gamma}{R_0^2\varepsilon^2}, \qquad \boldsymbol{u}^* = \boldsymbol{u}\Big/\frac{\Gamma}{R_0\varepsilon},\\ &(\dot{R}^*, \dot{Z}^*) = (\dot{R}, \dot{Z})\Big/\frac{\Gamma}{R_0}.\end{aligned}\tag{18}$$

A glance at the equations written in this moving frame tells the dependence, on θ, of the solution in a power series in ε to be [22]

$$\begin{aligned}\psi &= \psi^{(0)}(r) + \varepsilon\psi_{11}^{(1)}(r)\cos\theta\\ &\quad + \varepsilon^2\left[\psi_0^{(2)}(r) + \psi_{21}^{(2)}(r)\cos 2\theta\right] + O(\varepsilon^3),\end{aligned}\tag{19}$$

$$\begin{aligned}\zeta &= \zeta^{(0)}(r) + \varepsilon\zeta_{11}^{(1)}(r)\cos\theta\\ &\quad + \varepsilon^2\left[\zeta_0^{(2)}(r) + \zeta_{21}^{(2)}(r)\cos 2\theta\right] + O(\varepsilon^3).\end{aligned}\tag{20}$$

We solve the Euler equations in a frame moving with the vortex ring. The origin of this moving frame should have some bearing with the core center in the meridional plane, but, for a core of finite thickness, the definition of the center is subtle. We expand the radial position R of the center in powers of ε as

$$R = 1 + \varepsilon^2 R^{(2)} + O(\varepsilon^3). \tag{21}$$

Keeping the first term to be unity by adjusting the origin of the moving frame would be helpful to the analyses that follow.

For axisymmetric flows, the kinetic energy (9) and the hydrodynamic impulse (7) reduces, respectively, to

$$H = -\pi \iint \psi\zeta \, \mathrm{d}\rho \mathrm{d}z, \qquad \boldsymbol{P} = \pi \iint \zeta\rho^2 \mathrm{d}\rho \mathrm{d}z \boldsymbol{e}_z. \tag{22}$$

Correspondingly to (18), these are normalized as

$$H^* = H/\Gamma^2 R_0, \qquad P_z^* = P_z/\Gamma R_0^2, \tag{23}$$

where P_z is the z component of $\boldsymbol{P}$. Upon substitution from (19)–(21), we obtain a representation of (23) to $O(\varepsilon^2)$, as

$$H = -2\pi^2 \int_0^\infty \left\{ r\zeta^{(0)}\psi^{(0)} + \varepsilon^2 r \left[\frac{1}{2}\zeta_{11}^{(1)}\psi_{11}^{(1)} + \zeta^{(0)}\psi_0^{(2)} + \zeta_0^{(2)}\psi^{(0)} \right] \right\} \mathrm{d}r + O(\varepsilon^3), \tag{24}$$

$$P_z = \pi + \varepsilon^2 \pi \left[2R^{(2)} + \pi \int_0^\infty \zeta^{(0)} r^3 \mathrm{d}r + 2\pi \int_0^\infty \zeta_{11}^{(1)} r^2 \mathrm{d}r \right] + O(\varepsilon^3). \tag{25}$$

It is noteworthy that the kinetic energy H and the impulse P_z are gained, to $O(\varepsilon^2)$, without knowledge of the quadrupole components $\psi_{21}^{(1)}$ and $\zeta_{21}^{(1)}$ of $O(\varepsilon^2)$. Except for cores of uniform ζ/ρ, calculation of $\psi_{21}^{(2)}$ and $\zeta_{21}^{(1)}$ requires numerical integration and stands as an obstacle, though this is not the case with the monopole component $\psi_0^{(2)}$ and $\zeta_0^{(2)}(r)$ of $O(\varepsilon^2)$ and $O(\varepsilon)$ field. Relying on the variational principle, the kinetic energy H and the impulse P_z, to $O(\varepsilon^2)$, are sufficient to deduce the formula for $\boldsymbol{U}$ valid to $O(\varepsilon^3)$. Advent of the variational principle dispenses not only with the quadrupole field of $O(\varepsilon^2)$ but also with the $O(\varepsilon^3)$ field. In the following sections, we enumerate the necessary expressions of flow field.

4. Outer solution

The energy (24) desires the flow field only in the region supported by vorticity, namely the inner solution. In spite of this, the outer solution is necessary to supply the boundary condition on the inner field.

The outer solution is nothing but the Biot–Savart law and is written, for the Stokes streamfunction, as

$$\psi(\rho, z) = -\frac{\rho}{4\pi} \int_{-\infty}^{\infty} \int_0^{2\pi} \int_0^\infty \mathrm{d}\rho' \mathrm{d}\phi' \mathrm{d}z' \zeta(\rho', z')\rho' \cos\phi' \Big/ \left\{ \rho^2 - 2\rho\rho'\cos\phi' + \rho'^2 + (z - z')^2 \right\}^{1/2}. \tag{26}$$

Dyson's shift-operator technique is adapted to manipulate the inner limit of (26) for an arbitrary distribution of vorticity in the form of (20) [22]. The asymptotic development of the Biot–Savart law valid to $O(\varepsilon^2)$, in a region $\varepsilon \ll r/R \ll 1$ surrounding the core, is

$$\begin{aligned}
\psi = & -\frac{\Gamma}{2\pi}\left[\log\left(\frac{8}{\varepsilon r}\right) - 2\right] \\
& + \varepsilon \left\{ -\frac{\Gamma}{4\pi}\left[\log\left(\frac{8}{\varepsilon r}\right) - 1\right] r\cos\theta + d^{(1)}\frac{\cos\theta}{r} \right\} \\
& + \varepsilon^2 \left\{ -\frac{\Gamma}{2^5\pi}\left(\left[2\log\left(\frac{8}{\varepsilon r}\right) + 1\right] r^2 \right.\right. \\
& \left. - \left[\log\left(\frac{8}{\varepsilon r}\right) - 2\right] r^2 \cos 2\theta \right) + \frac{d^{(1)}}{2}\left[\log\left(\frac{8}{\varepsilon r}\right) \right. \\
& \left.\left. + \frac{\cos 2\theta}{2}\right] - \frac{\Gamma R^{(2)}}{2\pi}\log\left(\frac{8}{\varepsilon r}\right) + q^{(2)}\frac{\cos 2\theta}{r^2} \right\} \\
& + O(\varepsilon^3),
\end{aligned} \tag{27}$$

where $\Gamma = 2\pi\int_0^\infty r\zeta^{(0)}\mathrm{d}r = 1$, when nondimensionalized, and $d^{(1)} = d_1/\Gamma\sigma^2$ is the strength of the dipole of $O(\varepsilon)$ whose dimensional form will be provided later by (39). The expression of $q^{(2)}$, the strength of the quadrupole at $O(\varepsilon^2)$, is left out, as this is unnecessary.

5. Inner solution

The radial coordinate r^* in (18), normalized by the core radius σ, is peculiar to the inner expansion. The inner solution is found by solving the Euler or Navier–Stokes equations made dimensionless with use of the inner variables (18), subject to the matching condition (27), in powers of the small parameter ε. In the following we write down the resulting expressions of the vorticity and the Stokes streamfunction. The detail is found in Ref. [22].

In the absence of viscosity, the vorticity profile $\zeta^{(0)}(r)$ may be left unspecified. The local radial velocity is $u^{(0)} = 0$, and the local azimuthal velocity $v^{(0)}$, $\psi^{(0)}$ and $\zeta^{(0)}(r)$ are linked with each other via

$$v^{(0)} = -\frac{\partial\psi^{(0)}}{\partial r}, \qquad \zeta^{(0)} = \Delta\psi^{(0)} = -\frac{1}{r}\frac{\partial}{\partial r}\left(r v^{(0)}\right). \tag{28}$$

Integrating the first of (28), we obtain the leading-order streamfunction, complying with $O(\varepsilon^0)$ of (27), as

$$\psi^{(0)} = -\int_0^r v^{(0)}(r')\mathrm{d}r' + \lim_{r\to\infty}\left\{ \int_0^r v^{(0)}(r')\mathrm{d}r' - \frac{1}{2\pi}\left[\log\left(\frac{8}{r}\right) - 2\right] \right\}. \tag{29}$$

Viscosity plays the role of selecting the functional form of $\psi^{(0)}$. We introduce a dimensionless parameter switching on the action of viscosity ν.

$$\hat{\nu} = 0 \quad \text{for the inviscid case}, \quad = 1 \text{ for the viscous case}. \tag{30}$$

For the viscous case, $\varepsilon = \sqrt{\nu/\Gamma}$ takes the place of the small parameter. The axisymmetric (or θ-averaged) part of the vorticity equation at $O(\varepsilon^2)$ leads to the heat conduction equation for $\zeta^{(0)}$. For the initial δ-function core (4), the Oseen vortex (5) is picked out.

The first-order solution comprises a dipole field. The streamfunction corresponding to the uniform flow $-\dot{Z}^{(0)}\boldsymbol{e}_z$ in the z direction is given by $-\dot{Z}^{(0)}\rho^2/2$. Here a dot stands for differentiation with respect to time. Denote the dipole coefficient of the streamfunction for the flow, relative to the moving frame, to be $\tilde{\psi}_{11}^{(1)} = \psi_{11}^{(1)} + r\dot{Z}^{(0)}$. The coefficient function $\tilde{\psi}_{11}^{(1)}$ admits an explicit expression, in the form of a repeated integral, as

$$\tilde{\psi}_{11}^{(1)} = \Psi_{11}^{(1)} + c_{11}^{(1)} v^{(0)}, \tag{31}$$

where $c_{11}^{(1)}$ is a constant (which may depend on t), and

$$\Psi_{11}^{(1)} = -v^{(0)} \left\{ \frac{r^2}{2} + \int_0^r \frac{\mathrm{d}r'}{r'[v^{(0)}(r')]^2} \int_0^{r'} r'' \left[v^{(0)}(r'') \right]^2 \mathrm{d}r'' \right\}. \tag{32}$$

The vorticity is calculable through

$$\zeta_{11}^{(1)} = a\tilde{\psi}_{11}^{(1)} + r\zeta^{(0)}, \tag{33}$$

where

$$a(r,t) = -\frac{1}{v^{(0)}} \frac{\partial \zeta^{(0)}}{\partial r}. \tag{34}$$

The Fourier coefficient $\tilde{\psi}_0^{(2)}(r)$ of the monopole component of $O(\varepsilon^2)$, relative to the moving coordinate frame, is defined by $\tilde{\psi}_0^{(2)} = \psi_0^{(2)} + \dot{Z}^{(0)} r^2/4$. The vorticity equation is integrated for this component, resulting in

$$\frac{\partial \tilde{\psi}_0^{(2)}}{\partial r} = \frac{1}{r}\int_0^r r'\zeta_0^{(2)} \mathrm{d}r' + \frac{r}{2}\frac{\partial \tilde{\psi}_{11}^{(1)}}{\partial r} + \left(\frac{r^2}{2} - R^{(2)}\right) v^{(0)}. \tag{35}$$

The $O(\varepsilon^2)$ monopole component $\zeta_0^{(2)}$ of vorticity obeys

$$\frac{\partial \zeta_0^{(2)}}{\partial t} - \hat{\nu}\frac{1}{r}\frac{\partial}{\partial r}\left(r\frac{\partial \zeta_0^{(2)}}{\partial r}\right) = \frac{1}{r}\frac{\partial}{\partial r}\left\{ -\frac{r}{2v^{(0)}} \left[\frac{\partial \zeta_{11}^{(1)}}{\partial t} - \hat{\nu}\left(\frac{\partial^2}{\partial r^2} + \frac{1}{r}\frac{\partial}{\partial r} - \frac{1}{r^2}\right)\zeta_{11}^{(1)} \right] \tilde{\psi}_{11}^{(1)} + \frac{\dot{R}^{(2)} r^2}{2}\zeta^{(0)} \right\}. \tag{36}$$

This equation is extracted from the axisymmetric part of the vorticity equations at $O(\varepsilon^4)$. The constraint that no net vorticity is created, $2\pi\int_0^\infty r\zeta_0^{(2)}\mathrm{d}r = 0$, is compatible with (36).

6. Asymptotics of energy and impulse

There are no terms of $O(\varepsilon)$ in the energy (24) and impulse (25). By substitution from (29), we obtain the leading-order term $H^{(0)}$ of (24), which is expressed, in terms of dimensional variables, as

$$H_0/\Gamma^2 = \frac{1}{2} R_0 \left\{ \log\left(\frac{8R_0}{\sigma}\right) + A - 2 \right\}, \tag{37}$$

where $H_0 = \Gamma^2 R_0 H^{(0)}$ and A is defined by (3).

Likewise, after some algebra, we obtain $H_2 = \Gamma^2 R_0 \varepsilon^2 H^{(2)}$, the dimensional form of the second-order term $H^{(2)}$ of (24), as follows:

$$\begin{aligned} \frac{H_2}{\Gamma^2} = &-\frac{\pi d_1}{2\Gamma R_0}\left\{ \log\left(\frac{8R_0}{\sigma}\right) - \frac{1}{2} + \frac{4\pi R_0}{\Gamma}U_0 \right\} + \frac{\pi^2 B}{R_0} \\ &- \frac{\pi^2}{\Gamma^2 R_0}\left[\frac{1}{2}\int_0^\infty r^4 \zeta_0 v_0 \mathrm{d}r + \int_0^\infty r a (\tilde{\psi}_{11}^{(1)})^2 \mathrm{d}r \right] \\ &- \frac{4\pi^2 R_0}{\Gamma^2}\int_0^\infty v_0(r)\left[\int_0^r r'\zeta_0^{(2)}(r') \right]\mathrm{d}r \\ &+ \frac{R_2}{2}\left\{ \log\left(\frac{8R_0}{\sigma}\right) + A - 1 \right\}, \end{aligned} \tag{38}$$

where $v_0 = \Gamma v^{(0)}/\sigma$, $\zeta_0 = \Gamma\zeta^{(0)}/\sigma^2$, $U_0 = \Gamma\dot{Z}^{(0)}/R_0$ and $R_2 = R_0\varepsilon^2 R^{(2)}$ are dimensional variables, and

$$d_1 = -\frac{1}{4}\left(\int_0^\infty r^3\zeta_0 \mathrm{d}r + 2R_0\int_0^\infty r^2\zeta_{11}^{(1)}\mathrm{d}r \right), \tag{39}$$

$$\begin{aligned} B = \lim_{r\to\infty} &\left\{ \frac{1}{\Gamma^2}\int_0^r r' v_0 \tilde{\psi}_{11}^{(1)} \mathrm{d}r' + \frac{r^2}{16\pi^2}\left[\log\left(\frac{r}{\sigma}\right) + A \right] \right. \\ &\left. + \frac{d_1}{2\pi\Gamma}\log\left(\frac{r}{\sigma}\right) \right\}. \end{aligned} \tag{40}$$

It is to be understood that, in the above, the dimensional variables v_0 and ζ_0 are used in place of $v^{(0)}$ and $\zeta^{(0)}$, respectively.

In the inviscid case, (36) is integrated to produce

$$\int_0^r r'\zeta_0^{(2)}(r')\mathrm{d}r = -\frac{r}{4v^{(0)}} a\tilde{\psi}_{11}^{(1)} + \frac{R^{(2)}}{2} r^2 \zeta^{(0)}, \tag{41}$$

and cancellation among several terms is effected in (38).

The second-order term $P^{(2)}$ in (25), the z component of the hydrodynamic impulse, has a link with the strength d_1 of a dipole defined by (39), in such a way that

$$P_2 = \pi\left(2\Gamma R_0 R_2 - 4\pi d_1\right), \tag{42}$$

where $P_2 = \Gamma R_0^2 \varepsilon^2 P^{(2)}$ [22].

7. Third-order correction to speed

We are now ready to implement the variational calculation (8) to produce the translation speed of an axisymmetric vortex ring. We set, as a natural profile of local velocity field featuring a vortex ring,

$$v_0(r) = -\frac{\Gamma}{2\pi r} f\left(\frac{r}{\sigma}\right), \qquad \zeta_0 = \frac{\Gamma}{2\pi r}\frac{\mathrm{d}}{\mathrm{d}r} f\left(\frac{r}{\sigma}\right), \tag{43}$$

where f is an arbitrary function, except for the requirement that

$$f(\xi) = O(\xi^2) \quad \text{as } \xi \to 0, \qquad f(\xi) \to 1 \quad \text{as } \xi \to \infty. \tag{44}$$

The parameter σ introduces the scale for the core thickness, and (43) includes both the constant vorticity, within the core, and the Gaussian distribution (5).

Suppose that the fluid particles occupying a toroidal region of radius r around the center circle of radius R are mapped to another toroidal region of radius $\hat{r}$ around the center circle of radius $\hat{R}$. To maintain these flow fields on an iso-vortical sheet, it is necessary for the circulation Γ to remain unchanged. Preservation of volume enforces

$$2\pi^2 r^2 R = 2\pi^2 \hat{r}^2 \hat{R}, \qquad 2\pi^2 \sigma^2 R = 2\pi^2 \hat{\sigma}^2 \hat{R}, \tag{45}$$

from which follows $r/\sigma = \hat{r}/\hat{\sigma}$. Consequently, the local circulation around the circle of radius r

$$\Gamma(r) = 2\pi \int_0^r \zeta_0(r')r'\mathrm{d}r' = \Gamma f(r/\sigma) \tag{46}$$

is invariant: $\Gamma(r) = \Gamma(\hat{r})$. Under an infinitesimal perturbation of $R \to \hat{R} = R+\delta R, \sigma \to \hat{\sigma} = \sigma+\delta\sigma$, with $R = R_0+R_2$, (45) demands that, at each order, $\sigma^2 R_0 =$ const. and $\sigma^2 R_2 =$ const., and therefore that

$$2\delta\sigma/\sigma = -\delta R_0/R_0 = -\delta R_2/R_2. \tag{47}$$

We can show that, under this perturbation, $\hat{A} = A + O\left((\delta R)^2\right)$, or $\delta A = 0$. It follows from this and the first of (47) that the variation of (37), under an iso-vortical perturbation, is

$$\delta H_0 = \frac{\Gamma^2}{2}\left[\log\left(\frac{8R_0}{\sigma}\right) + A - \frac{1}{2}\right]\delta R_0. \tag{48}$$

The variation of the leading term of impulse $P_0 = \Gamma\pi R_0^2$ is $\delta P_0 = 2\pi\Gamma R_0 \delta R_0$, and application of $\delta H_0 = U_0 \delta P_0$ restores Fraenkel–Saffman's formula (2). This result supplements the list in Ref. [29].

A great care should be exercised to proceed to a higher order. Because of the space limitation, we cannot help omitting the detail, and write out the resulting expressions only. The variation of (38) leads, after some manipulations, to

$$\begin{aligned}\delta H_2/\delta R_0 = {} & \frac{2\pi\Gamma d_1}{R_0^2}\left\{\log\left(\frac{8R_0}{\sigma}\right) + \frac{A}{2} - \frac{5}{4}\right\} - \frac{2\pi^2\Gamma^2}{R_0^2}B \\ & + \frac{\pi^2}{R_0^2}\left[\int_0^\infty r^4\zeta_0 v_0 \mathrm{d}r - \int_0^\infty ra(\tilde{\psi}_{11}^{(1)})^2\mathrm{d}r\right] \\ & - 4\pi^2\int_0^\infty v_0(r)\left[\int_0^r r'\zeta_0^{(2)}(r')\right]\mathrm{d}r \\ & + \frac{\Gamma^2 R_2}{2R_0}\left\{\log\left(\frac{8R_0}{\sigma}\right) + A + \frac{1}{2}\right\}.\end{aligned} \tag{49}$$

The hydrodynamic impulse, the second-order term of which is (42), varies as

$$\delta P = [2\pi\Gamma R_0 + 4\pi(\Gamma R_2 + \pi d_1/R_0)]\,\delta R_0. \tag{50}$$

Enforcement of (8) or $\delta H_0 + \delta H_2 = (U_0 + U_2)\,\delta P$, eventually gives rise to the desired correction term of $O(\varepsilon^3)$ to the traveling speed:

$$\begin{aligned}U_2 = {} & \frac{d^{(1)}}{2R_0^3}\left\{\log\left(\frac{8R_0}{\sigma}\right) - 2\right\} - \frac{\pi\Gamma}{R_0^3}B \\ & + \frac{\pi}{2\Gamma R_0^3}\left[\int_0^\infty r^4\zeta_0 v_0\mathrm{d}r - \int_0^\infty ra(\tilde{\psi}_{11}^{(1)})^2\mathrm{d}r\right] \\ & - \frac{2\pi}{\Gamma R_0}\int_0^\infty v_0(r)\left[\int_0^r r'\zeta_0^{(2)}(r')\right]\mathrm{d}r \\ & - \frac{\Gamma R_2}{4\pi R_0^2}\left\{\log\left(\frac{8R_0}{\sigma}\right) + A - \frac{3}{2}\right\}.\end{aligned} \tag{51}$$

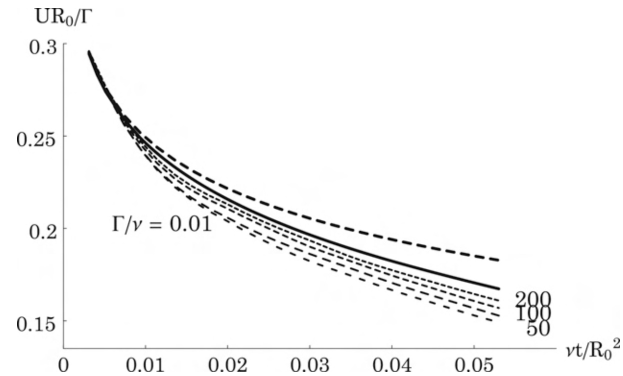

Fig. 1. Variation of speed of a viscous vortex ring with time. The thick line is the higher-order formula (53), while the thick dashed line is the Saffman's formula (6). The dashed lines are the values read off from the graph of numerical simulations [15]. $\Gamma/\nu = 200, 100, 50, 0.01$ from above.

The perturbation R_2 is retained, in order to deal with time variation of the ring radius. For an inviscid vortex ring, the ring radius is constant in time, and we may take $R_2 = 0$ without loss of generality. By exploiting (41) and (51) collapses to

$$\begin{aligned}U_2 = {} & \frac{1}{R_0^3}\left\{\frac{d_1}{2}\left[\log\left(\frac{8R_0}{\sigma}\right) - 2\right] - \pi\Gamma B\right. \\ & \left. + \frac{\pi}{2\Gamma}\int_0^\infty r^4\zeta_0 v_0\mathrm{d}r\right\}.\end{aligned} \tag{52}$$

This is an extension, to $O(\varepsilon^3)$, of Fraenkel–Saffman's formula (2), and is expected to be applicable to a fat core.

The above derivation rests on the assumption of zero viscosity. However, even if viscosity comes into play, the resulting higher-order asymptotics (51) is not invalidated, presumably because, at a large Reynolds number, the action of viscosity is confined to selecting the vorticity profile. In the presence of viscosity ($\nu > 0$), we are forced to solve the inhomogeneous heat-conduction Eq. (36) for the axisymmetric part of the second-order vorticity $\zeta_0^{(2)}$. Taking the initial condition (4), a circular vortex line, of radius R_0, with vanishing thickness, avoids mathematical complication. For this initial condition, (36) is reduced to an ordinary differential equation, with an introduction of similarity variables. The parameters $c_{11}^{(1)}$ in (31) and R_2, both being functions of t, play a common role of specifying the radial position of the ring at $O(\varepsilon^2)$ relative to R_0. This redundancy is removed, for instance, by taking $c_{11}^{(1)} \equiv 0$ and by taking the constant $P_2 = 0$ in (42). This amounts to placing the center $r = 0$ of the local moving frame at the stagnation point relative to this frame [22]. Performing the integration of (36) and then integration in (51), we eventually arrive at an extension of Saffman's formula (6) as

$$U \approx \frac{\Gamma}{4\pi R_0}\left\{\log\left(\frac{4R_0}{\sqrt{\nu t}}\right) - 0.5580 - 3.6716\frac{\nu t}{R_0^2}\right\}. \tag{53}$$

Fig. 1 illustrates the comparison of the asymptotic formula (53) with the direct numerical simulation of the axisymmetric

Navier–Stokes equations [15]. The normalized speed UR_0/Γ of the ring is drawn as a function of normalized time $\nu t/R_0^2$ for its small values. The thick solid line is our formula (53), and the thick broken line is the first-order truncation (6). The thin lines are the results of the numerical simulations. The number attached to each line is the circulation Reynolds number Γ/ν, being no larger than 200. We observe that inclusion of the correction U_2 achieves a significant improvement in approximation. It is remarkable that the large-Reynolds-number asymptotics formula (53), valid to $O(\varepsilon^3)$, compares fairly well with the numerical result of even moderate and small Reynolds numbers.

Mathematical labor to reach the same formula for the speed of a vortex ring dramatically decreases in order of the method of matched asymptotic expansions [22], Lamb's method and the variational principle. By appealing to the variational principle, we have succeeded in achieving higher-order extension of Fraenkel–Saffman's and Saffman's formulae, which are applicable to fat cores, Hopefully this principle encompasses helical vortex tubes if allowance is made for the rotation of the system (*cf.* [35]).

Appendix. Unified view of topological invariants

The helicity is a topological invariant of an ideal fluid in three dimensions. Two-dimensional ideal flows admit an integral of any function of vorticity as topological invariants. This is extended to axisymmetric flows. However, Noether's theorem associated with the particle relabeling symmetry does not discriminate between two and three dimensions. Inspired by this fact, it can be shown that these are variants of the cross helicity [33]. This appendix gives a brief sketch of this unified view.

We start from the vorticity equations for a barotropic fluid filling a domain $\mathcal{D}$:

$$\frac{\partial \boldsymbol{\omega}}{\partial t} = \nabla \times (\boldsymbol{u} \times \boldsymbol{\omega})\,. \tag{A.1}$$

Since we are concerned with the kinematics of ideal barotropic flows, the advection velocity $\boldsymbol{u}$ may be an arbitrary smooth vector field so that the vorticity ω may be unrelated to $\nabla \times \boldsymbol{u}$. We take compressibility into account, and the fluid density ρ_{f} obeys the equation of continuity $D\rho_{\mathrm{f}}/Dt + \rho_{\mathrm{f}}\nabla \cdot \boldsymbol{u} = 0$, Here $\mathrm{D}/\mathrm{D}t = \partial/\partial t + \boldsymbol{u} \cdot \nabla$ is the Lagrangian derivative. The law of mass conservation holds true without reference to the detailed form of velocity field $\boldsymbol{u}$, and therefore pertains to the kinematics.

Suppose that $\mathcal{D}$ is simply connected. Impose the following boundary condition on ω:

$$\omega \cdot \boldsymbol{n} = 0 \quad \text{on } \partial\mathcal{D}, \tag{A.2}$$

or in the case the domain $\mathcal{D}$ is unbounded,

$$|\omega| \to 0 \quad \text{sufficiently rapidly as } |\boldsymbol{x}| \to \infty\,. \tag{A.3}$$

Then for a given solenoidal vector field $\omega(\boldsymbol{x}, t)$, there exists a vector potential $\boldsymbol{v}(\boldsymbol{x}, t)$ defined, over $\mathcal{D}$, by $\omega = \nabla \times \boldsymbol{v}$. The vector potential is determined only up to the gauge transformation. The evolution equation of $\boldsymbol{v}$, obtained by taking the uncurl of (A.1), is named the Euler–Poincaré equations [36], and, when specialized as $\boldsymbol{v} = \boldsymbol{u}$, is made coincident with the Euler equations.

Let us introduce another solenoidal vector field $\boldsymbol{B}(\boldsymbol{x}, t)$ which is frozen into the fluid. The equation of $\boldsymbol{B}$ takes the same form as (A.1), and the boundary condition to be imposed is the same as (A.2) or (A.3). The cross helicity

$$\mathcal{H}[\omega, \boldsymbol{B}] = \int_{\mathcal{D}} \boldsymbol{v} \cdot \boldsymbol{B} \, \mathrm{d}V \tag{A.4}$$

is invariant even if the advection velocity field $\boldsymbol{u}$ is different from $\boldsymbol{v}$ [33,37]. The helicity [6–9] is a special case of (A.4) of taking $\boldsymbol{B} = \boldsymbol{\omega}$ and $\boldsymbol{u} = \boldsymbol{v}$.

For two-dimensional flows on the xy-plane with velocity provided by $\boldsymbol{u}(\boldsymbol{x}, t) = (u_x(x, y, t), u_y(x, y, t), 0)$, there is a family of integral invariants for planar flows in a domain $\mathcal{A}$, namely integrals of arbitrary function of $\omega = \partial u_y/\partial x - \partial u_x/\partial y$. For a compressible barotropic fluid, it is superseded by

$$Q = \int_{\mathcal{A}} \omega f\left(\frac{\omega}{\rho_{\mathrm{f}}}\right) \mathrm{d}A, \tag{A.5}$$

where f is an arbitrary function. This integral is termed the generalised enstrophy [27]. Invariance of (A.5) is a direct consequence of the restriction of (A.1) to two dimensions,

$$\frac{\mathrm{D}}{\mathrm{D}t} f\left(\frac{\omega}{\rho_{\mathrm{f}}}\right) = 0, \tag{A.6}$$

and the conservation law of the vorticity flux or Kelvin's circulation theorem. Introducing $\boldsymbol{F} = \nabla \times f\boldsymbol{e}_z$, (A.6) is converted into

$$\frac{\partial \boldsymbol{F}}{\partial t} = \nabla \times (\boldsymbol{u} \times \boldsymbol{F})\,. \tag{A.7}$$

A topological invariant is manufactured by replacing $\boldsymbol{B}$ by $\boldsymbol{F}$ in (A.4) with the volume integral of unit length in z over the domain $\mathcal{A}$. This integral is reduced, after a partial integration, to (A.5), except for a boundary term. The latter vanishes in a typical case that $f(\omega/\rho)$ approaches zero sufficiently rapidly as the boundary $\partial\mathcal{A}$ recedes to infinity,

The axisymmetric counterpart of (A.5) is

$$Q_{\mathrm{A}} = \int_{\mathcal{A}} \zeta f\left(\frac{\zeta}{\rho_{\mathrm{f}}\rho}\right) \mathrm{d}\rho \mathrm{d}z, \tag{A.8}$$

for an arbitrary function f of $\zeta/(\rho_{\mathrm{f}}\rho)$ [32]. The vector $\boldsymbol{F} = \nabla \times f\boldsymbol{e}_\phi/\rho$ fulfills (A.4) and (A.7), taking $\boldsymbol{F}$ in place of $\boldsymbol{B}$, coincides with (A.8) except for a boundary term.

References

[1] L. Euler, Solutio problematis ad geometriam situs pertinentis, Commentarii academiae scientiarum Petropolitanae 8 (1741) 128–140.

[2] L. Euler, Elementa doctrinae solidorum, Novi commentarii academiae scientiarum Petropolitanae 4 (1752/3) 109–140.

[3] L. Euler, Principes généraux du mouvement des fluides, Mémoires de l'académie des sciences de Berlin 11 (1757) 274–315.

[4] H. von Helmholtz, On integrals of the hydrodynamical equations, which express vortex-motion, Crelle's J. 55 (1858) 485–513 (Also Philos. Mag. 4 (33) (1867)).
[5] R.L. Ricca, M. Berger, Topological ideas and fluid mechanics, Phys. Today 35 (1996) 24–30.
[6] L. Woltjer, A theorem on force-free magnetic fields, Proc. Natl. Acad. Sci. USA 44 (1958) 489–491.
[7] R. Betchov, Semi-isotropic turbulence and helicoidal flows, Phys. Fluids 7 (1961) 925–926.
[8] J.J. Moreau, Constants d'un ilot tourbillonnaire en fluide parfait barotrope, C. R. Acad. Sci. Paris 252 (1961) 2810–2812.
[9] H.K. Moffatt, The degree of knottedness of tangled vortex lines, J. Fluid Mech. 35 (1969) 117–129.
[10] G. Călugăreanu, Sur les classes d'isotopie des noeuds tridimensionnels et leurs invariants, Czechoslovak Math. J. 11 (1961) 588–625.
[11] H.K. Moffatt, R.L. Ricca, Helicity and the Călugăreanu invariant, Proc. R. Soc. Lond. A 439 (1992) 411–429.
[12] L.E. Fraenkel, On steady vortex rings of small cross-section in an ideal fluid, Proc. R. Soc. Lond. A 316 (1970) 29–62.
[13] P.G. Saffman, The velocity of viscous vortex rings, Stud. Appl. Math. 49 (1970) 371–380.
[14] C. Tung, L. Ting, Motion and decay of a vortex ring, Phys. Fluids 10 (1967) 901–910.
[15] S.K. Stanaway, B.J. Cantwell, P.R. Spalart, A numerical study of viscous vortex rings using a spectral method, NASA Technical Memorandum, 101041, 1988.
[16] K. Shariff, A. Leonard, Vortex rings, Annu. Rev. Fluid Mech. 24 (1992) 235–279.
[17] F.W. Dyson, The potential of an anchor ring.—part II, Philos. Trans. R. Soc. Lond. A 184 (1893) 1041–1106.
[18] L.E. Fraenkel, Examples of steady vortex rings of small cross-section in an ideal fluid, J. Fluid Mech. 51 (1972) 119–135.
[19] J. Norbury, A family of steady vortex rings, J. Fluid Mech. 57 (1973) 417–431.
[20] L. Ting, R. Klein, Viscous Vortical Flows, in: Lecture Notes in Physics, vol. 374, Springer, 1991.
[21] Y. Fukumoto, T. Miyazaki, Three-dimensional distortions of a vortex filament with axial velocity, J. Fluid Mech. 222 (1991) 369–416.
[22] Y. Fukumoto, H.K. Moffatt, Motion and expansion of a viscous vortex ring. Part 1. A higher-order asymptotic formula for the velocity, J. Fluid Mech. 417 (2000) 1–45.
[23] H. Lamb, Hydrodynamics, 6th ed., Dover, New York, 1932.
[24] N. Rott, B. Cantwell, Vortex drift. I: Dynamic interpretation, Phys. Fluids A 5 (1993) 1443–1450.
[25] V.I. Arnol'd, Sur la géométrie différentielle des groupes de Lie de dimension infinie et ses applicationsà l'hydrodynamique des fluids parfaits, Ann. Inst. Fourier Grenoble 16 (1966) 319–361.
[26] V.I. Arnol'd, B.A. Khesin, Topological Methods in Hydrodynamics, Springer-Verlag, 1998.
[27] G.K. Vallis, G.F. Carnevale, W.R. Young, Extremal energy properties and construction of stable solutions of the Euler equations, J. Fluid Mech. 207 (1989) 133–152.
[28] T.B. Benjamin, The alliance of practical and analytical insights into the nonlinear problems of fluid mechanics, in: Lecture Notes in Math., vol. 503, Springer-Verlag, 1976, pp. 8–29.
[29] R.J. Donnelly, Quantized Vortices in Helium II, Cambridge University Press, Cambridge, 1991 (Chapter 1).
[30] C.A. Jones, P.H. Roberts, Motions in a Bose condensate: IV. Axisymmetric solitary waves, J. Phys. A: Math. Gen. 15 (1982) 2599–2619.
[31] Y.-H. Wan, Variational principle for Hill's spherical vortex and nearly spherical vortices, Trans. Amer. Math. Soc. 308 (1988) 299–312.
[32] H.K. Moffatt, Structure and stability of solutions of the Euler equations: a lagrangian approach, Philos. Trans. R. Soc. Lond. A 333 (1990) 321–342.
[33] Y. Fukumoto, A unified view of topological invariants of fluid flows, Topologica 1 (2008) (in press).
[34] P.H. Roberts, A Hamiltonian theory for weakly interacting vortices, Mathematika 195 (1972) 169–179.
[35] Y. Fukumoto, V.L. Okulov, The velocity field induced by a helical vortex tube, Phys. Fluids 17 (2005) 107101-1–107101-19.
[36] D.D. Holm, J.E. Marsden, T.S. Ratiu, The Euler–Poincaré equations and semidirect products with applications to continuum theories, Adv. Math. 137 (1998) 1–81.
[37] H.K. Moffatt, Some developments in the theory of turbulence, J. Fluid Mech. 106 (1981) 27–47.

Available online at www.sciencedirect.com
ScienceDirect
Physica D 237 (2008) 2218–2222
PHYSICA D
www.elsevier.com/locate/physd

Circulation and trajectories of vortex rings formed from tube and orifice openings

Paul S. Krueger*

Department of Mechanical Engineering, Southern Methodist University, Dallas, TX, United States

Available online 8 January 2008

Abstract

A model for vortex ring circulation developed by the author [P.S. Krueger, An over-pressure correction to the slug model for vortex ring circulation, J. Fluid Mech. 545 (2005) 427–443] is discussed. Numerical simulations of vortex ring formation are used to provide model closure and validation data for orifice-type generators. The model results agree well with the simulation results for both tube and orifice configurations provided the jet duration is sufficiently long. For short jets, the model discrepancy is explained in terms of an interaction between the primary and stopping vortices.

PACS: 47.32.cf; 47.15.ki

Keywords: Vortex ring; Circulation; Vortex trajectories

1. Introduction

The sudden ejection of a finite duration jet from a nozzle or orifice is a frequently observed unsteady flow. It is a distinguishing feature of many important systems ranging from aquatic propulsion of squid and salps [9,11] to synthetic jet actuators [3]. A piston–cylinder mechanism is commonly used to generate such flows in the laboratory where the generation of the jet is due to the piston motion as illustrated in Fig. 1.

The formation and evolution of the vortex ring that results from the roll-up of the jet shear layer has been the subject of a substantial body of research (see Shariff and Leonard [10] for a review). A key vortex ring characteristic that is directly related to the formation process is the total circulation of the ring, namely

$$\Gamma_T = \int \omega_\theta \, \mathrm{d}r \, \mathrm{d}x, \tag{1}$$

where ω_θ is the azimuthal vorticity and integration is over the domain external to the vortex ring generator. Two common methods for determining Γ_T in terms of the formation parameters involve consideration of the flux of vorticity in the jet [2] and dynamics of the vortex sheet roll-up [7]. In the case of the former, assuming uniform flow across the jet and neglecting the transient start-up behavior leads to the so-called 'slug model' in which Γ_T is determined entirely by $U_J(t)$ [10]. The assumptions made in this approach limit it to long duration pulses where the flow approaches steady jet behavior. Moreover, it does not account for geometric differences in vortex ring generators, even though orifice-type generators produce rings with nearly twice the circulation as tube-type generators under the same conditions (see [5] and Section 5). Modeling the dynamics of the vortex sheet roll-up [7], on the other hand, does account for geometric differences through appropriate boundary conditions, but it treats the flow as 2D, which limits its applicability to short time behavior [6]. Neither approach provides good accuracy over a wide range of conditions.

A different approach, developed and refined by the author [4, 5], considers the integral of the incompressible vorticity transport equation over the domain external to the vortex ring generator. This provides two terms which can be modeled using primarily potential flow considerations to account for the jet development and geometry differences, but model

* Corresponding address: Department of Mechanical Engineering, Southern Methodist University, P.O. Box 750337, 75275 Dallas, TX, United States.
E-mail address: pkrueger@engr.smu.edu.

0167-2789/$ - see front matter © 2008 Elsevier B.V. All rights reserved.
doi:10.1016/j.physd.2008.01.004

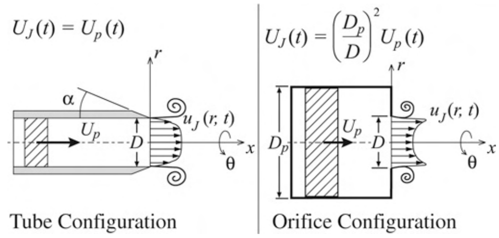

Fig. 1. Schematic of tube- and orifice-type vortex ring generators.

closure requires information about the trajectory of the vortex ring during formation. The present discussion begins with a summary of the model developed by the author. Then numerical simulations of vortex ring formation are utilized to provide model closure information in the case of the orifice configuration and data by which the model can be validated. Finally, the model and numerical results are compared and model error for short duration pulses are discussed in terms of vortex ring evolution and trajectories.

2. A model for vortex ring circulation

To aide further discussion, this section summarizes the key features of the model developed by the author [4].

For vortex ring formation by high Reynolds number jets, vorticity diffusion across the centerline may be ignored. Then integrating the vorticity transport equation over the domain external to the vortex ring generator and in time yields

$$\Gamma_T = \underbrace{\frac{1}{2}\int_0^{t_p} u_{cl}^2(t)\mathrm{d}t}_{\Gamma_U} + \underbrace{\frac{1}{\rho}\int_0^{\infty} (p_{cl}(t) - p_\infty)\mathrm{d}t}_{\Gamma_p}, \tag{2}$$

where u_{cl} and p_{cl} are the velocity and pressure at $(x, r) = (0, 0)$ and t_p is the jet duration. Since the jet ejection period dominates the contribution of u_{cl}^2 to circulation, Γ_U is integrated only up to t_p. The compact nature of the vorticity field for high jet Reynolds number results in irrotational flow at $(x, r) = (0, 0)$ so that Γ_T may be determined by potential flow analysis.

For rapidly initiated jets, the initial flow appears like that in front of a translating disk and Γ_p may be determined by integrating the unsteady Bernoulli equation for the appropriate potential flow solution. The result is

$$\Gamma_p \approx \frac{U_0 D}{C_p}, \tag{3}$$

where $C_p = \pi$ for the tube geometry and 2.00 for the orifice geometry. Here U_0 is the maximum value achieved by the jet velocity during the jet pulse. The jet termination process (which gives $p_{cl} < p_\infty$) is ignored in the evaluation of Γ_p because for sufficiently long pulse duration and rapid jet termination, the stopping vortex formed at jet termination travels back into the vortex ring generator and does not interact with the primary vortex ring. This issue is discussed further in Section 6.

To determine Γ_U, a model for $u_{cl}(t)$ is required. At jet initiation, $u_{cl}(t)$ can be determined by a potential flow solution inside the vortex ring generator. As time proceeds, however, the jet separates from the nozzle/orifice lip and the vortex ring propagates downstream. If the jet duration is long enough it approaches steady jet behavior. Based on these observations a model for $u_{cl}(t)$ may be developed using a modeling parameter σ to smoothly transition between the known initial and final states. The results for the tube and orifice configurations are, respectively,

$$u_{cl} = \frac{U_c(t)}{1 + 0.595(1 - \sigma(t))} \tag{4}$$

$$u_{cl} = \frac{U_J(t)}{2 + (C_c - 2)\sigma(t)}, \tag{5}$$

where U_c is the core velocity in the tube (outside the boundary layer) and $C_c < 1$ is the contraction coefficient (ratio of jet area at the *vena contracta* to the orifice area) for the steady state jet in the orifice configuration. Assuming a thin boundary layer, U_c may be approximated using the results of [1]. It should be noted that Eq. (5) is an *effective* centerline velocity that accounts for the downstream contraction of the jet at late time, making it appropriate for computing the vorticity flux term Γ_U; it is only equal to the actual centerline velocity at jet initiation. In either case $0 \le \sigma(t) \le 1$ where $\sigma \to 1$ at large t.

The specification of σ for model closure is based on the observation that the velocity of the forming ring ($W(t)$) increases and eventually the ring begins to move away from the vortex ring generator as steady jet behavior is approached. Taking $U_0/2$ as a reference ring velocity beyond which steady jet behavior is approximated, σ is modeled as

$$\sigma(t) = \begin{cases} \dfrac{W(t)}{U_0/2}: & W < U_0/2 \\ 1: & W \ge U_0/2. \end{cases} \tag{6}$$

For tube configurations, robust correlations are available for $W(t)$ [2,6] which, when used in Eq. (6), give Γ_T accurate to within 10% over a wide range of conditions [4], except for short pulses. In particular, for stroke ratios $L/D < 0.5$ where $L \equiv \int_0^{t_p} U_J(t)\mathrm{d}t$, Γ_T tends to be over-predicted by the model. For the orifice case, however, there was no data available on $W(t)$ throughout vortex ring formation when the model was originally formulated, so model closure was problematic. Closure based on an extension of the tube results was proposed by [4] giving reasonable results, but validation was extremely limited because there was very little Γ_T data available for orifice configurations. The present investigation builds on the numerical results of [5] to resolve the model validation and closure issues and investigate the source of the model error for $L/D < 0.5$.

3. Numerical method and computational domains

Vortex ring formation was studied numerically by simulating the axisymmetric, time dependent, incompressible Navier–Stokes equations. The equations were solved on the domains shown in Fig. 2 with the coordinate systems shown in Fig. 1. The motion of the piston was simulated using an inlet

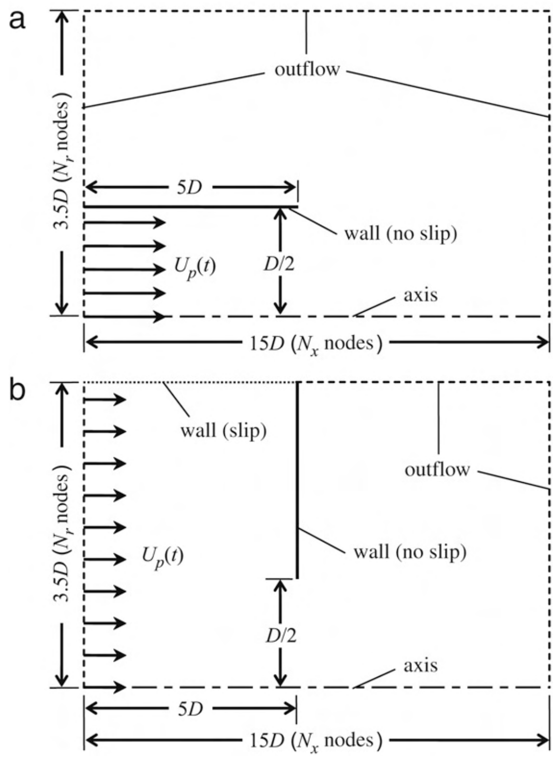

Fig. 2. Domains used in numerical simulation of vortex ring formation: (a) tube configuration, (b) orifice configuration.

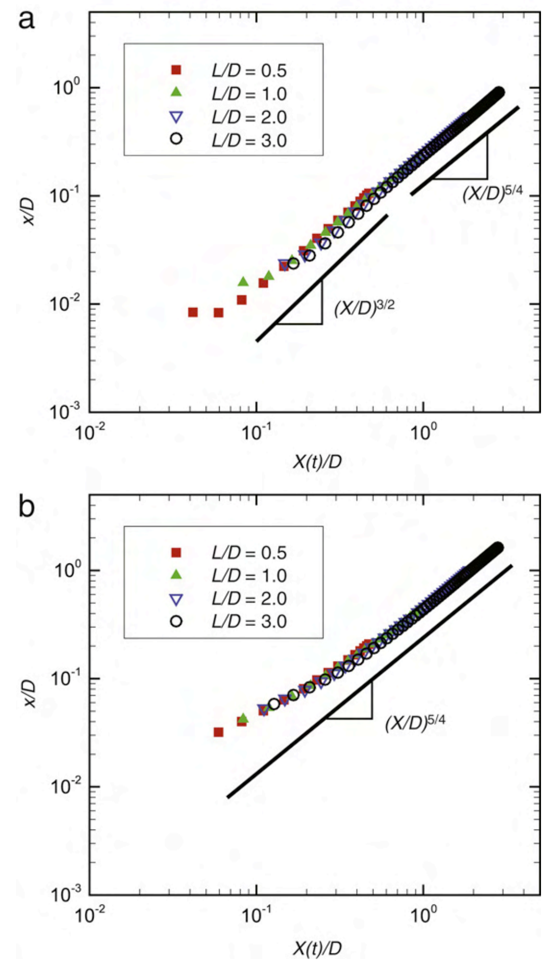

Fig. 3. Vortex trajectories during ring formation: (a) tube configuration, (b) orifice configuration.

boundary condition at the left of the domain. For the orifice case, $D_p/D = 7$ was simulated with a slip flow boundary condition at the top left of the domain to approximate the case of an orifice in an infinite plane ($D_p/D \to \infty$). A trapezoidal program (with acceleration and deceleration times specified as $0.1t_p$, each) was prescribed for the piston velocity $U_p(t)$ with a jet Reynolds number ($Re_J \equiv U_0 D/\nu$) of 2000. Stroke ratios of $0.1 \leq L/D \leq 3.5$ were simulated for both geometries.

The time dependent solutions were obtained using the Finite Volume method with the SIMPLE algorithm for pressure–velocity coupling and the QUICK scheme for approximation of the flux terms. A second-order implicit scheme was used for time integration.

The domain was discretized using a non-uniform, rectangular grid with the greatest node density near the exit plane and nozzle/orifice lip. To test grid independence, the $L/D = 1.0$ case was simulated on the orifice geometry with three grids having nodal dimensions $N_x \times N_r = 191 \times 53$, 388×120, and 571×180. Comparing Γ_T for the three cases gave less than 1% difference between the 388×120 and 571×180 grids for both geometries. Likewise, trajectories of the peak vorticity (obtained to subgrid resolution using a Gaussian fit of the local vorticity peak) showed a deviation of less than $0.01D$ between the 388×120 and 571×180 grids for $x/D < 4.4$. Thus, the 388×120 grid was used to obtain the results for this investigation.

A specified, but variable, time step was used for time integration. The base time resolution used at least four time steps during periods of jet acceleration/deceleration (to provide sufficient resolution of the initiation and termination transients) and limited the maximum time step to 5% of a convective time scale (D/U_0) during jet ejection. After jet termination, the time step for the base resolution was limited to a maximum of 5% of a convective time scale. More-coarse and less-coarse time stepping was investigated to confirm time step independence. Refining the base scheme to have 50% more time steps gave only a 1% difference in circulation. Likewise, time step refinement gave no discernible difference in vortex trajectories for $x/D < 0.75$ and less than $0.005D$ difference for $x/D > 0.75$. Consequently, the base time resolution was deemed sufficient for the present investigation.

4. Vortex ring trajectories and model closure

For model closure, the ring axial location during formation ($0 < t < 0.9t_p$) was considered for $0.5 \leq L/D \leq 3.0$. The results for the tube and orifice configurations are shown in Fig. 3. The horizontal axis in these plots is effectively a dimensionless time where $X(t) \equiv \int_0^t U_J(\tau)\mathrm{d}\tau$ is the time-varying length of the ejected fluid slug. In these coordinates, the ring trajectories collapse well.

The tube results show that $x/D \sim (X/D)^{3/2}$ for $0.5 \leq X/D < 1.5$. In fact, over this range the computational results agree, to within experimental error, with the empirical fit

$x/D = 0.28(X/D)^{3/2}$ proposed by Didden [2]. For $X/D > 1.5$ a $(X/D)^{5/4}$ scaling is approached as the flow transitions to steady jet behavior. Since $0.5 \leq X/D < 1.5$ encompasses the transition to the condition where the ring separation from the tube is significant, the present results concur with the use of Didden's result for model closure as implemented by [4]. Specifically, inserting the time derivative of Didden's empirical fit into Eq. (6) gives the following model closure for the tube configuration:

$$\sigma(t) = \begin{cases} 0.84\sqrt{X(t)/D}: & X(t)/D < 1.42 \\ 1: & X(t)/D \geq 1.42. \end{cases} \tag{7}$$

The orifice results, on the other hand, show that $x/D \sim (X/D)^{5/4}$ where the flow transitions to steady jet behavior ($X/D > 1.0$) and suggest a $(X/D)^0$ scaling as $X/D \to 0$ in agreement with [7]. In between there is no clear power-law behavior (although the results do collapse to a universal curve).

For the sake of simplicity, a power-law fit is preferred. Since W near the transition to steady jet behavior is most important for model closure, a best fit of the data for $X/D > 1.0$ was utilized, giving $x/D = 0.447(X/D)^{5/4}$. Applying this fit in Eq. (6), the model closure for the orifice configuration becomes

$$\sigma(t) = \begin{cases} 1.118(X(t)/D)^{1/4}: & X(t)/D < 0.64 \\ 1: & X(t)/D \geq 0.64. \end{cases} \tag{8}$$

5. Comparison between model and simulations

Comparison of the numerical results with the model predictions using Eqs. (7) and (8) for model closure is shown in Fig. 4. The orifice model results were obtained using $C_c = 0.61$, appropriate for a high Re_J jet issuing through a sharp-edged orifice. For display purposes, percentage error is only shown for $L/D \geq 0.5$. In the range $L/D \geq 0.5$ the model results compare very well with Γ_T calculated from the numerical results. In the tube case the results agree within 14% over this range, in agreement with [4]. The orifice results agree within 20% over the same range. The agreement achieved using Eq. (8) for closure gives an improvement of as much as 10% over the closure based on tube results proposed by [4]. Further discussion of the validity of the closure model for the orifice case can be found in [5]. For both configurations, the model performs significantly better than the slug model, which under predicts Γ_T by more than 20% for the tube geometry and greater than 60% for the orifice geometry.

At $L/D < 0.5$ the models do not perform well. The absolute error steadily increases as L/D decreases below 0.5 for the tube case and 0.2 for the orifice case.

6. Discussion

The performance of the model is satisfactory for $L/D > 0.5$. In particular, the model captures the nearly twofold difference in Γ_T between the two configurations at the same Re_J and L/D (cf. Fig. 4(a) and (b)). The ability of the model to capture the geometry effects is linked to its use of potential flow analysis, where different boundary conditions

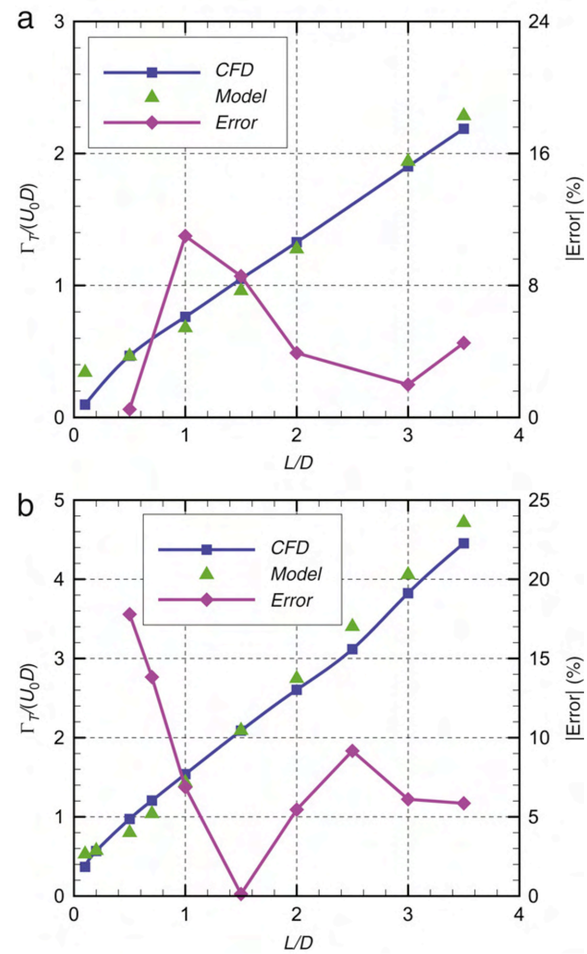

Fig. 4. Comparison of model and CFD results: (a) tube configuration, (b) orifice configuration.

can be naturally incorporated (e.g., through C_p), and through appropriate closure models for $\sigma(t)$. Although $D_p/D \to \infty$ was approximated in the orifice results, the orifice model is expected to work well for $D_p/D \geq 2$.

The use of potential flow analysis is noteworthy since the model predicts Γ_T even though vorticity is not explicitly addressed. The role played by vorticity is implicitly captured in the transition of u_{cl} to steady jet behavior at large time. In this regard, the analysis is analogous to classical airfoil theory, where the appropriate bound vortex circulation is determined by the empirically observed condition that the flow leaves the trailing edge smoothly.

In the short L/D regime, the model degradation could be tempered by fine tuning the closure models or by small adjustments to C_p related to deviations of the flow from the assumed form. The primary source of the error for $L/D < 0.5$, however, is the model prediction that Γ_p remains constant as $L/D \to 0$. In actuality Γ_p must decrease to zero along with Γ_U.

The model for Γ_p is based on the assumption that it may be determined by integrating the pressure term in Eq. (2) only over jet initiation because the stopping vortex generated at jet termination does not interact with the primary vortex and travels back into the vortex ring generator. In reality, the primary and stopping vortices are in close proximity at jet termination

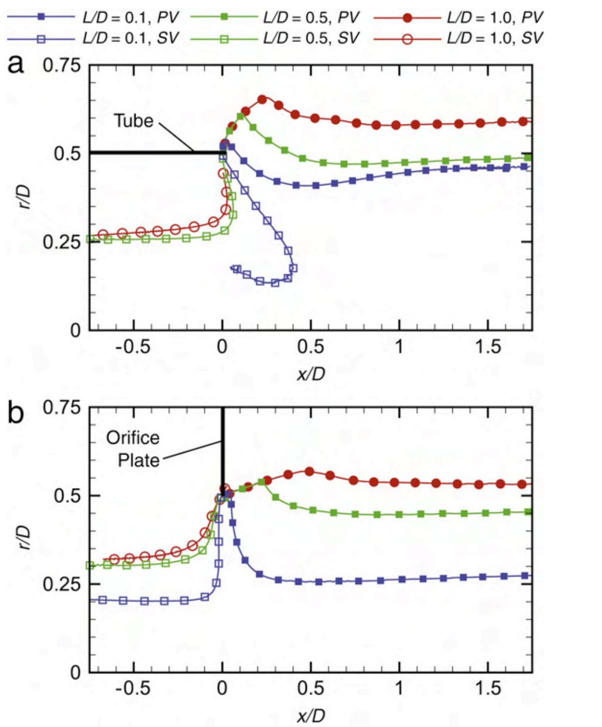

Fig. 5. Vortex trajectories: (a) tube configuration, (b) orifice configuration. PV = primary vortex, SV = stopping vortex.

for $L/D < 0.5$, as illustrated in Fig. 5. In fact, for $L/D = 0.1$, the stopping vortex for the tube configuration is actually drawn out of the vortex ring generator ($x > 0$) by its interaction with the primary vortex. Physically this occurs because immediately following jet termination the primary and stopping vortex act as a 2D vortex pair that convects toward the centerline until the self-induced velocity of each takes over and pulls them apart. The orifice results are similar except that the initial vortex trajectory after pulse termination is directed more toward the axis.

Clearly the stopping vortex can no longer be ignored as $L/D \to 0$. Rather, vorticity cancellation due to the adjacent opposite sign vorticity after jet termination tends to reduce the final circulation of the primary ring for small L/D. This effect is illustrated in Fig. 6 where the circulation of the ring only (Γ_{ring}) is shown to decrease after jet termination during the period where the stopping and primary vortices are in close contact for $L/D < 0.5$. In the limit of $L/D \to 0$ one might suppose that the primary and stopping vortices simply cancel each other and no net vortex is formed. The primary–stopping vortex interaction presents a challenge for development of a robust model for short L/D.

As a concluding remark, it is interesting to note that Fig. 5 gives no indication of the primary vortex returning into the

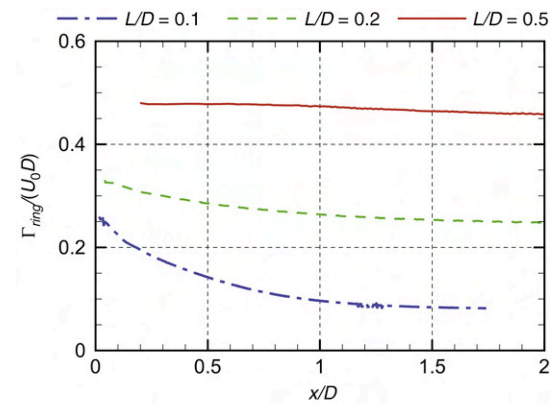

Fig. 6. Evolution of circulation of the ring only (Γ_{ring}) for the tube geometry.

vortex ring generator as L/D is reduced. This is in contrast to the potential flow prediction of Sheffield [8], which is not surprising since the stopping vortex was not included in his analysis.

Acknowledgment

This material is based upon work supported by the National Science Foundation under Grant No. 0347958.

References

[1] J.O. Dabiri, M. Gharib, A revised slug model boundary layer correction for starting jet vorticity flux, Theoret. Comput. Fluid Dyn. 17 (2004) 293–295.

[2] N. Didden, On the formation of vortex rings: Rolling-up and production of circulation, Z. Angew. Math. Phys. 30 (1979) 101–116.

[3] A. Glezer, M. Amitay, Synthetic jets, Annu. Rev. Fluid Mech. 34 (2002) 503–529.

[4] P.S. Krueger, An over-pressure correction to the slug model for vortex ring circulation, J. Fluid Mech. 545 (2005) 427–443.

[5] P.S. Krueger, Circulation of vortex rings formed from tube and orifice openings, in: Proc. ASME Fluids Eng. Div. Summer Mtg., Paper No. FEDSM2006-98268, 2006.

[6] M. Nitsche, Scaling properties of vortex ring formation at a circular tube opening, Phys. Fluids 8 (1996) 1848–1855.

[7] D.I. Pullin, Vortex ring formation at tube and orifice openings, Phys. Fluids 22 (1979) 401–403.

[8] J. Sheffield, Trajectories of an ideal vortex pair near an orifice, Phys. Fluids 20 (1977) 543–545.

[9] J. Siekmann, on a pulsating jet from the end of a tube, with application to the propulsion of certain aquatic animals, J. Fluid Mech. 15 (1963) 399–418.

[10] K. Shariff, A. Leonard, Vortex rings, Annu. Rev. Fluid Mech. 24 (1992) 235–279.

[11] D. Weihs, 1977 periodic jet propulsion of aquatic creatures, Fortschr. Zool. 24 (1977) 171–175.

Available online at www.sciencedirect.com
ScienceDirect
Physica D 237 (2008) 2223–2227
PHYSICA D
www.elsevier.com/locate/physd

Momenta of a vortex tangle by structural complexity analysis

Renzo L. Ricca*

Department of Mathematics and Applications, University of Milano-Bicocca, Via Cozzi 53, 20125 Milano, Italy
Institute for Scientific Interchange, Villa Gualino, 10133 Torino, Italy

Available online 6 January 2008

Abstract

A geometric method based on information from structural complexity is presented to calculate linear and angular momenta of a tangle of vortex filaments in Euler flows. For thin filaments under the so-called localized induction approximation the components of linear momentum admit interpretation in terms of projected area. By computing the signed areas of the projected graph diagrams associated with the vortex tangle, we show how to calculate the two momenta of the system by complexity analysis of tangle diagrams. This method represents a novel technique to extract dynamical information of complex systems from geometric and topological properties and provides a potentially useful tool to test the accuracy of numerical methods and investigate scale distribution of fluid dynamical properties of vortex flows.

PACS: 47.10.A-; 47.10.ab; 47.32.C-; 47.37.+q

Keywords: Vortex tangle; Structural complexity

1. Conservation of linear and angular momenta of a vortex tangle

In this paper we present new mathematical results concerning a method based on signed area of oriented graphs developed to evaluate linear and angular momenta of a tangle of vortex filaments in Euler's flows. In paying our tribute to celebrate more than 250 years of work on Euler's equations, we are particularly happy to present and discuss here new ideas that rely not only on such a fruitful setting, but also on another Euler's remarkable contribution, rooted in his 1735 solution of the famous Königsberg's Bridge Problem [1], namely the foundation of graph theory and what, arguably, we now call topology [2]. The idea of using graph theoretical information to study fluid dynamical properties was originally put forward by Kelvin in 1867 [3], but it remained little explored. What we present here benefits from the progress made in recent years in algebraic topology and geometric fluid mechanics and, we believe, has great potential for further developments and future applications in visiometric diagnostics of structural flow complexity [4,5].

For simplicity, let us consider the evolution of a vortex tangle in an unbounded, ideal fluid at rest at infinity, where vorticity remains localized on thin filaments of infinitesimal cross-sections. Such vortex tangles arise naturally in superfluid turbulence [6], where indeed vorticity remains confined on very thin filaments for very long time. In this context vortex evolution may be approximated by the so-called localized induction approximation, LIA for short [7,8]. The analytical results presented here are rigorously valid for LIA evolutions, and can, under mild assumptions, be adapted to evolutions of vortex filaments governed by the full Biot–Savart law (see the last section for a brief clarifying comment).

It is well-known that LIA is directly related to the nonlinear Schrödinger equation, that in one dimension is completely integrable, preserving an infinity of invariants of motion. It is remarkable that among such invariants two classical invariants of the Euler equations survive, namely the linear and angular momenta [9,10]. Let us consider these invariants for a vortex tangle. Let $\mathcal{T} = \{\bigcup_i \mathcal{L}_i\}_{i=1,\ldots,N}$ denote a tangle of N vortex lines $\mathcal{L}_i$, each line being a smooth curve in $\mathbb{R}^3$, parametrized by

* Corresponding address: Department of Mathematics and Applications, University of Milano-Bicocca, Via Cozzi 53, 20125 Milano, Italy. Fax: +39 02 6448 5705.
E-mail address: renzo.ricca@unimib.it.

0167-2789/$ - see front matter
doi:10.1016/j.physd.2008.01.002

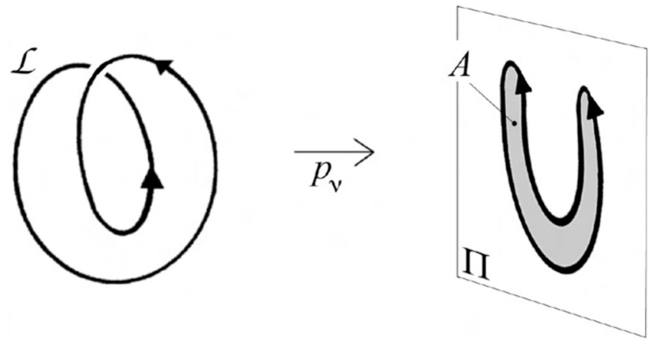

Fig. 1. The area A of the projected graph resulting from the projection p_ν of a vortex line $\mathcal{L}$ on the plane Π is proportional to the component of the linear momentum of $\mathcal{L}$ in the $\boldsymbol{\nu}$-direction.

arc-length s. Vorticity $\boldsymbol{\omega}$ is defined on $\mathcal{L}_i$, and is simply given by $\boldsymbol{\omega} = \bar{\omega}\mathbf{X}'$, where, in general, $\mathbf{X} = \mathbf{X}(s, t)$ denotes the position vector, $\bar{\omega}$ a constant and $\mathbf{t} \equiv \mathbf{X}'$ the unit tangent to $\mathcal{L}_i$ (the prime denoting the derivative with respect to s, and t is time). The linear momentum $\mathbf{P} = \mathbf{P}(\mathcal{T})$ corresponds to the hydrodynamic impulse, which generates the motion of $\mathcal{T}$ from rest, and from its standard definition [11] takes the form

$$\mathbf{P} = \frac{1}{2}\int_{\mathcal{T}} \mathbf{X} \times \boldsymbol{\omega} \mathrm{d}^3\mathbf{X} = \frac{1}{2}\sum_{i=1}^{N} \Gamma_i \int_{\mathcal{L}_i} \mathbf{X} \times \mathbf{X}' \,\mathrm{d}s, \tag{1}$$

where $\mathbf{P}$ is here intended per unit density, and Γ_i represents the circulation of $\mathcal{L}_i$. Similarly, for the angular momentum $\mathbf{M} = \mathbf{M}(\mathcal{T})$, that corresponds to the moment of the impulsive forces acting on $\mathcal{T}$; we have

$$\mathbf{M} = \frac{1}{3}\int_{\mathcal{T}} \mathbf{X} \times (\mathbf{X} \times \boldsymbol{\omega}) \mathrm{d}^3\mathbf{X}$$
$$= \frac{1}{3}\sum_{i=1}^{N} \Gamma_i \int_{\mathcal{L}_i} \mathbf{X} \times (\mathbf{X} \times \mathbf{X}') \mathrm{d}s, \tag{2}$$

where, again, $\mathbf{M}$ is intended per unit density. We remark that under both Euler's equations *and* LIA, we have

$$\frac{\mathrm{d}\mathbf{P}}{\mathrm{d}t} = 0, \qquad \frac{\mathrm{d}\mathbf{M}}{\mathrm{d}t} = 0. \tag{3}$$

2. Interpretation of momenta in terms of projected area

Arms and Hama [8], who first proved the conservation of the integral on the right-hand side of Eq. (1) for a single vortex line, showed that this quantity admits interpretation in terms of projected area (see Fig. 1). Indeed, by direct inspection of the integrand above, it is evident that under LIA the plane projected area of the vortex line is proportional to the component of the linear momentum of the vortex along the direction of projection.

Let $p = p_\nu$ denote the orthogonal projection onto the plane Π along the direction $\boldsymbol{\nu}$, and $\mathcal{L}_\nu = p_\nu(\mathcal{L})$ be the graph diagram of a smooth space curve $\mathcal{L}$ under p_ν. Evidently $\mathcal{L}_\nu$ depends on $\boldsymbol{\nu}$. For the moment let $\mathcal{L}_\nu$ be a smooth planar curve with no self-intersections, but in general $\mathcal{L}_\nu$ will be a *nodal* curve with self-intersections, the latter resulting from the projection of the apparent crossings of $\mathcal{L}$, when $\mathcal{L}$ is viewed along the line of sight $\boldsymbol{\nu}$.

By identifying the vortex line with its geometric support $\mathcal{L}$, the projected graph diagram $\mathcal{L}_\nu$ will be oriented, the orientation being naturally induced by the vorticity vector. Let $\mathcal{L}_{xy}$, $\mathcal{L}_{yz}$, $\mathcal{L}_{zx}$ be the three graph diagrams of the projected vortex line onto the mutually orthogonal planes $x = 0$, $y = 0$, $z = 0$, and let $A_{xy} = A(\mathcal{L}_{xy})$, $A_{yz} = A(\mathcal{L}_{yz})$, $A_{zx} = A(\mathcal{L}_{zx})$ be the corresponding areas of the plane regions bounded by $\mathcal{L}_{xy}$, $\mathcal{L}_{yz}$, $\mathcal{L}_{zx}$, respectively.

By applying the results of Arms and Hama [8], from (1) we have

$$P_{xy} = \Gamma A_{xy}, \quad P_{yz} = \Gamma A_{yz}, \quad P_{zx} = \Gamma A_{zx}, \tag{4}$$

where Γ is vortex circulation. Moreover:

Definition 2.1. The *resultant area* $A_{\max}$ is the maximal area obtained by $\max_\nu p(A) = p_{\max}(A)$ (along the *resultant axis* $\boldsymbol{\nu}_{\max}$) among all possible projected areas A.

The direction of the resultant axis $\boldsymbol{\nu}_{\max}$ is clearly that of the linear momentum. Hence, also from [8], we have

Theorem 2.2 (*Maximal Area Interpretation*). *The resultant linear momentum of a vortex line $\mathcal{L}$, of circulation Γ, under LIA is given by $\mathbf{P} = \Gamma A_{\max}\boldsymbol{\nu}_{\max}$, where $A_{\max}$ is the resultant area. The projected area of $\mathcal{L}$ on any plane perpendicular to that of the resultant area is zero.*

Similar results hold true for the angular momentum. With reference to the right-hand side of Eq. (2), the second integral can be interpreted in terms of areal moment, according to the following definition:

Definition 2.3. The *areal moment* around any axis is the product of the area A multiplied by the distance d between that axis and the axis $\mathbf{a}_G$, normal to A through the centroid G of A.

For a vortex line $\mathcal{L}$, the centroid G of the projected area A is the center weighted with respect to the vorticity distribution of $\mathcal{L}$. As for the linear momentum, the components of the angular momentum are determined by the areal moments:

$$M_{xy} = \Gamma d_z A_{xy}, \quad M_{yz} = \Gamma d_x A_{yz}, \quad M_{zx} = \Gamma d_y A_{zx}, \tag{5}$$

where evidently d_x, d_y, d_z are the distances between the rotational axis and the centroid axes through A_{yz}, A_{zx}, A_{xy}, respectively. Similar considerations apply to define the resultant areal moment of $\mathcal{L}$:

Definition 2.4. The *resultant areal moment* of $\mathcal{L}$ is the areal moment around the resultant axis $\mathbf{a}_G$ of the projected areas of $\mathcal{L}$ onto two mutually orthogonal planes, parallel to $\mathbf{a}_G$.

These observations are easily extended to a tangle $\mathcal{T} = \bigcup_i \mathcal{L}_i$ of N vortex lines $\mathcal{L}_i$, provided we carefully define the

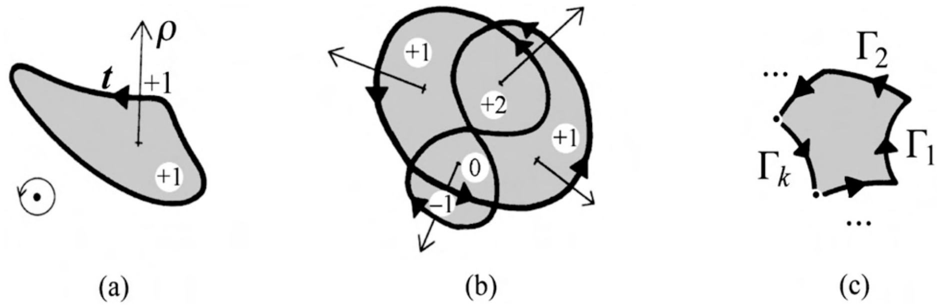

Fig. 2. (a) The number in the dashed region is the value of the index $\mathcal{I}_P(\mathcal{C})$ according to the right-hand rule convention and the algebraic intersection number calculated by Eq. (6). (b) The oriented nodal curve, resulting, for example, from the standard projection of a figure-8 knot, has 5 bounded regions. Note that one of the interior regions has index 0, due to the opposite orientation of the strands crossed by $\boldsymbol{\rho}$. (c) Contribution from each $A(\mathcal{R}_j)$ must be weighted according to the circulations on the boundary $\partial\mathcal{R}_j$.

area of the resulting oriented graph diagram. The difficulty here is precisely in the correct calculation of such area.

3. Signed area of oriented graph diagrams

The oriented graph diagram of a tangle of vortex lines is an oriented nodal curve (i.e. the "underlying universe" of the tangle) in $\mathbb{R}^2$, and this can easily attain considerable complexity, particularly as regards the localization of self-intersections. A necessary first step is to reduce nodal curves of any complexity to *good* nodal curves, that have (at most) double points. Nodal points are classified according to their degree of multiplicity $\mu(P)$ given by the number of arcs incident at the point of intersection P. If P is a double point, then $\mu(P) = 2$. If P is a point of multiplicity $\mu(P) = n$ ($n > 2$), we can always reduce its multiplicity by "shaking" the graph diagram (actually its pre-image) near P to get $m = \frac{1}{2}(n^2 - n)$ double points, by virtual perturbations of the incident arcs from their location. Thus, if $h^{(n)}$ is the total number of points of multiplicity n, by applying this shaking technique we can always replace these $h^{(n)}$ points with $h(n) = mh^{(n)}$ ($m \geq 3$) double points. We say that a graph diagram is a *good projection*, when it has at most double points. Hence, by the shaking technique, we can always reduce highly complex graph diagrams to good nodal curves.

Let $\mathcal{C}$ denote one such good nodal curve on Π, and let $A(\mathcal{C})$ be the corresponding total area. In order to calculate this area, first we need to define the index $\mathcal{I}_P(\mathcal{C})$ of $\mathcal{C}$ at the point P (for this see, for example, [12]). Let $P \notin \mathcal{C}$, $\mathbf{t}$ the tangent to $\mathcal{C}$ and $\boldsymbol{\rho}$ the radiant vector with foot at P, that intersects $\mathcal{C}$ transversally. At each intersection point $X \in \boldsymbol{\rho} \cap \mathcal{C}$ assign the algebraic sign $\epsilon(X) = \pm 1$, according to the standard convention given by the right-hand rule, that is $\epsilon(X) = +1$ when the frame $\{\boldsymbol{\rho}, \mathbf{t}\}$ is positive (see Fig. 2(a)). If X is a double point, then the intersection is computed with one of the neighbouring pairs of the incident, equi-oriented arcs.

Definition 3.1. The *index* $\mathcal{I}_P(\mathcal{C})$ of $\mathcal{C}$ at P is the algebraic intersection number given by

$$\mathcal{I}_P(\mathcal{C}) = \sum_{X \in \boldsymbol{\rho} \cap \mathcal{C}} \epsilon(X). \tag{6}$$

Hence, $\mathcal{I}_P(\mathcal{C}) \in \mathbb{Z}$.

Let us now consider the Z sub-domains $\{\mathcal{R}_j\}_{j=1,\ldots,Z}$ determined by $\mathcal{C} \cap \Pi$ and bounded by $\mathcal{C}$, and let $A(\mathcal{R}_j) > 0$ denote their standard area. Since every point $P \in \mathcal{R}_j$ has the same $\mathcal{I}_P(\mathcal{C})$, we shall call $\mathcal{I}_j$ the index associated with any point $P \in \mathcal{R}_j$ and assign this value to each sub-domain $\mathcal{R}_j$ of $\mathcal{C} \cap \Pi$ (see Fig. 2(b)). The signed area of an oriented graph, a concept that can be traced back to Gauss [13], is thus given by the following rule.

Rule 3.2 (*Signed Area*). *The signed area $A(\mathcal{C})$ of an oriented, planar nodal curve $\mathcal{C}$, is given by*

$$A(\mathcal{C}) = \sum_{j=1}^{Z} \mathcal{I}_j A(\mathcal{R}_j), \tag{7}$$

where $A(\mathcal{R}_j) > 0$ is the standard area of $\mathcal{R}_j$.

4. Linear and angular momenta of a vortex tangle by structural complexity analysis

By the signed area rule we can calculate the projected area of any nodal curve, be it the graph of a single vortex line, or that of a complex tangle of vortices. If the vortices have different circulations, a weighting factor defined in terms of contributions from each arc of $\partial\mathcal{R}_j$ must be assigned to $A(\mathcal{R}_j)$ (see Fig. 2(c)). The simplest correction comes from the algebraic weighting γ_j. Let $L_j = L(\partial\mathcal{R}_j) = \sum_{k=1,\ldots,M} L_{k,j}$ denote the total length of the boundary curve $\partial\mathcal{R}_j$ made of M oriented arcs, the k-th arc having length $L_{k,j}$ and circulation Γ_k. We have

Definition 4.1. The *circulation weighting factor* γ_j of $\mathcal{R}_j$ is given by

$$\gamma_j = \frac{\sum_{k=1}^{M} \Gamma_k L_{k,j}}{L_j}. \tag{8}$$

If all the vortices have same circulation Γ, then evidently $\gamma_j = \Gamma$. Appropriate weighting of circulation is necessary to determine the correct location of the centroid of the projected area. To summarize, we have the following result.

Theorem 4.2 (*Signed Area Interpretation*). *Let $\mathcal{T}$ be a vortex tangle evolving under LIA. Then, the linear momentum* $\mathbf{P} = \mathbf{P}(\mathcal{T})$ *has components*

$$P_{xy} = \sum_{j=1}^{Z} \gamma_j \mathcal{I}_j A_{xy}(\mathcal{R}_j), \quad P_{yz} = \cdots, \quad P_{zx} = \cdots, \tag{9}$$

and the angular momentum $\mathbf{M} = \mathbf{M}(\mathcal{T})$ *has components*

$$M_{xy} = d_z \sum_{j=1}^{Z} \gamma_j \mathcal{I}_j A_{xy}(\mathcal{R}_j), \quad M_{yz} = \cdots, \quad M_{zx} = \cdots, \tag{10}$$

where $A_{xy}(\mathcal{R}_j), \ldots,$ etc. denotes standard area of $\mathcal{R}_j$.

Proof of the above theorem is based on direct applications of (4) and (5), by using the signed area Rule 3.2.

5. Dynamical aspects based on signed area information

Signed area contributions provide useful information, that can be applied, predictively, to estimate and, postdictively, to understand some dynamical properties of the system. Remember that: (i) areas with index 0 do not contribute to the momentum; (ii) areas with high index (in absolute value) weight more and, proportionally, contribute more to the dynamical impulse of the system; (iii) areas of opposite sign determine contributions in opposite directions. Additional information on dynamical aspects may also come from index gradient analysis. Take the case of Fig. 2(b): here the alignment of regions, where the index gradually changes from -1 to $+2$, indicates the presence of a principal axis of revolution. The exact location of this axis, placed orthogonally to the alignment of such regions, is determined by an accurate estimate of the weighted areas and, in any case, it can be determined by signed area information.

Let us consider two other examples, assuming, for simplicity, equal circulations and maximal projected areas. In Fig. 3(a) we have the projection of a single coiled filament, that in space is wound up 5 times around a circular axis (not shown). Contribution from the 5 negative areas exceeds that from the positive area, hence the resultant momentum is oriented in the negative direction. If such a vortex configuration existed, it would propagate backwardly in space. Such an unusual behaviour may not be so unrealistic, as recent analytical solutions [14,15] and numerical tests [16] seem to suggest.

Another interesting case is illustrated by the following example. Consider the head-on collision of two anti-parallel vortex rings, propagating co-axially one against the other. The linear momentum of the two-ring system (as a whole) is obviously zero, and in ideal conditions this value is conserved until collisional time. In the case of real dynamics at sufficiently high Reynolds number, slight perturbations of the circular axes are likely to develop and, upon collision, we can expect that these will trigger sinusoidal disturbances along the two colliding ring axes. Here, analysis of the projected diagram may be rather illuminating. Without loss of generality and for the sake of simplicity, let us drastically simplify the situation and consider the perturbed circular axes as the elliptical curves sketched in Fig. 3(b) (realistic perturbations would obviously generate a far more complex diagram). The central region has index 0 and is surrounded by four regions (light grey) of alternating sign. Consistently with what we expect from the annihilation of the rings velocity, this gives zero contribution to the resultant linear momentum of the two-ring system.

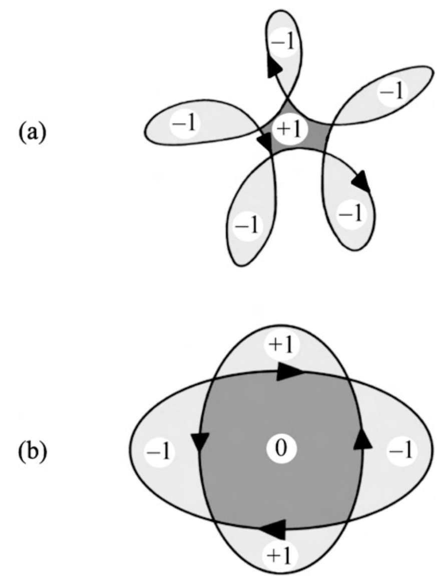

Fig. 3. (a) Projected diagram of a coiled vortex filament: contribution from negative areas (light grey) exceeds that from positive area (dark grey); hence, the resultant linear momentum of the vortex is negative. (b) Graph of the projection of two anti-parallel, elliptical vortex rings: opposite contributions from regions of index of alternating sign (light grey) cancel out; hence, the resultant linear momentum of the two-ring system is zero.

When the two rings collide, the alternating sign of the four surrounding regions is an indicator of an imminent structural instability, that produces the shoot-off of a pair of small vortex rings on either side of the collisional plane. In a realistic scenario, the precise number of surrounding regions will depend on geometric details of the perturbation, but in any case the production of an equal number of secondary small rings on either side of the collisional plane must be expected. These considerations seem confirmed by direct inspection of experimental results (see, for instance, [17]). In real experiments a diadem of a large number of secondary small vortex rings is clearly visible. This diadem grows from the instability of a fluid membrane that is produced in the collisional plane, upon collision of the primary large vortex rings. These secondary rings appear to be alternately distributed on either side of the collisional plane, surviving just for a short time before final dissipation.

6. Concluding remarks

The geometric method based on the signed area interpretation summarized by Theorem 4.2 provides a new and potentially useful tool for fluid dynamics research. The method exploits information from structural complexity analysis of a tangle of vortex filaments to estimate linear and angular momenta of the system. This is done by computing the signed areas of the projected graph diagrams associated with the vortex tangle, after application of appropriate shaking and weighting techniques. The results are rigorously valid in the LIA context, but, as mentioned earlier, in principle they could be extended to thin vortex filaments governed by the Biot–Savart law. This extension seems plausible as long as vorticity remains localized in a tubular domain of volume small compared with the fluid volume 'embraced' by the tangle. In terms of projected areas, this corresponds to assuming that the (standard) area of the vorticity domain is much smaller compared with the overall area enclosed by the outermost boundary projected curve, the order of approximation depending presumably on this ratio. Physically, this simply means that the higher the localization of vorticity, the most efficacious is the production and transfer of hydrodynamic impetus and moment, two quantities that are conserved under Euler's equations, regardless of the validity of the localized induction approximation.

In any case, for LIA systems the geometric method proposed here provides a potentially useful tool for predictive and postdictive diagnostics. By analyzing projected areas, it can be applied to implement tests of accuracy of numerical methods simulating vortex tangles. In superfluids, in particular, by analyzing the area distribution of the vortex projection one can judge about the scale distribution of linear and angular momenta, and compare this with the expected values of the spectrum of turbulence (Kolmogorov's two-thirds law). Moreover, since LIA preserves an infinity of invariants of motion, *all* of these admitting a geometric interpretation in terms of global curvature, torsion and higher-order gradients [18,10], these can be implemented to supply further information on dynamical properties (for instance, kinetic energy and helicity). Other features associated with the analysis of projected graphs can be related to dynamical issues, but this is beyond the scope of this article. We just like to conclude mentioning that the famous relation [19] $\chi(G) = v - e + r$, between the Euler characteristic $\chi(G)$ of a graph G (associated with vortex topology), of v vertices, e edges and r regions, may find also useful applications in the study of complex systems [20] and in the advanced diagnostics of complex flow patterns.

Acknowledgments

I would like to thank C. Weber for pointing out Ref. [13]. Financial support from Italy's MIUR (D.M. 26.01.01, n. 13 "Incentivazione alla mobilità di studiosi stranieri e italiani residenti all'estero") and from ISI-Fondazione CRT (Lagrange Project) is kindly acknowledged.

References

[1] L. Euler, Solutio problematis ad geometriam situs pertinentis, Commentarii Academie Scientiarum Imperialis Petropolitanae 8 (1741) 128–140.
[2] G.L. Alexanderson, Euler and Königsberg's bridges: A historical view, Bull. Am. Math. Soc. 43 (2006) 567–573.
[3] Lord Kelvin (W. Thomson), On vortex atoms, Proc. R. Soc. Edin. 6 (1867) 94–105.
[4] C.F. Barenghi, R.L. Ricca, D.C. Samuels, How tangled is a tangle? Physica D 157 (2001) 197–206.
[5] R.L. Ricca, Structural complexity, in: A. Scott (Ed.), Encyclopedia of Nonlinear Science, New York and London, Routledge, 2005, pp. 885–887.
[6] K.W. Schwarz, Three-dimensional vortex dynamics in superfluid ^{4}He: Homogeneous superfluid turbulence, Phys. Rev. B 38 (1988) 2398–2417.
[7] L.S. Da Rios, On the motion of an unbounded liquid with a vortex filament of any shape, Rend. Circ. Mat. Palermo 22 (1906) 117–135 (in Italian).
[8] R.J. Arms, F.R. Hama, Localized induction concept on a curved vortex and motion of an elliptic vortex ring, Phys. Fluids 8 (1965) 553–559.
[9] Y. Fukumoto, On integral invariants for vortex motion under the localized induction approximation, J. Phys. Soc. Japan 56 (1987) 4207–4209.
[10] R.L. Ricca, Physical interpretation of certain invariants for vortex filament motion under LIA, Phys. Fluids A 4 (1992) 938–944.
[11] P.G. Saffman, Vortex Dynamics, Cambridge University Press, Cambridge, 1991.
[12] R. Langevin, Differential geometry of curves and surfaces, in: R.L. Ricca (Ed.), An Introduction to the Geometry and Topology of Fluid Flows, in: NATO Science Series II, vol. 47, Kluwer Academic Publs., Dordrecht, 2001, pp. 13–33.
[13] C.F. Gauss, Letter to H. Olbers, Werke 8 (1825) 398–400.
[14] Y. Fukumoto, Stationary configurations of a vortex filament in background flows, Proc. R. Soc. Lond. A 453 (1997) 1205–1232.
[15] L. Kiknadze, Yu. Mamaladze, The waves on the vortex ring in He II, J. Low Temp. Phys. 126 (2002) 321–326.
[16] C.F. Barenghi, R. Hänninen, M. Tsubota, Anomalous translational velocity of vortex ring with finite-amplitude Kelvin waves, Phys. Rev. E 74 (2006) 1–5.
[17] T.T. Lim, T.B. Nickels, Instability and reconnection in head-on collision of two vortex rings, Nature 357 (1992) 225–227.
[18] H.K. Moffatt, R.L. Ricca, Interpretation of invariants of the Betchov–Da Rios equations and of the Euler equations, in: J. Jimenez (Ed.), The Global Geometry of Turbulence, Plenum Press, New York, 1992, pp. 257–264.
[19] W.S. Massey, Algebraic Topology: An Introduction, Harcourt, Brace and World, Inc., New York.
[20] R.L. Ricca, Structural complexity and dynamical systems, in: R.L. Ricca (Ed.), Lectures on Topological Fluid Mechanics, Springer-CIME Lecture Notes in Mathematics, Springer-Verlag, Berlin, 2008 (in press).

Available online at www.sciencedirect.com

ScienceDirect

Physica D 237 (2008) 2228–2233

PHYSICA D

www.elsevier.com/locate/physd

Final states of decaying 2D turbulence in bounded domains: Influence of the geometry

Kai Schneider[a,*], Marie Farge[b]

[a] M2P2–CNRS & CMI, Université de Provence, Marseille, France
[b] LMD–CNRS, Ecole Normale Supérieure, Paris, France

Available online 16 February 2008

Abstract

Direct numerical simulations of two-dimensional decaying turbulence in wall bounded domains are presented. The Navier–Stokes equations are solved using a Fourier pseudo-spectral method with volume penalization. Starting from random initial conditions, we study the influence of the geometry of the domain on the flow dynamics, in particular on the long time behaviour. Circular, square, triangular and annular domains are considered and we show how the geometry plays a crucial role regarding the decay scenario towards final states. Three stages can be distinguished: formation of coherent vortices from random initial conditions, vortex wall interactions, and finally relaxation towards a quasi-steady structure. The eigenvalues estimated from the decay rate of both energy and enstrophy depend on the geometry and agree well with the theoretical eigenvalues based on the Stokes mode of the corresponding domain. For the final states we find a linear functional relation between vorticity and streamfunction.

PACS: 47.27.Eq; 47.32.Cc

Keywords: 2D turbulence; Confined flows; Final states; Stokes eigenmodes

1. Introduction

Two-dimensional turbulence in wall-bounded domains has many applications in geophysical flows, *e.g.* the prediction of currents in oceanic basins, the transport and mixing of pollutants. Experiments in rotating tanks, *e.g.*, in [2], leading to quasi two-dimensional geostrophic flows, have shown the formation of long-lived coherent vortices. Quasi two-dimensional experiments in stratified fluids for square and circular containers have been presented in [10,6,16]. Several numerical simulations of two-dimensional turbulence in bounded domains have been performed so far, *e.g.*, in circular and square domains [15,5,4,22]. Compared to simulations in double periodic domains the decay scenario is altered in bounded domains with no-slip boundary conditions, since the role of viscous boundary layers is determinant, for a discussion see, *e.g.*, [7].

The aim of the present paper is to study the influence of the geometry of the domain on the flow dynamics, in particular on its long-time behaviour. Therefore we consider four different geometries: circular, square, triangular and annular domains. Typically, we observe the formation of stable large-scale structures which persist for a long time before they are finally dissipated.

Late states of decaying two-dimensional flows in periodic domains were investigated, *e.g.*, in [17,23]. Here we study the final states of wall-bounded flows considering different geometries with no-slip boundary conditions.

Several theoretical predictions of the long time behaviour of two-dimensional flows have been made for unbounded or periodic domains. Variational principles for predicting the final state are based on the 'selective decay' hypothesis supposing conservation of energy and decay of enstrophy [13]. In this heuristic approach enstrophy is minimized under constraint

* Corresponding author. Tel.: +33 491118529; fax: +33 491113502.
E-mail addresses: kschneid@cmi.univ-mrs.fr (K. Schneider), farge@lmd.ens.fr (M. Farge).

0167-2789/$ - see front matter
doi:10.1016/j.physd.2008.02.012

of conservation of energy and eventually additional conditions. Another variational hypothesis has been proposed, based on statistical mechanics, which introduces a measure of mixing, leading to the definition of an entropy. The final states then correspond to a maximum of entropy as turbulence maximizes mixing [8,19]. For two-dimensional flows in bounded domains, with either free-slip [9] or no-slip [10] boundary conditions, a different approach based on viscous eigenmodes of the Stokes flow has been used to predict the self-organization of the flow into 'final' states. Stokes eigenmodes in a square domain with no-slip boundary conditions have been computed in [14].

The paper is organized as follows. First, we briefly recall the volume penalization technique and the numerical method employed to solve Navier–Stokes equations in different geometries (Section 2). The construction of viscous eigenmodes is sketched in Section 3. Then, numerical results of decaying flows in four different geometries are presented in Section 4 and conclusions are drawn in Section 5.

2. Numerical scheme and geometry

The numerical technique we use here is based on a Fourier pseudo-spectral method with semi-implicit time discretization and adaptive time-stepping [21]. The Navier–Stokes equations are solved in a double periodic square domain of size $L = 2\pi$ using the vorticity–velocity formulation. The bounded domain Ω is imbedded in a periodic domain and the no-slip boundary conditions on the wall $\partial\Omega$ are imposed using a volume penalization method. A mathematical analysis of the method is given in [1], proving its convergence towards the Navier–Stokes equations with no-slip boundary conditions. Details on the code, together with its numerical validation, can be found in [21]. The governing equations in vorticity-velocity formulation, written in dimensionless form, are

$$\partial_t \omega + \vec{u} \cdot \nabla\omega - \nu \nabla^2 \omega + \nabla \times \left(\frac{1}{\eta} \chi \vec{u} \right) = 0, \quad (1)$$

where $\vec{u}$ is the divergence-free velocity field, *i.e.*, $\nabla \cdot \vec{u} = 0$, $\omega = \nabla \times \vec{u}$ the vorticity, ν the kinematic viscosity and $\chi(\vec{x})$ a mask function which is 0 inside the fluid, *i.e.*, $\vec{x} \in \Omega$, and 1 inside the solid wall.

Four different geometries are considered: a circle with radius $R = 2.8$, a square of sidelength $S = 5.712$, an equilateral triangle with sidelength $T = 5.8$ and an annulus with minor radius $R_m = 0.8$ and major radius $R_M = 2.8$. All domains are centred inside the periodic square domain of size $L = 2\pi$. The viscosity is set to $\nu = 0.001$. For all computations the resolution is $N = 256^2$ and the penalization parameter η is chosen to be sufficiently small ($\eta = 10^{-3}$) [21].

Different integral quantities, the energy E, enstrophy Z and palinstrophy P, can be defined as [11]

$$E = \frac{1}{2} \int_\Omega |\vec{u}|^2 \mathrm{d}\vec{x}, \qquad Z = \frac{1}{2} \int_\Omega |\omega|^2 \mathrm{d}\vec{x},$$
$$P = \frac{1}{2} \int_\Omega |\nabla\omega|^2 \mathrm{d}\vec{x}, \quad (2)$$

respectively.

Table 1
Properties for different geometries

	Circle	Triangle	Annulus	Square
t_ν	200	180	210	280
Theor. EV μ_1	1.87	–	2.73	1.60
Estim. EV	1.89	5.88	2.74	1.70
Estim. α	1.90	4.25	2.70	1.70

Viscous time, theoretical eigenvalues [10,12], eigenvalues estimated from the energy and enstrophy decay (Fig. 2) and estimated slope of the linear functional relationship at final instants (Fig. 4).

The energy dissipation is given by $\mathrm{d}_t E = -2\nu Z$ and the enstrophy dissipation by

$$\mathrm{d}_t Z = -2\nu P + \nu \oint_{\partial\Omega} \omega(\vec{n} \cdot \nabla\omega) \mathrm{d}s, \quad (3)$$

where $\vec{n}$ denotes the outer normal vector with respect to the boundary of the domain $\partial\Omega$. The line integral in (3) reflects the enstrophy production at the wall, involving the vorticity and its gradients, which is due to the no-slip boundary conditions. This second term is not present in the case of periodic boundary conditions.

3. Viscous eigenmodes of the Stokes flow

Final decay of two-dimensional turbulence in bounded domains with no-slip boundary conditions is characterized by a self-similar decay of the fundamental mode of the Stokes flow [5]. For a square domain an analytical expression was derived, either for stress-free [9], or for no-slip boundary conditions [10]. For the later case numerical computations of the Stokes eigenmodes and the corresponding eigenvalues were presented in [14]. The solution of the vorticity equation neglecting the nonlinear term

$$\partial_t \omega - \nu \nabla^2 \omega = 0 \quad (4)$$

is expressed as a superposition of exponentially decaying modes, each characterized by an eigenvalue μ_n,

$$\omega(\vec{x}, t) = \sum_\mu C_\mu \, \omega_\mu(\vec{x}) \, \mathrm{e}^{-\mu_n \nu t}, \quad (5)$$

with $\mu_n > 0$, and where the constants C_μ are determined by the initial conditions. For each value of μ_n the following Helmholtz equation for $\omega_\mu(\vec{x})$ has to be solved.

$$\nabla^2 \omega_\mu(\vec{x}) + \mu \, \omega_\mu(\vec{x}) = 0. \quad (6)$$

Since for the vorticity no boundary condition is available we consider instead the streamfunction ψ. Replacing in Eq. (6) $\omega = \nabla^2\psi$, we obtain a fourth order PDE

$$\nabla^4 \psi_\mu(\vec{x}) + \mu \nabla^2 \psi_\mu(\vec{x}) = 0. \quad (7)$$

The no-slip boundary condition of the velocity yields for the stream function $\psi = \frac{\partial\psi}{\partial n} = 0$.

The available theoretical lowest eigenvalues for the circular, annular and square geometry are given in Table 1. For the circle the eigenvalue is the square of the first zero crossing of the

Bessel function of order one, divided by the square of the radius R, to take into account the domain size. For the square domain, the value given in [10] has to be multiplied by $(\pi/(S/2))^2$, which corresponds to the value computed numerically in [14] divided by $(S/2)^2$, due to different normalizations. Analytical expressions for the Stokes eigenfunctions of the annular domain can be found in [12]. The corresponding eigenvalues are given by a transcendent equation containing Bessel functions of the first and second kind. More details on the eigenmodes of the circular and annular domains are given in the Appendix.

4. Numerical results

Starting with the same random initial conditions, *i.e.*, a correlated Gaussian noise with an energy spectrum $E(k) \propto k^{-4}$, we compute the flow evolution in the four different geometries for initial Reynolds numbers, $Re = 2D\sqrt{2E}/\nu$, of about 1000 (where D corresponds to the characteristic domain size). Fig. 1 shows the vorticity fields at early, intermediate and late times, for circular, square, triangular and annular domains. All flows organize into larger and larger scale structures until reaching the domain size and forming a structure which then no more evolves. For the circular geometry (Fig. 1, top) we observe the transition via a quasi-dipolar structure, before reaching the final state where a monopole is formed. It consists of a negative circular vortex surrounded by a band of positive vorticity which forms a kind of circular jet. The final state of the annular geometry (Fig. 1, bottom) corresponds to two ring-shaped bands of oppositely signed vorticity which corresponds to a circular jet. During the transition phase, a triangularly shaped vortical structure forms which is surrounded by three positive vortices. For the triangle and the square domain (Fig. 1, middle) we see that the final state is not yet completely reached. During the transition phase we observe a tripole which evolves towards a kind of circular jet as for the circular and annular domains. In the present simulations the infinite sequence of corner eddies of the Stokes eigenmodes, predicted by Moffatt [18] and computed numerically in [14], cannot be observed for the triangular and square domains. Indeed, the magnitude of these vortices decays exponentially and a high resolution spectral method where the basis functions satisfy the no-slip boundary conditions would be required for observing them.

Figs. 2 and 3 present the decay of different integral quantities, energy (Fig. 2, left), enstrophy (Fig. 2, right) and palinstrophy (Fig. 3, left) for the four geometries. All quantities exhibit at early times a rapid monotonuous decay, which is partly due to the fact that the flow has first to adjust to the boundary conditions, since the initial conditions do not satisfy them. For the square, circular and triangular geometries we observe an oscillatory behaviour in the palinstrophy decay, which is, however, less pronounced for the latter case. These oscillations are due to the enstrophy production at the wall. Considering the decay of the fundamental Stokes mode, we can characterize the long time decay of energy, enstrophy and palinstrophy, to be proportional to $\exp(-2\mu\nu t)$ according to Eq. (5). At later times we find indeed, for all geometries and all quantities, an exponential decay behaviour for which

Fig. 1. 2d decaying turbulence in bounded domains. Vorticity fields at early (left), intermediate (middle) and late times (right). From top to bottom: circle, square, triangle and annulus.

the decay rates depend on the geometry. Table 1 presents the time instant t_ν when viscous decay starts to dominate for the different geometries. It is identified by considering the palinstrophy evolution and detecting the moment when the decay slows down and becomes exponential. We computed slopes by fitting an exponential curve using a least square method, applied to both energy and enstrophy evolution, which yield similar results. The square domain shows the slowest decay for all quantities, followed by the circle, the annulus, while the triangle exhibits the fastest decay. To get an estimation of the eigenvalue μ we divide the slopes thus obtained by twice the viscosity. The resulting estimated eigenvalues μ are given in Table 1 and are compared with the theoretical values based on the Stokes eigenmodes, given in [10] for the circle and the square geometry, and in [12] for the annulus. Note that the theoretical values are adapted to our normalization. The estimated eigenvalues agree well with the available theoretical values for all geometries.

The time evolution of the mean square wavenumber $k_\lambda = \sqrt{Z/E}$, which is inversely proportional to the Taylor microscale λ, is plotted in Fig. 3, right. It is measuring the inverse average vortex size in the flow and is bounded from below by the size of the domain. For unbounded flows, one can show that $\frac{\mathrm{d}k_\lambda^2}{\mathrm{d}t} \leq 0$, *i.e.*, the average vortex size is monotonously increasing [17]. In the present cases we observe a monotonous decay at early times. At later times a nonmonotonous behaviour is found

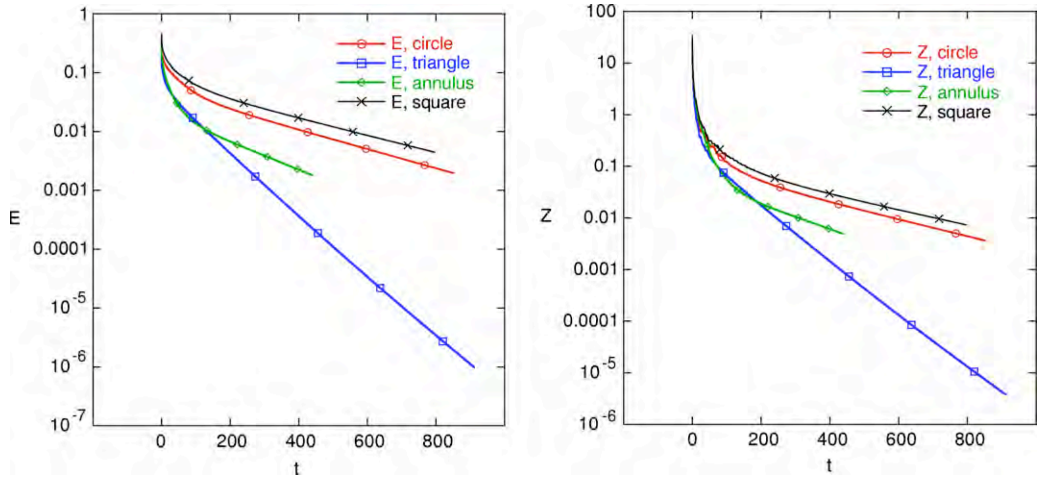

Fig. 2. Decay of energy $E(t)$ (left) and enstrophy $Z(t)$ (right) for circular, square, triangular and annular domains.

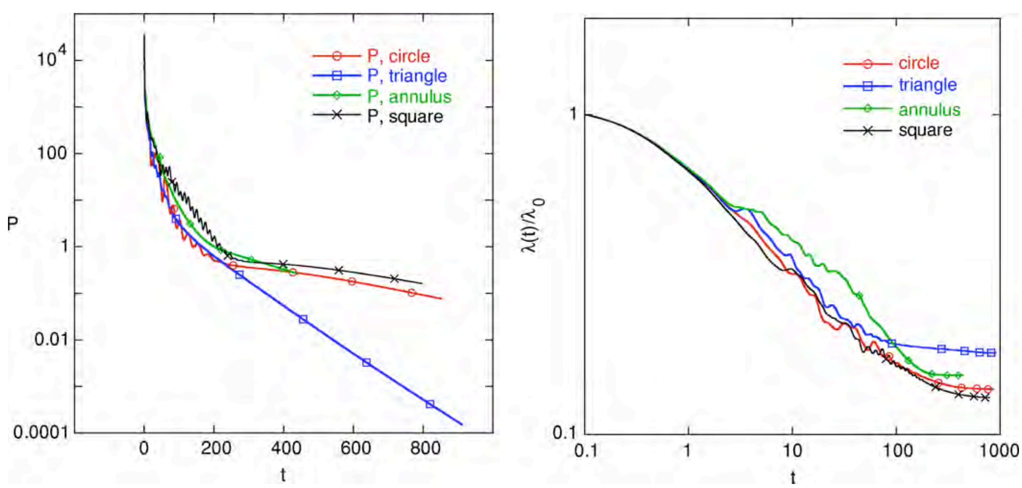

Fig. 3. Decay of palinstrophy $P(t)$ (left) and the normalized mean square wavenumber $k_\lambda(t)/k_\lambda(0)$ (right), for circular, square, triangular and annular domains.

which is due to the intermittent generation of vortices at the no-slip wall (cf. Fig. 3, right). Note that in [22] we also found a nonmonotonous behaviour for a circular domain at higher Reynolds number ($Re = 50\,000$). At late times, the mean square wavenumber becomes constant for all cases, which confirms that the size of the structure is not changing anymore. The coherence scatter plot, defined as the pointwise correlation between vorticity and stream function, is shown in Fig. 4 for the four geometries at the corresponding final instant of the simulations. The coherence plot measures the self-organization of the flow. A functional relationship between ω and ψ implies that the nonlinearity has been depleted, and that the flow has reached a quasi-stationary state.

For the flows in bounded domains considered here we find a linear functional relationship between ω and ψ, *i.e.*, $\omega = F(\psi)$ with $F(\psi) = \alpha\psi$ in the four cases. This is in agreement with the linear relationship found in [10] for the square domain. We also observe that close to the wall the linear relationship is less pronounced. For the triangular domain we still have some scattering which might be due to the persistence of higher order eigenmodes. The values of α, obtained by fitting a straight line in the scatter plot (Fig. 4), are given in Table 1 and they agree approximately with the eigenvalues of the corresponding geometry.

5. Conclusion

By means of DNS of wall-bounded flows in domains of different geometries, we have shown that no-slip boundary conditions and the geometry of the domain play a crucial role for the decay of turbulent flows. At early times, we observe a decay of the flow which leads to self-organization and the emergence of vortices in the bulk flow, similarly to flows in periodic domains. At later times, larger scale structures form which depend on the domain geometry, and they finally relax towards quasi-steady states. The present results confirm both numerical and experimental studies performed for circular and square domains [16,7].

In contrast to simulations of two-dimensional turbulence in periodic domains, we do not observe selective decay in bounded domains with no slip boundary conditions, since in this case energy is no more conserved but strongly dissipated. The viscous dissipation becomes the dominant mechanism of these final states, which correspond to the fundamental Stokes eigenmodes of the different geometries. The nonlinear

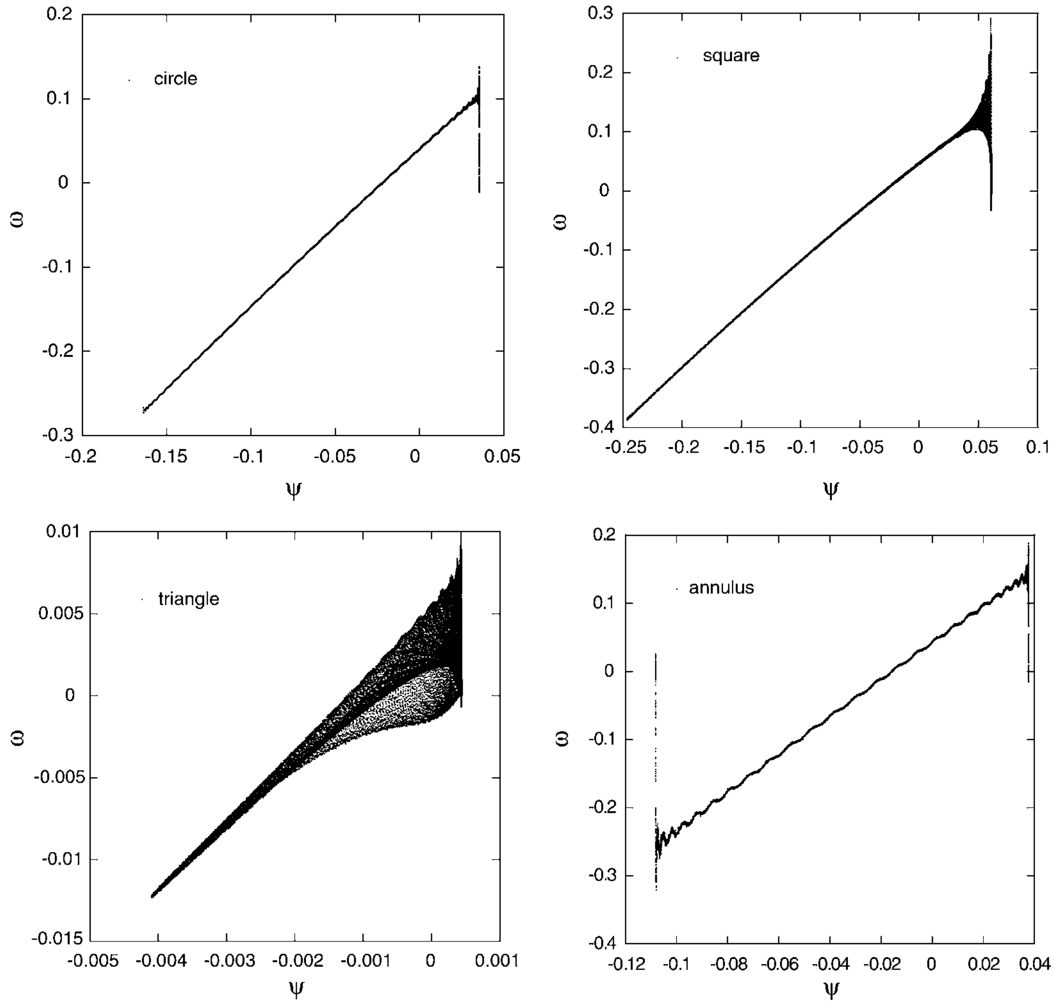

Fig. 4. Coherence scatter plot for the different geometries at final instants: circle (top, left), square (top, right), triangle (bottom, left) and annulus (bottom, right).

term in the Navier–Stokes equations is depleted and we observe a functional relationship between streamfunction and vorticity. For wall-bounded domains this relationship is linear, corresponding to the eigenmodes. This linear relationship, originally suggested by Batchelor [3], corresponds to steady motion of an inviscid fluid, or, when multiplied by $\exp(-\mu\nu t)$ to decaying motion of viscous fluid. The observed decay rates μ of the exponentially decaying energy and enstrophy agree well with the smallest eigenvalues of the Stokes eigenmodes of the different geometries.

Acknowledgements

We acknowledge financial support from the Agence Nationale de la Recherche, project "M2TFP". We thankfully acknowledge one of the referees for useful comments, and J. P. Kelliher for bringing to our knowledge Ref. [12].

Appendix

In the following we present the eigenfunctions and the corresponding eigenvalues for the circular and annular domains. Their derivation in velocity-pressure formulation can be found in the original papers [20,12].

For the circular domain with radius R the azimuthally symmetrical solutions of Eq. (7) are given by [20]

$$\psi_\mu(r) = J_0(\sqrt{\mu_n} r) - J_0(\sqrt{\mu_n} R) \tag{8}$$

with $r = |\vec{x}|$ and where J_0 denotes the Bessel function of first kind of order zero. The eigenvalues μ_n are obtained from the zeros of the Bessel function of first kind of order one, *i.e.*,

$$J_1(\sqrt{\mu_n} R) = 0 \tag{9}$$

which yields for the lowest eigenvalue, $\mu_1 = 1.873$ (with $R = 2.8$). Note that (8) satisfies $\psi_\mu(r = R) = 0$ and $\partial_r \psi_\mu(r = R) = 0$.

For the solution of the vorticity equation (5) we get correspondingly

$$\omega(r, t) = \sum_n c_n \mu_n J_0(\sqrt{\mu_n} r) \mathrm{e}^{-\mu_n \nu t}. \tag{10}$$

For the annular domain with minor radius R_m and major radius R_M the azimuthally symmetrical solutions of Eq. (7) are given by [12]

$$\psi_\mu(r) = J_0(\sqrt{\mu_n} r) - J_0(\sqrt{\mu_n} R_M)$$

$$-\frac{J_1(\sqrt{\mu_n}R_m)}{Y_1(\sqrt{\mu_n}R_m)}\left(Y_0(\sqrt{\mu_n}r)-Y_0(\sqrt{\mu_n}R_M)\right), \quad (11)$$

where Y_0 and Y_1 denote the Bessel functions of second kind (also called Weber functions) of order 0 and 1, respectively.

The eigenvalues μ_n are solutions of the transcendent equation

$$J_1(\sqrt{\mu_n}R_M)Y_1(\sqrt{\mu_n}R_m)-J_1(\sqrt{\mu_n}R_m)Y_1(\sqrt{\mu_n}R_M)=0 \quad (12)$$

which yields (using Maple) for the lowest eigenvalue, $\mu_1 = 2.731$ (with $R_m = 0.8$ and $R_M = 2.8$).

For the vorticity in eq. (5) we get

$$\omega(r,t)=\sum_n d_n\,\mu_n\left[J_0(\sqrt{\mu_n}r)-\frac{J_1(\sqrt{\mu_n}R_m)}{Y_1(\sqrt{\mu_n}R_m)}J_0(\sqrt{\mu_n}r)\right]\mathrm{e}^{-\mu_n\nu t}. \quad (13)$$

For the square and triangular domains there are to our knowledge no explicit expressions available.

References

[1] P. Angot, C.H. Bruneau, P. Fabrie, Numer. Math. 81 (1999) 497–520.

[2] J. Aubert, S. Jung, H.L. Swinney, Geophys. Res. Lett. 29 (2002) 1876.

[3] G.K. Batchelor, An Introduction to Fluid Mechanics, Cambridge University Press, 1967. Reprinted 1994.

[4] H.J.H. Clercx, A.H. Nielsen, D.J. Torres, E.A. Coutsias, Eur. J. Mech. B - Fluids 20 (2001) 557–576.

[5] H.J.H. Clercx, S.R. Maassen, G.J.F. van Heijst, Phys. Fluids 11 (3) (1999) 611–576.

[6] H.J.H. Clercx, S.R. Maassen, G.J.F. van Heijst, Phys. Rev. Lett. 80 (1998) 5129–5132.

[7] G.J.F. van Heijst, H.J.H. Clercx, D. Molenaar, J. Fluid Mech. 554 (2006) 411–431.

[8] G. Joyce, D. Montgomery, J. Plasma Phys. 10 (1973) 107.

[9] Y. Kondoh, M. Yoshizawa, A. Nakano, T. Yabe, Phys. Rev. E 54 (3) (1996) 3017–3020.

[10] J.A. van de Konijnenberg, J.B. Flor, G.J.F. van Heijst, Phys. Fluids 10 (3) (1998) 595–606.

[11] R.H. Kraichnan, D. Montgomery, Rep. Progr. Phys. 43 (1980) 547–619.

[12] D.-S. Lee, B. Rummler, Z. Angew. Math. Mech. 82 (6) (2002) 399–407.

[13] C.E. Leith, Phys. Fluids 27 (6) (1984) 1388–1395.

[14] E. Leriche, G. Labrosse, J. Comput. Phys. 200 (2004) 489–511.

[15] S. Li, D. Montgomery, B. Jones, Theoret. Comput. Fluid Dyn. 9 (1997) 167–181.

[16] S.R. Maassen, H.J.H. Clercx, G.J.F. van Heijst, Phys. Fluids 14 (2002) 2150–2169.

[17] W.H. Matthaeus, W.T. Stribling, D. Martinez, S. Oughton, Phys. Rev. Lett. 66 (1991) 2731–2734.

[18] H.K. Moffatt, J. Fluid Mech. 18 (1964) 1–18.

[19] R. Robert, J. Sommeria, J. Fluid Mech. 229 (1991) 291–310.

[20] B. Rummler, Z. Angew. Math. Mech. 77 (8) (1997) 619–627.

[21] K. Schneider, Comput. Fluids 34 (2005) 1223–1238.

[22] K. Schneider, M. Farge, Phys. Rev. Lett. 95 (2005) 244502.

[23] E. Segre, S. Kida, Fluid Dyn. Res. 23 (1998) 89–112.

Available online at www.sciencedirect.com
ScienceDirect
Physica D 237 (2008) 2234–2239
PHYSICA D
www.elsevier.com/locate/physd

The hydrodynamics of flexible-body manoeuvres in swimming fish

Kiran Singh*, Timothy J. Pedley

DAMTP, University of Cambridge, United Kingdom

Available online 12 February 2008

Abstract

Swimming in flexible-bodied animals like fish is characterised by a travelling wave passing along the spinal chord of the body. Symmetric transverse undulations of the body generate thrust and propel the fish forward. Turns are effected by generating an asymmetric transverse movement of the fish body, frequently as a C-shaped bend. Typical fish swimming speeds allow for simplifying assumptions of incompressible and inviscid flow. The objective of the current work is to use existing theoretical models developed for forward swimming, to analyse fish turns. Lighthill's classical elongated-body theory for fish swimming forms the fundamental basis for the 3D flow model and 'recoil' correction concept implemented here. In the methods developed here, transverse motion of a thin 'waving' plate is prescribed by a displacement signal acting along the midline, for finite time t_o. Lighthill's approach to calculate the rigid-body motion or 'recoil' correction is implemented to ensure zero net force and moments act on the body. Accordingly, angular and transverse motion are computed and final orientation of the plate after the manoeuvre is calculated. A 3D boundary-value algorithm has been developed using a vortex lattice method. The essential methodology, modifications for turning and comparisons with the analytical methods in the small and large aspect ratio limits are presented.

PACS: 47.63.M-; 47.15.ki; 47.11.Hj

Keywords: Swimming; Flexible-body motion; Manoeuvres; Vortex methods

1. Introduction

Fish are a typical example of flexible bodies swimming in an inviscid flow (Reynolds numbers $> 10^5$). Most fish swim in an aquatic environment that practically eliminates the effects of gravity. They have evolved different forms of swimming depending upon several factors, such as habitat and feeding habits. Gray's [1] pioneering experiments helped to characterise fish swimming in terms of a wave of muscular contraction passing down the length of the body. Symmetric transverse undulations of the body generate thrust and propel the fish forward. However, fish rarely swim in straight lines at constant speeds. More often, they tend to drift or swim slowly, occasionally indulging in rapid turns or a fast start in order to catch prey or escape from a predator. The objective of this paper is to examine the hydrodynamics of flexible bodied swimmers to understand the turning mechanics.

Lighthill [2] was the first to apply the methods of slender-body theory to an undulating body swimming in an inviscid fluid medium. Wu [3] modified the methods of thin airfoil theory to analyse the motion of a waving 2D plate. Both these methods allow for calculations of thrust, side force and yaw moment. Lighthill's theory is most likely to be applicable to long slender eel-like fish without prominent body-fins and a gradual taper in dimensions to the caudal fin. These theories have been further extended to account for body-taper at the caudal-peduncle and fin protrusions [4], time-varying forward speeds [5] and large amplitude motion [6]. Comparison of these methods is often done with numerical methods. Cheng et al. [7] first developed the vortex lattice method for rectangular, infinitely thin waving plates. Hill and Pedley [8,9] extended the method to examine large amplitude forward swimming. The full panel method for fish models of realistic thickness has been developed extensively by the Triantafyllou group at MIT [10, 11].

Significantly less attention, experimental or theoretical, has been devoted to studying turns however. Gray's investigations did include observations of turning fish [12]. Through

* Corresponding address: DAMTP, University of Cambridge, CMS, Wilberforce Road, CB3 0WA Cambridge, United Kingdom. Tel.: +44 (0) 1223760417.

E-mail address: kiran.singh@damtp.cam.ac.uk (K. Singh).

0167-2789/$ - see front matter © 2008 Elsevier B.V. All rights reserved.
doi:10.1016/j.physd.2008.02.002

time-sequence photographs, he was able to show the body-flexure involved in performing turns. In general however, most observations on manoeuvring fish have been on starts from rest [13]. Webb [14] recently examined turns in trout and bass to measure their turning radius and dependence on speed and acceleration. Theoretically, Weihs [15] applied the large amplitude version of Lighthill's theory [6] to model a turn, using Gray's experimental observations [12]. Although fins are important for turning in many species, they introduce complexities that Lighthill's theory of an undulating body does not account for. Recently Wolfgang et al. [10] qualitatively compared the flow field from PIV for a Giant Danio (*Danio Malabaricus*) performing a C-turn with their flow computations from an unsteady 3D numerical panel method. Other studies on manoeuvring swimmers have typically used methods based on linear control theory [16–18]. The key problem with large amplitude turns lies in the complex coupled interaction of the active bending body with the fluid, and in particular interaction with the vortex wake. Furthermore, the internal dynamics, both active muscle mechanics and passive visco-elastic deformations, depend on the inertial and hydrodynamic forces.

The essential 2D and 3D methods developed by Wu and Lighthill, respectively, have formed the basis from which the turning models were developed. Here we analyse how simple rectangular, thin, flexible-body swimmers manoeuvre. A numerical boundary value method using the 3D vortex lattice approach was developed to compare the validity and applicability of the theoretical methods, using a variation of the straight swimming techniques. The asymmetric manoeuvre is prescribed as a deflection about of the midline and the rigid-body motion or 'recoil correction' parameters are computed based on the inertial and hydrodynamic forces and moments. The straight swimming methods are summarised in Section 2 and the turning methods and corresponding results are presented in Section 3.

2. Forward swimming

This section examines the methodologies employed for analysing forward swimming in undulating bodies and compares some results from the analytical and numerical vortex methods.

2.1. Analytical swimming models

The linear swimming models assume the flexible-body swims at constant forward speed such that the thrust force balances fluid viscous resistance. Reynolds number is considered to be high enough ($\sim > 10^5$) for viscous effects to be confined to the boundary layer. Equations are solved in a body frame of reference with the fluid moving at velocity U_∞ along the x direction (from head to tail). For both analytical models, the fish is represented by an undulating midline with prescribed mass distribution. In this paper, Lighthill's 3D 'elongated-body' theory is examined briefly [2]. The 2D 'waving plate' method developed by Wu [3] will not be discussed here although results from this theory will be compared with those from the numerical methods.

Lighthill's elongated-body theory: This theory assumes transverse-body dimensions and deflections are an order of magnitude smaller than the body length and there exists a gradual variation in cross-section profile. The body has a stretched-straight configuration such that no resultant normal force acts at any point along the body. It executes transverse motion $h_z(x, t)$ along the perpendicular z direction.

Slender-body theory describes flow around the body to be a linear combination of the ambient steady flow and perturbations in the fluid flow induced by body deflections. The transverse velocity is given by,

$$v(x,t) = \frac{\partial h_z}{\partial t} + U_\infty \frac{\partial h_z}{\partial x} \quad (1)$$

relative to the free-stream. This imparts a momentum $\rho A(x) v(x, t)$ per unit length of the body, where $m(x) = \rho A(x)$ is the added mass per unit body length. In Lighthill's model $m(x)$ is approximately the mass of the circular cylinder of water C_x of diameter equal to the depth of the body at cross-section S_x, while moving in the transverse z direction.

The transverse force per unit length is now given by,

$$L(x,t) = -\rho \left(\frac{\partial}{\partial t} + U_\infty \frac{\partial}{\partial x} \right) (v(x,t) A(x)), \quad (2)$$

whose integral along the length of the fish must balance the rate of change of lateral momentum. Similarly the yaw moment about the spanwise axis must balance the rate of change of angular momentum. This forms the basis for Lighthill's 'recoil correction' principle, which requires that for a prescribed backbone displacement, an imbalance in force and moment can be corrected with a recoil translation and rotation about the centre of mass. This is the basic concept used to analyse turning and is examined in more detail in Section 3.

An extension of 'elongated-body' theory for large amplitude motion assumes that the body is inextensible, with the independent Lagrangian variable s indicating position along the body from nose ($s = 0$) to tail ($s = 1$). The inextensibility condition is represented by,

$$\left(\frac{\partial h_x}{\partial s} \right)^2 + \left(\frac{\partial h_z}{\partial s} \right)^2 = 1. \quad (3)$$

Spatial integration of Eq. (3) gives $h_x(s, t)$. For small amplitude motion, x and s are interchangeable.

2.2. Numerical panel methods

Current computational capabilities now permit numerical solutions to fish swimming problems. These may then be compared with the analytical methods. Cheng et al. [7] considered an infinitesimally thin waving plate modelled as a network of rectangular vortex rings. The wake was modelled as a spanwise row of rings shed at each time step so as to satisfy the Kutta condition. Hill [9] extended Cheng's method for large amplitudes. (For details on vortex methods see [19].)

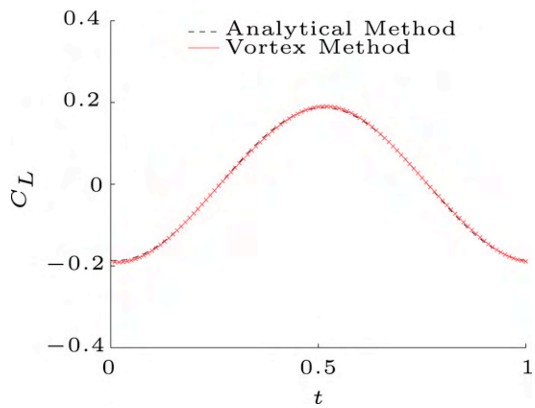

(a) Lift coefficient: C_L.

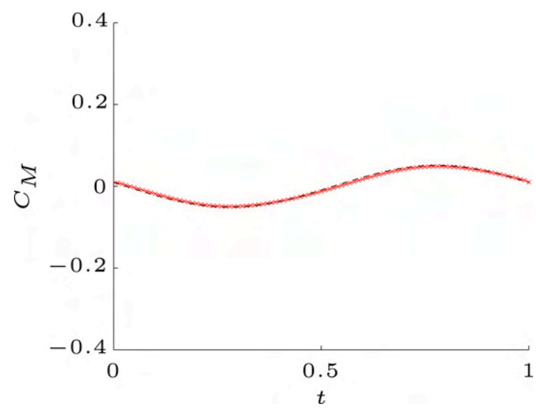

(b) Moment coefficient: C_M.

Fig. 1. Small amplitude pitch–heave motion of 2D flat plate, heave leading pitch by $\pi/2$.

The essential problem is to calculate the flow field generated by a prescribed displacement, $h_z(x, t)$ of the spinal chord of the fish swimming in a background flow ($\mathbf{Q}_\infty$). The boundary value problem [19] examines the flow due to a body, S_B, moving in a volume V in an irrotational, incompressible fluid bounded at infinity by a surface, S_∞. Viscous effects are confined to the surface, S_W, which is the wake shed at vorticity shedding edges subject to the Kutta condition. The continuity condition in an irrotational fluid requires the perturbation velocity potential, ϕ, to satisfy the Laplace equation, and singularity solutions are sought to represent this flow. Thus the body is discretised into finite elements or 'panels' which are represented by a distribution of singular elements. Discrete vortices form the simplest singularity solution in 2D. The corollary in 3D are quadrilateral rings constructed from a lattice of vortex lines.

Body and wake vorticity are calculated by applying the condition of zero normal relative velocity and prescribed body position at each panel. The Kutta condition is applied at the trailing edge. Green's identity is used to solve the Laplace equation in terms of vortex ring circulation strength. In integral form this is given by the Biot–Savart law, which prescribes the velocity induced at a position $\mathbf{r}$ with respect to a closed vortex filament, C, of circulation Γ to be,

$$\mathbf{q_{ind}} = \nabla\phi = \frac{\Gamma}{4\pi}\int_C \left(\frac{\mathbf{dl}\times\mathbf{r}}{r^3}\right). \tag{4}$$

The normal velocity boundary condition applied at the collocation point of each body panel,

$$(\mathbf{q_{ind}} - \mathbf{Q}_\infty)\cdot\mathbf{n} = 0, \tag{5}$$

gives a system of linear equations. Eqs. (4) and (5) are solved for the instantaneous circulation strength of each vortex ring. The unsteady Bernoulli equation is then applied to compute the differential pressure across the body due to the full velocity potential, $\Phi = \phi + \phi_\infty$,

$$\Delta P = -\rho\left(\frac{1}{2}\nabla\Phi\cdot\nabla\Phi + \frac{\partial\Phi}{\partial t}\right), \tag{6}$$

where ϕ_∞ is the velocity potential function for the background flow, $\mathbf{Q}_\infty$. The pressure may be integrated spatially to solve for thrust, side force and yaw moment.

2.3. Results

This section compares results from the theoretical and numerical methods developed for forward swimming, which give an estimate of the accuracy of the numerical algorithms. The variables in these computations are non-dimensionalised with respect to body swimming parameters. The dimensional scales are body length $\bar{l}$, steady swimming speed $\bar{U}$, time $\bar{t}$ and fluid density $\bar{\rho}$.

2D *model-small amplitude pitch–heave*: In these results, Wu's waving plate model is restricted to two degrees of freedom, heave and pitch (phase difference of $-\pi/2$). The plate is allowed to move at speed U_o and flap about its midchord, $x_{cg} = 0.5$. Fig. 1 plots the side force and moment computed for one time period. The results suggest the numerical panel method agrees well for small amplitude pitch and heave.

3D *model-large amplitude swimming*: The results in this section examine the role of undulations on the lift generated by a swimmer. The transverse displacement of the waving plate is given by the waveform,

$$h_z(s, t) = \Re\left([A + B(s - s_{cg})]e^{i(\omega t - ks)}\right). \tag{7}$$

For small enough amplitudes s is the same as x. A wavenumber range of -3 to 5 is considered. In Fig. 2 (a) results for side force from Wu's 2D model are compared with the large aspect ratio (20) 3D vortex lattice method for a heaving ($A = 0.1$, $B = 0$) and a pitching ($A = 0$, $B = 0.1$) swimmer. The general trends agree between analytical and numerical models, although at $k = 5$, numerics differ from the analytical predictions, reasons for which are not apparent at this point. In Fig. 2(b) the small aspect ratio (0.5) numerical swimming model is compared with the results by Lighthill. The waveforms are the same as for the 2D case for heave and pitch swimming. For this case, the maximum side force generated is predicted to be less than from the analytical model. This is to be expected as Lighthill's method does not account for the shed wake. For increasingly positive wavenumber, side-force predictions asymptote to zero for both.

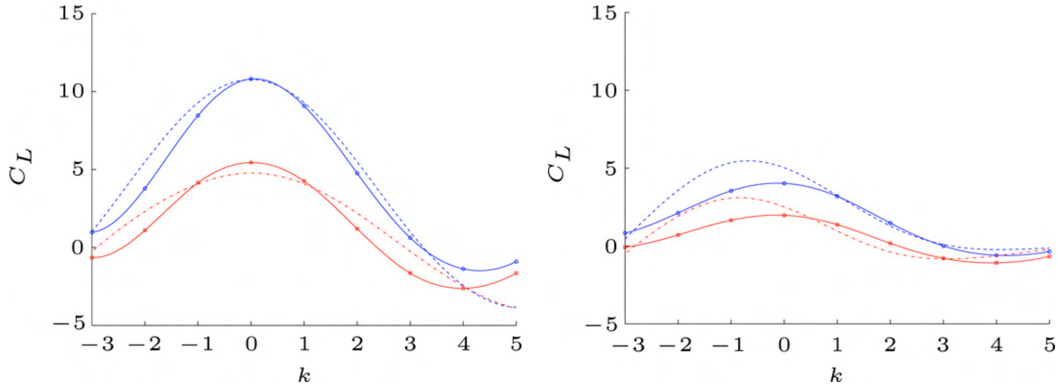

(a) 2D lift: C_L.

(b) 3D lift: C_L.

Fig. 2. Side force per unit span vs. wavenumber for steady swimming: (a) 2D and (b) Small aspect ratio 3D waving plate in heave (upper two curves) and pitch (lower two curves) flexible swimming. (Analytical results: dash curves, numerical results: solid curves).

3. Turning manoeuvres

A model based on Lighthill's method modified for turns is presented in this section. The fish is represented as a thin rectangular plate with constant mass per unit body length, m_b. The motion is assumed to be such that while initially gliding along at speed U_∞, it executes an asymmetric manoeuvre given by a prescribed function $h_z(x, t)$.The initially unknown recoil parameters (side translation, $R(t)$ and yaw rotation, $\Theta(t)$) are computed at the centre of mass, from the spatial integral of the inertial and hydrodynamic force and yaw moment. Thus the actual trajectory is worked out by including the rigid-body or recoil terms. The turning methodology is developed here for the Lighthill model, although the results presented include comparisons between the modified 2D Wu and 3D Lighthill methods with the numerical vortex lattice method. Similarly, the recoil approach is applied to the 3D numerical method developed in Section 2.2. Here the recoil parameters are solved instantaneously from the force and moment balance equations, using Newton's iterative root-finding technique.

3.1. 3D turns: Modified lighthill theory

The theory presented in Section 2.1 is modified to compute the instantaneous trajectory in response to a prescribed asymmetric manoeuvre for a swimming rectangular plate of finite span. The basic assumptions remain the same and similar terminology applies except where specified. Small perturbations are assumed, thus the independent spatial variable of choice is the x coordinate. Transverse deflection $h_z(x, t)$ is specified as a linear combination of the prescribed function $\bar{h}_z(x, t) = f(x)g(t)$ and recoil variables $R(t)$, $\Theta(t)$ as,

$$h_z(x, t) = \bar{h}_z(x, t) + R(t) + (x - x_{cg})\Theta(t), \tag{8}$$

where x_{cg} is the position of the centre of mass of the body. The linear and angular momentum conservation equations are,

$$\int_0^1 \left(m_b \frac{\partial^2 h_z}{\partial t^2} + \left(\frac{\partial}{\partial t} + U_\infty \frac{\partial}{\partial x} \right) m v \right) \mathrm{d}x = 0, \tag{9}$$

$$\int_0^1 (x - x_{cg}) \left(m_b \frac{\partial^2 h_z}{\partial t^2} + \left(\frac{\partial}{\partial t} + U_\infty \frac{\partial}{\partial x} \right) m v \right) \mathrm{d}x = 0 \tag{10}$$

where v is given by Eq. (1) and $m = \rho A(x)$ is the added mass per unit length of the body. For a prescribed function representing the transverse manoeuvre, a pair of second-order differential equations in time are obtained. The coefficients depend on body inertia and added mass, spanwise distribution of mass and the transverse deflection function, $f(x)$. Eqs. (9) and (10) may be spatially integrated depending upon the body profile and mass distribution to yield a pair of second-order ODES for the time-dependent recoil parameters R, Θ. Solutions of these differential equations give us the actual trajectory of the body performing a prescribed manoeuvre, subject to the coupled inertial-hydrodynamic model. Once again, note that Lighthill's model does not account for the wake shed off the trailing edge (or the caudal fin).

3.2. Results

Results for prescribed transverse motion from Lighthill's model discussed in Section 3.1 as modified for turning as well as the modified 2D Wu method (not developed in this paper) are compared with numerical vortex methods. The input function, $\bar{h}_z(x, t) = f(x)g(t)$ is specified such that the body performs a C-bend for a time, t_o, given by,

$$f(x) = (x - x_{cg})^2 \tag{11}$$

$$\begin{aligned} g(t) &= \frac{(1 - \cos(2\pi t))}{8}, \quad 0 < t < t_o \\ &= 0, \quad t > t_o. \end{aligned} \tag{12}$$

2D: *Wu vs. numerics*: Fig. 3 compares recoil parameters for 2D Wu method and large aspect ratio ($AR = 20$) 3D numerical methods. Recoil predictions agree quite well for this simplified turn problem. However, a comparison of the force and moment contributions indicates that the pressure distributions differ between analytical and numerical solutions. Moment predictions agree reasonably well, but the side-force predictions between the 3D large aspect ratio numerics and analytical model differ in phase, which is possibly due to the wake shed at the trailing edge. The planar wake assumption as applied in the numerical models (no wake rollup) may need to be revisited.

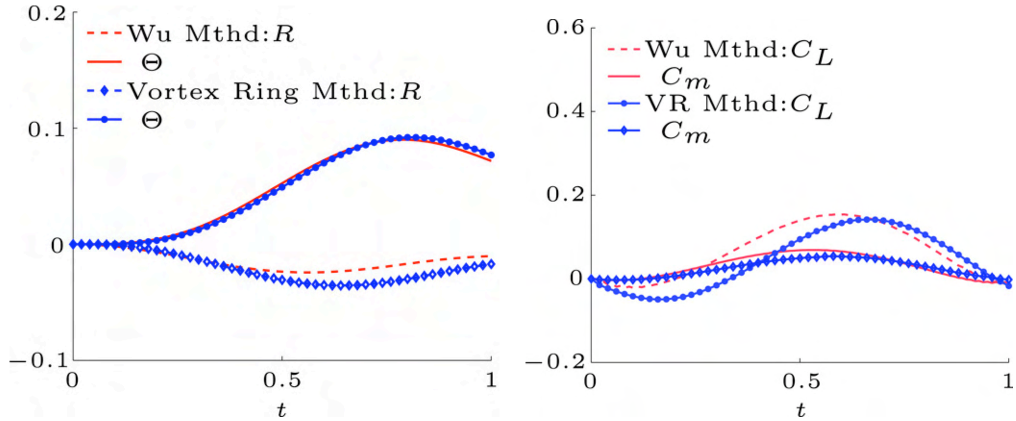

(a) Recoil parameters: R, Θ. (b) Side force, yaw moment: C_L, C_M.

Fig. 3. Recoil parameters and force and moment comparisons for 2D Turns. Analytical calculations are in red, numerics in blue (Analytical calculations are the solid and dashed curves, numerics are shown with symbols). (For interpretation of the references to colour in this figure legend, the reader is referred to the web version of this article.)

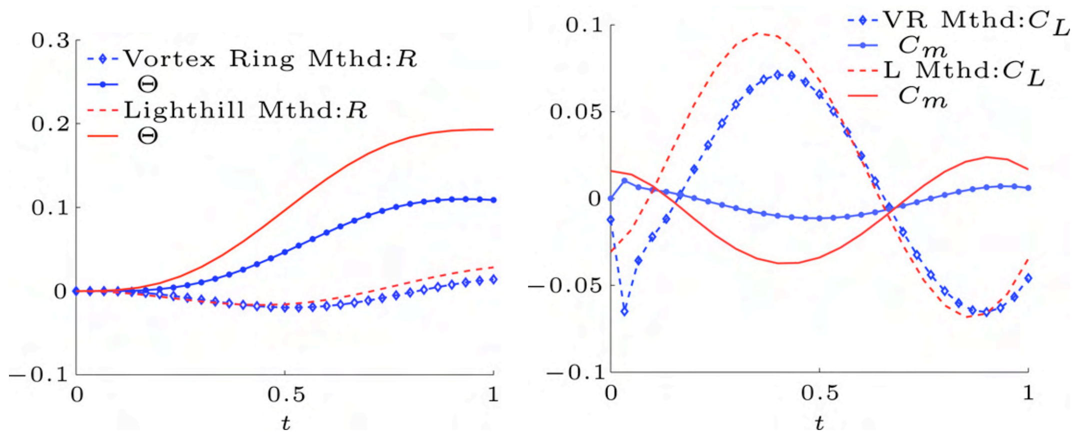

(a) Recoil parameters: R, Θ. (b) Side force, yaw moment : C_L, C_M.

Fig. 4. Recoil parameters and force and moment comparisons for 3D Turns. Analytical Lighthill model calculations are the solid and dashed curves, 3D numerics are given by symbols (C_L-dashed curves, C_M-solid curves).

3D: *Lighthill vs numerics*: Fig. 4 compares results for the 3D vortex method with Lighthill's approach for the same transverse displacement function. Here, a small aspect ratio plate is considered ($AR = 0.2$). Translational recoil agrees fairly well but angular recoil computations are off by a factor of almost 2. Lighthill's prediction of hydrodynamic pressure distribution around the body differs considerably from the numerical computations. This presumably explains the difference between analytical and computational side force and moment and therefore the higher recoil values predicted by Lighthill. Lighthill's theory ignores the shed wake while the discrete vortex method explicitly includes the wake through the Kutta condition at the trailing edge.

4. Future work

The research developed here extends the forward flexible-body swimming models to analyse turning manoeuvres for rectangular waving plates. The results suggest that for these simplified geometries, the modified Lighthill elongated-body method overpredicts the hydrodynamic side force and corresponding yaw moments. As a result the actual turning angles are expected to be lower than predicted by Lighthill. The subsequent steps to this work include extension of the 3D numerical methods to include realistic body profiles, representative body thickness, internal muscle dynamics and fluid viscous effects. These will be implemented by modifying the discretisation module to include various planforms. Body thickness will be included through a source-doublet panel method. The internal structural dynamics of the fish will be modelled initially using Euler's beam theory as implemented by Cheng et al. and Hill and Pedley [20,8,9]. These studies will initially be conducted for fish manoeuvres that involve swimming turns. They will be extended to model manoeuvres from rest, like C and S starts. Comparisons of these studies will be made with the analytical methods discussed here to understand the extent of their applicability.

Acknowledgments

The authors wish to acknowledge the contributions of the DAMTP, University of Cambridge and Fitzwilliam College in supporting this work.

References

[1] J. Gray, Animal Locomotion, Weidenfeld and Nicolson, London, 1968.
[2] M.J. Lighthill, Note on swimming of slender fish, J. Fluid Mech. 9 (part 2) (1960) 305–317.
[3] T.Y.T. Wu, Swimming of a waving plate, J. Fluid Mech. 10 (1961) 321–344.
[4] T.Y.T. Wu, Hydromechanics of swimming propulsion. Part 3. Swimming and optimum movements of slender fish with side fins, J. Fluid Mech. 46 (3) (1971) 545–568.
[5] T.Y.T. Wu, Hydromechanics of swimming propulsion. Part 2. Some optimum shape problems, J. Fluid Mech. 46 (3) (1971) 521–544.
[6] M.J. Lighthill, Large-amplitude elongated-body theory of fish locomotion, Proc. R. Soc. 179 (1971) 125–138.
[7] J.Y. Cheng, L.X. Zhuang, B.G. Tong, Analysis of swimming three-dimensional waving plates, J. Fluid Mech. 232 (1991) 341–355.
[8] T.J. Pedley, S.J. Hill, Large-amplitude undulatory fish swimming: Fluid mechanics coupled to internal mechanics, J. Exp. Biol. 202 (1999) 3431–3438.
[9] S.J. Hill, Large amplitude fish swimming, Ph.D. Thesis, University of Leeds, Department of Applied Mathematics, 1998.
[10] M.J. Wolfgang, J.M. Anderson, M.A. Grosenbaugh, D.K.P. Yue, M.S. Triantafyllou, Near-body flow dynamics in swimming fish, J. Exp. Biol. 202 (1999) 2303–2327.
[11] Q. Zhu, M.J. Wolfgang, D.K.P. Yue, M.S Triantafyllou, Three dimensional flow structures and vorticity control on fish-like swimming, J. Fluid Mech. 468 (2002) 1–28.
[12] J. Gray, Directional control of fish movement, Proc. R. Soc. Lond., Ser. B 113 (770) (1933) 115–125.
[13] P. Domenici, R.W. Blake, The kinematics and performance of fish fast-start swimming, J. Exp. Biol. 200 (1997) 1165–1178.
[14] P.W. Webb, Speed, acceleration and manoeuvrability of two teleost fish, J. Exp. Biol. 102 (1983) 115–122.
[15] D. Weihs, Hydrodynamic analysis of fish turning manoeuvres, Proc. R. Soc. 182 (1972) 59–72.
[16] J.M. Anderson, N.K. Chhabra, Maneuvering and stability performance of a robotic tuna, Integr. Comput. Biol. 42 (2002) 118–126.
[17] P.R. Bandyopadhyay, Maneuvering hydrodynamics of fish and small underwater vehicles, Integr. Comput. Biol. 42 (2002) 102–117.
[18] D. Weihs, Stability versus maneuverability, Integr. Comput. Biol. 42 (2002) 127–134.
[19] J. Katz, A. Plotkin, Low Speed Aerodynamics, 2nd edition, Cambridge University Press, 2001.
[20] J.Y. Cheng, T.J. Pedley, J.D. Altringham, A continuous dynamic beam model for swimming fish, Philos. Trans. R. Soc. Lond. B. 353 (1998) 981–997.

Available online at www.sciencedirect.com
ScienceDirect
Physica D 237 (2008) 2240–2246
PHYSICA D
www.elsevier.com/locate/physd

Acoustic streaming flows in a cavity: An illustration of small-scale inviscid flow

Josué Sznitman*, Thomas Rösgen

Institute of Fluid Dynamics, ETH Zurich, CH-8092 Zurich, Switzerland

Available online 5 December 2007

Abstract

Low Reynolds number flows are typically described by the equations of creeping motion, where viscous forces are dominant. We illustrate using particle image velocimetry (PIV) an example of small-scale boundary driven cavity flows, where forcing relies on viscous mechanisms at the boundary but resulting steady flow patterns are inviscid. Namely, we have investigated acoustic streaming flows inside an elastic spherical cavity. Here, the inviscid equations of fluid motion are not used as an approximation, but rather velocity fields independent of viscosity come as a result from the general solution of the creeping motion equations solved in the region interior to a sphere.

PACS: 47.15.G-; 47.15.km; 47.80.Jk; 47.63.mf

Keywords: Acoustic streaming; Particle image velocimetry; Low-Re; Creeping motion; Cavity flow

1. Introduction

Low Reynolds number flows characterize flow phenomena where fluid velocities are very slow, viscosities are high or alternatively length scales of the flow are very small (e.g. microfluidics [1]), such that inertial forces are small compared to viscous forces. For incompressible Newtonian fluids, in the limit of vanishing Reynolds numbers, where $Re = \rho UL/\mu \ll 1$ (U is a characteristic fluid speed, L a characteristic length scale; μ and ρ the fluid's dynamic viscosity and density, respectively), the equations of creeping motion reduce to [2]

$$\nabla p - \mu\nabla^2\underline{u} = 0, \tag{1}$$

$$\nabla \cdot \underline{u} = 0, \tag{2}$$

where inertial and transient terms may be neglected and the above equations describe, respectively, the conservation of momentum and mass (i.e. Stokes flow). Here, $\underline{u}$ is the velocity field and p the pressure. In three-dimensional (3D) flows, the component velocities, $\underline{u} = (u, v, w)^T$, may be related to a scalar stream function ψ [3,4]:

$$\underline{u} = \nabla\psi \times \underline{n} = \nabla \times \underline{\Psi}, \tag{3}$$

where $\underline{\Psi} = \psi\underline{n}$ is the stream function vector and $\underline{n}$ the unit normal vector perpendicular to the plane of $\nabla\psi$ and $\underline{u}$. For planar two-dimensional (2D) flows, Eq. (3) reduces effectively to a single stream function ψ where $u = \partial\psi/\partial y$ and $v = -\partial\psi/\partial x$. Under creeping motion, it is readily shown that $\underline{\Psi}$ satisfies the biharmonic equation [5]:

$$\nabla^4\underline{\Psi} = 0, \tag{4}$$

where $\nabla^4\underline{\Psi} = -\nabla^2\underline{\omega}$, and $\underline{\omega} = \nabla \times \underline{u} = -\nabla^2\underline{\Psi}$ defines the vorticity vector field. Neither the fourth-order differential equation for $\underline{\Psi}$ nor its boundary conditions, which govern the spatial distribution of $\underline{\Psi}$, contain Re such that streamlines are independent of viscosity μ [6].

Classic examples of such low Reynolds number flow phenomena are cavity flows which may illustrate slow internal recirculation induced by the translation of one or more of the containing walls [7,8], or driven by a shear flow over the cavity [9,10]. Here, we illustrate using flow visualization techniques (i.e. PIV), an original example of such low Reynolds number cavity flows, where forcing relies on viscous mechanisms at a solid–fluid interface, but resulting flow patterns are steady and inviscid. Namely, we have investigated acoustic streaming flows generated inside thin elastic spherical cavities. We demonstrate analytically that the resulting velocity fields are independent of viscosity as they may be captured by spherical harmonic functions which arise from the general

* Corresponding author.
E-mail address: sznitman@ifd.mavt.ethz.ch (J. Sznitman).

0167-2789/$ - see front matter
doi:10.1016/j.physd.2007.11.020

solution of the creeping motion Eqs. (1) and (2) in spherical coordinates.

2. Solution to creeping motion inside a sphere

Following Lamb [11] and Happel and Brenner [2], the general solution to Eqs. (1) and (2) in spherical coordinates (r, θ, ϕ) may be given in terms of the velocity field:

$$\underline{u} = \sum_{n=1}^{\infty} \left[\nabla \times (\underline{r}\chi_n) + \nabla \Phi_n + \frac{(n+3)\,|r|^2\,\nabla p_n - n\underline{r}\,p_n}{2\mu(n+1)(2n+3)} \right], \quad (5)$$

with the assumption of finite velocities at the origin $(r = 0)$, and where the scalar functions χ_n, Φ_n, and p_n are solid spherical harmonics defined as

$$\begin{aligned} \chi_n &= \frac{1}{n(n+1)} \left(\frac{r}{a}\right)^n Z_n^m(a, \theta, \phi), \\ \Phi_n &= \frac{a}{2n} \left(\frac{r}{a}\right)^n \left[(n+1) X_n^m(a, \theta, \phi) - Y_n^m(a, \theta, \phi) \right], \\ p_n &= \frac{\mu(2n+3)}{na} \left(\frac{r}{a}\right)^n \\ &\quad \times \left[Y_n^m(a, \theta, \phi) - (n-1) X_n^m(a, \theta, \phi) \right]. \end{aligned} \quad (6)$$

The above formulation makes use of the surface harmonics $Z_n^m(r, \theta, \phi)$, $Y_n^m(r, \theta, \phi)$, and $X_n^m(r, \theta, \phi)$ of degree m and order n. Each harmonic function takes the form $r^n P_n^m(\cos\theta)\, e^{im\phi}$, where $P_n^m()$ are the associated Legendre functions.

The unknown scalar functions χ_n, Φ_n, and p_n are determined by matching the appropriate velocity and vorticity boundary conditions at the surface of the sphere $(r = a)$. These conditions are described as follows:

$$\begin{aligned} u_n &= \frac{1}{|r|} \left(\underline{r} \cdot \underline{u}_s\right)\Big|_{r=a} = \sum_{n=1}^{\infty} X_n^m(a, \theta, \phi), \\ -|r| \left(\nabla \cdot \underline{u}_s\right)\Big|_{r=a} &= \sum_{n=1}^{\infty} Y_n^m(a, \theta, \phi), \\ |r|\,\underline{\omega}_n = \underline{r} \cdot \left(\nabla \times \underline{u}_s\right)\Big|_{r=a} &= \sum_{n=1}^{\infty} Z_n^m(a, \theta, \phi), \end{aligned} \quad (7)$$

where the velocity vector $\underline{u}_s(\theta, \phi)$ describes the surface velocity field at $r = a$ and ω_n is the vorticity component normal to the surface. For the problem at hand, one may use the fact that there is no normal velocity component, $u_n = 0$, at the surface of the sphere, such that

$$X_n^m(a, \theta, \phi) \equiv 0. \quad (8)$$

As a consequence, the full velocity field, $\underline{u}(r, \theta, \phi)$, in the region interior to the sphere can be described in terms of its surface normal vorticity, ω_n, and any contribution of source/sink distributions on the surface of the sphere resulting from $\nabla \cdot \underline{u}_s \neq 0$. By definition, $\underline{u}(r, \theta, \phi)$ is a solution of the biharmonic Eq. (4) and furthermore, it follows from Eqs. (5) and (6) that $\underline{u}(r, \theta, \phi)$ is independent of viscosity μ.

3. Acoustic streaming inside a thin elastic cavity

The propagation of sound waves in a fluid may lead to a bulk non-periodic motion of the fluid. This nonlinear phenomenon is called acoustic streaming [12] and is directly related to the quadratic convective terms of the flow field. We have investigated acoustic streaming flows generated at a solid–fluid interface by a sound wave of angular frequency ω. Experimental measurements of the resulting flow fields are based on particle image velocimetry (PIV) conducted inside millimeter-sized thin elastic spherical cavities of characteristic diameter $D = 2a$. The streaming phenomenon relies on a thin viscous boundary layer (Stokes layer) of thickness $\delta = (2\mu/\rho\omega)^{1/2}$ at the solid wall, where the no-slip boundary condition applies, while a steady-state solution independent of viscosity μ arises in the bulk of the flow away from the wall $(\delta \ll D)$. Conceptually, outside the boundary layer δ, the driving force behind acoustic streaming is absorbed into the background hydrostatic pressure p in the momentum Eq. (1) [13].

3.1. Experimental methods

The experimental apparatus consists of a test cell allowing for optical access, enclosing a thin silicone elastomer film (50 μm thickness, $\rho = 1260$ kg/m^3), a loudspeaker and an imaging system (Fig. 1). The bottom of the test cell is connected to a graduated syringe such that spherical cavities may be inflated by injecting air which distends the silicone membrane. Typical cavities are generated at a 6 mm circular orifice opening, by inflating ∼1.5–2 ml of air, resulting in a spherical cap with a characteristic diameter of $D \sim 6.5$–7 mm.

Depending on the excitation frequency, $f = \omega/2\pi$, acoustic waves are generated using a piezoelectric loudspeaker (3–20 kHz) or an electrostatic transducer (20–50 kHz) mounted onto one of the test cell faces and connected to a signal generator which delivers a sinusoidal electrical waveform. The imaging system consists of a progressive scan CCD camera with 15 Hz image acquisition rate and a resolution of 1008 × 1008 pixels triggered under computer control. The CCD camera is fitted onto a microscope with a field of view of about 7 × 7 mm, resulting in a spatial resolution of ∼6.9 μm. The laser sheet is generated by a 150 mW diode laser making use of a light sheet optic. Due to the lighting and flow conditions (driven flows are typically ≪1 mm/s for the acoustic output power range), a pulsed illumination is not required. Rather, consecutive images with an exposure time of 1/15 s are recorded in a horizontal plane cutting through the inflated membrane at approximately maximum diameter. Since the elastomer film is not perfectly transparent, scattering effects of the light sheet may be observed close to the wall, perhaps compromising slightly PIV results in close proximity to the membrane, while the bulk of the measurement plane remains unaffected.

The syringe barrel is filled with air, seeded with oil droplets. 2D vector displacements are obtained with a custom PIV algorithm based on cross-correlation pattern matching with sub-pixel interpolation [14]. Typical measurements consist in the acquisition of 100 consecutive frames and velocity vectors obtained from independent image pairs are then time averaged following an average correlation method [17].

3.2. Flow fields

For the range of frequencies investigated, several steady streaming flows were observed (Fig. 2), with $U \ll 1$ mm/s

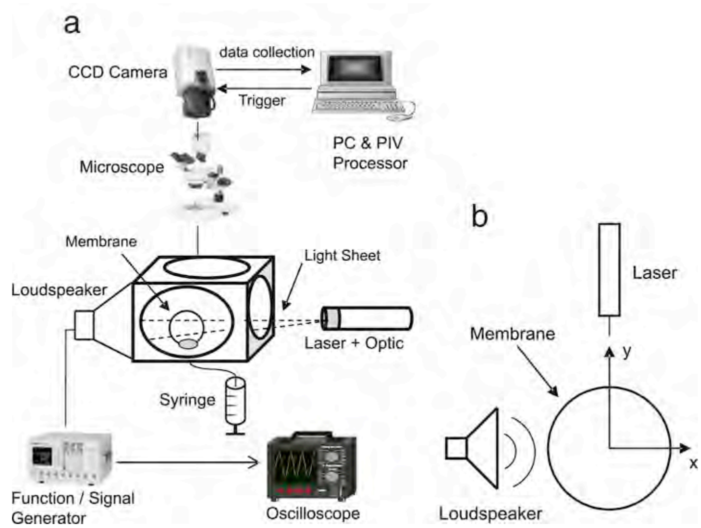

Fig. 1. (a) Schematic of the experimental apparatus. (b) Top view of the measurement plane.

resulting in $Re \approx O(0.01–0.1)$. Streaming flows may be categorized using the dimensionless parameter $M = D/2(\omega/\nu)^{1/2} \gg 1$ [15], where ν is the kinematic viscosity. M may be interpreted as the ratio of a body length scale to a viscous length scale. For the cavity sizes and frequencies investigated, $M \approx 120–450$ and the resulting flows are reproducible.

Generally, we observed a small degree of asymmetry in several streaming flows generated. We suspect this may result from the fact that the inflated elastic membranes are not perfectly axisymmetric in nature. Indeed, this may be a consequence of local differences in the tension present in the membrane wall when inflated at the orifice opening. Furthermore, in contrast to the solutions for the creeping motion Eqs. (5)–(7), which are valid for the region interior to an ideal sphere, the present cavities are, rather, truncated spheres (i.e. spherical caps) illustrating at best axisymmetry along the out-of-plane z-axis only. Therefore, we expect resulting flow patterns to be influenced by such geometrical differences.

The simplest flow perhaps observed in the measurement plane was encountered at $M = 454$ (Fig. 2, bottom row), resembling the structure of a simple vortex flow (i.e. 2D potential flow theory). To reconstruct analytically the 2D flow measured in the plane from a 3D creeping flow solution in the region interior to the sphere, we may consider the single surface harmonic $Z_1^0(a, \theta, \phi)$. This boundary condition is equivalent to applying in Eq. (7) a vorticity field, $\omega_n = \Omega \cos\theta \underline{e}_r$, on the surface of the sphere, where Ω is a constant and a radius of unity is chosen ($a = 1$). Solving Eq. (5) in cartesian coordinates yields a velocity field, $\underline{u}$, of the form

$$\begin{bmatrix} u \\ v \\ w \end{bmatrix} = K r \sin\theta \begin{bmatrix} -\sin\phi \\ \cos\phi \\ 0 \end{bmatrix} = K \begin{bmatrix} -y \\ x \\ 0 \end{bmatrix}, \tag{9}$$

where K is a constant. Physically, this 3D flow is analogous to a "solid body rotation" of the sphere where the velocity distribution is independent of z and holds directly in the equatorial x–y plane ($z = 0$). The analytical flow field (Fig. 3) bears a striking resemblance to the experimental measurement.

At $M = 120$, the resulting streaming flow in the equatorial plane resembles qualitatively a spiraling counterclockwise vortex flow with a source located approximately at the origin (Fig. 2, top row). Analytically, the flow inside the cavity may be constructed by superimposing a "solid body rotation", $Z_1^0(a, \theta, \phi)$, as described in Eq. (9), with a surface harmonic $Y_1^0(a, \theta, \phi)$. This latter boundary condition is equivalent to imposing a surface velocity, $\underline{u}_s = U_0 \sin\theta \underline{e}_\theta$, from Eq. (7), where U_0 is a constant. The resulting 3D velocity field is found from Eqs. (5) and (6) and takes the form

$$\begin{bmatrix} u \\ v \\ w \end{bmatrix} = U_0 \begin{bmatrix} xz \\ yz \\ 1 - 2(x^2 + y^2) - z^2 \end{bmatrix} + K \begin{bmatrix} -y \\ x \\ 0 \end{bmatrix}, \tag{10}$$

in cartesian coordinates. Note that in the equatorial plane ($z = 0$), $u = v = 0$ and only an out-of-plane w velocity component persists. However, since the elastic cavity is a spherical cap, as mentioned earlier, and thus not entirely axisymmetric, we evaluate $\underline{u}$ at a small finite value $z = \epsilon$, slightly off the symmetrical plane. The resulting analytical velocity field, $\underline{u}$ Eq. (10), captures qualitatively well the planar experimental measurement at $M = 120$, with $K/U_0 = 0.01$ (Fig. 4).

At $M = 178$, the planar flow is approximately axisymmetric (Fig. 2, second row) and consists qualitatively of two distinct regions: (i) a thin annular shaped region near the membrane wall, separated from (ii) a central circular region with a radially oriented flow. Fluid flows in the plane towards the discernible ring, originating both from the center of the cavity where it moves radially outwards, and from the outer wall where it flows inwards. Analytically, the 3D flow inside the cavity may be constructed by considering the surface harmonic $Y_2^0(a, \theta, \phi)$, which is equivalent to imposing a surface velocity, $\underline{u}_s = U_0 \cos\theta \sin\theta \underline{e}_\theta$, in Eq. (7). To capture the slight rotational motion observed in the experimental planar flow field, we superimpose again $Z_1^0(a, \theta, \phi)$ Eq. (9). The resulting

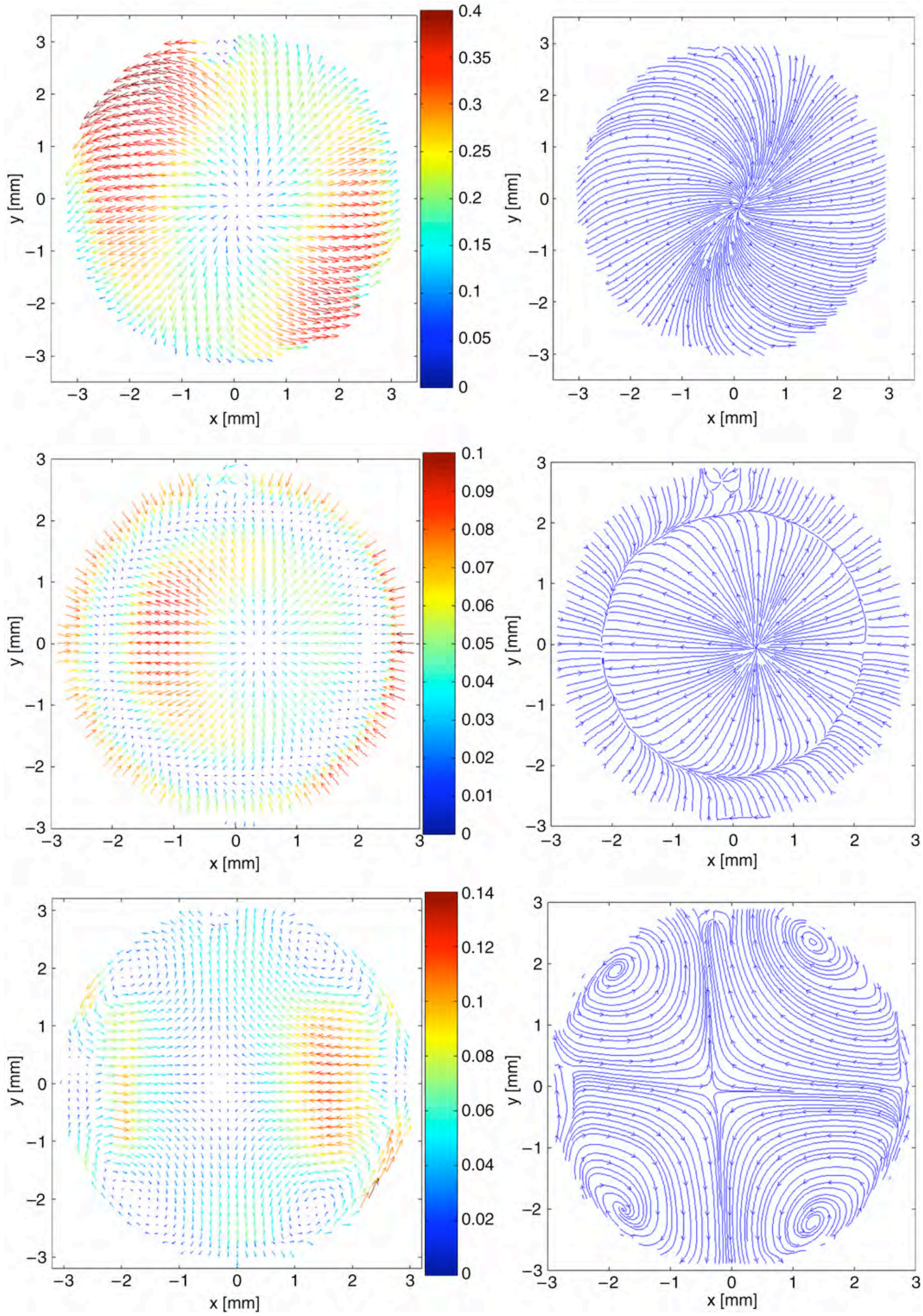

Fig. 2. Acoustic streaming flows inside the elastic cavity. Left column: Time averaged PIV (scale in mm/s). Right column: Reconstructed streamlines. From top to bottom: $M = 134$, 180, 306, 405, and 454.

3D velocity field is solved in cartesian coordinates from Eqs. (5) and (6):

$$\begin{bmatrix} u \\ v \\ w \end{bmatrix} = U_0 \begin{bmatrix} -x(x^2+y^2+3z^2-1)/4 \\ y(x^2+y^2+3z^2-1)/4 \\ z(2x^2+2y^2+z^2-1)/2 \end{bmatrix} + K \begin{bmatrix} -y \\ x \\ 0 \end{bmatrix}. \quad (11)$$

Here, we evaluate again $\underline{u}$ at $z = \epsilon$. The resulting analytical velocity field, $\underline{u}$ Eq. (11), resembles closely the planar flow at $M = 178$, with $K/U_0 = -0.05$ (Fig. 5).

At $M = 306$, the streamsurfaces form a nested family of tori and a circle of elliptic fixed (stagnation) points lies at the center of each of the four vortices (Fig. 2, third row).

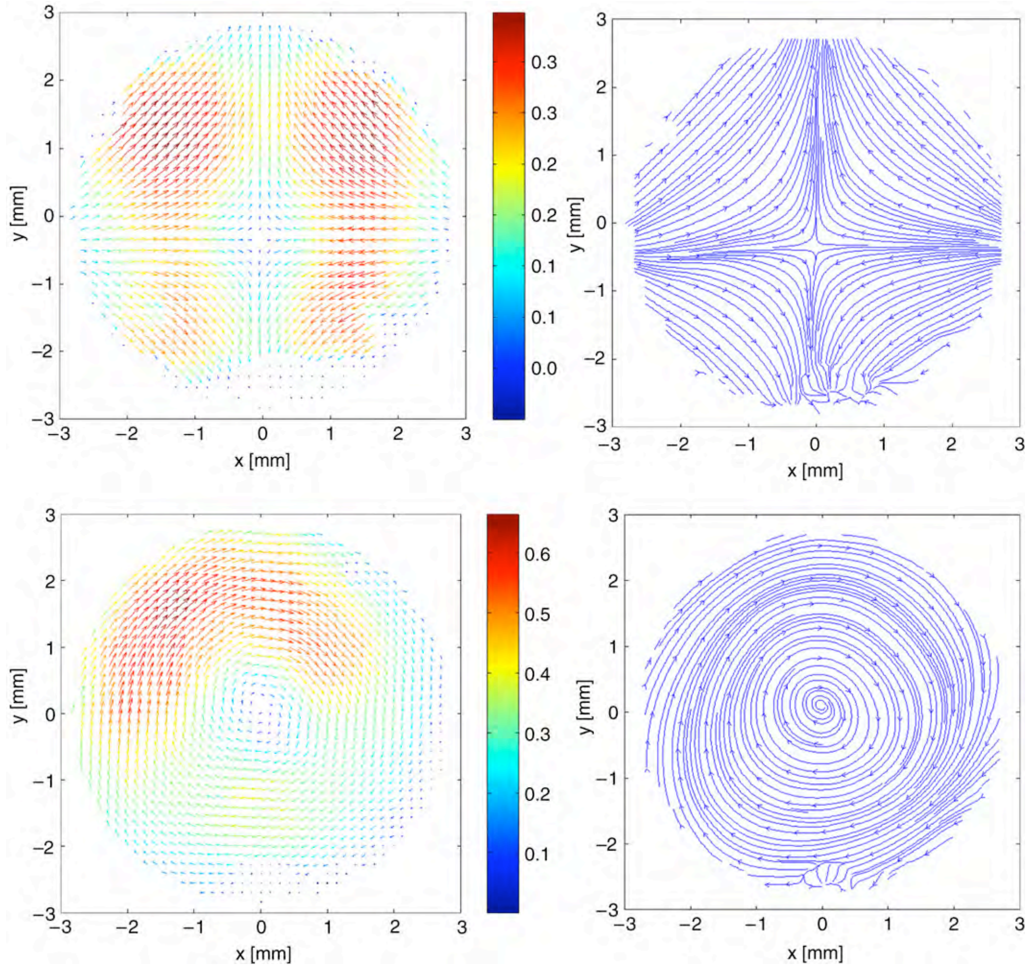

Fig. 2. (*continued*)

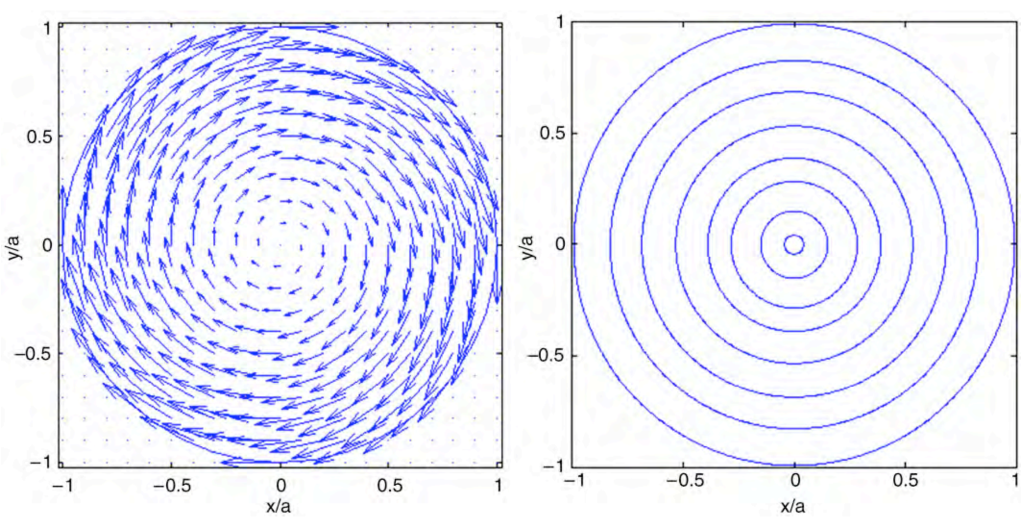

Fig. 3. Velocity field (left) and reconstructed streamlines (right) at $z = 0$ ($K = -1$) obtained from Eq. (9).

For this characteristic streaming flow, the streamline patterns resemble closely internal circulation flows described for a levitated drop in an acoustic field [15] or similarly for an immersed drop in Stokes flow [16]. The measured planar flow may be reconstructed by considering the boundary condition $\nabla \cdot \underline{u}_s = Y_2^2(a, \theta, \phi) = \sin^2\theta(2\cos^2\phi - 1)$ in Eq. (7). This

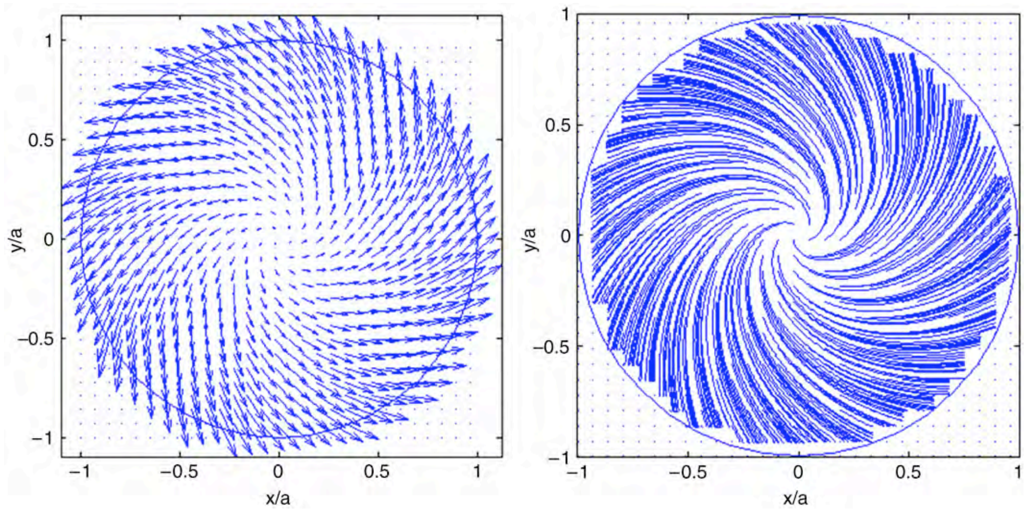

Fig. 4. Velocity field (left) and reconstructed streamlines (right) at $z = 0.01$ ($K/U_0 = 0.01$) obtained from Eq. (10).

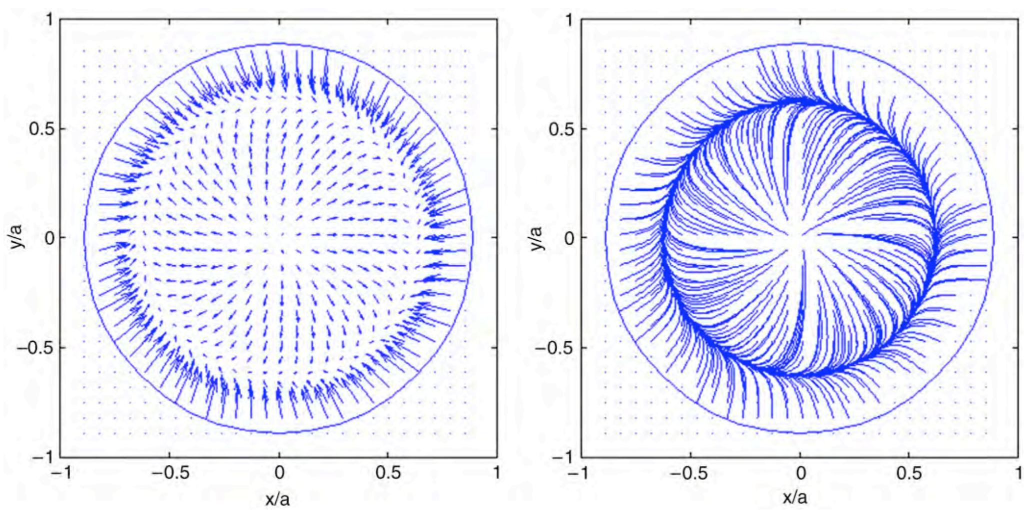

Fig. 5. Velocity field (left) and reconstructed streamlines (right) at $z = 0.4$ ($K/U_0 = -0.05$) obtained from Eq. (11).

leads to the 3D velocity field:

$$\begin{bmatrix} u \\ v \\ w \end{bmatrix} = U_0 \begin{bmatrix} x(3x^2 + 7y^2 + 5z^2 - 3)/2 \\ -y(7x^2 + 3y^2 + 5z^2 - 3)/2 \\ -z(x - y)(x + y) \end{bmatrix}. \tag{12}$$

Evaluated at the equatorial plane ($z = 0$), the resulting analytical planar flow, $\underline{u}(x, y)$, captures closely the experimental flow pattern (Fig. 6).

Finally at $M = 405$, the four vortices have now disappeared, giving place to open streamlines in each quadrant of the plane (Fig. 2, fourth row). The stagnation (saddle) point at $r = 0$ is preserved and the poles remain saddle fixed points. This planar flow may be captured by imposing the boundary condition $\omega_n = Z_2^2(a, \theta, \phi) = \sin^2\theta(2\cos^2\phi - 1)\underline{e}_r$ in Eq. (7). Solving Eqs. (5) and (6) leads to the 3D velocity field

$$\begin{bmatrix} u \\ v \\ w \end{bmatrix} = K \begin{bmatrix} -zy \\ -zx \\ 2xy \end{bmatrix}. \tag{13}$$

Note again that $u = v = 0$ in the equatorial plane ($z = 0$), where only w persists. Hence, $\underline{u}$ is evaluated at $z = \epsilon$, slightly off the equatorial plane. The resulting analytical flow field (Fig. 7) resembles closely the experimental measurement, although here the orientation of the flow in the plane is slightly altered with respect to Fig. 2 (fourth row). This difference may perhaps result from the arbitrary location of the acoustic source (i.e. loudspeaker/transducer) relative to the cavity.

4. Conclusions

We have illustrated, using PIV, an original example of low Re boundary driven cavity flows: acoustic streaming inside elastic spherical cavities. The generation of such flows relies on viscous mechanisms at the solid–fluid boundary; in the bulk of the fluid, however, velocity fields are steady and independent of viscosity. Analytically, the measured planar flows may be captured from the general solution of the creeping motion equations inside a sphere. Inviscid 3D flow patterns are constructed from the superposition of surface harmonics, defining

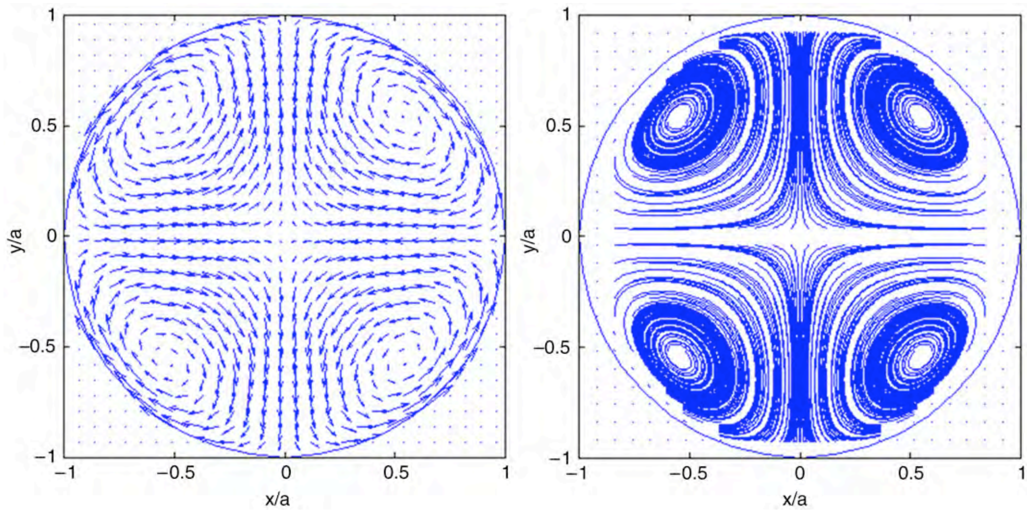

Fig. 6. Velocity field (left) and reconstructed streamlines (right) at $z = 0$ ($U_0 = 1$) obtained from Eq. (12).

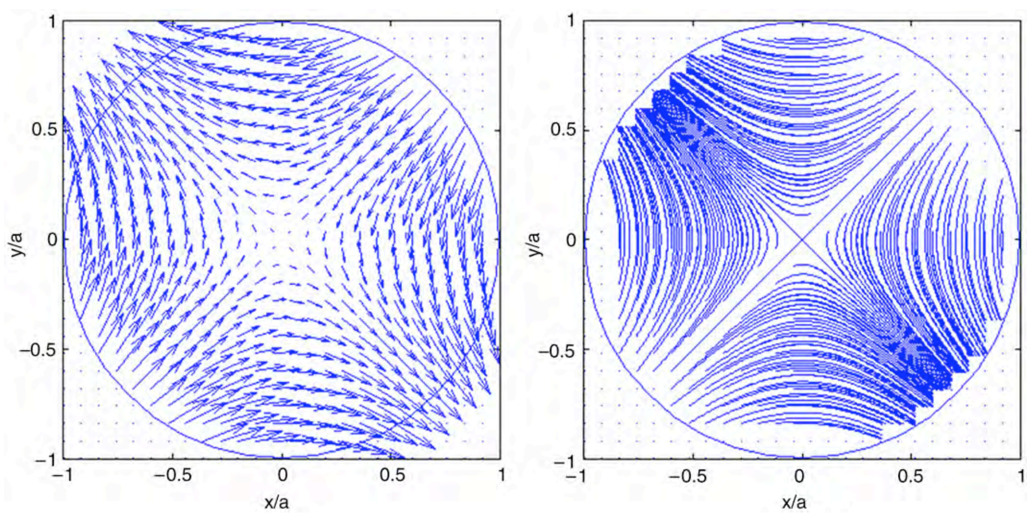

Fig. 7. Velocity field (left) and reconstructed streamlines (right) at $z = 0.01$ ($K = 1$) obtained from Eq. (13).

the flow boundary conditions on the surface of the sphere. The inviscid equations of fluid motion are not used as an approximation here, but rather inviscid flow fields come as a result.

Acknowledgments

The authors thank T.H. Ho (Imperial College, UK) as well as R. Holliger and P. Stachel (ETH Zurich).

References

[1] P. Tabeling, Introduction to Microfluidics, Oxford University Press, 2006.
[2] J.H. Happel, H. Brenner, Low Reynolds Number Hydrodynamics, Kluwer, 1983.
[3] T.J. Chung, Applied Continuum Mechanics, Cambridge University Press, 1996.
[4] A.M. Elshakba, T.J. Chung, Numerical solution of three-dimensional stream function vector components of vorticity transport equations, Comput. Methods Appl. Mech. Engrg. 170 (1999) 131–153.
[5] R.L. Panton, Incompressible Flow, Wiley & Sons, 1996.
[6] F.S. Sherman, Viscous Flow, McGraw-Hill, 1990.
[7] F. Pan, A. Acrivos, Steady flows in rectangular cavities, J. Fluid Mech. 28 (1967) 634–655.
[8] C.W. Leong, J.M. Ottino, Experiments on mixing due to chaotic advection in a cavity, J. Fluid Mech. 209 (1989) 463–499.
[9] C. Shen, J.M. Floryan, Low Reynolds number flow over cavities, Phys. Fluids 28 (1985) 3191–3202.
[10] J.J.L. Higdon, Stokes flow in arbitrary two-dimensional domains: Shear flow over ridges and cavities, J. Fluid Mech. 158 (1985) 195–226.
[11] H. Lamb, Hydrodynamics, 6th ed., Dover Publications, 1993.
[12] J. Lighthill, Acoustic streaming, J. Sound Vibration 61 (1978) 391–418.
[13] C.P. Lee, T.G. Wang, Outer acoustic streaming, J. Acoust. Soc. Am. 88 (1990) 2367–2375.
[14] T. Rösgen, Optimal subpixel interpolation in particle image velocimetry, Exp. Fluids 35 (2003) 252–256.
[15] H. Zhao, S.S. Sadhal, E.H. Trinh, Internal circulation in a drop in an acoustic field, J. Acoust. Soc. Am. 106 (1999) 3289–3295.
[16] H.A. Stone, A. Nadim, S.H. Strogatz, Chaotic streamlines inside drops immersed in steady Stokes flow, J. Fluid Mech. 232 (1991) 629–646.
[17] C.D. Meinhart, S.T. Wereley, J.G. Santiago, A PIV algorithm for estimating time-averaged velocity fields, J. Fluids Eng. 122 (2000) 285–289.

Available online at www.sciencedirect.com
ScienceDirect
Physica D 237 (2008) 2247–2250
PHYSICA D
www.elsevier.com/locate/physd

Index of authors and papers to this issue

doi:10.1016/S0167-2789(08)00247-9